



AFRL-RZ-WP-TR-2011-2028

**VERSATILE AFFORDABLE ADVANCED FUELS AND
COMBUSTION TECHNOLOGIES**

S. Zabarnick, D.R. Ballal, J.S. Ervin, A. Briones, J.L. Graham, M.J. DeWitt, R. Adams, Z.J. West, S.D. Stouffer, P.H. Taylor, L.M. Shafer, T.F. Williams, E.A. Guliants, R. Striebich, and L.M. Balster

University of Dayton Research Institute

**NOVEMBER 2010
Final Report**

Approved for public release; distribution unlimited.

See additional restrictions described on inside pages

**AIR FORCE RESEARCH LABORATORY
PROPULSION DIRECTORATE
WRIGHT-PATTERSON AIR FORCE BASE, OH 45433-7251
AIR FORCE MATERIEL COMMAND
UNITED STATES AIR FORCE**

NOTICE AND SIGNATURE PAGE

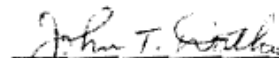
Using Government drawings, specifications, or other data included in this document for any purpose other than Government procurement does not in any way obligate the U.S. Government. The fact that the Government formulated or supplied the drawings, specifications, or other data does not license the holder or any other person or corporation; or convey any rights or permission to manufacture, use, or sell any patented invention that may relate to them.

This report was cleared for public release by the Wright-Patterson Public Affairs Office and is available to the general public, including foreign nationals. Copies may be obtained from the Defense Technical Information Center (DTIC) (<http://www.dtic.mil>).

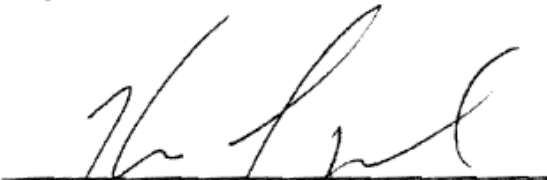
AFRL-RZ-WP-TR-2011-2028 HAS BEEN REVIEWED AND IS APPROVED FOR PUBLICATION IN ACCORDANCE WITH ASSIGNED DISTRIBUTION STATEMENT.



ROBERT W. MORRIS, JR.
Contract Monitor, Fuels and Energy Branch
Energy/ Power/ Thermal Division
Propulsion Directorate



JOHN DATKO
Acting Chief, Fuels and Energy Branch
Energy/ Power/ Thermal Division
Propulsion Directorate



KIRK L. YERKES, PhD
Deputy for Science
Energy/ Power/ Thermal Division
Propulsion Directorate

This report is published in the interest of scientific and technical information exchange, and its publication does not constitute the Government's approval or disapproval of its ideas or findings.

*Disseminated copies will show “//signature//” stamped or typed above the signature blocks.

REPORT DOCUMENTATION PAGE

Form Approved
OMB No. 0704-0188

The public reporting burden for this collection of information is estimated to average 1 hour per response, including the time for reviewing instructions, searching existing data sources, gathering and maintaining the data needed, and completing and reviewing the collection of information. Send comments regarding this burden estimate or any other aspect of this collection of information, including suggestions for reducing this burden, to Department of Defense, Washington Headquarters Services, Directorate for Information Operations and Reports (0704-0188), 1215 Jefferson Davis Highway, Suite 1204, Arlington, VA 22202-4302. Respondents should be aware that notwithstanding any other provision of law, no person shall be subject to any penalty for failing to comply with a collection of information if it does not display a currently valid OMB control number. **PLEASE DO NOT RETURN YOUR FORM TO THE ABOVE ADDRESS.**

1. REPORT DATE (DD-MM-YY) November 2010		2. REPORT TYPE Final		3. DATES COVERED (From - To) 14 April 2003 – 30 September 2010	
4. TITLE AND SUBTITLE VERSATILE AFFORDABLE ADVANCED FUELS AND COMBUSTION TECHNOLOGIES				5a. CONTRACT NUMBER F33615-03-2-2347	
				5b. GRANT NUMBER	
				5c. PROGRAM ELEMENT NUMBER 0602203F	
6. AUTHOR(S) S. Zabarnick, D.R. Ballal, J.S. Ervin, A. Briones, J.L. Graham, M.J. DeWitt, R. Adams, Z.J. West, S.D. Stouffer, P.H. Taylor, L.M. Shafer, T.F. Williams, E.A. Guliants, R. Striebich, and L.M. Balster				5d. PROJECT NUMBER 3048	
				5e. TASK NUMBER 04	
				5f. WORK UNIT NUMBER 304804AK	
7. PERFORMING ORGANIZATION NAME(S) AND ADDRESS(ES) University of Dayton Research Institute 300 College Park Dayton, OH 45469				8. PERFORMING ORGANIZATION REPORT NUMBER	
9. SPONSORING/MONITORING AGENCY NAME(S) AND ADDRESS(ES) Air Force Research Laboratory Propulsion Directorate Wright-Patterson Air Force Base, OH 45433-7251 Air Force Materiel Command United States Air Force				10. SPONSORING/MONITORING AGENCY ACRONYM(S) AFRL/RZPF	
				11. SPONSORING/MONITORING AGENCY REPORT NUMBER(S) AFRL-RZ-WP-TR-2011-2028	
12. DISTRIBUTION/AVAILABILITY STATEMENT Approved for public release; distribution unlimited.					
13. SUPPLEMENTARY NOTES Report contains color.					
14. ABSTRACT <p>This report is a compilation of highlights of research accomplishments completed under Cooperative Agreement No. F33615-03-2-2347, "Versatile Affordable Advanced Fuels and Combustion Technologies," with the Air Force Research Laboratory, Propulsion Directorate, Turbine Engine and Energy/Power/Thermal Divisions. This report covers work performed during the period April 14, 2003 to September 30, 2010. Research efforts covered a wide range of topics toward development of advanced fuels and combustion systems. These efforts included analysis, analytical measurement, and diagnostics technologies for fuels, additives, and combustion processes; advanced/alternate fuels development, evaluation, demonstration, and management; advanced, affordable fuel/combustion additive technologies; materials compatibility; modeling and simulation; technology integration and demonstration for thermal management and fuel system operability, supportability, and maintainability.</p>					
15. SUBJECT TERMS Jet fuel, JP-8+100, JP-8+100LT, alternative fuels, fuel additives, low temperature flowability, thermal stability, particulates, combustion, turbine engines, high heat sink fuels, combustion emissions					
16. SECURITY CLASSIFICATION OF:			17. LIMITATION OF ABSTRACT: SAR	18. NUMBER OF PAGES 446	19a. NAME OF RESPONSIBLE PERSON (Monitor) Robert W. Morris, Jr.
a. REPORT Unclassified	b. ABSTRACT Unclassified	c. THIS PAGE Unclassified			

Standard Form 298 (Rev. 8-98)
Prescribed by ANSI Std. Z39-18

INTENTIONALLY LEFT BLANK

Table of Contents

<u>Section</u>	<u>Page</u>
List of Figures	vii
1.0 Summary	1
2.0 Introduction.....	3
3.0 Highlights of Research Studies.....	5
3.1 Analysis, Analytical Measurement, and Diagnostics Technologies for Fuels, Additives, and Combustion Processes	5
3.2 Advanced/Alternate Fuels Development, Evaluation, Demonstration, and Management....	9
3.3 Advanced, Affordable Fuel/Combustion Additive Technologies	16
3.4 Materials Compatibility.....	22
3.5 Modeling and Simulation.....	28
3.6 Technology Integration and Demonstration for Thermal Management and Fuel System Operability, Supportability, and Maintainability.....	32
4.0 References.....	39
Appendix A. A Statistical Approach to Estimating the Compatibility of Alternative Fuel	47
Appendix B. Effects of a Reacting Cross Stream on Turbine Film Cooling	63
Appendix C. Community Dynamics and Phylogenetics of Bacteria Fouling Jet A and JP-8 Aviation Fuel	73
Appendix D. Emissions Characteristics of Military Helicopter Engines with JP-8 and Fischer-Tropsch Fuels.....	85
Appendix E Compatibility of DiEGME and TriEGME Fuel System Icing Inhibitor Additives with BMS 10-39 Aircraft Tank Topcoat Material.....	95
Appendix F. Flame Stabilization in Small Cavities.....	111
Appendix G. Soot Studies of Laminar Diffusion Flames with Recirculation Zones	125
Appendix H. Identification of Polar Species in Aviation Fuels using Multidimensional Gas Chromatography-Time of Flight Mass Spectrometry.....	135
Appendix I. Sonochemically Assisted Thermal Decomposition of Alane <i>N,N</i> - Dimethylethylamine with Titanium (IV) Isopropoxide in the Presence of Oleic Acid to Yield Air-Stable and Size-Selective Aluminum Core-Shell Nanoparticles	147
Appendix J. Spontaneous Hydrogen Generation from Organic-Capped Al Nanoparticles and Water.....	153

Table of Contents (continued)

<u>Section</u>		<u>Page</u>
Appendix K.	Effects of Aromatic Type and Concentration in Fischer-Tropsch Fuel on Emissions Production and Material Compatibility	159
Appendix L.	Characterization of Particulate Matter and Gaseous Emissions of a C-130H Aircraft	169
Appendix M.	Combustion Performance and Emissions Characteristics for a Well-Stirred Reactor for Low Volatility Hydrocarbon Fuels	181
Appendix N.	Use of Measured Species Class Concentrations with Chemical Kinetic Modeling for the Prediction of Autoxidation and Deposition of Jet Fuels	195
Appendix O.	A Laboratory Assessment of the Compatibility of Fischer-Tropsch Derived (ISO Paraffinic Kerosene) and Blended FT-Petroleum-Derived Fuels with Non-Metallic Materials	213
Appendix P.	Formation of Protein-Metal Oxide Nanostructures by the Sono-chemical Method: Observation of Nanofibers and Nanoneedles	235
Appendix Q.	Emissions Characteristics of a Turbine Engine and Research Combustor Burning a Fischer-Tropsch Jet Fuel	243
Appendix R.	Density Functional Theory Calculations of the Energetics and Kinetics of Jet Fuel Autoxidation Reactions	257
Appendix S.	Swelling of Nitrile Rubber by Selected Aromatics Blended in a Synthetic Jet Fuel	269
Appendix T.	Pressure Effects on Flowing Mildly-Cracked n-Decane	279
Appendix U.	Soot Reduction Research Using a Well-Stirred Reactor	293
Appendix V.	Determination of Hydroperoxides in Jet Fuel via Reaction with Triphenylphosphine	309
Appendix W.	Estimation of Selected Specification Tests for Aviation Turbine Fuels Using Fast Gas Chromatography (GC)	319
Appendix X.	Computational Model of the Freezing of Jet Fuel	331
Appendix Y.	Simulations of Flow Mildly-Cracked Normal Alkanes Incorporating Proportional Product Distributions	345
Appendix Z.	Simulation of the Effect of Metal-Surface Catalysis on the Thermal Oxidation of Jet Fuel	358
Appendix AA.	Evaluation of Soot Particulate Mitigation Additives in a T63 Engine	373
Appendix BB.	Modeling Soot Formation in a Stirred Reactor	391

Table of Contents (continued)

<u>Section</u>	<u>Page</u>
Appendix CC. Modeling the Liquid-Phase Oxidation of Hydrocarbons over a Range of Temperatures and Dissolved Oxygen Concentrations with Pseudo-Detailed Chemical Kinetics	399
Appendix DD. List of UDRI Publications, Patents, Presentations, Honors and Awards Obtained during the Contract Period	409
LIST OF ACRONYMS, ABBREVIATION, AND SYMBOLS	445

INTENTIONALLY LEFT BLANK

List of Figures

<u>Figure</u>	<u>Page</u>
1. U-2 Simulator Isometric Drawing with Images of Actual Components.....	18
2. Low-flow Thermodenuder	31
3. Dilution Chamber Computational Domain, Engineering Design, and Final Product.....	31

INTENTIONALLY LEFT BLANK

PREFACE

This final report was submitted by the University of Dayton Research Institute (UDRI) under Cooperative Agreement No. F33615-03-2-2347, sponsored by the U.S. Air Force Research Laboratory, Propulsion Directorate, Wright-Patterson AFB, OH. Mr. Robert W. Morris, Jr. of AFRL/RZPF was the Contract Monitor and Dr. Dilip R. Ballal of the Energy & Environmental Engineering Division of UDRI, was the Principal Investigator. This report covers work performed during the period April 14, 2003 to September 30, 2010.

The authors would like to acknowledge the support and encouragement of Mr. Bill Harrison, Dr. Tim Edwards, Mr. Bob Morris, Mr. Edwin Corporan of the AFRL Fuels Branch; Dr. Rick Fingers of the AFRL Energy/Power/Thermal Division; Mr. Bill Koop of the AFRL Turbine Engine Division; and Dr. Mel Roquemore, Dr. Robert Hancock, and Dr. Joe Zelina of the AFRL Combustion Branch.

This material is based on research sponsored by Air Force Research Laboratory under agreement numbers F33615-03-2-2347. The U.S. Government is authorized to reproduce and distribute reprints for Governmental purposes notwithstanding any copyright notation thereon. The views and conclusions contained herein are those of the authors and should not be interpreted as necessarily representing the official policies or endorsements, either expressed or implied, of Air Force Research Laboratory or the U.S. Government.

INTENTIONALLY LEFT BLANK

1.0 EXECUTIVE SUMMARY

This report is a compilation of highlights of research accomplishments completed under Cooperative Agreement No. F33615-03-2-2347, "Versatile Affordable Advanced Fuels and Combustion Technologies," with the Air Force Research Laboratory, Propulsion Directorate, Turbine Engine and Energy/Power/Thermal Divisions. This report covers work performed during the period April 14, 2003 to September 30, 2010. Research efforts covered a wide range of topics toward development of advanced fuels and combustion systems. These efforts included Analysis, Analytical Measurement, and Diagnostics Technologies for Fuels, Additives, and Combustion Processes; Advanced/Alternate Fuels Development, Evaluation, Demonstration, and Management; Advanced, Affordable Fuel/Combustion Additive Technologies; Materials Compatibility; Modeling and Simulation; Technology Integration and Demonstration for Thermal Management and Fuel System Operability, Supportability, and Maintainability.

INTENTIONALLY LEFT BLANK

2.0 INTRODUCTION

The University of Dayton is pleased to submit this final report to the Air Force Research Laboratory, Propulsion Directorate (AFRL/RZ) under Cooperative Agreement No. F33615-03-2-2347, "Versatile Affordable Advanced Fuels and Combustion Technologies." The goal of this program was to investigate and evaluate advanced fuels and fuel technologies, fuel system component development, advanced combustor designs, advanced fuel properties measurement, fuel system component development and safety, combustion emissions, and their integration into advanced aerospace applications. Another goal was to extend the technology base for development, validation, and fielding of high heat sink fuels, low-temperature fuels, fuel-additive material compatibility, additive injection techniques, and reduced emissions of gaseous and particulate matter. Additional objectives were to establish an experimental database needed to validate and refine computer models for designing future fuels and fuel system components, develop in-field fuel diagnostics to qualify locally purchased fuels, identify and mitigate biological contaminants, determine combustion properties, and address fuel management and quality issues associated with both ground and flight fuel handling systems. Finally, these advanced technologies are to be integrated to demonstrate optimum thermal management and fuel system operability, supportability, and maintainability for use in 21st century aircraft and weapons systems. This program was comprised of six parts: (1) Analysis, Analytical Measurement, and Diagnostics Technologies for Fuels, Additives, and Combustion Processes; (2) Advanced/Alternate Fuels Development, Evaluation, Demonstration, and Management; (3) Advanced, Affordable Fuel/Combustion Additive Technologies; (4) Materials Compatibility; (5) Modeling and Simulation; (6) Technology Integration and Demonstration for Thermal Management and Fuel System Operability, Supportability, and Maintainability.

Here we highlight the research accomplishments during the program; provide a list of publications, presentations, honors, and awards; and provide copies of publications that show the most important research successes achieved during the research period.

INTENTIONALLY LEFT BLANK

3.0 HIGHLIGHTS OF RESEARCH STUDIES

3.1 Analysis, Analytical Measurement, and Diagnostics Technologies for Fuels, Additives, and Combustion Processes

3.1.1 HPLC Analysis of Fuel Polars

High performance liquid chromatography (HPLC) based techniques were used to investigate the role of polar species in deposit formation during jet fuel autoxidation and to explore the relative contributions of the various species classes which constitute the polar fraction (Balster et al., 2006). More specifically, HPLC with UV-visible absorption detection was employed to quantify the polar species in jet fuel as a class, and a technique which combines solid-phase extraction (SPE) with HPLC and gas chromatography with mass spectrometric detection (GC-MS) was used to identify the species classes which comprise the polar fraction in typical jet fuels. The analytical results were combined with surface deposit data obtained in a Quartz Crystal Microbalance (QCM) system for a series of twenty jet fuels. The results indicate a relationship between the total amount of polar species measured and the amount of surface deposits produced. Results also suggest that phenols, various other oxygenated polar species, indoles, and carbazoles have a significant positive correlation with jet fuel surface deposit formation, while pyridines, anilines, and quinolines do not demonstrate a strong correlation with the tendency of a fuel to form surface deposits.

3.1.2 Multi-Dimensional Gas Chromatography of Jet Fuel

Aviation fuel is so complex that it is virtually impossible to separate all of the major components of the mixture, much less the minor components. The minor components are typically separated from the major components using preparative techniques (such as solid phase extraction - SPE) and then re-examined by gas chromatography-mass spectrometry (GC-MS). Without SPE, GC-MS is not capable of a comprehensive determination of the trace polar components in jet fuel due to fuel complexity. In this contribution (Striebich et al., 2009a), jet fuel mixtures are pre-separated by normal-phase SPE, followed by a single analysis using multidimensional gas chromatography-time of flight mass spectrometry (MDGC-TOFMS), which is similar to the recently popularized technique of GCxGC. This two-column sequential analysis followed by TOFMS identifications is able to accurately identify more of the polar components of jet fuel. Automated data analysis routines, based on improved mass spectral library identifications (due to the better chromatographic separations), are able to determine individual components in the polar fractions that are of interest. Spreadsheet-based sorting of the highest quality identifications was also performed and used to quantify important polar fuel classes such as amines, indoles, pyridines, anilines, sulfur compounds, oxygenates, aromatics, and others. The relative amounts of each group were determined and related to similar measurements found in the literature. The ability to identify and quantify polar components in fuel may be useful in developing relationships between fuel composition and properties such as thermal stability.

3.1.3 Fast Gas Chromatography for Fuel Property Determination

The quality of aviation turbine fuels is measured largely by specification tests, which are routinely conducted for every large fuel supply purchased by the United States Air Force. Because military operations insist on more mobility than ever before, fuels are often purchased

locally where the military is located. To test the fuels being purchased from unfamiliar sources, the military is examining mobile laboratories. With modern instrumentation such as gas chromatography (GC) with microbore columns and multiple detectors, compositional data can be easily and quickly obtained and related directly to specification test properties. By investigating composition-property relationships, a single GC experiment can be used to estimate several properties. In this work (Striebich et al., 2005), the development and validation of specification test prediction using compositional data obtained via fast (<5 min) GC is presented. Simple correlations and relationships between properties and composition are suggested as possible ways to predict specification results without the expense and time required for testing. In this initial work, the properties investigated were simulated distillation, flash point, freeze point, and sulfur content. Results indicated that these tests could be reasonably predicted in minutes using correlations to fast GC data. Instrumentation developed for predicting specification tests was delivered to a field location and used to predict the specification results of locally purchased and captured fuels in wartime. These same fuels were also analyzed in regional laboratories, for validation of results.

3.1.4 Hydrocarbon Type Analysis

An analysis technique to classify the major components of aviation turbine fuels, rocket fuels and alternate fuels was investigated in this effort. This method was developed to classify the major constituents in most fuel: paraffins, cycloparaffins, dicycloparaffins, tricycloparaffins, alkylbenzenes, indans/tetralins, indenenes, naphthalene, alkylnaphthalenes, and selected aromatics. This group-type separation was tested, refined, and finally reported (Edwards et al., 2006b) for commercial fuels and specialty kerosene fuels. The method consists of an HPLC group type separation to measure and fractionate saturates and aromatic fuel constituents. GC-MS techniques are then used in conjunction with a modified ASTM D2425 procedure to obtain weight or volume percent levels for each of the above-mentioned categories of fuel compounds, according to mass spectral ions associated with each of the groups. The method was validated using model mixtures, and used to measure more than 60 JP-8, JP-5 and Jet A fuels from a recent world survey (Shafer, 2010). This laboratory is one of only three laboratories in the country performing this method, which is the only method currently approved for alternative fuels specification in hydrocarbon type analysis.

3.1.5 Fuel Hydroperoxide Determination via TPP Method

The development of an analytical method for quantification of thermally labile organic hydroperoxides in jet fuel via reaction with triphenylphosphine (TPP) was explored (West et al., 2005). The primary goal of this work is to devise a technique for hydroperoxide detection in jet fuel, for use in fuel oxidation studies, that will use only small sample volumes (<1 mL), have a low detection limit (<0.02 mM), have a broad dynamic range, and be fast, reproducible, and accurate. The reported technique uses the reaction of TPP with hydroperoxides to form triphenylphosphine oxide (TPPO) and the subsequent alcohol, which proceeds rapidly in jet fuel (less than 1 min) at ambient conditions. Elemental sulfur was used prior to analysis as a novel means to prevent the oxidation of TPP during chromatographic analysis by converting excess TPP into triphenylphosphine sulfide (TPPS) via another rapid, ambient condition reaction. Gas chromatographic (GC) analysis with flame ionization detection (FID) was used to quantify the

resulting TPPO and TPPS, and the relative TPPO peak area was observed to be proportional to the hydroperoxide concentration. The production of TPPO by an interfering reaction was observed; however, TPPO produced via this reaction occurred predominantly in thermally stressed fuels, when large amounts of excess TPP were used. By limiting the amount of excess TPP used during the analysis we were able to control this interfering source of TPPO. The accuracy of the reported TPP method compares favorably with ASTM D6447. Finally, we report that the resulting method requires a small sample volume (0.5 mL), has a very low detection limit (0.002 mM), has a wide dynamic range, and is accurate and reproducible.

3.1.6 Development of Analytical Techniques for Pilot Plant Fuel Production

Methods for the analysis of Fischer Tropsch generated waxes and products distilled from these waxes were developed and reported. Gas chromatographs with on-column injection, flame ionization detectors (FID) and high temperature metal columns were selected, evaluated and used to examine fuel distributions and processing success for high temperature wax material (from C7 to C73 hydrocarbons) being processed into jet fuel. In addition, distilled products from pilot plant wax processing were evaluated on similar GC-FID systems for hydrocarbon distribution and impurity analysis. Alcohol and other oxygenate formation was also monitored in the aqueous products from these same processes. Output from these analytical techniques is typically a spreadsheet listing hydrocarbon composition for each carbon number of material, specified as weight percent. These measurements allow the operators of the pilot plant to evaluate their processes and change conditions.

3.1.7 HPLC-MS (High Performance Liquid Chromatography-Mass Spectrometry) Analyses

HPLC-TOFMS (Time-of-Flight Mass Spectrometry) analysis techniques were developed during this effort. This project required a large effort to select the HPLC instrumentation appropriate for our laboratory. Samples were prepared and sent to multiple vendors as a part of a thorough evaluation process. The instrument selected, HPLC with a time of flight mass spectrometer, is important because it allows research to be conducted on fuel components which may be important in thermal stability issues. The analytes detected by this instrument are those which we have not been able to investigate before, due to the fact that they cannot be measured in more conventional gas chromatographic instrumentation. These components which may include metal complexes and high polarity compounds, may provide new insight to problems which have been investigated for decades. Publications from this relatively new research will be forthcoming in the new contractual research effort.

3.1.8 Core-Shell CdS Nanoparticles For Optochemical Sensing

This effort was focused on development of a prototype miniature fuel sensor based on optochemical sensing scheme (Gulians et al., 2004). Strong radiative transitions characteristic of direct band gap II-VI semiconductor compounds combined with quantum confinement effects inherent to particles on the nanoscale have secured a very vivid interest in studying the photophysics of CdS nanoparticles for the past two decades. Moreover, CdS nanoparticles exhibit very interesting photochemical and photophysical properties when foreign species adsorb

on the surface of the particles under irradiation. Interfacial reactions affect the transitions between energy levels and lead to changes in both absorption and luminescence kinetics. Respective shifts in the emission spectra offer an excellent mechanism for opto-chemical sensing. However, in order to utilize these nanoparticles in planar solid-state fiber-optic sensors, they have to be immobilized on solid surfaces while maintaining their unique optical properties. We studied and compared the emission spectra collected for thin films of CdS nanoparticles prepared in a number of ways and analyzed the photophysical changes in the emission mechanism. Spectral properties of CdS nanoparticles prepared by the reverse-micelle approach were studied in thin films coated on the surface of Si wafers. The nanoparticles synthesized in hexane were extracted from the solution and spin-cast into films using polymethylmethacrylate (PMMA) and tetraethyl orthosilicate (TEOS)-based sol-gel silica as matrix materials. The matrix material was observed to significantly influence the position of the photoluminescence (PL) peak in thin films containing CdS nanoparticles. The sensing mechanism was proposed.

3.1.9 Bio-Nano Composites and Structures

Currently, there is particular interest in the synthesis of nano-bio composite materials. Such compounds may find application as drug delivery agents, in pathogen detection and separation applications, and as hybrid electronic devices. Recent examples of such materials produced using other synthesis methods include the formation of Ag-BSA and CdS-BSA nanocomposites from supercritical fluid expansion, Au-BSA nanocomposites from chemical reduction, CdTe-BSA nanocomposites using L-cysteine as a linker, iron oxide-BSA nanocomposites using 3-aminopropyltrimethoxysilane as a linker, and Au nanoparticles bonded to double stranded DNA modified with thiol groups. These methods can be described as either direct or indirect, with indirect involving the use of a linker molecule. Indirect methods potentially suffer from increased molecular size, less access to the nanoparticle surface, and loss of the unique chemical or physical properties of the nanoparticles. Because of this, direct methods for the production of nano-bio composite materials are of great interest.

The sonochemical method has potential as a direct synthesis approach, noting that only volatile components and compounds at very high concentrations (*i.e.*, the solvent) appear to be exposed to the extreme temperature conditions produced by acoustic cavitation. Heavy, low volatility compounds such as BSA likely remain intact and thus are available for secondary reaction with or for capping of the newly formed nanoparticles. In this work, we have synthesized Iron oxide nanostructures using both BSA and DNA as a template (Stachler et al., 2007). It was found that both bio-compounds significantly affect the structure, morphology, phase composition, as well as magnetic properties of iron oxides, offering control over the overall composite properties.

3.1.10 Speciated Naphthalene Analysis in Liquid Transportation Fuels

This study (Shafer et al., 2010) presented data for naphthalene species concentrations (naphthalene, 1-methyl naphthalene, and 2-methyl naphthalene) present in a range of 166 fuel samples procured from various locations throughout the world. Gas chromatography with mass spectrometric detection and selected ion mode was used to quantify the naphthalenes. The naphthalene contents in the suite of test fuels was determined to improve the understanding of the specific naphthalene-based species in transportation fuels. The particular specific naphthalene species were found in much lower concentrations than the total “naphthalenes.”

Ranging from 500 – 3000 µg/mL (roughly 500-3000 ppmv or 0.05-0.3 vol%), these speciated naphthalene levels were only roughly correlated with total naphthalenes. Gasoline had the lowest level of total naphthalenes, but had naphthalene (C₁₀H₈) levels comparable to jet fuel and marine diesel fuel, averaging approximately 1500 µg/mL.

3.2 Advanced/Alternate Fuels Development, Evaluation, Demonstration, and Management

3.2.1 Coal-based Jet Fuel (Penn State fuel)

A candidate coal-based fuel was evaluated both for use as a substitute for conventional petroleum-derived JP-8 fuel and as a candidate for advanced applications (Balster et al., 2008). Numerous properties and performance behavior were monitored through a combination of specification tests and research-type evaluations. This testing included a variety of physical and chemical property tests in the areas of high temperature thermal stability, low temperature flowability, and combustion emissions characteristics, as well as a thorough series of chemical analysis evaluations. The fuel was found to meet the vast bulk of the testing, but had some off-specification test results (for example, hydrogen content and API gravity) due to the unusual hydrocarbon constituents present in the fuel. In general, the fuel performed extremely well in thermal stability testing, but exhibited a higher viscosity than conventional fuels in low temperature evaluations. The significant oxidative and pyrolytic thermal stability benefits of the coal-based fuel could be used in the future to greatly improve the fuel heat sink for engine and aircraft technologies that are currently limited by thermal concerns.

3.2.2 Greenhouse Gas Life Cycle Analysis

UDRI has been involved in two efforts in the area of life cycle analysis of greenhouse gases of aviation fuels. In the first, a working group was tasked to provide a framework and guidance for estimating the life cycle greenhouse gas emissions for transportation fuels, specifically aviation fuels (Allen et al., 2009). The focus on aviation fuels was driven by the patterns of fuel use by the federal government. Policies such as those outlined in Section 526 of EISA 2007 cause federal agencies to institute enforceable guidelines for procuring low carbon alternative fuels. Federal consumption of fuels is dominated by the Department of Defense and the Air Force consumes more fuel than any of the other military services or federal agencies. Thus, aviation applications may become early adopters of low carbon transportation fuels. The U.S. Air Force convened a working group of individuals from government agencies, universities and companies actively engaged in assessing greenhouse gas emissions from transportation fuels, and requested that this group develop guidance on procedures for estimating greenhouse gas emissions in aviation applications, using currently available data and tools. This report provides methodological guidance for the development of greenhouse gas emission estimation from aviation fuels and is based on the collective consensus of a working group with extensive experience in aviation fuels and LCAs. The methodological guidance is directed toward the analysts who will perform and interpret the LCAs of fuel systems. The methodological guidance addresses issues of system boundaries, allocation and data quality and the need for comprehensive analyses, transparency of methodologies and data, and well characterized uncertainties. The working group anticipates this methodological guidance will evolve over time and the modeling of life cycle greenhouse gas emissions from transportation fuels will have its

own life cycle. This report is intended as a first step toward a well documented and evolving approach to applying life cycle greenhouse gas emission models in a regulatory or contractual context.

In the second effort, a subcontract with the University of Texas at Austin was implemented to begin the assessment of the greenhouse gas life cycle emission of three alternative fuels (Allen et al., 2010). Using methodologies recommended by the Aviation Fuel Life Cycle Assessment Working Group, estimates of life cycle greenhouse gas emissions for FT aviation fuels were made for three types of processes: 1) Steam methane reforming followed by FT wax production (cobalt catalyst) and upgrading (US average natural gas as a feed), 2) Coal (Kittanning #6 coal) gasification followed by FT wax production (cobalt catalyst) and upgrading, 3) Coal/biomass (mixtures of switchgrass and Kittanning #6 coal) gasification followed by FT wax production (cobalt catalyst) and upgrading. These greenhouse gas emission estimates were compared to a petroleum baseline fuel. The results indicate that the greenhouse gas footprints of natural gas derived FT fuels are less than the petroleum baseline and coal-derived FT fuels have greenhouse gas footprints that are 110% larger than the petroleum baseline. These estimates assume extensive heat recovery, but no carbon dioxide capture and sequestration. Mixing biomass with coal has a moderate impact on the greenhouse gas footprint directly attributed to fuel production, decreasing the footprint by about 1% for each 1% of biomass added to the feed. The emission estimates are reduced further if indirect effects are considered.

3.2.3 Assured Aerospace Fuels Research Facility

In 2007 the Fuels Branch of the Air Force Research Laboratory tasked UDRI with the design and construction of an Assured Aerospace Fuels Research Facility (AAFRF) for aviation fuels research. This facility was to be initially located in Building 490, Test Cell 154 and the adjoining external ground in Area B of Wright-Patterson Air Force Base, Ohio. The ultimate goal is the construction of a system capable of (i) the production of synthesis gas by natural gas reforming, (ii) Fischer-Tropsch synthesis, and (iii) wax separation and upgrading for production of the desired fuel product/molecular weight range. The AAFRF will ultimately produce 10 to 15 gallons/day of jet fuel product via Fischer-Tropsch (FT) synthesis.

For Phase I of the program, UDRI solicited proposals for the design, fabrication, and installation of a product upgrading system for converting the hydrocarbon wax produced via the Fischer-Tropsch process to synthetic jet fuel. UDRI selected Battelle (for engineering design and consulting) and a team of subcontractors including Xytel Corporation (design and construction of the upgrader) and Idaho National Laboratory (ASPEN simulations). UDRI executed analysis of the system design and related safety issues as well implementation of the design. The upgrading system was received in summer 2009 and UDRI performed tasks associated with installation, such as supplying the proper utilities to the system. UDRI led the efforts to commission and troubleshoot the unit. The upgrader is being successfully operated under UDRI's scientific leadership by UDRI operations technicians with engineering assistance from Battelle.

Small scale research support for both FT synthesis and hydrocarbon upgrading is being provided through the Shroyer Park Center Alternative Fuels Synthesis facility. Initially, two continuous stirred tank (CSTR) FT synthesis reactors were commissioned to identify catalysts and conditions suitable for operating the foreseen AAFRF FT slurry reactor. With a change to a fixed-bed design, the CSTRs were replaced by two tubular fixed-bed reactors which are in

operation. For the purposes of selecting the best catalysts for use in the AAFRF upgrader, for identifying the most appropriate operating conditions, as well as for conducting fundamental research into hydrocarbon conversion reactions, two fixed-bed upgrading systems were also installed and are in operation.

For Phase II of the program, UDRI solicited proposals for the design, fabrication, and installation of subsystems for producing synthesis gas by natural gas reforming, a slurry bubble column FT reactor subsystem for FT synthesis, and FT products recovery. Phase II was awarded to Battelle with a team of subcontractors including Idaho National Laboratory (ASPEN simulations), RTI International (design, build, and install the slurry bubble system), and other collaborators. The Steam Methane Reformer (SMR) system was received in June 2009 and placed in storage until Building 496 is ready for installation of the system. In February 2010 the slurry bed FT reactor task was put on hold as revised completion cost estimates greatly exceeded the original contract. In addition, it was concluded that a tubular fixed-bed FT reactor would be more suitable for the scale of the proposed system. Currently, this task is on hold pending further funding.

Battelle was also tasked with providing an engineering analysis for the design of an off-gas system capable of accommodating the exit streams from the combined operation of the SMR, FT reactor, and the relocated upgrader. As a result, an analysis of gaseous output during individual and integrated operation was performed, as well as analysis of treatment options. The treatment options identified were enclosed flares, thermal oxidizers, and regenerative thermal oxidizers, all of which also require a suitable relief stack. The thermal oxidizer was determined to be the most cost-effective approach and a full design basis for a detailed design was provided to the vendor. Implementation of a final design and installation is on hold pending further funding.

3.2.4 Emissions Program

Characterization of the major and minor gaseous and particulate matter emissions from aircraft engines continues to receive significant interest. In recent years, this interest has increased due to the potential impact of aircraft emissions on the environment and public health. In addition, emissions levels can affect aircraft basing in non-attainment areas and the trackability of aircraft during flight. Despite the technological advances made for reducing emissions on aircraft turbine engines, the total emissions of the global aviation fleet have not decreased. This is due to the growth in the aviation industry and the increased demand in global transportation services, which was projected to increase at a rate of 3–5% per year before the September 11, 2001 terrorist attacks. Sampling and quantitation of turbine engine emissions, especially particulate matter aerosol characteristics and trace compounds, such as Hazardous Air Pollutants, is a daunting task. UDRI and AFRL/RZPF performed extensive efforts to develop viable sampling methodologies and quantitation strategies for accurate and reliable sampling of turbine engine exhaust, both in test cells and on-wing. Implementation of these efforts included the evaluation and characterization of (1) the emission propensity from varying types of engines/aircraft, (2) the effect of fuel composition and additives on emissions and combustion performance, and (3) the emissions propensity during operation with alternative fuels. In addition, efforts were performed to develop an experimental system and methodologies to simulate and investigate the effect of environmental conditioning on emissions characteristics.

A major accomplishment was the development of the Turbine Engine Research Transportable Emissions Laboratory (TERTEL), which has been used for numerous in-house studies and in-

field measurement campaigns. The TERTEL is equipped with state-of-the art instrumentation for the measurement and analysis of turbine engine emissions. The TERTEL was used in a joint SERDP program with researchers from Oak Ridge National Laboratory (ORNL) to characterize and determine emissions factors from military aircraft. UDRI supported the development of extractive sampling methodologies and hardware for the on-wing measurement of emissions from varying aircraft platforms. Successful on-wing measurements were made from two T56-A-15 turboprop engines of a C-130H aircraft stationed at the 123rd Airlift Wing in the Kentucky Air National Guard (Corporan et al., 2008), two TF33 turbofan engines of a B-52 bomber at Barksdale AFB (Corporan et al., 2009), and T700 series helicopter engines used in Black Hawk and Apache helicopters at Hunter Army Air Field (Corporan et al., 2010a). These studies provided a comprehensive measure of the emissions levels of these various engines and demonstrated the capability to perform robust and detailed measurements from complex platforms. These efforts were recognized by receiving the 2008 SERPD Project of the Year Award for Weapon Systems and Platforms.

Extensive efforts were made to characterize the effect of additive chemistry and fuel composition on the emissions propensity during combustion. These efforts provide valuable guidance related to the potential effect of additives (Corporan et al., 2004a) and fuel chemical composition on particulate matter emissions (Corporan et al., 2004b; DeWitt et al., 2008) and provided a basis for evaluation of alternative aviation fuels. UDRI and RZPF were instrumental in the characterization and evaluation of the emission propensity and combustion performance of alternative fuels, primarily Synthetic Paraffinic Kerosenes (SPKs), and performed the initial studies which assisted in implementation and certification of alternative fuels for use on military and commercial aircraft. This included emission characterization on research combustors and a turbine engine at AFRL (Corporan et al., 2007a), TF33 engines used in the B-52 FT fuel certification process at both Tinker and Edwards AFB (Corporan et al, 2007b), CFM56 engines both on-wing of a NASA DC-8 in Palmdale, CA (Bulzan et al., 2010) and a test stand at GE Aviation Peebles Test Operation Facility (Timko et al., 2011), and a PW308 engine at Pratt and Whitney's West Palm Beach Test Facility (Timko et al., 2010). These various efforts have provided significant guidance regarding the emission propensity during operation with alternative aviation fuels and have assisted in the certification process. In addition, the first-ever emissions evaluation of a military aircraft, a C-17, operated with a 50/50 blend of Hydroprocessed Renewable Jet (HRJ) and conventional JP-8 was performed at Edwards AFB in August 2010 (Corporan et al., 2010b). This and related efforts will further assist to increase the potential types of alternative fuels approved for use on military and commercial aircraft.

3.2.5 'General Support' of Alternative Fuels Efforts

The USAF interest in the use and certification of alternative (non-petroleum) derived fuel blends was initiated with efforts in support of the B-52 FT-fuel certification effort in 2006. These efforts included basic studies related to the physical and chemical properties of alternative fuels and the effect of blending with JP-8 on the resulting properties (Striebich et al, 2009b; Shafer et al., 2010), the characterization of thermal stability and fit-for-purpose behavior, and the combustion and emission performance with the alternative fuels. UDRI provided extensive support of these efforts, primarily interacting with AFRL/RZPF on the numerous tasks required to provide the basis for on-aircraft approval and the B-52 alternative fuel blend certification. The overall understanding achieved during these efforts has significantly assisted with the subsequent

certification of alternative fuels for additional USAF aircraft and the pursuit of approval of Hydroprocessed Renewable Jet (HRJ) fuels.

3.2.6 Novel High Energy Release Materials on the Nanoscale

Novel reactive materials structured on the nanoscale offer tremendous advantages over their bulk counterparts due to increased surface-to-volume ratios and strong electronic coupling, which offers higher stored energy densities and decreased warhead size. Current technologies produce nano-aluminum (Al) – the most attractive high-energetic candidate for the use in fuel additives, jet propellants, and explosives because of its density and high relative heat of oxide formation – on the scale of 40 nm to as large as a few microns. However, formation of a thin oxide layer on the surface of such Al nanoparticles prevents further oxidation of the particle core which results in incomplete combustion. This project was aimed at developing new synthetic approaches to produce zerovalent Al nanoparticles on the sub -10nm scale using sonochemistry. Moreover, air sensitivity of these highly reactive metallic particles becomes even a bigger issue on the nanoscale. Combination of sonochemistry with the careful selection of capping protective agents coating the metallic particle had been successfully demonstrated by our research group before on the iron compounds, allowing the synthesis of “triggerable” reactive nanoparticles stable in air and reacting at certain conditions. Exploring these novel concepts in such nanoparticles was utilized here to lead to better understanding and therefore control over chemical/thermodynamic/kinetic reactions in nanoscale energetic materials and potentially to a major breakthrough in the area of explosive materials (Li et al., 2009).

3.2.7 Spontaneous Hydrogen Generation from Organic-Capped Al Nanoparticles and Water

Development of technologies that would lead toward the adoption of a hydrogen economy requires readily available, safe, and environmentally friendly access to hydrogen. This can be achieved using the aluminum-water reaction; however, the protective nature and stability of aluminum oxide is a clear detriment to its application. In this effort, we demonstrated the spontaneous generation of hydrogen gas from ordinary room-temperature tap water when combined with aluminum-oleic acid core-shell nanoparticles obtained via sonochemistry (Bunker et al., 2010). The reaction is found to be near-complete (>95% yield hydrogen) with a tunable rate from 6.4×10^{-4} to 0.01 g of H₂/s/g of Al and to yield an environmentally benign byproduct. The potential of these nanoparticles as a source of hydrogen gas for power generation was demonstrated using a simple fuel cell with an applied load. We have shown that the reaction of aluminum with water to yield hydrogen gas can be performed in a simple fashion, requiring no promoters or initial energy to initiate the reaction. This capability is achieved through the combined effect of using nanoscale aluminum particles coupled with an organic-provided oxide shell, which demonstrates remarkable air and organic solvent stability but allows easy reaction of the aluminum in water. We have shown that the reaction is near-complete, that the rate of hydrogen production can be tuned by controlling the nanoparticle- to-water mass ratio, and that the hydrogen generated by this reaction is sufficient to perform useful work. The simplicity of the reaction, the high energy density of the aluminum-water reaction, and the tremendous stability of these novel aluminum nanoparticles make this system a viable approach for providing power based on hydrogen without requiring the direct storage of large quantities of hydrogen;

one need only to add water to produce hydrogen on demand, where and when needed. Future efforts will focus on a better understanding of the nature of the protective shell, the particular role the synthetic method plays in developing these properties, and the effect of the organic capping agent on the reaction parameters.

3.2.8 Chemical Dynamics of Metal Nanoparticles in Energetic Systems

The primary attraction of aluminum nanoparticles for propulsion applications is the rapid release of large amounts of energy during the oxidation of the aluminum metal core. Tests were designed and conducted to evaluate the chemistry and reaction kinetics of organically-capped metal nanoparticles in model energetic systems, and to compare them with those obtained traditional oxide-passivated Al nanoparticles (Stauffer et al., 2010). Aluminum nanoparticles were mixed into ammonium nitrate and ammonium perchlorate (typical oxidizers used in solid fuel rocket motors and low-brisance explosives) matrices and ignited with a laser pulse. The resulting chemistry was characterized using time-resolved optical emission spectroscopy and time-of-flight mass spectrometry (TOF-MS). The results of these tests suggested that the organically-capped aluminum is significantly more reactive than traditional oxide-passivated particles, particularly on short timescales. It was also determined that the organically-capped aluminum nanoparticles are able to access chemical reaction pathways not available to oxide-passivated materials, at least in the systems studied. These results were very encouraging in terms of confirming the potential of organically-capped metal nanoparticles to increase the energy density and energy release rate in fuels and propellants. This is a particularly promising result in view of propulsion systems where available reaction timescales are short, such as scram-jet engines. In addition to these studies, we have also developed optical spectroscopy methods based upon atomic emission lines to permit time and space-resolved temperature measurements to be made on reacting systems with temporal resolutions of millisecond or even shorter.

3.2.9 Metal-Decorated Carbon Allotropes

We extended our research in the past few years to explore the decoration of carbon allotropes with metal nanoparticles, such as silver (Ag) and gold (Au) (Fernando et al., 2010). The decoration of carbon allotropes (carbon nanotubes, graphene oxide (GO) and carbon nanoparticles) with metals gained attention because these novel materials have been shown to be useful for many different applications. As an example, Ag decorated single-walled carbon nanotubes (SWNTs) have been used for biomedical applications; SWNTs are biocompatible and silver has a wide antibacterial spectrum which has allowed the use of Ag decorated carbon nanotubes in enhanced the artificial heart valves. In addition, metal decorated carbon allotropes might be used to develop photocatalysts for water cleavage and carbon dioxide conversion. Also, the composites that are made using the metal decorated carbon allotropes and polymers show improved physical properties, such as higher electrical or thermal conductivity and better optical properties.

3.2.10 Photocatalytic Cleavage of Water to Generate Hydrogen.

The sun is continuously emitting a large amount of energy ($\sim 10^{34}$ J/year) to the earth's surface and photosynthesis, nature's most efficient solar energy capturing mechanism, fixes only 0.1% of that solar energy. The decomposition of water into hydrogen and oxygen using a photocatalyst is another method for the conversion of solar energy to chemical energy. Early work on the cleavage of water to generate hydrogen and oxygen gas using a photoelectrochemical cell was pioneered by Honda and Fujishima. Since then various photocatalysts were developed to cleave water to generate hydrogen gas. Low efficiency was the main drawback of these photocatalysts; most of the photocatalysts generate only a few microliters of hydrogen gas after an hour of photoirradiation. Furthermore, most of these photocatalysts are metal based and therefore, not environmentally friendly. We developed a carbon based photocatalyst: carbon nanoparticles decorated with metal nanoparticles such as Ag and Au. Carbon nanoparticles are known to absorb visible light and therefore, these carbon nanoparticles will be a suitable candidate to develop an environmentally friendly photocatalyst to convert water to hydrogen gas. Mechanistically, carbon nanoparticles absorb visible light and create photoexcited hole-electron pairs. The metal nanoparticles on the carbon surface act as a co-catalyst; these metal nanoparticles pull electrons from the carbon and prevent the recombination of hole-electron pairs. The newly accumulated electrons on the metal surface are readily available and the water cleavage reaction takes place at the metal-water interface. In addition to carbon nanoparticles, we will further investigate graphene oxide and carbon nanotubes for similar applications.

3.2.11 Photocatalytic Conversion of CO₂ to Hydrocarbon Fuels.

Humans have relied heavily on the fossil fuels: coal, petroleum and natural gas. Unfortunately, the combustion of fossil fuels emits a large amount of greenhouse gases, such as carbon dioxide. The emission of carbon dioxide triggers air pollution, human health risks and possibly even global warming. Therefore, a decrease in carbon dioxide emission and conversion of carbon dioxide that is already in air to useful sources, such as hydrocarbons, is essential. In addition the use of biomass to convert carbon dioxide to ethanol and biodiesel, a few other techniques including thermochemical, electrochemical and photochemical processes were also developed. Among these methods, photochemical conversion of carbon dioxide to hydrocarbon fuel in the presence of water is a versatile method. Scientists have already examined many semiconducting metal powders, such as TiO₂, ZnO, CdS, SiC and WO₃, for carbon dioxide reduction; the results showed that a small amount of formic acid, formaldehyde, methyl alcohol and methane can be generated from carbon dioxide. Unfortunately, most of the metal powders are toxic, none are environmentally friendly, and they have low efficiency of carbon dioxide conversion. We propose here to replace the metal powders with carbon nanoparticles for the carbon dioxide conversion reaction in order to minimize the aforementioned disadvantages. Carbon nanoparticles are known to absorb visible light very efficiently with high quantum yield. Photocatalytic conversion of carbon dioxide to a hydrocarbon fuel should be possible with metal decorated carbon nanoparticles; metals, such as Ag and Au, might act as a co-catalyst. The electron transfer and carbon dioxide conversion to a hydrocarbon fuel will occur at the metal-water interface. In addition to carbon nanoparticles, we will further investigate the possibility of using other carbon allotropes for a similar application.

3.3 Advanced, Affordable Fuel/Combustion Additive Technologies

3.3.1 Minimum FSII Study on Microbial Contaminants in Aviation Fuel

The Air Force has an interest in reducing the amount of DiEGME used in JP-8 fuel for the purpose of reducing cost. A study was completed during the cooperative agreement period which explored the effects of reducing the amount of DiEGME added to the fuel on a number of fuel properties. As part of the larger effort, a study was performed to explore the effect of DiEGME reduction on the tendency of the fuel to form microbial growth (Balster et al., 2010b). DiEGME has been well documented as having biostatic properties, so the question arose as to whether a decrease in DiEGME concentration would lead to an increase in microbial growth. In this study, it was found that $>0.02\%$ by volume of DiEGME in the fuel was adequate for controlling microbial growth, which was a fraction of the 0.10 to 0.15 % by volume typically used as the concentration of DiEGME in fuel. As a result, the study found that DiEGME present in the fuel at a lower concentration would still have a beneficial biostatic effect.

3.3.2 Replacement FSII Study (RTOC) on Microbial Contamination in Aviation Fuel

Studies have been performed to look at the benefits of replacing the current fuel system icing inhibitor (FSII), DiEGME, with an alternative additive, TriEGME. The use of DiEGME has caused problems with fuel tank topcoat peeling in the B-52, and it was expected that the low volatility of TriEGME would ameliorate this problem. However, the effect of switching to TriEGME on microbial contamination in jet fuel was unknown, and it was suspected that TriEGME might be less toxic and therefore might cause an increase in microbial contamination problems. The study performed by our lab during the contract period suggested that DiEGME or TriEGME levels of $\sim 0.01\text{--}0.02\%$ by volume in the fuel phase were adequate to control microbial growth (Balster et al., 2010c and Balster et al., 2009). TriEGME was found to be a suitable replacement for DiEGME in terms of its biostatic effectiveness.

3.3.3 Simulations of Jet Fuel Solidification

A computational fluid dynamics model was developed to simulate the solidification of jet fuel due to freezing in forced and buoyancy driven flows (Atkins et al., 2005a). Flow resistance caused by porous crystal structures that exist in liquid–solid regions is simulated through the use of a momentum resistance source term. Experiments were performed in which jet fuel samples were cooled below their pour point temperatures in an optical cell which induced buoyancy driven flow. In addition, low-temperature properties of jet fuel samples were determined, using a differential scanning calorimeter, pycnometer, and a low-temperature viscometer. To study the freezing behavior of jet fuel under forced flow conditions, we fabricated a quartz duct. The duct walls were cooled below the solidification temperatures of Jet A, JP-8, and JPTS fuel samples by means of an environmental chamber. The validity of the computational fluid dynamics calculations was established by comparing them with experimental measurements (Assudani et al., 2006 and Assudani et al., 2007). The calculated temperature and solidified area of the fuel inside both the optical cell and duct agreed well with those values measured in the experiments. The effect of flow rate on solidification was also simulated, and it was found that lower flow rates result in relatively more solidification of the fuel than do higher flow rates. The simulations of the freezing behaviors of JP-8 and JPTS samples were found to have essentially same value of

morphology constant. However, the crystal structures of these two fuels were studied in experiments and were found to be very different. This shows the inability of the model to capture small-scale details like the crystal microstructure. However, this limitation is not fatal here because the focus is on the overall flow and freezing behavior of jet fuels.

3.3.4 Low Temperature Viscosity Studies

A low-temperature Brookfield scanning viscometer and visualization techniques were used to evaluate the viscosity behavior of kerosene-based jet fuels from -20 °C to sample cloud point temperatures (Atkins et al., 2005b). The uncertainty of using this rotational viscometer technique was evaluated and determined to be acceptable. The viscometer was used to perform shear rate studies on JP-8, Jet A, and JP-8 blended with a low-temperature additive designed to improve fluidity. Clouding of the neat fuel samples during cooling, visualized in a unique optical cell using cross-polarized light and a He-Ne laser, was determined to not cause non-Newtonian viscosity behavior. The use of polarized light demonstrated that neat fuel clouding during cooling is likely due to free droplets of a water/diethylene glycol monomethyl ether (water/DIEGME) mixture, while clouding of the jet fuel/additive blend was caused by crystallization. Our viscosity measurements obtained in this work were compared with viscosity measurements from other methods and were determined to be in good agreement. Complex non-Newtonian viscosity behavior, including both pseudo-plasticity and dilatancy, was identified for the fuel/additive blend. Viscosity results and the effects of shear rate changes matched observed solidification behavior.

3.3.5 JP-8+100LT Studies

AFRL and UDRI began a JPTS fuel replacement program (referred to here as the “JP-8+100LT Program”) in 1999 (Ervin et al., 1999) and the program was essentially completed with the submission of a final report in 2010 (Ervin et al., 2010). The initial objective of this program was to find a cost effective JP-8 based replacement fuel for use in the U-2 that provides both thermal stability and low-temperature fluidity at the U-2 high altitude flight conditions. The improved high temperature thermally stable fuel/additive combination known as JP-8+100, was designed to provide high temperature thermal stability performance equivalent to JPTS and was selected for this program. The cold flow requirement was pursued through the introduction of additives that modify flow properties to provide equivalent flowability at low temperatures to that of JPTS, while retaining the thermal stability characteristics of JP-8+100.

With regard to research for the U-2, potential LT flow improving additive candidates were obtained from several additive and petroleum companies. The goal was to produce a JP-8+100 fuel which also contained a LT additive that provided the equivalent low temperature flow performance of specification limit JPTS fuel. Candidate additives were evaluated for their effect on a number of important jet fuel properties. Initially, candidates were evaluated only for their effectiveness in improving LT flow properties. Additive candidates that provided promising improved LT performance were subsequently further evaluated for their effect on other properties, including: high temperature thermal stability, combustion performance, altitude relight, and a series of JP-8 and JPTS fuel specification tests.

Initial candidates were evaluated for the ability to improve LT performance on the scanning Brookfield viscometer and cold additive screening test (CAST). Subsequently, the most promising candidates were evaluated in the U-2 Fuel System Simulator, which provides an evaluation of the additive efficacy in a relevant environment that includes actual U-2 fuel system hardware, including: fuel system valves, pumps, and strainers. Two candidate additives (LT candidates A and B) successfully passed the LT screening and simulator tests, demonstrating that they improved the LT flowability of a marginal specification freeze point JP-8 fuel beyond that of borderline specification freeze point JPTS samples. A misconception held by some is that solidified JPTS has insulating properties assumed to benefit the U-2 by reducing the cooling rate to the ambient. Simulations in the U-2 Fuel System Simulator (Figure 1) and flow visualization in an optical cell (Atkins et al., 2005) together demonstrated that frozen JPTS does not effectively insulate cooled surfaces. Thus, solidified JPTS does not offer insulating benefits.

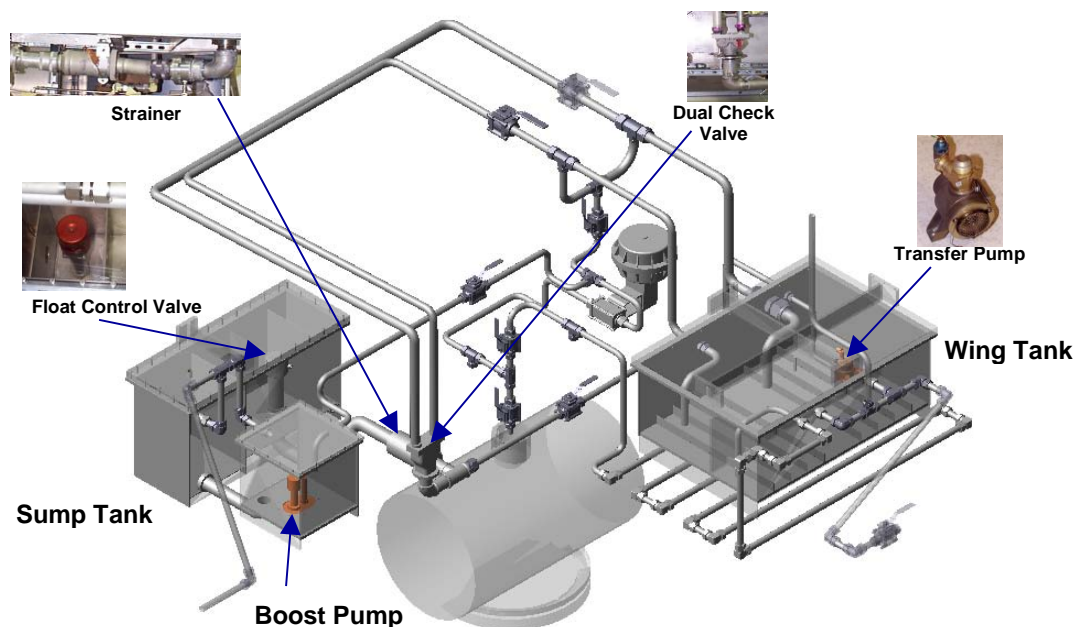


Figure 1. U-2 Simulator Isometric Drawing with Images of Actual Components

Additive candidates A and B also were evaluated for their effect on fuel properties not involved with LT flowability. It is essential that the LT flow-improving additives not detrimentally affect important fuel properties such as high temperature thermal stability, altitude relight, and combustor and nozzle coking. Thus, these promising candidates were evaluated in a series of tests to determine their effect on fuel properties and performance. High temperature thermal stability was evaluated in the Quartz Crystal Microbalance (QCM) and the Extended Duration Thermal Stability Test (EDTST). The thermal stability performance of candidates A and B was equivalent to that of JPTS. Altitude relight testing was conducted at the Royal Military College of Canada, and the altitude relight results indicated no negative impact of the additives on the relight capability of JP-8+100. Combustor and nozzle coking were evaluated in the T63 engine and swirl stabilized combustor systems. The combustion coking testing showed some additional combustor liner and nozzle face deposits due to the presence of the additives. A second

generation of LT candidates A and B were synthesized with the goal of reducing combustion deposits. As anticipated, this second generation of additives successfully passed the low-temperature screening tests. Moreover, combustor testing showed improved performance from the first to the second generation of LT additives, and there was no detriment to the T63 engine from the use of these additives. The LT additive technology was demonstrated in system/subsystem models in relevant environments and achieved USAF Technology Readiness Level 6 for the U-2 aircraft.

A second phase of LT additive research was directed toward the Global Hawk. Due to the high cost of fielding two additives for use in the Global Hawk, the decision was made to retain only one additive for further screening. Preliminary studies performed in a combustor sector rig within LibertyWorks facilities indicated better combustion performance for candidate B. Thus, LT candidate B was selected for further consideration and is referred to as JP-8+100LT. Additional combustion tests showed that JP-8 formed substantial fouling deposits on the fuel nozzle under 28-hour simulated cruise conditions. In contrast, JP-8+100LT formed no observable nozzle deposits. JP-8+100LT was more inclined to form deposits in the sector liner, but none of the observed deposits would impair engine operation. In addition, the use of JP-8+100LT did not reduce the lean blow out or ignition combustor stability margins. Lastly, JP-8+100LT did not significantly affect NO_x and CO emissions but reduced smoke emission by ~30%. When the concentration of the LT additive was doubled, the nozzles did not have detectable internal fouling. However, there was significant combustor liner deposition, and the ignition using piloted nozzles was significantly degraded. In this case, lean blow out was unaffected.

In addition to the combustion tests, a variety of additional tests were performed using JP-8+100LT. Because of fuel system differences between the U-2 and the Global Hawk, additional LT testing in the glass wing rig with conditions similar to those encountered in the Global Hawk were performed, and no concerns were raised. Hot section materials testing was performed using a (LibertyWorks) Becon rig and alloys relevant to current and future engine components. After analyzing (via scanning electron microscopy, optical microscopy, weight loss measurements, and X-ray diffraction) the pin specimens that were exposed to JP-8+100LT in the Becon rig, it was concluded that the combustion products of JP-8+100LT were not detrimental to the hot section materials of the Global Hawk. For (non-hot section) materials compatibility testing, it was concluded that JP-8+100LT presents no adverse materials compatibility concern for the Global Hawk for concentrations below 1.5 times the recommended concentration. Water filtration studies performed by Southwest Research Institute found that there were no concerns if the LT additive was added to the base fuel at the aircraft skin. In addition, tests were performed to study the compatibility of the LT additive with the other additives found in JP-8 and with the JP-8+100 additive. No additive compatibility problems were found. Lastly, a portable spectroscopic method for detecting the LT additive within fuel was developed. The LT additive technology was demonstrated in system/subsystem models in relevant environments and achieved USAF Technology Readiness Level 6 for the Global Hawk aircraft.

3.3.6 Minimum FSII Program

Fuel System Icing Inhibitor (FSII) additive, a mandatory additive in JP-8, is used to prevent solidification of free water in the fuel and to provide protection against microbial growth in fuel

systems. The current FSII additive approved for use is Diethylene Glycol Monomethyl Ether (DiEGME). The fuel specifications require that JP-8 be procured with 0.10 to 0.15% by volume of FSII (MIL-DTL-83133G) with an on-aircraft minimum use limit of 0.07% (USAF T.O. 42B-1-1). There is significant interest in determining if the on-board use concentration of FSII can be reduced due to both economic and material compatibility concerns. More specifically, a lower FSII concentration would yield significant logistical and economic cost savings and potentially reduce the occurrence of FSII-related Fuel Tank Topcoat Peeling (FTTP) occurring in aircraft fuel tanks (primarily the B-52). UDRI performed extensive experimental studies and analyses to determine if the use concentration of FSII could be reduced while still providing similar icing inhibition and biostatic capability as the current 0.07% requirement

Due to the complexity of independently determining a minimum use limit for each USAF aircraft, numerous experimental studies and conservative analyses were performed to provide an aircraft-independent recommendation. The primary efforts performed included: estimation of the expected total water content on-board aircraft, the characterization of the partitioning of FSII from fuel to any free water present, and small- and large-scale icing studies (DeWitt et al., 2005; DeWitt et al., 2009). In addition, studies were performed to characterize the bio-efficacy (Balster et al., 2010) and potential for reduced occurrence of Fuel Tank Topcoat Peeling (FTTP) (Zabarnick et al., 2010) with a lower FSII concentration in the base fuel. Results from the numerous efforts support the feasibility of a reduced use limit while maintaining safe operation of aircraft. Estimations of the total water content expected on aircraft and in-field measurements from B-52 aircraft at both Barksdale and Andersen AFBs indicated that low quantities of water (< 120-130 ppm) should be encountered during standard operation. Partitioning measurements showed FSII readily migrates from fuel into free water and the propensity and percentage of the migration increases with reduced temperature and concentration. Biological growth studies indicated that even at reduced levels of FSII in the base fuel, the resulting aqueous phase concentration will be sufficient to provide comparable performance to current use levels. Extensive small-scale icing studies with strainer filter elements used on B-52 aircraft and metal screens show that concentrations much lower than currently required can prevent ice formation of large water concentrations, even at the specification temperature limit of JP-8 (-47°C). Large-scale component testing performed with a B-52 strainer housing provided validation of the small-scale testing with improved definition of the required use limit. Overall, it was determined that a minimum use limit of 0.040% FSII will provide for safe operation under expected water levels and flight conditions for aircraft operating with JP-8. Implications of FSII-loss during fuel transfer and storage were addressed in a separate effort by the United States Air Force Petroleum Agency (Regoli, 2009) to define the required FSII procurement range required to insure the minimum use limit is achieved at the aircraft. Flight testing of a B-52 with JP-8 at the 0.040% FSII level and 125 ppm total water in a test fuel tank will be performed FY2011; this testing will assist in implementation of the reduced FSII concentration in both DoD and NATO fuels.

3.3.7 Fuel System Icing Inhibitor Replacement Program (RTOC)

In recent years there has been an increasing incidence of reports of the peeling of topcoat material (Boeing Material Specification 10-39, aka BMS 10-39) in the ullage space of integral wing tanks in B-52 aircraft. This increase in delamination phenomena coincides with the change from JP-4 to JP-8 as the primary U.S. Air Force fuel and also the change in primary icing inhibitor additive from ethylene glycol monomethyl ether (EGME) to diethylene glycol

monomethyl ether (DiEGME). Recent work indicates that with the JP-8/DiEGME combination, the icing inhibitor additive can concentrate in the tank ullage and condense at these high concentrations on the upper tank walls. These high concentrations of DiEGME cause swelling and subsequent peeling of the epoxy-based topcoat. In this work, we report on the identification and evaluation of alternative icing inhibitor additives that do not cause topcoat delamination in fuel tank upper surfaces. The U.S. Air Force, with funds provided by the Reduction in Total Ownership Cost (RTOC) program of the Department of Defense, has undertaken the task of finding a replacement FSII which does not cause fuel tank topcoat peeling. This program consisted of four phases: additive development, safety of flight certification, specification development, and field implementation/logistics.

Initially, prospective additives need to be evaluated for their ability to inhibit the formation of ice in aircraft fuel systems. Additives which perform well as icing inhibitors then need to be evaluated for their compatibility with fuel tank topcoat material. The initial group of additive candidates evaluated consisted of glycol ether species with decreased volatility (Zabarnick et al., 2007). These low volatility species should be less able to concentrate in the ullage and cause topcoat failure. The selection process identified triethylene glycol monomethyl ether (TriEGME) as the most promising candidate for replacement of DiEGME. TriEGME was shown to exhibit equivalent icing inhibition performance to DiEGME, but also exhibits a much lower tendency to negatively impact BMS 10-39 topcoat on aircraft fuel tank ullage surfaces at typical use concentrations (≤ 0.15 vol%). Following the ASTM D4054 standard practice guidelines, the additive was evaluated in jet fuel for its effect on both specification (MIL-DTL-83133) and fit-for-purpose properties. Testing was performed to determine the impact of TriEGME on compatibility with other fuel system materials, evaluation of the effect on fuel properties such as thermal stability, impact on fuel filtration, impact on functionality of other additives, and testing of the biostat capabilities of the additive (Zabarnick et al., 2010; Bessee and Zabarnick, 2008; Zabarnick et al. 2011; Balster et al., 2010c). Where practical this testing was performed at both 1x and 4x concentrations of the additives. In all cases TriEGME was found to compare favorably with DiEGME in these properties.

3.3.8 Spectral Characterization of the Composition and Structure of Organically-Capped Metal Nanoparticles

Significant attention has been paid in recent years to organically-capped metal nanoparticles for use as next-generation additives in fuels and propellants. Aluminum has been of interest due to its high energy density, but other metals such as iron have shown promise for deoxygenation of fuel at elevated temperatures. In any case, the purpose of the organic capping layer is to provide a triggerable coating and to enable metal nanoparticles to be dissolved in jet fuels. The synthesis of these materials is described elsewhere in the report. But to evaluate and optimize such materials, it is necessary to characterize their composition and structure. A combination of spectroscopic methods including Fourier-Transform Infrared (FTIR) spectroscopy, Inductively-Coupled Plasma Mass Spectrometry (ICP-MS) and Temperature Programmed Desorption (TPD) were employed to measure the metal content of candidate nanoparticles and to elucidate the bonding structures at the metal-organic interface (Lewis et al., 2010). These methods were used to characterize the composition and structure of organically-capped aluminum, iron, Fe-doped Al, and Si-doped Al nanoparticles. Many of the results were quite surprising. In the case of oleic acid-capped Al nanoparticles, a previously unknown type of bonding at the metal-organic

interface was identified, which may account for the unique properties of this nanomaterial. Also, the Fe-doped Al nanoparticles were observed to sequester sufficient oxygen in the nanoparticle to permit combustion of the organic layer even in vacuum. The results of these studies gave us an unprecedented understanding of these materials, not only allowing us to optimize their properties for intended applications, but also highlighting possible applications that could not have been foreseen otherwise.

3.3.9 Synthesis of Metal Decorated Carbon Allotropes.

It is well documented that there are many different technologies available for the decoration of carbon allotropes with metal nanoparticles including photoreduction, microwave heating reduction, laser assisted reduction, potentiostatic reduction, solid state reduction, ball milling reduction, and traditional wet chemistry reduction of metal salts using reducing agents. Low efficiency, low yield and difficulty of scale up to produce large quantities are the major drawbacks of the aforementioned methods. In our laboratory, carbon allotropes were decorated with metal nanoparticles using sonochemistry. Among these methods, sonochemistry might be the most efficient for the decoration of carbon allotropes with metals because of its simplicity, lower metal salt requirement, shorter reaction time and ease of scale up. In a typical procedure of SWNT decoration using sonochemistry, 50 mg of SWNTs was mixed with 25 mg of metal acetate in 15 ml of DMF and sonicated for 10 minute active time. After the sonication, the sample was allowed to cool for a few minutes to cool down and transferred to a round bottom flask. The DMF solvent was removed using a rotary evaporator and the metal decorated SWNTs were washed with water, ethanol and acetone to remove unreacted metal acetate. Additionally, we synthesized metal decorated graphene oxide and carbon nanoparticles in a similar fashion.

3.4 Materials Compatibility

3.4.1 Topcoat Compatibility for Fuel Tank Topcoat Peeling

In recent years, the fuel system icing inhibitor (FSII) diethylene glycol monomethyl ether (DiEGME) has been implicated in an increasing incidence of peeling of topcoat material in the ullage space of integral wing tanks in the B-52 and other military aircraft. Work has indicated that for the combination of DiEGME in JP-8 fuel, the icing inhibitor additive can concentrate in the tank ullage and condense at elevated concentrations on cooled tank walls. These high concentrations of DiEGME cause swelling and subsequent peeling of the epoxy-based topcoat. Here we report on detailed studies of the compatibility of DiEGME and FSII replacement candidate triethylene glycol monomethyl ether (TriEGME) with BMS 10-39 fuel tank topcoat material (Adams et al., 2010). Tests were designed to simulate fuel tank wall exposures with subsequent topcoat degradation measured by icing inhibitor uptake analyses and pencil hardness evaluations. The lower volatility of TriEGME relative to the JP-8 fuel components results in it being less able to concentrate in the tank ullage and promote topcoat failure, as compared to DiEGME. This was confirmed with lower additive levels measured in the ullage, condensed vapors, and the exposed topcoat material. The pencil hardness of topcoat material exposed to fuel vapors was significantly improved upon changing from DiEGME to TriEGME exposure. Simulation experiments were able to reproduce the fuel tank topcoat peeling observed in the

field, as well as determine the conditions (concentration and temperature) required for topcoat degradation.

3.4.2 KC-130J “Brown Goo” Study

Forward deployed KC-130J aircraft, outfitted with AE2100D3 engines, were experiencing an engine coking problem with production of an unknown brown sticky substance (deemed “brown goo”) that was rendering the variable inlet guide vanes of the engine inoperable. We provided extensive analytical support to elucidate the exact cause of the “brown goo” by analyzing field samples and comparing the results to those of possible chemical source materials (Swigart, 2006). Ultimately, we devised an experiment in which jet fuel was subjected to severe oxidation conditions (440°C in flowing air) using a modified micro-carbon residue tester (MCRT) and collected the resulting vapors in a room temperature knock out trap. The condensed, heavily oxidized material collected from the knock out trap closely matched the chemical and physical composition of the “brown goo” field samples regardless of the jet fuel examined. Based on this finding, and additional engine information provided by ASC/EN, we were able to conclude with good confidence that fuel vapors from the engine nozzle were back diffusing into the end stage of the engine compressor. Once in the compressor the fuel vapors were severely oxidized to become “brown goo” and were then able to transport throughout the fan and compressor stages via engine bleed air lines. Our reported findings helped to directly impact efforts to mitigate the problem.

3.4.3 Alternative Fuels and Microbial Contamination

The Air Force is interested in using cleaner fuels and reducing its dependence on foreign oil. For this reason, work is being performed on incorporating alternative fuels and fuel blends into current aviation fuel systems. One facet of the introduction of alternative fuels is the question of changes in microbial growth and biofilm formation compared to ordinary aviation fuel, i.e., will the introduction of alternative fuels and fuel blends make microbial growth and biofilm formation worse than before? One study conducted by this lab, utilizing an ATP assay as a rough indicator of microbial growth, suggested that microbial growth in an Fischer-Tropsch alternative fuel may be somewhat retarded compared to regular aviation fuel (Mueller et al., 2010). Another study conducted by this lab compared the microbial growth/biofilm forming tendencies of six alternative fuels versus a typical Jet A fuel. Alternative fuels investigated were: coal to liquid (CTL) fuel, gas to liquid (GTL) fuel, beef tallow hydrotreated renewable jet fuel (HRJ), camelina HRJ, and animal fat HRJ. No significant differences in microbial growth tendency were found for the alternative fuels tested vs. regular jet fuel. However, the CTL fuel, comprised of unusual highly substituted isoparaffins and no straight chain paraffins, seemed to prevent biofilm growth. In comparison, the other alternative fuels and the Jet A fuel experienced substantial biofilm growth over the 45 day test period (Balster et al., 2010a). More work on the ability of the CTL to suppress biofilm formation is planned.

3.4.4 Biodiesel and Microbial Contamination

In biodiesel fuels, microbial contamination has led to filter plugging and system malfunctions. As the Air Force moves toward the use of more alternative fuels, including biodiesel, these

problems are expected to continue in the future. Biodiesel is a renewable alternative fuel that can be produced from a wide range of vegetable oils and animal fats. Manufactured, biodiesel is a liquid fuel comprised of fatty acid alkyl esters, fatty acid methyl esters (FAME), or long-chain mono alkyl esters. It is a cleaner-burning replacement for petroleum-based fuel and is non-toxic and biodegradable. However, a disadvantage to the fact it is so easily biodegradable is the ability of microorganisms to live within the fuel. Additionally, the presence of water with a fuel system can also increase the likelihood of microbial growth causing widespread contamination of the system. Various laboratory techniques including visual inspection of the fuel, traditional microbiological plating of microbes, commercial lab test kits, and molecular testing has been utilized in recognizing contamination problems and identifying the causative organisms (Bowen et al., 2009). This research into microbial contamination of biodiesels showed the consortia within the fuel varied from sample to sample and also by location. Some fuel contained a variety of organisms while other fuels had only one to two dominate microorganisms. The most significant identification results came from using the polymerase chain reaction (PCR) with primers from the 16S and 18S small ribosomal subunits and then sequencing the gene regions while traditional plating yielded fewer identifications. Some commonly identified microbes included *Pseudomonas*, *Burkholderia*, and *Ralstonia*. A variety of fungus and yeast organisms such as *Hyphozyma* and *Geotrichum* were also present in fuel. A strategy for mitigating microbial contamination in biodiesels is needed because of the fuel susceptibility to biodegradation.

3.4.5 Bioinformatics

It has been previously established that microbes survive and proliferate in hydrocarbon environments where water is present. This microbial growth fouls filter units, fuel storage tanks, and other equipment where water has the opportunity to collect in very small amounts. In order to develop a plan to help mitigate microbial growth, we needed to determine if the bacterial communities in different types of fuel were similar. In order to answer this question, clonal libraries consisting of 16S DNA from several hundred bacteria surviving in JP-8 and Jet A were analyzed for community dynamics and phylogenetics (Brown et al., 2010). DNA extraction, PCR, TOPO cloning, sequencing, and bioinformatics programs were used in order to investigate any commonalities between the multiple libraries. It was discovered that bacterial communities surviving in the same type of fuel can be significantly (<0.05) different from one another depending on length of storage of the fuel and the environmental factors surrounding the storage unit.

3.4.6 Microarray Studies

Work has recently begun using DNA microarray multiplex technology to gain information on which genes aid microbes in resisting biostatic additives such as DiEGME and TriEGME. Once the gene activity is known, it might become possible to manipulate the genes to turn off, making the additive effective again against microbes that had become resistant. The first challenge of this task was finding microbes that were resistant to biostatic additives that were currently in use by the Air Force or might be in the future. Through a large field study, this lab was able to harvest many wild type microbes, which tend to be “tougher” than lab grown microbes. Of these, two field microbes of the genera *Clostridium* and *Bacillus* were found to be resistant to DiEGME

and TriEGME. The second step was to compare these microbes under two gene expression conditions: one where they are exposed to jet fuel + additive, and one where they are only exposed to jet fuel. Through a customized microarray slide prepared by Agilent, the differences in gene expression will become clear, enabling our lab to approach gene down regulation, shutting off genes that enable the microbe to survive additized conditions.

3.4.7 Microbial Identifications: PCR Advancements

It has been estimated that only 5% or fewer environmental microbes can be cultured on standard laboratory media. Although cultured microbes provide excellent DNA for identification, especially when paired with standard PCR (polymerase chain reaction)—which amplifies the DNA present, making identification much easier, even when only tiny amounts of DNA are isolated—the fact remains that these standard methods only account for a small amount of the microbial community. During the contract period, this lab developed a new technique called “direct PCR” where PCR is used on the direct fuel sample instead of the few cultures isolated from fuel samples (Denaro et al., 2006). In this way, many more microbes were detected in current fuel samples than ever before, presenting for the first time a comprehensive view of the microbial consortia in the current CONUS air fleet. This knowledge of microbial consortia is useful for developing mitigation strategies.

3.4.8 Material Compatibility of Alternative Fuels

Basic Research

In recent years there has been increasing interest in developing alternative sources of jet propulsion fuels, particularly from non-petroleum sources such as natural gas, coal, biomass, agricultural, and biological sources. It has been shown that many of these sources can provide high quality liquid fuels that in some ways are superior to conventional jet fuel. However, a significant concern inhibiting the wide acceptance of these fuels is that their composition is often significantly different than a petroleum distillate fuel. For example, the earliest alternative fuels were produced from coal and natural gas which produced a clean paraffinic fuel that performed exceptionally well as a fuel, but unlike a petroleum distillate fuel these new fuels did not contain aromatics which normally comprise 13-23% of a conventional fuel. This lack of aromatics reduces the propensity of the fuel to act as a solvent making it far more inert with respect to how it interacts with polymeric materials which in some cases can be a source of problems and concerns. Most notably is the potential impact on the performance of O-ring seals which ordinarily swell and soften to some extent when exposed to conventional jet fuel but may shrink and harden when exposed to a low-swell alternative fuel. Several potential solutions to this problem have been considered including adding aromatics to an alternative fuel, developing a swelling promoter that could be added to an alternative fuel at very low concentration, and blending an alternative fuel with conventional jet fuel.

Before embarking on examining various solutions to the anticipated challenges of using alternative fuels a series of studies were performed to better understand exactly how all of the major components of jet turbine fuels interact with polymeric fuel system materials so that potential problems with the use of these fuels could be anticipated and strategies to mitigate these issues could be formulated in an effective and timely manner. This work also resulted in

new methods of assessing material compatibility and measuring the composition of the fuel absorbed by polymeric materials. Briefly, the initial studies showed that the response to jet turbine fuel was very material-dependent and that while the strength of interaction generally increased with aromatic content, all of the fuel components participate in the volume swell process with the solubility on the major class fractions increasing as alkanes < aromatics < di-aromatics (Graham, et al., 2004). This study also illustrated the potential utility of solubility parameters in predicting the strength of interaction between polymers and specific fuel components. The concept of applying general solubility theories and the thermodynamics of polymer solutions to the issue of polymer-fuel interactions was further developed which lead to a general framework for describing the strength of these interactions (Graham, et al., 2006, Graham, 2006). Briefly, it was shown that the strength of interaction between a specific component of a jet fuel and a polymer is a balance between polymer-polymer, fuel-fuel, and potential fuel-polymer interactions as well as the size and shape of the fuel molecule. Generally, it was found that the strength of interaction, and hence the volume swell character of a fuel component, tends to increase as the molar volume of the fuel component decreases and as the polarity and hydrogen bonding of the component increases.

Developing a Statistical Approach to Estimating the Material Compatibility of Alternative Fuels

In the spring of 2006 plans were being made to conduct a flight test using a fuel blend consisting of 50% Fischer-Tropsch and 50% JP-8. Prior to conducting this test it was necessary to conduct an assessment of the material compatibility of this fuel and given the lead-time required, means had to be developed to conduct a preliminary screening of representative materials from all of the critical fuel system components as quickly as possible. To achieve the goal a statistical approach to material compatibility was developed (Graham, et al., 2007). Briefly, this approach was based on taking the volume swell of a material immersed in fuel as a measure of how that material responds to that fuel. To assess the potential compatibility of a material with an alternative fuel, volume swell data is obtained using a set of reference JP-8 fuels and the alternative fuel. The overlap in the 90% prediction intervals for these two data sets is then used as a measure of the comparability, and by extension the degree of compatibility, between 'typical' JP-8 and the alternative fuel. In the specific case of the preparations for the flight test, a study was conducted that examined the acute response (volume swell) of 29 fuel-wetted materials to a neat FT fuel, selected petroleum-derived jet fuels (JP-8 fuels), and selected FT/JP-8 blends (Graham, et al., 2007). The results of this study suggested that it was unlikely that acute problems associated with the use of 50% FT fuel blends with respect to their compatibility with common polymeric materials used in aircraft fuel systems would be encountered. Furthermore, although problems were considered unlikely, the greatest concern is with soft plasticized materials (O-rings, fuel barrier materials, and sealants) as these showed the largest volume swell and the strongest correlations with the aromatic content of the fuel. The least concern was for hard, fuel resistant materials (coatings, adhesives, films) as these showed only limited responses to the test fuels. Comparing the 90% prediction intervals for the volume swell showed that if the materials used in this study are exposed to arbitrarily selected JP-8 fuels blended with 50% FT fuel (with the same boiling range as JP-8) the probability that the material will behave as it does in a low aromatic JP-8 (a JP-8 with at least 10% aromatics) is greater than 50%. This means that with an arbitrarily blended JP-8 there is less than a 50% chance that the polymeric materials will show a volume change that is outside the range currently being

experienced by materials in normal use. This suggests a high degree of compatibility between 50% FT/JP-8 fuel blends and low-aromatic JP-8 fuels.

Development of Standardized Tests to Assess the Overall Material Compatibility of Alternative Fuels

The statistical approach to material compatibility described above proved to be an effective method of assessing the degree of comparability between different fuels and provided a means of estimating the extent of material compatibility. This general approach was modified to form the basis for standardized screening tests for fuel that are being considered for advanced testing and certification. The overall approach is to measure the volume swell character of the proposed fuel in a small set of representative fuel system materials (at present up to 4 O-ring materials and 2 sealants) and compare these results with the volume swell in a set of reference JP-8 fuels. The primary difference between this method and the work described above is that this approach uses a smaller number of selected materials (4 to 6 versus 29) and at present uses a larger number of reference JP-8 fuels (33 versus 9) and longer exposures to the fuel (40 hours versus 16). A second, more comprehensive screening protocol has also been developed that uses more materials (up to 38) and fewer reference JP-8 fuels (1 under the present protocol). During this reporting period 44 fuels and fuel blends were evaluating using the simple screening protocol and 6 have been evaluated using the more extensive protocol.

3.4.9 Biological Relevance of Novel Nanoenergetic Materials

Due to the rapid development of nanoenergetics research, consideration of their impact on biological systems is of great interest. It has been established that every chemical is toxic under certain conditions of exposure and is considered biologically safe up to specific exposure levels. The USAF is interested in ensuring that environmental and health related issues concerning production, handling, use, and disposal of nanoenergetic materials are minimized as they relate to the future mission requirements. However, there is a significant gap in our knowledge about biological interactions of these highly energetic nanomaterials and subsequent health implications associated with their increasing use. Recent nanotoxicity studies associated with Al nanoparticles (NPs) have been limited in that they failed to address realistic human exposure levels and identification of interactions that occur following low levels to the nanoparticles' exposure. Furthermore the effects of different properties of NPs such as size, shape, morphology, and surface chemistry on the overall nanomaterials' behavior in live organisms have not been extensively studied. This project was a systematic study of synthetic conditions to produce Al NPs with varying size, shape, morphology, and chemical properties, and their consequent impact on human health (Smith et al., 2008). For this project, the sonochemical method was employed to synthesize Al⁰ NPs with varying parameters followed by exploring the effect of these parameters on the mechanisms of nanostructure interaction with biological systems. The primary technical objectives of this research were as follows: (1) to synthesize capped Al nanoparticles of various particle size, shape, and chemical reactivity, (2) to functionalize the surface of these nanoparticles with various organic and bio-organic capping agents (i.e., carboxylic acids, proteins, DNA, biopolymers), and examine their uptake, (3) to label the nanoparticles with fluorescent markers for determining translocation and uptake, (4) to understand the mechanisms

of their interaction with biological systems. The project was carried out in collaboration with the Human Effectiveness Directorate of AFRL.

3.4.10 Development of New Jet Reference Fluid (JRF-3)

In 2005 it was decided that a more appropriate jet reference fluid needed to be developed for material compatibility testing. At that time the two fluids being used were a two-component fluid and a five-component fluid (ASTM D4054-93). Some of the criteria for the new fluid included adding JP-8 additives (fuel system icing inhibitor and corrosion inhibitor/lubricity improver), and targeting the concentrations of the aromatics (total and naphthalenes), sulfur (total and mercaptan), and FSII to be at the specification maximums. In addition, it was desirable to use multi-component surrogates (as opposed to a single component) to more closely simulate the paraffin, cycloparaffin, and aromatic fractions in jet fuel. Previous chemical analysis research had been performed to compare the aromatic fraction of a JP-8 jet fuel to a combination of three aromatic solvents (Aromatic 100, 150, 200), which verified that the blend encompassed the range of the majority of the aromatics found in jet fuel. Additional work was performed to adjust the relative concentrations of the individual aromatic solvents in the blend to resemble the aromatic fraction of a jet fuel, as well as to yield a naphthalenes concentration at the specification maximum when the blend was combined with the other components at the specification maximum concentration for total aromatics. Exxsol D40 and D80 were the surrogates chosen for the saturate fraction of the reference fluid. Through qualitative and quantitative analyses, it was discovered that in combination (50:50) they approximate the volatility and hydrocarbon type of the saturate fraction of jet fuel. As in ASTM D4054-93, single components were added for each of the two sulfur types.

JRF-3 is currently being used by a number of organizations for materials testing. The latest version of ASTM D4054 lists it as one of the two baseline test fluids that “are approved for use for determining compatibility of a new fuel or new fuel additive with fuel system materials.”

3.5 Modeling and Simulation

3.5.1 Thermal Stability Modeling

The production of detrimental carbonaceous deposits in jet aircraft fuel systems results from the involvement of trace heteroatomic species in the autoxidation chain that occurs upon fuel heating. Although it has been known for many years that these sulfur, nitrogen, and oxygen containing species contribute to the tendency of a fuel to form deposits, simple correlations have been unable to predict the oxidation rates or the deposit forming tendencies over a range of fuel samples. In this work (Kuprowicz et al., 2007), a chemical kinetic mechanism developed previously is refined to include the roles of key fuel species classes, such as phenols, reactive sulfur species, dissolved metals, and hydroperoxides. The concentrations of these fuel species classes in the unreacted fuel samples are measured experimentally and used as an input to the mechanism. The resulting model is used to simulate autoxidation behavior observed over a range of fuel samples. The model includes simulation of the consumption of dissolved oxygen, as well as the formation and consumption of hydroperoxide species during thermal exposure. In addition, the chemical kinetic mechanism is employed with a global deposition sub-mechanism in computational fluid dynamics (CFD) simulations of deposit formation occurring in near-

isothermal as well as non-isothermal flowing environments. Experimental measurements of oxygen consumption, hydroperoxide formation, and deposition are performed for a set of seven fuels. Comparison with experimental measurements indicates that the methodology offers the ability to predict both oxidation and deposition rates in complex flow environments, such as aircraft fuel systems, using only measured chemical species class concentrations for the fuel of interest.

3.5.2 Quantum Calculations for Thermal Stability Modeling

Density functional theory (DFT) calculations of the energetics and kinetics of important reactions for jet fuel oxidation were reported (Zabarnick and Phelps, 2006). The B3LYP functional along with 6-31G(d) and larger basis sets are used for calculation of peroxy radical abstraction reactions from hydrocarbons and heteroatomic species; the reaction of sulfides, disulfides, and phosphines with hydroperoxides to produce non-radical products; and the metal catalysis of hydroperoxide decomposition. Reaction enthalpies and activation energies are determined via DFT calculations of the structures and energies of stable species and transition states. The peroxy radical abstraction study shows the high reactivity (E_a 's of 6 to 11 kcal/mol) of H atoms which are weakly bonded to heteroatoms, including nitrogen, oxygen, and sulfur. These species, at part-per-million levels, are able to compete for peroxy radicals with the bulk fuel hydrocarbon species. Benzylic hydrogens on aromatic hydrocarbons are shown to be significantly more reactive (by 4 to 5 kcal/mol) than paraffinic hydrogens with the result that the aromatic portion of fuel sustains the bulk of the autoxidation process. Sulfides and disulfides are found to react readily with fuel hydroperoxides (E_a 's of 26 to 29 kcal/mol) to produce alcohols and the oxidized sulfur species. Triphenylphosphine reacts with hydroperoxides with a very low activation energy (12.9 kcal/mol). The metal catalysis of hydroperoxide decomposition is calculated to occur through the formation of a complex with subsequent decomposition to form radical species without regeneration of the metal ion. The reaction pathways found and activation energies calculated can be used to improve chemical kinetic models of fuel autoxidation and deposition.

3.5.3 Kinetic Modeling of Hydrotreated Paraffins Blend

The ability of pseudo-detailed chemical kinetic modeling to simulate the oxidation behavior of Exxsol D-80, a paraffin blend whose oxidative characteristics are representative of severely hydrotreated jet fuels, was assessed (Kuprowicz et al., 2004). The effects of temperature and initial dissolved O_2 concentration on oxidation were considered. A 17-step pseudo-detailed mechanism is shown to provide reasonable simulations of Exxsol D-80 oxidation over a range of temperatures, but not over a range of initial dissolved O_2 concentrations. The addition of alkyl-peroxy radical isomerization to the pseudo-detailed mechanism did not reconcile the initial dissolved O_2 limitation. With the addition of a peroxy radical decomposition reaction to the original 17-step pseudo-detailed mechanism, reasonable simulations of Exxsol D-80 oxidation over a range of temperatures and initial dissolved O_2 concentrations were obtained. Analysis of the rate parameters associated with peroxy radical decomposition suggests that aromatic hydrocarbons play a significant role in the oxidation of fuels, even at low (<1% by weight) aromatic levels.

3.5.4 Modeling and Simulation of Emission Sampling

Soot-particulate Dilution Probe under Gas Turbine Conditions

An extensive numerical investigation was conducted to quantify the aspiration efficiency (A_{eff}) of a soot-particulate sampling probe with dilution under ground idle and normal rated power gas-turbine conditions. The axisymmetric turbulent air flow around and inside the cone-shaped probe was simulated using a Lagrangian-Eulerian approach. The external flow fields of the probe were measured in the University of Dayton (UD) Low Speed Wind Tunnel (LSWT) using various Particle Image Diagnostics Techniques (PIDTs). The Particle Image Velocimetry (PIV) measurements provided excellent qualitative and quantitative agreements with the numerical results. A range of conditions from sub- to super-isokinetic sampling were numerically examined by varying the dilution ratio. The major conclusion was that the soot-particle sampling at ground idle and normal rated power conditions is highly efficient with our cone-shaped probe. Further details of this investigation can be found in Briones et al., 2008a.

Modeling and Simulation of Thermodenuder

A numerical investigation was conducted to examine the performance of a low-flow thermodenuder (Briones et al., 2008b). The commercial code FLUENT was used to model the three-dimensional laminar nitrogen flow inside the thermodenuder. A steady, one-way coupling Lagrangian approach is used to track the NaCl particles, whose trajectory depends on the balance between the particle inertia, flow drag, and thermophoretic forces. The thermodenuder operates horizontally and buoyancy acts vertically. Without buoyancy the flow is axisymmetric and the flow permeates the screen and the particle losses occur downstream along the screen. By switching on the buoyancy force the flow becomes non-axisymmetric and two non-aligned counter-rotating vortices are formed on each side of the inlet flow (see Figure 2). Due to these vortices, particles traveling near the screen are pushed towards the centerline, reducing particle losses. Even though the total particle losses are reduced with buoyancy, particle losses due to thermophoretic force are enhanced with it. Increasing the operating temperature also enhances particle losses.

Dilution Chamber

With the assistance of computational fluid dynamics (CFD) an experimental apparatus (Dilution Chamber) was designed and manufactured. This Dilution Chamber can be used to condition the exhaust flow in research combustors and turbine engines on-stands and on-wing to effectively evaluate the effect of dilution rate, temperature, and humidity on gaseous and particulate matter transformations (see Figure 3).

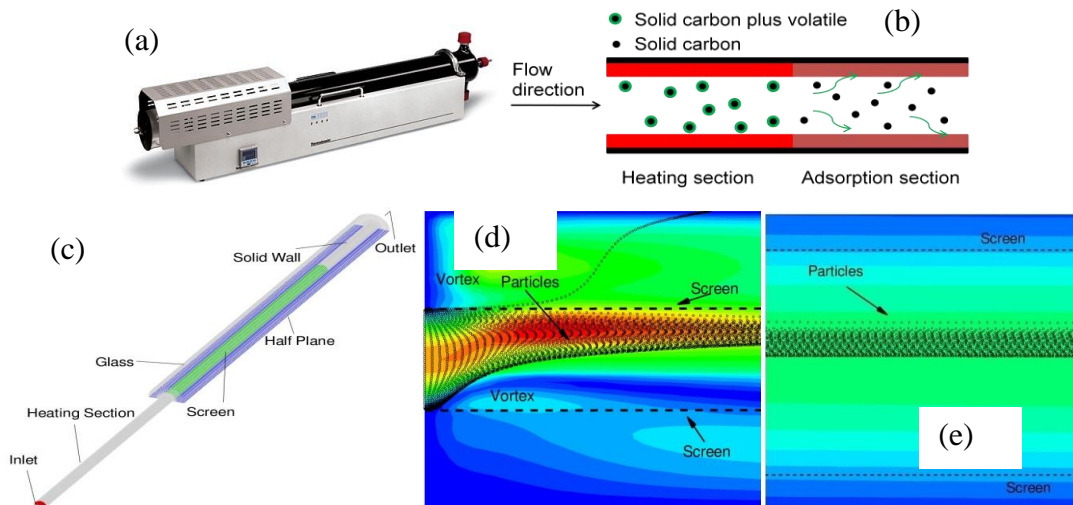


Figure 2. Low-flow Thermodenuder (a) Photograph, (b) Schematic Showing General Operation, (c) Computational Model, and (d) Upstream and (e) Downstream Predicted Velocity Contours and NaCl Particle Distribution in the Adsorption Section

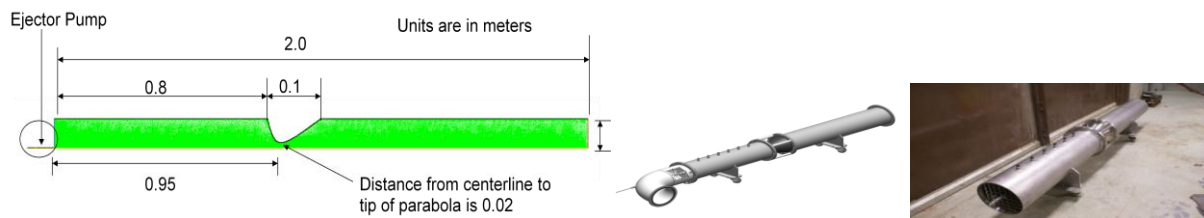


Figure 3. Dilution Chamber Computational Domain, Engineering Design, and Final Product

3.5.5 Modeling and Simulation of Advanced Combustor Technology

Well-Stirred Reactor (WSR)

A comprehensive numerical investigation was conducted to characterize the combustion performance of a toroidal WSR burning a stoichiometric mixture of C_2H_4 and air. Multiple premixed-like flames are established at the fuel-air injector exits. These flames are stabilized in high velocity regions and positioned at the same relative location with respect to their corresponding fuel-air injectors. The average number of turbulent mixing operations per residence time indicated that the flow field is almost homogeneous (Briones et al., 2008c). The results also indicated regions of jet impingement on the reactor walls causing flow recirculation and high shear stresses leading to non-homogenous flow and destruction of the reactor, respectively. Therefore, the eight exhaust ports of the reactor were replaced by a single circular slot in order to reduce both flow non-homogeneity and shear stresses. The new WSR design was manufactured and is now operational.

Cavity-in Cavity Numerical Study

This research was motivated by the necessity to improve the performance of ultra compact combustors, which requires flame stabilization in small cavities. An extensive computational investigation on the characteristics of cavity-stabilized flames was conducted. A high-fidelity, time-accurate, implicit algorithm that uses a global chemical mechanism for JP-8/air combustion and includes detailed thermodynamic and transport properties as well as radiation effects was used for simulation. Based on the results obtained in this investigation, important recommendations are provided to designers/engineers to reduce flame unsteadiness in these cavities (Briones et al., 2010a).

Inter-Turbine Burner

This study presents an alternative concept for the UCC that uses a Trapped Vortex Cavity (TVC) to replace the high swirling circumferential cavity combustion to enhance mixing rates via a double vortex system in the TVC, followed by further mixing of the free stream air through the vane with a notch. Numerical simulations were performed with FLUENT using three-dimensional geometry with temperature- and species-dependent thermodynamic and transport properties with global chemistry. Although the TVC with vane and notch enhances mixing the exit temperature profiles were not yet satisfactory for implementing the novel concept in an experimental setup (Sekar et al., 2009). We further investigated various notch designs and ramps typically found in high speed combustion applications in order to improve pressure losses and exit temperature profiles (Briones et al., 2010b).

Bluff-body Stabilized Turbulent Flames

Insight into the fundamental mechanisms responsible for augmentor's static and dynamic instabilities can be obtained from single flameholder studies with pre-vaporized fuel and premixed mixture in order to isolate the turbulence-chemistry interactions from the complex physical processes. The commercial code FLUENT was used in this regard for modeling two-dimensional and three-dimensional non-reacting and reacting flows past typical flameholder geometries, comprising of square, rectangular, and triangular cross sections, so as to form cylinders in three-dimensional space. The flow field and the flow/flame stability was found to be particularly unique to the flameholder geometry and also depend on the non-reacting and reacting condition (Sekar et al., 2010a; Sekar et al., 2010b; Briones et al., 2011).

3.6 Technology Integration and Demonstration for Thermal Management and Fuel System Operability, Supportability, and Maintainability

3.6.1 Modeling of Endothermic Fuels

It is anticipated that traditional methods of cooling that employ the sensible heat transfer provided by fuels will not be sufficient to meet the cooling requirements of future high performance aircraft. One potential solution is the use of endothermic fuels which absorb heat through chemical reactions. However, few studies have analyzed the effects of pressure on a chemically reacting, flowing fuel. We have performed experiments which study the effects of pressure on flowing, mildly-cracked, supercritical n-decane (Ward et al., 2005). Mild-cracking is

defined as a low conversion of n-decane in which the primary degradation products are smaller carbon number n-alkanes and 1-alkenes. Mild-cracking reactions of n-alkanes do not form aromatics in substantial quantities. Aromatics are known to increase soot and pollutant emissions during combustion, reduce the heat-absorbing potential of the reaction, and are thought to be deposition precursors. Deposition is undesirable because it can obstruct fuel pathways resulting in catastrophic system failure. Therefore, mild-cracking reactions of n-alkanes are of interest in endothermic fuel systems. A single pass heat exchanger, designed for mild-cracking reactions, could potentially provide a beneficial heat sink with minimal deposition and its associated detrimental effects.

A two-dimensional computational fluid dynamics model was used to further the understanding of the behavior of the transport properties of the fuel and simulate the fuel chemistry (Ward et al., 2004). Most previous pyrolytic modeling efforts have involved several different types of chemical kinetics mechanisms including: detailed, lumped, and global. Our simulations involved a unique two-dimensional computational fluid dynamics model which represented the formation of cracked products from experimentally derived proportional distributions. This model was used to study the effect of pressure on the flow properties of the fuel. This proportional product distribution (PPD) mechanism was used to simulate the chemical composition changes of a fuel as it underwent pyrolysis over a range of temperatures, pressures, and flow rates. The PPD mechanism requires only one rate expression defining n-decane degradation. The experiments indicated that increasing pressure enhanced bimolecular pyrolysis reactions, relative to unimolecular reactions. Increasing pressure also increased the overall conversion rate of supercritical n-decane flowing through the reactor. This was primarily because pressure increases the density, which increases the residence time of n-decane flowing through the reactor. It is anticipated that this model could serve as a building block to computational models involving more complex endothermic fuels and cooling systems.

3.6.2 Soot Modeling for Ethylene/Ethanol in Well-Stirred Reactor

An experimental/modeling study, in which a modified version of the CHEMKIN-based code for ‘perfectly stirred reactors’ was used to model soot particle formation, was conducted (Colket et al., 2004). The three fuels used in the current study were neat ethylene and two ethylene-ethanol mixtures: one with 5% of the fuel mass from the oxygen in the ethanol (14.4% ethanol by mass) and the second with 10% oxygen. With these fuels the WSR operates stably at high equivalence ratios ($1.8 < \phi < 2.6$), which allows measurement particulates and smoke in a range of conditions from soot inception through the formation of carbonaceous soot. Qualitative experimental trends were found to be accurately modeled by the code with quantitative accuracies generally within 50%. Through this work, it was found that scatter in the earlier experiments can be largely attributed to inadequate temperature control in the reactor, which has since been improved. Speculation for differences between the model and experiment are offered while additive effects and the well known ‘soot bell’ are discussed. For the initial experiments examined by Stouffer et al, the effect of the additive is largely due to temperature differences. Initial experiments investigating additive effects have been performed on the high temperature side of the soot bell. A temperature shift (decrease) due to the presence of the additive is the primary cause of the increase in soot observed in the initial experimental study by Stouffer, et al. (2003). Better thermal control of the conditions in the work by Reich et al. (2003) enabled investigation of the kinetic mechanisms by which additives effect soot production.

3.6.3 Effect of Additives on Soot Reduction for Heptane-Toluene Combustion

A study was conducted to examine the effect of six different compounds (nitromethane, nitroethane, nitropropane, cyclohexanone, pyridine, and quinoline) as additives for soot reduction (Stouffer et al., 2005). The base fuel for the study was a mixture of 80% n-heptane - 20% toluene by volume. The effect of the temperature on the chemical kinetics vs. the chemical effect of the additives was addressed for the nitroalkane additives by controlling the inlet temperatures into the reactor in order to produce the same combustion temperatures for the neat and additive cases. Equivalence ratios between 1.90 and 2.10 were studied. The WSR was limited to this equivalence ratio range on the low side by the melting point of the fused silica and on the high side by the rich blow out limit. However, this range of equivalence ratios captures the peak along with the low temperature and high temperature sides of the so-called “soot bell.” The study showed that quinoline increased volatile and carbonaceous carbon mass across the entire range of test conditions and is shown to be a poor additive for soot reduction. Pyridine showed little effect near the peak of the soot bell, increased the soot mass on the low temperature side of the soot bell and decreased it on the high temperature side of the soot bell. All of the nitroalkane additives were shown to give similar reductions in the soot produced and were the most effective additives explored. While some of the reduction in soot mass for the nitroalkane additives is due to the increased combustion temperatures, simply increasing the temperature of the neat combustion products (by increasing the inlet air/fuel temperature) did not account for the all of the change in the particulate mass and it is concluded that the effect of the nitroalkane additive was not solely due to an increase in combustion temperature. Cyclohexanone reduced the soot mass over the range of equivalence ratios tested. At the high temperature side of the soot bell the effect of the cyclohexanone was shown to be chemical rather than due to a change in combustion temperature, while the decrease in soot at for the high equivalence ratio cases was due to the change in the combustion temperature.

3.6.4 Comparison of JP-8 and FT Fuels in a WSR

An exploratory study of the performance and gaseous emissions were measured (Stouffer et al., 2007) for a well-stirred reactor operating under lean conditions for two fuels: JP-8 and a synthetic Fisher-Tropsch fuel, over a range of equivalence ratios from 0.6 down to the lean blowout. The lean blowout (LBO) characteristics were determined in experiments at loading parameter values from 0.7 to 1.4. The lean blowout characteristics were then explored under higher loading conditions by simulating higher altitude operation with the use of nitrogen as a dilution gas for the air stream. The experiments showed that the lean blowout characteristics and combustion temperatures were similar for the two fuels under both low loading and high loading conditions. The gaseous emissions were similar for the two fuels and the differences in the H₂O and CO₂ emissions appear to be directly relatable to the C/H ratio for the fuels.

3.6.5 Effects of Heat Release on Film Cooling

A study was conducted to examine the potential for heat release to occur within a turbine as a result of the interaction of film cooling air with the exhaust of a fuel-rich well-stirred reactor operating at high temperatures over a flat plate (Anderson et al., 2010). A test rig was designed

and mounted downstream of the well-stirred reactor and constructed with modular components to allow the study of different cooling hole geometries. This investigation focused on three common configurations used in modern turbines—normal holes, angled holes, and fan-shaped cooling holes. The cooling holes could be fed with either air or nitrogen, which enabled a direct comparison of the impact of the reactions to be isolated. The investigation showed that reactions do occur downstream of the introduction of cooling film in the presence of a combustor exhaust stream containing unburned fuel. These reactions occurred close to the surface and resulted in augmented heat transfer to the metal and only happened for rich equivalence ratios. The relative impact of the reactions on the surface heat transfer was quantified for the three cooling arrangements. The normal holes resulted in the lowest enhancement of heat transfer to the surface. This was attributed to the high amount of separation resulting in the reactions occurring off the wall surface. The angled holes were more susceptible to reaction as the coolant was introduced along the wall, significantly raising the local driving temperature to the wall. The fan-shaped holes exhibited the greatest degradation of performance since the well-attached film of coolant that was produced by this design resulted in reactions occurring even closer to that wall and more spread along the wall. This resulted in the highest overall heat load and the greatest difference between the nitrogen injection and the air injection.

3.6.6 Centerbody Flame Studies

The centerbody flame rig was redesigned by UDRI to improve the flame stability and has been used in several laminar flame studies of gaseous fuels. The unusual sooting characteristics of three ethylene/Air/N₂ flames established by the laminar recirculation zones of a centerbody burner were investigated (Roquemoire et al., 2009) using flame photographs, laser sheet visualizations, and calculations with a 2D CFD-based code. The different flames were obtained by varying the N₂ dilution in the fuel and oxidizer streams while maintaining a constant fuel and oxidizer velocities (~1.2 m/s). All three flames have the unusual characteristic that the soot, entrained into the recirculation zone established by the bluff-body, followed path lines that spiral towards the vortex center. Calculations indicated that the unusual shapes of the sooting flames result from the exponential dependence of the soot radiation that biases the radiation to the high-temperature surfaces, changes in the location of the stoichiometric flame surface with respect to the vortex center established by the centerbody, and complete oxidation of the soot following path lines that intersect the high temperature flame zone. The location of the stoichiometric flame surface moved radially towards the vortex center as N₂ was added to the fuel jet. The observed soot particles are the ones that follow path lines between the flame and the vortex center. To the eye, the soot surface will appear as tighter and tighter spirals as N₂ is added to the fuel, thus resulting in the donut- and ring-shaped flames. This accounts for the size variations of the spiral soot path lines in the flames with different N₂ additions. The spiral soot path-lines depend on particle size with massless particles giving a closed streamline like trajectory and 50 μm particles travel downstream without being entrained. The spiral path lines disappear when the thermophoretic force is removed from the calculation. Thus, it is predicted that the spiral soot path lines result from thermophoresis.

3.6.7 Impact of Additives on Soot Yields at 20 bar

Particulates emitted to the atmosphere from various sources of combustion are a major environmental and health concern. The use of additives due to its cost effective nature is considered as an attractive approach to reduce particulate emissions from combustors. In this study (Kahandawala et al., 2005a), the impact of nitrogenated and oxygenated additives on soot formation was investigated using a modified single pulse shock tube. Soot was generated under fuel-rich (equivalence ratio of 3.0) conditions over a temperature range of 1100 to 1550 K and a pressure of 20 bar. A fuel mixture of n-heptane and toluene (4:1 vol.) was used as the base fuel. 1-nitropropane, cyclohexanone and a mixture of cyclohexanone/1-nitropropane were the additives that were used in this study to mitigate soot formation. The combustion generated particles from the gas phase premixed combustion were collected on quartz filters and the particle yield was determined using a carbon burn-off method (Leco carbon analyzer). Lower particulate yields were observed with the addition of cyclohexanone and its mixture at all temperatures. However, the addition of 1-nitropropane reduced particulate yields only at the higher temperatures. Kinetic modeling of related nitromethane reactions showed that the effect of addition of 1-nitropropane on particle yields is primarily a chemical effect. Also, the observed ignition delay times decreased with the addition of 1-nitropropane but increased with the addition of cyclohexanone. The observed increase in ignition delay with cyclohexanone may have reduced the time available for soot surface growth and thereby reduced the soot yields.

3.6.8 Investigation of Heptane Combustion at P=50 atm

In order to reduce NO_x and PM emissions a better understanding of pollution formation from hydrocarbon fuels at high pressures is required. Unfortunately there is very little data available on high pressure hydrocarbon combustion. To remedy this situation, a new single pulse reflected shock tube was designed (Sidhu et al., 2005) to enable us to conduct experiments at pressures approaching or exceeding 50 atmospheres. This new high-pressure shock tube was built to investigate various gaseous and liquid hydrocarbon fuels (heptane, decane, and Jet A) at high pressures (~50 atm). For each experiment, ignition delay, particle yield and product distribution data was collected. The observed experimental trends (ignition delay-equivalence ratio) were also consistent with the predictions of NIST n-heptane model. The alkenes were the major gaseous combustion products. An appreciable soot yield could only be observed after addition of toluene. These initial results from the high pressure shock tube show the need for reaction temperature calibration and more detailed soot formation study. The initial results have also shown that the data obtained from this high pressure shock tube will be very useful in developing an ignition model, database on low-residence time chemical kinetics, and formation of intermediate radicals and species for pollutant emissions studies. Such studies will help refine models of ignition and turbulent combustion used to design the ultra-high pressure, ultra-fuel lean advanced gas turbine combustors of the future.

3.6.9 Investigation of the Kinetics of iso-Octane Ignition for Scramjet Conditions

Most shock tube derived ignition data are outside of the range of interest for scramjet combustor inlet conditions. Accordingly, as an initial step to improve the database for jet fuel kinetics for which alkanes are a major component, a study of iso-octane ignition at low temperatures and

pressures was initiated (Kahandawala et al., 2006). A single pulse reflected shock tube was used to investigate iso-octane ignition over the temperature range of 900–1400 K at a pressure of ~1 atm. To account for the anticipated long ignition delay times at the lower temperatures, long shock tube dwell times (~12 ms) at lower temperature and near atmospheric pressure were achieved by using argon–helium mix as a driver gas. Chemical thermometer experiments were conducted to remove any uncertainties in determining post reflected shock temperatures. The ignition delay data obtained in this study are in good agreement (in the overlap region) with the iso-octane ignition data from a previous shock tube study. However, the activation energy of iso-octane ignition obtained in this study in the lower temperature region (<1300 K) is significantly lower (~15 kcal vs. ~40 kcal) than that obtained in a previous higher temperature study. The deflagration may be responsible for lowering of activation energy under the conditions of this study. Two detailed iso-octane kinetic models (AFRL and Curran et al.) were used to model the experimental results of this study. The AFRL mechanism showed a good agreement with the experimental iso-octane ignition delays and their temperature dependence.

3.6.10 Support of Endothermic Fuels Efforts

A major complication to the development and implementation of advanced liquid-hydrocarbon-fueled hypersonic vehicles is achieving sufficient heat sink capability in the fuel, which is used to regeneratively cool the vehicle and engine structure and subsystems. One approach, termed an “Endothermic Fuel,” achieves high levels of heat sink by supplementing the “sensible heating ($C_p\Delta T$)” via bulk reactions of the fuel, such as thermal and/or catalytic cracking. The use of endothermic fuel cracking to facilitate high speed (mach 5) flight was demonstrated using the X-51A Waverider flight test vehicle in May 2010. A major limitation to viable implementation for extended/reusable operation with endothermic fuels is the undesirable formation of carbonaceous deposits. The deposition can reduce fuel flow, increase resistance to heat transfer and foul injector nozzles. The supercritical pyrolytic reaction pathways produce a wide range of products, with smaller alkanes/alkenes and aromatics being predominant products, all of which can form carbonaceous deposits. Improved understanding in the controlling reaction chemistry and deposition mechanisms will assist in developing viable implementation strategies for high speed applications. Additionally, the use of alternative (non-petroleum derived) aviation fuels derived has received significant attention recently. As synthesized, neat SPK exhibits excellent thermal-oxidative stability with minimal deposition propensity, however, the behavior under endothermic conditions requires evaluation.

Based on the need for improved understanding of the effect of fuel composition on the relative endothermic reactivity and deposition propensity and the interest in applicability of alternative fuels, UDRI performed initial experimental studies and analyses with the goal to identify major differences in the controlling reaction and deposition mechanism (Edwards et al., 2006a). The studies were performed using fully formulated middle distillate fuels rather than using model compounds. Studies were performed with two specification petroleum-derived jet fuels (a Jet A-1 and JP-8) and an SPK which conforms to the commercial and military neat specification requirements. The paraffinic alternative fuel was found to be significantly more reactive and have a much higher deposition propensity than petroleum-derived fuels. Extensive characterization of the major and minor fuel products assisted in identifying the primary reaction pathways applicable within supercritical fuel environments and provided guidance regarding the governing deposition pathways. These efforts will provide a basis for future efforts related to

understanding and improving the capability of endothermic fuels. Additionally, UDRI supported endothermic combustion studies being performed on Pulse Detonation Engines (PDE), where the approach is being used to both provide system cooling and to convert the neat fuel into compounds which have a higher combustion efficiency in the system (Nagley et al., 2008)

4.0 REFERENCES

1. D.T. Allen, C. Allport, K. Atkins, J.S. Cooper, R.M. Dilmore, L.C. Draucker, K.E. Eickmann, J.C. Gillen, W. Gillette, W.M. Griffin, W.E. Harrison, III, J.I. Hileman, J.R. Ingham, F.A. Kimler, III, A. Levy, C.F. Murphy, M.J. O'Donnell, D. Pamplin, G. Schivley, T.J. Skone, S.M. Strank, R.W. Stratton, P.H. Taylor, V.M. Thomas, M.Q. Wang, and T. Zidow, "Advanced Propulsion Fuels Research and Development Subtask: Framework and Guidance for Estimating Greenhouse Gas Footprints of Aviation," AFRL-RZ-WP-TR-2009-2206, 2009.
2. D.T. Allen, C. Murphy, K.S. Rosselot, S. Watson, J. Miller, J. Ingham, and W. Corbett, "Characterizing the Greenhouse Gas Footprints of Aviation Fuels from Fischer-Tropsch Processing," Final report from the University of Texas to the University of Dayton Research Institute, Agreement No. RSC09006, 2010.
3. W.S. Anderson, M.D. Polanka, J. Zelina, D.S. Evans, S.D. Stouffer, and G. Justinger, "Effects of a Reacting Cross-Stream on Turbine Film Cooling," ASME Journal of Engineering for Gas Turbines and Power, Vol. 132, pp. 051501/1-051501/7, 2010.
4. R. Assudani, J.S. Ervin, and S. Zabarnick, "Experimental and Modeling Studies of Jet Fuel Flow Near the Fuel Freeze Point Temperature," AIAA Journal of Propulsion and Power, Vol. 22, pp.534-541, 2006.
5. R. Assudani, J.S. Ervin, and L. Riehl, "Experiments and Simulations of the Freezing of Jet Fuel in Forced Flow," AIAA J. Propulsion and Power, Vol. 23, pp. 1123-1133, 2007.
6. D.L. Atkins, J.S. Ervin, and A. Saxena, "Computational Model of the Freezing of Jet Fuel," AIAA J. Propulsion and Power, Vol. 21, pp. 356-367, March-April 2005a.
7. D. Atkins, J.S. Ervin, and L. Shafer, "Experimental Studies of Jet Fuel Viscosity at Low Temperatures, Using a Rotational Viscometer and an Optical Cell," Energy & Fuels, Vol. 19, pp. 1935-1947, 2005b.
8. L. M. Balster, S. Zabarnick, R. C. Striebich, L. M. Shafer, and Z. J. West, "Analysis of Polar Species in Jet Fuel and Determination of Their Role in Autoxidative Deposit Formation," *Energy & Fuels*, Vol. 20, pp. 2564-2571, 2006.
9. L.M. Balster, E. Corporan, M.J. DeWitt, J.T. Edwards, J.S. Ervin, J.L. Graham, S.-Y. Lee, S. Pal, D.K. Phelps, L.R. Rudnick, R.J. Santoro, H.H. Schobert, L.M. Shafer, R.C. Striebich, Z.J. West, G.R. Wilson, R. Woodward, and S. Zabarnick, "Development of an Advanced, Thermally Stable, Coal-Based Jet Fuel," *Fuel Proc. Tech.*, Vol. 89, pp. 364-378, 2008.
10. L. M. Balster, E. M. Strobel, M. D. Vangsness, L. L. Bowen, S. S. Mueller, L. M. Brown, D. D. Pike, and D. L. Dalrymple, "Effect of FSII on Microbial Contamination in Jet Fuel: DiEGME and TriEGME," Proceedings of the 11th Conference of the International Association for Stability, Handling, and Use of Liquid Fuels (IASH), Prague, Czech Republic, October 18-22nd, 2009.

11. L. M. Balster, L. L. Bowen, L. M. Brown, S. S. Mueller, L. M. Shafer, E. M. Strobel, M. Tsao, M. D. Vangsness. "Microbial Growth and Biofilm Formation: GC-MS Analysis and Traditional Culture of Jet A-1 and Alternative Fuels," Central Regional Meeting of the American Chemical Society (CeRMACS) Dayton, OH, June 16-19, 2010a.
12. L. M. Balster, M. D. Vangsness, L. L. Bowen, S. S. Mueller, L. M. Brown, E. M. Strobel, 2010. "The Effect of DiEGME on Microbial Contamination of Jet Fuel: A Minimum Concentration Study," Technical report AFRL-RZ-WP-TR-2010-2002, Wright Patterson Air Force Base, 2010b.
13. L. M. Balster, M. D. Vangsness, L. L. Bowen, S. S. Mueller, L. M. Brown, E. M. Strobel, D. D. Pike, "Effects of Diethylene Glycol Monomethyl Ether (DiEGME) and Triethylene Glycol Monomethyl Ether (TriEGME) on Microbial Contaminants in Aviation Fuel," Technical report AFRL-RZ-WP-TR-2010-2094, Wright Patterson Air Force Base, 2010c.
14. G. Bessee and S. Zabarnick, "Evaluation of the Effects of TriEGME Fuel System Icing Inhibitor Candidate on Aviation Fuel Filtration," Proceedings of the 9th International Filtration Conference, 2008.
15. L. L. Bowen, M. D. Vangsness, E. M. Strobel, L. M. Balster, S. S. Mueller, L. M. Brown, D. L. Dalrymple, "Microbial Contaminants of Biodiesel and Diesel Fuel," Poster Presentation, Society for Industrial Microbiology (SIM) meeting in Toronto, ON Canada, July 26-29, 2009.
16. A.M. Briones, S. Stouffer, A. Bichal, H. Kang, A. Aaron, E. Corporan, and V. Belovich, "Aspiration Efficiencies of a Soot-particulate Sampling Probe with Dilution under Gas Turbine Conditions," AIAA-2008-4877, 44th Joint Propulsion Conference & Exhibit, Hartford, CT, 21 July 2008a.
17. A.M. Briones, M. Dewitt, S. Stouffer, C. Klingshirn, M.-D. Cheng, E. Corporan, "A Numerical Investigation on the Performance of a Low-flow Thermodeuder," DESS08-0015, 4th Annual Dayton Engineering Science Symposium, October, 2008b.
18. A.M. Briones. B. Sekar, J. Zelina, R. Pawlik, S. Stouffer, "Numerical Modeling of Combustion Performance for a Well-stirred Reactor for Aviation Fuels," AIAA-2008-4565, 44th Joint Propulsion Conference & Exhibit, Hartford, CT, 21 July 2008c.
19. A.M. Briones, J. Zelina, V. Katta, "Flame Stabilization in Small Cavities," *AIAA Journal*, **48**, 224-235 (2010a).
20. A.M. Briones, B. Sekar, H. Thornburg, J. Zelina, "Effect of Vane Notch and Ramp Design on the Performance of a Rectangular Inter-Turbine Burner," AIAA-2010-581, 48th AIAA Aerospace Sciences Meeting including the New Horizons and Aerospace Exhibition," Orlando, FL, January 4-7, 2010b.

21. A.M. Briones, B. Sekar, H. Thornburg, "Characteristics of Bluff Body Stabilized Turbulent Premixed Flames," GT2011- 45089, *Proceedings of the ASME Turbo Expo 2011: Power for Land, Sea, and Air*, Vancouver, British Columbia, Canada, June 6-10, 2011.
22. L. M. Brown, J. P. McComb, M. D. Vangsness, L. L. Bowen, S. S. Mueller, L. M. Balster, C. A. Bleckmann, "Community Dynamics and Phylogenetics of Bacteria Fouling Jet A and JP-8 Aviation Fuel," *International Biodeterioration & Biodegradation*, Vol. 64, pp. 253-261, 2010.
23. D. Bulzan et al., "Gaseous and Particulate Emissions Results of the NASA Alternative Aviation Fuel Experiment (AAFEX)," *Proceedings of ASME Turbo Expo*, GT 2010-23524, Glasgow, Scotland, June 14-18, 2010.
24. C.E. Bunker, M.J. Smith, K.A.S. Fernando, B.A.Harruff, W.K. Lewis, J.R. Gord, E.A. Guliants, and D.K.Phelps "Spontaneous Hydrogen Generation from Organic-Capped Al Nanoparticles and Water," *ACS Appl. Mater. Interfaces*, Vol. 2, pp. 11-14, 2010.
25. M.B. Colket, R.J. Hall, and S.D. Stouffer, "Modeling Soot Formation in a Well-Stirred Reactor," Paper GT2004-54001, *Proceedings of the ASME Turbo Expo 2004 Power for Land, Sea and Air*, June 14-17, 2004 Vienna, Austria.
26. E. Corporan, M.J. Dewitt, and M. Wagner, "Evaluation of Soot Particulate Mitigation Additives in a T63 Engine," *Fuel Processing Technology*, Vol. 85(6-7), pp. 727-742, 2004a.
27. E. Corporan, M.J. Dewitt, and M. Wagner, "Evaluation of Soot Particulate Mitigation Additives in a T63 Engine," *Fuel Processing Technology*, Vol. 85(6-7), pp. 727-742, 2004a.
28. E. Corporan, O. Monroig, M. Wagner, and M.J. DeWitt, "Influence of Fuel Chemical Composition on Particulate Matter Emissions of a Turbine Engine," *Proceedings of ASME Turbo Expo*, GT2004-54335, Vienna, Austria, 14-17 June 2004b.
29. E. Corporan, M.J. DeWitt, V. Belovich, R. Pawlik, A.C. Lynch, J.R. Gord, and T.R. Meyer, "Emissions Characteristics of a Turbine Engine and Research Combustor Burning a Fischer-Tropsch Jet Fuel," *Energy & Fuels*, Vol. 21, pp. 2615-2626, 2007a.
30. E. Corporan, M.J. DeWitt, C.D. Klingshirn and R. Striebich, "DOD Assured Fuels Initiative: B-52 Aircraft Emissions Burning a Fischer-Tropsch/JP-8 Fuel Blend," *Proceedings of the 10th International Conference on Stability, Handling and Use of Liquid Fuels*, 2007b.
31. E. Corporan, A. Quick, and M.J. DeWitt, "Characterization of Particulate Matter and Gaseous Emissions of a C-130H Aircraft," *Journal of Air & Waste Management Association*, Vol. 58, pp. 474-483, 2008.

32. E. Corporan, M.J. DeWitt, C.D. Klingshirn, S.M. Mahurin, M.-D. Cheng, "Emissions Characteristics of a Legacy Military Aircraft," Proceedings of ASME Turbo Expo, Power for Land, Sea and Air, Paper GT2009-59255, June 8-12, 2009.
33. E. Corporan, M.J. DeWitt, C.D. Klingshirn, R. Striebich, and M.-D. Cheng, "Emissions Characteristics of Military Helicopter Engines with JP-8 and Fischer-Tropsch Fuels," Journal of Propulsion and Power, 26(2), p 317-324, 2010a.
34. E. Corporan, M.J. DeWitt, C.D. Klingshirn, and D. Anneken, "Alternative Fuels Tests in a C-17 Aircraft: Emissions Characteristics," AFRL-RZ-WP-TR-2010-XXXX, *submitted for publication*, 2010b.
35. T. R. Denaro, S. K. Chelgren, J. N. Lang, E. M. Strobel, L. M. Balster, and M. D. Vangsness, "DNA Isolation of Microbial Contaminants in Aviation Turbine Fuel via Traditional Polymerase Chain Reaction (PCR) and Direct PCR--Preliminary Results," AFRL-WP-TR-2006-2049, 2006.
36. M. J. DeWitt, T. Williams, L. Shafer, R. Striebich, and L. Riehl, "Investigation of the Effectiveness of DiEGME to Suppress Solidification of Water in Aircraft Fuel Systems. Appendix A: Requirement for Static Dissipater Additive in Military Jet Fuels : An Evaluation of Safety Considerations for the Removal of Static Dissipater Additive," AFRL-PR-WP-TR-2005-2167.
37. M.J. DeWitt, E. Corporan, J.L. Graham and D. Minus, "Effects of Aromatic Type and Concentration in Fischer-Tropsch Fuel on Emission Production and Material Compatibility," *Energy & Fuels*, Vol. 22, pp. 2411-2418, 2008.
38. M.J. DeWitt, S. Zabarnick, T.F. Williams, Z. West, L. Shafer, R. Striebich, S. Breitfield, R. Adams, R. Cook, D.K. Phelps, and C.L. Delaney, "Determination of the Minimum Use Level of Fuel System Icing Inhibitor (FSII) in JP-8 that will Provide Adequate Icing Inhibition and Biostatic Protection for Air Force Aircraft," AFRL-RZ-WP-TR-2009-2217.
39. T. Edwards, M.J. DeWitt, L. Shafer, D. Brooks, H. Huang, S.P. Bagley, J.O. Ona, M.J. Wornat, "Composition Influence on Deposition in Endothermic Fuels," Paper 2006-7973, Proceedings of the 14th AIAA/AHI Hypersonics Technology Conference, Canberra, Australia, 2006a.
40. T. Edwards, L. Shafer, R. Striebich, and J. Gomach, "Chemical Class Composition of Commercial Jet Fuels and Other Specialty Kerosene Fuels," Paper 2006-7972, Proceedings of the 14th AIAA/AHI Hypersonics Technology Conference, Canberra, Australia, 2006b.
41. J.S. Ervin, S. Zabarnick, E. Binns, G. Dieterle, D. Davis, and C. Obringer, "Investigation of the Use of JP-8+100 with Cold Flow Enhancer Additives as a Low-Cost Replacement for JPTS," *Energy & Fuels*, Vol. 13, pp. 1246-1251, 1999.
42. J.S. Ervin, S. Zabarnick, L.J. Shafer, M.D. Vangsness, K.E. Binns, T.F. Williams, G.L. Dieterle, D.G. Davis, R.J. Strong, M.J. DeWitt, D.K. Phelps, C. Obringer, D.K. Atkins, and

- W.E. Harrison, "Development of an Advanced Jet Fuel with Improved Low Temperature Flow Performance – the JP-8+100 LT Program," AFRL-RZ-TR-2010-xxxx, in press, 2010.
43. K.A.S. Fernando, B. Harruff, M. Smith, C.E. Bunker, E. Guliants, and N.D. McNamara, "Sonochemical Assisted Synthesis of Silver Nanoparticles and the Decoration of Single-Walled Carbon Nanotubes and Graphene Oxide," 42nd Central Regional Meeting of the American Chemical Society, Dayton, OH, June 16-19, 2010.
 44. J. L. Graham, R. C. Striebich, D. K. Minus, W. E. Harrison, "The Swelling of Selected O-Ring Materials in Jet Propulsion and Fischer-Tropsch Fuels," Prepr. Pap.-Am. Chem. Soc., Div. Pet. Chem., 49 (3&4), 2004.
 45. J.L. Graham, R.C. Striebich, K.J. Myers, D.K. Minus, W.E. Harrison, "The Swelling of Nitrile Rubber by Selected Aromatics Blended in a Synthetic Jet Fuel," *Energy and Fuels*, 20, pp. 759-765, 2006.
 46. J.L. Graham, "The Swelling of Nitrile Rubber by Selected Species in a Synthetic Jet Turbine Fuel," Ph.D. Thesis, University of Dayton, August, 2006.
 47. J. L. Graham, R. C. Striebich, D. K. Minus, W. E. Harrison, "A Statistical Approach to Estimating the Compatibility of Alternative Fuels with Materials used in Seals and Sealants," Proceedings of the 43rd AIAA/ASME/SAE/ASEE Joint Propulsion Conference and Exhibit, Cincinnati, Ohio, July 8-11, 2007.
 48. J. L. Graham, R. C. Striebich, D. K. Minus, W. E. Harrison, "A Laboratory Assessment of the Compatibility of Fischer-Tropsch Derived (Iso-Paraffinic Kerosene) and Blended FT-Petroleum-Derived Fuels with Non-Metallic Materials," Proceedings of the 10th International Conference on Stability, Handling and use of Liquid Fuels, Tucson, Arizona, October 7-11, 2007.
 49. E.A. Guliants, B.A. Haruff, J.R. Gord, and C.E. Bunker, "Photophysical Properties of CdS Nanoparticles in Thin Films for Opto-Chemical Sensing", *Nanoengineered Assemblies and Advanced Micro/ Nanosystems*, MRS Proceedings, Vol. 820, pp. 69-74, 2004.
 50. M. S. Kahandawala, S. A. Corera and S. S. Sidhu, "Impact of additives on Soot Yields at 20 bar – A Shock Tube Study," *Shock Wave, Proc. 25th International Shock Tube and Shock Wave Symposium*, Paper No. 1085-2a, 636-644, (2005).
 51. M. S. Kahandawala, S. A. Corera, S. Williams, C. D. Campbell, and S. S. Sidhu, "Investigation of kinetics of iso-octane ignition under scramjet conditions," *Int. J. Chem. Kinet.* 38, 194-201 (2006).
 52. N.J. Kuprowicz, J.S. Ervin, and S. Zabarnick, "Modeling the Liquid-Phase Oxidation of Hydrocarbons over a Range of Temperatures and Dissolved Oxygen Concentrations with Pseudo-Detailed Chemical Kinetics," *Fuel*, Vol. 83, pp. 1795-1801, 2004.

53. N. J. Kuprowicz, S. Zabarnick, Z. J. West, and J. S. Ervin, "The Use of Measured Species Class Concentrations with Chemical Kinetic Modeling for the Prediction of Autoxidation and Deposition of Jet Fuels," *Energy & Fuels*, 2007, Vol. 21, pp. 530-544, 2007.
54. W.K. Lewis, A.T. Rosenberger, J.R. Gord, C.A. Crouse, B.A. Harruff, K.A.S. Fernando, M.J. Smith, D.K. Phelps, J.E. Spowart, E.A. Guliants, and C.E. Bunker "Multispectroscopic (FTIR, XPS, and TOFMS-TPD) Investigation of the Core-Shell Bonding in Sonochemically-Prepared Aluminum Nanoparticles Capped with Oleic Acid," accepted *J. Phys. Chem. C*, 2010.
55. H. Li, M.J. Meziani, F. Lu, C.E. Bunker, E.A. Guliants, Y.-P. Sun, "Templated Synthesis of Aluminum Nanoparticles – A New Route to Stable Energetic Materials," *J. Phys. Chem. C.*, Vol 113, pp. 20539-2542, 2009.
56. S. S. Mueller, M. D. Vangsness, L. M. Balster, L. L. Bowen, L. M. Brown, "Comparing Microbial Contamination in Different Types of Fuel," 4th Annual Alternative Energy NOW Conference, February 9-10, 2010.
57. E.A. Nagley, P.I. King, F.R. Schauer, M.J. DeWitt and J.L. Hoke, "Fuel Composition Analysis of Endothermically Heated JP-8 Fuel for Use in a Pulse Detonation Engine," AIAA-2008-0109.
58. M. Regoli, "Loss of Fuel System Icing Inhibitor Additive During the Transport and Storage of JP-8," AFPET-TR-14092009, 2009.
59. M. Roquemore, V. Katta, S. Stouffer, V. Belovich, R. Pawlik, M. Arstingstall, G. Justinger, J. Gord, A. Lynch, J. Zellina, and S. Roy, "Soot Studies of Laminar Diffusion Flames with Recirculation Zones," *Proceedings of the Combustion Institute*, in press (2009).
60. B. Sekar, H. J. Thornburg, A. M. Briones, J. Zelina, "Effect of Trapped Vortex Combustion with Radial Vane Cavity Arrangements on Predicted Inter-Turbine Burner Performance," AIAA-2009-4603, *Joint IECEC/JPC Opening Panel: 40th Anniversary Apollo Panel*, Denver, CO, August 2-5, 2009.
61. B. Sekar, A.M. Briones, H. Thornburg, "Analysis of Wake Characteristics of Several Two-dimensional Flame Holders for Combustion Systems," *Augmentor Design Systems Conference*, Jacksonville, FL, March, 2010a.
62. B. Sekar, H. Thornburg, A.M. Briones, "Design and Analysis of Flame Holders for Instability-Free Operation of Combustion Systems," *Proceedings of the HPCMP User's Group Conference*, Schaumburg, IL, June 14-17, 2010b.
63. E. Shafer, R. Striebich, M. J. DeWitt, T. Edwards, and W. Harrison III, "Variation of JP-8 Properties in the Continental United States (CONUS) and Potential Implications During Blending with Synthetic Paraffinic Kerosene," AFRL-PZ-WP-TR-2010-2079.
64. L. Shafer, "Hydrocarbon-Type Analysis of Aviation Turbine Fuels Using Semi-automated Modified ASTM D2425," manuscript in preparation, 2010.

65. L. Shafer, J. Hinz, T. Edwards, B. Curtis, and W. Weisman, "Speciated Naphthalene Analysis in Liquid Transportation Fuels," manuscript in preparation, 2010.
66. S. S. Sidhu, J.L. Graham, D. R. Ballal, and H.C. Mongia, "Investigation of Heptane Combustion at 50 ATM Using a Shock Tube," AIAA 2005-1447, 2005.
67. M.J. Smith, K.A.S. Fernando, E.A. Guliants, S.M. Hussain, L.K. Stolle, C.E. Bunker, "Active Aluminum Core-shell Nanoparticles and Their Biological Relevance", US-Korea Conference on Science, Technology, and Entrepreneurship, San Diego, CA, August 2008.
68. M.M. Stachler, J. Gord, E.A. Guliants, and C.E. Bunker, "Synthesis and Characterization of Bionanocomposite Materials", South-Eastern Regional ACS meeting, Greenville, SC October, 2007.
69. H.U. Stauffer, S. Roy, C.E. Bunker, J.R. Gord, and W.K. Lewis, "Optical Visualization of Energy Release Following Ignition of Energetic Nanomaterials, 42nd Central Regional Meeting of the American Chemical Society, June 16-19, 2010.
70. S.D. Stouffer, B.M. Mortimer, D.M. Ostdiek, M.D. DeWitt, R. Pawlik, R. Reich, and R. Mayfield, "Soot Reduction Research Using a Well-Stirred Reactor," AIAA 2005-1317, 2005.
71. S.D. Stouffer, R. Pawlik, G. Justinger, J. Heyne, J. Zelina, and D. Ballal, "Combustion Performance and Emissions Characteristics for a Well-Stirred Reactor for Low Volatility Hydrocarbon Fuels", AIAA 2007-5663, 2007
72. R.C. Striebich, M.A. Motsinger, M.E. Rauch, S. Zabarnick, and M. DeWitt, "Estimation of Select Specification Tests for Aviation Turbine Fuels Using Fast Gas Chromatography," *Energy and Fuels*, Vol. 19, pp. 2445-2454, 2005.
73. R. Striebich, J. Contreras, L. Balster, Z. West, L. Shafer, and S. Zabarnick, "Identification of Polar Species in Aviation Fuels using Multidimensional Gas Chromatography-Time of Flight Mass Spectrometry," *Energy & Fuels*, Vol 23, pp 5474-5482, 2009a.
74. R. Striebich, L. Shafer, M. J. DeWitt, Z. West, T. Edwards, and W. Harrison III, "Dependence of Fuel Properties During Blending of Iso-Paraffinic Kerosene and Petroleum-Derived Jet Fuel," AFRL-PZ-WP-TR-2009-2034, 2009b.
75. T. C. Swigart, "C-130J Brown Contamination," AFRL/MLS 06-064, June 2006.
76. M.T. Timko et al., "Particulate Emissions of Gas Turbine Engine Combustion of a Fischer-Tropsch Synthetic Fuel," *Energy & Fuels*, *submitted for publication*, 2010.
77. M.T. Timko et al., "Combustion Products of Jet Fuel, Fischer Tropsch Synthetic Fuel, and Biomass Jet Fuel for a Gas Turbine Engine," *Combustion Science and Technology*, *submitted for publication*, 2011.

78. T.A. Ward, J.S. Ervin, R.C. Striebich, and S. Zabarnick, "Simulations of Flowing Mildly-Cracked Normal Alkanes Incorporating Proportional Product Distributions," *AIAA Journal of Propulsion and Power*, Vol 20, No 3, pp. 394-402, 2004.
79. T. A. Ward, J. S. Ervin, S. Zabarnick, and L. Shafer, "Pressure Effects on Flowing Mildly-Cracked n-Decane," *AIAA Journal of Propulsion and Power*, Vol. 21, pp. 344-355, 2005.
80. Z. West, S. Zabarnick and R. Striebich, "Determination of Hydroperoxides in Jet Fuel via Reaction with Triphenylphosphine," *Ind. Eng. Chem. Res.*, Vol. 44, pp. 3377-3383, 2005.
81. S. Zabarnick and D.K. Phelps, "Density Functional Theory Calculations of the Energetics and Kinetics of Jet Fuel Autoxidation Reactions," *Energy & Fuels*, Vol. 20, pp. 488-497, 2006.
82. S. Zabarnick, Z. West, M.J. DeWitt, L. Shafer, R. Striebich, C. Delaney, and D. Phelps, "Development of Alternative Fuel System Icing Inhibitor Additives that are Compatible with Aircraft Tank Topcoat Material," *Proceedings of the 10th International Conference on Stability, Handling and Use of Liquid Fuels*, 2007.
83. S. Zabarnick, R. Adams, Z. West, M.J. DeWitt, L. Shafer, R. Striebich, C.L. Delaney, and D.K. Phelps, "Compatibility of DiEGME and TriEGME Fuel System Icing Inhibitor Additives with BMS 10-39 Aircraft Tank Topcoat Material," *Energy & Fuels*, Vol. 24, pp. 2614-2627, 2010.
84. S. Zabarnick, M.J. DeWitt, R. Adams, Z.J. West, L.S. Shafer, T.F. Williams, R. Cook, R. Striebich, L.M. Balster, D.K. Phelps, and C.L. Delaney, "Evaluation of Triethyleneglycol Monomethyl Ether (TriEGME) as an Alternative Fuel System Icing Inhibitor for JP-8 Fuel, submitted for publication, AFRL-RZ-WP-TR-2011-2030, 2011.

APPENDIX A

A Statistical Approach to Estimating the Compatibility of Alternative Fuel with Materials used in Seals and Sealants

INTENTIONALLY LEFT BLANK

A Statistical Approach to Estimating the Compatibility of Alternative Fuels with Materials used in Seals and Sealants

John L. Graham* and Richard C. Striebich†
University of Dayton Research Institute, Dayton, Ohio 45469

and

Donald K. Minus‡ and William E. Harrison III§
Air Force Research Laboratory, Wright Patterson AFB, Dayton, Ohio 45433

In this study a method of statistically comparing the volume swell behavior of selected materials in representative JP-8s and alternative fuels is described. This approach is based on obtaining volume swell data on a set of reference JP-8s and the alternative fuel. The overlap in the 90% prediction intervals is then used as a measure of the comparability, and by extension the degree of compatibility, between 'typical' JP-8 and the alternative fuel. In the specific case examined here the alternative fuel is a 50% v/v blend of JP-8 and a Fischer-Tropsch fuel. The results of the statistical analysis showed that in a arbitrarily blended JP-8 fuel there is greater than 50% chance that this fuel would exhibit volume swell behavior that is within the range of 'typical' low-aromatic JP-8s. From this it was concluded that the chances of an acute failure of O-ring seals and sealants with a 50% JP-8/FT fuel blend was low and there was no compelling evidence in the data that there was a significant likelihood of an acute sealing failure resulting from the use of this blend.

Nomenclature

A_0, A_i	=	the cross sectional areas in image 0 and i (area counts)
FT	=	Fischer-Tropsch fuel
JP	=	jet propulsion fuel
K_s	=	swelling coefficient (%/%, % swell/% aromatics)
LL, UL	=	lower and upper limit of the 90% prediction interval
R^2	=	coefficient of determination

I. Introduction

SINCE the synthesis of a liquid hydrocarbon fuel from coal by Franz Fischer and Hans Tropsch in 1923, there has been cyclic interest in developing this fuel for military and commercial applications.¹ In recent years the U.S. Department of Defense has taken interest in producing a unified battlespace fuel using the Fischer Tropsch (FT) process for a variety of reasons including cost, quality, and logistics. In the past year there has been a particular emphasis on moving quickly to demonstrate that an FT fuel can be used in the form of a blend with conventional petroleum-derived jet fuel. The initial objective is to employ this semi-synthetic fuel with blend ratios as high as 50% FT with longer range goals to use even higher blend ratios and ultimately a fully synthetic jet fuel.

A significant concern associated with the use of a semi-synthetic jet fuel with high FT blend ratios is the effect these low-aromatic fuels will have on fuel-wetted polymeric materials, most notably seals and sealants. These

* Senior Research Engineer, Energy & Environmental Engineering Division, University of Dayton Research Institute, Member

† Senior Research Engineer, Energy & Environmental Engineering Division, Room 135, Bldg. 490, Wright Patterson Air Force Base, Non-member

‡ Research Chemist, Fuels Branch, Turbine Engine Division, Propulsion Directorate, Air Force Research Laboratory, Wright Patterson Air Force Base, Non-member.

§ Chief, Fuels Branch, Turbine Engine Division, Propulsion Directorate, Air Force Research Laboratory, Wright Patterson Air Force Base, Non-member.

materials typically swell and soften to some degree when exposed to jet fuel and the aromatic content of these fuels contribute to this effect.² Semi-synthetic jet fuels with very low aromatic contents may cause seals and sealants to shrink and harden leading to acute or chronic failure. Unfortunately, most of the material qualification tests are more concerned with excessive swelling than shrinkage (see for example Ref. 3) and there is little guidance offered as to an acceptable level of shrinkage or other changes in physical properties related to low aromatic content. Given the pressing need for guidance data, a program was developed to rapidly estimate the compatibility of synthetic and semi-synthetic fuels with fuel-wetted polymeric materials.

II. Background

The Fischer-Tropsch (FT) process is one whereby a hydrocarbon feedstock (typically coal or natural gas) is converted into a mixture of carbon monoxide and hydrogen (synthesis gas) which is then recombined over a catalyst to form a very complex mixture of hydrocarbons superficially resembling a petroleum distillate jet propulsion (JP) fuel (Fig. 1). However, an analysis of the composition of FT fuel shows its composition is actually much simpler than JP fuel. The exact composition of JP fuels is so complex it defies complete analysis,⁴ but in terms of broad class fractions JP fuels are typically 75-90% v/v alkanes (linear, branched, and cyclic), 10-25% v/v aromatics (alkyl substituted benzenes), 1-3% v/v diaromatics (naphthalenes), and thousands of other species that total less than 1% v/v (heteroatomic species containing sulfur, nitrogen, and/or oxygen). In contrast, FT fuel contains only linear and branched alkanes.

The compositional difference between JP and FT fuels can have a significant effect on how these fuels interact with polymeric materials. For example, the aromatic components of JP fuel are smaller and more absorptive than the aliphatic components. This often results in the aromatic species preferentially absorbing into the fuel-wetted polymeric components.⁵⁻⁷ The overall effect is that JP fuels can act as mild solvents towards polymeric materials including those commonly used as seals and sealants. The absorption of fuel by a polymeric

component causes the material to swell and soften to an extent proportional to the volume of components absorbed by the fuel. This has a particularly significant impact on the performance of O-ring seals which rely on the compressive stress between the O-ring and the surrounding gland to form a tight seal and a small amount of swelling is usually considered beneficial as it can improve the quality of the seal.

In contrast to the solvent characteristic of JP fuel, the absence of aromatics from FT fuel renders it relatively inert with respect to its interactions with polymeric materials. Specifically, alkanes in general do not exhibit the absorptive behavior of aromatics and their molar volume is greater than that of the aromatics typically found in JP fuel. Consequently, FT fuel generally does not interact with polymeric materials to the same extent as conventional JP fuel. The inert nature of FT fuel results in a lower potential to swell and soften polymeric fuel-wetted components. This behavior by itself may not be detrimental, however, it suggests that if FT fuel is used interchangeably with conventional JP fuel polymeric materials that have been used with JP fuel will shrink and harden when they come into contact with FT fuel.

An example of the volume change that can occur when typical O-ring materials are aged in a JP-8 and then switched to an FT fuel with the same boiling range is summarized in Fig. 2. This shows that the volume change behavior can be quite dramatic depending on the specific material involved. The question becomes; is this type of behavior acceptable, or will it result in the failure of a particular seal? Answering this question is potentially a very prolonged and difficult process particularly considering the large number of materials, designs, and ages of the components potentially involved.

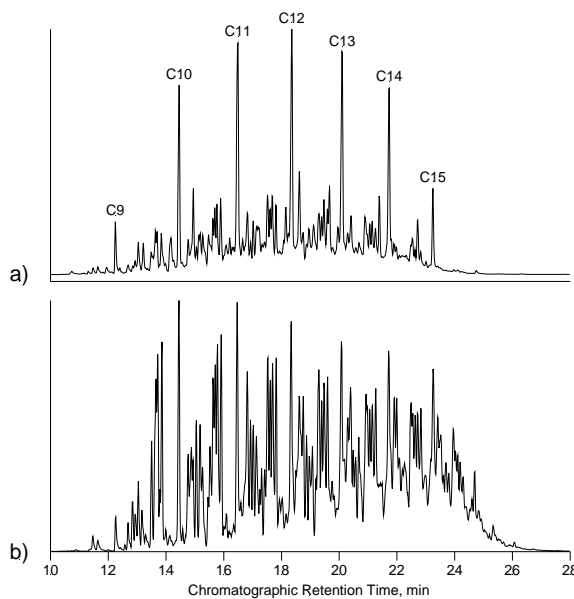


Figure 1. Example Chromatograms of a typical JP-8 (a) and an FT fuel produced with a boiling range comparable to JP-8 (b).

In early 2006 plans were put into motion to initiate a series of ground and flight tests with a semi-synthetic fuel consisting of a blend of 50% JP fuel with 50% FT fuel and information was needed very early in this process to provide guidance as to the potential for problems with the polymeric seals. To address this need the statistical approach described below was developed to determine the degree of comparability (and by extension infer a degree of compatibility) between JP-8 and this 50% JP-8/FT fuel blend.

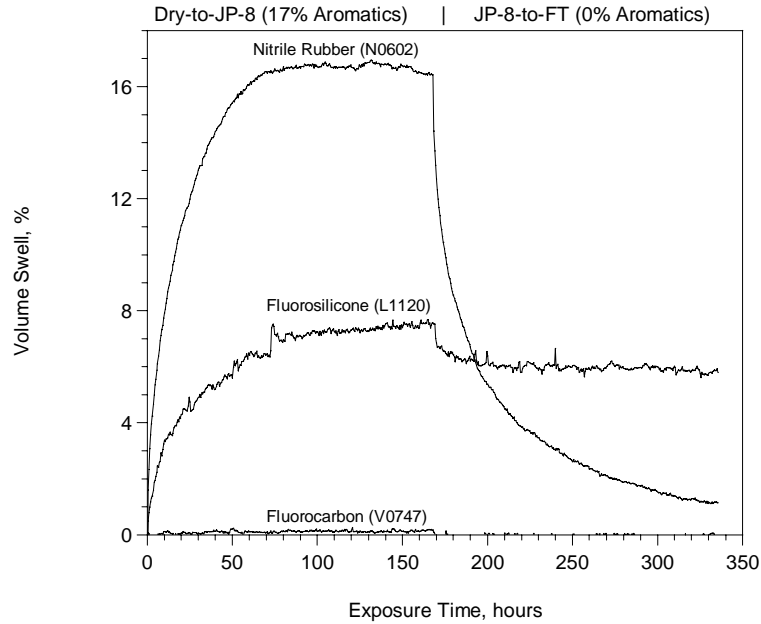


Figure 2. Volume swell as a function of time for three different O-ring materials aged in a typical JP-8, then switched to an FT fuel with a comparable boiling range.

III. Experimental Approach

A. Materials

The materials used in this study included 4 O-ring and 6 sealants as listed in Table 1. The O-ring samples (Parker-Hannifin, Lexington, KY) were size -001 (0.74 mm I.D. 1.02 mm D.) and used as-received. The sealant samples were cut into small squares (3 mm by 3 mm by 1 mm) from sheets prepared as per the respective manufacturer’s instructions (PRC-DeSoto International, Pittsburg, PA, and Dow Corning, Midland, MI).

Table 1
Seal Materials Selected for Fuel Compatibility Testing

Category	ID	Material
O-rings	N0602	Nitrile Rubber
	L1120	Fluorosilicone
	V0747	Fluorocarbon
	V0835	Fluorocarbon (Low Temperature)
Sealants	PR-1422	Dichromate cured Polysulfide
	PR-1440	Manganese dioxide cured Polysulfide
	PR-1776	Manganese dioxide cured Polysulfide
	PR-1828	Epoxy cured Polythioether
	PR-2911	Polythioether/Polyurethane
	Q4-2817	Fluorosilicone

The fuels used in this study are listed in Table 2. These included an FT fuel produced by Syntroleum Corporation (Tulsa, OK), and 9 JP-8s provided by AFRL/PRTG. Note that POSF(4908) was received from Tinker AFB and POSF(4911) was received from Edwards AFB where the ground and flight tests were performed, respectively. In the data presented below the volume swell for the 50% JP-8/FT blends associated with these fuels is indicated in the figures. JP-8/FT fuel blends were prepared by mixing the appropriate volumes of the JP-8s listed in Table 3 (with the exception of POSF(3773)) with the FT fuel (POSF(4909)) to give a set of fuels with 25%, 37.5%, 50%, and 75% v/v FT fuel.

Table 2
Stock Fuels Selected for Fuel Compatibility Testing

POSF	Aromatics	Notes
4909	0.0%	FT with JP-8 additives ¹
4908	13.6%	Fuel from Tinker AFB ²
3773	15.9%	Not used in blended fuels
4911	16.5%	Fuel from Edwards AFB ³
3694	16.6%	
4177	16.9%	
3166	17.3%	
4751	18.8%	
3804	20.3%	
3602	23.6%	

¹Syntroleum

²Ground tests

³Flight tests

Table 3
Summary of the Analysis of the Volume Swell of the O-ring Samples

ID	Material	Mean Volume Swell		Swelling Coefficient Ks	R2	Overlap 90% P.I.
		0% Arom.	25% Arom.			
N0602	Nitrile Rubber	-1.1%	10.5%	0.465	0.949	57%
L1120	Fluorosilicone	6.5%	8.2%	0.069	0.363	95%
V0747	Fluorocarbon	0.2%	0.3%	0.005	0.141	100%
V0835	Fluorocarbon	0.3%	0.4%	0.002	0.008	100%

B. Volume Swell

The principal measure of the samples' response to exposure to the fuel was volume swell. This was measured using the optical dilatometry system described in Fig. 3. Briefly, this system consisted of a back-lit fuel reservoir fitted with an optical window. The window was designed so that its inner face was immersed in the test fuel to prevent condensation from obscuring the view of the sample resting on the bottom of the reservoir. Mounted above the reservoir was a digital camera which periodically photographed the sample and stored the image on a dedicated desktop computer.

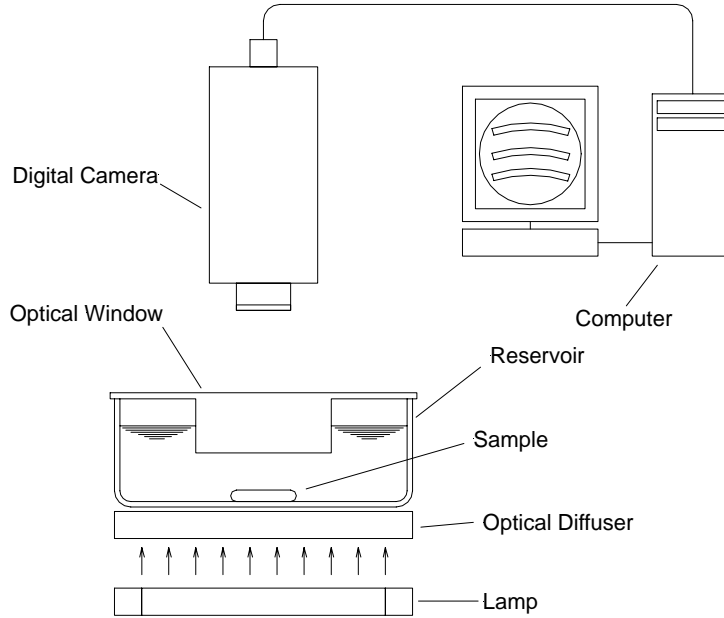


Figure 3. Schematic of the optical dilatometry system used to measure volume swell as a function of time.

For each test the sample was placed in the reservoir which was then filled with 10 mL of fuel and covered the optical window. The sample was then photographed every 15 minutes over the next 16 hours providing a record of the cross sectional area of the sample as a function of time. The cross sectional area was extracted from the digital images using a commercial image processing system (MetaMorph, Universal Imaging Corp.). Assuming isotropic swelling the change in cross sectional area was taken as a characteristic dimension proportional to the change in volume as:

$$\text{Volume Swell} = \left[\left(\frac{A_i}{A_0} \right)^{3/2} - 1 \right] \times 100\% \quad (1)$$

where A_i and A_0 are the cross sectional areas in image i and 0 (the reference image taken at time zero), respectively. The volume swell at the end of the aging period was the value used in the statistical analysis.

C. Statistical Analysis

The primary basis for comparing the sample populations of the volume swell in the neat JP-8s and 50% JP-8/FT fuel blends was the overlap in the 90% prediction intervals;

$$\text{Overlap 90\% Prediction Interval} = \frac{(\text{UL Blend}) - (\text{LL Reference})}{(\text{UL Blend}) - (\text{LL Blend})} \times 100\% \quad (2)$$

where UL and LL denote the upper and lower limit of the 90% prediction intervals, respectively for the JP-8/FT fuel blends and the reference set of JP-8s. The prediction intervals were calculated with a linear fit to the volume swell data using SAS v8.0 (SAS Institute, Raleigh, North Carolina). The concentration range for aromatics in JP-8 was taken as being from 10% to 25% v/v and from 5% to 12.5% v/v for 50% JP-8/FT fuel blends.

In addition to the core analysis of the overlap in the 90% confidence intervals for the neat JP-8s and the 50% v/v JP-8/FT fuel and overall statistical analysis was done on the volume swell as a function of aromatic content using all of the JP-8, FT, and JP-8/FT fuel blends. Specifically, the volume swell from these analyses were fit with a linear model from which the mean volume swell with 0% and 25% v/v aromatics was estimated along with the slope, a value referred to as the swelling coefficient (K_s , % swell/% aromatics), and the coefficient of determination (r^2) which proves a measure of the strength of the correlation between the aromatic content of a fuel and the volume swell.

IV. Results and Discussions

A. Overall Volume Swell Behavior

Before presenting the final results from the volume swell analysis there are two characteristics of the volume swell behavior that are of general interest. Specifically, the time-dependence of the volume swell and the overall affect of diluting a variety of fuels with a single diluent.

Because of the large number of samples in the overall study in which the O-rings and sealants were a part the aging time for each sample was limited to 16 hours. To accelerate the approach to equilibrium very small samples were used which offered relatively high surface area to volume ratios. However, as shown in Fig. 4, the samples actually reached varying degrees of complete volume swell. Specifically, these figures summarize the average time-dependent volume swell for the O-ring and sealant materials, respectively, in the source JP-8s. Although in many cases complete equilibrium was not achieved, the volume swell had proceeded to a point where the relative ranking of the volume swell for each material had been established (for example see Fig. 5). The caution here is that while the data does represent the relative volume swell behavior of each fuel, it does not necessarily reflect the complete equilibrium volume swell.

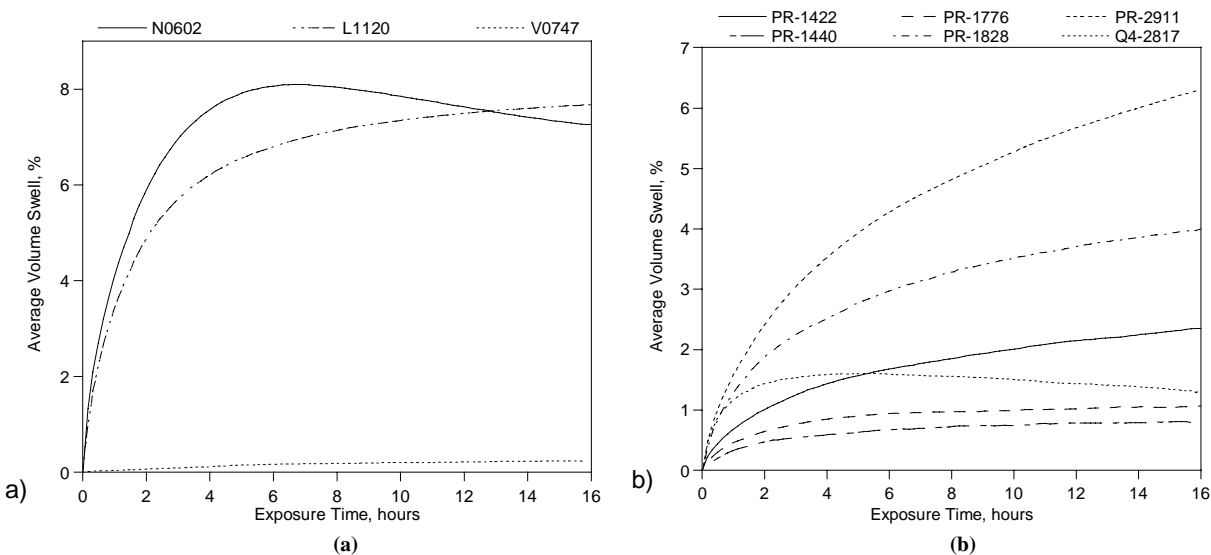


Figure 4. The average volume swell of the O-ring (a) and sealant (b) samples in the source JP-8s.

Another characteristic shown in Fig. 4 is there are two distinctly different volume swell behaviors. The first is a gradual approach to equilibrium such as illustrated by the fluorosilicone O-ring material (L1120 in Fig. 4a) and the manganese dioxide cured polysulfide sealants (PR-1440 and PR-1776 in Fig. 4b). This is very common behavior which shows the gradual absorption of fuel and the accompanying volume swell. The other behavior is an initial rapid increase in volume followed by an gradual loss of volume as illustrated by the nitrile rubber O-ring material (N0602 in Fig. 4a) and the fluorosilicone sealant (Q4-2817 in Fig. 4b). This behavior is common in materials with a significant extractable fraction such as plasticizers, oligomers, or residual solvent. In these materials the initial increase in volume represents the relatively rapid absorption of fuel while the gradual loss of volume represents the

concurrent extraction of components by the fuel. This emphasizes the utility of an in situ, near real-time analytical method such as optical dilatometry.

Another general characteristic of the JP-8/FT fuel blends is summarized by the example volume swell summary for nitrile rubber (N0602) in the source JP-8s and their respective JP-8/FT fuel blends as shown in Fig. 6. Specifically, as described above the aromatic content of JP-8s can vary over a wide range, typically from about 10-25% by volume. Furthermore, the individual species of aromatics can also vary. This results in the source JP-8s having a varying volume swell potential depending on both their overall aromatic content and the specific types of aromatics they contain. However, since these fuels are all being diluted with a single type of fuel with not aromatics the swelling characteristic approaches that of the diluent fuel as the concentration of the JP-8 approaches zero. This causes distribution of volume swell behavior to narrow as the blending ratio of FT fuel increases. The overall effect is the volume swell behavior of JP-8/FT fuel blends tend to lie closer to the mean behavior than the source JP-8s improving the overall compatibility of the JP-8/FT fuel blends in terms of giving a blended fuel that behaves like an average JP-8.

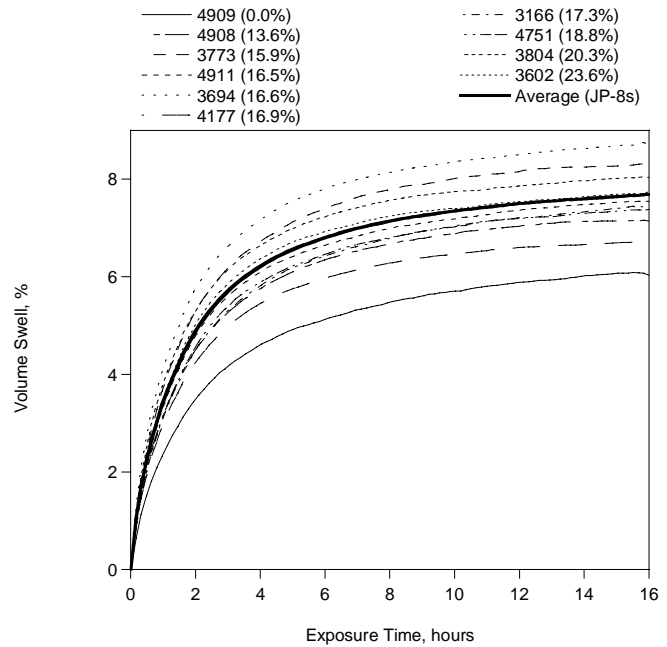


Figure 5. The volume swell of the fluorosilicone O-ring material (L-1120) in the source JP-8s showing that the relative volume swell is established by the end of the aging period.

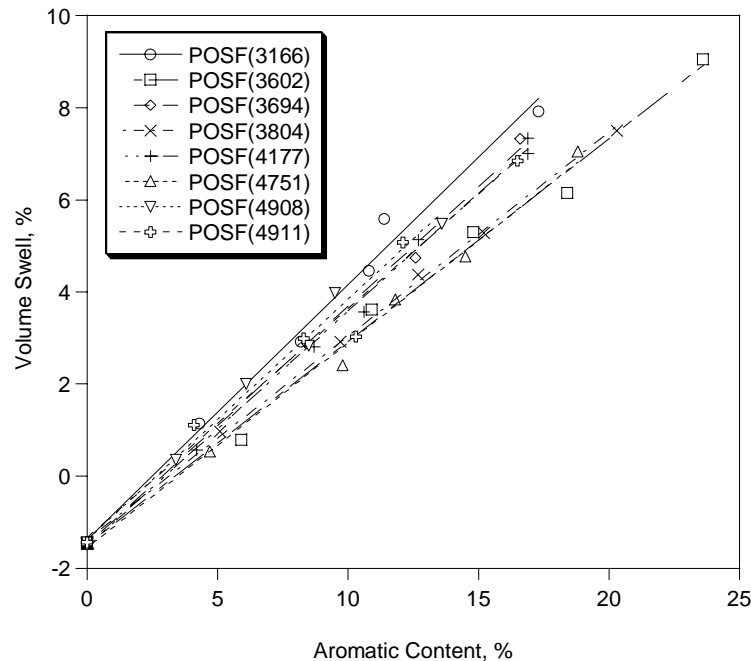


Figure 6. Example volume swell data for the nitrile rubber O-ring material grouped by each source JP-8 showing how the distribution in volume swell behavior approaches the mean as the blending ratio increases.

B. O-rings

The volume swell results for the four O-ring materials are summarized in Fig. 7 through 10 and Table 3. Comparing these results shows that nitrile rubber has the highest mean swelling coefficient (0.465%/%) and coefficient of determination (0.949) and the lowest overlap in the 90% prediction intervals (57%). The nitrile rubber also shrank slightly (-1.1%) in the neat FT fuel, a fact attributed to the relatively high plasticizer loading of this material (10.1% as measured by thermogravimetric analysis). Interestingly, the fluorosilicone showed considerable volume swell even in the neat FT fuel (6.5%) with a comparably lower mean swelling coefficient (0.069%/%) and a very low coefficient of determination (0.363) resulting in a nearly complete overlap in the 90% prediction intervals (95%). This behavior indicates a material with moderate fuel resistance and no plasticizer. The fluorocarbon materials, V0747 and V0835, respectively, showed the greatest fuel resistance with very low mean swelling coefficients (0.005%/% and 0.002%/%) and coefficients of determination (0.141 and 0.008) and a complete overlap in the 90% prediction intervals (100%).

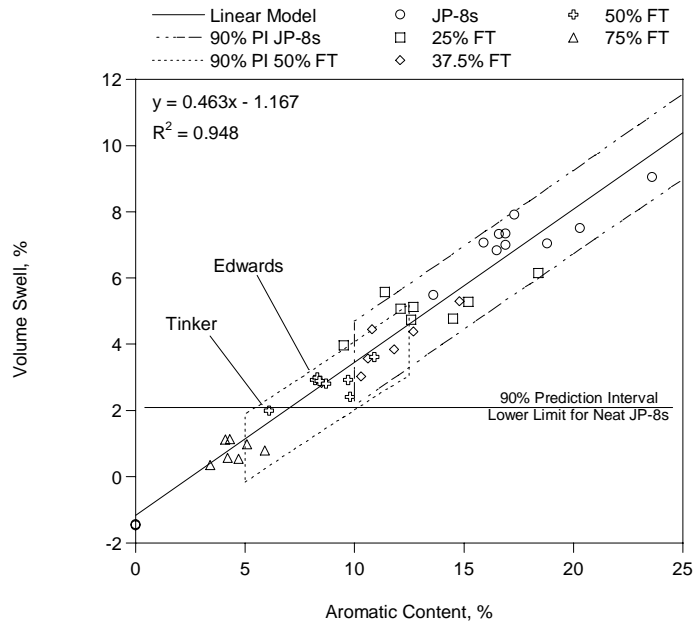


Figure 7. Summary of the volume swell data for nitrile rubber O-rings (N0602).

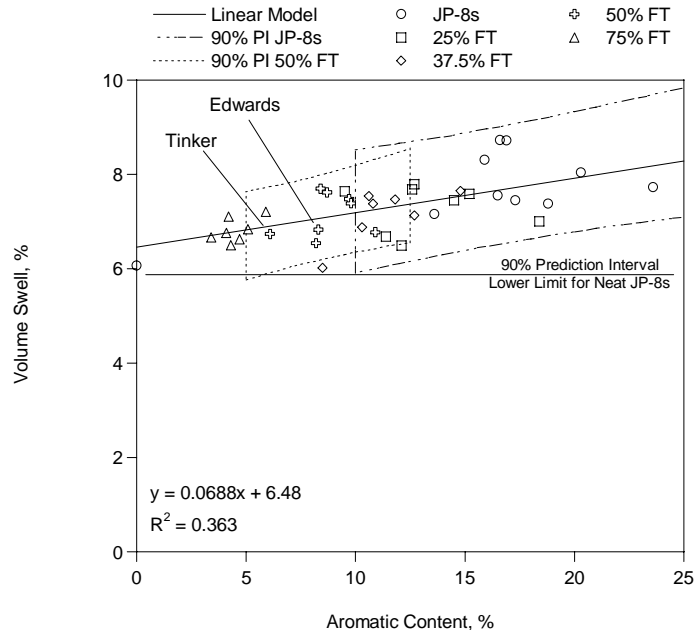


Figure 8. Summary of the volume swell data for fluorosilicone O-rings (L1120).

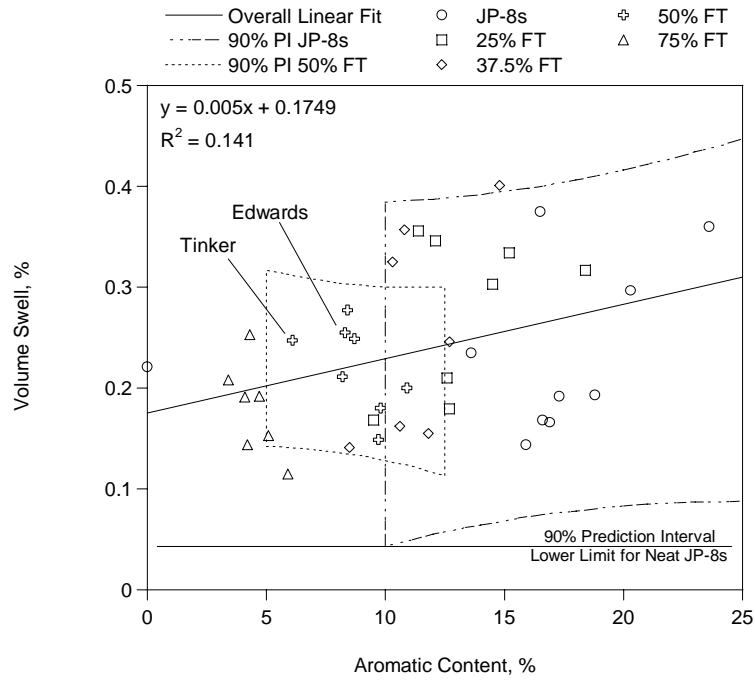


Figure 9. Summary of the volume swell data for fluorocarbon O-rings (V0747).

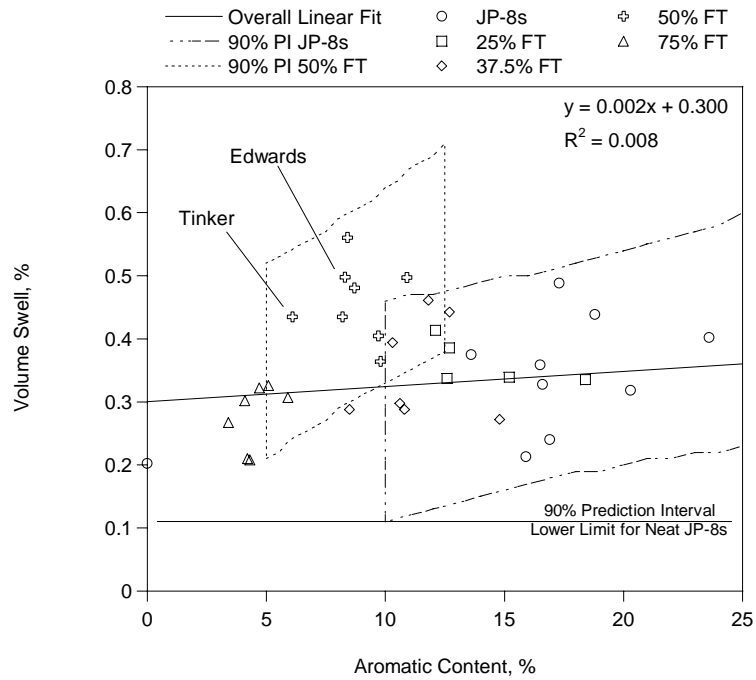


Figure 10. Summary of the volume swell data for fluorocarbon O-rings (V0835).

These results illustrate that among these O-ring materials the greatest concern with respect to compatibility with the 50% JP-8/FT fuel blends would be with nitrile rubber. However, even in this worst-case material this study indicates that in an arbitrarily selected 50% JP-8/FT fuel blend there is a 57% chance that the volume swell of nitrile rubber O-rings will be within the 'normal' range for JP-8s.

C. Sealants

The volume swell results for the four O-ring materials are summarized in Fig. 11 through 16 and Table 4. Comparing these results shows that the three polysulfide materials (PR-1422, PR-1440, and PR-1776) had intermediate performance with respect to their swelling coefficients (0.101%/%, 0.077%/%, and 0.094%/%), coefficients of determination (0.744, 0.795, and 0.871) and overlap in the 90% prediction intervals (83%, 84%, and 75%). The epoxy cured polythioether (PR-1828) showed a larger swelling coefficient (0.181%/%), a moderate coefficient of determination (0.780), and the highest overlap in the 90% prediction intervals among the sealants (90%). The polythioether/polyurethane (PR-2911) proved to be the least fuel resistant of the sealants with the highest swelling coefficient (0.206%/%), a moderate coefficient of determination (0.782), and the lowest overlap in the 90% prediction intervals (61%). The fluorosilicone (Q4-2817) was one of the more fuel resistant sealants with the lowest swelling coefficient (0.052%/%), the lowest coefficient of determination (0.419), and a one of the lowest overlaps in the 90% prediction intervals (69%).

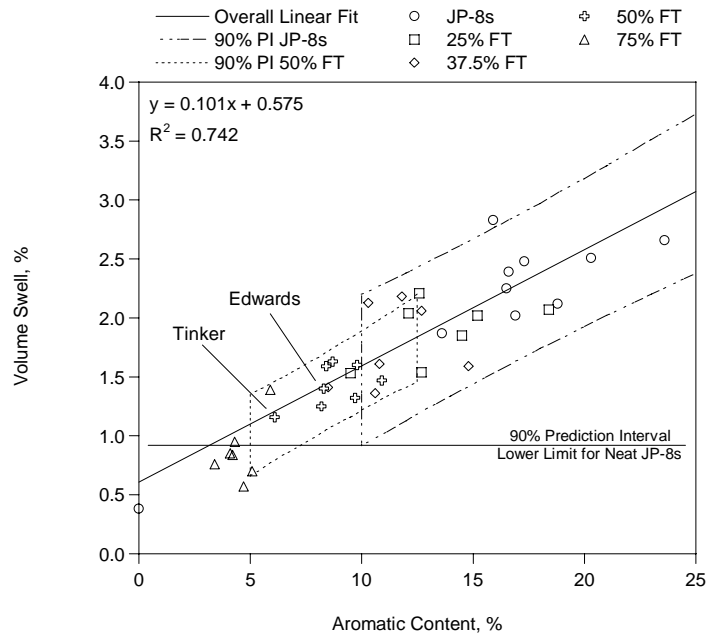


Figure 11. Summary of the volume swell data for the dichromate cured polysulfide sealant (PR-1422).

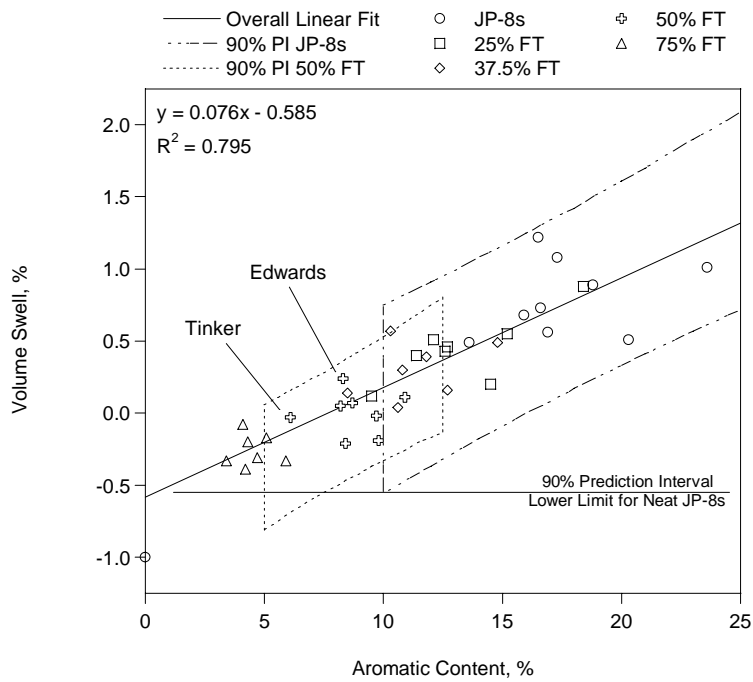


Figure 12. Summary of the volume swell data for the manganese dioxide cured polysulfide sealant (PR-1440).

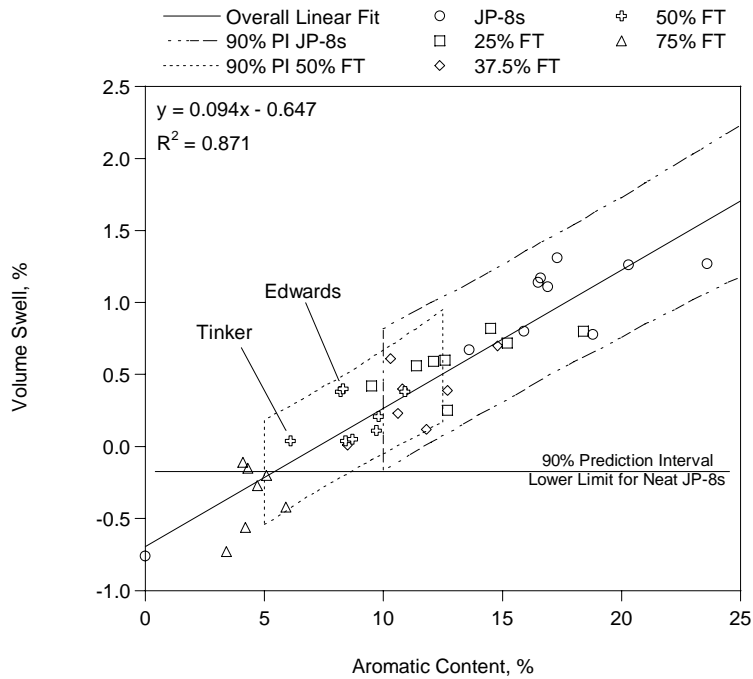


Figure 13. Summary of the volume swell data for the manganese dioxide cured polysulfide sealant (PR-1776).

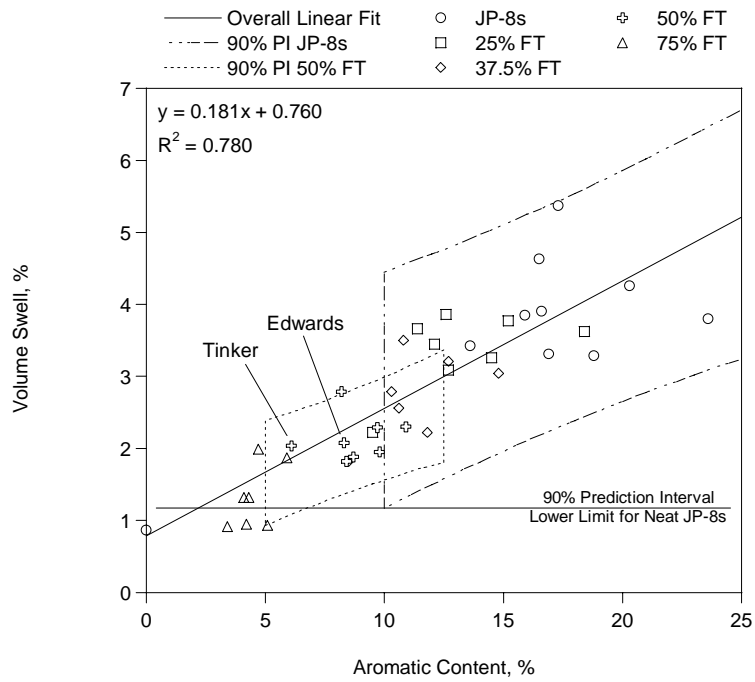


Figure 14. Summary of the volume swell data for the epoxy cured polythioether sealant (PR-1828).

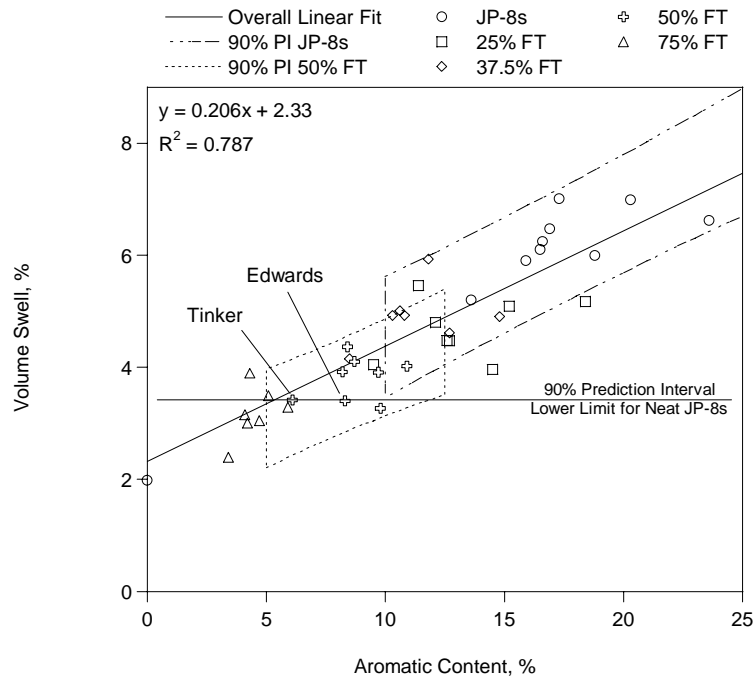


Figure 15. Summary of the volume swell data for the polythioether/polyurethane sealant (PR-2911).

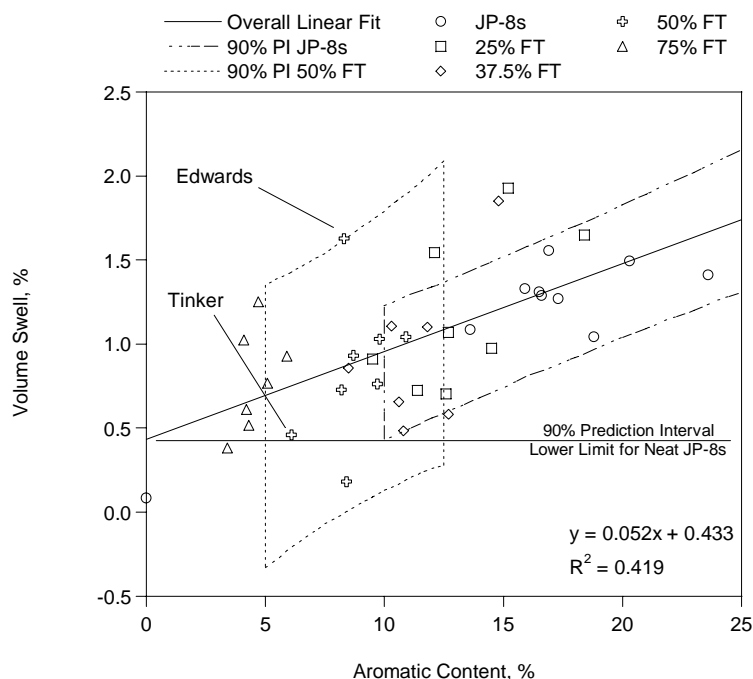


Figure 16. Summary of the volume swell data for the fluorosilicone sealant (Q4-2817).

Table 4
Summary of the Analysis of the Volume Swell of the Sealants

ID	Material	Mean Volume Swell		Swelling Coefficient Ks	R2	Overlap 90% P.I.
		0% Arom.	25% Arom.			
PR-1422	Dichromate cured Polysulfide	0.6%	3.1%	0.101	0.744	83%
PR-1440	MnO2 cured Polysulfide	-0.6%	1.3%	0.076	0.795	84%
PR-1776	MnO2 cured Polysulfide	-0.6%	1.7%	0.094	0.871	75%
PR-1828	Epoxy cured Polythioether	0.8%	5.3%	0.181	0.780	90%
PR-2911	Polythioether/Polyurethane	2.3%	7.5%	0.206	0.787	61%
Q4-2817	Fluorosilicone	0.4%	1.7%	0.052	0.419	69%

These results illustrate that the sealants showed more moderate volume swell behavior than the O-rings. This could be a result of differences in the way these materials are cured. Specifically, O-rings are cured during manufacture which may give a more consistent product whereas sealants are cured in-place possibly under less controlled conditions leading to a less consistent final product. However, even in the worst-case material among the sealants evaluated here, the polythioether/polyurethane (PR-2911), and the results of this study indicates that in an arbitrarily selected 50% JP-8/FT fuel blend there is a 61% chance that the volume swell of this material will be within the 'normal' range for JP-8s.

V. Conclusion

With respect to O-ring seals, this study indicates that the material most likely to show excessive shrinkage upon switching from JP-8 to a 50% JP-8/FT fuel blend is nitrile rubber. However, even with this worst-case material the data reported here indicates that 57% of all arbitrarily selected 50% JP-8/FT fuel blends will show volume swell character that is within the normal range of low-aromatic JP-8s (fuels with at least 10% v/v aromatics). Furthermore, nearly all fluorosilicone and fluorocarbon O-rings would exhibit volume swell that is within the range of low-aromatic JP-8s. Similarly, the worst-case sealant, the polythioether/polyurethane, 61% would be expected to exhibit volume swell behavior comparable to that in low-aromatic JP-8s. Given that in all cases more than 50% of the volume swell behavior is expected to be within the bounds currently being experienced with low-aromatic JP-8s it was concluded that the chances of an acute failure of O-ring seals and sealants with a 50% JP-8/FT fuel blend was low and there was no compelling evidence in the data that there was a significant likelihood of an acute sealing failure resulting from the use of this blend.

Acknowledgements

We would like to thank the National Energy Technology Laboratory (NETL), Department of Energy Contract #DE-AI26-01NT41110, Bonnie Dowdell Contract Monitor, for their funding support to co-sponsor this effort.

References

- ¹Davis, B.H., "Overview of Reactors for Liquid Phase Fischer-Tropsch Synthesis," *Catalysis Today*, Vol. 71, 2002, pp. 249-300.
- ²Moses, C.A., Valtierra, M.L., "Impact Study of Synthetic and Alternative Fuel Usage in Army Aircraft Propulsion Systems," Final Report, SRWI-MED-134, Cont. No. N00140-80-C-2269, 1981.
- ³MIL-P-5315B, "Packing, Preformed, Hydrocarbon Fuel Resistant," ASSIST [online database] URL: <http://assist.daps.dla.mil/online/start/>, [cited 1 May 2007].
- ⁴Bacha, J., Barnes, F., Franklin, M., Gibbs, L., Hemighaus, G., Hogue, N., Lesnini, D., Lind, J., Maybury, J., and Morris, J.; *Aviation Fuels Technical Review*, Chevron Products Company, Houston, TX, 2000.
- ⁵Sombatsompop, N., Christodoulou, K.J., "Penetration of Aromatic Hydrocarbons into Natural Rubber," *Polymers and Polymer Composites*, Vol. 5 (5), pp. 377-386, 1997.
- ⁶Mathai, A.E., Singh, R.P., Thomas, S., "Transport of Substituted Benzenes through Nitrile Rubber/Natural Rubber Blend Membranes," *Journal of Membrane Science*, Vol. 202, 2002, pp. 35-54.
- ⁷Graham, J.L., Striebich, R.C., Myers, K.J., Minus, D.K., Harrison, W.E., "Swelling of Nitrile Rubber by Selected Aromatics Blended in a Synthetic Jet Fuel," *Energy & Fuels*, Vol. 20, No. 2, 15 March 2006, pp. 759-765.

APPENDIX B

Effects of a Reacting Cross-Stream on Turbine Film Cooling

INTENTIONALLY LEFT BLANK

Effects of a Reacting Cross-Stream on Turbine Film Cooling

Wesly S. Anderson

Marc D. Polanka

Joseph Zelina

Air Force Research Laboratory,
Propulsion Directorate,
Wright Patterson AFB,
Dayton, OH 45433

Dave S. Evans

Naval Air Systems Command,
NAS,
Patuxent River, MD 20670

Scott D. Stouffer

Garth R. Justinger

University of Dayton Research Institute,
Dayton, OH 45469

Film cooling plays a critical role in providing effective thermal protection to components in modern gas turbine engines. A significant effort has been undertaken over the last 40 years to improve the distribution of coolant and to ensure that the airfoil is protected by this coolant from the hot gases in the freestream. This film, under conditions with high fuel-air ratios, may actually be detrimental to the underlying metal. The presence of unburned fuel from an upstream combustor may interact with this oxygen rich film coolant jet resulting in secondary combustion. The completion of the reactions can increase the gas temperature locally resulting in higher heat transfer to the airfoil directly along the path line of the film coolant jet. This secondary combustion could damage the turbine blade, resulting in costly repair, reduction in turbine life, or even engine failure. However, knowledge of film cooling in a reactive flow is very limited. The current study explores the interaction of cooling flow from typical cooling holes with the exhaust of a fuel-rich well-stirred reactor operating at high temperatures over a flat plate. Surface temperatures, heat flux, and heat transfer coefficients are calculated for a variety of reactor fuel-to-air ratios, cooling hole geometries, and blowing ratios. Emphasis is placed on the difference between a normal cylindrical hole, an inclined cylindrical hole, and a fan-shaped cooling hole. When both air and nitrogen are injected through the cooling holes, the changes in surface temperature can be directly correlated with the presence of the reaction. Photographs of the localized burning are presented to verify the extent and locations of the reaction. [DOI: 10.1115/1.3204616]

1 Introduction

Film cooling is the primary means of maintaining turbine surface temperatures below the critical melting temperature. The most common cooling hole configurations are normal cylindrical holes, angled cylindrical holes, and fan-shaped holes. Countless studies have been conducted over the past forty years that have investigated the merits of different cooling schemes under nearly all conditions encountered in a turbine. A review article by Bogard and Thole [1] addresses many of the relevant issues. The impact of the inclination angle was studied by Baldauf et al. [2] revealing that at low blowing ratios the angled holes exhibit better performance because the coolant flow remains attached to the surface over a longer distance. At the higher blowing ratios, the relative differences between normal and angled holes diminish and the normal holes can be more effective. The relative benefits of cylindrical, fan-shaped, and laidback fan-shaped holes were also studied by Saumweber et al. [3]. The laidback fan-shaped hole ejects more coolant flow at a lower blowing ratio. Because of the increasing area of the hole near the exit, this configuration also reduces the tendency of the jet to separate. These benefits associated with shaping are dramatic, particularly at high blowing ratios, resulting in higher effectiveness.

One area that has not been investigated thoroughly is the impact of combustion gases on the film cooling process. Historically, the combustion sections of gas turbine engines operated at overall equivalence ratios (Φ) much less than one [4]. Additionally, a relatively long flow path within the combustor (in the order of 25–50 cm) compared with chemical and mixing times ensured that reactions were complete before leaving the combustor. Therefore, no unburned species enter the turbine and subsequently little concern has been expressed in literature. Recently, however, the desire to increase performance has led to the development of com-

burners that operate at a Φ much closer to one. With these designs, the chance of fuel-rich streaks entering the turbine increases. At the same time, advanced combustors are being designed more compact to increase the thrust to weight ratio [5]. One such design is the ultracompact combustor/interturbine burner (UCC/ITB) currently being developed at the Air Force Research Laboratories (AFRL) [5,6]. Figure 1 contains images of a conventional annular combustor (left) and the UCC (right). This concept directs the flow of combustion air into a circumferential cavity for providing sufficient residence times while at the same time reducing the axial length of the component. Fuel is injected into this cavity, where combustion occurs in a fuel-rich regime [5]. The flow is then entrained into a radial cavity that is integrated with the vane. Because of the close proximity, the gases in this cavity still contain intermediate combustion products.

The possibility of unburned fuel entering the turbine, therefore, can no longer be ignored. The primary location where the fuel can find an oxygen rich stream to complete the reaction is at the film cooling hole. The chances of reactions occurring in the turbine vastly increase. When the unburned fuel mixes with oxygen rich compressor bleed air in the turbine cooling film, the conditions become conducive for burning in the turbine. Heat release in the cooling film, whether it results from the recombination of dissociated species or from the combustion of unburned fuel, would drastically reduce the cooling effectiveness of the turbine cooling scheme with potentially severe effects on engine component durability. The challenges presented by this design require a fuller understanding of the interaction between turbine cooling films and incomplete combustion products as well as the relationship between boundary layer reactions and turbine durability.

The potential effect of heat release in the turbine was studied by Lukachko et al. [7] who found that the potential local temperature rise depends strongly on the amount of chemical energy remaining in the flow. The research showed that the local temperature increase in a flow simulating a fuel streak in a future combustor at a stoichiometric fuel-to-air ratio could become large and potentially

Manuscript received March 23, 2009; final manuscript received June 2, 2009; published online March 3, 2010. Review conducted by Dilip R. Ballal.

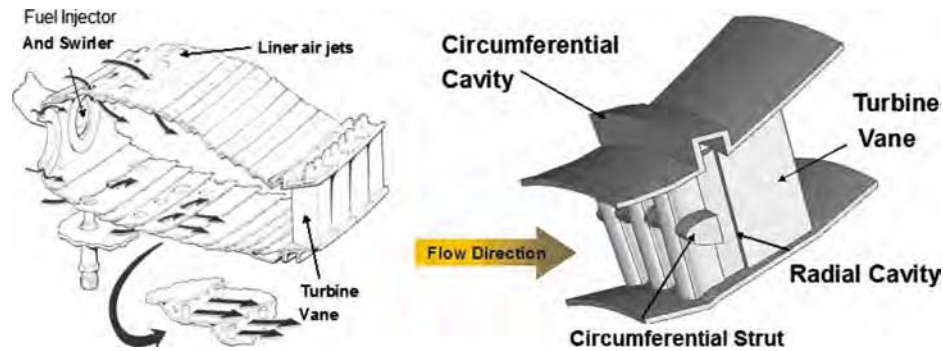


Fig. 1 Conventional axial combustor (left) and ultracompact combustor (right) [5]

catastrophic. In a subsequent effort by Kirk et al. [8], a series of shock tube experiments were conducted that examined the impact of near wall reactions in a cooling film. Their experimental setup allowed concurrent heat flux measurements for a reacting (air) coolant flow and a nonreacting (N_2) coolant flow through a 35 deg injection angle into a freestream mixture of ethylene and argon. Blowing ratios in the test ranged from 0.5 to 2.0, for a range of unburned fuel concentrations. Their research showed that at high concentrations of unburned fuel, as much as a 30% increase in heat flux may occur. At moderate CO concentrations, the increase reaches approximately 10%. At low concentrations, the difference between reacting and nonreacting flows is insignificant. The objective of the present research is to explore the effect of reactions on turbine film cooling. Specifically, the impact of blowing ratio, equivalence ratio, and cooling hole shape on the occurrence of heat release on a flat plate geometry are quantified. A well-stirred reactor (WSR) was employed to provide a well characterized source of combustion products utilizing propane as a fuel source. Propane was chosen due to its similar heat release as liquid jet fuel while being more chemically accurate to the molecular weight of the species expected to be present within the turbine section. This research will serve as an incremental step toward understanding the physics of reacting boundary layers as they relate to compact combustion systems such as the UCC, where the turbine vane is integrated into the combustor design. The ultimate goal of this program is to provide a sufficient understanding for the development of turbine cooling schemes that will enable the application of the UCC/ITB to future systems.

2 Experimental Setup

A WSR, as developed by Nenniger et al. [9] and modified by Zelina and co-workers [10–12], was used to simulate the turbine entry conditions of a notional combustor. In a WSR, a high rate of mixing of products and incoming reactants is induced, which results in a very nearly uniform distribution of temperature and species within the reactor and at the exit. Because of the uniformity of the flow at the exit, it is possible to assume a uniform species and temperature distribution at a given distance within the test section. The mass flow rate and Φ into the reactor were controlled by thermal mass flow controllers.

The reactor is composed primarily of two toroidal half sections of cast zirconia-oxide ceramic, an Inconel® jet ring, and a metal housing. A schematic of the WSR is shown in Fig. 2. Premixed air and fuel is fed through the fuel-air tubes into the jet ring, into the jet ring manifold, and through 48 fuel-air jets into the reactor toroid. The two toroidal half sections fit together on the top and bottom of the jet ring, forming a 250 ml internal volume. Once in the reactor, the fuel-air mixture reacts and then exits through eight exhaust ports. The flow then enters a common exhaust section, which turns the flow upwards into the test section. A temperature limit of 1970 K restricted the use of the reactor at equivalence ratios close to one at the high overall air flow rates that were

desired to match the inlet Reynolds number. A gas sample was fed from the WSR to a standard emissions test bench for characterization of gas concentrations. CO_2 and CO were measured with a California Analytical Instruments Fourier transform infrared (FTIR) analyzer. O_2 was measured with a Horiba magnetopneumatic analyzer.

From the WSR the exhaust flowed upwards through a shaped ceramic chimney, over a forward facing step that served as a turbulent trip, and into the test section. The test section consisted of a thick flat plate base that was enclosed by three quartz window side walls. Slots were machined in the piece to allow for the insertion of two cooling air assemblies and four heat transfer gauge assemblies. Each of these assemblies was inserted through the back of plate with their surfaces flush with the surface of the plate.

The cooling air assemblies were made up of the cooling hole slot inserts and the plena. The cooling air or nitrogen was fed to the plena from the facility supply. In the plena, the cooling air temperature and pressure were measured. The plena were attached to the cooling hole inserts and sealed with a high temperature adhesive sealant. Thermocouples were inserted to a location 5.1 mm from the outside surface of the cooling hole inserts. The cooling air assemblies were inserted through the back of the flat plate. The cooling hole geometries were machined into the surface of the inserts. Three film cooling configurations were tested as part of this study: normal holes, angled holes, and fan-shaped laidback holes (Fig. 3). All the holes were 0.51 mm in diameter. The normal holes had a length to diameter ratio (L/D) of 5. The spacing between the holes was 3.81 mm.

The angled holes were machined at an angle of 30 deg to the surface. To maintain a L/D of 5, the surface was thinner. The fan-shaped laidback holes were based on the angled hole geometry, being equal in size, angle, and depth. However, at the surface

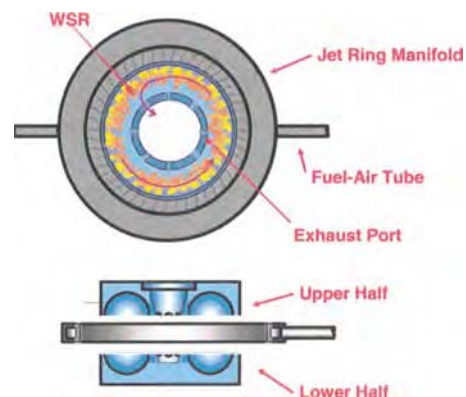


Fig. 2 WSR schematic, modified from Stouffer [12]

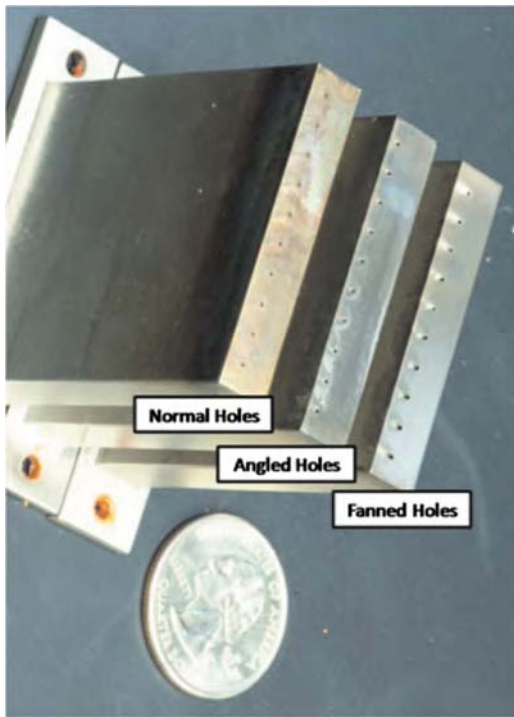


Fig. 3 Cooling insert geometries

that sees the flow, the sides of the hole flared out 10 deg and lay back 10 deg and provided an exit hole length of 0.91 mm on the surface.

In the current study, the heat transfer to the surface is utilized to determine the amount of heat release in the film. The heat transfer is calculated from measurements of two thermocouples embedded in instrumentation blocks downstream of the film cooling holes. The upper gauge was located 3.8 mm from the surface of the block. A second thermocouple was inserted through the bottom of the block to a depth of 19.1 mm from the surface. This provided a known distance between these thermocouples (15.3 mm). The conductivity of the Hastelloy-X[®] was determined locally by utilizing a linearization of the conductivity of Hastelloy-X[®] as a function of temperature from the manufacturer's material property data sheets. With these parameters being known, the heat flux can be determined directly from Fourier's Law. Steady, one dimensional conduction was confirmed by analyzing a typical set of boundary conditions with an ANSYS thermal conduction solver. Within the instrumentation blocks the temperature was determined to be nearly one dimensional. Based on this result, the surface temperature was extrapolated using the embedded measurements and the calculated heat transfer. Four instrumentation blocks were installed, two at nominally 20 hole diameters downstream of the film coolant hole and the other two at approximately 75 diameters downstream. The surface of the flat plate with all inserts installed is shown in Fig. 4. Also shown in this figure is the location of the film cooling row of 11 holes and the location of a second, upstream, film cooling port that was intended to simulate an upstream coolant row that will be used in future tests. What was not shown in Fig. 4 is a trip strip that was installed at the leading edge (bottom of the picture) of the plate to ensure a turbulent boundary layer at the film cooling hole location.

One necessary addition to the test section was water channels to maintain the entire film cooled surface below the melting temperature of the material. A simple heat balance calculation indicated that the Hastelloy-X[®] would achieve a surface temperature of 1600 K without active cooling. Because of the uncooled leading edge section and the desire to run at low coolant flow rates, it was necessary to water cool this surface. As shown in Fig. 4, a

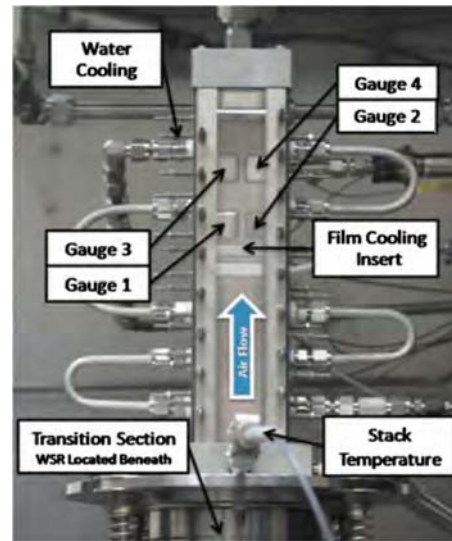


Fig. 4 Flat plate heat transfer gauge and cooling hole insert location

five pass water circuit was included. To maintain a one-dimensional temperature profile in the area of interest, the wall thickness was 5.1 cm and the circuits were 6.4 mm in diameter and installed about 13 mm from the bottom of the flat plate. The impact of the water circuit was investigated by Evans et al. [13]. The water circuit controlled the temperatures between 850 K on the hot surface and 450 K at the deep thermocouple location.

For a comparison with the current literature it was beneficial to calculate the heat transfer coefficient in the presence of film cooling h_f . The traditional means of determining h_f in a film cooling layer would be with the use of Eq. (1) where T_f is the driving temperature for the heat transfer and is the temperature of the film located adjacent to the surface and T_s is the temperature of the surface.

$$q'' = h_f(T_f - T_s) \quad (1)$$

It is a goal of this program to be able to experimentally measure T_f locally above the surface with the use of laser diagnostics, but at the current time T_f has not been measured. Therefore, Eq. (1) is modified with T_∞ as the reference temperature, and h_f is replaced with the effective heat transfer coefficient, h_{eff} . This effective heat transfer coefficient will therefore take into account changes locally of the film temperature due to heat release as this cannot currently be separated. Equation (2) is the form of the convective heat transfer equation used in the analysis of the results of this study.

$$q'' = h_{\text{eff}}(T_\infty - T_s) \quad (2)$$

Many fluid mechanical factors influence the film cooling behavior. The current study explores a number of these in addition to the chemistry of the flow: blowing ratio, injection angle, and hole shape. The blowing ratio M , also referred to as the mass flux ratio, is given in Eq. (3) as a ratio of densities and velocities.

$$M = \frac{\rho_c U_c}{\rho_\infty U_\infty} \quad (3)$$

The calculation of M directly from Eq. (3) requires precise knowledge of the density of the gases. The determination of this property in reacting systems is imprecise. Therefore, M was calculated in this experiment using the conservation of mass for a constant area flow in an incompressible fluid for both coolant flow and reactor exhaust flow. This yields the following:

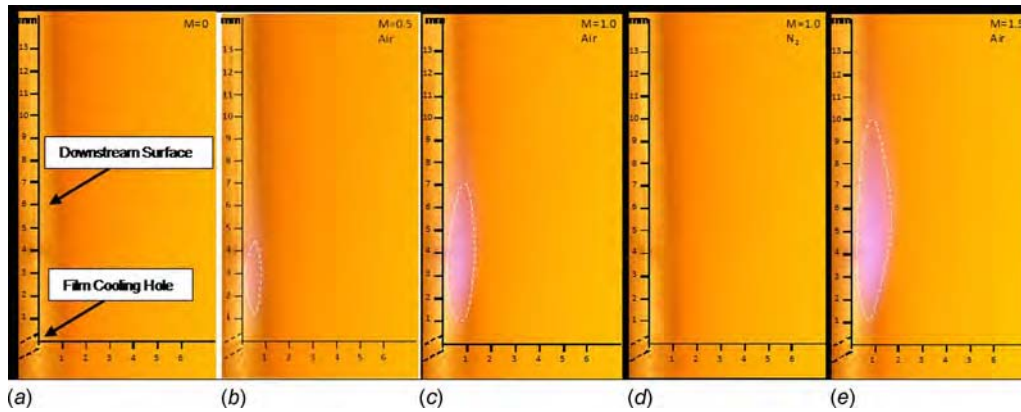


Fig. 5 Angled hole visible burning for (a) $M=0$, (b) $M=0.5$, air, (c) $M=1.0$, air, (d) $M=1.0$, N_2 , and (e) $M=1.5$, air

$$M = \frac{\dot{m}_{c,\text{total}} A_\infty}{\dot{m}_\infty A_{c,\text{total}}} \quad (4)$$

Here, $\dot{m}_{c,\text{total}}$ is the total mass flow of the coolant through all cooling holes, $A_{c,\text{total}}$ is the metered area of all cooling holes, A_∞ is the cross-sectional area of the test rig, and \dot{m}_∞ is the mass flow of the reactor exhaust, equaling the sum of \dot{m}_{fuel} and \dot{m}_{air} .

The ratio of \dot{m}_{fuel} to \dot{m}_{air} is the fuel-air ratio. This ratio compared with the value at the stoichiometric condition is the equivalence ratio. This ratio is given as

$$\Phi = \frac{\left(\frac{\dot{m}_{\text{fuel}}}{\dot{m}_{\text{air}}} \right)}{\left(\frac{\dot{m}_{\text{fuel}}}{\dot{m}_{\text{air}}} \right)_{\text{stoich}}} \quad (5)$$

where the stoichiometric value of the fuel-air ratio is 0.06395 for propane. With this definition, a Φ greater than one would be fuel-rich and, conversely, a Φ less than one would be fuel lean. More details of the measurements and calculations can be found in Evans et al. [13].

3 Results

An extensive test matrix was built to understand the impact of heat release on a film cooled surface. This matrix focused on investigating the three typical film cooling hole arrangements shown in Fig. 3. For each of these test plates, a series of experiments was performed with both nitrogen as the film coolant and then with air ejecting from the holes. A sequence of blowing ratios was established covering $M=0, 0.5, 1.0, 1.5$, and 2.0 . Each test configuration was performed at equivalence ratios of $0.6, 0.8, 1.5, 1.6$, and 1.7 at a relatively high air flow of 1020 g/min . This set the freestream velocity to be 34 m/s , which correlated with a freestream Reynolds number of about $60,000$ based on the channel height or 600 based on the hole diameter. Equivalence ratios closer to 1.0 could not be achieved at this air flow rate because of the resultant WSR and stack exit temperature being too high. The materials used in the reactor were not capable of withstanding these higher temperatures. Therefore, a few cases were performed at equivalence ratio of 0.8 and 0.95 at lower air flows of 720 g/min and 480 g/min . These lower air flows were also repeated at the $\Phi=1.5$ condition to permit comparison. A previous effort, Evans et al. [13], provides the impact of main airflow on the results.

In performing these tests, a prominent white flame was evident just downstream of the coolant holes for the higher equivalence ratios. The flame was not present for any condition of Φ less than 1.0 . While readily visible to the naked eye, it was somewhat challenging to capture digitally mainly because of the viewing angle

and the amount of light saturating the camera. The photographs were taken from the side of the rig with the field of view restricted to the area immediately around the cooling holes. One good set of images was captured in Fig. 5 for the angled hole case at a $\Phi = 1.5$ showing the differences between the blowing ratio of $0, 0.5, 1.0$, and 1.5 for the air flow and the stark contrast at $M=1.0$ for the nitrogen coolant flow. As the coolant jet met and mixed with the reactor exhaust flow, local combustion occurred. The combustion is visible as a white plume emanating from the coolant hole and progressing downstream.

These photographs demonstrate that boundary layer reactions can occur in fuel-rich conditions as a result of the introduction of air from cooling holes. The reactions happen in close proximity to the surface and cause significant heat transfer to the surface in the immediate vicinity of the cooling holes. This visual evidence is proof of the cause for the heat transfer augmentation that will follow and is discerning to the turbine cooling designer. Instead of the film cooling flow serving to maintain the airfoil surface below a specific temperature, this oxygen rich flow is serving as a flame holder for any remaining combustion products to reach completion. As shown for this fuel-rich condition, as the blowing ratio is increased, the amount of burning is also increased. One small benefit is that for these angled holes at the higher blowing ratio, the jet itself is lifted off the surface. Therefore, the highest temperatures are achieved away from the airfoil surface.

While the photographs of the visible flame provide qualitative proof of what was occurring in the flowfield, the measurements of temperature within the block and the subsequent reduction in heat flux provided the quantitative impact of that flame. The primary comparison made was a relative comparison between the air coolant flow and the nitrogen coolant flow. These two conditions were always obtained on the same day of testing for each configuration and the order was often alternated as the blowing ratio was varied to ensure that the trends were consistent. Also a given blowing ratio was occasionally repeated later in the test program to verify that the facility was not changing throughout the testing window. This was done for a number of reasons, the most significant was that the two set of blocks on either side of the rig often produced results with a substantial side to side variation. That is while the changes between gauges 1 and 3 were consistent with the changes between gauges 2 and 4 within approximately 5 K , gauge 1 could be higher or lower than block 2 by 20 K or more for a given test day or period within a test. It was thought that some residual variation within the well-stirred reactor occurred because of some localized plugging of some of the feed holes that caused different flow to the different areas of the rig. Over the course of a test window, the characteristics of this distribution could change. Laser diagnostics are planned to further quantify these localized variations in the inlet condition.

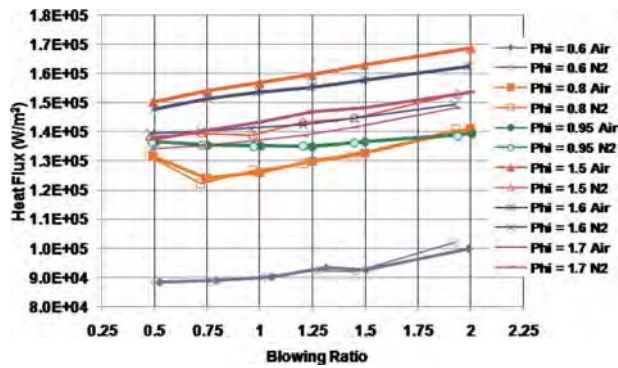


Fig. 6 Angled hole heat flux as a function of equivalence ratio and coolant gas at $x/D=20$

What was ultimately verified was that the side to side trend in the blocks held true throughout when the results for air were compared with those for nitrogen. An uncertainty of about 1% was measured in surface temperature and subsequent heat flux between repeat points within a test period. A greater variation of closer to 5% occurred in an individual surface temperature with about a 4% change in the resultant heat flux when trying to re-establish the same condition on a different day. This was often due to changes in the WSR exit stack temperature and or the coolant exit temperature, which were both difficult to control day to day. However the difference between the air results and the nitrogen results was consistent, with variation within 2%. To account for some of the overall variation, the results presented in the following figures are mean values of measurements for gauges 1 and 2 for the 20 D location and between gauges 3 and 4 for the 75 D location.

The heat flux for the three cooling hole arrangements at an $x/D=20$ is provided in Figs. 6–8. In Fig. 6 the angled hole results are shown for Φ of 0.6, 0.8, 0.95, 1.5, 1.6, and 1.7. It is noted that the $\Phi=0.95$ data were obtained at a lower overall airflow of 720 g/min. Two primary results were realized. First, the overall heat flux levels differ at the different equivalence ratios, which is mostly due to the difference in the freestream temperature as Φ was changed. There was some variability between test days for this value but Table 1 provides the nominal variation in stack temperature with equivalence ratio. Again, this is the temperature achieved at the lower overall airflow for the $\Phi=0.95$ case. This variation was absorbed by utilization of the effective heat transfer coefficient to be discussed in detail later. The second result was the marked difference in heat flux between the air and nitrogen coolant gases at the same Φ and blowing ratio for the equivalence ratios greater than 1.0. This is attributed to the local heat addition

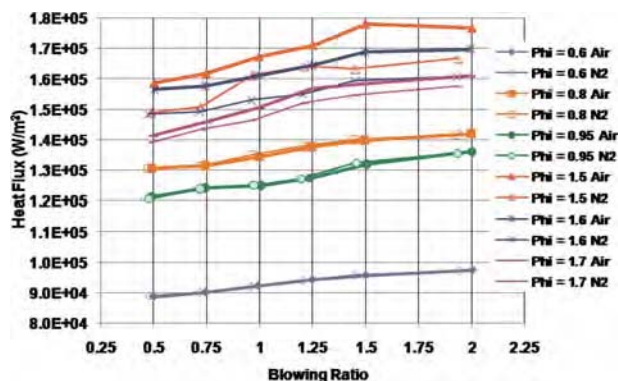


Fig. 7 Normal hole heat flux as a function of equivalence ratio and coolant gas at $x/D=20$

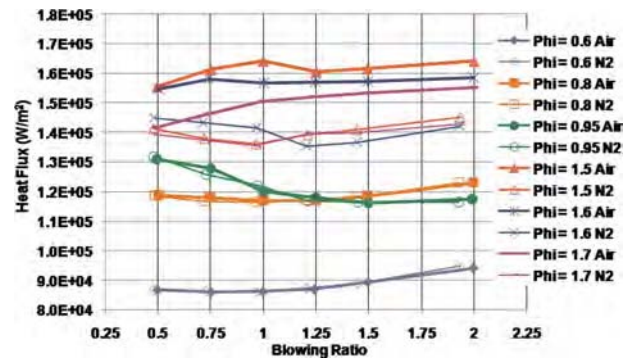


Fig. 8 Fan shaped hole heat flux as a function of equivalence ratio and coolant gas at $x/D=20$

due to the reaction chemistry shown in Fig. 5. It is likely that the reactions were initiated by auto-ignition as the inlet temperatures run in the experiment were well above those necessary for auto-ignition in hydrocarbon fuels. It is also possible that the flame contained in the WSR propagated into the test section causing ignition.

A similar result is depicted in Fig. 7 for the normal hole case. Here, the heat flux at each equivalence ratio for nitrogen is somewhat higher than that found for the angled holes, which is consistent with literature (Baldauf et al. [2], for example). What is different is that the heat flux augmentation was substantially higher for the angled holes than for the normal holes when the equivalence ratio was over 1.0. This can be directly attributed to the poorer film cooling coverage of the normal holes. Since, particularly at higher blowing ratios, the normal holes separate from the airfoil surface, the reaction is occurring off the surface, thus transferring less additional heat to the wall. Laser diagnostic measurements are planned in later experiments to try to determine exactly where the reactions are taking place for all three test conditions.

A contrary result is revealed in Fig. 8 for the heat flux for the shaped hole configuration. Here, the heat flux values are lower than those for the angled hole configuration because of the more effective spread of coolant as is often observed in literature (Saumweber et al. [3], as an example). But as clearly seen in Fig. 8, when the equivalence ratio was over 1.0, the augmentation experienced by the air fed cooling condition is the greatest of any case because the coolant flow was maintained very close to the surface. An attached flow is traditionally desirable for an effective cooling arrangement. However, in this case, having air close to the wall caused the heat release due to reaction to also be maintained near the wall. This resulted in a marked increase in the heat transfer.

Looking further downstream for the shaped holes, Fig. 9 reveals that the reaction still has an impact at 75 hole diameters. The difference between the air and nitrogen injections has diminished at this distance but it is still prevalent causing about a 5–10% enhancement with air particularly at the lower blowing ratios. At the higher blowing ratios, little coolant would be expected at this downstream location, so it is not surprising to see little variation. One note is that the overall heat flux is calculated to be higher at this location than at $x/D=20$. This is attributed to the greater amount of cooling water present downstream pulling more heat out of the test surface. The actual surface temperatures are 30–80 K lower at $x/D=75$ than at $x/D=20$. Table 2 gives the varia-

Table 1 Comparison of stack temperatures at different equivalence ratios

Equivalence ratio	0.6	0.8	0.95	1.5	1.6	1.7
Stack temperature (K)	1525	1777	1827	1845	1805	1760

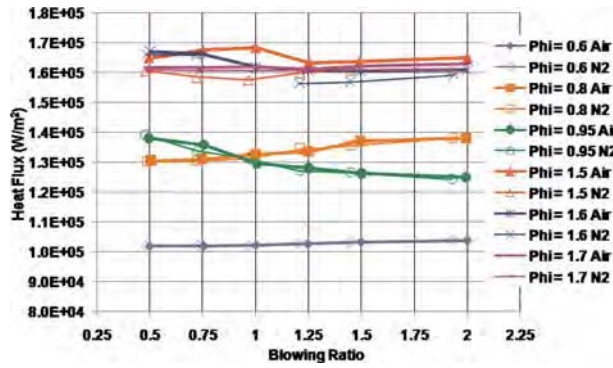


Fig. 9 Fan shaped hole heat flux as a function of equivalence ratio and coolant gas at $x/D=75$

tion in surface temperature for the fan holes for four different equivalence ratios at a blowing ratio of 1.0. Readily apparent is the larger differences at the higher Φ .

One means of normalizing the differences in these results for the various cooling configurations was to utilize an effective heat transfer coefficient (h_{eff}). The values of h_{eff} for each of the geometries are compared in Figs. 10–12. Figure 10 displays h_{eff} for the angled, fan-shaped, and normal holes at $\Phi=0.6$. The data for cooling air (closed symbols) and cooling nitrogen (open symbols) are nearly coincident for the three geometries, indicating that boundary layer reactions had no effect on h_{eff} at this Φ . Furthermore, the basic trends of the data show the angled holes performed better (maintained a lower h_{eff}) than the normal holes at lower M , however performance degrades at higher M due to separation. The fan-shaped hole design provided much lower h_{eff} over the entire range of tested values of M .

Figure 11 shows the h_{eff} data for the same cooling geometries at $\Phi=1.5$. The effect of boundary layer reactions can be clearly ob-

Table 2 Comparison of surface temperatures at different equivalence ratios for $M=1.0$ for the shaped holes

Φ	X	$T_{s,Air}$ (K)	$T_{s,N2}$ (K)	Difference (%)
1.7	20D	790.0	767.1	3.0
	75D	730.4	725.4	0.7
1.5	20D	813.6	764.7	6.4
	75D	739.2	717.5	3.0
0.8	20D	720.2	719.5	0.1
	75D	671.7	669.7	0.3
0.6	20D	632.2	631.5	0.1
	75D	597.9	597.4	0.1

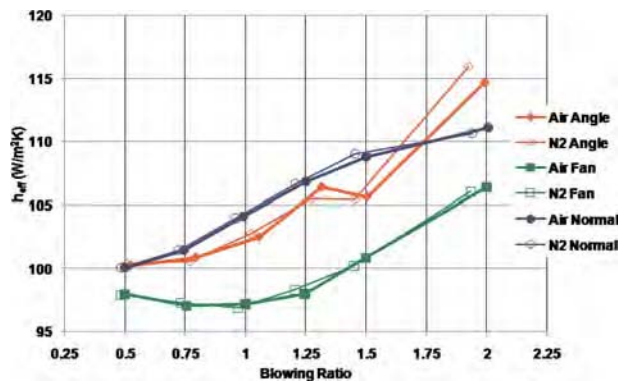


Fig. 10 Comparison of cooling hole geometries: dependence of h_{eff} on M , $\Phi=0.6$, and $x/D=20$

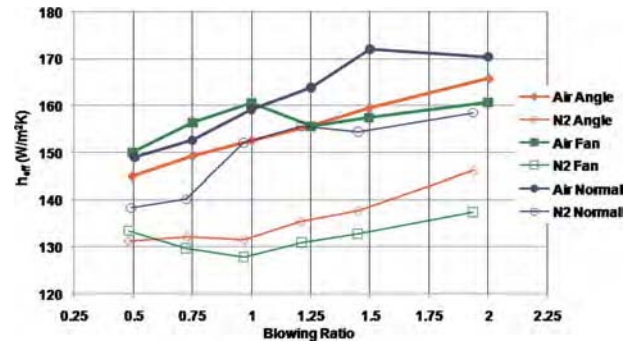


Fig. 11 Comparison of cooling hole geometries: dependence of h_{eff} on M , $\Phi=1.5$, and $x/D=20$

served by comparison of the air and nitrogen data. When air is introduced, a significant increase in effective heat transfer coefficient was experienced for each geometry. The h_{eff} of the normal jets increased by an average of 8% when coolant was switched from nitrogen to air. The h_{eff} for angled holes increased by an average of 14%, while the fan-shaped holes increased by 19%. This caused the fan-shaped holes, which were the most effective in the nonreactive flow conditions, to be the least effective (highest h_{eff}) for the lower blowing ratios. Interestingly, the shape of the curve changed for the fan-shaped holes as well. The previous minimum value of h_{eff} at $M=1$ has increased by 25% to one of the highest levels of h_{eff} . This reemphasizes that the fan-shaped holes which, by design, maintain the film coolant close to the wall, has a negative impact in a reacting flow. Any reactions that occur do so next to the wall for this cooling scheme, resulting in a significant increase in the surface temperature.

Looking farther downstream to the 75 D location, Fig. 12 provides similar results at the equivalence ratio of 1.5. While the overall levels have been reduced, the same trends are readily apparent, which suggests one of two potential drivers. One explanation is that the reaction times are sufficiently long to last an additional 55 hole diameters downstream. In other words the Damkohler number (Da), near 0.68 for this experiment, is such that this reaction was still completing over this surface length. Some simple reaction rate calculations were performed, which shows that the carbon and air reaction would require about 1.62 ms to complete in this experiment and that the flow would take about 1.1 ms to traverse from the cooling hole to the downstream set of gauges so it is possible the reaction was still occurring at the downstream location. The second potential driver stems from the belief that the reaction was only occurring on the edge of the coolant jets. Literature showed (Moore et al. [14], for example) that high vorticity is generated along the interface with the freestream and this mixing zone is where combustion is likely to

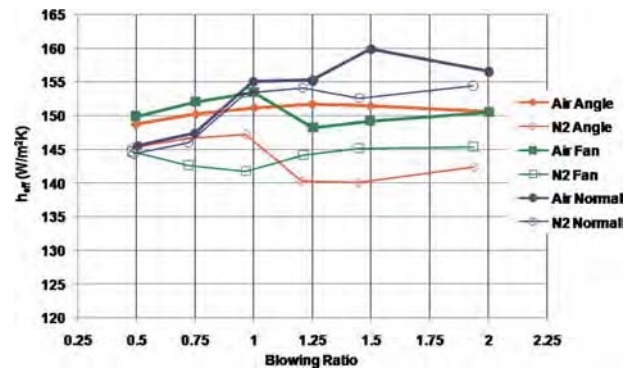


Fig. 12 Comparison of cooling hole geometries: dependence of h_{eff} on M , $\Phi=1.5$, and $x/D=75$

occur. As the jet progresses downstream, more oxygen was convected out of the core where it could react with the fuel-rich freestream. This process continued with downstream distance until the air was depleted from the core. The fact that the normal holes show little enhancement at this downstream position for low blowing ratios further reinforces these drivers. The normal jet ejected the flow further away from the wall leaving less oxygen near the wall at the downstream location.

4 Conclusions

This study has focused on the potential for heat release to occur within a turbine as a result of the interaction of air rich cooling flow with the exhaust of a fuel-rich well-stirred reactor operating at high temperatures over a flat plate. A test rig was designed and constructed with modular components to allow the study of different cooling hole geometries. This investigation focused on three common configurations used in modern turbines—normal holes, angled holes, and fan-shaped cooling holes. The cooling holes could be fed with either air or nitrogen, which enabled a direct comparison of the impact of the reactions to be isolated. The heat flux and effective heat transfer coefficient were calculated for a variety of equivalence ratios and blowing ratios for the three cooling hole geometries.

This investigation has shown that reactions do occur downstream of the introduction of cooling film in the presence of a combustor exhaust stream containing unburned fuel. These reactions occurred close to the surface and resulted in augmented heat transfer to the metal and only happened for equivalence ratios above stoichiometric. The relative impact of the reactions on the surface heat transfer was quantified for the three cooling arrangements. The normal holes resulted in the lowest enhancement of heat transfer to the surface. This was attributed to the high amount of separation resulting in the reactions occurring off the wall surface. The angled holes were more susceptible to reaction as the coolant was introduced along the wall, thus significantly raising the local driving temperature to the wall. The fan-shaped holes exhibited the greatest degradation of performance since the well attached film of coolant that was produced by this design resulted in reactions occurring even closer to that wall and more spread along the wall. This resulted in the highest overall heat load and the greatest difference between the nitrogen injection and the air injection. Overall, the results were consistent with blowing ratio from the perspective of understanding where the jet would be located for the specific case. A turbine cooling scheme designed to take advantage of the improved performance of the fan-shaped holes in a nonreactive condition could underpredict the magnitude of augmented heat release due to fuel streaks, potentially resulting in turbine durability degradation.

Further investigations are planned to better understand the two main areas of concern. First, an improved quantification of the inlet chemistry in the upstream boundary condition to the film cooling jet is desired. Laser diagnostics will be used to aide in the identification of the species that has a significant impact on the reaction. Second, diagnostic lasers will also be used to help quantify the location of the reaction and, more precisely, the extent of the reaction. Clearly reactions can occur in a configuration such as an intra turbine burner and further investigations are needed to address relevant design issues.

Acknowledgment

The authors are grateful to Dr. Jeff Brown and Lt. Joe Beck of the Air Force Research Laboratory Structures Branch in the Tur-

bine Engine Division for their model of the temperature distributions within the test block. We are further grateful to Dr. Paul King of the Air Force Institute of Technology for his advice during this project. We also wish to acknowledge Chuck Abel of ISSI and Mike Arstingstall of UDRI for their assistance in machining the test pieces and running the experiments, respectively.

Nomenclature

A	= area (m ²)
D	= diameter (m)
Da	= Damkohler number
H	= heat transfer coefficient (W/m ² K)
M	= blowing ratio
\dot{m}	= mass flow rate (g/min; g/s)
q''	= heat flux (W/m ²)
T	= temperature (K)
U	= velocity (m/s)
x	= location; distance (m)
Φ	= equivalence ratio
ρ	= density (kg/m ³)

Subscripts

∞	= freestream; reactor exhaust stream
c	= coolant; convection
eff	= effective
f	= film
s	= surface

References

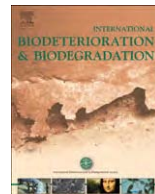
- [1] Bogard, D. G., and Thole, K. A., 2006, "Gas Turbine Film Cooling," *J. Propul. Power*, **22**, pp. 249–269.
- [2] Baldauf, S., Schulz, A., and Wittig, S., 2001, "High-Resolution Measurements of Local Effectiveness From Discrete Hole Film Cooling," *ASME J. Turbomach.*, **123**, pp. 758–765.
- [3] Saumweber, C., Schulz, A., and Wittig, S., 2003, "Free-Stream Turbulence Effects on Film Cooling With Shaped Holes," *ASME J. Turbomach.*, **125**, pp. 65–73.
- [4] Mattingly, J. D., Heiser, W. H., and Daley, D. H., 1987, *Aircraft Engine Design*, AIAA, Washington, DC.
- [5] Zelina, J., Sturgess, G. J., Shouse, D. T., 2004, "The Behavior of an Ultra-Compact Combustor (UCC) Based on Centrifugally Enhanced Turbulent Burning Rates," AIAA Paper No. 2004-3541.
- [6] Zelina, J., Shouse, D. T., and Hancock, R. D., 2004, "Ultra-Compact Combustors for Advanced Gas Turbine Engines," Paper No. 2004-GT-53155.
- [7] Lukachko, S. P., Kirk, D. R., Waitz, I. A., 2002, "Turbine Durability Impacts of High Fuel-Air Ratio Combustors, Part 1: Potential For Intra-Turbine Oxidation of Partially-Reacted Fuel," Paper No. GT-2002-30077.
- [8] Kirk, D. R., Guenette, G. R., Lukachko, S. P., and Waitz, I. A., 2002, "Gas Turbine Engine Durability Impacts of High Fuel-Air Ratio Combustors Part 2: Near Wall Reaction Effects on Film-Cooled Heat Transfer," Paper No. GT-2002-30182.
- [9] Nenniger, J. E., Kridiotis, A., Chomiak, J., Longwell, J. P., and Sarofim, A. F., 1984, "Characterization of a Toroidal Well Stirred Reactor," *Twentieth Symposium (International) on Combustion*, Combustion Institute, pp. 473–479.
- [10] Zelina, J., "Combustion Studies in a Well-Stirred Reactor," Ph.D. thesis, University of Dayton, Dayton OH, 1995.
- [11] Stouffer, S. D., Striebich, R. C., Frayne, C. W., and Zelina, J., 2002, "Combustion Particulates Mitigation Investigation Using a Well-Stirred Reactor," AIAA Paper No. 2002-3723.
- [12] Stouffer, S., Pawlik, R., Justinger, G., Heyne, J., Zelina, J., and Ballal, D., 2007, "Combustion Performance and Emissions Characteristics for a Well-Stirred Reactor for Low Volatility Hydrocarbon Fuels," AIAA Paper No. 2007-5663.
- [13] Evans, D. S., King, P. I., Polanka M. D., Zelina, J., Anderson, W. S., and Stouffer, S. D., 2009, "The Impact of Heat Release in Turbine Film Cooling," AIAA Paper No. 2009-298.
- [14] Moore, K., Wolff, J. M., Polanka, M. D., and Sondergaard, R., 2005, "A Large Scale Investigation of a Flat Plate Vortex Generator Jet in Crossflow Using PIV," 41st AIAA/ASME/SAE/ASEE Joint Propulsion Conference and Exhibit, Tucson, AZ, July 10–13, Paper No. AIAA-2005-4221.

INTENTIONALLY LEFT BLANK

APPENDIX C

Community Dynamics and Phylogenetics of Bacteria Fouling Jet A and JP-8 Aviation Fuel

INTENTIONALLY LEFT BLANK



Community dynamics and phylogenetics of bacteria fouling Jet A and JP-8 aviation fuel

L.M. Brown^a, J.P. McComb^b, M.D. Vangsness^a, L.L. Bowen^a, S.S. Mueller^a, L.M. Balster^a, C.A. Bleckmann^{b,*}

^aEnergy and Environmental Engineering, University of Dayton Research Institute, Dayton, OH, USA

^bDepartment of Systems and Engineering Management, Air Force Institute of Technology, 2950 Hobson Way, Wright-Patterson AFB, OH 45433-7765, USA

ARTICLE INFO

Article history:

Received 8 October 2009

Received in revised form

13 January 2010

Accepted 13 January 2010

Available online 17 March 2010

Keywords:

Aviation fuel

JP-8

Jet A

Fuel fouling

Fuel degradation

Fuel microbiology

Microbial diversity

PCR

Phylogeny

ABSTRACT

Aviation fuel and fuel systems support the proliferation of microorganisms. Fuel and fuel system fouling by microbes, and associated problems, have been reported since the 1960s. This study compares the community dynamics and phylogenetics of bacteria extracted from different types of aviation fuel, Jet A and JP-8, collected within the United States, and JP-8, collected abroad, in order to determine if bacterial communities differ between fuels and locations. Clone libraries containing 16S rDNA sequences of bacteria collected from Jet A and JP-8 fuel located within the U.S. were compared and results showed significant differences in the phylogenetic structure of each community. Both bacterial communities from fuel collected within the U.S. (Jet A and JP-8) were also shown to be significantly different ($P < 0.05$) from the bacterial community collected in JP-8 abroad. Results demonstrate that the survival and proliferation of bacteria in hydrocarbon sources is dependent on a variety of influences, including type of fuel and geographic location.

Published by Elsevier Ltd.

1. Introduction

It has been acknowledged since 1895 that microorganisms are capable of utilizing hydrocarbons as a source of metabolic energy (Miyoshi, 1895). Microbial degradation of hydrocarbons can foul any hydrocarbon source, from underground oil reserves to processed paraffin wax. Microbes can be found in every step of petroleum fuel production, except in high-temperature refinery process equipment, causing concern for operators of fuel storage and distribution systems. The fouling of aviation fuel, in particular, has been an issue for commercial and military institutions since the 1960s. Aviation fuel, a middle distillate fuel, is particularly susceptible to microbial degradation (Ratlidge, 1978) because "...microbes tend to prefer low molecular weight ($<C_{18}$), straight-chain aliphatic hydrocarbons to large ($>C_{20}$) complex molecules" (Passman and McFarland, 1997).

Aviation fuel systems promote proliferation of microorganisms, as all physiological requirements for growth (essential nutrients, an energy source, and water) are normally present. Water, nutrients, and microbes enter fuel storage tanks through some or all of the

following routes: vapor in humid air and dust entering tank vents, rain water through a floating tank roof, ballast water from tankers during shipping, and seepage of groundwater into leaky tanks. Once water enters the fuel tank it may be emulsified in the fuel layer, condense on the inner surface of the tank, and/or sink to the bottom of the tank where a water/fuel interface is established (Smith, 1991). In the absence of water, microbial growth and contamination is not an issue (Smith, 1991); however, exclusion of all water from a fuel system may be nearly impossible (Neihof, 1988).

Bacterial and fungal growth problems in aviation fuel storage tanks and aircraft wing tanks usually occur as a biofilm attached to the inner surface of a fuel storage tank, at the fuel/water interface, and/or in the sediment that falls to the bottom of the tank (Passman, 2003). Biofilm growth has caused fuel filter plugging, injector fouling (Smith, 1991), tank corrosion (Beech and Gaylarde, 1999; McNamara et al., 2005), and fuel degradation (Watkinson, 1978), among other issues. Along with these fouling issues come increased maintenance and repair costs (Rauch et al., 2006).

Several studies have focused on microbial proliferation in, and degradation of, hydrocarbon sources. These previous studies employed traditional culture-based techniques to identify the bacterial populations within aviation fuel (Swift, 1988; Ferrari et al., 1998; Donlan, 2002; McNamara et al., 2005; Rauch et al., 2006).

* Corresponding author. Tel.: +1 937 255 3636x4721; fax: +1 937 656 4699.

E-mail address: Charles.Bleckmann@afit.edu (C.A. Bleckmann).

However, due to the high percentage (88–99%) of environmental organisms that are suspected to be non-cultivable (Bull et al., 1992; Amann et al., 1995; Hugenholtz et al., 1998; Donlan, 2002), these previous fuel/microbe studies may have missed a large percentage of the fouling microbes that exist in aviation fuel. A preliminary report from the continental U.S. (CONUS) sampling effort identified many of the sequences originating from non-cultivable microbes in the JP-8 and Jet A libraries to the genera taxonomic level (Denaro et al., 2005). However, to date, little data describing the phylogenetic diversity and community structure of microorganisms in current aviation fuel systems is available.

In order to understand and abate these fouling problems it is necessary to characterize the microbial consortia affecting aviation fuels and the systems that use those fuels. An alternative to the limited culture-based method of identification is the molecular-based polymerase chain reaction (PCR). This method exponentially amplifies a designated gene found in an organism's deoxyribonucleic acid (DNA). The result is a concentration of the gene or segment of DNA selected for analysis (Mullis and Faloona, 1987). Once the gene of interest is amplified, it can be inserted into a plasmid and cloned through replication. The gene is then easily excised from the plasmid and sequenced. Sequence data is compiled into DNA libraries, referred to as a clone library, and analyzed.

This study compared the 16S ribosomal DNA of bacterial communities extracted from different types of aviation fuel, Jet A and JP-8, collected within the U.S., as well as JP-8 collected from outside the U.S. The comparison of the community structure and phylogenetics within each bacterial community extracted from aviation fuel demonstrated that bacterial communities differ between fuels and locations.

2. Materials and methods

2.1. Sampling

Eight Jet A fuel samples from aircraft wing tanks at two different commercial sites, and 17 JP-8 fuel samples from aircraft wing tanks at six different CONUS Air Force bases (AFBs) were collected. Some CONUS samples were taken from aircraft wing tanks whose fuel had the potential to be mixed with fuel collected outside the continental U.S. (OCONUS) as the aircraft's flight schedule may have necessitated re-fueling at an OCONUS base. Twenty-two JP-8 fuel samples were collected from R-19 filter units, fuel bladders, in-ground multi-million gallon storage tanks, and flight line pumping carts at six different OCONUS AFBs. The OCONUS samples were limited to base supply tanks and did not include any aircraft samples.

Fuel/water samples were collected into 1-l sterile, high-density polyethylene (HDPE) bottles. A variety of sterile collection procedures and tools were employed, as there was considerable variation in tank sampling ports and accessibility among the different bases. The fuel was packaged for shipment back to Wright Patterson AFB, Dayton, OH, for microbial contaminant testing. The CONUS samples generally arrived at the laboratory within 1–2 days after collection and were processed for DNA extraction within a week of arrival at the laboratory. The OCONUS samples generally took from 2 to 4 weeks to arrive at the laboratory and were extracted as above. Samples were not refrigerated during shipment or prior to extraction.

2.2. DNA extraction

Once received at Wright Patterson AFB, all CONUS fuel samples were shaken by hand for 30 s and 60-ml aliquots of the mixed fuel sample were pushed through a clean 0.45- μ m hydrophobic filter

(Corning, Corning, NY) attached to a disposable 60-ml syringe (Becton Dickinson and Co., Franklin Lakes, NJ). Filters were removed from the syringe and air-dried in a sterile biosafety cabinet to remove any residual fuel. When additional drying was needed, 60 ml of clean air pulled from a sterile biosafety cabinet were pushed repeatedly through the filter using a clean syringe. Dry filters were attached to a clean syringe and 1.5 ml of sterile water was pulled through the filter and into the syringe to wash captured bacteria from the filter. The water was transferred to a clean 1.5-ml microcentrifuge tube (Eppendorf, Westbury, NY), centrifuged at 13,000 rpm for 30 s, and then stored at -20°C .

The OCONUS fuel samples were shaken by hand for 30 s and, depending on turbidity, aliquots of 75–200 ml of the mixed fuel sample were vacuum filtered through a 0.45- μ m cellulose membrane filter (Nalgene, Rochester, NY). Filters were removed from the vacuum unit, placed in a 50-mm petri dish (Fisher Scientific, Hanover Park, IL) and air-dried in a sterile fume hood to remove any residual fuel. Dry filters were covered with 2.5 ml of sterile water and vortexed for 15 s to wash microbes from the filter. Neat wash water samples were stored at -20°C .

Aliquots (100 μ l), of the neat wash water from all CONUS and OCONUS samples were heated in a Mastercycler ep gradient S thermal cycler (Eppendorf, Westbury, NY) for 10 min at 99°C to rupture the bacterial cells and release genomic DNA. Samples were removed from the thermal cycler, centrifuged at 13,000 rpm for 30 s, and stored at -20°C .

2.3. PCR and sequencing

The first 500 base pairs (bp) of DNA coding for the 16S ribosomal gene was selected for amplification. Individual PCR reactions were 50 μ l which included 2 μ l 5 μ M forward primer (5'-TGGAGAG TTTGATCCTGGCTCA) (Integrated DNA Technologies, Coralville, IA); 2 μ l 5 μ M reverse primer (5'-GCTGCTGGCACGTAGTTAGC) (IDT, Coralville, IA); 4 μ l (CONUS samples) or 5 μ l (OCONUS samples) genomic DNA; 25 μ l Quick Load Taq (New England BioLabs, Ipswich, MA); and 16 μ l (OCONUS samples) or 17 μ l (CONUS samples) sterile water. The PCR program was initiated by a 2-min denaturing step at 94°C followed by 30 cycles of denaturing (94°C , 30 s), annealing (51°C , 20 s), and extension (72°C , 30 s). The program was finalized with an extension step of 72°C for 5 min. Samples were centrifuged at 13,000 rpm for 30 s and stored at -20°C .

PCR reactions were examined for 500 bp products by agarose gel electrophoresis. Each sample containing a 500 bp product was cloned into One Shot Top 10 chemically competent *Escherichia coli* cells using the pCR[®] 2.1 TOPO vector from the TOPO TA Cloning kit following manufacturers' protocols with an extra streaking step (Invitrogen, Carlsbad, CA). Clones expressing a DNA insert by white colony growth were streaked onto Luria-Bertani agar (LB) (Sigma Aldrich, St. Louis, MO) plus Kanamycin ($50\ \mu\text{g ml}^{-1}$) (Fisher Bioreagents, Hanover Park, IL) and X-gal ($25\ \mu\text{g ml}^{-1}$) (Invitrogen), and then incubated overnight at 37°C . The streaks provided a larger surface area, making it easier to distinguish between a pale blue colony that may not contain an insert and a white colony that did contain an insert. White colonies, 48 from each fuel sample, were processed using the QIAprep Spin Mini Prep Kit following the manufacturer's protocol but eluting with 75 μ l of EB Buffer (Qiagen, Valencia, CA). CONUS plasmids were sequenced on an ABI 3100 (Applied Biosystems, Foster City, CA) by MWG Biotech Inc. (High Point, NC). OCONUS plasmids were sequenced on a Beckman CEQ 8000 (Beckman Colter Inc., Fullerton, CA) by the Environmental, Evolutionary and Ecological Genomics Laboratory (Wright State University, Dayton, OH).

2.4. DNA sequence analysis

Chromatograms from the OCONUS raw data were loaded into the Ribosomal Database Project (RDP) Release 10 (Cole et al., 2007). The RDP program identified the chromatogram peaks as DNA bases (guanine, adenosine, thymine, or cytosine), then removed vector sequences. The library was cleaned according to the default settings on the RDP-pipeline website; then the sequences were prepped for alignment. Both CONUS sequence libraries (Jet A and JP-8) were loaded into BioEdit software (Ibis Biosciences, Carlsbad, CA) as the raw chromatogram data was not available. Sequences shorter than 300 bp were manually removed along with sequences containing numerous Ns, meaning unidentified base. The cleaned sequence libraries were then uploaded to the RDP. Non-overlapping sequences were removed from each library using a script written in the Python Programming Language personally provided by Benli Chai of the RDP. Once non-overlapping sequences were removed, each library was analyzed using the RDP classifier to gather taxonomic data on sequences that were identifiable.

Jukes–Cantor corrected distance matrices were downloaded from the RDP for all three libraries (CONUS Jet A, CONUS JP-8, and OCONUS JP-8) and run on the Distance Based Operational Taxonomic Unit and Richness Determination (DOTUR) program (Schloss and Handelsman, 2005). Using the furthest neighbor method in the DOTUR program, sequences from each library were separately grouped into operational taxonomic units (OTUs) at every possible distance level. An OTU is a group of sequences that cluster together at a given distance level without regard to taxonomic rank. In Figs. 2, 3, and 7, where the 5% distance level was used, the sequences within an OTU are a maximum of 5% distant from any other sequence in the OTU. The 5% distance level was chosen as it was not so specific as to separate nearly every sequence into its own OTU nor did it cluster sequences into so few OTUs that data were minimal. A Shannon diversity index, frequency distribution plot, and rarefaction curve (Figs. 1–3, respectively) were generated from DOTUR output files for each library.

The three libraries were then compared to each other using the s-Library Shuffling (s-LIBSHUFF) program, which calculates the integral form of the Cramér-von Mises statistic (Schloss et al., 2004) to determine if any compared libraries are drawn from the same population (Figs. 4–6). The coverage versus evolutionary distance

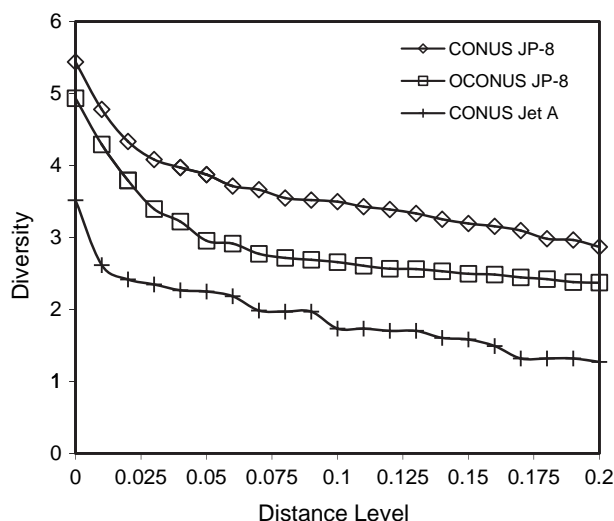


Fig. 1. Shannon Index of each clone library for each distance level from 0.01 to 0.20.

of two libraries is determined as follows: The coverage of library A is calculated using sequence data from library A (homologous comparison), then calculated a second time using combined sequence data from the library A and B (heterologous comparison). The two libraries are then transposed and the coverage of library B is calculated from library B data (homologous comparison), then from data combined from library A and B (heterologous comparison) (Good, 1953; Singleton et al., 2001).

The DOTUR .list output file and a user generated .names file were then run in the Shared Operational Taxonomic Units and Similarity (SONS) program (Schloss and Handelsman, 2006). Generated data were used to identify which OTUs, if any, were shared between the Jet A and CONUS JP-8, the CONUS and OCONUS JP-8, and the Jet A and OCONUS JP-8 libraries (Fig. 7).

3. Results

The Python script used to remove non-overlapping sequences from a library identified 11 sequences to be removed from the CONUS JP-8 library. No sequences were removed from the CONUS Jet A or OCONUS JP-8 libraries.

The Jet A clone library had the fewest number of sequences (195), the lowest diversity at each distance level (Fig. 1), and the fewest number of observed OTUs (Figs. 2 and 3). The largest OTU in the Jet A clone library (Fig. 2A) contained 71 sequences. This is 36% of the entire clone library, which indicates the fuel samples were dominated by a group of bacteria that clustered together at the 5% distance level. The second largest OTU contained 24 sequences or 12% of the library. Of the 195 clones in the Jet A library, nearly half were clustered into only two OTUs.

In the CONUS Jet A library, 83% of the sequences were identified while 67% of the CONUS JP-8 and 35% of the OCONUS JP-8 sequences were identified. The RDP classifier identified 71 sequences from the Jet A library to be in the genus *Methylobacterium* (Table 1). The DOTUR program found the largest OTU in the Jet A library to contain 71 sequences (Fig. 2). Reasonable deduction concludes that the Jet A fuel was dominated by bacteria in the genus *Methylobacterium*.

The CONUS JP-8 clone library had the largest number of sequences (803), the highest diversity at each distance level (Fig. 1), and the highest number of observed OTUs (Figs. 2 and 3). The frequency plot (Fig. 2B) shows the CONUS JP-8 library was not dominated by a few clusters. The two largest OTUs in the CONUS JP-8 library each contained 49 sequences, only 12% of the library. The top nine OTUs of the CONUS JP-8 library nearly equaled the coverage (48%) of the top two OTUs of the Jet A library.

The RDP classifier identified 91 sequences from the CONUS JP-8 as the genus *Pseudomonas* (Table 1), while the DOTUR program identified the largest OTU contained 49 sequences (Fig. 2). The *Pseudomonas* genus recognized by the RDP likely contains multiple OTUs identified at the 5% distance level by DOTUR, suggesting genus level does not equate to a 5% distance level. However, several *Pseudomonas* species were contaminating the CONUS JP-8.

While the number of observed OTUs and the diversity level of the OCONUS library falls between that of the Jet A and CONUS JP-8 libraries, it is important to note that the frequency plot (Fig. 2C) was similar to that of Jet A. Over 37% of the clones (186 sequences) from the OCONUS JP-8 library belonged to the same OTU. The top three OTUs made up 47% of the total library, suggesting that, like the Jet A library, the OCONUS library was dominated by bacteria that clustered together at the 5% distance level. This does not indicate that these dominant bacteria in these two fuels are the same, only that the bacterial community within the fuel is similarly structured.

The most common identifiable genus, *Chryseobacterium*, in the OCONUS JP-8 library contained 17 sequences (Table 1). The DOTUR

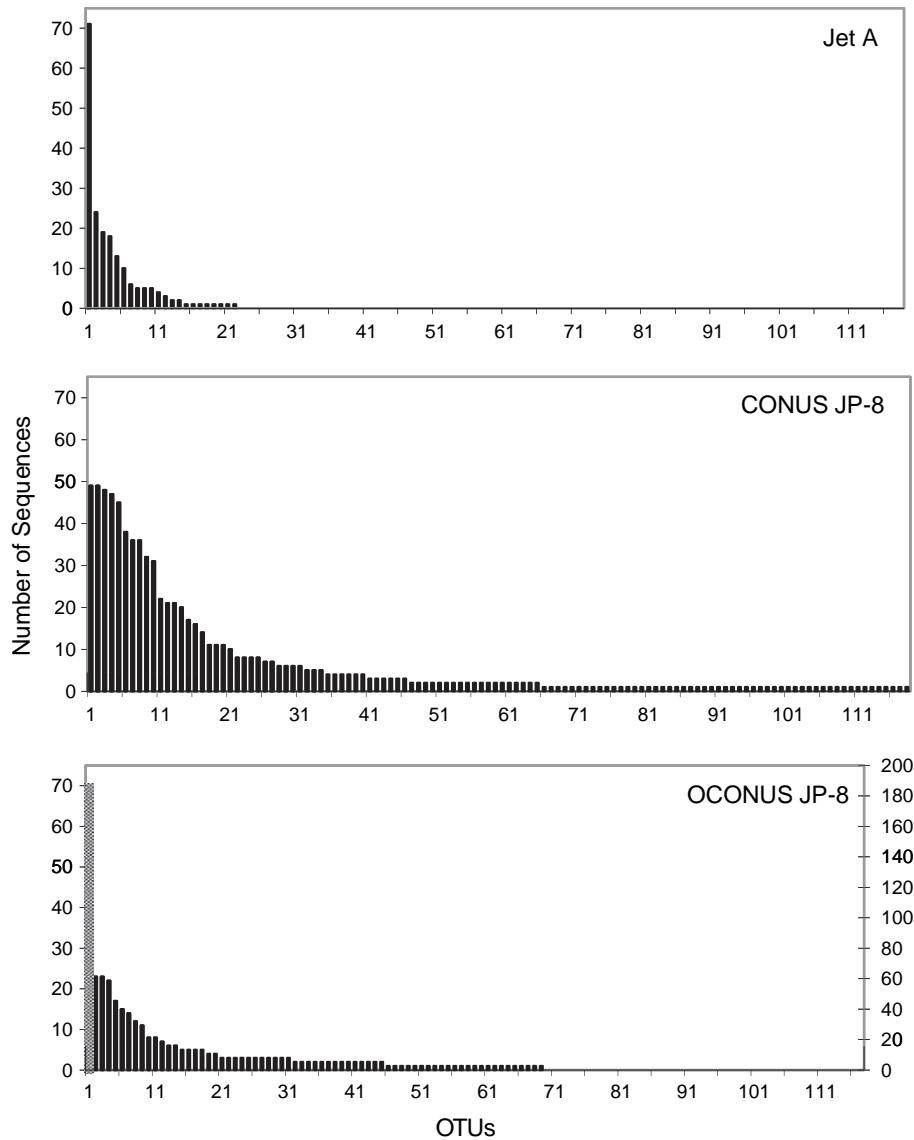


Fig. 2. Frequency distribution of OTUs at the 5% distance level for Jet A clone library, CONUS JP-8 clone library, and OCONUS JP-8 clone library. The first data point (186) of the OCONUS library (bottom chart) is scaled to the second y-axis, to the right of the chart.

program found the OCONUS JP-8 library to have 186 sequences in the largest OTU (Fig. 2). This suggests that the No. 1 OTU in OCONUS JP-8 is a type of bacteria yet to be identified and/or included in the RDP classifier reference library. Since their purposes are not identical, it is perhaps not surprising that the two taxonomic tools, DOTUR versus RDP, did not produce the same results.

In Fig. 3, the boundary level of the rarefaction curve was set at a 5% distance level. The observed OTUs in each clone library increased as the number of sequences added to the library increased. The Jet A community approaches an asymptote, indicating the sequences being added to the library cluster within an already observed OTU and new OTUs were not being identified. The slope of the CONUS and OCONUS JP-8 curves do not appear to approach an asymptote. These curves suggest that increasing the number of sequences in both JP-8 clone libraries would have increased the number of observed OTUs and, therefore, diversity. Shaw et al. (2008) stated that “because we currently do not know the true diversity of any free-living microbial community, it is impossible to test the accuracy of these estimates.”

An issue that affects measured diversity in a bacterial community is that the ease of amplifying the 16S rDNA gene via PCR is not equally distributed among all microbes (Polz and Cavanaugh, 1998). Though universal 16S primers were used in the PCR process, they may not have aligned with some bacterial DNA as well as others, resulting in a preference of certain amplified species. Therefore, the presence, absence, or abundance of a particular species within a community becomes difficult to assess and quantify. Primer alignment does not appear to have been biased in the CONUS JP-8 library, as Fig. 2 shows sequences were distributed across multiple OTUs; however, the Jet A and OCONUS JP-8 libraries show one OTU dominating the clone library.

The *P*-values (<0.05) generated when comparing the coverage of the Jet A library to the CONUS JP-8 library using s-LIBSHUFF (Fig. 4A), showed that the bacterial populations were significantly different from one another. This was also the case when the two libraries were transposed (Fig. 4B). The phylogenetics of each of the clone libraries were unique to the fuel in which the bacteria had grown.

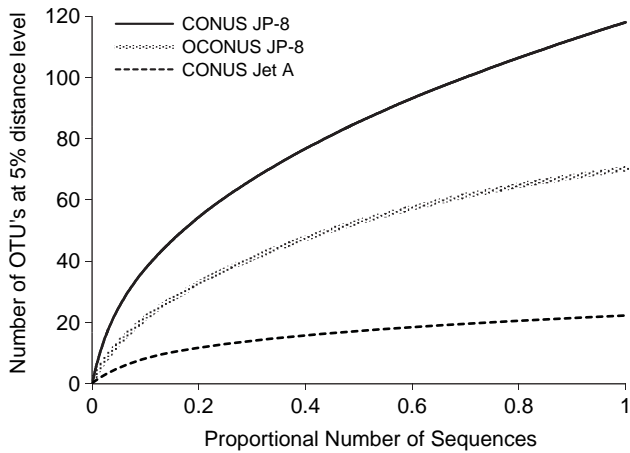


Fig. 3. Rarefaction curves of CONUS JP-8, OCONUS JP-8, and CONUS Jet A bacterial communities at the 5% distance level. The x-axis is the proportional number of sequences in each clone library in order to better compare the unequal number of sequences from each fuel.

The bacterial communities sequenced from the CONUS and OCONUS JP-8 fuel samples were also found to be significantly different from one another ($P < 0.05$). When the coverage of the CONUS JP-8 was calculated by the OCONUS JP-8 (Fig. 5A) and vice versa (Fig. 5B), the phylogenetics of each clone library were unique to the location from which the fuel had been collected. As expected, when the Jet A and OCONUS libraries were compared, the phylogenetics of each library was significantly different, with a P -value of < 0.05 (Fig. 6A and B).

The .otu files (output files generated by the SONS program which list the sequences from each library found in each OTU) were used to create the Venn diagrams in Fig. 7. All comparisons are at the 5% distance level. One discrepancy found in the data using the SONS program was that the number of OTUs in the CONUS and OCONUS JP-8 library (Fig. 7) varied depending on which library was used for comparison. The variance was not great but slightly inconsistent even though neither library was modified for any comparison. Also, the number of OTUs within each library calculated with the SONS program varied slightly from the number of OTUs calculated with the DOTUR program (Figs. 2 and 7).

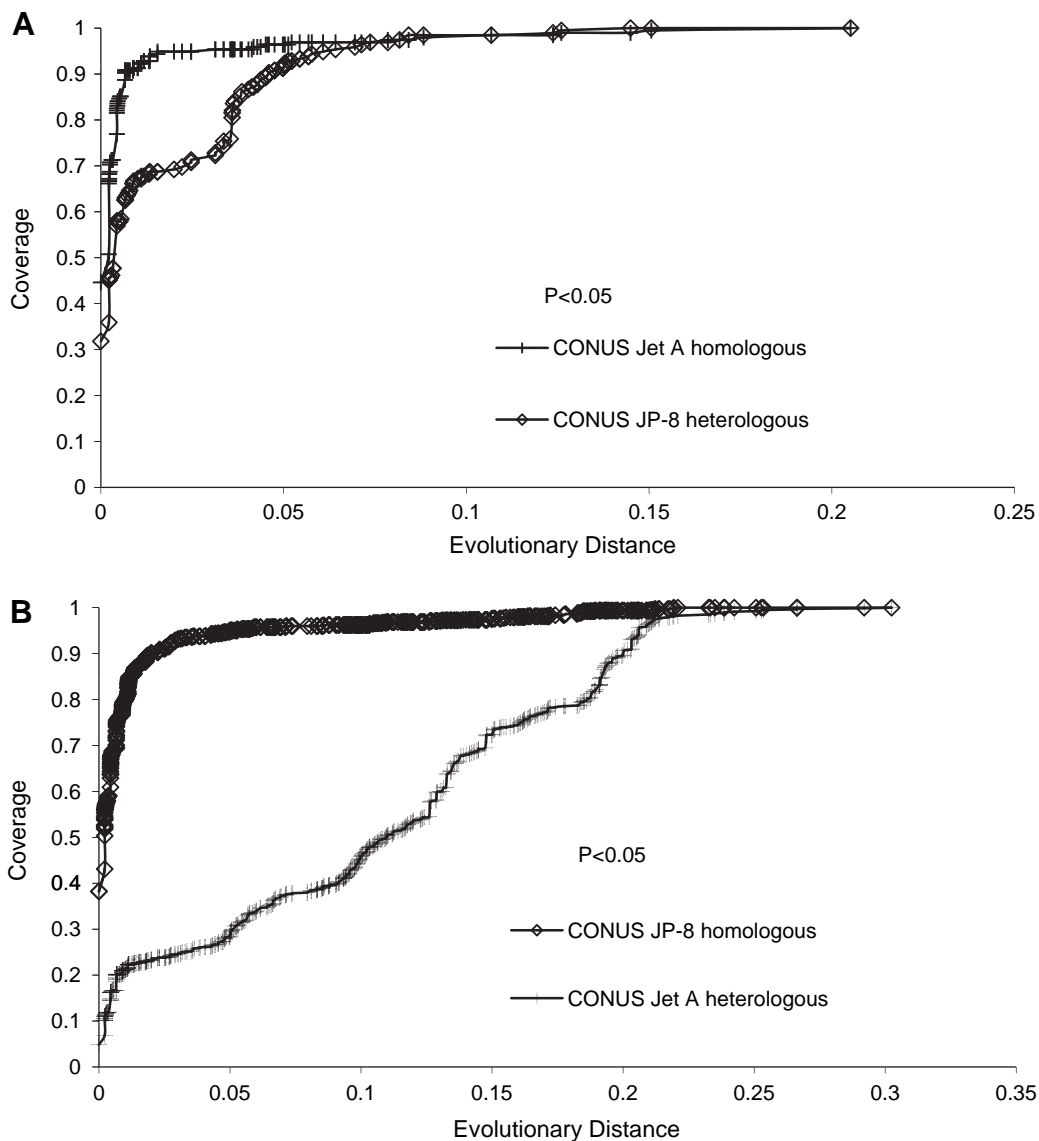


Fig. 4. (A) Coverage of CONUS Jet A measured by CONUS Jet A (homologous) and coverage of CONUS Jet A measured by CONUS JP-8 (heterologous). (B) Coverage of CONUS JP-8 measured by CONUS JP-8 (homologous) and coverage of CONUS JP-8 measured by CONUS Jet A (heterologous).

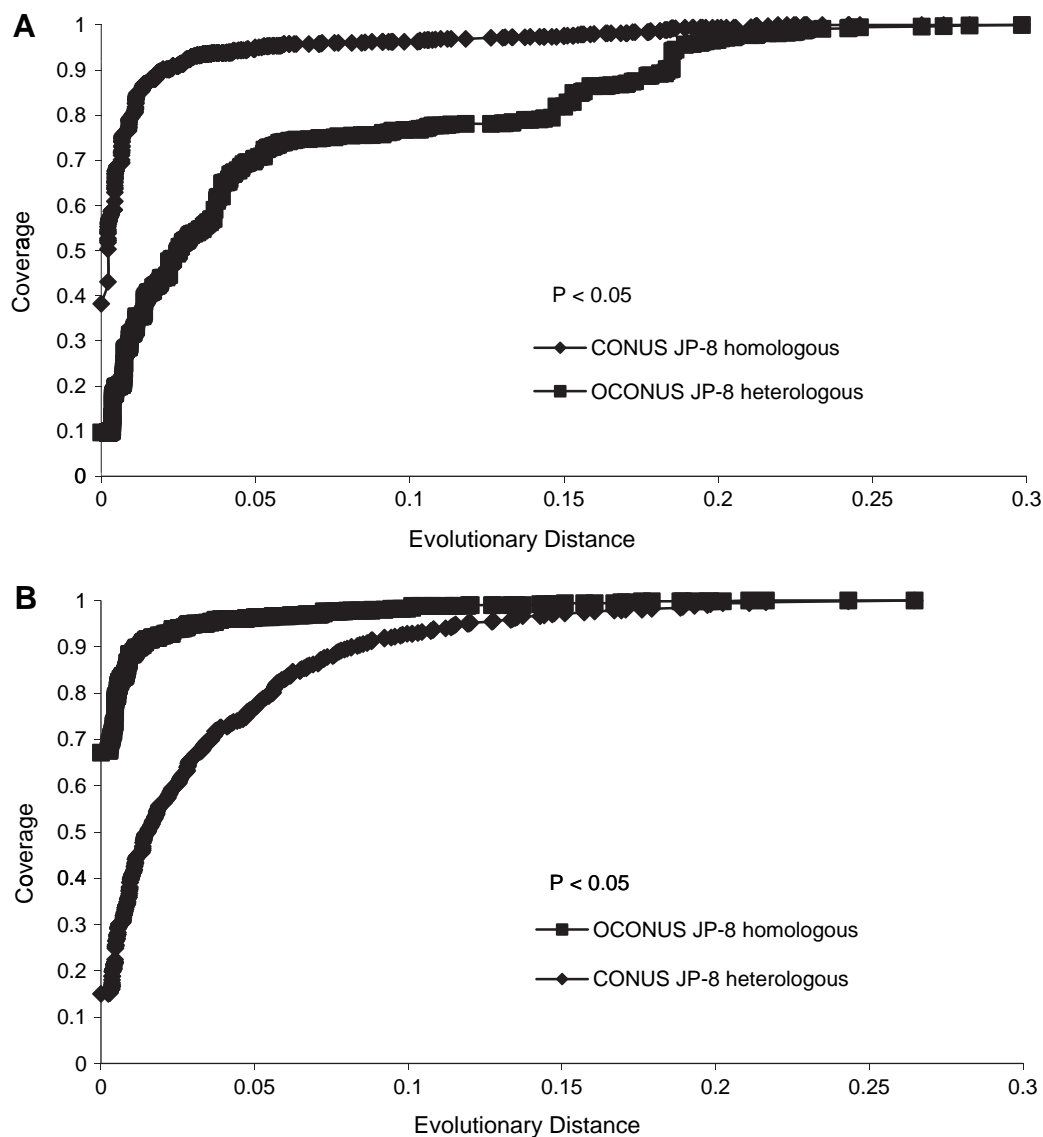


Fig. 5. (A) Coverage of CONUS JP-8 measured by CONUS JP-8 (homologous) and coverage of CONUS JP-8 measured by OCONUS JP-8 (heterologous). (B) Coverage of OCONUS JP-8 measured by OCONUS JP-8 (homologous) and coverage of OCONUS JP-8 measured by CONUS JP-8 (heterologous).

Of the 13 shared OTUs in Fig. 7A the largest OTU of the CONUS Jet A library (71 sequences) was shared as the third largest OTU in the CONUS JP-8 library (47 sequences). Both the Jet A and CONUS JP-8 libraries shared some OTUs with the OCONUS JP-8 library (Fig. 7B and C); however, the largest OTU in the OCONUS JP-8 library (186 sequences) was not one that was shared with either the CONUS JP-8 or Jet A libraries. This further suggests the OCONUS JP-8 clone library is very different in community structure and phylogenetics from the other libraries.

4. Discussion

The phylogenetic structures of the clone libraries from Jet A and JP-8 fuel collected within the U.S. were found to be significantly different ($P < 0.05$). Frequency plots from the CONUS Jet A and CONUS JP-8 clone libraries also showed a difference in the community structure of bacteria that were extracted from these fuels. The CONUS Jet A clone library had one OTU that dominated the library while the CONUS JP-8 clone library did not have a dominant OTU.

Clone libraries from the CONUS and OCONUS JP-8 were found to be significantly different ($P < 0.05$). Frequency plots from the CONUS and OCONUS JP-8 clone libraries revealed different bacterial community structures within each type of fuel. The OCONUS JP-8 clone library, like the CONUS Jet A, was dominated by one OTU.

The CONUS Jet A and OCONUS JP-8 clone libraries were found to be significantly different ($P < 0.05$). Frequency plots of the Jet A and OCONUS JP-8 libraries showed similar bacterial community structures between the two fuels, as each was dominated by one OTU. However, the largest OTU within each library was not a shared OTU.

There were two logistical elements to consider that may have influenced the results from the Jet A clone library. First, it is unknown if the Jet A collected from the commercial aircraft had a fuel system icing inhibitor (FSII) with biocidal properties (Hill et al., 2005). The FSII additive was required in JP-8 military fuel at the time of sampling but was optional for commercial fuel supplies. If the Jet A fuel did not contain FSII, there would have been an increased opportunity for microbes to proliferate at elevated levels. Second, and more important, the two commercial airframes

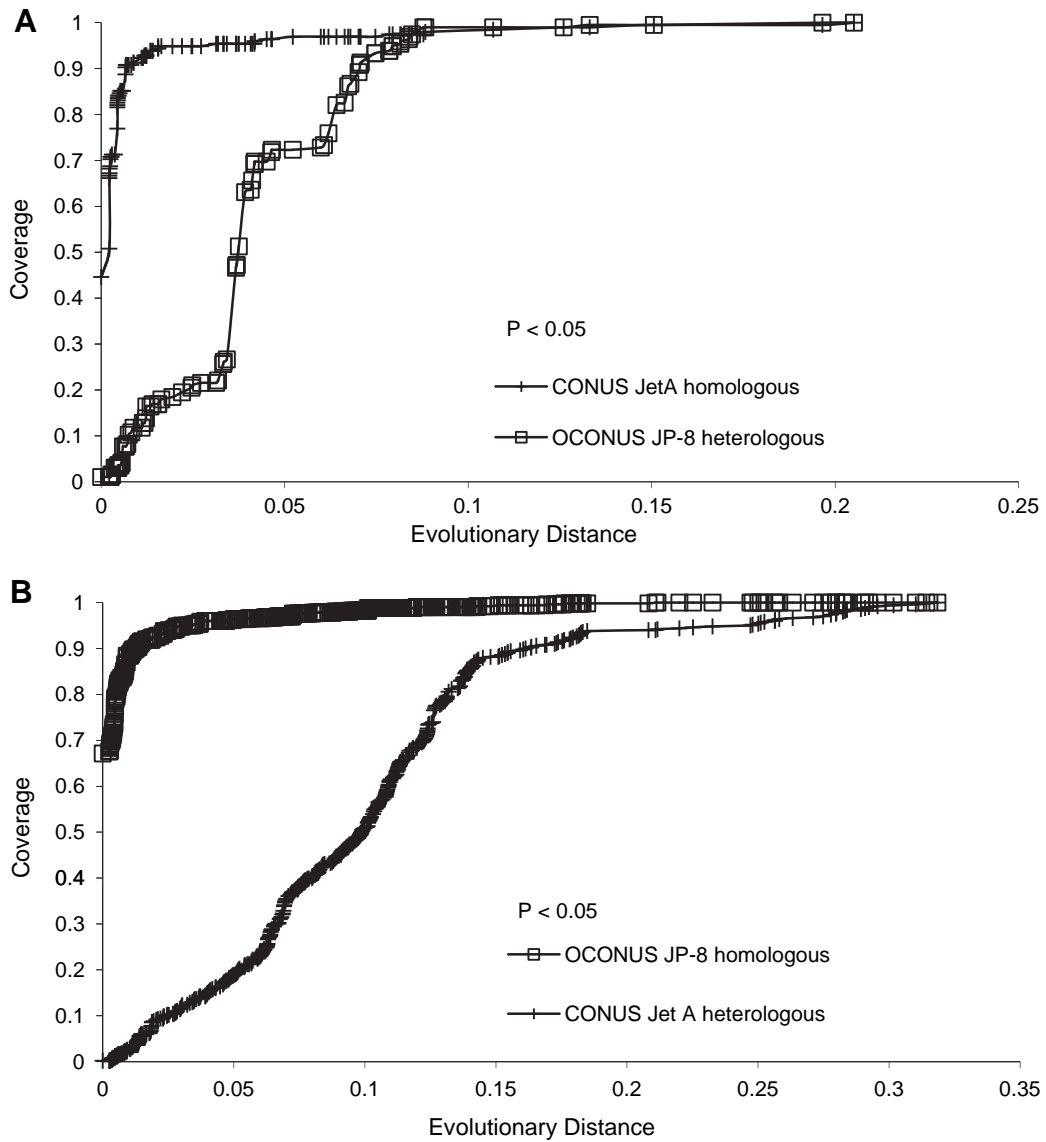


Fig. 6. (A) Coverage of CONUS Jet A measured by CONUS Jet A (homologous) and coverage of CONUS Jet A measured by OCONUS JP-8 (heterologous). (B) Coverage of OCONUS JP-8 measured by OCONUS JP-8 (homologous) and coverage of OCONUS JP-8 measured by CONUS Jet A (heterologous).

containing the Jet A fuel had been in outdoor long-term storage (longer than six months) in the southwestern U.S. Long-term storage of fuel in hot desert temperatures greater than 90 °F in the summer, without tank sumping and fresh fuel turnover, could provide an environment that would enhance the growth of

a dominant type of bacteria in the fuel, leading to a high bacterial load but a low bacterial diversity level within the samples. None of the JP-8 samples, whether CONUS or OCONUS, had been in long-term storage. It is not likely that the Jet A bacterial community was under-sampled, although the library contains the fewest number of

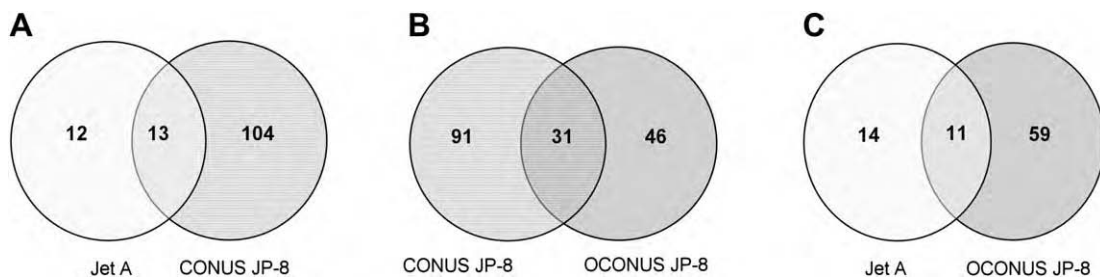


Fig. 7. Number of shared OTUs at the 5% distance level between the (A) CONUS Jet A and CONUS JP-8 libraries, (B) CONUS and OCONUS JP-8 libraries and (C) the CONUS Jet A and OCONUS JP-8.

Table 1

Five most common genera found in each clone library identified by the RDP classifier and the number of sequences in each genus. Unclassified designates sequences that were not identified to the genus taxonomic level by the RDP.

CONUS Jet A	CONUS JP-8	OCONUS JP-8
<i>Methylobacterium</i> – 71	<i>Pseudomonas</i> – 91	<i>Chryseobacterium</i> – 17
<i>Staphylococcus</i> – 24	<i>Nitrospira</i> – 49	<i>Streptococcus</i> – 16
<i>Bacillus d</i> – 18	<i>Methylobacterium</i> – 46	<i>Corynebacterium</i> – 11
<i>Rhodococcus</i> – 9	Streptophyta – 45	<i>Hydrogenophilus</i> – 11
<i>Bacillus a</i> – 7	<i>Rhodococcus</i> – 37	<i>Shigella</i> – 10
Others & Unclassified – 34	Others & Unclassified – 266	Others & Unclassified – 324

sequences. As shown in Fig. 3, the rarefaction curve of the Jet A library plateaus before either of the other libraries, indicating sufficient sampling.

Organisms recovered from the Jet A samples were dominated by the genus *Methylobacterium*, and the genus was third most common in the CONUS JP-8 samples. *Methylobacterium* was previously reported in fuels based on culture methods (Denaro et al., 2005) and is well known in biodegradation of the fuel additive MTBE (Mo et al., 1997) and from petroleum reservoirs (Orphan et al., 2000).

Chryseobacterium, formerly known as *Flavobacterium*, was the most numerous organism recovered from the OCONUS JP-8 samples and had previously been recovered from fuel samples using culture techniques (Rauch et al., 2006).

Somewhat unexpectedly, the fourth most common taxon recovered (8% of the total) for the CONUS JP-8 samples, based on the RDP classification, was Streptophyta, or green plants. However, when these sequences were compared to the NCBI BLAST dataset, they appeared to match the cyanobacteria at the 85–95% level. Clearly, assignment of organism identity requires consideration beyond the first answer from the various databases. Sample origin and history are also important.

Time from sample collection to extraction was somewhat variable, particularly for the OCONUS samples. Ongoing and previous laboratory studies of fuel biodegradation suggest that microbial population changes in fuel/water mixtures do not occur rapidly (weeks versus days). Therefore, we believe the variations in sample hold times had little impact on microbial population levels or species composition.

Results demonstrate that the survival and proliferation of bacteria in hydrocarbon sources is dependent on a variety of influences including type of fuel and geographic location. These environmental variables ultimately affect the community structure and phylogenetic diversity of the bacteria that survive in aviation fuel, which can greatly influence the microbial fouling potential.

Further research, including identification of additional house-keeping and hydrocarbon-degrading genes, needs to be conducted in order to better characterize the fouling bacterial communities and mitigate their effects on fuel systems.

Acknowledgements

We gratefully acknowledge funding from the U.S. Air Force, AFRL/RZPF, Wright Patterson AFB, under contract number F33615-03-2-2347, with Ms. Ellen Strobel serving as the technical monitor and Mr. Robert Morris serving as the contract monitor. The U.S. government is authorized to reproduce and distribute reprints for governmental purposes notwithstanding any copyright notation thereon. The view and conclusions contained herein are those of the authors and should not be interpreted as necessarily representing the official policies or endorsements, either expressed or

implied, of the Air Force Research Laboratory or the U.S. government.

References

- Amann, R., Ludwig, W., Schleifer, K., 1995. Phylogenetic identification and in situ detection of individual microbial cells without cultivation. *Microbiological Reviews* 59, 143–169.
- Beech, I., Gaylarde, C., 1999. Recent advances in the study of biocorrosion – an overview. *Revista de Microbiologia* 30, 177–190.
- Bull, A., Goodfellow, M., Slater, J., 1992. Biodiversity as a source of innovation in biotechnology. *Annual Review of Microbiology* 46, 219–252.
- Cole, J., Chai, B., Farris, R., Wang, Q., Kulam-Syed-Mohideen, S., McGarrell, D., Bandela, A., Cardenas, E., Garrity, G., Tiedje, J., 2007. The Ribosomal Database Project (RDP II): introducing myRDP space and quality controlled public data. *Nucleic Acids Research* 35 (Suppl. 1), D169–D172.
- Denaro, T., Chelgren, S., Lang, J., Strobel, E., Balster, L., Vangness, M., 2005. DNA Isolation of Microbial Contaminants in Aviation Turbine Fuel via Traditional Polymerase Chain Reaction (PCR) and Direct PCR – Preliminary Results. Interim Report AFRL-PR-WP-TR-2006-2049.
- Donlan, R., 2002. Investigation of Fuel/Water Samples Collected from Fuel Tanks of Military Aircraft. Centers for Disease Control and Prevention, Biofilm Laboratory, Atlanta, GA.
- Ferrari, M., Neirotti, E., Albornoz, C., 1998. Occurrence of heterotrophic bacteria and fungi in an aviation fuel handling system and its relationship with fuel fouling. *Revista Argentina de Microbiologia* 30, 105–114.
- Good, I., 1953. The population frequencies of species and the estimation of population parameters. *Biometrika* 40, 237–264.
- Hill, G., Hill, E., Collins, D., Anderson, S., 2005. Investigation of the anti-microbial characteristics of di-ethylene glycol mono methyl ether (Di-EGME) in relation to its use intermittently and at sub-lethal concentrations. In: IASH 2005 the Ninth International Conference on Stability, Handling and Use of Liquid Fuels, Sitges, Spain, September 18–22.
- Hugenholtz, P., Goebel, B., Pace, N., 1998. Impact of culture-independent studies on the emerging phylogenetic view of bacterial diversity. *Journal of Bacteriology* 180, 4765–4774.
- McNamara, C., Perry, T., Leard, R., Bearce, K., Dante, J., Mitchell, R., 2005. Corrosion of aluminum alloy 2024 by microorganisms isolated from aircraft fuel tanks. *Biofouling* 21, 257–265.
- Miyoshi, M., 1895. Die durchbohrung von membranen durch pilzfäden. *Jahrbücher für wissenschaftliche Botanik* 28, 269–289. Available from: <http://books.google.com/books?id=aDAVAAAAYAAJ&printsec=titlepage#v=onepage&q=&f=false> (Cited 14.05.09).
- Mo, K., Lora, C., Wanken, A., Javanmardian, M., Yang, X., Kulpa, C., 1997. Biodegradation of methyl *t*-butyl ether by pure bacterial cultures. *Applied Microbiology and Biotechnology* 47, 69–72.
- Mullis, K., Faloona, F., 1987. Specific synthesis of DNA *in vitro* via a polymerase-catalyzed chain reaction. *Methods in Enzymology* 155, 335–350.
- Neihof, R., 1988. Microbes in fuel: an overview with a naval perspective. In: Chesneau, H.L., Dorris, M.M. (Eds.), *Distillate Fuel Contamination, Storage, and Handling*. American Society for Testing and Materials, Philadelphia, PA, pp. 6–14.
- Orphan, V., Taylor, L., Hafenbradl, D., Delong, E., 2000. Culture-dependent and culture-independent characterization of microbial assemblages associated with high-temperature petroleum reservoirs. *Applied and Environmental Microbiology* 66, 700–711.
- Passman, F., McFarland, B., 1997. Understanding, Recognizing, and Controlling Microbial Contamination in Fuels and Fuel Systems – a Primer. Prepared for: Chevron USA. FQS Limited, Inc., Princeton, NJ.
- Passman, F., 2003. Fuel and Fuel System Microbiology: Fundamentals, Diagnosis, and Contamination Control. ASTM International, West Conshohocken, PA.
- Polz, M., Cavanaugh, C., 1998. Bias in template-to-product ratios in multitemplate PCR. *Applied and Environmental Microbiology* 64, 3724–3730.
- Ratledge, C., 1978. Degradation of aliphatic hydrocarbons. In: Watkinson, R.J. (Ed.), *Developments in Biodegradation of Hydrocarbons – 1*. Applied Science Publishers Ltd., London, UK, pp. 1–46.
- Rauch, M., Graft, H., Rozenzhak, S., Jones, S., Bleckmann, C., Kruger, R., Naik, R., Stone, M., 2006. Characterization of microbial contamination in United States Air Force aviation fuel tanks. *Journal of Industrial Microbiology and Biotechnology* 33, 29–35.
- Schloss, P., Handelsman, J., 2005. Introducing DOTUR, a computer program for defining operational taxonomic units and estimating species richness. *Applied and Environmental Microbiology* 71, 1501–1506.
- Schloss, P., Handelsman, J., 2006. Introducing SONS, a tool for operational taxonomic unit-based comparisons of microbial community memberships and structures. *Applied and Environmental Microbiology* 72, 6773–6779.
- Schloss, P., Larget, B., Handelsman, J., 2004. Integration of microbial ecology and statistics: a test to compare gene libraries. *Applied and Environmental Microbiology* 70, 5485–5492.
- Shaw, A., Halpern, A., Beeson, K., Tran, B., Venter, C., Martiny, J., 2008. It's all relative: ranking the diversity of aquatic bacterial communities. *Environmental Microbiology* 10, 2200–2210.

- Singleton, D., Furlong, M., Rathbun, S., Whitman, W., 2001. Quantitative Comparisons for 16S rRNA gene sequence libraries from environmental samples. *Applied and Environmental Microbiology* 67, 4374–4376.
- Smith, R., 1991. Developments in fuel microbiology. In: Rossmore, H.R. (Ed.), *Biodeterioration and Biodegradation* 8. Elsevier Applied Science, London, pp. 112–124.
- Swift, S., 1988. Identification and control of microbial growth in fuel handling systems. In: Chesneau, H.L., Dorris, M.M. (Eds.), *Distillate Fuel Contamination, Storage, and Handling*. American Society for Testing and Materials, Philadelphia, PA, pp. 15–26.
- Watkinson, R., 1978. *Developments in Biodegradation of Hydrocarbons – 1*. Applied Science Publishers Ltd., London.

INTENTIONALLY LEFT BLANK

APPENDIX D

Emissions Characteristics of Military Helicopter Engines with JP-8 and Fischer-Tropsch Fuels

INTENTIONALLY LEFT BLANK

Emissions Characteristics of Military Helicopter Engines with JP-8 and Fischer–Tropsch Fuels

Edwin Corporan*

U.S. Air Force Research Laboratory, Wright-Patterson Air Force Base, Ohio 45433

Matthew J. DeWitt, Christopher D. Klingshirn, and Richard Striebich

University of Dayton Research Institute, Dayton, Ohio 45469

and

Meng-Dawn Cheng

Oak Ridge National Laboratory, Oak Ridge, Tennessee 37831

DOI: 10.2514/1.43928

The rapid growth in aviation activities and more stringent U.S. Environmental Protection Agency regulations have increased concerns regarding aircraft emissions, due to their harmful health and environmental impacts, especially in the vicinity of airports and military bases. In this study, the gaseous and particulate-matter emissions of two General Electric T701C engines and one T700 engine were evaluated. The T700 series engines power the U.S. Army's Black Hawk and Apache helicopters. The engines were fueled with standard military JP-8 fuel and were tested at three power settings. In addition, one of the T701C engines was operated on a natural-gas-derived Fischer–Tropsch synthetic paraffinic kerosene jet fuel. Test results show that the T701C engine emits significantly lower particulate-matter emissions than the T700 for all conditions tested. Particulate-matter mass emission indices ranged from 0.2–1.4 g/kg fuel for the T700 and 0.2–0.6 g/kg fuel for the T701C. Slightly higher NO_x and lower CO emissions were observed for the T701C compared with the T700. Operation of the T701C with the Fischer–Tropsch fuel rendered dramatic reductions in soot emissions relative to operation on JP-8, due primarily to the lack of aromatic compounds in the alternative fuel. The Fischer–Tropsch fuel also produced smaller particles and slight reductions in CO emissions.

Introduction

AIRCRAFT have been identified as significant sources of local pollution at airports and military bases. The Federal Aviation Administration (FAA) estimated in 2002 that passenger air travel in the United States would increase about 4% per year [1], further increasing the environmental burden of aircraft and ground support equipment, especially in the vicinity of airports. Even in the absence of any growth in aviation, emissions from aircraft, especially particulate matter (PM), have been under increased scrutiny recently due to their proven harmful health and environmental effects. The more stringent environmental standards imposed by the U.S. Environmental Protection Agency (EPA) will likely impact commercial aviation growth and military operations, including the basing of advanced and legacy aircraft. Therefore, accurate determination of emission indices (EIs) of pollutants from aircraft is necessary to assess their environmental impact to take appropriate corrective action. Robust techniques and instrumentation are needed to perform these challenging measurements from full-scale turbine engines under actual operating conditions. Through several aircraft emissions research projects led by NASA (many in collaboration with the FAA, EPA, U.S. Department of Defense, academia, and industry), significant progress has been made in advancing the knowledge of instrumentation and methodologies for improved reliability of particulate measurements from turbine engines [2,3]. Recently, the SAE E-31 Committee generated an Aerospace Information Report describing instruments and techniques currently available for the measurement of nonvolatile PM emissions [4].

Several instruments that may be employed for these measurements were also assessed under the Strategic Environmental Research and Development Program (SERDP) project CP-1106 [5]. The ultimate goal is to develop methodologies to generate reliable data and reduce the uncertainties associated with existing and future emissions inventories from military and commercial aircraft. In this effort, several of these instruments/techniques were applied to quantify the emissions from the T700 series engines.

In recent years, there has been increased interest in the potential use of alternative jet fuels produced via the Fischer–Tropsch (FT) process for aviation applications. These fuels can be produced domestically from various nonpetroleum feedstocks such as coal, natural gas, and biomass and could therefore reduce reliance on foreign oil. FT fuels are typically comprised solely of iso- and normal paraffins and do not contain heteroatoms, cyclic compounds, or aromatics. Accurate emissions measurements for turbine engines operating with alternative fuels are needed to evaluate their environmental impact. Previous research conducted on turbine engines and combustors have shown significantly reduced PM emissions using FT/JP-8 fuel blends [6–8]. The U.S. Air Force has been very active in the analysis and testing of FT produced fuels and is currently certifying aircraft to operate with a 50/50% by volume FT/JP-8 fuel blend with the goal of certifying all U.S. Air Force weapon systems for use with the alternative fuel blend by 2011. In the present effort, a T701C engine, which powers the U.S. Army's Black Hawk and Apache helicopters, was operated with 100% natural-gas-derived FT fuel and specification JP-8, in order to compare emissions and engine performance. Favorable results from this and other studies will help expedite the certification of engines, aircraft, and ground support equipment for use of synthetic paraffinic kerosene (SPK)-type fuels in commercial and military systems.

T700 and T701C Engines

The General Electric T700-700 or T700-701C (referred to hereafter as T700 and T701C) is the turboshaft engine used to power the UH-60 Black Hawk and AH-64 Apache helicopters. The T701C

Received 19 February 2009; accepted for publication 15 November 2009. This material is declared a work of the U.S. Government and is not subject to copyright protection in the United States. Copies of this paper may be made for personal or internal use, on condition that the copier pay the \$10.00 per-copy fee to the Copyright Clearance Center, Inc., 222 Rosewood Drive, Danvers, MA 01923; include the code 0748-4658/10 and \$10.00 in correspondence with the CCC.

*Senior Research Engineer, Propulsion Directorate; edwin.corporan@wpafb.af.mil.

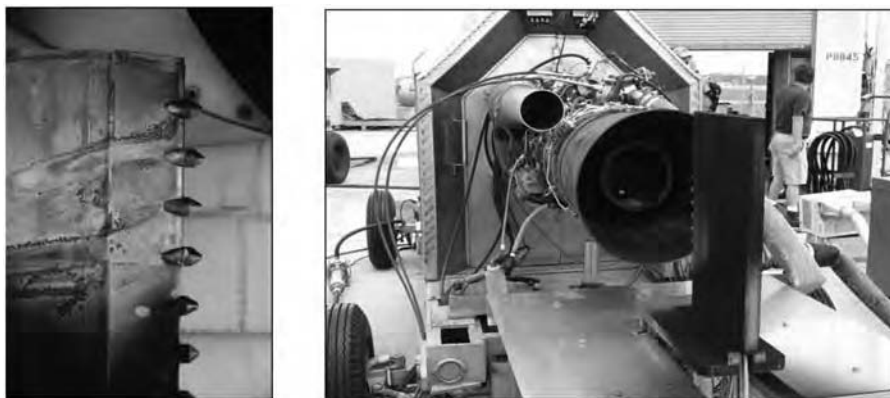


Fig. 1 Particle and gas probes mounted on a water-cooled rake installed 33 cm from the engine exit plane.

is a more powerful and upgraded version of the T700 and is installed in the latest Black Hawk and Apache attack helicopters. They both have six compressor stages and two low- and high-pressure turbines. The overall pressure ratio of the T700 is 17:1 versus 18:1 for the T701C. The T701C has slightly better specific fuel consumption and a higher maximum shaft horsepower than the T700 (1890 vs 1622 shp). The three engines used in this study had a few thousand hours of total operation.

Instrumentation

PM and gaseous emissions instrumentation were transported to the test site and housed during testing in the U.S. Air Force Research Laboratory, Fuels Branch, Turbine Engine Research Transportable Emissions Laboratory (TERTEL). The TERTEL is equipped with state-of-the-art instrumentation for the measurement and analysis of turbine engine emissions. Online analysis of the mostly nonvolatile PM emissions was performed using a TSI, Inc., model 3022A condensation particle counter (CPC) to provide a count of the total particles per unit volume (particle number) via light scattering techniques, and a scanning mobility particle sizer (SMPS) TSI model 3936 was used to measure particle size distributions via electrostatic classification. Basic descriptions of the CPC and SMPS systems can be found elsewhere.[†] The SMPS was composed of a long differential mobility analyzer (DMA) (TSI model 3081) coupled with a condensation particle counter (TSI model 3025). The long DMA was operated at a sheath flow rate of 10 lpm and a sample flow rate of 1.5 lpm, allowing for classification of particles in the range of 7 to 300 nm. An in-house-designed smoke sampler was used to collect PM samples for determination of engine smoke numbers following the techniques in Society of Automotive Engineers (SAE) Aerospace Recommended Practice (ARP) 1179 [9]. In addition, soot samples were collected on quartz filters for offline analysis using a LECO Corporation RC-412 multiphase carbon analyzer. In this method, total carbon mass and the fractions of organic and elemental carbon were inferred via quantitation of the CO₂ generated during the oxidation of volatile and nonvolatile organic species as a function of temperature. Species that oxidize at low temperatures (less than 325°C) are considered volatile organic species [e.g., polycyclic aromatic hydrocarbons (PAHs)], and those that oxidize at higher temperatures are assumed to be primarily elemental carbon (e.g., highly graphitic). The carbon was oxidized to temperatures up to 750°C. The total carbon mass is the sum of the volatile [i.e., organic carbon (OC)] and elemental carbon. Selected soot samples were also analyzed for adsorbed PAH content via ultrasonic extraction and analysis using gas chromatography/mass spectrometry (GC/MS). Direct real-time nonvolatile particle mass concentrations were measured with an Rupprecht & Pataschnick series 1105 tapered-element oscillating microbalance (TEOM). The TEOM measures the mass concentration based on the change in frequency of an oscillating tapered element as PM is deposited on a filter installed at the tip of the element.

Gaseous emissions were quantified using an MKS Instruments, Inc., MultiGas 2030 Fourier transform infrared (FTIR)-based gas analyzer. CO₂ in the diluted sample streams was measured with a nondispersive infrared analyzer. The total unburned hydrocarbons were quantified with an analyzer based on flame ionization detection; however, an instrument malfunction precluded its use for all test cases, and thus the data are not included.

Emissions Sampling System

PM and gaseous emissions were captured at the engine exit plane using three particle (N₂-diluted) and three gas (undiluted) probes mounted within a water-cooled probe rake. The probe rake was placed near the center and approximately 33 cm from the engine exhaust plane to capture representative samples and avoid diluting with surrounding air. The rake was mounted on a 15-cm-diam, 1.23-m-long stainless steel post supported on a stand restrained with the engine test bed. The particle and gas probes had nominal port diameters of 1.6 and 1.5 mm, respectively. The probes types were alternated within the rake and separated by 3.18 cm center to center (Fig. 1). The exhaust gas temperature was monitored using a thermocouple installed in a blank probe, and the exhaust pressure was measured using an open probe connected to a pressure gauge in the TERTEL. The aerosol sample was diluted with nitrogen (at room temperature) at the probe tip to minimize condensation of water and organic species and to minimize particle loss to the tubing walls. Although the dilution ratios were set using high-precision Brooks Instrument 5850i (0–10 slpm) flow controllers, the dilution ratios used for particle number (PN) and mass correction were determined by the ratio of the carbon dioxide (CO₂) concentration of the diluted and undiluted streams. The average of CO₂ measurements from two separate probes, typically within ±10% (95% confidence), was used for the calculations. Dilution ratios were between 8 and 50:1, with higher dilutions required at higher engine power. Emission samples were transported from the probe rake to a heated valve box using 6.35-mm-o.d., 4.6-mm-i.d. heated lines (150°C). Samples from each probe could be sent to the desired instrument by means of fast-response ball valves within the box (also maintained at 150°C). Since the required sample dilution varied based on the analytical instrument, two six-way valves with three dilution schemes (diluted for PN and TEOM, undiluted for the smoke sampler) were used to provide the required dilution to the appropriate probe. Undiluted and diluted particle samples were kept at 150 and 75°C, respectively, from the valve box to the instruments to help maintain sample integrity. The total length of the heated sample lines from the probe stand to the instruments was approximately 23 m. The emissions samples were drawn into the instruments via vacuum pumps. A simplified flow diagram of the sampling system is shown in Fig. 2.

Jet Fuel Characteristics

JP-8 is Jet A-1 commercial aviation fuel with a military additive package that includes a fuel system icing inhibitor (FSII) at ~1000–1500 ppm, corrosion inhibitor/lubricity enhancer at

[†]Data available online at <http://www.tsi.com> [retrieved 11 April 2008].

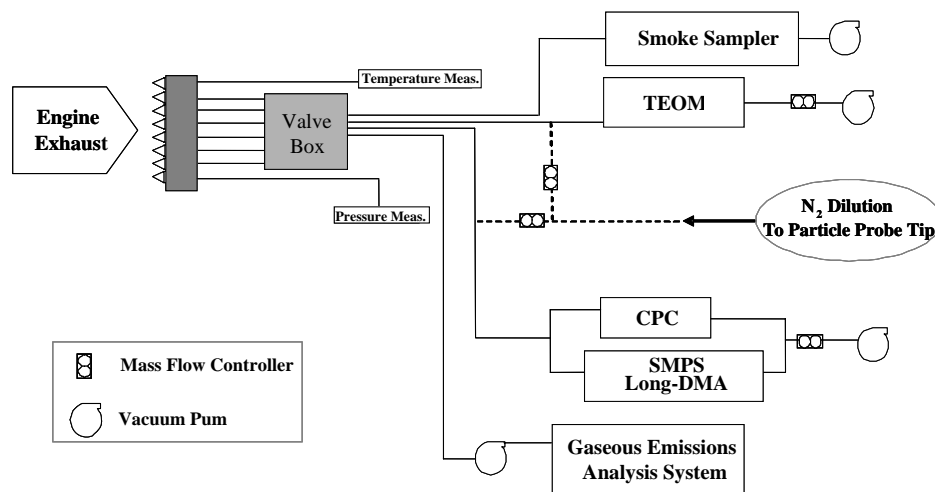


Fig. 2 Simplified emissions sampling system.

~20 ppm, and a static dissipater additive at ~5 ppm. JP-8 contains hundreds of different types of hydrocarbons. In a typical JP-8 fuel, branched (iso) and normal (*n*) paraffins account for approximately 60% of the total hydrocarbons. The *n* paraffins typically range from *n*-octane (*n*-C₈) to *n*-hexadecane (*n*-C₁₆), with maximum concentrations from *n*-decane (*n*-C₁₀) to *n*-dodecane (*n*-C₁₂). JP-8 also contains approximately 20% mono-, di-, and tricycloparaffins. Aromatics are the other significant fraction (~15–20%) of JP-8 fuel. The alternative fuel used in this study was produced by Syntroleum Corporation from natural gas via the FT process. Extensive details on this fuel have been previously provided [6,7,10]. The fuel is comprised solely of iso (82%) and normal (18%) paraffins with a distillation (i.e., molecular weight) range consistent with that typically observed for an aviation fuel. The isoparaffins in this fuel are mainly monomethyl-substituted species. The chemical composition of fuels was determined using a variety of chromatographic techniques, including GC/MS and high-performance liquid chromatography. ASTM International specification conformance tests [11–22] were conducted to verify fuel compliance with all JP-8 specifications and to determine the concentration of known PM precursor species, such as aromatics and sulfur. Table 1 shows the specification limits of several JP-8 properties and the properties of the JP-8 and FT fuel used in this effort. This FT fuel conforms to the recently released specifications for SPK, which can be blended up to 50 vol % with JP-8 and was recently certified on B-52 platforms [23].

Table 1 ASTM specification test results for JP-8 and FT fuels used during tests

ASTM test	Standard	JP-8	FT fuel
Aromatics, vol % (D1319 [11])	Max 25.0	19.2	0
Total sulfur, wt % (D4294 [12])	Max 0.30	0.140	0
Initial boiling point, °C (D86 [13])	Report	173	150
10% Recovered, °C (D86 [13])	Max 205	189	173
20% recovered, °C (D86 [13])	Report	192	181
50% recovered, °C (D86 [13])	Report	207	208
90% recovered, °C (D86 [13])	Report	234	245
Final boiling point, °C (D86 [13])	Max 300	248	258
Distillation-residue, vol % (D86 [13])	Max 1.5	1.3	1.5
Loss, %vol (D86 [13])	Max 1.5	1.5	0.5
Freeze point, °C (D5972 [14])	Max -47	-51	-49
Existent gum, mg/100ml (D381 [15])	Max 7.0	1.1	0.6
Viscosity at -20°C, cSt (D445 [16])	Max 8.0	5.0	4.9
FSII (DiEGME), vol % (D5006 [17])	0.10–0.15	0.12	0.05
Smoke point, mm (D1322 [18])	Min 19.0	25	35
Flash point, °C (D93 [19])	Min 38	62	63
Specific gravity at 15.5°C (D4052 [20])	0.775–0.840	0.806	0.756
Heat of combustion, Btu/lb (D3338 [21])	Min 18,400	18,500	18,980
Hydrogen content, % mass (D3343 [22])	Min 13.4	13.7	15.3

Test Conditions

The test plan for this campaign is shown in Table 2. A total of 30 test runs were conducted. All three engines (one T700 and two T701C) were operated on JP-8 at three power settings: ground idle (or idle), 75%-maximum power, and maximum power. One cycle consisted of consecutive tests at the three conditions. Four cycles were run for the T700 and two for each T701C. For the second T701C, two cycles were also performed with the FT fuel. The engine was operated at each power setting for approximately 30 min to acquire multiple measurements from two probe locations. The tests were conducted in the test sequence shown, i.e., from low to high power. The engine conditions were set by controlling the turbine rotational speed. For tests with the neat FT fuel, the fuel was stored in an external tank and supplied to the engine fuel pump via an air-driven diaphragm pump.

Test Results and Discussion

Engine Operation

The engines were observed to operate normally during the tests. As anticipated, no discernible difference in engine operation (performance parameters were within measurement variability) was observed between JP-8 and neat FT fuel. After test completion with the FT fuel, the engine was thoroughly inspected and no anomalies were found. The total engine run time with the neat FT fuel was approximately 2.5 h.

Table 2 Test plan for emissions tests on T700 and T701C engines

Test run	Power setting
T700 with JP-8	
1,4,7,10	Ground idle
2,5,8,11	75%
3,6,9,12	Max
T701C-1 with JP-8	
13,16	Ground idle
14,17	75%
15,18	Max
T701C-2 with JP-8	
19,22	Ground idle
20,23	75%
21,24	Max
T701C-2 with FT	
25,28	Ground idle
26,29	75%
27,30	Max

Particulate-Matter Emissions

Particle Number

PN emissions were quantified with a CPC and corrected for dilution based on the CO₂ measurement of the diluted and raw samples. Dilution ratios ranged from an average of 8:1 at idle to 50:1 at maximum power. Higher dilution was required to maintain the particle counts within the CPC measurement range. Particle-number emission indices (PN-EIs), the number of particles produced per unit mass of fuel consumed, were calculated using the following relationship derived from fluid flow fundamentals:

$$\text{PN-EI} = 2.833 \times 10^3 \times \text{PN}_{\text{corrected}} \times (1 + F/A)/(F/A) \times T/P \quad (1)$$

where PN-EI is the number of particles per kilogram of fuel, PN_{corrected} is the dilution-corrected PN in number of particles per cubic centimeters, T is the sample temperature at the instrument in Kelvin (~ 293 K), P is the sample pressure at the instrument in atmospheres, F/A is the engine fuel-to-air ratio, and 2.833×10^3 is a unit conversion factor.

The engine F/A ratios were determined based on the CO and CO₂ emissions following the SAE ARP 1533A guidelines [24]. The average PN-EI (not corrected for sample line losses) varied from 1.25×10^{15} at idle to 4.12×10^{15} #/kg fuel at maximum continuous power for the T700 and 4.56×10^{14} to 2.11×10^{15} #/kg fuel for the T701C. The PN uncertainty for each individual test run was excellent at less than $\pm 8\%$ (95% confidence), reflecting the steadiness of the engine operation. The average PN-EI corrected for estimated line losses are shown in Fig. 3. The losses are based on an unreported in-house study designed to quantify particle line losses through the 23 m heated line and valving system used in this campaign. The in-house study (conducted using particulate exhaust from a T63 helicopter engine) showed average losses between ~ 40 – 60% in PN (depending on engine condition) for particulate emissions, with a similar size-distribution range as for the T700 engines. The reported values in Fig. 3 represent averages of multiple runs from two probes. The uncertainty for each average value varied depending on engine condition. At idle, the average uncertainty was higher ($\pm 25\%$) than at both the 75%-maximum ($\pm 12\%$) and maximum power ($\pm 10\%$) conditions. Higher uncertainties at the idle condition are likely due to the higher concentrations of unstable volatile and semivolatile species at the lower power setting. The physical properties of these species are believed to be extremely sensitive to temperature and pressure, and therefore any small change in these may affect gas-to-particle conversion processes in the sampling system, which subsequently influence the number of particles measured. For the higher power settings, the concentration of semivolatile species (i.e., organic carbon) is significantly reduced and particles are more stable, which reduces the data variation. It was observed that the difference between the PN measurements from the two individual probes

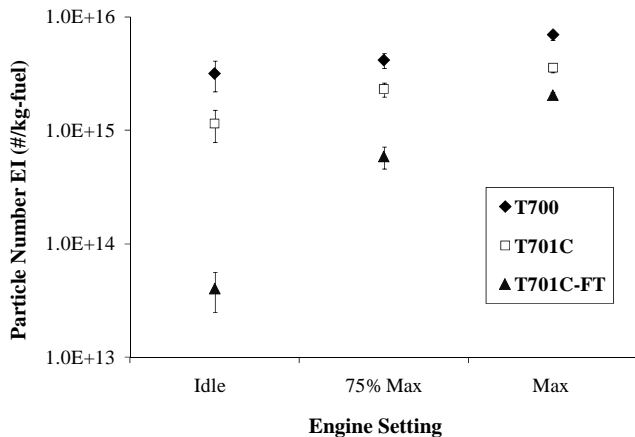


Fig. 3 Particle-number emission indices at three power settings for T700 and T701C engines operating with JP-8 and the T701C operating with FT fuel.

(separated by 6.4 cm) was also highly dependent on engine condition. This difference was larger at idle ($\sim 40\%$) than at both the 75%-maximum ($\sim 20\%$) and maximum power ($\sim 13\%$) conditions. However, the trends observed for samples from both probes were consistent for all power settings and engines. The relatively small difference in PN at higher power demonstrates the fairly uniform PM profile in the exhaust. As shown in Fig. 3, the PN-EI varied directly with engine power at an average of 3.0 – 6.9×10^{15} #/kg fuel for the T700 and significantly lower 1.1 – 3.5×10^{15} #/kg fuel for the T701C operating on conventional JP-8 fuel. For the T701C engine operating with FT fuel, lower particle emissions for all conditions were evident. Reductions of 40–97% in PN-EI were observed with the FT fuel, with the highest reductions occurring at engine idle. The higher impact at idle is likely due to the smaller particles produced at this condition and the production of even smaller and more easily oxidized particles with the FT fuel. The lower PM emissions with the FT fuel are primarily due to its aromatic-free nature. Aromatics are known soot precursors that act as seeds for the growth of PAHs, which subsequently nucleate into soot particles. The propensity of aromatics to produce soot has been demonstrated in large-scale combustors and laboratory flames. A summary of several efforts and the role of aromatics in soot formation have been presented by Richter and Howard [25]. Reduction in the fuel aromatic content decreases precursors that contribute to the formation of soot nuclei. The FT fuel is comprised solely of normal and branched paraffinic compounds, which are believed to produce soot primarily via fragmentation and polymerization reactions, which are much slower (i.e., less efficient) than condensation reactions with aromatics [26]. Reductions in PM emissions with FT fuels have been observed previously in a T700 engine and other test platforms [6–8]. Because of the sampling methodology employed, most of the PM measured are nonvolatile (mostly soot) particles; therefore, the lack of sulfur in the FT fuel did not have a significant impact on the measured particle reductions observed here. However, significant reductions in volatile particles (which nucleate as the exhaust is cooled and mixed in the atmosphere) are anticipated, as most of these are sulfur-based.

Particle Size Distributions

Particle size distributions of the PM emissions were measured over a range of 7–300 nm in aerodynamic mobility diameter. The average particle size distributions for operation of both engines with JP-8 for the power settings evaluated are shown in Fig. 4. The y axis is represented by $dN/d\log D_p$ (a size-bin normalized particle number), which is a common practice in aerosol measurements to remove artificial counts due to the raw nonuniform voltage settings used in the DMA. Each curve represents the average of a minimum of eight size-distribution scans (four per probe). Data reproducibility for each power setting was excellent at maximum and 75%-maximum settings, with averages of ± 7 and 15% (1σ), respectively, but relatively poor at idle power ($\pm 40\%$). As discussed in the

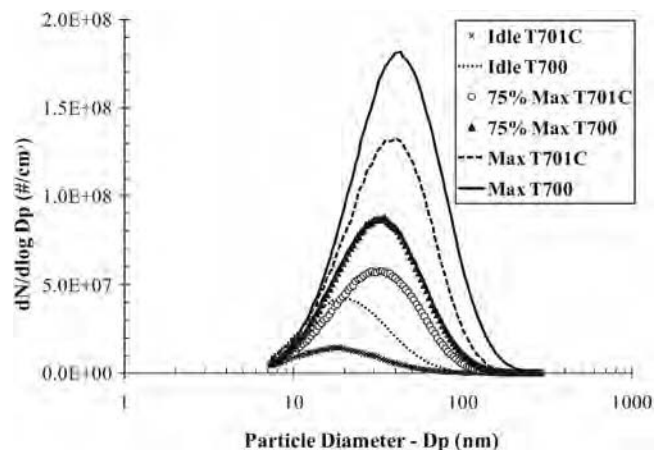


Fig. 4 Particle size distributions of PM emissions from T700 and T701C engines operated with JP-8 at three power settings.

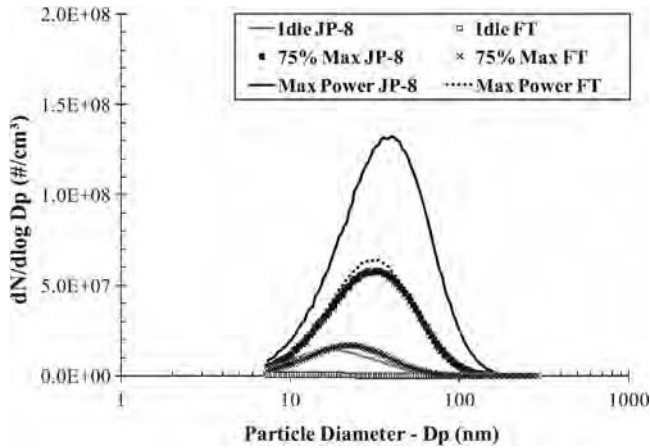


Fig. 5 Particle size distributions of PM emissions from T701C engine operated with JP-8 and FT fuel at three power settings.

previous section, the poorer PN repeatability at low power is likely due to the higher concentration of semivolatile (organic) particles in the exhaust. Size-distribution curves for both engines and for all three conditions are observed to follow a single-mode lognormal distribution with average geometric mean diameters of approximately 21 nm for idle, 30 nm for 75%-maximum power, and 37 nm for maximum power. Although the particle concentrations were significantly lower for the T701C compared with the T700, the average particle diameters for both engines were very similar. The particle mean diameters for both engines were approximately 24, 35, and 42 nm from low to high power.

Comparison of the particle size distributions of the T701C with the JP-8 (solid symbols) and FT (open symbols) fuels is shown in Fig. 5. Consistent with the particle-number data, dramatic reductions in particle concentrations (magnitude of size-distribution peak) are observed with the FT fuel. Additionally, average reductions of 25% in the mean particle diameter were observed with the FT fuel at all conditions. The reduced particle mean diameter is the result of fewer soot nuclei available for surface growth (by agglomeration and aggregation) as a consequence of the lower concentration of soot precursors in the fuel (aromatics). These trends are consistent with previous FT emissions tests in engines and combustors [6,7].

PM Mass Emissions

Engine PM mass emissions were measured online using a TEOM and offline via temperature programmed oxidation (carbon burn-off) of soot samples collected on quartz filters. Mass measurements with the TEOM varied significantly at idle, in which uncertainties up to $\pm 75\%$ (95% confidence) were observed. The high error at low engine power is primarily due to the relatively low particulate load and insufficient sensitivity of the TEOM. For the 75%-maximum and maximum power settings, the uncertainty was significantly reduced to an average of $\pm 15\%$ (95% confidence). The TEOM PM mass-EI was calculated in a manner similar to that used for the PN-EI:

$$\text{PM mass-EI} = 2.83 \times 10^{-6} \times \text{PM mass}_{\text{conc}} \times \frac{1 + F/A}{F/A} \times \frac{T}{P} \quad (2)$$

where PM mass-EI is the grams of PM per kilogram of fuel, PM mass_{conc} is dilution-corrected PM mass concentration in mg/m^3 , T is the standard temperature (293 K), P is the sample pressure at the instrument in atmospheres (1 atm), F/A is the engine fuel-to-air ratio, and 2.83×10^{-6} is a unit conversion factor.

The PM mass-EI varied directly with power setting and ranged (uncorrected for losses) from 0.053 to 1.04 g/kg fuel for the T700 and from 0.049 to 0.49 g/kg fuel for the T701C with JP-8. The PM-EIs corrected for estimated line losses (25% at high power and 60% at idle, determined from in-house experiments) ranged from 0.2–1.4 g/kg fuel for the T700 and from 0.2–0.6 g/kg fuel for the T701C. The PM mass-EIs as a function of engine power setting are

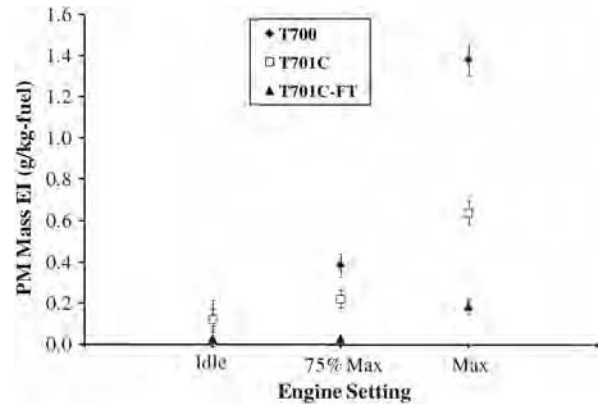


Fig. 6 Measured particulate-matter mass emission indices for T700 and T701C engines using a TEOM.

shown in Fig. 6. As shown, the trends of PM mass-EIs as a function of power are similar to those of the PN-EI. It is noted that the PM mass-EIs for the T700 engine are significantly lower than those reported by Wade [27] for a T700 engine, which ranged between 1.5–2.6 g/kg fuel for the same range of engine conditions. Differences in the measurement techniques may explain the disagreement between the PM mass measurements. Compared with PM mass emissions of military engines tested recently (T56 and TF33) under this SERDP project, both the T700 and T701C engines produced significantly lower PM emissions [7,28].

Carbon mass measurements via the carbon burnoff method (LECO) showed significantly higher fractions of OC at engine idle, compared with the higher power settings. Average ratios of organic carbon to total carbon (OC/TC) of 0.41, 0.28, and 0.16 were observed for idle, 75%-maximum, and maximum power, respectively, for the engines operating with JP-8. For the T701C with FT fuel, the OC/TC ratios averaged 0.40, 0.37, and 0.27, which were moderately higher than those observed with JP-8 for the two high-power cases. However, it should be noted that although the OC/TC ratios were higher for the FT fuel, the absolute OCs were lower for the FT; thus, the lower OC/TC for the FT were due to the significant decrease in soot formation. As with the TEOM, the mass measurements with the LECO were highly variable at low engine power.

Comparison of the mass concentration measurements determined using the TEOM and LECO is shown in Fig. 7. The error bars represent one standard deviation based on a minimum of three measurements. The LECO measured mass was observed to be significantly higher (up to 7.2 times) than for the TEOM for engine idle (PM mass $< \sim 2.0$). The high concentrations of OC at low power combined with the ineffectiveness of the TEOM to quantify the OC mass and lack of instrument sensitivity for these low-mass loadings

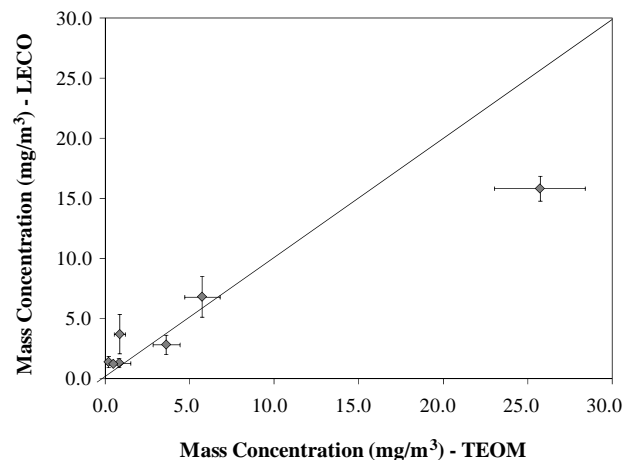


Fig. 7 Comparison of particulate-matter mass concentration measured online with a TEOM and offline via carbon oxidation using a LECO RC-412 multiphase carbon analyzer.

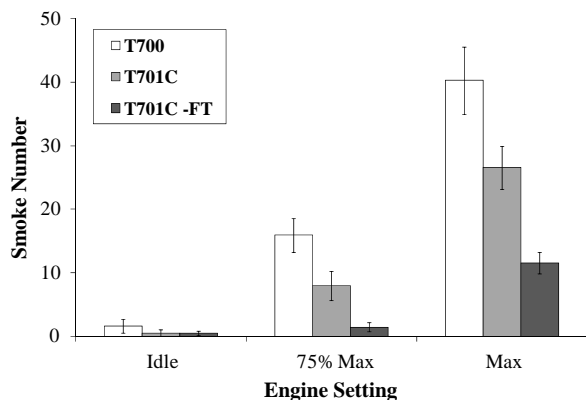


Fig. 8 Smoke numbers for T700 and T701C engines operated with JP-8 at three power settings and data for the T701C operating on the FT fuel.

are believed to be the cause for the large discrepancies. These results suggest that at low engine power, where there is a higher fraction of unburned hydrocarbons (i.e., OCs), the TEOM may underestimate the total particle mass. For the two high-power cases, the agreement between the two techniques is significantly better because of the higher total mass and increased elemental carbon; however, significant discrepancies are still observed. For the higher-mass concentrations (maximum power), the TEOM measurement is 1.6 to 2.1 times higher than the LECO. Differences in filter efficiency between the two instruments may explain the discrepancy between the two techniques. In addition, the TEOM sample was diluted, whereas the LECO sample was undiluted; error due to sample dilution correction can also affect the measured value. Overall, further research is warranted to understand the discrepancies between these techniques in order to develop a reliable methodology for PM mass measurement.

Smoke Number

Engine smoke numbers (SNs) were measured following SAE ARP 1179 [9]. The SN measures the relative difference in filter reflectance between a clean (unused) and stained (test) filter. Average SNs (minimum of eight samples per engine condition) for all test conditions are shown in Fig. 8. As anticipated, the SN varied directly with engine power. At idle, the SNs were essentially zero for both engines and fuels. At maximum power, average SNs of 40 were observed for the T700, whereas significantly lower SNs were observed for the T701C operating on both JP-8 and FT fuel. The average SNs for the T701C were approximately 40% lower than those for the T700, and average reductions of 65% were observed for the T701C when operated with the FT fuel. The SN trends as a function of engine, fuel, and power setting agree qualitatively with the PN-EI trends.

Analysis of PAHs from Soot Samples

Soot samples collected on quartz filters were analyzed to preliminarily investigate potential differences in the quantity and type of PAH compounds absorbed onto the particulate samples. Samples were prepared for analysis using ultrasonic extraction with methylene chloride and were analyzed via GC/MS to quantify PAH compounds and evaluate the impact of engine type, power setting, and fuel on the relative and absolute formation [7]. Using this

technique with the limited available sample quantities, only fluoranthene and pyrene were above the quantifiable detection limit. Results in nanograms (ng) of PAH per m^3 of exhaust gas volume are shown in Table 3. Larger and smaller PAHs are likely present in the samples but could not be detected with the sampling and analytical techniques employed here. As shown in Table 3, the total PAH concentration increased with increasing power setting, whereas the more efficient T701C engine and FT fuel both produced lower PAH emissions. These results were expected, as PAHs are believed to be intermediates in the soot-formation pathway, and the trends follow those observed for the overall soot mass and PM emissions. An attempt was made to normalize the PAH quantity to the mass of soot collected to provide insight into the relative selectivity of PAH formation in the soot-formation process (e.g., a lower ratio for FT fuel would imply an alternate pathway for soot formation rather than being solely due to reduced overall formation rate.) However, this analysis was inconclusive due to the limited available samples for analysis. Future efforts will be made to improve the sensitivity of the PAH detection and to provide additional samples for better statistical analysis.

Gaseous Emissions

Carbon Monoxide and Nitrogen Oxides

Gaseous emissions were quantified with an FTIR-based gas analyzer. As criteria pollutants, only CO and NO_x emissions are discussed in detail. Average CO and NO_x EIs for the T700 and T701C engines as a function of power setting are shown in Figs. 9 and 10. The CO-EIs ranged from 2.3–53.7 g/kg fuel for the T700 and from 2.8–31.0 g/kg fuel for the T701C. These CO-EIs are in excellent agreement with previous T700 engine emissions tests by Jones et al. [8] and Wade [27]. The NO_x -EIs ranged from 2.0–9.9 g/kg fuel for the T700 and from 2.8–15.0 g/kg fuel for the T701C. As anticipated, the engines produced higher CO and lower NO_x emissions at the lower power conditions as a result of the lower engine efficiency and exhaust temperatures, respectively. The T700 generated nearly twice the CO emissions as the T701C, which reflects a higher combustion efficiency for the latter. The approximately 40% higher NO_x emissions of the T701C over the T700 is the result of the higher-performance and higher-operating-temperature capabilities of the T701C. As anticipated, operation with the FT fuel rendered negligible differences in NO_x , since the production of these are temperature-driven and not significantly influenced by fuel type. The CO emissions for the T701C were only slightly reduced (~5–10%) with the FT fuel.

Analysis of Aldehydes

Aldehydes are produced during the combustion of hydrocarbons, and several have been identified as toxic compounds. Analysis of aldehydes was performed to determine the EIs and to assess any differences in their formation between the FT and JP-8 fuels. The analysis of aldehydes was performed using the MKS FTIR-based analyzer and a modified EPA Compendium Method TO-11A [29]. For the latter, silica-gel cartridges (Supelco, part number H30, 1 g bed weight) treated with 2,4-dinitrophenylhydrazine (DNPH) were used to capture and derivatize aldehydes from the engine exhaust and ambient air. In this analysis, 1 slpm of engine exhaust was sampled through the ambient-temperature silica-gel cartridge. Aldehydes in the gas sample reacted with the derivatizing agent to form aldehyde-diphenylhydrazone. The cartridges were capped and placed into

Table 3 Concentrations of measurable PAHs for operation of the T700 and T701C engines as a function of power setting and fuel type

Engine/fuel	Fluoranthene, ng/ m^3			Pyrene, ng/ m^3		
	Idle	75%	Max	Idle	75%	Max
T700-JP-8	— ^a	9.6E + 03	2.3E + 04	4.2E + 02	2.0E + 04	5.0E + 04
T701C-JP-8	— ^a	3.6E + 03	2.1E + 04	— ^a	9.4E + 03	4.1E + 04
T701C-FT	— ^a	— ^a	3.5E + 03	— ^a	3.5E + 02	9.0E + 03

^aDenotes below the detection limit.

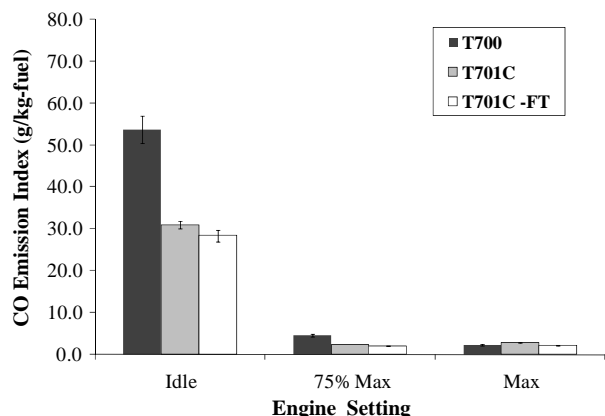


Fig. 9 CO Emission Indices at three power settings for T700 and T701C engines operating with JP-8 and the T701C operating with FT fuel.

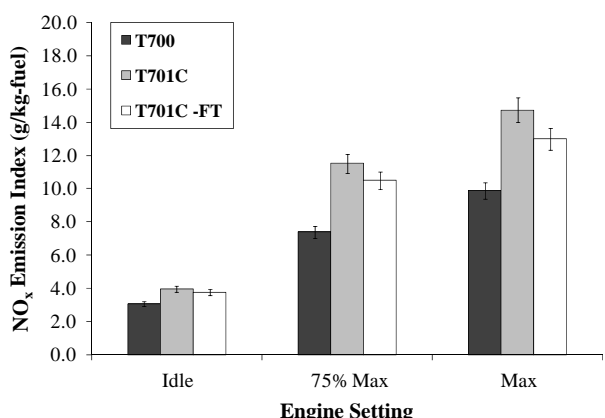


Fig. 10 NO_x emission indices at three power settings for T700 and T701C engines operating with JP-8 and the T701C operating with FT fuel.

foil-lined bags in coolers for transport from the field. The cartridges were subsequently treated with 10 ml of acetonitrile to extract the derivatized aldehydes; the extracts were analyzed by GC/MS using a DB5-MS column, operating in the selected ion-monitoring mode. Quantification ions were selected based on the most abundant and unique ions for each of the components. Standard solutions of all aldehydes were prepared and analyzed to develop a calibration range between 0 and 15 mg/liter of each derivatized aldehyde. Comparison to the calibration standards was performed to quantify the mass of each aldehyde per volume of gas.

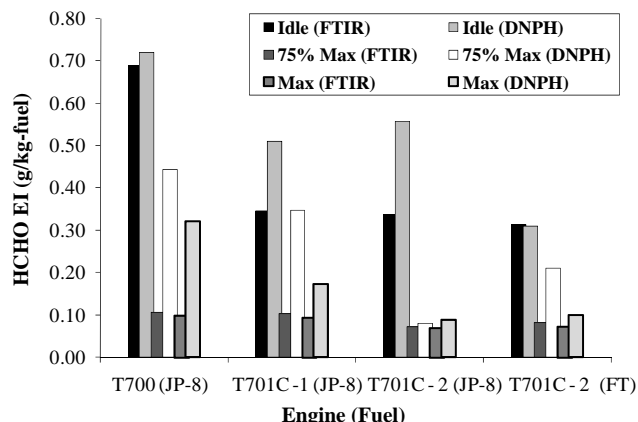


Fig. 11 Formaldehyde emission indices for T700 and T701C engines using a modified EPA Compendium Method TO-11A (DNP) [29] and an FTIR-based analyzer.

Tests results show that formaldehyde (HCHO) was the only aldehyde produced at quantities above the sensitivity of this technique (~ 0.1 ppm). Figure 11 displays the HCHO emission indices using both analytical methods for the three engines with JP-8 and the T701C with FT fuel. The average errors were $\pm 25\%$ (1σ) and $\pm 10\%$ (1σ) for the DNP and FTIR measurements, respectively. The average HCHO-EIs ranged from 0.50 g/kg fuel at idle to 0.13 g/kg fuel at maximum engine power. Relatively good agreement (within uncertainty) is observed between the measurement techniques at the idle condition, in which the concentrations were largest. At the 75%-maximum and maximum power conditions, large discrepancies between the methods are likely the result of their reduced concentration and lack of measurement sensitivity. The T700 produced significantly higher concentrations of HCHO at the idle condition, compared with the T701C. All HCHO measurements with the FTIR and DNP methods (except the 75%-maximum DNP) show that operation of the T701C with the FT fuel had minimal impact on the production of HCHO.

Conclusions

Aircraft have been identified as significant sources of local pollution at airports and military bases. Accurate determination of emission indices from aircraft is necessary to assess their environmental impact in order to take appropriate action. In this effort, conventional aerosol instruments and an FTIR-based gas analyzer were used to measure the particulate matter (PM) and gaseous emissions of three T700 series engines (one T700 and two T701C), to determine emission indices and to assess the validity and performance of the instrumentation and measurement techniques. In general, the aerosol instrumentation and sampling methodology employed provided consistent and reliable measurements throughout the test campaign. Test results show that the T701C engine emitted significantly lower soot emissions than the T700 for all conditions tested. Corrected PM mass emission indices ranged from 0.2–1.4 g/kg fuel for the T700 and from 0.2–0.6 g/kg fuel for the T701C. Particle number and smoke numbers trends are consistent with those of the PM mass-EI. Excellent agreement in PM emissions measurements were observed between the two T701C engines. Slightly higher NO_x and lower CO emissions were observed for the T701C compared with the T700, which demonstrates higher operation temperatures and combustion efficiency for the T701C. Consistent with previous studies on TF33 and T63 engines, the FT fuel significantly reduced soot emissions (~ 40 – 97% in particle number), with smaller mean particle sizes and minimum impact on gaseous emissions, compared with operation on JP-8. The reduction in PM emissions is largely attributed to the lack of aromatic compounds in the FT fuel.

Acknowledgments

This work was funded by the Department of Defense Strategic Environmental Research and Development Program (SERDP) office within the Weapon Systems and Platforms focus area under the Project WP-1401 led by Oak Ridge National Laboratory (ORNL). ORNL is managed by UT-Battelle, LLC, for the U.S. Department of Energy under contract DE-AC05-00OR22725. The work of the University of Dayton Research Institute (UDRI) was supported by the U.S. Air Force Research Laboratory (AFRL) under the cooperative research agreement F33615-03-2-2347. Special thanks to Joe Lukas from the Aviation Branch Maintenance Division at Fort Stewart for his support and coordination of these tests and to Daniel Houck, Robert Henson, Jason Mikelonis, and Robert Shell for operating the test facility. The authors are also very grateful to Joe Mantz from UDRI and Tom Greene from Taitech, Inc., for their technical support during the tests and to Linda Shafer and Rhonda Cook of UDRI for the polycyclic aromatic hydrocarbon analysis.

References

- [1] "For Greener Skies-Reducing Environmental Impacts of Aviation," Committee on Aeronautics Research and Technology for Environmental Compatibility, National Research Council, 2002.

- [2] Anderson, B. E., Branham, H.-S., Hudgins, C. H., Plant, J. V., Ballenthin, J. O., Miller, T. M., et al., "Experiment to Characterize Aircraft Volatile Aerosol and Trace-Species Emissions (EXCAVATE)," NASA TM-2005-213783, 2005.
- [3] Wey, C. C., Anderson, B.E., Hudgins, C., Wey, C., Li-Jones, X., Winstead, E., et al., "Aircraft Particle Emissions eXperiment (APEX)," NASA TM 2006-214382, 2006.
- [4] "Non-Volatile Particle Exhaust Measurement Techniques," SAE International, Aerospace Information Report, SAE AIR 5892, Warrendale, PA, 2004.
- [5] Kelly, K. E., Sarofim, A. F., Lighty, J. S., Wagner, D. A., Arnott, W. P., Rogers, C. F., Zielinska, B., and Prather, K. A., "User Guide for Characterizing Particulate Matter. Evaluation of Several Real-Time Methods," College of Engineering, Univ. of Utah, Salt Lake City, UT, 1 Oct. 2003
- [6] Corporan, E., DeWitt, M. J., Belovich, V., Pawlik, R., Lynch, A. C., Gord, J. R., and Meyer, T. R., "Emissions Characteristics of a Turbine Engine and Research Combustor Burning a Fischer-Tropsch Jet Fuel," *Energy and Fuels*, Vol. 21, No. 5, 2007, pp. 2615–2626. doi:10.1021/ef070015j
- [7] Corporan, E., DeWitt, M. J., Klingshirm, C. D., and Striebich, R. C., "DoD Assured Fuels Initiative: B-52 Aircraft Emissions Burning a Fischer-Tropsch/JP-8 Fuel Blend," *Proceedings of the 10th International Conference on Stability and Handling of Liquid Fuels* [CD-ROM], International Association for Stability, Handling and Use of Liquid Fuels, Atlanta, 2007.
- [8] Jones, X. L., Penko, P.F., Williams, S., Moses, C., "Gaseous and Particle Emissions in the Exhaust from a T700 Helicopter Engine," ASME International Turbo Expo Conference, ASME International, Paper GT2007-27522, 2007.
- [9] "Aircraft Gas Turbine Exhaust Smoke Measurement," SAE Aerospace Recommended Practice, Rept. SAE ARP 1179. Society of Automotive Engineers, Warrendale, PA, 1970.
- [10] DeWitt, M. J., Striebich, R., Shafer, L., Zabarnick, S., Harrison, W. E., III, Minus, D. E., and Edwards, T., "Evaluation of Fuel Produced via the Fischer-Tropsch Process for Use in Aviation Applications," American Institute of Chemical Engineers, Spring National Meeting, Paper 58b, 2007.
- [11] "Standard Test Method for Hydrocarbon Types in Liquid Petroleum Products by Fluorescent Indicator Adsorption," ASTM International, Std. ASTM D1319, Alexandria, VA, Oct. 2008.
- [12] "Standard Test Method for Sulfur in Petroleum and Petroleum Products by Energy Dispersive X-Ray Fluorescence Spectrometry," ASTM International, Std. ASTM D4294, Alexandria, VA, Oct. 2008.
- [13] "Standard Test Method for Distillation of Petroleum Products at Atmospheric Pressure," ASTM International, Std. ASTM D86, Alexandria, VA, April 2007.
- [14] "Standard Test Method for Freezing Point of Aviation Fuels (Automatic Phase Transition Method)," ASTM International, Std. ASTM D5972, Alexandria, VA, Nov. 2005.
- [15] "Standard Test Method for Gum Content in Fuels by Jet Evaporation," ASTM International, Std. ASTM D381, Alexandria, VA, Nov. 2004.
- [16] "Standard Test Method for Kinematic Viscosity of Transparent and Opaque Liquids (and Calculation of Dynamic Viscosity)," ASTM International, Std. ASTM D445, Alexandria, VA, May 2006.
- [17] "Standard Test Method for Measurement of Fuel System Icing Inhibitors (Ether Type) in Aviation Fuels," ASTM International, Std. ASTM D5006, Alexandria, VA, Dec. 2003.
- [18] "Standard Test Method for Smoke Point of Kerosene and Aviation Turbine Fuel," ASTM International, Std. ASTM D1322, Alexandria, VA, June 1997.
- [19] "Standard Test Methods for Flash Point by Pensky-Martens Closed Cup Tester," ASTM International, Std. ASTM D93, Alexandria, VA, May 2007.
- [20] "Test Method for Density, Relative Density, and API Gravity of Liquids by Digital Density Meter," ASTM International, Std. ASTM D4052, Alexandria, VA, April 1996.
- [21] "Standard Test Method for Estimation of Net Heat of Combustion of Aviation Fuels," ASTM International, Std. ASTM D3338, Alexandria, VA, May 2008.
- [22] "Standard Test Method for Estimation of Net Heat of Combustion of Aviation Fuels," ASTM International, Std. ASTM D3343, Alexandria, VA, Nov. 2005.
- [23] "Turbine Fuel, Aviation, Kerosene Type, JP-8 (NATO F-34), NATO F-35, and JP-8+100 (NATO F-37)," U.S. Dept. of Defense, MIL-DTL-83133F, 11 April 2008.
- [24] "Procedure for the Analysis and Evaluation of Gaseous Emissions from Aircraft Engines," Aerospace Recommended Practice SAE ARP 1533A, SAE International, Warrendale, PA, 2004.
- [25] Richter, H., and Howard, J. B., *Progress in Energy and Combustion Science*, Vol. 26, Nos. 4–6, 2000, pp. 565–608. doi:10.1016/S0360-1285(00)00009-5
- [26] Lefebvre, A. H., *Gas Turbine Combustion*, 1st ed., McGraw-Hill, New York, 1983, Chap. 11.
- [27] Wade, M. D., "Aircraft/Auxiliary Power Units/Aerospace Ground Support Equipment Emission Factors," U.S. Air Force Rept. IERA-RS-BR-SR-2003-0002, 2004.
- [28] Corporan, E., Quick, A., and DeWitt, M. J., "Characterization of Particulate Matter and Gaseous Emissions of a C-130H Aircraft," *Journal of the Air & Waste Management Association*, Vol. 58, No. 4, April 2008, pp. 474–483. doi:10.3155-1047-3289.58.4.474
- [29] "Compendium Method TO-11A: Determination of Formaldehyde in Ambient Air Using Adsorbent Cartridge Followed by High Performance Liquid Chromatography (HPLC) [Active Sampling Methodology]," Compendium of Methods for the Determination of Toxic Organic Compounds in Ambient Air, 2nd ed., Center for Environmental Research Information, U.S. Environmental Protection Agency, Rept. EPA/625/R-96/010b, Cincinnati, OH, www.epa.gov/ttn/amtic/files/ambient/airtox/to-11ar.pdf [retrieved 21 March 2008].

A. Gupta
Associate Editor

APPENDIX E

Compatibility of DiEGME and TriEGME Fuel System Icing Inhibitor Additives with BMS 10-39 Aircraft Tank Topcoat Material

INTENTIONALLY LEFT BLANK

Compatibility of DiEGME and TriEGME Fuel System Icing Inhibitor Additives with BMS 10-39 Aircraft Tank Topcoat Material

Steven Zabarnick,^{*,†} Ryan Adams,[†] Zachary West,[†] Matthew J. DeWitt,[†] Linda Shafer,[†] Richard Striebich,[†] Charles L. Delaney,[‡] and Donald K. Phelps[§]

[†]University of Dayton Research Institute, Dayton, Ohio 45469, [‡]Consultant, 10011 Bennington Drive, Cincinnati, Ohio 45241, and [§]Air Force Research Laboratory, Fuels and Energy Branch AFRL/RZPF, Wright-Patterson AFB, Ohio 45433

Received December 17, 2009. Revised Manuscript Received February 17, 2010

In recent years, the fuel system icing inhibitor (FSII) diethylene glycol monomethyl ether (DiEGME) has been implicated in an increasing incidence of peeling of topcoat material in the ullage space of integral wing tanks in the B-52 and other military aircraft. Work has indicated that, for the combination of DiEGME in JP-8 fuel, the icing inhibitor additive can concentrate in the tank ullage and condense at elevated concentrations on cooled tank walls. These high concentrations of DiEGME cause swelling and subsequent peeling of the epoxy-based topcoat. Here, we report on detailed studies of the compatibility of DiEGME and FSII replacement candidate triethylene glycol monomethyl ether (TriEGME) with BMS 10-39 fuel tank topcoat material. Tests were designed to simulate fuel tank wall exposures with subsequent topcoat degradation measured by icing inhibitor uptake analyses and pencil hardness evaluations. The lower volatility of TriEGME relative to the JP-8 fuel components results in it being less able to concentrate in the tank ullage and promote topcoat failure, as compared to DiEGME. This was confirmed with lower additive levels measured in the ullage, condensed vapors, and the exposed topcoat material. The pencil hardness of topcoat material exposed to fuel vapors was significantly improved upon changing from DiEGME to TriEGME exposure. Simulation experiments were able to reproduce the fuel tank topcoat peeling observed in the field as well as determine the conditions (concentration and temperature) required for topcoat degradation.

Introduction

At high altitudes, the exteriors of aircraft are subjected to cold temperatures (≤ 60 °C) from the surrounding environment. While the current USAF fuel, JP-8, has a low freezing point (-47 °C maximum), any free water within the fuel will readily freeze at altitude. To remedy this situation, a fuel system icing inhibitor (FSII) was developed and introduced as a fuel additive to selectively partition into any free water present and suppress the freezing point of the aqueous mixture. This additive became required by the U.S. military in 1961 after a B-52 Stratofortress crash, which was attributed to ice formation that caused fuel line blockages. Initially, ethylene glycol monomethyl ether (EGME)/glycerol mixtures were employed as the FSII additive during the period that JP-4 was used by the United States Air Force (USAF). However, EGME was subsequently shown to have a relatively high toxicity, and problems arose with the volatility of JP-5, the fuel used by the Navy, as it became difficult for EGME-containing fuels to meet the flashpoint specification (≥ 60 °C).¹ Diethylene glycol monomethyl ether (DiEGME) was found to be an acceptable alternative FSII additive, and transition to this species began in 1987 for JP-5 and was authorized for use in JP-8 in 1992. DiEGME is currently required in both JP-5 and JP-8 fuels, with a specification procurement level of 0.10–0.15 vol % for both fuels.

The current aircraft use limits for DiEGME are currently 0.03 vol% for the U.S. Navy and 0.07 vol % for the U.S. Air Force.

Recently, DiEGME has been implicated in causing degradation and peeling of the protective fuel tank topcoat layer in B-52 aircraft, a process referred to as fuel tank topcoat peeling (FTTP).^{2,3} This epoxy topcoat layer is Boeing Material Specification (BMS) 10-39 and serves as a physical barrier between the fuel/air environment and the aluminum tank wall. Peeled surfaces are more likely to support corrosion and pitting of the aluminum substrate. Also, the topcoat flakes that have lost adhesion can cause blockages in fuel filters and valves, resulting in catastrophic failure of the aircraft. Figure 1 shows examples of fuel tank topcoat peeling and the problems it causes.

The BMS 10-39 epoxy topcoat was originally formulated to resist degradation from prolonged exposure to JP-4 fuel. Despite this formulation, FTTP has occurred in fuel containing DiEGME, and high concentrations of DiEGME in fuel and water have been shown to promote swelling and peeling of the topcoat layer.^{2,3} FTTP has primarily been observed above the fuel level on the tank walls in the headspace (ullage) of the tank and at the bottom of the tank where water accumulates (Figure 1). Mechanisms of deterioration have been proposed for both of these peeling areas. For the ullage space above the

*To whom correspondence should be addressed. E-mail: zabarnick@udayton.edu.

(1) Martel, C. R. Air Force Wright Aeronautical Laboratories Technical Report AFWAL-TR-2062, Wright-Patterson AFB, OH, 1987.

(2) Aliband, A.; Lenz, D.; Dupois, J.; Alliston, K.; Sorhaug, V.; Stevenson, L.; Whitmer, T.; Burns, D.; Stevenson, W. *Prog. Org. Coat.* **2006**, *56*, 285–296.

(3) Aliband, A.; Lenz, D.; Stevenson, L.; Whitmer, T.; Cash, R.; Burns, D.; Stevenson, W. *Prog. Org. Coat.* **2008**, *63*, 139–147.

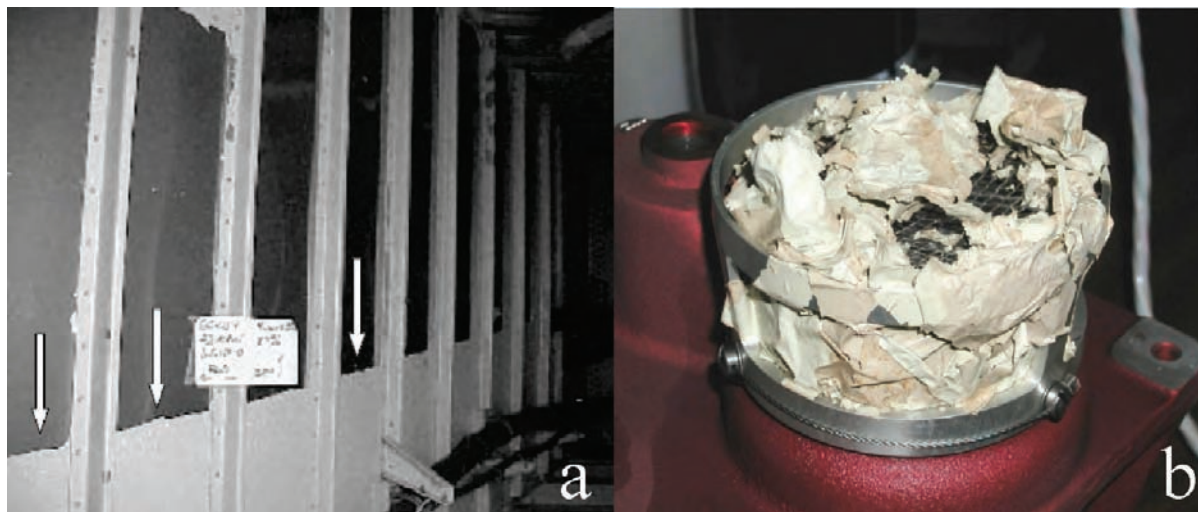


Figure 1. (a) Fuel tank topcoat peeling in a B-52 wing fuel tank² and (b) a B-52 boost pump intake screen (4-mesh) clogged with BMS 10-39 flakes.

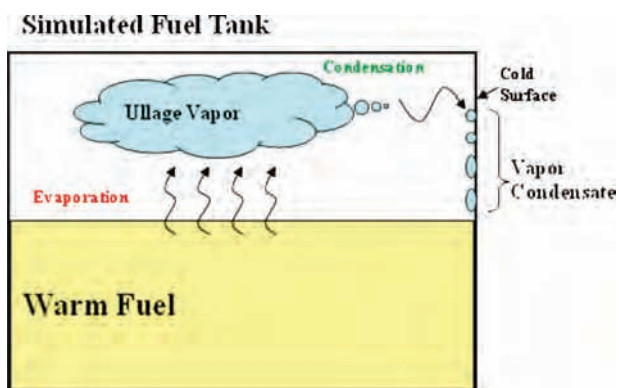


Figure 2. FTTP phenomenon initiated by a DiEGME-rich ullage vapor and condensation on a cold topcoat surface.

fuel level, DiEGME concentrates in the vapor phase due to its high vapor pressure relative to the JP-8 fuel.² This DiEGME-rich vapor phase can then condense on cold topcoat surfaces, resulting in a wall wetted with condensate that has a DiEGME concentration which is significantly higher than that of the base fuel. The presence of relatively warm bulk fuel and vapor along with a cold fuel tank wall encourages this process, as demonstrated graphically in Figure 2.

The conditions of relatively warm bulk fuel and a cold wall to promote selective condensation are possible under several scenarios during aircraft operation. For example, after take-off, the fuel tank walls will cool down quickly due to the low outside air temperature at altitude, while the large thermal mass of bulk fuel will result in the fuel cooling down significantly more slowly. These conditions will be repeated for each flight, resulting in continued exposure of DiEGME-rich condensate in contact with the topcoat. Another scenario involves aircraft on the ground in warm climates. If the aircraft is left exposed to the sun throughout a hot day, the bulk fuel temperature in the aircraft fuel tanks can rise substantially. In studies of the temperature of refueling tankers, it was found that the tanker trucks showed fuel temperatures above 55 °C during the middle of the day in a desert location.⁴ As the

sun sets, the outside air temperature will decrease quickly, especially in arid climates, while the wall will cool more quickly due to the differences in thermal mass and promote surface condensation. These conditions can be repeated daily if the ambient temperature is sufficiently warm to vaporize the lighter fuel components, such as DiEGME.

Topcoat degradation at lower fuel tank surfaces is likely initiated by high concentrations of DiEGME in water bottoms. The specific gravities of water and DiEGME (1.00 and 1.023, respectively) are higher than that of JP-8 (~0.8), and thus free water that phase-separates will collect at the bottom of the tank. DiEGME and water are completely miscible, and DiEGME typically concentrates in water in the range of 30 to 50 vol % within the fuel tank. Higher concentrations of DiEGME in aqueous solutions have been shown to cause FTTP with seven day liquid exposures.⁵ Severe swelling of topcoat flakes has also been shown to occur at similar exposure concentrations.²

The chemical and physical mechanisms which result in FTTP are still not fully understood, and thus it is difficult to eliminate or minimize future occurrences. More information needs to be obtained on the required concentrations, temperatures, and time of exposure to induce FTTP. Along with attempting to confirm the mechanisms which cause FTTP, a number of solutions have been proposed to prevent future problems. To reduce the occurrence of peeling in water bottom areas, regular sumping of aircraft tanks ensures that water/FSII mixtures do not accumulate in the fuel tanks and high concentrations of FSII are not in contact with the topcoat for extended periods of time. For the issue of FTTP on the tank ullage surfaces, one solution is to reduce the concentration of DiEGME in JP-8. Decreasing the concentration of DiEGME in the fuel would reduce the concentration in the vapor phase and lower the concentration in the condensate which collects on the ullage topcoat. This approach would also lower the DiEGME levels in tank water bottoms. However, the DiEGME concentration still needs to be high enough to provide the required anti-icing performance. Ideally, a proper balance between reducing the occurrence of FTTP and retaining the inhibiting icing performance of the additive would be found.

(4) Williams, T. F.; Vangness, M.; Shardo, J.; Ervin, J. Air Force Research Laboratory Report, AFRL-PR-WP-TR-2005-2103, Wright-Patterson AFB, OH, February 2005.

(5) Hufnagle, D. University of Dayton Research Institute Report UDR-TR-2008-00032, Dayton, OH, 2008.

Table 1. Selected Properties of DiEGME and TriEGME

FSII additive	vapor pressure (mmHg) @ 20 °C	density (g/mL) @ 20 °C	molecular weight (g/mol)	freezing point (°C)
DiEGME	0.19	1.023	120	−85
TriEGME	<0.01	1.026	164	−47

Another approach is to replace DiEGME with an alternative FSII additive which does not promote FTTP. With the current hypothesized mechanisms for FTTP on the tank ullage walls, a suitable replacement would provide equivalent anti-icing efficacy but exhibit a lower vapor pressure. One such species that may fit these requirements is triethylene glycol monomethyl ether (TriEGME), which has a vapor pressure that is more than an order of magnitude lower than DiEGME, as shown in Table 1.⁶ TriEGME should not volatilize as readily from the bulk fuel, resulting in a lower effective concentration in any condensate in contact with the topcoat surfaces. Table 1 also shows other selected property differences between DiEGME and TriEGME.

It is apparent that further investigation of the requisite conditions for the occurrence of FTTP in aircraft is required. A comparison of the topcoat compatibility between DiEGME and TriEGME is also essential to assess TriEGME as an alternative icing inhibitor additive. Determination of the anti-icing efficacy of DiEGME and TriEGME at lower concentrations is being evaluated separately.^{6,7} The experiments in this study were designed to assess the effects of DiEGME and TriEGME on BMS 10-39 topcoat degradation using the most probable scenarios relating to FTTP. The absorption of FSII into BMS 10-39 was quantified to analyze the effects of concentration in aqueous or fuel solutions under various exposure conditions. This work also studied differences between DiEGME and TriEGME using topcoat panels that were recently fabricated and those that were exposed to fuel for many years, as well as the conditions which will reduce the topcoat integrity below the minimum specification requirement. After being softened due to DiEGME exposure, BMS 10-39 topcoat has been observed to “rearden”,² which is most likely due to FSII molecules desorbing from the coating. Thus, preliminary studies were also performed to investigate the desorption rates of FSII from the topcoat. An ultimate goal of this work was to reproduce FTTP in a controlled laboratory setting to assess the differences between DiEGME and TriEGME, as well as to investigate the degradation process and to provide a knowledgebase of the conditions necessary for FTTP.

Experimental Section

BMS 10-39 Panels. Experimental studies were performed to investigate the compatibility of FSII additives with both aged and new BMS 10-39 topcoat panels. The AFRL Coatings Technology Integration Office fabricated one-sided topcoat panels on 1/32 in. aluminum (2024-T3) to meet the 1-mm-thickness specification of BMS 10-39. Prior to coating, the

aluminum panels were cleaned, acid etched with an alcoholic phosphoric acid solution, and chemically treated with Alodine 1200S, which is a chromium chemical conversion coating surface treatment. These manufactured panels are referred to as “new” panels, as they have not been exposed to fuel or FSII before these studies. The “old” BMS 10-39 panels were obtained from a scrapped B-52G aircraft from Boeing Wichita which had been operated for many years with JP-4 and JP-5/EGME and/or JP-5/DiEGME fuels.

FSII Exposure Solutions. Interactions with the BMS 10-39 topcoat can occur with FSII in solution with various liquids. Three different bulk solutions were used in the experimental studies while varying the FSII concentrations: water, fuel, and a surrogate fuel condensate. Aqueous solutions were used for many of the studies to evaluate the required concentrations for FTTP to occur in water bottoms. The water used to create the solutions was purified via reverse osmosis. A clay treated Jet A-1 (POSF-4877) was used as the base fuel in the experimental studies. The clay treatment was necessary to remove any FSII contamination in the fuel that may have occurred during transportation and storage. Finally, a surrogate fuel was developed to simulate the fuel condensate which would be in contact with the BMS 10-39 coating in the ullage of aircraft tanks. This surrogate was comprised of Exxsol D40 (85% by volume), Aromatic 100 (9%), and Aromatic 150 (6%). The mixture closely simulates the lighter components that are initially vaporized from the bulk fuel and subsequently condense on cold surfaces.⁶

FSII Absorption Study. The uptake study investigated the liquid–solid interactions between FSII and the BMS 10-39 layer by quantifying the FSII absorbed into the topcoat. Aluminum topcoat panel squares (0.25 in.²) are submerged in 20 mL of fuel or water with specific concentrations of DiEGME or TriEGME in 30 mL capped vials. This volume of liquid was used to ensure there would not be a significant change in the FSII concentration of the liquid phase due to partitioning into the topcoat. This was verified by analyzing the concentration of the solution before and after exposure to a BMS 10-39 panel.

The aqueous solutions ranged from 0 to 100% DiEGME or TriEGME, while the fuel or surrogate solutions ranged from 0 to 2%. This difference in concentration ranges resulted from the typical concentrations expected in these phases. Initially, the solutions were placed into a shaker to be agitated throughout the exposure period; however, further studies revealed that agitation was unnecessary due to the short time required for the FSII in the liquid and topcoat layer to equilibrate. The initial exposure time used was five days, as further time did not increase the absorption of FSII in the topcoat. Later, this was shortened on the basis of the absorption study discussed below. After the exposure period, the panels were removed from the vials and cleaned to remove any liquid droplets by rinsing with a small volume of hexane (1–2 mL) and then blotted dry with Kimwipes. The panel was then submerged in 2 mL of acetone for 1 h to extract the absorbed FSII component from the topcoat. Consecutive acetone extractions on the same panel failed to yield detectable levels of FSII, showing that all of the extractable FSII was removed. The acetone extract was collected and analyzed by GC-MS to obtain the total mass of absorbed FSII. The FSII absorption quantity was normalized by the topcoat volume, measured via thickness measurements, and reported as moles of FSII absorbed per liter of topcoat. Each experimental condition was performed in triplicate to obtain a measure of reproducibility.

This basic approach was modified to investigate the rate of FSII absorption and desorption. To evaluate the absorption rate, the exposure time of the topcoat in contact with a FSII solution was varied to determine when the uptake concentrations reached a plateau. A plateau in the uptake absorption vs time suggests that the topcoat no longer absorbs FSII and equilibrium is reached with the FSII in solution. The panels

(6) Zabarnick S.; West Z.; DeWitt M.; Shafer L.; Striebich R.; Adams R.; Delaney C.; Phelps D. IASH 2007, the 10th International Conference on Stability, Handling and Use of Liquid Fuel, Tucson, AZ, October 2007.

(7) DeWitt, M. J.; Zabarnick, S.; Shaeffer, S.; Williams, T.; West, Z.; Shafer, L.; Striebich, R.; Breitfield, S.; Adams, R.; Cook, R.; Delaney, C. L.; Phelps, D. IASH 2009, the 11th International Conference on Stability, Handling and Use of Liquid Fuel, Prague, Czech Republic, October 2009.

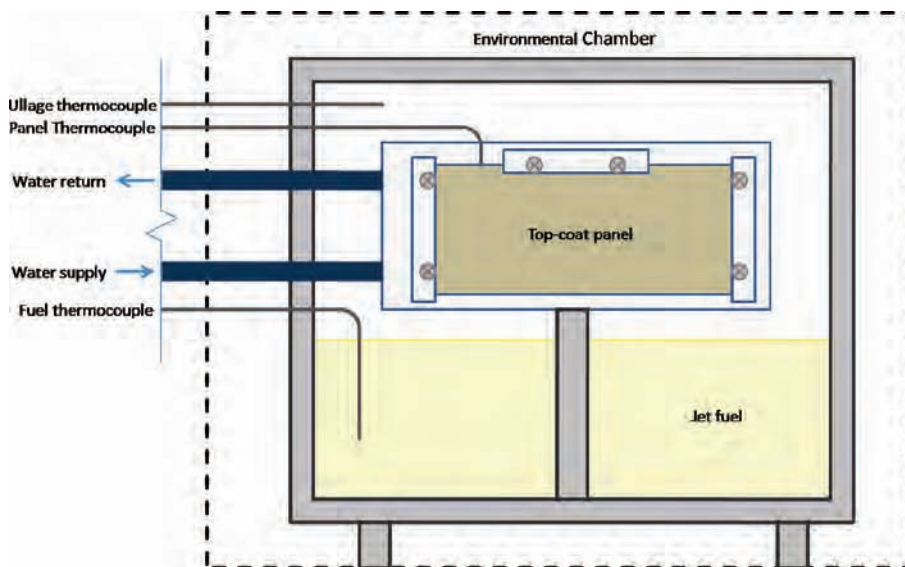


Figure 3. FSII simulation box apparatus.

were removed from the solutions at varying times between 10 s and 144 h. This was performed with new panels and 50% aqueous solutions of DiEGME and TriEGME. The results indicated that equilibrium was reached in less than 24 h. These data were used to validate reducing the exposure time for the absorption study to one day for later experiments from the initial five days. Alternatively, the desorption rate was qualitatively analyzed by varying the time between the cleaning of the panel (after removal from the solution) and the acetone extraction.

Pencil Hardness Study. To correlate the quantity of FSII absorbed with the integrity of the coating after exposure, pencil hardness tests were performed. These were performed according to ASTM D3363 procedures. The pencil leads used for this analysis along with the range of acceptable hardness for BMS 10-39 are shown below:

Acceptable Range for BMS 10-39

6B – 5B – 4B – 3B – 2B – B – HB – F – H – 2H – 3H – 4H – 5H – 6H
 Softest → → → Hardest

The pencil hardness study was performed on 1" × 2" panels of new and old BMS 10-39 on aluminum. The panel size was chosen to allow the use of all leads required to determine the hardness. Two such panels were submerged in 100 mL beakers with 80 mL of a FSII solution for two days. This exposure time permitted two data sets to be collected per week while maintaining equilibrium between the solution and the topcoat. As in the uptake study, this volume of liquid was used to ensure that the concentration of FSII in the solution did not decrease during the duration of exposure. This was verified by analyzing the concentration of DiEGME in a solution before and after exposure, which did not change significantly over the two days.

When the panels were removed, they were washed with a small amount of hexane to remove the remaining solution from the BMS 10-39 panel. One of the panels was immediately tested for its pencil hardness, while the other was allowed to dry in a fume hood for 2 h prior to evaluation. The latter approach was performed to determine the ability of the topcoat to reharder over time as the FSII evaporates from the topcoat material.

Fuel Tank Topcoat Peeling (FTTP) Simulation Study. This study was designed to simulate the conditions in aircraft fuel tanks which promote topcoat degradation, as well as to quantify the effects of FSII concentration and temperature on the resulting pencil hardness of exposed BMS 10-39 panels.

The experiment was used to test the hypothesis that DiEGME concentrates in the ullage and condenses at high concentrations on the topcoat surface, which results in degradation. This simulation was also used to determine if the lower vapor pressure of TriEGME results in a decreased potential for creating a FSII-rich ullage. The system (Figure 3) consisted of a 28.3 L (1 ft³) aluminum box which contained the fuel along with a plate heat exchanger with an attached BMS 10-39 panel. The box containing the fuel was placed inside an environmental chamber, allowing control of the fuel and box surface temperatures. The heat exchanger/panel placed above the fuel allowed independent temperature control of the topcoat panel, which was secured by clamps on the edges and top of the panel. A recirculating cooling water bath was used to control the heat exchanger temperature and the surface temperature of the topcoat panel. This heat exchanger was maintained at a lower temperature than the fuel to promote selective condensation onto the topcoat specimen.

The BMS 10-39 panels used for the simulation were 3" × 6" in size to provide a large surface area for contact with the condensate, and for visible confirmation of topcoat peeling. The box was typically filled with 9 L (approximately 1/3 of the total volume) of jet fuel and agitated throughout the duration of the experiment with a magnetic stir bar. This volume was used to create a similar ratio of total mass of FSII to area of topcoat as shown in the Uptake and Pencil Hardness Study, such that any absorption of FSII in the topcoat panel would not reduce the FSII concentration in the bulk fuel. Thermocouples were placed in the vapor headspace of the box, submerged into the fuel, and placed between the topcoat panel and heat exchanger surface. During the experiment, the box was closed after the fuel was added, and then the environmental chamber was heated to a specified temperature. After the desired test duration (2 to 5 days) and cooling to near ambient temperatures, samples of the bulk fuel and condensate were collected. Condensate samples were obtained using a chromatographic syringe to collect droplets on the panel or the heat exchanger. The initial fuel samples, final fuel samples, and condensate samples were analyzed by GC-MS to obtain FSII concentrations. Data were collected at varying initial FSII concentrations in the bulk fuel, temperatures of the box and/or heat exchanger, and exposure durations of FSII in contact with the topcoat panel. The topcoat panel was removed from the apparatus and immediately evaluated for its hardness at five locations: the center of the panel and each of the four corners.

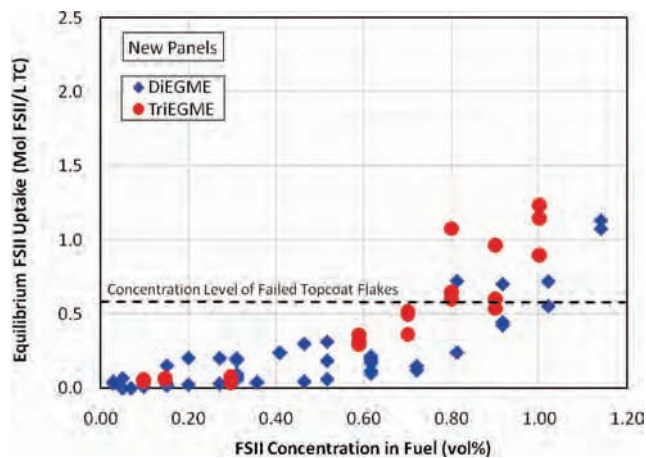


Figure 4. Equilibrium uptake of new panels exposed to DiEGME and TriEGME in Jet A-1.

Analytical Techniques Used for Quantification of FSII. Analytical techniques were developed for quantification of levels of FSII in water, acetone, and fuel. While there is an ASTM standard for determination of DiEGME in fuel (ASTM D5006), the technique requires a large volume of fuel (80 to 160 mL), which was not available for the current studies. In addition, the variability of this method is greater than required for these studies.

Verification of the FSII concentration in water before exposure to the topcoat material was performed by refractive index using a Reichert AR200 Digital Refractometer over a concentration range of 0 to 100% FSII. Individual calibration curves were determined for DiEGME and TriEGME at approximately 10 vol % increments. The reproducibility is approximately $\pm 10\%$ of the FSII concentration.

Quantifying the concentration of FSII in acetone solutions was required for the topcoat absorption study and was performed by gas chromatography with flame ionization detection (GC-FID). An HP 5890 Series II GC-FID was used to quantify the dilute FSII component in acetone in ranges from 0 to 0.20 vol % to a reproducibility of $\pm 10\%$ of the FSII concentration.

For analysis of FSII in the fuel, fuel surrogate, and fuel condensate, a method was developed which employed gas chromatography with a mass spectrometer (GC-MS) detector. The FSII component in fuel could not be separated chromatographically due to coelution with the other fuel components. Thus, the selective ion mode of the detector was used to monitor the 45, 59, and 89 ions. These ion peaks are selective for both DiEGME and TriEGME, which allows the FSII peak to be resolved from the other fuel components. The reproducibility is approximately $\pm 10\%$ of the FSII concentration.

Results and Discussion

FSII Fuel Absorption Results. Studies were performed to investigate the absorption of DiEGME and TriEGME into BMS 10-39 topcoat panels as a function of concentration and time. The exposure studies were performed at ambient temperature and pressure as these were representative of ground conditions for aircraft fuel tanks. Unless specified, the panels were submerged in 20 mL FSII solutions for five days. The uptake data obtained using new panels in Jet A-1 are shown in Figure 4, with each data point representing the average of two or three panel measurements. The line labeled “concentration level of failed topcoat flakes” at 0.66 mol of FSII/L topcoat is from an uptake measurement obtained from failed topcoat flakes from the field. These failed topcoat flakes, which were obtained from B-52 aircraft, were analyzed by the same acetone extraction methodology as used to analyze the test panels

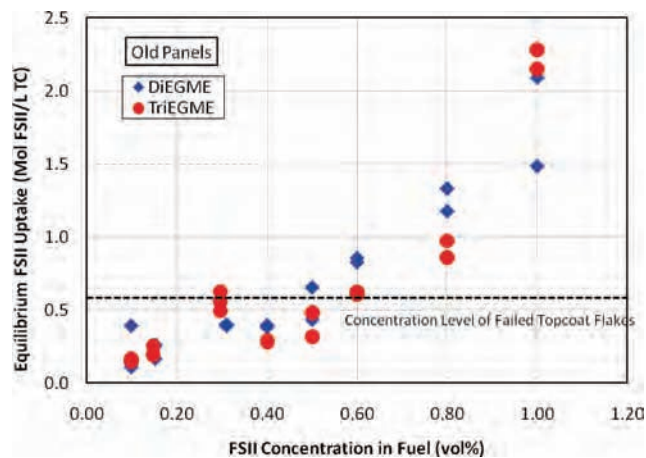


Figure 5. Uptake of DiEGME and TriEGME in Jet A-1 obtained for old panels that were in service for over 40 years.

during the absorption studies. Three separate flakes were analyzed in this fashion, and the level of DiEGME was averaged with a reproducibility of $\pm 20\%$ of this concentration.

The figure shows that increasing the initial concentration of FSII in the fuel increases the quantity of FSII absorbed into the topcoat layer. The uptake increases significantly at concentrations greater than 0.50 to 0.80 vol % FSII. The figure shows that DiEGME and TriEGME performed similarly and follow the same trend. The FSII uptake increases above the level of failed topcoat flakes at approximately 0.80 vol % FSII in the fuel. This suggests that the concentration in the fuel required for failure to occur is at least 0.80% FSII in cases of direct contact, although additional analysis and correlation with topcoat integrity (e.g., pencil hardness measurements) is needed for verification. It is likely that the concentration of FSII in these flakes has decreased over time due to evaporation from the coating. The reproducibility of the absorption data can be fairly poor at some concentrations, with the data varying up to $\pm 100\%$ of an average concentration. There are a number of factors that may contribute to this, including variations in the GC analysis, a slightly unequal topcoat thickness, and possible degradation of the topcoat after repeated use of some panels.

To provide an understanding of changes that can occur in the topcoat after 40 years of aging and contact with fuel, the absorption of FSII into BMS 10-39 was also determined using old panels. The absorption data for old panels in Jet A-1 fuel are shown in Figure 5 under ambient temperatures and an exposure time of five days.

The old panels show a significant increase in the topcoat uptake relative to the newer panels at equivalent FSII concentrations. This may be due to the old topcoat having a reduced resistance to absorption due to weakening of the polymer matrix which allows more molecules to absorb into the coating. The old panels reach an uptake value higher than the failed topcoat flakes at 0.50 vol % FSII, which is significantly lower than the 0.80 vol % level found for the new panels. If the ability of the topcoat to absorb FSII correlates with the tendency to exhibit degradation, these data imply that old panels would be expected to exhibit much higher levels of degradation. This correlation is addressed in the Pencil Hardness Study Report below.

When comparing DiEGME and TriEGME on a molar basis, the additives show similar extents of absorption in both the old and new topcoat panels, but on a mass basis,

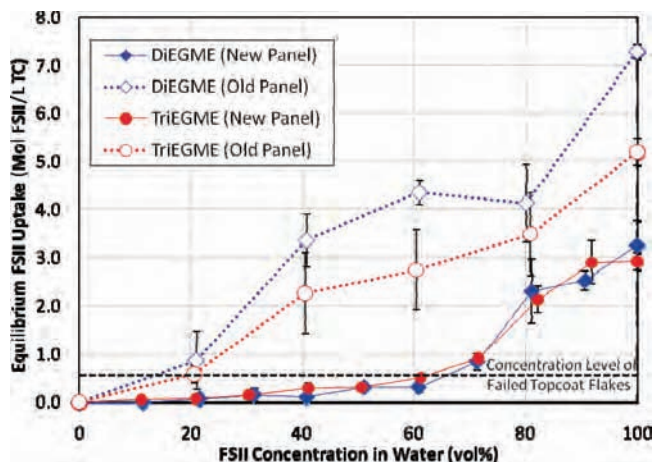


Figure 6. Uptake of DiEGME and TriEGME with new and old panels in aqueous solutions.

TriEGME has a higher equilibrium uptake than DiEGME. This can be explained by the molecular weight of TriEGME (164 g/mol) being one-third higher than DiEGME (120 g/mol), while the absorption of FSII is likely a function of the number of molecules a given volume of topcoat can absorb, rather than the mass. This FSII absorption data agree qualitatively with the equilibrium solvent uptake (ESU) measurements of topcoat flakes performed by Aliband et al.² which were performed via gravimetric differences following exposure. Their data show a relatively level 6% ESU uptake from 0 to 0.75 vol % DiEGME in the fuel, which then increases rapidly at higher DiEGME levels. The higher uptake observed by Aliband et al.² is likely caused by absorption of other fuel components into the topcoat, as their technique measures total uptake of all species into the topcoat flakes.

FSII Aqueous Absorption Results. To better understand the occurrence of FTTP from exposure to water bottoms of fuel tanks, measurements were performed to determine the absorption of FSII into the topcoat from FSII/water solutions. These measurements were performed at ambient temperature with the panels exposed to aqueous solutions for five days. Figure 6 shows the results for new and old panels with each data point representing the average of two or three uptake measurements.

The new panels show little uptake until a concentration of approximately 70 vol % FSII is achieved, while the uptake for older panels increases relatively smoothly with increasing FSII concentration. At concentrations greater than approximately 80 vol % FSII, the new panel uptake appears to plateau, or at least not increase as rapidly. These trends are similar to the aqueous ESU data obtained by Aliband et al.² Their data show a distinct “S” shaped curve with the ESU measurements reaching a plateau at levels above 75 vol % DiEGME.

The new panel uptakes shown in Figure 6 are above the failed topcoat flakes concentration at 70 vol % FSII and greater, while the old panels achieve this level at a significantly lower concentration of approximately 20 vol % FSII. The older panels absorb more FSII from aqueous mixtures than the newer panels, as also observed in the fuel absorption studies. Overall, the aqueous solutions show a much higher maximum uptake than the FSII in fuel solutions. The maximum uptake for aqueous solutions is ~7.2 mol FSII/L TC at 100 vol % FSII, while the maximum uptake for fuel

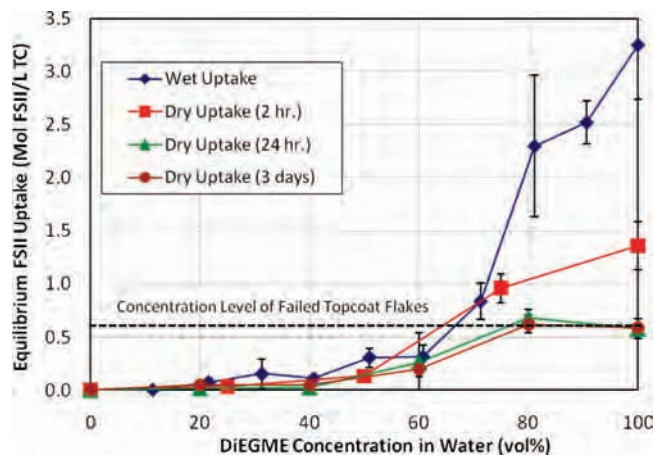


Figure 7. Uptake of DiEGME in aqueous solutions as a function of drying time with new panels.

exposures was ~2.3 mol FSII/L TC at 1.0 vol % FSII. This may be due to the significantly higher concentration of FSII in the aqueous solutions. While the topcoat was still physically intact after exposure to 100% solutions of DiEGME and TriEGME, it was easily damaged upon contact.

FSII Desorption Results. While the results show that DiEGME and TriEGME have similar absorption rates, it is important to assess relative desorption rates, as a slower desorption can contribute to increased topcoat degradation over time. To evaluate the relative desorption rate of FSII from the topcoat polymer matrix, the exposed panels were allowed to dry in a fume hood at ambient temperatures for various periods of time, rather than being immediately analyzed after exposure. The uptake for aqueous solutions of DiEGME was measured as a function of time and is shown in Figure 7.

The figure shows evidence for DiEGME desorption from the topcoat at the higher concentrations studied. At DiEGME concentrations less than 70 vol %, the equilibrium uptake is very similar for the four tested time periods. At concentrations greater than 70 vol %, there is a very large decrease in the DiEGME absorbed in the topcoat after only 2 h, and at longer times the desorption rate slows down significantly. The DiEGME concentration in the coating reaches its final equilibrium level in less than 24 h. It is interesting to note that DiEGME does not completely desorb from the topcoat, and the resulting final concentration of DiEGME in the topcoat is the same as the uptake level from the failed topcoat flakes at ~0.7 mol FSII/L topcoat for concentrations greater than 80 vol % in the water. In order for the dried flakes to have such a high concentration of FSII, they must have been exposed to an even greater concentration of DiEGME. Once the topcoat is exposed to a sufficient concentration of FSII to cause a failure, it is possible that the FSII in the coating will tend to desorb to this level.

As shown in Figure 8, the equilibrium uptake of TriEGME as a function of time is low up to a concentration of 50 vol % TriEGME. At higher concentrations, the data show evidence of desorption, but the TriEGME desorption is significantly slower at the 2 h mark. At the 100% FSII level, TriEGME is only reduced to 78% of the original concentration after 2 h, while the DiEGME concentration is reduced to 42%. This difference is likely due to the lower vapor pressure of TriEGME, which will cause it to evaporate

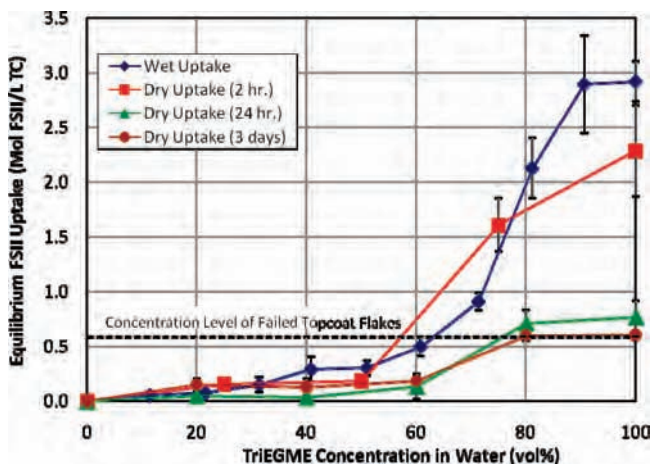


Figure 8. Uptake of TriEGME in aqueous solutions as a function of drying time with new panels.

more slowly from the topcoat. The slower rate of TriEGME desorption may also result from its larger molecular size, causing slower diffusion of the molecules through the polymer matrix. DiEGME and TriEGME desorb to a similar final concentration when given enough time to reach equilibrium.

The results show that TriEGME and DiEGME desorb to similar final equilibrium values, although their initial desorption rates vary. This difference in desorption rates at high concentrations of FSII indicates that it might be possible for high concentrations of TriEGME in the topcoat to be maintained for longer periods of time, with a resulting higher occurrence of topcoat degradation. However, it is expected that these high concentrations of TriEGME will not be achieved due to the lower vapor pressure of the additive, resulting in a reduced concentration in the condensate. This absorption/desorption study does not fully evaluate the entire FTTP process; however, it provides insight into the required concentration of FSII in jet fuel or water that will promote high absorption levels and subsequent topcoat degradation.

Pencil Hardness Study Results. Further studies were performed to evaluate topcoat integrity after the absorption of FSII has occurred. These studies provide insight into what concentration ranges of FSII in fuel or water provide sufficient absorption to cause topcoat degradation and promote FTTP. Pencil hardness measurement after exposure was selected as a simple technique to indicate topcoat degradation. A two day exposure time was selected to complete measurements in a reasonable time, while still maintaining the minimum exposure duration for equilibrium to be reached between the solution and topcoat. Each pencil hardness data point represents a single panel that was tested at the given FSII concentration. The first study used the surrogate condensate, discussed in the Experimental Section, which simulates the condensable fuel components from the fuel ullage. As it is hypothesized that the condensed vapors are the fuel components in contact with the fuel ullage tank walls where FTTP occurs, it is reasonable to study this using the fuel condensate surrogate mixture. Figure 9 shows a plot of the equilibrium uptake and pencil hardness of new panels in the surrogate as a function of the FSII concentration.

The figure shows a strong correlation between the pencil hardness of BMS 10-39 and the equilibrium uptake. The pencil hardness of the panel is unaffected at low FSII concentrations, but as the uptake begins to increase (> 0.80 vol %), a very sharp

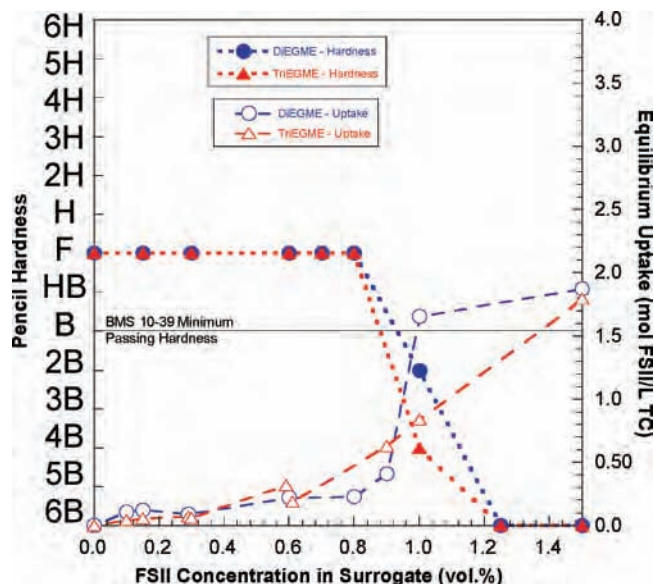


Figure 9. New panel uptake and wet pencil hardness in a fuel condensate surrogate.

decrease is observed. DiEGME and TriEGME behave very similarly in this pencil hardness evaluation. The equilibrium uptake level corresponding to the degradation of BMS 10-39 occurs at uptake levels greater than approximately 1.0 mol FSII/L topcoat. The topcoat integrity continues to decrease, and adhesion is lost as the concentration in the topcoat increases further. Exposure of BMS 10-39 topcoat panels to jet fuel (Jet A-1) containing FSII was compared to the surrogate mixture exposures, and in all cases it was found that the surrogate and jet fuel uptake and pencil hardness measurements were identical within experimental uncertainty. As both fuel and surrogate produce similar results, the surrogate was used for further pencil hardness studies to more closely simulate the conditions for FTTP.

Pencil hardness measurements were also performed with old panels to determine the effect of increased uptake on the hardness of the topcoat. If the older panels represent a worst-case scenario for the current BMS 10-39 coating in B-52 aircraft, then studying the pencil hardness of these panels after exposure to FSII is critical for investigating the requisite conditions for FTTP. The results are shown in Figure 10, along with FSII uptake measurements for old panels in the condensate surrogate.

The pencil hardness begins to decline rapidly at approximately 0.30 vol % FSII, which corresponds to an increase in the uptake. This FSII concentration is only twice the maximum procurement concentration for JP-8. The pencil hardness falls below the minimum passing rating of “B” at a FSII concentration of approximately 0.40 vol % FSII in the surrogate. This is a significant decrease from the concentration necessary to fail newer panels (approximately 1.0 vol % FSII). Overall, the older panels show a highly decreased ability to maintain coating hardness, as is evident by the increased absorption of FSII. These data imply that older panels have increased void spaces and weakened polymer bonds, resulting in a degradation of the topcoat matrix. These results indicate that older panels should be used for conservative analysis of aircraft fuel tank scenarios, due to the degraded properties of the topcoat after exposure to fuel and environmental conditions over many years.

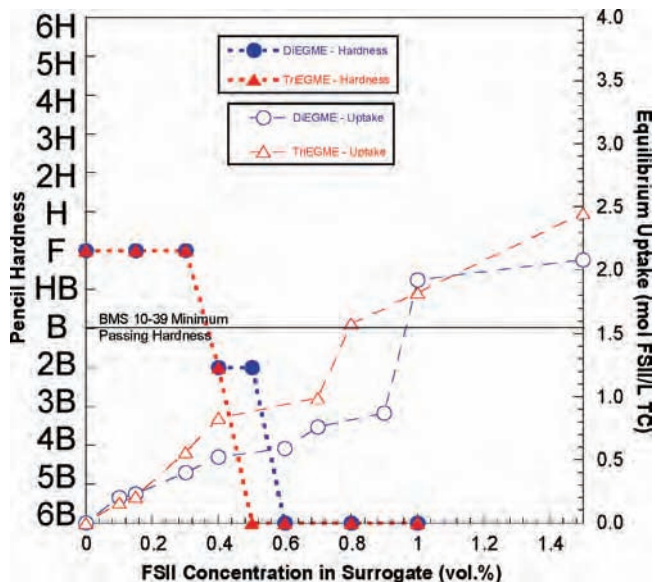


Figure 10. Uptake and pencil hardness of DiEGME and TriEGME in the condensate surrogate for old panels.

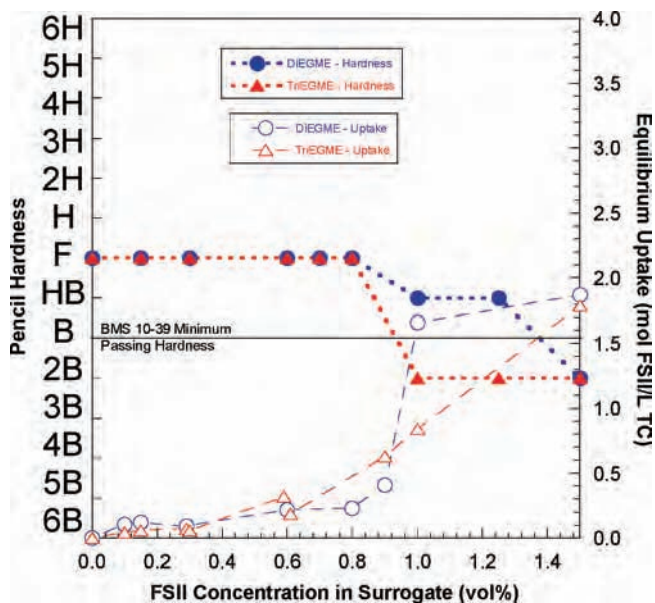


Figure 11. Pencil hardness for new panels in surrogate after 2 h of drying.

Pencil hardness testing was adapted to investigate the effect of FSII desorption from the topcoat. Instead of evaluating the hardness immediately after removal from the solution, testing was performed after drying for 2 h in a fume hood. This study was performed using the condensate surrogate and new panels under ambient conditions. The data are shown in Figure 11. It should be noted that the uptake data included in Figure 11 were obtained from extractions performed without adding a drying time before analysis.

The pencil hardness of BMS 10-39 topcoat decreases as the concentration of FSII in the surrogate increases; however, the hardness does not decrease to nearly the same extent as the panels evaluated immediately after contact with FSII. Panels exposed to DiEGME remain above the minimum passing hardness for BMS 10-39, except for 1.5 vol %

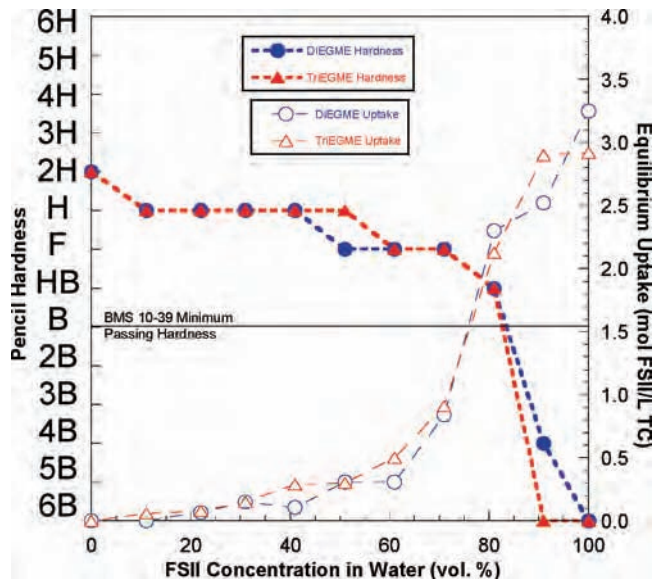


Figure 12. Pencil hardness and equilibrium FSII uptake of new panels in aqueous solutions with varying concentrations of FSII.

DiEGME in the surrogate. Panels exposed to TriEGME fall below the passing level at a concentration of 1.0 vol %. When the panels were evaluated “wet” (Figure 9), both DiEGME and TriEGME decreased the hardness at the same concentration of 1.0 vol % FSII. As discussed above, this difference could be due to the lower vapor pressure of TriEGME, which causes it to desorb and evaporate more slowly from the coating. It would be expected for the pencil hardness to reach the same level in both DiEGME and TriEGME if more time is given for desorption to occur, as the desorption data show that these additives reach the same final level in the topcoat. These data show that BMS 10-39 exposed to high concentrations of TriEGME will have a reduced hardness for a longer period of time compared to DiEGME. This could potentially increase the time frame for FTTP to occur, although these high concentrations of TriEGME in the topcoat are not expected to occur on tank ullage walls, as discussed below.

To study FTTP occurring in fuel tank water bottom areas, the pencil hardness was evaluated for new BMS 10-39 panels after exposure to aqueous solutions. Similar to the fuel and surrogate pencil hardness testing, this provides insight into the requisite concentrations in water bottoms for degradation. Figure 12 shows the “wet” pencil hardness testing and uptake as a function of aqueous FSII concentration for new panels.

The uptake dramatically increases at approximately 70 vol % FSII, while the pencil hardness also begins to decrease rapidly. New topcoat exposed to surrogate or fuel has been shown to degrade at approximately 2.0 mol FSII/L topcoat, and the aqueous solutions also show a very similar uptake concentration for failure. This degradation requires concentrations greater than 70 vol % DiEGME or TriEGME in water in contact with the topcoat. This is much higher than expected concentrations (30 to 50 vol %) in tank bottoms at ambient conditions with specification FSII levels in fuel.⁸ The initial hardness of these panels exposed to aqueous solutions was slightly higher than those exposed to fuel surrogate solutions. While there was some variation with the initial hardness from both the new and

(8) West, Z.; Shafer, L.; Striebich, R.; Zabarnick, S.; Delaney, C.; Phelps, D.; DeWitt, M. J. Manuscript in preparation, 2009.

panels used, the surrogate alone seemed to have a very slight softening effect of one pencil lead on the topcoat. This could potentially be due to some slight swelling due to absorption of unknown fuel species into the BMS 10-39 coating.

The pencil hardness testing has been able to provide a comparison between DiEGME and TriEGME, which has shown statistically identical behavior for nearly all absorption measurements. It has also provided a greater understanding into what concentrations are necessary to initiate FTTP. Concentrations of FSII greater than 1.0 vol % are required to severely weaken the topcoat of new panels in a fuel or surrogate. Older panels only require concentrations of FSII greater than approximately 0.40 vol % FSII in the fuel or surrogate to degrade the topcoat below the minimum hardness. As discussed above, this difference in concentration is a result of the reduced capability of the older panels to resist FSII absorption. Aqueous solutions require concentrations greater than 80 vol % for new panels to fail.

The only differences between DiEGME and TriEGME were observed in the desorption studies. The more rapid recovery in the hardness of DiEGME-exposed panels is most likely due to its higher vapor pressure. Because there is less FSII remaining in the topcoat, there is less swelling and the coating retains a higher hardness. While DiEGME and TriEGME performed similarly in the absorption study, different pencil hardness results are expected when the vaporization process of FSII in the bulk fuel is combined with the condensation process of the fuel/FSII vapor onto the topcoat. It is expected for TriEGME to have a much lower concentration in the vapor, and thus a much lower concentration in contact with the topcoat, because of its reduced vapor pressure. The next section demonstrates a simulation system which attempts to reproduce the overall behavior of the fuel/FSII/topcoat system.

Fuel Tank Topcoat Peeling (FTTP) Simulation Results.

A fuel tank simulation system was developed to attempt to recreate the required conditions for FTTP, as well as to evaluate the ability of TriEGME to reduce FTTP. In previous work,⁶ the concentrations of DiEGME and TriEGME in the fuel condensate were compared. The results show that the concentration of DiEGME in the condensate increased with each distillate fraction and further vaporization, while the concentration of TriEGME in the condensate maintained a level below the initial concentration in the bulk fuel. While this previous work focused only on collecting and analyzing the fuel condensate, the FTTP simulation described here will promote fuel/FSII vaporization with subsequent selective condensation of the fuel vapor on an old topcoat panel. This simulation was designed to recreate all necessary steps for FTTP in a controlled setting. It also serves to investigate the effects of specific conditions on FTTP, such as the initial concentration of FSII in the bulk fuel, the temperature of the fuel, and the temperature of the condensing topcoat surface. Selective condensation on the topcoat panel was achieved by attaching a heat exchanger with a recycling cooled water bath to the back of the panel. Old panels were employed to provide a conservative measure of the effect of the FSII additives. The concentration range of FSII in the fuel was from 0 to 0.15 vol %, while the temperatures investigated were 50 or 60 °C in the environmental chamber, and a cooled panel surface of 10 to 30 °C. These ranges of concentrations and temperatures were selected, as they are believed to closely represent the worst-case ground conditions for FTTP in aircraft fuel tanks.

Table 2. DiEGME and TriEGME Experiments with the Environmental Chamber at 60 °C and the Condensation Surface at 20 °C

	Initial FSII Conc. (vol%)	Final FSII Conc. (vol%)	Condensate FSII Conc. (vol%)	Exposure Time (Days)	Pencil Hardness
DiEGME	0	0.006	0.033	3	3H
	0.030	0.026	0.031	3	2H
	0.047	0.049	0.062	3	H-2H
	0.055	0.047	0.077	3	H-2H
	0.067	0.067	0.12	3	F-4H
	0.067	0.069	0.076	5	F-4H
	0.078	0.076	0.14	3	4H-1H
	0.100	0.094	0.67	3	<6B-4B
	0.101	0.100	0.25	4	<6B-4B
	0.140	0.135	0.72	2	<6B
0.156	0.138	1.09	5	<6B	
TriEGME	0.051	0.052	0.065	3	2H
	0.080	0.101	0.12	4	2H
	0.135	0.135	0.15	3	H-2H

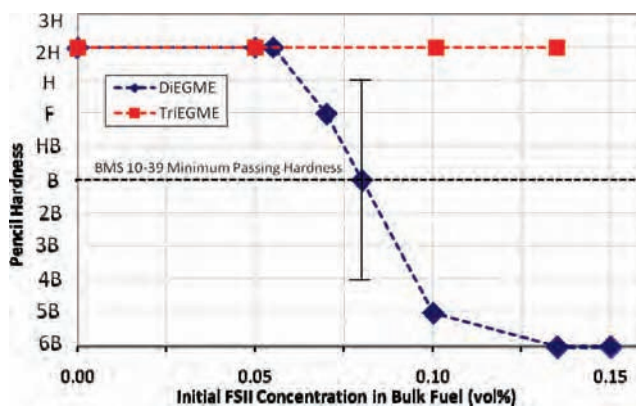


Figure 13. Pencil hardness of older panels after exposure to varying initial FSII concentrations in the bulk fuel.

Fuel and condensate samples were collected, their DiEGME and TriEGME concentrations were quantified after three to five days. This was shown to be sufficient for equilibrium to be reached, as discussed below. The data obtained from this set of experiments, at a fuel temperature of 60 °C and a cooling surface temperature of 20 °C, along with the quantified FSII concentrations are summarized in Table 2. Figure 13 presents the pencil hardness data as a function of the initial concentration for the experimental conditions in Table 2.

At concentrations equal to or below approximately 0.05 vol % DiEGME in the fuel, there were no visible changes in the panel after exposure, and the hardness of the topcoat was unaffected. This is evident by Figure 14, which shows the BMS 10-39 panel exposed to condensate from 0.05 vol % DiEGME in the fuel for three days. At concentrations of 0.06 to 0.10 vol % DiEGME in the fuel, there were initial signs of swelling in the panels. The hardness began to degrade quickly with any further increase in the DiEGME concentration in the fuel, although the panels were still relatively intact and did not show any severe signs of swelling and blistering. Figure 15 shows BMS 10-39 panels after



Figure 14. Old panel exposed to condensed vapors from 0.05 vol % DiEGME in the bulk fuel.

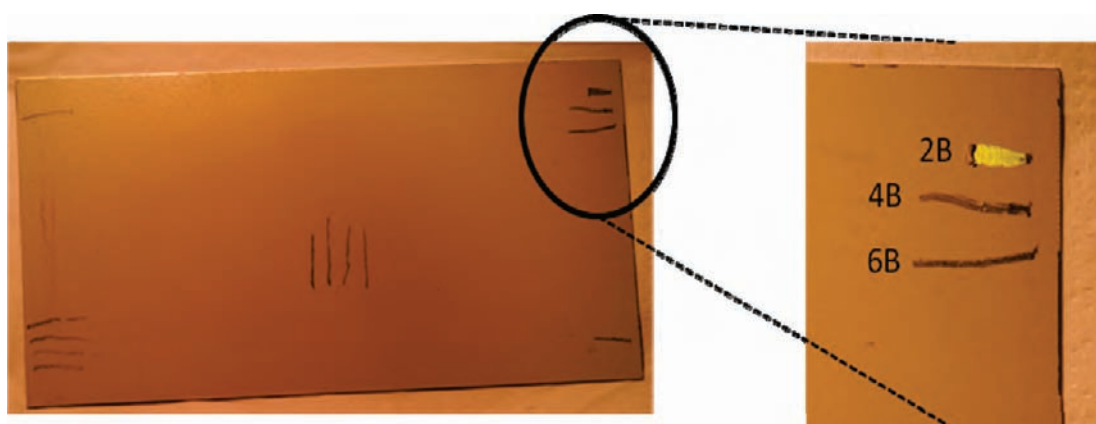


Figure 15. Old panel exposed to condensed vapors from 0.08 vol % DiEGME in the fuel with the pencil hardness measurements shown.



Figure 16. Old panel exposed to condensed vapors from 0.10 vol % DiEGME in the bulk fuel.

a three day exposure to condensate from ~ 0.08 vol % DiEGME in the bulk fuel. There were no visible changes in the topcoat panel after exposure to the DiEGME-rich condensate in this range; however, the hardness of the panel did decrease significantly on some portions of the coating. The center of the panel did pass a hardness of “H,” which is above the minimum passing hardness for BMS 10-39; however, the edges only yielded a hardness of “4B.”

A complete failure of the topcoat panels was evident for initial concentrations of approximately 0.10 vol % DiEGME in the fuel or greater. Along with the hardness decreasing below the minimum specification, the coating itself exhibited signs of severe swelling and blistering as well as a loss of adhesion from the aluminum substrate. Figure 16 shows a topcoat panel after three days’ exposure to condensate from ~ 0.10 vol % DiEGME in the fuel. The center of the panel



Figure 17. Old panel exposed to condensed vapors from 0.10 vol % TriEGME in the bulk fuel.

yielded a hardness of 4B, while the edges of the panel were not tested, as they were severely swollen and delaminated from the aluminum substrate. The largest failure regions on the panel typically occurred on the sides and edges of the panel, while the center showed slightly less degradation. This could be explained by a nonuniform condensation on the surface of the panel due to nonuniform surface temperatures created by inadequate contact with the heat exchanger. The panel was attached to the cooled steel heat exchanger plate by clamps on the edges and along the top of the panel. This may have provided better contact to the heat exchanger and a colder surface that selectively condensed the FSII-rich vapor in these regions.

The use of TriEGME in this FTTP simulation study in place of DiEGME provided completely different results for all aspects of this experiment. BMS 10-39 panels showed no degradation after exposure to condensed vapors from TriEGME-containing fuels at all of the concentrations tested. Figure 17 shows a topcoat panel after exposure to condensate from ~0.10 vol % TriEGME in the bulk fuel. The figure shows a topcoat panel that was completely unaffected by contact with concentrations of approximately 0.12 vol % TriEGME in the condensate. There is no visible discoloration or swelling after exposure, and the pencil hardness of the coating did not decrease. At these concentration levels, TriEGME exhibits excellent anti-icing performance.⁶

As DiEGME and TriEGME performed almost identically in the uptake and pencil hardness testing shown above, the reason for the decreased degradation caused by TriEGME is due to the lower concentration in contact with the topcoat, which results from the lower vapor pressure of TriEGME. Gas chromatograms of fuels, DiEGME, and TriEGME (not shown) suggest that DiEGME is more volatile than most jet fuel components, while TriEGME is slightly less volatile than the average fuel components. Thus, at temperatures below the initial fuel boiling point (< 200 °C), DiEGME will preferentially concentrate in the vapor relative to most fuel components, while TriEGME will vaporize along with the fuel components and not increase in concentration in the vapor. Thus, the topcoat will be exposed to concentrations of TriEGME which are far below that shown to cause degradation in the absorption studies reported above.

Table 2 shows a significant difference between the DiEGME and TriEGME concentrations in the sampled condensate. It should be noted that these FSII concentration determina-

tions were difficult to perform, as only microliter volumes could be collected from the panel surface using a GC syringe. The concentrations of DiEGME in the condensate increased by a factor of up to seven compared to the initial bulk fuel concentration. Typically, higher concentrations of DiEGME in the fuel yielded much higher concentrations in the condensate. For example, a concentration of approximately 0.15 vol % DiEGME in the fuel resulted in a condensate of 1.09 vol % DiEGME. TriEGME does not show this large increase in the condensate concentration and only increases by a factor of 1.2 on average for the runs. A maximum value of 0.15 vol % TriEGME in contact with the topcoat is not sufficient to cause degradation, as was also confirmed by the previous pencil hardness study experiments (Figure 10). In the pencil hardness study, the pencil hardness of old panels after exposure to concentrations of 1.0 vol % DiEGME in the surrogate resulted in a hardness of <6B, which is seen under these simulation conditions. The increase in DiEGME concentrations in the condensate is also supported by the ullage box data obtained from previous work.⁶ Table 2 shows that the concentration of DiEGME in the condensate clearly increased from the initial concentration in the fuel for each experimental condition. However, the TriEGME result differs from the previous work. The data from Table 2 show an increase of TriEGME in the condensate, while the previous study showed a significant decrease in the TriEGME condensate. This difference could be explained by the relatively low distillation percentage collected in the previous work. Also, the glass collector used previously condensed the fuel condensate at a much lower temperature of -10 °C. This lower temperature may not selectively condense TriEGME from the vapor, but rather, lighter fuel components may be more likely to condense, lowering the concentration of TriEGME.

The time needed to reach equilibrium between the vapor, the condensate, and the topcoat was also studied as shown in Table 2. Degradation could be seen as early as one day for concentrations of 0.07 vol % DiEGME or greater in the bulk fuel; however, more time was given to ensure the entire panel reached equilibrium. Figure 18 shows a BMS 10-39 panel clamped to the heat exchanger while exposed to approximately 0.10 vol % DiEGME after one day. It is evident that there are droplets of the FSII-rich condensate in contact with the topcoat surface, which has begun to swell and blister. Figure 18 also serves to show the increased condensation on



Figure 18. Old BMS 10-39 panel in the FTTP simulation box showing severe swelling after one day of exposure to vapors from 0.10 vol% DiEGME in the fuel.

the edges of the panel, where greater amounts of fluid are present. Three days of exposure was found to be sufficient in reaching an equilibrium state between the fuel and the topcoat, as well as to obtain a visual confirmation of the integrity of the topcoat. This was confirmed by running two experiments at 0.067 vol % DiEGME in the fuel, with one panel being exposed for three days and the other for five days. While there was a small difference in the DiEGME concentration in the condensate, the pencil hardness and visual appearance of the panels were identical.

The effects of temperature on the degradation process were also studied to determine the conditions necessary for FTTP to occur. The temperature of the environmental chamber and the cooling surface were varied to determine how they affected the vaporization and condensation processes and topcoat degradation. These additional DiEGME experiments also served to evaluate the minimum concentration of DiEGME in the bulk fuel which would no longer produce FTTP. BMS 10-39 panels were evaluated on the basis of their pencil hardness as a function DiEGME concentration and temperature, as shown in Table 3. The bulk fuel and condensate DiEGME concentrations were also measured.

The environmental chamber was heated to 50 or 60 °C, while the cooling surface temperature was varied between 10 and 30 °C for this study. These temperatures were used to simulate the expected ground conditions in a fuel tank, as well as determine what temperatures will cause the most severe degradation. The initial runs at 60 °C fuel, 20 °C cooling (60/20 °C) showed a significant amount of degradation, especially at concentrations greater than 0.10 vol % DiEGME in the fuel. To further investigate the other temperatures, an initial fuel concentration of approximately 0.07 vol % DiEGME was used, as this was within the transition range for topcoat failure at the 60/20 °C conditions. This concentration could then be altered on the basis of the topcoat behavior to further evaluate the effect of temperature.

Table 3. Experimental Simulations with DiEGME Performed at Various Temperatures and Concentrations

Fuel Temperature (°C)	Cooling Surface Temperature (°C)	Initial Conc. (vol%)	Final Conc. (vol%)	Condensate Conc. (vol%)	Test Period (days)	Pencil Hardness
60	20	0	0	0	3	H-2H
		0.047	0.049	0.062	3	H-2H
		0.055	0.047	0.077	3	H-2H
		0.067	0.067	0.12	3	F-H
		0.078	0.076	0.14	3	4B-H
		0.100	0.094	0.67	4	<4B
		0.101	0.100	0.25	4	<4B
	0.140	0.135	0.72	2	<6B	
	0.156	0.138	1.09	5	<6B	
	60	30	0.070	0.069	0.046	3
0.088			0.087	0.087	3	H-2H
10		0.070	0.060	0.19(56.4%)*	3	HB-H
50	20	0.109	0.086	0.28(62.5%)*	3	2B-F
		0.072	0.070	0.10	3	H-2H
	0.093	0.091	0.20	14	F-H	
	10	0.079	0.072	0.25(57.1%)*	3	H-2H

(* denotes 2nd aqueous phase concentration)

Increasing the cooling surface to 30 °C increased the hardness of the panel compared to a cooling surface of 20 °C, for the two tested concentrations of approximately 0.07 and 0.09 vol % DiEGME in the bulk fuel. This is most likely due to the surface temperature being high enough such that DiEGME no longer selectively condensed relative to fuel vapors on the panel. The condensate samples did contain lower concentrations of DiEGME than was measured in the 20 °C cooling surface experiments. Lowering the cooling surface temperature to 10 °C also did not promote FTTP as readily. While increasing the initial DiEGME concentration in the fuel to approximately 0.11 vol % did reduce the pencil hardness below the minimum passing hardness at this condition, it was still not as severe of a failure as the 60/20 °C condition at a similar initial concentration. Lowering the cooling surface to 10 °C appeared to promote condensation of two phases on the topcoat panel, an aqueous and a hydrocarbon phase. Two condensed liquid phases were observed visually on the topcoat surface. The identity of

the phases was confirmed by refractive index as well as GC-MS analysis of the composition and DiEGME concentration. The addition of an aqueous phase on the topcoat surface may provide a benefit to the topcoat integrity, as DiEGME will partition readily into the aqueous phase, reducing the concentration in the hydrocarbon phase. This benefit will only be realized as long as high concentrations (> 70%) are not reached in the aqueous phase.

The other runs involved reducing the fuel temperature to 50 °C to determine if lowering the temperature would significantly reduce the vaporization of DiEGME. The 50/20 °C experiment at approximately 0.07 vol % DiEGME did not produce any detectable change in the pencil hardness, or any visual evidence of failure. It was unclear if sufficient exposure time was given to reach equilibrium at this lower temperature, as it would require more time to vaporize DiEGME and accumulate sufficient amounts in the topcoat to cause degradation. The second run at a higher concentration of approximately 0.09 vol % DiEGME was exposed for 14 days. The BMS 10-39 panel did decrease in pencil hardness slightly, although the coating was still two pencil leads above the minimum passing hardness. This decrease in hardness was most likely a function of the increased concentration of DiEGME in the fuel and subsequent condensate, and not the increased exposure time. An environmental chamber temperature of 50 °C reduced the vaporization of DiEGME in the system such that the condensate concentration did not cause a significant decrease in the topcoat hardness or initiate severe swelling. The final run of 50/10 °C also did not degrade the topcoat panel. This condition created two phases on the panel surface, which seemed to indicate that a cooling surface of 10 °C was sufficient to condense any water within the system.

Overall, experimental simulation of FTTP in this system provided data for the determination of the concentrations and temperatures necessary to promote this phenomenon. The initial conditions of 60/20 °C were ideal for creating an FTTP scenario. While other temperatures did produce some deterioration of the BMS 10-39 coating, the hardness of the panel was still above the minimum specification. The fuel temperature needs to be sufficiently warm such that high concentrations of DiEGME are vaporized, and the condensing surface temperature needs to be low enough to selectively condense DiEGME, but not so low as to condense water. On the basis of this study, continued use of DiEGME as the FSII additive will require a significant decrease in concentration, as FTTP will occur at current procurement concentrations if the correct temperature conditions are reached. The highest concentration that did not cause the hardness of the topcoat to fall below the minimum specification was approximately 0.07 vol % DiEGME. TriEGME did not cause topcoat degradation at any of the concentrations tested in this simulation (up to 0.135 vol %).

Conclusions

The compatibility of DiEGME and TriEGME with BMS 10-39 topcoat material was studied to provide a better understanding of the fuel tank topcoat peeling mechanisms, to determine the requisite conditions for degradation to occur, and to determine the conditions under which degradation can be prevented. Under liquid exposure conditions, both fuel system icing inhibitor additives were found to partition equally, on a molar basis, into the topcoat over a wide

range of concentrations. This was demonstrated for aqueous, fuel, and fuel surrogate solution exposures for both old and new topcoat panels. The absorption of FSII was found to increase dramatically for old panels relative to new panels. The old panels are considered to be representative of topcoat surfaces of real fuel tank walls in the current USAF fleet. The new panels studied are likely more resistant to FSII absorption than what is currently present in B-52 aircraft.

The desorption rate of FSII out of the topcoat differed between DiEGME and TriEGME. Initially, TriEGME showed a slower desorption rate than DiEGME, which can be explained by its lower vapor pressure and greater molecular size. After 2 h, the DiEGME and TriEGME concentrations in the panel began to reach similar levels, and eventually reached a final concentration of approximately 0.7 mol FSII/L topcoat after aqueous exposures of 80 vol % FSII or greater. This concentration was similar to that from failed topcoat flakes, which suggests that the FSII component in the topcoat will not completely desorb or evaporate after exposure to high concentrations. In the pencil hardness study, both DiEGME and TriEGME performed identically within experimental error. There was a large difference between the new and old panels, with the old panels falling below the passing hardness lead of “B” when exposed to FSII concentrations as low as 0.40 vol % in the fuel surrogate, while the new panels required concentrations of 1.0 vol % for failure. In pencil hardness measurements of FSII desorption, the hardness of the topcoat was found to increase as desorption occurs. This hardening effect is indicative of relamination of the topcoat after FSII exposure and topcoat softening.

The experimental simulation that was developed to recreate FTTP in a controlled setting was the first laboratory system able to reproduce the entire FTTP process and to determine the requisite conditions for topcoat failure. DiEGME was found to concentrate in the ullage vapor by a factor of 2 to 7 times the initial concentration in the fuel. These high condensate concentrations resulted in severe degradation of the topcoat. The highest concentration in the bulk fuel that did not cause a failure, as rated by the pencil hardness of the coating, was at ~0.07 vol % DiEGME. However, TriEGME proved very effective as it did not lower the pencil hardness of the topcoat panel up to approximately 0.14 vol % TriEGME. The resulting TriEGME condensate concentration did increase on average by a factor of 1.2, although this small increase did not prove detrimental to the BMS 10-39 panel. The lower vapor pressure of TriEGME was determined to be the major reason for its improved topcoat compatibility for fuel tank ullage surfaces. On the basis of these results, TriEGME has been shown to be an excellent FSII replacement in terms of BMS 10-39 topcoat material compatibility. During the scenarios analyzed in these studies, TriEGME would not cause degradation to the topcoat at the current concentrations employed for DiEGME in JP-8. If DiEGME continues to be used as the specification FSII additive, it is recommended that the maximum concentration in aircraft tanks be no more than 0.07 vol % to prevent topcoat degradation. This should prevent high concentrations of DiEGME vaporizing and condensing on topcoat surfaces. Adherence to required maintenance practices, such as sumping of fuel tanks, is essential to the prevention of FTTP in water bottoms when either FSII additive is used.

The occurrence of FTTP in the simulated fuel tank box was dependent on the temperatures of the fuel and condensing

surfaces. Fuel temperatures of 60 °C were able to selectively vaporize levels of DiEGME sufficient to cause swelling and blistering. Lower temperatures were unable to provide condensate concentrations that were sufficient to cause degradation of the coating during the test period. The optimum cooled surface temperature for selective condensation of DiEGME and topcoat degradation is near 20 °C. At higher temperatures, the surface condensate had reduced DiEGME concentrations, and below 20 °C, an aqueous phase condensed on the topcoat surface, which decreased the concentration of DiEGME in contact with the polymer.

Acknowledgment. This material is based on research sponsored by the Air Force Research Laboratory under agreement number F33615-03-2-2347. The U.S. Government is authorized to reproduce and distribute reprints for Governmental purposes notwithstanding any copyright notation thereon. The view and conclusions contained herein are those of the authors and should not be interpreted as necessarily representing the official policies or endorsements, either expressed or implied, of Air Force Research Laboratory or the U.S. Government. The authors would like to acknowledge funding support from the U.S. Department of Defense Reduction of Total Ownership Cost program through Ed Wells of USAF ASC/ENFA.

APPENDIX F

Flame Stabilization in Small Cavities

INTENTIONALLY LEFT BLANK

Flame Stabilization in Small Cavities

Alejandro M. Briones*

University of Dayton Research Institute, Dayton, Ohio 45469

Joseph Zelina†

U.S. Air Force Research Laboratory, Wright-Patterson Air Force Base, Ohio 45433

and

Viswanath R. Katta‡

Innovative Scientific Solutions, Inc., Dayton, Ohio 45440

DOI: 10.2514/1.44162

This research is motivated by the necessity to improve the performance of ultracompact combustors, which requires flame stabilization in small cavities. An extensive computational investigation on the characteristics of cavity-stabilized flames is presented. A high-fidelity, time-accurate, implicit algorithm that uses a global chemical mechanism for JP8-air combustion and includes detailed thermodynamic and transport properties as well as radiation effects is used for simulation. Calculations are performed using both direct numerical simulation and standard $k-\epsilon$ Reynolds-averaged Navier–Stokes model. The flow unsteadiness is first examined in large axisymmetric and small planar cavities with nonreactive flows. As with previous investigations on axisymmetric cavities, multiple flow regimes were obtained by varying cavity length (x/D_o): wake backflow regime, unsteady cavity vortex regime, steady cavity vortex regime, and compressed cavity vortex regime. However, planar cavities only exhibit steady cavity vortex and compressed cavity vortex regimes. Two opposed nonaligned air jets were positioned in this planar cavity: the outermost air jet in coflow with the mainstream flow (i.e., normal injection). The fuel jet was injected either in coflow, crossflow, or counterflow with respect to the mainstream flow. Flow unsteadiness was observed to be relatively small for coflow- and crossflow-fuel-jet injection. By reversing the air jet positions (i.e., reverse injection), the flow unsteadiness is promoted regardless of fuel jet positioning. Finally, the effect of combustion and cavity equivalence ratio (ϕ_{CAV}) on flame unsteadiness is addressed. With normal injection (reverse injection), low and high ϕ_{CAV} leads to low (high) and high (low) flame unsteadiness, respectively. Based on these results recommendations are provided to designers/engineers to reduce flame unsteadiness in these cavities.

Nomenclature

C_p	=	pressure coefficient
D	=	planar cavity depth
D_o	=	forebody diameter
D_s	=	spindle diameter
L	=	planar cavity length
Re_D	=	global Reynolds number based on cavity depth, D
Re_x	=	cavity Reynolds number based on axisymmetric cavity length, x
R_o	=	forebody radius
x	=	axisymmetric cavity length
ΔC_D	=	change in drag
$\Delta C_{D,P}$	=	change in pressure drag
$\Delta C_{D,S}$	=	change in shear drag
λ_{CAV}	=	cavity air to fuel jet momentum ratio
ϕ_{CAV}	=	cavity equivalence ratio

I. Introduction

MAJOR advances in combustor technology are required to meet the conflicting challenges of improving performance, increasing durability, reducing weight, lowering emissions, and

maintaining cost. A novel approach proposed by the U.S. Air Force Research Laboratory/RZTC [1,2] is the development of the ultracompact combustor (UCC). The UCC design uses high swirl in a circumferential cavity (cavity refers to a space lacking of solid and filled with gas) to enhance mixing rates via high cavity gravity loading on the order of 3000g. The UCC shows how the primary, intermediate, and dilution zones of a conventional combustor can be incorporated into a much smaller footprint using compressor and turbine features that enable a shorter and potentially less complex gas turbine. It combines the high-gravity combustor circumferential cavity and strut with the compressor exit vanes and the high-pressure turbine inlet guide vanes (IGV). Because recent investigations [3] on the UCC have shown promising improvements on performance for future engine implementation, it is envisioned that the UCC could be either used as the main combustor or as an interturbine burner between the high- and low-pressure turbines to operate in a reheat cycle engine.

A schematic of the current UCC is shown in Fig. 1. The main air (or vitiated) flow enters the combustor and flows around the bullet nose of the center body. The turning vanes (indicated as “guide vane”) simulate the swirl that would be coming from the compressor rotor in a real gas turbine engine. The flow from the trailing edge of these turning vanes impinges on the IGV (indicated as “blade”). The function of the IGV is the same as that of a conventional gas turbine engine. A radial cavity located in the IGV, aligned with the circumferential cavity, facilitates transport of gases from the circumferential cavity to the main stream. Additional air is admitted through 24 holes equally spaced around the circumferential cavity and angled at 45 deg to the radial direction to promote high swirl in the cavity. At the cavity-in-cavity (CIC), a small amount of air is injected and fuel is sprayed into the circumferential cavity. This allows fuel-rich combustion to occur in the circumferential cavity. Consequently, combustion primarily takes place in the engine circumferential direction rather than in the axial direction as is conventionally done. The circumferential cavity is analogous to a centrifuge; hence, cold nonreactive fuel–air mixture migrates radially outward, whereas hot

Received 5 March 2009; revision received 5 August 2009; accepted for publication 10 August 2009. Copyright © 2009 by the American Institute of Aeronautics and Astronautics, Inc. The U.S. Government has a royalty-free license to exercise all rights under the copyright claimed herein for Governmental purposes. All other rights are reserved by the copyright owner. Copies of this paper may be made for personal or internal use, on condition that the copier pay the \$10.00 per-copy fee to the Copyright Clearance Center, Inc., 222 Rosewood Drive, Danvers, MA 01923; include the code 0001-1452/10 and \$10.00 in correspondence with the CCC.

*Research Engineer, Energy and Environmental Engineering Division, 300 College Park/0043. Member AIAA.

†Senior Research Engineer, 1950 Fifth Street. Associate Fellow AIAA.

‡Senior Research Engineer, 2766 Indian Ripple Road. Senior Member AIAA.

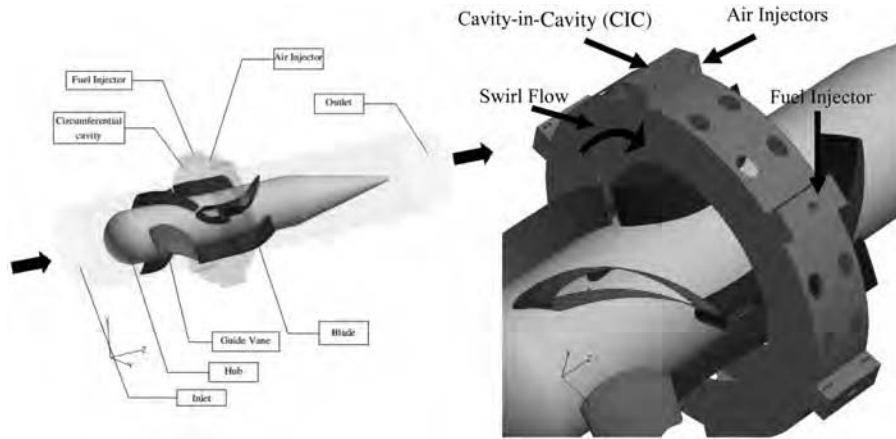


Fig. 1 Ultracompact combustor; inlet, hub, guide vane, blade, circumferential cavity, outlet, cavity-in-cavity, air injectors, and fuel injectors are indicated. The swirl flow is also indicated by the bent arrow on the circumferential cavity.

reacted mixture migrates radially inward. The cold mixture remains in the circumferential cavity for a longer period of time to evaporate, mix, and burn. The large density gradient in the cavity along with the high-gravity flow enhances mixing of cold and hot mixtures creating a very well-mixed combustion zone. The intermediate products of combustion are transported by lower wake pressures into the radial cavities where fuel-lean combustion occurs.

Numerous design variations of the selected configurations have been evaluated, leading to improved configurations with optimized performance and higher efficiency [3–7]. Although the UCC exhibits many advantageous features over conventional burners, it poses a particular difficulty regarding lean blowout and flame stability. The CIC shown in Fig. 1 was one of the latest additions to the UCC. Without the CIC, the gaseous flow high speed and acceleration in the circumferential cavity demands fuel injection with low residence times. In addition, the high-gravity loading enhances strain rates and, consequently, promotes extinction. The CIC is a workaround to these problems by channeling a second cavity inside the primary one. The fuel injected with additional air jets through the CIC is to increase fuel-injection residence times and to reduce local strain rates, while enhancing the fuel-air mixing. Hence, the small CIC with dimensions of a few millimeters and inherent global Reynolds number $Re_D \approx 10,000$ acts as a flame holder. [We refer to small cavities as those whose dimensions are very small in comparison with the characteristic length of the combustor. For instance, our planar cavity exhibits cavity length to combustor length of $\sim 10\%$ (cf. Fig. 1). It turns out that these cavities generally exhibit global Reynolds number (Re_D) $\approx 10,000$. On the other hand, we refer to large cavities as those with cavity length to combustor length greater than $\sim 50\%$ with usual Re_D greater than 10,000 (e.g., (Re_D) $\approx 70,000$). Large cavities reported in the literature usually exhibit one order of magnitude larger residence time than small cavities.] Even though the CIC concept has proven to enhance the performance of the UCC, there is still further need for improvement [3]. The fuel and air jets in the CIC create vortices, which, depending on the cavity dimensions, equivalence ratio, and injector positions, could lead to highly unstable flow. This in turn leads to flame instability, which induces higher residence times and promotes fuel-rich environments that increase pollution and soot formation. Therefore, current efforts are oriented toward determining design criteria for reducing flame fluctuations in the CIC.

Most previous investigations have dealt with nonreactive and reactive flow stability criteria in large axisymmetric [8–11] and planar [12–15] cavities with dimensions on the order of a few centimeters, $Re_D > 10,000$, and an order of magnitude larger residence time than those expected in the CIC.[§] Consequently, the flow/flame stabilization in the CIC is more complicated than in previous studies [8–15]. For instance, for large cavities, the fuel is nearly fully consumed inside the cavity and the flame is contained in

the cavity [10,11,15]. On the contrary, in CIC-like cavities, very little amount of the fuel is burned in the cavity, extending the flame outside it [16]. Despite these facts, it is worth discussing the flow/flame stabilization criteria in large cavities because it provides insights into flame stabilization in CIC-like cavities. Mair [8] experimentally examined the effect of an afterbody disk on the drag of a blunt-based forebody-spindle object. His experiments showed that the drag of the forebody-spindle object is significantly reduced by mounting an afterbody disk. Further reduction in drag was observed by mounting a secondary afterbody disk. Little and Whipkey [9] performed similar experiments. They identified three regimes associated with drag. These are the wake backflow (WBF), unsteady cavity vortex (UCV), and the steady cavity vortex (SCV) regime. In the WBF, flow downstream the afterbody spills upstream into the cavity and the cavity exhibits a counter-rotating vortex[†] with high-drag coefficient. By moving the afterbody disk downstream from where WBF regime exists, the flow in the cavity transitions to the UCV regime. The cavity exhibits a corotating vortex^{**} and the wake backflow does not move upstream past the afterbody disk. The drag coefficient C_D fluctuates from low- to high-drag condition. When the disk is positioned at its optimum from the forebody, the flow in the cavity is said to be in the SCV regime. Here, the vortex rotates (with edge velocity) in the same direction as the mainstream velocity, fits the cavity nearly perfectly, mass transfer into or out of the cavity is minimum, there is no backflow, and is characterized by low drag. Their cavity optimization criterion was based so that, to reduce C_D , the afterbody disk needs to be large enough to separate the wake backflow from the cavity flow so that a locked vortex can exist in the cavity. Therefore, with the proper choice of cavity dimensions, vortices in the cavity can be made stationary. However, a steady vortex yields minimum mass exchange between the vortex and the main flow, which in the CIC means that additional air must be supplied within the cavity for combustion to be sustainable. Consequently, Katta and Roquemore [10,11] conducted an extensive numerical investigation to determine the effect of combustion on cavity-stabilized flames. They showed that, for nonreactive flow, both standard $k-\varepsilon$ Reynolds-averaged Navier–Stokes (RANS) model and direct numerical simulation (DNS) can be used to predict ΔC_D with cavity size. They also showed that the optimum cavity length determined from nonreactive flows yields to nonshedding cavity flows, even with combustion and primary injection into the cavities.

Planar cavities better emulate the shape of the CIC (cf. Figure 1). Zdanski et al. [12,13] numerically studied the nonreactive flow past two-dimensional trenchlike cavities and showed that, with increasing

[†]Throughout the text, counter-rotating vortex means that the vortex edge velocity is in the opposed direction to the mainstream velocity. The mainstream flow is not rotating.

^{**}Throughout the text, corotating vortex means that the vortex edge velocity is in the same direction as the mainstream velocity. The mainstream flow is not rotating.

[§]The residence time scales with length for turbulent flows.

Table 1 Transport coefficients and source terms appearing in governing equations

Equations	Φ	Γ^Φ	S^Φ
Continuity	1	0	0
Axial momentum	u	μ	$-\frac{\partial p}{\partial z} + (\rho_0 - \rho)g + \frac{\partial}{\partial z}(\mu \frac{\partial u}{\partial z}) + \frac{\partial}{\partial r}(\mu \frac{\partial v}{\partial z}) + \frac{\mu}{r} \frac{\partial v}{\partial z} - \frac{2}{3} \frac{\partial}{\partial z}(\mu \frac{\partial u}{\partial z}) + \frac{\partial}{\partial z}(\mu \frac{\partial v}{\partial r}) + \frac{\partial}{\partial z}(\mu \frac{v}{r})$
Radial (transverse) momentum	v	μ	$-\frac{\partial p}{\partial r} + \frac{\partial}{\partial r}(\mu \frac{\partial u}{\partial r}) + \frac{\partial}{\partial r}(\mu \frac{\partial v}{\partial r}) + \frac{\mu}{r} \frac{\partial v}{\partial r} - 2\mu \frac{v}{r^2} - \frac{2}{3} \frac{\partial}{\partial r}(\mu \frac{\partial u}{\partial z}) + \frac{\partial}{\partial r}(\mu \frac{\partial v}{\partial r}) + \frac{\partial}{\partial r}(\mu \frac{v}{r})$
Species mass fraction	Y_i	$\rho D_{i-\text{mix}}$	$\dot{\omega}_i$
Energy	H	$\frac{\lambda}{c_p}$	$\nabla \left[\frac{\lambda}{c_p} \sum_1^{N_s} \left(L e_i^{-1} - 1 \right) H_i \nabla Y_i \right] - \sum_1^{N_s} \left\{ h_{f,i}^0 \dot{\omega}_i \right\} + q_{\text{rad}}$

the cavity aspect ratio, two vortices in the cavity appear. At a critical aspect ratio, the external flow reattaches to the surface that is parallel to the mainstream flow. Similarly, D'yanchenko et al. [14] experimentally studied the nonreactive flow past heated two-dimensional trenchlike cavities with inclined frontal and rear walls. They showed that, for an interval of wall inclination angles, the flow in the cavity becomes unstable with the primary vortex changing its structure from single cellular to double cellular. Recently, Puranam et al. [15] investigated experimentally the flame stabilization in a curving, contracting channel with an inner large cavity. They showed that, at low Reynolds number (1000–10,000), the flame extends outside the cavity, whereas at high Reynolds number ($\geq 40,000$), combustion occurs inside the cavity. In between these regimes, the flame was unstable.

Because flow/flame stabilization in small cavities is so specialized, there are (to the best of our knowledge) only two investigations reported in the literature. Zelina et al. [3] experimentally studied multiple air injection strategies on the performance of the CIC, while the fuel was injected radially as in Fig. 1. The configurations included the following: (config. 1) two-nonaligned opposed air jets with the outermost jet in coflow with the mainstream flow, (config. 2) one single innermost air jet in counterflow with the mainstream flow, and (config. 3) no air jets. Cavity equivalence ratio ϕ_{CAV} at lean blowout was found to be as low as 0.08 for config. 3 and as high as 1.5 for config. 1. Decreasing the cavity air to fuel momentum ratio λ_{CAV} led to higher ϕ_{CAV} at lean blowout for all configurations. Moreover, Katta et al. [16] performed two-dimensional, unsteady, reacting flow numerical simulations on a trenchlike cavity with fuel and air injections. The parametric investigation indicated that there is a cavity optimum size that minimizes flow unsteadiness. Therefore, the purpose of this investigation is to enhance our understanding regarding cavity-stabilized flames that might lead to the development of concepts for the design of higher performance CIC. First, we will start by reviewing and expanding the discussion on the criteria of flow unsteadiness in large axisymmetric cavities. Second, we will apply the concepts related to large axisymmetric cavities to small planar cavities. Third, the effect of fuel and air injections on flow unsteadiness will be addressed for small planar cavities. Fourth, the effect of fuel-injection positioning to flow unsteadiness will be examined in small planar cavities. Then, the effect of air injection positioning on flow unsteadiness will also be investigated in these

cavities. Finally, we will discuss the effect of combustion and cavity equivalence ratio on flow/flame unsteadiness.

II. Physical-Numerical Procedure

A. Gas-Phase Numerical Model

The numerical model is based on the solution of the time-dependent governing equations for a two-dimensional unsteady reacting flow [17,18]. Using cylindrical coordinates (r, z) these equations can be written as

$$\frac{\partial(\rho\Phi)}{\partial t} + \frac{\partial(\rho v\Phi)}{\partial r} + \frac{\partial(\rho u\Phi)}{\partial z} = \frac{\partial}{\partial r} \left(\Gamma^\Phi \frac{\partial\Phi}{\partial r} \right) + \frac{\partial}{\partial z} \left(\Gamma^\Phi \frac{\partial\Phi}{\partial z} \right) - \frac{\rho v\Phi}{r} + \frac{\Gamma^\Phi}{r} \frac{\partial\Phi}{\partial r} + S^\Phi \quad (1)$$

Here, t denotes the time, ρ the density, and u and v the axial z and radial r velocity components, respectively. The general form of the equation represents conservation of mass, momentum, species, or energy conservation, depending on the variable used for Φ . The diffusive transport coefficient Γ^Φ and source terms S^Φ are described in Table 1. Introducing the overall species conservation equation and the state equation completes the equation set. In addition, a sink term based on an optically thin gas assumption is included in the energy equation to account for thermal radiation from the flame [19]. The sink term due to the radiation heat loss is expressed as $q_{\text{rad}} = -4\sigma K_p (T^4 - T_o^4)$ [20] where T denotes the local flame temperature. The term K_p accounts for the absorption and emission from the participating gaseous species (CO_2 , H_2O , CO , and CH_4) and is expressed as

$$K_p = P \sum_k X_k K_{p,i}$$

where $K_{p,i}$ denotes the mean absorption coefficient of the k th species. Its value is obtained by using a polynomial approximation to the experimental data provided in [21].

The finite difference forms of the momentum equations are obtained using QUICKEST scheme [22], whereas those of the species and energy are obtained using a hybrid scheme of upwind and central differencing. The pressure field is calculated at every time

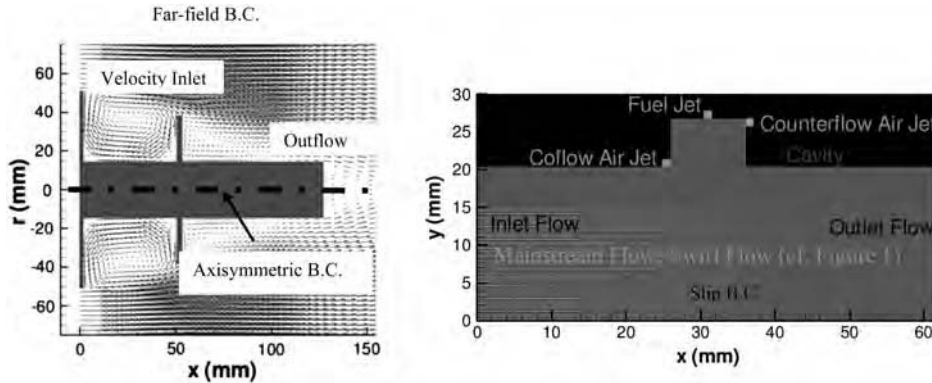


Fig. 2 Computational domains for the axisymmetric cavity (left) and the planar cavity (right). The axisymmetric cavity has been mirrored. The sample axisymmetric cavity corresponds to the case in which the afterbody disk is placed at $x/D_o = 0.5$. The whole computational domain is not shown here. The planar cavity indicates the location of the injections in its normal configuration. The boundary conditions are also indicated. The air mainstream flow direction is also indicated for the small planar cavity case. Note that the swirl flow corresponds to the swirl flow in Fig. 1.

step by solving all of the pressure Poisson equations simultaneously and using the lower and upper diagonal matrix-decomposition technique.

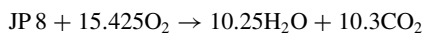
Figure 2 illustrates the computational domains for the large axisymmetric and small planar cavities. They consist of 229×229 mm and 62×30 mm in the axial x and radial r (vertical y) directions, respectively, and are represented by a staggered, non-uniform grid system (300×300 and 401×421 , respectively). The axisymmetric cavity contains a forebody with diameter D_o of 101.6 mm, spindle diameter D_s of 28.6 mm, afterbody disk diameter D_1 of 38.1 mm, afterbody disk thickness of 1.5 mm, and spindle length of 127 mm. The upstream flow approaches the forebody-spindle-afterbody geometry at uniform and constant velocity and temperature of 30.5 m/s and 300 K, respectively. Throughout this investigation, only the distance of the afterbody disk to the forebody is varied. Only nonreactive flow conditions and standard $k-\varepsilon$ RANS simulations are performed on the axisymmetric cavities. The planar cavity consists of a forebody and an afterbody of equal depth D . Although the separation distance of the forebody and afterbody is varied in this study, the depth D is maintained constant at 6.4 mm. For nonreactive flow conditions, the air mainstream approaches the cavity at uniform and constant velocity and temperature of 40 m/s and 300 K. Both DNS and RANS simulations and both nonreactive and reactive flow conditions are performed on the planar cavities. Fuel and air injections are also used in planar cavities. The cavity equivalence ratio ϕ_{CAV} is also varied. Additional details are provided in subsequent sections.

B. Thermodynamic and Transport Properties

The thermodynamic and transport properties appearing in the governing equations are temperature and species dependent. The mixture density is computed using the ideal gas law assuming that the pressure remains constant in the flowfield at 101,325 Pa. The specific heat capacity of individual species is computed with piecewise polynomials [10]. The viscosity, thermal conductivity, and binary diffusivity of the individual species were based on kinetic theory [23]. Whereas the mixture viscosity and thermal conductivity are computed using the Wilke semi-empirical formulas [24], mixture-averaged formulation is used to compute species diffusivities that are used in the governing equations. The Wilke semi-empirical correlations are used because they apply to nonpolar low-density gases; hence, these correlations are useful in our investigation. The mixture-averaged diffusivity is a particularly useful simplification when all species, but one, are not abundant. For instance, the mass fraction of N_2 is ~ 0.72 . The formulation used for the calculation of individual and mixture properties is a common practice used in many in-house source codes [25] and commercial codes [26,27].

C. Combustion Model

The JP8-air chemistry is modeled using a global reaction mechanism involving five species, namely JP8, O_2 , CO_2 , H_2O , and N_2 . JP8 is treated as a surrogate mixture consisting of six parent species: 30% n dodecane, 20% n tetradecane, 10% i octane, 20% methyl-naphthalene, 5% tetralin, and 15% m xylene [28]. The global reaction for this surrogate mixture is



III. Results and Discussion

A. Validation of Numerical Model

The validation of the numerical model has been presented in a previous investigation by Katta and Roquemore [10]. They compared the change in pressure drag $\Delta C_{D,P}$ as a function of afterbody disk distance from the forebody x/D_o for two spindle sizes. Both results of DNS and standard $k-\varepsilon$ RANS models were compared with the measurements of Little and Whipkey [9]. Although their RANS simulations did not result in the dynamic flow observed in the experiments, the drag coefficients compared favorably with those

from the experiments. On the contrary, the DNS yielded dynamic flows similar to those observed in the experiments and the drag coefficients were not as favorable with the experiments. For the small and large spindle sizes used in their investigation, the RANS simulations predicted a minimum $\Delta C_{D,P}$ similar to that of the measurements. Moreover, the DNS and RANS algorithms have been extensively validated in many unsteady reacting flow simulations, such as opposed jet flames [29] and buoyant jet diffusion flames [30]. Furthermore, the numerical simulations of the trapped-vortex combustor (TVC) [11], which is similar to our large axisymmetric cavity except that it has fuel and air injections, yielded only qualitative comparison with the experiments in terms of temperature profiles. The DNS results were in closer agreement to the experiments than those obtained with RANS. However, the ability of incorporating standard $k-\varepsilon$ RANS model in predicting reacting flows was tested in vertically mounted turbulent jet flames [11]. Good qualitative and quantitative agreements were predicted by both the models. Based on these results and the discrepancies presented in the TVC, it was speculated that the standard $k-\varepsilon$ RANS model is only inadequate to predict reacting flows in TVC and in large axisymmetric cavities. Nevertheless, the standard $k-\varepsilon$ RANS model can qualitatively obtain general features of large axisymmetric cavities exposed to non-reacting flows as shown in Fig. 2 of [10]. Therefore, in this investigation, the standard $k-\varepsilon$ RANS model is used for nonreacting flows, whereas the DNS is used for both nonreacting and reacting flows.

B. Flow Unsteadiness in Large Axisymmetric Cavities

This section is concerned with the drag and flow characteristics of a locked vortex afterbody shapes formed by thin disks spaced along a central spindle. Figure 3 presents the velocity vector flowfields and streamlines for conditions when the afterbody disk is placed at $x/D_o = 0.2, 0.4, 0.5,$ and 0.7 . Similar simulations were conducted by Katta and Roquemore [10]. In this figure, the upstream flow diverges due to increased cross-sectional area and, consequently, flow separation occurs at the sharp corner of the forebody. The streamwise pressure gradient increases until the flow reattaches to the spindle downstream the afterbody. For $x/D_o = 0.2$, the flow recirculates behind the afterbody disk. This flow spills over the afterbody disk into the cavity and two vortices are formed in the cavity. The innermost vortex is counter-rotating with respect to the direction of the mainstream, whereas the outermost vortex is corotating with the mainstream. There is also a freestanding stagnation point inside the flowfield, indicating the presence of opposed flows. This flow configuration is called the wake backflow regime and the characteristic cavity Reynolds number Re_x is less than 84,000. For $x/D_o = 0.4$, there is still spillover and two vortices within the cavity exist. However, in comparison with the WBF, there are velocity vectors pointing toward the afterbody disk still with the presence of a stagnation point in the flowfield. This contraction around the disk and backflow is responsible for inducing flow oscillations [9] and the flow is said to be in the unsteady cavity vortex regime with Re_x ranging from 84,000 to 105,000. For $x/D_o = 0.5$, there is no longer backflow over the afterbody disk and the stagnation point has moved to the top of the afterbody wall and the vortex fits nearly perfectly in the cavity. The location of the stagnation point is consistent with that reported by Gharib and Roshko [31] for this type of flow. The flow is in the steady cavity vortex regime, exhibiting $Re_x \approx 105,000$. At $x/D_o = 0.7$, the vortex in the cavity becomes elongated, the mainstream impinges on the afterbody disk, and the stagnation point moves to the front of the afterbody wall. This impingement compresses the vortex and the flow becomes unsteady. We named this flow the compressed cavity vortex regime (CCV) and it exhibits $Re_x > 105,000$. Furthermore, the streamlines suggest that the SCV exhibits minimum mass exchange with the mainstream flow, as expected.

Figure 4 presents the change in pressure drag $\Delta C_{D,P}$ coefficient as a function of axial distance x/D_o , resulting from the addition of disk to forebody-spindle geometry, discussed in the context of Fig. 3. Katta and Roquemore [10] presented in their Fig. 2 the total change in

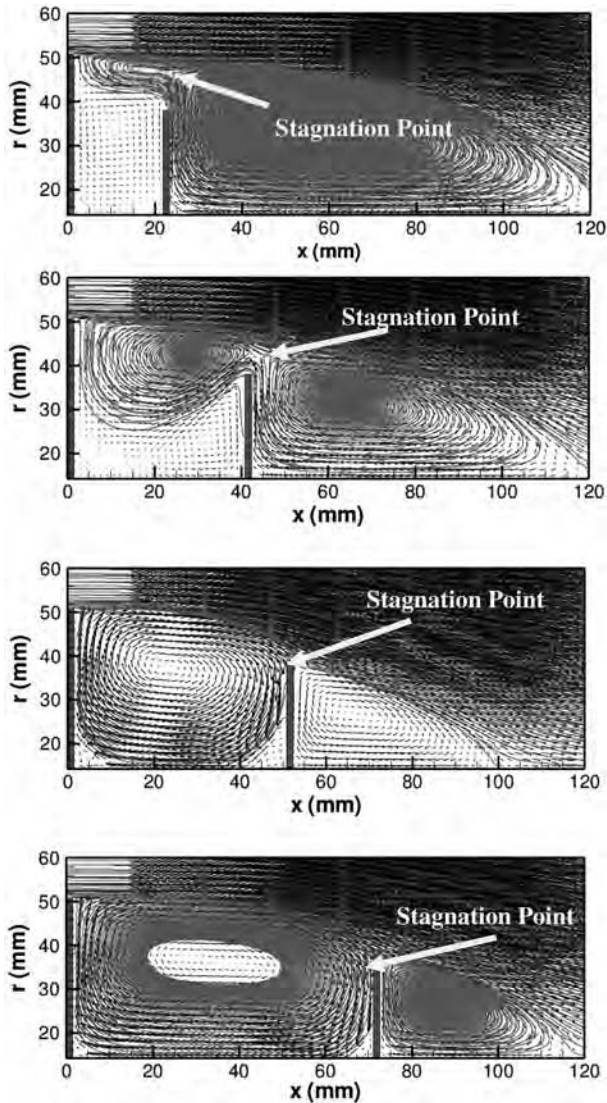


Fig. 3 Velocity vectors for the afterbody disk placed at $x/D_o = 0.2, 0.4, 0.5,$ and 0.7 . The calculations were performed using the standard $k-\epsilon$ RANS model. The velocity vector lengths are scaled with magnitude. The streamlines are shown. The stagnation points due to reattachment are also indicated.

total drag. By comparing our Fig. 4 with Fig. 2 of [10], it is clear that shear drag is nearly negligible. The calculated $\Delta C_{D,P}$ indicates that the drag coefficient decreases monotonically to a minimum value at $x/D_o = 0.5$ and then increases for x/D_o greater than 0.6. Momentum balance on the cavity provides the drag force expressed in terms of the direct forces on the cavity walls or in term of integrated turbulent momentum flux out of the cavity [31]. This momentum flux is inherently unsteady. Increase on the momentum flux indicates increase on flow unsteadiness and thereby increase on drag and drag coefficient (i.e., increase on unbalance forces in the cavity walls). Consequently, the large pressure drag exhibited by the WBF yields oscillations. Similarly, UCV and CCV exhibits larger pressure drags than SCV and these regimes are more unsteady. The flow structure that reduces oscillations is that depicted in Fig. 3 for $x/D_o = 0.5$. Now, in the subsequent paragraph, we relate the minimum $\Delta C_{D,P}$ to the pressure distribution on the forebody face and the upstream face of the afterbody disk.

Figure 5 presents the pressure coefficient C_p as a function of radial coordinate r/R_o at the forebody. The local minima represent the projections of the centers of the vortices on the walls. For the forebody spindle alone without disk, C_p slightly increases from the spindle edge until it reaches an absolute maximum. Further outwardly C_p decreases until it reaches an absolute minimum, 117

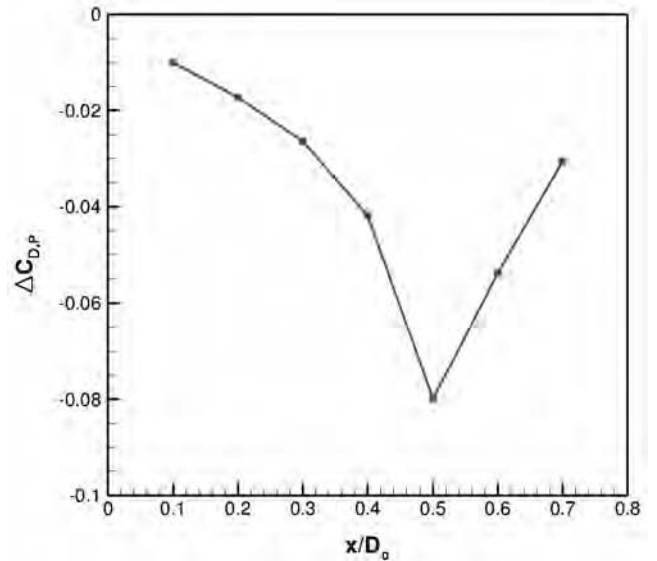


Fig. 4 Change in pressure drag $\Delta C_{D,P}$ coefficient as a function of axial distance x/D_o , resulting from the addition of disk to forebody-spindle geometry. The calculations were performed using the standard $k-\epsilon$ RANS model.

indicating the radial location of the center of the vortex. From the center of this vortex, C_p increases to either side at a rate proportional $\sim (r/R_o)^n$, where n is $-1 \leq n \leq 1$. This indicates that this is a free-like vortex structure. When the disk is added at $x/D_o = 0.2$, C_p decreases drastically, suggesting that velocity magnitude increases. However, the C_p distribution is nearly flat with an increase in the outermost edge and a slight increase near the spindle edge. This indicates that velocity magnitudes and circulations corresponding to the outermost corotating and the innermost counter-rotating vortices are comparable, as shown in Fig. 3. Further increase in x/D_o decreases C_p until it reaches a minimum at $x/D_o = 0.5$. When the disk is at this position, the C_p distribution is no longer flat. First, C_p decreases to a local minimum and then it increases to an absolute maximum. This section of the profile indicates the location of a small vortex near the corner of the cavity, as shown in Fig. 3. Further outwardly C_p decreases to an absolute minimum and then rises. This section indicates the existence of a larger vortex in the cavity. In contrast to $x/D_o < 0.5$, the two vortices indicated by the C_p profile suggest that these vortices are forced-like vortex. This statement is reached because from the center of the vortices C_p now increases with the square of the radius [i.e., $\sim (r/R_o)^2$], which is characteristic of forced vortices. From Fig. 3, note that the velocity magnitude has increased from $x/D_o = 0.2$ to 0.5 as indicated by the length of the velocity vectors. When the disk is positioned further downstream at $x/D_o = 0.6$, C_p increases again. By positioning the disk even further downstream, C_p increases monotonically with the same qualitative radial distribution as for when the disk was positioned at $x/D_o = 0.5$ and 0.6 (i.e., $n = 2$). The increase in C_p is associated with decrease in velocity magnitudes in the cavity (as indicated by velocity vector lengths in Fig. 3). It is important to point out that the minimum $\Delta C_{D,P}$, which is associated with steady flow, is also associated with minimum C_p on the forebody face. This is in contradiction with the results of Mair [8] which suggested exactly the opposite (i.e., minimum C_p yields maximum $\Delta C_{D,P}$). We believe that the minimum C_p yields minimum $\Delta C_{D,P}$ since $\Delta C_{D,P} = (1/A) \cdot \int C_p \cdot dA$, where A is the area. In fact, Mair [8] suggested that, in the high-drag regime, the flow was unsteady and the pressures recorded by the manometer may not have been the true mean values. This could have led to data misinterpretation.

Figure 6 presents pressure coefficient C_p as a function of radial coordinate r/R_o at the upstream face of the afterbody disk. At $x/D_o = 0.2$, C_p exhibits a small local minimum near the spindle and then decreases continuously with r/R_o . This indicates that the flow near the disk is moving from the inner regions of the cavity toward

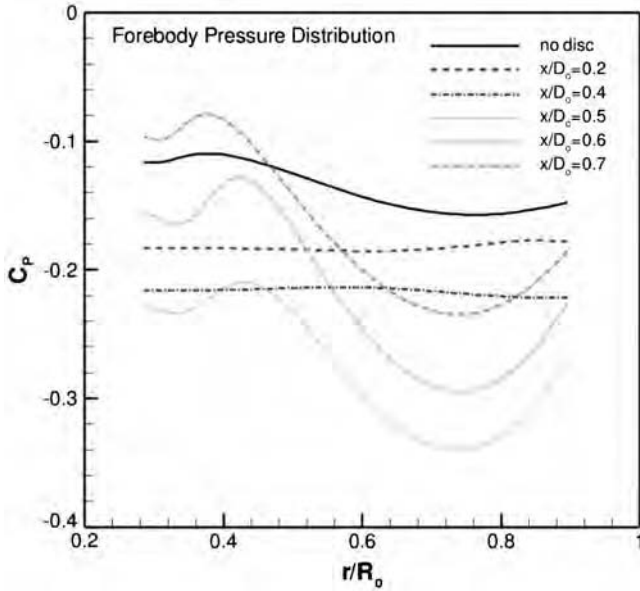


Fig. 5 Pressure coefficient C_p as a function of radial coordinate r/R_o at the forebody. The calculations were performed using the standard $k-\epsilon$ RANS model.

outside (i.e., counter-rotating vortex). With increasing x/D_o to 0.4, the magnitude of C_p decreases and the profile is still nearly similar to that of $x/D_o = 0.2$ because there is still a counter-rotating vortex, as depicted in Fig. 3. Further increase of x/D_o to 0.5 shifts C_p slightly above that of $x/D_o = 0.4$. An absolute minimum C_p is observed to occur. As x/D_o increases to 0.6 and 0.7, the minimum is shifted toward the inside of the cavity. This is due to larger impingement area of the mainstream flow on the afterbody disk, which pushes the vortex toward the spindle. That is why at $x/D_o = 0.6$ and 0.7 the flow is in the CCV regime. According to Zdanski et al. [12,13], if we were to further increase x/D_o , two major vortices would form inside the cavity which depending on x/D_o these vortices could be either encapsulated (i.e., without flow reattachment) or nonencapsulated.

In summary, our results presented from Figs. 3–6 indicate that low flow unsteadiness is achieved when a large corotating vortex with the mainstream, exhibiting forcedlike vortex characteristics, fits the cavity. This leads to low-pressure drag and low-pressure coefficients in both the forebody face and upstream face of the

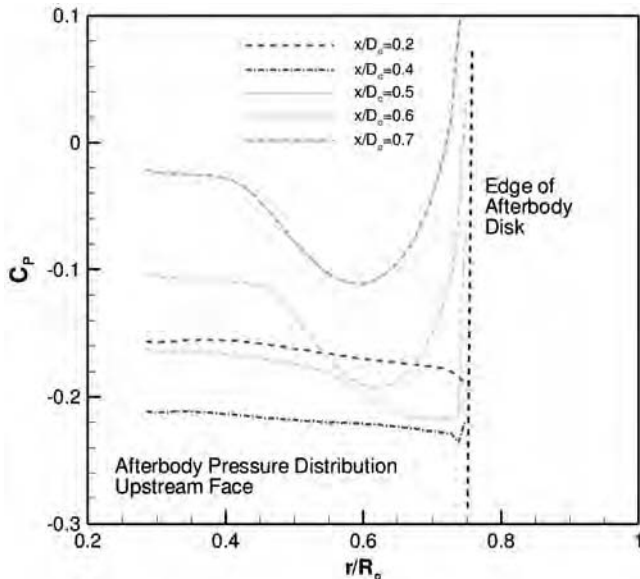


Fig. 6 Pressure coefficient C_p as a function of radial coordinate r/R_o at the upstream face of the afterbody disk. The calculations were performed using the standard $k-\epsilon$ RANS model.

afterbody. RANS simulations are sufficient for determining flow configuration exhibiting low flow unsteadiness.

C. Flow Unsteadiness in Small Planar Cavities

From Fig. 1, it is noticed that the CIC has two major geometrical differences with the large axisymmetric cavities studied in the previous section. In the CIC, the thickness of the afterbody is infinitely long and the heights of the afterbody and forebody walls are equal. Therefore, the CIC is modeled as the small planar cavity shown in Fig. 2. Based on the results from the previous section, we expect the wake spillover to be nonexistent, and, consequently, WBF and UCV regimes will be nonexistent as well.

Figure 7 presents the velocity vectors for the planar cavity with dimensions of $L/D = 1$ and 6. These calculations were performed using the standard $k-\epsilon$ RANS model. As with axisymmetric cavities, flow separation occurs at the sharp corner of the forebody. The streamwise pressure gradient increases until the flow reattaches at the sharp corner of the afterbody for $L/D = 1$ and impinges on the afterbody for $L/D = 6$. For the latter case, the flow momentum is not sufficient, hence flow impingement occurs. For $L/D = 1$, a corotating vortex is seen inside the cavity with its center nearly at the center of the cavity. Thereby, this configuration resembles that of $x/D_o = 0.5$ (shown in Fig. 3). We, consequently, state that the flow is in the SCV regime. Nonetheless, at $L/D = 6$, the vortex is elongated and characterized by flow impingement, exhibiting similarities to that corresponding to $x/D_o = 0.7$ (shown in Fig. 3). Thus, this flow corresponds to the CCV regime. Furthermore, these results plainly suggest that there is a critical cavity length to depth ratio L/D , at which a single vortex does no longer fit in the cavity. For instance, Zdanski et al. [12] showed that, for a trench cavity like this one, vortex encapsulation takes place at $L/D \sim 6.65$. Recall from the previous section that vortex encapsulation refers to two vortices in the cavity without inside-cavity flow reattachment.

Figure 8 presents the change on drag ΔC_D as a function of cavity length to depth ratio L/D . The individual contributions of pressure $\Delta C_{D,p}$ and shear $\Delta C_{D,s}$ drag are also plotted. Both pressure and shear drag increases with increasing L/D . $\Delta C_{D,p}$ increases due to flow impingement on the afterbody wall, as suggested by Fig. 7. It is obvious that shear drag is negligible for both axisymmetric and planar cavities. In comparison with Fig. 4, it is interesting to note that, for our planar cavity, there is no absolute minimum $\Delta C_{D,p}$. This is, however, expected because we modified the cavity to avoid flows in the WBF and UCV regimes. It is evident that, by increasing L/D , the flow transitions from the SCV to the CCV regime. This also suggests that the vortex for the range of L/D studied here exhibits characteristics of forced vortices (i.e., $n = 2$ and the pressure increases almost quadratically with increasing vortex radius). Now it is

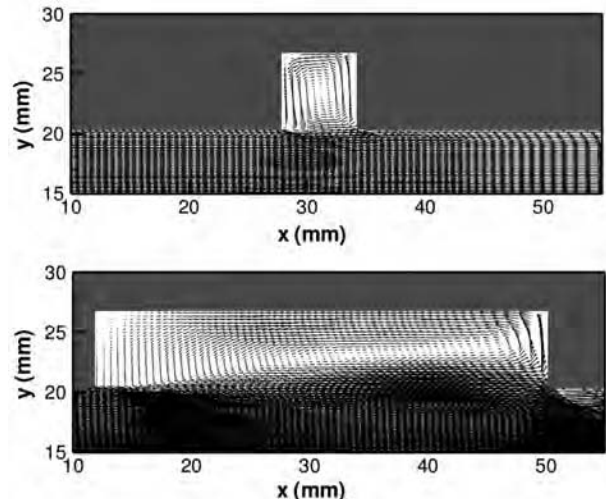


Fig. 7 Velocity vectors for the planar cavity with dimensions of $L/D = 1$ and 6. The calculations were performed using the standard $k-\epsilon$ RANS model.

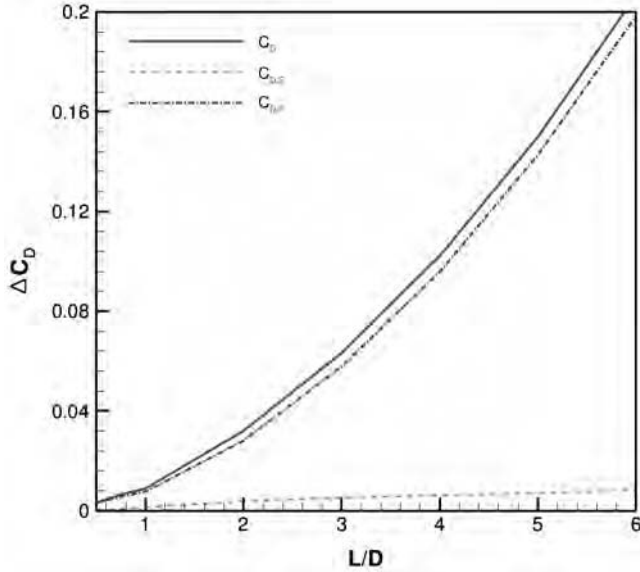


Fig. 8 Change in drag coefficient ΔC_D as function of cavity length to depth ratio L/D . The individual contributions of pressure $\Delta C_{D,p}$ and shear $\Delta C_{D,s}$ drag are also plotted.

important to examine the pressure distribution on the forebody and afterbody walls.

Figure 9 presents the pressure coefficient C_p as function of vertical distance y at the forebody (solid) and afterbody (dashed) walls. For $L/D = 1$, the absolute minimum C_p occurs at the center of the forebody and afterbody walls, indicating that the vortex center is located at the cavity center. Both C_p profiles and magnitudes in the forebody and afterbody walls are very similar, indicating that the horizontal forces are nearly balanced, exhibiting minimum flow oscillations. With increasing length to depth ratio L/D , C_p on the afterbody wall increases, whereas that on the forebody wall decreases. Because both C_p profiles and magnitudes in the forebody and afterbody walls are very different, horizontal forces are not balanced and the flow would exhibit large oscillations. The location of the absolute minimum C_p on the afterbody wall is shifted inward due to flow impingement on the afterbody wall. Note that this shift is consistent with that observed for $x/D_o = 0.6$ and 0.7 in Fig. 5.

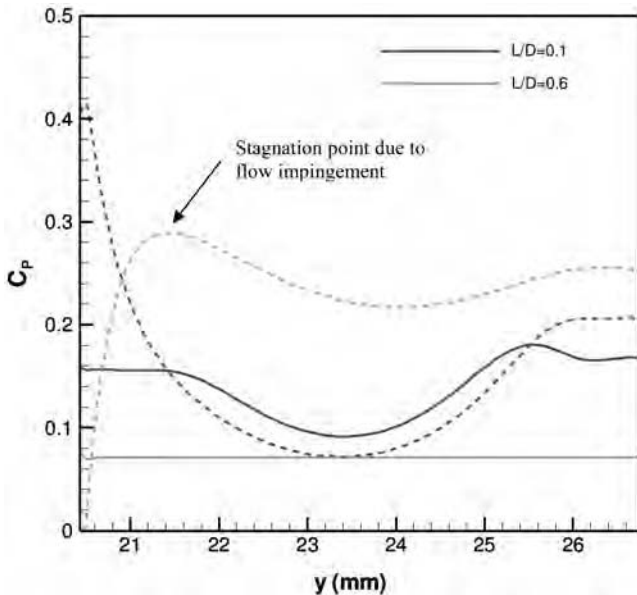


Fig. 9 Pressure coefficient C_p as function of vertical distance y at the forebody (solid) and afterbody (dashed) walls. The calculations were performed using the standard $k-\epsilon$ RANS model. The location of the stagnation point due to flow impingement is also indicated.

This again confirms qualitative similarities between that flow configuration in the axisymmetric cavity with afterbody disk at $x/D_o = 0.7$ and the flow in the planar cavity with $L/D = 6$.

DNS calculations were performed for the cavity sizes discussed in the context of Fig. 9 and the change in pressure drag $\Delta C_{D,p}$ as a function of dimensionless time τ^* is presented in Fig. 10. Whereas the RANS simulation provided steady values of $\Delta C_{D,p}$, the DNS provides unsteady values of $\Delta C_{D,p}$. Nevertheless, similar to the results of Fig. 8, the DNS results indicate that with increasing L/D , $\Delta C_{D,p}$ increases. Note that, for $L/D = 1.0$, the average $\Delta C_{D,p}$ is nearly 0.0 consistent with the result in Fig. 8. However, when $L/D = 6.0$, the average $\Delta C_{D,p}$ is ~ 0.7 , which is several times larger than that of Fig. 8. DNS and RANS simulations provide qualitative results; however, they might differ on their quantitative results.

D. Effect of Fuel and Air Injections on Flow Unsteadiness in Small Planar Cavities

This section is concerned with the pressure drag and flow characteristics in the small planar cavity due to fuel and air injection configurations. The schematic of normal injection (NI) and reverse injection (RI) configurations for air jets is presented in Fig. 11. In this figure, three possible fuel jet injection configurations are also depicted: coflow, crossflow, and counterflow with respect to the mainstream flow. As discussed in the Introduction, NI with crossflow corresponds to config. 1 examined by Zelina et al. [3]. The temporal pressure drag evolution for the configurations discussed in the context of Fig. 11 is presented in Fig. 12. For the NI of air jets, pressure drag oscillations start to fluctuate after a finite time of ~ 0.4 ms, whereas for RI, pressure drag fluctuations start immediately as the simulation starts. This suggests that flow disturbances propagate faster when RI is used. For NI, the crossflow-fuel-jet position exhibits the lowest pressure drag amplitudes, followed very closely by the coflow fuel jet position. The counterflow fuel jet position, on the other hand, exhibits the highest pressure drag amplitudes. Recall from Secs. III.B and III.C that the optimum flow configuration that leads to lowest flow unsteadiness is that of the SCV regime, which contains a corotating forcedlike vortex with the mainstream with minimum flow impingement on the afterbody wall. Therefore, when the fuel jet is injected in counterflow with respect to the mainstream, the corotating vortex existing in the cavity is distorted. On the contrary, when fuel jet is injected in crossflow or coflow, the corotating vortex is not distorted and possibly enhanced. This explains why the crossflow and coflow fuel-injection positions exhibit superior flow steadiness with respect to the counterflow fuel-injection position. Moreover, RI promotes a counter-rotating cavity

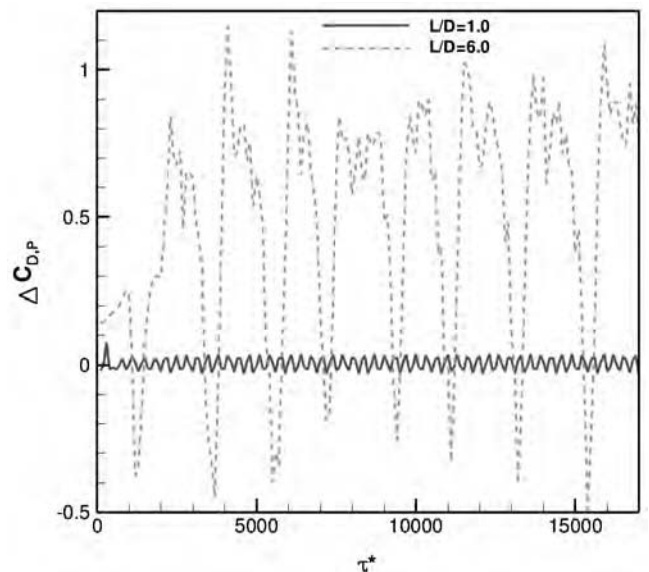


Fig. 10 Change in pressure drag $\Delta C_{D,p}$ as a function of dimensionless time τ^* . The calculations were performed using DNS.

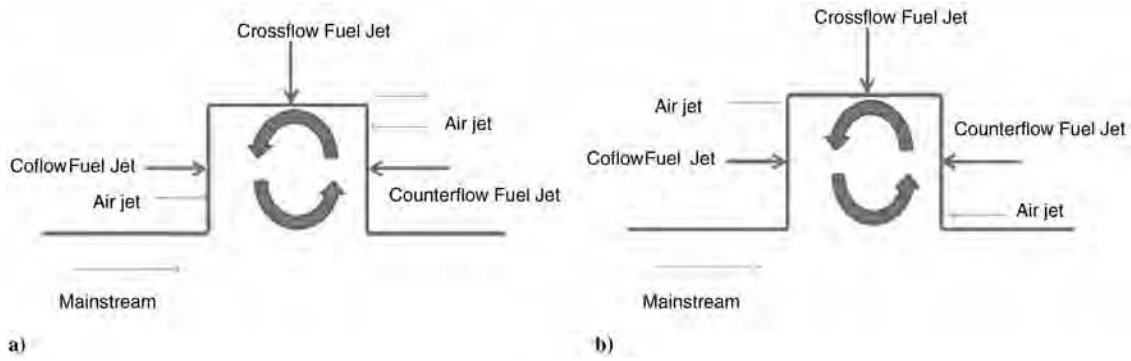


Fig. 11 Schematic of the a) normal injection and b) reverse injection configuration of air jets. The multiple positions of fuel jets are also indicated.

vortex (with respect to the mainstream flow). This in turn increases the flow unsteadiness as demonstrated by the larger pressure drag amplitudes. The flow in the RI is nearly insensitive to the fuel-jet injection positions. Counterflow-fuel-jet position and RI provide the worst-case scenario in terms of flow unsteadiness.

E. Effect of Cavity Equivalence Ratio and Combustion to Flame/Flow Unsteadiness

This section is concerned with the pressure drag and flow/flame characteristics in the small planar cavity due to combustion under various cavity equivalence ratios ϕ_{CAV} . The cavity equivalence ratios ϕ_{CAV} used are 0.85, 1.42, 2.15, 5.67, 8.5, and 11.33. As ϕ_{CAV} is increased, the cavity air to fuel jet momentum ratio λ_{CAV} decreases from 9.9 to 5.85, 3.87, 1.47, 0.97, and 0.74, respectively. The velocity in the main stream is equaled to the velocity of the air jets to reduce the effect of shear between the air mainstream flow and the outermost air jet. The mainstream temperature is constant at 533 K and its profile is uniform. The cavity walls are assumed isothermal at 533 K. A total number of 12 simulations were run corresponding to the six ϕ_{CAV} and two injection configurations for the air jets (cf. Figure 11). The fuel jet is injected in crossflow with the respect to the mainstream air flow. The instantaneous temperature contours, streamlines (lines), and streak lines (dots) for $\phi_{CAV} = 2.15, 5.67, 8.5,$ and 11.33 using NI and RI are presented in Fig. 13. The streamlines are computed from the fuel and air jets, whereas the streak lines are computed from the fuel jet only. These streak lines, in fact, represent massless particles injected through the fuel jet. Temperature contours and streamlines reveal that, when NI is used, two nonpremixed flames attached to the air jet ports are formed. On the other hand, the nonpremixed flames are attached to the fuel jet and the counterflow air jet ports when RI is used. A plausible explanation is that, if the flame were to be attached to the coflow air jet port, the curvature-induced stretch would be high

enough to extinguish the flame. Consequently, the flames established in the NI configuration appeared to be more parallel to the mainstream than the flames in the RI configuration. With NI, the particles are accumulated toward the forebody face of the cavity. On the contrary, particles are clustered toward the afterbody face of the cavity when RI is used. This plainly indicates that fuel is transported toward the forebody face of the cavity and afterbody face of the cavity when NI and RI are used, respectively. Moreover, this fact is consistent with the relatively high temperature encountered in the forward and backward cavity regions for the NI and RI, respectively. Qualitatively, it appears that, regardless of ϕ_{CAV} , it is more difficult for particles to escape the cavity when RI is used. This is because the particles have to go against the flow when they are still in the cavity as illustrated by the streamlines and streak lines.

Figure 14 shows the temporal temperature profiles for the NI (solid) and RI (dashed) for the conditions discussed in the context of Fig. 13. The temperatures are probed at $x = 34$ mm and $y = 22$ mm (cf. Figs. 3 and 13). Note that, at $\phi_{CAV} = 0.85, 1.42, 2.15, 5.67, 8.5,$ and 11.33 , the temperature starts increasing and/or oscillating at $\sim 1.5, 0.5, 0.25, 0.11, 0.09,$ and 0.19 ms, respectively, for the NI case. For ease of discussion, we refer to this time as the ignition time. It is reasonable to qualitatively observe that the mixture ignition time is the slowest at off-stoichiometric conditions (i.e., $\phi_{CAV} = 8.5$ and 11.33). The ignition time is, however, not the lowest at $\phi_{CAV} = 1.42$ because the chemistry model used in this investigation does not account for CO_2 and H_2O dissociation. Therefore, these results can only be interpreted qualitatively. The ignition time for RI is always larger than for their NI counterparts. This is a reasonable result because the large pressure drag fluctuations observed in Fig. 12 for RI would tend to inhibit ignition. For low ϕ_{CAV} , the amplitude of the temperature fluctuations is larger for RI than it is for NI. Nevertheless, as ϕ_{CAV} increases, the amplitude and frequency of temperature oscillations decrease for RI, whereas those for NI

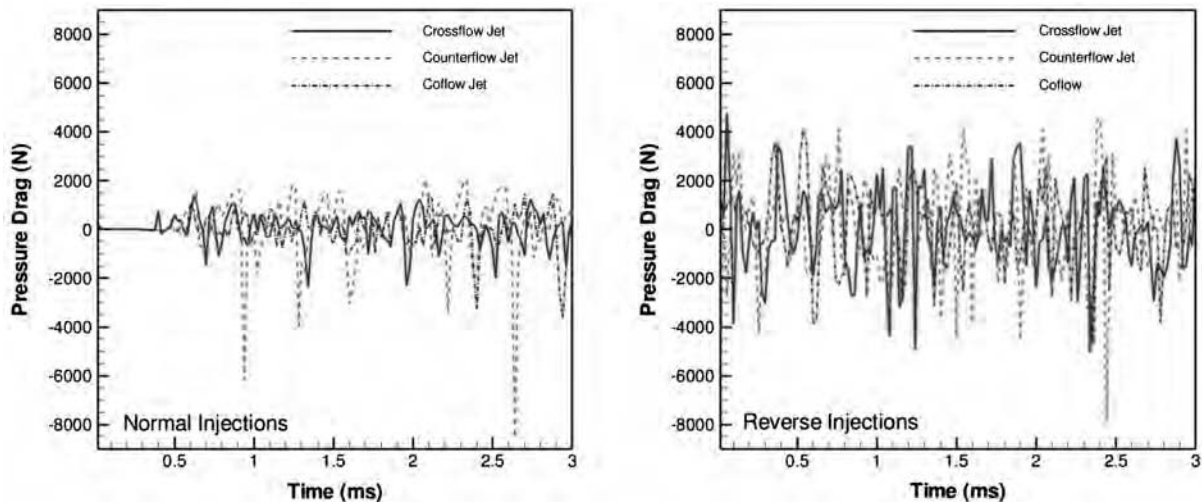


Fig. 12 Pressure drag as a function of time for the normal and reverse injection configurations. DNS were performed for these calculations.

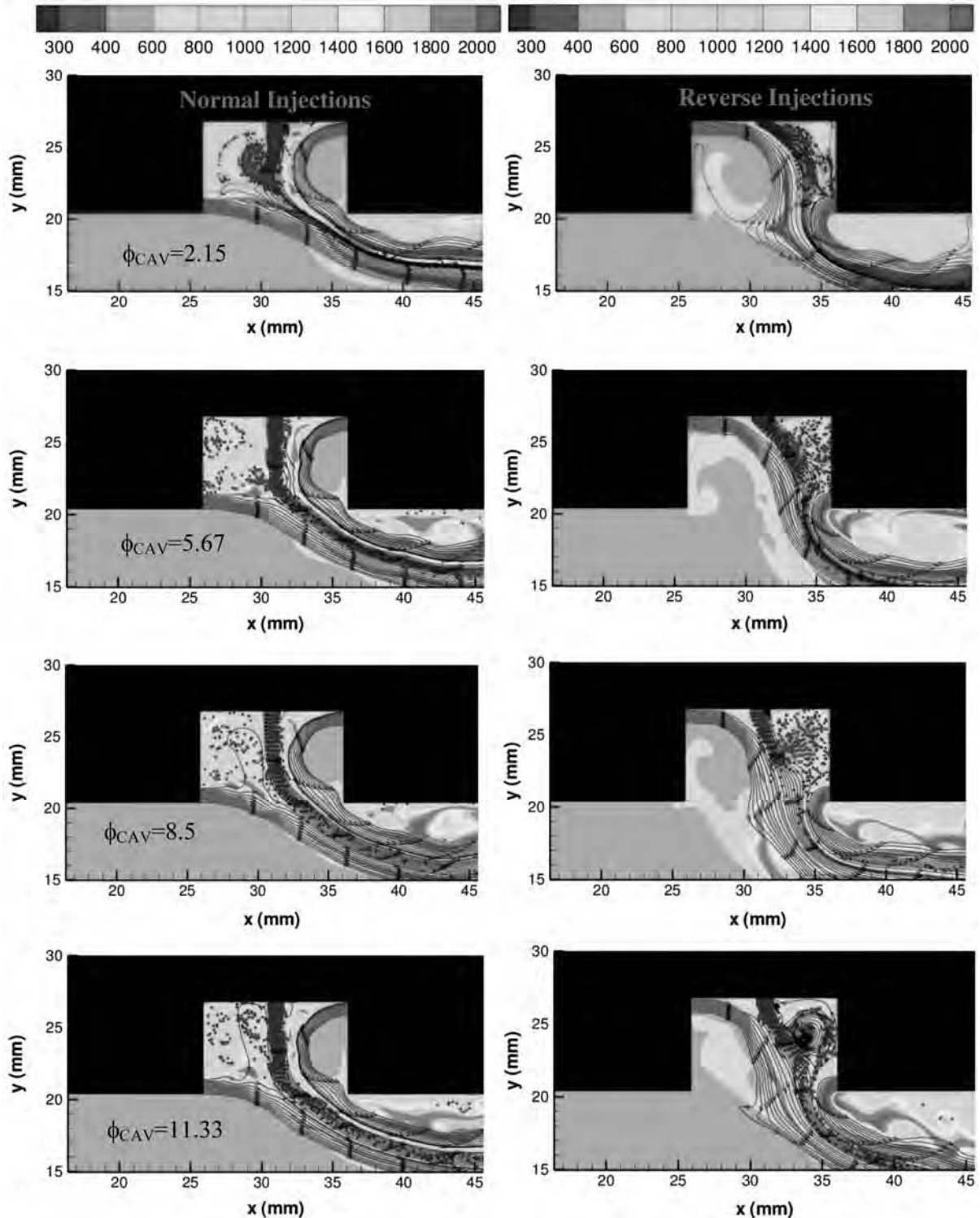


Fig. 13 Instantaneous temperature contours, velocity streamlines (lines), and streak lines (dots) after 3 ms for cavity equivalence ratios ϕ_{CAV} of 2.15, 5.67, 8.5, and 11.33 under NI (left) and RI (right) configurations.

generally increase. However, the effect of ϕ_{CAV} appears to be more pronounced for RI. So, at high ϕ_{CAV} , the amplitude and frequency of the temperature fluctuations is larger for NI than it is for RI.

To further examine the effect of ϕ_{CAV} on flow unsteadiness, Fig. 15 presents the pressure drag as a function of time for relatively low and high ϕ_{CAV} (i.e., 2.15 and 8.5). It is evident from Figs. 14 and 15 that, at low ϕ_{CAV} , flow unsteadiness is more pronounced for NI; nonetheless, at high ϕ_{CAV} , the flow unsteadiness for NI and RI become comparable. A possible explanation can be mentally visualized as follows:

1) For NI conditions, as $\phi_{CAV} \rightarrow 0$ $\lambda_{CAV} \rightarrow \infty$, and the effect of the fuel jet on the air jets becomes negligible. Consequently, we would expect a flow structure resembling that of an axisymmetric cavity with afterbody disk at $x/D_o = 0.5$ (cf. Figure 3) or that of a planar cavity with $L/D = 1.0$ (cf. Figure 7) (i.e., steady cavity vortex). Therefore, low ϕ_{CAV} leads to low flow unsteadiness.

2) For NI, as $\phi_{CAV} \rightarrow \infty$ $\lambda_{CAV} \rightarrow 0$, and the effect of the fuel jet on the air jets becomes significant. The previously established structure becomes distorted and the flow unsteadiness increases. Therefore, high ϕ_{CAV} leads to high flow unsteadiness. This is consistent

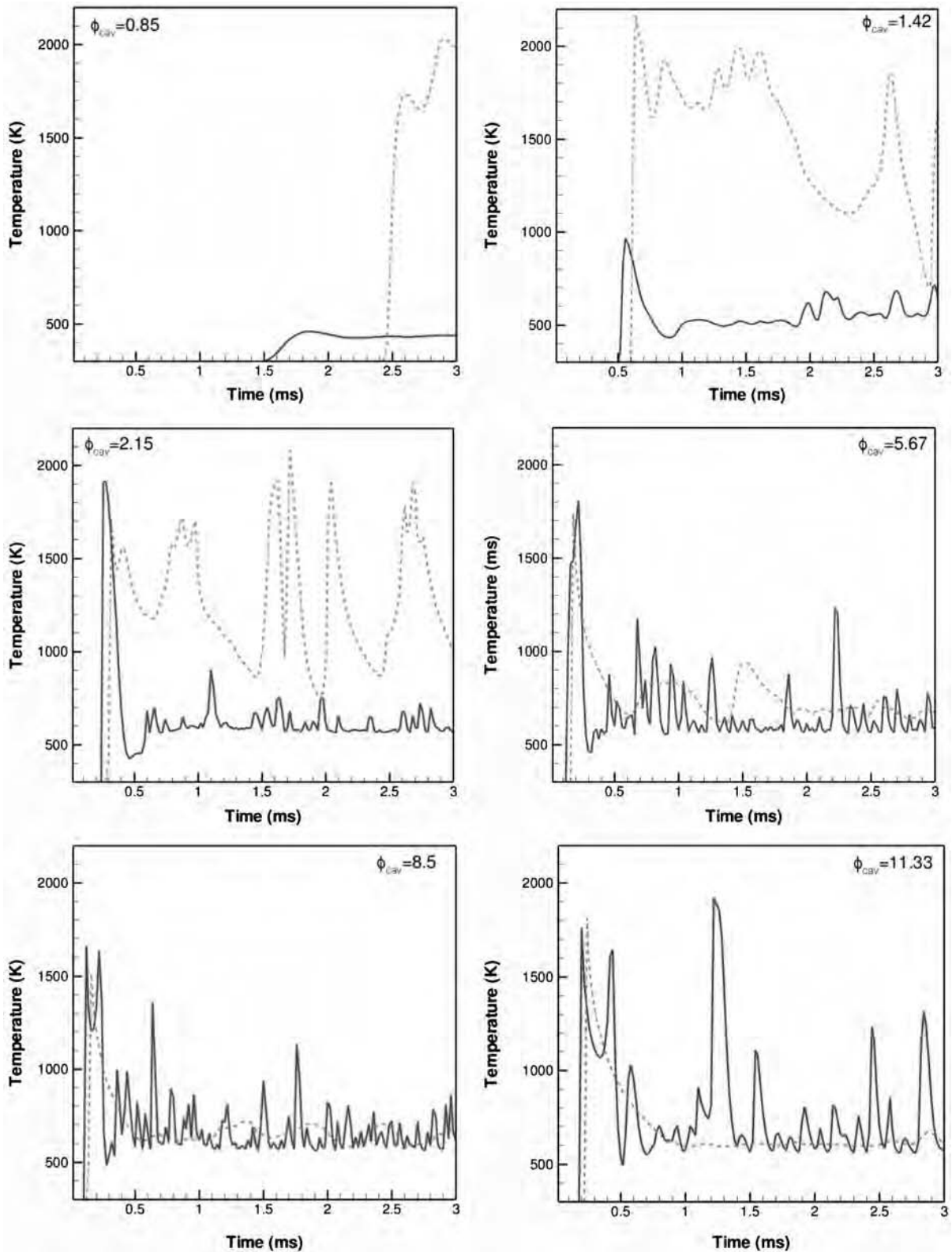


Fig. 14 Temporal temperature profiles for the normal (solid) and reverse (dashed) Injections. The simulations were performed using DNS. The temperatures are probed at $x = 34$ mm and $y = 22$ mm (cf. Figs. 3 and 13).

with Zelina et al. [3] who showed, as discussed in the Introduction, that decreasing λ_{CAV} leads to higher ϕ_{CAV} at lean blowout for NI of air and crossflow fuel injection. Because near-extinction conditions are associated with flow oscillations [32], the higher ϕ_{CAV} at lean blowout is interpreted here as higher flow unsteadiness. Nevertheless, blowout was not observed for any of our simulations because the global chemistry does not include elementary reactions needed for the correct assessment of flame extinction [33].

3) For RI conditions, as $\phi_{CAV} \rightarrow \infty$ $\lambda_{CAV} \rightarrow 0$, and the effect of the fuel jet on the air jets becomes negligible. Consequently, the flow inside the cavity resembles that presented for axisymmetric cavity with afterbody disk at $x/D_o = 0.2$ (cf. Figure 3) (i.e., wake backflow). Therefore, high ϕ_{CAV} leads to high flow unsteadiness.

4) For RI, as $\phi_{CAV} \rightarrow 0$ $\lambda_{CAV} \rightarrow \infty$, and the effect of the fuel jet on the air jets becomes significant. The previously established structure becomes distorted and the flow unsteadiness decreases.

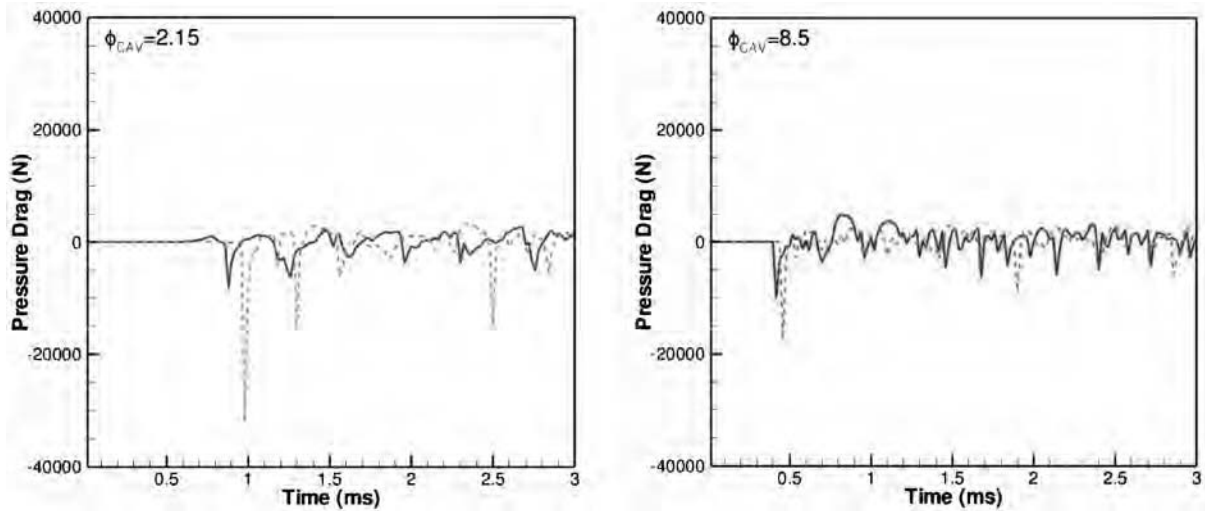


Fig. 15 Pressure drag as a function of time for cavity equivalence ratio ϕ_{CAV} of 2.15 and 8.5. The simulations were performed using DNS. Normal and reverse injections are indicated in solid and dashed lines, respectively.

IV. Conclusions

An extensive computational investigation on the characteristics of cavity-stabilized flames was presented. We examined the flow unsteadiness in both axisymmetric and (nonreactive and reactive flow past) planar cavities. Important conclusions are as follows:

1) Results indicate that shear drag coefficient $\Delta C_{D,S}$ is negligible in comparison with pressure drag coefficient $\Delta C_{D,P}$, and the former is proportional to flow unsteadiness.

2) The axisymmetric cavity, which consists of a forebody and an afterbody disk, exhibits multiple flow regimes depending on the distance between the forebody and afterbody disk. When the distance between the forebody and afterbody disk x/D_o is small, multiple vortices are formed in the cavity. However, it contains a main counter-rotating freelike vortex with respect to the mainstream flow that is formed due to the backflow (wake backflow regime). As with previous investigations on axisymmetric cavities, results indicate that with increasing cavity length the drag decreases as the flow transitions to the unsteady cavity vortex regime, characterized by backflow and flow contraction around the afterbody disk. Further increase on cavity length reduces the drag to an absolute minimum as the flow transitions to the steady cavity vortex regime. This regime is characterized by a corotating forcedlike vortex with neither backflow nor mainstream flow impingement. With further increase in x/D_o , the drag increases again as the flow transitions to the compressed cavity vortex regime, characterized by an elongated corotating forcedlike vortex with mainstream flow impingement on the afterbody disk.

3) Results indicate that with increasing planar cavity length the pressure drag increases monotonically as the flow in the cavity transitions from SCV to CCV regime. The vortex formed in the cavity exhibits forced-vortex pressure profiles as those present in the axisymmetric cavities. The planar cavity does not exhibit characteristics of the WBF and UCV regimes due to two reasons: 1) the forebody and afterbody depth D are equal, and 2) the afterbody thickness for the planar cavity is infinitely long in comparison with that of the axisymmetric cavity.

4) Normal injections (i.e., the outermost air jet is in coflow with the air mainstream flow, and the innermost air jet is in counterflow) present superior flow steadiness characteristics than their reverse injection counterpart (i.e., the outermost jet is in counterflow with the air mainstream flow and the innermost air jet is in coflow). This is because RI promotes counter-rotating vortex formation, resembling WBF. In the NI, the crossflow fuel jet promotes superior flow steadiness than the counterflow fuel jet. Crossflow-fuel-jet injection is slightly better in terms of flow steadiness than the coflow fuel jet injection. However, with RI, the three fuel jet injection positions (crossflow, coflow, and counterflow) exhibit comparable flow unsteadiness.

5) Cavity-stabilized flames were established at various cavity equivalence ratios ϕ_{CAV} under NI and RI. For NI, low ϕ_{CAV} (with high air to fuel momentum ratio λ_{CAV}) leads to low flow unsteadiness because the air jets promote corotating vortex formation in the cavity. At high ϕ_{CAV} (low λ_{CAV}), on the other hand, the fuel jet distorts the corotating vortex; hence, flow unsteadiness increase. For RI, low ϕ_{CAV} leads to high flow unsteadiness because the air jets promote counter-rotating vortex formation in the cavity. On the contrary, at high ϕ_{CAV} , the fuel jet distorts the formation of corotating vortex(es), increasing flow steadiness.

6) The results presented in this investigation suggest that, for minimizing cavity flow unsteadiness, designers need to focus on geometric dimensions, and fuel/air injection positioning and ϕ_{CAV} that promote corotating forcedlike vortex formation, and reduce both backflow and flow mainstream impingement on the afterbody wall.

Acknowledgments

This material is based on research sponsored by U.S. Air Force Research Laboratory under agreement number F33615-03-2-2347. We also thank W. M. Roquemore from the U.S. Air Force Research Laboratory/RZTC for his insightful comments. The views and conclusions contained herein are those of the authors and should not be interpreted as necessarily representing the official policies or endorsements, either expressed or implied, of U.S. Air Force Research Laboratory or the U.S. Government.

References

- [1] Zelina, J., Sturgess, G. J., and Shouse, D. T., "The Behavior of an Ultra-Compact Combustor (UCC) Based on Centrifugally-Enhanced Turbulent Burning Rates," *40th AIAA/ASME/SAE/ASEE Joint Propulsion Conference and Exhibit*, AIAA Paper 2004-3541, 2004.
- [2] Greenwood, R. T., Anthenien, R. A., and Zelina, J., "Computational Analysis of the Ultra Compact Combustor," *43rd AIAA Aerospace Sciences Meeting and Exhibit*, AIAA Paper 2005-220, 2005.
- [3] Zelina, J., Anderson, W., Koch, P., and Shouse, D. T., "Compact Combustion Systems Using a Combination of Trapped Vortex and High-g Combustor Technologies," *Proceedings of ASME Turbo Expo 2008: Power for Land, Sea, and Air*, American Society of Mechanical Engineers, GT2008-50090, 2008.
- [4] Zelina, J., Ehret, J., Hancock, R. D., Shouse, D. T., and Roquemore, W. M., "Ultra-Compact Combustion Technology Using High Swirl for Enhanced Burning Rate," *38th AIAA/ASME/SAE/ASEE/ Joint Propulsion Conference & Exhibit*, AIAA Paper 2002-3725, 2002.
- [5] Zelina, J., Sturgess, G. J., and Shouse, D. T., "The Behavior of an Ultra-Compact Combustor (UCC) Based on Centrifugally-Enhanced Turbulent Burning Rates," *40th AIAA/ASME/SAE/ASEE/ Joint Propulsion Conference & Exhibit*, AIAA Paper 2004-3541, 2004.
- [6] Greenwood, R. T., Anthenien, R. A., and Zelina, J., "Computational Analysis of the Ultra Compact Combustor," *43th Aerospace Sciences*

- Meeting & Exhibit*, AIAA Paper 2005-220, 2005.
- [7] Mawid, M. A., Park, T. W., Thornburg, H., Sekar, B., and Zelina, J., "Numerical Analysis of Inter-turbine Burner (ITB) Concepts for Improved Gas Turbine Engine Performance," *43th Aerospace Sciences Meeting & Exhibit*, AIAA Paper 2005-1162, 2005.
- [8] Mair, W. R., The Effect of a Rear-mounted Disc on the Drag of a Blunt-based Body of Revolution, *The Aeronautical Quarterly*, Vol. 16, Pt. 4, Nov. 1965, pp. 350–360.
- [9] Little, B. H., Jr., and Whipkey, R. R., "Locked Vortex Afterbodies," *Journal of Aircraft*, Vol. 16, No. 5, 1979, pp. 296–302. doi:10.2514/3.58522
- [10] Katta, V. R., and Roquemore, W. M., "Numerical Studies on Trapped-Vortex Concepts for Stable Combustion," *Transactions of the ASME: Journal of Engineering for Gas Turbines and Power*, Vol. 120, No. 1, 1998, pp. 60–68. doi:10.1115/1.2818088
- [11] Katta, V. R., and Roquemore, W. M., "Numerical Studies of Trapped-vortex Combustor," *32nd AIAA/ASME/SAE/ASEE/Joint Propulsion Conference & Exhibit*, AIAA Paper 1996-2660, 1996.
- [12] Zdanski, P. S. B., Ortega, M. A., and Fico, N. G. C. R., Jr., "On the Flow over Cavities of Large Aspect Ratio: A Physical Analysis," *International Communications in Heat and Mass Transfer*, Vol. 33, No. 4, 2006, pp. 458–466. doi:10.1016/j.icheatmasstransfer.2006.01.007
- [13] Zdanski, P. S. B., Ortega, M. A., and Fico, N. G. C. R., Jr., "Numerical Study of the Flow over Shallow Cavities," *Computers and Fluids*, Vol. 32, No. 7, 2003, pp. 953–974. doi:10.1016/S0045-7930(02)00067-1
- [14] D'yanchenko, A. Y., Terekhov, V. I., and Yarygina, N. I., "Vortex Formation and Heat Transfer in Turbulent Flow Past a Transverse Cavity with Inclined Frontal and Rear Walls," *International Journal of Heat and Mass Transfer*, Vol. 51, Nos. 13–14, 2008, pp. 3275–3286. doi:10.1016/j.ijheatmasstransfer.2007.11.039
- [15] Puranam, S., Arici, J., Sarzi-Amade, N., and Dunn-Rankin, D., Sirignano, "Turbulent Combustion in a Curving, Contracting Channel with a Cavity Stabilized Flame," *Proceedings of the Combustion Institute*, Vol. 32, No. 2, 2009, pp. 2973–2981. doi:10.1016/j.proci.2008.06.161
- [16] Katta, V. R., Zelina, J., and Roquemore, W. M., "Numerical Studies on Cavity-Inside-Cavity-Supported Flames in Ultra Compact Combustor," *Proceedings of the ASME Turbo Expo 2008: Power for Land, Sea, and Air*, American Society of Mechanical Engineers, GT2008-50853, 2008.
- [17] Shu, Z., Aggarwal, S. K., Katta, V. R., and Puri, I. K., "Flame-Vortex Dynamics in an Inverse Partially Premixed Combustor: The Froude Number Effects," *Combustion and Flame*, Vol. 111, No. 4, 1997, pp. 276–286. doi:10.1016/S0010-2180(97)00018-7
- [18] Azzoni, R., Ratti, S., Puri, I. K., and Aggarwal, S. K., "Gravity Effects on Triple Flames: Flame Structure and Flow Instability," *Physics of Fluids*, Vol. 11, No. 11, 1999, pp. 3449–3464. doi:10.1063/1.870203
- [19] Qin, X., Puri, I. K., Aggarwal, S. K., and Katta, V. R., "Gravity, Radiation and Coflow Effects on Partially Premixed Flames," *Physics of Fluids*, Vol. 16, No. 8, 2004, pp. 2963–2974. doi:10.1063/1.1764835
- [20] Siegel, R., and Howell, J. R., *Thermal Radiation Heat Transfer*, Hemisphere, New York, 1981.
- [21] Lee, B. J., and Chung, S. H., "Stabilization of Lifted Tribachial Flames in a Laminar Nonpremixed Flame," *Combustion and Flame*, Vol. 109, Nos. 1–2, 1997, pp. 163–172. doi:10.1016/S0010-2180(96)00145-9
- [22] Katta, V. R., Goss, L. P., and Roquemore, W. M., "Numerical Investigations of Transitional H₂/N₂ Jet Diffusion Flames," *AIAA Journal*, Vol. 32, No. 1, 1994, pp. 84–94. doi:10.2514/3.11954
- [23] Bird, R. B., Stewart, W. E., and Lightfoot, E. N., *Transport Phenomena*, Wiley, New York, 1960.
- [24] Reid, R. C., Prausnitz, J. M., and Poling, B. E., *The Properties of Gases and Liquids*, McGraw-Hill, New York, 1987.
- [25] Chu, W.-W., Yang, V., and Majdalani, J., "Premixed Flame Response to Acoustic Waves in a Porous-Walled Chamber with Surface Mass Injection," *Combustion and Flame*, Vol. 133, No. 3, 2003, pp. 359–370. doi:10.1016/S0010-2180(03)00018-X
- [26] "Ansys Fluent 12.0 Theory Guide," Ansys, Ann Arbor, MI, www.fluent.com.
- [27] Kee, R. J., Rupley, F. M., Miller, J. A., Coltrin, M. E., Grcar, J. F., Meeks, E., Moffat, H. K., Lutz, A. E., Dixon-Lewis, G., Smooke, M. D., et al., "Chemkin Release 4.1.1," Reaction Design, San Diego, CA, 2007.
- [28] Katta, V. R., Mawid, M., Sekar, B., Corporan, E., and Montgomery, C. J., "Comparison of Chemical-Kinetics Models for JP-8 Fuels in Predicting Premixed and Nonpremixed Flames," *42nd AIAA/ASME/ASEE Joint Propulsion Conference and Exhibit*, AIAA Paper 2006-4745, 2006.
- [29] Katta, V. R., Meyer, T. R., Brown, M. S., Gord, J. R., and Roquemore, W. M., "Extinction Criterion for Unsteady, Opposing-Jet Diffusion Flames," *Combustion and Flame*, Vol. 137, Nos. 1–2, 2004, pp. 198–221. doi:10.1016/j.combustflame.2004.02.004
- [30] Grisch, F., Attal-Tretout, B., Bresson, A., Bouchardy, P., Katta, V. R., and Roquemore, W. M., "Investigation of a Dynamic Diffusion of H₂ in Air with Laser Diagnostics and Numerical Modeling," *Combustion and Flame*, Vol. 139, Nos. 1–2, 2004, pp. 28–38. doi:10.1016/j.combustflame.2004.08.002
- [31] Gharib, M., and Roshko, A., "The Effect of Flow Oscillations on Cavity Drag," *Journal of Fluid Mechanics*, Vol. 177, April 1987, pp. 501–530. doi:10.1017/S002211208700106X
- [32] Füre, M., Papas, M., and Monkewitz, P. A., "Non-Premixed Jet Flame Pulsations Near Extinction," *Proceedings of the Combustion Institute*, Vol. 28, Pt. 1, 2000, pp. 831–838.
- [33] Takahashi, F., and Katta, V. R., "A Reaction Kernel Hypothesis for the Stability Limit of Methane Jet Diffusion Flames," *Proceedings of the Combustion Institute*, Vol. 28, Pt. 2, 2000, pp. 2071–2078.

T. Jackson
Associate Editor

APPENDIX G

Soot Studies of Laminar Diffusion Flames with Recirculation Zones

INTENTIONALLY LEFT BLANK



ELSEVIER

Available online at www.sciencedirect.com

ScienceDirect

Proceedings of the Combustion Institute xxx (2009) xxx–xxx

 Proceedings
of the
Combustion
Institute
www.elsevier.com/locate/proci

Soot studies of laminar diffusion flames with recirculation zones [☆]

M. Roquemore ^{a,*}, V. Katta ^c, S. Stouffer ^b, V. Belovich ^a, R. Pawlik ^a,
M. Arstingstall ^b, G. Justinger ^b, J. Gord ^a, A. Lynch ^a, J. Zelina ^a, S. Roy ^c

^a Air Force Research Laboratory, Propulsion Directorate, AFRL/RZTC BLDG 490,
1950 Fifth Street, Wright-Patterson AFB, OH 45433-7251, USA

^b University of Dayton Research Institute, Dayton, OH 45469-0114, USA

^c Innovative Scientific Solutions, Inc. (ISSI), Dayton, OH 45440-3638, USA

Abstract

This paper describes the unusual sooting structure of three flames established by the laminar recirculation zones of a centerbody burner. The vertically mounted burner consists of an annular air jet and a central fuel jet separated by a bluff-body. The three ethylene fueled flames are identified as: fully sooting, donut-shape, and ring-shape sooting flames. Different shapes of the soot structures are obtained by varying the N₂ dilution in the fuel and air jets while maintaining a constant air and fuel velocity of 1.2 m/s. All three flames have the unusual characteristic that the soot, entrained into the recirculation zone, follows discrete spiral trajectories that terminate at the center of the vortex. The questions are what cause: (1) the unusual sooting structures and (2) the spiral trajectories of the soot? Flame photographs, laser sheet visualizations, and calculations with a 2D CFD-based code (UNICORN) are used to answer these questions. The different sooting structures are related to the spiral transport of the soot, the spatial location of the stoichiometric flame surface with respect to the vortex center, and the burnout of the soot particles. Computations indicate that the spiral trajectories of the soot particles are due to thermophoresis. Published by Elsevier Inc. on behalf of The Combustion Institute.

Keywords: Soot; Recirculation zone; Flame structure; Centerbody; Laminar-flow

1. Introduction

The Strategic Environmental Research and Development Program (SERDP) office recently started a comprehensive soot-research initiative

to establish the science base needed to develop and validate soot models that can be used to design low soot emission combustors in future gas turbine engines burning practical hydrocarbon fuels. The SERDP-sponsored programs involve strongly coupled, mutually supportive, experimental and modeling efforts that investigate soot processes in different burners. The burner designs progress in complexity from laminar, transitional, to turbulent flames.

A centerbody configuration has been selected for soot studies of laminar flames stabilized by recirculation zones. It has been used for many

[☆] Submitted to: The Thirty-Second International Symposium on Combustion, The Combustion Institute, August 3–8, 2008, Montreal, Canada.

* Corresponding author. Fax: +1 937 255 1125.
E-mail address: william.roquemore@wpafb.af.mil (M. Roquemore).

years in fundamental studies to aid the evaluation and development of combustion models [1–7]. It has a simple geometry with clean inlet conditions for modeling, clear optical access for use of laser diagnostics, and can be operated at conditions that give radically different flow fields and flame structures which are advantageous for evaluating and developing models. The ability to dramatically change the flow field by changing the inlet flow rates was first observed by Yule [8] for non-reacting flows and by others in reacting flows [9–13].

In this paper, the effects due to changing the flow field are not exploited. Instead, laminar diffusion flames are studied in which the flow fields are maintained nearly the same but their sooting surfaces are radically changed by using mixtures of N_2 in both the inlet fuel and air flow. To our knowledge, a centerbody burner has never been used in this type of study.

Three flames are investigated that have almost the same flow fields but have very different sooting structures. An interesting and perhaps unique aspect of these flames is that the soot entrained into the large recirculation zone, established by the centerbody, is transported towards the vortex center in discrete spiral trajectories. These interesting flames raise two questions: (1) what causes the different shapes of the soot structures and (2) what causes the soot spiral path lines? Flame photographs, Mie scattering from a laser sheet, and 2D CFD computations with a code called UNICORN (UNsteady Ignition and COMbustion using ReactionS) are used to address these questions.

2. Simulations and modeling (UNICORN)

UNICORN is a time-dependent, axisymmetric mathematical model that is used to investigate 2D steady and unsteady reacting flows. It has been developed over a 14-year period [14] and has evolved hand-in-hand with experiments designed to test its ability to predict ignition, extinction, stability limits, and the dynamic and steady-state characteristics of diffusion and premixed flames burning various fuels [15]. UNICORN uses a simplified soot model [16] and a detailed chemical-kinetics model for ethylene with 99 species and 1066 elementary reactions [17]. A simple radiation model, based on the optically thin-media assumption, is incorporated into the energy equation for treating radiation heat loss from gaseous species [18]. Only CH_4 , CO , CO_2 , and H_2O are considered as radiating species in this study. Soot is modeled assuming it is a separate gaseous species. It is computed by solving conservation equations for its volume fraction and number density. Heat losses from “gaseous” soot are computed assuming blackbody radiation from the carbon soot particles [19]. More detailed descriptions of UNICORN are given in [20–22].

3. Experiment

The centerbody burner set-up is shown in Fig. 1 and is similar to that used for studies of dynamic flames [23]. The centerbody is contained in a vertical wind tunnel designed to provide low turbulence inlet flows with a flat velocity profile. The centerbody is a 46-mm-diameter disk with a 7.6-mm-diameter fuel jet located at its center. It is symmetrically mounted in an 80-mm-ID quartz tube that extends 25 cm from the face of the centerbody. A Nd:YAG laser and cylindrical lens are used to form a laser sheet for visualizing the soot characteristics of the flames. Mie scattering images from soot particles are collected with a digital camera mounted normal to the laser sheet and triggered by the laser.

The centerbody configuration can be thought of as an annular air jet and a central fuel jet separated by a bluff-body. Mixtures of ethylene/ N_2 are ejected from the fuel jet and air/ N_2 mixtures are ejected from the annular jet. All of the flows are metered with mass-flow controllers. Ethylene is selected as the fuel because detailed chemistry mechanisms exist [17]. It is been widely used in soot studies [24].

Three sooting flames with very different and unusual sooting structures are selected for study. The flames are identified as: the fully sooting, donut-shaped, and ring-shaped flame. The different sooting structures are achieved by diluting the air and ethylene fuel with nitrogen (N_2) while maintaining the air/ N_2 and fuel/ N_2 flow rates constant, which mean that the average velocities at the exit of the annular air and central fuel jets (the inlet to the burner) are also constant. The impact of this is that the flow fields of the three flames are nearly the same [23]. That is, the size, shape, velocity, and other flow characteristics of the recirculation zones established by the centerbody are nearly the same for three flames. This is confirmed by the presented flow field calculations. Maintaining constant fuel and air flow rates greatly simplifies the experiments because it removes the flow field as a variable when trying to account for the different shaped sooting structures and the unusual spiral vortices.

The volumetric flow rates for the air and fuel jets are given in Table 1. The average inlet velocity of the air and fuel was 1.2 m/s, which corresponds to a fuel jet that just penetrates the recirculation zone [23].

4. Results and discussion

4.1. Soot flame structure

The unusual sooting structures for the fully sooting, donut-shaped, and the ring-shaped flames are shown by the color flame photographs

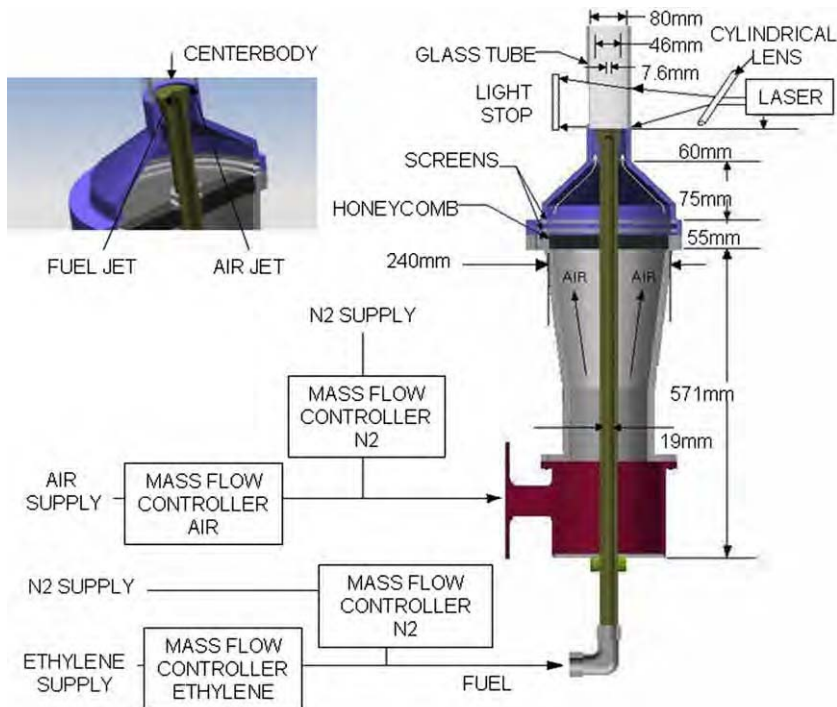


Fig. 1. Experimental set-up showing flow controllers, test section, and laser-sheet-lighting arrangement. A digital camera (not shown) is mounted normal to the laser sheet and triggered by the laser.

Table 1
Volumetric flow rates (standard liters/minute, SLPM) of studied flames

		Fully sooting	Donut-shape	Ring-shape
Annular	Air	250	200	200
	N ₂	0	50	50
Annular flow	Total	250	250	250
Fuel jet	C ₂ H ₄	3.4	2.1	1.5
	N ₂	0	1.3	1.9
Fuel flow	Total	3.4	3.4	3.4

in Figs. 2a–4a, respectively. The yellow part of the flame represents what we call the sooting structure. Although it is hard to see in the photographs, a thin blue flame, adjacent to the outer surface of the sooting flame, is “nearly attached” at the outer rim of the centerbody. The blue flame results from chemiluminescence of species such as CH and C₂ and is a reasonable marker for the stoichiometric flame surface. In all three flames, soot forms on the fuel-rich side of the stoichiometric surface just as one would expect for diffusion flames.

UNICORN, with a simple soot model, has been used to calculate the characteristics of the

fully sooting, donut-, and ring-shaped flames. These results are shown in (b) and (c) of Figs. 2–4. Caution must be used in comparing photographed and computed flames. The flame photographs are 2D images of 3D surfaces. The computed flames are 2D cross sections through the centerline of the centerbody. Only the outer edges of the observed and computed flame surfaces should be compared because this is the only location where the images overlap.

UNICORN calculations in (b) and (c) of Figs. 2–4 seem to capture the global features of the flames and their unusual shapes. Using enlarged transparent overlays of scaled photographs will show that the blue flames in Figs. 2, 3a, and 4a overlay almost perfectly with the stoichiometric surface, shown in white, and the computed high temperature colored contour images in the (b) figures. Very good agreement is obtained when the observed yellow sooting flame surface in Fig. 2a is compared with the computed radiation-intensity surface in Fig. 2c. When similar comparisons are made for the donut- and ring-shaped flames in Figs. 3 and 4, agreement is reasonably good but there are some noticeable differences. The experimentally observed donut-shaped and especially the ring-shaped sooting surfaces are thinner and located upstream of those calculated using the soot radiation intensity. Even with these

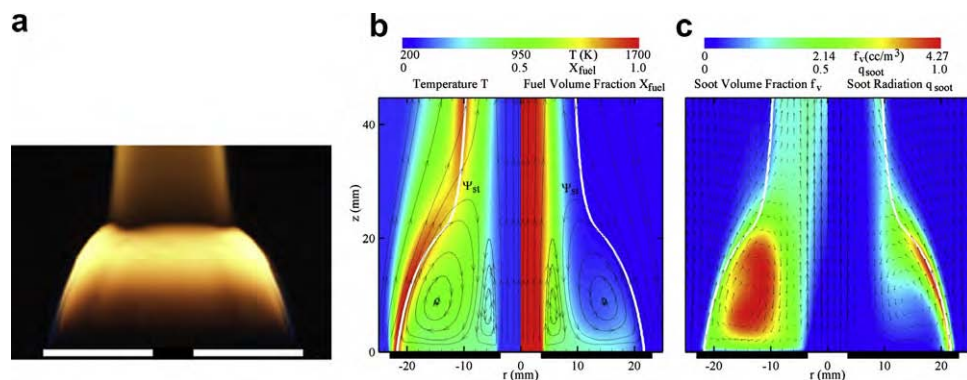


Fig. 2. (a) Photograph of fully sooting flame, (b) computed temperature (left) and fuel volume fraction (right); and (c) relative soot volume (left) and normalized soot-radiation intensity (right). White line is calculated stoichiometric surface.

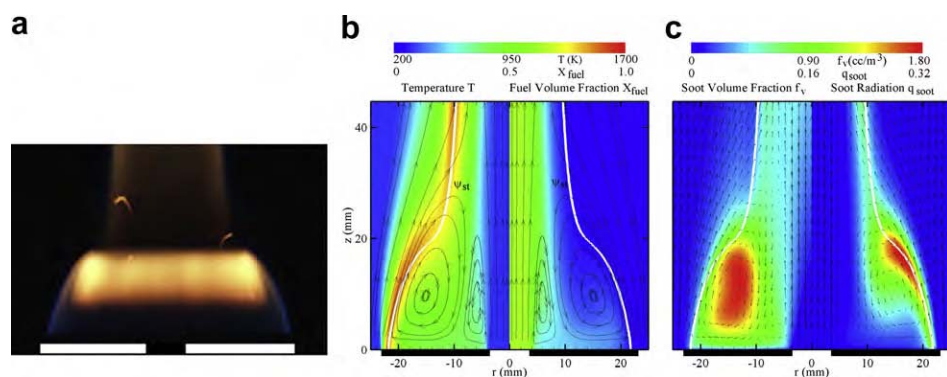


Fig. 3. (a) Photograph of donut-shaped flame, (b) computed temperature (left) and fuel volume fraction (right), and (c) relative soot volume (left) and normalized soot-radiation intensity (right).

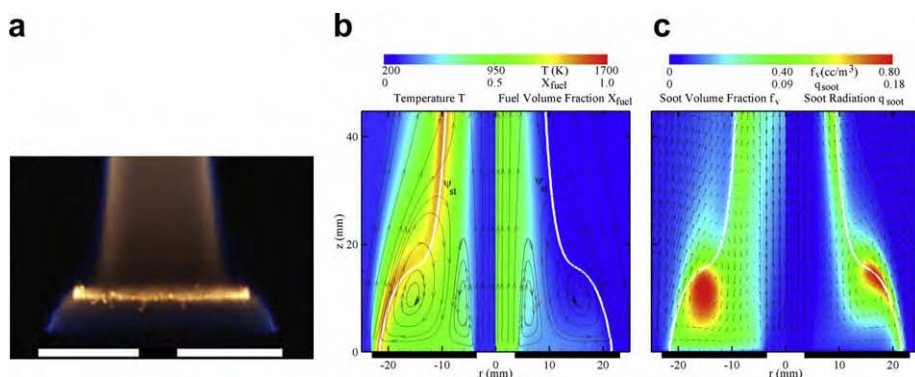


Fig. 4. (a) Photograph of ring-shaped flame, (b) computed temperature (left) and fuel volume fraction (right), and (c) relative soot volume (left) and normalized soot-radiation intensity (right).

differences, UNICORN does a reasonable job capturing the global sooting flame shapes.

It is encouraging that UNICORN, with a simple soot model, does reasonably well in capturing the unusual shapes of the sooting flames. How-

ever, comparing the observed and computed sooting flame surfaces is not adequate to evaluate a soot model and can even be misleading because the radiation intensity depends exponentially on temperature. Comparing sooting flame surfaces

can have more to do with a models' ability to predict temperature fields than soot fields. However, Mie scattering is a good way of evaluating soot models because it gives a direct way of visualizing the location of the soot particles. Also, the Mie scattering images provide new insights into the unusual sooting structures. These points are discussed in the next section.

4.2. Spiral soot path-lines

Laser sheet-lit images in Figs. 5 and 6a show the fully sooting and donut-shaped flames, respectively, and the soot path lines that result for the Mie scattering from the soot particles. The soot appears to form in the outer shear layer just above the edge of the centerbody face in Fig. 5a. Some of the soot particles are entrained into the recirculation zone and follow spiral paths towards the center of the outer vortex. The soot particles tend to accumulate at the vortex center, where visual

observations indicate they either oxidize or grow sufficiently large so they fall to the centerbody face. Also, the soot formed in the shear layer appears, to the eye, to be much larger than the submicron size particles one might expect. This is probably due to an enhanced soot growth process resulting from the long residence times in the recirculation zone.

The donut-shaped flame in Fig. 6a also shows that the entrained soot particles follow path lines that spiral towards the vortex center; however, the path lines have a tighter spiral shape than that in Fig. 5a. This is also evident when visually observing the ring-shaped flame in Fig. 4a. The thin sooting ring is actually composed of soot particles with very tight spiral path lines swirling about the center of the vortex. Indeed, laser sheet lit images of the ring-shaped flame (not shown) and visual observations of the Mie scattered laser light show that there are very few soot particles between the centerbody face and soot ring. As will be

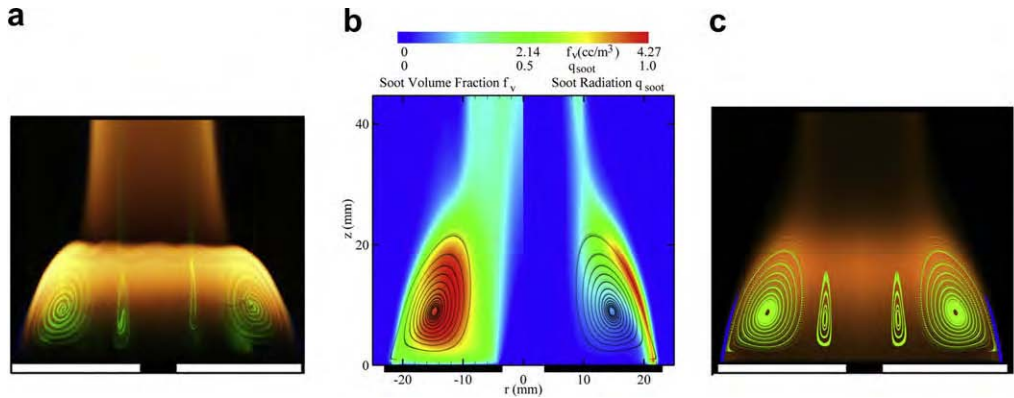


Fig. 5. (a) Photograph of fully sooting flame, (b) computed soot volume fraction (left) and radiation intensity (right) with particle tracks, and (c) computed fully sooting flame with solid body rotation and false colors (For interpretation of colour mentioned in this figure, the reader is referred to the web version of this article.).

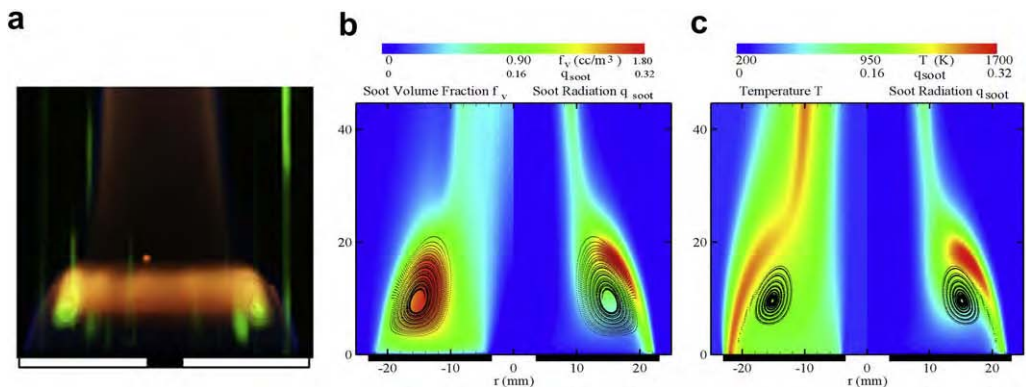


Fig. 6. (a) Photograph of donut-shaped sooting flame, (b) computed soot volume fraction (left) and radiation intensity (right) with particle tracks, and (c) computed temperature (left) and radiation intensity (right) and oxidation of spiraling soot (right).

discussed, considerable insight can be gained from this observation. Before pursuing this, it is advantageous to consider the results of UNICORN calculations.

Spiral vortices are often observed in spatial and time evolving flows such as a Kármán vortex street and Kelvin–Helmholtz vortices. However, we are only aware of one example where spiral vortices have been observed for particles and that is for another centerbody flow [23]. As shown in the (b) Figs. 2–4, the fluid follows closed path lines as expected for a stable, laminar recirculation zone. The spiral path lines represent a computational challenge and an intellectual stimulus to understand their origin.

The current version of UNICORN, with a simple soot model, does not simulate the spiral motion of the soot particles. This is evident from the soot-volume-fraction calculations shown in Figs. 2–4c and results because the current model treats soot as a gas. However, UNICORN has a tracking program that can be used to follow the path of released particles with defined mass and size. It is a Lagrangian-based program with Newtonian particle dynamics that include drag, thermophoresis [25], gravitational forces, and flow-field characteristics calculated with UNICORN. This particle-tracking program is used to explore the path lines of particles released in the sooting zone of the flames.

Particle trajectories are obtained by tracking the particles as they are released in the shear layer at the soot-inception point near the edge of the centerbody face as noted in Fig. 2c. Several different diameter particles were selected for UNICORN calculations with particle tracking. As will be illustrated later, the calculations show that the number of spirals is determined by the diameter of the particles. The larger particles have the fewer number of spirals. Figure 5b illustrates that 5- μm -diameter carbon particles are entrained into the recirculation zone and follow spiral path lines similar to those experimentally observed (Fig. 5a). Note the size and shape of the observed and computed spiral path lines are almost identical. This suggests that the observed soot particles may have a diameter of about 5- μm .

Figure 5c uses a solid-body rotation of the blackbody-radiation intensity and false coloring to illustrate how a 3D computed flame appears as a 2D image. The agreement with the flame photograph in Fig. 5a is considered very good. Also, the observed (Fig. 5a) and computed (Fig. 5c) outer and inner recirculation zones are nearly the same.

UNICORN, with particle-tracking calculations shown in Fig. 6b, captures some but not all of the observed details. For example, UNICORN correctly predicts the location of the vortex center; but, the tightly spiraling path lines shown in Fig. 6a are not predicted. That is, the

computed particle path lines in Fig. 6a have a larger diameter than those experimentally observed in Fig. 6a. However, tight spiral path lines can be computed if additional physics is imposed on the calculation. As will be shown, this will have a significant impact on shape of the soot structures.

To gain an insight into the physics needed to compute and understand the observed tight spiral path lines, note that the donut- and ring-shaped flames result because N_2 is added to the fuel and air jets (Table 1). The addition of N_2 causes the stoichiometric flame surface to move towards the center of the vortex. This is evident by comparing the location of the blue flames and calculated stoichiometric surfaces (white lines) in Figs. 2 and 3. Indeed, the stoichiometric blue ring flame is very near the vortex center in Fig. 3a. This means that a considerable number of soot particles, with larger soot path line diameters, pass through the flame front. As the soot passes through the flame, oxidation takes place.

Soot oxidation is an important process missing in the soot-particle tracking model and, as we will illustrate, plays an important role in determining the shape of the sooting flame surface. A simple soot oxidation model, added to UNICORN's particle tracking program, removes all soot particles from the calculations that encounter temperatures larger than 1300 K [26]. Thus, soot particles, following path lines that pass through the high-temperature flame zone, are completely oxidized. The only observable soot particles are the ones that follow path lines that do not pass through the flame zone. That is, the only soot particles that survive are the ones that follow path lines which pass between the vortex center and the temperature zone at which complete soot oxidation takes place. As N_2 dilution moves the flame location towards the vortex center, the surviving soot particles appear in tighter and tighter spirals around vortex center. To the eye, the soot surface appears as the donut- and ring-shaped flames in Figs. 6a and 7a, respectively. UNICORN has captured this process in Fig. 6c.

UNICORN/particle-tracking calculations show that spiral soot path lines depend on particle size. Figure 7a illustrates that mass-less particles do not spiral toward the vortex center but follow a large closed orbit similar to a streamline. Particle-tracking calculations with 1- and 5- μm diameter carbon particles result in spiral path lines as noted in Figs. 5b and 7b but the 1- μm diameter soot particles only make 4 spirals before they are terminated at the vortex center; whereas, the 5- μm diameter particles make more than 10 revolutions. Figure 7c shows that the 50- μm diameter particles have sufficient momentum to carry them downstream without being entrained into the recirculation zone. A particle density of 1900 kg/m^3 is used in the calculation [16].

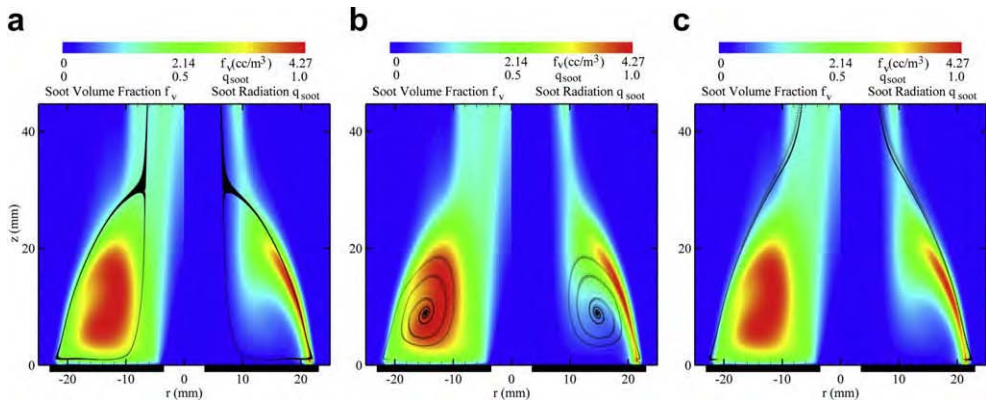


Fig. 7. (a) Fully sooting flame with mass-less particles, (b) soot volume fraction (left) and radiation intensity (right) with 1- μ m-diameter particles, and (c) temperature (left) and radiation intensity (right) with 50- μ m-diameter soot particles.

The path line calculations in Figs. 5b, 7a, and b indicate that the force, causing the spiral motion of the particles, depends on particle size and appears to have more impact on the smaller particles. The result is that they complete fewer revolutions. This suggests that the thermophoretic force may be involved. When thermophoresis is removed from the 5- μ m particles calculation in Fig. 5b, the calculation looks just like that for the mass-less particle in Fig. 7a. Thus, thermophoresis is predicted to be the cause of the spiral transport of the soot particles.

5. Summary and conclusions

The unusual sooting characteristics of three flames established by the laminar recirculation zones of a centerbody burner are investigated. The three ethylene fueled flames are identified as: fully sooting, donut-shape, and ring-shape flames. Different sooting structures are obtained by varying the N_2 dilution in the fuel and air jets while maintaining a constant air and fuel velocity of 1.2 m/s. All three flames have the unusual characteristic that the soot, entrained into the recirculation zone established by the bluff-body, follows path lines that spiral towards the vortex center. The questions are what causes: (1) the unusual sooting structures and (2) the spiral trajectories of the soot? Flame photographs, laser sheet visualizations, and calculations with a 2D CFD-based code (UNICORN) are used to answer these questions. Calculations indicate that the unusual shapes of the sooting flames result from: (1) the exponential dependence of the soot radiation that biases the radiation to the high-temperature surfaces, (2) changes in the location of the stoichiometric flame surface with respect to the vortex center established by the centerbody, and (3) complete oxidation of the soot following path lines that intersect the high temperature flame zone. The location of the stoichiometric flame surface

moves radically towards the vortex center as N_2 is added to the fuel jet. The observed soot particles are the ones that follow path lines between the flame and the vortex center. To the eye, the soot surface will appear as tighter and tighter spirals as N_2 is added to the fuel, thus resulting in the donut- and ring-shaped flames. This accounts for the size variations of the spiral soot path lines in the flames with different N_2 additions. The spiral soot path-lines depend on particle size with massless particles giving a closed streamline like trajectory and 50- μ m particles travel downstream without being entrained. The spiral path lines disappear when the thermophoretic force is removed from the calculation. Thus, it is predicted that the spiral soot path lines result from thermophoresis. It is concluded that the laminar centerbody burner is an excellent tool for studying fundamental soot processes and evaluating soot models.

Acknowledgments

The authors acknowledge the financial support of Bruce Sartwell of the SERDP program office and the Turbine Engine Division of the Propulsion Directorate of the Air Force Research Laboratory. We also appreciate the work of Kyle Frische and Keith Grinstead, Jr., on the camera and laser-interface electronics; Jack Yoder for the illustration of the experimental set-up; and Jennifer James for editorial assistance.

References

- [1] W.M. Roquemore et al., *AGARD CP 353* 19 (1984) 36-1-36-21.
- [2] G.J. Sturgess, K.R. McManus, *Calculations of Turbulent Mass Transport in a Bluff-body Diffusion-flame Combustor*, American Institute of Aeronautics and Astronautics, Aerospace Sciences Meeting, 22nd, Reno, NV, Jan. 9-12, 1984.

- [3] S.M. Correa, A. Gulati, *Combust. Flame* 89 (2) (1992) 195–213.
- [4] L. Fallot, *Combust. Flame* 110 (1997) 298–318.
- [5] Kai Liu et al., *Combust. Flame* 141 (2005) 89–117.
- [6] A. Kempf et al., *Combust. Flame* 144 (2006) 170–189.
- [7] Bart Mercier et al., *Combust. Flame* 144 (2006) 109–130.
- [8] A.J. Yule et al., *AIAA J.* 19 (1980) 752–760.
- [9] W.M. Roquemore et al., *Preliminary Evaluation of a Combustor for Use in Modeling and Diagnostics Development*, ASME Publication, 1980, 80-GT-93.
- [10] A.R. Masri, R.W. Bilger, *Twentieth Symposium (International) on Combustion*, The Combustion Institute, Pittsburgh, 1984, pp. 319–320.
- [11] B.B. Dally, A.R. Masri, *Combust. Flame* 114 (1998) 119–148.
- [12] M. Namazian et al., *Exp. Fluids* 8 (3–4) (1989) 216–228.
- [13] H.T. Esquiva-Dano et al., *Combust. Flame* 127 (2001) 2167–2180.
- [14] V.R. Katta et al., *AIAA J.* 32 (1) (1994) 84.
- [15] W.M. Roquemore, V.R. Katta, *J. Vis.* 2 (2000) 257–272.
- [16] R.P. Lindstedt, *Simplified Soot Nucleation and Surface Growth Steps for Non-Premixed Flames*, in: H. Bockhorn (Ed.), *Soot Formation in Combustion: Mechanisms and Models*, Springer-Verlag, Heidelberg, 1994, pp. 417–439.
- [17] H. Wang, M. Frenklach, *Combust. Flame* 110 (1997) 173–221.
- [18] Annon., *Computational Submodels, International Workshop on Measurement and Computation of Turbulent Nonpremixed Flames*, 2001, available at <http://www.ca.sandia.gov/tdf/Workshop/Submodels.html>.
- [19] H. Guo, F. Liu, G.J. Smallwood, *Combust. Theory Model.* 8 (2004) 475–489.
- [20] V.R. Katta, W.M. Roquemore, GT2004-54165, *Proceedings of ASME Turbo Expo* (2004) June 14–17, Vienna, Austria.
- [21] V.R. Katta, *Paper # D 37*, 5th US Combustion Meeting, 2007.
- [22] V.R. Katta, L.G. Blevins, W.M. Roquemore, *Combust. Flame* 142 (2005) 33–51.
- [23] W.M. Roquemore et al., *Exp. Fluids* 4 (1986) 205–213.
- [24] M.D. Smooke et al., *Combust. Flame* 143 (2005) 613–628.
- [25] I. Goldhirsch, D. Ronis, *Phys. Rev. A* 27 (1983) 3.
- [26] Kelly J. Higgins et al., *J. Phys. Chem. A* 106 (2002) 96–103.

APPENDIX H

Identification of Polar Species in Aviation Fuels using Multidimensional Gas Chromatography-Time of Flight Mass Spectrometry

INTENTIONALLY LEFT BLANK

Identification of Polar Species in Aviation Fuels using Multidimensional Gas Chromatography-Time of Flight Mass Spectrometry

Richard C. Striebich,^{*,†} Jesse Contreras,[‡] Lori M. Balster,[†] Zachary West,[†] Linda M. Shafer,[†] and Steven Zabarnick[†]

[†]University of Dayton Research Institute (UDRI), Dayton, Ohio, and [‡]Department of Chemical and Materials Engineering, University of Dayton, Dayton, Ohio

Received May 4, 2009. Revised Manuscript Received September 15, 2009

Aviation fuel is so complex that it is virtually impossible to separate all of the major components of the mixture, much less the minor components. The minor components are typically separated from the major components using preparative techniques (such as solid phase extraction—SPE) and then re-examined by gas chromatography—mass spectrometry (GC-MS). Without SPE, GC-MS is not capable of a comprehensive determination of the trace polar components in jet fuel due to fuel complexity. In this contribution, jet fuel mixtures are pre-separated by normal-phase SPE, followed by a single analysis using multidimensional gas chromatography-time of flight mass spectrometry (MDGC-TOFMS), which is similar to the recently popularized technique of GC×GC. This two-column sequential analysis followed by TOFMS identifications is able to accurately identify more of the polar components of jet fuel. Automated data analysis routines, based on improved mass spectral library identifications (due to the better chromatographic separations), are able to determine individual components in the polar fractions that are of interest. Spreadsheet-based sorting of the highest quality identifications was also performed and used to quantify important polar fuel classes such as amines, indoles, pyridines, anilines, sulfur compounds, oxygenates, aromatics, and others. The relative amounts of each group were determined and related to similar measurements found in the literature. The ability to identify and quantify polar components in fuel may be useful in developing relationships between fuel composition and properties such as thermal stability.

Introduction and Background

The chemical complexity of natural products, in general, and aviation fuel mixtures, specifically, is significant. Research has been conducted over the past 30 years to identify the components of petroleum-based aviation fuel, in order to better understand their behavior in fuel systems. This research has shown that jet fuel is a complex mixture with hundreds of species, including normal alkanes, branched alkanes, cycloalkanes (naphthenes), and aromatics.¹ These compounds make up the bulk of the composition of the fuel. Each of the major groups contains short alkyl substitutions of the parent compounds, which while chemically different from their parents, have similar properties. To relate fuel composition to fuel properties, it is often sufficient to measure concentrations of components in “group-type” separations,^{2,3} where the total saturates, total monocycloparaffins, or total alkylbenzenes may be measured. With some exceptions, the quantitation of individual components within a group is often not necessary to relate composition to overall fuel properties.

Many of the important properties of fuel result from the presence of trace polar species that are present in extremely

low concentrations (<0.1% by mass) in matrices that may contain several hundred major components (Figure 1). The important classes of these trace compounds include phenols, indoles, thiophenes, amines, and others. Certain classes may affect important properties, including fuel thermal stability,^{4,5} storage stability, combustion efficiency, or combustion emissions.⁶ Polar components have also been used to characterize gasoline, diesel fuel, and other mixtures since these compounds survive most environmental degradation, unlike many of the major components.⁷ To identify the important trace components, advanced separation techniques have been used, including high performance liquid chromatography (HPLC)⁸ and solid phase extraction (SPE),¹ followed by gas chromatography—mass spectrometry (GC-MS).^{1,9} All of these techniques provide more resolving power with a pre-separation or some separation improvement over conventional gas chromatography. HPLC and normal-phase SPE have been very successful in separating the polar components from the nonpolar matrix of jet fuel in order to uncover components that are of great interest due to their effect on properties.^{1,8,9} By using calibration mixtures simulating the

*To whom correspondence should be addressed. E-mail: Richard.striebich@wpafb.af.mil.

(1) Zabarnick, S.; Striebich, R. C.; Straley, K.; Balster, L. M. T. *Prep. Pap. — Am. Chem. Soc., Div. Pet. Chem.* **2002**, *47*, 223–2261.

(2) Shafer, L. M.; Striebich, R. C.; Gomach, J.; Edwards, J. T. *Chemical Class Composition of Commercial Jet Fuels and Other Specialty Kerosene Fuels*. AIAA 2006–7972, 14th AIAA/AHI Space Planes and Hypersonic Systems and Technologies Conference, 2006.

(3) ASTM D2425–04, *Hydrocarbon Types in Middle Distillates by Mass Spectrometry*; ASTM International: 2004.

(4) Jones, E. G. *Energy Fuels* **1996**, *10*, 509–515.

(5) Heneghan, S. P.; Zabarnick, S.; Ballal, D. R. *JP-8 + 100: The Development of High Thermal Stability Jet Fuel*. AIAA 96–0403, January 1996.

(6) Sidhu, S.; Gullett, B.; Striebich, R.; Klosterman, J.; Contreras, J.; DeVito, M. *Atmos. Environ.* **2005**, *39*, 801–811.

(7) Rostad, C. E. *Energy Fuels* **2005**, *19*, 992–997.

(8) Balster, L. M.; Zabarnick, S.; Striebich, R. C. *Prep. Pap. — Am. Chem. Soc., Div. Pet. Chem.* **2004**, *49* (4), 223–226.

(9) Balster, L. M. T.; Zabarnick, S.; Striebich, R. C.; Shafer, L. M.; West, Z. J. *Energy Fuels* **2006**, *20*, 2564–2571.

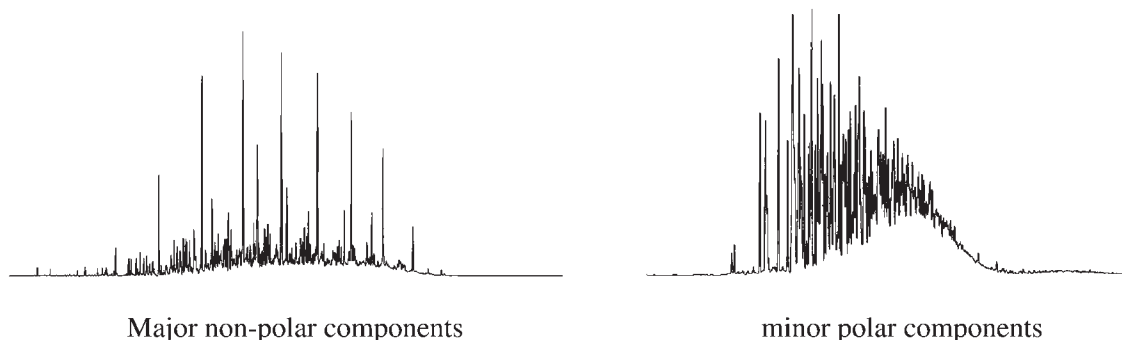


Figure 1. Jet A sample analyzed by GC-MS, showing the major components (greater than $\sim 0.1\%$) on the left and minor components (less than 0.1% , isolated using SPE) on the right. Each peak represents at least one compound.

polar components of similar types of fuels, quantitation can be conducted for total polar content by combining the quantified individual polar species. These data can then be related to properties such as thermal stability.⁹ One unfortunate aspect to this analysis is the effort required for separation: an HPLC polar separation and quantitation, a polar fraction collection in a separate HPLC analysis, a concentration of the collected polar fraction, analysis of the concentrated collected polar fraction by GC-MS, and associated quantitation schemes for each step.

In the analysis of trace polar components by SPE, the polar fraction is collected and most typically analyzed via GC-MS in order to identify the components of interest. Although this analysis is readily performed, it results in mixtures of polar compounds, which appear equally as complex as the fuel from which they were extracted (Figure 1). It is possible to identify and even quantify the components of the SPE extract, but trace components (less than 0.005% by weight) typically have been ignored. Some of the major components of this analysis may be 2–3 orders of magnitude more concentrated than other components of interest. Trace polar nitrogen or sulfur-containing compounds may be 10 mg/L or lower. It is important to find techniques that can identify both the high concentration components and low concentration components in the mixture. Significant separation power is required after SPE prefractionation to characterize this fraction.

To demonstrate the relationship of these compounds to fuel properties, previous work has involved the use of devices (such as the quartz crystal microbalance, QCM) to evaluate oxidative stability of particular fuels at $140\text{ }^\circ\text{C}$ for a period of 15 h .¹⁰ A thermally unstable fuel, that is, one that readily forms deposits on surfaces at these elevated temperatures, was examined using the QCM and was found to create large surface deposits. Upon removal of the polar components in the fuel by SPE treatment and retesting using QCM, deposits were consistent with the levels of a high quality, low-depositing fuel. When the removed polar components were readded to a thermally stable fuel, the thermally stable fuel showed decreased stability. Analysis of the fraction collected from the poor fuel revealed a complex collection of alkyl-phenols and other oxygenates as major components. Both nitrogen and sulfur compounds can also be observed in samples such as these, but not in all cases, since their concentrations are low in comparison to phenol concentrations. In addition, many sulfur components in jet fuel are decidedly nonpolar, whereas nitrogen compounds are almost always polar. If these important compounds could be better separated and identified,

in spite of their concentrations or polarity, it may then be possible to better relate composition to fuel stability. Refiners could potentially improve fuel quality by predicting fuel stability from analytical measurements. In addition, engine designers could more effectively select fuels for high heat sink applications to improve performance when needed.

This contribution describes research that attempts to apply more chromatographic resolution (and therefore, identification power) to the analysis of the polar fractions of jet fuel, using multidimensional gas chromatography-time of flight mass spectrometry (MDGC-TOFMS). This technique, similar to the recently popularized technique $\text{GC}\times\text{GC}$,^{11,12} essentially conducts two independent gas chromatographic separations: a slow, high-resolution nonpolar column separation (primary), followed by a fast, polar column separation (secondary) of each peak eluting from the primary column. Using this technique, compounds are better separated and can be more readily compared to mass spectral libraries for automated analyses with higher confidence in qualitative identification.¹³ MDGC-TOFMS is similar to $\text{GC}\times\text{GC}$ in this case because MDGC here is comprehensive, that is, all peaks from the primary column are directed to the secondary column, rather than just a few heartcuts, as in conventional MDGC. Primary column ramping rates were slowed ($3\text{ }^\circ\text{C}/\text{min}$) to create wider peaks so as not to “undo” resolution attained in the primary column. Heartcut or modulation time ($\text{GC}\times\text{GC}$ terminology) was increased to match expanded peak width due to slow temperature programming. Longer modulation time allowed for an increased secondary column length and longer times (15 s).

The analytical techniques that are available for these types of samples are compared in Table 1 below. SPE with MDGC-TOFMS provides the best combination of compound resolving power, along with speed of the pre-separation process (HPLC vs SPE). Analysis of petroleum products using MDGC or $\text{GC}\times\text{GC}$ is becoming more commonplace.^{13–17} The technique offers benefits for analysis of petroleum samples because of the significant complexity of the sample and the mixture of saturate (nonpolar), cycloalkane (slightly polar), aromatic (midpolar), diaromatic (more polar), and heteroatomic components (most polar). If a primary separa-

(11) Liu, Z.; Phillips, J. B. *J. Chromatogr. Sci.* **1991**, *29*, 227.

(12) Frysinger, G. S.; Gaines, R. B. *J. High Resol. Chromatogr.* **1999**, *22* (5), 21–255.

(13) Striebich, R. C.; Rubey, W. A.; Klosterman, J. R. *Waste Manage.* **2002**, *22*, 413–420.

(14) Bertsch, W. J. *J. High Resol. Chromatogr.* **1999**, *22*, 647–665.

(15) Bertsch, W. J. *J. High Resol. Chromatogr.* **2000**, *23*, 167–181.

(16) Blomberg, J.; et al. *J. High Resol. Chromatogr.* **1997**, *20*, 539–544.

(17) Klosterman, J. R.; M.S. Thesis, University of Dayton: 2002.

(10) Zabarnick, S. *Ind. Eng. Chem. Res.* **1994**, *33*, 1348–1354.

Table 1. Comparison of Techniques for Preparative Separation, Instrumental Separation, and Detection

	SPE	SPE	HPLC
preparative separation	SPE	SPE	HPLC
instrumental separation	MDGC-TOFMS	GC-MS	GC-MS
	Preseparation		
time of preseparation	20 min	20 min	90 min
number of polar fractions	1	1	several (~4)
resolution of polarity separation	fair	fair	high
	Final GC Separation (GC-MS or MDGC-TOFMS)		
time of final separation	slow (~100 min)	20–30 min	20–30 min for each collected fraction
compound resolving power	high	poor	moderate
identification of target compounds	moderate	high	fair
identification of unknown compounds	high	fair	moderate

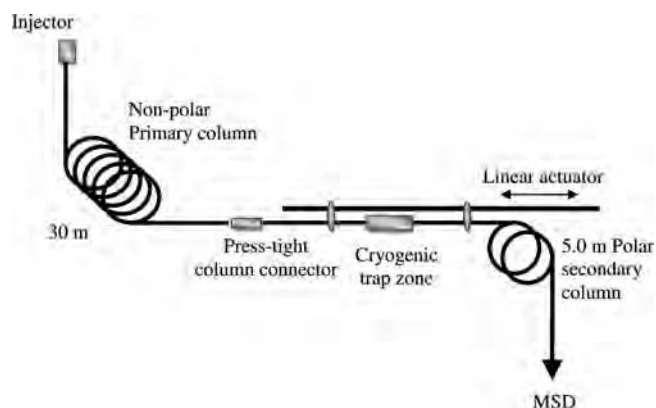
tion is ineffective because many compounds have similar vapor pressure, then a secondary separation is conducted using polarity. By identifying the separated components in an automated fashion, great improvements in the ability to speciate important compounds can be realized.

Experimental Procedures

SPE Conditions. Solid phase extraction (SPE) was used to separate polar fuel components from each nonpolar fuel matrix.¹ A silica gel cartridge (1 mL volume, Bakerbond) was rinsed with 1 column volume (5 mL) of methanol to preclean the cartridge. Then the cartridge was further prepared by rinsing with 15 mL of hexanes, followed by 25 mL of fuel at a flow rate of 1–3 mL/min. A vacuum manifold with stopcock was used to set the appropriate flow rate. As fuel flowed through the silica gel bed, the polar components were retained, typically creating a yellow or brown band at the top of the bed. The 25 mL of fuel was then followed by a 15 mL wash of hexanes to remove nonpolars from the bed. Methanol was then used to elute the polars from the cartridge. The collected 1.0 mL sample could then be used in subsequent analyses by conventional GC-MS and MDGC-TOFMS.

GC-MS and MDGC-TOFMS Analysis. The polar mixtures from SPE separation were analyzed with conventional GC-MS instrumentation (Agilent 6890/5973) using an HP-5 column (30 m, 0.25 mm, 0.25 μ m) in splitless mode. An initial temperature of 40 °C, held for 3 min and ramp rate of 10 °C/min to 280 °C (3 min hold) was used for the GC separation. The MS system was operated in the scanning mode, from 35 to 450 atomic mass units (amu).

The MDGC-TOFMS work was conducted using an Agilent 6890 gas chromatograph attached to a Pegasus III (Leco Corporation) time of flight mass spectrometer (TOFMS). Multidimensional GC-MS as practiced in this laboratory has been previously described.¹³ The GC was modified to accommodate a cryogenic trap and release device, which captured small portions of the effluent from a primary capillary column and then released the portions into a secondary capillary column for further separation. This trapping device focused effluent from the main column into a single zone and then pulled the column out of the cryogenic zone into the heated region of the oven to release the zone onto the secondary column, every 15 s. Figure 2 shows a schematic of the entire analytical system and Figure 3 shows a portion of the trapping/releasing system. Since the secondary capillary column was short and narrow bore, very fast analyses were conducted for the secondary separation, in order to “keep up” with the primary column separation. This resulted in a 100 min analysis, but contained a separation using two columns of different polarities. GC \times GC is typi-

**Figure 2.** Schematic of the MDGC-TOFMS system.**Table 2. Experimental Conditions for MDGC-MS Analysis of Jet Fuel Polars**

primary column	DB-5MS, 30 m, 0.25 mm ID, 0.25 μ m
secondary column	RTX-200, 5 m, 0.18 mm ID, 0.5 μ m
sample size	3 μ L, splitless
oven programming	40 (10) – 300 (5) at 3 °C/min
trap/release interval	15 s
approximate cryogenic trapping temp	–20 at 100 °C GC oven temperature
TOFMS sampling	35–500 at 50 Hz
GC column connection	direct, press tight union with back-up fittings

cally performed much faster, with shorter secondary columns in many other laboratories.

TOFMS provided important improvements to the previous work using conventional quadrupole mass spectrometers.¹⁸ The TOFMS has a much higher scanning speed than conventional quadrupole instrumentation. With more data available, the software for the TOF instrument is able to deconvolute complex GC-MS data, making better identifications possible. Experimental conditions for the GC-TOFMS are included in Table 2. Information on the fuels analyzed is provided in Table 3. A standard mixture of polar components in hexane/toluene solvent (60/40 by volume) was also prepared to determine the concentration of polars as measured by MDGC-TOFMS. The components used in this mixture are provided in Table 4. The mixture represents a typical collection of polar compounds found in fuel as determined in previous studies⁹.

The intent of the analysis with MDGC-TOFMS is to be able to use SPE with MDGC-TOFMS to identify and quantify various types of polar compounds in jet fuel. After analyzing as many compounds as possible, the compounds identified by MDGC-TOFMS were sorted into compound

(18) Contreras, J., M.S. Thesis, University of Dayton: 2004.

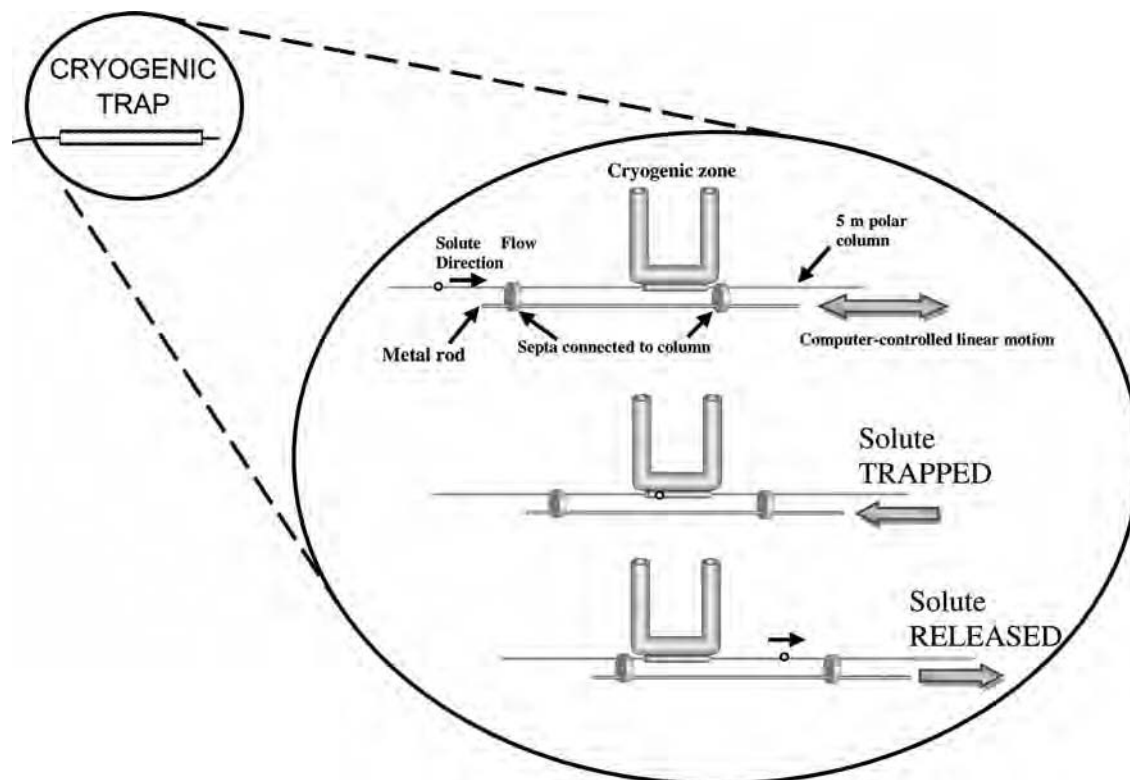


Figure 3. Trapping/releasing device for MDGC-TOFMS¹⁴.

Table 3. Fuel Types and Refinery Process Information Where Available

identification No.	fuel type*	refinery process information
2985	JP-5	unknown
3166	Jet A	straight run
3603	Jet A	hydrotreated
3633	Jet A	clay treated
3658	Jet A	hydrocracked
3084	Jet A	unknown
3684	JP-8	unknown
3686	Jet A	hydrocracked
3688	Jet A	hydrocracked
3773	JP-8	unknown
3804	JP-8	unknown
4108	Jet A	unknown
4110	Jet A	unknown
4195	JP-8	unknown

*JP-5 is the US Navy aviation fuel; Jet A is commercial aviation fuel; JP-8 is US Air Force aviation fuel

classes for group-type characterization. These measurements were compared to existing group-type separations as determined by HPLC; the ultimate purpose of the group-type information is to be able to relate these measurements to important fuel properties.

Results and Discussion

Figure 4 shows an example of the separation of individual components of a petroleum product separation, where the primary column separation was enhanced with a secondary separation, to produce a high-resolution analysis.⁶ This work was not conducted for this effort, but rather as an exaggeration of the resolution available in a “slow” secondary separation. A wide chromatographic peak (for the example in Figure 4), 45 s in width, was captured and eluted from a secondary column. The secondary column separated based on

Table 4. Concentration of Polars in Calibration Mixture

polar constituent name	compound class	concentration (mg/L)
2,4 dimethyl phenol	phenols	541.0
3,5 dimethyl phenol	phenols	242.6
2-methyl phenol (o-cresol)	phenols	173.3
2 (1-methyl ethyl) phenol	phenols	348.6
3,4,5 trimethyl phenol	phenols	126.1
4 (1-methyl propyl) phenol	phenols	153.6
2-methyl-5-(1methylethyl)phenol	phenols	159.3
trans-2-hexanoic acid	acids	212.7
2-indanol	alcohols	252.5
9-hydroxyfluorene	alcohols	16.8
2 ethyl aniline	amines	16.7
2-methyl indole	indoles	85.8
carbazole	carbazoles	129.6
2,6 lutidine (2,6 dimethyl pyridine)	pyridines	13.1
quinoline	quinolines	29.5
total		2501
classes of compounds:		totals (mg/L)
total phenols		1745
total acids		212.7
total alcohols		269.3
total amines		16.7
total indoles		85.8
total carbazoles		130
total pyridines		13.1
total quinolines		29.5

polarity, with the most polar compound (an organic acid) eluting with a time greater than 45 s. The secondary column separates those peaks that the primary column is unable to separate. Although the chromatographic conditions of the current study are different than those in Figure 4, the effect is the same: one peak width of information from a primary column is separated on a secondary column into many (in this case, more than 8–10) peaks, each represen-

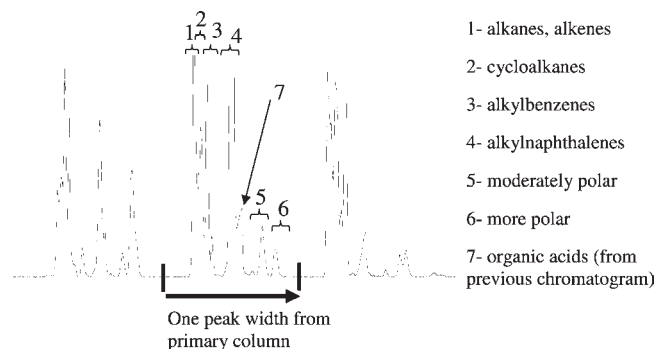


Figure 4. Multidimensional GC-MS (quadrupole) of a portion of jet fuel.⁶

ting individual compounds. These compounds, now separated, can more readily be identified using automated library searching.

Whereas Figure 4 shows major components from jet fuel, the current interest is in the separation of the minor components, and specifically, those components in the polar fraction. Separations of the polar compounds in the SPE fractions were performed using both conventional GC-MS and MDGC-TOFMS (Figure 5). These three examples shown are typical of all of the analyses conducted in that: (1) the conventional GC-MS routines show a great deal of peak coelution as evidenced by the elevated baseline throughout most of the analysis and (2) MDGC-TOFMS has better baseline resolution, as it is performing a secondary separation. Although the times of the two analyses are different, the lack of resolution in conventional GC-MS would not be overcome by this time difference.

It has been shown in several other sources that improvements in separations are possible using MDGC-TOFMS as compared to GC-MS.^{9,13,18} Many components, hidden by coelution with other larger peaks, are better separated and able to have mass spectral patterns with less interference, as shown in Figure 6. In addition, automated library searching is more effective since the algorithm is able to determine where a peak is present and where to subtract the peak background to reduce interferences. In true unknown analysis, where there is no preconceived determination of what compounds should be or may be in a mixture, it is difficult or impossible (with conventional techniques) to identify unknowns without random selection of shoulders of peaks or elevated baselines. MDGC-TOFMS can examine compounds when there is little or no prior knowledge about which compounds may be present.

By examining a wide variety of aviation fuels, it was possible to obtain an overview of the different types of compounds that can be observed in jet fuel polar fractions. However, the amount of information for this many fuels is enormous. Many of the components, once identified uniquely, can then be added to a group of compounds in spreadsheet format, which, along with their relative amounts, can be used to determine the concentration of particular classes, such as total indoles or total pyridines. The totals for the classes observed can then be used to compare to thermal stability and other important properties for various fuels. These relationships can be developed for the purposes of predicting

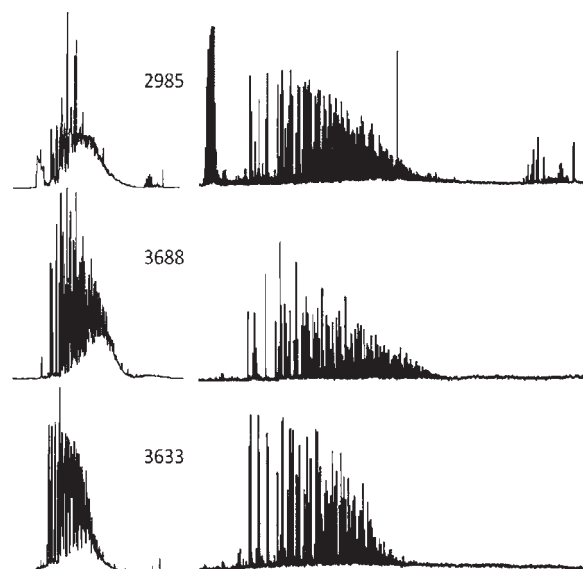


Figure 5. GC-MS (left) and MDGC-TOFMS (right) for the SPE-derived polar fractions from fuels (a) 2985, (b) 3688, and (c) 3633.

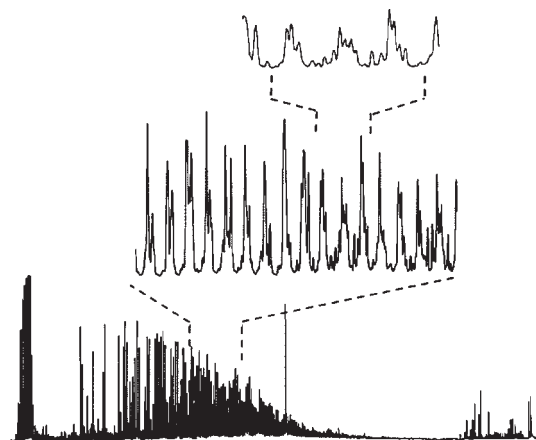


Figure 6. MDGC-TOFMS chromatogram of high nitrogen fuel, showing a single peak that was re-separated on the secondary column, resulting in at least 4 peaks from the single peak group.

fuel thermal stability from composition or for use in modeling efforts.¹⁹

Identification of Individual Polar Compounds from Various Classes. The identifications of separated compounds were determined by automated search and deconvolution routines within the TOFMS software. The search routines returned 2000 background subtracted peaks in the MDGC analysis which were imported into an Excel spreadsheet. Sorting and filtering were used to obtain the top hits (greater than 700 of 1000 match quality) from each identification and then classify the peaks according to compound nomenclature and molecular formula. Using this technique, a large number of peaks can be readily sorted and categorized in an automated way.

Identification of individual compounds in the polar fractions of jet fuels is difficult to summarize, since different fuels have many different compounds. In order to show the wide diversity of compounds that can be identified in the SPE extracts, Table 5 shows compounds identified from a particular group and names the fuel from which it was identified. While no particular fuel probably has all of these compound

(19) Kuprowicz, N. J.; Ervin, J. S.; Zabarnick, S. *Fuel* **2004**, *83*, 1795–1801.

Table 5. Library Matches to Various Compound Classes^a

R.T. (s)	name	match quality (out of a possible 1000)
Phenols Fuel Example 3166		
1688.08	phenol, 2,6-dimethyl-	940
1790.14	phenol, 3-ethyl-	704
1836.36	phenol, 2,3-dimethyl-	932
1897.2	phenol, 3,5-dimethyl-	933
1941.38	phenol, 2-ethyl-6-methyl-	916
1972.9	phenol, 3,4-dimethyl-	907
1984.6	phenol, 2-(1-methylethyl)-	881
2001.78	phenol, 2,4,6-trimethyl-	909
2016.2	phenol, 3,4,5-trimethyl-	920
2045.12	phenol, 2-propyl-	709
2075.94	phenol, 4-(1-methylethyl)-	856
2092.18	phenol, 2,3,6-trimethyl-	927
2180.98	phenol, 4-propyl-	818
2195.62	phenol, 2-methyl-6-propyl	851
2211.3	phenol, 2-ethyl-5-methyl-	748
2223.94	phenol, 2-(1-methylpropyl)-	918
2225.28	phenol, 2,3,5,6-tetramethyl-	886
2239.26	phenol, 2-methyl-5-(1-methylethyl)-	732
2255.64	phenol, 2-ethyl-4,5-dimethyl-	860
2314.78	phenol, 3-methyl-6-propyl-	839
2329.9	phenol, 4-(1-methylpropyl)-	793
2435.62	phenol, 3,5-diethyl-	779
2463.74	phenol, 2-(1,1-dimethylethyl)-5-methyl-	772
2481.82	2-allyl-4-methylphenol	796
2555.56	2-ethyl-5-n-propylphenol	808
2748.22	phenol, 2,5-bis(1-methylethyl)-6- <i>tert</i> -butyl-2,4-dimethylphenol	719
2928.2	3,4-diethylphenol	703
2974.02	phenol, 2-cyclohexyl-	756
3079.92	4-methyl-2-phenylphenol	777
3156.8		
Quinolines Fuel Example 2985		
2014.14	6-methyl-1,2,3,4-tetrahydroquinoline	734
2171.76	quinoline	966
2185.2	quinoline, 5,6,7,8-tetrahydro-	759
2269.8	quinoline, 5,6,7,8-tetrahydro-3-methyl-	749
2303.38	quinoline, 1,2,3,4-tetrahydro-2-methyl-	799
2327.92	3-ethyl-5,6,7,8-tetrahydroquinoline	726
2349.7	quinoline, 2-methyl-	895
2363.28	quinoline, 8-methyl-	798
2487.54	quinoline, 5-methyl-	899
2503.32	quinoline, 3-methyl-	878
2529.76	isoquinoline, tetrahydro-3-methyl-	826
2559.96	dimethyl-1,2,3,4-tetrahydroisoquinoline	729
2664.24	2,8-dimethylquinoline	805
2803.32	quinoline, 5,8-dimethyl-	704
2856.98	dihydro-dimetquinolinylidene methane	733
Pyridines Fuel Example 3658		
1252.16	pyridine, 2,4,6-trimethyl-	918
1311.72	pyridine, 2,3,6-trimethyl-	836
1358.48	pyridine, 2-ethyl-6-methyl-	718
1522.1	2-ethyl-3,5-dimethylpyridine	798
1535.68	pyridine, 2-ethyl-4,6-dimethyl-	740
1667.5	pyridine, 2-ethyl-6-isopropyl	812
1935.08	pyridine, 3-ethyl-5-methyl-	726
2134.16	pyridine, 2-methyl-4,6-dipropyl-	761
2227.72	pyridine, 4-methyl-2-(2-methyl-1-C3-tetrahydropyridine, 4-[4-hydroxyphenyl]-	775
2658.18	2,4-dimethyl-6-phenylpyridine	717
3159.34		769
Amines Fuel Example 2985		
1070.9	2-benzoyloxyethylamine	715
1587.64	benzenamine, 3-methyl-	944

Table 5. Continued

R.T. (s)	name	match quality (out of a possible 1000)
1613.32	benzenamine, 2,5-dimethyl-	740
1840.68	benzenamine, 2-ethyl-	933
1862.82	benzenamine, N,N,3,5-tetramethyl-	774
1900.18	benzenamine, 3,5-dimethyl-	931
1938.02	benzenamine, 2,3,4,5,6-pentamethyl-	725
1991.56	benzenamine, 2,3-dimethyl-	939
2112.08	benzenamine, 2-(1-methylethenyl)-	769
2124.2	benzenamine, 4-propyl-	884
2168.26	benzenamine, 2-ethyl-6-methyl-	889
2347.56	benzenamine, 2,6-diethyl-	729
2450.84	naphthalenamine, tetrahydro-N,N-dimethyl-	732
2514.56	1-naphthalenamine, 5,6,7,8-tetrahydro-	735
Indoles Fuel Example 3658		
2065.26	2-methylindoline	919
2259.2	1H-indole, 2,3-dihydro-1-methyl-	849
2308.34	indole	926
2505.1	1H-indole, 5-methyl-	922
2561.94	1H-indole, 3-methyl-	846
2565.48	1H-indole, 1-methyl-	871
2580.18	1H-indole, 2-methyl-	864
2747.42	2H-isoindole, 4,7-dimethyl-	831
2830.7	1H-indole, 1,3-dimethyl-	863
2833.78	1H-indole, 2,3-dimethyl-	912
2910.42	1H-indole, 5,6,7-trimethyl-	869
2984.28	1H-indole, 1,2,3-trimethyl-	871
2986.82	2,3,7-trimethylindole	702
2998.42	1H-indole, 2,3,5-trimethyl-	758
3030.14	1H-indole, dihydro-trimethyl-2-methylene-	803
3162.48	2H-isoindole, 4,5,6,7-tetramethyl-	803
3294.4	ethanone, 1-(1,3-dimethyl-1H-indol-2-yl)-	718
3311.16	1H-indole, 3-methyl-2-propanoyl-	716
3340.64	1,2,3,4,7-pentamethylindole	735
3388.5	1H-indole, 1-butyl-3-methyl-	807
Carbazoles Fuel Example 2985		
3674.3	carbazole	924
3686.9	carbazole, 1,2,3,4-tetrahydro-3-methyl-	741
3811.16	3-methylcarbazole	927
3917.12	carbazole, 1,6-dimethyl-	913
3945.12	3-ethylcarbazole	740
4035.64	carbazole, 3,6-dimethyl-	913
4064.36	carbazole, 2,5-dimethyl-	888
4123.34	carbazole, 1,3-dimethyl-	705
4125.88	carbazole, 2,4,6-trimethyl-	853
4154.66	carbazole, 2,3,5-trimethyl-	868
Sulfur Fuel Example 2985		
1631.96	cyclothiazide	596
1968.46	1,2-dithiane	924
2376.54	benzothiazole	957
3635.16	2-benzothiophene, dihydro-5,6-dimethyl-	743

^a Groups of compounds were taken from a particular fuel, as noted.

classes, some of the trace polar compounds listed in this table may be in particular fuels. Some general information about each of these classes follows:

Phenols. Phenols were, by far, the most pervasive of the components in the polar fraction. They could easily be determined by conventional GC-MS because they are major

components in the extracted polar fraction. However, significant separation is required for isomer specific identification, and MDGC did reasonably well at this task. Table 5 shows some examples of isomer specific determinations and match qualities (of a possible 1000 score) to provide some idea of the certainty of the match. The high match quality provides accurate information about the identity of the unknown compounds in the polar mixture, which are largely alkyl-substituted components of the major compound class: methyl phenol, dimethyl phenol, and the like.

Quinolines. These nitrogen-containing compounds were observed only infrequently during the analysis of aviation fuel. Although there is no specification for nitrogen-containing compounds, quinolines can affect the properties of fuels dramatically, especially in the area of thermal or storage stability. Most of the quinolines identified were, as might be expected, methyl- and ethyl-substituted quinolines. However, there were also several isomers of tetrahydroquinoline identified in the sample 2985, a fuel with a high nitrogen concentration.

Carbazole. Carbazoles are nitrogen-containing aromatic compounds that are often present in larger concentrations in less-volatile diesel fuel fractions. However, there are many fuels in the JP-8 range that contain substituted carbazoles. Mostly, the carbazoles contain methyl through propyl substitutions.

Amines. Amines are also very common components of the high-nitrogen fuel 2985. These particular amines are almost exclusively aromatic amines, either benzeneamine (aniline) or naphthalene amine. Alkyl amines are generally stronger bases than aliphatic amines, making the alkyl amines more reactive and less likely to survive processing steps.

Indoles. A wide variety of indoles and *iso*-indoles were identified from the MDGC-TOFMS analysis. Several groups have investigated various indoles as thermally unstable and reactive chemicals from poor quality fuels.²⁰

Pyridines. The fuel 3658 contained several pyridines and *iso*-pyridines that were well-identified. The effect that these compounds would have on any fuel properties is largely unknown, other than moderate decreases in thermal stability with higher concentrations of pyridines.²⁰

Other Classes. There are several other compounds that impart important properties to fuels; one such collection of compounds is that of hindered phenols (phenol compounds with large alkyl groups near the C–OH phenol functionality). With the exception of electrochemical methods, it is very difficult to individually identify (and quantitate) the levels of hindered phenolic compounds in fuel without searching for each phenol individually. In this case, the compound hit lists can be queried for phenols and for “2,6” substitution (adjacent to the C–OH bond). Some of the compounds observed were 6-*tert*-butyl-2,4-dimethylphenol; 2-ethyl-6-methylphenol; 2,3,6-trimethylphenol; and 2,3,5,6-tetramethylphenol, to name a few. Compounds like butylated hydroxytoluene (BHT), a common antioxidant, were not observed because of their lack of polarity. These highly hindered phenols are not part of the polar fraction obtained from these SPE pre-separations.

Sulfur Compounds. Very few sulfur compounds were identified in these polar fractions, probably because sulfur-containing compounds are typically not polar until they are oxidized.

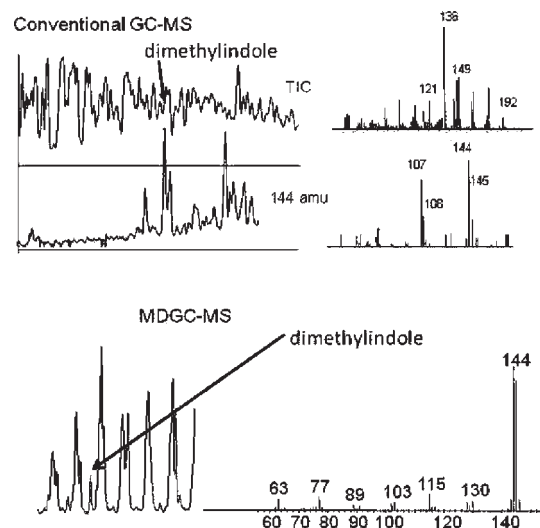


Figure 7. Total ion current (TIC) and extracted ion chromatogram of polar fraction give a complicated chromatogram (top, left) and mass spectral pattern (top, right) which is not well identified. MDGC-MS provides separation where the peak of interest is completely isolated and the mass spectral pattern is accurate.

Thianes, thiophenes, and benzothiophenes are slightly polar and therefore could be extracted and observed in these samples.

To summarize, the ability of MDGC-TOFMS to identify unknowns in complex mixtures is superior to similar analysis using conventional GC-MS, due to the multiple separations that occur in the MDGC-TOFMS. Although there is clearly an advantage using the dual chromatographic separation, the TOFMS, with its deconvolution software, also provides an additional separation that the conventional MS cannot provide, due to its slower scanning rate. Arguably, the acceptance of automated library search routines which provide top hits is an inadequate way to examine unknowns in a polar jet fuel mixture. However, the sheer number of identifications that need to be made from this complex sample is too great to perform analysis manually (peak by peak). This is especially true when performing a nontarget analysis (qualitative analysis). In addition, the degree of coelution in conventional GC-MS means that background subtraction routines are not as effective as they could be. MDGC-TOFMS improves these situations by providing more resolution for complex samples.

Many analyses in GC-MS are “target” analyses¹³ in which a complex mixture is separated by chromatography and an ion is extracted to examine a particular compound. In order to examine mixtures with no target analysis in mind, the total ion chromatogram must be used, and separate, distinct chromatographic peaks must be observable. Frequently, however, peaks of interest appear like those shown in Figure 7: a shoulder of a collection of peaks. There is no particular reason to select this shoulder to examine among all the thousands of other peaks and shoulders available to examine. It is only after deciding to look for dimethylindole (which has a strong 144 ion), performing extracted ion analysis, background subtracting the 144 response at the proper retention time and comparing against the library, that the substituted indole is identified. Even with these actions, the library hit is extremely low (38 match quality), which does not provide confidence for this identification. Clearly, these difficult separations are

(20) Hazlett, R. N., Ed. *Thermal Oxidation Stability of Aviation Turbine Fuels*; American Society for Testing and Materials, Monograph 1: Philadelphia, PA, p 82.

Table 6. Calibration Data for Total Polar Compounds

compound class (No. of components)	calibration levels (mg/L)	slope	intercept	R ²
phenols (7)	1750, 1310, 875, 438, 0	121 000	20 000 000	0.965
anilines (1)	16.7, 12.5, 8.35, 4.18, 0	357 000	−396 000	0.929
indoles (1)	85.8, 64.4, 42.9, 21.5, 0	216 000	451 000	0.965
carbazoles(1)	129.6, 97.2, 64.8, 32.4, 0	163 000	−208 000	0.971
pyridines(1)	13.1, 9.83, 6.55, 3.28, 0	32 700	−35 054	0.926
quinolines(1)	29.5, 22.1, 14.8, 7.38, 0	290 000	−376 000	0.974

Table 7. Classification of Compounds Using MDGC-TOFMS Analysis Compared to Total HPLC Polars Analysis

fuel	phenols (mg/L)	pyridine (mg/L)	carbazole (mg/L)	indole (mg/L)	amine (mg/L)	quinolines (mg/L)	sum of groups (mg/L)	HPLC polars (mg/L)
3084	92.8	4.4	0.1	2.7	6.7	0.8	106.6	
2985	736.4	540.4	0.2	57.1	65.4	87.6	1399.4	2400
3166	119.9	13.0	0.2	2.2	1.9	1.1	137.3	514
3603	< 1.0	0.7	0.1	0.5	0.5	0.7	2.5	110
3633	361.8	3.2	0.1	1.5	3.8	4.2	370.4	470
3658	200.5	507.3	3.0	63.3	133.6	60.4	907.8	2200
3684	21.2	0.5	0.1	0.8	0.6	0.8	23.2	240
3686	432.8	16.8	0.2	10.4	8.4	4.9	468.6	710
3688	199.9	37.3	0.3	6.6	15.8	6.1	260.1	510
3773	73.8	1.4	0.1	0.9	19.4	0.7	95.6	190
3804	37.0	0.0	0.1	0.7	0.6	1.5	38.5	190
4108	122.4	10.3	0.1	1.7	4.0	1.0	138.5	
4110	69.1	0.3	0.1	0.4	0.6	0.1	70.5	
4195	111.3	42.5	0.1	2.6	2.3	1.2	158.7	

better handled using additional separation schemes (such as MDGC).

MDGC-TOFMS is used to perform a primary column separation equal to that of the conventional separation, but then enhances the separation by subjecting one peak width of material to the additional separation on the polar column. The significant polarity of the indole insures that it is separated from its less polar neighbors, which are substituted phenols. The bottom portion of Figure 7 shows the MDGC-TOFMS chromatogram and mass spectral identification, with a match quality over 700 (out of 1000). The identification of this compound was performed automatically because the peak was visible and apparent due to the additional separation.

Compound Class Identification. Although it is interesting to examine the different types of individual chemical constituents, it may be more useful to combine identified component concentrations together and determine a compound class concentration. For example, it may be more useful to determine the total indole concentration or the total carbazole concentration. While different types of indoles may have different reactivities and properties, the general levels of these compounds may be important for purposes of modeling and property prediction. In order to determine this level, several calibration analyses were conducted with a mixture representing the polar constituents in a typical fuel.⁹ These components of the calibration mixture and their concentrations were previously provided in Table 4.

This mixture was then diluted to several other concentrations. The response from each of the components from Table 3 was used to develop calibration curves for individual polar classes by summing the responses from similar compounds in Table 3. The results of the five-point calibration curves are shown in Table 6 for MDGC-TOFMS analysis. The calibration mixture was examined by MDGC-TOFMS using the same procedures as would be used in examining unknowns. That is, identifications were made automatically by the library searching software and the produced spreadsheets were manipulated to group together all compounds

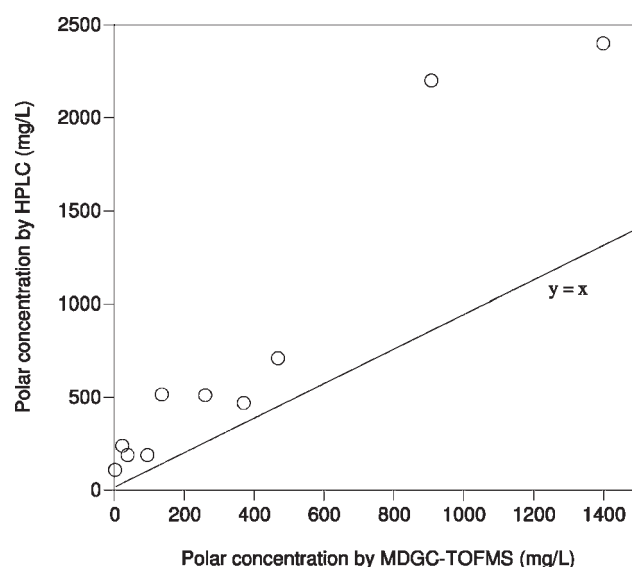


Figure 8. Relationship between HPLC-based polar concentrations and MDGC-TOFMS-based polar concentrations. The $y = x$ line would represent perfect agreement between the two techniques.

identified as each of the compound classes. The area sum of each of the peaks identified in each compound class was then used to determine the linearity of detection (slope and intercept) as given in Table 6. These analyses were performed without the use of an internal standard solution.

By separating the complex mixture as completely as possible using MDGC-TOFMS, it is then possible to filter the results so that individual compounds may be quantified using the appropriate calibration curve, that is, dimethylindole concentration could be measured using the “indole” curve, trimethylquinoline measured using the quinoline curve, etc. Although HPLC techniques are being used for total quantitation, the polar components may have very different response factors, which would make the results difficult to quantify with a single stock solution. Using total

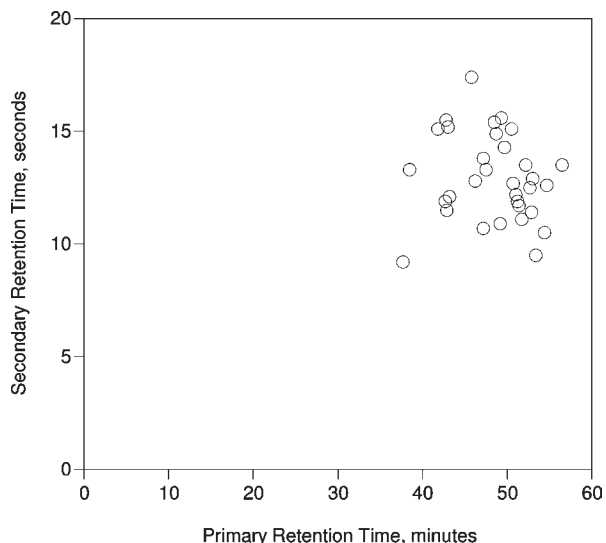


Figure 9. Polarity mapping for substituted indoles identified using MDGC-TOFMS.

ion response would likely generate more consistent response factors for different compound types.

In this work, the MDGC-TOFMS separations allowed for this type of analysis. Although these measurements can only be considered estimations, they may provide more information in less time than the HPLC separation, quantitation, fraction collecting, sample concentration, and subsequent GC-MS analysis of each fraction that was used to collect quantitative information on polars in previous work.⁹ Table 7 shows a summary of the quantitation of the compound classes using MDGC-TOFMS with data analysis using spreadsheet file filtering and sorting.

Of the fuels evaluated by the HPLC/GC-MS versus the MDGC-TOFMS techniques, there is a relationship between the data, but not agreement between the absolute results obtained. Figure 8 shows the MDGC results plotted versus the HPLC results for the same fuels, indicating that qualitative agreement between the data is evident, but there is certainly not quantitative agreement.

The HPLC polar technique gave consistently higher results for fuels than did the MDGC-TOFMS. It is possible that the HPLC responded to all polars in SPE, and not specific ones, as was the case in MDGC. The ketone, acid, and aldehyde levels, for example, were not evaluated in MDGC-TOFMS. Future studies may also include the analysis for these compounds. The analysis by HPLC included a category of polars species referred to as “% other oxygenates”, which could be between 0 and 92.1% of the polar fraction.⁹ In addition, the response factors of these compounds on a diode array detector may be different for acids than ketones or alcohols. In addition, total ion mass spectrometer response factors may more dependable for different compounds in the same class. However, since it is not practical to purchase or synthesize standards for each of hundreds of compounds, it is appropriate to use general response factors to estimate concentration.

The multidimensional technique took only a fraction of the time of the HPLC/GC-MS analysis for individual chemical classes. The analysis of the polar mixture was easily performed in both qualitative identification and quantitative analysis, with a single SPE separation and a single analysis. In addition to phenol and nitrogen compounds, it is also possible to observe sulfur-containing species, although relatively few of these are polar enough to be in the SPE fraction. Oxidation products of the sulfur compounds may, however, make possible the use of SPE and MDGC-TOFMS.

It is often useful to “map” polars analysis as shown in Figure 9.⁶ This can be performed by plotting both the primary column retention time along with the polar or secondary column retention time. Groups type analysis may be possible by identification of the regions of the two-dimensional space that contain certain important compounds. Screening for specific compounds may allow the speed of the analysis to be increased. If patterns of polarity can be determined, it may be possible to perform group type separations with the help of a less-sophisticated detector (such as the more common flame ionization detector, FID) which would allow more laboratories to investigate polarity separations using MDGC.

Conclusions and Recommendations

MDGC-TOFMS is an elegant way to identify and measure both individual compounds and compound classes in the polar fraction of jet fuel. These complex fractions are extremely difficult to measure by conventional GC-MS, except for the most abundant components. The measurements obtained did not agree quantitatively to existing HPLC compound class measurements. However, the two techniques did generally agree in a qualitative sense. The MDGC-TOFMS technique was shown to be a superior qualitative analysis technique compared to traditional GC-MS and HPLC. MDGC-TOFMS is also superior in trace analysis of complex mixtures because peak identifications can be made in an automated way with more confidence. Work is continuing to examine the complex results obtained; chemometrics and other statistical methods may be appropriate to apply to these measurements. In addition, improvement of the separations by changing columns, column lengths, phases, and other chromatographic parameters is also possible. Distinguishing improvements achieved because of multidimensional separations versus improvements made due to TOFMS deconvolution needs to be performed to direct further experiments in this area.

Acknowledgment. This material is based on research sponsored by Air Force Research Laboratory under agreement No. F33615-03-2-2347. The views and conclusions contained herein are those of the authors and should not be interpreted as necessarily representing the official policies or endorsements, either expressed or implied, of Air Force Research Laboratory or the U.S. Government. The authors recognize the efforts of Mr. Wayne Rubey for his assistance.

INTENTIONALLY LEFT BLANK

APPENDIX I

Sonochemically Assisted Thermal Decomposition of Alane *N,N*-Dimethylethylamine with Titanium (IV) Isopropoxide in the Presence of Oleic Acid to Yield Air-Stable and Size-Selective Aluminum Core-Shell Nanoparticles

INTENTIONALLY LEFT BLANK

Sonochemically Assisted Thermal Decomposition of Alane *N,N*-Dimethylethylamine with Titanium (IV) Isopropoxide in the Presence of Oleic Acid to Yield Air-Stable and Size-Selective Aluminum Core–Shell Nanoparticles

K. A. Shiral Fernando,[†] Marcus J. Smith,[†] Barbara A. Harruff,[†] William K. Lewis,[†]
Elena A. Guliants,[†] and Christopher E. Bunker^{*,‡}

Sensors Technology Office, University of Dayton Research Institute, Dayton, Ohio 45469, Air Force Research Laboratory, Propulsion Directorate, Wright-Patterson Air Force Base, Ohio 45433-7103

Received: October 21, 2008; Revised Manuscript Received: December 08, 2008

Using sonochemistry to provide the thermal energy and mixing, we demonstrate the ability to synthesize air-stable aluminum nanoparticles of two different size distributions from the titanium-catalyzed thermal decomposition of alane. Characterization data indicate the presence of spherical face-centered-cubic aluminum nanoparticles with average sizes of either 5 or 30 nm that are capped with an organic shell. The average size of the nanoparticles correlates with the concentration of the passivation agent oleic acid, where a higher concentration results in smaller particles. Thermal analysis data demonstrates that at elevated temperatures (>550 °C), these particles react via a typical aluminum oxidation mechanism, whereas at low temperatures (<550 °C), the behavior of these particles is unique and directly related to the presence of the organic shell.

Introduction

The synthesis of aluminum particles is of particular interest due their high heat of reaction to form aluminum oxide ($\Delta H_f = 31$ kJ/g).¹ Applications that utilize the stored chemical potential of aluminum often will benefit from a reduction in particle size because this can lead to an increase in mass transport and energy release rates.^{2–6} However, due to the highly reactive nature of aluminum particles, passivation of the surface is necessary to prevent early oxidation of the bulk aluminum metal. In most cases, this takes the form of the naturally occurring aluminum oxide Al₂O₃ shell. Although the aluminum oxide shell provides no energetic benefit, its contribution to overall particle mass is small, and it serves to protect and prevent early reaction of the remaining aluminum metal. However, when particles begin to range into the nanoscale, the contribution of the oxide shell to particle mass becomes significant. To realize the benefits of the enhanced mass transport and energy release rates of aluminum nanoparticles, facile methods for the synthesis of such particles that can provide alternatives to Al₂O₃ passivation are required. The thermal decomposition of alane with the catalyst titanium isopropoxide is a well-known approach to making aluminum films and aluminum nanoparticles.^{7–11} Researchers have used this method to produce core–shell nanoparticles, including perfluoroalkyl carboxylic acid^{9,10} and transition-metal-capped aluminum nanoparticles.¹¹ The characterization showed large particles or broad size distributions and indicated the possibility of agglomerations. Here, we utilize this reaction in the sonochemical environment,^{12,13} noting that the reaction still follows a thermal decomposition mechanism, to yield stable

aluminum nanoparticles. By including an organic passivation agent during the reaction, we achieve both air-stable nanoparticles and the ability to control the size of the nanoparticles.

Experimental

Materials. Alane *N,N*-dimethylethylamine in a 0.4 M toluene solution, titanium (iv) isopropoxide (98%), aluminum chloride (1 g water solution atomic spectroscopy standard), oleic acid (99%), and dodecane (99% and anhydrous) were all obtained from Aldrich and used as received. Hexane (Optima grade) was obtained from Fisher Scientific.

Synthesis. To synthesize the aluminum core–shell nanoparticles, an initial solution of dodecane with 3.8 mM oleic acid was subjected to five cycles of a freeze–pump–thaw process to reduce dissolved oxygen concentration. This solution was then transferred to a dry nitrogen glovebox for the addition of alane and titanium (iv) isopropoxide catalyst. This working solution with alane and catalyst concentrations of 50 and 0.55 mM, respectively, was then transferred to a sonication flask (Sonics Inc., Suslick flask) and moved from the glovebox to a nitrogen-filled glovebag encompassing the sonication instrument (Sonics Inc. Vibra Cell). The instrument consisted of a 0.5-in.-diameter solid titanium horn operated at 20 kHz. The working solution was then sonicated for 7.5 min active time at an amplitude of 37% (~22 W) following a 1-s-on, 1-s-off procedure. The bulk reaction solution reached a maximum temperature of 70 °C. The above conditions produced a black solution that gradually precipitated, yielding a grayish-black powder. The powder was recovered by evaporation of the solvent under vacuum, followed by repeated washings with hexane. A second aluminum nanoparticle sample was prepared following the same procedure, except that the oleic acid concentration was increased 3-fold (11.4 mM). The application

* To whom correspondence should be addressed. E-mail: christopher.bunker@wpafb.af.mil.

[†] University of Dayton Research Institute.

[‡] Air Force Research Laboratory.

of the sonochemical energy again produced a black solution that precipitated to yield a grayish-black powder.

Measurements. Infrared absorption spectra were obtained using a Perkin-Elmer L100 FTIR (Fourier Transform Infrared) absorption spectrophotometer equipped with an attenuated total reflectance sample attachment. X-ray powder diffraction (XRD) analysis was performed on a Bruker D8-Advanced equipped with a Cu α source, monochromator, and a Sol-X detector. Identification of the observed patterns was accomplished by comparison with the ICDD crystallographic database. TEM (transmission electron microscopy) images were obtained using a Hitachi H-7600 operated at 100 kV. Samples were prepared from solution by drip-spotting on carbon-coated copper grids. The energy and mass dependence on temperature of these particles was recorded using a TA Instruments STD Q600 dual DSC/TGA (differential scanning calorimetry/thermal gravimetric analysis) instrument with open pan alumina sample cups. Samples were analyzed from room temperature to 700 °C using a 10 °C/min temperature profile under a constant flow of air or argon. The aluminum content of the nanoparticles was determined with a Varian UltraMass ICP-MS (inductively coupled plasma-mass spectrometry) instrument measured against a five-point aluminum chloride calibration curve. Samples were digested in concentrated nitric acid and then analyzed as aqueous samples. This technique was found to be responsive only to active aluminum, yielding no signal for Al_2O_3 samples.

Results and Discussion

Aluminum–oleic acid core–shell nanoparticles have been synthesized using the titanium-catalyzed thermal decomposition of alane in which the thermal energy was supplied via acoustic cavitation. TEM analysis of the first nanoparticle sample indicated the formation of spherical nanoparticles with an average size of ~ 30 nm and a size distribution estimated at 20–70 nm (Figure 1, top). XRD analysis revealed the powder to be face-centered-cubic (fcc) aluminum metal (Figure 2, top). The broad feature located around 20° was attributed to the organic, because the feature was observed to decrease in intensity with exposure of the sample to increasing temperatures, disappearing completely by 350 °C. FTIR analysis clearly identified the presence of the reacted oleic acid (Figure 3), showing the same C–H stretch pattern before and after reaction (around 2900 cm^{-1}), but demonstrating the loss of the C=O peak at ~ 1700 cm^{-1} and the formation of the O–H band at 3350 cm^{-1} . These results differ somewhat from the traditional role of oleic acid in passivating metal nanoparticles. It has been well-demonstrated that oleic acid and carboxylic acids in general, will bond to a metal surface either in a bridged M–O–C–O–M configuration, or in a monodentate, dangling configuration.^{14–16} The formation of this bond is indicated by a characteristic two-band feature at ~ 1450 and 1540 cm^{-1} . Jouet et al. proposed such a bonding with the postreaction capping of their aluminum nanoparticles with a series of perfluoroalkyl carboxylic acids.^{9,10} Our sample, however, does not indicate such a bond. Instead, the FTIR suggests the possible decomposition of the oleic acid as it reacted to passivate the aluminum nanoparticle surface.

TEM of the second sample prepared with the 3-fold higher concentration of oleic acid revealed spherical nanoparticles of a much smaller diameter (Figure 1, bottom). Analysis of the particles indicates an average size of ~ 5 nm with a size distribution of 2–15 nm. XRD analysis again indicates the formation of fcc aluminum. FTIR analysis produced the same spectrum shown in Figure 3. The decrease in particle diameter

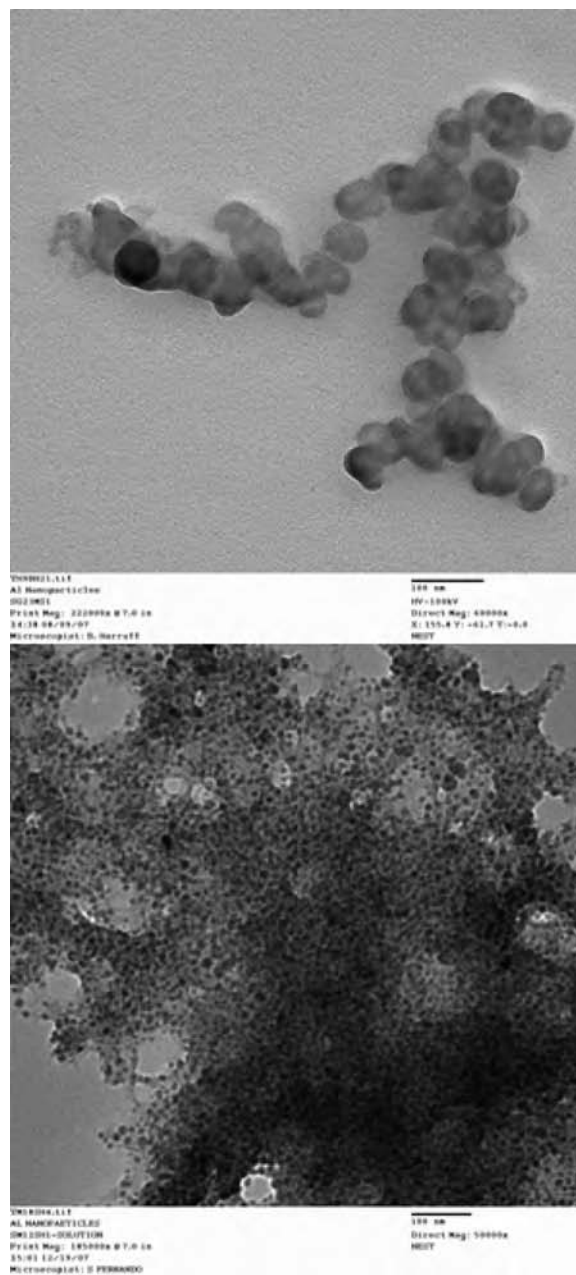


Figure 1. TEM images of the aluminum–oleic acid core–shell nanoparticles prepared with 3.8 mM oleic acid (top) and 11.4 mM (bottom). The size bar indicates 100 nm.

correlates with the increase in oleic acid concentration, indicating that oleic acid may act to cap the surface of the growing nanoparticles, thus limiting particle size.¹⁷

The first aluminum nanoparticle sample with the average size of 30 nm was analyzed for stability and energetic content using simultaneous DSC/TGA.¹⁸ For a known quantity of sample placed under flowing air at 30 °C, only a slight decrease in mass ($<5\%$) was observed over a 24 h period. Figure 4 (top) shows the TGA data obtained with sample heating to 700 °C in air and also in argon for comparison. Templates for understanding the mass changes and heat flow in these materials within the context of aluminum oxidation have been established.^{2,5} For the TGA data, the temperature range covered corresponds to aluminum oxidation regions I and II, where region I is characterized by the formation of amorphous aluminum oxide and region II shows a transition to $\gamma\text{-Al}_2\text{O}_3$.² For region I ($T < 550$ °C), oxidation of the aluminum nanoparticles is reported

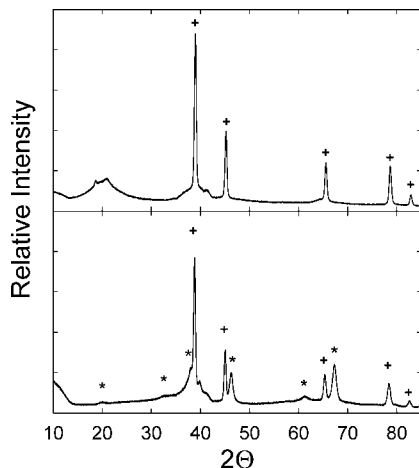


Figure 2. XRD spectra of the aluminum-oleic acid core-shell nanoparticles as prepared (top) and after heating in air to 700 °C (bottom). Peaks identified with the ICPSD database as fcc aluminum (+) and γ - Al_2O_3 (*) are indicated.

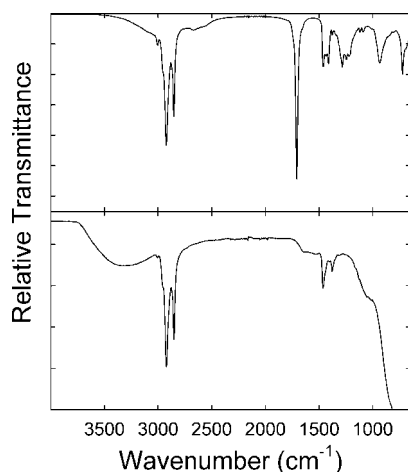


Figure 3. FTIR spectra of oleic acid (top) and the aluminum-oleic acid core-shell nanoparticles (bottom).

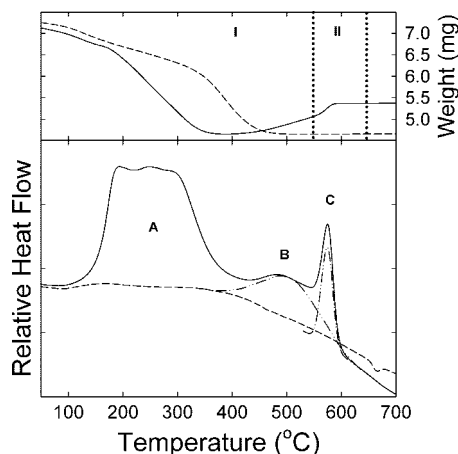


Figure 4. TGA (top) and DSC (bottom) data for the aluminum-oleic acid core-shell nanoparticles measured in air (—) and in argon (---). I and II identify the separate oxidation regions, and A, B, and C identify exothermic heat flows from organic (A), initial oxide layer (B), and the oxide coated aluminum nanoparticles (C), respectively. Peaks B and C are estimated by a simple curve fit (- · · - · · -).

as very slow and subject to the availability of outwardly migrating Al cations. Thus, TGA plots show minimal change.^{2,18} Our results are somewhat different, showing an $\sim 35\%$ decrease

in mass by 350 °C. This decrease in mass is attributable to the thermal loss of the organic passivation layer (supported by the exothermic heat flow, peak A, observed under air due to combustion of the organic).¹⁹ For region II (550 °C > T > 650 °C) it is reported that the amorphous aluminum oxide grown through region I converts to γ - Al_2O_3 , forming platelets that expose additional aluminum metal.² The rate of oxidation is observed to increase and produce a significant increase in mass until the γ - Al_2O_3 platelets fully cover the remaining aluminum metal. Our results appear to correlate well with this description of the aluminum oxidation process—we observe a rapid increase in mass just after 550 °C that plateaus just before 600 °C, suggesting exposure of aluminum metal followed by oxide passivation. Additionally, our XRD analysis of a sample taken to 700 °C confirmed the formation of γ - Al_2O_3 while still showing unreacted fcc aluminum (Figure 2, bottom). Particle sizes estimated from the XRD peak widths using the Scherrer formula indicate a change from ~ 15 nm at room temperature to ~ 11 nm at 700 °C for the fcc aluminum and ~ 3 nm for the γ - Al_2O_3 formed at 700 °C.

A difference in our data, however, is that the rapid increase in mass just past 550 °C was preceded by a somewhat slower increase in mass that started at ~ 400 °C. The rate is greater and the mass increase more significant than typical region I growth, indicating a somewhat different process. These observations appear to be corroborated by the DSC data. The two oxide growth steps we observe correlate with two exothermic peaks (B and C in Figure 4, bottom). The sharp peak C, which aligns with the region II mass increase, can be attributed to the exothermic reaction of oxide-coated aluminum nanoparticles and agrees well with literature reports for this process.⁵ The broad peak B, which yields a maximum near 500 °C, is both too broad and too early to be comfortably explained the same way. It would also suggest that the sample exists as a bimodal distribution of particles sizes, which is something not supported by the TEM data. Instead, we attribute the heat flow exhibited in peak B and the slow mass increase that precedes region II to oxide growth that occurs after the organic passivation layer is displaced at high temperatures. We should note that although these particles are passivated by oleic acid, oleic acid does provide oxygen from which an initial aluminum oxide layer can be formed. The presence of such a layer is supported by the ICP-MS data, which indicates 40% of the sample mass is active aluminum,²⁰ and TGA in argon data, which confirms 35% of the mass is organic, leaving 25% of the sample mass to be an organic-provided aluminum oxide layer. The nature of this layer is currently unknown; however, the observation of the somewhat different region I oxidation behavior suggests it is unlike that of a naturally occurring aluminum oxide passivation layer. Although not yet achieving an oxide-free passivation of these aluminum nanoparticles, the results presented here do suggest the use of organic passivation compounds alters the reactivity such that energy is released at lower temperatures. Further investigations will focus on the effect of particle size on the oxidation properties and the role the organic passivation compound plays in forming the stabilizing shell (i.e., the nature of the initial oxide layer).

Conclusion

We have demonstrated the ability to produce stable aluminum nanoparticles of two different sizes using a sonochemically assisted technique. The size control is achieved by the organic passivation agent as it caps the growing nanoparticle surface to stop particle growth. We believe that an organic-provided oxide

layer is formed in this process, and it is that layer that provides the observed particle stability. Both the FTIR and the thermal analysis confirm the presence of the organic passivation layer, and the thermal analysis combined with the ICP-MS data suggests the oxide layer. Further, the thermal analysis indicates aluminum oxidation occurring at relatively low temperatures once the organic has been removed and that the oxidation behavior differs from that of naturally formed oxide-coated aluminum particles. With the ability to tune the size of the aluminum nanoparticles and to manipulate the organic passivation layer, these organic passivated aluminum nanoparticles provide an interesting and valuable variation with which to study the oxidation process.

Acknowledgment. We thank Drs. J. E. Spowart, C. A. Crouse, and D. K. Phelps for helpful discussions. We acknowledge the financial support of the Defense Threat Reduction Agency (DTRA, Grant no. HDTRA-07-1-0026), the Air Force Office of Scientific Research (AFOSR) through the continued support of Dr. Julian Tishkoff, the Air Force Research Laboratory (AFRL) through the support of nanoenergetics, and the Dayton Area Graduate Studies Institute (DAGSI) for support for M.J.S.

Supporting Information Available: TGA/DSC analysis was performed following the same procedure reported in this manuscript for three commercially available Al nanopowders. These nanopowders are the Alpha Aesar, Sigma Aldrich, and MTI samples. The energy and mass dependence on temperature of these samples was recorded using a TA Instruments STD Q600 dual DSC/TGA instrument with open pan alumina sample cups. Samples were analyzed from room temperature to 700 °C using a 10 °C/min temperature profile under a constant flow of air. This material is available free of charge via the Internet at <http://pubs.acs.org>

References and Notes

- (1) Cooper, P. W. *Explosives Engineering*; Wiley-VCH: New York, 1996.
- (2) Trunov, M. A.; Schoenitz, M.; Zhu, X.; Dreizin, E. L. *Combust. Flame* **2005**, *140*, 310–318.
- (3) Jeurgens, L. P. H.; Sloof, W. G.; Tichelaar, F. D.; Mittemeijer, E. J. *J. Appl. Phys.* **2002**, *92*, 1649–1656.
- (4) Jeurgens, L. P. H.; Sloof, W. G.; Tichelaar, F. D.; Mittemeijer, E. J. *Thin Solid Film* **2002**, *418*, 89–101.
- (5) Sun, J.; Pantoya, M. L.; Simon, S. L. *Thermochim. Acta* **2006**, *444*, 117–127.
- (6) Il'in, A. P.; Gromov, A. A.; Yablunovskii, G. V. *Combust., Expl., Shock Waves* **2001**, *37*, 418–422.
- (7) Frigo, D. M.; van Eijden, G. J. M. *Chem. Mater.* **1994**, *6*, 190–195.
- (8) Haber, J. A.; Buhro, W. E. *J. Am. Chem. Soc.* **1998**, *120*, 10847–10855.
- (9) Jouet, R. J.; Warren, A. D.; Rosenberg, D. M.; Bellitto, V. J.; Park, K.; Zachariah, M. R. *Chem. Mater.* **2005**, *17*, 2987–2996.
- (10) Jouet, R. J.; Granholm, R. H.; Sandusky, H. W.; Warren, A. D. In *Shock Compression of Condensed Matter—2005*; Proceedings of the Conference of the American Physical Society Topical Group on Shock Compression of Condensed Matter, Baltimore, MD, July 31–August 5, 2005; Furnish, M. D., Elert, M., Russell, T. P., White, C. T., Eds.; American Institute of Physics: 2006, 1527.
- (11) Foley, T. J.; Johnson, C. E.; Higa, K. T. *Chem. Mater.* **2005**, *17*, 4086–4091.
- (12) Suslick, K. S. *Science* **1990**, *247*, 1439–1445.
- (13) Thompson, L. H.; Doraiswamy, L. K. *Ind. Eng. Chem. Res.* **1999**, *38*, 1215–1249.
- (14) Shafi, K. V. P. M.; Ulman, A.; Yan, X.; Yang, N.-L.; Estournès, C.; White, H.; Rafailovich, M. *Langmuir* **2001**, *17*, 5093–5097.
- (15) Wu, N.; Fu, L.; Su, M.; Aslam, M.; Wong, K. C.; Dravid, V. P. *Nano Lett.* **2004**, *4*, 383–386.
- (16) Bunker, C. E.; Karnes, J. K. *J. Am. Chem. Soc.* **2004**, *126*, 10852–10853.
- (17) It has been suggested that oleic acid may react with alane such that the mechanism for limiting particle growth is somewhat more complex.
- (18) DCS/TGA data for a commercially available aluminum nanoparticle sample obtained under the same experimental conditions are provided as supporting information.
- (19) Hucknall, D. J. *Chemistry of Hydrocarbon Combustion*; Chapman and Hall: New York, 1985.
- (20) All ICP-MS analyses were performed on purified samples; however, any contribution by other aluminum products to the sample would result in an overestimated active aluminum content.

JP809295E

APPENDIX J
Spontaneous Hydrogen Generation from Organic-Capped
Al Nanoparticles and Water

INTENTIONALLY LEFT BLANK

Spontaneous Hydrogen Generation from Organic-Capped Al Nanoparticles and Water

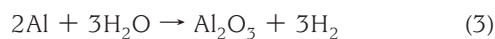
Christopher E. Bunker,^{*,†} Marcus J. Smith,[‡] K. A. Shiral Fernando,[‡] Barbara A. Harruff,[‡] William K. Lewis,[‡] Joseph R. Gord,[†] Elena A. Guliants,[‡] and Donald K. Phelps[†]

Air Force Research Laboratory, Propulsion Directorate, Wright–Patterson Air Force Base, Ohio 45433-7103, and Metals and Ceramics Division, University of Dayton Research Institute, Dayton, Ohio 45469

ABSTRACT The development of technologies that would lead toward the adoption of a hydrogen economy requires readily available, safe, and environmentally friendly access to hydrogen. This can be achieved using the aluminum–water reaction; however, the protective nature and stability of aluminum oxide is a clear detriment to its application. Here, we demonstrate the spontaneous generation of hydrogen gas from ordinary room-temperature tap water when combined with aluminum–oleic acid core–shell nanoparticles obtained via sonochemistry. The reaction is found to be near-complete (>95% yield hydrogen) with a tunable rate from 6.4×10^{-4} to 0.01 g of H₂/s/g of Al and to yield an environmentally benign byproduct. The potential of these nanoparticles as a source of hydrogen gas for power generation is demonstrated using a simple fuel cell with an applied load.

KEYWORDS: energy • hydrogen • nanoparticles • aluminum

In obtaining hydrogen from water, it is well-known that aluminum metal will react with water to yield hydrogen gas (1, 2):



The three reactions represent the products that result from varying water conversion efficiencies (bayerite, boehmite, and aluminum oxide, respectively, with hydrogen). These reactions are limited in their utility because of the natural occurrence of a protective aluminum oxide shell on the surface of the aluminum metal. The stability of the aluminum oxide prevents air and moisture from accessing the underlying metal (3, 4). To circumvent this problem and facilitate the generation of hydrogen, researchers have applied various reaction-promoting schemes. These have included the use of strong bases (5, 6), application of high temperature (7), or activation of the aluminum metal (8–11). Recently, Woodall demonstrated the activation concept and produced large quantities of hydrogen from a gallium–aluminum mixture (8, 9). By dissolving the aluminum in liquid gallium, the researchers prevented the formation of the aluminum oxide shell, thus allowing the aluminum–water reaction to proceed.

While able to provide hydrogen from the aluminum–water reaction, the above-mentioned approaches are more complex than what eqs 1–3 imply. A simpler solution might be achieved if the nature of the protective aluminum oxide shell could be altered. Recent research on the combustion of aluminum nanoparticles protected by aluminum oxide shells suggests that this may be possible with data demonstrating enhanced reactivity over micrometer- or bulk-scale aluminum (12, 13). These results can be attributed to the role surfaces and interfaces play in nanoparticle chemistry, noting that, as the particle size decreases, the surface and interfacial areas increase and become dominant in determining the physical and chemical properties. Methods for producing aluminum nanoparticles are well-documented (14–24). However, having particles on the nanoscale alone is not sufficient; commercial aluminum nanoparticles possessing an aluminum oxide shell will not readily react in water under ambient conditions. In fact, the mixing of aluminum oxide protected aluminum nanoparticles with water ice has been demonstrated as a stable and viable propellant formulation (25, 26).

To achieve our desired goal, chemical modification of the aluminum oxide shell is also required. Previously, we reported the synthesis of air-stable AIOA core–shell nanoparticles via the sonochemically assisted thermal decomposition of alane in the presence of the catalyst titanium(IV) isopropoxide (18). The physical and thermal analysis of these particles suggested a structure consisting of an inner aluminum core surrounded by an oxide shell, followed by an outer organic shell, each accounting for ~40, 25, and 35% of the total particle mass, respectively. Because the reaction solutions were vigorously deoxygenated prior to the reaction, the oxide shell is believed to have formed from the oxygen atoms brought to the aluminum surface by the capping agent oleic acid. Thermal analysis of the AIOA particles demon-

* E-mail: christopher.bunker@wpafb.af.mil.

Received for review November 3, 2009 and accepted December 29, 2009

[†] Wright–Patterson Air Force Base.

[‡] University of Dayton Research Institute.

DOI: 10.1021/am900757r

© 2010 American Chemical Society

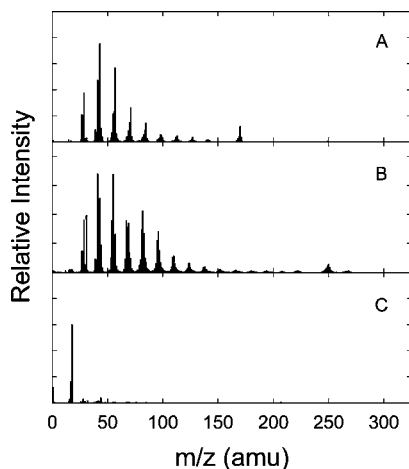


FIGURE 1. TOF mass spectra for the AIOA nanoparticles at (A) 150 °C and (B) 500 °C and for the commercial aluminum nanoparticles with an aluminum oxide coating at (C) 500 °C. The spectra are identified as (A) dodecane, (B) 9-octadecen-1-ol, and (C) water by comparison with the NIST database.

strated that this oxide shell does not behave as natural aluminum oxide, instead allowing reaction of the nanoparticles at a much lower temperature (~ 420 vs 600 °C for commercial aluminum nanoparticles) (18). Using a home-built time-of-flight (TOF) mass spectrometer equipped with a thermal desorption stage, we find that the AIOA nanoparticles release dodecane at temperatures between 100 and 150 °C (Figure 1A) and 9-octadecen-1-ol from ~ 200 to 500 °C (Figure 1B). The dodecane is a residual solvent entrained in the sample. 9-Octadecen-1-ol is consistent with an oleic acid molecule bound to the aluminum particle through the carbonyl oxygen [RC(OH)OAl] and cleaved between carbon and oxygen. The data correlate well with the observed Fourier transform infrared spectrum, showing a strong O–H stretch and no carbonyl band (18). Commercial aluminum nanoparticles (Alpha Asar) analyzed under the same conditions yield only water vapor (Figure 1C).

The AIOA samples were found to be air-stable; however, to provide a more quantitative measure of the stability, an experimental procedure involving exposure of these samples to air-saturated solvents while agitated in a sonic bath was devised. Specifically, samples (~ 20 mg) were suspended in a series of solvents (5 mL) and agitated in a sonic bath for 90 min. The solvents included nonpolar hydrocarbons (hexane and toluene), heteroatom and halogenated hydrocarbons [tetrahydrofuran (THF) and chloroform], and polar solvents (ethanol, methanol, and water). In each solvent except one, the particles remained unchanged as measured by powder X-ray diffraction (Figure 2A and 2B). Only water showed a change in the particles with a significantly altered X-ray spectrum (Figure 2C). The spectrum is not identifiable as a single aluminum oxide material, but the main peaks suggest the formation of bayerite and boehmite. To test this reaction, a small quantity of sample was mixed with water and the headspace sampled using the mass spectrometer. After subtraction of a background spectrum, the data showed a strong signal for hydrogen gas (Figure 3). It should be noted that, in the above experiments, the AIOA:H₂O mass ratio is

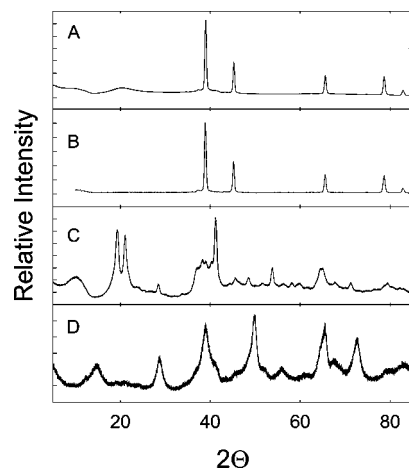


FIGURE 2. Powder X-ray diffraction spectra for (A) the as-synthesized AIOA nanoparticles, (B) the AIOA nanoparticles after exposure to methanol, and representative of exposure to hexane, toluene, THF, chloroform, and ethanol, (C) the product of their reaction with water at an AIOA:H₂O ratio of 10^{-3} , and (D) the product of their reaction with water at an AIOA:H₂O ratio of 0.5. The spectra were identified by comparison with the ICPSD database; (A and B) fcc aluminum, (C) a mixture with the main peaks indicating bayerite and boehmite, and (D) boehmite.

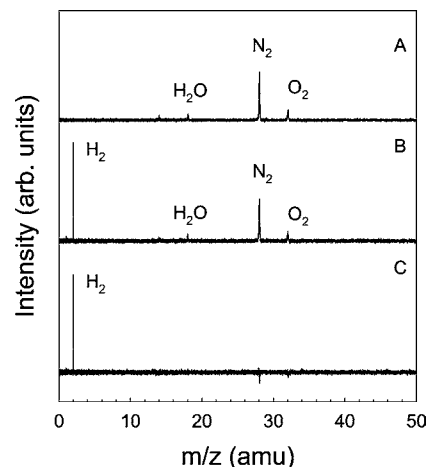


FIGURE 3. Mass spectra demonstrating hydrogen production from reaction of the AIOA nanoparticles and water: (A) background spectrum; (B) reaction spectrum; (C) background-subtracted spectrum.

fairly small (AIOA:H₂O = 10^{-3}). When performed at a much larger value (e.g., 0.5), the reaction appeared far more vigorous and generated considerable heat. The X-ray spectrum of the oxide product formed under those conditions is quite different (Figure 2D), demonstrating a clear pattern for boehmite (eq 2).

A second experiment was performed to directly measure hydrogen generation (pressure) versus time. To a 25 mL stainless steel pressure vessel was added 1 g of a AIOA sample and 2 mL of water (AIOA:H₂O = 0.5). The pressure is plotted versus time in Figure 4 and shows a rapid rise, which then slows to reach a plateau. The pressure at the plateau is 309 psi, or 21 atm. From the knowledge that our samples are $\sim 40\%$ aluminum metal, using the stoichiometry of eq 2 and applying the ideal gas law, we calculate a $>95\%$ yield for the formation of hydrogen gas. More importantly, if we examine the rate at which hydrogen gas is generated under continuously reacting conditions (i.e., the

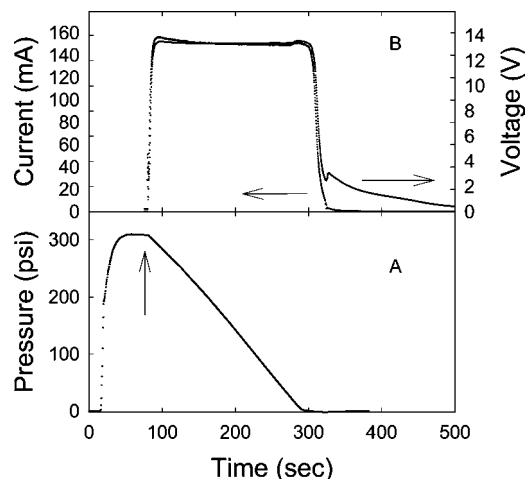


FIGURE 4. Plots of pressure versus time (A) and voltage and current versus time (B) for the reaction of 1.0 g of the AIOA nanoparticles with 2.0 mL of water in a 25 mL stainless steel pressure vessel. The pressure was allowed to stabilize before the fuel cell was brought in line. The operating power was approximately 2 W. In plot A, the arrow indicates the point at which the fuel cell was brought in line. In plot B, arrows indicate the applicable axes.

rapid-rise region), we obtain a rate of ~ 0.01 g of $\text{H}_2/\text{s/g}$ of Al. The utility of this hydrogen was also demonstrated in Figure 4, where just after the plateau was reached the pressure vessel was placed in line with a fuel cell (TDM Fuel Cell Technology, 20-stack polymer electrolyte membrane cell) using a pressure regulator set to deliver under 5 psi of hydrogen. Attached to the fuel cell was a simple computer fan to serve as the electrical load, and the voltage and current were recorded as the hydrogen was consumed. As can be seen from the plot, once the hydrogen was delivered to the cell, the voltage and current quickly reached stable working values (~ 13 V and 0.15 A). The power consumed by this system is ~ 2 W for a continuous 2.3 min.

Because the reaction appeared to demonstrate a strong dependence on the AIOA: H_2O ratio, a small-scale temperature measurement system was assembled using a thermocouple affixed to an alumina cup to probe this dependence. Water (a constant $60 \mu\text{L}$) was added to AIOA samples varying in mass from ~ 2 to 15 mg (AIOA: $\text{H}_2\text{O} = 0.03\text{--}0.25$). The temperature was then recorded as a function of time, and the data are plotted in Figure 5. The traces of temperature versus time are all similar in that they exhibit an induction phase, a rapid rise, a maximum, and then a steady decrease, eventually returning to room temperature. The data can be fit using a model that accounts for the heat generated by the reaction q_{rxn} , the heat lost from the system q_{loss} , and the total heat capacity of the system $C_{\text{p,total}}$ (a detailed description of the model with definitions for all terms is given in the Supporting Information):

$$T(T) = T(0) + \frac{\int_0^t [q_{\text{rxn}}(t) - q_{\text{loss}}(t)] dt}{C_{\text{p,total}}(t)} \quad (4)$$

The q_{rxn} term is obtained assuming a pseudo-first-order kinetic equation modified to account for the time-dependent surface area (SA) of the reacting nanoparticles:

$$q_{\text{rxn}} = \Delta H_{\text{rxn}} \int_0^t (1 - e^{-k(t)t}) m_{\text{nanoAl}} dt \quad (5)$$

where $k(t)$ is

$$k(t) = ASA(m_{\text{nanoAl}}) e^{-E_a/RT(t)} \quad (6)$$

The fits to the data are shown in Figure 5 (fit parameters are also provided in the Supporting Information). From the model, we obtain an average activation barrier of 15 kJ/mol. With this information, we can convert the temperature data in Figure 5 to hydrogen volume versus time and obtain the rate of hydrogen production versus the AIOA: H_2O ratio. The modeled data demonstrate a mass-normalized tunable rate between 6.4×10^{-4} and 5.6×10^{-3} g of $\text{H}_2/\text{s/g}$ of Al (Figure 5), where the aluminum mass was taken as 40% of the total sample weight. Extending the model to a AIOA: H_2O value of 0.5, we obtain a predicted rate of 0.017 g of $\text{H}_2/\text{s/g}$ of Al, in very good agreement with the experimentally measured value of ~ 0.01 g of $\text{H}_2/\text{s/g}$ of Al (Figure 5).

We have demonstrated that the reaction of aluminum with water to yield hydrogen gas can be performed in a simple fashion, requiring no promoters or initial energy to initiate the reaction. This capability is achieved through the combined effect of using nanoscale aluminum particles coupled with an organic-provided oxide shell, which demonstrates remarkable air and organic solvent stability but allows easy reaction of the aluminum in water. We have shown that the reaction is near-complete, that the rate of hydrogen production can be tuned by controlling the nanoparticle-to-water mass ratio, and that the hydrogen generated by this reaction is sufficient to perform useful work. The simplicity of the reaction, the high energy density of the aluminum–water reaction, and the tremendous stability of these novel aluminum nanoparticles make this system a

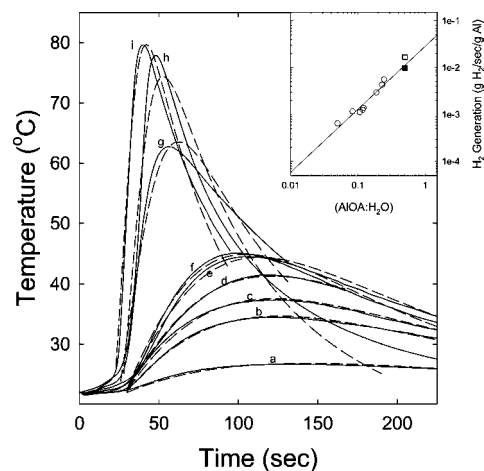


FIGURE 5. Plot of temperature versus time for reaction of the AIOA nanoparticles with water; experimental (—) and calculated (---) data for AIOA masses of 3.0, 4.9, 5.0, 6.4, 7.1, 7.3, 11.3, 13.7, and 14.7 mg (curves a–i, respectively). Inset: plot of the hydrogen production rate versus the AIOA: H_2O ratio as calculated from the kinetic model for the data in the main figure (○), calculated for an AIOA: H_2O ratio of 0.5 (□), and measured at a AIOA: H_2O ratio of 0.5 (■).

viable approach for providing power based on hydrogen without requiring the direct storage of large quantities of hydrogen; one need only to add water to produce hydrogen on demand, where and when needed. Future efforts will focus on a better understanding of the nature of the protective shell, the particular role the synthetic method plays in developing these properties, and the effect of the organic capping agent on the reaction parameters.

Acknowledgment. The authors thank Dr. S. Hussain and N. McNamara for helpful discussion and experimental assistance. We acknowledge financial support of the Defense Threat Reduction Agency (Grant HDTRA-07-1-0026), the Air Force Office of Scientific Research through continued support of Dr. Julian Tishkoff, the Air Force Research Laboratory through support of nanoenergetics, and the Dayton Area Graduate Studies Institute for support for M.J.S.

Supporting Information Available: Additional experimental details for the work presented herein, a full description of the kinetic model and definition of all terms, and a table of fit parameters for the data presented in Figure 5. This material is available free of charge via the Internet at <http://pubs.acs.org>.

REFERENCES AND NOTES

- Wang, H. Z.; Leung, D. Y. C.; Leung, M. K. H.; Ni, M. *Renewable Sustainable Energy Rev.* **2009**, *13*, 845–853.
- Roach, P. J.; Woodward, W. H.; Castleman, A. W., Jr.; Reber, A. C.; Khanna, S. N. *Science* **2009**, *323*, 492–495.
- Vedder, W.; Vermilyea, D. A. *Trans. Faraday Soc.* **1969**, *65*, 561–584.
- Digne, M.; Sautet, P.; Raybaud, P.; Toulhoat, H.; Artacho, E. *J. Phys. Chem. B* **2002**, *106*, 5155.
- Belitskus, D. J. *Electrochem. Soc.* **1970**, *117*, 1097.
- Soler, L.; Candela, A. M.; Macanás, J.; Muñoz, M.; Casado, J. *J. Power Sources* **2009**, *192*, 21–26.
- Astankova, A. P.; Godymchuk, A. Y.; Gromov, A. A.; Il'in, A. P. *Russ. J. Phys. Chem. A* **2008**, *82*, 1913–1920.
- Cuomo, J. J.; Woodall, J. M. U.S. Patent 4,358,291, Nov 9, 1982.
- Cuomo, J. J.; Leary, P. A.; Woodall, J. M. U.S. Patent 4,745,204, May 17, 1988.
- Parmuzina, A. V.; Kravchenko, O. V. *Int. J. Hydrogen Energy* **2008**, *33*, 3073–3076.
- Deng, Z.-Y.; Liu, Y.-F.; Tanaka, Y.; Ye, J.; Sakka, Y. *J. Am. Ceram. Soc.* **2005**, *88*, 977–979.
- Shafirovich, E.; Diakov, V.; Varma, A. *Combust. Flame* **2006**, *144*, 415.
- Sun, J.; Pantoya, M. L.; Simon, S. L. *Thermochim. Acta* **2006**, *144*, 117.
- Haber, J. A.; Buhro, W. E. *J. Am. Chem. Soc.* **1998**, *120*, 10847–10855.
- Jouet, R. J.; Warren, A. D.; Rosenberg, D. M.; Bellitto, V. J.; Park, K.; Zachariah, M. R. *Chem. Mater.* **2005**, *17*, 2987–2996.
- Jouet, R. J.; Carney, J. R.; Granholm, R. H.; Sandusky, H. W.; Warren, A. D. *Mater. Sci. Technol.* **2006**, *22*, 422–429.
- Foley, T. J.; Johnson, C. E.; Higa, K. T. *Chem. Mater.* **2005**, *17*, 4086–4091.
- Fernando, K. A. S.; Smith, M. J.; Harruf, B. A.; Lewis, W. K.; Guliants, E. A.; Bunker, C. E. *J. Phys. Chem. C* **2009**, *113*, 500–503.
- Meziani, M. J.; Bunker, C. E.; Lu, F.; Li, H.; Wang, W.; Guliants, E. A.; Quinn, R. A.; Sun, Y.-P. *ACS Appl. Mater. Interfaces* **2009**, *1*, 703–709.
- Chung, S. W.; Guliants, E. A.; Bunker, C. E.; Hammerstroem, D. W.; Deng, Y.; Burgers, M. A.; Jelliss, P. A.; Buckner, S. W. *Langmuir* **2009**, *25*, 8883–8887.
- Li, H.; Meziani, M. J.; Lu, F.; Bunker, C. E.; Guliants, E. A.; Sun, Y.-P. *J. Phys. Chem. C* **2009**, *113*, 20539–20542.
- Weigle, J. C.; Luhrs, C. C.; Chen, C. K.; Perry, W. L.; Mang, J. T.; Nemer, M. B.; Lopez, G. P.; Phillips, J. J. *Phys. Chem. B* **2004**, *108*, 18601–18607.
- Kwon, Y.-S.; Gromov, A. A.; Strokova, J. I. *Appl. Surf. Sci.* **2007**, *253*, 5558–5564.
- Mahendiran, C.; Ganesan, R.; Gedanken, A. *Eur. J. Inorg. Chem* **2009**, *14*, 2050–2053.
- Ingenito, A.; Bruno, C. *J. Propul. Power* **2004**, *20*, 1056.
- Risha, G. A.; Son, S. F.; Yetter, R. A.; Yang, V.; Tappan, B. C. *Proc. Combust. Inst.* **2009**, *31*, 2007.

AM900757R

APPENDIX K

Effects of Aromatic Type and Concentration in Fischer-Tropsch Fuel on Emissions Production and Material Compatibility

INTENTIONALLY LEFT BLANK

Effects of Aromatic Type and Concentration in Fischer–Tropsch Fuel on Emissions Production and Material Compatibility

Matthew J. DeWitt,^{*,†} Edwin Corporan,[‡] John Graham,[†] and Donald Minus[‡]

University of Dayton Research Institute, 300 College Park, Dayton, Ohio 45469, and Air Force Research Laboratory, Fuels Branch AFRL/PRTG, Wright-Patterson AFB, Ohio 45433

Received February 17, 2008. Revised Manuscript Received April 18, 2008

The use of synthetic fuels produced via the Fischer–Tropsch (FT) process is being considered for U.S. military applications as an approach to provide secure and stable fuel resources. Many potential operational benefits have been observed while employing this type of paraffinic fuel for aviation applications. However, operational limitations with respect to seal-swell and lubricity may need to be improved for ultimate implementation. Studies were performed to investigate the feasibility of adding aromatic solvents as an option to achieve “fit-for-purpose” (FFP) requirements. Aromatics are known to improve seal-swell characteristics, but also increase engine soot emissions. Three aromatic solvents, which encompass the molecular weight range typically found in military jet fuel (JP-8), were added both individually and as a blend to an FT fuel at varying concentrations. The seal-swell capability of the solvents was inferred using nitrile, fluorosilicone, and fluorocarbon O-rings while the solvent effect on combustion emissions was evaluated using a T63 engine. The studies showed that particulate matter (PM) emissions increased with increasing aromatic molecular weight and concentration, which was attributed to an increase in soot precursors. The seal-swell of nitrile rubber was most strongly affected by the addition of aromatics in the form of alkyl-naphthalenes as compared to alkyl-benzenes. This result was attributed to the decreasing molar volume and increasing polarity and hydrogen-bonding potential for the larger aromatics, primarily naphthalene and corresponding derivatives. Results showed that the desired swell characteristics and relatively low PM emissions can be achieved with the solvents evaluated in this study. The overall relation between PM emissions production and volume swell showed that all solvents considered had comparable dependence, which suggests that it may be possible to predict these interdependent variables. Overall, this study provided an initial assessment and basis for subsequent evaluations of potential feedstocks for blending in FT fuels to achieve FFP requirements. Future studies will evaluate additional elastomer materials and individual aromatic species while characterizing the emissions production on varying combustion platforms.

Introduction

In recent years, there has been increased interest in the potential use of fuels produced via the Fischer–Tropsch (FT) process for aviation applications. These fuels can be produced domestically from various nonpetroleum feedstocks, such as coal, natural gas, and biomass and, therefore, could reduce reliance on foreign supply. FT-derived fuels have been shown to exhibit excellent thermal-oxidative stability characteristics with significantly lower particulate matter (PM) combustion emissions compared to conventional petroleum-derived fuels.^{1–4} FT fuels are typically comprised solely of *iso*- and *n*-alkanes and do not contain heteroatoms, cyclic compounds, or aromatics. The latter are believed to provide seal-swell and other needed

“fit-for-purpose” (FFP) properties, but have also been shown to increase undesirable PM and gaseous emissions.^{5–8} The eventual widespread use of FT fuels may require blending with an additional feedstock or additive to provide the required FFP properties. With respect to volume swell, there are also potential concerns that transition of operation from petroleum-derived fuels (typically 10–25% aromatic content) will result in seal shrinkage and leaks due to the poor swelling characteristics of the FT fuel. One approach is to blend the FT fuel directly with petroleum-derived fuel,^{9,10} but this approach will negate the

* Corresponding author. E-mail: matthew.dewitt@wpafb.af.mil.

[†] University of Dayton Research Institute.

[‡] Air Force Research Laboratory.

(1) Edwards, T.; Minus, D.; Harrison, W.; Corporan, E.; DeWitt, M.; Zabarnick, S.; Balster, L. Fischer–Tropsch Jet Fuels—Characterization for Advanced Aerospace Applications. *40th AIAA/ASME/SAE/ASEE Joint Propulsion Conference and Exhibit*, July 11–14, 2004, Fort Lauderdale, FL AIAA-2004-3885; American Institute of Aeronautics and Astronautics: Reston, VA, 2004.

(2) Harrison, W. E., III; Zabarnick, S. The OSD Assured Assured Fuels Initiative - Military Fuels Produced From Coal. *Proceedings of 31st International Technical Conference on Coal Utilization & Fuel Systems*, Clearwater, FL, May 21–26, 2006.

(3) Corporan, E.; DeWitt, M. J.; Belovich, V.; Pawlik, R.; Lynch, A. C.; Gord, J. R.; Meyer, T. R. *Energy Fuels* **2007**, *21* (5), 2615–2626.

(4) Corporan, E.; DeWitt, M. J.; Klingshirn, C. D.; Striebich, R. C. DoD Assured Fuels Initiative: B-52 Aircraft Emissions Burning a Fischer–Tropsch/JP-8 Fuel Blend. *Proceedings of the 10th International Conference on Stability and Handling of Liquid Fuels*, Tucson, AZ, Oct 7–11, 2007.

(5) Bittner, J. D.; Howard, J. B. *Prog. Astronautics Aeronautics* **1978**, *62*, 335.

(6) Moses, C. A.; Valtierra, M. L. Impact Study of Synthetic and Alternative Fuel Usage in Army Aircraft Propulsion Systems: Final Report, SRWI-MED-134, Cont. No. N00140-80-C-2269, Southwest Research Institute: San Antonio, TX, 1981.

(7) Richter, H.; Howard, J. B. *Prog. Energy Combust. Sci.* **2000**, *26*, 565–608.

(8) Monroig, O.; Corporan, E.; DeWitt, M. J. Effects of Aromatic and Sulfur Concentration in Jet Fuel on the Emissions of a T63 Engine. *Proceedings of the 9th International Conference on Stability and Handling of Liquid Fuels*, Sitges, Spain, Sept 18–22, 2005.

(9) Moses, C. A.; Stavinoha, L. L.; Roets, P. *Qualification of SASOL Semi-Synthetic Jet A-1 as Commercial Jet Fuel*, Report No. SWRI 8531; Southwest Research Institute: San Antonio, TX, 1997.

forementioned advantages of a fully petroleum-free fuel and will limit the beneficial operational properties of the synthetic fuel by significantly increasing the concentration of thermal deposition and emission precursors.¹¹ Although an ambitious goal would be to introduce a specific additive at very low concentration, an alternative and affordable option is to blend aromatic solvents into the paraffinic fuel. Since varying aromatic type, molecular weight and total concentration may impart different degrees of volume swell, it is of interest to investigate the effect of these variables in the FT fuel. This will assist in determining the minimum concentration required to achieve desired swell while maximizing the benefits of the FT blend and reducing logistics and cost. An improved understanding into the effect of the type and concentration of the aromatic solvent will assist in identifying potential aromatic candidates to meet the aircraft system operational requirements. Of specific interest are the extents to which the combustion emissions and seal-swell behavior are affected. In this effort, three petroleum-derived aromatic solvents of varying molecular weight, which encompass the range typically found in JP-8 fuels, were added both independently and as a blend to an FT fuel to assess their effects on the swelling of typical aircraft fuel system seal materials and on the emissions of a T63 engine. Test procedures, analysis techniques, and results are presented.

Experimental Details

Baseline Fuel. The baseline fuel used for this study was a natural gas-derived fuel produced by the Syntroleum Corporation. The fuel is comprised solely of *iso*-paraffins (82%) and *n*-paraffins with a distillation range similar to a typical JP-8 fuel. Details of the specific physical and chemical properties have been previously reported.^{3,11}

Aromatic Solvents. The purpose of this study was to investigate the effect of aromatic solvent type and concentration on the resulting emissions and seal-swell characteristics of relevant elastomers. Compared to evaluating individual aromatic species, the solvents are readily available, affordable and feasible options for blending to obtain desired fuel properties. Three commercially available aromatic solvents produced by Exxon (Aromatic 100, 150, and 200), which encompass the molecular weight range of typical jet fuels, were used. A comparison of the molecular weight range for each solvent obtained using gas chromatography/mass spectrometry (GC/MS) is shown in Figure 1. These solvents were added both independently and as a blend to simulate the typical aromatic distribution in JP-8. A previous study showed that overall, 25, 53, and 22% of the Aromatic 100, 150, and 200 solvents, respectively, were found to provide the best match to a typical JP-8 distribution without significantly altering the volatility of the mixture.⁸ The individual aromatic solvents and blend were added to the FT fuel at volume concentrations of 5, 10, 15, 20, and 25% to represent the aromatic range found in typical aviation fuels. A comparison of the relative molecular weight ranges and total naphthalene content in the solvents and the aromatic extract of a typical (e.g., specification) JP-8 is provided in Table 1. The aromatic extract from the JP-8 was obtained via pre-separation of the chemical class using high pressure liquid chromatography (HPLC) followed by GC/MS analysis. It can be observed that the naphthalene content of the Aromatic 200 and solvent blend is relatively high, which is anticipated to have an adverse impact on emissions. Also of note is that although the naphthalene concentration in the JP-8 aromatic extract was 9.3%, the actual concentration in the fuel was only 1.9%.

(10) Muzzell, P.; Sattler, E.; Terry, A.; McKay, B.; Freerks, R.; Stavinoha, L. SAE Paper No. 2006-01-0702, Society of Automotive Engineers: Warrendale, PA, 2006.

(11) DeWitt, M. J.; Striebich, R.; Shafer, L.; Zabarnick, S.; Harrison, W. E., III; Minus, D. E.; Edwards, J. T. Evaluation of Fuel Produced via the Fischer-Tropsch Process for Use in Aviation Applications. *Proceedings of the AIChE Spring National Meeting*, Houston, TX, April 22–27, 2007; Paper 58b.

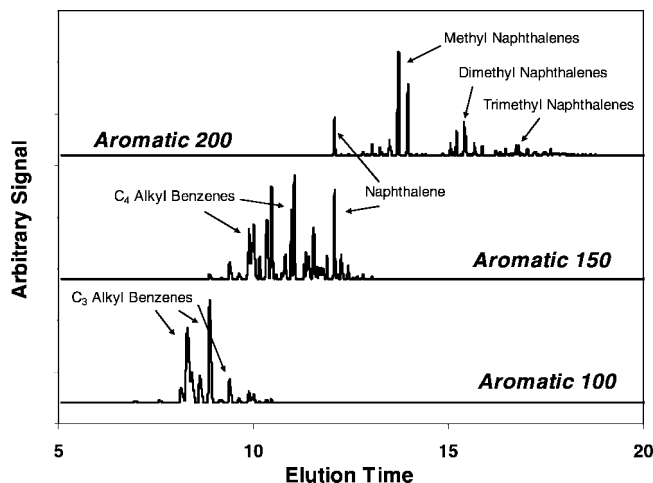


Figure 1. Comparison of the molecular weight range and composition for the Aromatic 100, 150, and 200 solvents from GC/MS analysis.

Table 1. Comparison of Molecular Weight Ranges and Naphthalene Content for Aromatic Solvents, Aromatics in a Typical JP-8, and the Paraffinic FT Fuel

solvent	MW range (g/mol)	average MW (g/mol)	naphthalenes (% volume)
aromatic 100	106–134	121	
aromatic 150	118–148	135	6
aromatic 200	120–196	151	82
aromatic blend (25:53:22)	106–196	135	21
JP-8 aromatic extract	106–170	138	9.3
FT fuel	100–240	169	

Emissions Testing. A T63-A-700 turboshaft engine was used in this study to investigate the effect of aromatic solvent addition on PM and gaseous emissions relative to neat FT fuel combustion. The engine is located in the Engine Environment Research Facility (EERF) in the Propulsion Directorate at Wright-Patterson Air Force Base and is used to evaluate turbine engine lubricants, fuels, and sensors in an actual engine environment. Detailed descriptions of the engine and operating methodology have been provided in previous publications.^{3,8,12} For these studies, the engine was operated at idle and cruise conditions. The FT fuel was supplied to the engine from an external tank. The required aromatic solvents were injected via two ISCO Model 1000D syringe pumps to achieve the desired concentration. Due to capacity limitation with the injection pumps, testing of the 20 and 25% mixtures at engine cruise was performed by premixing the FT and solvent in the external tank. For all tests, the fuel flow rate was adjusted to maintain a constant turbine outlet temperature (T_5). This approach assured the best run-to-run repeatability. The engine was initially operated on JP-8 at the two power conditions and then transitioned to operation with the synthetic fuel and solvents. The JP-8 used in this study (POSF 3773) has ~15.9% aromatics by volume; other properties and extensive emissions results are reported elsewhere.³

Both nonvolatile PM and gaseous emissions were extracted using oil-cooled probes and transported to the analytical instruments via heated lines to maintain sample integrity. PM samples were diluted with nitrogen at the probe tip to prevent water condensation and particle loss to the wall due to high wall-sample temperature gradients and to prevent saturation of the particle instrumentation. All measurements were corrected for dilution using the raw and diluted CO_2 measurement. The PM emissions were characterized using commercially available aerosol instruments. A TSI Model 3022A condensation particle counter (CPC) was used to provide a count of particles per unit volume (particle number (PN)), a TSI Model 3936 scanning mobility particle sizer (SMPS) with a model 3081 long differential mobility analyzer and 3022A CPC was used

(12) Corporan, E.; DeWitt, M. J.; Wagner, M. *Fuel Process. Technol.* **2004**, *85* (6–7), 727–742.

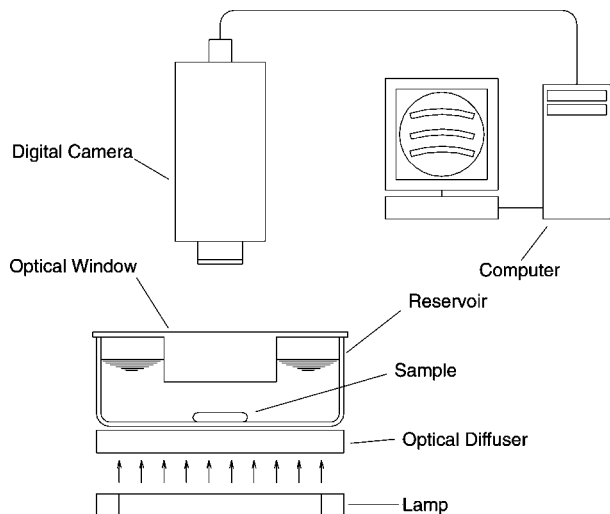


Figure 2. Schematic of the optical dilatometry system used to measure volume swell as a function of time.

to obtain the particle size distribution from 7–300 nm, and a Rupprecht & Patashnick Series 1105 tapered element oscillating microbalance (TEOM) was used to obtain real-time particle mass emissions. An in-house-designed smoke sampler was used to collect undiluted soot samples on quartz filters to allow for off-line analysis of the soot quantity and composition. Major and minor gaseous emissions were quantified using an MKS Multi Gas 2030 fourier transform infrared (FTIR) based analyzer while total unburned hydrocarbons were quantified using a CAI 600 heated flame ionization detector.

Material Compatibility. One characteristic of conventional JP-8 fuels is their solvent-like interactions with polymeric material. This behavior expresses itself in the form of swelling and softening polymeric materials, most notably O-rings seals since this behavior can impact their performance. The solvent character of JP-8 is largely due to its aromatic content. Since FT fuels do not have similar seal swelling characteristics as JP-8, the seals that have swollen as a consequence of their service with JP-8 may shrink, harden, and fail when exposed to FT and similar aromatic-free fuels. The degree of swelling is dependent on both the seal material and the composition of the overlying fuel. The seals are typically comprised of polymeric materials, such as nitriles, fluorosilicones, and fluorocarbons. Swelling occurs due to diffusion of solvent (e.g., fuel) molecules into the polymer matrix, which increase the distance between the polymer chains. The more energetically favorable the overall diffusion and equilibrium processes become, the greater the corresponding volume swell. In general, the swelling ability of a species increases with increasing polarity and hydrogen bonding and decreasing molar volume. The paraffinic species within the FT fuel are relatively large and inert, having only dispersive intermolecular bonding. In contrast, aromatic compounds of similar molecular weight have a smaller molar volume and exhibit both polar and hydrogen bonding, typically resulting in enhanced volume swell characteristics.^{13–15}

The volume swell of varying O-ring material types was measured using optical dilatometry. A schematic of the system is shown in Figure 2. This system consisted of a backlit fuel reservoir fitted with an optical window. The window was designed such that the inner face is immersed in the test fuel to prevent condensation from obscuring the view of the sample resting on the bottom of the reservoir. A digital camera is mounted above the reservoir which periodically photographed the sample. For each test, the O-ring

sample was placed in the reservoir and filled with 10 mL of fuel and then covered with the optical window. The sample was photographed every 15 min over a 16 h period providing a record of the cross sectional area of the sample as a function of time. Representative images collected during testing with a nitrile rubber O-ring in an FT fuel blended with 25% Aromatic 200 are shown in Figure 3.

The cross-sectional area was extracted from the digital images using a commercial image processing system (MetaMorph, Molecular Devices Corp., Downingtown, PA). Assuming isotropic swelling, the change in cross sectional area was taken as a characteristic dimension proportional to the change in volume. The O-rings used in this study were nitrile rubber (N0602), fluorosilicone (L1120), and fluorocarbon (V0747). The specific O-rings were size -001 (0.029 in. I.D. 0.109 in. O.D.) and used as-received (Parker-Hannifin, Lexington, KY). These materials represent those typically used in aircraft fuel systems. Tests were conducted with the FT fuel, which was blended with specification levels of the JP-8 additives (fuel system icing inhibitor, static dissipater, and corrosion inhibitor/lubricity improver) and the aromatic solvents at concentrations discussed above.

Results and Discussion

Emissions Testing. Particle Number (PN) and Size Distribution. The PN emissions (particles per volume of exhaust gas) were found to be strongly dependent on aromatic type, concentration, and engine condition. The average dilution-corrected PN for neat FT and JP-8 at idle were approximately 3.1×10^6 and 7.1×10^7 particles/cm³, respectively, with a variability of $\pm 8\%$. A comparison of the ratio of the measured PN for the blended fuel to that for neat FT fuel at the engine idle condition as a function of aromatic solvent type and concentration is shown in Figure 4. The ratio observed for operation with JP-8 was approximately 23:1 (i.e., 23 times higher PN for JP-8 compared to FT fuel). The data were normalized to neat FT emissions to best account for small variations in engine operation as the solvents were evaluated during separate test periods. As shown, the PN significantly increased with both aromatic concentration and molecular weight, with the dependence appearing to be linear. Results from studies conducted at the engine cruise condition are shown in Figure 5. The average dilution-corrected particle numbers for neat FT and JP-8 at cruise were approximately 7.1×10^7 and 1.9×10^8 particles/cm³, respectively, with a variability of $\pm 10\%$. The testing at cruise showed similar trends with respect to aromatic content and type, but the increases were significantly lower (although the absolute emissions were higher). For example, the ratio for the test with 25% Aromatic 200 was approximately 8:1 at cruise versus 71:1 at idle. The significantly higher ratio at idle is most likely due to increased volatile hydrocarbon emissions and inefficient combustion of the aromatic species at the lower temperature and pressure conditions. This effect is intensified as the molecular weight of the aromatics increases. It is notable that the relative PM emission production for the aromatic blend at 15% and 20% total content is comparable to that for a typical JP-8 for both engine conditions.

The particle size distributions were observed to follow a single mode log-normal distribution for both engine conditions. The relative size distribution profiles shifted slightly to larger particle sizes and increased with the higher aromatic content. The mean particle diameter was found to increase linearly with aromatic content. The mean particle diameters for testing with the individual solvents are shown in Table 2. The mean values at a constant aromatic concentration were similar for the testing with Aromatic 100 and 150, while the mean diameter increased

(13) Sombatsompop, N.; Christodoulou, K. J. *Polym. Polym. Compos.* **1997**, 5 (5), 377–386.

(14) Mathai, A. E.; Singh, R. P.; Thomas, S. J. *Membr. Sci.* **2002**, 202, 35–54.

(15) Graham, J. L.; Striebich, R. C.; Myers, K. J.; Minus, D. K.; Harrison, W. E. *Energy Fuels* **2006**, 20 (2), 759–765.

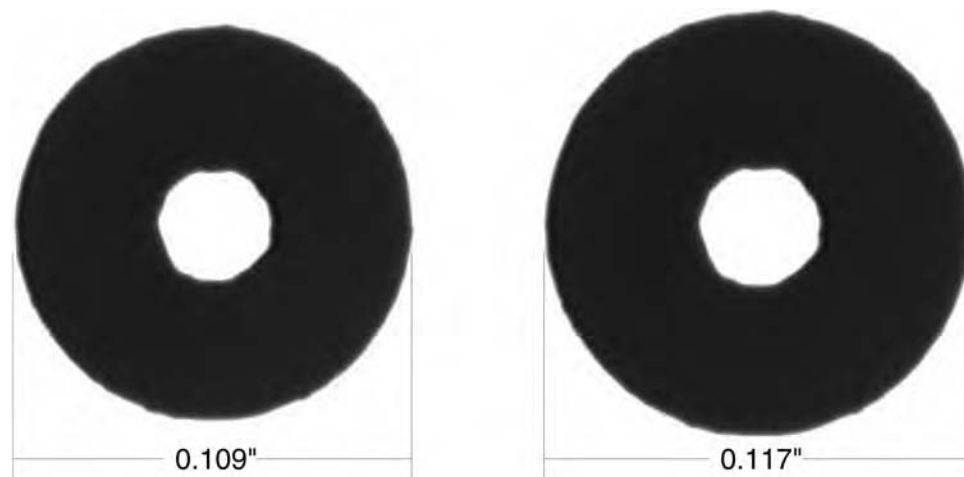


Figure 3. Representative optical dilatometry images collected during testing with a nitrile rubber O-ring in an FT fuel with 25% Aromatic 200 for 0 (left) and 16 h (right) at room temperature.

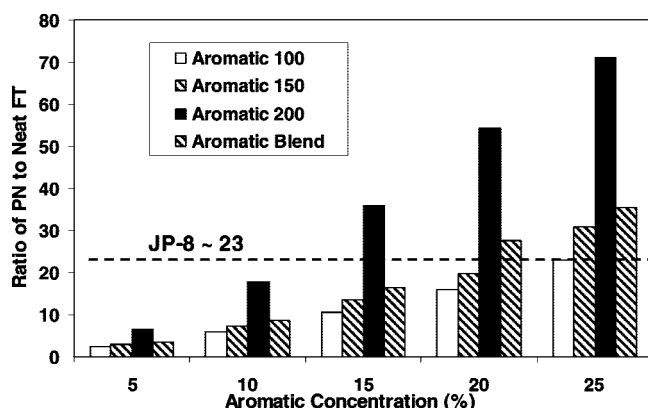


Figure 4. Comparison of the ratio of the measured particle number (PN) to neat FT fuel at engine idle as a function of aromatic solvent type and concentration.

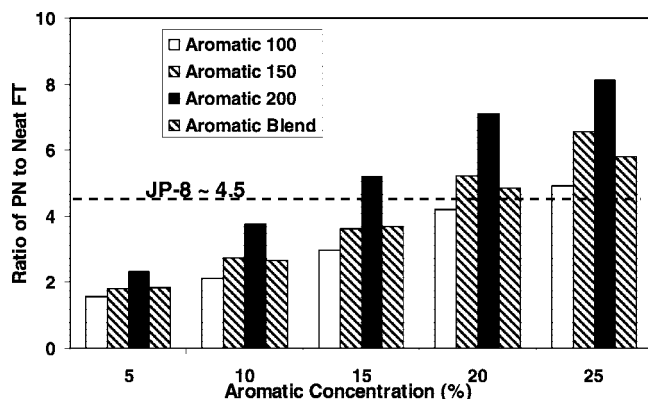


Figure 5. Comparison of the ratio of the measured particle number (PN) to neat FT fuel at engine cruise as a function of aromatic solvent type and concentration.

more rapidly for the Aromatic 200. The trends for the particle size data obtained previously with the solvent blend⁸ were consistent with those observed herein for the individual solvents; however, the mean particle diameters were slightly different due to the use of a different SMPS system. Overall, these trends are consistent with those previously observed during evaluation of blends of this FT fuel directly with the JP-8 at varying concentrations on this platform.³ The increase in mean particle size without significant alteration to the distribution shape indicates that the aromatic species increase the concentration of soot nuclei, but do not alter the particle growth mechanisms.^{3,8}

Particulate Matter (PM) Mass. The ratio of the measured mass concentration quantified with the TEOM to that for neat FT fuel at the engine idle and cruise conditions as a function of aromatic solvent type and concentration are shown in Figures 6 and 7. The mass concentration emissions for neat FT were approximately 0.76 and 1.43 mg/m³ at idle and cruise, respectively, while the values for testing with JP-8 were 2.43 and 11.04 mg/m³. The trends for the normalized ratios were consistent with those for the PN, but the ratios were substantially lower in absolute value. This occurs because the mass of PM emitted is strongly related to particle size, with larger particles contributing more strongly to the total mass emission. It is evident that significant increases in the measured PM mass results with increasing concentration of multiring aromatics in the fuel. This was also reflected in the larger increase in the mean particle diameter with increasing concentrations of Aromatic 200 as compared to the Aromatic 100, 150, and blend studies.

Soot Analysis. Particulate samples were also collected on quartz filters for offline analysis for soot quantity and relative composition. Analysis was performed using temperature programmed oxidation (TPO) of the filters. Carbon mass was determined via quantitation of the CO₂ evolved using a LECO RC412 multiphase carbon analyzer. Qualitative compositional information was obtained based on the temperature at which the soot oxidized; oxidation below 350 °C was termed “organic” while that above was termed “elemental” or “carbonaceous.” The differences in total soot were evident via visual inspection of the filters. Figure 8 shows particulate collected during tests with Aromatic 200 at the engine idle condition. For these samples, volumes of 2.0 ft³ of exhaust gas were collected for the 0–10% blend concentrations and 1.5 ft³ for 15–25%. The trends in visible particulate loading were similar for testing with the other solvents. The changes in soot loading with increasing aromatic concentration shown in Figure 8 was consistent with the PN and mass emissions discussed in the previous sections. The general trends in the particulate mass quantitation using the TPO technique were consistent with those from the TEOM measurements. Lower absolute organic and elemental carbon were observed for both engine conditions with the aromatic-free FT fuel. Also, with respect to composition, the lowest elemental fraction for particulate was observed for the neat FT, with values of approximately 30% and 57% at engine idle and cruise respectively as compared to 45% and 72% for tests with JP-8. The percentage increases in elemental particulate relative to FT fuel at cruise as a function of the solvent type and

Table 2. Comparison of Mean Particle Diameters as a Function of Aromatic Solvent Type, Concentration, and Engine Condition

concentration	idle			cruise		
	Aromatic 100	Aromatic 150	Aromatic 200	Aromatic 100	Aromatic 150	Aromatic 200
0	13	15	13	21	21	21
5	14	15	16	23	24	26
10	16	16	20	26	26	30
15	17	18	23	28	29	34
20	19	20	26	32	33	38
25	21	22	29	34	35	41

concentration are shown in Figure 9. The trends at idle were consistent with those at cruise, but the magnitude of the increases were even larger. As shown, the carbonaceous fraction significantly increased with the addition of the aromatic components. It is believed that this occurs since the aromatics can readily promote larger polycyclic aromatic hydrocarbon (PAH) growth which readily nucleate into soot particles. These particles oxidize less readily and are more likely to exit the engine, rendering the observed increased particulate emissions.

Gaseous Emissions. Most gaseous emissions were observed to be slightly affected with increasing molecular weight and concentration of the aromatic solvents. Significant changes were only observed for the carbon monoxide (CO) and unburned hydrocarbon (UHC) emissions. The increases for testing at engine idle are shown in Table 3. The average CO and UHC emissions for neat FT at idle were approximately 900 and 585 ppm, respectively. The JP-8 used in this study had approximately 22% higher CO and 44% higher UHC than the neat FT. Both CO and UHC were observed to increase significantly with aromatic molecular weight at the idle engine condition. For example, compared to the CO produced with neat FT, addition

of Aromatic 100, 150, and 200 solvents at a concentration of 20% increased CO by 9, 11, and 32%, respectively, as compared to ~22% higher with JP-8. The UHC emission trends at idle were even more pronounced than the CO trends; increases of 13, 26, and 58% at a concentration of 20% for the aromatic 100, 150, and 200 solvents respectively were observed. The relative changes in CO and UHC were significantly lower and somewhat negligible at the higher power condition (<30 ppm total). The increase in CO and UHC is attributed to the reduced combustion efficiency as the fuel aromatic concentration and molecular weight increases. These trends are consistent with those for the PN, as discussed previously. The carbon dioxide (CO₂) emissions slightly increased (1–5%) while the water emissions slightly decreased (<10%) with addition of aromatics and were comparable to those with JP-8. These trends were attributed to a decrease in the overall H/C ratio of the fuel with increasing blend concentration. The total nitrogen oxide (NO plus NO₂) emissions were not observed to vary with the aromatic solvents. This was anticipated since NO_x production is primarily thermally driven and the engine was operated at a constant turbine exit temperature (T_5).

Volume Swell Testing. The volume swell was found to be linearly dependent on fuel total aromatic concentration and solvent type for all materials evaluated. The volume swell as a function of total concentration and aromatic type are summarized in Figures 10–12 for nitrile rubber, fluorosilicone, and fluorocarbon, respectively. Volume swell measurements were previously made with these elastomers in ten JP-8 fuels which encompassed typical property range (aromatics from 14–24%).¹⁶ The data were then extrapolated to determine the 90% prediction intervals for an aromatic range from 10–25%; these lower and upper prediction intervals are also shown on the plots for reference. For the nitrile rubber, the volume swell was strongly influenced by hydrogen bonding, polarity, and molar volume. The Aromatic 100 and 150 solvents provided similar swell efficacy, which was slightly enhanced for the solvent blend. The swell with comparable total aromatic content was within that for typical JP-8s. However, the swell was significantly higher for the Aromatic 200, with typical JP-8 swell achieved with only approximately 5–10% total volume. These results imply that the overall swell is highly dependent on the naphthalene content within the fuel. For fluorosilicone, all of the FT/aromatic blends produced swells within the typical JP-8 swell range. This indicates that this material is weakly influenced by polarity and hydrogen bonding and primarily influenced by molar volume. The volume swell of the fluorocarbon material was slightly higher with the blends than that of “normal” JP-8s, but the absolute difference was minimal. In addition, there was no distinct trend for the solvents. In fact, the neat FT fuel appears to provide adequate swell for this material. This

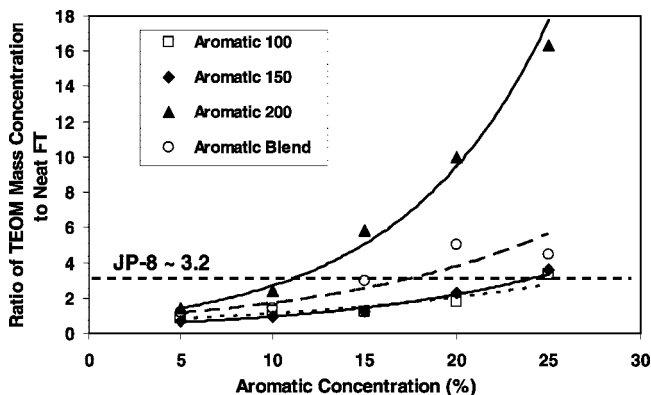


Figure 6. Comparison of the ratio of the TEOM mass concentration emission to neat FT fuel at engine idle as a function of aromatic solvent type and concentration.

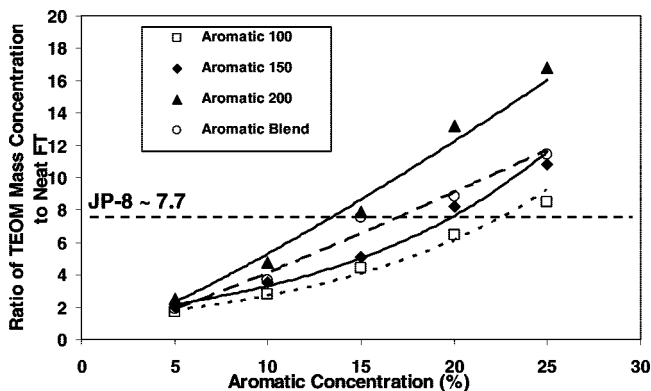


Figure 7. Comparison of the ratio of the TEOM mass concentration emission to neat FT fuel at engine cruise as a function of aromatic solvent type and concentration.

(16) Graham, J. L.; Minus, D. K. Investigation of the Utilization of Undiluted Fischer–Tropsch-Derived Jet Fuels and Mixtures of Fischer–Tropsch-Derived and Petroleum Derived Jet Fuels in Aviation Systems, Final Report, Department of Energy Contract No. DE-AI26-01NT41110, March, 2007.

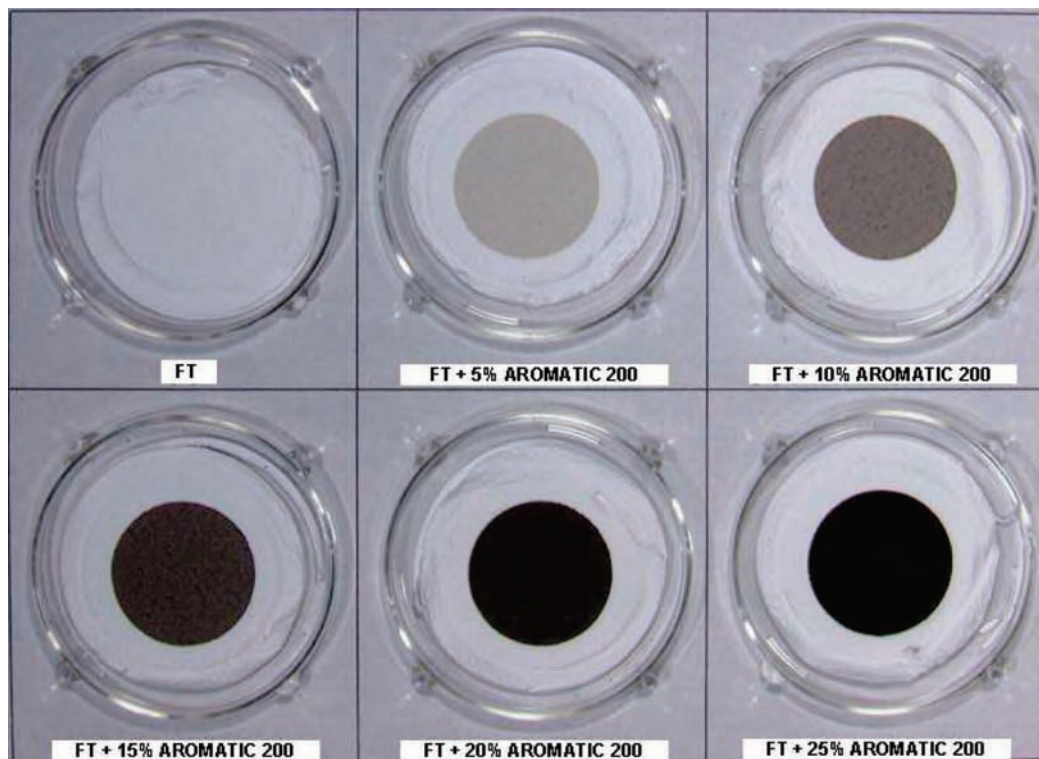


Figure 8. Comparison particulate samples collected for tests with Aromatic 200 at engine idle.

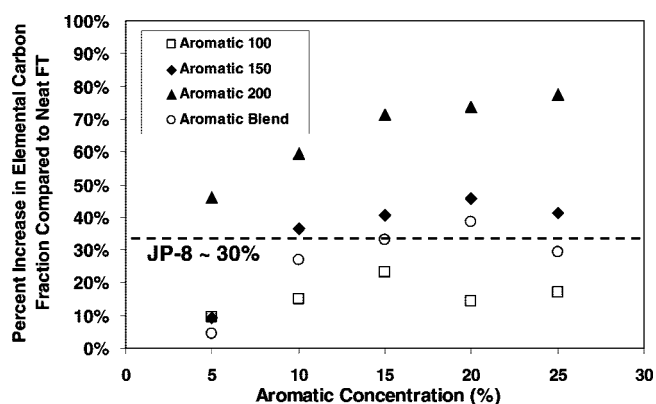


Figure 9. Percent increase in elemental carbon fraction of particulate emissions at engine cruise as a function of Aromatic solvent type and concentration.

elastomer is highly fluorinated and relatively inert, as evident by the very low percentage of volume swell.

Previous studies have shown that the partitioning of fuel components from the bulk fuel into polymeric materials (and hence contributing to volume swell) is a function of the molar volume of the fuel component and the nature of the intramolecular bonding of the polymer. In addition, it is a function of the interaction of the fuel component to the polymer, and the fuel component to the bulk fuel (i.e., the chemical physics of forming gel-phase polymer solutions).^{17–20} With respect to molar volume, partitioning tends to decrease within a given boiling

range as *alkanes* > *alkyl benzenes* > *naphthalenes*; therefore, diffusion processes dominated by molecular size should follow the inverse order. The effect of intermolecular bonding is highly material-specific and depends both on the polymer–polymer bonding and the fuel–fuel bonding. However, partitioning generally increases with the polarity and hydrogen donor ability of the fuel component. The latter can be strongly influenced by hydrogen acceptors in the polymer (which tends to increase partitioning) and in the fuel (which tends to decrease partitioning). Normal and branched alkanes are nonpolar and are inefficient hydrogen donors while the polarity of alkyl benzenes is variable and many can serve as weak hydrogen donors. The polarity of alkyl naphthalenes tends to vary to a greater extent than the alkyl benzenes and they can serve as more efficient hydrogen donors. Consequently, the partitioning of fuel components typically increases as:



However, the specific net effect on volume swell is a combination of many factors.

Relationship Between Volume Swell and Emissions. As observed, the composition and concentration of aromatic solvents added to FT fuel had a significant effect on the resulting emission production and corresponding elastomer volume swell. As previously discussed, it is desirable to satisfy required FFP properties while maintaining the operational benefits of the FT fuel. Therefore, determination of optimal aromatic concentration and type is needed. In general, the emission propensity and volume swell are inversely proportional; i.e., for a given blend concentration, the propensity of an aromatic component to impart swell increased with decreasing molar volume and the ability to serve as a hydrogen donor, especially in nitrile rubber, but also produced higher soot emissions. The relation for nitrile rubber can be observed in Figure 13. The PN data at idle are used as a reference for the engine emissions. The box corresponds to the 90% confidence limits for volume swell of typical JP-8s with an upper emission for the JP-8 used in this study.

(17) Flory, P. J. *Principals of Polymer Chemistry*; Cornell University Press: Ithaca, NY, 1953.

(18) Hildebrand, J. H.; Scott, R. L. *The Solubility of Nonelectrolytes*, 3rd ed.; Dover Publications: New York, NY, 1964.

(19) Schwarzenbach, R. P.; Gschwend, P. M.; Imboden, D. M. *Environmental Organic Chemistry*; John Wiley and Sons, Inc.: New York, NY, 1993.

(20) Miller-Chou, B. A.; Koenig, J. L. *Prog. Polym. Sci.* **2003**, *28*, 1223–1270.

Table 3. Comparison of Percent Increase in Carbon Monoxide and Unburned Hydrocarbon Emissions Relative to Neat FT Fuel at Engine Idle as a Function of Aromatic Solvent Type and Concentration

concentration	carbon monoxide			unburned hydrocarbon		
	Aromatic 100	Aromatic 150	Aromatic 200	Aromatic 100	Aromatic 150	Aromatic 200
5	6%	3%	7%	3%	7%	8%
10	7%	8%	14%	9%	14%	24%
15	8%	9%	27%	12%	19%	47%
20	9%	11%	32%	13%	26%	58%
25	9%	16%	41%	18%	31%	77%

As shown, it is possible to achieve typical JP-8 seal swell with different concentrations of the varying solvents. However, it can be observed that the swell can be achieved while maintaining particulate emissions below those observed for the JP-8. For example, the Aromatic 200 at 5% volume provided midlevel swell but was about 50–70% lower in PN and PM mass emissions than a typical JP-8. This is somewhat surprising since the total naphthalene content of the blend is 4.1%, which is above the current JP-8 specification limit (3.0%). The fuel

specification requires a naphthalene limit of 3% with a measured smoke point of 19.0 (ASTM D1322) or a smoke point of 25.0. Testing of blends showed measured smoke points of >40.0, 24.0, 20.0, 17.0, and 15.0 for concentrations of Aromatic 200 from 5–25%. Therefore, addition of slightly less than 10% Aromatic 200 should be capable of passing the fuel specification while still satisfying seal-swell with improved emissions characteristics. These results indicate that for petroleum-derived fuels, the relationship between naphthalene content and measured smoke point is also affected by the quantity and types of single-ring aromatic species. The desired swell characteristics can also be achieved using the lower molecular weight solvents

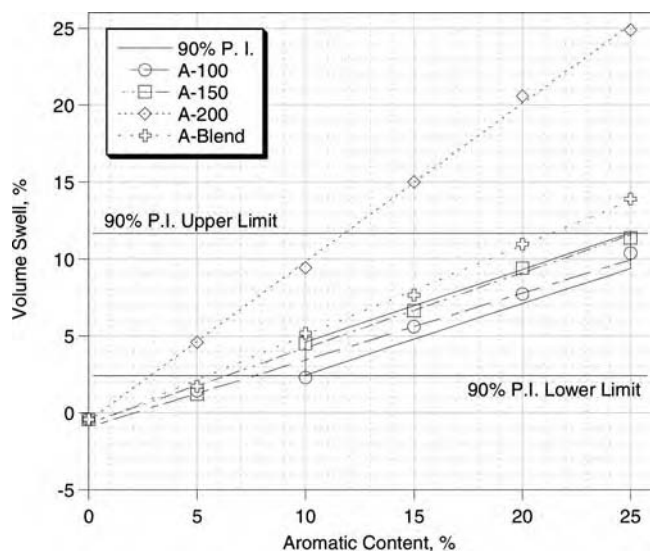


Figure 10. Comparison of the volume swell of nitrile rubber O-rings (Parker N0602) aged for 16 h at room temperature as a function of aromatic solvent type and concentration.

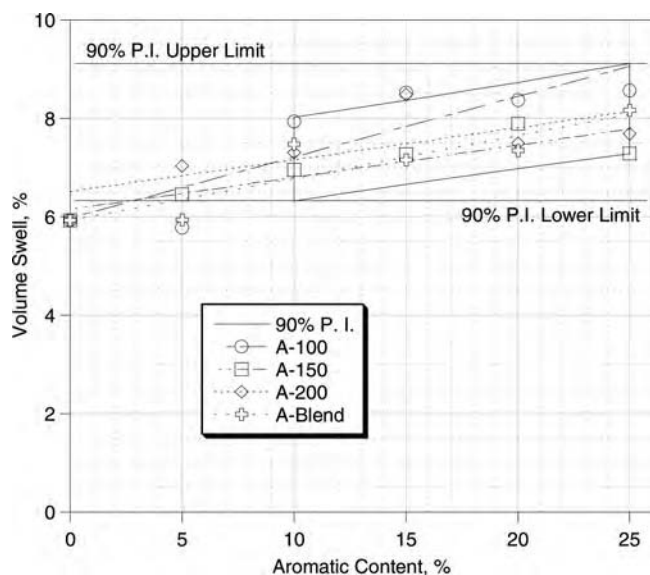


Figure 11. Comparison of the volume swell of fluorosilicone O-rings (Parker L1120) aged for 16 h at room temperature as a function of aromatic solvent type and concentration.

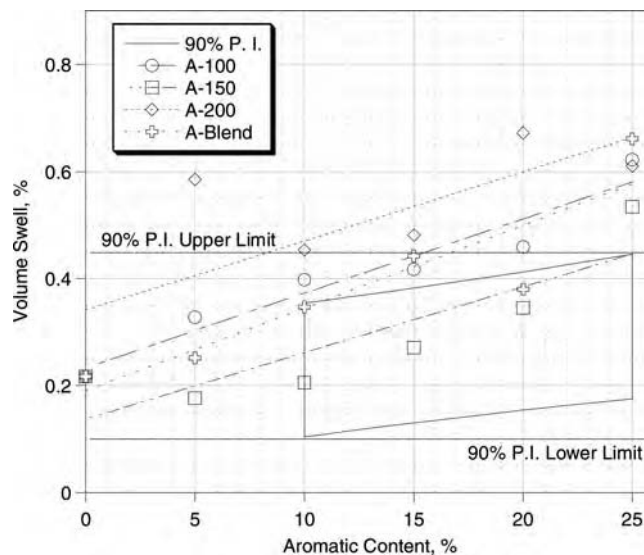


Figure 12. Comparison of the volume swell of fluorocarbon O-rings (Parker V0747) aged for 16 h at room temperature as a function of aromatic solvent type and concentration.

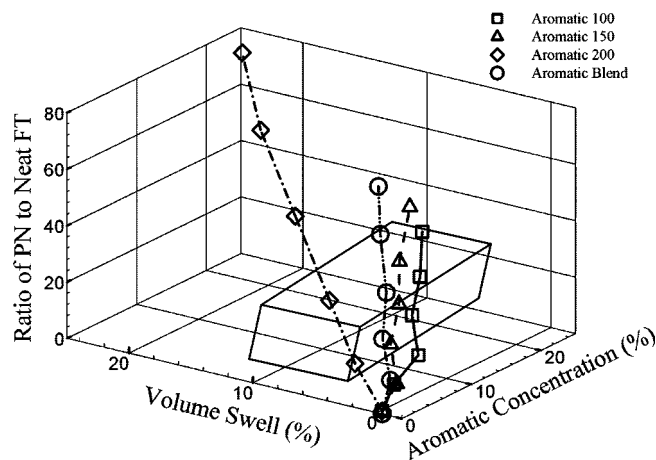


Figure 13. Comparison of the emission propensity (normalized particle number) at engine idle and volume swell of nitrile rubber O-Rings as a function of aromatic solvent type and concentration.

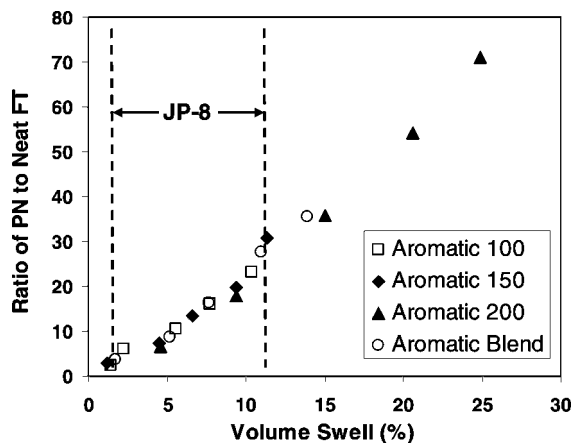


Figure 14. Interdependence of the emission propensity (normalized particle number) at engine idle and volume swell of nitrile rubber O-rings as a function of aromatic solvent type.

at concentrations greater than 10%, while significant emission reductions relative to JP-8 would still be possible.

The relationship between PM emissions and volume swell for the various aromatic solvents can also be considered via a comparison which is independent of solvent concentration. This comparison for engine idle is shown in Figure 14 with the corresponding volume-swell range for JP-8s. It is notable that the relation between PM emissions and volume swell appears to be independent of aromatic type. Obviously, the strong dependence on concentration exists (see Figures 4–13), but this comparison shows that if either the PM emission production or volume swell are known, it may be possible to predict the other. The applicability of this relationship may be limited to the types of solvents used in this study; therefore, comparison to other aromatic solvents and individual components is merited. This comparison at the cruise condition was similar to that shown in Figure 14, but the overall magnitude of emission increase was significantly lower (see Figure 5).

Summary

The use of synthetic fuels produced via the Fischer–Tropsch (FT) process for aviation applications has the potential to provide many operational benefits and reduce the dependence on foreign oil. However, required “fit-for-purpose” (FFP) properties, such as seal-swell and lubricity may need to be improved for ultimate implementation. In this effort, the feasibility of adding aromatic solvents was investigated as an option to achieve the FFP requirements, specifically for volume swell of elastomer seals. However, aromatics increase undesirable engine soot emissions. The extent to which these emissions increase was evaluated using a T63 engine fueled with FT fuel blended with several aromatic solvents. The studies showed that both the PM emissions and volume swell in nitrile rubber increased with

aromatic molecular weight and concentration. The emission increase was attributed to an increase in the seed molecule concentration for PAH formation (soot precursor), while the volume swell trends were attributed to decreasing molar volume and increased polarity and hydrogen-bonding potential. Results showed that the desired swell characteristics and relatively low PM emissions can be achieved with solvents evaluated in this study. The relationship between emission production and volume swell showed that all solvents considered within this study had comparable dependence. This relationship is important since both seal swell and PM production depend on the type of aromatics within the fuel, not solely on the total concentration. Therefore, improved understanding and development of strong correlations for these properties as a function of aromatic type allow for the possibility to predict these interdependent fuel-related characteristics. It would be highly desirable to determine the optimal aromatic type and concentration to provide required FFP properties while maximizing the beneficial properties of FT fuels.

Overall, this study provided an initial assessment and basis for subsequent evaluations of potential blend feedstocks. An ambitious goal is to identify a specific component which can provide volume swell at very low concentrations, which will require different classes of compounds to be considered. Future studies should evaluate additional elastomer materials and individual aromatic and other species while characterizing the emissions production on varying combustion platforms. In addition, the effect of the blend component(s) and concentration on the effect of fuel specification properties should be investigated. It is known that *iso*-paraffinic FT fuels such as the one in this study (specific gravity of 0.756) will most likely not satisfy the minimum required JP-8 specific gravity (0.775), blending with higher density aromatic solvents can increase the value to acceptable levels while still retaining beneficial operational properties.

Acknowledgment. The authors would like to thank Capt. Orvin Monroig for experimental testing with the aromatic blend solvent, Linda Shafer, Christopher Klingshirn, Mark Laber, and David Brooks of UDRI for their significant assistance with chemical analysis of the fuels and solvents and assistance with data collection and analysis, and Matthew Wagner of AFRL/PRTM for operating the T63 engine. This material is based on research sponsored by Air Force Research Laboratory under agreement number F33615-03-2-2347. The U.S. Government is authorized to reproduce and distribute reprints for governmental purposes notwithstanding any copyright notation thereon. The views and conclusions contained herein are those of the authors and should not be interpreted as necessarily representing the official policies or endorsements, either expressed or implied, of the Air Force Research Laboratory or the U.S. Government.

EF8001179

APPENDIX L
Characterization of Particulate Matter and Gaseous
Emissions of a C-130H Aircraft

INTENTIONALLY LEFT BLANK

Characterization of Particulate Matter and Gaseous Emissions of a C-130H Aircraft

Edwin Corporan and Adam Quick

U.S. Air Force Research Laboratory, Propulsion Directorate, Wright Patterson Air Force Base, OH

Matthew J. DeWitt

University of Dayton Research Institute, Dayton, OH

ABSTRACT

The gaseous and nonvolatile particulate matter (PM) emissions of two T56-A-15 turboprop engines of a C-130H aircraft stationed at the 123rd Airlift Wing in the Kentucky Air National Guard were characterized. The emissions campaign supports the Strategic Environmental Research and Development Program (SERDP) project WP-1401 to determine emissions factors from military aircraft. The purpose of the project is to develop a comprehensive emissions measurement program using both conventional and advanced techniques to determine emissions factors of pollutants, and to investigate the spatial and temporal evolutions of the exhaust plumes from fixed and rotating wing military aircraft. Standard practices for the measurement of gaseous emissions from aircraft have been well established; however, there is no certified methodology for the measurement of aircraft PM emissions. In this study, several conventional instruments were used to physically characterize and quantify the PM emissions from the two turboprop engines. Emissions samples were extracted from the engine exit plane and transported to the analytical instrumentation via heated lines. Multiple sampling probes were used to assess the spatial variation and obtain a representative average of the engine emissions. Particle concentrations, size distributions, and mass emissions were measured using commercially available aerosol instruments. Engine smoke numbers were determined using established Society of

Automotive Engineers (SAE) practices, and gaseous species were quantified via a Fourier-transform infrared-based gas analyzer. The engines were tested at five power settings, from idle to take-off power, to cover a wide range of operating conditions. Average corrected particle numbers (PNs) of $(6.4\text{--}14.3) \times 10^7$ particles per cm^3 and PN emission indices (EI) from 3.5×10^{15} to 10.0×10^{15} particles per kg-fuel were observed. The highest PN EI were observed for the idle power conditions. The mean particle diameter varied between 50 nm at idle to 70 nm at maximum engine power. PM mass EI ranged from 1.6 to 3.5 g/kg-fuel for the conditions tested, which are in agreement with previous T56 engine measurements using other techniques. Additional PM data, smoke numbers, and gaseous emissions will be presented and discussed.

INTRODUCTION

Aircraft emissions contribute to the degradation of air quality near airports and military bases. Emissions include particulate matter (PM), nitrogen oxides (NO_x), sulfur oxides (SO_x), carbon monoxide (CO), carbon dioxide (CO_2), and others. Because traffic at airports is expected to continue to increase, the impacts from commercial aircraft activities will likely exacerbate the local and global environments. Impacts at higher altitudes are also of concern because aircraft pollutants contribute to stratospheric ozone layer depletion, radiative forcing of climate change, and changes in tropospheric chemical composition.¹ NO_x and PM have been shown to contribute to the formation of photochemical smog in addition to undesirable health-related effects. In 1997, the U.S. Environmental Protection Agency (EPA) established a new air quality standard for airborne fine PM with diameter of 2.5 μm or less ($\text{PM}_{2.5}$). The $\text{PM}_{2.5}$ standard was established based on human health studies, which showed that the previous standard for PM with diameters of 10 μm or less (PM_{10}) was insufficient to address the harmful effects caused by these smaller particles. PM emissions from turbine engines are of particular concern because most are smaller than 2.5 μm in diameter. The more stringent environmental standards imposed by EPA have increased interest into the research and development of methodologies to better characterize and reduce PM emissions from combustion sources. Improved characterization of turbine engine emissions will increase the fundamental knowledge on the formation and oxidation of soot particles and

IMPLICATIONS

Aircraft emissions contribute to the degradation of air quality near airports and military bases. The more stringent environmental standards imposed by the U.S. Environmental Protection Agency may adversely impact commercial and military aircraft operations. Therefore, there is a need for reliable and accurate PM and gaseous emissions data from aircraft to properly estimate the environmental burden of aviation activities. However, standards for the measurement of PM emissions from turbine engines are lacking. In this effort, conventional aerosol instruments were used to assess their viability to measure PM emissions from actual military aircraft engines.

assist in the development of viable strategies for the reduction of undesirable PM emissions. Accordingly, robust techniques and instrumentation are needed to perform these difficult and tedious measurements from full-scale aircraft engines under actual operating conditions. The National Aeronautics and Space Administration (NASA), through several aircraft emissions research projects (many in collaboration with the Federal Aviation Administration [FAA], EPA, Department of Defense [DoD], academia, and industry), have made significant progress in advancing the knowledge of instrumentation and methodologies for improved reliability of particulate measurements from turbine engines.^{2,3} Recently, the Society of Automotive Engineers (SAE) E31 committee generated an Aerospace Information Report describing instruments and techniques that may be used for the measurement of nonvolatile particulate emissions.⁴ The ultimate goal is to develop techniques to generate reliable data and reduce the uncertainties associated with existing and future emissions inventories from military and commercial aircraft. To support this goal, the effort presented here focused on the characterization of gaseous and nonvolatile PM emissions of two T56-A-15 turboprop engines of a C-130H aircraft. The emissions campaign supports the Strategic Environmental Research and Development Program (SERDP) project WP-1401 to determine emissions factors from military aircraft.

EXPERIMENTAL SYSTEMS

Emissions Sampling System

Three particle (diluted) and three gas (undiluted) probes were used to extract engine exhaust samples for transport to the analytical instrumentation. The probes (separated by 3.18 cm center-to-center) were installed in a multi-probe rake (Figure 1) placed near the center and approximately 35 cm from the engine exhaust plane (measured horizontally from probe 6) to capture a "representative" sample of the engine exhaust and avoid diluting or contaminating with surrounding air. Although the exhaust nozzle of the T56 directs the flow at an angle ($\sim 60^\circ$ from

the horizontal), the probe rake was installed close enough to the nozzle to be exposed to nearly parallel flow. In addition, calculations for a nonparallel sample flow of 60° show negligible particle losses for this sampling configuration. The probe rake was mounted on a 15.2-cm diameter, 2.3-m long steel post supported on a stand restrained with three 300-gal water tanks to prevent movement during engine operation (Figure 2). For PM measurements, the exhaust sample was diluted with nitrogen at the probe tip to prevent water condensation and particle loss to the wall because of high wall-sample temperature gradients (thermophoresis). Sample dilution also prevented the saturation of the analytical instrumentation. Although the probes are designed to be water-cooled, they were operated uncooled for these tests because of leaks. Target dilution and total sampling flows (10 SLPM) were set using high precision Brooks 5850i flow controllers. Dilution ratios used for particle number (PN) and mass correction were determined using the ratio of the CO concentration of the diluted and undiluted streams. The sampling system was configured to allow for switching of sampling probes (2,4,6 particle and 1,3,5 gas) via fast-response ball valves to direct the sample from each probe to different instruments. The routing valves were installed in a heated box (150°C) located between the aircraft the instruments.

Because the required dilution varied based on the analytical instrument, two six-way valves fed with three dilution schemes (undiluted for the smoke sampler) were used to provide the desired dilution flow to the appropriate probe. All sample lines from the probe stand base to the valve box (16 m long) were kept at 150°C . The smoke and gas sample lines were maintained at 150°C , and the diluted particle samples were maintained at 75°C from the valve box to the instruments (~ 8.3 m long) to help maintain sample integrity. All emissions samples were drawn into the instruments via vacuum pumps. The inner diameter of the sample lines was 4.6 mm and total length from the aircraft to the instruments was approximately 25 m.

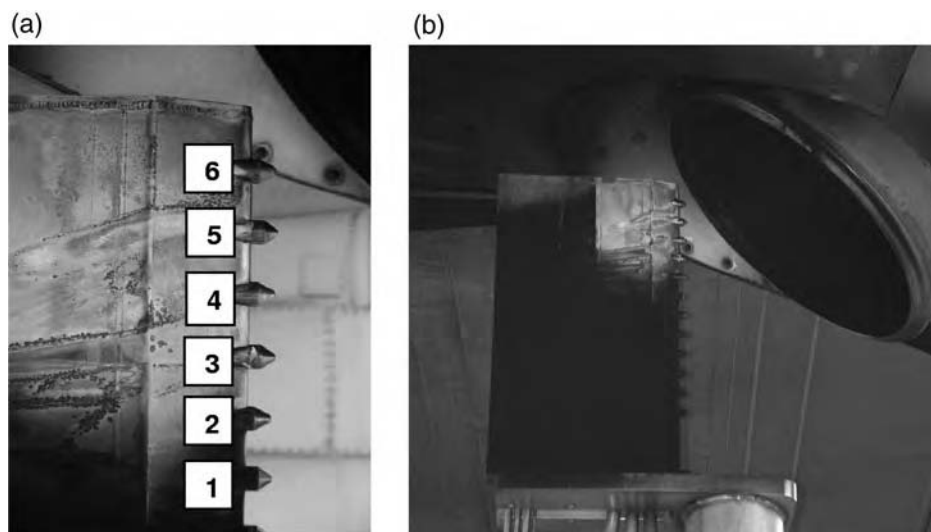


Figure 1. (a) Particle and gas probes mounted on a water-cooled rake. (b) Emissions rake installed approximately 35 cm from T56-A-15 engine exit plane.

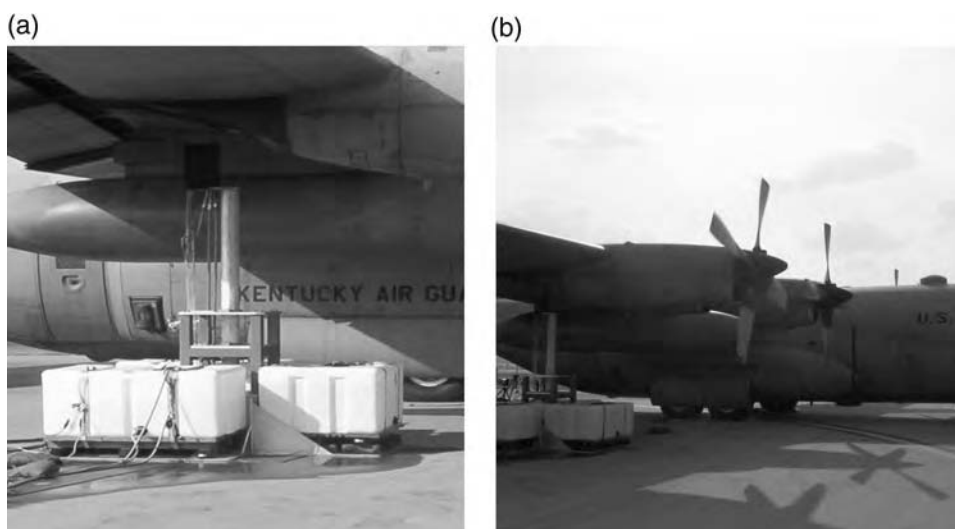


Figure 2. (a) Emissions rake and stand assembly used during C-130H emissions campaign. (b) C-130H aircraft at the Kentucky Air National Guard.

Instrumentation

The emissions instrumentation was transported to the test site and housed during the campaign in the U.S. Air Force Research Laboratory (AFRL)/RZTG (Fuels Branch–Turbine Engine Division) Turbine Engine Research Transportable Emissions Lab (TERTEL; see Figure 3). TERTEL is a mobile laboratory equipped with state-of-the-art instrumentation for the measurement and analysis of turbine engine emissions. Online analysis of the mostly nonvolatile PM emissions was performed using a TSI Model 3022A condensation particle counter (CPC) to provide a count of the total particles per unit volume (PN) and a TSI Model 3936 scanning mobility particle sizer (SMPS) to measure particle size distribution. For the SMPS, a long differential mobility analyzer (DMA) TSI Model 3081 with a Model 3022A CPC were used to classify and quantify the particles in the range of 7–300 nm in diameter. A Met One laser particle counter was used to measure particles larger than 300 nm in diameter. The contribution of these larger particles to particle concentration and mass was found to be negligible (<1%), and as such, is not reported herein. An in-house designed smoke sampler was used to collect

smoke samples on paper filters to determine engine smoke numbers (SNs). An R&P Series 1105 tapered element oscillating microbalance (TEOM) measured real-time total mass concentration of the nonvolatile particle emissions. The relatively high particle count from this engine required dilution ratios (nitrogen-to-sample) of approximately 10:1 to 25:1 for the CPC/SMPS and 6:1 for the TEOM. Gaseous emissions (except for total unburned hydrocarbons) were quantified using an MKS MultiGas 2030 Fourier-transform infrared (FTIR)-based gas analyzer.

JET FUEL CHARACTERISTICS

The Jet Propellant-8 (JP-8) fuel used during the campaign was evaluated using the ASTM specification conformance tests to verify that the fuel complied with all JP-8 specifications (MIL DTL-83133E) and to determine the concentration of recognized particle precursor species such as aromatics and sulfur. Table 1 shows the specification limits of several JP-8 properties, the mean property values of JP-8 fuel purchased by DoD in 2004,⁵ and properties of

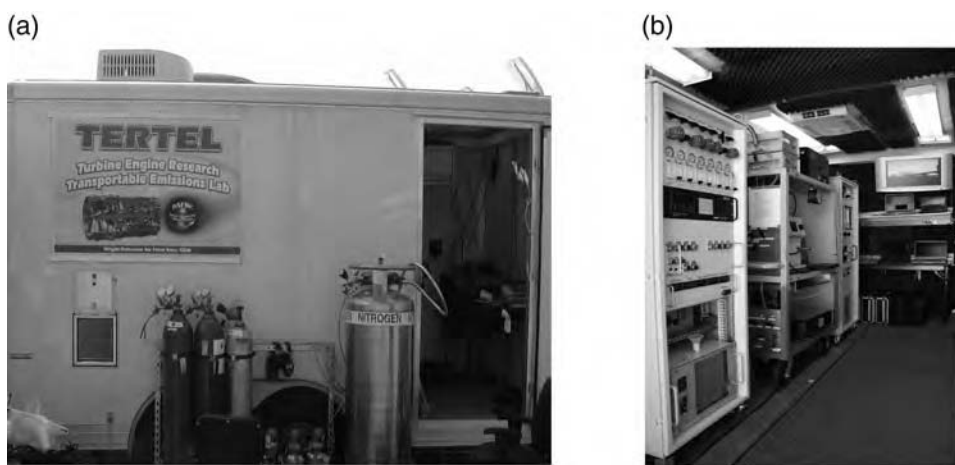


Figure 3. (a) The AFRL/RZTG TERTEL. (b) Instrumentation in the TERTEL for the measurement of gas and PM emissions.

Table 1. Results of fuel specification tests for average JP-8 procured in 2004 and fuel used in C-130H emission campaign.

ASTM Tests	Standard	Average JP-8 (CY 2004)	JP-8 Fuel (C-130 tests)
Aromatics, % volume (D1319)	Max 25.0	17.16	16.10
Total sulfur, % weight (D4294)	Max 0.30	0.062	0.090
Total acid number, mg KOH/g (D3242)	Max 0.015	0.0055	0.0020
Initial boiling point, °C (D86)	Report	159	171
10% Recovered, °C (D86)	Max 205	177	195
20% Recovered, °C (D86)	Report	183	201
50% Recovered, °C (D86)	Report	202	216
90% Recovered, °C (D86)	Report	238	240
Final boiling point, °C (D86)	Max 300	260	255
Distillation-residue, % volume (D86)	Max 1.5	1.0	1.2
Loss, % volume (D86)	Max 1.5	0.64	0.90
Freeze point, °C (D5972)	Max -47	-51.7	-47.0
Existent gum, mg/100 mL (D381)	Max 7.0	1.1	2.6
Viscosity at -20 °C, centistokes (D445)	Max 8.0	4.5	6.1
Naphthalenes, % volume (D1840)	Max 3.0	1.2	1.6
FSII (DiEGME), % volume (D5006)	0.10-0.15	0.12	0.13
Smoke point, mm (D1322)	Min 19.0	23.3	22.0
Flash point °C (D93)	Min 38	49.6	62.0
Heat of combustion, Btu/lb (D3338)	Min 18,400	18,500	18,582
Hydrogen content, % mass (D3343)	Min 13.4	13.8	13.8

Notes: KOH = potassium hydroxide; FSII = fuel system icing inhibitor; DiEGME = diethylene glycol monomethyl ether.

the fuel used in this campaign. As shown, the JP-8 passed the jet fuel specifications and has very similar properties to the average JP-8 procured by DoD in 2004.

TEST CONDITIONS AND PROCEDURE

The objective of this effort was to measure the C-130H emissions from two of the four T56-A-15 turboprop engines at typical operating conditions to characterize the aircraft emissions throughout its operating envelope. The test matrix used is shown in Table 2. Testing two engines increased confidence that the emissions were not unique to one particular engine. Engine nos. 3 and 4 (inboard and outboard on the aircraft's right wing) were evaluated. Testing started at the three low power conditions (idle) followed by cruise and maximum power. Six idle-to-maximum power cycles were completed during the campaign.

Operation at the cruise and maximum power conditions required running an engine on the opposite wing to maintain aircraft balance. For the idle conditions, only the test engine was operated. During the tests, the engines were allowed to reach steady-state before commencing data acquisition. Each test condition was run for approximately 30 min to provide sufficient time for multiple measurements of PN, size distribution, mass concentration, SN, and gaseous emissions from at least two probes.

TEST RESULTS

PM Emissions

PN. The raw PN (measurements from the CPC) for the conditions tested ranged from 8.0×10^5 to 4.4×10^6 . Random errors were usually less than 5% (1σ) for each test run (typically 180 scans), thus reflecting the steadiness of

the engine operation. Data reproducibility between multiple runs was observed to be highly dependant on the engine, engine setting, and probe used. The raw PN were consistently higher for probe 2 than for probe 4, which could be attributed to differences in exhaust velocity or particle concentration at each probe location. The raw PN repeatability was significantly worst (average of 21%) for the outboard engine (no. 4) than for the inboard engine (no. 3) (average error 9%), likely because of the larger degree of engine/wing movement as the fuel was consumed. For both engines, low-speed ground idle produced the least repeatable PN measurements. Differences in ambient temperature between test runs (up to 15 °C lower in the early morning runs) and their effect on the semi-volatile aerosols are believed to have contributed to the poorer data reproducibility.

Dilution-corrected PN of $(3.8-6.2) \times 10^7$ particles per cubic centimeter (no./cm³) were observed for both engines over the range of conditions tested. The PN were corrected for dilution by multiplying the measured PN by the ratio of undiluted (gas probe) to diluted (particle probe) CO concentration. The undiluted CO measurements represent the average from two probes, and were typically within $\pm 5\%$ (1σ). The dilution ratios were observed to vary significantly between engines, settings, and probes despite having the same settings for dilution flow rate. The high velocity (i.e., dynamic pressures) and highly turbulent flowfields at the probe tip appear to affect the sample flow through the probe and thus, the effective dilution ratio. Consistently higher dilution ratios were observed for probe 4 (15:1 to 25:1) than for probe 2 (11:1 to 20:1). The dilution ratios for the high power conditions were usually lower (i.e., higher particle

Table 2. Test matrix for C-130H emissions characterization.

Cycle No.	Run No.	Engine No.	Engine Condition	Percent Maximum Engine Torque (measured)
1	1	4	Low-speed ground idle	4
1	2	4	High-speed ground idle	7
1	3	4	Flight idle	20
2	4	4	Low-speed ground idle	4
2	5	4	High-speed ground idle	7
2	6	4	Flight idle	20
2	7	4	Cruise	41
2	8	4	Max power	100
3	9	4	Low-speed ground idle	4
3	10	4	High-speed ground idle	7
3	11	4	Flight idle	20
3	12	4	Cruise	41
3	13	4	Max power	100
4	14	3	Low-speed ground idle	4
4	15	3	High-speed ground idle	7
4	16	3	Flight idle	20
4	17	3	Cruise	41
4	18	3	Max power	100
5	19	3	Low-speed ground idle	4
5	20	3	High-speed ground idle	7
5	21	3	Flight idle	20
5	22	3	Cruise	41
5	23	3	Max power	100
6	24	3	Low-speed ground idle	4
6	25	3	High-speed ground idle	7
6	26	3	Flight idle	20
6	27	3	Cruise	41
6	28	3	Max power	100
7	29	3	Low-speed ground idle	4
7	30	3	Cruise	41
7	31	3	Max power	100
7	32	3	Low-speed ground idle	4
7	33	3	High-speed ground idle	7
7	34	3	Flight idle	20

penetration) than for the idle cases; however, trends of dilution ratio as a function of engine condition were inconsistent. The low-speed ground idle condition for engine no. 4 was the most erratic as dilution ratios varied from 18:1 to 110:1. This may be due to the influence of ambient conditions on semi-volatile particle concentration and variations in engine position. Despite the discrepancy of dilution ratios and raw PN, the corrected PN and profiles for each engine agreed reasonably well. Figure 4 shows the corrected PN as a function of engine power setting. These PN were also corrected for estimated particle losses in the sample line. The losses were based on a recent laboratory study conducted by the authors in which particle losses were observed to be between 40 and 60%, with the largest losses observed at the lowest engine power setting. Therefore, the average PN including the estimated line losses ranged from 6.4×10^7 to 14.3×10^7 no./cm³.

On the basis of measurements with probes 2 and 4, the particle concentration profiles were relatively uniform for all conditions. Because small variations in the engine fuel-to-air (F/A) ratios may have a significant impact on PM emissions, the PN emission indices (EI; number particles per kg-fuel) provide a more valid comparison of the particle emissions between engines and test conditions. The PN-EI were calculated using eq 1, derived from fluid flow fundamentals and the assumption that the molecular weight of the exhaust gases averages that of air (28.96 g/g · mol).

$$PN-EI = 2833 * PN_{corrected} * (1 + F/A) / (F/A) * T_{sample} / P_{sample} \quad (1)$$

where PN-EI is in number particles per kg-fuel, $PN_{corrected}$ is the corrected PN in no./cm³, T_{sample} is the sample temperature at the instrument in Kelvin (~293 K), P_{sample} is the sample pressure at the instrument in atmospheres (~1 atm), and F/A is the engine fuel-to-air ratio.

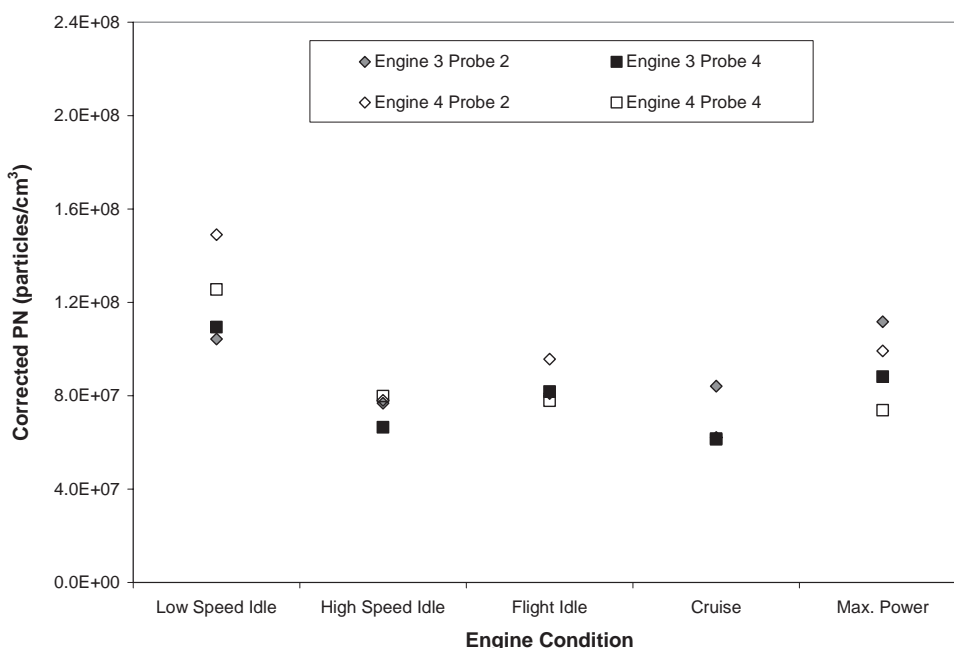


Figure 4. Corrected PN for engine nos. 3 and 4.

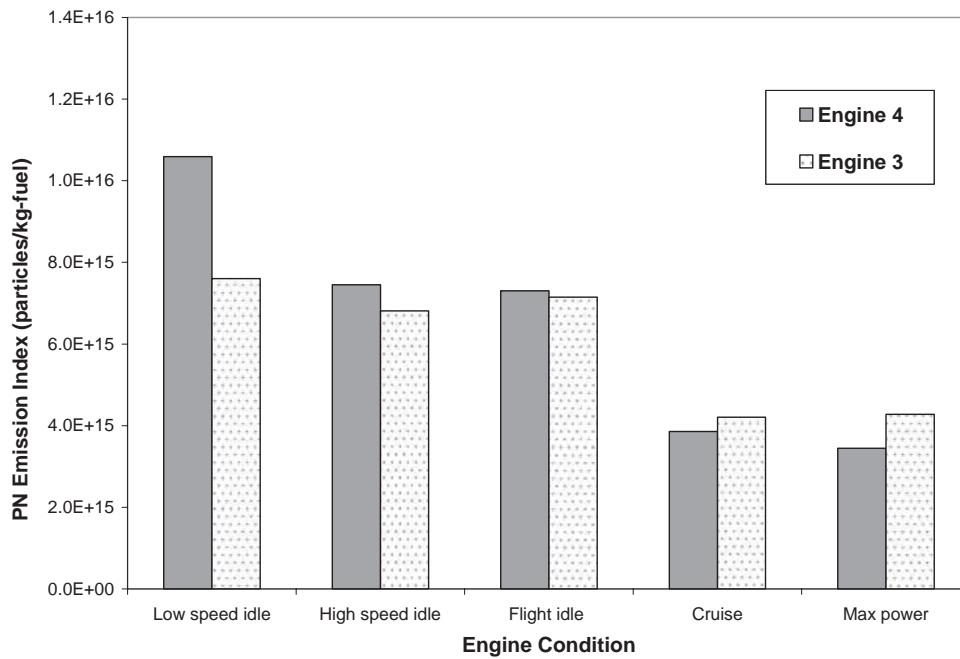


Figure 5. PN EI for each engine and condition.

The F/A ratios were calculated based on stoichiometry of the reactants and the primary gaseous products (CO and CO₂). Excellent agreement was observed between the F/A ratios for each condition for both engines and probes with ratios ranging from 0.0085 at high-speed idle to 0.021 at maximum power. The PN-EI (corrected for estimated line losses) for both engines are shown in Figure 5. Very good agreement between the particle emissions for both engines for all power settings was observed except for the low-speed idle setting. The PN-EI was moderately higher (40–50%) for the three idle conditions than for the two high power cases, which suggests improved combustion of soot particles and precursors (semi-volatiles). A

significant concentration of particles formed at the idle settings is believed to be semi-volatile aerosols from the incomplete combustion of fuel rather than actual soot nuclei particles. These particles appear to condense and grow to detectable levels in the probe and sampling line. As observed, the PN-EI were significantly lower (~25%) for engine no. 3 at the low-speed ground idle, the only condition in which the particle emissions between the two engines were significantly different.

Particle Size Distribution. The average particle size distributions for all test points are shown in Figure 6. These data

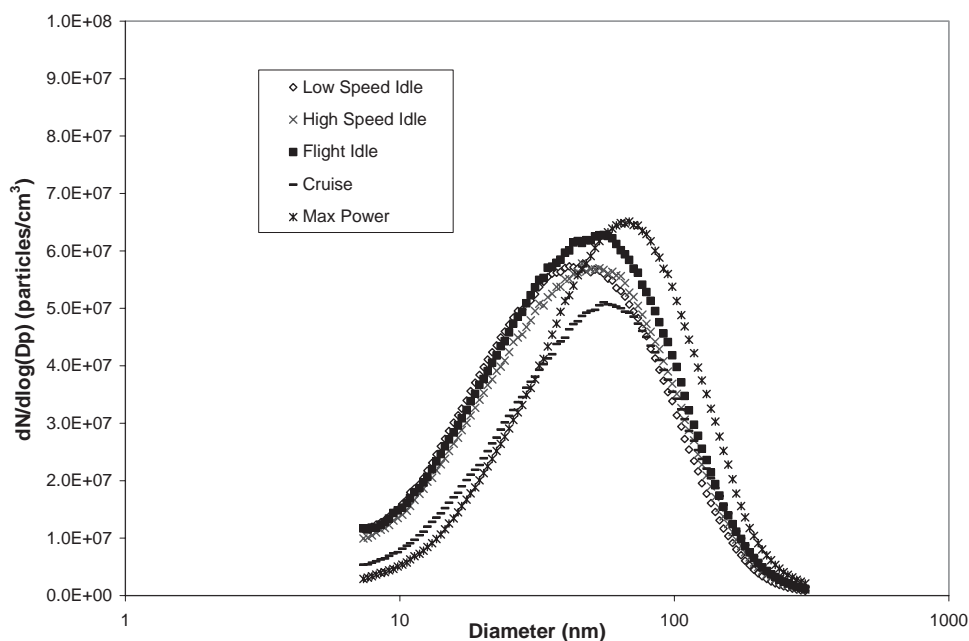


Figure 6. Average dilution-corrected particle size distribution for the T56 engines.

were not corrected for line losses because the shape of the distributions is not significantly altered by line losses. The size distributions follow a typical single mode lognormal profile with mean particle diameters between 50 and 70 nm. The size distribution curves shift to the right as the engine power increases, evidence of the production of larger diameter particles. The larger particles are likely the result of increased formation, growth, and agglomeration of soot nuclei as combustion temperatures increase. It also reflects the decrease of the smaller soot particles and semi-volatile aerosols via combustion. Excellent agreement was observed between the total particle counts (integrated number) with the SMPS and the CPC. For the inboard engine (no. 3), particle size distribution data for the three idle conditions were very repeatable ($\pm 9\%$) but poorer at cruise and maximum power. Consistent with the CPC, data reproducibility between runs was significantly poorer for the outboard engine because of engine movement during the SMPS analysis, which required approximately 200 sec/scan. However, despite the variability, the mean particle diameter remained relatively constant for each condition.

PM Mass Emissions. A TEOM was used to directly quantify the total PM mass emissions of the T56 engines. The sample was extracted using probes 2 and 6. A total sample flow rate of approximately 4 standard liters per minute (SLPM) was maintained during all tests with a target nitrogen dilution of 10:1 using mass flow controllers. The primary purposes for dilution were to obtain a measurement with sufficient sensitivity without loading the filter element too rapidly and to prevent condensation of water vapor and volatiles within the transfer line. The TEOM dilution ratio was calculated using the CO concentration of the diluted sample and the CO measurement while the

flow controllers targeted a 1:1 dilution. The CO concentration at a 1:1 dilution was used to estimate the undiluted concentration (i.e., multiply by 2) for each sampling probe. This approach was used to validate using the gas probe CO measurements for the correction because differences in CO values were observed as a function of probe position. In general, the average CO measurements using gas probes were in excellent agreement with the computed values using the 1:1 dilution ratio.

Dilution-corrected PM mass concentrations of 10–25 mg/m^3 were observed for the conditions tested. The total PM mass concentrations were lower for low-speed ground idle and relatively similar for all other conditions. Excellent agreement was observed for the measurements between probes and each engine except for low-speed ground idle. Overall, the data reproducibility for each engine setting was between 5 and 15% (1σ), with the largest deviation observed for the maximum power condition, likely because of extensive instrument vibration inherent at this condition.

Dilution-corrected PM mass EI averaged 0.9–2.2 g/kg-fuel. Considering the estimated losses in the sample transfer line, the corrected PM mass EI averaged 1.6–3.5 g/kg-fuel, which are in excellent agreement with those reported by Wade⁶ of 1.2 and 3.6 g/kg-fuel for a similar range of engine conditions, and significantly higher than those reported for a commercial engine.³ The agreement between these and previous results increase confidence that the techniques and instrumentation used in this study are viable for the measurement of PM emissions from turbine engines. Comparison of the corrected PM mass EI as a function of engine and power setting is shown in Figure 7. As observed, there was very good agreement between the mass emissions for both engines for all power settings. Except for the low-speed idle, the

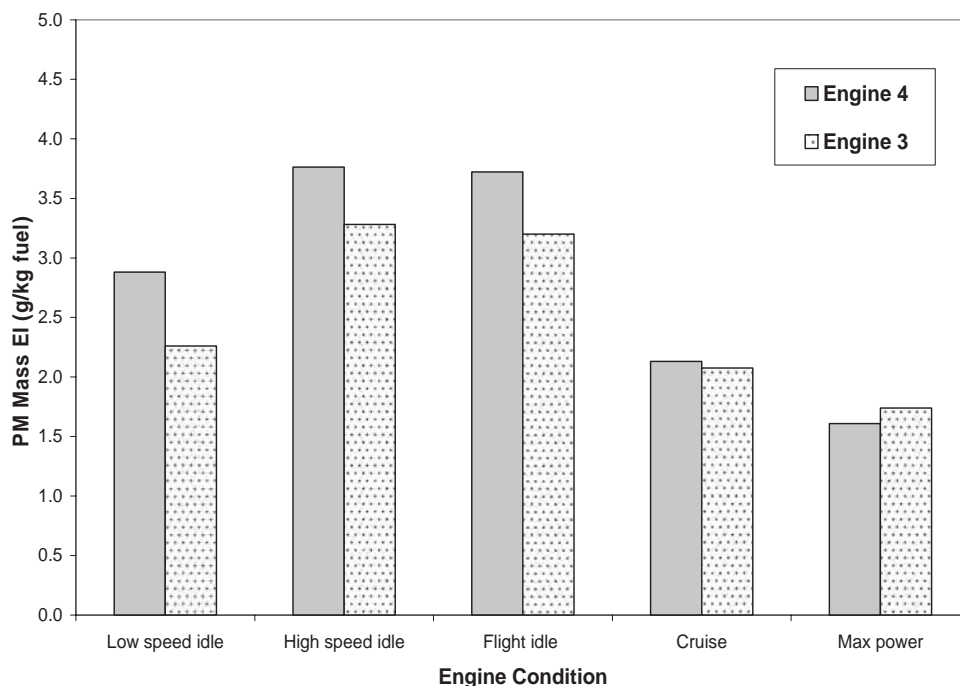


Figure 7. TEOM measured PM mass EI as a function of engine power and condition measured PM mass EI as a function of engine and power condition.

trends in the PM mass EI were consistent to those observed for the PN-EI (Figure 5). As previously discussed, the lower PM mass EI at the higher power settings is likely related to improved combustion efficiency at the elevated temperatures. The net effect is that although the engine releases an equivalent total concentration of particles there is a decrease in the relative production as a function of fuel usage. Of note is the relatively low PM mass EI for the low-speed idle considering that this condition produced the highest PN-EI. The relatively small contribution of the semi-volatile particles on mass may explain the low PM mass EI observed at this engine setting.

PM mass emissions can also be estimated using the aerosol size distribution data collected with the SMPS. The calculation requires assumptions for the soot particle geometry and density. Typically, soot particles within the submicrometer size range are assumed to have a spherical geometry. With respect to density, soot particles are composed of volatile polycyclic aromatic hydrocarbons ($\rho \sim 1\text{--}1.4 \text{ g/cm}^3$) to graphitic carbon ($\sim 2.2 \text{ g/cm}^3$), with the majority of the mature soot near the latter. However, the particles can contain significant voids that reduce the overall density. Therefore, a density value of 1.2 g/cm^3 was used as a compromise for these calculations. The average PM mass was calculated using the size distribution data (corrected for dilution and line losses) and by multiplying the total particle count by the mass contribution for each bin size. Relatively good agreement (better than $\pm 30\%$) was observed between the average mass concentrations measured with the TEOM and estimated with the size distribution. The variability for the SMPS data was observed to be higher than for the TEOM. It was expected that the general trends for both techniques would be consistent, but the similarity in the magnitude

for most cases was unanticipated considering the assumptions required for the calculation. Although good agreement was observed in these tests between the TEOM and size-distribution-based PM mass, the assumptions of particle geometry and density may produce significant error in the calculated mass. Therefore, direct mass measurement techniques (e.g., TEOM, filter gravimetric) are recommended to obtain more accurate and reliable measurements of PM mass.

SN. Engine SNs for each engine and condition were measured following the guidelines in the SAE ARP 1179.⁷ Undiluted smoke samples were collected on paper filters (Whatman no. 4) from probes 4 and 6, and the change in reflectance between the clean and stained filters were compared with determine the SN. The results, summarized in Figure 8, show excellent agreement between the SN for the two engines.

In general, the SN were very similar for all conditions at $SN \approx 42\text{--}45$ except the low-speed ground idle, which had a $SN \approx 31$. The smaller particles generated at the low-speed ground idle do not contribute significantly to the mass and SN, thus, yielding lower values of both. These results correlate very well with the absolute PM mass concentration trends measured with the TEOM. Although SN is considered to be the result of larger soot particles, these results suggest that even for PM with mean diameters as small as 50 nm, trends for PM mass and SN are similar if sufficient material is sampled.

Gaseous Emissions

Gaseous emissions were measured using an FTIR-based MKS Type MultiGas 2030 analyzer. The undiluted sample was drawn through probes 3 and 5 and transferred to the

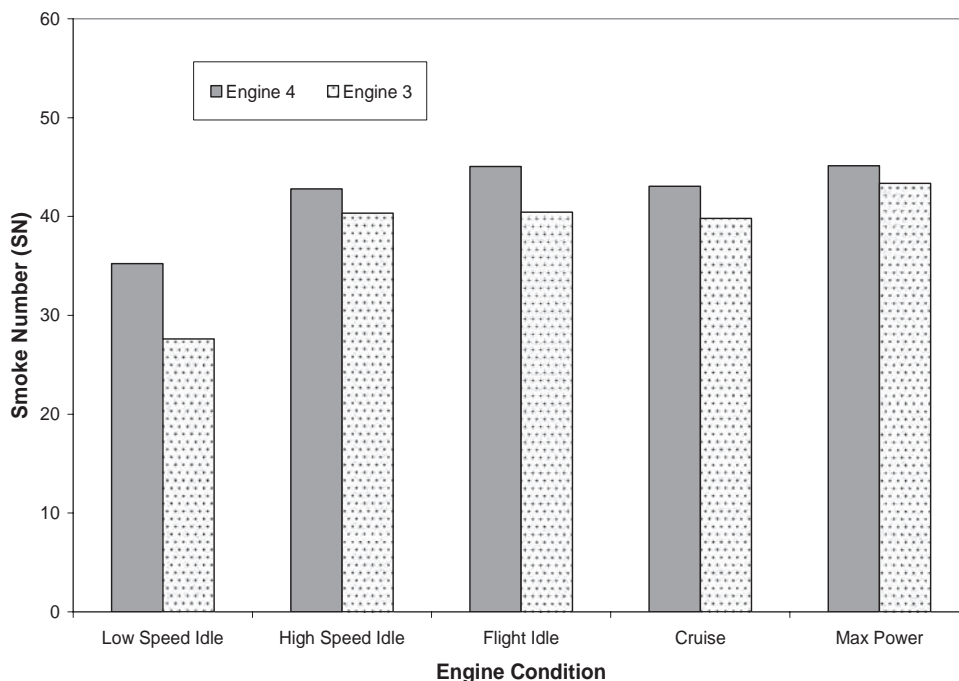


Figure 8. SNs as a function of engine power and condition.

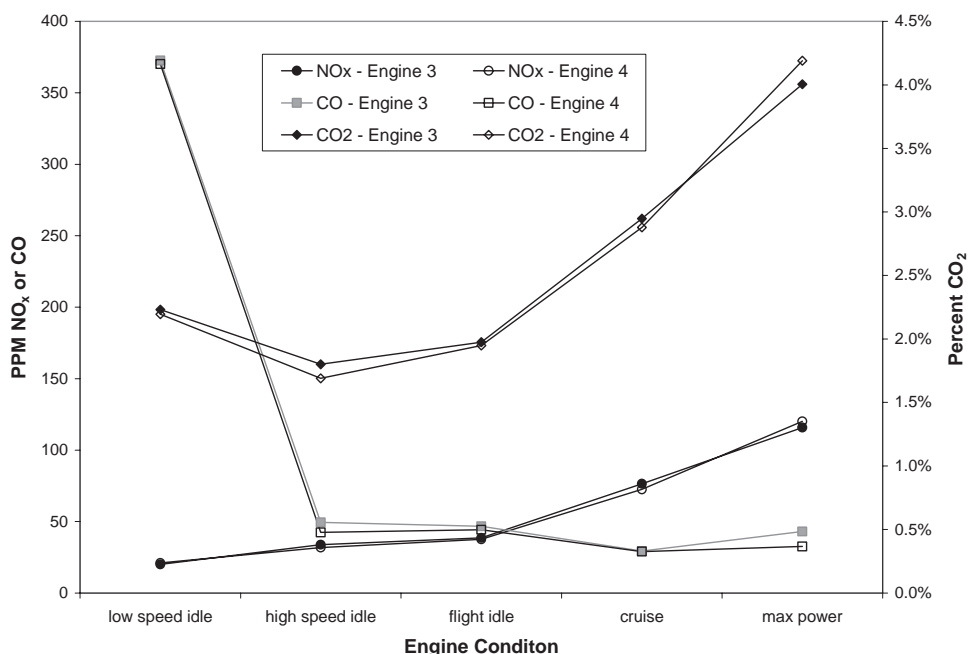


Figure 9. CO, CO₂, and NO_x emissions as a function of engine and power condition.

instrument via a heated sample line (150 °C) following the guidelines of the SAE ARP 1256.⁸ All emissions data are reported on a wet basis. Figure 9 shows the combustion species of interest (CO, CO₂, and total NO_x) as a function of engine condition. As shown, excellent agreement between the two engines was observed, which further demonstrates that both engines performed similarly.

At the low-speed ground idle, the CO concentrations were approximately 7 times higher than those observed at the other engine conditions, evidence of this being the least efficient condition. The concentrations of NO_x (sum of NO and NO₂) appear very similar for the idle conditions, and increase as the F/A (i.e., combustor temperatures) increase for the cruise and maximum power conditions. This behavior was expected because the primary route for NO_x formation is via thermal pathways. Table 3 lists the EI for CO and NO_x calculated following the SAE ARP 1533.⁹ The trends and values of these EI are in good agreement with those reported by Wade⁶ for the range of engine conditions. As expected, the absolute SO₂ emissions (not shown) were observed to vary directly with the fuel flow because of the increased concentration of fuel-bound sulfur reacting in the engine combustor. Unburned hydrocarbon species, inferred with the FTIR, showed the highest concentrations at low-speed ground idle and negligible concentrations for all other conditions. The total unburned hydrocarbons were not

quantified in this campaign because of problems with the flame-ionization detector (FID)-based hydrocarbon analyzer.

SUMMARY

The gaseous and PM emissions of two T56-A-15 engines of a C-130H aircraft were characterized. The exit plane measurements show that both engines yielded very similar and relatively uniform emissions profiles. Corrected PN_s of (6.4–14.3) × 10⁷ no./cm³ were observed, whereas the PN-EI ranged from 3.5 × 10¹⁵ to 10.0 × 10¹⁵ particles/kg-fuel. The highest PN were observed for the idle power condition, whereas the PN-EI was slightly lower for cruise and maximum power than for the idle settings. Particle size distribution curves followed a single-mode lognormal profile and displayed an increase in mean particle diameter as a function of engine power. The mean particle diameter varied between 50 nm at idle to 70 nm at maximum engine power. PM mass EI (corrected for line losses) ranged from 1.6 to 3.5 g/kg-fuel, which are in good agreement with previously reported measurements and significantly higher than for modern commercial engines. As expected, high concentrations of CO and unburned hydrocarbons were observed at the lowest engine power, which as anticipated was the least efficient condition.

In general, this emissions campaign successfully demonstrated the viability and reliability of conventional aerosol characterization instruments for the measurement of PM emissions from aircraft turbine engines. However, considering that the particle losses in the probe and sample line may be substantial, these must be determined (preferably experimentally) to improve the accuracy and reliability of the measurements. Although it is difficult to assess the accuracy of these measurements because of the lack of a standard, the consistent reproducibility of PM

Table 3. Average EI (g/kg-fuel) for gaseous pollutants for T56 engine.

Gaseous Pollutant	Low-Speed Ground Idle	High-Speed Ground Idle	Flight Idle	Cruise	Maximum Power
CO	32.9	5.5	4.7	2.0	2.0
NO _x	3.3	6.3	6.5	8.5	9.6

mass and PN measurements at all power conditions for both engines and the excellent agreement of the mass concentrations using two different techniques increases confidence that these instruments and sampling methods are adequate for the measurement of PM emissions from turbine engines.

ACKNOWLEDGMENTS

This work was a collaborative effort with Oak Ridge National Laboratory—Meng Dawn Chen, Principal Investigator—funded by the DoD SERDP office. The work of the University of Dayton Research Institute (UDRI) was supported by AFRL under the cooperative research agreement F33615-03-2-2347. Special thanks to SMSgt Wayne Ashley and SMSgt Gary Dunlap from the 123rd Airlift Wing at the Kentucky Air Guard for their technical and logistical support. The authors are also very grateful to Mark Laber, Joe Mantz, Scott Brietfield, and Ed Strader from UDRI and Tom Greene from Taitech Inc. for their technical support during the tests.

REFERENCES

1. Committee on Aeronautics Research and Technology for Environmental Compatibility, National Research Council. *For Greener Skies-Reducing Environmental Impacts of Aviation*; National Academy Press: Washington, DC, 2002.
2. Anderson, B.E.; Branham, H.-S.; Hudgins, C.H.; Plant, J.V.; Ballenthin, J.O.; Miller, T.M.; Viggiano, A.A.; Blake, D.R.; Boudries, H.; Canagaratna, M. *Experiment to Characterize Aircraft Volatile Aerosol and Trace Species Emissions (EXCAVATE)*; NASA TM-2005-213783; National Aeronautic and Space Administration; Langley Research Center: Hampton, VA, 2005.
3. Wey, C.C.; Anderson, B.E.; Hudgins, C.; Wey, C.; Li-Jones, X.; Winstead, E.; Thornhill, L.K.; Lobo, P.; Hagen, D.; Whitefield, P.; Yelvington, P.E.; Herndon, S.C.; Onasch, T.B.; Miake-Lye, R.C.; Wormhoudt, J.; Knighton, W.B.; Howard, R.; Bryant, D.; Corporan, E.; Moses, C.; Holve, D.; Dodds, W. *Aircraft Particle Emissions eXperiment (APEX)*; NASA TM 2006-214382 and ARL-TR-3903; National Aeronautics and Space Administration; John H. Glenn Research Center at Lewis Field, Cleveland, OH, 2006.
4. *Non-Volatile Particle Exhaust Measurement Techniques*. SAE Aerospace Information Report AIR 5892. Society of Automotive Engineers: Warrendale, PA, 2004.
5. *Petroleum Quality Information System 2004*; Defense Logistics Agency; Product Technology and Standardization Division; Defense Energy Support Center: Fort Belvoir, VA, 2004; available at <http://www.desc.dla.mil/DCM/DCMPage.asp?pageid=99>.
6. Wade, M.D. *Aircraft/Auxiliary Power Units/Aerospace Ground Support Equipment Emission Factors*; U.S. Air Force Report IERA-RS-BR-SR-2003-0002; Karta Technology: San Antonio, TX, 2004.
7. *Aircraft Gas Turbine Exhaust Smoke Measurement*. Society of Automotive Engineers (SAE) Aerospace Recommended Practice ARP 1179; SAE: Warrendale, PA, 1970.
8. *Procedure for the Continuous Sampling and Measurement of Gaseous Emissions from Aircraft Turbine Engines*. Society of Automotive Engineers (SAE) Aerospace Recommended Practice ARP 1256; SAE: Warrendale, PA, 1971.
9. *Procedure for the Analysis and Evaluation of Gaseous Emissions from Aircraft Engines*. Society of Automotive Engineers (SAE) Aerospace Recommended Practice ARP 1533; SAE: Warrendale, PA, 2004.

About the Authors

Edwin Corporan and Adam Quick are senior research engineers in the Propulsion Directorate at AFRL at Wright-Patterson Air Force Base, OH. Matthew DeWitt is a senior research engineer at the University of Dayton Research Institute. Please address correspondence to: Edwin Corporan, AFRL/PRTG 1790 Loop Road North, Wright Patterson Air Force Base, OH 45433; phone: +1-937-255-2008; fax: +1-937-255-3893; e-mail: edwin.corporan@wpafb.af.mil.

APPENDIX M

Combustion Performance and Emissions Characteristics for a Well-Stirred Reactor for Low Volatility Hydrocarbon Fuels

INTENTIONALLY LEFT BLANK

Combustion Performance and Emissions Characteristics for a Well-Stirred Reactor for Low Volatility Hydrocarbon Fuels

Scott D. Stouffer*

University of Dayton Research Institute, Dayton, OH, 45469

Robert Pawlik†

Air Force Research Laboratory, Wright-Patterson AFB, OH, 45433

Garth Justinger‡, Joshua Heyne§

University of Dayton, Dayton, OH, 45469

Joe Zelina**

Air Force Research Laboratory, Wright-Patterson AFB, OH, 45433

Dilip Ballal††

University of Dayton Research Institute, Dayton, OH, 45469

The performance and gaseous emissions were measured for a well-stirred reactor operating under lean conditions for two fuels: JP8 and a synthetic Fischer-Tropsch fuel over a range of equivalence ratios from 0.6 down to lean blowout. The lean blowout characteristics were determined in LBO experiments at loading parameter values from 0.7 to 1.4. The lean blowout characteristics were then explored under higher loading conditions by simulating higher altitude operation with the use of nitrogen to dilute the air. The results show that the two fuels have very similar combustion performance and lean blowout characteristics. Most of the differences observed in the emissions characteristics can be directly attributed to the difference in the C/H ratio of the two fuels.

Nomenclature

n_{air}	=	Flow rate of air (moles/sec)
EI	=	Emissions Index, g/kg of fuel
FT	=	Fischer-Tropsch Fuel
LHV	=	Lower Heating Value (J/kg)
MW	=	Molecular Weight
R_u	=	Universal Gas constant
slpm	=	Standard Liters Per Minute
UHC	=	Unburned Hydrocarbons

* Senior Research Engineer, Energy and Environmental Engineering Division, Senior Member AIAA.

† Chemist, AFRL/PRTC.

‡ Student, School of Engineering, Mechanical Engineering Department.

§ Student, School of Engineering, Mechanical Engineering Department.

** Senior Research Engineer, AFRL/PRTC, Wright Patterson AFB, AIAA Associate Fellow.

†† Division Head, Energy and Environmental Engineering Division, AIAA Fellow.

V	=	Reactor Volume
ϕ	=	Equivalence ratio
ρ	=	Density (kg/m^3)
τ	=	Residence time (ms)

I. Introduction

The fundamental understanding of pollutant formation coupled with new technologies will be required to produce cleaner burning, robust combustors and to offset the increased NO_x produced by higher combustor inlet pressures and temperatures. To develop advanced combustors in a cost-effective manner by true design-by-analysis approach requires validated unsteady aero design analysis codes that include transient combustion behavior and detailed chemical kinetics. Conventional design practice for combustion systems requires design iterations via expensive component rig testing because current state-of-the-art design codes cannot accurately capture the turbulent-chemistry interaction occurring in the combustor's complex flow environment. Therefore, experimental data from focused smaller-scale experiments to obtain the data for extension of current code capabilities is required.

The Well-Stirred Reactor (WSR) is a versatile laboratory research combustor that simulates the highly turbulent combustion process in a practical gas turbine combustor. The WSR has been used to study high temperature chemical kinetics of gaseous and liquid fuel combustion, combustion stability, lean extinction and blowout limits, and gaseous pollutants (NO_x, CO, and unburned hydrocarbons) and particulate emissions in previous studies.¹⁻⁵

Interest in alternative fuels has led to the consideration of the Fischer-Tropsch (FT) process for converting non-conventional hydrocarbon feedstocks into a practical gas turbine fuel. The FT process allows the use of non-conventional hydrocarbons by converting the fuel into synthesis gas (CO and H₂), which can then be converted to hydrocarbon fuel sources. The raw feedstock fuel for the process can be natural gas, coal or other sources. The Department of Defense is currently working with the Department of Energy to develop, test, and certify usage of the FT fuels leading to their use in military and commercial aircraft.⁶ The work reported in this paper examines the combustion performance, and emissions characteristics for a well-stirred reactor operating under steady lean combustion for JP8 and a synthetic Fischer-Tropsch jet fuel. Lean blowout limits and gaseous emissions while approaching lean blowout are also examined for the two fuels in the WSR.

II. Experimental Apparatus

The most important characteristic that separates the WSR from other premixed combustion systems is the high rate of continuous mixing of the products and incoming reactants. Ideally, for a "Perfectly-Stirred Reactor" the intense mixing will result in a uniform profile of species and temperature throughout the reactor. However, because of practical limitations on mixing and reaction rates, it is impossible to achieve a perfectly stirred reactor over the entire combustor. For example, in the immediate vicinity of the fuel/air jets there will be a higher fraction of incoming reactants than products of combustion. However, over most of the reactor volume the products and incoming reactants are well mixed. The high degree of mixing with the current design is evident by the high equivalence ratio associated with the soot inception limits and by the temperature profiles across the WSR cross-section measured in previous studies.^{3,5}

The 250-ml toroidal WSR, as designed by Nenniger et al.¹ and modified by Zelina² and later Stouffer³, was used for the current experiments. The photo in Fig. 1 shows the WSR rig during operation. A schematic cross section of the reactor and jet ring are shown in Fig. 1(b). The four key parts of the WSR system are: a vaporizer (not shown), the fuel-air injector ring, toroidal WSR combustor, and the plug flow exit section. The two halves of the WSR fit around the jet ring assembly to form the toroidal WSR combustor section. A variety of ceramic and metallic materials have been used for the WSR fabrication in previous studies, and the material used depends

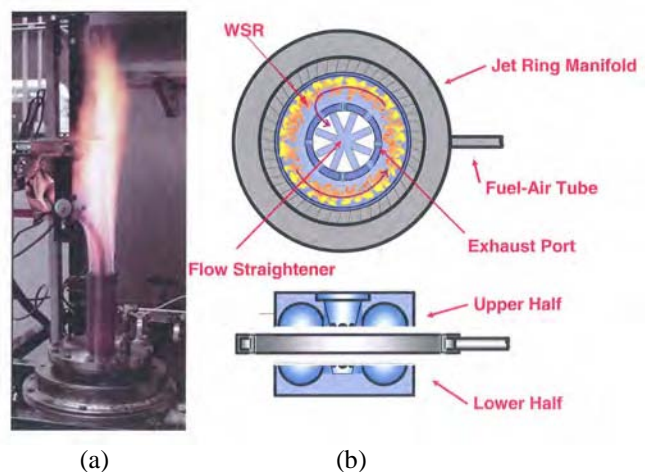


Figure 1. (a) The Well-Stirred Reactor shown during operation, (b) Cross-section of the WSR.

on the anticipated test conditions. For the current experiment the desire was to operate the combustor under fuel-lean conditions with minimal heat loss through the walls, and so fused-silica ceramic was used for the reactor walls because of its low thermal conductivity, to reduce heat loss, and its low thermal expansion coefficient, which helps to reduce cracking under the fast thermal transients associated with blow out. The Inconel jet ring has 48 fuel/air jets of 0.86 mm diameter that are used to inject the pre-vaporized/premixed reactants at high subsonic or sonic velocity from the outer radius of the toroidal WSR combustor. At low flow rates, the jet ring is cooled by nitrogen impingement to avoid autoignition of the fuel-air mixture within the jet ring manifold. It was found that as the total air flow to the reactor was increased, the need to actively cool the jet ring was reduced. For the experiments, a 6 g/min nitrogen cooling flow rate was used to purge the steel reactor housing. In the reactor, the high velocity reactants continually stir and mix with the combusting gases producing high turbulence and mixing levels in the reacting flow field. The WSR has several access ports for temperature, pressure, and emissions samples, located at the bottom of the WSR. Oil-cooled gas-sampling emissions probes are used for extracting emissions from the reactor. The mixture is then exhausted through eight radial ports at the toroid inner diameter, and turned and straightened before entering the 5-cm diameter plug flow reactor (PFR), where additional measurements can be made.

A facility schematic, shown in Fig. 2, identifies components and instrumentation used for operation of the rig and acquisition of emissions. Air and gaseous fuel flow rates are measured and controlled using thermal mass flow controllers. The uncertainty of the gas flow measurements was +/- 1.5%. The fuel system uses a three-diaphragm pump to continuously supply the fuel mixture to a combination of several pulse dampers and regulators to create a steady pressure source from the pulsing pump. Two parallel control valves, a coarse manual valve and fine adjustment valve are used to control the flow measured by a constant displacement piston flow meter using a PID loop for controlling a fine control valve. The piston flow meter is accurate to within +/- 0.5%, and the estimated overall uncertainty of the liquid flow measurement including calibration was +/-1.4%.

PID-controlled electric heaters heat the fuel and air streams entering the reactor. The liquid fuel was sprayed into the vaporizer using an air swirl atomizer nozzle, which uses approximately 10-20% of the total air consumed in the reactor as vaporizer nozzle air to atomize the fuel. The rest of the air (main air) consumed in the reactor was added as a coaxial stream in the vaporizer. The combination of the fuel temperature (~420K), main air temperature (~470-490K), vaporizer nozzle air temperature (~430-460K), and the flow rates were used to control the temperature of the air-fuel mixture entering the reactor. The temperatures of both the fuel and the air were at all times below the known autoignition limits of JP8 fuel. The autoignition limit of the FT fuel was not known but it was assumed that it was between that of JP8 and heptane.

Proper vaporization of all of the lower volatility hydrocarbons is a particular concern for the experiment. The temperature levels of the fuel and air were sufficient to maintain the temperatures of the flow entering the jet ring of the reactor at temperatures above 444K which was above the maximum estimated dew point (404K) of the JP8 mixtures used in the study. As evidence of vaporization it should be noted that the reactor and vaporizer has been used for long duration materials testing experiments which included multiple continuous 12-hr periods of operation on JP8 fuel. During these long-duration experiments, the pressures at the jet ring, and the vaporizer were continuously monitored to assess any potential problems caused by condensation/coking in a filter and check valve located in the line between the vaporizer and the jet ring. The absence of any pressure changes upstream of the reactor at constant flow rates has served as a secondary check for vaporizer effectiveness.

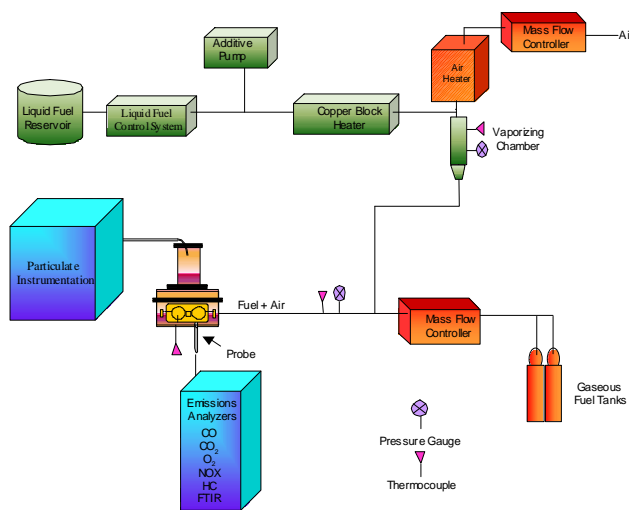


Figure 2. Well Stirred Reactor Air, Fuel and Instrumentation Systems.

A retractable spark igniter was used to initiate combustion within the reactor. When the reactor is operated on a liquid fuel, it is first started on a gaseous fuel (usually ethylene) and allowed to warm-up to operating temperatures to prevent fuel condensation in the small passages of the jet ring. After allowing the reactor to warm up to operational temperatures, the fuel is smoothly transitioned from a gaseous fuel to a liquid fuel.

Two fuels; JP8 and S8 Fischer-Tropsch were studied and their properties are shown in Table 1. JP8 is the standard fuel used in U.S. military aircraft. Syntroleum Corporation of Tulsa, OK,

produced the S8 fuel from a feedstock of natural gas. However, because the initial step in the fuel manufacturing is to produce synthesis gas, which is then converted to the jet fuel, the properties of the FT fuel considered here are similar to those that would be made by the FT process using other feedstocks, such as coal. The FT fuel is primarily composed of normal and branched alkanes, in contrast to JP8, which can have significant (10-24%) aromatic content. As shown in Table 1 many of the properties of the S8 are similar to those for JP8. A noted disadvantage of the FT fuel is the lower density, which is partially offset by its increased heat of combustion. Further investigations of the properties and of FT and JP8 fuels are discussed in Refs. 6-9.

Table 1. Properties of the JP8 and FT Fuels

Property	JP8 (3773)	FT (5018)
Molecular Formula	C _{11.9} H _{22.8}	C _{11.9} H _{25.9}
H/C ratio	1.916	2.165
Stoichiometric Fuel/air	0.0682	0.0666
Molecular Weight	165.9	169.5
Density (g/ml)	0.80	0.755
Heat of Combustion (J/kg)	43276	44135
% Aromatics	17.2	0
Freezing Point (°C)	-51	-51
Flash Point (°C)	45	48

A. Instrumentation

The reactor temperature was measured by a bare wire type B thermocouple (0.2 mm diameter) which was placed at a distance of 4.8 mm up from the bottom of the toroidal reactor section. The radial position of the thermocouple in the toroid corresponds to the position of 50% of the cross-sectional area of toroid. Facility operation was monitored using thermocouples in the air lines, WSR jet ring, inlet, reactor, housing, and stack. The pressure rise in the reactor was determined using an absolute pressure transducer.

The gaseous emissions were sampled from an oil-cooled probe placed at an equivalent position from the emissions sampling probe, which was located 90 degrees around the major axis of the toroid and at the same height (4.8 mm) from the bottom of the reactor as the thermocouple. The outer diameter of the cooled probe was 9.5 mm. The probe was constructed of stainless steel and had an inner tube with a diameter of 1.27 mm that was used to extract emission gases and was surrounded by two concentric tubes that formed a cooling jacket around the probe. A circulating oil heater is used to cool the emissions probes to a temperature of 420 K. Electrically heated sampling lines, maintained at above 150°C, were used to transport samples to the emissions instrumentation.

Gaseous emissions analyzers were used for on-line measurement of CO, CO₂, NO_x, O₂, and unburned hydrocarbons within the reactor and water and minor species were measured by the use of a multigas FTIR. A sketch of the sample train is shown in Fig. 3. Flow from the probe was sent to either the FTIR or the rest of the analyzers shown on the right side of Fig. 3. With the setup it was possible to sample to either the FTIR or the other

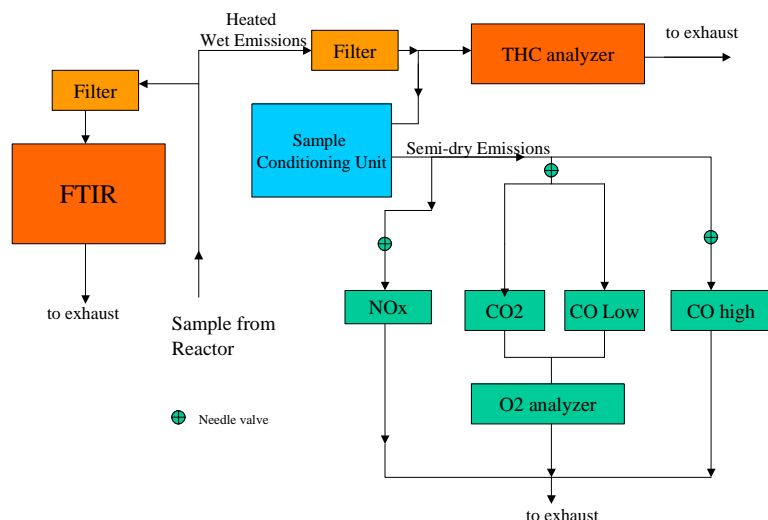


Figure 3. Sample Train for Gaseous Emissions Measurements.

analyzers, but not to both sets of instruments simultaneously. Each of the analyzer trains had a filter in series with it for protection from particulate matter. The volume associated with the filters caused a lag in the time response of the analyzers.

The FTIR system used an MKS 2030 with a 5.11-m long gas cell path length. The analyzer is heated and allows online detection of major gaseous species along with subsequent detailed investigation of the spectra saved. It is capable of measuring species of CO, CO₂, H₂O, NO, NO₂, and other compounds that absorb infrared radiation. Flow to the FTIR was limited to 1-2 lpm. At the lowest reactor flow rates (lowest reactor pressures) an

ejector mounted on the exhaust side of the FTIR was used to pull gas through the analyzer. This typically lowered the pressure in the analyzer by less than 0.02 atm. At higher reactor flow rates the pressure in the reactor was sufficient to push the gas through the analyzer. Uncertainty for the FTIR measurements was typically +/- 3%.

The emissions train for the rest of the instruments is shown on the right side of Fig. 3. The unburned hydrocarbons were measured using a heated Flame Ionization Detector (FID) analyzer (VIG model 600), which measures the unburned hydrocarbons on a wet basis. The analyzer had adjustable ranges of 100 to 100000 ppm propane. The rest of the sample stream was routed to a sample conditioning unit, which consists of a pump and a chiller-based sample dryer that dried the sample to a dew point of roughly 5°C before allowing the semidry sample to flow to the other analyzers, which were arranged in a parallel-series arrangement. The CO₂ and CO were measured by a three-cell non-dispersive infrared analyzer (California Analytical model 600). There are two CO cells, a low concentration cell, which has a maximum range of 3000 ppm, and a high CO that was set at a range of 2%. A paramagnetic analyzer (Horiba MPA) was used to measure the oxygen. Repeatability for the gas analyzers was within +/-1% over the course of a day and the calibration gases used to set the span of the analyzers were certified to +/- 2%.

The response time of the analyzers to a fast transient such as a lean blowout was an issue during the study. The requirement to continuously pass the emissions through sample volumes associated with the filters and sample-conditioning units slows the time response of the system. Another consequence of the finite time response of the sample system components is that the time response of each of the analyzers may be different. Because of the finite volumes associated with the system the measurement from an analyzer is a running time average of the emissions produced in the combustor, which is not an issue for the characterization of steady operation, but it presents limitations on capturing fast transients. Fig. 4 shows the response of the sample train to a typical blowout. The blowout event (at time = 0 s) is marked by a steep decrease in the temperature in the reactor. The UHC analyzer was the first to respond to the blowout, which is expected because of its faster response time (5 seconds), shorter length to the source, and smaller system volume. The rest of the analyzers have slower response times and have the added system volume associated with the filters and the sample-conditioning unit, resulting in a slower overall response. The response of the FTIR analyzer (not shown) was typically within 16-24 seconds of an event in the reactor. The results reported as blowout conditions from the sample train are those that occur at the time of blowout as indicated by the reactor temperatures.

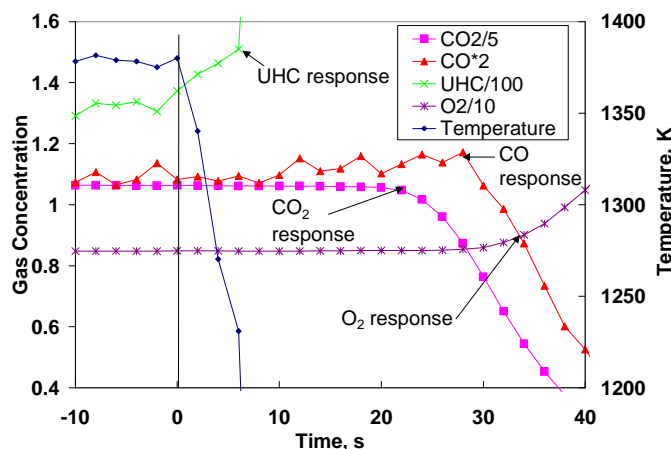


Figure 4. Time Response of the Emissions Analyzers During a Typical Lean Blowout.

B. Experimental conditions

During the experiments, the reactor was operated under a range of air flow rates from 300-600 g/min (250 to 500 slpm). The fuel/air mixture entering the jet ring was held to a constant temperature of 444 +/-6 K, and the pressure ratio across the injector ring nozzles was greater than 2, implying from one-dimensional compressible flow theory that the flow across the nozzles was choked and that the fuel/air mixture entering the WSR was sonic. The fuel flow was varied to obtain the desired equivalence ratio for the two fuels. All of the penetration paths to the reactor are sealed allowing the reactor to maintain a pressure slightly (1-3 kPa) above ambient pressure.

For the emissions measurements the air and fuel flows were established at the levels required and the reactor temperature was allowed to level out before taking emissions data. Emissions data were taken for a fixed experimental condition using both the FTIR and the other analyzers in sequence.

The lean blowout tests were conducted by gradually reducing the fuel equivalence ratio at fixed air flow rates until the flammability limit was reached in the reactor. A lean blowout was noted to correspond to an immediate drop in temperature of the reactor and usually coincided with a sharp change in the noise generated by the reactor. After the lean blowout in the reactor the fuel flow was diverted from the vaporizer, the reactor was then re-lit using

lower liquid fuel and air flow rates. Typically two to four separate LBO events were measured for each fuel at a given air flow rate.

III. Experimental Results

The experimental results for combustion performance and emissions that will be presented were determined for two constant air flow rates 300 g/min and 600 g/min.

The average residence time, τ , is defined by the following equation:

$$\tau \equiv \frac{\rho V}{\dot{m}}, \quad (1)$$

Where V is the reactor volume, \dot{m} is the mass flow and the density, ρ , is calculated by the ideal gas law,

$$\rho = \frac{P(MW)}{R_u T}, \quad (2)$$

The pressure and the temperature were measured during the experiments and the molecular weight of the products was estimated from equilibrium values. For the range of lean combustion conditions explored in this study, the changes in the molecular weight and reactor pressure are small, so that the variations in the residence time are principally caused by changes in the reactor temperature and mass flow. At the highest air flow rates studied (600 g/min) the residence time ranged from 6.3 ms near lean blowout to 5 ms at $\phi = 0.6$, while the residence time was approximately twice as much for the lowest air flow rates (300 g/min) studied. For the plots shown below blue is used to indicate the results for the FT fuel and red for the JP8 fuel. Also, squares are used to indicate the lower flow rate (higher residence time) and the triangles are used to show the results for the higher mass flows (lower residence times).

One of the primary measures of combustor performance in the WSR is the temperature in the combustor. Figure 5 shows the temperatures in the WSR. As expected, the temperature increased with the increases in equivalence ratio. The temperatures show close agreement for both fuels at the two flow rates. For equivalence ratios at or above 0.45, the reactor was operated at point for long periods of time and multiple 30-second averages of temperature and emissions were measured using both sample trains. At equivalence ratios less than 0.45 the reactor equivalence ratio was gradually lowered toward lean blow out and the data points shown also represent 30-second averages. But, for the points below $\phi = 0.45$ the reactor was not held at the same condition for as long, and it is thought that the non-equilibrium between the gas temperature and the wall temperature, as the reactor was cooling down, may be responsible for the small scatter in the WSR temperature data at the lower equivalence ratios.

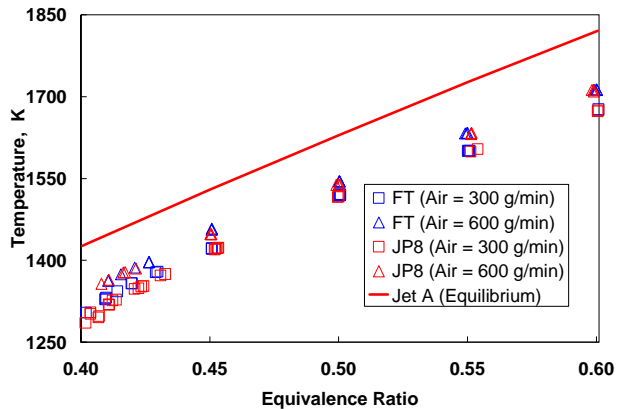


Figure 5. Temperatures Measured in the WSR.

The temperature results are also compared to equilibrium calculations of the adiabatic flame temperature from the NASA Chemical Equilibrium Code.¹⁰ The difference between the experimental temperatures and the calculated adiabatic flame temperature were highest for the lower flow rate conditions implying that the effect of heat loss was less for the higher flow rate cases.

The measured O_2 and CO_2 data are shown plotted along with the equilibrium values for JP8 and the ideal concentration for the FT fuel in Figs. 6 and 7, respectively. The overall results show the expected increased oxygen consumption and CO_2 production as the equivalence ratio is increased. It was found that with both of the fuels the CO_2 production was higher and the O_2 consumption was higher at the higher mass flow cases. This result is also consistent with trends of temperature vs. mass flow observed in Fig. 5. The CO_2 observed for the JP8 was higher than that for the FT fuel, which was expected based on the higher carbon fraction for the JP8 fuel. For $\phi > 0.5$ the

ratio of the CO_2 produced for the JP8 to that for the FT ranged from 1.033-1.044, while the ideal ratio of the CO_2 produced under complete oxidation to CO_2 and H_2O for the two fuels was 1.044. For the higher equivalence ratios shown the results parallel the ideal limits, but as lean blowout was approached the oxygen consumption and CO_2 production depart further from the ideal limits. The departure from the ideal as lean blowout is approached is also consistent with the temperature trends shown above; as less CO_2 is formed the combustion temperatures decrease.

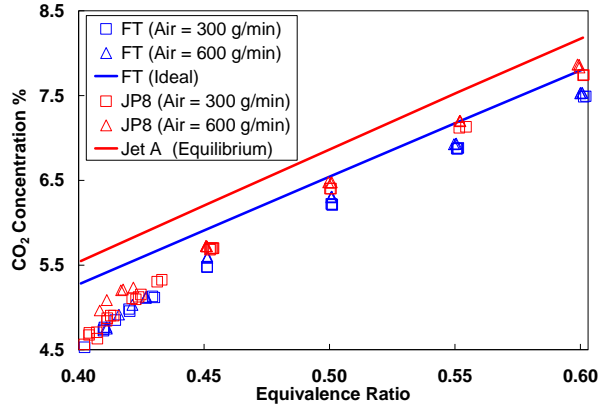


Figure 6. CO_2 Concentration Measured in the WSR.

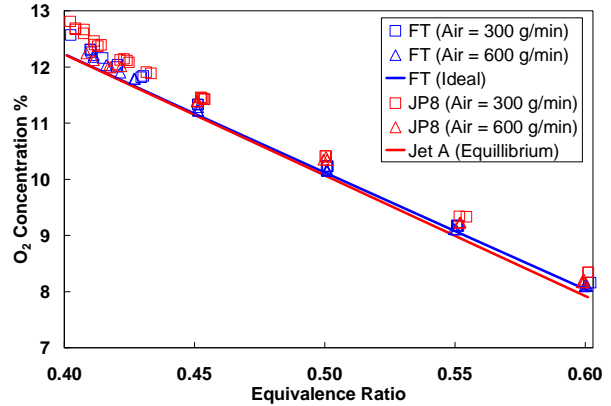


Figure 7. Oxygen Concentration Measured in the WSR.

The water produced in the WSR was measured by the FTIR. The results are shown in Fig. 8 along with an equilibrium and ideal calculation for the water in the exhaust based on complete conversion of the fuel to CO_2 and H_2O . The results show the expected increase in H_2O concentration with equivalence ratio and show good agreement with the equilibrium and ideal water concentrations. The H_2O levels were higher for the FT fuel cases across all of the equivalence ratios studied. Because of the higher H/C ratio of the FT fuel, it was expected that the H_2O concentration in the exhaust would be higher for the FT than that for the JP8 fuel. A comparison of the experimental values in the range from $\phi = 0.45$ to 0.6 showed that the ratio of the water concentration for the FT exhaust to that of the JP8 was 1.07-1.09, which brackets the value of the ideal ratio (1.08) of the water produced for complete combustion of the two fuels. As the equivalence ratio was lowered toward lean blowout the water production in the reactor was shown to drop as it did for the CO_2 .

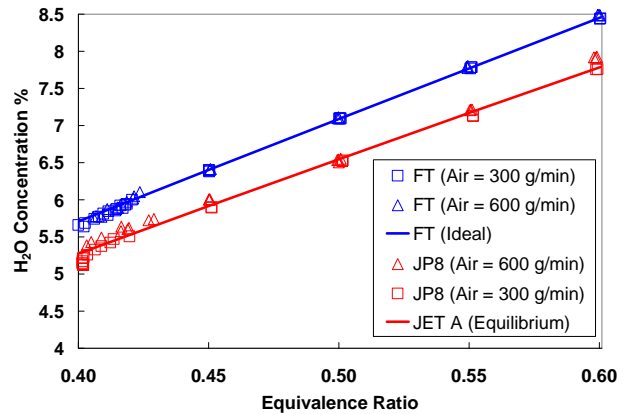


Figure 8. Water Concentration Measured in the WSR.

As the equivalence ratio was lowered toward lean blowout the water production in the reactor was shown to drop as it did for the CO_2 .

The unburned hydrocarbons (UHC) measured in the WSR are shown in Fig. 9 expressed as an emissions index. Above $\phi = 0.45$ the UHC level was low and the UHC level increased dramatically as ϕ was decreased below $\phi = 0.45$. The results are plotted vs. temperature to emphasize the effect of reactor temperature on the unburned hydrocarbon level. It can be seen that in the region leading up to lean blowout that UHC production is more dependant on reactor temperature than the residence time or fuel type.

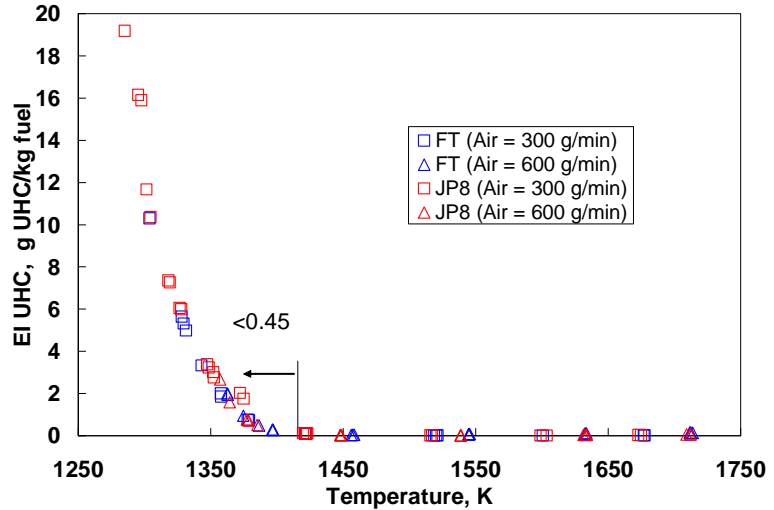


Figure 9. Emissions Index of Unburned Hydrocarbons.

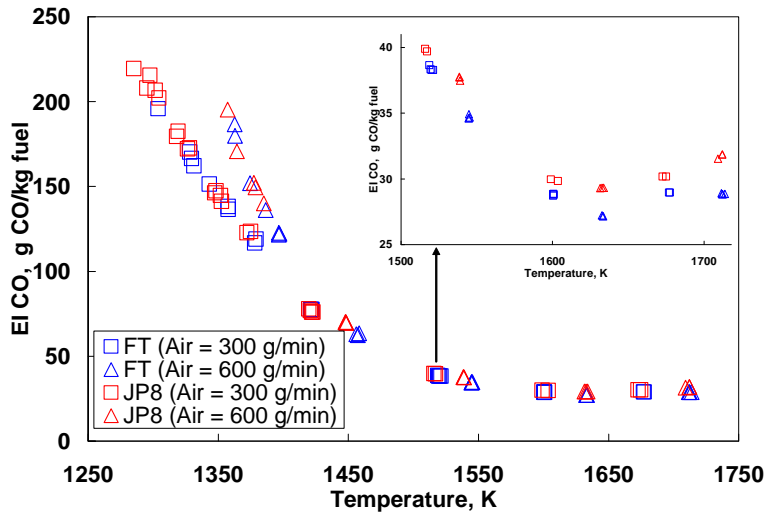


Figure 10. Emissions Index of Carbon Monoxide.

The carbon monoxide emissions are shown in Fig. 10 plotted vs. temperature. The results show that for temperatures above 1400 K ($\phi > 0.45$) the CO is dependant of the temperature and is almost independent of the residence time for the flow rates considered. Also, in this region the CO levels in this region are slightly higher for the JP8 cases. The CO is shown to decrease to a minimum at approximately 1630 K and then gradually increases as temperature is increased. This existence of a minimum CO value has been seen previously for other fuels.^{2,4} As the temperature is increased further more CO is formed as a result of CO₂ dissociation. As the temperature is lowered below 1630 K the CO increases due to quenching of the reactions before

CO₂ can be formed, resulting in higher CO levels. As lean blowout is approached for temperatures below 1400 K there is an effect of the residence time on the CO production, with lower residence times (higher mass flows) leading to higher CO values than the higher residence time cases. Note that in this region, for the same temperature and residence time, the CO levels are approximately equal for the two fuel types.

The combustion efficiency was calculated from the SAE Aerospace recommended Practice ARP 1533¹¹ using measurements of CO and UHC:

$$\eta_c = 1 - 10109 \frac{EI_{CO}}{LHV} - \frac{EI_{UHC}}{1000} \quad (3)$$

where: EI is emissions index and LHV is the lower heating value of the fuel.

The results show that the combustion efficiency is almost identical for the two fuels. For equivalence ratio values above $\phi = 0.5$ the combustion efficiency was higher than 99% for both of the fuels. The major portion of the combustion inefficiency is due to the production of CO rather than the production of UHC, and so the efficiency results strongly resemble a mirror image of the plot for the CO vs. temperature in Fig. 10. As the lean blowout is approached at the lower equivalence ratios the combustion efficiency drops dramatically. The efficiency decrease with temperature drop is more pronounced for the shorter residence time cases.

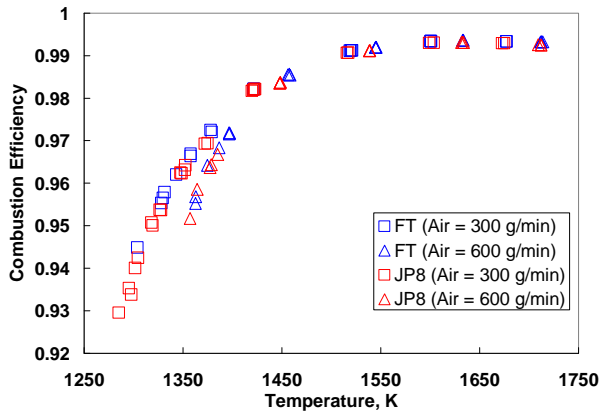


Figure 11. Combustion Efficiency vs. Temperature in the WSR.

Figure 12 shows the lean blowout data expressed as equivalence ratio at LBO vs. Loading parameter where the loading parameter is determined from:¹²

$$LP = \frac{n_{air}}{VP^{1.75}} \quad (4)$$

where: n_{air} = flow rate of air in moles/sec
 V = volume of the reactor in liters
 P = pressure in the reactor in atm

The LBO data for the JP8 show that the equivalence ratio at blowout varied only about 1% as the LP was doubled. This variation is actually less than the uncertainty of the measurement of the equivalence ratio. The data for the FT fuel show that the equivalence ratio at lean blowout is slightly less than that for the JP8 fuel and shows less than 2.8% increase in equivalence ratio with loading parameter as loading parameter is doubled.

Figure 13 shows that the temperature at lean blowout increased as the loading parameter increased. Note that the higher loading parameter cases correspond to lower residence times in the reactor and thus less time for reactions to complete, therefore higher temperatures are required to maintain the reaction rates. The temperatures at blowout for the two fuels are very similar.

While the equivalence ratio and temperatures at lean blow out was well defined and very repeatable, it was found that the emissions varied for a given blowout condition. The carbon monoxide and total hydrocarbon levels at lean blowout are shown in Figs. 14 and 15, respectively. The CO levels at blowout are relatively flat but scattered within a +/-16% band. In contrast, the results for unburned hydrocarbons show a decreasing trend of UHC with loading parameter. Note that the condition of higher loading also corresponds to higher mass flows, and as shown in Fig. 13, the temperature in the reactor at LBO increases with higher temperatures.

All of the data shown above was obtained under quasi-steady conditions. The response of the reactor to the lean blowout will now be examined. In general as lean blowout was approached the temperature began to drop and the hydrocarbons and carbon monoxide increased. As the reactor cooled, the combustion efficiency decreased resulting in less heat release and further production of CO and UHC. Eventually there is not enough energy released in the reactor to sustain combustion and the flammability limit is reached.

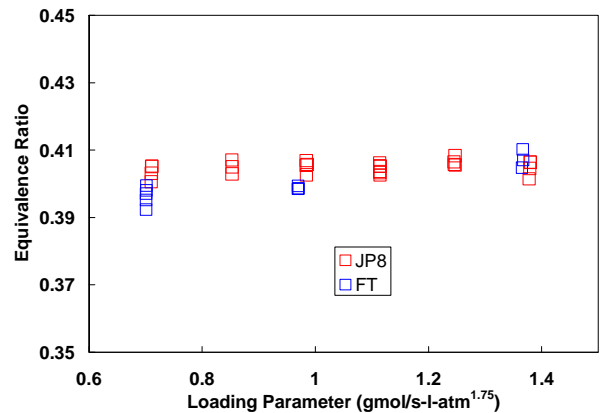


Figure 12. Equivalence Ratio at Lean Blowout vs. Air Loading Parameter.

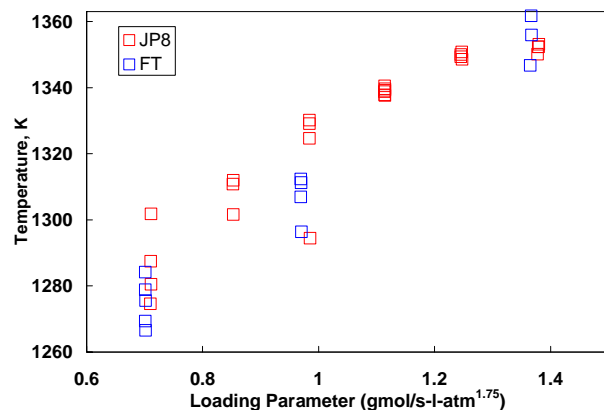


Figure 13. Temperatures Measured in the WSR at Lean Blowout.

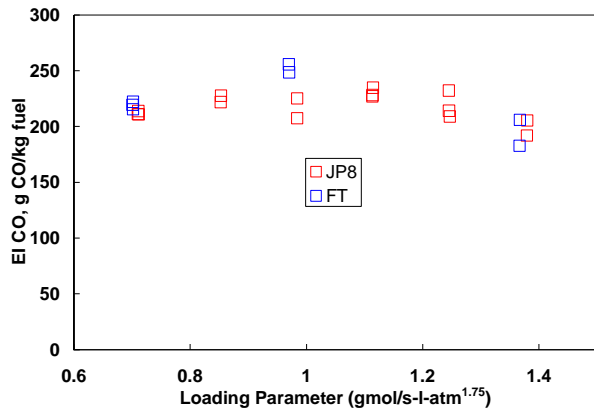


Figure 14. Emissions Index of Carbon Monoxide Measured at LBO.

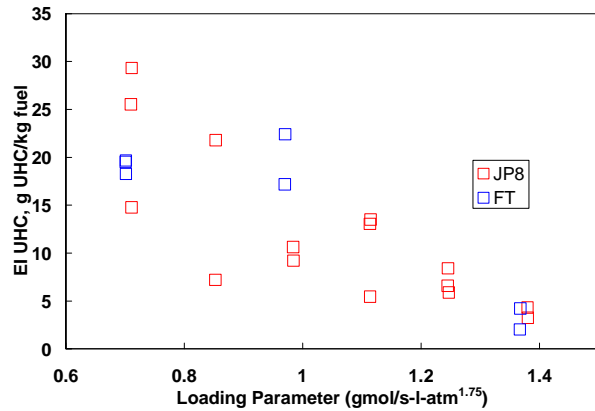


Figure 15. Emissions Index of Unburned Hydrocarbon Level Measured at LBO.

Details of the chemical constituents of the UHC were determined by FTIR analysis and it was found that ethylene, formaldehyde, and acetylene were found to be present in the exhaust at conditions near lean blowout and not found in significant quantities at temperatures above 1450 K. The results are shown in Figs. 16 and 17 where ethylene, formaldehyde, and acetylene are plotted along with temperature vs. time for the two flow rates. The data for all of the conditions show that as the temperature decreased on the approach to blow out the concentrations of the individual hydrocarbons all increased. Close examination of the plots shows the sensitivity of the individual hydrocarbon concentrations to the fluctuations of the temperatures, as changes in the temperature are followed by changes in the opposite direction by the hydrocarbon concentrations. As the flowrate increased, the unburned hydrocarbons dropped for both of the fuels, this observed trend is in agreement with the trends shown for all of the UHC's shown in Fig. 15. For the cases shown here, the levels of the ethylene and the formaldehyde at blowout were slightly higher for the FT fuel, however, it should be noted that the temperature levels at blowout for the FT fuels shown here are lower than those for the JP8.

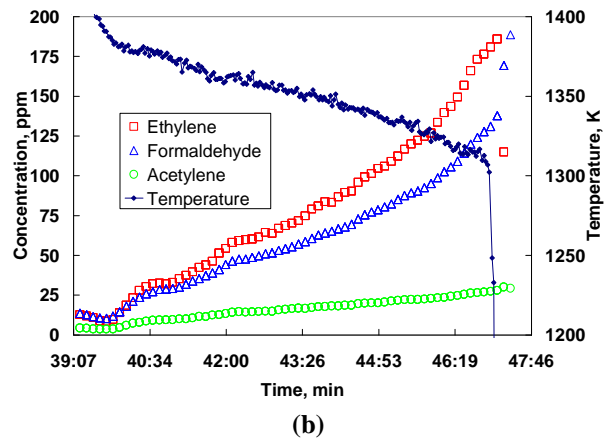
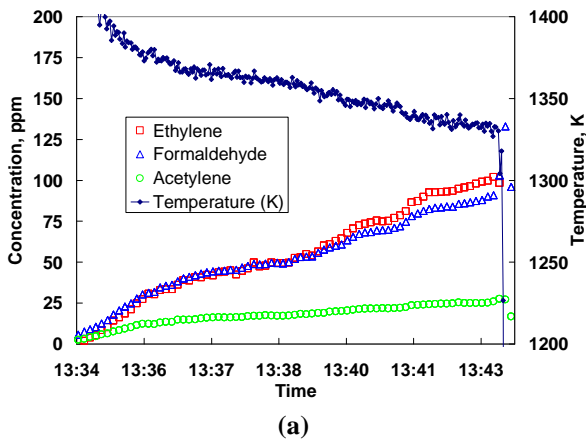


Figure 16. Ethylene, Acetylene, and Formaldehyde Formation as LBO is Approached for Total Air Flow of 420 g/min (a) JP8, (b) FT.

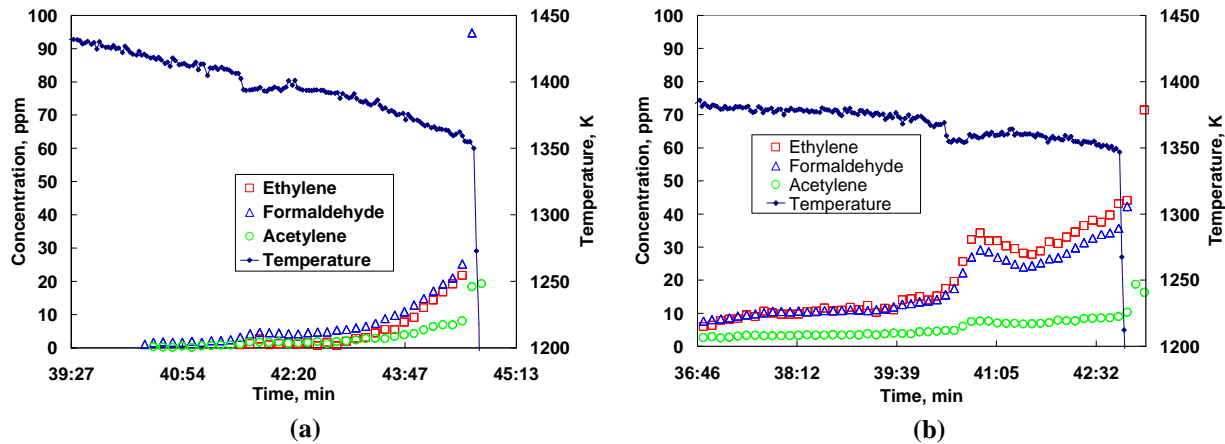


Figure 17. Ethylene, Acetylene, and Formaldehyde Formation as LBO is Approached for Total Air flow of 600 g/min (a) JP8, (b) FT.

The lean blowout at higher reactor loading was explored using the method outlined by Sturgess¹³ to simulate high altitude (lower pressures) by nitrogen dilution of the air stream in the reactor. The combined volume flow rate of nitrogen and air was maintained at a constant value and the mole fraction of the oxygen in the air and nitrogen was adjusting the N₂/Air balance. The results shown in Fig. 18 show an increase of equivalence ratio at LBO as the oxygen content of the air decreased. Similar to the results for the lower combustor loading cases, the equivalence ratio at LBO was almost identical for the two fuels under the higher combustor loading conditions shown in Fig. 18. It is possible to estimate the effective altitude and assign a loading parameter by the procedure outlined in Ref. 13; however, this analysis will be performed at a later time.

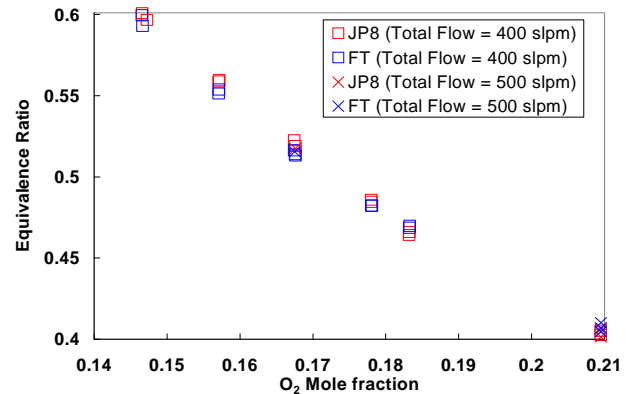


Figure 18. Equivalence Ratio at Lean Blow Out vs. Oxygen Fraction in Air Stream.

IV. Summary and Conclusions

The performance and gaseous emissions were measured for a well-stirred reactor operating under lean conditions for two fuels: JP8 and a synthetic Fisher-Tropsch fuel over a range of equivalence ratios from 0.6 down to the lean blowout. The lean blowout characteristics were determined in LBO experiments at loading parameter values from 0.7 to 1.4. The lean blowout characteristics were then explored under higher loading conditions by simulating higher altitude operation with the use of nitrogen as a dilution gas for the air stream. The experiments showed that:

1. The lean blowout characteristics for the two fuels were close under both low loading and high loading conditions.
2. The combustion temperatures and observed combustion efficiencies were similar for the two fuels.
3. The gaseous emissions were similar for the two fuels and the differences in the H₂O and CO₂ emissions appear to be directly relatable to the C/H ratio for the fuels.

Acknowledgments

The authors are grateful for the help of Mr. Mike Arstingstall of UDRI for technical support on the construction of the WSR and associated systems. The efforts of Mr. Edward Strader of UDRI on the instrumentation and Mr.

Tom McCray of ISSI for data acquisition support are also gratefully acknowledged. This work was funded by GE Aviation subcontract No. 200-18-14U38773, under a NASA prime award no. NAS3-01135 with Dr. Timothy J. Held serving as the contract monitor.

References

- ¹Nenniger, J. E., Kridiotis, A., Chomiak, J., Longwell, J. P., and Sarofim, A. F., "Characterization of a Toroidal Well Stirred Reactor," *Twentieth Symposium (International) on Combustion*, The Combustion Institute, pp. 473-479, 1984.
- ²Zelina, J., "Combustion Studies in a Well-Stirred Reactor," Ph.D. Thesis, University of Dayton, Dayton, OH, 1995.
- ³Stouffer, S. D., Striebich, R. C., Frayne, C. W., and Zelina, J., "Combustion Particulates Mitigation Investigation Using a Well-Stirred Reactor," AIAA Paper No. 2002-3723, 2002.
- ⁴Blust, J.W., Ballal D.R., Sturgess, G.J., "Fuel effects on the Lean Blowout and Emissions from a Well-Stirred Reactor," *Journal of Propulsion and Power*, Volume 15, Number 2. pp. 216-223, 1999.
- ⁵Stouffer, S. D., Ballal, D. R., Zelina, J., Shouse, D. T., Hancock, R. D., and Mongia, H. C.: "Development and Combustion Performance of a High Pressure WSR and TAPS Combustor," AIAA Paper 2005-1416, 2005.
- ⁶Harrison, W.E., and Zabarnick, S., "The OSD Assured Fuels Initiative-Military Fuels Produced from Coal," Proceedings of 31st International Technical Conference on Coal Utilization and Fuel Systems, 2006.
- ⁷Dewitt, M.J., Striebich, R.C., Shafer, L., Zabarnick, S., Harrison, W.E., Minus, D.E., Edwards, T., "Evaluation of Fuel Produced by the Fischer-Tropsch Process for Aviation Applications," Preprints of the AIChE, 2007.
- ⁸Edwards, T, Minus, D.E., Harrison, W.E., Corporan, E., DeWitt, M.J., Zabarnick, S., and Balster, L., "Fischer-Tropsch Jet Fuels-Characterization for Advanced Aerospace Applications," AIAA 2004-3885, 2004.
- ⁹Shafer, L.M., Striebich, R.C., Gomach, J., and Edwards, T, "Chemical Class Composition of Jet Fuels and Other Specialty Kerosene Fuels," AIAA 2006-7972, 2006.
- ¹⁰Gordon, S., and McBride, B., "Computer Program for Complex Chemical Equilibrium Compositions and Applications," NASA Reference Publication 1311, October, 1994.
- ¹¹Aerospace Recommended Practice 1533, "Procedure for the Calculation of Gaseous Emissions from Aircraft Turbine Engines," Society of Automotive Engineers, Inc., Warrendale, PA, pp. 1-36, 1994.
- ¹²Lefebvre, A.H., *Gas Turbine Combustion*, Hemisphere Publishing Corp., McGraw-Hill, NY, 1983.
- ¹³Sturgess, G.J., Heneghan, S.P., Vangsness, M.D., Ballal, D.R., Lesmerises, A.L. "Lean Blowout in a Research Combustor at Simulated Low Pressures," *ASME Journal of Engineering for Gas Turbines and Power*, Volume 118, pp. 145-153, 1996.

APPENDIX N

Use of Measured Species Class Concentrations with Chemical Kinetic Modeling for the Prediction of Autoxidation and Deposition of Jet Fuels

INTENTIONALLY LEFT BLANK

Use of Measured Species Class Concentrations with Chemical Kinetic Modeling for the Prediction of Autoxidation and Deposition of Jet Fuels

Nicholas J. Kuprowicz,^{†,§} Steven Zabarnick,^{*,†,§} Zachary J. West,^{†,§} and Jamie S. Ervin^{†,§}

Air Force Research Laboratory, Propulsion Directorate, Wright-Patterson Air Force Base, Ohio 45433, Energy & Environmental Engineering Division, University of Dayton Research Institute, Dayton, Ohio 45469-0116, and Department of Mechanical & Aerospace Engineering, University of Dayton, Dayton, Ohio 45469-0232

Received August 17, 2006. Revised Manuscript Received November 27, 2006

The production of detrimental carbonaceous deposits in jet aircraft fuel systems results from the involvement of trace heteroatomic species in the autoxidation chain that occurs upon fuel heating. Although it has been known for many years that these sulfur-, nitrogen-, and oxygen-containing species contribute to the tendency of a fuel to form deposits, simple correlations have been unable to predict the oxidation rates or the deposit forming tendencies over a range of fuel samples. In the present work, a chemical kinetic mechanism developed previously is refined to include the roles of key fuel species classes, such as phenols, reactive sulfur species, dissolved metals, and hydroperoxides. The concentrations of these fuel species classes in the unreacted fuel samples are measured experimentally and used as an input to the mechanism. The resulting model is used to simulate autoxidation behavior observed over a range of fuel samples. The model includes simulation of the consumption of dissolved oxygen, as well as the formation and consumption of hydroperoxide species during thermal exposure. In addition, the chemical kinetic mechanism is employed with a global deposition submechanism in computational fluid dynamics (CFD) simulations of deposit formation occurring in near-isothermal as well as non-isothermal flowing environments. Experimental measurements of oxygen consumption, hydroperoxide formation, and deposition are performed for a set of seven fuels. Comparison with experimental measurements indicates that the methodology offers the ability to predict both oxidation and deposition rates in complex flow environments, such as aircraft fuel systems, using only measured chemical species class concentrations for the fuel of interest.

Introduction

Prior to being combusted for propulsion, jet fuel is heated during passage through aircraft fuel system components. This heating occurs incidentally while passing through fuel pumps but is promoted via heat exchangers, particularly in advanced military aircraft, to remove excess heat from numerous aircraft subsystems. Systems which may require cooling include avionics, hydraulics, lubrication, and environmental control. The use of fuel to cool fuel system, engine, and airframe components is an enabling technology for advanced military aircraft due to the large quantity of excess heat produced. Unfortunately, the heat absorbed by the fuel is not always innocuous. When fuel temperatures approach ~ 140 °C, the fuel begins to react via an autoxidation chain mechanism with the small amount of dissolved oxygen (65–75 ppmwt)¹ present from exposure to air. These autoxidation reactions ultimately result in the formation of detrimental surface deposits and bulk insolubles.² These deposits can plug narrow passageways in valves, filters, and nozzles and can inhibit the desired heat transfer in heat

exchangers. Numerous techniques have been investigated to limit the formation of deposits, including the following: fuel system designs to minimize fuel temperatures, fuel additives to inhibit autoxidation and/or deposit formation, fuel deoxygenation, fuel system surface coatings, and inclusion of “sacrificial” or coke tolerant components.³ But, no single method is able to eliminate the deposition problem under all current and proposed aircraft fuel system conditions.

In recent years, chemical kinetic models have been developed which simulate the major autoxidation pathways that occur in jet fuels.^{4–6} The development of a widely applicable autoxidation mechanism, which enables the prediction of deposit formation, would greatly aid the fuel system design process and enable the more efficient use of the fuel as a heat sink.⁷ As jet fuels consist of hundreds of individual species, which vary in their identity and concentration in different fuel samples, it is impractical to build detailed chemical kinetic mechanisms. Grouped or lumped mechanisms, sometimes referred to as

* Corresponding author. Tel.: 937-255-3549. E-mail: Steven.Zabarnick@wpafb.af.mil.

[†] Air Force Research Laboratory.

[‡] University of Dayton Research Institute.

[§] University of Dayton.

(1) Striebich, R. C.; Rubey, W. A. *Prepr. Pap., Am. Chem. Soc., Div. Pet. Chem.* **1994**, *39*, 47–50.

(2) Hazlett, R. N. *Thermal Oxidation Stability of Aviation Turbine Fuels*; ASTM: Philadelphia, 1991.

(3) Heneghan, S. P.; Zabarnick, S.; Ballal, D. R.; Harrison, W. E. *J. Energy Res. Tech.* **1996**, *118*, 170–179.

(4) Zabarnick, S. *Ind. Eng. Chem. Res.* **1993**, *32*, 1012–1017.

(5) Zabarnick, S. *Energy Fuels* **1998**, *12*, 547–553.

(6) Kuprowicz, N. J.; Ervin, J. S.; Zabarnick, S. *Fuel* **2004**, *83*, 1795–1801.

(7) Balster, L. M.; Zabarnick, S.; Ervin, J. S.; Striebich, R.; DeWitt, M. J.; Doughty, T. Predicting the Thermal Stability of Jet Fuel: Analytical Techniques Toward Model Validation. *Proceedings of the 8th International Conference on Stability, Handling, and Use of Liquid Fuels*, Steamboat Springs, CO, 2004.

“pseudo-detailed” mechanisms, have been used to simulate the most important reactive pathways, including the effects of antioxidants and catalytic surfaces.^{4–6,8} In addition, these mechanisms have been combined with computational fluid dynamics techniques with the goal of simulating the complex time and temperature variation during fuel flow in aircraft fuel system components.^{8,9} Most recently, initial efforts at including global deposit formation reactions in these mechanisms have been performed.^{7,10} An initial goal in the development of these models is to allow prediction of oxidation and deposition under simple laboratory flow systems with near-isothermal temperatures, with the ultimate goal of simulation of complex flow systems, such as engine nozzles, which exhibit highly non-isothermal fuel exposure.

The present work details the development of an approach which offers the potential to enable the prediction of the liquid-phase autoxidation and deposition of jet fuels. A chemical kinetic mechanism developed previously is refined to include the roles of key fuel species classes, such as phenols, reactive sulfur species, dissolved metals, and hydroperoxides. The concentrations of these fuel species classes are determined for the unreacted fuel samples and used as an input to the mechanism. The resulting model is used to simulate the autoxidation behavior observed over a range of fuel samples. The model includes simulation of the consumption of dissolved oxygen, as well as the formation and consumption of hydroperoxide species during thermal exposure. In addition, the chemical kinetic mechanism is employed with a global deposition submechanism in computational fluid dynamics (CFD) simulations of deposit formation occurring in near-isothermal as well as non-isothermal flowing environments.

Experimental Details

Both laminar and turbulent flow conditions can occur during aircraft fuel system operation. Under laminar flow conditions, the low flow rates result in relatively long residence times and slower rates of species and heat transport relative to those occurring in turbulent flow. Thus, it is important to perform experiments under both laminar and turbulent flow conditions to develop and validate models of oxidation and deposition. Two experimental rigs were used in the present work. The first rig, a near-isothermal flowing tube reactor (NIFTR), involved laminar flow and was used to evaluate the oxidation and deposition characteristics of seven jet fuels. The second rig employed turbulent flow and is a single-tube, non-isothermal flowing reactor system referred to as the ECAT.

The NIFTR system consists of a single-tube heat exchanger (32 in. length, 0.125 in. o.d., 0.085 in. i.d.) which has been described in detail previously.¹¹ Fuels are exposed to a temperature of 185 °C at 300 psig for all NIFTR experiments in the present work. The constant wall temperature provided by the copper block heater, along with low flow rates, provides a near-isothermal reaction environment for the fuel. In the oxidation experiments, where the oxygen consumption is monitored at various residence times, flow rates are varied over the range 0.25–5.0 mL min⁻¹ (Reynolds numbers of 10–205 at the tube exit) using a syringe pump. Average residence times are calculated using the known reactor tube volume, flow rates, and a correction for fuel expansion with temperature. Oxygen profiles (dissolved oxygen fraction vs residence time) are determined by in-line sampling of the fuel and injection to a gas chromatographic system and are reproducible to ±5%.¹² Hydro-

peroxide profiles (hydroperoxide concentration vs residence time) are determined by reaction of collected fuel sample aliquots with triphenylphosphine, and quantification of the triphenylphosphine oxide produced via gas chromatography.¹³ The oxidation experiments are performed using tubes coated with Silcosteel (Restek Corp.) to minimize surface catalysis and changes in fuel oxidation rates due to surface fouling if bare metal tubes were employed. Surface deposition is measured in separate 72 h runs utilizing the NIFTR system with a continuous flow rate of 0.25 mL min⁻¹. Uncoated stainless steel (SS316) tubes are used for the deposition experiments, with deposits produced during the first 10–12 h providing a noncatalytic surface for the vast majority of the test time. At the end of each deposition experiment, the tube is segmented into 2 in. long sections. The segments are washed with hexane to remove any residual fuel and, then, dried in a vacuum oven at 100 °C for at least 2 h. The total carbon deposition within each tube segment is then determined using standard carbon burnoff methods (LECO RC-412 Multiphase Carbon Determinator).

The deposition characteristics of one fuel, F4177, are also evaluated in a non-isothermal flowing environment utilizing the ECAT. A detailed description of the design and operation of the ECAT flow reactor system was presented in previous studies.^{14–16} A single-tube Lindberg furnace is used to provide the heated reaction zone during testing. The furnace has a 36 in. actively heated zone with 5.25 in. insulating adapters at each end. Stainless steel tubing (SS316, 50 in. length, 0.125 in. o.d., 0.085 in. i.d.) is used for the ECAT deposition experiments. The tubing is positioned horizontally such that the 8–44 in. section is within the actively heated zone. Outer wall temperatures are monitored using thermocouples that are strap welded to the wall at various axial locations. The bulk fuel outlet temperature is measured using a thermocouple that is inserted into the fuel flow approximately 7 in. downstream of the heated reaction zone. Three ECAT deposition experiments at varying temperatures were performed, each with a fuel flow rate of 10 mL min⁻¹ and system pressure of 550 psig. This flow rate for the fuel temperatures considered translates to Reynolds numbers in the range of 780–1000 at the tube exit. Such Reynolds numbers usually correspond to laminar flow. However, for the flows in the present heated horizontal tubes, buoyancy was assumed to prematurely induce turbulent flow. Others have demonstrated a similar premature transition to turbulence within horizontal heated tubes.¹⁷ In addition, Katta et al.¹⁸ have used this assumption to simplify simulations of the flow within heated horizontal tubes while providing good agreement between measured and calculated exit bulk temperatures. Thus in the simulations of the ECAT experiments, we assumed the flow to be turbulent. Upon completion of the 6 h of reaction time, the tubing is removed from the system and segmented, rinsed, and dried in a manner consistent with that previously described for the NIFTR deposition experiments. The total carbon deposition in each segment is measured using standard carbon burnoff methods. Table 1 provides a summary of the conditions of the NIFTR and ECAT jet fuel deposition experiments discussed in this work. The techniques used to quantify species class composition of the fuels are detailed in the following section.

Methodology

Jet fuels are comprised of hundreds, or perhaps thousands, of chemical species. The composition of a typical jet fuel is

(12) Rubey, W. A.; Striebich, R. C.; Tissandier, M. D.; Tirey, D. A.; Anderson, S. D. *J. Chromatogr. Sci.* **1995**, *33*, 433–437.

(13) West, Z. J.; Zabarnick, S.; Striebich, R. C. *Ind. Eng. Chem. Res.* **2005**, *44*, 3377–3383.

(14) DeWitt, M. J.; Zabarnick, S. *Prepr. Pap.—Am. Chem. Soc., Div. Pet. Chem.* **2002**, *47*, 183–186.

(15) Minus, D. K.; Corporan, E. *Prepr. Pap.—Am. Chem. Soc., Div. Pet. Chem.* **2000**, *45*, 484–487.

(16) Minus, D. K.; Corporan, E. *Prepr. Pap.—Am. Chem. Soc., Div. Pet. Chem.* **1998**, *43*, 360–363.

(17) Kakac, S.; Shah, R.; Aung, W. *Handbook of Single-Phase Convective Heat Transfer*; Wiley-Interscience: New York, 1987.

(18) Katta, V. R.; Blust, J.; Williams, T. F.; Martel, C. R. *J. Thermophys. Heat Transfer* **1995**, *9*, 159–168.

(8) Doughty, T.; Ervin, J. S.; Zabarnick, S.; Williams, T. F. *Energy Fuels* **2004**, *18*, 425–437.

(9) Ervin, J. S.; Zabarnick, S. *Energy Fuels* **1998**, *12*, 344–352.

(10) Doughty, T. Ph.D. Thesis, University of Dayton, Dayton, OH, 2004.

(11) Jones, E. G.; Balster, L. M.; Balster, W. J. *Energy Fuels* **1998**, *12*, 990–995.

Table 1. Summary of Deposition Experiments

	(a)	(b)
test rig	NIFTR	ECAT
no. experiments	7	3
Jet-A-1 fuels	F2747	N/A
Jet-A fuels	F2959, F3084, F3166, F3219	N/A
JP-8 fuels	F3804, F4177	F4177
tubing type	stainless steel (SS316)	stainless steel (SS316)
tube o.d.	0.125 in.	0.125 in.
tube i.d.	0.085 in.	0.085 in.
tube length	32 in.	50 in.
tube orientation	horizontal	horizontal
flow rate	0.25 mL min ⁻¹	10.0 mL min ⁻¹
flow pressure (inlet)	2.3 MPa	3.9 MPa
inlet temperature	room temperature	room temperature
wall temperature	constant (185 °C)	variable (21–400 °C), maximum wall temps of 340, 370, and 400 °C
active heating	0–32 in. section of tubing	8–44 in. section of tubing
exit temperature	185 °C	300–355 °C
exit Reynolds nos.	10	780–1000
test duration	72 h	6 h

approximately 80% alkanes, 10–25% alkylated aromatics, and parts per million to parts per thousand quantities of heteroatomic species. The heteroatomic species consist of oxygen-containing molecules, such as phenols and hydroperoxides; sulfur-containing molecules, such as thiols, sulfides, disulfides, benzothio-phenes, dibenzothiophenes, and elemental sulfur; and, lastly, nitrogen-containing molecules, such as anilines, pyridines, indoles, amines, and carbazoles. Although the heteroatomic species represent less than 1% of the typical fuel content, they are the primary species responsible for differences among oxidation and deposition behavior of fuel samples. As all of the species in jet fuel may contribute to jet fuel oxidation and deposition behavior to some degree, ideally it would be desirable to identify and quantify them individually and to understand how they affect oxidation and deposition processes. Unfortunately, due to the complex mixture that constitutes jet fuel and the variation between fuel samples (which are specified via properties rather than chemical composition), it is impractical to consider the detailed concentrations and reactions of hundreds of varying species. Therefore, the oxidation and deposition behavior of jet fuel has been characterized in a pseudo-detailed (i.e., simplified) chemical kinetic mechanism in which the fuel is treated as a mixture of classes of compounds, rather than individual species. Thus, the relevant species classes need to be identified, quantified, and incorporated into a reaction mechanism which includes the chemical behavior of interest.

Chemical Kinetic Mechanism. The basic autoxidation mechanism has been described in detail previously^{4–6} and is shown schematically in Figure 1. The mechanism is limited to the most important reactions in determining fuel oxidation behavior. The species classes represented in the cycle are: hydrocarbons (RH), dissolved oxygen (O₂), peroxy radical inhibitors or antioxidants (AH), hydroperoxide decomposers (SH), and hydroperoxides (ROOH). The cycle begins with a poorly understood initiation process that produces a hydrocarbon radical, R[•]. The resultant radical reacts rapidly with dissolved oxygen, forming a peroxy radical, RO₂[•]. This peroxy radical can extract a hydrogen atom from a fuel hydrocarbon (likely an alkyl-substituted aromatic species), forming a hydroperoxide and regenerating the R[•] radical, thereby continuing the cycle. Due to the reactivity of benzylic hydrogen atoms relative to those in paraffinic species, the hydrocarbon radical, R[•], which propagates the chain is likely a benzylic radical.¹⁹ This process

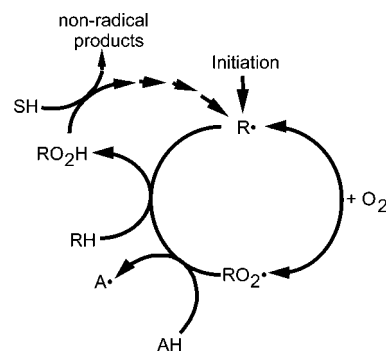


Figure 1. Diagram of the autoxidation reaction process showing the role of peroxy radical inhibiting (AH) and hydroperoxide decomposing (SH) species classes.

Table 2. Chemical Kinetic Mechanism of Liquid-Phase Oxidation

#	reaction	A (mol, L, s)	E _a (kcal mol ⁻¹)
1	I → R [•]	1 × 10 ⁻³	0
2	R [•] + O ₂ → RO ₂ [•]	3 × 10 ⁹	0
3	RO ₂ [•] + RH → RO ₂ H + R [•]	3 × 10 ⁹	12
4	RO ₂ [•] + RO ₂ [•] → termination	3 × 10 ⁹	0
5	RO ₂ [•] + AH → RO ₂ H + A [•]	3 × 10 ⁹	5
6	A [•] + RH → AH + R [•]	1 × 10 ⁵	12
7	A [•] + RO ₂ [•] → Products _{AH}	3 × 10 ⁹	0
8	R [•] + R [•] → R ₂	3 × 10 ⁹	0
9	RO ₂ H → RO [•] + •OH	1 × 10 ¹⁵	39
10	RO [•] + RH → ROH + R [•]	3 × 10 ⁹	10
11	RO [•] → R _{prime} [•] + carbonyl	1 × 10 ¹⁶	15
12	•OH + RH → H ₂ O + R [•]	3 × 10 ⁹	10
13	RO [•] + RO [•] → RO _{term} [•]	3 × 10 ⁹	0
14	R _{prime} [•] + RH → alkane + R [•]	3 × 10 ⁹	10
15	RO ₂ H + SH → Products _{SH}	3 × 10 ⁹	18
16	RO ₂ [•] → R [•] + O ₂	1 × 10 ¹⁶	19
17	RO ₂ [•] + R [•] → termination	3 × 10 ⁹	0
18	RO ₂ H + M → RO [•] + •OH + M	3 × 10 ¹⁰	15

can be slowed by the presence of antioxidant species, AH, which can be naturally occurring fuel species or added synthetic antioxidants. These species intercept the peroxy radical, slowing the chain by preventing the reformation of hydrocarbon radicals. The presence of hydroperoxide decomposing species, SH, can also slow the oxidation of the fuel. These species slow oxidation by decomposing hydroperoxides via a nonradical-producing pathway. Hydroperoxides act as initiators in the mechanism, increasing the free radical pool and the resulting oxidation rate. Thus, at temperatures where the oxidation rate is being influenced by hydroperoxide initiation, the removal of hydroperoxides results in a reduction of the oxidation rate.²⁰

The chemical kinetic mechanism and associated Arrhenius rate parameters describing the basic autoxidation cycle of Figure 1 have been previously published.⁶ The enhanced version used in the present work is shown in Table 2. Use of the mechanism to model individual fuel samples requires analytical techniques to quantify the important species classes, AH, SH, and ROOH, as well as dissolved metals (denoted as M in Table 2). Techniques used for the identification and quantification of these species classes, as well as evidence of their involvement in fuel autoxidation and deposition, are now presented.

AH Species Class. There is much evidence indicating that polar species, and phenols which comprise the bulk of the jet fuel polars, play an important role in determining the oxidation and deposition characteristics of fuel samples. Phenols are known to act as antioxidants in hydrocarbons²¹ and have been shown to slow oxidation in jet fuel samples.^{22,23} It is known

(19) Zabarnick, S.; Phelps, D. K. *Energy Fuels* **2006**, *20*, 488–497.

(20) Zabarnick, S.; Mick, M. S. *Ind. Eng. Chem. Res.* **1999**, *38*, 3557–3563.

Table 3. Polar, Hydroperoxide, and Reactive Sulfur Content of the Seven Fuels Studied

fuel sample	polars concentration		hydroperoxides conc (μM)	reactive sulfurs conc (ppmw)
	(relative) ^a	(mg L^{-1}) ^b		
F2747 (Jet A-1)	0.32	167	21	1
F2959 (Jet A)	0.43	222	3	911
F3084 (Jet A)	0.90	465	13	426
F3166 (Jet A)	1.00	515	11	519
F3219 (Jet A)	0.43	223	5	286
F3804 (JP-8)	0.34	177	21	366
F4177 (JP-8)	0.94	486	13	1069

^a Integral of 254 nm UV response obtained using the normal-phase HPLC method for polar species quantification²⁵ divided by that obtained for fuel F3166. ^b Estimate of absolute polar concentrations based on phenol calibration mixture studies.³²

from the experience gained studying many fuel samples that jet fuels with high concentrations of naturally present phenol species tend to oxidize slowly and jet fuels with low concentrations of these phenols tend to oxidize quickly.²⁴ In addition to having important effects on oxidation, there is also evidence which suggests that phenols have significant effects on surface deposition. For example, the deposits produced over a wide range of fuel samples have been correlated with measured concentrations of polar fuel fraction,²⁵ and the removal of polar phenols via solid-phase extraction²⁶ or silylation²⁷ results in increased oxidation rates and decreased deposition. In addition, experiments in blending jet fuels with solvents, which is a method to decrease the concentration of these species in the fuels, also suggest the involvement of phenols in slowing oxidation and increasing deposition.^{28,29} These observations provide compelling evidence that naturally occurring phenols are responsible for slowing oxidation and causing deposition in jet fuels.

A number of techniques have been developed to measure polar fuel species. These species can be separated and quantified by normal-phase HPLC with UV absorption detection.²⁵ Solid-phase extraction techniques using silica gel cartridges can also separate these fuel components which can be subsequently quantified by gas chromatography.³⁰ In addition, liquid-liquid extraction followed by chromatographic analysis has also been employed.³¹ While hydrocarbon fuel polars may consist of a number of species classes, for jet fuels the polars have been found to consist mostly of phenolic species.³² For example, analysis of the polar fraction of jet fuels via silica gel solid-phase extraction yielded a series of alkyl-substituted phenols almost exclusively.³⁰ The concentration of polar species determined by the normal-phase HPLC method is shown in Table 3

(21) Taylor, W. F.; Frankenfeld, J. W. *Ind. Eng. Chem. Prod. Res. Dev.* **1978**, *17*, 86–90.

(22) Zabarnick, S.; Whitacre, S. D. *J. Eng. Gas Turbines Power* **1998**, *120*, 519–525.

(23) Jones, E. G.; Balster, L. M. *Energy Fuels* **2000**, *14*, 640–645.

(24) Heneghan, S. P.; Zabarnick, S. *Fuel* **1994**, *73*, 35–43.

(25) Balster, L. M.; Zabarnick, S.; Striebich, R. C. *Prepr. Pap.—Am. Chem. Soc., Div. Pet. Chem.* **2002**, *47*, 161–164.

(26) Zabarnick, S. *Ind. Eng. Chem. Res.* **1994**, *33*, 1348–1354.

(27) Zabarnick, S.; Mick, M. S.; Striebich, R. C.; Grinstead, R. R. *Energy Fuels* **1999**, *13*, 154–159.

(28) Jones, E. G.; Balster, W. J.; Balster, L. M. *Energy Fuels* **1996**, *10*, 509–515.

(29) Zabarnick, S.; Zelesnik, P.; Grinstead, R. R. *J. Eng. Gas Turbines Power* **1996**, *118*, 271–277.

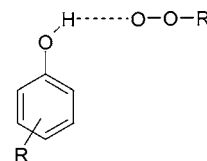
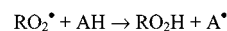
(30) Zabarnick, S.; Striebich, R.; Straley, K.; Balster, L. *Prepr. Pap.—Am. Chem. Soc., Div. Pet. Chem.* **2002**, *47*, 223–226.

(31) Link, D. D.; Baltrus, J. P.; Zandhuis, P.; Hreha, D. C. *Energy Fuels* **2005**, *19*, 1693–1698.

(32) Balster, L. M.; Zabarnick, S.; Striebich, R. C.; Shafer, L. M.; West, Z. J. *Energy Fuels* **2006**, *20*, 2564–2571.

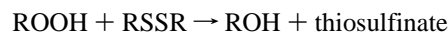
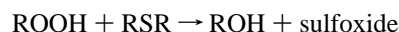
for the seven fuels studied here. The table shows that the polar concentrations in these fuels cover the range 167–515 mg L^{-1} . Analysis of a wide range of jet fuel samples indicates that the vast majority contain from 100 to 600 mg L^{-1} of polars.³²

Use of the measured polar species class concentrations for numerical modeling purposes is complicated by the fact that various species measured within a class have a range of reactivities. For example, a given fuel sample may have many dozens of naturally occurring phenols, including methyl-substituted, dimethyl-substituted, and larger phenols. During fuel autoxidation each of these phenols is capable of intercepting peroxy radicals via,



where AH is a phenol species and A^* is a phenoxy radical. The Arrhenius rate parameters of the reaction vary for different phenol species. In later sections, a method to relate the measured polar (phenol) species class concentration to the AH concentration used in the model is discussed.

SH Species Class. Another important class of species in fuel oxidation and deposition are those species which react with fuel hydroperoxides via a nonradical-producing pathway. Alternatively, hydroperoxides can decompose thermally or catalytically to produce radicals which accelerate the autoxidation chain. In jet fuels, these nonradical-producing hydroperoxide decomposing species include a subset of sulfur compounds, such as sulfides and disulfides. These can react with hydroperoxides via



where RSR is a sulfide and RSSR is a disulfide. These sulfur-containing species are referred to as “reactive sulfur” to differentiate them from the relatively unreactive thiophenes, benzothiophenes, and dibenzothiophenes that are commonly found in jet fuels. It has been shown in previous work that jet fuels which contain high levels of reactive sulfur species tend to produce only very low levels of hydroperoxides during autoxidation, while fuels with low levels of reactive sulfur species tend to produce relatively high levels of hydroperoxides.²⁸ Hydroperoxide-decomposing species serve to reduce the oxidation rate by reducing thermal or catalytic hydroperoxide decomposition and have been shown to act synergistically with peroxy radical inhibiting species in slowing oxidation.²⁰ Thus, the reactive sulfur species (sulfides and disulfides) are believed to be the primary components of the SH species class denoted in Figure 1. In addition to affecting oxidation, there is also evidence that oxidizable sulfur compounds promote surface deposition.³³ Thus, the reactive sulfur species (sulfides and disulfides) may also contribute to deposit formation.

A hydroperoxide reaction technique is used to quantify these reactive sulfur species in fuel.^{34,35} Fuels are reacted with hydrogen peroxide and/or iodine and the remaining sulfur

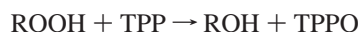
(33) Kauffman, R. E. *J. Eng. Gas Turbines Power* **1997**, *119*, 322–327.

(34) Stumpf, A.; Tolvaj, K.; Juhasz, M. *J. Chromatogr., A* **1998**, *819*, 67–74.

(35) Link, D. D.; Baltrus, J. P.; Rothenberger, K. S.; Zandhuis, P.; Minus, D. K.; Striebich, R. C. *Energy Fuels* **2003**, *17*, 1292–1302.

species are quantified by gas chromatography with atomic emission detection. As iodine only reacts with mercaptan sulfur, the mercaptan level can be determined by subtraction. Hydrogen peroxide reacts with sulfides, disulfides, and mercaptans, so that the sulfide plus disulfide level can be determined by subtraction and the use of the previously determined mercaptan level. These techniques show that jet fuels usually have very low mercaptan levels (<5 ppmwt) and the levels of reactive sulfur, i.e., sulfide plus disulfide classes, typically vary over the range 0–1000 ppmwt. The concentrations of reactive sulfur determined for the seven fuels of the present work are shown in Table 3. Use of the measured reactive sulfurs for numerical modeling is also complicated by the fact that various species measured within the class have a range of reactivities. Again, various sulfides and disulfides react with hydroperoxides at different rates, and the measured reactive sulfur content of the fuel needs to be related to the SH concentration used in the model.

ROOH Species Class. Hydroperoxides are important species in fuel oxidation which greatly affect the overall oxidation rate. These highly reactive species are usually present at only very low concentrations. Hydroperoxides are produced and destroyed during fuel autoxidation but also exist in fuel prior to thermal exposure. A technique to quantify fuel hydroperoxides as a species class using reaction with triphenylphosphine via



has recently been developed.¹³ The triphenylphosphine oxide (TPPO) produced is quantified by gas chromatography. This technique uses small sample volumes (≤ 0.5 mL), has a low detection limit (0.002 mM) and a wide dynamic range, and is fast, reproducible, and accurate. The small required sample volume allows laboratory-scale oxidation tests to be sampled readily for hydroperoxide content. The low detection limit allows the determination of hydroperoxide levels in fuels prior to thermal exposure. As various fuel hydroperoxides have very similar reactivity, this measurement of the hydroperoxide content of the unstressed fuel can be used directly as an input to the kinetic mechanism. We find that most fuels have hydroperoxide concentrations of 3–30 μM . Results on the hydroperoxide content of the seven fuels studied here are shown in Table 3. Kinetic analysis shows that at 185 °C, thermal decomposition (via reaction 9 of Table 2) of these low levels of hydroperoxides creates a radical pool which is sufficient to initiate the autoxidation chain. Thus, reaction 1 of Table 2, which is used to create an artificial source of radical production to start the autoxidation chain, is unnecessary but is still used in the present modeling to retain consistency with previous work. Low levels of hydroperoxides, such as those found in jet fuels, may also be responsible for initiating autoxidation in other hydrocarbon oxidation systems.³⁶

Dissolved Metals. Dissolved metals are known to play important roles in the oxidation and deposition of jet fuels.² Metals increase the decomposition rate of hydroperoxides via a catalytic pathway and may also provide catalysis of other reactions. It is essential to accurately quantify these species which can be active at very low concentrations (e.g., dissolved copper has been shown to be active at a concentration as low as 25 ppb). Inductively coupled plasma (ICP) techniques with either atomic emission spectroscopy (AES) or mass spectrometric detection provide promising ways for their identification and quantitation. Metals concentrations via ICP-AES for the seven fuels of the present work are shown in Table 4. The metals

Table 4. Dissolved Metal Content of the Seven Fuels Studied (via ICP-AES)

fuel	Cu ($\mu\text{g L}^{-1}$)	Mn ($\mu\text{g L}^{-1}$)	Fe ($\mu\text{g L}^{-1}$)	Mg ($\mu\text{g L}^{-1}$)	Zn ($\mu\text{g L}^{-1}$)
F2747 (Jet A-1)	40	<10	93	33	89
F2959 (Jet A)	<18	58	174	34	153
F3084 (Jet A)	25	<10	142	34	101
F3166 (Jet A)	111	13	142	34	100
F3219 (Jet A)	58	<10	182	40	128
F3804 (JP-8)	<18	<10	196	29	131
F4177 (JP-8)	<18	88	144	26	69

quantified here (Cu, Mn, Mg, Fe, and Zn) were selected for their known ability to catalyze autoxidation or deposition, as well as their being commonly found in fuel samples. Other metals, such as vanadium, are known to be detrimental to fuel thermal stability but are not generally found in jet fuel distillate cuts. The table shows that Cu and Mn exhibit a wide variation in measured concentrations, from below the detection limit to over 100 $\mu\text{g L}^{-1}$, while Fe, Mg, and Zn display significantly less variability. All of the fuels contain measurable levels of Fe, Mg, and Zn. Fuels with high measurable amounts of Cu tend to have low Mn levels, while fuels with measurable amounts of Mn tend to have low Cu levels. Fe, Mg, and Zn usually affect fuel thermal stability only at levels greater than those found in these fuels.² For these reasons, in using the measured metals content in the kinetic mechanism, the Cu and Mn concentrations were employed in the current work. Future studies need to more closely examine the role and catalysis rates of various metal species present in fuels.

Incorporating Measured Species Class Concentrations into the Kinetic Model. Measurement of species concentrations as grouped species classes provides a way to characterize differences between fuel samples and begins to reveal why various fuel samples have varying oxidation rates and deposit forming tendencies. Above, justification was provided for using the measured polars (primarily phenols) concentration as the peroxy radical inhibiting species class, AH, as well as the measured sulfur species which react with hydroperoxides as the hydroperoxide decomposing species class, SH. Again, these species classes represent an ensemble of individual species with a range of reactivities, and as such, a means to incorporate these species class measurements into the kinetic mechanism is required. The relationship between measured species classes and the concentrations used in the model should ideally be proportional so that, for example, a doubling of the measured phenol content results in a doubling of the AH concentration used in the model. The approach taken here was to model the initial AH and SH concentrations via linear relationships which define constants of proportionality,

$$\text{Const}_{\text{AH}} = \frac{\text{Simulated AH}_0[\text{M}]}{\text{Measured polars}[\text{mg/L}]}$$

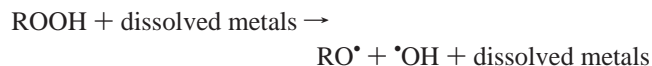
$$\text{Const}_{\text{SH}} = \frac{\text{Simulated SH}_0[\text{M}]}{\text{Measured reactive sulfurs}[\text{ppmwt}]}$$

between fuel species class composition measurements and simulated initial concentrations. Values of these constants are constrained such that the molar concentrations employed in the kinetic mechanism are less than or equal to the molar concentrations of the measured species classes. This constraint derives from the selection of Arrhenius parameters for the more reactive members of the species class. For example, Arrhenius parameters for the peroxy radical reaction with phenols, reaction 5 in Table 2, were selected for very reactive phenolic species, such

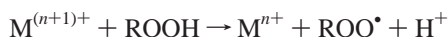
(36) Benson, S. W.; Nangia, P. S. *Acc. Chem. Res.* **1979**, *12*, 223–228.

as hindered phenols, but most naturally occurring fuel phenols are likely to be less reactive. Thus, the species class concentrations used in the model for AH and SH must be less than the measured species class concentrations.

For simplicity, dissolved metals were not included in previous pseudo-detailed chemical kinetic mechanisms of fuel oxidation. To assess the relative importance of dissolved metals in influencing oxidation behavior in the present work, a single metal-catalyzed reaction is appended to the kinetic mechanism (reaction 18 of Table 2):

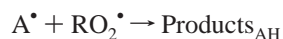
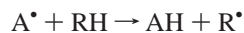


This reaction increases the rate of hydroperoxide decomposition via a catalytic pathway but is a simplification of the complex chemistry associated with dissolved metal catalysis in a number of respects. For example, the varied reactivity of individual dissolved metals such as Cu and Mn which are known to catalyze hydroperoxide decomposition³⁷ is not included here. In addition, the reaction is a simplification of the steps that may be involved in the catalysis of hydroperoxide decomposition. Two-step redox schemes of the form



have been proposed³⁸ for the catalytic decomposition of hydroperoxides involving dissolved metal ions with multiple oxidation states. However, recent studies utilizing density functional theory suggest that metal-catalyzed decomposition of hydroperoxides involves the formation of a complex and its subsequent decomposition to form radicals without regeneration of the metal ion.¹⁹ Another simplification associated with using the above single reaction is the exclusion of other catalytic reaction pathways that may be important. That is, in addition to the catalytic decomposition of hydroperoxides, dissolved metals may catalyze fuel oxidation and deposition via other reaction pathways. In addition, the single-step reaction cannot truly be catalyzed by metals, as the thermal hydroperoxide decomposition reaction is known to not contain a barrier.¹⁹ While the single catalysis reaction is a simplification of the poorly understood metal catalysis process, its inclusion in the mechanism provides a relatively simple method to assess the importance of metal catalysis in jet fuel autoxidation and deposition.

The mechanism of Table 2 also employs a refined set of reactions for peroxy radical inhibition compared to previous studies.⁴⁻⁶ These reactions (reactions 6 and 7 of Table 2),



replace a series of reactions which begin with reaction of A[•] with O₂ in the previous mechanism. As phenoxy radicals do not readily react with O₂, the previous mechanism is incorrect for phenol type AH species. The previous work employed reactions which represented AH species more broadly as the many different species capable of reacting with peroxy radicals,

as opposed to the current work where the AH species class is being associated with phenol species only. These new reactions have A[•] reacting with the fuel species RH or terminating with an RO₂ radical. In addition to more closely representing the important reactions which occur in this system, the new reactions provide improved agreement for the hydroperoxide profiles reported below.

Numerical Simulations. All chemical kinetic simulations presented here were performed using the LSODA solver³⁹ to integrate the multiple differential equations defined by the reaction mechanisms considered in a manner consistent with Whitbeck's methodology⁴⁰ for chemical kinetic simulations. It is important to note that these simulations do not solve the energy equation, so temperature changes due to exothermic or endothermic reactions are not modeled. At the relatively low temperature autoxidation conditions and low levels of dissolved oxygen considered here, energy changes should not be large enough to significantly affect the fuel temperature. In addition to individual chemical reactions and their associated rate parameters (*A* and *E_a*), the initial species concentrations for all species are required as inputs along with the reaction time, temperature, and tolerances for precision of the LSODA integration. Initial concentrations of [I]₀ = 1 × 10⁻⁸ M, [O₂]₀ = 1.8 × 10⁻³ M, and [RH]₀ = 4.7 M are used for all simulations of the present work. Individual fuel samples are modeled via initial concentrations of polar species ([AH]₀), reactive sulfurs ([SH]₀), hydroperoxide species ([ROOH]₀), and dissolved metals ([M]₀). The concentrations employed in the model for these species for each of the seven fuel samples are discussed in later sections. The initial concentrations of all remaining species in the mechanism are modeled as zero. The output for the kinetic simulations is concentration versus time for all species present in the reaction mechanism.

The computational fluid dynamics (CFD) simulations presented here were performed utilizing the commercially available FLUENT software package (Fluent, Inc., Lebanon, NH). The fuel flow within the tubing of the deposition experiments was assumed to be axisymmetric and steady. Thus, the conservation equations that are solved here may be expressed as

$$\frac{\partial(\rho V_z \Phi)}{\partial z} + \frac{\partial(\rho V_r \Phi)}{\partial r} = \frac{\partial}{\partial z} \left(\Gamma_\Phi \frac{\partial \Phi}{\partial z} \right) + \frac{\partial}{\partial r} \left(\Gamma_\Phi \frac{\partial \Phi}{\partial r} \right) - \frac{\rho V_r \Phi}{r} + \frac{\Gamma_\Phi}{r} \frac{\partial \Phi}{\partial r} + S^\Phi$$

In this equation, ρ is the fuel density, V_r is the radial velocity component, V_z is the axial velocity component, r represents a radial coordinate, and z represents an axial coordinate. Table 5 provides a list of the transport coefficients (Γ^Φ) and source terms (S^Φ) corresponding to solution variables represented by Φ . In Table 5, c_p is the specific heat, κ is the thermal conductivity, and μ is the absolute viscosity. The variables k , ϵ , h , P , and Y_i are the turbulent kinetic energy, its dissipation, enthalpy, pressure, and the mass fraction of species i , respectively. D is the diffusion coefficient, M_{w_i} is the molecular weight of species i , and $M_{w_i} \sum_{j=1}^{N_R} R_{i,j}$ is the rate of production. All simulations incorporate relationships describing the temperature dependence of fuel properties (density, thermal conductivity, specific heat, and absolute viscosity). The relationships used are based on curve fits of fuel property data.⁴¹ Here, we simulate the rate of initial surface deposition. The presence of the time-

(37) Syroezhko, A. M.; Begak, O. Y. *Russ. J. Appl. Chem.* **2004**, *77*, 1301–1307.

(38) Walling, C. *Free Radicals in Solution*; John Wiley & Sons: New York, 1957.

(39) Radhakrishnan, K.; Hindmarsh, A. C. 1993, UCRL-ID-113855.

(40) Whitbeck, M. *Tetrahedron Comput. Methodol.* **1990**, *3*, 497–505.

(41) Nixon, A. C.; Ackerman, G. H.; Faith, L. E.; Henderson, H. T.; Ritchie, A. W. 1967, AFAPL-TR-67-114.

Table 5. Transport Coefficients and Source Terms Appearing in Steady-State Axisymmetric Conservation Equation^a

Φ	Γ^Φ	S^Φ
1	0	0
Y_i	$\rho D + \frac{\mu_t}{\sigma_{Y_i}}$	$M_{W_i} \sum_{j=1}^{N_R} R_{ij}$
h	$\frac{k}{c_p} + \frac{\mu_t}{\sigma_h}$	0
V_r	$\mu + \mu_t$	$-\frac{\partial P}{\partial r} + \frac{\partial}{\partial z} \left(\Gamma^\Phi \frac{\partial V_z}{\partial r} \right) + \frac{\partial}{\partial r} \left(\Gamma^\Phi \frac{\partial V_r}{\partial r} \right) + \frac{\Gamma^\Phi}{r} \frac{\partial V_r}{\partial r} - 2\Gamma^\Phi \frac{V_r}{r^2}$
V_z	$\mu + \mu_t$	$-\frac{\partial P}{\partial z} + \frac{\partial}{\partial z} \left(\Gamma^\Phi \frac{\partial V_z}{\partial z} \right) + \frac{\partial}{\partial r} \left(\Gamma^\Phi \frac{\partial V_r}{\partial z} \right) + \frac{\Gamma^\Phi}{r} \frac{\partial V_r}{\partial z}$
k	$\mu + \frac{\mu_t}{\sigma_k}$	$G - \rho \epsilon$
ϵ	$\mu + \frac{\mu_t}{\sigma_\epsilon}$	$C_{1\epsilon} G \frac{\epsilon}{k} - C_{2\epsilon} \rho \frac{\epsilon^2}{k}$

$$^a \mu_t = \rho C_\mu \frac{k^2}{\epsilon}$$

$$G = \mu_t \left\{ 2 \left[\left(\frac{\partial V_z}{\partial z} \right)^2 + \left(\frac{\partial V_r}{\partial r} \right)^2 + \left(\frac{V_r}{r} \right)^2 \right] + \left[\left(\frac{\partial V_r}{\partial z} \right)^2 + \left(\frac{\partial V_z}{\partial r} \right)^2 \right] \right\}$$

$$C_{1\epsilon} = 1.44, C_{2\epsilon} = 1.92, C_\mu = 0.09, \sigma_k = 1.0, \sigma_\epsilon = 1.3, \sigma_{Y_i} = 0.70, \sigma_h = 0.85.$$

evolving surface deposits on the flow and heat transfer was not included in the simulations.

For NIFTR CFD simulations, a constant wall temperature boundary condition of 185 °C is prescribed. The flow is assumed to be laminar within the NIFTR tubing based on previous analysis of the flowfield under similar experimental conditions.⁸ A uniformly spaced computational grid of 180 axial elements by 15 radial elements is used to model the axisymmetric geometry. Analysis of the effects of grid resolution on the simulated centerline temperature in the entry region of the NIFTR tubing was used as a basis for determining required grid resolution. Simulations of the centerline temperature in the NIFTR experiments indicate that the temperature is isothermal over more than 90% of the tubing length. This result has important ramifications in later analyses of chemical reactions occurring in the flowfield and along the wall boundary.

For ECAT CFD simulations, a fit of the measured outer wall temperatures is used to prescribe an axially varying temperature profile along the flowfield outer boundary (interior wall). As the tube wall is thin (0.02 in. thickness), the radial temperature gradient between the outer and inner wall is not modeled for simplicity. The flow is modeled as turbulent within the ECAT tubing based on previous flowfield analysis of non-isothermal experiments performed with the same tubing at similar flowrates. A standard $k-\epsilon$ turbulence model is used. A uniformly spaced computational grid of 360 axial elements by 30 radial elements is used to model the axisymmetric geometry. Analysis of the effects of grid resolution on simulated mass-averaged bulk exit temperatures over the range of ECAT experiments was used as a basis for determining the required grid resolution. The simulated bulk exit temperatures (not shown) are within 1% of the measurements for all experiments.

Results and Discussion

Chemical Kinetic Modeling of Fuel Oxidation. A series of thermal oxidative test runs were performed on seven fuel samples to generate an experimental data set suitable for evaluation of the role of the species classes discussed above in the autoxidation mechanism. NIFTR experiments were conducted at 185 °C on each of the seven fuels, and dissolved

oxygen and hydroperoxide concentrations were measured as a function of flow rate (i.e., at varying residence time). This temperature was selected as representative of the highest temperatures of fuel exposure in aircraft fuel system engine nozzles, where deposition is most problematic. Flow rate ranges were selected so that the complete oxygen consumption profile would be measured. As each fuel experiment is performed under identical conditions, the variances in oxidation behavior observed are due to chemical composition differences between the fuels. Figure 2 shows the dissolved oxygen consumption profiles of the seven fuels in these NIFTR experiments. The figure shows that the dissolved oxygen consumption rates of the fuel samples vary by almost an order of magnitude, with complete oxygen consumption times ranging from ~1.5 to almost 9 min. The observed differences in oxidation rates are due to the varied species class compositions of the fuels. Fuel-like hydrocarbon mixtures with essentially zero heteroatom and metals content, such as Exxsol D80, display very fast oxidation curves with complete oxygen consumption in <1 min.⁴² The slower oxidation rates observed for these fuels are due to the

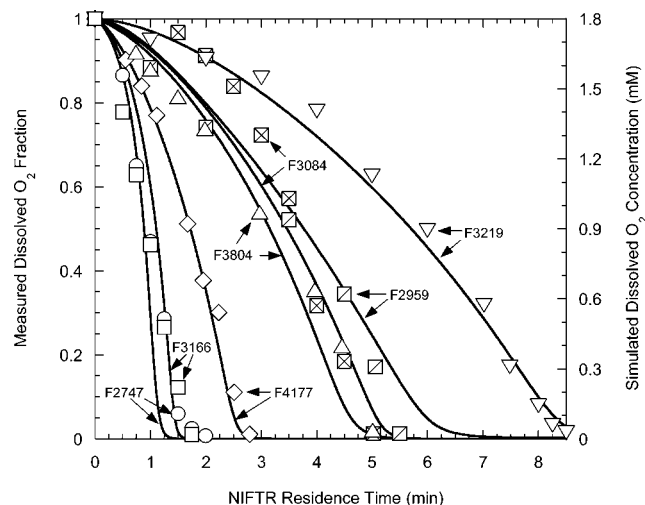


Figure 2. Comparison of measured and simulated dissolved oxygen consumption for seven fuels stressed at 185 °C. Symbols denote measurements. Curves denote chemical kinetic simulations.

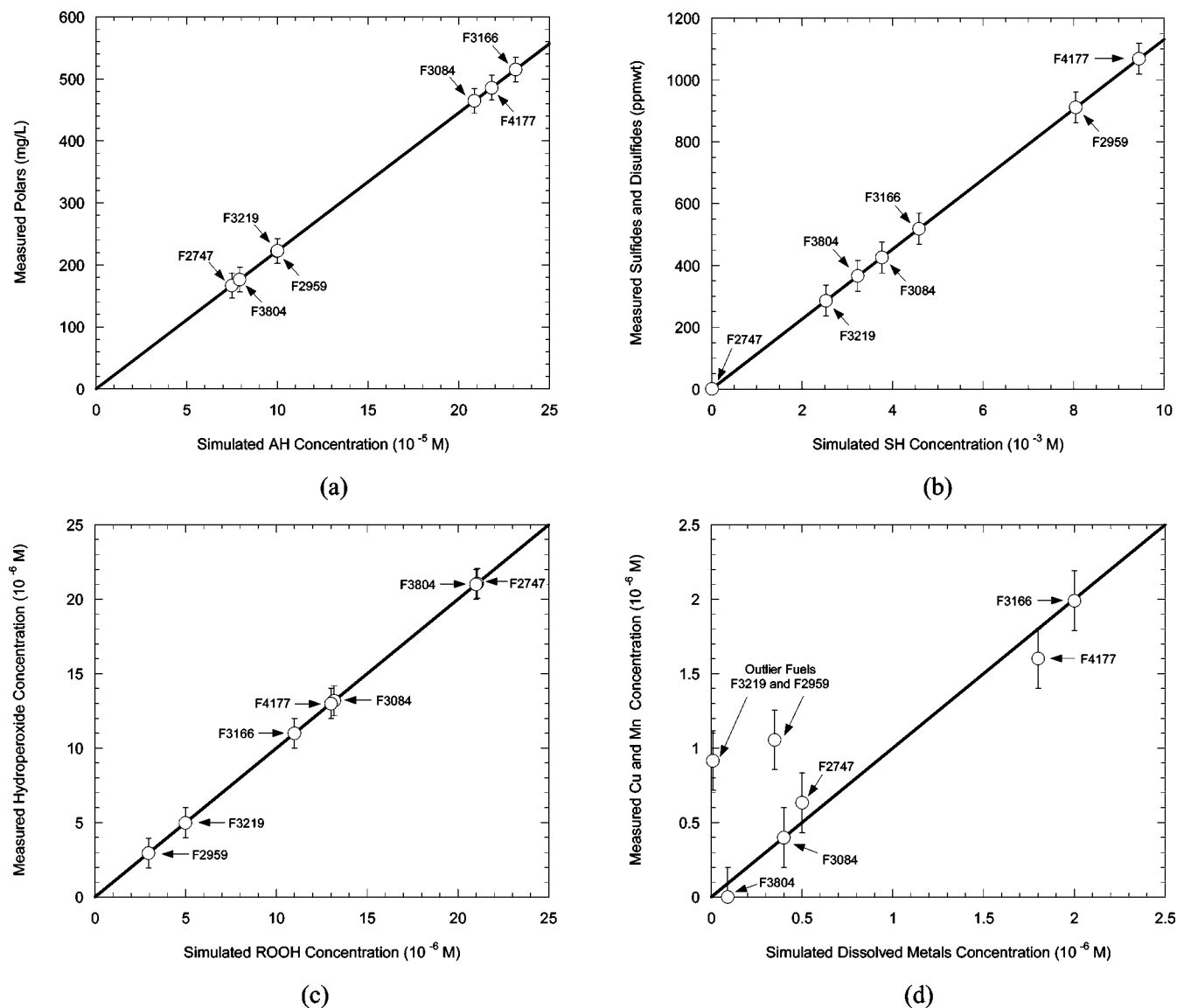


Figure 3. Plots of measured concentrations for various species classes vs concentrations used to model fuel samples in numerical simulations: (a) polars vs AH; (b) reactive sulfurs vs SH; (c) hydroperoxides vs ROOH; (d) dissolved metals (Cu + Mn) vs M.

presence of species that slow the autoxidation chain. The curved lines in Figure 2 are chemical kinetic simulations for each of the fuels. The figure shows that very good agreement between the measured oxidation profiles and the modeled profiles were obtained for all seven fuels. The kinetic modeling results reported here utilize the mechanism of Table 2 for each of the fuels. The mechanism and Arrhenius parameters employed were not adjusted for the different fuel samples, rather, the AH, SH, ROOH, and metals species class input concentrations to the model were different for each fuel. The relationships developed between the measured species class concentrations (Tables 3 and 4) and initial concentrations input to the model for these species classes are shown in Figure 3. The figure shows that proportional relationships were used for the peroxy radical inhibiting (AH) and hydroperoxide decomposing (SH) species classes and that the measured hydroperoxide concentrations were used directly in the model. A proportional relationship in metals content did not allow good agreement for all seven fuels with the measured oxygen profiles. Figure 3 shows that for the metals species a proportional relationship only holds for five of the

seven fuels; for two of the fuels (F3219 and F2959), agreement with the oxidation curves could only be obtained if lower concentrations of metal content than the measured values were employed. Further study of the metals content of these fuels was performed to determine the cause of this discrepancy.

The concentrations of dissolved metals found in the seven fuels is summarized in Table 4. As stated above, only the Cu and Mn concentrations were employed in the model, as the concentrations of the other metals do not differ appreciably among the various fuels. In addition, it is known that Cu and Mn play a role in catalysis of hydroperoxide decomposition³⁷ and that Fe, Mg, and Zn are thought to affect fuel oxidation and deposition only at higher levels.² It was hypothesized that if some of the fuels contained metal deactivator additive (MDA), this could be inhibiting the catalytic activity of the metal and result in a nonproportional modeling relationship. If MDA is present in a fuel, the metal activity would be reduced, resulting in a measured metal content which is too high for use in the model. Ultimately, it is desirable to measure only metals which are not complexed with MDA and thus available for catalytic activity, but the standard ICP analysis yields the total metals content of each metal (i.e., both complexed and uncomplexed

(42) Balster, L. M.; Balster, W. J.; Jones, E. G. *Energy Fuels* **1996**, *10*, 1176–1180.

metals). To address this hypothesis, MDA analyses⁴³ of each of the fuels was performed, which yielded measurable uncomplexed MDA in fuel F3219 only (the technique employed only responds to uncomplexed MDA). This is one of the two outlier fuels in the metals plot of Figure 3. Finding uncomplexed MDA in this fuel indicates that this fuel contains excess MDA and that all metal species are likely complexed. Thus, the metals concentration used in the model for this fuel should be zero or very low, which is precisely where the F3219 data point needs to be to fall on the $y = x$ line shown in the metals plot of Figure 3. Thus, MDA can account for the first outlier fuel in the metals plot. MDA was not detected in the second outlier fuel (F2959), but again, the analysis technique employed only measures uncomplexed MDA. The metals plot of Figure 3 suggests that for fuel F2959, while MDA may be present, its concentration is not high enough to complex all the metal species present, and thus, an excess of uncomplexed MDA would not be expected. These results indicate that techniques need to be developed to quantify “reactive metals”, i.e., dissolved metals in the fuel that are actively involved in catalysis reactions. Unfortunately, most metal analysis techniques do not distinguish between inactive (e.g., complexed with MDA) and active (or reactive) metals. One promising method which is able to provide this differentiation uses HPLC to separate the metals species, with flame atomic absorption detection of the metal atoms.^{44,45}

While being able to simulate the dissolved oxygen consumption of seven fuels using measured species classes shows that the kinetic mechanism and species class method is promising, a more stringent evaluation is provided by comparing the simulated and measured changes in hydroperoxide concentrations that occur during thermal stressing. These results are shown in Figure 4. The hydroperoxide quantities produced vary by over an order of magnitude for the seven fuels, ranging from ~ 0.05 (F3804) to ~ 1.3 mM (F2747). In addition, the residence times of the peak hydroperoxide concentration vary substantially from ~ 1.3 min (F3166) to fuels for which the hydroperoxide concentration is still increasing at 7 min (e.g., F3219). This varied behavior reflects the different quantities of species involved in the production and destruction of hydroperoxides for each fuel. Reactive metals catalyze oxidation and hydroperoxide decomposition and thus increase the oxidation rate and both the hydroperoxide production and removal rate, while reactive sulfur species remove hydroperoxides and thus lower the hydroperoxide level and increase the removal rate. Also, polar phenols react with peroxy radicals and slow the oxidation rate, thus slowing the rate of production of hydroperoxides. Figure 4 also shows the hydroperoxide concentrations simulated by the kinetic mechanism. Although the hydroperoxide simulations are not as accurate as the dissolved oxygen simulations, the model predictions of hydroperoxide peak location and absolute peak concentration agree reasonably well with the measurements. This work is the first successful modeling of hydroperoxide concentration vs time over a range of jet fuel samples and does so concurrently with the modeling of dissolved oxygen consumption.

The ability to simulate oxidation rates and hydroperoxide profiles using a kinetic mechanism and measured species class concentrations over a range of fuel samples provides confidence that the mechanism correctly includes the most important reaction chemistry and that measured species class concentrations can be used to determine autoxidation reactivity of fuels.

(43) Striebich, R. C.; Grinstead, B.; Zabarnick, S. *J. Chromatogr. Sci.* **2000**, *38*, 393–398.

(44) Taylor, D. B.; Synovec, R. E. *Talanta* **1993**, *40*, 495–501.

(45) Taylor, D. B.; Synovec, R. E. *J. Chromatogr.* **1994**, *659*, 133–141.

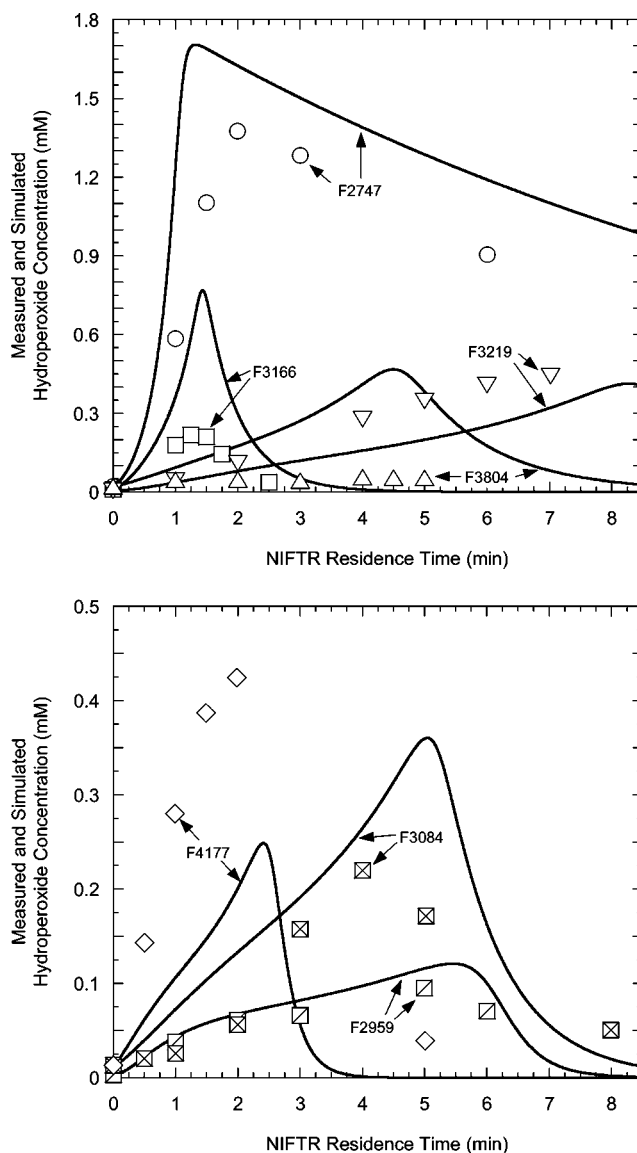


Figure 4. Comparison of measured and simulated hydroperoxide concentrations for seven fuels in the NIFTR at 185 °C. Symbols denote measurements. Curves denote chemical kinetic simulations: (a) F2747, F3166, F3219, and F3804; (b) F2959, F3084, and F4177.

These results also give confidence in beginning the next step, which is the development of a submechanism for production of surface deposits, toward the goal of enabling the prediction of jet fuel oxidation and deposition over a range of fuels, temperatures, and flow environments.

Computational Fluid Dynamics (CFD) Simulations of Jet Fuel Deposition.

Despite numerous studies of the production of surface deposits during fuel autoxidation, very little is known about the chemical mechanisms which initiate and propagate this process. Here, it is hypothesized that deposits result, at least in part, from subsequent reactions of the autoxidation products of peroxy radical inhibitors (AH), such as naturally occurring phenols, and hydroperoxide decomposers (SH), such as fuel sulfides and disulfides. Such processes would account for the tendency of slow oxidizing fuels to form relatively high levels of deposits and fast oxidizing fuels to generate only low amounts of deposits,²⁴ as the same species which slow oxidation also increase deposition. In addition, it is likely that some subclass, or subclasses, of fuel nitrogen compounds (e.g., indoles and/or carbazoles) also contributes to surface deposition,^{2,46} but the role of nitrogen species has not been explored in the present

Table 6. Candidate Global Deposition Submechanisms

deposit submechanism	reaction number	reaction type	reaction
a	19	wall	Products _{AH} → deposits
b	19	wall	Products _{AH} + O ₂ → deposits
c	19	bulk	Products _{AH} → solubles
	20	bulk	Products _{AH} → insolubles
	21	wall	insolubles → deposits

work. In this section, the reactions which play a role in initiating surface deposition and the kinetics involved in these reactions are further explored. As the deposition process is poorly understood and extremely complex, the reactions employed here for the deposit submechanism are necessarily global in nature. That is, the reactions employed simulate a large amount of poorly understood chemistry and do not represent individual elementary reactions. Thus, Arrhenius parameters used in the deposition submechanism have no chemical significance, in contrast to the reactions of the oxidation mechanism (Table 2).

Various global reactions are available as candidates for the deposit submechanism. It is important to select a reaction or series of reactions that is able to reproduce the observed deposition profiles as well as the time, temperature, and flow dependencies of deposition. Reaction selection is also complicated by the fact that deposit formation reactions can occur directly at the wall surface, or initially in the bulk fuel with subsequent reaction or adherence on the wall. In selecting candidate global deposition reactions, the goal is to select the simplest reaction set which yields the observed deposition profiles over a range of fuels and reaction conditions. It is important to note that the deposition submechanism is closely coupled to the autoxidation mechanism discussed above. As deposition is directly related to the oxidation process, it is essential to correctly simulate the rates and oxidation profiles of a range of fuels to have an opportunity to model deposition properly. One limitation of the current autoxidation mechanism is that, while the hydrocarbon/oxygen part of the mechanism was developed over a range of temperatures,⁶ the reactions of the species classes AH, SH, and metals have only been validated at a single temperature. This limitation needs to be considered in the non-isothermal deposition study reported below.

Three global deposition submechanisms were examined in this work, and they are listed in Table 6. Initial computational modeling indicated that, for the AH and SH species levels found in the current fuels and the conditions of the experiments reported here, deposit production due to SH reaction products was negligible relative to those produced via AH reaction products. Thus, for the current study, SH reaction products were not included in the deposition submechanism, although SH reaction products may need to be included in the future for deposition submechanisms employed for a larger set of fuels and/or other reaction conditions.

The first global deposition submechanism (submechanism a in Table 6) consists of a single, direct reaction of Products_{AH} (i.e., the termination products of the reaction of RO₂^{*} with A^{*}) at the wall to form deposits. This is the simplest and most direct path to deposits using the assumption that deposits result from AH oxidation reaction products. The second global deposition submechanism considered (submechanism b in Table 6) is also a single reaction where Products_{AH} species react with dissolved oxygen at the wall to form deposits. The third global deposition submechanism (submechanism c in Table 6) consists of three reactions, where AH reaction products form both soluble and

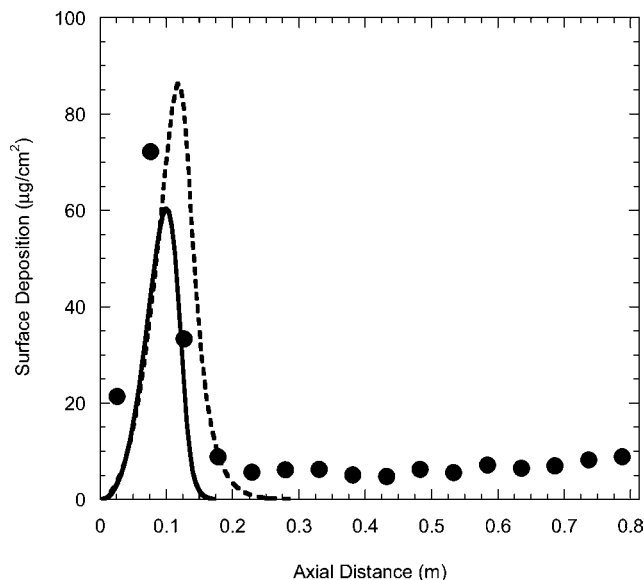


Figure 5. Comparison of measured and simulated deposit profiles for near-isothermal testing of jet fuel F2747. Symbols denote measurements, and curves denote computational fluid dynamics simulations for submechanism b (solid curve) and submechanism c (dashed curve).

insoluble species in the bulk fuel, with subsequent reaction of the insoluble species at the wall to form deposits. The first two submechanisms are adaptations of initial reactions studied recently,¹⁰ where oxygen was added in the second submechanism to provide improved deposition profiles. The third submechanism was created in the current study to provide improved agreement for the absolute deposit magnitude between the model calculations and the experiment measurements. These results are detailed below in studies of the modeling of deposition in near-isothermal (NIFTR) and non-isothermal (ECAT) reactors.

Near-Isothermal Deposition. NIFTR deposition experiments on each of the seven fuels were performed at identical conditions of flowrate (0.25 mL min⁻¹), temperature (185 °C), and stress time (72 h). Thus, differences in deposition profiles and magnitudes among the fuel samples are driven by the varying chemical composition of the fuels and the resulting changes in oxidation rate and deposit forming tendencies. Figures 5–11 show the measured deposition of the seven jet fuel samples from these experiments. The figures show that the measured peak deposition varies by over an order of magnitude, ranging from ~10 (for fuel F3219) to ~160 µg cm⁻² (for fuel F3166). The axial locations in the tube at which the peak deposition occurs also vary significantly from ~0.08 (F2747) to ~0.48 m (F2959 and F3219) and appear to be related to the oxidation rate. That is, fuels that oxidize quickly tend to exhibit peak deposition further upstream than those that oxidize more slowly. In addition, slow oxidizing fuels tend to have broader deposition peaks than fast oxidizing fuels.

In previous work under similar near-isothermal conditions, it has been noted that the axial location of the fuel autoxidative peak deposition is usually observed near the location of maximum oxidation rate.⁴⁷ Thus, if a proper deposition submechanism is employed, the CFD simulations should provide a good estimation of the location of the peak deposition over the range of fuels, as the autoxidation mechanism utilized here closely simulates the measured oxidation profiles. For a given global deposition submechanism, it is important to note that the only model inputs that are varied are the initial concentra-

(46) Taylor, S. E. *Prepr. Pap.—Am. Chem. Soc., Div. Pet. Chem.* **2002**, 47, 165–169.

(47) Jones, E. G.; Balster, W. J.; Post, M. E. 1993, ASME 93-GT-334.

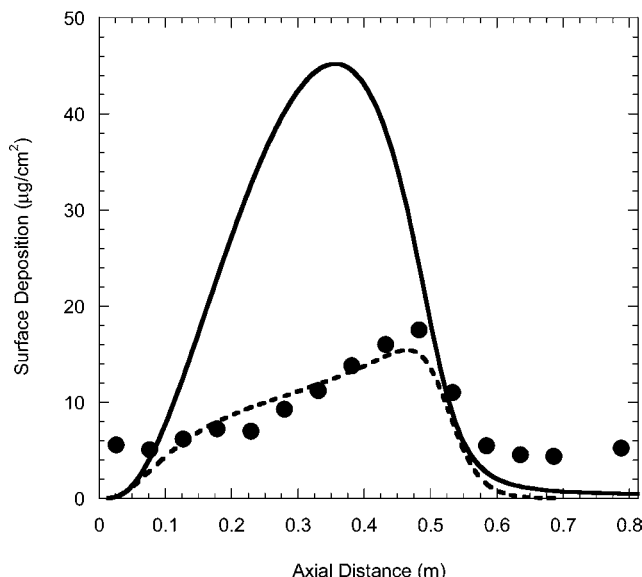


Figure 6. Comparison of measured and simulated deposit profiles for near-isothermal testing of jet fuel F2959. Symbols denote measurements, and curves denote computational fluid dynamics simulations for submechanism b (solid curve) and submechanism c (dashed curve).

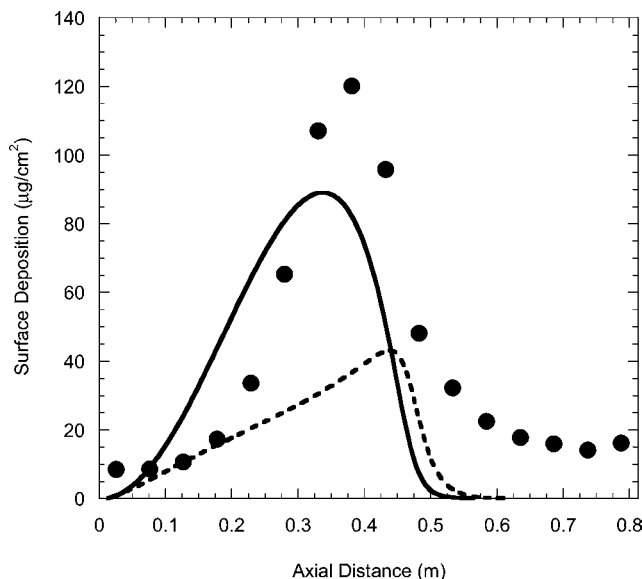


Figure 7. Comparison of measured and simulated deposit profiles for near-isothermal testing of jet fuel F3084. Symbols denote measurements, and curves denote computational fluid dynamics simulations for submechanism b (solid curve) and submechanism c (dashed curve).

tions of species classes (AH, SH, ROOH, and dissolved metals) for the various fuel samples. Reactions comprising the global deposit submechanisms are appended to the oxidation kinetic mechanism of Table 2. The rate constants at 185 °C of the global reactions in the deposit submechanism are calibrated by iterative adjustment of these values to provide the best match of deposit magnitude and axial location to the measured deposition profiles over the range of fuel samples. No constraints are placed on the values of the rate constants in the deposition submechanism as the reactions are global and are not meant to represent elementary chemical reactions.

The first global mechanism considered (submechanism a) is a single, direct reaction of AH reaction products at the wall to form deposits. This submechanism was found to yield reasonable simulations (not shown here) of the peak deposit locations for the NIFTR deposition experiments but was unable to simulate

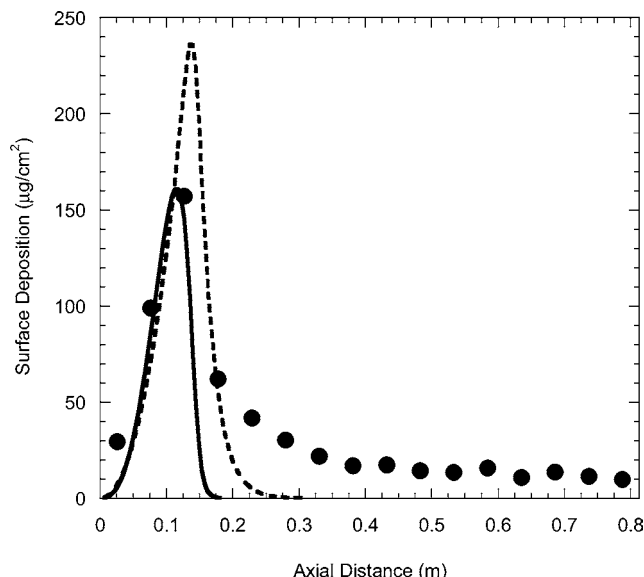


Figure 8. Comparison of measured and simulated deposit profiles for near-isothermal testing of jet fuel F3166. Symbols denote measurements, and curves denote computational fluid dynamics simulations for submechanism b (solid curve) and submechanism c (dashed curve).

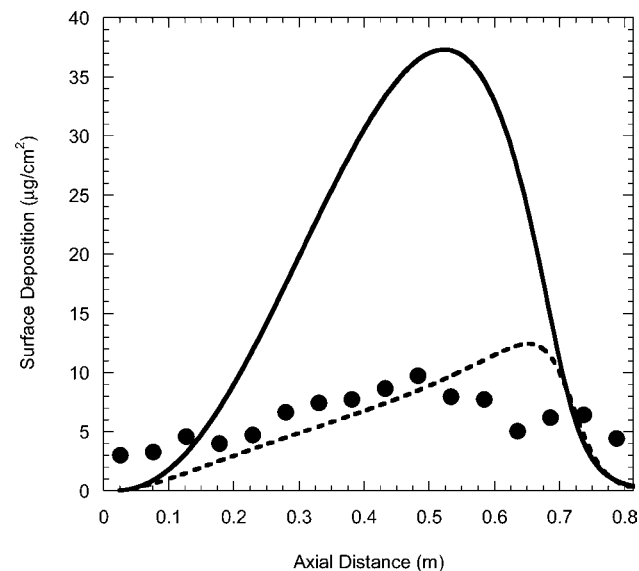


Figure 9. Comparison of measured and simulated deposit profiles for near-isothermal testing of jet fuel F3219. Symbols denote measurements, and curves denote computational fluid dynamics simulations for submechanism b (solid curve) and submechanism c (dashed curve).

the magnitude of the deposition correctly. For relatively high values of the 185 °C rate constant for the deposition reaction, where all $\text{Products}_{\text{AH}}$ species result in the formation of deposits, the simulated peak deposit magnitude was orders of magnitude greater than the measurements. Reduction of the 185 °C rate constant resulted in a reduced magnitude of the simulated peak deposition, due to the resultant slowing of the reaction, but also yielded unacceptably large simulated deposits downstream of the peak. Thus, this simple deposit submechanism does not provide the correct reactions to allow proper simulation of the measured deposition and was not considered further.

Submechanism b was created to address the deficiencies in submechanism a, by adding oxygen as a reactant to the wall reaction of $\text{Products}_{\text{AH}}$. This modification should result in reduced deposition downstream of the oxygen consumption curve, as the deposition reaction rate is now proportional to the oxygen concentration. The results of using submechanism b are

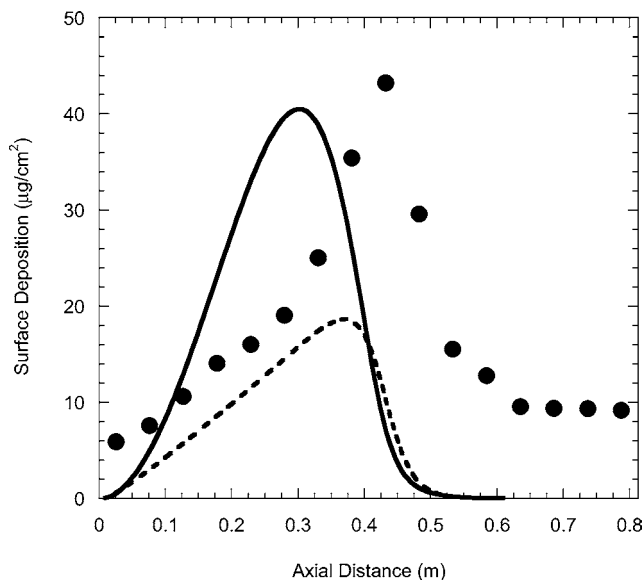


Figure 10. Comparison of measured and simulated deposit profiles for near-isothermal testing of jet fuel F3804. Symbols denote measurements, and curves denote computational fluid dynamics simulations for submechanism b (solid curve) and submechanism c (dashed curve).

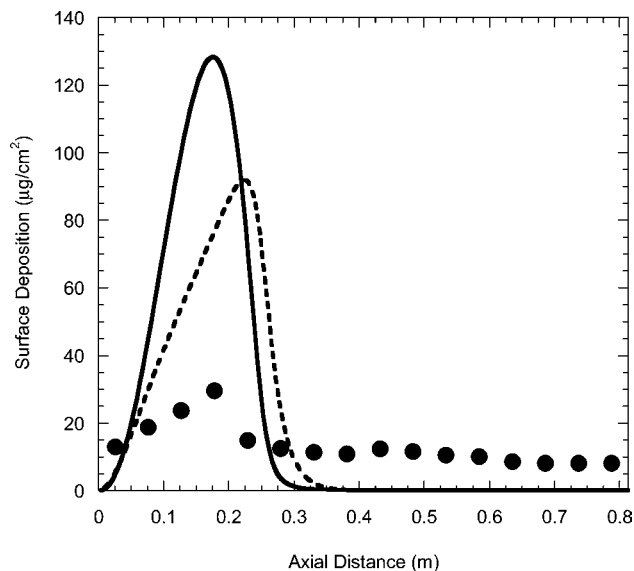


Figure 11. Comparison of measured and simulated deposit profiles for near-isothermal testing of jet fuel F4177. Symbols denote measurements, and curves denote computational fluid dynamics simulations for submechanism b (solid curve) and submechanism c (dashed curve).

compared with the experimental measurements in Figures 5–11 for each of the fuels. A 185 °C rate constant value of $k_{19b} = 5 \times 10^{-4} \text{ L mol}^{-1} \text{ s}^{-1} \text{ m}^{-1}$ was found to most closely simulate the measured deposits. The plots show that the submechanism does a very good job of simulating the deposit peak location for all the fuels but does a better job of simulating the deposition magnitude for higher peak deposit fuels (e.g., F2747, F3084, and F3166) than for lower depositing fuels. For these higher peak deposit fuels, the simulation is within 30% of the measurement, but for the lower depositing fuels, the simulation is only within a factor of 4 and always greater than the measurement.

Submechanism c was created to address the deficiencies in submechanism b. This submechanism consists of a three-step scheme with two bulk reactions and a single wall reaction. In the two bulk reactions, $\text{Products}_{\text{AH}}$ can react to form either soluble or insoluble precursors, and in the wall reaction, the

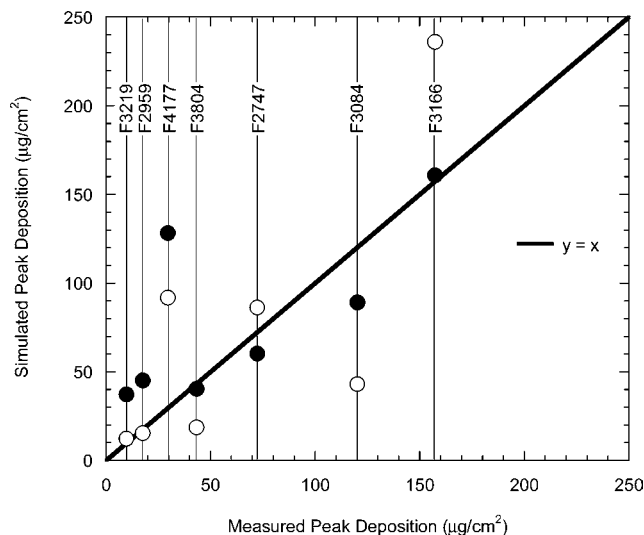


Figure 12. Comparison of measured and simulated peak deposition for seven jet fuel samples using global deposition submechanisms b and c of Table 6. Closed circles correspond to submechanism b, and open circles correspond to submechanism c.

insoluble precursors can react to form deposits. This submechanism creates a competition in which only a fraction of the products may react at the wall and provides the ability to more readily calibrate the model for deposition magnitude. With this submechanism, the location of the deposit peak is primarily a function of the oxidation rate and the rate of the wall reaction, while the deposit magnitude is primarily a function of the competition between the bulk reactions. It also provides for the formation of soluble and insoluble products, as well as wall deposits, all of which are known to form in fuel autoxidative systems. The plots in Figures 5–11 show that this submechanism also does a very good job at simulation of the axial location of the deposition peak for each of the fuels, but it also provides improved agreement with the measurements for the low peak depositing fuels. Rate constant values (185 °C) of $k_{19c} = 1 \times 10^9 \text{ s}^{-1}$, $k_{20c} = 3 \times 10^7 \text{ s}^{-1}$, and $k_{21c} = 5 \times 10^{-5} \text{ s}^{-1} \text{ m}^{-1}$ are used in the simulations and were again selected based on iterative analysis over the entire range of fuel samples. For the two lowest depositing fuels, F2959 and F3219, the submechanism provided very good agreement for the deposit magnitudes (within 30%) and profiles. For the other five fuels, the simulations yield deposit peak magnitudes that are from 20% to a factor of 3 of the measurements, without a propensity for being too high or low.

Figure 12 provides a comparison of the measured and simulated peak deposition magnitude over the range of fuel samples using global deposit submechanisms b and c. For the lowest depositing fuels (F2959, F3219, and F4177), the three-reaction submechanism is more accurate than the single-reaction mechanism. For all remaining, higher depositing fuels, the single-reaction model is as accurate (F2747) or more accurate (F3804, F3084, and F3166) than the three-reaction mechanism. The results appear to indicate a change in the global deposit submechanism with increasing fuel deposit level. This may be due to a change of deposition chemistry which occurs as the tube surface develops an increasingly thick layer of deposit, perhaps because of entrapment of fuel in the deposit structure. Further elucidation of this effect will require additional studies with a significantly larger set of fuels. Both submechanisms are able to quantitatively simulate the deposit production magnitude and location within a factor of 4 for the fuel with the worst agreement and, more typically, within a factor of 2

Table 7. Rate Parameters for Three-Reaction Global Deposition Submechanism

reaction number	reaction	A	E_a (kcal mol ⁻¹)	k_{185C}
19	Products _{AH} → solubles	1×10^9 s ⁻¹	0	1×10^9 s ⁻¹
20	Products _{AH} → insolubles	3.8×10^{10} s ⁻¹	6.5	3×10^7 s ⁻¹
21	insolubles → deposits	3×10^3 s ⁻¹ m ⁻¹	16.3	5×10^{-5} s ⁻¹ m ⁻¹

for these conditions and range of fuels. Overall, the results show the ability to quantitatively simulate the deposit production magnitude and location in flow systems for various fuels using only readily measured species class concentrations. Further evaluation of the usefulness of the approach is performed in the next section via simulations of deposition occurring in a non-isothermal flowing environment.

Non-Isothermal Deposition. The near-isothermal deposition experiments and modeling reported above show the promise of utilizing the methodology described here for prediction of jet fuel deposition. The single-temperature, near-isothermal environment provides a simplified temperature condition which enabled development of the autoxidative and deposition mechanisms, as well as inclusion of measured species class concentrations. As fuel is subjected to severe temperature changes in aircraft fuel systems, it is essential to perform experimental and modeling simulations of such non-isothermal flow environments. The ECAT test rig is utilized here to evaluate the assumed oxidation and deposition mechanism and species class methodology on a flow environment in which the fuel undergoes substantial temperature increases throughout the test tube. Here, fuel F4177, a JP-8 fuel that is included in the set of seven fuels, is run in the ECAT at three temperature conditions (maximum wall temperatures of 340, 370, and 400 °C) with subsequent determination of the surface deposit axial profiles. As each of the ECAT experiments was performed with the same tubing, flow rate, and fuel, the differences in observed deposition behavior are controlled by differences in the thermal environment (e.g., the temperature-dependent chemistry). The oxidation mechanism and input species class concentration profiles are the same as those employed in the previous section. The three-reaction global deposition submechanism (submechanism c) is employed as it provided the best agreement for the near-isothermal deposition of this fuel. It is important to note that the 185 °C rate constant values determined for the global deposition reactions in analysis of the near-isothermal deposition are maintained here. However, in contrast to the near-isothermal simulations, the Arrhenius parameters of the deposit submechanism reactions need to be determined for these non-isothermal conditions. The approach taken here was to first “calibrate” the rate parameters (A and E_a) of the three global reactions for the mid-temperature experiment, subject to the constraint of matching the 185 °C rate constant values. The resulting mechanism is then utilized without any further modifications in simulations of the two additional non-isothermal experiments (one at a higher wall temperature and one a lower wall temperature). Thus, the accuracy of the simulated deposition for the higher and lower temperature experiments provides an indication of the predictive capability of the model with changes in temperature.

The calibration of the rate parameters for the global deposition reactions involved iterative comparisons of deposition simulations and measurements for the mid-temperature experiment. The rate parameters determined for these global reactions are shown in Table 7. The AH, SH, metals, and global deposit submechanism parts of the model have not previously been validated at varying temperature conditions, so these non-isothermal experiments, with temperatures from 21 to ~400 °C, provide a

stringent evaluation of both the oxidation mechanism and deposition submechanism.

Figure 13 shows measurements of deposition for the three F4177 ECAT experiments. The figure shows that the peak deposition locations (~0.6–0.8 m) and magnitudes (~90–160 μg cm⁻²) are temperature-dependent, where increasing the temperature results in a larger deposition peak which occurs earlier in the tube. The resulting deposit simulations are shown as curves in the figure and indicate that the axial locations of the simulated peak deposition agree quite well with the measurements for the three experiments. Although the rate parameters of the global reactions were constrained to match the 185 °C rate constant values established in the NIFTR deposition analysis, it was found that quite reasonable simulations of the magnitude and distribution of deposition were still obtained. It should be noted that while many sets of rate parameters for the global reactions can fit this constraint, the parameters employed here were found to provide the best fit to the data. These results indicate that the oxidation mechanism is useful over a broader and higher range of temperatures than has been previously validated.

For the mid-temperature case, which was used to calibrate the global reaction rate parameters, Figure 13 shows that the simulated peak deposition is within 5% of the measurement. In the transition from the mid-temperature case to the low-temperature case, the model correctly predicts a reduction in peak deposition magnitude along with a downstream shift in peak deposit location. In contrast, for the transition from the midtemperature case to the high-temperature case, the model does not predict an increase in peak deposit as is seen in the experimental measurements, although the simulated peak deposit

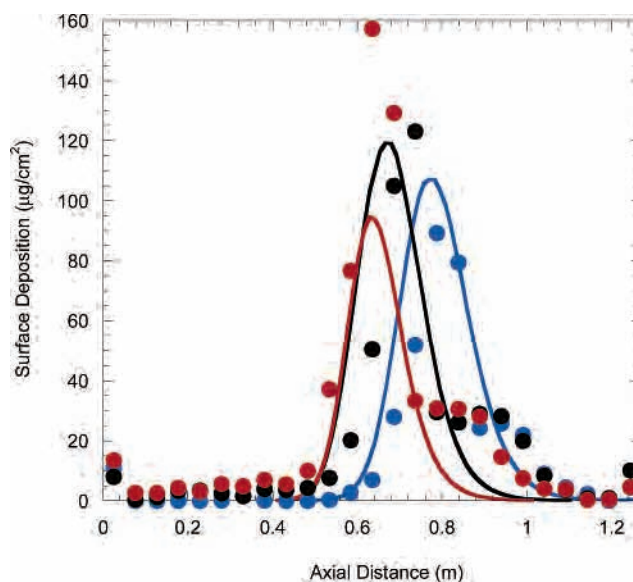


Figure 13. Comparison of measured and simulated deposition occurring in non-isothermal flowing environments for jet fuel sample F4177. Symbols denote measurements, and curves denote computational fluid dynamics simulations. The blue symbols/curve indicate the lowest-temperature experiment (340 °C maximum wall temperature), the black symbols/curve indicate the mid-temperature experiment (370 °C maximum wall temperature), and the red symbols/curve indicate the highest-temperature experiment (400 °C maximum wall temperature).

of the high-temperature case is within 60% of the measurement. Further analysis of species profiles for the high-temperature case indicates that the reduction in peak deposition in the simulation is due to reaction 16, $\text{RO}_2^\bullet \rightarrow \text{R}^\bullet + \text{O}_2$, of the mechanism becoming increasingly fast with temperature. Ultimately, this results in a slowing of the oxidation process and a corresponding reduction in deposition. Future work needs to examine in more detail the effect of this reaction, and the entire mechanism, on the temperature dependence of deposition.

The measured deposition profiles shown in Figure 13 each exhibit a shoulder on the downstream side of the deposition peak that is not predicted by the simulations. Additional work was performed (not shown here) to ascertain the source of this downstream shoulder. In these runs, ECAT deposits were measured at various test times. The results indicate that the shoulder becomes more prominent at shorter test times than the studies reported here. These results indicate that the shoulder is likely due to deposition which occurs during fuel/tube temperature stabilization during the startup of the test. During oven heatup, as the fuel approaches the ultimate test temperature, the fuel will be at various temperatures below the final temperature. At these lower temperatures, deposition will occur further downstream in the tube than at the final test temperature, thus generating an apparent shoulder in the deposition. Thus, the CFD model, which simulates the steady portion of the test run where the temperature at any point in the tube is constant, would not be expected to simulate this shoulder, which can be considered to be an artifact of the startup procedure of the experimental test.

Overall, the model does a very good job of simulating the deposit location and peak magnitude for this fuel over the wide range of temperatures to which the fuel is exposed during its transit through the tube. These results indicate that combining a suitable chemical kinetic mechanism with CFD modeling provides promise in simulating oxidation and deposition in the complex temperature and flow environment encountered in actual aircraft fuel system components.

Future Work. While the results reported here indicate that the methodology of using species class measurements along with a chemical kinetic mechanism for the simulation of oxidation and deposition is quite feasible, the method needs to be further refined in a number of important areas. These include improved species class analyses, improved understanding of the role of species classes and their interactions, refinements in the chemical kinetic mechanism, additional deposition and oxidation experimental data over wider ranges of conditions, and additional experimental data on a larger set of fuel samples. In particular, the role of metal and nitrogen species in the autoxidation process needs to be better understood so that these species can be properly included in the mechanism. In addition, improved analysis methods are needed for both the metal and nitrogen species classes. The metal species need to be measured accurately in the parts per billion range and speciated into reactive and nonreactive components, while methods need to be developed to quantify the nitrogen species by species class (e.g., indoles, carbazoles, etc.). In addition, more work needs to be performed to determine the concentrations and temperatures at which various fuel metals species begin to play a role in catalysis. The mechanism needs to be modified to include the differences in reactivity between hindered and non-hindered phenols, as hindered phenols are more efficient at intercepting peroxy radicals but are likely less efficient at producing deposition. Analysis techniques need to be developed to differentiate between these species as classes. Also, the mech-

anism needs to be modified to include the different roles of paraffinic and aromatic species, as it currently does not differentiate between these species which have very different reactivities in these systems. Additional experimental data needs to be acquired over a wide range of temperatures to better simulate the range of temperatures to which fuel is exposed in aircraft fuel systems. This additional data will help better determine the proper Arrhenius parameters that are required in the mechanism. Data over a wide range of temperature may also indicate other reactions that may need to be included under extrapolated conditions, e.g., relatively high and low temperatures. The increasingly important role of peroxy radical decomposition at higher temperatures is an example of the type of information which resulted from the present study. In addition, further studies of fuel autoxidation are needed to better understand the complexities of acid/base catalysis on autoxidation, the role of metal surfaces on the catalysis of deposition, and the role of metal deactivators on bulk and surface deposition. Improvements in all of the reactions of the mechanism will come with future studies on techniques to determine the Arrhenius parameters of the reactions of interest.

Ultimately, the fuel system and fuel component designer are concerned with the deposition which occurs over the lifetime of the component, which is exposed to many fuels over thousands of hours. Thus, future work also needs to address the expected average deposition produced over a typical variety of fuel samples, so that designers can use simulations such as these to modify their component designs and/or limit temperatures to minimize deposition in critical areas. In addition, studies of flow and deposition in complex geometries which simulate the aircraft engine nozzle environment are necessary.

Conclusions

This paper describes the development of a modeling methodology to enable the prediction of liquid-phase autoxidation and deposition of jet fuels. A chemical kinetic mechanism developed previously is refined to include the roles of key fuel species classes, such as phenols, reactive sulfur species, dissolved metals, and hydroperoxides. The concentrations of these fuel species classes in the unreacted fuel samples are measured experimentally and used as an input to the mechanism. The resulting model is used to simulate the autoxidation behavior observed over a range of seven fuel samples. The model includes simulation of the consumption of dissolved oxygen, as well as the formation and consumption of hydroperoxide species during thermal exposure. Proportional relationships were developed to incorporate the measured species class concentrations into the chemical kinetic mechanism. The fuel catalytic metal species are modeled using the Cu and Mn species measured in the fuels. The presence of metal deactivating additive is shown to result in a lower required level of metals in the model input than the experimental measurements for two of the seven fuels. Oxygen consumption and hydroperoxide profiles are obtained in a near-isothermal flow system at a temperature of 185 °C. The model is able to satisfactorily simulate these oxidation and hydroperoxide profiles for each of the seven fuels, using a constant chemical kinetic mechanism and by only varying the species class concentrations to differentiate the fuels.

Computational fluid dynamics simulations of isothermal and non-isothermal deposition experiments were performed to evaluate candidate global deposition submechanisms. Three global deposition submechanisms were evaluated, and two were found to yield reasonable simulations of deposit peak location and magnitude. These deposit submechanisms involve the

reaction products of polar phenol species in the formation of deposits. Including reactive sulfur species in the global deposition mechanisms did not improve agreement with the experiment, and as such, these species were not employed in the deposit submechanisms. CFD simulations were also performed for one fuel sample stressed in a non-isothermal flowing system at three different tube wall temperatures. The model simulations closely matched the location of the deposition peaks but were less satisfactory at simulating the increasing deposit peak magnitude with temperature due to limitations of the oxidation mechanism at high temperatures. Future work to improve the methodology was presented and included improved species class analyses, improved understanding of the role of species classes and their interactions, refinements in the chemical kinetic mechanism, additional deposition and oxidation experimental data over wider ranges of conditions, and additional experimental data on a larger set of fuel samples.

Acknowledgment. This work was supported by the Air Force Research Laboratory, Propulsion Directorate, Turbine Engine Division, Fuels Branch, Wright-Patterson AFB, OH, under Contract

No. F33615-03-2-2347. This work was also supported in part by the Air Force Office of Scientific Research (AFOSR). Julian Tishkoff is the AFOSR Program Manager. The U.S. Government is authorized to reproduce and distribute reprints for Governmental purposes notwithstanding any copyright notation thereon. The views and conclusions contained herein are those of the authors and should not be interpreted as necessarily representing the official policies or endorsements, either expressed or implied, of the Air Force Research Laboratory or the U.S. Government. The authors would also like to acknowledge Lori Balster of UDRI for the polars analysis, Donald Minus of AFRL for the reactive sulfurs analysis, Tony Viscomi of the Air Force Petroleum Office (WR-ALC Det 3) for the dissolved metals analysis, and Matthew DeWitt and Dave Brooks of UDRI for the ECAT deposition experiments.

Note Added after ASAP Publication. In the version of this paper published on February 1, 2007, there were some errors in Table 5. These have been corrected in the version published on February 7, 2007.

EF060391O

INTENTIONALLY LEFT BLANK

APPENDIX O

A Laboratory Assessment of the Compatibility of Fischer-Tropsch Derived (ISO Paraffinic Kerosene) and Blended FT-Petroleum-Derived Fuels with Non-Metallic Materials

INTENTIONALLY LEFT BLANK

**10TH INTERNATIONAL CONFERENCE ON STABILITY,
HANDLING AND USE OF LIQUID FUELS
October 7-11, 2007
Tucson, Arizona**

**A LABORATORY ASSESSMENT OF THE COMPATIBILITY OF FISCHER-TROPSCH
DERIVED (ISO PARAFFINIC KEROSENE) AND BLENDED FT-PETROLEUM-DERIVED
FUELS WITH NON-METALLIC MATERIALS**

John L. Graham¹, Richard C. Striebich¹, Donald K. Minus², William E. Harrison III²

¹University of Dayton Research Institute, 300 College Park, Dayton, OH 45469,
John.Graham@udri.udayton.edu

²Air Force Research Laboratory/Propulsion Directorate, 1790 Loop Rd. N. Bldg. 490, WPAFB,
OH 45433

Keywords: Jet fuel, JP-8, Fischer-Tropsch, FT, compatibility, swell, polymer

ABSTRACT

A study has been completed that examined the acute response (volume swell) of 29 fuel-wetted materials to a neat FT fuel, selected petroleum-derived jet fuels (JP-8s), and selected FT/JP-8 blends. Based on the results of this study there does not appear to be any acute problems associated with the use of 50% FT fuel blends with respect to their compatibility with common polymeric materials used in aircraft fuel systems. The greatest concern is with soft plasticized materials (O-rings, fuel barrier materials, and sealants) as these show the largest volume swell and the strongest correlations with the aromatic content of the fuel. The least concern is for hard, fuel resistant materials (coatings, adhesives, films) as these show very little response to any of the test fuels. Comparing the 90% prediction intervals for the volume swell show that if the materials used in this study are exposed to arbitrarily selected JP-8s blended with 50% FT fuel (with the same boiling range as JP-8) the probability that the material will behave as it does in a low aromatic JP-8 (a JP-8 with at least 10% aromatics) is greater than 50%. This means that with an arbitrarily blended JP-8 there is less than a 50% chance that the polymeric materials will show a volume change that is outside the range currently being experienced by materials in normal use. This suggests a high degree of compatibility between 50% FT/JP-8 fuel blends and low-aromatic JP-8s.

INTRODUCTION

In the spring of 2006, plans were initiated to perform a series of ground and flight tests using a Fischer-Tropsch (FT)/petroleum-derived fuel blend in a B-52 Stratofortress. At the time there was considerable experience by Sasol in South Africa flying FT/petroleum-derived blends that averaged approximately 25% FT fuel by volume with progress towards fuels with higher FT fuel blends. Although the ultimate goal is to fly a fuel consisting entirely of at FT derived iso-paraffinic kerosene few would have expected to fly a 100% FT fuel without at least some significant problems. This implies that problems are anticipated between 25% and 100% FT fuel

and the consequences of using an intermediate FT fuel blend were uncertain. A significant concern with the proposed demonstration tests was the possibility of encountering problems, particularly given the age of the test aircraft and the number of legacy materials involved. Of particular concern was the effect the fuel blend would have on the seals and sealants, specifically that the fuel may cause these materials to shrink causing acute failures of these components.¹ Given the lead times needed to secure and prepare the necessary fuels, guidance was needed fairly quickly as to whether to proceed with a 50% FT fuel blend or to select a more conservative approach.

To provide the necessary guidance two material compatibility programs were initiated; one based on traditional material qualification-type tests through Air Force Research Laboratory's (AFRL) Materials Lab, the other through AFRL's Fuels Branch using research methods developed through prior work with the compatibility of FT fuels with O-ring materials. This paper summarizes the results of the later study.

BACKGROUND

The basic interaction between a fuel and a polymeric material is essentially a shift in equilibrium. Specifically, when a material is exposed to a fuel for the first time, mobile components within the polymer are slowly extracted by the fuel, causing the material to shrink and harden. Concurrent with this extraction process is the influx of components from the fuel, causing the material to swell and soften. The net effect of the fuel on the material will be the relative magnitude of these two processes. Once a material has been in service long enough, all of the original extractable components will have been removed, and subsequent changes in physical properties will be a consequence of the changing composition of the fuel to which the piece is exposed.

The overall process of the exchange of material between the fuel and the polymer is governed by the chemical physics of polymer solutions.²⁻⁴ Thermodynamically, this process can be described as a series of discrete steps.⁵⁻⁷ The process begins by separating adjacent polymer strands and opening a cavity large enough to accept fuel molecules; energetically, this evolves breaking polymer-polymer intermolecular bonds and overcoming elastic strain in the polymer matrix surrounding the cavity. Next, fuel penetrant molecules must be separated from the bulk fluid; energetically this involves breaking fuel-fuel intermolecular bonds. Finally, the fuel molecule is inserted into the polymer and creates polymer-fuel bonds, a process that releases energy to make up for the deficit introduced by the first two steps. Considering the overall energy balance of this process, the strength of interaction between the fuel and polymer depends on the intermolecular bonding of the polymer, the physical properties of the polymer, the intermolecular bonding of the fuel, and the molar volume of the fuel components.

With respect to the fuel, hydrogen bonding is one of the most important characteristics when considering the propensity to interact with fuel resistant polymers.⁸ Note that in the solubility sense, hydrogen bonding involves hydrogen bound to nearly any electrophilic structure not just a highly electrophilic atom such as oxygen and nitrogen. Moreover, hydrogen bonding is often significant for molecules which do not have a highly localized hydrogen acceptor site or have a hydrogen acceptor site that is hindered. These molecules do not efficiently develop hydrogen

bonds to themselves or other species in the fuel, thereby reducing the energy burden of separating them from the fuel. Next, fuel species with significant polar character as well as those with low molar volumes can have a significant impact on how strongly they interact with polymeric materials.⁹⁻¹³

The overall intermolecular bonding characteristics of fuel species and polymers may be found in the form of Hansen solubility parameters (HSPs).^{14,15} Briefly, HSPs describe the relative the intermolecular bonding of pure solvents in terms of the relative contributions of non-polar (dispersive), polar, and hydrogen bonding forces. HSPs and molar volumes of species typically found in JP-8 and FT fuel are summarized in Table 1.¹⁴ This illustrates that the paraffinic component of these fuels are relatively large and inert, having only dispersive intermolecular bonding. In contrast, the aromatics components are comparatively small and exhibit both polar and hydrogen bonding character and diaromatics components and some fuel additives are even more so. What this means is that within JP-8 it is the non-paraffinic species that give the fuel its solvent characteristic and hence determine the strength of its interaction with polymeric materials. It is important to note that while the non-paraffinic species harbor this characteristic, the paraffinic species are the major component in JP-8 (typically 75%-90% v/v) and for many materials the paraffins are the major contributor to the overall volume swell.¹⁶ However, it is the non-paraffinic species that determine the differences in the volume swell character from one fuel to another.

This analysis forms the basis for the concerns regarding the use of FT fuels interchangeably with JP-8. Specifically, FT fuel represents an extreme case of a fuel in that it does not have any non-paraffinic species and would therefore have a much lower solvent potential than a typical JP-8 fuel. Interestingly, the concern is not that FT fuels will be too aggressive in their interactions with polymeric materials, but rather FT fuels will be too mild as compared to typical JP-8s. For example, in normal service materials exposed to JP-8 absorb components from the fuel and typically swell and soften to some extent and the selection of these materials has evolved over time to accommodate this behavior. However, when these materials are subsequently exposed to FT fuel the components the materials absorbed from their exposure to JP-8 will be extracted by the FT fuel, but these components will not be replaced because of the much lower solvent activity of the FT fuel. Consequently, there is concern materials that have been in service with JP-8 will shrink and harden when exposed to 100% FT fuel potentially resulting in acute failure of some fuel system components.

As illustrated in Figure 1, this behavior does indeed occur, though the magnitude of the volume change is a strong function of the specific material evolved. The present strategy to mitigate potential problems associated with the use of FT fuels is to blend the neat FT fuel with JP-8; essentially producing a fuel that is compositionally identical to conventional JP-8 but with a lower non-paraffinic content. The question becomes, how much JP-8 must be blended with FT fuel to obtain satisfactory performance? In the present study the specific question is whether there is a significant likelihood of acute problems associated with using a blend consisting of 50% JP-8 in FT fuel. Ideally, there would be specifications established that describe how much in-service variation in physical properties such as volume swell is allowed, but unfortunately such limits are not presently available. Alternatively, a statistical approach was developed to establish the degree of comparability between JP-8 and alternative fuels and this approach is

used to provide a basis for estimating the likelihood of acute problems associated with the use of the alternative fuel interchangeably with JP-8.

EXPERIMENTAL APPROACH

The basis for a statistical approach is outlined in Figure 2. Specifically, this approach is based on the fact that all materials presently in use have passed their respective qualification tests and have been accepted for use with JP-8. Through the course of normal use the materials are exposed to a range of JP-8s with a commensurate range of compositions (including aromatic content) which results in a range of fuel/material interactions. If the behavior of an alternative fuel falls within the bounds of 'normal' JP-8 behavior then the fuel should be compatible with materials used JP-8 systems. If the behavior of the material in an alternative fuel falls outside the bounds of behavior of the materials 'normal' JP-8, the magnitude of the discrepancy will provide at least basic guidance information as to the potential for problems with that fuel.

The overall experimental approach is to obtain representative physical property data in a range of JP-8s to develop a statistical description of how the material behaves in 'normal' JP-8; in this study 'normal' JP-8 was taken as JP-8s with 10-25% aromatics. The same data is then taken in the alternative fuel (in this case 50% FT/JP-8 fuel blends) and compare these two statistical populations to obtain a measure of the overlap between them.

Materials

The materials used in this study are listed in Table 2. As necessary, samples were prepared as per the manufacturer's procedures (sealants, adhesives, coatings); all others were used as-received. The fuels used in this study are listed in Table 3. These included an FT fuel produced by Syntroleum Corporation (Tulsa, OK), and 9 JP-8s provided by AFRL/PRTG. Note that fuel POSF(4908) was received from Tinker AFB and fuel POSF(4911) was received from Edwards AFB where the ground and flight tests were performed, respectively. JP-8/FT fuel blends were prepared by mixing the appropriate volumes of the JP-8s listed in Table 3 with the FT fuel (POSF(4909)) to give a set of fuels with 25%, 37.5%, 50%, and 75% v/v FT fuel.

Volume Swell

The principal measure of the samples' response to exposure to the fuel was volume swell. This was measured using the optical dilatometry system described in Figure 3. Briefly, this system consisted of a back-lit fuel reservoir fitted with an optical window. The window was designed so that its inner face was immersed in the test fuel to prevent condensation from obscuring the view of the sample resting on the bottom of the reservoir. Mounted above the reservoir was a digital camera which periodically photographed the sample and stored the image on a dedicated desktop computer.

For each test the sample was placed in the reservoir which was then filled with 10 mL of fuel and then covered with the optical window. The sample was then photographed every 15 minutes over the next 16 hours providing a record of the cross sectional area of the sample as a function of time. The cross sectional area was extracted from the digital images using a commercial image processing system (MetaMorph, Universal Imaging Corp.). Assuming isotropic swelling the

change in cross sectional area was taken as a characteristic dimension proportional to the change in volume as:

$$\text{Volume Swell} = \left[\left(\frac{A_i}{A_0} \right)^{3/2} - 1 \right] \times 100\% \quad (1)$$

where A_i and A_0 are the cross sectional areas in image i and 0 (the reference image taken at time zero), respectively. The volume swell at the end of the aging period was the value used in the statistical analysis.

Statistical Analysis

The primary basis for comparing the sample populations of the volume swell in the neat JP-8s and 50% JP-8/FT fuel blends was the overlap in the 90% prediction intervals;

$$\text{Overlap 90\% Prediction Interval} = \frac{(\text{UL Blend}) - (\text{LL Reference})}{(\text{UL Blend}) - (\text{LL Blend})} \times 100\% \quad (2)$$

where UL and LL denote the upper and lower limit of the 90% prediction intervals, respectively for the JP-8/FT fuel blends and the reference set of JP-8s. The prediction intervals were calculated with a linear fit to the volume swell data using SAS v8.0 (SAS Institute, Raleigh, North Carolina). The concentration range for aromatics in JP-8 was taken as being from 10% to 25% v/v and from 5% to 12.5% v/v for 50% JP-8/FT fuel blends.

In addition to the core analysis of the overlap in the 90% confidence intervals for the neat JP-8s and the 50% v/v JP-8/FT fuel, overall statistical analysis was done on the volume swell as a function of aromatic content using all of the JP-8, FT, and JP-8/FT fuel blends. Specifically, the volume swell from these analyses were fit with a linear model from which the mean volume swell with 0% and 25% v/v aromatics was estimated along with the slope, a value referred to as the swelling coefficient (K_s , % swell/% aromatics), and the coefficient of determination (r^2) which proves a measure of the strength of the correlation between the aromatic content of a fuel and the volume swell.

Supporting Data

In addition to the core volume swell measurements and the accompanying statistical analysis, supporting data was obtained on the dry source materials and samples aged in fuel. This included an analysis of the semi-volatile and fuel-extractable fraction using thermogravimetric analysis (TGA) and gas chromatography-mass spectrometry (GC-MS). GC-MS analysis was also conducted on the fuel species absorbed by each sample to directly observe the exchange of material between the fuel and polymer.

RESULTS AND DISCUSSION

Space does not permit a detailed description of all of the data from this study; however, data from the three principal O-ring materials (nitrile rubber, fluorosilicone, and fluorocarbon) illustrate the type of volume swell behavior observed for most of the materials used in this study.

Specifically, nitrile rubber is an example of a material that shows relatively low fuel resistance and contains a significant extractable fraction (plasticizer), fluorosilicone is an example of a material that shows relatively low fuel resistance and does not have a significant extractable fraction, and fluorocarbon is an example of material that shows relatively high fuel resistance and also does not have a significant extractable fraction.

Example source data from the optical dilatometry system for the three O-ring materials is given in Figure 4. The data for nitrile rubber shows an initial period of rapid swelling followed by a period of gradual shrinking. This type of behavior is often seen in materials with a significant extractable fraction, primarily plasticizers. Specifically, there is a concurrent rapid absorption of fuel and a more gradual extraction of the extractable fraction resulting in this characteristic swell/shrink behavior. Once the extractable fraction has been removed, the volume swell behavior becomes monotonic such as that shown for the fluorosilicone O-ring material. Finally, fuel resistant materials such as the fluorocarbon typically show relatively slow monotonic changes in volume as a function of time.

Another general characteristic of the JP-8/FT fuel blends is summarized by the example volume swell summary for nitrile rubber (N0602) in the source JP-8s and their respective JP-8/FT fuel blends as shown in Figure 5. As described above the aromatic content of JP-8s can vary over a wide range, typically from about 10-25% by volume. Furthermore, the individual species of aromatics can also vary. This results in the source JP-8s having a range of volume swell potentials dependent on their overall aromatic content and the specific types of aromatics they contain. However, since these fuels are all being diluted with a single type of fuel the overall swelling characteristic approaches that of the diluent fuel as the concentration of the JP-8 approaches zero. This causes distribution of volume swell behavior to narrow as the blending ratio of FT fuel increases. The overall effect is the volume swell behavior of JP-8/FT fuel blends tend to lie closer to the mean behavior than the source JP-8s, increasing the overlap between the distribution of the swelling behavior of the blends and the parent fuels. The result is an improvement in the overall compatibility of the JP-8/FT fuel blends in terms of giving a blended fuel that behaves like an average low-aromatic JP-8.

An example of source data and the overlap of the 90% prediction intervals for nitrile rubber is shown in Figure 6. The overall results of the volume swell measurements for all of the test materials are summarized in Table 4. This table lists the volume swell extrapolated from 0% to 25% v/v aromatics using a linear fit, the swelling coefficient (K_s), which reflects the relative strength of the mean interaction between the aromatics and the test material, the coefficient of determination (r^2), which reflects the strength of the correlation between the observed effect and the aromatic content, and the overlap in the 90% prediction intervals of the 50% FT fuel blends and the reference JP-8s, which reflects the fraction of 50% FT fuel blends that would exhibit volume swell behavior comparable to a low-aromatic JP-8 (a JP-8 with at least 10% aromatics). In the paragraphs that follow a brief overview of the results for each group of materials is presented.

O-rings

O-rings belong to the family of relatively soft manufactured materials. Their softness is an issue because this characteristic is often a compromise between its fuel resistance and its hardness

(modulus). The fact they are manufactured indicates they meet the manufacturer's specifications and should be relatively consistent, at least within a given production batch. For the most part this was found to be the case, although a proportionally higher amount of variability was found in the fluorosilicone samples.

As listed in Tables 2 and 4, the O-ring materials tested included a nitrile rubber (Parker N0602), a fluorosilicone (Parker L1120), and three fluorocarbons (Parker V0747, V0835, and V1226). All of the samples tested were in the form of size -001 O-rings. Analysis of the dry source samples showed that the nitrile rubber included a significant amount of plasticizer (10.1% by mass) that was found to be extracted by the fuels. The V1226 was also found to have a small plasticizer content, though in this case the plasticizer was not extracted by the fuel on the time-scales used here.

The overall volume swell data for the O-ring materials showed that only nitrile rubber was strongly influenced by the aromatic content of the fuel with a mean volume swell that varied from -1.1% to 10.5% (swelling coefficient of 0.451) as the aromatic content of the fuel varied from 0% (FT) to 25% (JP-8). Note that the volume loss of this material at low aromatic levels is due to the extraction of the plasticizer by the fuel. Fluorosilicone showed significant volume swell at all levels of aromatics from 6.5% to 8.2% with a swelling coefficient of only 0.069. The fluorocarbon materials showed very little volume swell in any of the fuels with swelling coefficients from 0.002 to 0.007. The coefficients of determination (r^2) also showed that only the volume swell of nitrile rubber exhibited a strong correlation with aromatic content. Note that this does not mean the volume swell of the other materials does not correlate with aromatic content, but rather the swelling coefficient is so low that other factors (specific aromatic types, variations in the samples, experimental uncertainty, etc.) become significant relative to the contribution from the aromatic content alone. The overlap in the 90% prediction intervals showed that in the worst case 57% of the nitrile rubber O-rings exposed to a 50% FT/JP-8 fuel blend would exhibit volume swell behavior that is within the bounds of 'normal' behavior for a low-aromatic (10% aromatic) JP-8. For all of the other O-ring materials tested the overlap was 80% or greater. Furthermore, of these materials only nitrile rubber stood out as having a significant potential for significant shrinkage (and potential hardening) in neat FT fuel. Therefore, these results indicate that the performance of these O-ring materials in 50% FT fuel blends should compare well with their performance in low-aromatic JP-8s. Extending these results to neat FT fuel suggests there may be significant shrinking and possible hardening of nitrile O-rings, though the performance of the other O-rings materials should be similar to their performance in low-aromatic JP-8s.

Hoses and Bladders (Fuel Barrier Materials)

In a manner similar to the O-ring materials, the four examples of hoses and bladders listed in Table 2 and 4 were grouped together as relatively soft manufactured materials. These materials share many of the same basic characteristics of the materials used in O-rings including establishing a balance between softness and fuel resistance through the use of plasticizers or by the nature of their molecular structure. The materials evaluated included an acrylic nitrile aerial refueling hose (AC-603-01), an epichlorohydrin ground refueling hose (EC-614-01), a nitrile rubber bladder (EF-51956), and a polyurethane bladder (EF-5904C). Analysis of the dry source materials showed that the nitrile rubber materials had significant initial loadings of plasticizer

while the epichlorohydrin material had a more moderate plasticizer content. In all three cases the plasticizer was efficiently extracted by the fuels.

The overall volume swell data for the fuel barrier materials showed that the volume swell of all of these materials was strongly influenced by the aromatic content of the fuel. Furthermore, all of the plasticized materials shrank in the neat FT fuel despite the fact they also absorbed a significant amount of fuel. This illustrates the potentially important role of the extraction of mobile phases from polymeric materials when considering their performance in alternative fuels (or even in conventional fuels). The swelling coefficients for all of these materials were significant, varying from 0.167 to 0.507, and the coefficients of determination were all relatively high, varying from 0.854 to 0.939.

The relatively high swelling coefficients and coefficients of determination resulted in the lowest overlaps in the 90% confidence intervals of any set of materials. However, even in this case the overlaps varied from 53% to 68%, meaning that over half of the fuel barrier materials exposed to 50% FT fuel blends would show performance (based on their volume swell) that is comparable to that in a low aromatic JP-8. These results indicate that the performance of fuel barrier materials in 50% FT fuel blends should be nominal and compare well with their performance in low-aromatic JP-8s. In a manner similar to that of nitrile rubber O-rings, these results suggest that there may be significant shrinking and possible hardening of plasticized fuel barrier materials and the use of these materials with 100% FT fuels should proceed with caution until experience indicates otherwise. This may not be the case for non-plasticized materials such as polyurethane.

Sealants

Sealants are similar to the O-rings and fuel barrier materials in that they are generally somewhat soft and pliable so there is a balance between fuel resistance and the desirable physical properties. Unlike the manufactured materials, sealants are cured in-place and the composition and physical properties of the final product may be more variable than the former. Furthermore, because they are typically cured at or near ambient temperature, as-applied sealants may contain significant amounts of residual solvents, plasticizers, and various processing aids that may be extracted by exposure to fuel at varying rates. This variability is reflected in the analysis of the source sealants summarized in Table 4. The semi-volatile content tended to be relatively low for all of the sealants, but still significant compared to the amount of fuel absorbed. In most cases the semi-volatile content included residual solvents and a single component that was tentatively identified as being either a plasticizer or uncured polymer (oligomer). Generally, the material identified as solvents were extracted by the fuel, while the material identified as oligomer or plasticizer was not, indicating this particular plasticizer is strongly bound to the polymer.

The swelling coefficients for the sealants tended to be lower than those found for nitrile rubber O-rings and the fuel barrier materials. Specifically, the swelling coefficients varied from 0.076 to 0.206 with coefficients of determination that varied from 0.419 to 0.871. The moderate to low swelling coefficients resulted in significant overlaps in the 90% confidence intervals from 61% to 90%, indicating that for the most part nominal performance of the sealants could be expected in 50% FT fuel blends. Furthermore, while some slight shrinkage (-0.6%) was noted in the neat FT fuel for some of the sealants, this behavior may not have a significant adverse effect on their

performance, though caution is warranted as the impact on adhesion and hardness is not yet known.

Coatings

Coatings are similar to sealants in that they are usually applied to surfaces and cured in-place. However, unlike sealants, coatings are usually relatively hard and the mechanisms by which they obtain this hardness make a significant contribution to their fuel resistance as well as other characteristics. Specifically, the mechanisms that make polymers hard include extensive crosslinking (curing), very strong intermolecular forces (polarity and hydrogen bonding), and crystallinity.

An interesting consequence of the relatively high fuel resistance of these materials is that as they cure they become increasingly impermeable to the solvents that were used to apply them. This is reflected in the amount of residual solvents present in the source samples. Specifically, the source samples were found to contain from 7.0% to 24.3% residual solvents and plasticizers and much of this material remained after the aging period in fuel.

The effect of the rigid molecular structure of these coatings strongly influenced their volume swell behavior. As summarized in Table 4, none of these materials showed much in the way of a change in volume when exposed to fuel and the coefficients of determination were all very low, indicating very weak correlations with the aromatic content. Based on this finding the performance of these materials in 50% FT fuel blends as well as neat FT fuel should compare well with their performance in low aromatic JP-8s. However, some caution is warranted as the performance of these materials relies on their ability to bond to a substrate and the impact of the exposure to fuel on adhesion was not evaluated as part of this study.

Adhesives

Adhesives are similar to coatings in that they tend to be relatively rigid polymers that are cured in-place and they share many of the same molecular structure and characteristics with the coatings. Specifically, the mechanisms that contribute to the physical properties of adhesives include extensive crosslinking (curing), very strong intermolecular forces (polarity and hydrogen bonding), and crystallinity. These same characteristics contribute to the fuel resistance of these materials as they do with the coatings.

The rigid molecular structure of these adhesives rendered them relatively inert with respect to their volume swell in the test fuels. As shown in Table 4 these adhesives showed very little volume change during the aging time. Based on this finding the performance of these materials in 50% FT fuel blends as well as neat FT fuel should compare well with their performance in low aromatic JP-8s. However, some caution is warranted as the performance of these materials relies on their ability to bond to a substrate and the impact of the exposure to fuel on adhesion was not evaluated as part of this study.

Composites

The composites share many of the same characteristics as the coatings and adhesives. The polymer matrices tend to be very rigid materials that obtain their stiffness through a combination of extensive crosslinking, very strong intermolecular forces, and crystallinity. Also, as in the case

of the coatings and adhesives, adhesion plays a very important role in these materials performing their intended function. The difference is the adhesion is internal to the material between the polymer matrix and graphite fibers. Furthermore, the volume fraction of fibers is quite high, meaning there is relatively little polymer matrix available to interact with the fuel. Composites are also different in that they are typically manufactured materials and are often cured at high temperatures, a process that results in a higher extent of curing and removes most of the residual solvents as compared to the cured in-place materials.

The results for the volume swell analysis showed that these materials are essentially inert with respect to their interactions with fuel. Table 4 shows the volume swell is very small and a very weak function of aromatic content. Based on these findings the performance of these materials in 50% FT fuel blends as well as neat FT fuel should compare well with their performance in low aromatic JP-8s. However, some caution is warranted as the performance of these materials relies on the adhesive bond between the polymer matrix and the composite fibers the impact of the exposure to fuel on adhesion was not evaluated as part of this study.

Films

Polymeric films share some characteristics that are common to all of the materials described above. They tend to be rigid materials that rely primarily on very strong intermolecular forces and crystallinity for their physical properties. Films are manufactured materials and are thus very consistent and tend to be free from residual solvents and partially cured polymer.

The fuel volume swell data showed these materials are relatively inert with regard to their interactions with fuel. The exception is polyethylene. This sample is unique in this set in that it is a non-polar waxy material that relies primarily on its crystallinity for its fuel resistance. However, although it shows more volume swell than the other materials, the volume swell was a very weak function of aromatic content so its response to FT fuel is comparable to JP-8. Based on these findings the performance of these materials in 50% FT fuel blends as well as neat FT fuel should compare well with their performance in low aromatic JP-8s.

Foam

The material selected for this study included one open-celled foam: Foamex polyurethane. Overall, this material was found to be similar to the other manufactured polyurethane used in this study: the EF-5904C polyurethane bladder material.

The volume swell showed a moderate dependence on the aromatic content, though this measurement proved somewhat problematic due to the geometry of the open-celled foam. The overall result is that since the material has very little plasticizer and absorbs a significant amount of fuel, including FT fuel, it is unlikely to harden from its as-installed state from the extraction of the plasticizer relative to the absorption of fuel. Furthermore, the swelling coefficient is weak-to-moderate. Based on these findings the performance of this materials in 50% FT fuel blends as well as neat FT fuel should compare well with their performance in low aromatic JP-8s. However, some caution is warranted in the latter until there is confirming data available that the material remains soft and pliable after prolonged exposure to neat FT fuel.

CONCLUSIONS

Based on the results of this study there does not appear to be any acute problems associated with the use of 50% FT fuel blends with respect to its compatibility with common polymeric materials used in aircraft fuel systems. The greatest concern is with soft plasticized materials (O-rings, fuel barrier materials, and sealants) as these showed the largest volume swell and the strongest correlations with the aromatic content of the fuel. The least concern is for hard, fuel resistant materials (coatings, adhesives, films) as these showed little response to any of the test fuels. Comparing the 90% prediction intervals for the volume swell showed that if the materials used in this study were exposed to arbitrarily selected JP-8s blended with 50% FT fuel (with the same boiling range as JP-8) the probability that the material will behave as it does in a low aromatic JP-8 (a JP-8 with at least 10% aromatics) is greater than 50%. This means that with an arbitrarily blended JP-8 there is less than a 50% chance that the polymeric materials will show a volume change that is outside the range currently being experienced by materials in normal use. This suggests a high degree of compatibility between 50% FT/JP-8 fuel blends and low-aromatic JP-8s. The statistical analysis of the performance of these materials in neat FT fuel is less complete. However, this study suggests that there is a significant probability that soft, plasticized materials will shrink and possibly harden when exposed to this type of fuel. It is not clear that this behavior will result in the acute failure of any given material or component, only that this behavior will likely be outside the present experience-base. Additional work should be done to specifically explore the use of neat FT fuels as compared to JP-8. Additional work should also be done to specifically examine the effect of the use of neat FT fuel and FT fuel blends on other critical physical properties such as hardness (modulus), adhesion, glass transition temperature (low temperature materials), and others as well as the chronic behavior of materials that response slowly to changes in fuel chemistry.

ACKNOWLEDGEMENTS

This work was supported by the Air Force Research Laboratory (AFRL), Contract F33615-03-2-2347, Mr. Robert Morris, Contract Monitor. Additional funding was provided by the National Energy Technology Laboratory (NETL), Department of Energy Contract #DE-AI26-01NT41110, Bonnie Dowdell Contract Monitor. The authors would also like to acknowledge Mr. Doug Wolf, Mr. Larry Sqrow, and Ms. Betty Ciani of the University of Dayton Research Institute's Micro Analytical Laboratory for their contributions to this work.

REFERENCES

1. Moses, C.A., Valtierra, M.L., "Impact Study of Synthetic and Alternative Fuel Usage in Army Aircraft Propulsion Systems," Final Report, SRWI-MED-134, Cont. No. N00140-80-C-2269, 1981.
2. Miller-Chou, B.A., Koenig, J.L., "A Review of Polymer Dissolution," *Prog. Polym. Sci.*, 28, pp. 1223-1270, 2003.
3. Sperling, L.H., *Introduction to Physical Polymer Science*, 2nd Edition, John Wiley & Sons, Inc., New York, 1992.

4. Billmeyer, F.W., Textbook of Polymer Science, John Wiley & Sons, Inc., New York, 1984.
5. Flory, P.J., Principals of Polymer Chemistry, Cornell University Press, Ithaca, NY, 1953.
6. Hildebrand, J.H., Scott, R.L., The Solubility of Nonelectrolytes, 3rd edition, Dover Publications, New York, N.Y., 1964.
7. R.P. Schwarzenbach, P.M. Gschwend, D.M. Imboden, Environmental Organic Chemistry, John Wiley and Sons, Inc., New York, NY, 1993.
8. Graham, J.L., Striebich, R.C., Myers, K.J., Minus, D.K., Harrison, W.E., "Swelling of Nitrile Rubber by Selected Aromatics Blended in a Synthetic Jet Fuel," *Energy & Fuels*, Vol. 20, No. 2, 15 March 2006, pp. 759-765.
9. Saleem, M., Asfour, A., De Kee, D., "Diffusion of Organic Penetrants Through Low Density Polyethylene (LDPE) Films; Effects of Size and Shape of the Penetrant Molecules," J. Appl. Polym. Sci., Vol. 37, pp. 617-625, 1989.
10. Mathai, A.E., Thomas, S., "Transport of Aromatic Hydrocarbons Through Crosslinked Nitrile Rubber Membranes," J. Macromol. Sci. - Phy, Vol. B35(2), pp. 229-253, 1996.
11. Mathai, A.E., Singh, R.P., Thomas, S., "Transport of Substituted Benzenes Through Nitrile Rubber/Natural Rubber Blend Membranes," J. Membrane Sci. Vol. 202, pp. 35-54, 2002.
12. Sombatsompop, N., Christodoulou, K.J., "Penetration of Aromatic Hydrocarbons into Natural Rubber," Polym. & Polym. Compos., Vol. 5 (5), pp. 377-386, 1997.
13. Sombatsompop, N., "Investigation of Swelling Behavior of NR Vulcanisates," Polym.-Plast. Technol. Eng., Vol. 37 (1), pp. 19-39, 1998.
14. Hansen, C.M., Hansen Solubility Parameters: A Users Handbook, CRC Press LLC, New York, NY, 2000.
15. Burke, J., "Solubility Parameters: Theory and Application," AIC Book and Paper Group Annual, Craig, J., Editor, Vol. 3, pp. 13-58, Washington, D.C., 1984.
16. Graham, J.L. "The Swelling of Nitrile Rubber by Selected Species in a Synthetic Jet Turbine Fuel," Ph.D. Thesis, University of Dayton, August, 2006.

Table 1
Hansen Solubility Parameters for Selected Fuel Components

Fuel Component	Dispersion MPa ^{1/2}	Polar MPa ^{1/2}	H-Bond MPa ^{1/2}	MV mL/mol
Alkanes				
Nonane	15.7	0.0	0.0	180
Decane	15.7	0.0	0.0	196
Dodecane	16.0	0.0	0.0	229
Hexadecane	16.3	0.0	0.0	294
Aromatics				
Ethyl Benzene	17.8	0.6	1.4	123
1,2,3-Trimethyl Benzene	17.8	0.4	1.0	134
1,3,5-Trimethyl Benzene	18.0	0.0	0.6	140
o-Diethyl Benzene	17.7	0.1	1.0	154
p-Diethyl Benzene	18.0	0.0	0.6	157
N-Butyl Benzene	17.4	0.1	1.1	157
o-N-Butyl Toluene	17.6	0.1	1.0	171
p-N-Butyl Toluene	17.4	0.1	1.0	174
Diaromatics				
Naphthalene	19.2	2.0	5.9	112
1-Methyl Naphthalene	20.6	0.8	4.7	139
Additives				
DiEGME	16.2	7.8	12.6	118

Table 2
Polymeric Materials Selected for Fuel Compatibility Testing

Category	ID	Material	Notes
O-rings	N0602	Nitrile Rubber	General Purpose
	L1120	Fluorosilicone	General Purpose
	V0747	Fluorocarbon	General Purpose
	V0835	Fluorocarbon	Low-temperature
	V1226	Fluorocarbon	Low-temperature
Hoses	AC-603-01	Acrylic Nitrile	Hose, Aerial
	EC-614-01	Epichlorohydrin	Hose, Ground
Bladders	EF-51956	Nitrile Rubber	Bladder
	EF-5904C	Polyurethane	Bladder
Sealants	PR-1422	Polysulfide	Dichromate cured
	PR-1440	Polysulfide	Manganese dioxide cured
	PR-1776	Polysulfide	Manganese dioxide cured
	PR-1828	Polythioether	Epoxy cured
	PR-2911	Polythioether/Polyurethane	
	Q4-2817	Fluorosilicone	
Coatings	EC-776	Nitrile	
	C-27725	Polyurethane	
	BMS 10-20	Epoxy	
	BMS 10-39	Epoxy	
Adhesives	AF-10	Phenol-formaldehyde/ nitrile	
	Epon 828	Epoxy	
	FM-47	Vinyl Phenolic	
Composites	AS4-3501-6	Graphite/Epoxy	Low Polymer Loading
	IM7-5250-4	Graphite/Bismaleimide	Low Polymer Loading
Films	PE	Polyethylene	Non-polar
	PTFE	PTFE	
	Upilex	Kapton	
	Zytel	Nylon	
Foam	Foamex	Polyurethane	Open-celled foam

Table 3
Ft and JP-8 Fuels and Fuel Blends for Fuel Compatibility Testing

POSF	Aromatic Content					Notes
	Source	25% FT	38% FT	50% FT	75% FT	
4909	0.0%	n.a.	n.a.	n.a.	n.a.	FT with JP-8 additives
4908	13.6%	10.2%	8.5%	6.8%	3.4%	Fuel from Tinker AFB
3773	15.9%	11.9%	9.9%	8.0%	4.0%	
4911	16.5%	12.4%	10.3%	8.3%	4.1%	Fuel from Edwards AFB
3694	16.6%	12.5%	10.4%	8.3%	4.2%	
4177	16.9%	12.7%	10.6%	8.5%	4.2%	
3166	17.3%	13.0%	10.8%	8.7%	4.3%	
4751	18.8%	14.1%	11.8%	9.4%	4.7%	
3804	20.3%	15.2%	12.7%	10.2%	5.1%	
3602	23.6%	17.7%	14.8%	11.8%	5.9%	

Table 4
Summary of Volume Swell Summary Results

Category	ID	Mean Swell		Statistical Analysis		
		0% Aro	25% Aro	Ks	r ²	Overlap
O-rings	N0602	-1.1	10.5	0.465	0.949	57%
	L1120	6.5	8.2	0.069	0.363	95%
	V0747	0.2	0.3	0.005	0.141	100%
	V0835	0.3	0.4	0.002	0.008	100%
	V1226	0.2	0.4	0.007	0.358	80%
Hoses	AC60301	-8.2	4.5	0.507	0.939	53%
	EC61401	-0.6	3.6	0.167	0.903	59%
Bladders	EF-5904	7.9	24.1	0.647	0.915	62%
	EF-51956	-2.8	3.4	0.248	0.854	68%
Foam	Foamex	6.4	10.3	0.154	0.070	98%
Sealants	PR-2911	2.3	7.5	0.206	0.787	61%
	Q4-2817	0.4	1.7	0.052	0.419	69%
	PR-1776	-0.6	1.7	0.094	0.871	75%
	PR-1422	0.6	3.1	0.101	0.744	83%
	PR-1440	-0.6	1.3	0.076	0.795	84%
	PR-1828	0.8	5.3	0.181	0.780	90%
Coatings	C-27725	0.1	0.2	0.004	0.022	63%
	BMS 10-20	0.0	0.0	0.00	0.009	92%
	EC-776	0.0	0.5	0.017	0.059	100%
	BMS 10-39	-0.1	0.1	0.005	0.119	100%
Adhesives	Epon 828	-0.1	-0.3	-0.007	0.025	98%
	AF-10	0.4	0.6	0.009	0.099	100%
	FM-47	0.0	-0.1	-0.002	0.012	100%
Composites	AS4-3501-6	-0.1	0.0	0.003	0.288	85%
	IM7-5250-4	-0.1	0.1	0.006	0.099	91%
Films	PE	2.4	3.0	0.022	0.060	83%
	TFE	-0.1	-0.1	-0.001	0.006	100%
	Upilex	-0.1	0.0	0.001	0.009	100%
	Zytel	-0.1	0.0	0.005	0.039	100%

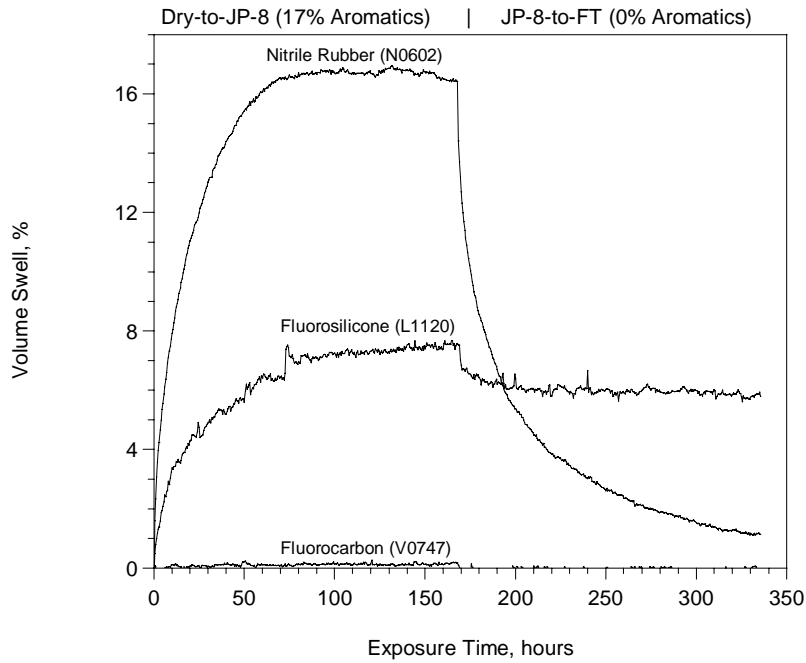


Figure 1. Volume swell as a function of time for three different O-ring materials aged in a typical JP-8, then switched to an FT fuel with a comparable boiling range.

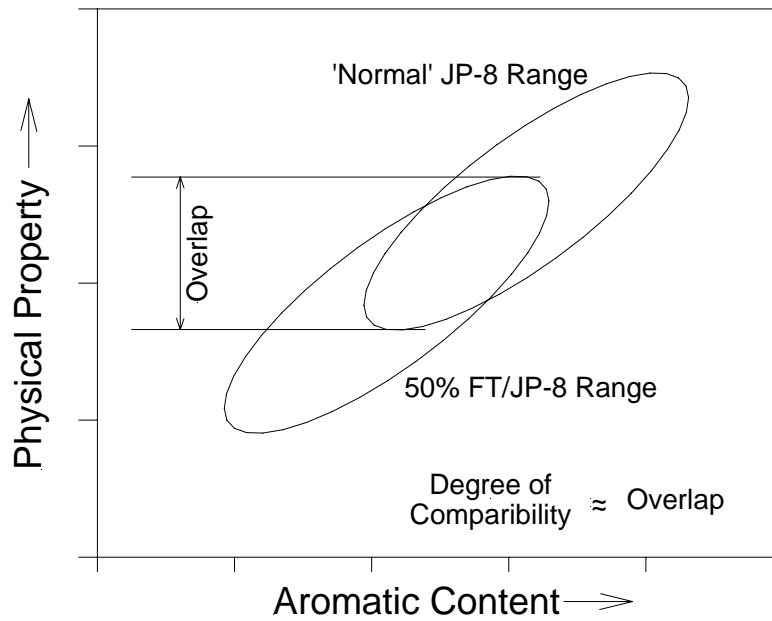


Figure 2. Graphical representation of a statistical approach to fuel compatibility.

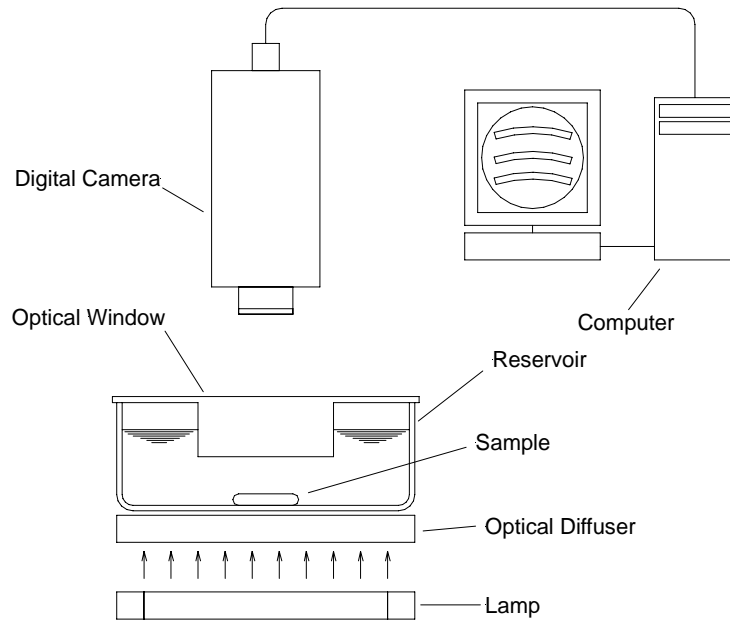


Figure 3. Schematic of the optical dilatometry system used to measure volume swell as a function of time.

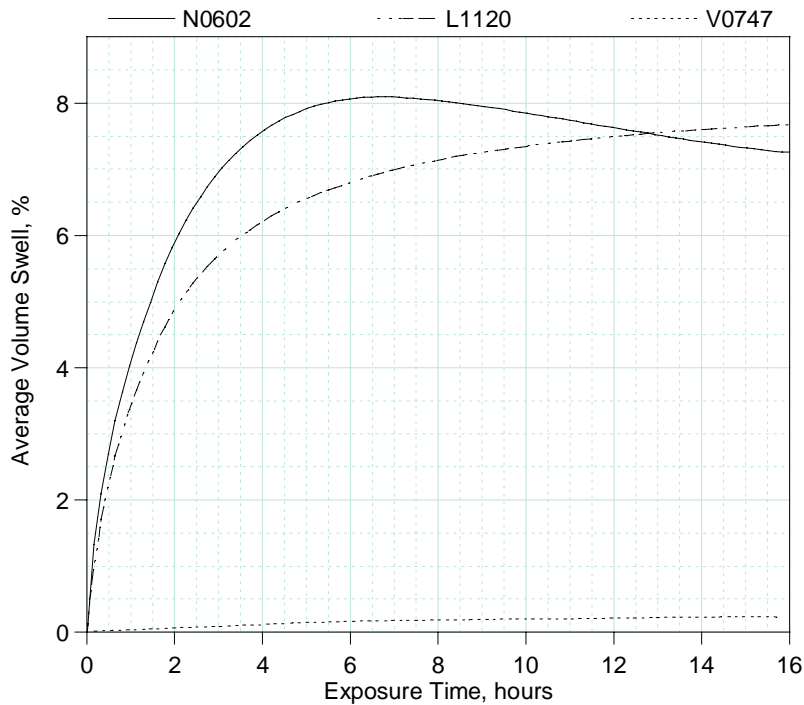


Figure 4. The average volume swell of the nitrile rubber (N0602), fluorosilicone (L1120), and fluorocarbon (V0747) O-rings in the reference JP-8s.

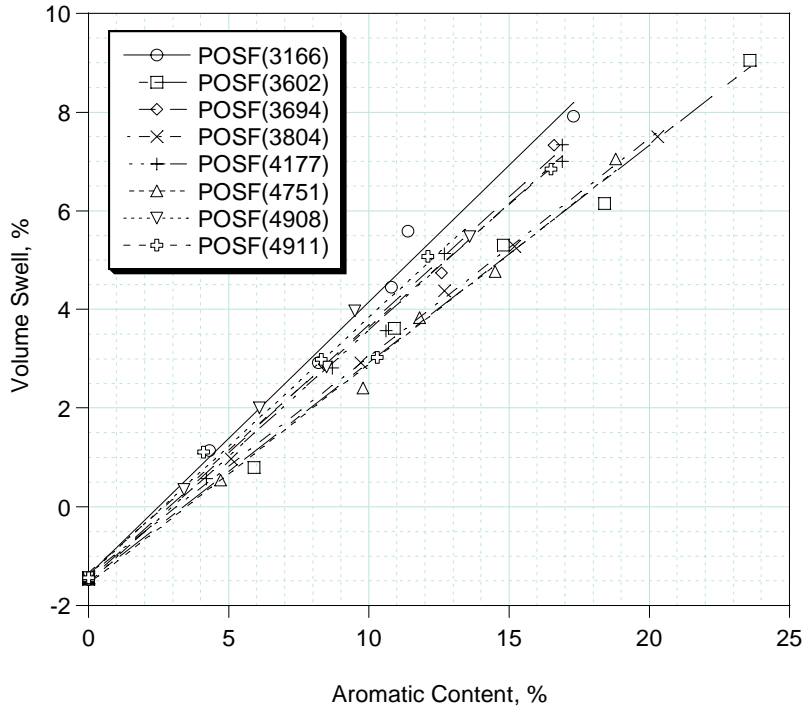


Figure 5. Example volume swell data for the nitrile rubber O-ring material grouped by each source JP-8 showing how the distribution in volume swell behavior approaches the mean as the blending ratio increases.

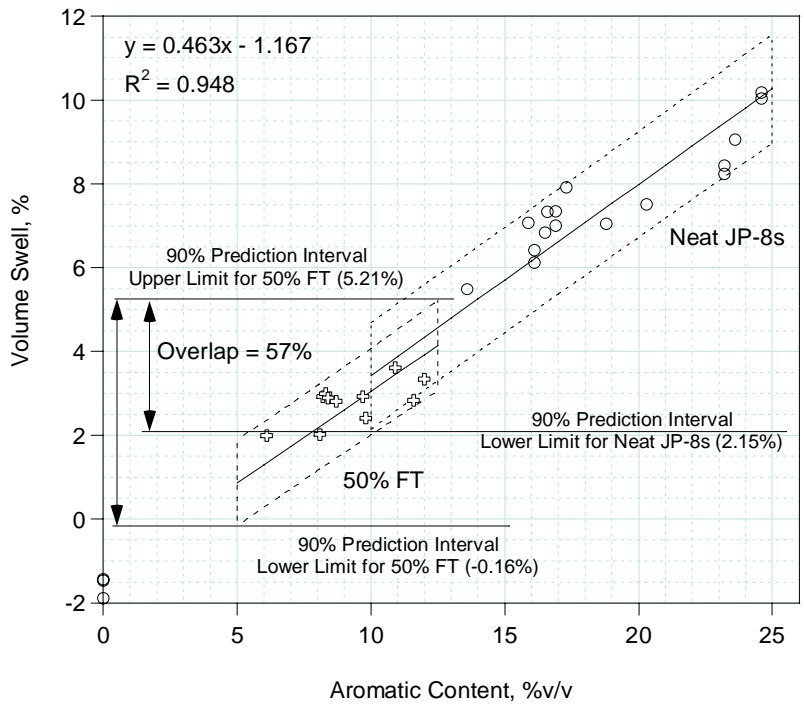


Figure 6. Example showing the calculation of the overlap of the 90% prediction intervals for the 50% FT fuel blends and the reference JP-8s.

INTENTIONALLY LEFT BLANK

APPENDIX P

Formation of Protein-Metal Oxide Nanostructures by the Sonochemical Method: Observation of Nanofibers and Nanoneedles

INTENTIONALLY LEFT BLANK

Formation of Protein–Metal Oxide Nanostructures by the Sonochemical Method: Observation of Nanofibers and Nanoneedles

Christopher E. Bunker,^{*,†} Kyle C. Novak,[‡] Elena A. Gulians,[‡] Barbara A. Harruff,[§]
M. Jaouad Meziani,[§] Yi Lin,[§] and Ya-Ping Sun[§]

Air Force Research Laboratory, Propulsion Directorate, Wright-Patterson Air Force Base, Ohio 45433-7103, University of Dayton Research Institute, Nonmetallic Materials Division, Dayton, Ohio 45469, and Department of Chemistry, Howard L. Hunter Chemistry Laboratory, Clemson University, Clemson, South Carolina 29634-0973

Received May 11, 2007. In Final Form: July 6, 2007

The sonochemical reaction of iron pentacarbonyl is explored in water and in water with the protein BSA (bovine serum albumen). In water, the reaction is found to produce spherical nanoparticles of magnetite (Fe_3O_4) with a particle size distribution of <10 to ~60 nm. In water with BSA, the reaction produces either nanofibers or nanoneedles, depending on the concentration of BSA. The nanofiber and nanoneedle samples are found to be mixtures of goethite, lepidocrocite, and hematite ($\alpha\text{-FeOOH}$, $\gamma\text{-FeOOH}$, and $\alpha\text{-Fe}_2\text{O}_3$, respectively). The sonochemical reaction of iron pentacarbonyl with BSA in water is thought to proceed through the thermal decomposition mechanism for iron pentacarbonyl with BSA acting as a templating agent.

Introduction

Sonochemistry and nanoparticle formation via the sonochemical method have been the subjects of intensive scientific research.^{1–8} The sonochemical method is fairly well understood for simple systems; iron pentacarbonyl in hydrocarbon solvents being a good example.² The addition of capping agents, stabilizers, and secondary reactants results in a much more complex reaction,

but with more versatile and interesting products. To date, the sonochemical method has produced a number of valuable nanoparticle systems, including luminescent nanoparticles,⁴ nanoscale catalysts,⁵ nanoparticles with application to devices,⁶ nanostructures with interesting geometries,⁷ and reactive nanoparticles with protective coatings.⁸

Currently, there is particular interest in the synthesis of nanobio composite materials.^{9–14} Such compounds may find application as drug delivery agents, in pathogen detection and separation applications, and as hybrid electronic devices. Recent examples of such materials produced using various synthetic methods include the formation of Ag–BSA and CdS–BSA nanocomposites from supercritical fluid expansion,¹⁰ Au–BSA nanocomposites from chemical reduction,¹¹ CdTe–BSA nanocomposites using L-cysteine as a linker,¹² iron oxide–BSA nanocomposites using 3-aminopropyltrimethoxysilane as a linker,¹³ and Au nanoparticles bonded to double stranded DNA modified with thiol groups.¹⁴ These methods can be described as either direct (i.e., direct conjugation of the biomolecule to the metallic nanoparticles) or indirect (i.e., incubation of biomolecules with highly passivated nanoparticles or attachment of the

* To whom correspondence should be addressed.

[†] Air Force Research Laboratory.

[‡] University of Dayton Research Institute.

[§] Clemson University.

(1) (a) Suslick, K. S.; Hammerton, D. A.; Cline, R. E., Jr. *J. Am. Chem. Soc.* **1986**, *108*, 5641–5642. (b) Didenko, Y. T.; McNamara, W. B., III; Suslick, K. S. *J. Phys. Chem. A* **1999**, *103*, 10783–10788. (c) Suslick, K. S.; Didenko, Y.; Fang, M. M.; Hyeon, T.; Kolbeck, K. J.; McNamara, W. B., III; Mdeleleni, M. M.; Wong, M. *Phil. Trans. R. Soc. Lond. A* **1999**, *357*, 335–353. (d) Flannigan, D. J.; Suslick, K. S. *Nature* **2005**, *434*, 52–55. (e) Shchukin, D. G.; Möhwald, H. *Phys. Chem. Chem. Phys.* **2006**, *8*, 3496–3506.

(2) (a) Suslick, K. S.; Schubert, P. F.; Goodale, J. W. *J. Am. Chem. Soc.* **1981**, *103*, 7342–7344. (b) Suslick, K. S.; Goodale, J. W.; Schubert, P. F.; Wang, H. *J. Am. Chem. Soc.* **1983**, *105*, 5781–5785. (c) Suslick, K. S.; Johnson, R. E. *J. Am. Chem. Soc.* **1984**, *106*, 6856–6858. (d) Suslick, K. S.; Flint, E. B.; Grinstaff, M. W.; Kemper, K. A. *J. Phys. Chem.* **1993**, *97*, 3098–3099.

(3) (a) Gedanken, A. *Ultrasound Sonochem.* **2004**, *11*, 47–55. (b) Suslick, K. S.; Fang, M.; Hyeon, T. *J. Am. Chem. Soc.* **1996**, *118*, 11960–11961. (c) Shafi, K. V. P. M.; Ulman, A.; Yan, X.; Yang, N.-L.; Estournès, C.; White, H.; Rafailovich, M. *Langmuir* **2001**, *17*, 5093–5097.

(4) (a) Dhas, N. A.; Raj, C. P.; Gedanken, A. *Chem. Mater.* **1998**, *10*, 3278–3281. (b) Zhu, L.; Liu, X.; Liu, X.; Li, Q.; Li, J.; Zhang, S.; Meng, J.; Cao, X. *Nanotechnology* **2006**, *17*, 4217. (c) Murcia, M. J.; Shaw, D. L.; Woodruff, H.; Naumann, C. A.; Young, B. A.; Long, E. C. *Chem. Mater.* **2006**, *18*, 2219–2225.

(5) (a) Suslick, K. S.; Hyeon, T.; Fang, M.; Cichowlas, A. A. *Materials Science and Engineering* **1995**, *A204*, 186–192. (b) Hyeon, T.; Fang, M.; Suslick, K. S. *J. Am. Chem. Soc.* **1996**, *118*, 5492–5493. (c) Suslick, K. S.; Hyeon, T.; Fang, M. *Chem. Mater.* **1996**, *8*, 2172–2179. (d) Dantsin, G.; Suslick, K. S. *J. Am. Chem. Soc.* **2000**, *122*, 5214–5215. (e) Basnayake, R.; Li, Z.; Katar, S.; Zhou, W.; Rivera, H.; Smotkin, E. S.; Casadonte, D. J., Jr.; Korzeniewski, C. *Langmuir* **2006**, *22*, 10446–10450.

(6) (a) de Caro, D.; Ely, T. O.; Mari, A.; Chaudret, B.; Snoeck, E.; Respaud, M.; Broto, J.-M.; Fert, A. *Chem. Mater.* **1996**, *8*, 1987–1991. (b) Ge, J.-P.; Li, Y.-D. *J. Mater. Chem.* **2003**, *13*, 911–915. (c) Nikitenko, S. I.; Koltypin, Y.; Felner, I.; Yeshurun, I.; Shames, A. I.; Jiang, J. Z.; Markovich, V.; Gorodetsky, G.; Gedanken, A. *J. Phys. Chem. B* **2004**, *108*, 7620–7626. (d) Park, J.-E.; Atobe, M.; Fuchigami, T. *Electrochim. Acta* **2005**, *51*, 849–854. (e) Xu, H.; Wang, W.; Zhu, W. *Mater. Lett.* **2006**, *60*, 2203–2206.

(7) (a) Shafi, K. V. P. M.; Felner, I.; Mastai, Y.; Gedanken, A. *J. Phys. Chem. B* **1999**, *103*, 3358–3360. (b) Dhas, N. A.; Suslick, K. S. *J. Am. Chem. Soc.* **2005**, *127*, 2368–2369. (c) Zhang, J.; Du, J.; Han, B.; Liu, Z.; Jiang, T.; Zhang, Z. *Angew. Chem. Int. Ed.* **2006**, *45*, 1116–1119.

(8) Bunker, C. E.; Karnes, J. J. *J. Am. Chem. Soc.* **2004**, *126*, 10852–10853.

(9) (a) Huang, P. M.; Naidja, A.; Liu, C. J. *Col. Interface Sci.* **2002**, *251*, 46–56. (b) Tedesco, A. C.; Oliveria, D. M.; Lacava, Z. G. M.; Azevedo, R. B.; Lima, E. C. D.; Morais, P. C. *J. M. Mater.* **2004**, *272*–276, 2404–2405. (c) Chen, Y.; Aveyard, J.; Wilson, R. *Chem. Commun.* **2004**, 2804–2805. (d) Krämer, S.; Xie, H.; Gaff, J.; Williamson, J. R.; Tkachenko, A. G.; Nouri, N.; Feldheim, D. A.; Feldheim, D. L. *J. Am. Chem. Soc.* **2004**, *126*, 5388–5395. (e) Xu, G.; Xu, K.; Gu, H.; Zhong, X.; Guo, Z.; Zheng, R.; Zhang, X.; Xu, B. *J. Am. Chem. Soc.* **2004**, *126*, 3392–3393. (f) Wang, Y.; Tang, Z.; Tan, S.; Kotov, N. A. *Nano Lett.* **2005**, *5*, 243–248. (g) Portney, N. G.; Singh, K.; Chaudhary, S.; Destito, G.; Schneemann, A.; Manchester, M.; Ozkan, M. *Langmuir* **2005**, *21*, 2098–2103. (h) Liang, J.-G.; Ai, X.-P.; He, Z.-K.; Xie, H.-Y.; Pang, D.-W. *Mater. Lett.* **2005**, *59*, 2778–2781. (i) Pan, B.-F.; Gao, F.; Ao, L.-M. *J. Magn. Magn. Mater.* **2005**, *293*, 252–258.

(10) (a) Meziani, M. J.; Pathak, P.; Harruff, B. A.; Hurezeanu, R.; Sun, Y.-P. *Langmuir* **2005**, *21*, 2008–2011. (b) Meziani, M.; Sun, Y.-P. *J. Am. Chem. Soc.* **2003**, *125*, 8015–8018.

(11) Burt, J. L.; Gutiérrez-Wing, C.; Miki-Yoshida, M.; José-Yacamán, M. *Langmuir* **2004**, *20*, 11778.

(12) Mamedova, N. N.; Kotov, N. A.; Rogach, A. L.; Studer, J. *Nano Lett.* **2001**, *1*, 281–286.

(13) Mikhaylova, M.; Kim, D. K.; Berry, C. C.; Zagorodni, A.; Toprak, M.; Curtis, A. S. G.; Muhammed, M. *Chem. Mater.* **2004**, *16*, 2344–2354.

(14) Tsai, C.-Y.; Shiau, A.-L.; Cheng, P.-C.; Shieh, D.-B.; Chen, D.-H.; Chou, C.-H.; Yeh, C.-S.; Wu, C.-L. *Nano Lett.* **2004**, *4*, 1209–1212.

biomolecules to the nanoparticles through a linker molecule).¹¹ Indirect methods potentially suffer from increased molecular size, less access to the nanoparticle surface, and loss of the unique chemical or physical properties of the nanoparticles. Because of this, direct methods for the production of nano–bio composite materials are of great interest.

The sonochemical method has potential as a direct synthesis approach, noting that only volatile components and compounds at very high concentrations (i.e., the solvent) appear to be exposed to the extreme temperature conditions produced by acoustic cavitation. Heavy, low volatility compounds such as BSA likely remain intact and thus are available for secondary reaction with or for capping of the newly formed nanoparticles.¹⁵ Previously, Suslick et al. demonstrated the formation of hollow protein microspheres from the reaction of BSA in oxygenated water during acoustic cavitation.¹⁶ The authors determined that the microspheres were formed through crosslinking of cysteine groups on adjacent BSA molecules and that the crosslinking occurred by the action of the reactive intermediate superoxide. By removing dissolved oxygen, they showed that the formation of superoxide could be suppressed and the formation of microspheres prevented. Following the work of Suslick, Gedankin et al. formed protein microspheres simultaneous with the decomposition of iron pentacarbonyl.¹⁷ The result was hollow microspheres coated inside and out with iron oxide nanoparticles. Since these early reports, work on sonochemically produced microspheres has continued,¹⁸ including the recent report of spheres generated using polyglutamic acid.^{18c} Our interest has been in obtaining metal nanoparticle–BSA conjugates, with the BSA serving as coating or protecting agent. By performing the reactions under degassed conditions and at relatively low power (~22 W), we have succeeded in generating iron oxide–BSA conjugates from the reaction of iron pentacarbonyl with BSA in water solution as opposed to protein microspheres. Interestingly, the composite material produced here does not display simple core–shell morphology but implies a rich interaction between the protein and the iron during synthesis demonstrated by the formation of protein-coated nanofibers and nanoneedles. Here, we report the synthesis and the results of the characterization of these materials, examine the effects of BSA and iron concentration on the morphology of the product, and discuss these observations within the context of both the sonochemical and thermal decomposition mechanisms for iron pentacarbonyl.^{2,19}

Experimental Section

Materials. Iron pentacarbonyl (99.99%) and bovine serum albumen (BSA, 98%) were purchased from Aldrich and used without further purification. Deionized water was produced using a Barnstead NANOpure II water-filtration system.

(15) Gülsersen, I.; Güzey, D.; Bruce, B. D.; Weiss, J. *Ultrason. Sonochem.* **2007**, *14*, 173–183.

(16) (a) Suslick, K. S.; Grinstaff, M. W. *J. Am. Chem. Soc.* **1990**, *112*, 7807–7809. (b) Grinstaff, M. W.; Suslick, K. S. *Proc. Natl. Acad. Sci. U.S.A.* **1991**, *88*, 7708–7710.

(17) Avivi, A.; Felner, I.; Novik, I.; Gedanken, A. *Biochim. Biophys. Acta* **2001**, *1527*, 123–129.

(18) (a) Avivi, S.; Nitzan, Y.; Dror, R.; Gedanken, A. *J. Am. Chem. Soc.* **2003**, *125*, 15712–15713. (b) Avivi, S.; Gedanken, A. *Ultrason. Sonochem.* **2005**, *12*, 405–409. (c) Dibbern, E. M.; Toublan, F. J.-J.; Suslick, K. S. *J. Am. Chem. Soc.* **2006**, *128*, 6540–6541.

(19) (a) Smith, T. W.; Wychick, D. *J. Phys. Chem.* **1980**, *84*, 1621–1629. (b) van Wonteghem, J.; Mørup, B.; Charles, S. W.; Wells, S.; Villadsen, J. *Phys. Rev. Lett.* **1985**, *55*, 410–413. (c) Park, S.-J.; Kim, S.; Lee, S.; Khim, Z. G.; Char, K.; Hyeon, T. *J. Am. Chem. Soc.* **2000**, *122*, 8581–8582. (d) Hyeon, T.; Lee, S. S.; Park, J.; Chung, Y.; Na, H. B. *J. Am. Chem. Soc.* **2001**, *123*, 12798–12801. (e) Burke, N. A. D.; Stöver, H. D. H.; Dawson, F. P. *Chem. Mater.* **2002**, *14*, 4752–4761. (f) Woo, K.; Hong, J.; Choi, S.; Lee, H.-W.; Ahn, J.-P.; Kim, C. S.; Lee, S. W. *Chem. Mater.* **2004**, *16*, 2814–2818.

Samples of nanophase iron oxide with BSA were prepared by the sonochemical method.^{1,2} To begin, a water solution of BSA (ranging from no BSA to 5.0 mg/mL) was deoxygenated using a vacuum system coupled with a sonication bath. This solution was then transferred to a specialized sonochemical reaction flask (~14 mL) and bubbled continuously with dry nitrogen gas. The reaction flask was contained within an ice bath to remove excess heat produced during the sonochemical process. Iron pentacarbonyl (150 or 300 μ L) was then injected on top of the water/BSA solution. Sonication was performed using a Sonics VC750 operating at 20 kHz equipped with a 0.5 in. diameter solid titanium horn. Energy was applied for 15 min of active time using a 1-s-on, 1-s-off procedure, with power adjusted to ~22 W per pulse. At the conclusion of the sonochemical process, a cloudy black (with no BSA) or red (with BSA) solution was obtained. The sample was purified using a centrifuge, thus removing suspended material and yielding a transparent, colored solution. The solution was then dried, leaving a powdery solid. Total protein content was evaluated using the modified Lowry procedure (Aldrich, total protein kit, micro Lowry, Onishi and Barr modification).

Measurements. Fourier transform infrared (FTIR) absorption spectra of the samples were collected using a Perkin-Elmer 2000 instrument. A small quantity of the sample was blended with dry KBr for analysis. X-ray powder diffraction (XRD) analysis was performed on a Bruker D8-Advanced equipped with a Cu α source and a Sol-X detector. Transmission electron microscopy (TEM) images were obtained using a Hitachi HD-2000 STEM instrument. Sample grids were prepared by first sonicating the powder sample in hexane to disperse the material, and then spotting the hexane solution onto a 300 mesh carbon coated grid for imaging. Thermal gravity analysis (TGA) was conducted with a TA Instruments Q500 Analyzer.

Results

The sonochemical method was used to decompose iron pentacarbonyl in the presence of the protein molecule BSA in water. Figure 1 shows the TEM images obtained for BSA concentrations of 0, 0.5, and 5.0 mg/mL. In the case of no BSA, iron pentacarbonyl decomposes to yield a black precipitate. The TEM image of this material shows nanoparticles ranging in size from <10 nm to ~60 nm (Figure 1a). Powder X-ray diffraction (Figure 2) indicates the structure of these nanoparticles to be either magnetite (Fe₃O₄) or maghemite (γ -Fe₂O₃), noting that the XRD patterns for these two phases of iron oxide are nearly identical. However, the black color of the sample suggests magnetite as the most likely phase. Macroscopically, the material is magnetic and easily responds to the influence of a magnetic field.

When the reaction is performed with BSA present in solution, the nature of the product is very different. At a BSA concentration of 0.5 mg/mL, the reaction produces a reddish solution that when dried yields a reddish powder. Figure 1b shows the TEM image of the material and is characterized by long (~200 nm), fiber-like structures, with aspect ratios of approximately 20:1. These structures range from well-defined, showing clear periodicity (Figure 3), to cloudy or wispy, which may indicate amorphous structure. Also evident are regions of small nanoparticles which appear to be 20 nm or less in diameter. XRD analysis of this sample reveals a mixture of α - and γ -FeOOH and α -Fe₂O₃ (Figure 4). In addition, the baseline appears somewhat distorted, possibly due to broad underlying features that correspond to amorphous or polycrystalline material.

At a higher concentration of BSA (5.0 mg/mL), sonication of iron pentacarbonyl produces needles, much shorter than the fibers, ~30 nm in length, and contained within a dense, amorphous material (Figure 1c). XRD analysis shows primarily a broad, featureless structure which is identical to that obtained when the

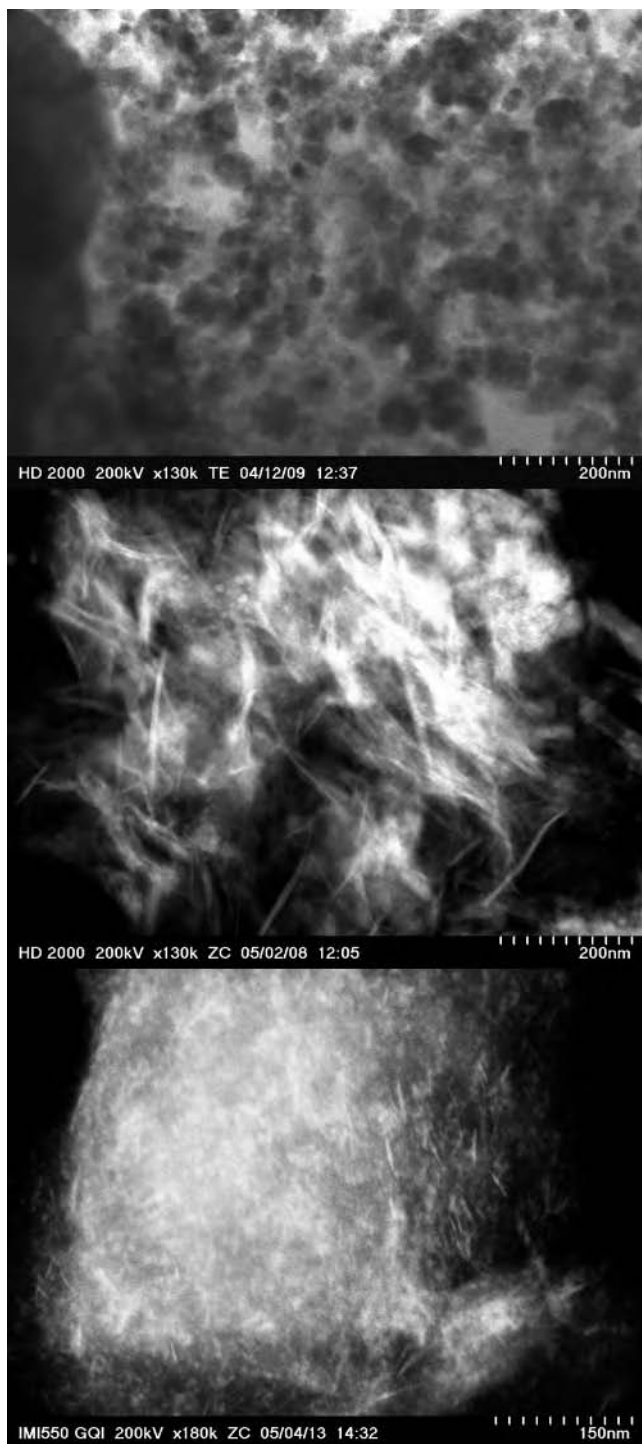


Figure 1. TEM images of the nanostructures produced from the sonication of iron pentacarbonyl with BSA in water solution (top, 0 mg/mL BSA; middle, 0.5 mg/mL BSA; bottom, 5.0 mg/mL BSA).

protein BSA is analyzed independently (Figure 5). Five minor peaks are observed that can be assigned to γ -FeOOH. This material was again a reddish powder.

To investigate the effect of iron concentration on product morphology and crystal structure, two samples were prepared with different iron pentacarbonyl injection volumes (150 and 300 μ L) at a constant BSA concentration of 0.5 mg/mL. TEM images of the two samples are shown in Figure 6. Both samples demonstrate similar fiber structures and amorphous material. XRD analysis indicated no significant differences between the

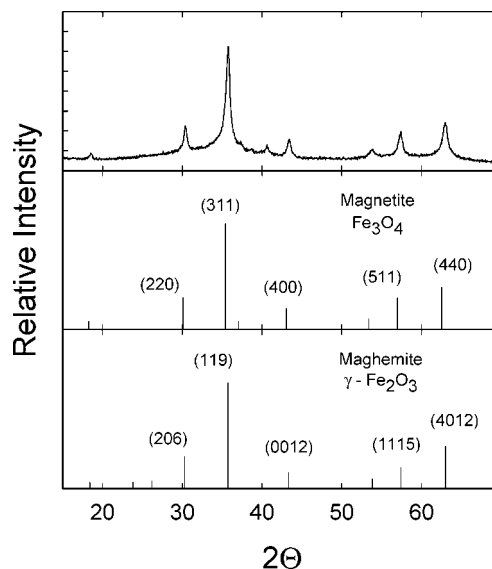


Figure 2. Top. XRD spectrum of the spherical nanoparticles formed from iron pentacarbonyl decomposition in water. Bottom. ICCD reference pattern for magnetite (Fe_3O_4) and maghemite ($\gamma\text{-Fe}_2\text{O}_3$).

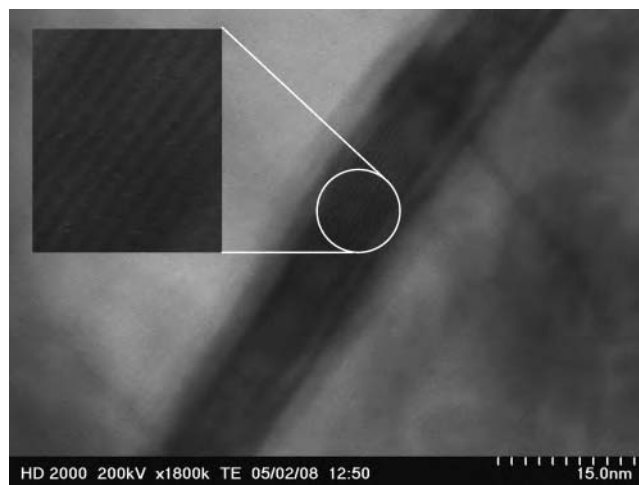


Figure 3. High-resolution image of a single fiber obtained from the sonication of iron pentacarbonyl with 0.5 mg/mL BSA. The expanded region shows the presence of lattice fringes.

two samples and produced results similar to those shown in Figure 4, again indicating mixtures of α - and γ -FeOOH and α -Fe $_2$ O $_3$.

FTIR analysis of the BSA-iron oxide samples was performed to verify the presence of the BSA protein. Figure 7 shows the FTIR absorption spectrum for (a) neat BSA and the spectrum for (b) the 0.5 mg/mL BSA-iron oxide sample. The similarities between the two spectra confirm the presence of BSA in the nanocomposite. The modified Lowry total protein analysis was performed on the 5.0 mg/mL BSA-iron oxide sample. This analysis determines the number of free tryptophan and tyrosine units in the protein. The assay indicated a high yield (\sim 70% recovery) suggesting the BSA protein remained intact. TGA analysis of the same sample showed about a 60% mass loss accumulated over the temperature range room temperature to 800 $^\circ\text{C}$, followed by no further mass loss up to 1000 $^\circ\text{C}$, the highest temperature measured. The change in mass is primarily due to loss of BSA and water, with a small contribution ($<$ 10%) due to conversion of the mixed iron oxide phases to pure hematite (α -Fe $_2$ O $_3$).

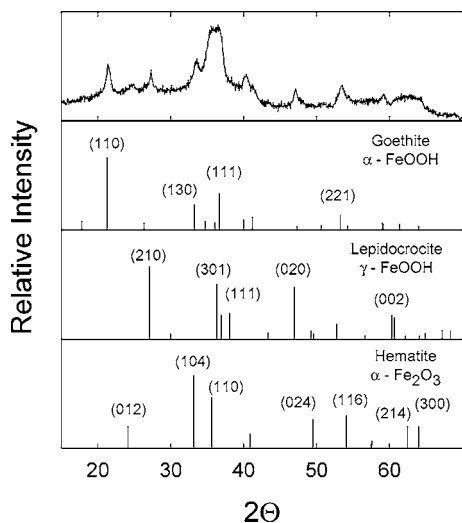


Figure 4. Top. XRD spectrum of the fibrous nanostructures formed by the sonochemical reaction of iron pentacarbonyl in water with 0.5 mg/mL BSA. Bottom. ICCD patterns for goethite, lepidocrocite, and hematite for comparison to the sample.

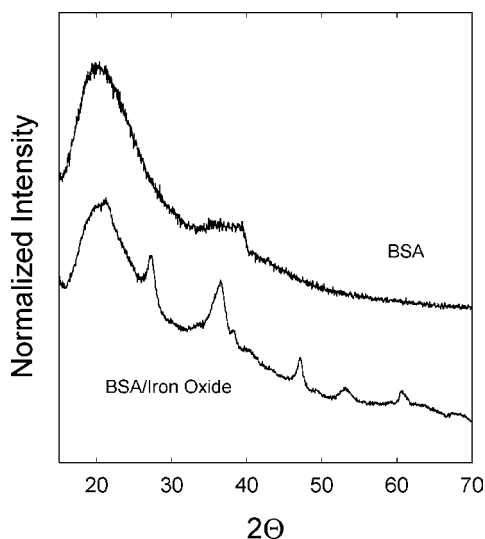


Figure 5. XRD spectra for the sample containing nanoneedles (5.0 mg/mL BSA) and for BSA alone.

Discussion

The sonochemical method has been used quite extensively for the production of metal nanoparticles.^{2–8} For simple systems such as iron pentacarbonyl in dodecane, the mechanism for particle formation is fairly well understood.² A thermally labile compound such as iron pentacarbonyl decomposes within the extreme-temperature (~ 5000 K) regions created by acoustic cavitation



The resulting free metal atoms nucleate to form the nanoparticles. Under the conditions produced by acoustic cavitation, it is speculated that iron pentacarbonyl can go directly to free metal iron, minimizing the role of any intermediates. In addition, because of the very fast cooling rates ($\sim 10^{10}$ K/s), the nanoparticles formed are often amorphous.

The conditions of the reaction performed here are somewhat different; iron pentacarbonyl is reacted in water (with no BSA), a solvent for which it is not soluble. The reaction is started with the injection of the iron pentacarbonyl on top of deoxygenated water; no mixing is observed. Only the action of the sonochemical

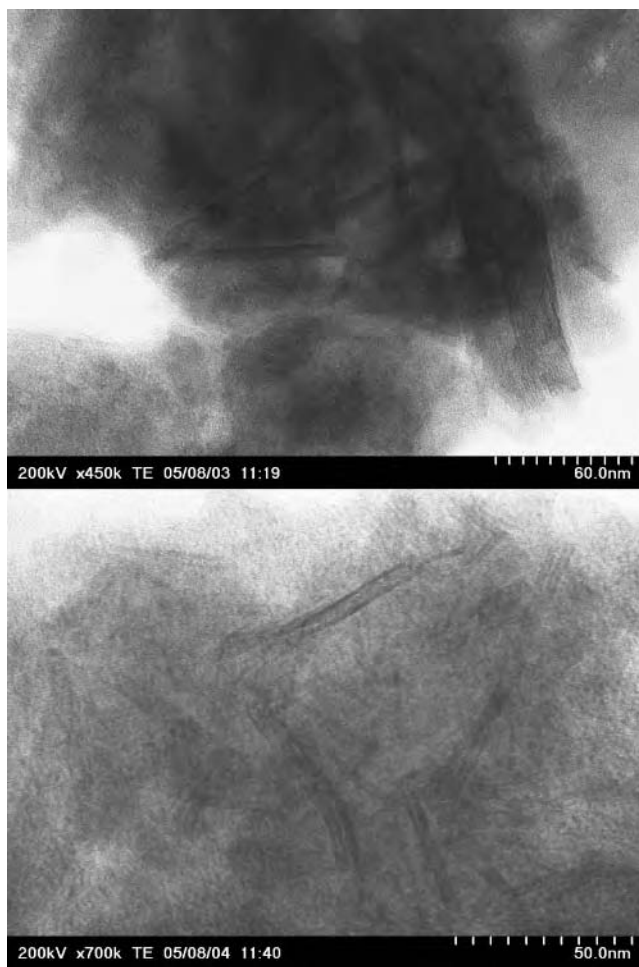


Figure 6. TEM images of the nanostructures produced by the sonochemical reaction of iron pentacarbonyl with 0.5 mg/mL BSA in water, using 300 μL (top) and 150 μL (bottom) of iron pentacarbonyl.

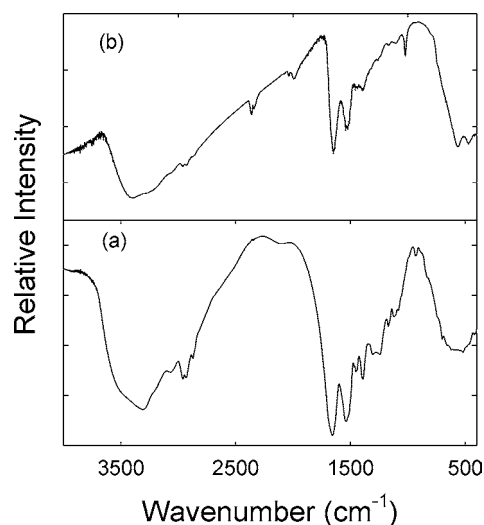


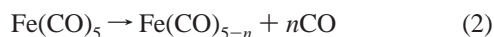
Figure 7. FTIR spectra of (a) BSA alone and (b) BSA–iron oxide nanofibers sample.

probe results in mixing and the formation of an emulsion. The emulsion remains intact only as long as the acoustic energy is applied. During the reaction, the iron pentacarbonyl decomposes to yield a black precipitate. TEM images of this material show particles ranging in size from <10 nm to ~ 60 nm (Figure 1a). The size distribution of these particles is larger than those obtained

from the sonochemical reaction of $\text{Fe}(\text{CO})_5$ in hydrocarbon solvents (~ 3 to 12 nm).⁸ The broad distribution could be due to an inhomogeneous distribution of droplet sizes within the emulsion formed during acoustic cavitation: different sized droplets would result in different sized nanoparticles. This, coupled with the observation of a Fe_3O_4 crystal structure (Figure 2), suggests a somewhat different reaction path for the formation of these particles; one that possibly involves a slower secondary step conducive to crystal growth (i.e., oxidation of the particles, formation of the particles from oxidized intermediates, or reaction via a thermal decomposition pathway).

When the same reaction is performed with the protein BSA (0.5 mg/mL) present in solution, the behavior of the reaction and the products formed are very different. The BSA readily dissolves in water and upon application of acoustic energy incorporates the iron pentacarbonyl into solution. This time the solution is stable, remaining a homogeneous mixture when acoustic cavitation is halted. This observation indicates that BSA may act like a surfactant; taking the iron pentacarbonyl into solution, isolating it from the water, and preventing bulk-phase separation. This reaction produces a reddish solution that when dried, yields a reddish powder. This material is characterized by long (~ 200 nm), fiber-like structures, with widths on the order of 5 – 10 nm (Figure 1b), and a well-defined crystal structure showing a mixture of α - and γ - FeOOH and α - Fe_2O_3 (Figure 4).

The fact that incorporation of BSA into the reaction made such a significant change in product morphology and structure indicates a change to the reaction mechanism. As shown by eq 1, the sonochemical reaction can be fairly simple, producing free metal iron from iron pentacarbonyl in a single step, followed by particle formation.² It is known that the thermal reaction of iron pentacarbonyl is much more complex, involving a number of decomposition intermediates¹⁹



where $n = 1$ – 5 . From the reaction of the decomposition intermediates, a number of product intermediates have been identified that lead to cluster formation [e.g., $\text{Fe}_2(\text{CO})_8$, $\text{Fe}_2(\text{CO})_9$, and $\text{Fe}_3(\text{CO})_{12}$]. Of the decomposition intermediates, $\text{Fe}(\text{CO})_4$ has also been shown to be reactive toward other compounds¹⁹



where L is a suitable ligand compound (e.g., Lewis base). This is further supported by studies of the reactivity of $\text{M}(\text{CO})_{x-1}$ species toward Lewis bases where efficient metal–ligand binding is well-known.²⁰ Another approach has indicated $[\text{Fe}_n(\text{CO})_{m-1}\text{C}(\text{O})\text{L}]^-$ as a likely intermediate for iron pentacarbonyl with a Lewis base, where n and m can be 1 and 5 , 2 and 9 , and 3 and 12 , respectively.²¹ It is possible that the formation of the iron oxide nanofibers proceeds through a mechanism similar to the thermal decomposition mechanism (eq 2 and 3), as opposed to the sonochemical path (eq 1). The observation that BSA acts to bring iron pentacarbonyl into solution suggests a strong interaction between BSA and iron pentacarbonyl. As a result, it is likely that the vapor pressure of the iron pentacarbonyl associated with BSA is much lower than the freely solubilized iron pentacarbonyl. The reduced vapor pressure would result in a greatly reduced concentration of iron pentacarbonyl in the

extreme temperature regions formed from acoustic cavitation, making the formation of nanoparticles via the sonochemical path unlikely. The reaction would instead proceed through exposure to high-temperature regions created as the heat generated from the acoustic cavitation events is dissipated by the solvent.

To probe the role of BSA on the growth of the nanofibers, the same reaction was performed at a much higher BSA concentration (5.0 mg/mL). At this concentration, sonication of iron pentacarbonyl produces needles; much shorter (~ 30 nm), thinner (~ 3 – 5 nm), and contained within a dense, amorphous material (Figure 1c). XRD analysis shows primarily a broad, featureless structure which is identical to that obtained when the protein BSA is analyzed independently (Figure 5).²² Three minor peaks are observed that can be assigned to γ - FeOOH . This material was again a reddish powder. If iron pentacarbonyl is truly associating with the BSA in solution, then an increase in BSA concentration would likely reduce the local or molecular-level concentration of the iron pentacarbonyl and its intermediates. A reduced local concentration of reactant would result in less iron available for the growth and propagation of the nanofibers, thus producing shorter and more numerous fibers, or needles, as is observed.

We also investigated the effect of concentration by varying the amount of iron pentacarbonyl injected (150 and 300 μL) while maintaining a constant protein concentration (0.5 mg/mL). For the sonochemical reaction of $\text{Fe}(\text{CO})_5$ in hydrocarbon solvents, it is well-known that a change in the concentration of $\text{Fe}(\text{CO})_5$ results in a change in nanoparticle size. This effect is attributed to a higher local concentration of the $\text{Fe}(\text{CO})_5$ being exposed to the extreme temperature regions and thus a greater number of iron atoms available to nucleate and form the nanoparticle. In our case, the TEM images of the two samples formed in water/BSA solution show no significant differences (Figure 6). Both samples demonstrate similar fiber structures and amorphous material. XRD analysis also indicated no significant differences and the spectra were similar to the spectrum shown in Figure 4. These results again support an alternate reaction pathway for the formation of the nanofibers (i.e., not via eq 1). Since it is likely that the strong interaction of $\text{Fe}(\text{CO})_5$ with BSA prevents the $\text{Fe}(\text{CO})_5$ from being exposed to the extreme temperature regions formed by acoustic cavitation, an increase in the $\text{Fe}(\text{CO})_5$ concentration in the presence of BSA would have no effect (via the sonochemical reaction path). However, analysis of the two previous samples prepared by varying the BSA concentration indicates that the thermal reaction pathway is also sensitive to concentration. Since changing the $\text{Fe}(\text{CO})_5$ concentration is conceptually similar to changing the BSA concentration, one would expect to observe some change in the nanostructures. Because this was not observed, we conclude that the change in $\text{Fe}(\text{CO})_5$ concentration (one-half) is too small compared to the change in BSA concentration (an order of magnitude) to effect the nanostructure results.

Conclusion

The sonochemical method has been used to decompose iron pentacarbonyl in an aqueous environment, both with and without the protein BSA. The reaction with BSA has led to the formation of BSA-iron oxide composites showing nanofiber and nanoneedle morphologies with well-defined crystal structures. Even though the reaction is performed using the sonochemical method, analysis of the results within the context of known iron pentacarbonyl decomposition chemistry suggests the reaction proceeds through

(20) (a) Zhang, S.; Dobson, G. R. *Organometallics* **1992**, *11*, 2447–2452. (b) Dobson, G. R. *Inorg. Chem.* **1974**, *13*, 1790–1791.

(21) (a) Belousov, Y. A.; Brin, E. F. *Polyhedron* **2001**, *20*, 2765–2769. (b) Kraihanzel, C. S.; Maples, P. K. *Inorg. Chem.* **1968**, *7*, 1806–1815.

(22) Reference 9h shows an XRD spectrum of CdS/BSA nanocomposite with a very similar profile to that of BSA shown here in Figure 5; however, the authors attributed their spectrum to CdS.

the thermal reaction pathway as opposed to the sonochemical. It is interesting to note that reports of nanoparticle formation from iron pentacarbonyl decomposed using the thermal reaction pathway tend to show spherical nanoparticles;¹⁹ however, very little is known about the thermal decomposition of iron pentacarbonyl to produce nanoparticles in water environment²³ or with proteins such as BSA. The observed difference in morphology could be due to either the presence of BSA and its apparent ability to template the growth of these nanostructures, or the fact that the sonochemical method provides a unique reaction environment—very rapid mixing supporting intimate contact

(23) Reports of iron pentacarbonyl and the water–gas shift reaction are known. See, for example: Pearson, R. G.; Mauermann, H. *J. Am. Chem. Soc.* **1982**, *104*, 500–504.

between the iron pentacarbonyl and the protein in water, and very localized hot spots provided by acoustic cavitation. Future work with this system will target other parameters such as pH, the state of the protein (viable or denatured), and the effect of co-reactants. Data from these proposed studies should help in determining mechanistic details for this reaction and the exact role BSA plays in the formation of these interesting nanostructures.

Acknowledgment. We acknowledge the continuing support of Dr. Julian Tishkoff and the Air Force Office of Scientific Research (AFOSR) for high-temperature fluids research and nanomaterials for propulsion applications.

LA7013682

APPENDIX Q

Emissions Characteristics of a Turbine Engine and Research Combustor Burning a Fischer-Tropsch Jet Fuel

INTENTIONALLY LEFT BLANK

Emissions Characteristics of a Turbine Engine and Research Combustor Burning a Fischer–Tropsch Jet Fuel

Edwin Corporan,^{*,†} Matthew J. DeWitt,[‡] Vincent Belovich,[†] Robert Pawlik,[†]
Amy C. Lynch,[†] James R. Gord,[†] and Terrence R. Meyer[§]

AFRL/PRTG, Loop Road N Bldg 490, Wright Patterson Air Force Base, Ohio 45433, University of Dayton
Research Institute, 300 College Park, Dayton, Ohio 45469, and Iowa State University,
2034 H.M. Black Engineering Bldg., Ames, Iowa 50011

Received January 10, 2007. Revised Manuscript Received June 6, 2007

The emissions characteristics of two combustion platforms, a T63 turboshaft engine and an atmospheric swirl-stabilized research combustor, fueled with conventional military jet fuel (JP-8), a natural-gas-derived Fischer–Tropsch synthetic jet fuel (also referred herein as synjet or FT), and blends of the two were investigated. Nonvolatile particulate matter (PM) and gaseous emissions were analyzed to assess the impacts of the aromatic- and sulfur-free synjet fuel on the combustion products of the two platforms. The engine was operated at two power settings, and the combustor at several equivalence ratios, to evaluate the emission production over a wide range of combustion temperatures. Conventional aerosol instrumentation was used to quantify particle number (PN), size, and PM mass emissions, while a Fourier Transform Infrared analyzer was used to quantify the gaseous species. Planar laser-induced fluorescence and laser-induced incandescence techniques were employed on the research combustor to study the effects of the FT fuel on the formation and oxidation of particles in the combustor primary zone. Test results show dramatic reductions in particle concentrations and mean size on both combustion platforms with the neat FT and synjet fuel blends relative to operation with JP-8. Reductions of over 90% in PN were observed on both platforms for several operating conditions with neat FT fuel. For the engine, over an 80% reduction in smoke number was observed with neat synjet relative to operation on JP-8. As expected, reductions in sulfur oxide emissions and slight increases in water vapor (measured only in the atmospheric combustor) resulted due to the sulfur-free nature and higher hydrogen-to-carbon ratio of the synthetic fuel. Minor impacts were observed for other gaseous emissions. American Society for Testing and Materials fuel specification tests showed that JP-8/synjet blends up to 50/50% by volume satisfied the JP-8 military fuel requirements and that only the minimum specific gravity requirement was not satisfied at higher synjet concentrations. Impacts of the synjet fuel on the emissions of the atmospheric combustor and the T63 engine, a comparison of emissions between the two platforms, and results of in situ laser-based measurements in the combustor reaction zone are discussed.

Introduction

It is estimated that the U.S. imports approximately 63% of its oil and consumes over 25% of the oil produced worldwide.¹ U.S. dependence on foreign oil is projected to increase gradually and reach imports of nearly 77% by the year 2025. Increases in the price of petroleum crude, currently over \$60 a barrel, and uncertainties in the political and socio-economic status in oil-rich countries have renewed interest into the production of liquid transportation fuels from alternative (domestic) sources. The primary benefits of domestic fuel production are the reduction in required oil imports and protection against future shortages or interruptions in supply, which adversely affects both the economy and national security of the U.S. In addition, increased domestic production could help control the rate of future OPEC price increases. Domestic resources considered for the production of liquid transportation fuels during the oil shortages of

the 1970s and 1980s included coal, oil shale, and tar sands.^{2–6} It has been estimated that the equivalent of 2.5×10^{12} barrels of oil lie in shale deposits, 1.5×10^{12} barrels in tar sands, 53×10^{12} barrels in coal, and 3.0×10^{12} barrels in natural gas.¹ Crude oil from shale and tar sands may be refined into transportation fuels using techniques similar to those used for petroleum; however, the final product is relatively high in sulfur, nitrogen, and aromatic compounds, and the initial handling and processing of these feedstocks is difficult. Natural gas and coal

(2) Sikonia, J. G.; Hilfman, L.; Wilcox, J. R.; Board, T. G.; Gembicki, V. A.; Yu, E.; Gatsis, J. G.; Latos, E. J. *USAF Shale Oil to Fuels*; U.S. Air Force Wright-Aeronautical Labs., AFWAL-TR-81-2116, Vol. II, Dayton, OH, July 1982.

(3) Reif, H. E.; Schwedock, J. P.; Schneider, A. *An Exploratory Research and Development Program Leading to Specifications for Aviation Turbine Fuel From Whole Crude Shale Oil*; U.S. Air Force Wright-Aeronautical Labs., AFWAL-TR-81-2087, Part V, Dayton, OH, Mar. 1982.

(4) Moore, H. R.; Henton, L. M.; Johnson, C. A.; Fabry, D. A. *Refining of Military Jet Fuels from Shale Oil*; U.S. Air Force Wright-Aeronautical Labs., AFWAL-TR-81-2056, Dayton, OH, 1982.

(5) Smith, E. B.; Guffey, F. D.; Nickerson, L. G. *Production of Jet Fuels from Coal Derived Liquids, Vol. III – Jet Fuels Potential of Liquid By-Products from the Great Plains Gasification Project*; U.S. Air Force Wright-Aeronautical Labs., AFWAL-TR-87–2042, Vol. III, Dayton, OH, May 1988.

(6) Talbot, A. F.; Swesey, J. R.; Magill, L. G. *Turbine Fuels from Tar Sands Bitumen and Heavy Oil*; U.S. Air Force Wright-Aeronautical Labs., AFWAL-TR-2043, Vol. II, Dayton, OH, Sept 1987.

* Corresponding author. E-mail: edwin.corporan@wpaaf.af.mil.

[†] Wright Patterson Air Force Base.

[‡] University of Dayton Research Institute.

[§] Iowa State University.

(1) Energy Information Administration. www.eia.doe.gov/aer (accessed Jan 2005).

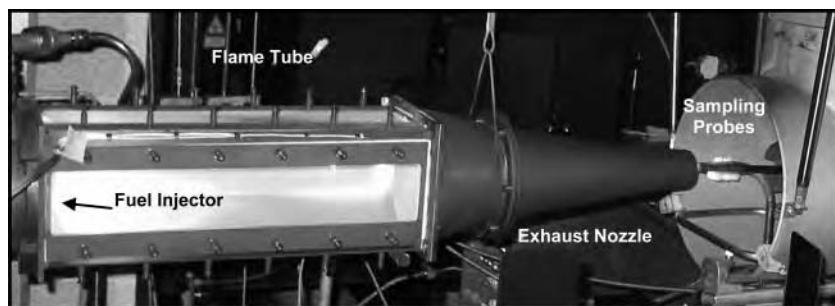


Figure 1. Swirl-stabilized atmospheric pressure research combustor.

can be converted into a highly refined transportation fuel via indirect liquefaction processes, such as a gas-to-liquid (GTL) or coal-to-liquid (CTL) processes. GTL and CTL technologies were discovered in Germany in the mid-1910s and further developed in 1923 by German scientists Drs. Franz Fischer and Hans Tropsch. In the GTL/CTL processes, the feedstock (e.g., natural gas or coal) is partially oxidized in the presence of steam, oxygen, and a catalyst to produce synthesis gas (carbon monoxide and hydrogen). The Fischer–Tropsch (FT) reaction converts the synthesis gas (syngas) into paraffinic hydrocarbons, which are then refined to the desired liquid products via product upgrading (e.g., cracking, fractionation, and isomerization). During World War II, FT technology was used by the Germans to produce liquid fuels from coal. The FT product is nearly free of heteroatoms and aromatics, thus making it attractive for diesel and jet fuel applications. Blends of FT-processed jet fuels produced from coal and natural gas with conventional petroleum-derived jet fuel have been studied recently to assess their suitability for aircraft use.^{7–8} A specific fuel blend, namely, Sasol semisynthetic jet fuel (SSJF), has undergone extensive evaluation. Studies conducted by the Southwest Research Institute demonstrated that the properties of this “semisynthetic” fuel were well within the Jet A-1 fuel specifications and that the fuel was compatible with aircraft and engine components.⁷ As a result, the United Kingdom Ministry of Defence DEF STAN 91-91 Turbine Fuel Standard currently allows the use of up to 50% by volume of the *iso*-paraffinic FT fuel with petroleum-derived Jet A-1 provided the mixture has a minimum aromatic content of 8% and conforms to all Jet A-1 specification requirements. SSJF is currently being used in commercial aircraft in South Africa.

The Department of Energy (DOE) National Energy Technology Laboratory and the Fuels Branch of the Air Force Research Laboratory (AFRL/PRTG) established a collaborative research and development program in 2000 to study and demonstrate clean aviation fuels as part of the DOE Ultra Clean Transportation Fuels Initiative. More recently (2006), the Department of Defense (DOD) established an Assured Fuels Initiative to develop, test, certify, and use jet fuels produced from alternative sources.⁹ Various studies have been performed to investigate the potential use of fuels produced via the FT process for aviation applications.^{9–17} Some have demonstrated that the FT

fuels can provide significant improvements in thermal oxidative stability and emission production with adequate low-temperature properties. However, as synthesized, the FT-processed paraffinic fuels will not satisfy required density specifications and possibly other fit-for-purpose properties. Therefore, compatibility with aircraft and engine materials, minimum aromatic content to ensure proper elastomer swell for seals to prevent fuel leaks, and lubrication properties of the FT fuel and blends are being addressed by the Air Force.^{16–17} In order to further assess the potential benefits of FT fuels on the emissions of legacy and more current combustor technologies, the present effort investigated the effects of a natural-gas-derived FT fuel on the emissions of a T63 turboshaft engine and of a CFM56-based low-emissions atmospheric combustor. Testing was performed on these platforms using neat FT and JP-8 fuels, and blends of these at varying volumetric ratios.

Experimental Section

Combustion Systems. The turboshaft engine and the atmospheric pressure swirl-stabilized combustor are located in the Propulsion Directorate at Wright–Patterson Air Force Base. The T63 engine is used primarily for helicopter applications and is employed in-house to evaluate turbine engine lubricants, fuels, fuel additives, and sensors. A detailed description of the engine has been provided in an earlier publication.¹⁸ JP-8 fuel was supplied to the engine from an underground facility tank. Neat FT fuel and JP-8/FT blends were supplied from an external tank pressurized with nitrogen to feed the engine pump. The engine was initially operated on JP-8 and then transitioned to operation with the fuel blends or the neat FT fuel. Each test condition was run for approximately 30 min. For a given engine setting, the fuel flow rate was controlled to obtain a constant turbine exit temperature (T_5). This approach ensured the best run-to-run repeatability with respect to engine power output and combustor temperature for the conditions considered. For these tests, the engine was operated at idle and cruise power.

The swirl-stabilized combustor is used for fundamental studies of complex combustion phenomena and to assess the impact of

(7) Moses, C. A.; Stavinoha, L. L.; Roets, P. *Qualification of Sasol Semi-Synthetic Jet A-1 as Commercial Jet Fuel*; 1997; SwRI-8531, San Antonio, TX, Nov. 1997.

(8) Roets, P.; Botha, J.; Moses, C.A.; Stavinoha, L. *Stability and Handling of Sasol Semi-Synthetic Jet Fuel*, Proceed. 6th Int'l Conf. on Stab. and Hand. of Liq. Fuels; Department of Energy, Rept. DOE/CONF 971014, Vol. II, 1998.

(9) Harrison, W. E.; Zabarnick, S. *The OSD Assured Fuels Initiative-Military Fuels Produced From Coal*, Proceed. 2006 Clearwater Coal Conf.; Clearwater, FL, May 2006.

(10) Edwards, J. T.; Minus, D.; Harrison, W.; Corporan, E.; DeWitt, M.; Zabarnick, S.; Balster, L. *AIAA 2004–3885*, 2004.

(11) Bauldreay, J. M.; Heins, R. J.; Smith, J. *Synthetic Jet Fuels and Their Role in the Future*, Proceed. 8th Int'l Conf. on Stab. and Hand. of Liq. Fuels; Steamboat Springs, CO, 2003.

(12) Freerks, R. L.; Muzzell, P. A. *Preprint ACS Div. Petr. Chem.* **2004**, 49 (4), 407.

(13) Muzzell, P. A.; Freerks, R. L.; Baltrus, J. P.; Link, D. D. *Preprint ACS Div. Petr. Chem.* **2004**, 49 (4), 411.

(14) Chang, P. H.; Colbert, J. E.; Hardy, D. R.; Leanoard, J. T. *Preprint ACS Div. Petr. Chem.* **2004**, 49 (4), 414.

(15) Lamprecht, D. *Energy Fuels* **2007**, 21 (3), 1448–1453.

(16) DeWitt, M. J.; Striebich, R.; Shafer, L.; Zabarnick, S.; Harrison, W. E.; Minus, D. E.; Edwards, T. *Evaluation of Fuel Produced via the Fischer-Tropsch Process for Use in Aviation Applications*, Proceed. AIChE Spring Meeting, Houston, TX, 2007.

(17) Graham, J. L.; Striebich, R. C.; Myers, K. J.; Minus, D. K.; Harrison, W. E., III. *Energy Fuels* **2006**, 20 (2), 759.

(18) Corporan, E.; DeWitt, M. J.; Wagner, M. *Fuel Process. Technol.* **2004**, 85, 727–742.

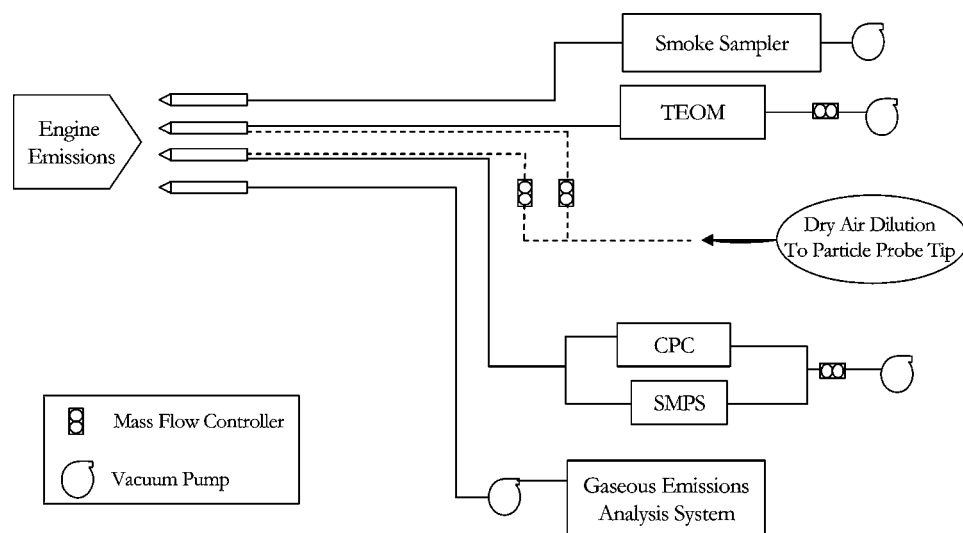


Figure 2. Simplified flow diagram of emissions sampling and instrumentation system.

research fuels and additives on soot formation/oxidation processes. The combustor consists primarily of a fuel injector, a square cross-sectional flame tube (combustion section), and an exhaust nozzle (Figure 1). The injector is a generic swirl-cup liquid-fuel nozzle consisting of a commercial pressure-swirl atomizer (Delavan Model 27710-8) with a nominal flow number of 1.6. The 4-cm-exit-diameter fuel injector is centrally located in the 15.25 cm × 15.25 cm square cross-sectional dome. Most of the air to the combustor enters through the swirl-cup injector, while a small percentage enters through aspiration holes along the dome wall. The combustion products from the primary flame zone are allowed to mix thoroughly along the 48-cm-long flame tube before entering a 43-cm-long, 5.7-cm-exit-diameter converging exhaust nozzle designed to generate a uniform exhaust gas temperature and particle concentration profile. The combustor is optically accessible for in situ laser-based diagnostics and video images via 75-mm-wide quartz windows along the top and sides. For these tests, the combustor overall equivalence ratio (Φ) was varied from $\Phi = 0.60$ to 1.10 by changing the pressure drop across the fuel injector from approximately 1.5 to 10 atm, resulting in fuel mass flow rates of 1.0–2.2 g/s with constant mass air flow. The fuel flow rate was measured with a positive-displacement flow meter and the air flow with a sonic nozzle. The inlet air was heated with an electric heater and the flow rate kept constant at approximately 0.028 kg/s throughout the study. The air pressure drop across the combustor dome was approximately 5.0% of the main supply.

Emissions Instrumentation. Nonvolatile particulate matter (PM) and gaseous emissions were extracted from the research combustor and engine with oil-cooled probes (maintained at 150 °C) and transported to the analytical instruments via heated lines. Details on the particle probe configuration and design are provided in a previous publication.¹⁸ The probes used for the gaseous emissions and smoke sample were undiluted and consisted of a simple sampling port nominally 0.457 cm in diameter. The probes were installed facing the flow near the center and at the exit plane of the engine or combustor. A simplified flow diagram of the emissions sampling system is shown in Figure 2.

In order to minimize particle loss by diffusion and impaction, the probes and sample lines were stainless steel, and sharp bends were avoided. Also, the samples were immediately diluted with dry air at the probe tip, and the sample lines were maintained at 75 °C to minimize water condensation and particle loss to agglomeration and thermophoresis. Dilution also prevented the saturation (over-range) of the analytical equipment. Dilution ratios (air-to-sample) of nominally 10–16:1 were used in these studies. The diluted sample was drawn into the instruments via a vacuum pump, and the dilution air and sample flows were controlled and measured with high-precision flow controllers. All PM measurements presented herein were corrected for dilution. On-line analysis

of the mostly nonvolatile PM emissions was performed using a TSI Model 3022A condensation particle counter (CPC) to provide a count of the total particles per unit volume (particle number, PN) and a TSI Model 3936 scanning mobility particle sizer (SMPS) to obtain particle size distributions (PSDs). Details on the theory of operation of the CPC and SMPS can be found in Cheng¹⁹ and Flagan.²⁰ For the SMPS, a nano differential mobility analyzer TSI model 3085 with a model 3025 CPC were used to classify and quantify the particles in the 4–160 nm mobility diameter range. A tapered element oscillating microbalance (TEOM) R&P model 1105 diesel particle monitor was employed for the real-time measurement of the engine PM mass concentration (mg/m^3). The TEOM quantifies the mass on the basis of the change in the oscillating frequency of a tapered element as PM is collected on an attached filter. Due to its principle of operation, the TEOM can be prone to generating highly unsteady data in high-noise and -vibration environments. However, for these tests, the instrument (located in the control room and isolated from noise) was unaffected by engine vibration, resulting in stable data for all test conditions. An in-house-designed smoke sampler was used to collect soot samples to determine smoke numbers (SNs) following the SAE Aerospace Recommended Practice (ARP) 1179.²¹ Gaseous emissions were quantified using an MKS MultiGas 2030 Fourier-transform infrared based gas analyzer and a flame ionization detector based total hydrocarbon analyzer. The sample lines to the gaseous emissions systems and the smoke sampler were maintained at 150 °C to prevent the condensation of water or volatile organic species.

Laser-Based Diagnostics Systems. Effects of the fuel composition on soot formation in the combustor reaction zone were assessed using droplet and OH planar laser-induced fluorescence (PLIF) and soot laser-induced incandescence (LII). Details of the PLIF and LII systems have been provided previously,²² and only a brief description is included here. The PLIF system consisted of a frequency-doubled, Q-switched Nd:YAG laser operated at 50% power to pump a dye laser which was then frequency-doubled to the ultraviolet for droplet and OH PLIF. A 1.5-m-focal-length spherical plano-convex lens and a 75-mm-focal-length plano-concave lens were used to form a laser sheet of 330 μm at full-thickness-half-max (FTHM) that entered the combustor through the top window. Fluorescence was collected using an intensified charge-

(19) Cheng, Y. S. Condensation Detection and Diffusion Size Separation Techniques. In *Aerosol Measurement*, 2nd ed.; Wiley-Interscience: New York, 2001; Chapter 19.

(20) Flagan, R. C. Electrical Techniques. In *Aerosol Measurement*, 2nd ed.; Wiley-Interscience: New York, 2001; Chapter 18.

(21) *Aircraft Gas Turbine Exhaust Smoke Measurement*; SAE Aerospace Recommended Practice ARP 1179; SAE: Warrendale, PA, 1970.

(22) Meyer, T. R.; Roy, S.; Gogineni, S. P.; Belovich, V. M.; Corporan, E.; Gord, J. R. *Appl. Opt.* **2005**, *44* (3), 445–454.

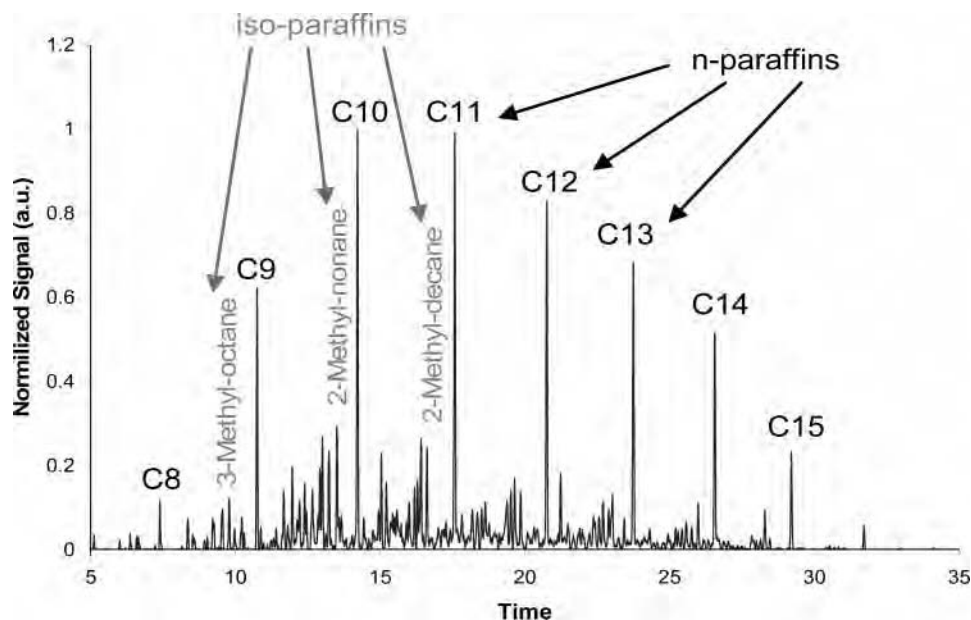


Figure 3. Gas chromatogram of JP-8 fuel.

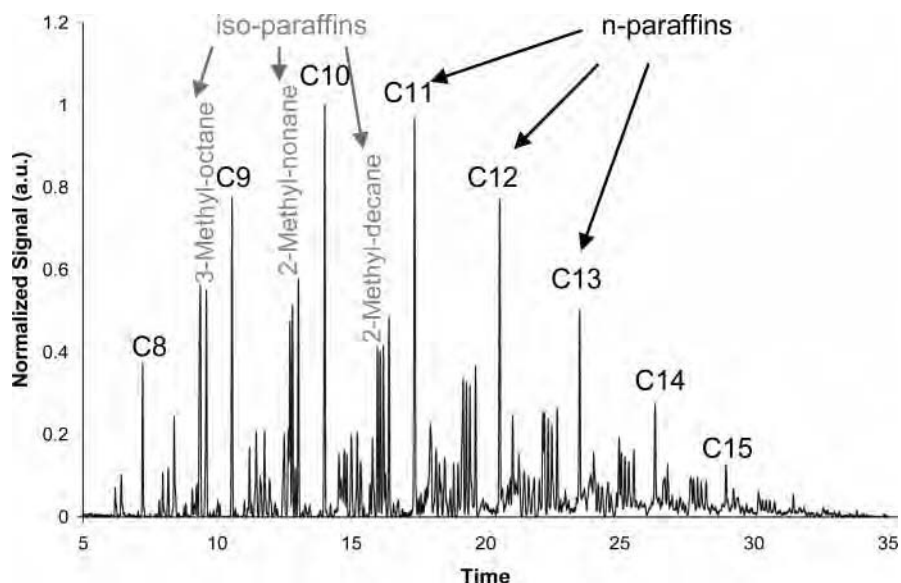


Figure 4. Gas chromatogram of synthetic jet fuel.

coupled device (ICCD) camera. Two 1 mm WG-295 filters were used to eliminate scattering from droplets (verified in a separate sample cell), and a UG11 filter was used to eliminate flame emission and scattering from the LII laser. A 105-mm-focal-length $f/4.5$ UV lens and an intensifier gate width of 20 ns were used to capture the droplet and OH PLIF signals. The two PLIF signals could be distinguished because the droplet PLIF signal intensity was approximately an order of magnitude higher than that for OH PLIF. In addition, the signal occurred primarily near the injector or at isolated points. OH signals, visible at low equivalence ratios or with low aromatic fuels, were verified by tuning the PLIF laser source on and off of the Q1(9) transition of OH at 283.922 nm (in air).

The LII system used 50% of the energy from a frequency-doubled Nd:YAG laser, formed into a laser sheet using a 2 m plano-convex spherical lens and a 50 mm plano-concave cylindrical lens. The FTHM of the laser sheet was about 700 μm . The LII signal, consisting of incandescence from laser-heated particles, was detected using an ICCD camera and an $f/1.2$, 58-mm-focal-length glass lens. The PLIF and LII cameras were synchronized for simultaneous imaging using an external delay generator driven by the Q-switch TTL output of the Nd:YAG laser.

Fuels. JP-8 fuel is petroleum-based commercial Jet A-1 with a military additive package that includes an icing inhibitor (~ 1000 – 1500 ppm), corrosion inhibitor/lubricity enhancer (~ 20 ppm), and a static dissipater additive (~ 5 ppm). JP-8 is the standard fuel used for all USAF aviation applications. The synthetic jet fuel (herein called synjet) used in this study was produced from natural gas by Syntroleum Corporation via a low-temperature FT process. The synjet fuel was not treated with the JP-8 additives; however, these are not expected to impact emissions due to their low concentration and mostly organic nature. The JP-8 and synjet fuels were analyzed using gas chromatography/mass spectrometry (GC/MS) and high-performance liquid chromatography techniques to determine their chemical composition. Their respective gas chromatograms are shown in Figures 3 and 4.

JP-8 is composed of various hydrocarbon types, with branched (*iso*-) and normal (*n*-) paraffins being the primary classes. The *n*-paraffins typically range from *n*-octane (*n*-C₈) to *n*-hexadecane (*n*-C₁₆), with maximum concentrations from *n*-decane (*n*-C₁₀) to *n*-dodecane (*n*-C₁₂). The molecular weight distribution is determined by the required volatility (e.g., distillation) range for the upgraded fuel. JP-8 also contains appreciable concentrations of cycloparaffins, olefins, and aromatics. During low-temperature FT synthesis, the

Table 1. Summary of GC/MS Results for the Synthetic Fuel and an Average JP-8²³

component	synthetic fuel	average jp-8 (jet-a 1)
<i>n</i> -paraffins	18.0	18.0
<i>iso</i> -paraffins	82.0	41.0
monocycloparaffins	<1.0	10.8
dicycloparaffins	<1.0	8.9
tricycloparaffins	<1.0	<1.0
alkyl benzenes	<0.5	13.3
indans + tetralins	<0.5	4.7
naphthalene	<0.5	<0.2
substituted naphthalenes	<0.5	1.6

primary products are linear paraffins of varying length. Although these could be used directly for certain combustion platforms, such as compression ignition diesel engines, upgrading must be performed to produce a suitable aviation fuel. This includes operations such as hydrocracking and hydro-isomerization to produce high yields of branched paraffins, which are required to provide acceptable low-temperature performance properties. Following the upgrading, the fuel is distilled to provide the appropriate volatility range for usage. The FT fuel used in this study had a high *iso*-/*n*-paraffin ratio, with the former composed primarily of monomethyl-substituted alkanes. The primary components and averages in JP-8 and the synthetic fuel used are listed in Table 1.²³

Results of several specification tests for the neat fuels and blends using standard American Society for Testing and Materials (ASTM) methods are listed in Table 2. As shown, the synjet fuel properties satisfy those required for JP-8 with the exception of the minimum specific gravity and the properties related to the required military additives. Overall, the physical properties vary linearly with blend ratio, which has been observed when blending with a wide range of petroleum-derived fuels.¹⁶ The lower density of the synthetic fuel may reduce aircraft range; however, this is slightly offset by its higher energy per mass content. The high concentration of *iso*-paraffins and low concentration of long-chain *n*-paraffins ($\geq C_{16}$) in this specific synthetic fuel (relative to the JP-8) result in a very low freezing point; the final freeze point of a FT fuel will be highly dependent on these factors. Various studies have shown that this type of paraffinic FT fuel possesses excellent thermal oxidative stability characteristics, making it a promising fuel for advanced high-speed aircraft applications.^{9–10} A lack of aromatic compounds in the synthetic fuel may be of concern since these are believed to have the ability to swell elastomers, which helps prevent leaks in fuel systems. Also, the lack of sulfur and a lubricity additive in the synthetic fuel may increase the wear in fuel pumps.

Results and Discussion

T63 Engine. Neat JP-8, synthetic jet fuel and several JP-8/synjet fuel blends in increments of 12.5% by volume were evaluated on the T63 engine. During testing, the engine power output was kept constant for each set point by adjusting the required fuel flow rate. This approach ensured the highest repeatability and provided a basis of comparison. Engine test data (e.g., pressure, temperatures, turbine rpm, etc.) demonstrated negligible impacts on engine performance or significant penalties on total engine fuel flow using the synjet fuel or blends. The engine was observed to operate smoothly (i.e., no instabilities) during the transitions between fuel types. In addition, no fuel leaks in the engine were observed during operation with the synjet fuel and blends.

PM Emissions. PN emissions for the T63 engine fueled with JP-8 averaged 6.0×10^7 ($\pm 5\%$) particles/cm³ at idle and 2.25×10^8 ($\pm 5\%$) particles/cm³ at cruise. The reductions in PN emissions as a function of the percentage of FT fuel blended in

JP-8 are shown in Figure 5. The PN emissions decreased proportionately with the concentration of FT fuel in the blend, although the slopes are slightly different for the two power conditions evaluated. The PN reductions at idle are clearly more pronounced than at cruise, which is likely the result of smaller-size PM exhaust at idle and the production of even smaller and more easily oxidized particles with the FT fuel. In addition, the unburned hydrocarbon emissions are significantly higher at the lower power condition (~ 800 – 1300 ppm) compared to cruise (<40 ppm), which can promote the formation of nanoscale particles or aerosols. The reduction in PM (soot) emissions with the FT fuel for this study is attributed primarily to the reduced aromatic components in the fuel blend. The propensity of aromatics to produce soot has been demonstrated in large-scale combustors and laboratory flames. A summary of several efforts and the role of aromatics in soot formation has been presented by Bittner and Howard.²⁴ Reduction in the fuel aromatic content decreases precursors that contribute to the formation of soot nuclei. In addition, the synjet fuel is comprised of only normal and branched aliphatic compounds, which are believed to produce soot primarily via fragmentation and polymerization reactions, which are much slower (i.e., less efficient) than condensation reactions with aromatics.²⁵ Reduced soot production with blends of paraffinic solvents in jet fuel has been previously observed on this platform.²⁶ The higher hydrogen-to-carbon (H/C) content in the synjet fuel also undoubtedly contributed to the reduction in soot. In fact, several studies have shown that the correlation of soot and fuel carbon (or hydrogen) content is stronger than the aromatic content.^{27–28} Studies by Mosier found that the fuel hydrogen content provided the best correlation to smoke numbers in several combustors.²⁷ Moses²⁸ showed that fuels containing low polycyclic aromatics ($<5\%$) exhibited very good correlations between the fuel H/C ratio and soot; however, fuels with higher polycyclic aromatic ($>5\%$) content produced more soot than their hydrogen content alone would predict, thus demonstrating the importance of aromatics. For the present study, it is proposed that aromatics are primarily responsible for the reduced soot emissions; however, it is recognized that deconvoluting the effects of aromatic and hydrogen content is difficult since both are interdependent and vary simultaneously. Testing with an FT-derived diesel fuel on heavy duty and passenger car diesel engines also showed significant reductions in PN emissions.²⁹ The PN reductions for the diesel application were primarily attributed to the lower sulfur content in the FT, which reduced the nucleation mode for particle formation. For the current study, the role of sulfur on the PN was not prominent due to the probe sampling location at the exhaust exit plane (high temperature) and immediate sample dilution, which minimizes subsequent condensation reactions. Previous testing on this platform showed a minimal effect of sulfur on PN emissions with up to a 3000

(24) Bittner, J. D.; Howard, J. B. *Prog. Astronautics Aero.* **1978**, *62*, 335.

(25) Lefebvre, A. H. *Gas Turbine Combustion*, 1st ed.; McGraw Hill: New York, 1983, Chap. 11.

(26) Corporan, E.; DeWitt, M. J.; Monroig, O.; Wagner, M. *Proc. ASME Turbo Expo 2004*, Paper No. GT2004-54335.

(27) Mosier, S. A. Fuel Effects on Gas Turbine Combustion Systems. *Comb. Prob. in Turbine Eng.*; AGARD-CP-353, SPS Limited: Essex, 1984; pp 5–1 to 5–15.

(28) Moses, C. U.S. Army Alternative Gas Turbine Fuels Research: Meradcom. *Comb. Prob. in Turbine Eng.*; AGARD-CP-353, SPS Limited: Essex, 1984; pp 7-1–7-10.

(29) Schaberg, P. W.; Zarling, D. D.; Waytulonis, R. W.; Kittleson, D. B. *SAE Tech. Pap. Ser.* **2002**, *SP-1724*, 55–67.

(23) Shafer, L. M.; Striebich, R. C.; Gomach, J.; Edwards, J. T. *AIAA Pap.* **2006**, *2006-7972*.

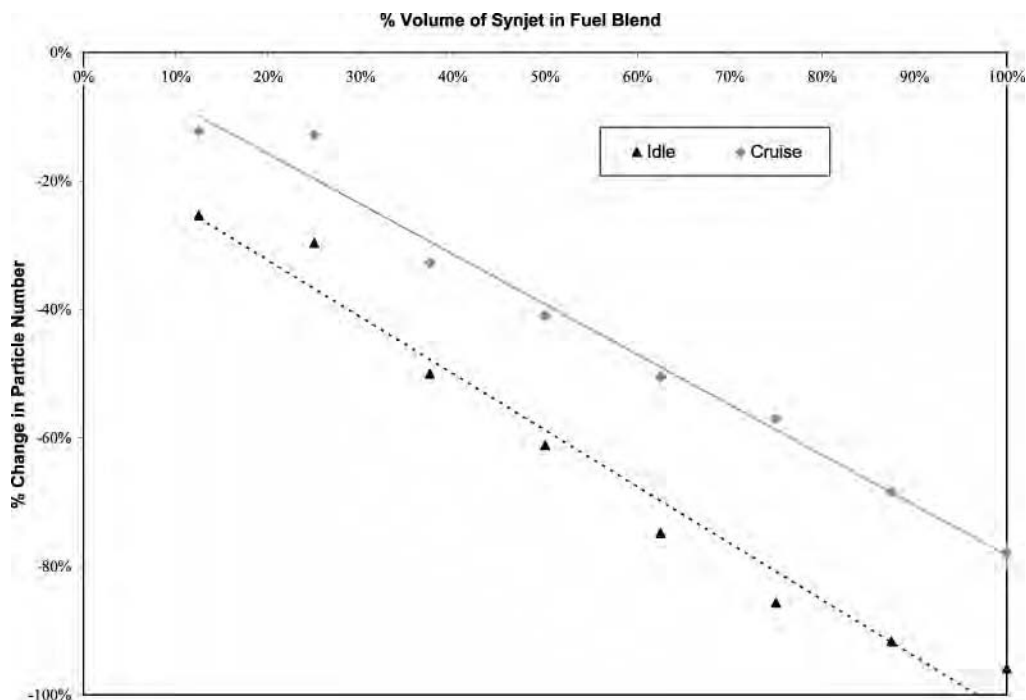


Figure 5. Reductions in PN emissions from T63 engine as a function of synjet in blend.

Table 2. ASTM Fuel Specification Test Results for JP-8, Synthetic Jet Fuel, and Blends

ASTM test	standard	JP-8 (POSF 3773)	25% synjet	50% synjet	75% synjet	100% synjet (POSF 4734)
aromatics, % vol (D1319)	max. 25.0	15.9	12.8	9.0	4.0	<0.1
hydrogen content, % by mass (D3343)	min. 13.4	13.9	14.2	14.6	15.2	15.3
total sulfur, % mass (D4294)	max. 0.30	0.06	0.05	0.04	0.02	<0.01
total acid number, mg KOH/g (D3242)	max 0.015	<0.001	<0.001	<0.001	<0.001	0.001
distillation-residue, % vol (D86)	max. 1.5	1.3	1.2	1.3	1.4	1.4
distillation-ep, °C (D86)	max. 300	256	265	268	271	271
freezing point, °C (D5972)	max. -47	-51	-52	-54	-56	-59
existent gum, mg/100 mL (D381)	max. 7.0	4.6	3.5	2.4	1.3	0.2
viscosity @ -20 °C, cSt (D445)	max. 8.0	4.1	4.6	4.3	4.6	4.6
specific gravity @ 15.5 °C (D4052)	0.775–0.840	0.799	0.788	0.778	0.767	0.757
smoke point, mm (D1322)	min. 19.0	25.0	29.0	37.5	46.0	>50
flash point, °C (D93)	38	48	48	48	48	49
heat of combustion, BTU/lb (D3338)	18 400	18 597	18 707	18 786	18 878	18 965

ppmV addition of tert-butyl disulfide into the FT fuel.³⁰ Only increases in the measured SO₂ were observed. These results demonstrated that the oxidized sulfur species did not participate in PM formation as would be expected if allowed to decrease in temperature and interact with moisture in the gas phase.

The effect of the FT fuel on the PSD is displayed in Figure 6. The PSD curves are observed to shift slightly to the left to smaller-diameter particles and lower peaks (concentrations) as the content of the FT fuel was increased. A strong correlation exists between the mean particle diameter and the concentration of FT in the fuel blend for both idle and cruise conditions. The particle mean diameters for operation on JP-8 were 28 and 42 nm at idle and cruise, respectively, which reduced linearly with the blend ratio to 17 and 27 nm, respectively, for the neat FT fuel. The resultant smaller-diameter particles are primarily attributed to the reduction in soot nuclei with the nonaromatic fuel, thereby reducing the pool of nascent particles available for coagulation and surface growth.

Reductions in PM mass as measured with the TEOM are shown in Figure 7. Data for the neat FT at idle and the 87.5%

FT blend were not collected due to incorrect setting of the dilution flow, which resulted in insufficient signal-to-noise data from the TEOM. The variability for each TEOM measurement was approximately ± 15 –25% at idle and ± 10 –20% at cruise; repeatability for successive measurements was better than ± 10 %. Reductions in the PM mass of 95% at cruise with neat synjet and approximately 50% for the 50% FT/JP-8 blend for both engine conditions were observed. The PM mass reduction trends as a function of synjet fuel are similar to the PN data with several exceptions at idle likely due to the reduced instrument sensitivity as the PM mass approached the TEOM lower measurement limit.

Smoke Number. Engine SNs for the test conditions studied are shown in Table 3. Three measurements were made for each condition. The measurement uncertainty (1σ) for SN above 4.0 was ± 10 % or better, and less than ± 20 % for SNs of 2.0–4.0. Consistent with the particle mass and number data, significant reductions in engine smoke numbers were observed using the FT fuel and blends relative to operation with JP-8. Although smoke numbers are largely the result of larger-diameter particles, these studies demonstrate very good correlation between the smoke number, PN, and PM mass for these nanometer-size particles.

(30) Monroig, O. R.; Corporan, E.; DeWitt, M. J.; Striebich, R.; Wagner, M. *Effects of Aromatic and Sulfur Concentration in Jet Fuel on the Emissions of a T63 Engine*, Proceed. 9th Int'l Conf. on Stab. and Hand. of Liq. Fuels; National Technical Information Services: Springfield, VA, 2005.

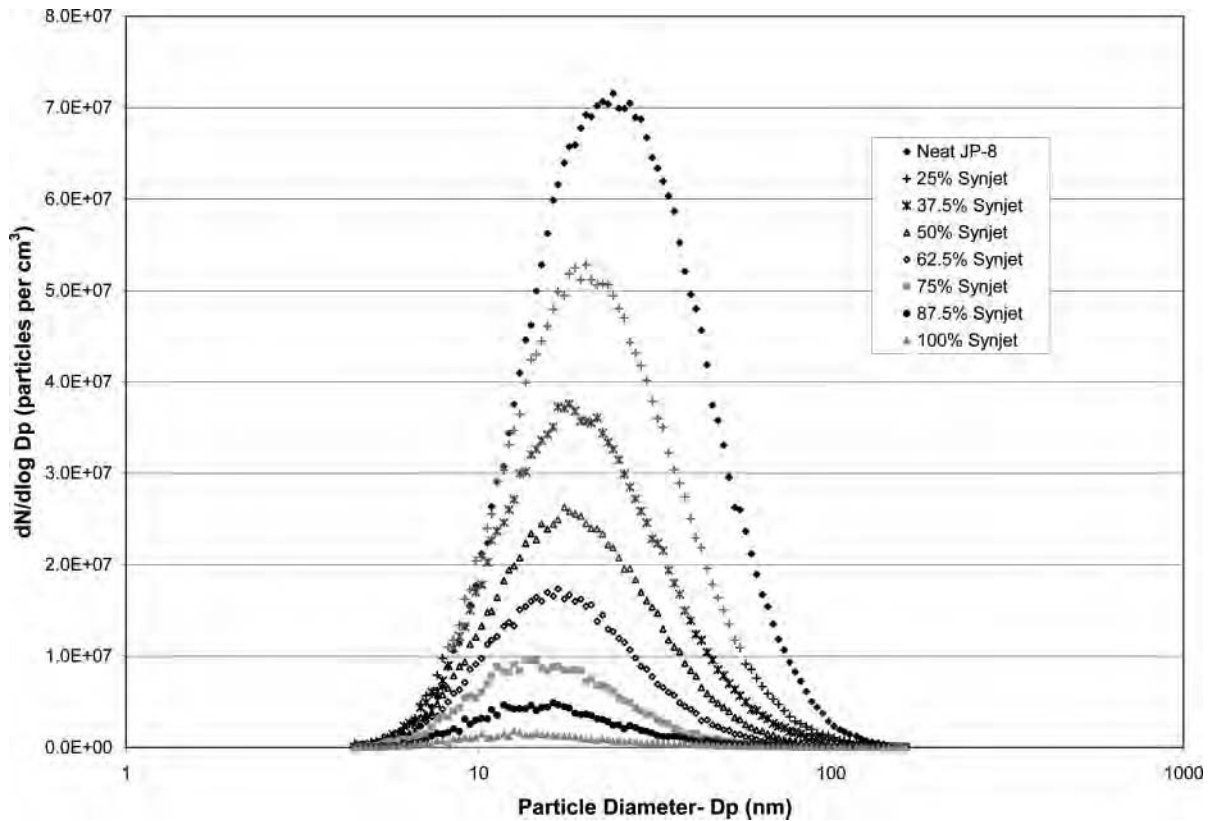


Figure 6. Effects of synjet fuel on T63 engine particle size distribution at idle.

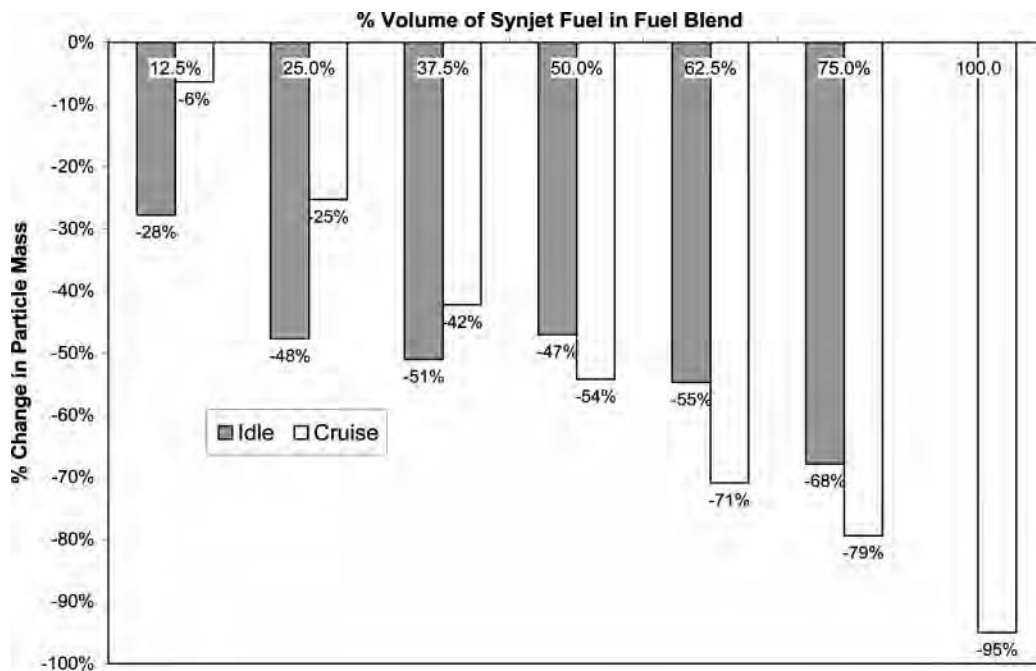


Figure 7. Reductions in PM mass emissions from T63 engine as a function of synjet fuel in blend.

Reductions in particle number and mass emissions with paraffinic FT fuels have also been observed in diesel applications both in the laboratory and on-road.^{31–34} Although these are reciprocating engines used for ground-based applications, the magnitudes of the reductions were comparable to the T63 engine results, thus further demonstrating the potential reduction of PM emissions with the use of these paraffinic fuels.

Gaseous Emissions. The synthetic fuel had a negligible effect on the primary gaseous emissions, specifically, CO, CO₂, and NO_x. Although a slight decrease (~1.5%) in CO₂ was expected

Table 3. Effects of Synthetic Jet Fuel on T63 Engine Smoke Numbers

engine condition	% synthetic fuel in fuel blend					
	0	12.5%	25%	37.5%	75%	100%
idle	6.4	4.0	3.8	2.7	<1.0	<1.0
cruise	29.7	26.6	23.7	19.7	8.7	3.8

due to the higher H/C ratio of the FT fuel, no appreciable difference in the measurements was observed. Only SO_x emissions were observed to change, decreasing linearly as the

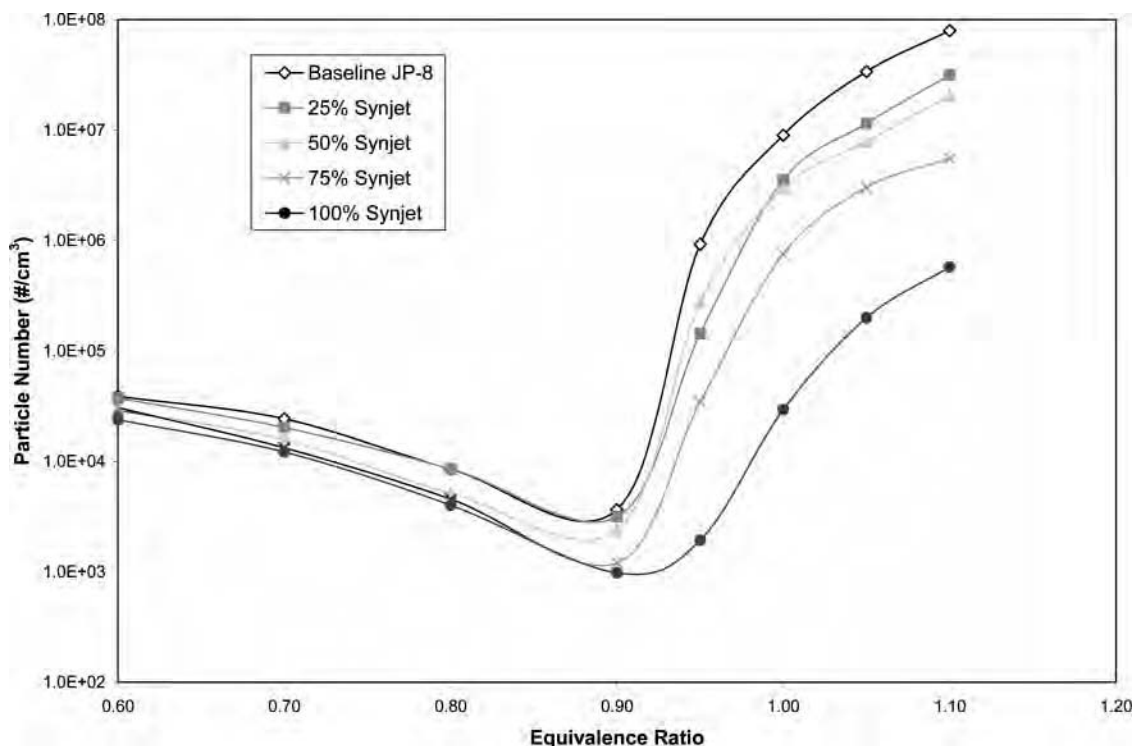


Figure 8. Swirl-stabilized combustor particle number as a function of equivalence ratio for several synjet/JP-8 blends.

result of the sulfur-free nature of the FT fuel. Negligible changes in NO_x emissions were observed, which was anticipated since these are primarily thermally driven and the engine operated at a constant turbine exit temperature (T_5). Testing with FT fuels has previously shown reductions in NO_x emissions for compression³² ignition applications.^{34–36} For these reciprocating engines, the NO_x production rate could be altered by varying the injection timing and heat release during the combustion event, intensifying the benefit of the synthetic fuels. Although these degrees of freedom are not typically available on turbine engine platforms, further investigation of potential reductions in undesirable NO_x formation with synthetic fuels is warranted.

Swirl-Stabilized Research Combustor. As with the engine, the combustor was operated with baseline JP-8, neat FT, and blends of the two. The combustor equivalence ratios (Φ) were varied from 0.60 to 1.10 by changing the fuel flow rates while maintaining a constant air flow. In order to set the correct fuel flow rates to match the desired equivalence ratio, the measured chemical formulations and densities of the blends were used to obtain the correct stoichiometry. The PM mass (TEOM) and smoke number were not measured for this platform due to its low magnitude of soot emissions, which resulted in extremely low signal-to-noise ratios.

PM Emissions. The PN range for this combustor, 3.6×10^3 to 8.0×10^7 particles/ cm^3 , was significantly lower than that

observed for the T63 engine. A semilog graph of PN versus Φ is shown in Figure 8. The corrected PNs for Φ between 0.60 and 0.90 were in the range of 3.6×10^3 to 4.0×10^4 particles/ cm^3 , which are in the low end (single-pulse count mode) of the CPC measurement capability considering that the raw instrument readings were only ~ 250 to ~ 2400 particles/ cm^3 , respectively. Despite the low PN at these Φ values, the average random uncertainty for the baseline JP-8 tests was less than $\pm 10\%$ (1σ), with the uncertainty increasing to near 25% for the higher Φ values. The larger uncertainty at the higher Φ is most likely due to the increased turbulence and unsteadiness in the primary zone and the shorter residence times of the fuel and combustion products. A trend of reduced PN with increasing Φ (as Φ approached 1.0) is observed for $\Phi < 0.90$ for all fuels. This is likely the result of enhanced vaporization and oxidation of semivolatile PM (uncombusted fuel) as the combustion temperatures increased.

As the equivalence ratio is increased above 0.90, it is evident that the richer mixtures caused a rapid increase in the soot formation rate (especially for blends with a higher JP-8 content). In contrast to the $\Phi \leq 0.90$ case, a further increase in equivalence ratio (>0.95) produced increases in PM emissions for all fuels tested. The dramatic increase in PN (soot production) at higher Φ values suggests an increase in the rate of soot nuclei formation accompanied by a decrease in the rate of soot oxidation due to the increasing fuel-rich pockets (e.g., poor fuel–air mixing), the deficiency of oxygen and OH radicals in the combustor, and the relatively short residence times. It is noteworthy that the effect of the FT on the reduction in PM emissions was significantly larger at the higher equivalence ratios. Reductions of 2 orders of magnitude ($>99\%$) were observed for the neat fuel for equivalence ratios of 0.95–1.10 compared to an average of 60% reduction at $\Phi = 0.60$ –0.90. This could potentially be of benefit for low- NO_x , fuel-rich combustor concepts (e.g., rich–quench–lean (RQL)) since the cooler fuel-rich primary zone tends to increase the production

(31) Norton, P.; Vertin, K.; Bailey, B.; Clark, N. M.; Lyons, D. W.; Goguen, S.; Eberhardt, J. *SAE Tech. Pap. Ser.* **1998**, SP-1391, 119–128.

(32) Clark, N. N.; Atkinson, C. M.; Thompson, G. J.; Nine, R. D. *SAE Tech. Pap. Ser.* **1999**, SP-1412, 9–22.

(33) Frame, E. A.; Alvarez, R. A.; Blanks, M. G.; Freerks, R. L.; Stavinoha, L. L.; Muzzell, P. A.; Villahermosa, L. *SAE Tech. Pap. Ser.* **2004**, 2004-01-2961.

(34) Friess, W.; Herrmann, H. O.; Maly, R. R.; Schnell, M.; Schaberg, P. *VDI-Ber.* **2003**, 265–279.

(35) Szybist, J. P.; Kirby, S. R.; Boehman, A. L. *Energy Fuels* **2005**, *19*, 1484–1492.

(36) Tsolakis, A.; Theinnoi, K.; Cracknell, R.; Megaritis, A.; Wyszynski, M. L.; Golunski, S. E. *Energy Fuels* **2006**, *20*, 2377–2384.

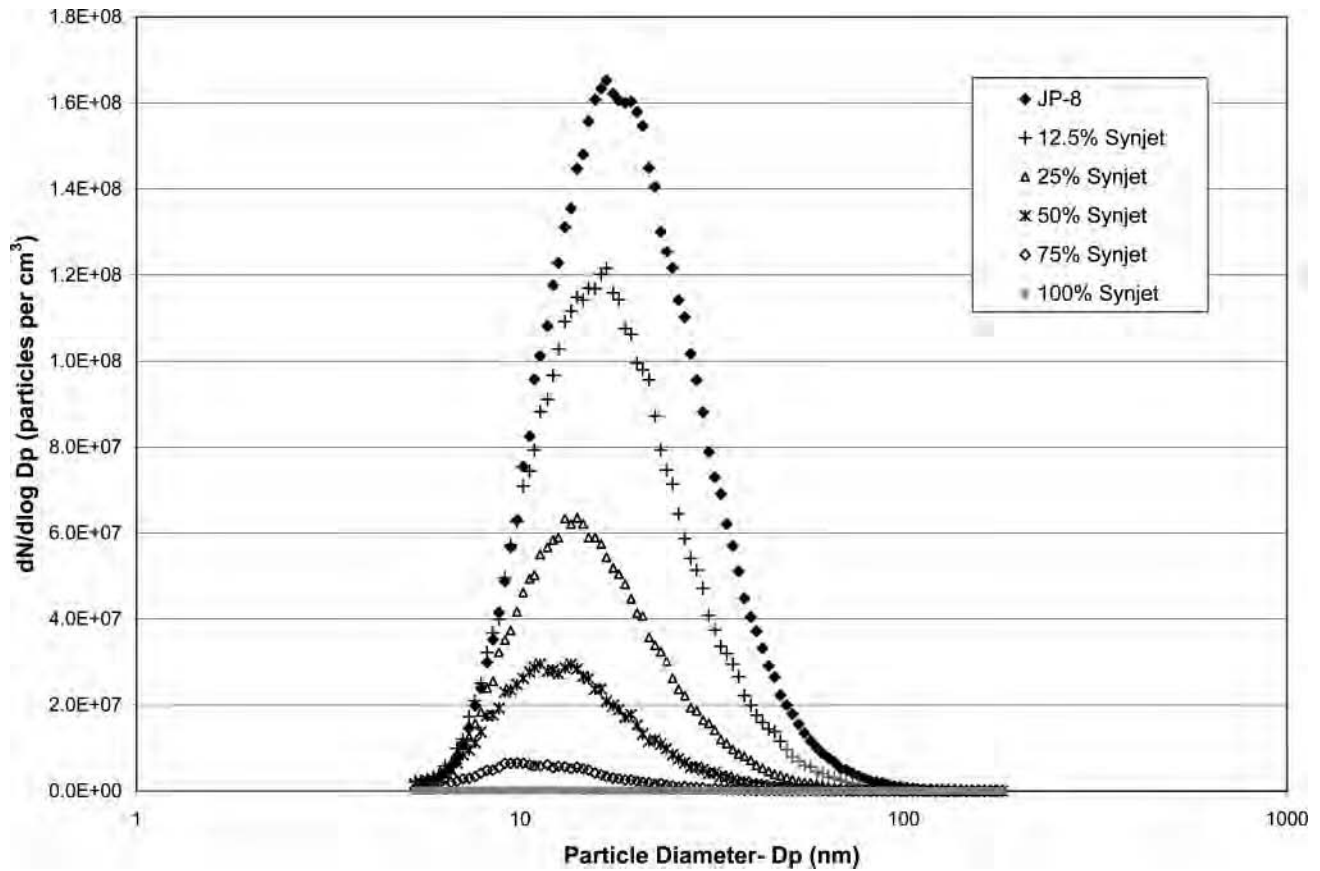


Figure 9. Effects of synjet fuel on swirl-stabilized combustor particle size distribution for $\Phi = 1.10$.

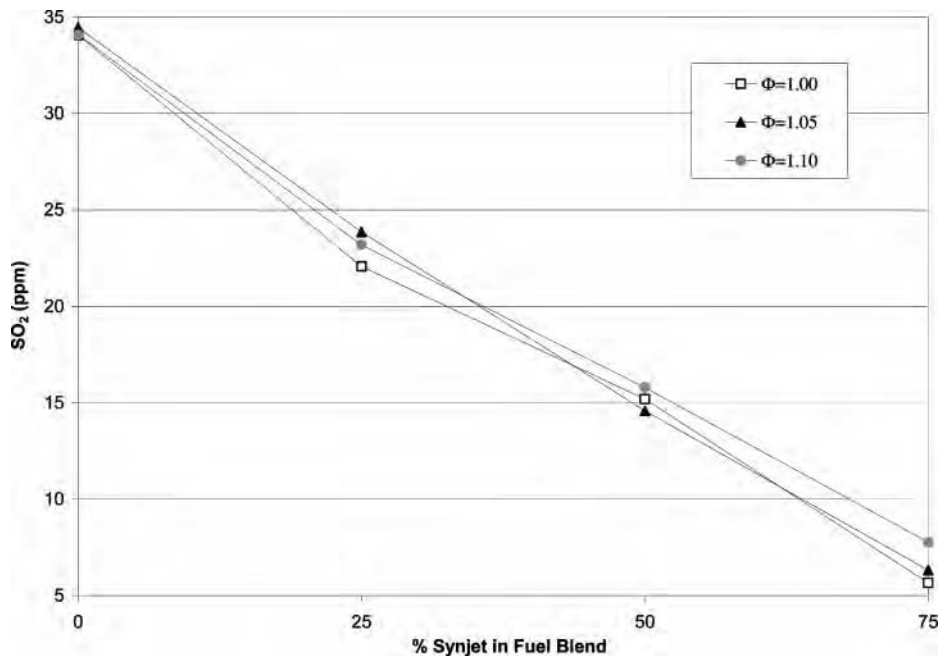


Figure 10. SO_2 emissions as a function of synjet concentration in JP-8/synjet blends.

of soot. Studies in advanced low- NO_x combustors employing similar synthetic fuels are warranted to demonstrate the potential of these for reduced soot emissions.

The effect of the synjet fuel on the particle size distribution for $\Phi = 1.10$ is illustrated in Figure 9. Consistent with the T63 engine results, the size distributions were unimodal for all fuels and decreased in concentration and particle size with increased synjet. The particle mean diameter ranged from 13 nm for the neat synjet to 21 nm for neat JP-8.

Gaseous Emissions. An analysis of gaseous emissions shows that the synjet fuel had only minor effects on the CO , CO_2 , and NO_x species. A measurable increase in water vapor (7% with neat synjet) was observed for the synjet fuel because of its higher H/C ratio. As anticipated due to the sulfur-free nature of the FT fuel, a linear decrease in SO_2 emissions resulted with the increased synjet concentration (Figure 10).

Chemical Analysis of Soot Samples. A chemical analysis was performed for soot samples collected on quartz filters for the

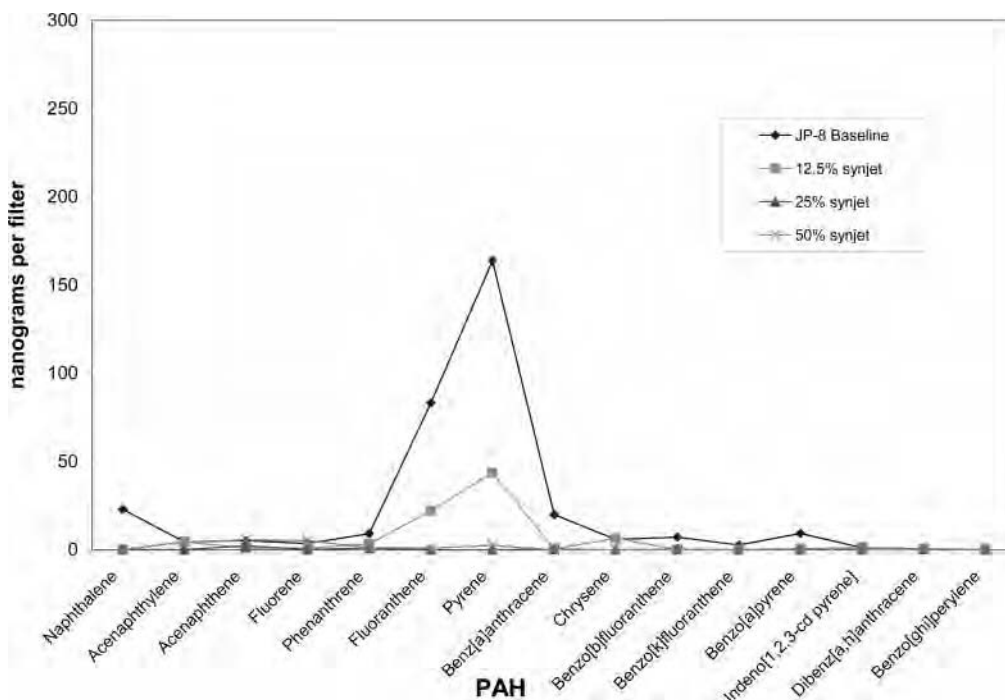


Figure 11. PAH species in soot samples as a function of synjet concentration for $\Phi = 1.10$.

combustor operating at $\Phi = 1.10$ using a thermal desorption technique with subsequent separation and analysis using GC/MS.^{37–38} Test results, depicted in Figure 11, show very low yields of polycyclic aromatic hydrocarbon (PAH) species for products from the 25% and 50% synjet/JP-8 blends. PAH species were below the detectable limit in the soot samples of fuels containing over 50% synjet fuel. The baseline JP-8 yielded the highest amount of PAH compounds; however, the concentrations of two- and three-ring species were very low. The only PAH compounds formed at relatively large concentrations, although still in the nanogram range, were pyrene and fluoranthene. The formation trend of these species correlates very well to the fuels' soot formation tendencies; therefore, these compounds may be potential markers in models to predict soot formation in combustors. The PAH detection limit is affected by both the efficiency of PAH adsorption on the quartz filter and the efficiency of the chromatographic separation and elution. Further refinements of the sampling and analysis techniques need to be made to improve the overall sensitivity and efficiency for quantitation.

Laser-Based in Situ measurements. In situ laser-based images for $\Phi = 1.10$ for the combustor operating with neat JP-8 and synjet are shown in Figure 12. The differences in fuel characteristics between JP-8 and the synjet fuel are evident in the flame zone just beyond the fuel injector. For this equivalence ratio, the flame is located about one injector diameter downstream, where the fuel and air have had sufficient time to mix and fall within the combustible limit. The laser-based imaging technique used to interrogate this region provides simultaneous droplet PLIF to track the liquid fuel and OH PLIF to track the flame. Droplet and OH PLIF images for JP-8 and the synjet are shown on the left-hand side of Figure 12. For JP-8, the fuel PLIF from liquid (unvaporized) droplets dominates the image

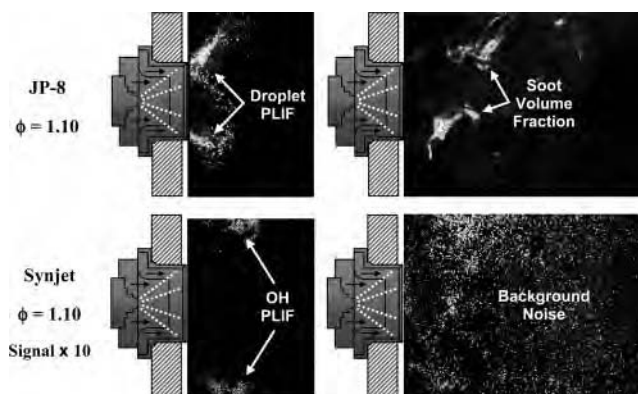


Figure 12. Images of droplet PLIF and OH PLIF (left) and soot volume fraction (right) for JP-8 and synjet fuels at $\Phi = 1.10$ (the signal levels for the images for the synjet fuel are scaled by a factor of 10 as compared with the images for JP-8).

and overwhelms the OH PLIF signal, clearly mapping the spray angle of the swirl injector. This is in contrast with the image for the synjet fuel, which shows little or no droplet PLIF near the injector even though the signal in the image has been scaled up by a factor of 10. Due to the low amount of fuel droplet PLIF for the synjet fuel, it is possible to detect OH PLIF just downstream of the fuel-rich mixing zone. The low fluorescence characteristics of the synjet fuel as compared with JP-8 were verified separately in a sample cell and can partially be attributed to differences in aromatic content between the two fuels.

The higher soot production with JP-8 is evident in the right-hand images of Figure 12, which show the soot-volume fraction recorded using LII. The lack of signal in the fuel-dense regions suggests that the LII images are free of contributions from fuel scattering or PLIF of unburned hydrocarbons. These interferences were suppressed using time-delayed detection of the relatively long-lived LII signal. In addition, the visible laser source used for LII is inherently inefficient at exciting fuel fluorescence. For JP-8, localized regions of soot formation

(37) Reich, R. F.; Stouffer, S. D.; Katta, V. R.; Mayfield, H. T.; Frayne, C. W.; Zelina, J. *AIAA Pap.* **2003**, 2003-0664.

(38) Klosterman, J. R.; Striebich, R. C.; Rubey, W. A. *Direct Thermal Desorption of Combustion Residues by GC-MS*, Pittcon, New Orleans, LA, 2001; Pittcon Paper No. 1034.

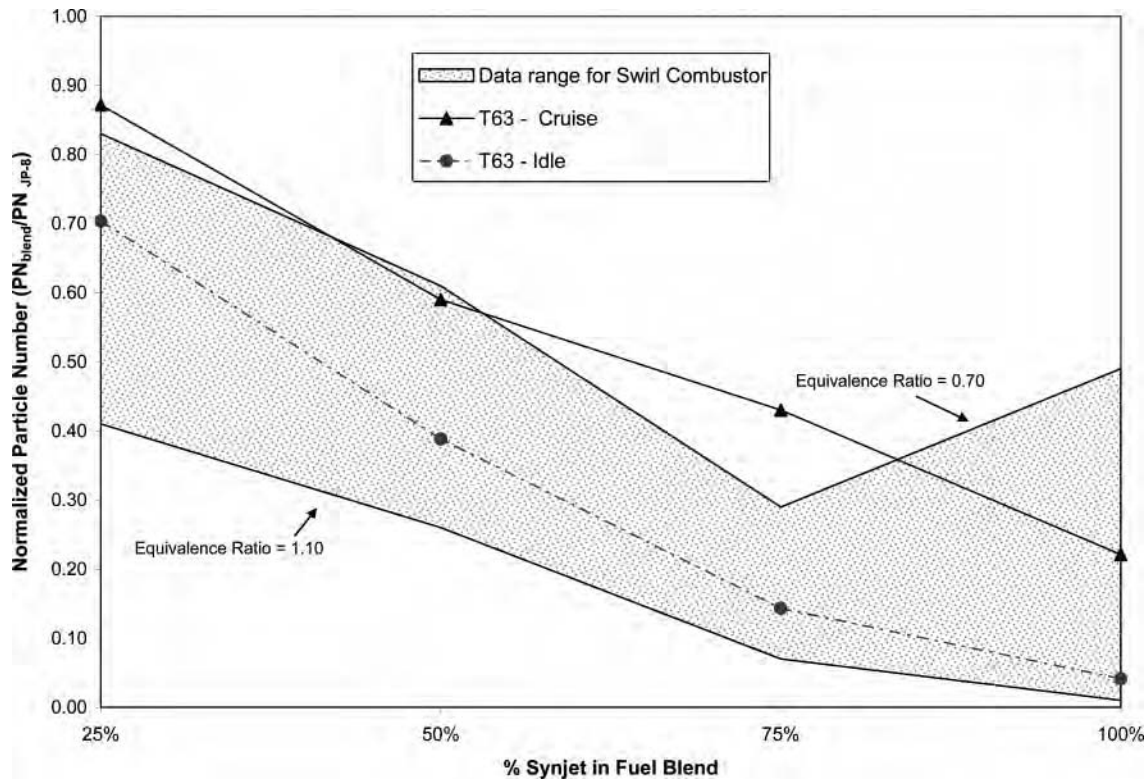


Figure 13. Comparison of synjet fuel effects on PM emissions for combustor and T63 engine.

Table 4. Swirl-Stabilized Combustor and T63 Operating Parameters

parameter	T63 engine	T63 engine	research combustor
power	idle	cruise	N/A
combustor pressure (atm)	2.37	5.43	1.0
combustor inlet temp. (°C)	122	259	177
fuel flow (kg/min)	0.40	1.32	0.056–0.123
air flow (kg/min)	43.1	76.6	1.68
equivalence ratio (Φ)	0.135	0.255	0.60–1.10
particle number (particles per cm ³)	5.0×10^7	1.5×10^8	3.6×10^3 to 8.0×10^7

are clearly visible, while soot is nearly undetectable for the synjet fuel despite scaling up the signal in the image by a factor of 10.

These images give strong evidence that the higher PM emissions with JP-8 relative to the synjet fuel are a result of increased soot production within the primary flame zone. This implies a fundamental change in the rate of soot formation and growth that takes place with JP-8 as compared with synjet. Future work will include comparisons of droplet scattering between the two fuels to discern any effects in droplet breakup and dispersion. Such nonintrusive diagnostics can provide insight into the complex two-phase combustion phenomena that may lead to changes in PM emissions in gas-turbine combustors.

Comparison of Emissions between Swirl Combustor and T63 Engine. A comparison of the operating parameters for the swirl combustor and T63 engine is provided in Table 4. At cruise, the engine operates at over 5 times the combustor pressure and at higher air inlet temperatures than the research combustor. In order to generate sufficient PM emissions from the combustor to generate a strong signal in the aerosol instruments, it was operated at relatively high equivalence ratios compared to the engine. The trends and magnitude of the PN reductions (shown as the actual PN divided by the neat JP-8 PN for each platform) for both the T63 engine and swirl combustor are shown in Figure 13. As depicted, the reduction in particle emissions for both combustion devices was directly related to the content of synjet in the fuel. Also, despite the

vast differences in combustor configuration, fuel injector, and operating conditions, the reductions in soot emissions for the research combustor are comparable in magnitude (or in some cases larger) to those observed for the T63 engine over the range of equivalence ratios considered. These results are encouraging since they demonstrate that aromatic/sulfur-free fuels may provide similar relative reductions in PM emissions for both legacy and more advanced engines. Note that the aromatic content of the baseline JP-8 is only 15.9%, which is lower than the average JP-8 aromatic content of 17.9%.³⁹ Therefore, further emissions benefits may be expected with synjet fuels when compared to average and higher aromatic content JP-8 fuels. Obviously, the absolute reductions in PM emissions will vary depending on the quality of the fuels, engine setting, and engine age and technology; however, it is feasible to infer that the trends and reductions should be relatively consistent with those observed in this study.

Conclusions

The effects of a natural-gas-derived synthetic jet (synjet) fuel on the PM and gaseous emissions of a T63 engine and a swirl-stabilized research combustor were evaluated. Reductions in PM emissions with the synjet fuel for both platforms were demonstrated. A greater than 90% reduction in PM mass and particle number and an over 80% reduction in engine smoke number were observed with neat synjet fuel relative to operation on JP-

8. The reductions varied directly with the concentration of synjet in JP-8 and were more pronounced at higher equivalence ratios for the research combustor. Except for reductions in sulfur oxides and slight increases in water vapor (observed in combustor only), a negligible impact on gaseous emissions was observed. In addition, no measurable fuel flow rate penalties or detrimental effects on engine performance were observed with neat synthetic fuel or the blends. The reductions in particulate matter emissions are primarily attributed to the reduced aromatic content of the synjet and blends relative to the neat petroleum-

(39) *Petroleum Quality Information System 2002*; Product Technology and Standardization Division, Defense Energy Support Center: Product Technology and Standardization Division, Defense Energy Support Center, 2002.

derived fuel. Similar results of the synjet fuel on both platforms increase confidence that these alternative fuels can reduce harmful PM emissions in both legacy and modern combustion systems.

Acknowledgment. The work of the University of Dayton Research Institute (UDRI) and Innovative Scientific Solutions Inc. (ISSI) were supported by the U.S. Air Force Research Laboratory (AFRL) under the cooperative research agreement F33615-03-2-2347 and contract F33615-03-D-M2329, respectively. Special thanks to Richard Striebich and Linda Shafer of UDRI for the chemical analysis of the fuel and soot samples, Sukesh Roy and Joseph Miller of ISSI and Sarah Chelgren of AFRL/PRTG for their assistance with the PLIF/LII measurements, and the Air Force Petroleum Agency (HQ AFPET/AFTLA) at WPAFB for performing the ASTM fuel specification testing.

EF070015J

APPENDIX R

Density Functional Theory Calculations of the Energetics and Kinetics of Jet Fuel Autoxidation Reactions

INTENTIONALLY LEFT BLANK

Density Functional Theory Calculations of the Energetics and Kinetics of Jet Fuel Autoxidation Reactions[§]

Steven Zabarnick^{*,†} and Donald K. Phelps[‡]

University of Dayton Research Institute & University of Dayton Mechanical & Aerospace Engineering Department, 300 College Park, Dayton, Ohio 45469, and Air Force Research Laboratory, Propulsion Directorate, 1790 Loop Rd. N., Wright-Patterson Air Force Base, Ohio 45433

Received October 21, 2005. Revised Manuscript Received December 16, 2005

Density functional theory calculations of the energetics and kinetics of important reactions for jet fuel oxidation are reported. The B3LYP functional along with 6-31G(d) and larger basis sets are used for calculation of peroxy radical abstraction reactions from hydrocarbons and heteroatomic species, the reaction of sulfides, disulfides, and phosphines with hydroperoxides to produce nonradical products, and the metal catalysis of hydroperoxide decomposition. Reaction enthalpies and activation energies are determined via DFT calculations of the structures and energies of stable species and transition states. The peroxy radical abstraction study shows the high reactivity (E_a 's of 6–11 kcal/mol) of the H atoms which are weakly bonded to heteroatoms, including nitrogen, oxygen, and sulfur. These species, at part-per-million levels, are able to compete for peroxy radicals with the bulk fuel hydrocarbon species. Benzylic hydrogens on aromatic hydrocarbons are shown to be significantly more reactive (by 4 to 5 kcal/mol) than paraffinic hydrogens with the result that the aromatic portion of fuel sustains the bulk of the autoxidation process. Sulfides and disulfides are found to react readily with fuel hydroperoxides (E_a 's of 26–29 kcal/mol) to produce alcohols and the oxidized sulfur species. Triphenylphosphine reacts with hydroperoxides with a very low activation energy (12.9 kcal/mol). The metal catalysis of hydroperoxide decomposition is calculated to occur through the formation of a complex with subsequent decomposition to form radical species without regeneration of the metal ion. The reaction pathways found and activation energies calculated can be used to improve chemical kinetic models of fuel autoxidation and deposition.

Introduction

Prior to being combusted for propulsion, jet fuel is heated during passage through aircraft fuel system components. This heating occurs incidentally while passing through fuel pumps, but it is encouraged via heat exchangers, particularly in advanced military aircraft, to remove excess heat from numerous aircraft subsystems. Systems which may require cooling include avionic, hydraulic, lubrication, and environmental control. The use of fuel to cool fuel system and combustion components is an enabling technology for advanced military aircraft because of the large quantity of excess heat produced. Unfortunately, the heat absorbed by the fuel is not always innocuous. When fuel temperatures approach ~ 140 °C, the fuel begins to react via an autoxidation chain mechanism with the small amount of dissolved oxygen (65–75 ppm wt/wt)¹ present from exposure to air. These autoxidation reactions ultimately result in formation of detrimental surface deposits and bulk insolubles.² These deposits can plug narrow passageways in valves, filters, and

nozzles and can inhibit desired heat transfer in heat exchangers. Numerous techniques have been investigated to limit the formation of deposits, including: fuel system designs to minimize fuel temperatures, fuel additives to inhibit autoxidation and deposit formation, fuel deoxygenation, fuel system surface coatings, and inclusion of “sacrificial” or coke tolerant components.³ Each of these solutions has corresponding advantages and disadvantages which are dependent on the application, but no single method is able to eliminate the deposition problem under all current and proposed aircraft fuel system conditions.

In recent years, chemical kinetic models have been developed which simulate the major autoxidation pathways that occur in jet fuels.^{4–6} Development of a widely applicable autoxidation mechanism, which enables the prediction of deposit formation, would greatly aid the fuel system design process and allow more efficient use of the fuel as a heat sink.⁷ As jet fuels consist of thousands of individual species, which vary in their identity and concentration in different fuel samples, it is impractical to build detailed chemical kinetic mechanisms. Grouped or lumped mechanisms, sometimes referred to as “pseudo-detailed” mech-

* To whom correspondence should be addressed.

[§] Disclaimer: The U.S. Government is authorized to reproduce and distribute reprints for Governmental purposes notwithstanding any copyright notation thereon. The views and conclusions contained herein are those of the authors and should not be interpreted as necessarily representing the official policies or endorsements, either expressed or implied, of Air Force Research Laboratory or the U.S. Government.

[†] University of Dayton.

[‡] Air Force Research Laboratory.

(1) Striebich, R. C.; Rubey, W. A. *Prepr.-Am. Chem. Soc., Div. Pet. Chem.* **1994**, *39*, 47–50.

(2) Hazlett, R. N. *Thermal Oxidation Stability of Aviation Turbine Fuels*; ASTM: Philadelphia, 1991.

(3) Heneghan, S. P.; Zabarnick, S.; Ballal, D. R.; Harrison, W. E. *J. Energy Res. Technol.* **1996**, *118*, 170–179.

(4) Zabarnick, S. *Ind. Eng. Chem. Res.* **1993**, *32*, 1012–1017.

(5) Zabarnick, S. *Energy Fuels* **1998**, *12*, 547–553.

(6) Kuprowicz, N. J.; Ervin, J. S.; Zabarnick, S. *Fuel* **2004**, *83*, 1795–1801.

(7) Balster, L. M.; Zabarnick, S.; Ervin, J. S.; Striebich, R.; DeWitt, M. J.; Doughty, T.; Kuprowicz, N. J. Predicting the Thermal Stability of Jet Fuel: Analytical Techniques Toward Model Validation. Presented at the 8th International Conference on Stability and Handling of Liquid Fuels, Steamboat Springs, CO, 2004.

anisms, have been used to simulate the most important reactive pathways, including the effects of antioxidants and catalytic surfaces.^{4–6} In addition, these mechanisms have been combined with computational fluid dynamics techniques with the goal of simulating the complex time and temperature variation during fuel flow in aircraft fuel system components.^{8,9} Most recently, initial efforts aimed at including global deposit formation reactions in these mechanisms have been performed.^{7,10}

Unfortunately, experimental kinetic parameters for autoxidation reactions are often not available for inclusion in these chemical kinetic mechanisms. It is desirable to have a consistent and reliable method to estimate such parameters. Recently, researchers have begun to apply semiempirical quantum mechanical¹¹ and density functional theory¹² methods to determine Arrhenius parameters for autoxidation reactions. These computational techniques promise to provide methods to readily estimate the rate parameters and evaluate the plausibility of candidate autoxidation and deposit-forming reactions. In the current work, we explore the use of density functional theory (DFT) quantum chemistry methods, specifically the B3LYP hybrid functional, for the calculation of the energetics and kinetics of autoxidation reactions. These DFT techniques promise to provide an accurate and consistent method for estimating the reaction energetics and Arrhenius parameters of fuel autoxidation reactions.

Computational Methodology

Calculations were performed using Gaussian 03 software (Gaussian, Inc.) on the USAF Aeronautical Systems Center Major Shared Resource Center computational facilities. All frequency and thermodynamic calculations were performed at 25 °C and one atmosphere of pressure. Transition state geometries were calculated using the synchronous transit-guided quasi-Newton (STQN) method or via saddle-point geometry optimizations starting with educated geometry estimates. All transition states reported were confirmed to contain a single imaginary frequency. Animations of the normal mode coordinate corresponding to the imaginary frequency of the transition state and intrinsic reaction coordinate (IRC) calculations were performed to confirm the connection between the reactants and products. Activation energies were calculated from the difference between the zero-point and thermal energy-corrected enthalpies of the transition state and the reactants. All calculations used unscaled frequencies, as the scaling factors for the functional/basis set combinations reported here result in negligible changes in the resulting thermodynamic and kinetic parameters. Unrestricted calculations were performed on open shell species (i.e., radicals and transition states), and restricted calculations were performed on closed shell (stable) species (i.e., the default behavior of Gaussian 03 was used). Basis set superposition error corrections were performed on the transition state complexes of the peroxy radical abstraction reactions by the counterpoise correction technique described below.

Basis Set Superposition Error. It is well-known that errors occur in ab initio and DFT calculations of the energetics of intermolecular interactions in complexes because of the effect of the basis functions of one molecule augmenting the other molecule. The error occurs because the individual molecule energetics are usually calculated without the presence of the basis functions of the additional species. This so-called basis set superposition error

Table 1. Calculated Bond Dissociation Enthalpies for the O–O Bond in *n*-Butylhydroperoxide

level of theory/basis set	bond dissociation enthalpy (kcal/mol)
HF/6-31G(d)	0.3
B3LYP/6-31G(d)	40.0
B3LYP/6-31G(d,p)	40.0
B3LYP/6-311G(d,p)	37.9
MP2/6-31G(d)	48.8
CBS-4M	45.0
G3B3	43.5
exptl (based on analogous reactions) ^{18,19}	44–45

(BSSE) results in an incorrect lowering of the overall energy of the complex. Techniques of correcting for BSSE's, such as the counterpoise correction of Boys and Bernardi,¹³ have been used extensively for the calculation of intermolecular complexes but have not generally been employed for transition states despite the fact that calculations of transition state interactions should lead to similar errors. Recently, counterpoise corrections of BSSE's have been used for a limited number of transition state calculations with good success.^{14,15} Here, for the peroxy radical abstraction reactions studied, we use the counterpoise correction method contained within Gaussian 03, which utilizes the techniques of Boys and Bernardi¹³ and Simon et al.¹⁶

Results and Discussions

Justification for Level of Theory and Basis Set Used and Technique Validation. The selection of the quantum chemical technique and basis set used for a given calculation represents a compromise between computational cost and accuracy. We would like to select the method that yields the most accurate results in a reasonable period of time. In addition, techniques which include electron correlation are required for the bond breaking and forming processes studied here. Unfortunately, the relatively large molecules which constitute jet fuel preclude the use of high accuracy compound methods, such as G3 theory and complete basis set methods, for calculation of transition states. Density functional theory, and in particular the B3LYP hybrid functional, is increasingly being proven to yield very good geometries and energies with relatively modest computational costs.¹⁷ Thus, it is particularly attractive for the relatively large molecular systems of interest in fuel autoxidation.

Initial validation runs for selecting the DFT functional/basis set combination were conducted on the calculation of the bond dissociation enthalpy of the O–O bond in *n*-butylhydroperoxide. Hydroperoxides are known to be important initiators of autoxidation and intermediates in the overall chain process. *n*-Butylhydroperoxide was chosen as a small model molecule of the larger hydroperoxides that are produced in fuel. Previous work indicates that the bond dissociation enthalpies of alkyl hydroperoxides, essentially independent of the identity of the alkyl group, is 44–45 kcal/mol.^{18,19} Calculated bond dissociation enthalpies at various levels of theory are shown in Table 1. The results indicate, as expected, that using methods which include the effects of electron correlation (all except the HF result) are

(13) Boys, S. F.; Bernardi, F. *Mol. Phys.* **1970**, *19*, 553.

(14) Kobko, N.; Dannenberg, J. J. *J. Phys. Chem. A* **2001**, *105*, 1944–1950.

(15) Sordo, J. A. *THEOCHEM* **2001**, *537*, 245–251.

(16) Simon, S.; Duran, M.; Dannenberg, J. J. *J. Chem. Phys.* **1996**, *105*, 11024–11031.

(17) Barckholtz, C.; Barckholtz, T. A.; Hadad, C. M. *J. Am. Chem. Soc.* **1999**, *121*, 491–500.

(18) Sebban, N.; Bockhorn, H.; Bozzelli, J. W. *Phys. Chem. Chem. Phys.* **2002**, *4*, 3691–3703.

(19) Reints, W.; Pratt, D. A.; Korth, H.-G.; Mulder, P. J. *Phys. Chem. A* **2000**, *104*, 10713–10720.

(8) Ervin, J. S.; Zabarnick, S. *Energy Fuels* **1998**, *12*, 344–352.

(9) Doungthip, T.; Ervin, J. S.; Zabarnick, S.; Williams, T. F. *Energy Fuels* **2004**, *18*, 425–437.

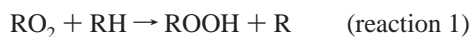
(10) Doungthip, T. Ph.D. Thesis, University of Dayton, Dayton, OH, 2004.

(11) Nikolaeva, E. V.; Shamov, A. G.; Khrapkovskii, G. M.; Kharlampidi, K. E. *Russ. J. Gen. Chem.* **2002**, *72*, 748–759.

(12) Denisova, T. G.; Emel'yanova, N. S. *Kinet. Catal.* **2003**, *44*, 441–449.

essential to obtain accurate values. The B3LYP DFT functional is similar in computational cost to HF but yields more accurate values. Ab initio (MP2), complete basis set (CBS-4M), and compound techniques (G3B3) yield even better results at a significantly higher computational cost. It was concluded that the DFT method resulted in the best compromise between accuracy and computational cost for the relatively large reaction systems that need to be studied in the autoxidation chemistry of jet fuel. All subsequent calculations reported here employ the B3LYP level of theory. The transition state calculations performed here are particularly costly and thus a relatively modest basis set, 6-31G(d), was selected for most of the calculations. We have performed limited studies to assess the change in accuracy of these calculations with increasing basis set size (e.g., 6-311G(d,p) and 6-311G(3df, 2p)), as reported below.

Peroxy Radical Abstraction Reactions. One of the most important reactions in autoxidation is the propagation reaction in which peroxy radicals abstract a hydrogen atom from a fuel species, producing a hydroperoxide and a hydrocarbon radical



This reaction tends to be the rate-limiting step in autoxidation, as the addition of O_2 to hydrocarbon radicals, $\text{R} + \text{O}_2 \rightarrow \text{RO}_2$, is a fast reaction. In addition, many antioxidants function by competing for peroxy reactions via



where AH is the antioxidant species and A is an antioxidant radical that does not propagate the autoxidation chain. As the strength of the O–H bond (85–86 kcal/mol) in hydroperoxides tends not to vary significantly with the identity of the R group,¹⁸ the reaction energetics are primarily determined by the strength of the R–H or A–H bond. It has been shown that antioxidants function by rapidly intercepting peroxy radicals, which occurs readily because of their relatively weak A–H bonds.^{20,21} In addition to synthetic antioxidants which are added after fuel processing, fuels can contain naturally occurring species which may have antioxidant properties. These species, such as phenols, thiols, amines, indoles, carbazoles, etc., though only present at low levels (ppm), determine the oxidation rate and the tendency of the fuel sample to produce deposits upon oxidation. Thus it is important to know the energetics of these reactions as well as the R–H and A–H bond strengths.

Unfortunately, very few measurements or calculations have been performed on the energetics or activation energies of reactions 1 and 2, although there are many measurements and calculations of bond strengths of some relevant R–H and A–H species.^{17,22,23} Recently, Nikolaeva et al.¹¹ used semiempirical quantum chemical methods (PM3) and DFT to estimate the energetics of some of these reactions. Denisova and Emel'yanov¹² used the intersecting parabolas method and DFT methods to estimate transition state geometries and energetics of peroxy radical reactions with various species.

In the present paper, we utilize DFT for the calculation of the activation energies of peroxy radical abstraction reactions from hydrocarbons and heteroatomic species. These species were

chosen to represent classes of species commonly found in jet fuels and include representatives of the following classes: alkanes, alkyl-substituted aromatics, alkyl-substituted phenols, indoles, carbazoles, and thiols. We have chosen the 2-butylperoxy radical as the abstracting radical in this study. This peroxy radical was chosen as a compromise between the larger hydrocarbon peroxy radicals (e.g., those with 9–16 carbon atoms) that likely dominate jet fuel autoxidation and the smaller radicals, such as methylperoxy, which may be too small and polar to approximate the reactivity of larger peroxy radicals. Analysis of the results obtained below demonstrates that the peroxy radicals most likely encountered in jet fuels are obtained from the reaction of fuel aromatic species, but it is likely that the hydrocarbon group of the peroxy radical has little effect on its reactivity, as the bond strength of the O–H bond in various hydroperoxides is largely independent of the identity of the hydrocarbon group.¹⁸ We show below, for a single abstraction reaction, that the identity of the abstracting peroxy radical (2-butylperoxy vs benzylperoxy) has no effect on the activation energy obtained. In addition, we have also used DFT for the calculation of the bond strengths of the weakest bonds to the hydrogen atom for relevant fuel species.

We have calculated the reaction enthalpies and activation energies with the B3LYP functional using the 6-31G(d) basis set for the reaction of 2-butylperoxy with a number of model fuel species, as shown in Table 2. Initial results indicated a problem with the values of the activation energies obtained for many of these reactions. As shown in the table, for many of these reactions, which tend to be slightly endothermic, the calculated activation energies were slightly lower than the calculated reaction enthalpies using the same level of theory and basis set. Obviously, a reaction cannot have an activation energy that is lower than the reaction enthalpy. Here we find that basis set superposition error (BSSE) can account for the activation energies that are too low. BSSE is well-known in the calculation of energies of intermolecular complexes (e.g., hydrogen-bonded complexes) but has only recently been applied to transition states.^{14,15} These errors occur when the basis functions of one species in the complex or transition state augments the basis functions of the other species, resulting in a lower overall energy of the complex or transition state. BSSE results in activation energies that are too low relative to the values obtained in the absence of basis function augmentation. BSSE can be corrected by the application of the counterpoise correction, in which the energies of the individual reactants are calculated in both the absence and presence of the augmented basis set resulting from other species.¹³ The error caused by this augmentation can then be assessed and subtracted from the system. In the present work, we have chosen to use the counterpoise correction as implemented in Gaussian 03, with the use of three molecular fragments. The three fragments chosen for each of the peroxy abstraction reactions are (1) the hydrogen being abstracted, (2) the peroxy radical, and (3) the resulting radical being formed. For example, in the case of the reaction of 2-butylperoxy and 3-ethylphenol, the three fragments used in the counterpoise correction are the phenol hydrogen, the 2-butylperoxy radical, and the 3-ethylphenoxy radical. Table 2 lists the activation energies calculated with the inclusion of the counterpoise correction for the BSSE. The use of the counterpoise correction results in an increase in the calculated activation energies from 3.1 to 4.7 kcal/mol relative to values obtained without the use of the correction. The activation energies calculated with the counterpoise correction are now more reasonable, being greater than the calculated reaction

(20) Heneghan, S. P.; Zabarnick, S. *Fuel* **1994**, *73*, 35–43.

(21) Scott, G. *Chem. Ind.* **1963**, 271–281.

(22) Nishiyama, T.; Suzuki, T.; Hashiguchi, Y.; Shiotsu, S.; Fujioka, M. *Polym. Degrad. Stab.* **2002**, *75*, 549–554.

(23) Bordwell, F. G.; Zhang, X.; Cheng, J.-P. *J. Org. Chem.* **1991**, *56*, 3216–3219.

Table 2. Calculated Reaction Enthalpies, Activation Energies, and Bond Strengths Using B3LYP/6-31G(d) for the Abstraction of Hydrogen from Model Fuel Species by 2-Butylperoxy Radicals

reacting species (hydrogen atom being abstracted)	ΔH (kcal/mol)	E_a without BSSE correction (kcal/mol)	E_a with BSSE correction (kcal/mol)	X–H bond strength (kcal/mol)
hydrocarbon species				
<i>n</i> -butane (secondary hydrogen)	20.9	20.1	23.9 (20.9) ^a	96.4 (98.3) ^b
ethylcyclohexane (ethyl CH ₂ hydrogen)	20.5	19.3	23.6	96.0
ethylcyclohexane (3-ring CH ₂ hydrogen)	21.2	21.6	25.0	96.6
ethylbenzene (benzylic hydrogen)	9.2	15.4	18.9 (16.5) ^a	84.6 (85.4) ^b
cumene (benzylic hydrogen)	7.5	14.8	18.9	83.0
heteroatomic species				
3-ethylphenol (phenolic hydrogen)	3.4	1.8	6.0 (5.9) ^a	78.9
3-ethylphenol (phenolic hydrogen) reaction with methylbenzylperoxy	3.4	1.6	6.0	78.9
2,6-di- <i>tert</i> -butyl-4-methylphenol (phenolic hydrogen)	-4.6	2.2	6.9 (6.7) ^a	70.8 (79.7–82.6) ^b
3-ethylbenzenamine (amine hydrogen)	9.9	5.6	9.6	85.4
2-methylindole (indole hydrogen)	10.4	6.8	11.0	85.8
3-methylindole (indole hydrogen)	8.7	6.5	10.1	84.2
carbazole (carbazole hydrogen)	9.4	5.6	9.8	84.9 (93.6) ^b
2-methylindoline (indole hydrogen)	3.6	2.4	6.6	79.0
2,5-dimethylpyrrole (pyrrole hydrogen)	7.6	6.7	11.2	83.0
ethylphenylthiol (thiol hydrogen)	-2.4	4.3	7.4	73.1

^a Activation energy values in parentheses are single point energies calculated via B3LYP/6-311G(d,p) DFT theory using B3LYP/6-31G(d) geometries with the counterpoise correction for the transition state. ^b Bond strength values in parentheses are experimental values tabulated by Luo.²⁵ All imaginary frequencies for these reactions were between -1626 and -1935 cm⁻¹.

enthalpy for all but one reaction (3-ethylbenzenamine). The cause of the benzenamine discrepancy is not known at this time. Presumably, the counterpoise correction would be successful in correcting previous calculations in which activation energies obtained appear too low or even negative.²⁴ The magnitude of the BSSE correction obtained here is relatively small compared to many reactions which exhibit moderate to large activation energies (>20 kcal/mol) and thus the correction may be unnecessary for such transition state calculations and has not been employed for the other reaction types studied in this paper (see sections below). In contrast, for the slightly endothermic reactions being studied here, the correction is quite significant relative to the reaction enthalpy.

The first five species in Table 2 are hydrocarbons which represent the types of these species present in fuel. *n*-Butane represents the normal and branched alkane fuel components that along with cycloalkanes and aromatic species compose the bulk of jet fuel. The *n*-butane reaction studied is the abstraction of one of the secondary hydrogens by the peroxy radical. The cycloalkanes are represented by ethylcyclohexane, and calculations were performed on the abstraction of both an ethyl CH₂ hydrogen and a CH₂ hydrogen on the 3-ring carbon. The fuel aromatics are represented by ethylbenzene and cumene (isopropylbenzene), which contain relatively reactive benzylic hydrogens. The enthalpy of the reaction calculations show that the enthalpies are similar for the *n*-butane and cyclohexane species but are substantially lower for ethylbenzene and cumene. The results reflect the well-known decrease in C–H bond strength through the series: secondary hydrogen, benzylic hydrogen, tertiary benzylic hydrogen. Our calculated bond strengths shown in the table also support this interpretation and agree well (within 2 kcal/mol) with the experimentally measured values for these C–H bonds.²⁵ The results show that the activation energies for *n*-butane and ethylcyclohexane are similar, while carbon bonds to benzylic hydrogens exhibit significantly lower activation energies. The changes in activation energy through the series of hydrocarbon species is reflected

in the corresponding C–H bond strengths and enthalpies of reaction. Also shown in the table is the counterpoise-corrected activation energies for a few of the hydrocarbon reactions using the B3LYP/6-31G(d) geometries with a single-point energy calculation with a larger basis set, B3LYP/6-311G(d,p). The larger basis set lowers the activation energies by 2.4 and 3.0 kcal/mol for the two hydrocarbons shown. Calculations using even larger basis sets (not shown), such as 6-311G(3df,2p), yield only slightly lower (<0.4 kcal/mol) activation energies.

In addition to the reaction of peroxy radicals with bulk fuel hydrocarbons, trace heteroatomic species are also involved in the autoxidation process, and these species have a significant effect on fuel oxidation and deposition. The remaining species in Table 2 represent some of the classes of heteroatomic species which contain X–H bonds, where X is a heteroatom, that are found in jet fuel. These heteroatomic species are present at trace levels, but they can greatly affect the fuel oxidation and deposition rate even at low concentrations.⁷ The results show that these species are significantly more reactive toward peroxy radicals than are the hydrocarbon bulk fuel species, with activation energies ranging from 6.0 to 11.2 kcal/mol. Even at very low concentrations (i.e., ppm levels), many of these species are likely to react with peroxy radicals more rapidly than the bulk fuel species. 3-Ethylphenol is a representative of the class of fuel phenols. Phenols are found in jet fuels at levels from 0 to 1600 mg/L, with concentrations of 100 to 600 mg/L being most common.²⁶ Low levels of species which react readily with peroxy radicals, such as phenols, have been implicated in causing the slowing of fuel oxidation, as well as the formation of deposits.^{20,27} The results show that the O–H bond strength and activation energy for reaction with peroxy radicals, 78.9 and 6.0 kcal/mol, respectively, are both substantially lower than for the C–H bonds of the hydrocarbons. This calculated bond strength is lower than most measurements of monosubstituted alkylphenols (by 2–10 kcal/mol).²⁵ The reaction is endothermic by 3.4 kcal/mol. Previous chemical kinetic modeling of fuel autoxidation⁴ grouped all phenolic species into a single species,

(24) Singh, N.; O'Malley, P. J.; Popelier, P. L. A. *Phys. Chem. Chem. Phys.* **2005**, *7*, 614–619.

(25) Luo, Y.-R. *Handbook of Bond Dissociation Energies in Organic Compounds*; CRC Press: Boca Raton, FL, 2003.

(26) Balster, L. M.; Zabarnick, S.; Striebich, R. C. **2005**, manuscript in preparation.

(27) Zabarnick, S.; Mick, M. S.; Striebich, R. C.; Grinstead, R. R. *Energy Fuels* **1999**, *13*, 154–159.

AH, which reacted with peroxy radicals with an activation energy of 5.0 kcal/mol. The 6.0 kcal/mol activation energy calculated here supports the value used previously. Also shown in the table are the results for the reaction of the methylbenzylperoxy radical with 3-ethylphenol. This calculation was performed to determine if the structure of the peroxy radical has a significant effect on the hydrogen abstraction rate. The results show that none of the calculated parameters changed significantly for the reaction of 3-ethylphenol with the two peroxy radicals. Thus, for these aliphatic and aromatic peroxy radicals, structural differences play no role in the calculated energetics, although differences in reaction rates have been observed previously for other peroxy radicals and largely attributed to steric effects.²⁸

Also shown in Table 2 are results for 2,6-di-*tert*-butyl-4-methylphenol, often referred to as BHT, which is a species commonly used as an antioxidant. Interestingly, the reaction of this species with 2-butylperoxy is calculated to be slightly exothermic (−4.6 kcal/mol) and the O–H bond strength is quite weak at 70.8 kcal/mol. This bond strength is lower than previously reported measurements of 79.6–80.7 kcal/mol.²⁵ Despite these differences, the very low bond strength and reaction exothermicity help explain the significant reactivity of BHT and its efficiency in slowing oxidation, even at very low concentrations, by intercepting peroxy radicals. The stability of the resulting BHT radical is also crucial to its effectiveness as an antioxidant.²⁹ The activation energies for reaction of 2-butylperoxy with either 3-ethylphenol and BHT were also calculated via a single energy calculation using the B3LYP/6-311G(d,p) basis set and B3LYP/6-31G(d) geometries. In contrast to the results on the hydrocarbon species, these reactions exhibited no significant changes in activation energy with the use of the larger basis set.

Nitrogen-containing compounds have been implicated in the formation of jet fuel deposits,² but little is known about the autoxidation reactivity of individual nitrogen-containing fuel species classes. In particular, indoles and pyrroles have been shown to increase fuel deposition.^{30–32} In the present study, we explore the reactivity of peroxy radicals with nitrogen compounds that have an abstractable H atom on their nitrogen atom. These include indoles, indolines, pyrroles, carbazoles, and anilines. Again we have selected one or two species as representative of each class of compounds. The calculated reaction enthalpies (Table 2) for these species classes cover the range of 3.6–10.4 kcal/mol, demonstrating that these are all slightly endothermic reactions. The resulting activation energies are in the range of 6.6–11.0 kcal/mol, showing that these species are quite reactive toward peroxy radicals. The carbazole, indole, pyrrole, and aniline (benzenamine) compounds all have similar activation energies (9.6–11.2 kcal/mol) and N–H bond strengths (83.0–85.8 kcal/mol). The indoline compound has a significantly lower activation energy, 6.6 kcal/mol, and N–H bond strength, 79.0 kcal/mol, implying that this nitrogen species class will be more reactive during fuel autoxidation than the other nitrogen species. Indeed, the addition of indoline compounds to hydrocarbon solvents greatly slows the oxidation rate at 140°C, but to date, indolines have not been found to be a major

Table 3. Calculated Bond Strengths of the O–H Bond Using B3LYP with Various Basis Sets

basis set	phenol O–H bond strength (kcal/mol)	BHT O–H bond strength (kcal/mol)
6-31G(d)	75.9	70.8
6-311G(d,p)	79.8	74.5
6-311G(3df,2p)	80.5	75.2
exptl ²⁵	88.0 ± 1.5	79.7–82.6

nitrogen component of jet fuels.³³ Overall, the N–H bond strengths calculated here compare favorably with those previously calculated using a similar computational method¹⁷ but agree less favorably with experimental measurements.

Also shown in Table 2 are the calculated reaction enthalpy and activation energy for reaction of peroxy radicals with the thiol hydrogen of ethylphenolthiol, along with the calculated S–H bond strength. The energetics of this reaction closely resembles that of BHT, with a small negative enthalpy (−2.4 kcal/mol) and quite a low activation energy of 4.3 kcal/mol. Again, the very low calculated bond strength of 73.1 kcal/mol explains these observations. These data predict that thiol species should be quite reactive, but their importance to autoxidation is minimized because they are usually found at only extremely low levels in jet fuels.^{34,35}

While the C–H bond strengths of the hydrocarbons calculated here agree well with experimental values, the heteroatomic X–H bond strengths appear to be low by up to 10 kcal/mol. To determine the cause of this discrepancy, we calculated the O–H bond strength of phenol and BHT using B3LYP/6-31G(d) geometries and various basis set sizes as shown in Table 3. Phenol was chosen because of its well-known experimental bond strength, although a recent study recommends that a slightly lower value be used.³⁶ The results show that, for both species, increasing the basis set size from 6-31G(d) to 6-311G(d,p) results in a stronger bond by nearly 4 kcal/mol but only minor increases (<1 kcal/mol) are observed on going from 6-311G(d,p) to 6-311G(3df,2p). Even the largest basis set employed yields bond strengths that are 4 to 8 kcal/mol lower than the experimental values. Interestingly, the difference in bond strength between phenol and BHT remains 5.2 ± 0.1 kcal/mol, independent of the size of the basis set. In contrast to these bond strength results, the results in Table 2 demonstrate that a larger basis set does not significantly change the B3LYP calculated activation energies of peroxy radical abstraction reactions from heteroatomic X–H bonds. Basis set size must not affect the relative stability of the reactants and transition states for the peroxy abstraction from the heteroatomic species as much as it affects the relative stability of the species involved in the homolytic bond dissociation. Although the calculated bond strengths of the heteroatomic X–H bonds appear to be too low using the B3LYP technique, it is unclear if the calculated transition state barriers have systematic errors, and what the magnitude of the errors would be.

To determine if a given species will react with peroxy radicals in the jet fuel autoxidation environment, we need to look at the competitive reaction rates. The competition for the RO₂ radical is a function of the rate constant for reaction and the relative concentrations of the species. Assuming a constant temperature

(28) Howard, J. A. In *Free Radicals*; Kochi, J. K., Ed.; Wiley: New York, 1973; Vol. 2, Chapter 12.

(29) Mahoney, L. R. *Angew. Chem., Int. Ed. Engl.* **1969**, *8*, 547–555.

(30) Taylor, W. F. *SAE Trans.* **1968**, *76*, 2811.

(31) Taylor, S. E. *Prepr.-Am. Chem. Soc., Div. Pet. Chem.* **2002**, *47*, 165–169.

(32) Musherush, G. W.; Beal, E. J.; Hazlett, R. N.; Hardy, D. R. *Energy Fuels* **1990**, *4*, 15–19.

(33) West, Z.; Zabarnick, S. **2004**, unpublished data.

(34) Link, D. D.; Minus, D. K.; Striebich, R. C.; Rothenberger, K. S.; Baltrus, J. P. *Prepr.-Am. Chem. Soc., Div. Pet. Chem.* **2002**, *47*, 212–215.

(35) Link, D. D.; Baltrus, J. P.; Rothenberger, K. S.; Zandhuis, P.; Minus, D. K.; Striebich, R. C. *Energy Fuels* **2003**, *17*, 1292–1302.

(36) Mulder, P.; Korth, H.-G.; Pratt, D. A.; DiLabio, G. A.; Valgimigli, L.; Pedullì, G. F.; Ingold, K. U. *J. Phys. Chem. A* **2005**, *109*, 2647–2655.

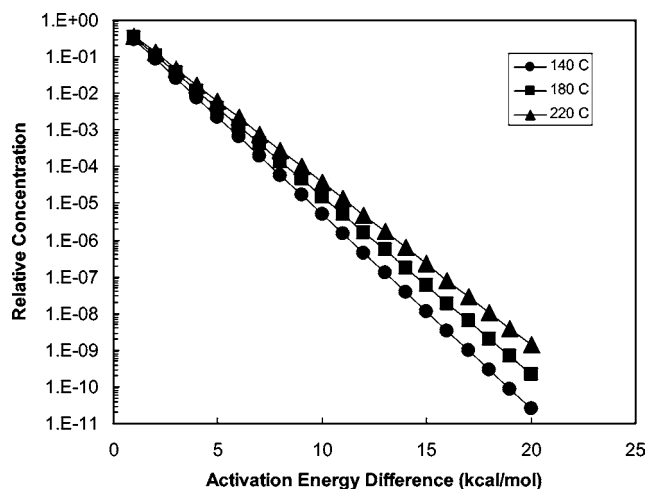


Figure 1. Plots of relative concentration vs activation energy difference at three temperatures.

and equivalent Arrhenius preexponential factors for the reactions, this becomes a function of the activation energies and species concentrations via

$$\exp\left(\frac{-(E_{a1} - E_{a2})}{RT}\right) = \frac{[\text{species2}]}{[\text{species1}]} \quad (1)$$

where E_{a1} and E_{a2} are the activation energies for the reaction of species1 and species2, respectively. The result of this equation can be plotted at various temperatures, as shown in Figure 1. The plot shows that at relative concentrations in the range of $1-10 \times 10^{-6}$, reactions with activation energy differences in the range of 8–13 kcal/mol have equivalent rates in the temperature range of 140–220 °C.

Assuming the fuel paraffins consist of molecules which behave similar to *n*-butane (i.e., $E_a=23.9$ kcal/mol) and the fuel aromatics behave similar to ethylbenzene or cumene (i.e., $E_a=18.9$ kcal/mol), we can calculate the relative rates for reaction with peroxy radicals of these two fuel species classes. For a fuel which consists of 80% paraffins and 20% aromatics, this yields relative rates of a factor of 258 at 180 °C. Thus, this analysis indicates that the peroxy radicals are 65 times more likely to react with fuel aromatic species than paraffinic species. The paraffinic species can thus be considered essentially unreactive for our current kinetic analysis. Previous chemical kinetic modeling of jet fuel oxidation treated the fuel hydrocarbon species as single species, RH, with the properties of a normal alkane.^{4,5} Future kinetic models of jet fuel autoxidation need to take into account that the paraffins are essentially unreactive, while the aromatic species likely provide reactive hydrocarbon species. The previous chemical kinetic models typically used an activation energy of 12 kcal/mol for the reaction of peroxy radicals with bulk fuel species.⁵ The current results indicate that a somewhat higher activation energy (16–19 kcal/mol) may be more correct.

To better understand peroxy radical reactions, one can now envision jet fuel as a mixture of unreactive paraffins (ca. 80%), reactive aromatics (ca. 20%), and trace amounts of heteroatomic species (<1%). Using the activation energies obtained here for peroxy radical abstractions, one can calculate the concentrations required for heteroatomic species to have equivalent reaction rates with peroxy radicals (i.e., the concentrations required for these species to become competitive for reaction with peroxy radicals). For example, the activation energy difference between 3-ethylphenol and ethylbenzene is 12.9 kcal/mol, using eq 1

this corresponds to a phenol concentration of only 0.12 ppm at 180 °C. Thus, fuel phenols and other reactive species can readily compete with the hydrocarbons for reaction with peroxy radicals. These results show how very low concentrations of heteroatomic species can play a large role in determining oxidation and the deposition which results from subsequent reactions.

The calculations reported above do not consider the effects of the fuel solvent on reaction energetics and kinetics. Preliminary calculations which attempt to account for these effects using the self-consistent reaction-field method (SCRf) were performed for the bond strength calculations. The use of the SCI-PCM technique with heptane as the solvent resulted in negligible (<0.4 kcal/mol) changes in the bond strengths. Other autoxidation reactions, such as the catalysis reactions discussed below, may be more susceptible to solvent effects. Transition state SCRf calculations were not performed in the present work. While solvent calculations using heptane provide a preliminary assessment of the effect of the fuel on reactivity, the complex jet fuel mixture contains quantities of other species (e.g., 15–20% aromatics and small amounts of heteroatomic species) which may have more significant effects. It is unclear at this point how to properly simulate the solvent effects of jet fuels in DFT calculations. One option would be to use dipole moments in the SCRf calculation which approximate the average dipole moment of the complex mixture. This option would not account for the effects of the microenvironment which may occur if a particular solvent molecule or molecules (e.g., an acidic species) preferentially associates itself with, for example, a transition state.

Despite the uncertainties in the calculations of bond strengths and activation energies for peroxy radical abstraction reactions using DFT, the present calculations provide important information about the relative, if not absolute, reactivities of various important fuel species classes with peroxy radicals. The work here has shown that the counterpoise correction for BSSE is crucial for these near thermoneutral reactions. Future work needs to further explore the effect of the jet fuel solvent, acid and metal catalysis, and complex formation on these reactions.

Nonradical-Producing Peroxide Decomposition Reactions. Hydroperoxides are extremely important species in the autoxidation of fuels and hydrocarbon liquids. These species are involved in the initiation reactions which begin the autoxidation chain, their decomposition into free radicals causes autoacceleration, and their decomposition reactions are greatly affected by bulk and surface metal catalysis as well as acid catalysis. The homolytic decomposition of hydroperoxides via



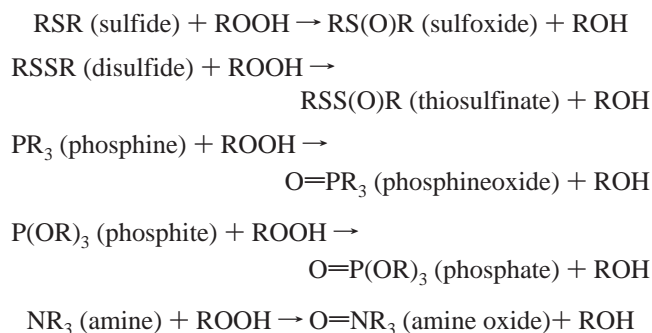
provides an increased source of radicals to the autoxidation process, thereby increasing the oxidation rate. With an uncatalyzed activation energy of ca. 45 kcal/mol,¹⁸ this process begins to become a key player in determining the overall autoxidation rate at temperatures of 140–180 °C, depending on the reaction time of the system. It has been demonstrated that even very small amounts of hydroperoxide decomposition (<0.02% decomposition) can have significant effects on the overall oxidation rate.⁴ Thus, at temperatures and reaction times where peroxide decomposition is important, any process that removes hydroperoxides from the system without the formation of radicals will result in a slowing of the oxidation rate.

There are a number of species which are known to react with hydroperoxides via nonradical producing pathways. These species include phosphines, phosphites, sulfides, disulfides,

Table 4. Calculated Reaction Enthalpies and Activation Energies Using B3LYP/6-31G(d) Density Functional Theory for Reaction of Hydroperoxides with Sulfides and Phosphines

reaction species	ΔH (kcal/mol)	E_a (kcal/mol)	transition state imaginary frequency (cm ⁻¹)
diethyl sulfide + <i>n</i> -butylhydroperoxide	-26.3	26.1	-668
diethyl disulfide + <i>n</i> -butylhydroperoxide	-27.7	28.7	-716
triphenylphosphine + 2-butylhydroperoxide	-75.0	12.9	-369

selenides, amines, thiophosphates, and thiocarbamates.³⁷⁻⁴¹ Of these, sulfides, disulfides, and amines are the only ones that are commonly found in fuels and other petroleum products. The other species have been used as antioxidants in various petroleum products. In the case of the sulfides, disulfides, phosphines, phosphites, and amines, the reaction occurs by the transfer of a hydroperoxide oxygen atom resulting in the formation of an oxidized form of the species and the corresponding alcohol via



These reactions do not produce radicals and can greatly slow autoxidation by consumption of the corresponding peroxide,³⁸ thereby preventing its decomposition into additional radicals which would accelerate the chain. In addition, it has been proposed that the reactions of sulfides and disulfides may contribute to the formation of bulk and surface deposits during jet fuel autoxidation.⁷ The reaction of these species to slow oxidation and produce increased deposition agrees with observations that slow oxidizing fuels tend to produce greater levels of deposition than fast oxidizing fuels.²⁰ The role of fuel amines is less clear as these species have not been associated with increased fuel deposition and slow oxidation rates.²

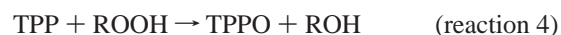
Despite the importance of these nonradical-producing hydroperoxide decomposition reactions, there have been few studies of their energetics or kinetics. Recently in model studies of biological reactions, Bach and Dmitrenko⁴¹ used DFT to calculate the transition state geometries and energetics of the reactions of hydroperoxides with trimethylamine, dimethyl sulfide, dimethylselenide, and trimethylphosphine. These calculations demonstrated for the first time that oxygen atom transfer of the hydroxyl oxygen from the hydroperoxide occurs through a concerted pathway via a rotation of the hydroperoxide hydroxyl group. The transition state imaginary frequency was related to the type of motion which occurs. Activation energies for these reactions were found to cover the range of 4–31 kcal/mol, with the lower activation energies found for trimethylphosphine and the higher range found for trimethylamine and dimethyl sulfide. Here we further explore these reactions by performing DFT calculations on species which are more representative of those found in fuels to better understand the reaction mechanisms and estimate activation energies and reaction energetics.

We have chosen *n*-butylhydroperoxide (*n*-BHP) and 2-butylhydroperoxide (2-BHP) as model species to represent fuel hydroperoxides. Fuel sulfides are represented by diethyl sulfide

and fuel disulfides by diethyl disulfide. We have also performed calculations on the reaction of triphenylphosphine (TPP) with 2-BHP to explore this reaction, as it is important in fuel hydroperoxide analysis⁴² and in the use of TPP as a fuel additive to slow oxidation.^{43,44} Attempts at locating transition states via DFT for the reaction of 2-BHP with trimethylamine and triphenylamine were unsuccessful in the present work.

Table 4 shows results for B3LYP/6-31G(d) calculations of reaction enthalpies and activation energies of the reaction of hydroperoxides with these species. The results show that the sulfide and disulfide reactions display similar reaction energetics. Both reactions are quite exothermic (ca. -27 kcal/mol), but they have significant activation barriers (26–29 kcal/mol). Bach and Dmitrenko⁴¹ demonstrated that reaction with hydroperoxide dimers results in a significant decrease in the activation energies of these type of reactions. As hydroperoxide concentrations in jet fuels are typically quite low (<<1 mmol/L), dimer formation is unlikely, and the resulting lower activation energies pathways are unlikely to occur. The magnitudes of these barriers imply an interesting competition for the fate of fuel peroxides, which can decompose unimolecularly with an uncatalyzed activation energy of 45 kcal/mol, and a catalyzed activation energy pathway (see next section) which can be substantially lower (ca. 20 to 30 kcal/mol). The similar activation energies for the catalyzed and nonradical bimolecular pathways imply that the two reactions will be competitive over a range of temperatures. Obviously, the concentration of the sulfides, disulfides, or both present, the relative activation energies, temperature, and resulting rates of these two hydroperoxide removing pathways will determine the fate of the fuel hydroperoxides. This implies that this fate is quite fuel sample dependent, as the concentrations of these species can vary greatly between fuels.

Also shown in Table 4 are calculated results for the reaction of fuel peroxides with triphenylphosphine (TPP) via



TPP is known to react readily with peroxides and has been used in their detection and quantitation.^{42,45} The results show that the reaction is highly exothermic with a relatively small barrier. The low activation energy (12.9 kcal/mol) supports the observation that this reaction proceeds readily at ambient temperatures.^{42,45} Also shown in the table are the calculated values of

(37) Denisov, E. T.; Denisova, T. G. *Handbook of Antioxidants*; CRC Press: Boca Raton, FL, 2000.

(38) Zabarnick, S.; Mick, M. S. *Ind. Eng. Chem. Res.* **1999**, *38*, 3557–3563.

(39) Denison, G. H.; Condit, P. C. *Ind. Eng. Chem.* **1945**, *37*, 1102–1108.

(40) Denison, G. H.; Condit, P. C. *Ind. Eng. Chem.* **1949**, *41*, 944–948.

(41) Bach, R. D.; Dmitrenko, O. *J. Phys. Chem. B.* **2003**, *107*, 12851–12861.

(42) West, Z. J.; Zabarnick, S.; Striebich, R. C. *Ind. Eng. Chem. Res.* **2005**, *44*, 3377–3383.

(43) Beaver, B.; DeMunshi, R.; Heneghan, S. P.; Whitacre, S. D.; Neta, P. *Energy Fuels* **1997**, *11*, 396–401.

(44) Heneghan, S. P.; Zabarnick, S. S.; Mick, M. S. U.S. Patent 6475252, 2002.

(45) Perkel, A. L.; Krutskaya, L. V.; Freidin, B. G. *J. Anal. Chem.* **1994**, *49*, 768–772.

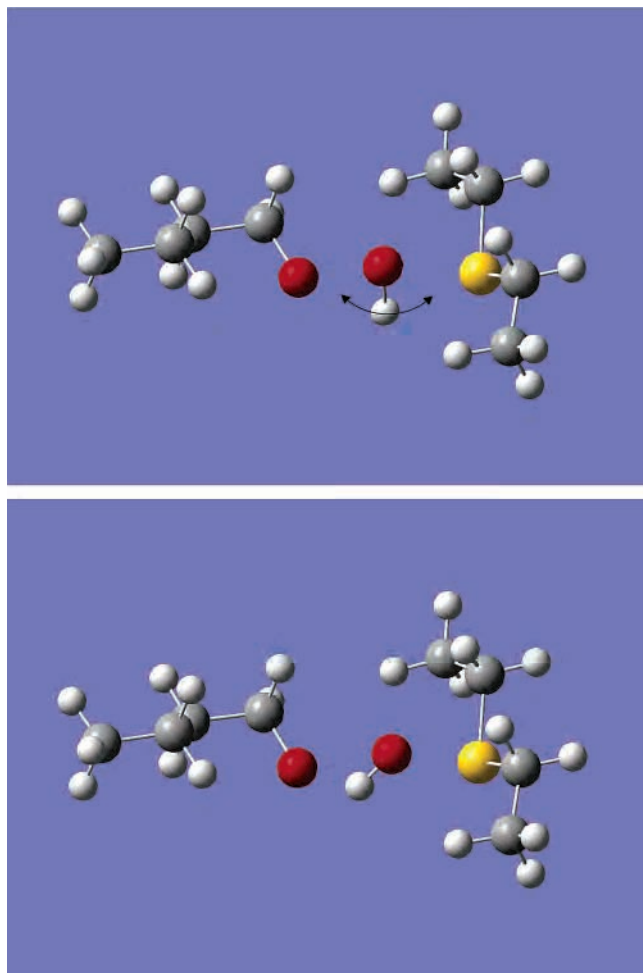


Figure 2. Visualization of the transition state imaginary frequency ($\nu = -668 \text{ cm}^{-1}$) during the reaction of diethyl sulfide with *n*-butylhydroperoxide demonstrating the rotation of the OH group with a relatively stationary O atom. The transition state geometry is shown in the lower graphic.

the transition state imaginary frequencies (reaction coordinate) for each of these reactions with hydroperoxides. Previous workers have shown that the magnitude of this frequency indicates the type of molecular motion of the OH group in the transition state.⁴¹ Figure 2 shows a visualization of the transition state imaginary frequency obtained for the reaction of diethyl sulfide with *n*-butylhydroperoxide. The figure demonstrates that the imaginary frequency is dominated by a relatively stationary O atom and a rapidly moving H atom in a “windshield-wiper” type of motion. The movement of the H atom results in a relatively large negative frequency (-668 cm^{-1}). Figure 3 shows a visualization of the transition state imaginary frequency for the reaction of TPP with 2-butylhydroperoxide. This motion is dominated by the movement of the relatively heavy O atom with less movement of the light H atom resulting in a relatively small negative frequency (-369 cm^{-1}). Thus, in agreement with previous calculations on similar reactions,⁴¹ the magnitude of the imaginary frequency is an indicator of the type of atomic motion which occurs during the oxygen atom transfer.

Metal Catalysis of Hydroperoxide Decomposition. As mentioned previously, the decomposition of hydroperoxides to free radical species (reaction 3) is an important process which under many conditions contributes significantly to the overall oxidation rate. This decomposition causes the characteristic autoaccelerating oxidation rate observed in the oxidation of liquid hydrocarbons and may also contribute significantly to

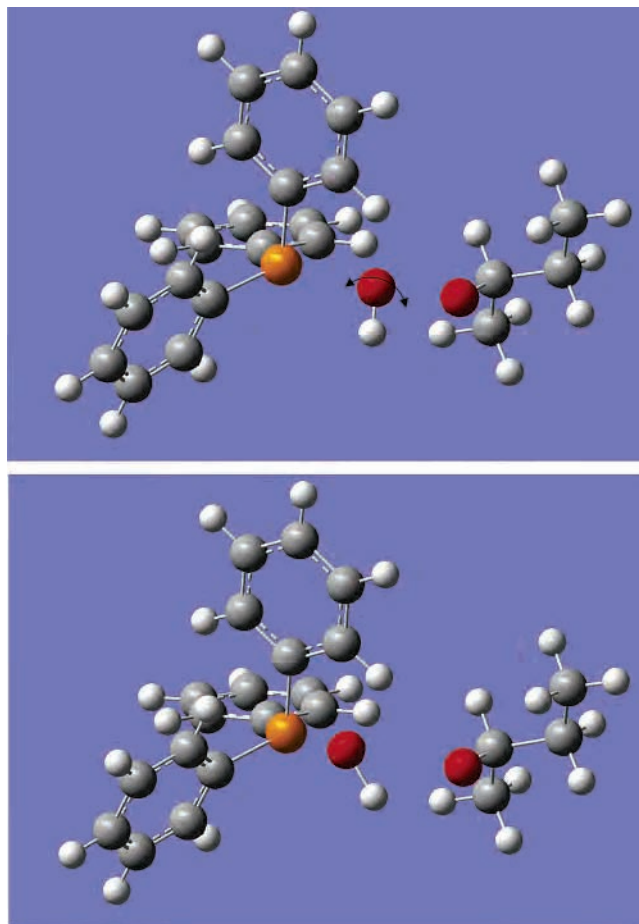


Figure 3. Visualization of the transition state imaginary frequency ($\nu = -369 \text{ cm}^{-1}$) during the reaction of triphenylphosphine with 2-butylhydroperoxide demonstrating the rotation of the OH group with a relatively stationary H atom. The transition state geometry is shown in the upper graphic.

the poorly understood initiation process which produces initial free radicals and begins the autoxidation process. Such initiation can occur because small ($\leq 20 \mu\text{M}$) but significant quantities of hydroperoxides are commonly found in on-specification jet fuels.⁴² This quantity is enough to produce a pool of radicals upon thermal exposure that begins the autoxidation chain. As mentioned previously, reaction 3 has been determined to have a gas-phase activation energy of $\sim 45 \text{ kcal/mol}$ independent of the identity of hydrocarbon group of the hydroperoxide. In addition to this unimolecular decomposition process, hydroperoxide decomposition is known to undergo a catalyzed decomposition by various species, particularly metal ions such as those of copper.² This catalysis can greatly increase the fuel oxidation rate at a given temperature or reduce the temperature at which a given extent of oxidation occurs. A two step redox scheme is often cited⁴⁶ as the process by which this catalysis occurs



This process produces two free radicals and results in no net change in the oxidation state of the metal ion. We have performed B3LYP/6-31G(d) calculations of the energetics of this scheme for three different ion pairs. The calculated reaction

(46) Walling, C. *Free Radicals in Solution*; Wiley: New York, 1957.

Table 5. Enthalpies of Reaction for Two-Step Redox Catalysis of Hydroperoxide Decomposition (reactions 5 and 6) via B3LYP/6-31G(d)

metal ion pair	ROOH + M ⁿ⁺ → RO + OH ⁻ + M ⁿ⁺¹⁺ reaction enthalpy (kcal/mol)	ROOH + M ⁿ⁺¹⁺ → RO ₂ + H ⁺ + M ⁿ⁺ reaction enthalpy (kcal/mol)
Cu ¹⁺ , Cu ²⁺	447	-17.3
Co ²⁺ , Co ³⁺	870	-440
Fe ²⁺ , Fe ³⁺	789	-359

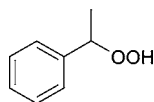
enthalpies are shown in Table 5. For all three ion pairs studied, the oxidation of the ion (reaction 5) is highly endothermic (447 to 789 kcal/mol), while reduction back to the original ion is quite exothermic (-17 to -440 kcal/mol). The overall process (i.e., the sum of the two reactions) is endothermic by ca. 430 kcal/mol independent of the ion pair. Obviously, at the temperatures and time scales of fuel autoxidation the overall process will not be favored. In polar and aqueous solvents, the energetics may change enough for this scheme to occur, but this is not likely in the jet fuel environment. It is unfortunate that the coordination environment of metal ions in jet fuel is not well-known, as it can have substantial impact on the reaction energetics of the ion. Here we explore alternate mechanisms to explain the observed metal catalysis of hydroperoxide decomposition in nonpolar solvents, such as jet fuels.

The unimolecular hydroperoxide decomposition is expected to occur by a simple O-O homolytic bond cleavage and is an endothermic process of ~45 kcal/mol. The reaction is believed to have no barrier. Thus, a direct reaction of the hydroperoxide with the metal ion, producing radicals and regenerating the metal ion via



cannot result in a lower activation energy than the uncatalyzed pathway as there is no barrier to be lowered. Interestingly, the formation of a complex between metal ions and hydroperoxides has been proposed and studied.⁴⁷⁻⁴⁹ Hiatt et al.⁵⁰ have even postulated that the OH⁻ and H⁺ ions of reactions 5 and 6 “may not be formed as free ions, but as part of the metal-ligand complex.” Formation of a metal ion and hydroperoxide complex may provide additional reaction pathways which offer lower energy routes to free radical formation than unimolecular hydroperoxide decomposition.

Here we perform B3LYP/6-31G(d) DFT calculations on the complex formation of a model fuel hydroperoxide, 1-phenylethyl hydroperoxide,



with Cu²⁺, along with calculations on possible decomposition pathways for the complex. The resulting energy level diagram is shown in Figure 4. The calculations predict a stable complex which is 222.1 kcal/mol lower in energy than the separated reactants. The geometry of the complex is shown in Figure 5, which illustrates that the copper ion primarily interacts with the hydroxyl oxygen atom with a Cu-O bond length of 1.799 Å. Calculations show that transition states exist on both the exit and entrance channels of the complex. The entrance channel transition state, referred to in the figure as “entrance TS”, in

which the copper ion approaches the hydroperoxide, is 40 kcal/mol above the complex (Cu-O distance 3.872 Å). The presence of the entrance TS implies the existence of a local minima or prereaction complex, LM1, whose energy and geometry we did not successfully calculate. The exit channel transition state, referred to in the figure as “exit TS”, in which the O-O bond is extended (3.523 Å) with the copper ion attached to the hydroxyl group, is 7 kcal/mol above the ROOH-Cu²⁺ complex. Formation of the species 1-phenylethyl alkoxy (RO) and CuOH⁺² is 14.3 kcal/mol below the reactants. Thus, the calculations show that formation of these products is an exothermic pathway for the production of a radical species from the decomposition of a hydroperoxide via complexation with a metal ion. The relative levels of the exit transition state and the RO + CuOH⁺² species imply that another local minimum, LM2, and transition state, RO-CuOH⁺², are necessary, but these were not calculated. Another transition state was found for the decomposition of CuOH⁺² to Cu²⁺ + OH, which is located 22 kcal/mol above the reactants. The relative energies of this transition state and the products imply the existence of a third local minimum, LM3, between these states.

The energy level diagram shows that while the reaction to products via reaction 7 is endothermic by 40 kcal/mol and does not lower the energy required to break the O-O bond in the hydroperoxide, there are additional pathways to radical forma-

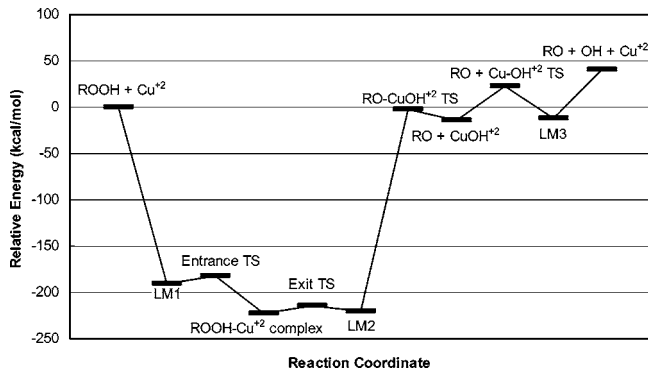


Figure 4. Energy level diagram for formation and decomposition of the 1-phenylethyl hydroperoxide (ROOH) complex with Cu²⁺. The geometries and energies of the local minima, LM1, LM2, and LM3, and transition state “RO-CuOH TS” were not calculated; the energies shown are gross estimates based on the relative energy levels of local minima and transition states to the nearby stationary points.

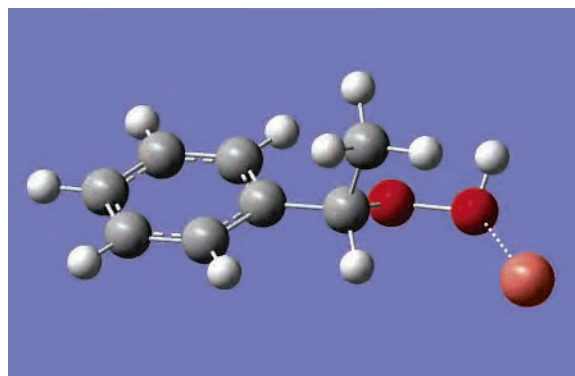


Figure 5. Geometry of 1-phenylethyl hydroperoxide-Cu²⁺ complex.

(47) Black, J. F. *J. Am. Chem. Soc.* **1978**, *100*, 527-535.

(48) Syroezhko, A. M.; Proskuryakov, V. A. *Russ. J. Appl. Chem.* **2004**, *77*, 1987-1993.

(49) Syroezhko, A. M.; Begak, O. Y. *Russ. J. Appl. Chem.* **2004**, *77*, 1301-1307.

(50) Hiatt, R.; Mill, T.; Mayo, F. R. *J. Org. Chem.* **1968**, *33*, 1416-1420.

tion that have significantly lower energy requirements. Such pathways appear to involve the consumption of the metal ion, forming CuOH^{+2} in the case of copper, and thus are not strictly catalytic. Interestingly, recent results indicate that dissolved copper ions are removed from the liquid fuel during thermal exposure and accumulate in filterable and surface deposits.⁵¹ These observations support the low energy, noncatalytic reaction pathways revealed by the present calculations. More generally, the formation of complexes between hydroperoxides and metal ions may provide alternative reaction pathways for radical formation. No attempt was made here to look exhaustively at additional possible complex formation pathways that could provide lower energy pathways for hydroperoxide decomposition. In addition to Cu^{2+} ions, it is likely that other metal ions may provide equivalent or alternative reaction pathways. Additionally, other species, such as acids and hydroperoxides, may also reduce the energy required for hydroperoxide decomposition by formation of complexes. For example, reaction of hydroperoxide dimers with dimethyl sulfide has been shown to provide a significantly lower activation energy pathway for (nonradical) product formation than reaction of individual hydroperoxides.⁴¹ Actually, it is unlikely that metal ions exist in the jet fuel mixture without being paired with one or more polar species, such as the conjugate base of a naphthenic acid. Thus the reaction of dissolved metals with species such as hydroperoxides needs to be studied in the presence of the complexed metal ion. In fact, the potential energy surfaces of reactions 5 and 6 need to be studied for the existence of complexed metal ions, as complexation can alter the energetics significantly.

Conclusions

Density functional theory was employed for the calculation of reaction enthalpies and activation energies for important reactions involved in the autoxidation of jet fuel. Basis set superposition error was found to significantly affect the

(51) Morris, R. E.; Evans, T.; Hughes, J. M.; Colbert, J. E.; Kamin, R. A.; Nowack, C. J. Oxidation of JP-5 in Single and Multipass Flow Testing. Presented at the 9th International Conference on Stability and Handling of Liquid Fuels, Sitges, Spain, 2005.

calculated activation energies of the near-thermoneutral peroxy radical abstraction reactions, and the counterpoise technique was used to provide reasonable corrections. The calculated peroxy radical abstraction reaction enthalpies, activation energies, and bond strengths show the important role of heteroatomic species with weak heteroatom bonds with hydrogen, as well as aromatic species which contain benzylic hydrogens. The calculated energetics provide insight into the relative reactivity of various fuel species during autoxidation. Reaction enthalpies and activation energies were calculated for the reaction of hydroperoxides via nonradical pathways with sulfides, disulfides, and phosphines. The results support the observed fast room-temperature phosphine reaction and predict activation energies for the sulfur species which provide insight into their reactivity with temperature. The transition state imaginary frequencies calculated provide information on the atomic motion which occurs during the reaction. Calculations of reactions in the metal catalysis of hydroperoxide decomposition indicate that a two-step redox scheme often shown in the literature is unlikely to be energetically favorable in the jet fuel environment. An alternative low-energy pathway for production of radicals from the reaction of Cu^{2+} with hydroperoxides was found which does not regenerate copper ions. This pathway may explain observations that dissolved copper is consumed during thermal exposure in flowing systems. Overall, the results show that DFT computational techniques can yield information that is useful for better understanding the autoxidation process and in the development of chemical kinetic mechanisms for these systems. These methods are particularly useful in estimating activation energies for reactions that have no previous experimental measurements. Future work needs to further explore the effect of the jet fuel solvent on the reaction energetics and kinetics and to employ the generated parameters in advanced chemical kinetic models of fuel autoxidation.

Acknowledgment. This material is based on research sponsored by Air Force Research Laboratory under agreement number F33615-03-2-2347. This work is also supported in part by the Air Force Office of Scientific Research (AFOSR). Julian Tishkoff is the AFOSR Program Manager. The authors would also like to thank Bill Harrison and Tim Edwards of AFRL for support of this work.

EF050348L

APPENDIX S

Swelling of Nitrile Rubber by Selected Aromatics Blended in a Synthetic Jet Fuel

INTENTIONALLY LEFT BLANK

Swelling of Nitrile Rubber by Selected Aromatics Blended in a Synthetic Jet Fuel

John L. Graham,^{*,†} Richard C. Striebich,[†] Kevin J. Myers,[‡] Donald K. Minus,[§] and William E. Harrison III[§]

University of Dayton Research Institute, Environmental Engineering Group, 300 College Park, Dayton, Ohio 45469-0114, University of Dayton, 300 College Park, Dayton, Ohio 45469-0246, and Air Force Research Laboratory, Propulsion Directorate, Wright-Patterson Air Force Base, WPAFB, Ohio 45433-7103.

Received June 27, 2005. Revised Manuscript Received November 8, 2005

To examine the contributions of different types of aromatics, the volume swell of nitrile rubber O-rings was determined in aromatic-free synthetic JP-5 fuel and in synthetic JP-5 fuel blended with selected aromatics. Additionally, partition coefficients between the O-ring and fuel phases were measured for the fuel and aromatic species. Volume swell was measured using an in situ optical dilatometry technique that provided temporal data, while partition coefficients were measured using direct thermal desorption GC–MS analysis of swollen O-ring samples. For the hydrocarbons studied, the data indicate a correlation between partition coefficient and volume swell. The propensity to swell nitrile rubber was found to increase with the polarity and hydrogen-bonding character of the aromatics, suggesting that swelling of nitrile rubber requires disrupting the attractive forces between cyano groups on adjacent polymer chains and replacing them with cyano group–aromatic interactions. Volume swell was also found to decrease with increasing molecular weight.

Introduction

Throughout the history of engine development there has been a parallel development of the fuels used to power them. This relationship between fuels and power plants is often synergistic with new engines requiring better fuels, better fuels enabling new engine designs, and so on. The design of engines has also evolved to utilize, or at least accommodate, the physical and chemical characteristics of the fuels they use. Consequently, if there is a significant change in the physical or chemical composition of a fuel, either the fuel system design may have to be altered to accommodate these changes or the fuel must be formulated so its behavior mimics the fuel the systems were originally designed to use.

This issue of the impact of making a significant change in the composition of a fuel is particularly acute for synthetic fuels. A well-known process for the production of synthetic fuel is the Fischer–Tropsch (FT) process. The fuels typically produced using an FT-type process are very complex mixtures of paraffins and isoparaffins.¹ Depending on the process conditions, a high-quality liquid fuel can be produced that has physical properties comparable to those of conventional petroleum distillate fuels.² However, unlike conventional fuels, FT fuels usually contain neither aromatics nor sulfur as compared to a typical jet fuel which may contain as much as 25% v/v aromatics and 0.3% m/m sulfur.^{1–3} The absence of aromatics and sulfur is attractive

as it reduces the propensity of the fuel to produce soot and sulfur gases.^{4,5} However, the lack of sulfur species reduces the lubricity of the fuel, reducing the lifetime of parts that are lubricated by the fuel such as fuel pumps and fuel injectors. The lack of aromatics reduces the propensity of the fuel to swell elastomer seals such as O-rings which is of particular concern as the use of synthetic fuels in engines that have been using conventional fuel may actually cause elastomer seals to shrink and fail.^{3,6,7}

A potential strategy to reduce the seal-swell problem is to blend an appropriate amount of aromatics with the synthetic fuel to give it the desired swelling character. While conceptually simple, this has the potential to significantly increase the cost of the fuel and is also likely to increase the propensity of the fuel to produce soot. Alternatively, nonaromatic additives could be developed that impart the desired swell character but at a much lower concentration and potentially lower cost. A combination of these two approaches could also be used in which aromatics would be blended with synthetic fuels to make them compositionally more like conventional fuels along with an additive to promote elastomer swelling. Assuming it is desirable, at least in the near-term, to blend aromatics with synthetic fuel, this raises the question as to which aromatics to

(3) Bacha, J.; Barnes, F.; Franklin, M.; Gibbs, L.; Hemighaus, G.; Hogue, N.; Lesnini, D.; Lind, J.; Maybury, J.; Morris, J. *Aviation Fuels Technical Review*; Chevron Products Company: Houston, TX, 2000.

(4) Song, C. *Catal. Today* **2003**, *86*, 211–263.

(5) MacLean, H. L.; Lave, L. B. *Prog. Energy Combust. Sci.* **2003**, *26*, 1–69.

(6) Moses, C.; Roets, P. Status Report on Use of Semi-Synthetic Jet Fuel and the Development of Synthetic Jet Fuel. Presented at the CRC Aviation Group Meeting, Alexandria, VA, April 30, 2003.

(7) Moses, C. A.; Valtierra, M. L. *Impact Study of Synthetic and Alternative Fuel Usage in Army Aircraft Propulsion Systems*; Final Report, SRWI-MED-134, Contract No. N00140-80-C-2269; U.S. Department of Commerce, NTIS: Springfield, VA, 1981.

* Corresponding author. E-mail: graham@udri.udayton.edu.

[†] University of Dayton Research Institute, Environmental Engineering Group.

[‡] University of Dayton.

[§] Wright-Patterson Air Force Base.

(1) Burtron, H. D. *Catal. Today* **2002**, *71*, 249–300.

(2) Dry, M. E. *J. Chem. Technol. Biotechnol.* **2001**, *77*, 43–50.

use. Do all aromatics offer the same swell potential, or do some aromatics swell more than others and could therefore be blended at a lower concentration?

Saleem et al. investigated the effect of the size and shape of penetrant molecules on the rate of diffusion through low-density polyethylene (LDPE).⁸ They found that diffusivity generally decreases with increasing molar volume. For example, for a series of alkyl benzenes they found the diffusivity decreased as benzene > toluene > *p*-xylene. They also found that the diffusivity was higher for linear, flexible, or symmetrical molecules. For example they found the diffusivity of xylenes decreased as *p*-xylene > *m*-xylene > *o*-xylene, which is also the order of decreasing molar volume. This deviation was attributed to the asymmetry of the *o*-xylene making it less mobile than either the *m*- or *p*-xylene. Mathai and co-workers investigated the transport of alkyl benzenes through membranes of nitrile rubber (NBR), natural rubber (NR), and NBR/NR blends.^{9,10} They found the diffusivity and sorption coefficient for benzene, toluene, and *p*-xylene in NBR decreased with increasing molecular weight and molar volume: benzene > toluene > *p*-xylene. The same trend was found in NR and the NBR/NR blends, though as the NBR/NR ratio decreased, the solvent uptake increased reflecting the solvent resistance of NBR relative to that of NR. Sombatsompop and Christodoulou reported the penetration behavior of aromatic hydrocarbons into NR.¹¹ They found the rate of swelling decreased with increasing molar volume: toluene > *p*-xylene > 1,3,5-trimethyl benzene. Sombatsompop later extended this work to include *o*-, *m*-, and *p*-xylene.¹² In this work it was found the rate of swelling and the swelling coefficient at the equilibrium state decreased with increasing molar volume: toluene > *p*-xylene > 1,3,5-trimethyl benzene. It was also found that within the family of xylenes the swelling coefficient at equilibrium decreased as *p*-xylene > *m*-xylene > *o*-xylene, and in a manner similar to that of Saleem they attributed this to the order of increasing asymmetry.

Previous work, such as the examples cited above, often report results of polymer samples aged in pure solvents which is an established method of investigating specific polymer–penetrant interactions. The present study extends this work to investigate polymer–penetrant interactions of specific species present in very complex mixtures. Specifically, the authors present the results of a study on the polymer–fuel partitioning and volume swell of a commercial nitrile rubber O-ring material upon aging in a synthetic jet propulsion (JP) fuel blended with selected aromatics.

Background

Nitrile rubber, a random copolymer of poly(acrylonitrile) and poly(butadiene), was selected as the model system for this study as it is one of the oldest and most widely used O-ring materials in fuel applications. In this system the poly(butadiene) contributes to the softness and pliability of the material, while the poly(acrylonitrile) contributes the fuel resistance.^{13,14} These physical

(8) Saleem, M.; Asfour, A.; De Kee, D. *J. Appl. Polym. Sci.* **1989**, *37*, 617–625.

(9) Mathai, A. E.; Thomas, S. J. *Macromol. Sci., Phys.* **1996**, *B35* (2), 229–253.

(10) Mathai, A. E.; Singh, R. P.; Thomas, S. J. *Membr. Sci.* **2002**, *202*, 35–54.

(11) Sombatsompop, N.; Christodoulou, K. J. *Polym. Polym. Compos.* **1997**, *5* (5), 377–386.

(12) Sombatsompop, N. *Polym.–Plast. Technol. Eng.* **1998**, *37* (1), 19–39.

(13) *Handbook of Elastomers*, 2nd ed.; Bhowmick, A. K., Stephens, H. L., Eds.; Marcel Dekker: New York, 2001.

Table 1. Hansen Solubility Parameters For Selected Polymers^a

polymer	δ_D	δ_P	δ_H
poly(acrylonitrile)	18.2	16.2	6.8
poly(butadiene)	17.0	0.0	1.0
poly(acrylonitrile- <i>co</i> -butadiene) ^b	17.4	4.9	2.7
poly(acrylonitrile- <i>co</i> -butadiene) ^c	19.8	17.8	3.2

^a Dispersive (δ_D), polar (δ_P), hydrogen bonding (δ_H), units = MPa^{1/2} from ref 16. ^b Estimated using volume additivity assuming 30% poly(acrylonitrile). ^c From ref 18.

characteristics arise from the intermolecular bonding that occurs between the poly(acrylonitrile) and poly(butadiene) chain segments. Briefly, poly(butadiene) is largely nonpolar with the chain segments attracted to one another by relatively weak dispersive (van der Waals) forces and weak polar forces from the olefinic groups. In contrast, the poly(acrylonitrile) chain segments are attracted to one another by strong dipole–dipole bonds between highly polar cyano groups (–C≡N) on adjacent polymer chains.¹⁵ Finally, there is likely intermolecular bonding of intermediate strength between the highly polar cyano and slightly polar olefinic groups.

This qualitative description of the intermolecular-bonding structure of nitrile rubber can be quantified somewhat by considering the Hansen solubility parameters (HSPs) of poly(acrylonitrile) and poly(butadiene) as summarized in Table 1.¹⁶ Briefly, HSPs describe the relative contribution to the bulk intermolecular bonding (cohesive energy density) of polymers and solvents in terms of dispersive (δ_D), polar (δ_P), and hydrogen-bonding forces (δ_H).^{16,17} The HSPs for poly(acrylonitrile) and poly(butadiene) confirm that these are polar and nonpolar materials, respectively.

Solubility parameters are most effective when used to describe the intermolecular bonding of pure materials. However, volume additivity rules can be used to estimate the HSPs for solvent mixtures and copolymers.^{16,17} Noting that nitrile rubber O-rings used with fuel are typically 30% poly(acrylonitrile), the HSPs for this material have been estimated as shown in Table 1. This table also gives an example of measured values for a nitrile rubber from the literature showing that volume additivity may underestimate the polar character of this copolymer.¹⁸ Similarly, volume additivity was applied to estimate the HSP for JP-5 (see Table 2) using a surrogate composition proposed by the Air Force Research Laboratory for JP-8.¹⁹ Assuming this to be representative of JP fuel in general, this shows that the intermolecular-bonding forces in JP fuel are largely dispersive with only weak contributions from polar and hydrogen-bonding forces.

Consideration of the solubility parameters illustrates why nitrile rubber is a fuel-resistant material. Specifically, the general

(14) Hertz, D. L.; Bussem, H. Nitrile Rubber—Past, Present and Future. Presented at the National Meeting of the American Chemical Society, Pittsburgh, PA, October 11–14, 1994; Paper 58.

(15) Ipiotis, E. N. A Study on the Swelling Properties of the Butadiene-Acrylonitrile Copolymers. Masters Thesis, Department of Chemistry, University of Akron, Akron, OH, 1955.

(16) Hansen, C. M. *Hansen Solubility Parameters—A Users Handbook*; CRC Press LLC: New York, 2000.

(17) Burke, J. Solubility Parameters: Theory and Application. *AIC Book and Paper Group Annual*; Craig, J., Ed.; AIC: Washington, D.C., 1984; Vol. 3, pp 13–58.

(18) Buckley-Smith, M. K.; Fee, C. J. The Use of Hansen Solubility Parameters for the Selection of Materials for Organic/Organic Separations by Pervaporation. Proceedings of the 9th APCChe Congress and CHEME-CA 2002, September 29–October 3, 2002; Gostomski, P. A., Morison, K. R., Eds.; University of Canterbury: Christchurch, NZ, 2002.

(19) Risher, J.; Bittner, P. M.; Rhodes, S. *Toxicological Profile for Jet Fuels JP-5 & JP-8*; Agency for Toxic Substances and Disease Registry, U.S. Department of Health and Human Services, Public Health Service: Atlanta, GA, 1998.

Table 2. Hansen Solubility Parameters, Molar Volumes, Partition Coefficients (K_{pf}), and Volume Swell (μ) for the Source Fuels and Aromatics Blended at 10% v/v in S-5 with Nitrile Rubber^a

component	δ_D	δ_P	δ_H	molar vol ^b	K_{pf}	μ %
neat S-5 ^c	16.0	0.0	0.0	n/a	0.082	0.82
neat JP-5 ^d	16.5	0.2	0.5	n/a	0.181	14.83
benzene	18.4	0.0	2.0	89	0.489	7.47
toluene	18.0	1.4	2.0	107	0.404	8.94
ethyl benzene	17.8	0.6	1.4	123	0.344	8.67
propyl benzene ^e	n.a.	n.a.	n.a.	139	0.313	7.96
pentyl benzene ^e	n.a.	n.a.	n.a.	173	0.283	5.75
<i>o</i> -xylene	17.8	1.0	3.1	121	0.465	9.37
<i>m</i> -xylene ^e	n.a.	n.a.	n.a.	122	0.404	8.65
<i>p</i> -xylene ^e	n.a.	n.a.	n.a.	123	0.389	8.10
styrene	18.6	1.0	4.1	116	0.696	13.33

^a Dispersive (δ_D), polar (δ_P), hydrogen bonding (δ_H), units = MPa^{1/2} from ref 16. ^b Units = mL/mol. ^c HSP taken as dodecane, molar volume not applicable (n/a). ^d HSP estimated, molar volume not applicable (n/a). ^e HSP not available (n.a.).

description of the thermodynamics of solubility given by Hildebrand and Scott requires that the process of breaking polymer–polymer and penetrant–penetrant intermolecular bonds and forming polymer–penetrant intermolecular bonds must be energetically favorable.²⁰ As shown by their respective HSPs, nitrile rubber is a relatively polar material while JP fuel is relatively nonpolar, and it therefore is not energetically favorable for the polar intermolecular bonding of the polymer to be exchanged with the weaker polar bonds of the JP fuel. However, examination of the HSPs for individual species within JP fuel shows there are numerous individual components whose polar and hydrogen-bonding character compares more favorably with those of the polymer than the bulk fuel, and these are for the most part the aromatic species. Furthermore, noting that the cyano nitrogen atom in nitrile rubber has a net negative charge, fuel components containing electropositive sites, such as the aromatic hydrogens, would interact preferentially with the cyano group and are thus good candidates for contributing to the volume swell of nitrile rubber.

This analysis supports the general observation that the volume swell of nitrile rubber correlates with aromatic content as it is this family of fuel components that the solubility parameters suggest will interact most strongly with the elastomer. Furthermore, this provides some guidance as to which aromatics will interact more strongly than others. Specifically, the strength of interaction should increase with the polarity of the fuel component as the breaking of a polymer–polymer intermolecular bond to form a polymer–aromatic intermolecular bond becomes more favorable. Furthermore, species with significant hydrogen bonding (an unhindered electropositive site) should also be effective.

To investigate this proposed model a study was conducted using aromatics listed in Table 2. Briefly, this study included a series of alkyl benzenes to examine the effect of increasing the length of a single alkyl substitution on the benzene ring and thus diluting the aromatic character of the molecule, *o*-, *m*-, and *p*-xylene to examine the effect of polarity in a structurally similar family of molecules, and styrene to examine the effect of hydrogen bonding using an aromatic that is structurally similar to the other penetrant molecules. The data obtained in this study included measuring the polymer–fuel partition coefficient to quantify the strength of interaction between the

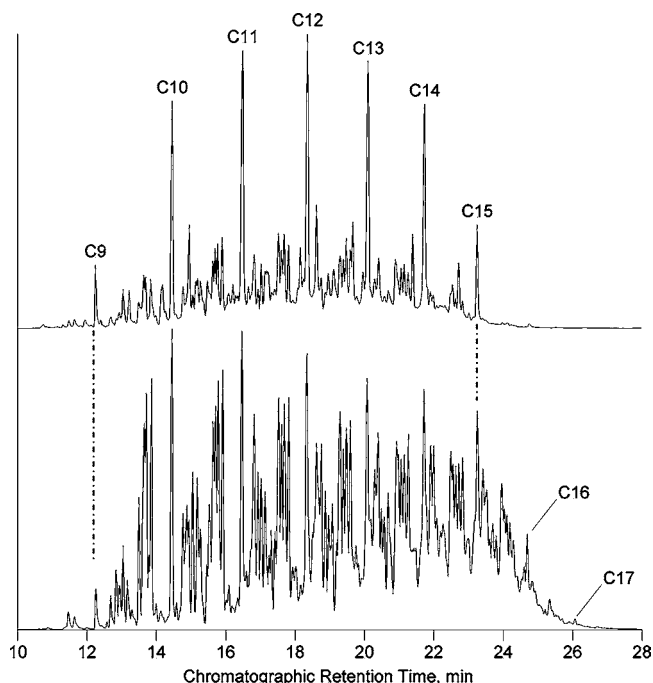


Figure 1. GC–MS chromatograms for JP-5 (top) and S-5 (bottom) showing the similar molecular weight range and complexity of these fuels.

polymer and the penetrants and the volume swell to quantify the result of this interaction.

Experimental Section

Materials. The O-rings used in this study were nitrile rubber N-602-70-214 (Parker Hannifin Corp., Lexington, KY). The baseline fuels included a JP-5 provided by the Naval Air Systems Command (Patuxent River, MD) and a synthetic JP-5 (S-5) that was provided by Syntroleum Corporation (Tulsa, OK).²¹ The overall composition of these two fuels is illustrated by the chromatograms shown in Figure 1. This analysis was conducted with the nonpolar stationary phase described below, and thus the solutes are separated in order of increasing boiling point: *n*-C₉ to *n*-C₁₅ for the JP-5 and *n*-C₉ to *n*-C₁₇ for the S-5. This figure shows the two fuels are of similar complexity and boiling range. However, compositional analysis provided by the suppliers showed that the JP-5 included 20% aromatics while the S-5 is entirely paraffinic (0% aromatics). The penetrants used in this study (see Table 2) were used as received from the supplier (Aldrich Chemical Co., Milwaukee, WI).

Polymer–Fuel Partition Coefficient: Direct Thermal Desorption GC–MS. The relative strength of interaction between a cross-linked (and therefore insoluble) polymer and a solvent is often expressed in terms of a measurable quantity such as a change in volume or weight. However, these are often convolutions of effects that can include loss of material from the polymer to the surrounding fluid as well as gain of components from the fluid into the polymer. In this study the polymer–fuel partition coefficient was used as measure of the strength of interaction between the polymer and the fuel in addition to the change in volume as described below. Specifically, the partition coefficient, K_{pf} , was taken as

(20) Hildebrand, J. H.; Scott, R. L. *The Solubility of Nonelectrolytes*, 3rd ed.; Dover Publications: New York, 1964.

(21) *Turbine Fuels, Aviation, Kerosene Types, NATO F-34 (JP-8) and NATO F-35; Military Specification MIL-T-83133E; ASD/ENES, Wright Patterson AFB: OH, April, 1999.*

$$K_{\text{pf}} = \frac{[A]_{\text{p}}}{[A]_{\text{f}}} \quad (1)$$

where $[A]_{\text{p}}$ is the concentration of fuel component A in the polymer and $[A]_{\text{f}}$ is the concentration of A in the fuel. The partition coefficient was found from GC–MS data by expressing the concentration in terms of the integrated peak areas per unit volume. The volume of the test fluid was taken as the volume of the injected sample, and the volume of the O-ring piece was determined from the measured mass of the sample before aging and the density as measured using ASTM method D-471.²²

The partition coefficient of each aromatic was measured using the direct thermal desorption gas chromatography–mass spectrometry (DT–GC–MS) system illustrated in Figure 2. This system consists of a thermal desorption assembly interfaced to a GC–MS through a cold trap. The thermal desorption assembly includes a liquid injection port where fuel samples are introduced using standard GC-type syringes and a solids insertion port where O-ring samples are introduced using quartz probes. The cold trap is a simple condenser-like device fabricated from fused quartz and is cooled with nitrogen gas that has been chilled by passing through a copper coil immersed in liquid nitrogen. The GC–MS is a Hewlett-Packard model 5890 fitted with a 5970B mass selective detector (MSD). The chromatographic column used was a 0.25 mm \times 15 m DB-1 (J&W Scientific, Folsom, CA) with a 25 μm film thickness and a 60:1 inlet split. The MSD was operated in scanning mode from 35 to 350 AMU with an electron multiplier potential of 1600 V.

For each measurement small sections of O-ring (typically 500–1000 μg) were weighed on a six-place analytical balance (Mettler-Toldeo model AX26). A stock supply of each fuel was prepared by blending 1 mL of the selected aromatic with 99 mL of S-5 giving a blend with approximately 1% v/v aromatics. This low level was selected as being representative of the concentration of an individual aromatic species in JP fuel and to minimize the swelling of the polymer matrix allowing the measured dry volume of the test piece to be used in the calculation of the partition coefficient. The weighed sample was then sealed in a 1.8 mL glass sample vial along with 1.0 mL of the fuel and allowed to age at room temperature. Since the partition coefficient measurement is an end-point technique in which each sample can only be analyzed once, an aging time was selected that was long enough to ensure the samples were at equilibrium with the fuel. Preliminary volume swell measurements with large O-ring sections indicated that these samples typically reached equilibrium in 3–6 days. Given that the samples used for the partition coefficient measurements were much smaller than those used for the volume swell tests it was estimated that 7 days was adequate to ensure that the partition coefficient samples would reach equilibrium with the fuel.

Following the aging period the fuel was analyzed with the DT–GC–MS system described above. For this analysis, 0.4 μL of the fuel was withdrawn from the sample vial using a standard 2.0 μL GC syringe and injected into the DT–GC–MS with the inlet temperature set at 280 $^{\circ}\text{C}$, dry helium flowing through the system, the cold trap cooled to approximately -130°C , and the splitter/vent open so the pressure in the system was near ambient. A period of 10 min was allowed to pass for the sample to evaporate in the inlet and flow through the system and into the cold trap. At this point the GC column was cooled to -60°C , the splitter/vent set to provide a 60:1 sample split, and the cold trap was heated to 280 $^{\circ}\text{C}$ at approximately 20 $^{\circ}\text{C}/\text{min}$, releasing the collected sample onto the GC column. Once this sample transfer process was complete the splitter/vent was adjusted to establish a head pressure on the GC column of 6 psig, and the GC oven was heated from -60°C to 280 $^{\circ}\text{C}$ at 20 $^{\circ}\text{C}/\text{min}$ and held at 280 $^{\circ}\text{C}$ for 20 min. Following this procedure the process was repeated using the O-ring sample. For this analysis the O-ring sample was removed from the vial, dabbed

dry with a laboratory tissue, sealed in the inlet of the DT–GC–MS and heated to 300 $^{\circ}\text{C}$ to thermally desorb the absorbed fluid from the sample.

Extracted ion chromatograms (EICs) were used to assist in obtaining integrated chromatographic peak areas for selected fuel components. Specifically, once the source total ion chromatograms (TICs) were obtained the EIC for the component of interest was obtained by extracting a specific ion that is characteristic of the analyte. For this study ion 43 used to isolate alkanes, 78 for benzene, 91, 105, 119, and 133 for alkyl benzenes, 96 for styrene, and 128, 142, and 156 for diaromatics. The partition coefficient was recorded as the average of three independent analyses.

Volume Swell: Optical Dilatometry. The volume swell of O-ring samples was measured using an optical dilatometry system illustrated in Figure 3. As shown, this system consisted of a backlit fuel reservoir fitted with an optical window. The window was designed so that its inner face was immersed in the test fluid to prevent condensation from obscuring the view of the O-rings resting on the bottom of the reservoir. The window also sealed the reservoir preventing the fuel from evaporating. A digital camera mounted above the reservoir periodically photographed the O-rings and stored the images on a dedicated desktop computer.

For each test, three sections of O-ring measuring approximately 2 cm long were cut from three different O-rings randomly selected from a stock supply. The fuel was prepared by mixing 10 mL of the selected aromatic with 90 mL of the S-5. The O-ring sections were placed in the reservoir which was then filled with 100 mL of fuel and covered the optical window. The O-ring sections were then photographed every 20 min over the next 72 h providing a record of the cross-sectional area of the specimens as a function of time. The cross-sectional area was extracted from the digital images using a commercial image processing system (MetaMorph, Molecular Devices Corp., Sunnyvale, CA). Assuming isotropic swelling, the change in cross-sectional area was taken as a characteristic dimension proportional to the change in volume as

$$\mu = \left[\left(\frac{A_i}{A_0} \right)^{3/2} - 1 \right] \times 100\% \quad (2)$$

where μ is the volume swell (%) and A_i and A_0 are the cross-sectional areas in image i and 0 (the reference image taken at time zero), respectively. The volume swell was recorded as the average volume swell of the three test specimens at the conclusion of the aging period.

Results and Discussion

The results from the partition coefficient and volume swell measurements are summarized in Table 2 and Figures 4–6.

The volume swell results for the nitrile rubber O-rings aged in S-5 and JP-5 illustrates why there is concern about O-rings that have been in service with JP-5 shrinking when they come into contact with S-5. Specifically, it was found that the nitrile rubber O-rings used here swelled 14.83% in JP-5, but only 0.82% in S-5, suggesting that considerable shrinkage would occur as the fuel is switched between JP-5 and S-5. Recalling the most significant difference in the composition of these two fuels is the aromatic content (20% in JP-5 vs 0% in S-5), this result is consistent with the general observation that aromatic species in JP fuels swell nitrile rubber.

As described previously, volume swell is often the convolution of competing processes: the extraction of material from the O-ring (such as plasticizers) causing it to shrink and partitioning of fuel into the O-ring causing it to swell. The partition coefficient (K_{pf}) provides a means of quantitatively measuring the relative equilibrium concentration of specific species between the O-ring and fuel. The simplest measure of this equilibrium for a fuel mixture is to consider the overall partition coefficient calculated using the total chromatographic

(22) *Standard Test Method for Rubber Property-Effect of Liquids*; Document No. ASTM D 471-98e1; ASTM International: West Conshohocken, PA, 1999.

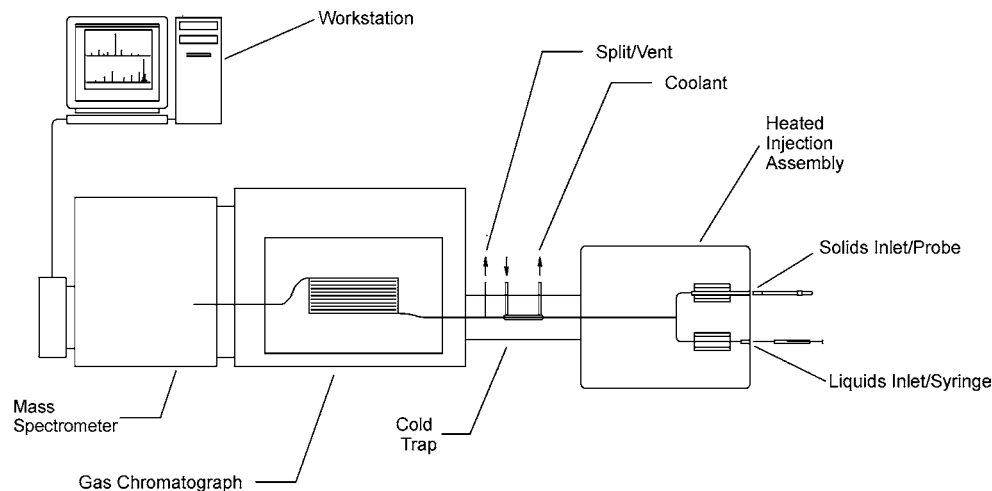


Figure 2. General schematic of the direct thermal desorption GC-MS system.

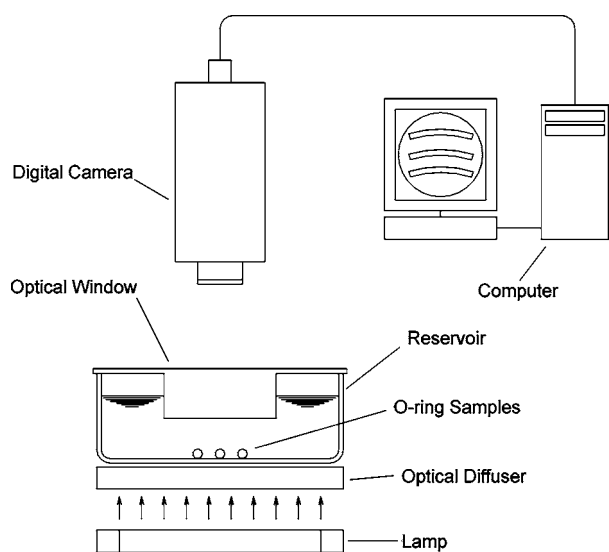


Figure 3. General schematic of the optical dilatometry system.

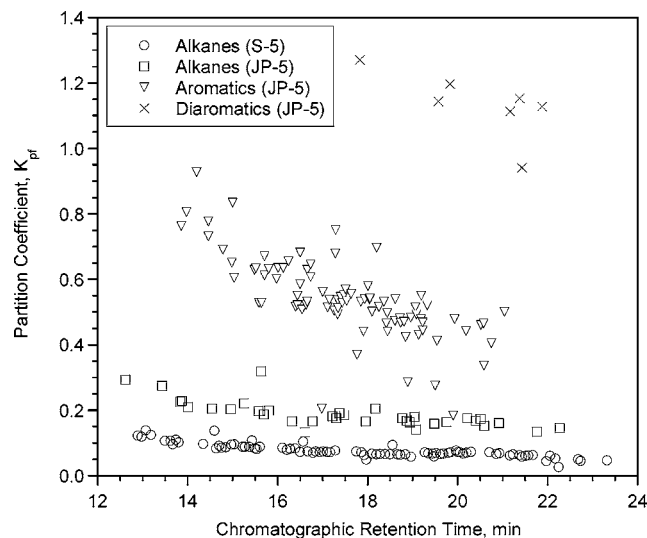


Figure 4. Partition coefficient between nitrile rubber and selected compound classes in S-5 and JP-5 vs chromatographic retention time after aging at room temperature for 7 days. Note that in this analysis molecular weight increases with increasing retention time.

peak areas from the analysis of the fuel and the O-ring. This analysis gives a value of K_{pr} for JP-5 of 0.181 as compared to 0.082 for S-5, illustrating that the mean equilibrium concentra-

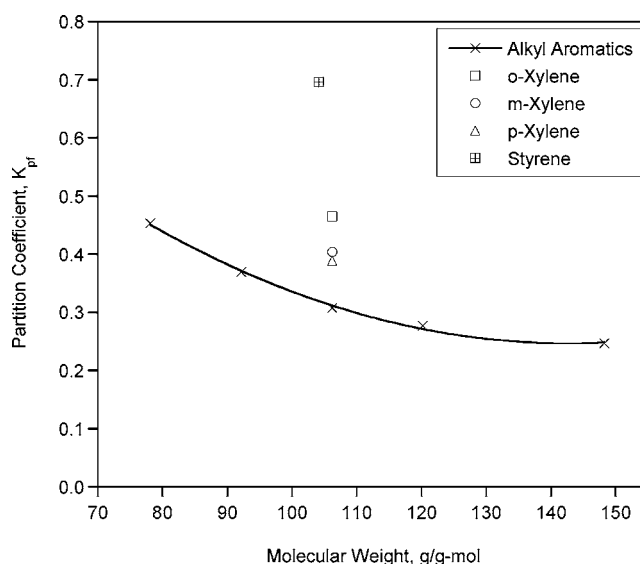


Figure 5. Partition coefficient between nitrile rubber and S-5 vs molecular weight for selected aromatics blended in S-5 after aging at room temperature for 7 days. Note the alkyl aromatics (from left to right) are benzene, toluene, ethyl benzene, *n*-propyl benzene, and *n*-pentyl benzene.

tion of JP-5 constituents in the O-ring is 2.2 times higher than S-5 showing that nitrile rubber has a higher affinity toward JP-5 than S-5.

The utility of the DT-GC-MS process is the ability to perform a variety of analyses using extracted ion chromatography (EIC) to isolate specific compounds or compound classes from complex mixtures such as JP fuels. Figure 4 summarizes one such class analysis for alkanes in S-5 and the alkanes, aromatics, and diaromatics in JP-5. Note that the relative chromatographic retention time was used to match peaks from the analysis of the fuel and O-ring. This figure shows that within each compound class the partition coefficient decreases with increasing molecular weight which is consistent with observations from the literature that diffusivity and swelling coefficient decrease with increasing molar volume. These data also shows the partition coefficient increases as alkanes < aromatics < diaromatics which is also the order of decreasing molar volume. However, there are also physical properties which could be significant contributing factors to this speciation. Specifically, reviewing the HSPs tabulated by Hansen shows that the intermolecular bonding of normal and branched alkanes are entirely dispersive with no contributions from polar or hydrogen

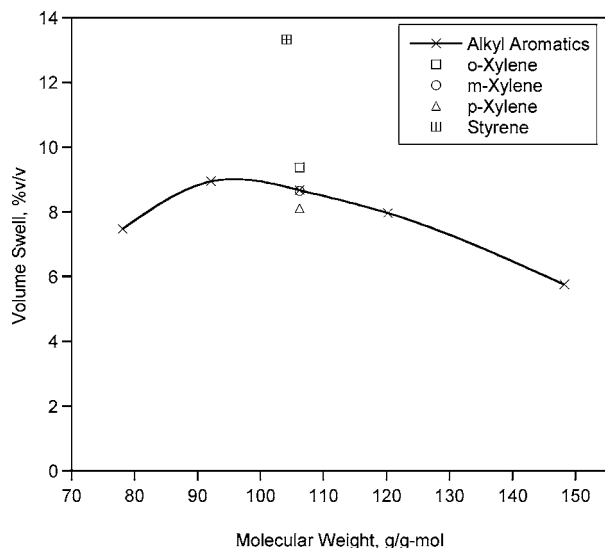


Figure 6. Volume swell of nitrile rubber vs molecular weight for selected aromatics blended in S-5 after aging at room temperature for 3 days. Note the alkyl aromatics (from left to right) are benzene, toluene, ethyl benzene, *n*-propyl benzene, and *n*-pentyl benzene.

bonding. Similarly, the naphthenes (cyclo-alkanes) are also nonpolar but may have some weak hydrogen-bonding character. In contrast, the aromatics show a considerable range of polar and hydrogen-bonding character depending on the number and type of substitutions on the benzene ring. Furthermore, the diaromatics (naphthalenes) show polar character that is similar to that of the single-ring aromatics but much higher hydrogen-bonding character. For example, the hydrogen-bonding contribution to the HSP for naphthalene is $5.9 \text{ MPa}^{1/2}$ as compared to $2.0 \text{ MPa}^{1/2}$ for benzene.¹⁷ From this we would conclude that the higher volume swell of nitrile rubber in JP-5 versus S-5 is a consequence of the smaller molar volume of the aromatic versus paraffinic species allowing them to more easily partition into the polymer coupled with the polar and hydrogen-bonding character of the aromatics resulting in the aromatics interacting specifically with the polar cyano sites within the nitrile rubber.

It is interesting to note that the alkanes in JP-5 show a partition coefficient that is about twice that found for those of S-5. This is likely a consequence of the higher degree of swelling of the nitrile rubber in the JP-5 as compared to the S-5.

The higher volume swell of nitrile rubber in JP-5 versus S-5 and the higher partition coefficients of aromatics versus alkanes indicate that aromatics are an important component of JP fuel with regard to O-ring swell. Information from the literature suggests that the smaller size of aromatics versus alkanes are a contributing factor, but measurements of polymer–fuel partitioning and solubility parameter analysis indicate that structure may also play a role, namely, polarity and hydrogen bonding. Furthermore, since it may be possible to coprocess aromatics with synthetic fuel, it is desirable to determine the relative importance of these factors: molar volume, polarity and hydrogen bonding. To perform this evaluation, a set of structurally similar aromatics was selected. Specifically, benzene, toluene, ethyl benzene, *n*-propyl benzene, and *n*-pentyl benzene were used to examine the effect of increasing the alkyl chain length of a singly substituted benzene ring, *o*-, *m*-, and *p*-xylene were used to examine the effect of polarity (substitution position), and styrene was used to examine the effect of hydrogen bonding.

As shown in Figure 5 the partition coefficients of the *n*-alkyl benzenes were found to steadily decrease with increasing

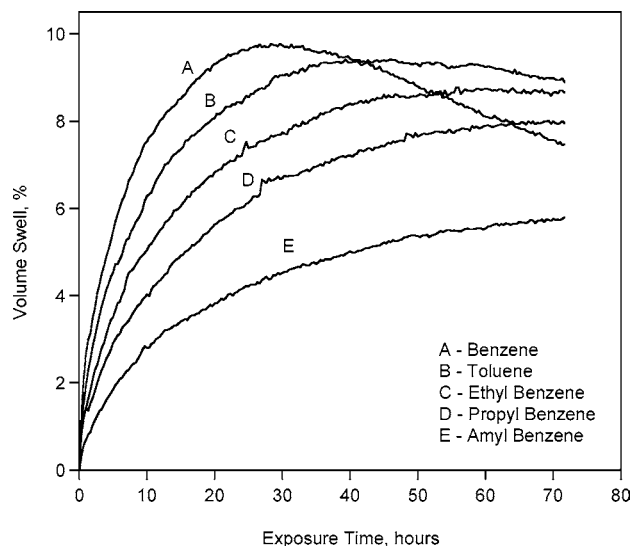


Figure 7. Volume swell as a function of time for nitrile rubber aged in S-5 + 10% v/v of each individual aromatic at room temperature showing the steady increase in the initial swelling rate with decreasing molecular weight and the onset of shrinking with toluene and benzene.

molecular weight, from 0.489 for benzene to 0.283 for *n*-pentyl benzene. The volume swell data summarized in Figure 6 shows a maximum at toluene even though the partition coefficient for benzene was greater, then a steady decline as the molecular weight increases. The decline in the partition coefficient and the overall decline in the volume swell is consistent with the observation that volume swell decreases with increasing molar volume. Furthermore, although the values tabulated by Hansen are incomplete, the available values for the HSPs for normal alkyl benzenes show that increasing the length of the alkyl substitution reduces the polarity and hydrogen-bonding character of these compounds.

An examination of the volume swell source data shows why the apparent maximum in the volume swell occurs at toluene. Specifically, the optical dilatometry data given in Figure 7 shows the initial rate of swelling follows the same order as the partition coefficient: benzene being the highest with a steady decline through pentyl benzene. However, in the case of benzene the volume swell shows a maximum at about 27 h, after which the sample shrinks. A much smaller effect is seen in the toluene data. This suggests that benzene is not only diffusing into the polymer but is also serving as a solvent to extract material from the O-ring with the net result being a loss of volume swell following an initial period of rapid swelling. This shows that it is possible to employ swelling promoters that can act too aggressively as solvents toward extractable components of the polymer.

With respect to polarity, it was found that both the partition coefficient and volume swell decreased as *o*-xylene > *m*-xylene > *p*-xylene which is consistent with the order of decreasing polarity and with the order of decreasing molar volume. However, this order is opposite that reported by Saleem et al.⁸ in LDPE and by Sombatsompop and Christodoulou¹¹ in NR who attributed this anomalous behavior to the order of increasing asymmetry of the xylene molecule. This contrast in findings may reflect the importance of the strongly polar cyano site in nitrile rubber and how penetrant molecules interact with this site. This result may also reflect a difference in the behavior of a neat polar penetrant versus a penetrant diluted in a nonpolar liquid phase. In the case of a neat penetrant, such as *o*-xylene, the exchange dipole–dipole intermolecular bonds in the liquid phase with dipole–dipole intermolecular bonds in the solid

phase must be energetically favorable. In the case of a polar penetrant diluted in a nonpolar liquid phase, such as *o*-xylene in S-5, the intermolecular bonding in the liquid phase will be largely dispersive as the solvated *o*-xylene molecules will encounter each other far less frequently and the exchange of dispersive intermolecular bonds in the liquid phase for dipole–dipole intermolecular bonds in the solid phase will be more likely to be energetically favorable.

The class analysis of the partitioning of JP-5 into nitrile rubber suggested that diaromatics are the most active aromatic species in JP-5. As described previously, a distinguishing feature in the intermolecular bonding of the naphthalenes is their relatively high hydrogen bonding as compared to that of the single-ring aromatics. To examine the potential role of hydrogen bonding, styrene was selected as a model penetrant because of its structural similarity to the other molecules used in this study, and among the singly substituted single-ring aromatic hydrocarbons for which HSPs are available, it has the strongest hydrogen-bonding component. Furthermore, considering the structure of styrene and comparing its HSPs with those of ethyl benzene, the source of the hydrogen bonding can be assigned to the olefinic group as opposed to molecules such as *o*-xylene where this character is distributed and possibly hindered. It was found that the partition coefficient of styrene was indeed exceptionally high with a value of 0.696, approximately twice that of the paraffinic analogue ethyl benzene with a solubility of 0.344. The volume swell was similarly high for this material: 13.33% for styrene as compared to 8.67% for ethyl benzene. It should be noted that styrene is a slightly smaller molecule than ethyl benzene and the xylenes, and this may be a contributing factor. However, the significant increase in the partition coefficient and the volume swell with this penetrant are consistent with the model that suggests hydrogen bonding can play an important role in the swelling of nitrile rubber by JP fuel.

The data described here suggests a correlation between partition coefficient and volume swell. Specifically, there is a general agreement in the trends observed in both sets of data. This correlation is illustrated in Figure 8 which summarizes the partition coefficient and volume swell data for the S-5 and S-5 blends. This observation is important in that it indicates that a speciation technique such as described here can be a valuable aid in understanding the volume swell of elastomers in very complex mixtures such as JP fuel by making available quantitative information on which species from the fuel are partitioning into the solid phase and are thus likely candidates for being the active species in imparting volume swell to the O-ring material.

Conclusions

The study presented here is consistent with the general observation that aromatic species in JP fuels swell nitrile rubber.

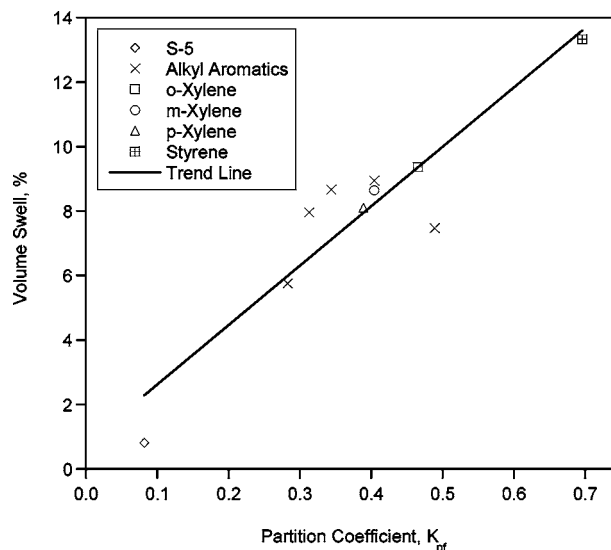


Figure 8. Volume swell vs partition coefficient between nitrile rubber and S-5 for neat S-5 and selected aromatics blended in S-5 showing the correlation between solubility and volume swell. Note the alkyl aromatics (from left to right) are *n*-pentyl benzene, *n*-propyl benzene, ethyl benzene, toluene, and benzene.

However, not all aromatics have the same propensity to induce swelling in nitrile rubber. Solubility parameter analysis indicates that solubility, and by extension polymer–fuel partitioning and volume swell, should increase with increasing polarity of the aromatic species. Furthermore, mechanistic considerations suggest that hydrogen-bonded species should also be effective due to a specific attraction to the electronegative cyano group which gives nitrile rubber its fuel resistance. The experiments show that there is an overall correlation between volume swell and solubility and that solubility and volume swell of nitrile rubber in synthetic JP fuel increases with increasing polarity and hydrogen bonding. Data also show that solubility and swelling tend to increase with decreasing molecular weight which is consistent with the general observation that smaller molecules make better solvents. Overall, this study indicates that the greatest volume swell in nitrile rubber by a highly paraffinic synthetic hydrocarbon fuel will be imparted by small aromatic molecules with significant hydrogen-bonding or polar character.

Acknowledgment. This paper is based on research sponsored by the Air Force Research Laboratory under Agreement No. F33615-03-2-2347 (Technical Monitor, Mr. Robert Morris). The U.S. Government is authorized to reproduce and distribute reprints for Governmental purposes notwithstanding any copyright notation thereon. The views and conclusions contained herein are those of the authors and should not be interpreted as necessarily representing the official policies or endorsements, either expressed or implied, of the Air Force Research Laboratory or the U.S. Government.

EF050191X

INTENTIONALLY LEFT BLANK

APPENDIX T

Pressure Effects on Flowing Mildly-Cracked n-Decane

INTENTIONALLY LEFT BLANK

Pressure Effects on Flowing Mildly-Cracked n-Decane

Thomas A. Ward,* Jamie S. Ervin,† and Steven Zabarnick‡

University of Dayton, Dayton, Ohio 45469-0210

and

Linda Shafer§

University of Dayton Research Institute, Dayton, Ohio 45469-0116

It is anticipated that traditional methods of cooling that employ the sensible heat transfer provided by fuels will not be sufficient to meet the cooling requirements of future high-performance aircraft. One potential solution is the use of endothermic fuels, which absorb heat through chemical reactions. However, few studies have analyzed the effects of pressure on a chemically reacting, flowing fuel. An experiment is described that studies the effects of pressure on flowing, mildly cracked, supercritical n-decane. The experimental results are studied with the aid of a unique two-dimensional computational fluid dynamics model that simulates the formation of cracked products from experimentally derived proportional distributions. This model is used to study the effect of pressure on the flow properties of the fuel. The experiments indicate that increasing pressure enhances bimolecular pyrolysis reactions, relative to unimolecular reactions. Increasing pressure also increases the overall conversion rate of supercritical n-decane flowing through a reactor. This is primarily because pressure increases the density, which increases the residence time of n-decane flowing through the reactor.

Nomenclature

A	= preexponential factor (A factor) in Arrhenius rate expression, s^{-1}
C_p	= specific heat, J/kg · K
C_μ	= coefficient in turbulent transport equations, const = 0.09
C_1	= coefficient in turbulent transport equations, const = 1.47
C_2	= coefficient in turbulent transport equations, const = 1.92
D_i	= diffusion coefficient of i th species, m^2/s
E_a	= activation energy in Arrhenius rate expression, cal/mole
G	= $\mu_i \{2[(\partial u/\partial z)^2 + (\partial v/\partial r)^2 + (v/r)^2] + [(\partial v/\partial z) + (\partial u/\partial r)]^2\}$
g	= gravitational acceleration, m/s^2
h	= enthalpy, kJ/kg
h_{sens}	= enthalpy due to sensible heat transfer, kJ/kg
h_{tot}	= total enthalpy, kJ/kg
i	= individual product species
k	= turbulent kinetic energy, kJ/kg
k_A	= Arrhenius rate constant, s^{-1}
p	= pressure, MPa
Q_{endo}	= heat transfer due to endothermic reactions, W
Q_{sens}	= sensible heat transfer, W
Q_{tot}	= total heat transfer, W
R	= gas constant, 1.987 cal/K · mole
r	= radial coordinate, (m)
S^Φ	= source term
T	= fuel temperature, °C or K

t	= time, s
u	= axial velocity component, m/s
v	= radial velocity component, m/s
Y_i	= mass fraction of i th cracked product species (fraction includes parent fuel)
Y_{RH}	= mass fraction of parent fuel
$Y_{\sum \text{products}}$	= mass fraction of total products
y_i	= product mass fraction of i th product species (fraction excludes parent fuel)
y_{iav}	= averaged y_i over a range of parent fuel conversions
z	= axial coordinate, m
Γ^Φ	= transport coefficient
Δh_{endo}	= enthalpy change due to endotherm, kJ/kg
ε	= turbulence dissipation rate, W
κ	= thermal conductivity, W/m · K
μ	= absolute viscosity, kg/m · s
μ_t	= turbulent viscosity, $C_\mu \cdot \rho \cdot k^2/\varepsilon$, kg/m · s
ρ	= density, kg/m ³
σ_k	= effective turbulent Prandtl number (kinetic energy), const = 1.0
σ_{y_i}	= effective turbulent Prandtl number (species), const = 1.0
σ_ε	= effective turbulent Prandtl number (dissipation rate), const = 1.3
Φ	= assigned variable in Eq. (2)
$\dot{\omega}_i$	= rate of production of i th species, kg/m ³ · s

Introduction

IN advanced military jet engines, fuel is used for cooling before combustion. It is envisioned that the heat dissipation requirements of future high-performance aircraft will increase beyond that which can be supplied by the sensible heat transfer provided by fuels.¹ Use of cryogenic fuels would add unacceptable weight, complexity, and cost. An alternative solution is to use a hydrocarbon fuel that absorbs heat through a series of endothermic chemical reactions. With an endothermic fuel, additional cooling is obtained by endothermic reactions occurring simultaneously with traditional convective heat transfer. The endothermic heat absorption rate can be over twice that of rate available by sensible cooling.¹

Significant thermal cracking of jet fuel occurs at temperatures above approximately 500°C, where the bonds of hydrocarbon molecules are broken to produce several smaller molecules.

281 This type of endothermic reaction is called thermal cracking or

Received 4 December 2003; revision received 19 July 2004; accepted for publication 2 July 2004. This material is declared a work of the U.S. Government and is not subject to copyright protection in the United States. Copies of this paper may be made for personal or internal use, on condition that the copier pay the \$10.00 per-copy fee to the Copyright Clearance Center, Inc., 222 Rosewood Drive, Danvers, MA 01923; include the code 0748-4658/05 \$10.00 in correspondence with the CCC.

*Aerospace Engineer, Department of Mechanical and Aerospace Engineering; Thomas.Ward@wpafb.af.mil. Member AIAA.

†Professor, Department of Mechanical and Aerospace Engineering; also Group Leader, Modeling and Simulation. Associate Fellow AIAA.

‡Professor, Department of Mechanical and Aerospace Engineering; also Distinguished Research Chemist, Fuels Science.

§Chemist, Fuels Science Group.

pyrolysis.² However, there are numerous factors that must be studied and understood before pyrolysis cooling can be applied to a new heat exchanger design. The effects of fuel temperature and residence time on pyrolytic fuel flow have been popular past topics of study, due to their strong influence on the reaction rate.³ Unfortunately, there is little work that addresses the effects of pressure on fuel properties and very few computational models capable of sufficiently representing the problem. A change of pressure on a flowing, supercritical hydrocarbon fuel may affect the flow properties. The effect of these properties on the velocity, heat transfer, and chemical kinetics is complex, especially if multidimensional geometries are considered. Furthermore, chemical changes in the fuel as it cracks also affect the behavior of flowing fuel. All of these factors must be taken into account to understand the effect of pressure completely.

Fabuss et al.⁴ conducted flow experiments to study the effects of pressure on the thermal cracking of *n*-hexadecane pumped at different flow rates (16–133 ml/min). The reactor was placed inside a furnace, which heated the reactor to wall temperatures over the range of 600–700°C. Analysis and measurements of the products were done by several methods, including gas chromatography. They concluded that, although the overall conversion of hexadecane increased with increasing pressure, the first-order reaction rate constants for the cracking of hexadecane was independent of pressure over the range studied (1.38–6.89 MPa). Unfortunately, they did not model the experiment or analyze the flow properties.

Similarly, Jones et al.⁵ conducted flow experiments using a mixture of *n*-alkanes (Norpar-13) pumped at a flow rate of 20 ml/min over a pressure range from 3.5–16.3 MPa. The reactor was electrically heated to produce an exit fuel temperature of 635°C. The gaseous products were collected in a bag after the fuel was cooled to room temperature and analyzed using gas chromatography. The liquid products were also analyzed by gas chromatography, but the measurements were lumped in carbon number groupings rather than differentiated as individual product species. Furthermore, a simple calculation of conversion was used and was defined as the fraction of liquid lost in the reaction region (with the final quantity of liquid being determined after cooling to room temperature). This definition of conversion ignores the liquid products and is, therefore, an inaccurate measure of conversion. Whereas they overlooked this inaccuracy due to their focus on deposition, the development of a computational model to study the flow properties of the fuel requires a more accurate definition of conversion that considers the liquid products.

The experiments of the present work study the effect of pressure on flowing *n*-decane undergoing mild-cracking reactions. Mild cracking is defined as a low conversion of *n*-decane in which the primary degradation products are smaller carbon number *n*-alkanes and 1-alkenes.^{6–8} Mild-cracking reactions of *n*-alkanes do not form aromatics in substantial quantities. Aromatics are known to increase soot and pollutant emissions during combustion, reduce the heat-absorbing potential of the reaction, and are thought to be deposition precursors.⁹ Deposition is undesirable because it can obstruct fuel pathways, resulting in catastrophic system failure. Therefore, mild-cracking reactions of *n*-alkanes are of interest in endothermic fuel systems. A single-pass heat exchanger, designed for mild-cracking reactions, could potentially provide a beneficial heat sink with minimal deposition and its associated detrimental effects. Research focused on suppressing surface deposition by use of surface coatings and additives is also ongoing.¹⁰

In this work, a two-dimensional computational fluid dynamics model is used to assist the understanding of the transport properties of the fuel. Many flow properties of interest in fuel experiments are difficult or costly to measure. Also measuring devices can sometimes interfere with the measurement of a flow property, providing erroneous data or resulting in undesirable conditions. Numerical models aid in understanding endothermic fuel experiments by simulating properties that are unavailable from measurement. Most past pyrolytic modeling efforts have involved several different types of chemical kinetics mechanisms including detailed, lumped, and global. Detailed¹¹ and lumped^{7,12} kinetic mechanisms

have generally been confined to nonflowing, analytical models. Detailed modeling of pyrolysis requires knowledge of thousands of elementary reaction pathways and rate constants, which are generally unavailable for high carbon number *n*-alkanes.¹¹ Thus, incorporation of a detailed model into multidimensional fluid dynamics problems is generally not practical. Lumped mechanisms group components of a fuel/product mixture into kinetic lumps, which are then treated as pseudocomponents. However, information about individual components comprising the product distribution is lost. Therefore, the transport properties associated with the mixture may not be adequately modeled. Most past numerical simulations of the thermal cracking of flowing jet fuel have employed global kinetic mechanisms.^{13–15} In global mechanisms, only the rate equations for the primary fuel species or components are defined. Because global mechanisms generally require fewer rate equations than detailed or lumped mechanisms, they are the most practical mechanisms for multidimensional fluid dynamics applications. However, most global models do not account for property changes due to the formation of cracked products.^{13–15}

In a previous study, we developed a new mechanism that calculated mildly cracked products based on experimentally measured proportional distributions.³ This proportional product distribution (PPD) mechanism is able to simulate chemical composition changes of a fuel as it undergoes pyrolysis. The PPD mechanism requires only one rate expression defining *n*-decane degradation. In this previous work, we demonstrated the advantages of using the PPD mechanism over a range of temperatures and flow rates, but for only one pressure, 3.45 MPa (Ref. 3). In the current work, we apply the PPD mechanism to a range of pressures to study the effect of pressure on a flowing, mildly cracked fuel.

Experimental

A set of experiments was performed to study the effect of pressure on the products of *n*-decane pyrolysis (Aldrich 99+%). *N*-decane was selected because it has a critical pressure and temperature similar to those of actual jet fuels, for example, jet-A and JP-8). Use of a pure compound avoids difficulties in differentiating specific product yields resulting from a complex mixture of reactants comprising an actual jet fuel. Studies have shown that *n*-alkanes (like *n*-decane) have product distributions that are similar to real jet fuels for experimental conditions similar to those studied in this work.¹⁶ The experimental apparatus used was the system for thermal diagnostic studies (STDS), shown in Fig. 1. The STDS consists of a thermal reaction chamber, gas chromatograph (GC) with mass spectrometer (MS), and hydrogen flame ionization detectors (FID).

The *n*-decane was sparged with gaseous helium before being pumped into the STDS to displace dissolved oxygen to prevent thermal-oxidative deposition in the heated reactor. A syringe pump was used to provide a constant flow rate through the reactor, and three different flow rates were used, 0.3, 0.5, 0.7 ml/min. The fuel was pumped into 316 stainless steel tubing (0.5 mm i.d.) and passed through a switch valve that either directed the fuel to the reactor assembly or allowed gaseous nitrogen to flow through the system (to prevent surface deposition in the reactor when not collecting data).

A series of backpressure regulators were used to obtain five different outlet pressures, 3.45, 5.17, 7.93, 9.31, and 11.38 MPa. An in-line pressure gauge was used to verify the pressure settings. The thermal reaction chamber was housed in a GC oven (Hewlett-Packard Model 5890A) kept at 200°C. The oven was used for temperature control of the fuel transfer lines into the reactor. Contained inside this oven was a smaller high-temperature furnace that completely surrounded the reactor and heated it by electrically resistive coils. The heating coils were surrounded by insulation to minimize convective heat loss to the surrounding GC oven. The reactor consisted of a continuous coiled, stainless steel fuel line (1.6 mm o.d. × 0.5 mm i.d. × 34.3 cm in length) lying inside an insulated quartz tube. The quartz tube was capped at both ends with a foam insulator to reduce convective heat loss. Six (type K) thermocouples were strap welded onto the outer wall of the reactor (Fig. 2).

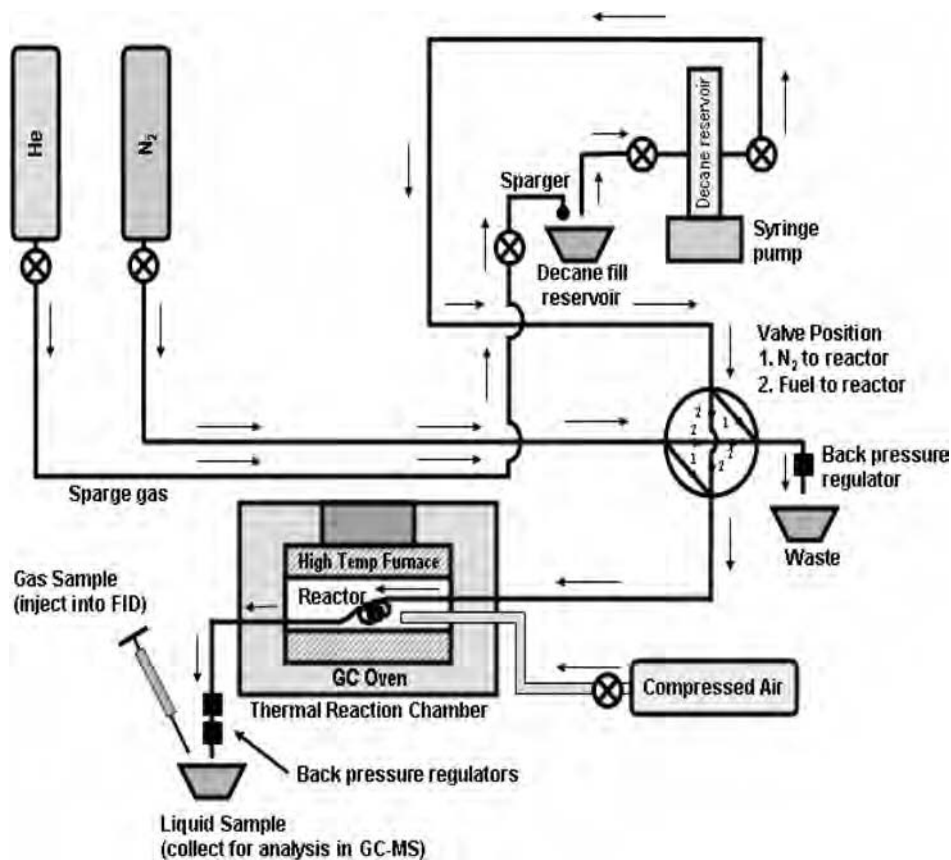


Fig. 1 STDS experimental apparatus.

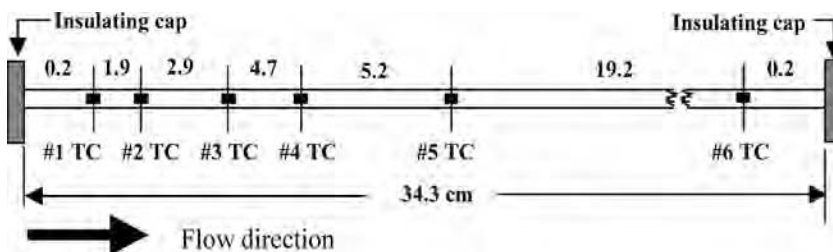


Fig. 2 Flow reactor Schematic, not to scale; all units in centimeters; thermocouples (TC) indicated.

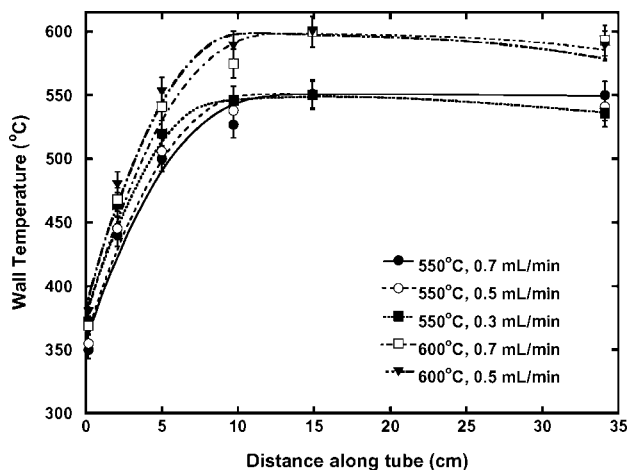


Fig. 3 Measured wall temperatures, 3.45 MPa.

The measured wall temperature profiles (uncertainty of $\pm 2^\circ\text{C}$) were used as boundary conditions for the numerical model. Two maximum wall temperature profiles were used, which had maximum temperatures of 550 or 600°C measured at the fifth thermocouple. As the fuel cracks, the endothermic reaction cools the fuel and the reactor wall. Because the magnitude of the endotherm varies with the different flow conditions, the electrical power supplied to the high-temperature furnace was adjusted (in response to different conditions) to maintain a constant maximum wall temperature (550 or 600°C) at the fifth thermocouple. Figure 3 shows the wall temperature profiles measured at a pressure of 3.45 MPa. The wall temperatures measured at the other pressure settings were similar to those shown in Fig. 3 and, thus, are not shown. The experiment was run at different flow rates for five pressure conditions and two maximum wall temperatures.

As fuel exited the reactor and cooled to room temperature, gas product samples were collected from a liquid/gas separator in a syringe and then injected into the FID. Ultrahigh purity helium (99.999%) was used as the carrier gas. The condensed-phase (liquid)

Table 1 Source terms and transport coefficients appearing in Eqs. (1) and (2)

Φ	Γ^Φ	S^Φ
u	$\mu + \mu_t$	$-\frac{\partial p}{\partial z} + \frac{\partial}{\partial z} \left(\Gamma^u \frac{\partial u}{\partial z} \right) + \frac{\partial}{\partial r} \left(\Gamma^u \frac{\partial v}{\partial z} \right) + \frac{\Gamma^u}{r} \frac{\partial v}{\partial z} + \rho g$
v	$\mu + \mu_t$	$-\frac{\partial p}{\partial r} + \frac{\partial}{\partial z} \left(\Gamma^v \frac{\partial u}{\partial r} \right) + \frac{\partial}{\partial r} \left(\Gamma^v \frac{\partial v}{\partial r} \right) + \frac{\Gamma^v}{r} \frac{\partial v}{\partial r} - 2\Gamma^v \frac{v}{r^2}$
k	$\mu + \mu_t/\sigma_k$	$G - \rho \varepsilon$
ε	$\mu + \mu_t/\sigma_\varepsilon$	$C_1 G(\varepsilon/k) - C_2 \rho(\varepsilon^2/k)$
h	$\kappa/c_p + \mu_t/\sigma_h$	0
Y_i	$\rho D_i + \mu_t/\sigma_{y_i}$	$\dot{\omega}_i$

product samples were collected for 15 min, weighed, and analyzed off-line using a GC–MS (Hewlett–Packard Model 5890A). The mass of the total gas products was determined by subtracting the weight of these liquid samples by a 15-min sample of unreacted n–decane (pumped through the STDS but unheated). The liquid and gas product fractions (determined from the GC–MS and FID, respectively) were normalized with the measured total gas and liquid product masses (for a 15-min sampling time) so that they could be directly related to one another. Once the product fractions were normalized (to the same sampling time), a product distribution including all products (gas and liquid) was calculated.

Both the FID and GC–MS were calibrated with external standards spanning the entire range of products formed in the experiment. All of the product species were quantified based on these calibrations. Six replicates of each experimental condition were performed to obtain an indication of the experimental error. The maximum standard deviation of the measured parent fuel mass fraction from all of the experimental conditions was $\pm 0.8\%$.

Computational Fluid Dynamics Simulations

The computational fluid dynamics (CFD) model is based upon the SIMPLE algorithm, which uses the Navier–Stokes turbulent energy, enthalpy, and species equations to simulate the flow and heat and mass transport within the reactor.¹⁷ The fluid motion inside the reactor was assumed to be axisymmetric and steady. The governing equations written in the cylindrical (z, r) coordinate system for axisymmetric flow are

$$\frac{\partial(\rho u)}{\partial z} + \frac{\partial(\rho v)}{\partial r} + \frac{\rho v}{r} = 0 \quad (1)$$

$$\begin{aligned} \frac{\partial(\rho u \Phi)}{\partial z} + \frac{\partial(\rho v \Phi)}{\partial r} &= \frac{\partial}{\partial z} \left(\Gamma^\Phi \frac{\partial \Phi}{\partial z} \right) + \frac{\partial}{\partial r} \left(\Gamma^\Phi \frac{\partial \Phi}{\partial r} \right) \\ &- \frac{\rho v \Phi}{r} + \frac{\Gamma^\Phi}{r} \frac{\partial \Phi}{\partial r} + S^\Phi \end{aligned} \quad (2)$$

Equation (1) is the continuity equation, and Eq. (2) represents the momentum, energy, or species equation depending on the variable represented by Φ . Here, ρ is the mixture density. Table 1 lists the transport coefficients Γ^Φ and the source terms S^Φ of the governing equations. The governing equations are discretized utilizing a second-order, central differencing scheme (except where the local Peclet number becomes greater than two, in which case a first-order upwind scheme is used). The solution was considered converged when the velocity, pressure, turbulent kinetic energy, turbulent dissipation, enthalpy, and species global error residuals were all reduced below four orders of magnitude from their maximum values.

The inlet velocity and temperature profile of the fuel are assumed to be uniform for simplicity. The inlet fuel temperature was 200°C. A wall temperature profile (obtained from measured data) was input as a boundary condition. Wall functions were used to determine the flow variables near the wall.¹⁸ Because the purpose of the model is to simulate mild thermal cracking, resulting in very low surface deposition, deposition was not modeled.

One of the salient features of the computational model is that it does not use idealized approximations such as plug flow or constant

properties. Because endothermic fuels will be expected to operate at supercritical temperatures and pressures, it is important to assess fuel behavior under supercritical conditions. Supercritical behavior occurs when both the temperature and pressure reach or exceed the critical point of the fuel. Supercritical fluids are characterized by having a low, gaslike viscosity and a high, liquidlike density. Transition from liquid phase to supercritical state may strongly influence the transport properties that ultimately determine the effects of pressure on the temperature field, reaction rates, and cooling capacity. The thermodynamic and transport properties were calculated at every grid point by incorporating SUPERTRAPP¹⁹ subroutines. SUPERTRAPP performs phase equilibrium calculations with the Peng–Robinson equation of state,²⁰ and transport properties are calculated with an extended corresponding states model. SUPERTRAPP provides well-behaved thermodynamic properties near the critical point and in the supercritical regime. However, it does not calculate the molecular diffusivity. Determination of diffusion coefficients for supercritical conditions is difficult, and there is little specific literature on the subject. In a previous work, we showed that the molecular diffusivity has a negligible effect on the reaction rate for reactions that have large activation energies (under conditions similar to those in this work).³ Stewart¹⁴ showed that for most supercritical fluid flow applications the diffusion coefficient is of the order of 10^{-7} m²/s. Liquids generally have a diffusion coefficient of the order 10^{-8} m²/s. In our experiment, the fluid transitions from an initial compressed liquid state into a supercritical fluid. Therefore, the diffusion coefficient was set to a constant value of 10^{-8} m²/s where the fluid is subcritical and 10^{-7} m²/s where the fluid is supercritical.

Several simulations of flow through the reactor (0.5 mm i.d. and 34.3 cm in length) were performed using different grid densities ($z \times r$): 80×15 and 200×25 . A comparison of the results obtained from the two grids indicated a negligible (less than 0.5%) difference in the bulk fuel temperature and reaction rate calculations. Because the 200×25 grid runs took five times longer to execute than the 80×15 grid and resulted in a negligible accuracy gain, all subsequent solutions were calculated using the 80×15 grid.

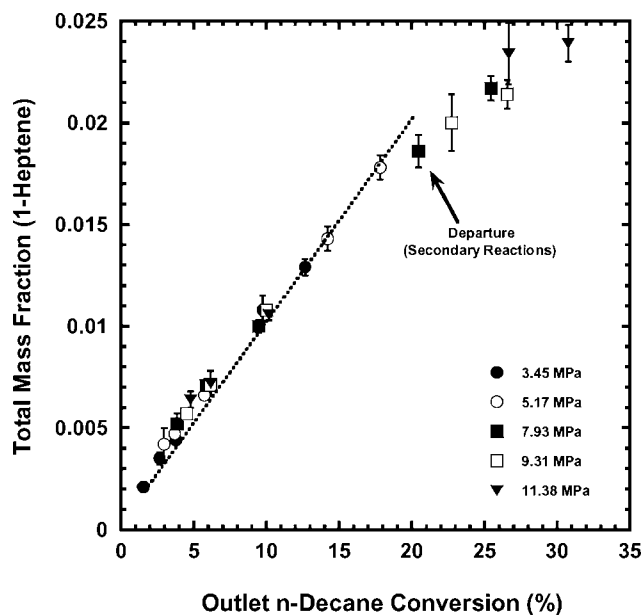
The formation of products from cracking n–decane is calculated using a PPD mechanism.³ The PPD mechanism is based on the observation that for mild cracking of n–alkanes each product forms at a constant proportion with respect to the other products. Therefore, it is possible to predict the mass fractions of the cracked products formed by taking advantage of these PPDs. However, in our previous work, the PPD mechanism was only validated for one pressure condition.³ Qualifying the expansion of the PPD mechanism to a range of pressures is an objective of the present work. The product mass fraction of species i (y_i) is measured from the experimental data,

$$y_i = Y_i / Y \sum_{\text{products}} \quad (3)$$

Equation (3) represents the fraction of species i of the sum of the products (excluding the parent fuel). By the PPD assumption, y_i remains approximately constant (small variations due to experimental uncertainty) over a range of n–decane conversions. The arithmetic average of several y_i , measured from different experimental conditions (n–decane conversions), is calculated to obtain species product distributions that can be used over the range of conversions

Table 2 Arrhenius rate constants used in the CFD calculations, n-decane, C₁₂H₂₆

Model	E_a , k cal/mol	A , s ⁻¹
Present ^a	63	1.6×10^{15}
Stewart et al. ^{21b}	64 ± 2.4	$1.10 \times 10^{15.9 \pm 1.5}$
Ward et al. ^{3c}	63	2.1×10^{15}

^a $P = 3.45$ – 11.38 MPa and $T = 550$ – 600°C .^b $P = 2.96$ MPa and $T = 440$ – 535°C .^c $P = 3.45$ MPa and $T = 500$ – 600°C .**Fig. 4** Measured 1-heptene formation.

considered. In Eq. (3), Y_i is the individual product species fraction of the total fuel mixture (including the parent fuel). It can be calculated by multiplying the total product mass fraction by the average product fractions of each individual species, y_{iav} ,

$$Y_i = (1.0 - Y_{RH}) \cdot y_{iav} \quad (4)$$

One rate expression is used to predict the conversion of n-decane into products [Eq. (5)]. RH denotes the concentration of the parent fuel,

$$-\frac{d(RH)}{dt} = k_A[RH] \quad (5)$$

The rate constant k_A for the reaction of Eq. (5) is expressed in the Arrhenius form:

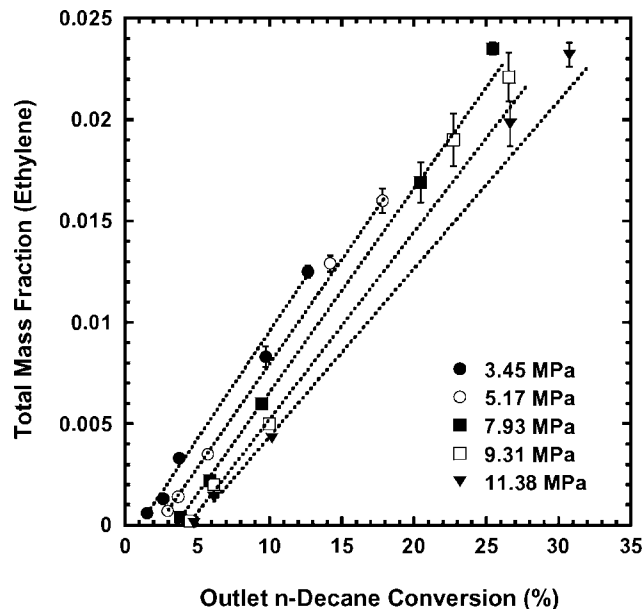
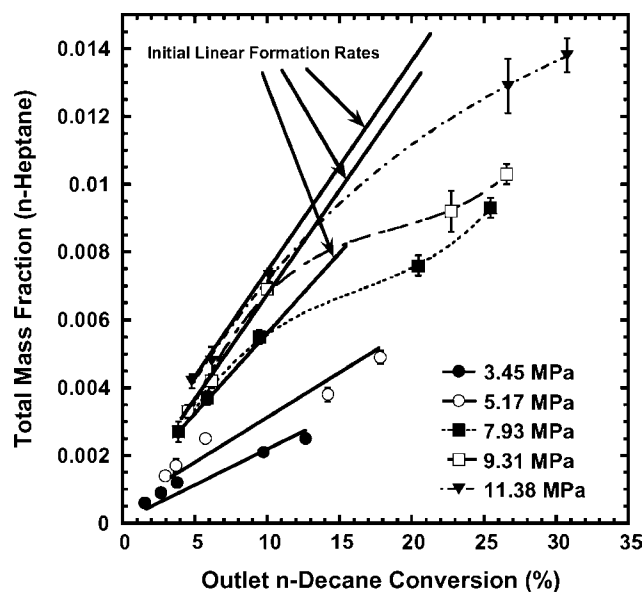
$$k_A = A \cdot \exp(-E_a/RT) \quad (6)$$

Table 2 shows the rate constants used in the simulations.

Therefore, the PPD mechanism described in Eqs. (3–6) is capable of calculating the chemical composition of a fuel as it cracks using only one rate expression governing the degradation of the parent fuel (n-decane).

Results and Discussion

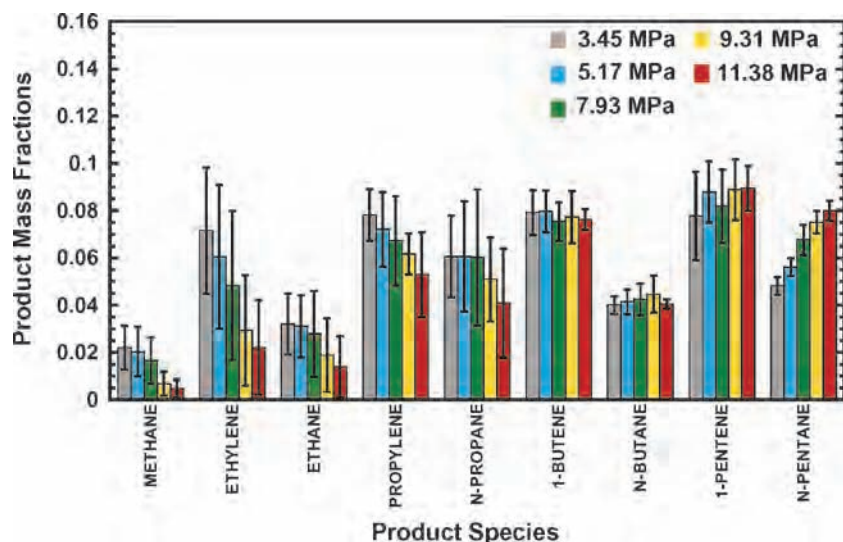
It has been observed that, for mild-cracking reactions of n-hexadecane, the first-order rate constant was independent of pressure over the ranges studied,⁴ 1.38–6.89 MPa. To examine whether this observation would be true for n-decane as well, the same set of rate constants were used in simulating the measurements over every pressure, temperature, and flow rate condition. The rate constants used to predict n-decane conversion are within the error bounds of those determined from flow reactor experiments at similar experimental

**Fig. 5** Measured ethylene formation.**Fig. 6** Measured n-heptane formation.

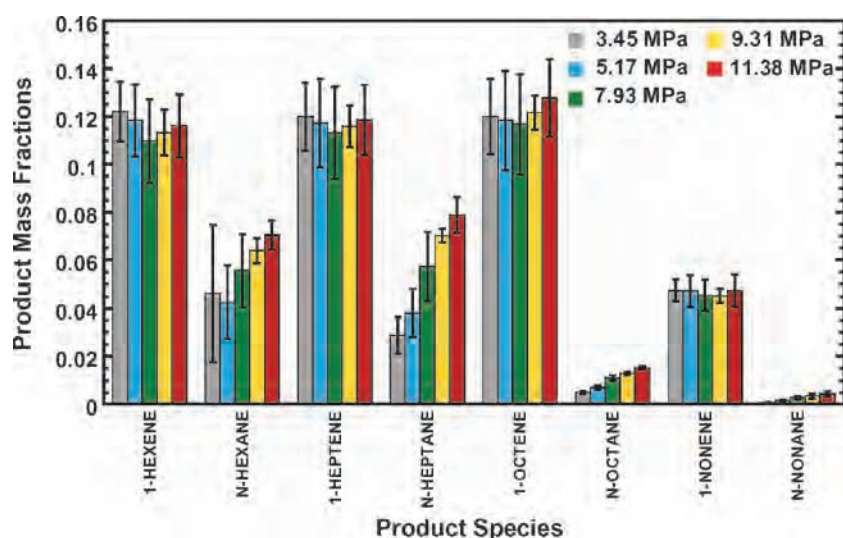
conditions. Because the rate constants were used to predict conversions at different conditions than the literature values, a small variation from the mean literature values was required. Table 2 shows that the rate constants used in this work are similar to that used in our previous work.³ (E_a is identical.) The A factor was slightly changed (but still within the error bounds of Table 2) for better agreement between the results and the experimental measurements.

The PPD mechanism has previously been defined as valid for mild-cracking conditions only. This is because significant secondary cracking of the initial products will cause the product distribution to become nonproportional.³ Therefore, it is important to determine the percent of n-decane conversion at which secondary cracking becomes significant. Figures 4–6 show the measured formation of several selected products with increased conversion of n-decane (obtained by varying the wall temperature, flow rate, and pressure). The selected products are representative of three behavior classes of products: C₄–C₉ n-alkane products (represented by 1-heptane), C₁–C₃ products (represented by ethylene), and C₄–C₉ 1-alkene products (represented by 1-heptene).

Figure 4 shows that 1-heptene initially forms at a linear rate as the conversion of n-decane increases, regardless of the pressure.



a)



b)

Fig. 7 PPDs for varying pressures, constant pressure PPDs: a) C_1 – C_5 products and b) C_6 – C_9 products.

However, at a conversion of approximately 20%, 1-heptene deviates from the initial linear formation rate. This indicates that, at conversions greater than 20%, a portion of the 1-heptene initial product is cracking into smaller secondary products. This is the same conversion where secondary cracking was first observed in previous n-decane experiments³ at a pressure of 3.45 MPa.

Figure 5 shows that, for conversions of less than 20%, ethylene also forms at a linear rate. However, for conversions greater than 20%, the measured ethylene begins to exceed the initial linear rate. The additional ethylene is likely formed from secondary cracking of higher carbon number initial products.³ Figure 5 shows that increasing pressure tends to decrease the amount of n-decane conversion to ethylene. The strong influence of pressure on formation rate of ethylene shown in Fig. 5 contrasts greatly with the weak influence pressure has on the formation of 1-heptene in Fig. 4.

Contrary to the linear formation rates observed in Fig. 4, the linear formation rates of ethylene in Fig. 5 do not extrapolate through the origin. This is because ethylene is primarily formed from the unimolecular decomposition of radicals resulting from the initial n-decane decomposition. At higher pressures, these radicals are more likely to react via bimolecular reactions, which do not form ethylene. Thus, the linear formation rates move away from the origin at higher pressures.

Similar to Figs. 4 and 5, Fig. 6 shows that the formation rate of n-heptane is approximately linear for n-decane conversions less

than 20%. However, as the conversion of n-decane becomes greater than 20%, the formation of n-heptane decreases, indicating that it is cracking into secondary products. Figure 6 also shows that increasing pressure significantly increases the formation of n-heptane.

Figures 4–6 indicate that significant secondary cracking occurs for n-decane conversions greater than 20%. Therefore, because of the mild-cracking assumption, the PPD mechanism loses validity for simulations involving n-decane conversions greater than 20%.

Figures 7a and 7b show the PPD obtained from the measured data [Eq. (3)] for each pressure. (Product distributions measured beyond the 20% limit were not averaged into the PPD models.) The error bars represent the standard deviation of the product mass fraction over each temperature and flow rate condition for a constant pressure. Figures 4–7 indicate that as pressure increases the C_4 – C_9 n-alkane products, for example, 1-heptane, form in greater proportions, whereas the smaller C_1 – C_3 products, for example, ethylene, proportionally decrease, and the formation of C_4 – C_9 1-alkene products, for example, 1-heptene, remains relatively constant. Previous experiments have shown similar results with increasing pressure.^{4,5} In both Refs. 4 and 5, an increased pressure increased the percentage of higher molecular weight normal alkane products at the expense of lower molecular weight products. This behavior can be better understood by considering the mechanism developed by Kossiakoff and Rice,²² which describes the decomposition of hydrocarbons through a series of free radical reactions.

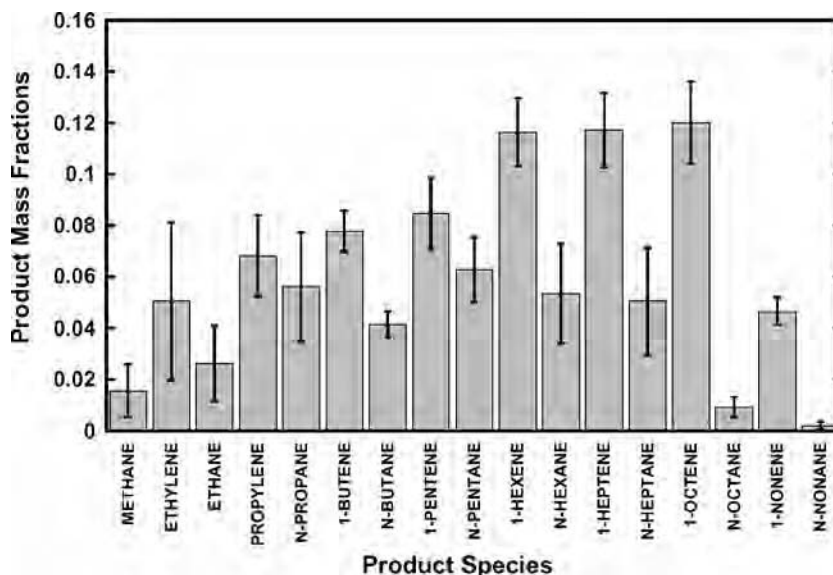
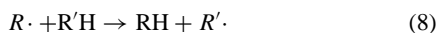


Fig. 8 Averaged PPD over all of the pressures, general PPD.

Initiation:



Bimolecular reaction:



Unimolecular reaction:



Equation (7) shows that decomposition initiates by a carbon-carbon bond fission along the parent n-alkane chain (RH) to form radicals ($R\cdot$). The radicals can then either react through bimolecular [Eq. (8)] or unimolecular reactions [Eq. (9)]. In a bimolecular reaction, the radicals abstract hydrogen atoms from surrounding molecules to form an n-alkane (RH) and another radical ($R'\cdot$). In a unimolecular reaction, $R\cdot$ decomposes by a β -scission reaction to form an alkene and a smaller radical ($R''\cdot$). The radicals formed can then repeat the reaction processes, shown in Eqs. (8) and (9), resulting in alkene and n-alkane products of different chain lengths. Pressure increases the molecular collision frequency, which enhances bimolecular processes more than the unimolecular processes. Thus, as pressure increases, more n-alkanes are produced relative to alkenes.

Because Figs. 7a and 7b show that the product distribution changes with pressure, one might presume the necessity of defining a different PPD model for each constant pressure. It would be more generally applicable if only one PPD could be defined over a range of pressures. Figures 7a and 7b show that the C_4 – C_9 1-alkene products form in greater proportions and vary less (nearly constant) with pressure relative to the other products. This observation suggests that a general PPD model (for a range of pressures) could be constructed by averaging the measured product fractions over the entire pressure range studied in the experiment, 3.45–11.38 MPa. The primary source of error of this general PPD model will be caused by averaging over the pressure-varying C_4 – C_9 n-alkane and C_1 – C_3 products. It is worth exploring if this error is acceptably small enough to provide a general PPD model that reasonably represents the behavior observed in the current experiments.

Figure 8 shows a new general PPD obtained by averaging all five of the constant pressure product distributions shown in Figs. 7a and 7b. Because ethylene experiences the greatest relative change over the range of pressures used in the experiment (Fig. 7a), it can be used to estimate the maximum error that this general PPD model

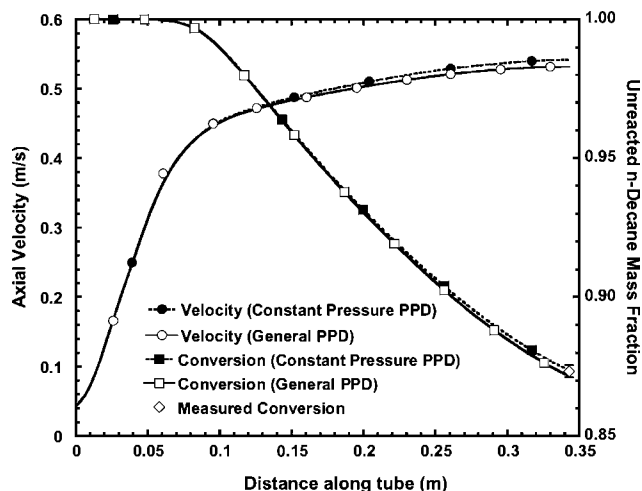


Fig. 9 Flow property calculation comparison between a constant pressure, 3.45 MPa, PPD and a general PPD mechanism.

(Fig. 8) will have in predicting a single product. Previous pyrolysis experiments also showed that ethylene underwent the largest product formation change with varying pressure.⁵ A comparison of the ethylene distribution in Fig. 7a (for both pressure extremes of 3.45 and 11.38 MPa) to the averaged ethylene distribution in Fig. 8 shows a maximum difference of 42%. Although this difference would be significant in isolation, it represents a difference of only 2.1% relative to the total product mixture. Also, the averaged ethylene distribution (Fig. 8) lies within the error bars of the measured ethylene for every pressure condition (Fig. 7a), with just one exception. (The upper error bar for 11.38 MPa in Fig. 7a falls just 0.005 under the average distribution.) Therefore, the general PPD model may be worth further investigation.

The maximum species mass fraction difference between any of the constant pressure PPDs (Fig. 7) and the general PPD (Fig. 8) occurs at 3.45 MPa. Figure 9 shows a comparison between the calculated axial velocities and n-decane mass fractions using the constant pressure (3.45 MPa) and general PPD models. The intent of Fig. 9 is to show the difference in the results obtained by using the general PPD model compared to the constant pressure PPD model. The axial velocity and n-decane mass fraction were selected for Fig. 9 because they are good indicators of differences in the flow property and cracking reaction results, respectively. The

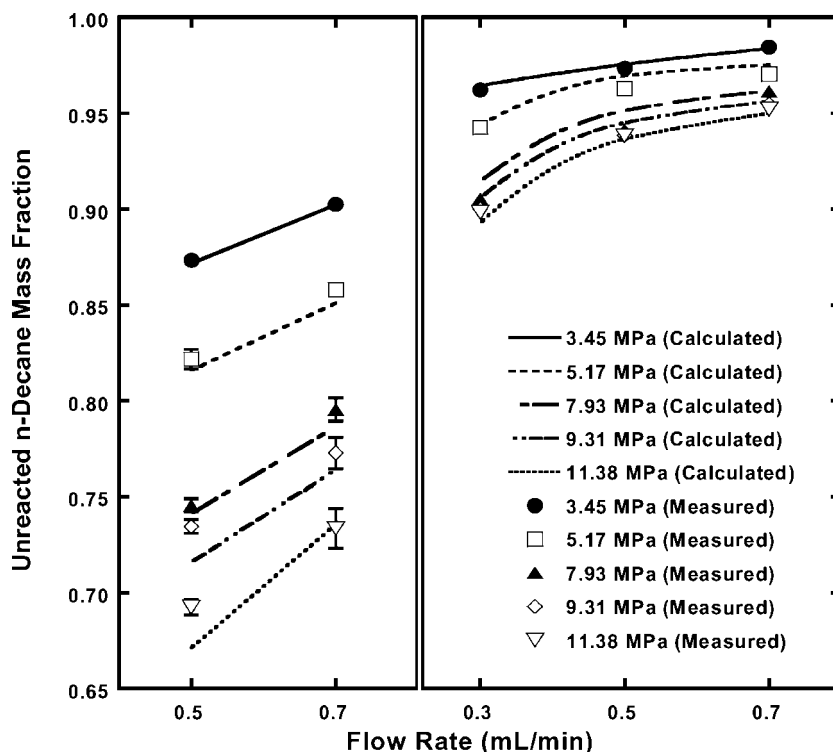


Fig. 10 Comparison of measured and simulated (general PPD) outlet unreacted n-decane mass fraction, maximum wall temperature a) 600°C and b) 550°C.

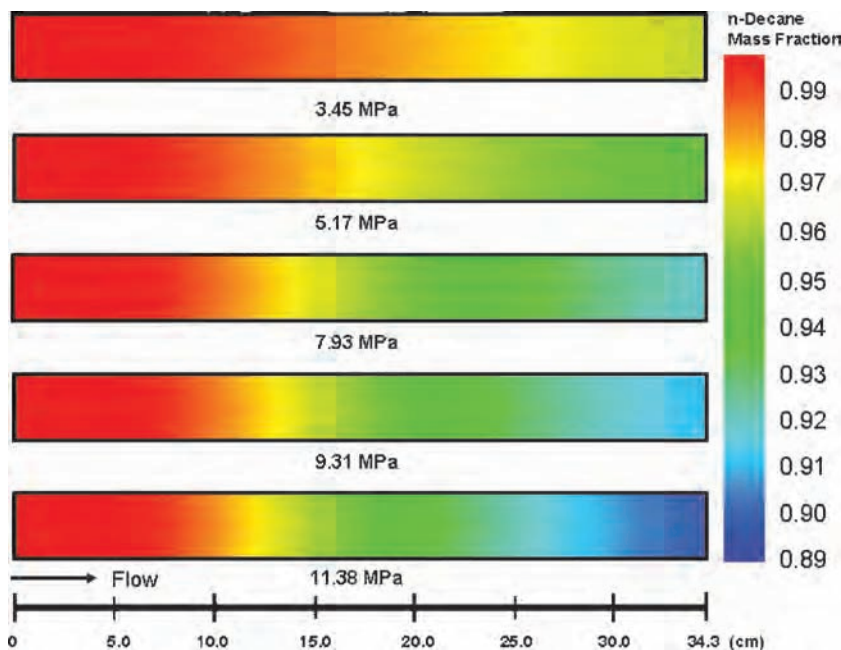


Fig. 11 Pressure effects on calculated n-decane mass fraction, two-dimensional plot.

experimental conditions (maximum wall temperature of 600°C and flow rate of 0.5 ml/min) of Fig. 9 correspond to maximum conversion at 3.45 MPa. Figure 9 shows that both n-decane conversion calculations agree closely (within the error bounds) of the measured outlet n-decane conversion. The maximum difference between the two predicted n-decane conversions is less than 0.25% conversion. The axial velocity calculations also agree reasonably well with a maximum difference of 1.8%. Because the n-decane conversion and velocity calculations do not vary appreciably using the general PPD relative to the constant pressure PPD, we conclude that the error

associated with the general PPD is within an acceptable tolerance, for our purposes, over the range of pressures studied. The general PPD model will now be used to study the behavior of pyrolytic fuel flow at varying pressures.

Figure 10 shows a comparison of the measured outlet n-decane conversion to the simulated results (general PPD model). Figure 10 shows that, as pressure increases, the conversion of n-decane also increases. The simulation agrees with the measured values within approximately $\pm 1\%$ (conversion), at conversions less than 20% (within the PPD mechanism accuracy limit). At conversions greater

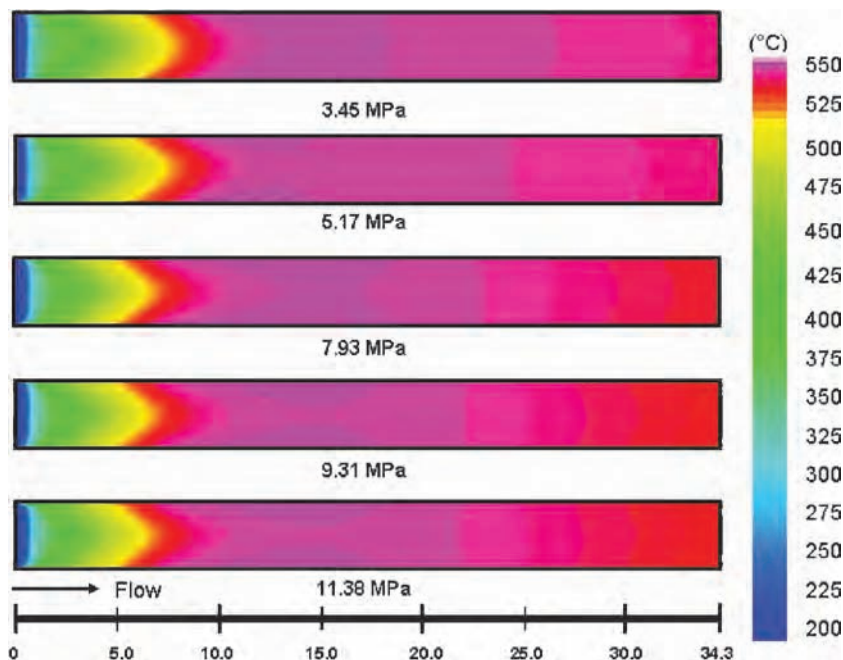


Fig. 12 Pressure effects on calculated fuel temperature, two-dimensional plot.

than 20%, the differences between calculated and measured values gradually increases as the conversion increases, possibly due to increased formations of products from secondary reactions.³ Figure 10 also shows that the effect of increased *n*-decane conversion with pressure is primarily due to factors other than a change in the rate constant. Because k_A was held constant in Eq. (5), the change in conversion rate must primarily be influenced by changes in the flow properties with pressure. A closer examination of the computed flow properties can assist in understanding the effect of pressure on conversion.

Figure 11 shows the calculated mass fraction of *n*-decane as it flows through the reactor at different pressures but at the same maximum wall temperature, 550°C, and flow rate, 0.3 ml/min. These conditions were selected because they yield the maximum conversion in the experiment, while still below the PPD conversion limitation for every pressure (Fig. 10). Because the same rate constants and input conditions (wall temperature and flow rate) were used for every simulation in Fig. 11, the change in the reaction rate is only due to the effects of pressure. Figure 11 shows that varying pressure does not significantly affect the radial mass fraction profile but dramatically affects the axial profile.

Figure 12 shows calculated fuel temperature as it flows through the reactor at the same conditions as Fig. 11. In both the experiment and the simulation, a constant wall temperature profile was input, regardless of pressure or flow rate. In the experiment, the heating source was adjusted to attain the same maximum wall temperature (550 or 600°C). Because the wall temperature and flow rate are held constant, the fuel temperature will only vary due to pressure induced effects.

Figure 12 shows that the fuel temperature reaches its peak and levels off at approximately 10 cm along the reactor for each pressure condition. However, as pressure increases, resulting in an increase in *n*-decane conversion (Fig. 11), the fuel cools more due to the higher endotherm generated by the pyrolytic reactions.

Several flow properties were examined (at the same conditions as Figs. 11 and 12, maximum wall temperature of 550° and flow rate of 0.3 ml/min) to determine which properties are most affected by pressure and their influence on the decomposition of *n*-decane. Figures 13–16 show the change in the bulk fuel temperature and several bulk flow properties as pressure varies. The bulk values are calculated by averaging properties at each grid point across the radial length of the reactor.

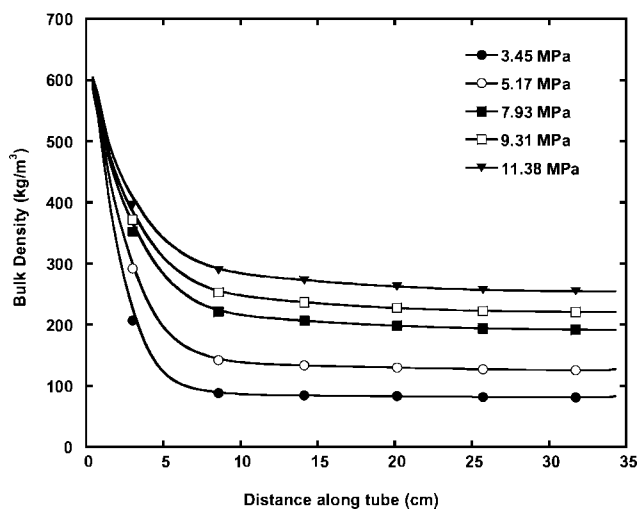


Fig. 13 Pressure effects on calculated bulk density.

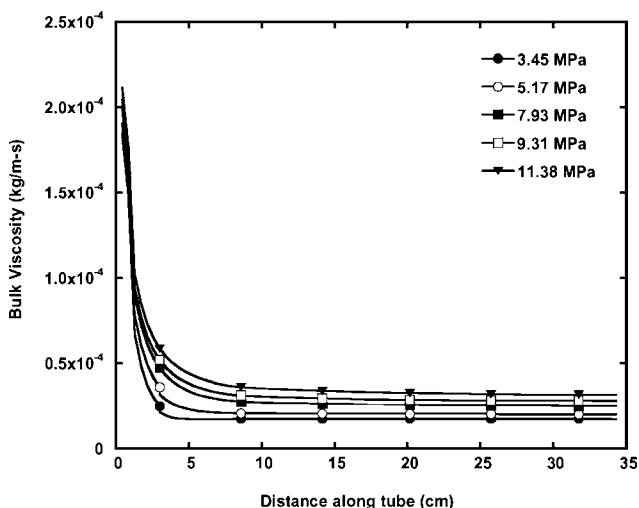


Fig. 14 Pressure effects on calculated bulk viscosity.

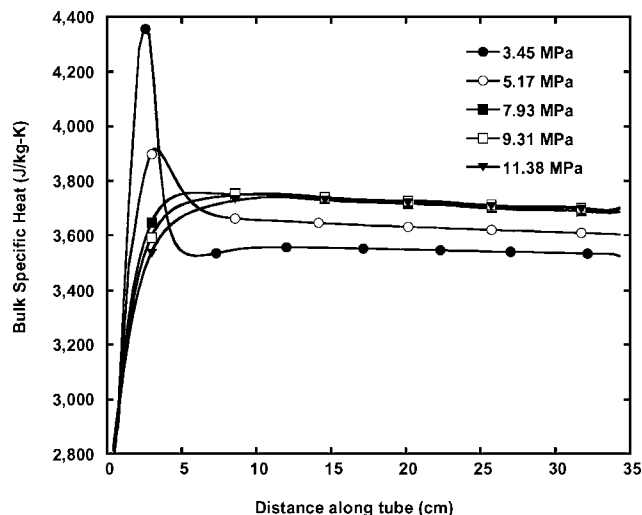


Fig. 15 Pressure effects on calculated bulk specific heat.

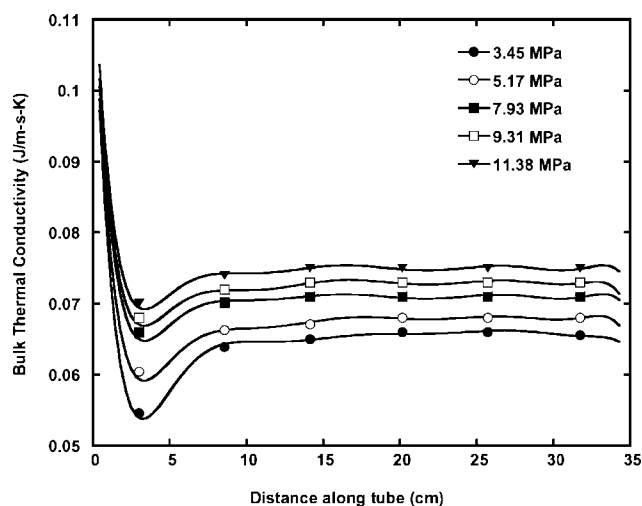


Fig. 16 Pressure effects on calculated bulk thermal conductivity.

Figure 13 shows that the bulk density is significantly affected by pressure changes. When only the portion of the tube after 10 cm is considered, density increases by about 200%, as pressure increases from 3.45 to 11.38 MPa. Figure 17 shows the calculated dimensionless density of the fuel and demonstrates that increasing pressure inhibits reduction of the fuel density within the reactor. By conservation of mass, as density increases, the velocity will decrease. Because velocity is proportional to residence time (which directly affects the extent of conversion), an increased density increases the conversion rate. However, conversion of *n*-decane into lighter cracked products also decreases the density. Density and the chemical decomposition of the reaction mixture are closely coupled.

Figure 14 shows (after 10 cm along the reactor) that the bulk viscosity increases by 60% over the range of pressures studied. An increased viscosity increases the residence time and, therefore, the heat transfer rate of flow near the walls. This observation justifies the use of a two-dimensional simulation. (A plug flow simulation is not capable of simulating property changes in the radial direction.)

At the critical point, the specific heat diverges and approaches infinity. In the vicinity of the critical point, the specific heat can be much larger than its subcritical or supercritical value. In Fig. 15 the specific heat for the pressure of 3.45 MPa initially rises and peaks at 3 cm along the reactor, which corresponds to the fuel's closest approach to the critical point, for *n*-decane $P_c = 2.10$ MPa and $T_c = 345^\circ\text{C}$. At this point, there is a 20% difference between the specific heat (for 3.45 MPa) and the specific heats corresponding to the higher pressures (7.93, 9.31, and 11.38 MPa). The specific heat (for 3.45 MPa) then declines as the fuel transitions from a compressed liquid to a supercritical fluid. After 10 cm along the tube, the difference between all of the specific heats (over the entire range of pressures) declines to only 7%. The specific heat (for 5.17 MPa) also peaks (at approximately the same point along the reactor) but below the specific heat peak (for 3.45 MPa). As pressures increases and moves away from the critical point (7.93, 9.31, and 11.38 MPa), the peaks disappear.

Figure 16 shows the variation of thermal conductivity along the reactor. At the critical point, the thermal conductivity approaches zero. In the vicinity of the critical point, the thermal conductivity can be much smaller than its subcritical or supercritical values. Figure 10e shows that the thermal conductivity declines and reaches a minimum point at 3 cm along the reactor (closest approach to the critical point). At these minima, there is a 20% difference in the thermal conductivities over the range of pressures. However, after

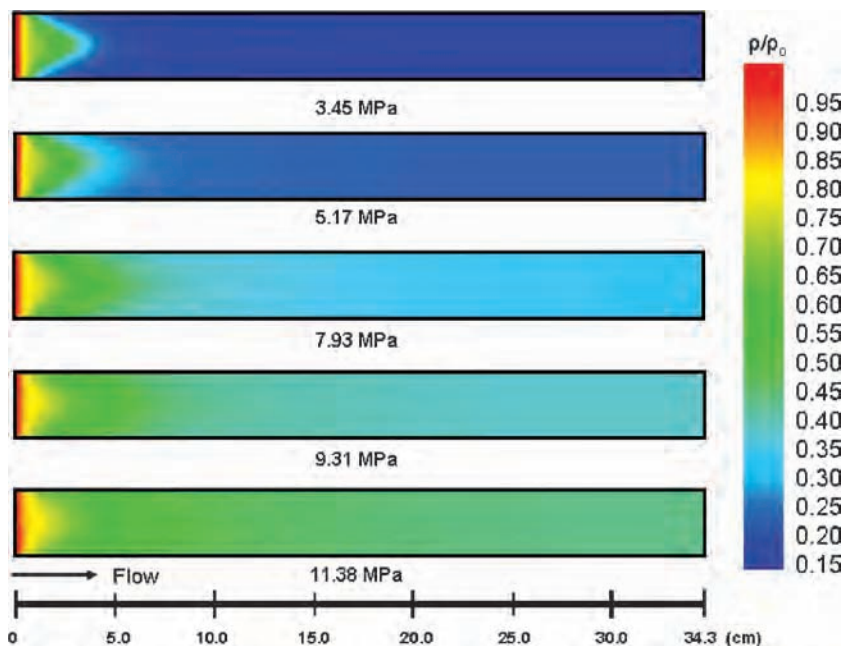


Fig. 17 Pressure effects on calculated fuel density, two-dimensional plot. (Maximum Wall Temperature: 550°C , Flow Rate: 0.3 mL/min).

10 cm along the tube, the bulk thermal conductivity changes by only 7% over the range of pressures. Figures 15 and 16 illustrate the importance of incorporating SUPERTRAPP into the CFD model to simulate accurately the flow properties near the critical point and in the supercritical region.

The effect of pressure on the endothermic heat sink (at the same conditions as Figs. 11–17) is shown in Fig. 18. The change in enthalpy of the fuel due only to the endothermic chemical reactions, Δh_{endo} , was calculated by

$$\Delta h_{\text{endo}} = h_{\text{tot}} - h_{\text{sens}} \quad (10)$$

In Eq. (10), enthalpy changes due only to sensible heat transfer h_{sens} are subtracted from the total enthalpy h_{tot} . The sensible enthalpy h_{sens} was obtained by running the CFD simulation without the cracking chemistry. The total enthalpy h_{tot} was obtained by running the simulation with the PPD chemistry mechanism and, therefore, includes the effects of both sensible heat transfer and the endothermic chemical reactions.

Figure 18 shows that as pressure increases the endothermic heat sink increases. The cracked products have a higher enthalpy than the n-decane parent fuel. As more products form, the overall enthalpy of the fuel mixture increases. Because increasing pressure increases the amount of cracked products formed (Fig. 10), increasing pressure also increases the endothermic heat sink. Figure 18 also shows that each of the Δh_{endo} curves peak before the end of the reactor. This is because the fuel cools as a result of the endothermic heat sink, which in turn cools the reactor wall. This can be seen in Fig. 3. As the wall cools, the heat transfer rate into the fuel declines, and therefore, the enthalpy decreases.

Figure 18 also shows a small peak in the heat sink curves near the beginning of the reactor (before 10 cm). This peak is not due to an endotherm, but is most likely just an anomaly caused by proximity of the fuel properties to the critical point. Near the beginning of the reactor, only a very small amount of fuel (near the wall) is cracked. Therefore, in this region, there should be very little difference between the flow properties of the reacting and nonreacting fuel flow simulations and the calculated endothermic heat sink should essentially be zero [Eq. (10)]. However, near the critical point, small differences in the flow properties can have a large effect on the enthalpy of the fuel. The variations of the two enthalpies in Eq. (10) (which each have slightly different flow properties due to the PPD mechanism being on or off) near the critical point are the most likely cause of the anomaly. As the flow properties of the fuel move away from the critical point, this anomaly vanishes (after 10 cm along the tube).

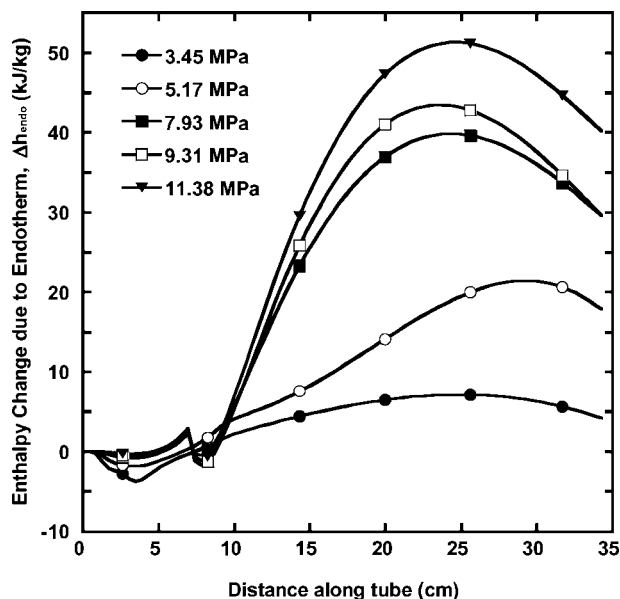


Fig. 18 Pressure effects on the calculated endothermic heat sink.

Table 3 Calculated heat transfer rates^a

Pressure, MPa	Q_{tot} , W	Q_{sens} , ^b W	Q_{endo} , ^c W
3.45	3.578	4.907	-1.329
5.17	3.566	4.941	-1.375
7.93	3.563	4.990	-1.427
9.31	3.544	5.012	-1.468
11.38	3.567	5.043	-1.477

^aMaximum wall temperature = 550°C and flow rate = 0.3 ml/min.

^bNo reactions.

^c $Q_{\text{tot}} - Q_{\text{sens}}$.

Table 3 shows calculated heat transfer rates of the simulations shown in Fig. 18. The calculations were done using a first-law analysis of the entire tube under conditions of steady flow. Bulk properties were used to simplify the calculation. The total endothermic heat transfer rate Q_{endo} was obtained by

$$Q_{\text{endo}} = Q_{\text{tot}} - Q_{\text{sens}} \quad (11)$$

Equation (11) is similar to Eq. (10). The sensible heat transfer Q_{sens} was calculated by using flow properties obtained from running the CFD simulation with the cracking chemistry mechanism disengaged. The total heat transfer Q_{tot} was calculated by using flow properties obtained from running the simulation with the PPD chemistry mechanism engaged and, therefore, includes the effects of both sensible heat transfer and the endothermic chemical reactions.

Table 3 shows that sensible heat transfer Q_{sens} is higher than the total heat transfer Q_{tot} . This is because the endothermic cracking reactions cool the fuel. Because the reactor wall is heated by the furnace at a constant rate, there is no additional heat to balance the cooling from the fuel as it reacts, and so the reactor wall cools. Table 3 shows that, as pressure increases, the total endotherm Q_{endo} also increases due to increased cracked products (Fig. 10). In this experiment, the magnitude of Q_{endo} is relatively small because the diameter of the reactor is very small, 0.5 mm i.d. Larger diameter tubes would have the potential to yield significantly higher endotherms.

Pressure affects both the reaction rates and the flow properties. The interaction among the properties is complex and coupled. All of the flow properties examined in Figs. 13–16 were affected by pressure and influenced the fuel's chemical kinetics. Density appears to be the most significant property because it increased by 200% over the 3.45–11.38 MPa pressure range. Viscosity is also significant because it increased by 60% over the pressure range. The specific heat and thermal conductivity were least significant because both increased by only 7% over the pressure range. The coupling of the chemical kinetics and flow properties illustrates the importance of simulating their complex interactions in a multidimensional CFD model. The observation that increasing pressure influences the conversion rate of the fuel implies possible applications to an endothermic heat exchanger system. Backpressure valves could potentially be used to throttle the pressure to attain a desired conversion rate and endotherm. These valves could potentially be controlled via a feedback loop to ensure that the fuel does not surpass mild-cracking limitations to ensure minimum surface deposition. It is believed that a multidimensional CFD simulation, using the techniques presented in this work, could be an invaluable tool in the design of future endothermic fuel systems.

Conclusions

The use of endothermic fuels is a promising alternative to meet the growing high-heat-sink requirements of future high-performance aircraft. However, little work has been done to analyze the effects of pressure on a chemically reacting, flowing fuel. The experiments performed in this work show that increasing pressure enhances the processes in which n-decane converts to (C₅–C₉) n-alkane products instead of decomposing into lower molecular weight products (C₁–C₄). A two-dimensional CFD model was developed that predicts the formation of pyrolysis products by using experimentally derived PPDs. It was shown that a general PPD mechanism could

be defined to simulate fuel pyrolysis over a range of pressures, temperatures, and flow rates. The model was used to simulate the effect of pressure on the complex coupling of the mass and transport properties involved with supercritical chemically reacting fuels. It was shown that increasing pressure increases the overall conversion rate (and, therefore, the endotherm) of flowing, supercritical n-decane. This is primarily because pressure increases the density, which decreases the residence time of n-decane flowing through the reactor. It is anticipated that this model could serve as a building block to computational models involving more complex endothermic fuels and cooling systems.

Acknowledgments

This work was supported by the U.S. Air Force National Aerospace Fuels Research Complex (AFRL/PRTG) at Wright-Patterson Air Force Base, Ohio; the University of Dayton Research Institute (under Contract F33615-03-2-2347); and the Dayton Area Graduate Studies Institute.

References

- ¹Sobel, D. L., and Spadaccini, L. J., "Hydrocarbon Fuel Cooling Technologies for Advanced Propulsion," *Journal of Engineering for Gas Turbines and Power*, Vol. 119, No. 2, 1997, pp. 344–351.
- ²Heinrich, B., Luc-Bouhali, A., Ser, F., and Vigot, C., "Endothermic Liquid Fuels: Some Chemical Considerations on the Cooling Process," AIAA Paper 2001-1785, April 2001.
- ³Ward, T. A., Ervin, J. S., Striebich, R. C., and Zabarnick, S., "Simulations of Flowing Mildly Cracked Normal Alkanes Incorporating Proportional Product Distributions," *Journal of Propulsion and Power*, Vol. 20, No. 3, 2004, pp. 394–402.
- ⁴Fabuss, B. M., Smith, J. O., Lait, R. I., Borsanyi, A. S., and Satterfield, C. N., "Rapid Thermal Cracking of n-Hexadecane at Elevated Pressures," *Industrial and Engineering Chemistry Process Design and Development*, Vol. 1, 1962, pp. 293–299.
- ⁵Jones, G. E., Balster, L. M., and Balster, W. J., "Effect of Pressure on Supercritical Pyrolysis of n-Paraffins," *Proceedings of the Symposium on General Papers Division of Petroleum Chemistry*, American Chemical Society, 1999, pp. 394–397.
- ⁶De Witt, M. J., and Broadbelt, L. J., "Binary Interactions between Tetradecane and 4-(1-Naphthylmethyl) Bibenzyl During Low- and High Pressure Pyrolysis," *Energy and Fuels*, Vol. 13, 1999, pp. 969–983.
- ⁷Nigam, A., and Klein, M. T., "A Mechanism-Oriented Lumping Strategy for Heavy Hydrocarbon Pyrolysis: Imposition of Quantitative Structure-Reactivity Relationships for Pure Components," *Industrial and Engineering Chemistry Research*, Vol. 32, 1993, pp. 1297–1303.
- ⁸Ranzi, E., Dente, M., Pierucci, S., and Biardi, G., "Initial Product Distributions from Pyrolysis of Normal and Branched Paraffins," *Industrial and Engineering Chemistry Fundamentals*, Vol. 22, 1983, pp. 132–139.
- ⁹Bozzano, G., Dente, M., Faravelli, T., and Ranzi, E., "Fouling Phenomena in Pyrolysis and Combustion Process," *Applied Thermal Engineering*, Vol. 22, 2002, pp. 919–927.
- ¹⁰Ervin, J. S., Ward, T. A., Williams, T. F., and Bento, J., "Surface Deposition within Treated and Untreated Stainless-Steel Reactors Resulting from Thermal-Oxidative and Pyrolytic Degradation of Jet Fuel," *Energy and Fuels*, Vol. 17, No. 3, 2003, pp. 577–586.
- ¹¹Lindstedt, R. P., and Maurice, L. Q., "Detailed Chemical-Kinetic Model for Aviation Fuels," *Journal of Propulsion and Power*, Vol. 16, 2000, pp. 187–195.
- ¹²Liguras, D. K., and Allen, D. T., "Comparison of Lumped and Molecular Modeling of Hydrolysis," *Industrial and Engineering Chemistry Research*, Vol. 31, 1992, pp. 45–53.
- ¹³LinhBao, T., and Chen, L. D., "Heat Transfer Calculation of an Endothermic Fuel at Supercritical Conditions," AIAA Paper 98-3762, July 1998.
- ¹⁴Stewart, J. F., "Supercritical Pyrolysis of the Endothermic Fuels Methylcyclohexane, Decalin, and Tetralin," Ph.D. Dissertation, Princeton Univ., Princeton, NJ, June 1999.
- ¹⁵Goel, P., and Boehman, A. L., "Numerical Simulation of Jet Fuel Degradation in Flow Reactors," *Energy and Fuels*, Vol. 14, 2000, pp. 953–962.
- ¹⁶Huang, H., Sobel, D. R., and Spadaccini, L. J., "Endothermic Heat-Sink of Hydrocarbon Fuels for Scramjet Cooling," AIAA Paper 2002-3871, July 2002.
- ¹⁷Patankar, V. S., *Numerical Heat Transfer and Fluid Flow*, McGraw-Hill, New York, 1980.
- ¹⁸Lauder, B. E., and Spalding, D. B., "The Numerical Computation of Turbulent Flows," *Computer Methods in Applied Mechanics and Engineering*, Vol. 3, 1974, pp. 269–289.
- ¹⁹Ely, J. F., and Huber, M. L., *NIST Standard Reference Database 4—NIST Thermophysical Properties of Hydrocarbon Mixtures*, Ver. 3.0, National Inst. of Standards and Technology, Gaithersburgh, MD, Oct. 1999.
- ²⁰Peng, D., and Robinson, D. B., "A New Two-Constant Equation of State," *Industrial and Engineering Chemistry Fundamentals*, Vol. 15, 1976, pp. 59–64.
- ²¹Stewart, J., Brezinsky, K., and Glassman, I., "Supercritical Pyrolysis of Decalin, Tetralin, and N-Decane at 700–800 K. Product Distribution and Reaction Mechanism," *Combustion Science and Technology*, Vol. 136, 1998, pp. 373–390.
- ²²Kossiakoff, A., and Rice, F. O., "Thermal Decomposition of Hydrocarbons, Resonance Stabilization and Isomerization of Free Radicals," *Journal of the American Chemical Society*, Vol. 65, 1943, pp. 590–595.

APPENDIX U
Soot Reduction Research Using a Well-Stirred Reactor

INTENTIONALLY LEFT BLANK

Soot Reduction Research Using a Well-Stirred Reactor

Scott D. Stouffer^{*}, Benjamin M. Mortimer[†], David M. Ostdiek[‡] and Matthew J. DeWitt[§]
University of Dayton Research Institute, Dayton, OH 45469

Robert Pawlik^{**}, Richard Reich^{††} and Charles W. Frayne^{‡‡}
Air Force Research Laboratory, Wright-Patterson AFB OH 45433

Howard Mayfield^{§§}
Air Force Research Laboratory, Tyndall AFB FL 32403

A comprehensive research program involving industry, academia and Government laboratories is developing a fundamental understanding of the complex interactions of fuel additives with the processes leading to particulate matter emissions from military gas turbine engines. The goal of this program is to eventually select promising additive compounds that would reduce particulate matter (PM) emissions. One experimental platform for assessing the performance of additives is the Well-Stirred Reactor (WSR) research combustor at the Air Force Research Laboratory. The WSR provides a unique capability for simulating the chemical kinetics within the primary zone of a gas turbine engine combustor. The current study presents results from six different compounds (nitromethane, nitroethane, nitropropane, cyclohexanone, pyridine, and quinoline) as additives for soot reduction. The effect of the temperature on the chemical kinetics vs. the chemical effect of the additives is addressed for the nitroalkane additives.

Nomenclature

GC/MS	= gas chromatograph/mass spectrometer
PAH	= polycyclic aromatic hydrocarbon
PM	= particulate matter
V	= reactor volume (ml)
WSR	= well-stirred reactor
Φ	= equivalence ratio
ρ	= density (kg/m ³)
τ	= residence time (ms)

I. Introduction

Because of practical concerns, including visibility, environmental, and maintenance costs, associated with combustion generated particulates for gas turbine powered aircraft, several research groups are conducting experiments to understand particle formation and mitigation strategies. Fundamental studies are underway that use

^{*} Senior Research Engineer, Energy and Environmental Engineering Division, Research Institute, AIAA Member.

[†] MS Candidate, Mechanical Engineering Department, AIAA Student Member.

[‡] MS Candidate, Mechanical Engineering Department, AIAA Student Member.

[§] Senior Research Engineer, Energy and Environmental Engineering Division, Research Institute, AIAA Member.

^{**} Research Chemist, Propulsion Directorate, Turbine Engine Division, Combustion Branch, AFRL/PRTC.

^{††} Research Chemist, Propulsion Directorate, Turbine Engine Division, Combustion Branch, AFRL/PRTC.

^{‡‡} Program Manager, Propulsion Directorate, Turbine Engine Division, Combustion Branch, AFRL/PRTC.

^{§§} Research Chemist, AFRL/MLQL

simplified combustion rigs to study the chemistry of particulate formation, investigate fuel additives to reduce particle formation, develop detailed models to predict soot formation, and identify mitigation strategies which could involve expensive combustor replacement, or modification. An economically attractive means of possibly reducing the soot produced is to use a fuel additive or additive package that can reduce soot while not requiring combustor modifications. It should be noted that the soot formation process is inherently complicated so that an additive that is found to be effective on one engine may be ineffective, or even counterproductive, on another engine. Therefore, an understanding of the fundamental processes and mechanisms at work for soot production is crucial for successful development and fielding of an effective additive. The well-stirred reactor (WSR) is a research combustor that is well suited for fundamental combustion studies of possible soot reducing additives. In addition to the WSR studies, several other groups are also examining the effects of fuel additives on other combustors in order to obtain a better understanding of how the proposed additive works over a range of conditions. This research will provide a fundamental understanding of the behavior occurring in these many processes, which may ultimately lead to the development of an additive composed of many compounds, each contributing specific capabilities to the overall soot reduction process.

Figure 1 shows a simplified pathway to soot and major product species during combustion. Large fuel molecules are broken down into smaller fuel fragments during pyrolysis, these fragments form soot precursors and PAH's which grow by ring addition, and subsequent primary soot particle inception and agglomeration into larger soot particles. At each step in the process of soot production, oxidation is competing for the carbon, and hydrogen atoms. Although there is agreement that soot formation follows this general model, the processes are much more complex because of the many competing reactions. A review of the chemical reaction pathways leading to soot is presented in Reference 1.

Two general types of additives were considered for the current study. The first type was intended to act as an oxidizer by virtue of the oxygen contained within the additive. The intent is to enhance oxidation of the precursors or primary soot particles. Oxidation of precursors or small PAH may provide a high leverage payoff if it occurs at a critical step in the soot formation process that reduces the formation of larger PAH and incipient soot particles. The second additive type is intended to indirectly enhance oxidation by inhibiting ring addition and growth of large PAH's and forming smaller PAH compounds that can be more rapidly oxidized before particle inception can occur.

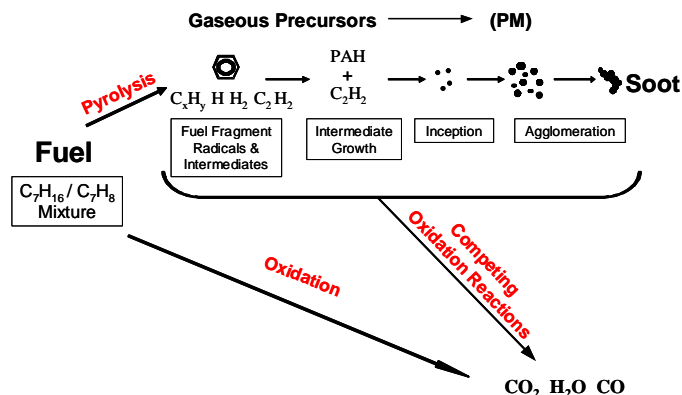


Figure 1. PM Formation and Destruction Processes.

II. WSR Background

The well-stirred reactor is a versatile laboratory research combustor that simulates the highly turbulent combustion process in a practical gas turbine combustor. The WSR has been used to study high temperature chemical kinetics of gaseous and liquid fuel combustion, combustion stability, lean extinction and blowout limits, and gaseous pollutants (NOx, CO, and unburned hydrocarbons) and particulate (soot and sulfur) emissions in previous studies²⁻⁷.

The purpose of the WSR is to create a combustion environment that allows chemical kinetic influences to be investigated without the physical complications associated with practical diffusion flame combustors. Specifically, the WSR uses premixed/pre-vaporized reactants to eliminate the complications of droplet combustion, a high velocity inlet flow to continuously stir the reactants at high turbulence levels, and low-conductivity refractory wall materials to decrease reactor heat loss. With these simplifications, the products are only a function of the inlet

temperatures, residence time, and heat loss, and can be readily modeled with existing chemical kinetic codes, without the need to model the complications of turbulence, spray, evaporation, and mixing.

The most important characteristic that separates the WSR from other premixed combustion systems is the high rate of continuous mixing of the products and incoming reactants. Ideally, for a "Perfectly-Stirred Reactor" the intense mixing will result in a uniform profile of species and temperature throughout the reactor. However, because of practical limitations on mixing and reaction rates, it is impossible to achieve a perfectly stirred reactor over the entire combustor. For example, in the immediate vicinity of the fuel/air jets there will be a higher fraction of incoming reactants than products of combustion. However, over most of the reactor the products and incoming reactants are well mixed. The high degree of mixing with the current design is evident by the high equivalence ratio associated with the soot inception limits and by the measured temperature profiles across the WSR cross-section.

III. WSR Design

The 250-ml toroidal WSR, as designed by Nenniger et al.⁶ and modified by Zelina⁷ and later Stouffer⁴, has been successfully used for the current experiments. Figure 2 shows the WSR rig during operation and shows a sampling probe penetrating the exhaust stack, entering the plug flow region above the reactor. A photo of the ceramic reactor and a schematic cross section of the reactor and jet ring are also shown. The four key parts of the WSR system are: a vaporizer chamber for liquid fuels (not shown), the fuel-air injector ring, toroidal WSR combustor, and the plug flow exit section. The two halves of the WSR fit around the jet ring assembly to form the toroidal WSR combustor section. A variety of materials, such as silicon carbide, fused silica, zirconia-oxide, and TBC-coated inconel have been used for the WSR fabrication. The reactor wall material used for the tests depends on the test conditions. For the current tests the desire was to operate the combustor under fuel-rich conditions with minimal heat loss through the walls, and fused silica was used for the reactor material because of its low coefficients of thermal conductivity and thermal expansion.

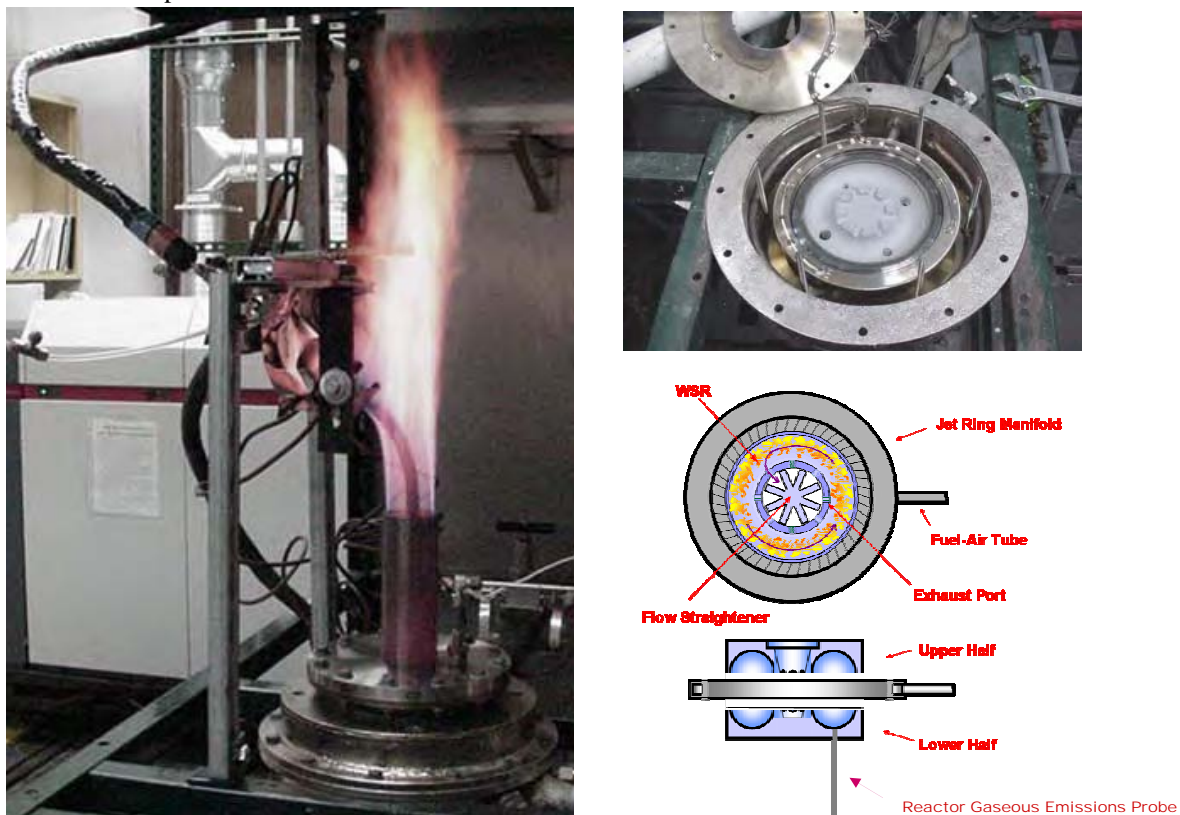


Figure 2. Well-Stirred Reactor Operation, Assembly, and Schematic Drawing.

The Inconel jet ring has 48 fuel/air jets of 0.034" diameter that are used to inject the pre-vaporized/premixed reactants at high subsonic or sonic velocity from the outer radius of the toroidal WSR combustor. The jet ring is cooled by nitrogen impingement cooling to avoid auto-ignition of the fuel-air mixture within the jet ring manifold. The high velocity reactants continually stir and mix with the combusting gases producing high turbulence and mixing levels in the reacting flow field. The WSR has several access ports for temperature, pressure, and emissions samples, located at the bottom of the WSR. Oil-cooled gas-sampling emissions probes are used for extracting emissions from the reactor. The mixture is then exhausted through eight radial ports at the toroid inner diameter, and turned and straightened before entering the plug flow reactor (PFR), which is a 5-cm diameter cylinder where additional measurements can be made along the axial length.

A facility schematic, shown in Figure 3, identifies components and instrumentation used for operation of the rig and acquisition of emissions samples. Heated air is mixed with fuel entering the WSR through a jet ring injector inside the reactor. Air and gaseous fuel flow rates are measured and controlled using thermal mass flow controllers. The fuel system uses a three-diaphragm pump to continuously pump the neat fuel mixture at a higher rate than required for the tests. Most of the fuel runs through a back-pressure regulator that sets the pressure downstream of the pump, before passing through a heat exchanger and back to the tank. A small fraction of the flow is then passed through a flow regulator that further reduces the pressure before it flows to the rest of the fuel control system. A combination of several pulse dampers and the two regulators creates a steady pressure source from the pulsing pump. Control valves are used to control the flow measured by a constant displacement piston flow meter using a PID loop for controlling the valve. For the first five additives considered, a single control valve was used; for the last additive considered, a combination of two valves in parallel were used, a course manual valve and a fine automatic control valve. The additives were pumped and metered with a set of high-pressure syringe pumps, and mixed with the neat fuel in a static mixer before passing through a heater and into the vaporizer nozzle. Because some of the additives in the study are sensitive to shock and rapid adiabatic compression, the syringe pumps were equipped with pressure relief valves.

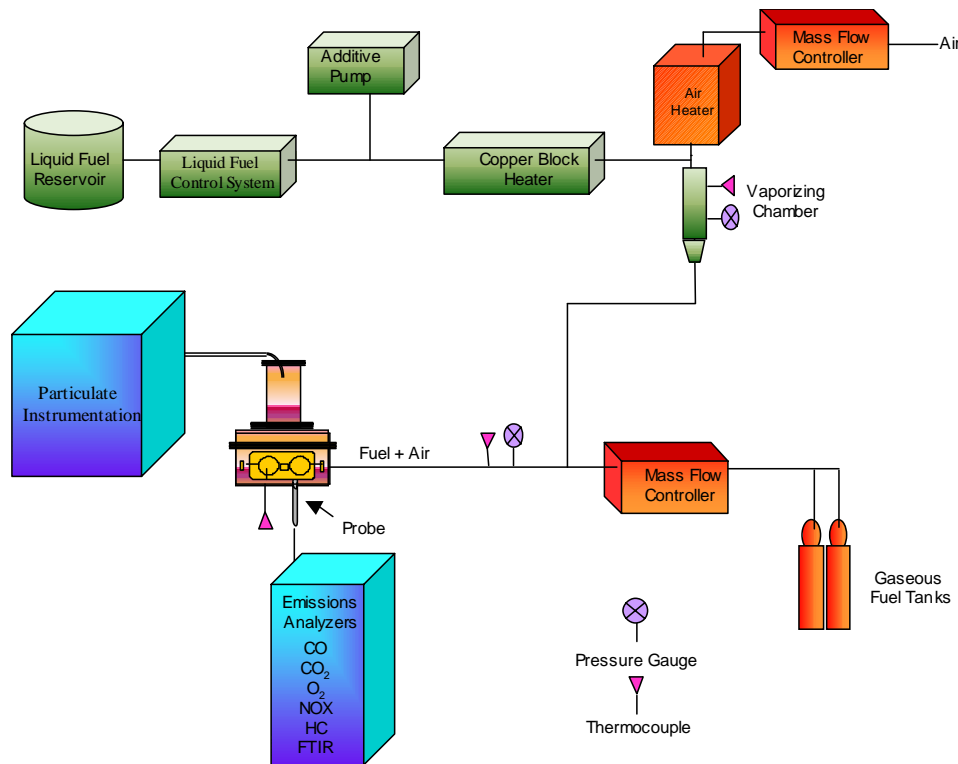


Figure 3. Well-Stirred Reactor Air, Fuel and Instrumentation Systems.

The liquid fuel is sprayed into the vaporizer using an air swirl atomizer nozzle, which passes approximately ¼ of the total air through the injector nozzle while the rest of the air is added as a coaxial stream in the vaporizer. The combination of the fuel temperature, air temperature, vaporizer air temperature and the flow rates are used to control the temperature of the air-fuel mixture entering the reactor. An automated fail-safe retractable spark igniter is used to initiate combustion within the reactor. When the reactor is to be operated on a liquid fuel, it is first started on gaseous ethylene and then smoothly transitioned from the gaseous to a liquid fuel. All of the penetration paths to the reactor are sealed allowing the reactor to maintain a positive pressure of around 3-5 kPa above atmospheric pressure while running.

IV. Experimental Measurements and Instrumentation

Thermocouples are located in the air line, WSR jet ring, inlet, reactor, housing and stack, and transducers are installed to indicate reactor pressure. The reactor temperature was measured by a type B thermocouple (0.008" diameter), which was not corrected for radiation effects. Late in the study, the capability to reliably scan the thermocouple across the cross-section of the toroidal reactor from the bottom to the top of the toroidal reactor was added to the experimental system⁹. Preliminary studies of the temperature scans have shown that the temperature can vary substantially with position across the reactor. For each of the data sets obtained for a specific additive, the thermocouple was maintained at the same location in the WSR. However, for a variety of reasons, including normal wear and tear on the reactor, emergency shutdowns, and reactor inspection, reactor reassembly resulted in small displacements of the thermocouple within the reactor. The position change of the thermocouple, in turn, affected the temperature recorded for a given set of conditions, due to the change in the spatial temperature distribution in the reactor. Thus the temperature data for any two different additives should not be directly compared.

A circulating oil heater is used to heat emissions and particulates probes to 420 K. Electrically heated sampling lines (300°F) were used to convey the particulate samples to the particulate instrumentation. The particulate results presented here are based on off-line determination of soot mass collected on quartz filters. Efforts have been made to determine particulate number densities and size distributions using CNC and SMPS, however because of the high



(A)



(B)

soot levels it is thought that further development of the dilution techniques used for these measurements is needed before reliable size distributions can be obtained. In general, mass measurements are less susceptible to transport system effects, such as coagulation, and are used here. At the start of the study a 26-year-old Roseco smoke sampling unit, which was near the end of its useful life, was used to obtain samples. This unit was replaced toward the end of the study by a custom-built smoke sampling unit (see Figure 4) optimized to reliably obtain samples from a rich combustion environment. The new sampling unit automated many of the operation tasks and has greatly improved the efficiency of collecting samples as well as the quality of the samples.

**Figure 4. (A) Old Smoke Sampling Unit
(B) Custom-Built Smoke Sampling Unit**

Gaseous emissions analyzers were used for on-line measurement of CO, CO₂, NO_x, O₂, and unburned hydrocarbons within the reactor. In addition, minor species were measured using FTIR and GC/MS analysis. The FTIR system used was an MKS 2030 with a 5.1-m long gas cell path length. The FTIR software allows quick online

detection of gaseous species along with subsequent detailed investigation of the spectra saved. The FTIR was also used to validate major species obtained from the on-line analyzers; it is capable of measuring species of CO, CO₂, H₂O, NO, NO₂, and other compounds that absorb infrared radiation. The FTIR system was made portable to aid with several in-house facility tests. The mobile FTIR system also contains a total hydrocarbon and O₂ analyzer, connected in series as indicated in Figure 5.

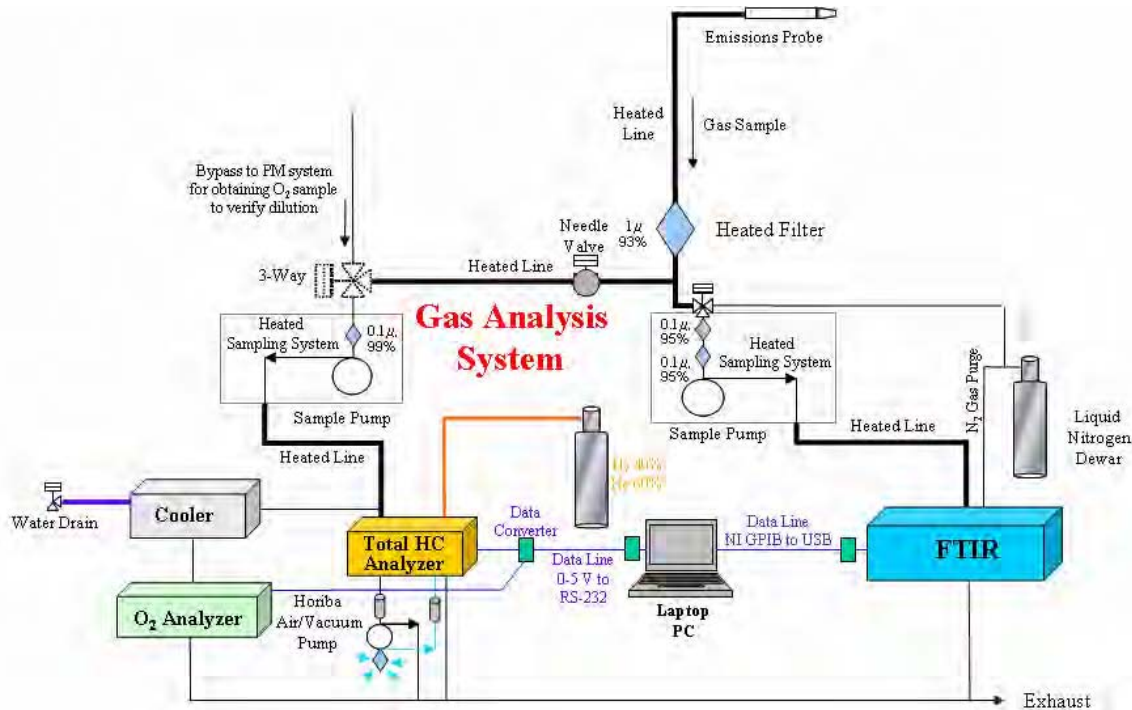


Figure 5. FTIR-Based Gas Sampling and Analysis System Schematic.

Soot samples were collected using the smoke sampling system on both quartz and paper filters. The smoke number, determined from a soot sample collected on a paper filter, was used for fast qualitative verification of the results for carbon mass. In general the smoke number trends agreed with the carbon mass results and will not be emphasized in the discussion of results. The samples collected on quartz filters were used for both particulate carbon mass determination and PAH analysis via GCMS analysis. The carbon mass was determined using a LECO RC-412 multiphase carbon analyzer, which measures the CO₂ produced as the filter is heated in the presence of an excess of oxygen. A typical plot of carbon given off by the filter vs. the filter temperature is shown in Figure 6. For each of the samples there are two distinct major peaks. The low temperature peak (below 325 C) is thought to be mainly volatile carbon due to PAH, while carbon mass above 325°C is thought to be mainly due to carbonaceous soot. Throughout the presentation of the results the carbon mass analysis will be discussed in terms of volatile, carbonaceous, and total (volatile + carbonaceous) soot.

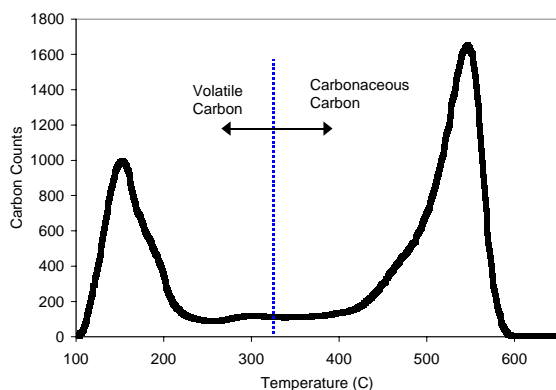


Figure 6. Carbon Signal vs. Burn-off Temperature For a Typical Sample on Quartz.

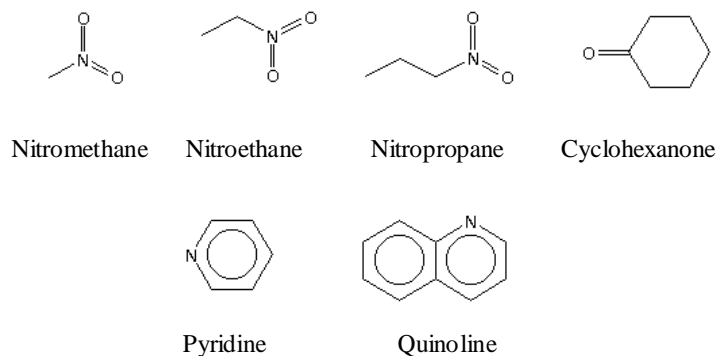
In addition to the carbon burn-off analysis, the quartz filter samples were also analyzed using gas chromatograph/mass spectrometry (GC/MS) Chromatoprobe analysis to determine the PAH content of the soot. The traces from the GC/MS were compared to the compounds in the EPA 610 standard. Further details of the analysis procedure are presented in References 5 and 8.

V. Additives and Experimental Conditions

The base fuel for the study was a mixture of 80% n-heptane -20% toluene by volume. This mixture was picked as a weak surrogate for JP8 as part of a larger research program¹⁰. Although this mixture is not a true surrogate for JP8, which contains hundreds of hydrocarbon compounds, it is studied because the kinetics of PAH and soot formation for C7 and aromatics are of interest to the modeling community.

Equivalence ratios between 1.90 and 2.10 were studied. The WSR was limited to this equivalence ratio range on the low side by the melting point of the fused silica and on the high side by the rich blow out limit. However, as will be shown later for the neat fuel under the conditions, this range of equivalence ratios captures the peak along with the low temperature and high temperature sides of the so-called "soot bell". The airflow was held at a constant 240 g/s and the average residence time in the reactor was 10 +/- 0.4 ms. The reactor pressure was slightly (0.1-0.2 psi) over the ambient pressure for all of the tests.

The performance of six different additive compounds, shown in Figure 7, was considered during the study. The first four additives (nitromethane, nitroethane, nitropropane, and cyclohexanone) contained oxygen, and it was thought that they could reduce soot by oxidation of soot precursors or small PAH. The use of the nitroalkanes as an



additive was suggested by previous studies with a commercial additive containing nitroalkanes that showed promise for reducing soot when used in large quantities¹¹. The other two additives are thought to reduce soot formation by trapping acetylene in a molecule that is unsuitable for ring growth and addition because of the presence of the nitrogen within the ring structure. All of the additives except for cyclohexanone contained nitrogen, which raises concern about the possibility of the generation of NO_x compounds.

Figure 7. Structure of the Additives Used in the Study.

The oxygenate additives were added to the fuel in concentrations such that the oxygen mass fraction of the fuel was 0% (neat heptane-toluene mixture), 2% and 4%. The mass flows of the additive and the base fuel were adjusted to maintain the same equivalence ratio as the neat case. The additives concentrations used to achieve the desired oxygen levels are listed in Table 1. For the tests with the pyridine and quinoline each additive was studied in quantities of 10,000 and 50,000 ppm. For each test of the first five additives, the indicated equivalence ratio was maintained to within +/- 0.006 of the target equivalence ratio, with most of the measurements occurring in a tighter band of equivalence ratio. For the tests with the last additive (quinoline), improvements in the fuel control systems allowed the indicated equivalence ratio to be maintained within +/- 0.0025.

Table 1. Additives and Concentration Levels (ppm by volume) Used in the Study

Additive	Formula	Low Concentration	High Concentration	Proposed Mechanism
Nitromethane	CH ₃ NO ₂	24,660 (2% O)	50,020 (4% O)	Oxidation
Nitroethane	C ₂ H ₅ NO ₂	32,820 (2% O)	66,620 (4% O)	Oxidation
Nitropropane	C ₃ H ₇ NO ₂	40,820 (2% O)	82,950 (4% O)	Oxidation
Cyclohexanone	C ₆ H ₁₀ O	96,140 (2% O)	198,280 (4% O)	Oxidation
Pyridine	C ₅ H ₅ N	10,000	50,000	Ring Growth Inhibitor
Quinoline	C ₉ H ₇ N	10,000	50,000	Ring Growth Inhibitor

VI. Experimental Results

The results for total carbon mass collected on quartz filters for the pyridine additive cases are shown in Figure 8. The carbon mass curve vs. equivalence ratio shows a bell shaped curve with a peak at $\Phi = 2.05$ for the neat case. Figure 9 shows the same data plotted against the WSR temperature, for each of the additive concentrations the carbon produced is also related to the temperature. This bell shaped curve is commonly referred to as the soot bell. On the high temperature (low phi) side of the soot bell, the soot produced increases as the equivalence ratio is increased. The decrease in the soot produced on the low temperature side of the soot bell with decreases in temperature (increased phi) is thought to be due to the temperature-related decrease in critical reaction rates within the soot formation mechanism. With the additive concentration at 10,000 ppm the effect on the soot is shown to be minimal over the entire range of equivalence ratios. In contrast, the pyridine at 50,000 ppm reduced carbon mass on the high temperature side of the soot bell, showed little effect near the peak, and increased the carbon mass produced on the low temperature side of the soot bell. The reduction in total carbon mass with the 50,000 ppm additive is most pronounced (-32%) at $\Phi = 1.9$, which is the highest temperature case considered. The total carbon vs. temperature in Figure 9 shows that the reduction of mass at the high temperature side of the curve may be due temperature effects only. The total carbon mass was broken into volatile and carbonaceous fractions and is shown in Figures 10 and 11, respectively. The volatile content of the carbon mass was shown to increase along with increases in the equivalence ratio for the neat and the additive cases. The trends for the carbonaceous carbon resemble those for the total carbon.

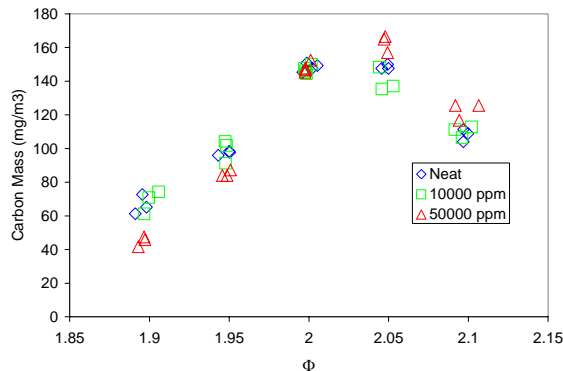


Figure 8. Total Carbon Particulate Mass vs. Φ for Pyridine Additive.

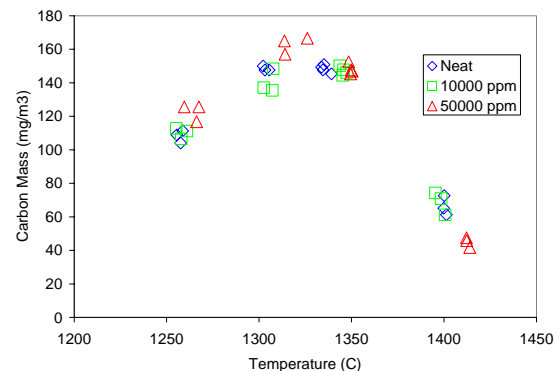


Figure 9. Total Carbon Particulate Mass vs. Temperature for Pyridine Additive.

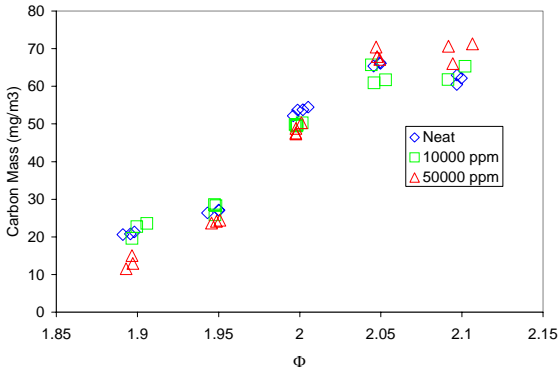


Figure 10. Volatile Carbon Mass for Pyridine Additive.

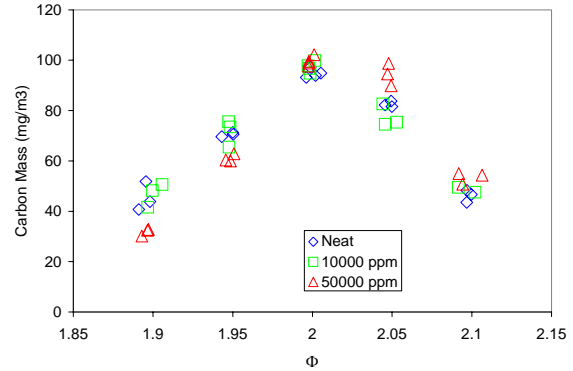


Figure 11. Carbonaceous Carbon Mass for Pyridine Additive.

For the tests with the pyridine additive, the acetylene concentration was of particular interest because of the proposed mechanism of trapping acetylene within the pyridine ring. The acetylene concentration was measured using the FTIR and the results shown in Figure 12 show little change as a result of pyridine addition.

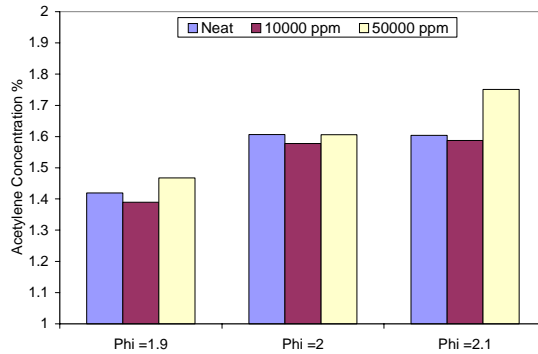


Figure 12. Acetylene Concentration from FTIR Measurements using Pyridine as an Additive.

The particulate carbon mass results for quinoline additive are shown in Figures 13 and 14 for the volatile and carbonaceous fractions of the carbon mass, respectively. Both the volatile and the carbonaceous fractions of particulate carbon mass increased with the quinoline addition over the entire range of equivalence ratios. Similar to the results for the pyridine, the volatile carbon content increased as the equivalence ratio increased for each of the concentrations. The carbonaceous carbon mass was shown to increase dramatically as a result of the 50,000 ppm quinoline addition increasing from 31% at $\Phi = 1.9$ to 91% at $\Phi = 2.1$. The effect of the quinoline on the combustion temperature was found to be small (less than 9°C) at each equivalence ratio, therefore the effect of the quinoline is thought to be predominately chemical rather than by the effect of a temperature shift on the chemical kinetics. Certainly the quinoline is a poor additive. Recall from Figure 7 that quinoline has a single nitrogen atom on only one of its aromatic rings. It is thought that while the presence of nitrogen on one of the aromatic rings may inhibit growth of that ring, the presence of the nitrogen on one ring does not effect addition to the other ring.

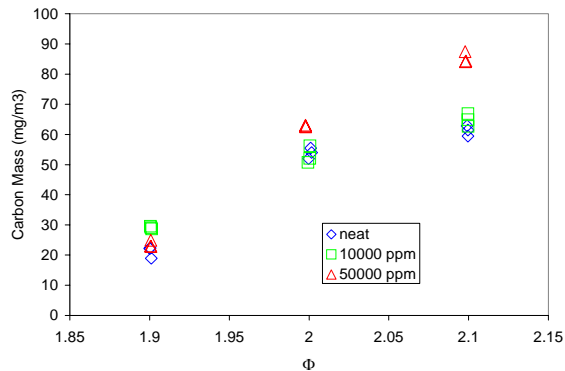


Figure 13. Volatile Carbon Mass for Quinoline Additive.

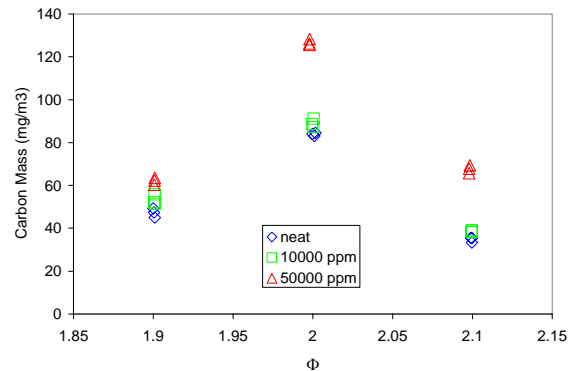


Figure 14. Carbonaceous Carbon Mass for Quinoline Additive.

Effect of the Nitroalkane additives

It has been shown previously in this study and others that the effect of a temperature increase is to decrease soot produced for the high temperature side of the soot bell and increase soot produced for the low temperature side. Highly energetic nitroalkane additive compounds, such as nitromethane, will increase the combustion temperature at the same inlet temperature and equivalence ratio. This increase in temperature as a result of the additive raises the question of whether difference in the soot production is only due to the increased combustion temperature, or if the change is due to other chemical effects of the additive. For each of the nitroalkane additives studied three test concentrations were considered (neat, additive with 2% O wt in the fuel, and a similar 4% O wt) with the same inlet fuel-air mixture temperature at each equivalence ratio. To explore the effect of temperature on the soot formation, a test point was also considered where the combustion temperature of the neat case was increased to match that of one of the additive cases. Increasing the inlet temperature of the fuel/air mixture increased the combustion temperature for this test point and allows differentiation between the thermal effect on the kinetic process and any chemical effect of the additive. Increased inlet temperatures were achieved by increasing the vaporizer, main air, and vaporizer air and fuel temperatures. Due to the large thermal mass of the vaporizer and associated fluid path upstream of the jet ring the process of matching the combustion temperatures required approximately 40-60 minutes between test points with matched temperatures. Note that over most of the range of conditions the increase in measured combustion temperature is less than the increase in the inlet temperature due to the difference in specific heats of the products and reactants. At the highest equivalence ratios tested ($\Phi = 2.1$), the increase in the inlet temperature has a larger effect on the combustion temperature due to the increase in the combustion efficiency, as shown by decreased measured oxygen levels in the exhaust emissions.

Figure 15 and 16 show the particulate carbon mass data for nitromethane plotted vs. temperature. For convenience of comparison, data at the same equivalence ratios is outlined within the ovals on the plots. The data clearly show that nitromethane decreases the total carbon particulate mass for $\Phi < 2.05$. As the concentration of nitromethane increased between the 2% O case and the 4% O case, the carbon mass dropped further. The reduction in carbon mass at $\Phi = 1.95$ was over 47% for the 4% O case. To explore the effect of temperature, the inlet temperature for the neat elevated inlet temperature case was increased until the WSR flame temperature was approximately the same for both the 2% O and the neat case. For the low temperature side of the soot bell the increased combustion temperature associated with the inlet temperature increased the soot mass production. On the high temperature side of the soot bell, the soot produced for the neat case decreased as temperature was increased. However, the soot mass production for the nitromethane additive case at the same temperature was less than or equal to the neat case at the same combustion temperature. Therefore, it is apparent that the drop in soot production observed over most of the test points with the additive addition is not merely due to an increase in temperature caused by the additive, but rather by other features of the reaction mechanism associated with the additive. At the lowest equivalence ratio considered ($\Phi = 1.90$) the additive case and the neat case had approximately the same total

carbon mass. The carbonaceous carbon mass is shown in Figure 16 and exhibited the same general trends as the total carbon mass results.

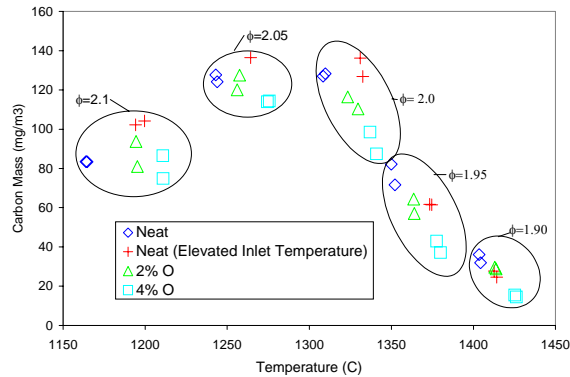


Figure 15. Total Carbon Mass for Nitromethane Additive.

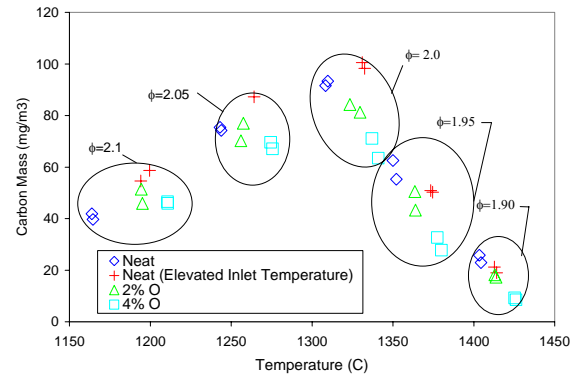


Figure 16. Carbonaceous Carbon Mass for Nitromethane additive.

Results from the PAH analysis of the Quartz filters are shown in Figure 17. Pyrene is considered here because of its importance as a soot precursor. At equivalence ratios below 2.0 the increase in temperature for the neat case decreases the pyrene mass, while it increases with temperature for equivalence ratios above 2.0. This pattern is similar to that shown for the total and carbonaceous carbon masses.

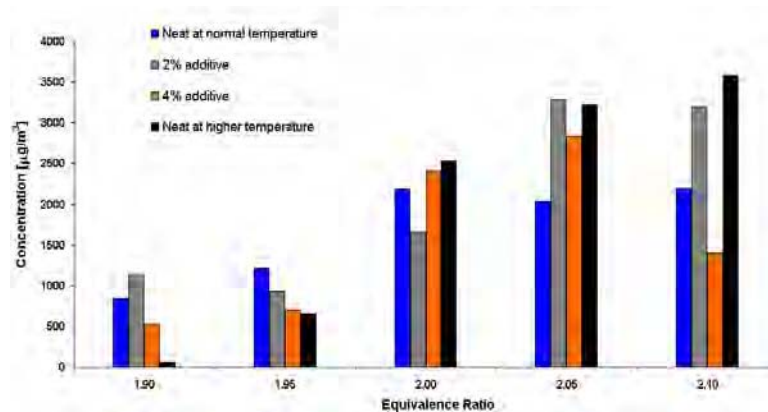


Figure 17. Pyrene Concentration for Nitromethane Additive.

The effect of the nitroethane additive is shown in Figures 18-19. For the high inlet temperature neat cases, the inlet temperature was increased enough so that combustion temperatures were matched with the 4% O additive cases. Note that the combustion temperature increase for the nitroethane was less than the increases seen with the nitromethane. Decreases in the total carbon particulate mass and carbonaceous carbon mass similar to those shown for the nitromethane cases were seen with the addition of the nitroethane. At $\Phi=1.95$ the total carbon mass is reduced by 51% for the 4% O case. The data plotted against temperature show that at all equivalence ratios, the high inlet temperature neat case produces more soot (as indicated by the total carbon mass) than the corresponding cases (same combustor temperature) with the additive. Therefore it is apparent that the effect of the nitroethane additive is not merely caused by the increase in the combustion temperature. Note that at $\Phi = 2.1$ the additive slightly increases soot generated above the neat case, however, for the same combustion temperature with 4% O in the fuel, less soot is produced with the nitroethane additive than for the neat case.

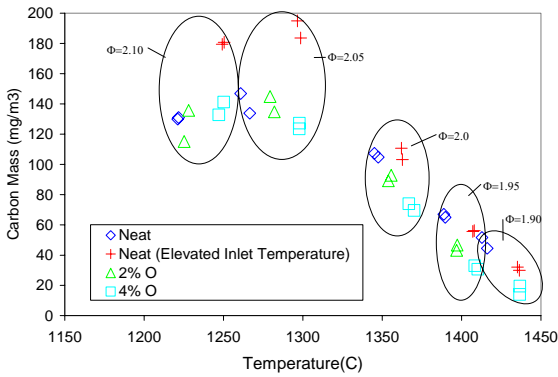


Figure 18. Total Carbon Mass for Nitroethane Additive.

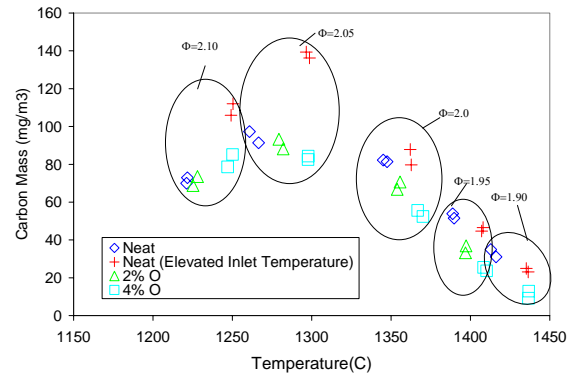


Figure 19. Carbonaceous Carbon Mass for Nitroethane Additive.

The carbon particulate mass data for the Nitropropane additive is shown in Figures 20 and 21. The trends are also similar to those shown previously for the nitromethane and nitroethane additives. The reduction in total carbon mass at $\Phi = 1.95$ was 48% for the 4% O additive case. The results for the carbonaceous carbon mass show similar trends to the total carbon mass. As for the other two nitroalkane additives the reduction of carbon mass is shown not to be due to an increase in the temperature only.

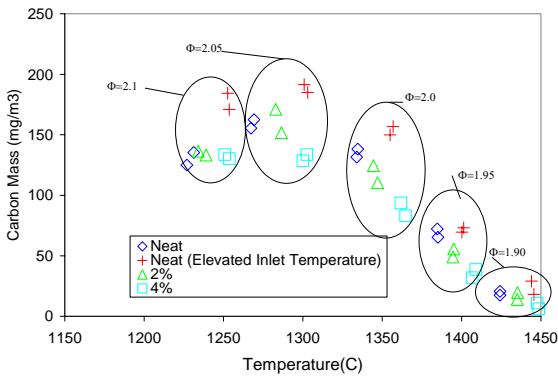


Figure 20. Total Carbon Mass for Nitropropane Additive.

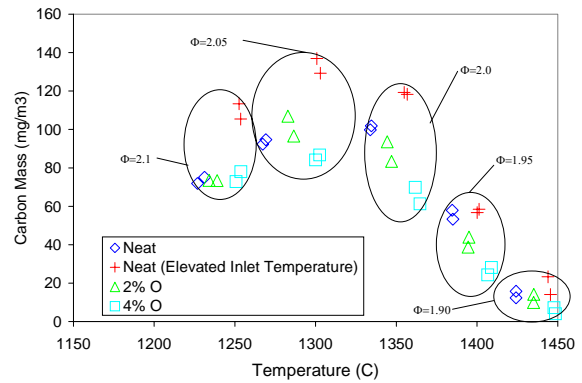


Figure 21. Carbonaceous Carbon Mass for Nitropropane Additive.

Effect of the Cyclohexanone Additive

Data for the Cyclohexanone tests are shown in Figures 22-23. The presence of Cyclohexanone was shown to reduce soot at all equivalence ratios. At $\Phi = 1.95$ the 4% O additive case produced 36% less carbon mass than the neat case. The effect of cyclohexanone on the temperature changed depending on the equivalence ratio. For the high temperature side of the soot bell the combustor temperature for the neat and the additive cases were nearly the same, implying that the effect of the additive in this region is chemical rather than thermal. On the low temperature side of the soot bell the combustor temperature decreased for the additive case relative to the neat case as the equivalence ratio was further increased. For the highest equivalence ratio case studied ($\Phi = 2.1$) the combustor temperature using the 4% O additive was increased for one data point by increasing the inlet conditions, and the soot mass increased to match that for the neat case, implying that for the low temperature side of the soot bell the effect of the additive is mainly due to a decrease in the combustor temperature.

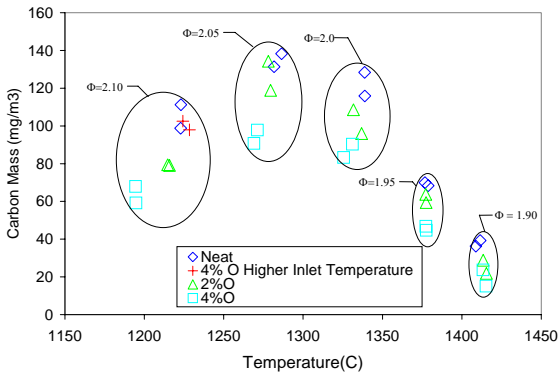


Figure 22. Total Carbon Mass for Cyclohexanone Additive.

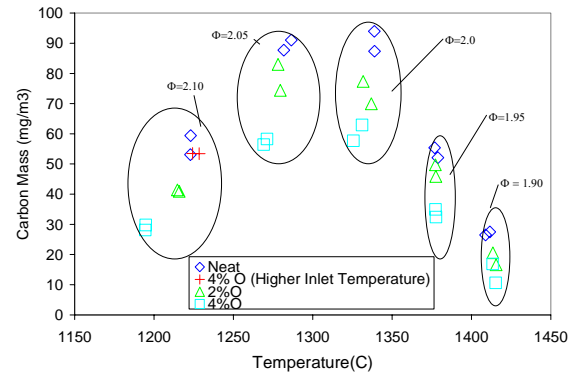


Figure 23. Carbonaceous Carbon Mass for Cyclohexanone Additive

Effect of the Additives on NO_x formation

Because of the presence of fuel bound nitrogen within the additives, the possibility of NO_x formation was a concern. The NO was measured using the FTIR for tests with cyclohexanone, quinoline, pyridine and nitromethane. As expected, the addition of the cyclohexanone did not increase the NO. The NO levels for the quinoline and pyridine additives also showed little increase above the low thermal NO_x levels associated with the neat fuel. In contrast, the NO_x levels increased dramatically (300-400 ppm) with the addition of nitromethane to the fuel.

VII. Summary and Conclusions

An experiment to evaluate the effect of six different additives (pyridine, quinoline, cyclohexanone, and nitromethane, nitroethane, and nitropropane) on the particulate carbon mass was conducted in a well-stirred reactor using a base fuel of 80% Heptane/ 20% toluene (by volume) at equivalence ratios from 1.9 to 2.1. It was concluded that:

1. Quinoline was shown to increase volatile, and carbonaceous carbon mass across the entire range of test conditions and is shown to be a poor additive for soot reduction.
2. Pyridine showed little effect near the peak of the soot bell, increased the soot mass on the low temperature side of the soot bell and decreased it on the high temperature side of the soot bell
3. The Nitroalkane additives were shown to give similar reductions in the soot produced and were the most effective additives explored.
4. While some of the reduction in soot mass for the nitroalkane additives is due to the increased combustion temperatures, simply increasing the temperature of the neat combustion products (by increasing the inlet air/fuel temperature) did not account for all of the change in the particulate mass and it is concluded that the effect of the nitroalkane additive was not solely due to an increase in combustion temperature.
5. The nitroalkanes, while reducing soot, were shown to dramatically increase the NO_x emissions.
6. Cyclohexanone reduced the soot produced over the entire range of equivalence ratios tested, at the high temperature side of the soot bell the effect of the cyclohexanone was shown to be chemical rather than due to a change in combustion temperature, while the decrease in soot at for the high equivalence ratio cases is due to the change in the combustion temperature.

VIII. Future Work

Work is ongoing to improve the gas sampling and particle sampling techniques. In particular, further interpretation of the current FTIR data set is under investigation and the methods used for dilution and particulate

sampling are being improved to allow collection of reliable size distributions. Modeling of the gas phase reactions is also underway to allow further interpretation and use of the experimental results.

Acknowledgments

This work is based on research sponsored by the US Air Force Research Laboratory under agreement number F33615-03-2-2347. Financial support for this work was also provided by the Strategic Environmental Research and Development Program (SERDP), project PP1179, Program Manager, Dr. Charles Pellerin. The authors are grateful for the help of Mr. Mike Arstingstall of UDRI for technical support on the construction of the WSR and associated systems. The efforts of Mr. Edward Strader of UDRI on the instrumentation are also gratefully acknowledged. The Authors also wish to acknowledge the contributions of David Brooks of UDRI for LECO analysis and Mr. Tom McCray of ISSI for data acquisition support.

References

- ¹Richter, H. and Howard, J.B., "Formation of Polycyclic Aromatic Hydrocarbons and their Growth to Soot – a Review of Chemical Reaction Pathways," *Prog. Energy Combust. Sci.* 26:565-608 (2000).
- ²Colket, M., Hall, R. J., and Stouffer, S. D., "Modeling Soot Formation in a Stirred Reactor," Paper No. GT2004-54001, ASME Turbo Expo, 2004, Vienna, Austria, June 2004.
- ³Ballal, D. R., and Zelina, J., "Assessment of Gas Turbine Combustor Performance and Emissions Using a Well-Stirred Reactor," ISABE-2001-1065, *Proceedings of International Society for Air Breathing Engines (ISABE)*, Bangalore, India, 2001.
- ⁴Stouffer, S. D., Striebich, R. C., Frayne, C. W., and Zelina, J., "Combustion Particulates Mitigation Investigation Using a Well-Stirred Reactor," AIAA Paper No. 2002-3723, 38th Joint Propulsion Conference, 2002.
- ⁵Reich, R., Frayne, C., Zelina, J., Mayfield, H., Stouffer S, and Katta V., "Particulate Matter and Polycyclic Aromatic Hydrocarbon Determination Using a Well-Stirred Reactor," AIAA Paper No. 2003-0664, 41st AIAA Aerospace Sciences Meeting, Reno, Nevada, January 2003.
- ⁶Nenniger, J. E., Kridiotis, A., Chomiak, J., Longwell, J. P., and Sarofim, A. F., "Characterization of a Toroidal Well Stirred Reactor," *Twentieth Symposium (International) on Combustion*, The Combustion Institute, pp. 473-479, 1984.
- ⁷Zelina, J., "Combustion Studies in a Well-Stirred Reactor," Ph.D. Thesis, University of Dayton, Dayton, OH 1995.
- ⁸Klosterman, J. R., Striebich, R. C. and Rubey, W. A., "Direct Thermal Desorption of Combustion Residues by GC-MS," Pittcon Paper No. 1034, New Orleans, LA, 5-8 March 2001.
- ⁹Stouffer, S. D., Ballal, D. R., Zelina, J., Shouse, D. T., Hancock, R. D., and Mongia, H. C. "Development and Combustion Performance of a High Pressure WSR and TAPS Combustor," AIAA Paper 2005-1416, 2005.
- ¹⁰Litzinger, T., Santoro, R., Colket, M., Liscinsky, D., McNesby, K., Reich, R., Frayne, C., Phelps, D., Sidhu, S., and Stouffer, S.D., "Reduction of Particulate Matter from Burners, Part 1: Effects of Ethanol", *Proceedings of the Third Meeting of the U. S. Sections of the Combustion Institute*, 2003.
- ¹¹Corporan, E., DeWitt, M., Wagner, M., "Evaluation of Soot Particulate Mitigation Additives in a T63 Engine," *Fuel Processing Technology*, Vol 85, pp727-742, 2004.

APPENDIX V

Determination of Hydroperoxides in Jet Fuel via Reaction with Triphenylphosphine

INTENTIONALLLY LEFT BLANK

APPLIED CHEMISTRY

Determination of Hydroperoxides in Jet Fuel via Reaction with TriphenylphosphineZachary J. West,^{*,†} Steven Zabarnick,^{†,‡} and Richard C. Striebich[†]*University of Dayton Research Institute and University of Dayton Department of Mechanical & Aerospace Engineering, 300 College Park, Dayton, Ohio 45469-0116*

The development of an analytical method for quantification of thermally labile organic hydroperoxides in jet fuel via reaction with triphenylphosphine (TPP) is explored. The primary goal of this work is to devise a technique for hydroperoxide detection in jet fuel, for use in fuel oxidation studies, that will use only small sample volumes (<1 mL), have a low detection limit (<0.02 mM), have a broad dynamic range, and be fast, reproducible, and accurate. The reported technique uses the reaction of TPP with hydroperoxides to form triphenylphosphine oxide (TPPO) and the subsequent alcohol, which proceeds rapidly in jet fuel (less than 1 min) at ambient conditions. Elemental sulfur was used prior to analysis as a novel means to prevent the oxidation of TPP during chromatographic analysis by converting excess TPP into triphenylphosphine sulfide (TPPS) via another rapid, ambient condition reaction. Gas chromatographic (GC) analysis with flame ionization detection (FID) was used to quantify the resulting TPPO and TPPS, and the relative TPPO peak area was observed to be proportional to the hydroperoxide concentration. The production of TPPO by an interfering reaction was observed; however, TPPO produced via this reaction occurred predominantly in thermally stressed fuels, when large amounts of excess TPP were used. By limiting the amount of excess TPP used during the analysis we were able to control this interfering source of TPPO. The accuracy of the reported TPP method compares favorably with ASTM D6447. Finally, we report that the resulting method requires a small sample volume (0.5 mL), has a very low detection limit (0.002 mM), has a wide dynamic range, and is accurate and reproducible.

Introduction

Modern military and commercial aircraft rely on jet fuel as both a propellant and a heat sink, or cooling medium. In particular, military aircraft require jet fuel to have a large heat sink potential to be able to properly cool auxiliary systems, extending service life and reducing operational costs. However, certain current and future fuel temperature requirements promote thermal decomposition of jet fuel via autoxidation and pyrolytic pathways. Products of jet fuel thermal decomposition often include gums, varnishes, and coke, which are detrimental because they can foul and plug fuel system components, such as filters, valves, fuel nozzles, and heat exchangers.

Trace fuel species have been linked to the production of deposits during the autoxidation of jet fuels. Fuel hydroperoxides, i.e., organic hydroperoxides, are known to play a major role in the autoxidation of jet fuels.^{1–4} Hydroperoxides are the primary, initial autoxidation product species at relatively low temperatures (<120 °C). At higher temperatures, they begin to decompose,

resulting in production of free radicals which accelerate the rate of fuel oxidation. Even very small extents of decomposition (<<1%) can greatly affect the oxidation rate.⁵ Decomposition of trace levels of hydroperoxides may be the source of initiation which begins the autoxidation chain. In addition, reaction of hydroperoxides with other fuel species, such as sulfides and disulfides, may result in precursors to bulk and surface deposits.³

For the development of jet fuels with improved heat sink capabilities, it is important to better understand the role hydroperoxides play during thermal exposure. Research toward this goal is hampered by the lack of a suitable technique for quantification of hydroperoxides in these studies. In fuel oxidation studies, it is typically desirable to quantify hydroperoxides in unstressed fuels, small volume samples from benchtop thermal testing devices, and samples from large scale rigs. Therefore, a hydroperoxide analysis technique is needed that exhibits a very low detection limit (<0.02 mM for unstressed fuels), requires only a small volume of fuel (≤1 mL), and exhibits a wide dynamic range (ca. 0.02 to 5 mM). While there are currently two ASTM techniques (D3703 and D6447) available for hydroperoxide quantification, they are of limited usefulness for these studies due to one or more of the following factors: inadequate lower detection limit, limited dynamic range, too large a sample volume, and poor reproducibility.^{6,7} The first method, ASTM D3703,⁶ makes use of the

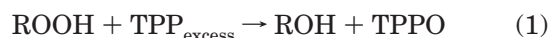
* To whom correspondence should be addressed. Tel.: (937) 255-4062. Fax: (937) 252-9917. E-mail: zachary.west@wpafb.af.mil.

† University of Dayton Research Institute.

‡ University of Dayton Department of Mechanical & Aerospace Engineering.

reaction of hydroperoxides with iodide ions resulting in the formation of iodine, which is subsequently determined by titration. This technique requires relatively large quantities of fuel (5 to 50 g), involves a subjective titration endpoint, and can have relatively poor reproducibility. The second method, ASTM D6447,⁷ also involves the conversion of the iodide ion to iodine, but uses a voltammetric method for determination of the iodine formed. This technique uses much smaller amounts of fuel (0.2 to 5 mL depending on the hydroperoxide level being measured), but does not exhibit a linear response at very low peroxide levels (<0.1 mM).

Previous workers^{8–13} have measured organic hydroperoxides using the well-known reaction of hydroperoxides (ROOH) with triphenylphosphine (TPP), forming triphenylphosphine oxide (TPPO) and the corresponding alcohol (ROH):



At room temperature, this reaction is rapid and goes to completion. With the use of an excess of TPP, the amount of TPP consumed can be measured by difference, or alternatively, the product alcohol or TPPO can be quantified. Measurement of the TPP consumed by difference requires two analyses and tends to be prone to poor reproducibility at low hydroperoxide levels. Measurement of the product alcohol allows identification of the original hydroperoxide, but in the present study we wish to quantify the hydroperoxides as a class of species, and therefore we have chosen to measure the TPPO product. Previous studies¹¹ using the measurement of TPPO were only performed at relatively high peroxide levels (>1 mM) and did not involve measurements in jet fuel matrices. In this paper, we report on the development of a technique to measure hydroperoxides in jet fuel using reaction with TPP over a wide range of hydroperoxide levels, including concentrations <<1 mM. We measure the TPPO reaction product via gas chromatography (GC) with flame ionization detection (FID).

Experimental Section

Preparation of Solvent and Reagents. Toluene (Optima 99.8+%, Fisher Chemical) is treated with basic alumina via Sorbent Technologies solid-phase extraction cartridges to remove hydroperoxide impurities. The maximum loading used is 15 mL of toluene per gram of sorbent (one cartridge holds 1 g of alumina sorbent) to ensure that the hydroperoxide impurities do not breakthrough.

Three reagent solutions of TPP in toluene are formulated to cover the range of anticipated fuel hydroperoxide concentrations. A typical set of solutions would be 0.75, 7.5, and 15.0 mM of TPP in toluene to cover maximum hydroperoxide concentrations of 0.15, 1.5, and 3.0 mM (due to dilution of the TPP reagent in the sample), respectively. For analysis of samples with hydroperoxide concentrations greater than 3.0 mM, a TPP solution must be formulated so that TPP will be in appropriate excess. Appropriate excess TPP is defined by the resulting TPPS/TPPO ratio as described in detail below. A reagent solution of elemental sulfur in toluene is made to be twice the molar excess of the TPP reagent with the highest molarity (typically 30 mM of sulfur in toluene). TPP (99%, Aldrich) and elemental sulfur (99.998%, Aldrich) are used without further purification.

TPPO and TPPS calibration solutions are prepared over a range of 0 to 4.5 mM by diluting a concentrated TPPO in toluene solution, or TPPS in toluene solution, with additional toluene. The TPPO (98%) and TPPS (98%) were from Aldrich and used without further purification.

All jet fuels were obtained from the U.S. Air Force Research Laboratory, Fuels Branch. As needed, fuels were thermally stressed at 140 °C for 15 h in a quartz crystal microbalance system that has been described previously.¹⁴ Also, cumene hydroperoxide (CHP, 88%) from Aldrich was used without further purification as a representative organic hydroperoxide for doped samples.

Sample Preparation and Analysis. Samples are prepared by delivering 0.1 ± 0.01 mL of the TPP reagent solution to 0.5 ± 0.01 mL of jet fuel in a 2 mL GC vial. The vial is capped and shaken vigorously, with the aid of a vortex mixer, for 20 s to ensure complete mixing. The sample is allowed to react at ambient conditions for 5 min. Subsequently, 0.1 ± 0.01 mL of sulfur reagent is delivered to the vial. Again the vial is capped and mixed vigorously for 20 s. A calibrated autopipet is used for delivering reagent and sample volumes with ± 0.01 mL accuracy.

Sample and calibration solution vials are transferred to an autosampler and analyzed with an Agilent 6890 series GC system, with a DB5MS column (30 m long, 0.25 mm i.d., and 0.25 μm film thickness) and an FID detector. One microliter of sample was injected into the inlet, which is operated in splitless mode at 280 °C. The oven profile is set with an initial temperature of 150 °C for 1 min and then ramped at a rate of 15 °C/min, with a 5 min hold at the final temperature of 320 °C. The total chromatographic run time is 18 min per sample.

Chemstation software (Agilent) is used to analyze the GC chromatograms and report the TPPO and TPPS relative peak areas, which are then recorded. TPPO and TPPS had retention times of about 11.02 and 11.59 min, respectively. Relative peak areas of TPPO and TPPS are then converted into concentrations using the following equations:

$$[\text{TPPO}] = \frac{\text{TPPO relative area response}}{\text{TPPO calibration slope}} \frac{7}{5} \quad (I)$$

$$[\text{TPPS}] = \frac{\text{TPPS relative area response}}{\text{TPPS calibration slope}} \frac{7}{5} \quad (II)$$

The fraction $7/5$ is a volume correction factor that accounts for the difference between the jet fuel volume (0.5 mL) and the analyzed sample volume (0.7 mL).

The relative excess TPP ratio (TPPS/TPPO) is calculated by dividing the result of eq II by the result of eq I. The TPPS/TPPO ratio is a gauge of the excess TPP used, with an acceptable operating range of 0.2 to 30 for stressed fuels and 0.2 to 50 for unstressed fuels. Figure 1 outlines a procedure for determining an appropriate TPP concentration, based on the resulting TPPS/TPPO ratio, for situations when the order of magnitude of hydroperoxides is unknown. In general, it is suggested that one use the least amount of TPP to still be in excess; however, it is also understood that TPP reagent solutions are formulated prior to analysis and will not always follow this guideline. On the basis of our experience, we found it useful to test unstressed fuel samples with a 0.75 mM TPP solution and stressed samples with a 7.5 mM TPP solution, since these TPP

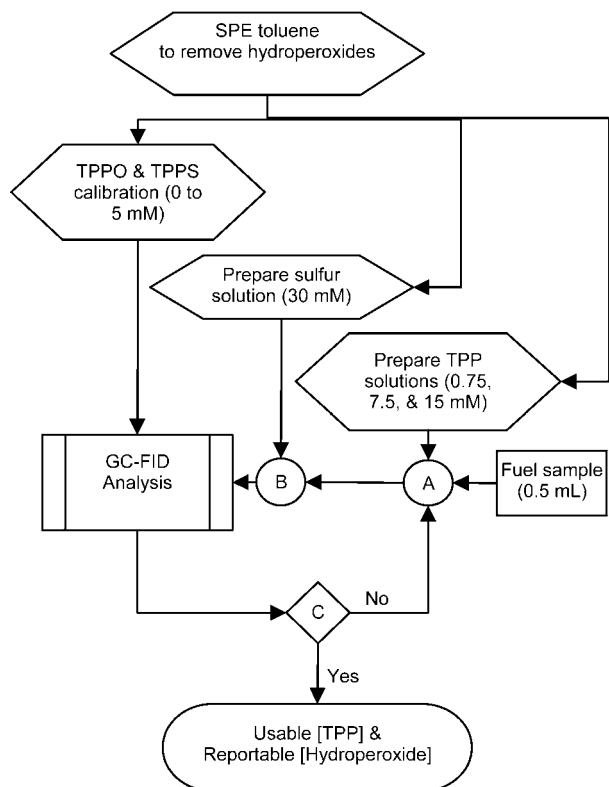


Figure 1. Flowchart to select an appropriate TPP concentration, for samples with unknown hydroperoxide levels, based on the TPPS/TPPO ratio. (A) For the first iteration, deliver 0.1 ± 0.01 mL of the 7.5 mM TPP solution; for iterations beyond the first, use an appropriate higher or lower TPP concentration solution based on the TPPS/TPPO ratio (e.g., if the TPPS/TPPO ratio is 0.01 [too low] then use a higher TPP concentration solution [15 mM]). (B) After the 5 min reaction time, add 0.1 ± 0.01 mL of the 30 mM sulfur solution. (C) Check the TPPS/TPPO ratio. If it is within the operating limits (i.e., unstressed fuels 0.2 to 50 and stressed fuels 0.2 to 30), then report the hydroperoxide concentration, and use the selected TPP concentration (from part A) for any further analysis. If the TPPS/TPPO ratio is not within the operating limits, then return to part A and adjust the TPP concentration accordingly.

concentrations often provided TPPS/TPPO ratios within the operating range for our fuel samples.

Results and Discussion

The reaction of TPP with hydroperoxides, reaction 1, has been well documented.^{8–13} These previous studies have shown that the reaction rapidly goes to completion at ambient temperatures, making it attractive for use in the quantification of fuel hydroperoxides. In this work, we have chosen to treat a sample of jet fuel with a dilute solution of TPP in toluene with subsequent GC–FID analysis to quantify the TPPO produced from reaction 1. Measurement of the product TPPO detects all hydroperoxides which react via reaction 1, and thus the peroxides are measured as a class. Identification of individual peroxide species was not a goal of the present work, but could be performed by analysis of the alcohol products of the reaction. Much previous work has involved the quantification of the TPP consumed upon treatment with excess TPP. This involves two analyses for each sample, and shows poor reproducibility at low peroxide levels due to the uncertainty involved in subtracting two analyses of relatively large TPP levels. The present method promises to provide significantly improved lower detection limits, required for quantifica-

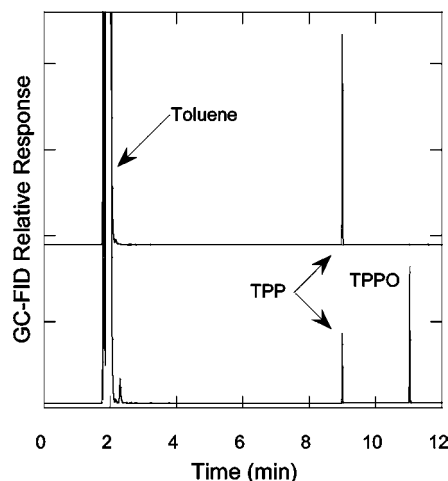


Figure 2. Chromatograms of toluene solutions with basic alumina SPE treatment (top) and without SPE treatment (bottom), both with subsequent addition of 1.0 mM of TPP.

tion of peroxides in unstressed fuels, by the analysis of the product TPPO via GC. Perkel et al.¹¹ have recently employed a similar methodology for the analysis of hydroperoxides in solvents. This work was limited to relatively high concentrations of hydroperoxides (>1 mM) and was not performed in complex jet fuel matrices. The goal of the present work is to demonstrate the viability of this analysis for hydroperoxides over a wide range of concentrations in unstressed and stressed jet fuels.

Initially we explored the separation of TPPO in the complex jet fuel matrices of interest. It was found that both TPPO and TPP could readily be separated from the matrix with excellent sensitivity using flame ionization detection. Unfortunately, dilute solutions of TPP in toluene (1.0 mM) showed a substantial TPPO response of 0.72 mM (Figure 2, lower chromatogram). Obviously, this is undesirable as it would severely limit our ability to detect low levels of hydroperoxides. Hydroperoxides are known to accumulate in organic solvents, such as toluene, during storage, and thus this large TPPO response may be due to the reaction of these species with the added TPP. Fortunately, treatment of solvents with basic alumina is known to remove hydroperoxides. We employed basic alumina solid-phase extraction (SPE) of the toluene solvent prior to the addition of TPP. The resulting chromatogram is shown in Figure 2 (upper chromatogram). The figure shows that the basic alumina treatment of the toluene solvent results in a substantial reduction in the TPPO peak. The measured TPPO concentration after basic alumina treatment is 0.003 mM. Further treatment of the toluene solvent provided no additional reductions in the TPPO level. The remaining TPPO observed can be due to residual peroxides in the toluene solvent, impurities in the TPP reactant, and/or TPP oxidized during the analysis procedure. Fortunately, this level of TPPO will not interfere with our lower detection limit goal. For reference, the 0.003 mM TPPO peak has an RMS signal-to-noise ratio of 40, which demonstrates that our lower detection limit will not be limited by the GC–FID sensitivity for TPPO.

Another possible cause of the TPPO observed, and a potential interfering process, is the reaction of TPP with oxygen (dissolved in the toluene or injected with the mixture) during the chromatographic analysis at the high temperatures in the GC injector port. It is well-

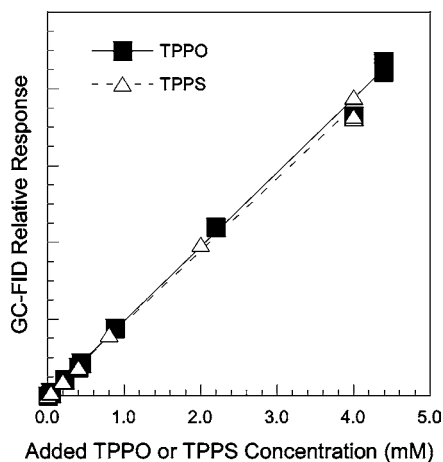


Figure 3. Calibration plots for TPPO and TPPS added to toluene.

known that TPP reacts with oxygen at elevated temperatures. Elemental sulfur can be used to limit the potential for oxidation of TPP after fuel treatment. An excess of elemental sulfur (excess over the TPP level) could be added to the toluene/fuel/TPP mixture to consume all of the remaining TPP via the reaction,^{15,16}



The resulting TPPS is much more stable to oxidation than TPP, thereby preventing further oxidation of TPP to TPPO. When excess elemental sulfur, along with basic alumina treatment of the toluene, is employed for the analysis of TPPO in the 1.0 mM TPP in toluene mixture, only 0.001 mM of TPPO is observed. This result shows that a significant amount (0.002 mM) of the observed TPPO is due to reaction during the chromatographic analysis. Using excess elemental sulfur treatment prior to the chromatographic procedure further improves the detection limit of the technique. We employed elemental sulfur treatment to prevent undesired reactions of TPP in all subsequent analyses.

Calibrations of separate solutions of TPPO and TPPS in toluene were run on the GC-FID system. The relative GC-FID peak area responses were recorded and linear calibration curves were observed over the range of calibration, 0.0010 to 5.14 mM and 0.040 to 4.0 mM for TPPO and TPPS, respectively. A representative calibration plot is shown in Figure 3. The overlapping TPPO and TPPS data seen in the figure demonstrates the almost identical response factors for both species on the FID. Calibrations were observed to be very reproducible on our system and were run on a monthly basis.

To determine the response in jet fuel matrices, known amounts of CHP were spiked into jet fuel samples and analyzed using the TPP method outlined in the Experimental Section. The results of these experiments are shown in Figure 4. The data demonstrates that in actual jet fuel matrices there is quantitative production of TPPO from the added CHP. Thus, this quantitative, room temperature reaction is very promising for use as an analysis technique for hydroperoxides.

As it is desirable for the analysis technique to be rapid, and it is important to ensure that the reaction has proceeded to completion, experiments were conducted to determine the reaction time required for the reaction of TPP with hydroperoxides. Various jet fuel samples were analyzed with the TPP method while

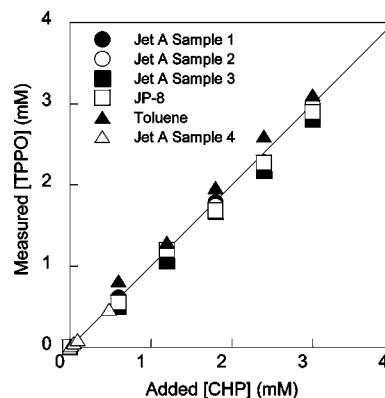


Figure 4. Measured TPPO concentration of fuel samples spiked with cumene hydroperoxide (CHP) showing the quantitative production of TPPO from hydroperoxide. The line shown represents $y = x$.

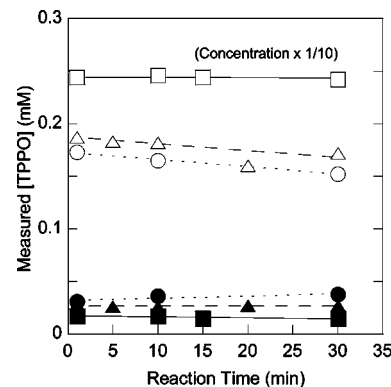


Figure 5. TPPO production dependence upon reaction time. Closed markers represent unstressed fuels while open markers represent the respective thermally stressed fuels. Circles (●, ○): JP-8. Squares (■, □): FT jet fuel. Triangles (▲, △): Jet A. The stressed FT jet fuel concentrations (open circles) are reduced by a factor of 10 to fit to scale.

varying the reaction time, i.e., the time from TPP solution addition to the time of sulfur solution addition, as shown in Figure 5. The figure shows that the measured TPPO concentration remains level over the entire reaction time range of 1 to 30 min, with the implication that the reaction is complete in less than 1 min. These results are in contrast to those of Perkel et al.,¹¹ who observed reaction times from 10 to 40 min. Apparently, the fuel matrix increases the reaction rate significantly beyond that of the solvent matrix used in the Perkel et al. work. Further discussion of the effect of the fuel matrix on the reaction is discussed below. Despite the less than 1 min reaction time observed, a reaction time of 5 min has been adopted for all subsequent analyses to ensure complete reaction for all samples.

To confirm that reactions 1 and 2 occur as expected, we monitored the concentrations of both TPPO and TPPS which result from the analysis of a 1.52 mM solution of CHP in a JP-8 fuel as a function of the amount of added TPP (both below and above the excess amount of TPP required). The hydroperoxide level present in the fuel prior to CHP addition was negligible in this case; therefore the hydroperoxide content of the fuel was considered to be the spiked amount, represented by the horizontal (equivalent to the amount of TPPO to be expected) and vertical (equivalent to the amount of TPP required to be in excess) lines drawn in Figure 6. The figure shows that as the TPP level is

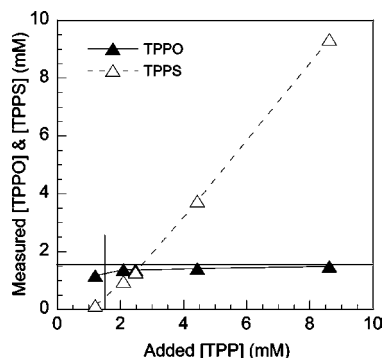


Figure 6. Plot of measured TPPO and TPPS concentrations for a JP-8 spiked with 1.52 mM of CHP with increasing amounts of TPP.

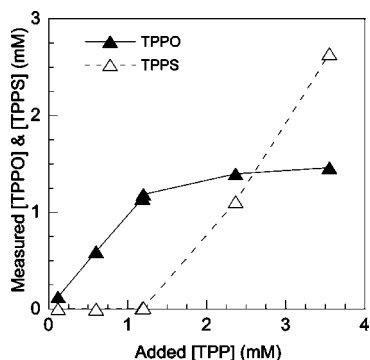


Figure 7. Plot of measured TPPO and TPPS concentrations for a stressed FT fuel with increasing amounts of TPP.

increased, the measured TPPO concentration rises to near the known hydroperoxide amount of 1.52 mM and stays level at greater amounts of added TPP. Also shown in the figure is the measured TPPS concentration. At low TPP levels, where TPP is less than the hydroperoxide concentration and thus not in excess, TPPS is not observed, implying that all the TPP is converted to TPPO by the hydroperoxides. However, as the TPP added was increased to an excess of the hydroperoxide concentration, the TPPS concentration rises, showing that TPP is now in excess of the CHP level. These results confirm that reactions 1 and 2 proceed as expected in our reaction system.

An analysis similar to that shown in Figure 6 was run using a thermally stressed Fischer–Tropsch process (FT) jet fuel, where TPP was added just above and below the excess point; however, in this case the hydroperoxide concentration was not known a priori. This stressed fuel was chosen because of its relatively high level of hydroperoxides produced during thermal oxidative exposure. The results for this second experiment are in Figure 7. Similar behavior is observed for the TPPO and TPPS concentrations of the FT fuel, compared to the JP-8 seen in Figure 6, with TPPO leveling off at a concentration (1.4 mM) which corresponds to the TPP level at which TPPS begins to form. These results provide further evidence that the reactions occur as expected in analysis of hydroperoxides produced from oxidative reactions (in contrast to the spiked cumene hydroperoxide used in Figure 6).

A complication observed in this analysis was that when very large excesses of TPP were employed, it was observed that the measured TPPO concentration became dependent on the amount of excess TPP added. This dependence on the TPP concentration is most

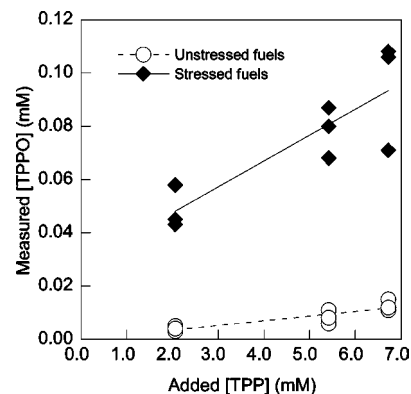


Figure 8. Plot of the measured TPPO concentration for stressed and unstressed jet fuel samples over a wide range beyond excess TPP.

noticeable when analyzing thermally stressed fuels. An example of the TPP concentration dependence of the measured hydroperoxide is shown in Figure 8. The plot shows that when very large excess TPP levels were used in stressed (TPPS/TPPO ratios above 30) and unstressed (TPPS/TPPO ratios above 300) fuels, increasing amounts of added TPP resulted in increased amounts of measured TPPO. Obviously, it is undesirable for the measured TPPO level to be dependent on the TPP added. Fortunately, this is only observed at very large excesses of TPP. In studies of hydroperoxides in carbonyl solvents, Perkel et al.¹¹ proposed that a competing reaction of TPP with carbonyl compounds could produce TPPO via a zwitterion pathway. Carbonyl species, such as aldehydes, ketones, and carboxylic acids, are well-known products from the autoxidation of jet fuel.¹ If carbonyl species cause the observed TPP dependence, we would expect to see a larger effect from thermally stressed fuels, as is observed. Obviously, it is important to limit this competing TPPO production pathway for accurate hydroperoxide quantification.

The preferred method to limit the TPPO produced by this competing carbonyl pathway is to limit the amount of excess TPP available for reaction. The amount of excess TPP can be gauged by the ratio of TPPS to TPPO concentrations measured, which provides a normalized measure of the excess TPP. Having tracked the TPPS/TPPO ratio over a multitude of samples, we have determined that an acceptable excess TPP ratio operating range for unstressed fuels is from 0.2 to 50 and from 0.2 to 30 for stressed fuel samples. The lower excess limit is to ensure that enough TPP is present for the hydroperoxides to react fully, while the upper excess limit is to prevent the overprediction of the hydroperoxide concentration from the competing reaction. Unstressed fuels have a higher excess limit because the competing pathway is less important than in stressed fuels. Fortunately, it is quite simple to monitor the TPPS to TPPO ratio, and the ranges suggested represent a very wide range of excess TPP levels that are acceptable. Table 1 lists some representative fuels that have been analyzed using a range of TPPS/TPPO ratios. It can be seen that the measured hydroperoxide concentration for the stressed JP-8 fuel is consistent at the lowest TPPS/TPPO ratio of 6; however, the concentration more than doubles at a ratio of 33 and triples at an excess ratio of 75. The JP-8, spiked JP-8, and Jet A-1 fuels seem less affected by the amount of excess TPP until the TPPS/TPPO ratio increases above 50. Interestingly, the TPP concentration has almost no effect on the

Table 1. Comparison of the Measured Hydroperoxide Concentration to the Amount of Excess TPP, or TPPS/TPPO Ratio, for Various Fuel Samples

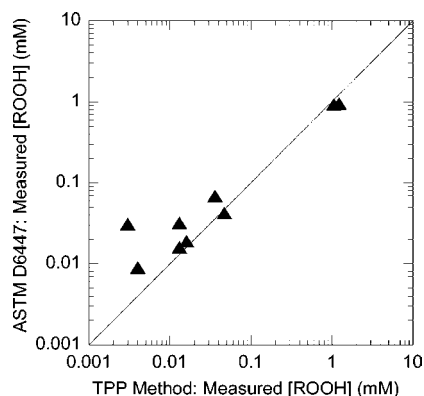
sample	[ROOH] (mM)	TPPS/TPPO
stressed JP-8	0.019	6
	0.021	6
	0.047	33
	0.065	75
spiked JP-8 (0.6 mM CHP)	0.611	9
	0.637	13
	0.641	40
	0.736	84
JP-8	0.005	29
	0.014	51
	0.025	139
	0.035	165
Jet A-1	0.007	23
	0.008	19
	0.014	52
	0.018	79
FT fuel	0.001	127
	0.002	330
	0.003	428
toluene	0.001	118
	0.004	423
	0.005	626

Table 2. Toluene Solutions with Known Concentrations of CHP Analyzed for Hydroperoxides Using Both the TPP Method and ASTM D6447

[CHP] in toluene (mM)	[ROOH] (mM)		TPPS/TPPO
	ASTM D6447	TPP method	
0.0	0.009	0.004	423
0.0105	0.034	0.012	130
0.105	0.092	0.097	15
1.050	0.986	0.950	0.7

measured hydroperoxide concentrations of the FT fuel and SPE treated toluene solvent (even at excess ratios over 100), illustrating the lack of carbonyl species in these samples.

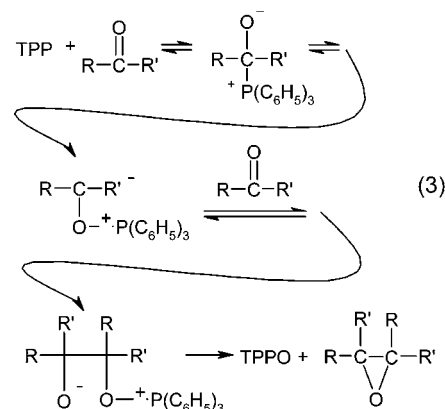
To show the utility of the TPP hydroperoxide method developed here, jet fuel samples (thermally stressed and unstressed), and samples of toluene spiked with known quantities of CHP, have been tested for hydroperoxides using both the TPP method and ASTM D6447. Table 2 shows the known hydroperoxide concentrations of the spiked toluene samples, along with the measured values from both methods. It can be seen that both methods are within 6–15% of the known values for the higher concentrations of CHP. However, at a CHP concentration of 0.0105 mM, ASTM D6447 overpredicts the

**Figure 9.** Log-log plot comparing measured hydroperoxide values using ASTM D6447 versus the TPP method for a group of eight stressed and unstressed jet fuels. The line shown represents $y = x$.**Table 3. Exxsol D-110 with Various Amounts of Added Carbonyl Compounds and/or Acids. Hydroperoxides Measured Using the TPP Method**

sample	added concentration (mM)				[ROOH] (mM)	TPPS/TPPO	[ROOH] increase
	aceto-phenone	cyclo-hexanone	acetic acid	nitric acid			
1	0	0	0	0	0.026	3.7	0
2	0	0	0	21.2	0.049	1.4	0.023
3	1.3	2.2	0	0	0.028	3.6	0.001
4	1.3	2.2	0	21.2	0.050	1.4	0.024
5	0	0	26.6	0	0.039	2.2	0.013
6	0.6	1.1	0	0	0.035	2.6	0.008
7	0.6	1.1	26.6	0	0.055	1.2	0.029

hydroperoxide concentration by a factor of 3. This is attributed to the fact that the hydroperoxide level is well below the reported linear detection limit of 0.2 mM for the ASTM method. Figure 9 is a log-log plot comparing the hydroperoxide measurements of real fuel samples obtained using both the ASTM D6447 method and the TPP method. As in the case of the CHP spiked samples, the plot demonstrates good agreement between the two methods, with the exception of when the ASTM method is used below the linear detection limit. The observations of Table 2 and Figure 9 show that the TPP method can correctly quantify jet fuel hydroperoxides over a wide range of concentrations in both spiked and real fuel samples.

Although we can minimize the production of extra TPPO from the interfering reaction with carbonyl species, we now further explore the source of this process. The pathway proposed by Perkel et al. for the reaction of TPP with carbonyl species,



involves the production of a zwitterion, which may be quite unfavorable in the nonpolar jet fuel matrix. We hypothesize that the formation of the zwitterion is likely catalyzed, in nonpolar media, by the presence of acids. An experiment was conducted where samples of Exxsol D-110 (a jet fuel like blend consisting mainly of normal paraffins and isoparaffins) were spiked with known amounts of representative carbonyl compounds, acids, and a combination of both acids and carbonyls. Hydroperoxides were analyzed using the TPP method and are reported in Table 3. The data show that acids, both organic and inorganic, increase these low levels of measured hydroperoxides. Whether this increase is due to catalysis of the carbonyl reaction or to a more direct reaction between the acids and TPP is difficult to conclude. The data show that carbonyl compounds alone also increase the measured hydroperoxides, but less efficiently than the acidic species. Since acetic acid is both an acid and carbonyl compound, it is difficult to

differentiate if the increase in hydroperoxide response is due to its acidic nature, carbonyl content, or combination of the two. However, the data clearly demonstrate that both carbonyls and acids have an impact on the results of the TPP analysis method, especially at very low hydroperoxide levels. The procedure we have described, utilizing low excess TPP levels, elemental sulfur addition, and short reaction times, is designed to minimize interferences from the species classes in unstressed and stressed jet fuel samples. Fortunately, fuels with relatively high levels of acids and carbonyls (such as thermally stressed samples) also tend to have relatively high levels of hydroperoxides, making the small interfering reaction relatively unimportant.

Conclusions

A technique to quantify hydroperoxides in jet fuel using reaction with TPP has been demonstrated to be effective over a wide range of hydroperoxide concentrations in both stressed and unstressed fuels. The experimental method shown here is rapid, uses small quantities of fuel (0.5 mL), has a very low detection limit (0.002 mM), has a wide dynamic range, and is accurate and reproducible. To obtain a lower detection limit adequate for analysis of unstressed fuels, contaminant hydroperoxides were removed from the toluene solvent via alumina SPE. Elemental sulfur was used as a novel means to prevent further reactions of TPP with non-hydroperoxide species during the analysis procedure. Also, interference in thermally stressed fuels caused by carbonyl species was observed, but was minimized by limiting the amount of excess TPP employed. The reaction of TPP with hydroperoxides to produce TPPO and alcohols is shown to proceed rapidly to completion, resulting in a convenient method for measuring hydroperoxide concentrations in jet fuels, and possibly other hydrocarbon systems.

Acknowledgment

This material is based on research sponsored by Air Force Research Laboratory under agreement number F33615-03-2-2347. The U.S. Government is authorized to reproduce and distribute reprints for governmental purposes notwithstanding any copyright notation thereon. The views and conclusions contained herein are those of the authors and should not be interpreted as necessarily representing the official policies or endorsements, either expressed or implied, of Air Force Research Laboratory or the U.S. Government. The authors thank Mr. Robert Kauffman (UDRI) for performing the ASTM D6447 measurements reported.

Literature Cited

- (1) Hazlett, R. N.; Hall, J. M.; Matson, M. Reactions of Aerated n-Dodecane Liquid Flowing over Heated Metal Tubes. *Ind. Eng. Chem. Res.* **1977**, *16*, 171.
- (2) Zabarnick, S.; Mick, M. S. Inhibition of Jet Fuel Oxidation by Addition of Hydroperoxide-Decomposing Species. *Ind. Eng. Chem. Res.* **1999**, *38*, 3557.
- (3) Balster, L.; Zabarnick, S.; Ervin, J. S.; Striebich, R.; DeWitt, M. J.; Douthip, T. Predicting the Thermal Stability of Jet Fuel: Analytical Techniques Toward Model Validation. Presented at the 8th International Conference on Stability and Handling of Liquid Fuels, Steamboat Springs, CO, 2003.
- (4) Zabarnick, S. Pseudo-Detailed Chemical Kinetic Modeling of Antioxidant Chemistry for Jet Fuel Applications. *Energy Fuels* **1998**, *12*, 547.
- (5) Zabarnick, S. Chemical Kinetic Modeling of Jet Fuel Autoxidation and Antioxidant Chemistry. *Ind. Eng. Chem. Res.* **1993**, *32*, 1012.
- (6) ASTM D 3703, "Standard test method for peroxide number of aviation turbine fuels," ASTM International.
- (7) ASTM D 6447, "Standard test method for hydroperoxide number of aviation turbine fuels by voltammetric analysis," ASTM International.
- (8) Barnard, D.; Wong, K. C. The Determination of Small Amounts of Organic Hydroperoxides with Triphenylphosphine. *Anal. Chim. Acta* **1976**, *84*, 355.
- (9) Stein, R. A.; Slawson, V. Spectrometric Hydroperoxide Determination by the Use of Triphenylphosphine. *Anal. Chem.* **1963**, *35*, 1008.
- (10) Dulog, L.; Burg, K. H. Bestimmung Organischer Peroxide. *Z. Anal. Chem.* **1964**, *203*, 184.
- (11) Perkel, A. L.; Krutskaya, L. V.; Freidin, B. G. Application of Triphenylphosphine to the Gas Chromatographic Determination of Peroxides in the Oxidation Products of Organic Compounds. *Zh. Anal. Khim.* **1994**, *49*, 768.
- (12) Denny, D. B.; Goodyear, W. F.; Goldstein, B. Concerning the Mechanism of the Reduction of Hydroperoxides by Trisubstituted Phosphines and Trisubstituted Phosphites. *J. Am. Chem. Soc.* **1960**, *82*, 1393.
- (13) Ruiz, A.; Cañada, M.; Lendl, B. A Rapid Method for Peroxide Value Determination in Edible Oils Based on Flow Analysis with Fourier Transform Infrared Spectroscopic Detection. *Analyst* **2001**, *126*, 242.
- (14) Zabarnick, S. Studies of Jet Fuel Thermal Stability and Oxidation Using a Quartz Crystal Microbalance and Pressure Measurements. *Ind. Eng. Chem. Res.* **1994**, *33*, 1348.
- (15) Heneghan, S. P.; Williams, T.; Whitacre, S. D.; Ervin, J. S. The Effects of Oxygen Scavenging on Jet Fuel Thermal Stability. *Prepr.-Am. Chem. Soc., Div. Pet. Chem.* **1996**, *41*, 469.
- (16) Clark, P. D.; Lesage, K. L. Quantitative Determination of Elemental Sulfur in Hydrocarbons, Soils, and Other Materials. *J. Chromatogr. Sci.* **1989**, *27*, 259.

Received for review October 4, 2004

Revised manuscript received March 1, 2005

Accepted March 3, 2005

IE0490379

INTENTIONALLY LEFT BLANK

APPENDIX W

Estimation of Select Specification Tests for Aviation Turbine Fuels Using Fast Gas Chromatography (GC)

INTENTIONALLY LEFT BLANK

Estimation of Select Specification Tests for Aviation Turbine Fuels Using Fast Gas Chromatography (GC)

R. C. Striebich,^{*,†} M. A. Motsinger,[†] M. E. Rauch,[‡] S. Zabarnick,[†] and M. Dewitt[†]

*University of Dayton Research Institute, 300 College Park, Ohio 45469-0116, and
Department of Chemistry, U.S. Air Force Academy, Colorado Springs, Colorado 80840*

Received May 6, 2005. Revised Manuscript Received August 2, 2005

The quality of aviation turbine fuels is measured largely by specification tests, which are routinely conducted for every large fuel supply purchased by the United States Air Force. Because military operations insist on more mobility than ever before, fuels are often purchased locally where the military is located. To test the fuels being purchased from unfamiliar sources, the military is examining mobile laboratories. With modern instrumentation such as gas chromatography (GC) with microbore columns and multiple detectors, compositional data can be easily and quickly obtained and related directly to specification test properties. By investigating composition–property relationships, a single GC experiment can be used to estimate several properties. In this work, the development and validation of specification test prediction using compositional data obtained via fast (<5 min) GC is presented. Simple correlations and relationships between properties and composition are suggested as possible ways to predict specification results without the expense and time required for testing. In this initial work, the properties investigated were simulated distillation, flash point, freeze point, and sulfur content. Results indicated that these tests could be reasonably predicted in minutes using correlations to fast GC data. Instrumentation developed for predicting specification tests was delivered to a field location and used to predict the specification results of locally purchased and captured fuels in wartime. These same fuels were also analyzed in regional laboratories, for validation of results.

Introduction

Aviation fuels have been an important component of the success of the gas turbine engine, which was first introduced by Han von Ohain in 1939. While early proponents of the gas turbine engine claimed to be able to fly these craft on any fuel ranging from peanut butter to whiskey,¹ there has always been a need to carefully control the quality of the fuel being used in gas turbine engines. Although the gas turbine engine may have, at one time, been more tolerant of fuel impurities than gasoline or diesel reciprocating engines, today's advanced turbine engines are not nearly as tolerant. Impurities in fuel can disable advanced turbine engines, interfere with the cooling of avionics and weapons systems, and disturb the control and gauging systems on board. Obviously, in-flight failures caused by aircraft fuel are more serious and potentially life-threatening than gasoline or diesel fuel failures on ground vehicles. Thus, fuel quality in an aircraft system is critical and is largely controlled by the fuel specification system.

Military and civilian fuel specifications are controlled under standards MIL-DTL-83133E (for military fuels) and ASTM D1655-01 (for commercial aviation).² These

two specifications detail properties for JP-8, which is military aviation fuel, and Jet A, which is the primary commercial aviation fuel. The current specification properties for JP-8 and Jet A are listed in Table 1.³ Although the military normally uses JP-8 jet fuel, the expeditionary (mobile) nature of today's Air Force, and the military in general, make it necessary to purchase local fuel from nearby sources. The benefit of not having to transport fuel is then offset by the inability to carefully control the quality of fuel purchased. Although fuel samples of locally purchased fuel can be sent to regional laboratories for specification testing, there is a benefit to operate mobile laboratories to measure important specification properties.

The specification tests, while all important to fuel performance, are often conducted using tests methods that are 20–50 years old. Some of these tests do not take advantage of today's modern analytical laboratory and may also be difficult to perform in the field. Standard ASTM-D86, for example, is a test designed to obtain a fuel's boiling range and most typically uses large glassware and mantle heaters.⁴ Standard ASTM D2386, which is the test for freezing point, requires that fuel be cooled to temperatures below $-47\text{ }^{\circ}\text{C}$.⁴ It also requires operators to watch a solution carefully to determine at which temperature the last solid crystal

* Author to whom correspondence should be addressed.

† University of Dayton Research Institute.

‡ Department of Chemistry.

(1) Martel, C. R. Military Jet Fuels, 1944–1987, Report No. AFWAL-TR-87-2062, Aero Propulsion Laboratory, Wright Patterson AFB, OH, November 1987.

(2) Aviation Fuel Properties, Coordinating Research Council, CRC Report No. 530, Atlanta, GA, 1983.

(3) Aviation Fuels; Chevron Products Company Technical Review, 2000.

(4) Distillation of Petroleum Products at Atmospheric Pressure, ASTM Standard Test Method D 86, *ASTM Annual Book of Standards*, American Society for Testing and Materials (ASTM), Philadelphia, PA.

Table 1. Military JP-8 and Commercial Jet A Specification Tests and Ranges^a

property	Value		ASTM test method
	Jet A or Jet A-1	JP-8	
	Composition		
acidity, total	0.10 mg KOH/g (max)	0.015 mg KOH/g (max)	D 3242
aromatics	25 vol % (max)	25 vol % (max)	D 1319
olefins	-	5 vol % (max)	D 3227
sulfur, mercaptan	0.003 mass % (max)	0.001 mass % (max)	D 3227
sulfur, total	0.30 mass % (max)	0.3 mass % (max)	D 1266, D 1552, D 2622, D 4294, or D 5453
	Volatility		
distillation			D 86
volume percent recovered			
initial boiling point, IBP	205 °C, max	report	
10	205 °C, max	205 °C (max)	
20		report	
50	report	report	
90	report	report	
final boiling point, FBP	300 °C (max)	300 °C (max)	
distillation yields			
residue	1.5 vol % (max)	1.5 vol % (max)	
loss	1.5 vol % (max)	1.5 vol % (max)	
flash point	38 °C (min)	38 °C (min)	D 56 or D 3828
density at 15 °C	775–840 kg/m ³	775–840 kg/m ³	D 1298 or D 4052
vapor pressure at 38 °C (kPa (max))			D 323 or D 5191
	Fluidity		
freezing point	−40 °C (max) (Jet A), −47 °C (max) (Jet A-1)	−50 °C (max)	D 2386, D 4305, D 5501, or D 5972
viscosity at −20 °C	8.0 mm ² /s (max)	8.0 mm ² /s (max)	D 445
	Combustion		
net heat of combustion	42.8 MJ/kg (min)	42.8 MJ/kg (min)	D 4529, D 3338, or D 4809
one of the following requirements:			
1. luminometer number	45 (min)	-	D 1740
2. smoke point	25 mm (min)	25 mm (min)	D 1322
3. smoke point	18 mm (min)	19 mm (min)	D 1322
naphthalenes	3.0 vol % (max)	-	D 1840
	Corrosion		
copper strip, 2 h at 100 °C (max)	No. 1	No. 1b	D 130
	Stability		
thermal stability, 2.5 h at 260 °C:			
filter pressure drop	25 mmHg (max)	25 mmHg (max)	D 3241
tube deposit, less than	<Code 3	<Code 3	D 3241
	Contaminants		
existent gum	7 mg/100 mL (max)	7 mg/100 mL (max)	D 381
particulates	1 mg/L (max)	1 mg/L (max)	D2276
water reaction, interface rating (max)	1b	1b	D 1094
water separation index modified	70	70	D 1094

^a Data taken from ref 3. See the current version of D 1655 for complete requirements.

disappears in the fuel as it is cooled, then heated. The flash point is a test in which samples must be heated to temperatures above 50 °C to measure fuel volatility. All of the tests can be well-conducted by technicians in laboratories under controlled conditions; however, because of excess power requirements, utilities, or bulky or breakable equipment, the tests are difficult to perform in a mobile laboratory. Although many of these tests have been miniaturized⁵ and modernized⁶ to some degree, they still entail conducting each performance test with a single piece of equipment.

In this contribution, we describe work that has been conducted to measure multiple specification properties for aviation fuel quickly with a single, rapid analytical measurement. This measurement will incorporate advanced laboratory instrumentation (gas chromatography (GC)), which can be more readily transported and

used in mobile laboratories. The goal of this testing is to conduct one fast (less than 5 min) GC experiment and to obtain accurate specification test results for multiple specification test properties. The specification test properties investigated in this initial work were distillation range, freeze point, flash point, and sulfur content. Empirical relationships with many fuels were developed for these properties and then validated using additional measurements made from fuels not used in the correlation development. After conducting the correlations of composition (as measured by GC) and properties, this instrumentation was sent to a military location to predict specification test results for the U.S. military. These correlations and the field usage of this technique demonstrate the ability of fast GC to quickly and accurately measure specification test properties with less time and equipment.

Background

A. Specification Test Prediction. Jet fuels are comprised of thousands of individual compounds. Prop-

(5) Standard test method for hydroperoxide number of aviation turbine fuels by voltammetric analysis, ASTM Standard Test Method D 6447, *ASTM Annual Book of Standards*, American Society for Testing and Materials (ASTM), Philadelphia, PA.

(6) Product information (available at <http://www.petrolab.com>).

erties of fuels, as measured by specification tests, are likely be related to the concentrations of these compounds and any interactions these compounds might have with each other. Therefore, it seems reasonable that properties may be directly related to composition, although the relationships may be complex. Chemometric procedures are continuing to be a popular way to define the complex relationships between composition and properties. The thermal stability of jet fuels, which is an extremely complex property that may be related to the trace composition of chemical constituents, has been attempted using chemometrics.⁷ Analysis of variance (ANOVA) techniques with GC \times GC data (two-dimensional gas chromatography) have also been used to predict the fuel types (e.g., Jet A vs JP-7 vs JP-5) of unknown petroleum samples.⁸

In addition to GC data as the source for chemometric procedures, spectroscopy has been used for the prediction of fuel properties. Near-infrared (NIR) spectroscopy-based predictions of octane number, aromatic content, API gravity, and vapor pressure have been conducted for gasoline⁹ and crude oil.¹⁰ Jet fuels and kerosenes were examined using NIR spectroscopy for viscosity, density, flash point, and other properties.^{11,12} Fourier transform infrared (FTIR) spectroscopy has also been used, along with chemometrics, to predict the Reid vapor pressure in commercial gasoline.¹³ Nuclear magnetic resonance (NMR) spectroscopy has been used to predict aromatic content, octane number, and other properties, based on the proton NMR spectra.¹⁴ In all of these cases, advanced laboratory instrumentation was used to predict property tests (density, viscosity, flash point, vapor pressure, etc.), in part, because of the potential to conduct multiple property measurements with one laboratory analysis. In addition, some of these analytical procedures may have been automated or may have been capable of on-line measurement, making the techniques of interest to fuel manufacturers and suppliers.

While chemometrics may indeed hold the ultimate answer to the prediction of these relationships, a simpler approach is described in this contribution. Because GC in nonpolar columns represents, in essence, a distillation, the use of simple GC retention would seem appropriate for flash point and distillation range. Indeed, in the case of simulated distillation, routines are available that predict single-plate distillation from GC data for mixtures from crude oils to finished gasolines.¹⁵ The flash point is directly related to the relative amount of low boiling (volatile) components available in a product. Thus, it would seem straightforward to use simpler relationships of composition to predict proper-

ties without resorting to the development of more-complex chemometric procedures.

A great deal of understanding about the low-temperature properties of fuels already exists. Several authors have reported that the freezing point of aviation fuel mixtures is dependent upon *n*-alkane concentrations^{16,17} and, specifically, the higher *n*-alkane concentrations in fuel. Thus higher *n*-C18 concentrations in fuel are more important than elevated C12 concentrations. This observation makes sense, with regard to the differences between diesel and jet fuel and the relative *n*-alkane concentrations in each. Thus, this work assumes the primary importance of these components and measures their concentration in a fast and reasonably accurate way to estimate the freeze point.

Gas chromatography is a versatile and convenient technique, in that general analysis can be conducted so that all components are measured. In addition, specific components can be measured if a detector exists that responds selectively to the property of interest. In the jet fuel specification, sulfur content is an important property, relating to emissions, catalyst poisoning, thermal stability, and general fuel quality. Sulfur detection by specification tests are conducted by techniques (such as X-ray fluorescence) which are appropriate for determining the differences between a specification "pass" and a "fail": that is, less than or greater than 0.3 wt % sulfur in fuel. Chromatographic detectors for sulfur are designed for low parts per million (ppm) determinations of individual sulfur levels; because the specification limit is 3000 ppm by weight, chromatographic detectors have more-than-adequate sensitivity to measure the sulfur content in fuel. The summation of a low resolution chromatographic determination of sulfur is directly related to total sulfur measurement.

In these four examples, (distillation range, flash point, freeze point, and sulfur content), we have selected properties that are directly related to and appropriate for GC measurement as an initial specification test prediction. Although other programs are being addressed to use these data with chemometric routines, it is clear that past experience about fuel properties and chromatography can reasonably predict some specification properties.

B. Fast Gas Chromatography. Fast GC analysis is useful for field determinations of jet fuel. Depending on the resolution required for a particular GC separation, analysis times can be greatly decreased using this technique rather than conventional GC. The need to analyze complex mixtures using GC is often a balance between the ability to separate adjacent peaks in a chromatogram (resolution) and analysis time. Especially in complex mixtures, analysts can use longer columns and much slower programming rates to increase resolution; however, there is a penalty to be paid in time of analysis. Because petroleum samples are arguably the most complex samples known, much work has been performed to provide the greatest possible resolution without the consideration of time. Some petroleum analyses that may take 2–4 hours and longer have been

(7) Johnson, K. J.; Rose-Pehrsson, S. L.; Morris, R. E. *Energy Fuels* **2004**, *18*, 844–850.

(8) Johnson, K. J.; Synovec, R. E. *Chemometr. Intell. Lab. Syst.* **2002**, *60*, 225–237.

(9) Latani-Barzilai, I.; Sela, I.; Bulatov, V.; Silberman, I.; Schechter, I. *Anal. Chim. Acta* **1997**, *339*, 193–199.

(10) Tuchler, W. *Pet. Coal* **2000**, *42* (1), 56–59.

(11) Seinsche, von K.; et al. *Erdoel, Erdgas, Kohle* **1996**, *112* (6), 261–263.

(12) Fodor, G.; Kohl, K.; *Energy Fuels* **1993**, *7*, 598–601.

(13) Flecher, P. E.; Welch, W. T.; Albin, S.; Cooper, J. B. *Spectrochim. Acta, Part A* **1997**, *199*–206.

(14) Meusinger R. *Fuel* **1996**, *75* (10), 1235–1243.

(15) Product information on automated software from Separation Systems (available via the Internet at <http://www.separationsystems.com/sde.htm>).

(16) Van Winkle, T. L.; Affens, W. A.; Beal, E. J.; Mushrush, G. W.; Hazlett, R. N.; DeGuzman, J. *Fuel* **1987**, *66*, 890–896.

(17) Ervin, J.; Zabarnick, S.; Binns, E.; Dieterle, G.; Davis, D.; Orbrun, C.; *Energy Fuels* **1999**, *13*, 1246–1251.

reported.¹⁸ However, because better resolution is frequently unnecessary for some analyses, there is a definite application for faster analysis.

The history, methods, and applications for conducting fast analyses via GC are delineated in several excellent reviews.^{19–23} In these works, the authors discuss the typical ways to shorten analysis time: (a) decrease the column length; (b) increase the carrier gas flow rate; (c) use multichannel columns;²³ and (d) provide rapid heating of the column with heating rates up to 1200 °C/min and higher.¹⁹ Fast GC, in these instances, is best-described as conducting analyses as fast as is possible to provide *sufficient* separation of the compounds of interest. Often, in the search for maximum resolution, compounds can be over-separated, which usually lengthens the time of analysis which can be possible. Fast GC could be described as that separation which can produce the desired analytical information in the shortest time.

In petroleum analyses, and specifically for aviation fuels, there are a good many separations where complete resolution is not needed. Fingerprinting of different types of fuels (diesel, gasoline, aviation fuels, kerosene, etc) can be performed quickly to characterize the mixtures in useful ways.²⁴ Simulated distillation²⁵ is one good example of a chromatographic analysis that has low resolution but can be conducted very fast ($\ll 5$ min). Fortunately, excellent resolution is not usually necessary to obtain the critical information about distillation range;²⁴ therefore, this application is a good example of fast GC where limited resolution is required. One must decide, therefore whether the speed of analysis allows enough resolution to provide compositional information about the fuel, which can be related to the results of the specification tests.

Experimental Section

The goal of this program was to conduct a rapid, single GC experiment using flame ionization detection and sulfur-specific detection, and to relate these results empirically to specification test results for total sulfur, distillation range, flash point, and freeze point. The instrumentation developed was to be transported for military installations in the field for use as a specification test predictor for the properties listed.

A. Fast Gas Chromatography Instrumentation. The fast GC system was developed to provide a 5-min analysis of the fuel in question with sufficient resolution for specification test prediction. Two fused-silica capillary columns were used with a two-holed ferrule into the injector of a gas chromatograph (Agilent model 6890). The first column, which is a 7.0-meter microbore HP-5 (0.1 mm inner diameter (ID), 0.17 μ m film thickness; Agilent Technologies), was connected to a flame

ionization detector (FID). The second column was a wide-bore 30-m model HP-5 (0.32 mm ID, 0.25 μ m film thickness, Agilent technologies) which was connected to a sulfur-specific flame photometric detector (FPD) on the GC. The columns were chosen because of their nonpolar nature, which ensured that compounds would elute essentially by boiling point, which is an important and necessary feature for these predictions. The detectors were also chosen to make use of the excellent linearity of the FID signal and the specificity of the FPD for sulfur detection. An Agilent Chemstation was used to monitor both signals from the two detectors simultaneously. Because the first column was a microbore (0.10 mm ID), peaks are typically much narrower than more-traditional columns (0.25 mm). Thus, the data rate for the FID was 100 Hz, instead of the more-common rate of 20 Hz. The FPD was operated at 20 Hz. An auto sampler was also used with this chromatographic system.

The conditions of temperature programming and pressure programming the GC system were chosen to balance the speed of analysis and the splitting of sample in the two dissimilar columns. The inlet pressure for the two columns was chosen to optimize (or nearly so) the separations being conducted in the microbore column to the FID. In this case, the average linear velocity was fixed at 41 cm/s in constant flow through the column. This setting resulted in a nominal initial inlet pressure of 29.4 psi, which increased throughout the analysis to maintain constant column flow. The wide-bore column to the FPD was not used optimally, resulting in poor resolution from the second column separation. However, because the analysis being conducted was total sulfur measurement, the need for optimal resolution per unit time was only required in the first column. A high split ratio (200:1) was used for all analyses in this study. All of these important flow rates were controlled using electronic pressure control features within the GC system.

The separations performed in the laboratory and used to develop the correlations were conducted in helium carrier gas. However, because this system was to be used in a mobile laboratory, no gas bottles were desired. The exclusive use of gas generation would allow the system to be more mobile and would not significantly detract from the resolution of the separations. Therefore, a nitrogen-air separation system (Domnick Hunter, Ltd., model UHPA0601W) was obtained to provide pure nitrogen for the carrier gas and makeup gas for each detector. It also provided dry, filtered air for the FID and FPD systems. A hydrogen generation system (Matheson/Airgas, Chrysalis model) was also used to provide hydrogen gas from the electrolysis of water for the FID and FPD systems. While hydrogen could have been used for carrier gases to increase speed and resolution, the safety aspect of using hydrogen in high-split ratio injections for a forward-operating mobile laboratory was not desirable.

Sample preparation required a constant dilution of the fuel to be analyzed. In this case, each fuel was diluted 1:20 in hexane solvent. Simulated distillation requires a standard of normal alkanes (C5 through C17) to be analyzed, to determine the retention times of each of the alkanes. In addition, Jet A fuel with 1700 ppm (by weight) of sulfur was used to calibrate the sulfur detector. Dilutions of this solution in hexane were performed using syringes, which were made available for the mobile laboratory.

B. Correlation Development. The goal of this program was to develop empirical correlations of GC data to specification test results so that one injection could be used to predict specification test results. Fuels from several test programs being analyzed by specification tests were used to develop the correlations to the properties of simulated distillation (distillation range), flash point, freeze point, and sulfur content. Table 2 lists the appropriate specification property and ASTM test method for each of the tests. Specification test results were

(18) Altgelt K. H., Gouw, T. H., Eds. *Chromatography in Petroleum Analysis*; Marcel Dekker: New York, 1979; pp 75–89.

(19) McNair, H. M.; Reed, G. L. *J. Microcolumn Sep.* **2000**, *12* (6), 351–355.

(20) Cramers, C. A.; Janssen, H.-G.; van Deursen, M. M.; Leclercq, P. A. *J. Chromatogr., A* **1999**, *856*, 315–329.

(21) Cramers, C. A.; Leclercq, P. A. *J. Chromatogr., A* **1999**, *842*, 3–13.

(22) David, F.; Gere, D. R.; Scanlan, F.; Sandra, P. *J. Chromatogr., A* **1999**, *842*, 309–319.

(23) van Lieshout, M.; van Deursen, M.; Derks, R.; Janssen, H.-G.; Cramers, C. *J. Microcolumn Sep.* **1999**, *11* (2), 155–162.

(24) Striebich, R. C. *Prepr.-Am. Chem. Soc., Div. Pet. Chem.* **2002**, *47* (3), 219–222.

(25) Boiling Range Distribution of Petroleum Fractions by Gas Chromatography, ASTM Standard Test Method D2887-93, *ASTM Annual Book of Standards*, American Society for Testing and Materials (ASTM), Philadelphia, PA.

Table 2. Specification Tests Used To Correlate to Fast Gas Chromatography (GC)

specification property	ASTM method	description
distillation range	D2887	simulated distillation, a GC-based method that can provide volatility data in place of the one plate D86 distillation data
flash point	D56, D93	ability of fuel vapors at specific temperatures to ignite when exposed to a flame
freeze point	D2386	temperature at which visual solids disappear upon warming
sulfur content	D1266, D2622	weight percent of sulfur-containing organics in fuel

Table 3. Specification Limits for Volatility, as Measured via ASTM D86

	Volatility Limit				
	JP-8	Jet A	JP-7	JP-5	Avgas(100/130)
initial boiling point, IBP	report		182 °C (min)		report
T 10% rec. max	186 °C (max)	186 °C (max)	196 °C (min)	205	75 (min)
T 20% rec. max	report		206 °C (min)		report
T 50% rec. max	report	report	report	Report	report
T 90% rec. max	report	report	260 °C (max)	Report	report
final boiling point, FBP	330 °C (max)	300 °C (max)	288 °C (max)	300 °C (max)	290 °C (max)
residue	1.5 vol %	1.5 vol %	1.5 vol %	1.5 vol %	
loss	1.5 vol %	1.5 vol %	1.5 vol %	1.5 vol %	

performed according to ASTM test methods by qualified quality control laboratories.

Results and Discussion

A. Development of Correlations and Validation of Predictions. The results of chromatographic determinations were related directly to specification test results for a collection of fuels. Training sets of fuels analyzed for the properties of interest were developed. Other fuel samples were then used to validate the correlations; fuels from the validation set were not used in the training set for the development of the correlation. The fuels used for training were Jet A or JP-8 fuels, with as wide a range of properties as the specification would allow. In some cases, off-spec fuels (diesel fuels or gasolines) were added to the training set to allow a broader range of property values with which to compare.

A.1. Simulated Distillation. In simulated distillation, the chromatographic column replaces the distillation apparatus of Standard Method ASTM D-86. In doing so, the distillation changed from a single-plate distillation to a more complete multiple-plate distillation using chromatography. This information is generally different than the specification results from distillation, which are primarily derived from Standard Method ASTM D-86. Several researchers have investigated the relationship of simulated distillation (D2887) data with D-86 data.²⁶ In fact, relationships exist for converting D2887 to D86 data and are used routinely in available software for conducting these methods on GC systems.¹⁵ Also, specification test levels for military jet fuel are available for D2887 data as well as D86 data. The existing specification levels for D86 distillation data are given in Table 3.

The use of simulated distillation for predicting D86 data is well-documented. The purpose of this work was to use Standard Method D2887 to predict specification-grade fuels, and also to predict D86 data from the D2887 data. Figure 1 shows a plot of the retention time versus *n*-alkane boiling point. Using the cumulative area of the chromatographic tracing along with the boiling points

for individual *n*-alkanes, one may construct a cumulative distribution for boiling range, as shown in Figure 2. The cumulative distribution of the peaks eluting from the FID analysis is compared to the total FID response to obtain the area percentage of the chromatogram (essentially, the percentage recovered), which was then related to the temperature to recover that fraction by comparison to Figure 1.

The retention time at which a percentage of the area was achieved was related to the boiling temperature by comparison with Figure 1 to generate a cumulative distribution, with respect to temperature. Through examination of this curve, it is possible to find the cut points (percentage recovered at various temperatures), as shown in Figure 2. With the cumulative distribution, one can predict the percentage of recovered fuel.

Unfortunately, it clear from Figure 2 that Standard Method ASTM D86, which is the current specification test for boiling range, does not agree precisely with Standard Method D2887, except near the midpoint of the cumulative distillation plot. This observation is well-established in the literature^{15,26} and empirical correlations now exist to perform the routines to transfer the D2887 chromatographic information to D86 data for comparison to the specification tests. However, the commercial product was unavailable to use at the time; therefore, a less-sophisticated adjustment (using the average deviation from the D86 to D2887 data for a

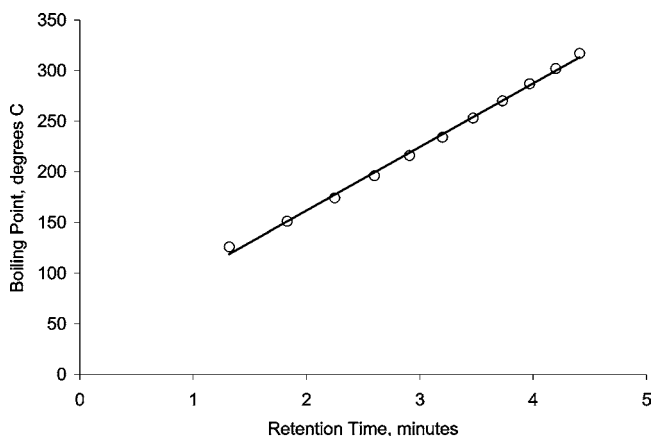


Figure 1. *n*-Alkane boiling points plotted against retention time from heptane (C7) through heptadecane (C17).

(26) Martel, C. R. Investigation of ASTM D2887 Test Method for use with Aircraft Turbine Engine Fuels, Report No. AFAPL-TR-74-122, Aero Propulsion Laboratory, Air Force Systems Command Wright Patterson AFB, OH, March 1975.

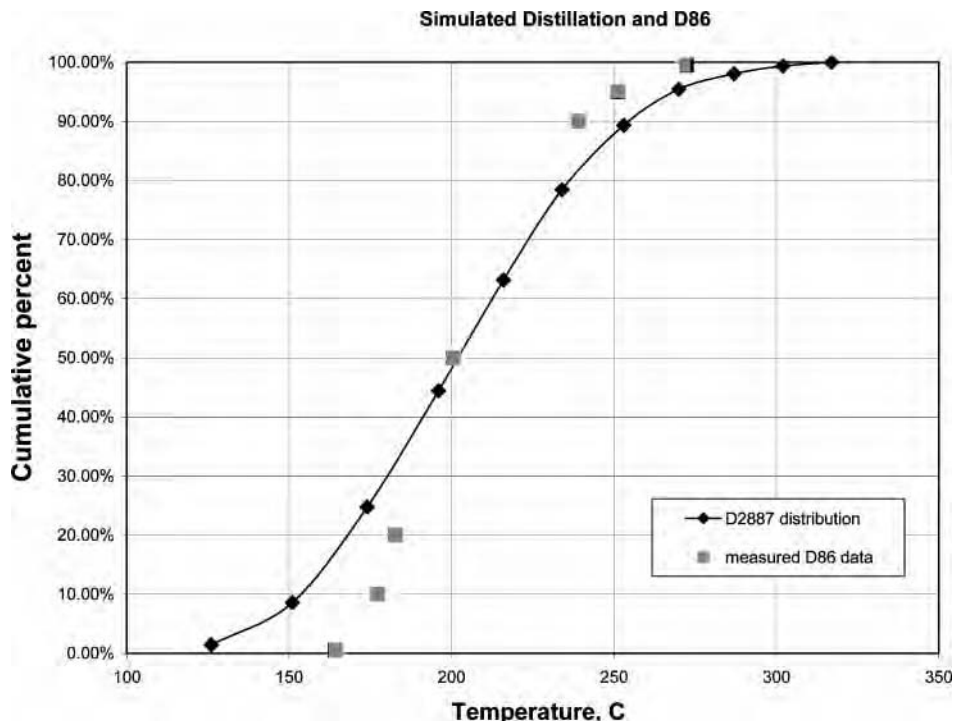


Figure 2. Curve showing the cumulative distribution of the boiling range distribution as predicted by Standard Method ASTM D2887 for one of the fuels used in the training set. The squares represent the D86 distillation temperatures as measured by the specification tests.

particular recovery point) was established with the training set and evaluated using the validation set. Additional commercial software will be incorporated in the future.

This work describes an empirical relationship of the cumulative chromatographic response (percentage recovered), compared to measured D86 responses for a large training set of fuels. These fuels were taken mostly from Jet A and JP-8 samples from the United States. The size of the training set was 99 fuels tested by D86 distillation. To relate the GC simulated distillation predictions to the D86 measurements, a relationship between the two data sets was developed using the $n = 99$ training set for each distillation recovery tested (10%, 50%, and 90%). Another set ($n = 33$) of data (not included in the training set) was then used to evaluate the accuracy of this prediction.

The results of the predictions for simulated distillation are shown in Figure 3. The results generally fall within 10 °C of the measured D86 temperature for 10%, 50%, and 90% recovery. The predominance of points below the $y = x$ line indicates a slight bias. By incorporating other software routines to change the D2887 data to D86 data, we may improve these correlations. Also, some jet fuel specifications (JP-5, JP-8) provide D2887 (simulated distillation) specification limits for the 10% recovered temperature (186 °C for JP-8). However, GC-based simulated distillation is a proven technique and can be conducted readily in the fast GC analysis.

To conduct simulated distillation, a normal alkane standard must be analyzed to determine the relationship between retention time and boiling point for the normal alkanes under the instrumental conditions selected. These standards need not be run if the chromatographic columns used are identical to those used in the current experiments. However, from a

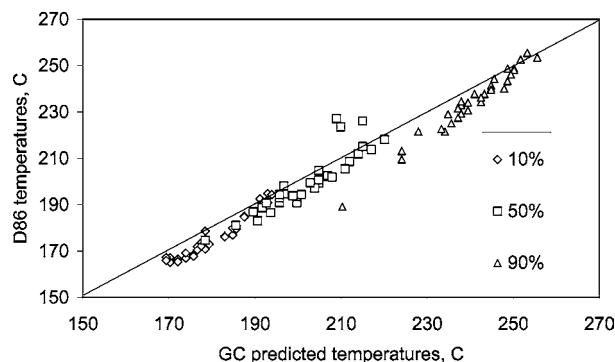


Figure 3. Gas chromatography (GC) predictions of ASTM D86 distillation data using the modified simulated distillation method. The predictions are compared to actual ASTM D86 data for a set of data that was not used to develop the correlations.

practical viewpoint, all columns are slightly different and the determination of retention times for alkanes is more straightforward after examining a standard mixture.

A.2. Flash Point. The flash point was determined simply by summing the area of the peaks eluting before the C9 *n*-alkane (see Figure 4). Although other compounds contribute some volatility, these compounds represent the great majority of the volatile compounds; that is, compounds that would be in the vapor phase at the temperatures indicated. Because the FID for this GC system provides a constant response factor for most of the volatile compounds, this semiquantitative estimation works reasonably. Several aromatic compounds have different response factors than the aliphatic compounds; because higher or lower concentrations of aromatic compounds, compared to aliphatic compounds, will change the volatility without changing the area response of this collection of peaks, there is error

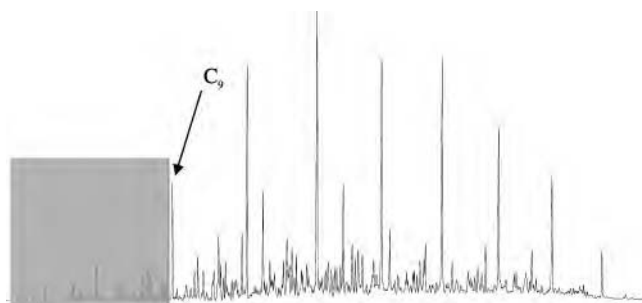


Figure 4. Calculation of flash-point area (small box) versus the total chromatographic area (large box). This ratio is then related to the ASTM measured flash point.

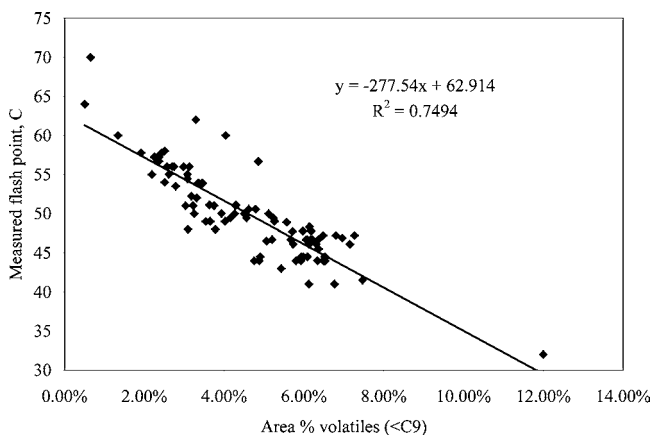


Figure 5. Area-percent response of hydrocarbons, relative to the total hydrocarbon response measured by a flame ionization detector (FID) ($n = 116$).

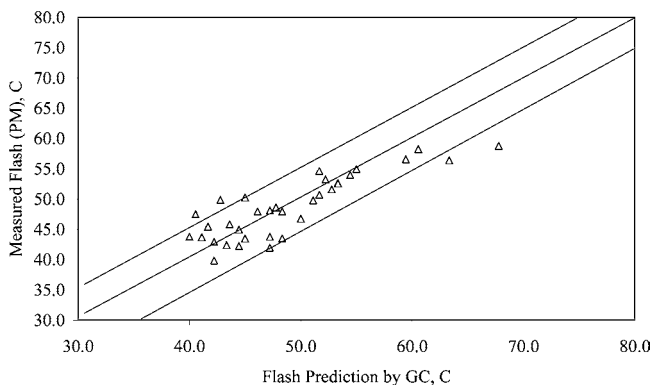


Figure 6. Actual versus predicted flash-point temperatures for World Survey program fuels.

associated with this measurement. Improvements could be made if retention times were tracked and aromatic compounds were distinguished from aliphatic and response factors for each class were calculated. However, because this technique needed to be field-portable and simple, the aromatic and aliphatic compounds were lumped together and used in this estimating fashion.

The calibration of this estimate is shown in Figure 5, where the area percentage of the chromatographic response is plotted against known measurements of flash point temperature. This correlation was used to predict the flash points of other fuels, not included in the training set. These results are shown in Figure 6.

Flash-point testing is normally performed using Standard Methods ASTM D56 (Flash Point by Tag Closed Tester) or ASTM D93 (Flash Point by Pensky Martens Closed Cup Tester). The development of the correlation

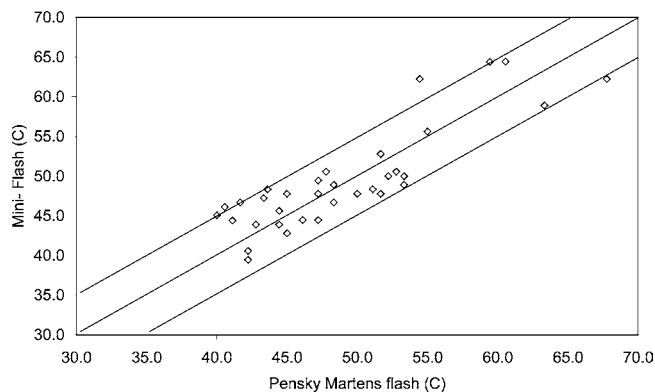


Figure 7. Comparison of two ASTM flash point tests methods (Mini flash versus Pensky Martens Flash).

did not distinguish between these two techniques, even though they generally show a slight bias. Several of the fuels examined in this effort were performed by both techniques (Standard Methods D56 and D93). Figure 7 shows the differences between the two techniques and the level of accuracy for the same sample measured by the same laboratory.

It is apparent that the ASTM methods themselves have some inherent error, with regard to the flash point. The great majority of the fuels tested by both methods show agreement to within 5 °C. The GC prediction technique is generally accurate to 5 °C, with some notable exceptions, as observed in Figure 6. The conclusion from these figures is that simple GC area percent calculations can be used to predict the flash point almost as well as the ASTM methods, and they can be conducted at different laboratories or via different methods. The error associated with the estimation by GC is not significantly different than that of the ASTM tests themselves. This is interesting, given the fact that the correlations were performed using the ASTM tests, with their associated errors. The fact that the GC-based calculations provide little additional error to this measurement is indication of its suitability as an estimator or screening tool.

A.3. Freeze-Point Predictions. Prediction of the freezing point is an important and useful measurement to perform for field applications, because of the difficulty of supporting the cryogenic or subambient conditions necessary for conducting the freeze-point test. It is an important measurement to be made in the field, because an accurate measurement of the freeze point could allow aircraft to be operated at temperatures closer to the fuel's measured freeze point, rather than at temperatures closer to the specification test limit. Currently, aircraft must be operated at temperatures above the fuels specification freeze point, rather than the measured freeze point.

In this application, we recognize the close relationship between freezing point and normal alkane concentration. This relationship has been shown in both diesel and jet fuel samples:²⁷ the higher the concentration of heavier normal alkanes, the higher the freezing temperature. Heavier *n*-alkanes, being the most likely components to freeze at high temperatures, have a tendency to align and agglomerate. Thus, a relationship

(27) Zabarnick, S.; Widmore, N.; Vangness, M. *Energy Fuels* **2002**, *16*, 1565–1570.

between n -alkane concentration in the fuel and the measured freeze point was anticipated. The higher n -alkanes were weighted to be more important in this relationship and the best, but non-unique, weighting relationship was determined empirically as a power-law equation. The higher n -alkanes were higher weighted by considering the boiling point of each carbon number alkane, as shown below in eq 1.

$$W_n = A(T_{mp,n} - T_c)^P \quad (\text{for each } n\text{-alkane}) \quad (1)$$

where W_n is the weighting factor for each n -alkane (C8–C20), A is a pre-exponential factor, $T_{mp,n}$ is the melting temperature of each n -alkane, T_c is the constant temperature used to reduce the power-law term, and P is a power-law factor.

The variables A and P —the pre-exponential factor and the power-law factor, respectively—are solved by successive iteration based on a minimization of error (prediction minus measured) using initial estimates for A and P . By multiplying these weights by the area-percent (approximately the weight-percent) concentrations for each normal alkane, one obtains a relationship that describes a value that gives the n -alkane concentrations weighted toward the heavier normal alkanes, taking into account both concentration and carbon number.

$$X = \sum_{n=20}^{n=8} W_n [C_n] \quad (2)$$

where $[C_n]$ is the area percent concentration of the n -alkane and X is the weighted n -alkane concentration factor.

This value, summed between the C8 and C20 weighted n -alkane concentrations, could then be compared empirically with measured freeze points. The weighting factor and concentrations for each normal alkane were summed and, using linear regression, were compared to the measured freeze point to obtain a slope and intercept for the linear relationship. With the slope and intercept, an estimation of the predicted freeze point was determined. By repeating this spreadsheet calculation with different values for T_c , A , and P , and then minimizing the residual between the measured and predicted values, we obtain the relationship in eq 3:

$$T_{fp} = \left[\sum_{n=20}^{n=8} 5.0 \times 10^{-14} (T_{mp,n} - 200)^{7.07} \times [C_n] \right] [\text{slope}] + \text{intercept} \quad (3)$$

where the slope and intercept were determined by the previously described relationships. These A factors, P values, slopes, and intercepts were calculated to minimize errors for 91 fuels for which freeze-point data were available. These final relationships, as described by eq 3, were used to predict the freeze points for an independent set of fuels. Figure 8 shows the agreement for these 38 fuels for which data were available.

In these data, it is apparent that the freeze-point predictions can differ by 5–7 °C from the measured freeze-point values. This prediction is probably not precise enough to be used to determine minimum in-flight temperatures. A field technique that could ac-

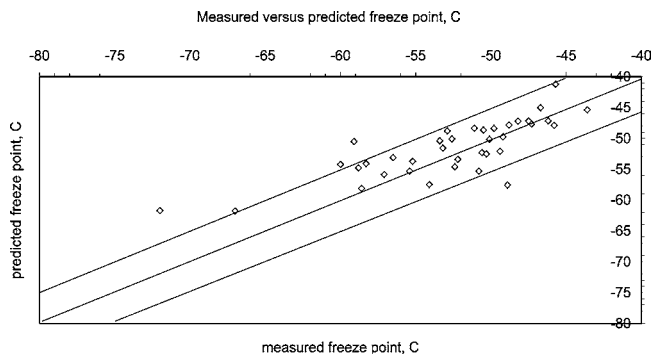


Figure 8. Measured versus predicted freeze point for a weighted concentration of normal alkanes using empirical data.

curately predict the freeze point would allow aircraft to fly at a temperature just above the freeze point of the particular fuel being used, instead of the specification limit of the fuel. Further work is need to improve these predictions using GC data.

Clearly, the higher normal alkanes are important factors in determination of the freeze point. The weighting factors used show the importance of the C15 through C20 normal alkanes, although the concentration effect also has an important role. That is, the low concentrations of heavily weighted C20 may not be as important as the high concentrations of C16 or C15 in the fuel. Also, the concentrations of alkanes less than C11 were determined to be virtually unimportant, no matter their concentration. These observations are apparent in the determination of the freeze point for diesel fuels as compared to jet fuels, because diesel fuel n -alkane concentrations, especially for C18 through C11 and above, are quite high. Freeze-point predictions for diesels are often greater than 0 °C; although not an accurate freeze point, this value shows the importance of the higher n -alkanes in freeze-point prediction.

A.4. Sulfur Content. Sulfur content is perhaps the most directly measured property for GC, because a sulfur detector is available as one of the two detectors on the system. Although the column connected to this system was not a microbore column, the column velocity and flow were so high that experiments could be performed within ~5 min, which is the length of time of the microbore separation. Although some resolution is lost in operating the column at this excessive flow rate, our goal was only to measure the total sulfur content of the fuel sample, meaning that the area response of the flame photometric detector (FPD) could be summed and that resolution of individual components was not an issue. The two chromatograms in Figure 9 show the simultaneous collection of FID data, representing the microbore GC separation of the hydrocarbon components of the fuel, and the sulfur signal from the low resolution separation in the second column.

The calibration of this system was performed using a single fuel sample. The fuel (Code POSF-2959) is a high-sulfur fuel that was measured using standard microcoulometry tests (ASTM D3120) to be 1700 ppm (wt/wt). Calibration was performed using syringes to dilute this sample. Every jet fuel sample analyzed had to be accurately diluted using syringes, or some other accurate dilution technique. The calibration curve,

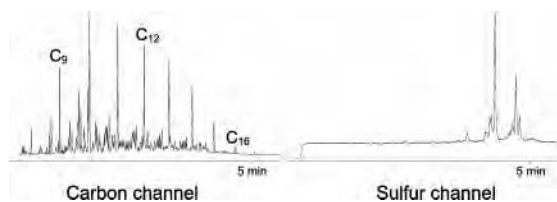


Figure 9. Simultaneous carbon and sulfur channels using the flame photometric detector in parallel with the FID for experiments with a duration of <5 min. Sulfur signal is summed to obtain a total sulfur concentration, compared to a calibration curve.

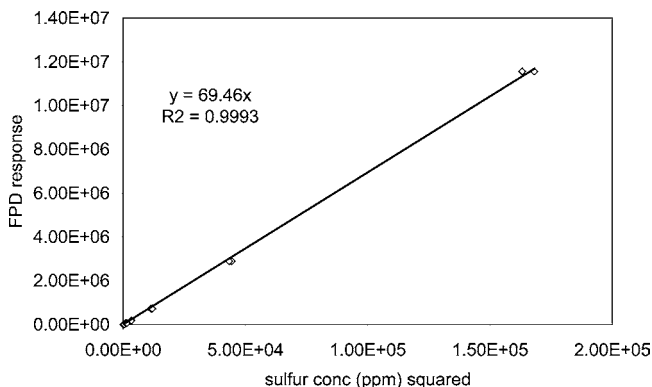


Figure 10. Sulfur calibration for the flame photometric detector (FPD) based on the square of the sulfur concentration.

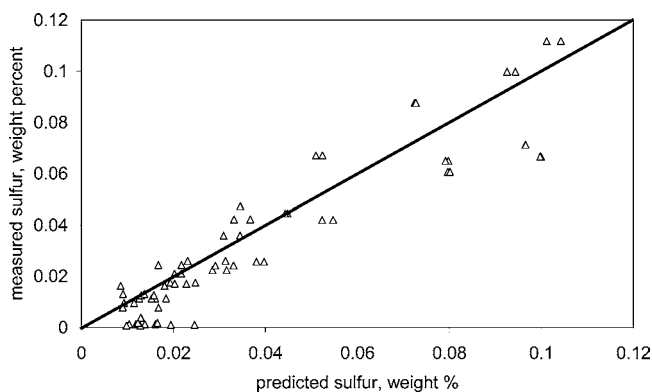


Figure 11. Predicted (by GC–FPD) versus measured (ASTM D2622) sulfur content for 38 fuels from the World Survey program.

based on the response of the square of the concentration, is shown in Figure 10.

Using this calibration curve, each of the unknown fuels was diluted using hexane or similar solvents and analyzed. The results in Figure 11 show the amount of sulfur measured by FPD response, compared to specification test results for Standard Method ASTM D2622, which is the X-ray fluorescence method. These data were obtained for the same set of fuels as previously mentioned, i.e., the survey set of 38 samples, from military bases and airports around the world.

Although the agreement may not be perfect in this plot, one must consider that the specification test results for sulfur are those determined using Standard Method ASTM 2622 (sulfur by X-ray fluorescence). This test is not particularly precise, and it is designed to be able to determine the differences between fuels that are of the near-specification limit of 0.3 and those that are above the specification limit. GC is more suited toward low-

level determinations of the amount of sulfur in a sample; indeed, the fuel sample itself is diluted by a factor of 50 before analysis begins. In any case, the technique is very capable of screening for nonspecification levels of sulfur in many different types of samples.

B. Use of Specification Test Prediction in the Field. The GC–FID–FPD system was outfitted so that it could be operated in the field from a near-automated fashion. Thus, a wireless laptop computer for system control, along with the correlations described here, was developed for the system.

The GC system also contained autosampling capability, so that the operator had only to dilute 20 μL of the sample in 1000 μL hexane, put the vial in the autosampler, and run the method. Each experiment was conducted within 5 min or less. The data analysis was not automated at this stage of development of the project. Therefore, data files were integrated manually to obtain (1) the total FID response for the entire chromatogram, excluding solvent; (2) the integrated sum of response for compounds up to normal C9; (3) the area of each n -alkane; (4) the total sulfur response; and (5) the CSV output of all peaks to be used in calculation of the simulated distillation profile

With these five pieces of information, the flash point, freeze point, simulated distillation, and sulfur content could all be predicted using the correlations previously described. All results were automatically printed out in summary format.

Although the specification data generated was an estimate from GC data, it provided a screening tool (with one 5-min automated chromatographic experiment and ~ 5 min for data analysis) for determining whether an unusual fuel was present. If the specification properties predicted were questionable or failing, the fuel sample could then be sent to a local or regional laboratory for routine specification analysis. This screening technique could save time and expense for an army quickly moving across a battlefield, by obtaining fuel from local unfamiliar or captured sources.

This instrumentation was provided for use in the screening of fuels for specification tests. Table 4 gives examples of results obtained from captured and locally purchase fuel samples. Specification predictions were made using the fast GC data and comparisons to the regional quality assurance laboratory were also obtained.

These data indicate that the great majority of specification properties of fuels tested were successfully predicted using the GC analysis. The instrument, as expected, was especially good at determining diesel fuel versus jet fuel, which is an important consideration when examining captured fuel. Flash-point predictions quickly and easily reveal the differences between JP-8, diesel fuel, and aviation gasoline. Fuels for trucks that may have catalytic conversion systems designed for lower-sulfur diesel are readily measured for sulfur. The system is relatively automated. It is also interesting to note that the volumes of fuels needed for testing are relatively low. Full specification tests for JP-8 generally require more than 1 gallon of fuel. Chromatographic analysis requires on the order of microliters of fuel, which may improve the speed and ease of sample shipment and storage.

Table 4. Specification Test Prediction by Fast GC in the Field^a

fuel type	sample location ^b	Freeze Point (°C)		Flash Point (°C)		Sulfur Content (wt %)	
		specification test	GC	specification test	GC	specification test	GC
TS-1	A	-53	-56.3	32	26.1	NA	<0.01
Diesel 1	A	pp, -22; cp, -25 ^c	-30.9	42	41.5	0.07	0.045
AvGas	B	-65	-65.4	NA	-197	0.01	<0.01
AvGas	B	-65	-65.5	NA	-197	0.01	<0.01
AvGas	B	-63	-65.4	NA	-198	0.03	0.0331
AvGas	B	-63	-65.4	NA	-197.7	0.03	<0.01
AvGas	B	-62	-64.5	NA	-197	0.02	<0.01
AvGas	B	-62	-65.4	NA	-197	0.02	<0.01
AvGas	B	-66	-65.4	NA	-198	0.01	<0.01
AvGas	B	-66	-65.4	NA	-197	0.01	<0.01
Diesel 1	C	NA	134	NA	58.6	NA	0.06
Diesel 1	C	NA	146	NA	58.3	NA	0.09
MoGas	C	NA	-64.6	NA	-113	NA	<0.01
MoGas	C	NA	-64.6	NA	-107	NA	<0.01
Diesel 2	D	pp, -9; cp, -7 ^c	101.2	71	56	0.69	0.4
Diesel 2	D	pp, -9; cp, -8 ^c	140.9	75	58.8	0.61	0.297
JP8	E	-52	-52.1	44	26.7	0.1	0.14
JP8	F	-47	-49.4	48	42.2	0.01	0.11
JP8	F	-49	-47.5	NA	41.9	0.006	<0.01
JP8	F	-46.8	-49.9	NA	39.3	0.005	<0.01
JP8	F	-47	-49.3	NA	38.3	0.005	<0.01
JP8	F	-48.2	-51	NA	38.7	0.005	<0.01
JP8	F	-48.3	-51.7	NA	39.7	0.005	<0.01
JP8	F	-48.6	-52.3	NA	29.5	0.003	<0.01
JP8	F	-49	-52	NA	28.9	0.003	<0.01
JetA1	G	-50	-55	58	51.2	0.14	0.14
JP8	H	-52	-53.6	46	40.5	0.05	0.05
JP8	I	-48	-50.6	45	41.9	0.05	0.05
JP8	J	-49	-50.7	44	43.4	0.1	0.1
JP8	D	-52	-52.5	46	25.9	0.001	<0.01
JP8	D	-47	-55.4	44	23.8	0.002	<0.01

^a NA = measurement not applicable. ^b All samples were taken from undisclosed locations outside the continental United States. ^c The pour point (pp) and cloud point (cp) are given because the freeze point is out of range.

Conclusions

Gas chromatography (GC) can be useful in quickly and accurately measuring compositional data that can then be used for specification test prediction. The predictions for distillation temperatures, freeze point, flash point, and sulfur content are generally within the range of accuracy for many of the specification tests if analyzed by multiple laboratories. Commercial simulated distillation software can greatly improve the predictions made to ASTM D86 data. However, the military is currently considering the use of an alternate simulated distillation specification test limit. The freeze point is typically accurate within 7 °C, and the flash point is typically accurate to within 5 °C. The sulfur content, as measured by chromatography, may be more accurate than the specification sulfur test, which is based on a specification limit of 0.3% sulfur. The GC method can handle low levels of sulfur better than the current X-ray spectrometry method (ASTM D2622) does. Thus, as a screening tool, and considering that only simple correlations were used for relating composition to properties, this estimation for jet fuel properties seems acceptable for screening purposes.

There are already many important specification or nonspecification tests that can be measured or estimated using compositional data from GC analysis. Using gas chromatography–mass spectroscopy

(GC–MS) or liquid chromatography (LC), it is likely that many more specification tests could be predicted from two or three analyses on advanced instrumentation. A gas or liquid chromatograph in a mobile laboratory allows for a versatile laboratory that is capable of a wide variety of test methods, including estimations of current specification tests, as well as advanced tests that are related to additive concentration or thermal stability.

Acknowledgment. This material is based on research sponsored by Air Force Research Laboratory, under Agreement No. F33615-03-2-2347. The U.S. Government is authorized to reproduce and distribute reprints for Governmental purposes notwithstanding any copyright notation thereon. The views and conclusions contained herein are those of the authors and should not be interpreted as necessarily representing the official policies or endorsements, either expressed or implied, of Air Force Research Laboratory or the U.S. Government. The authors recognize the efforts of the Air Force Petroleum Office (Major Andy Pittman) and Mr. William E. Harrison III for their support of this program. We also recognize the efforts of the Coordinating Research Council (especially J. M. Johnson and O.J. Hadaller, Boeing) for providing data from their recent World Survey of Aviation Fuels.

EF0501360

APPENDIX X
Computational Model of the Freezing of Jet Fuel

INTENTIONALLY LEFT BLANK

Computational Model of the Freezing of Jet Fuel

Daniel L. Atkins* and Jamie S. Ervin†

University of Dayton, Dayton, Ohio 45469-0210

and

Amit Saxena‡

CFD Research Corporation, Huntsville, Alabama 35805

A computational fluid dynamics model is developed that simulates the solidification of jet fuel due to freezing in a buoyancy-driven flow. Flow resistance caused by porous crystal structures that exist in liquid–solid regions is simulated through the use of a momentum resistance source term. Experiments are performed in which jet fuel samples are cooled below their pour point temperatures in an optical cell. Polarized light is used to record images during the freezing process. In addition, low-temperature properties of jet fuel samples are determined, using a differential scanning calorimeter, pycnometer, and a low-temperature viscometer. The validity of the simulations is demonstrated by comparing temperature and solid area measurements with predicted values for various thermal boundary conditions and fuel samples. Reasonable agreement between experiments and simulations is obtained. Thus, the modeling technique is useful for aircraft fuel system designers in the prediction of fuel tank hold-up.

Nomenclature

C	= morphology constant, m^{-2}
C_0	= Kozeny pore geometry constant
C^*	= product $C\mu$, $kg/m^3 \cdot s$
c	= specific heat, $J/kg \cdot K$
f_l	= liquid mass fraction
f_l^*	= normalized liquid mass fraction
$f_{n-alkane}$	= % weight n -alkane
f_s	= solid mass fraction
g	= gravity constant, m/s^2
H	= liquid and solid enthalpy, J/kg
h	= liquid enthalpy, J/kg
h_{ref}	= reference enthalpy for Boussinesq approximation at T_L , J/kg
K	= permeability, m^2
k	= thermal conductivity, $W/m^2 \cdot K$
P	= pressure, Pa
T	= temperature, K
T_H	= temperature at onset of solidification, K
T_L	= temperature at n -alkane phase change completion, K
t	= time, s
u	= superficial velocity, m/s
u_l	= actual velocity, m/s
v	= scalar velocity in y direction, m/s
w	= scalar velocity in z direction, m/s
y, z	= coordinate directions
β	= coefficient of thermal expansion, K^{-1}
ΔH	= latent heat, J/kg
ΔH_e	= effective latent heat, J/kg
λ	= porosity
μ	= absolute viscosity, $kg/m \cdot s$
ρ	= density, kg/m^3

Σ	= interstitial surface area of the pores per unit volume of porous material, m^{-1}
τ	= tortuosity (ratio of tortuous flow-path length to material length)

Introduction

JET fuel solidification must be considered when an aircraft flies at high altitudes (>14 km) or operates in arctic regions. Frozen fuel can remain trapped within tanks or obstruct flow by blocking fuel system components and, if unchecked, may result in the loss of human life and aircraft. The ability to simulate and predict jet fuel freezing is a necessary tool for fuel system designers. From a fundamental perspective, there has been much research using computational fluid dynamics (CFD) to simulate the freezing of mixtures. Unfortunately, the mixtures considered in past CFD simulations generally are much simpler in composition than jet fuel.^{1,2} Studies of metal alloy solidification have demonstrated the difficulties of modeling mixtures of three compounds.³ Moreover, many researchers believe that it is impossible to predict accurately the final solid properties of some well-known mixtures, such as iron alloys, which have been studied for centuries.³ Jet fuel is a mixture of thousands of hydrocarbon compounds, and the compositions of individual jet fuel samples vary with refinery source. Moreover, solidified jet fuel consists of crystals composed of solid solutions of normal alkanes (n -alkanes) and phase change takes place over a temperature range as species precipitate from the liquid fuel. The authors believe there are no published jet fuel CFD solidification simulations with experimental verification and that this is due to the complexities of the multiphase transport involved and experimental difficulties. Moreover, numerical techniques to simulate simultaneously both the microscopic and macroscopic phenomena occurring during solidification of complex mixtures are believed to be in their infancy.

Previous techniques used to simulate jet fuel freezing have had significant limitations. A previous one-dimensional numerical model incorporating the freezing of jet fuel relied entirely on empirical hold-up data.⁴ (Fuel frozen in tanks, unavailable for use, is referred to as hold-up.) An accurate extrapolation of the results of this one-dimensional model to more complex geometries and flow conditions is unlikely. A two-dimensional CFD model was also developed to predict the temperature in fuel tanks. However, a mixture of water and glycerin was used as a surrogate fuel, and the effects of solidification were represented by altering the viscosity of the mixture.^{1,2} Glycerin was used due to the opaqueness of jet fuel at low temperature and safety considerations. However, the appropriateness of using glycerin to represent jet fuel is unclear. There have

Received 10 December 2003; revision received 30 March 2004; accepted for publication 19 April 2004. Copyright © 2004 by the American Institute of Aeronautics and Astronautics, Inc. All rights reserved. Copies of this paper may be made for personal or internal use, on condition that the copier pay the \$10.00 per-copy fee to the Copyright Clearance Center, Inc., 222 Rosewood Drive, Danvers, MA 01923; include the code 0748-4658/05 \$10.00 in correspondence with the CCC.

*Ph.D. candidate, Mechanical and Aerospace Engineering Department, 300 College Park.

†Professor, Energy and Environmental Engineering Division, Research Institute, 300 College Park. Associate Fellow AIAA.

‡Engineer, Technical Support, Software Division, 215 Wynn Drive, Suite 501; currently with ESI Group, 215 Wynn Drive, Suite 503.

been efforts to develop a thermodynamic model for the equilibrium-phase compositions during the freezing of jet fuel.⁵ Although phase equilibrium models do not include flow and heat transfer effects, the thermodynamic modeling of the phase compositions of complex hydrocarbon mixtures remains an important avenue of fundamental research. In summary, the authors have not found previous CFD models of the freezing of jet fuel that include a detailed treatment of phase change. A large impediment to the simulation of jet fuel freezing has been the absence of published thermophysical properties of jet fuel at low temperatures. The primary objective of the present work is to develop a two-dimensional CFD model that uses measured fuel properties to predict the solidification of jet fuels within a buoyancy-driven flow. Buoyancy-driven flow is the dominate flow in many fuel tanks.

Early wing tank simulator studies led Leo and von Meerwall to conclude that optical techniques are ineffective as tools to study jet fuel solidification behavior due to poor optical properties at low temperatures.⁶ In contrast, our recent work has shown that high-quality images of the freezing of jet fuel are possible with the use of polarized light.⁷ The use of polarized light has shown that jet fuel freezing involves interactions between precipitating solids and flowing liquid. Flow visualization and temperature measurements within an optical cell were obtained to develop a better fundamental understanding of the freezing of jet fuel and to validate numerical simulations.

Experimental

The fidelity of a computational simulation is assessed by comparing experimental measurements to predicted values. Here, the computational model should reasonably predict the temperature at any location and time within the cooled fuel. In addition, the model should predict the location of an advancing liquid–solid boundary. In the current research, images of the solidification front and temperature measurements within the low-temperature optical cell (Fig. 1) are recorded for different thermal boundary conditions. The optical cell (88.9 × 38.1 mm) was fabricated from aluminum (6061) tubing and has a depth of 44.5 mm to establish the desired two-dimensional flow by minimizing heat transfer end effects. Copper block heat exchangers are clamped to opposite vertical sides of the cell to impose the desired surface temperatures. Temperature control is accomplished by the use of cryogenic solenoid valves, which meter the flow of liquid nitrogen into the copper blocks. Consequently, the resulting density differences within the fuel drive the flow within the cell. Calibrated (type T) thermocouples measure temperatures on the internal surfaces of the aluminum cell. Quartz windows permit illumination and image collection. Cross polariza-

tion eliminates light transmittance through the liquid fuel. As the fuel solidifies, crystals rotate the polarization plane and allow light to pass through the front polarization analyzer. Additional details of the low-temperature optical cell are given elsewhere.⁷

Samples of JP-8 (F3804) and Jet A (F3219) fuels and a Jet A fuel (F3219) mixed with 2000 mg/l of a proprietary low-temperature additive (F3607) were used. An additive mixture was included due to the potential commercial and military applications for additives that improve the low-temperature performance of Jet A and JP-8. The freeze-point [American Society for Testing and Materials (ASTM) D5972-96], cloud-point (ASTM D5773-95), and pour-point (ASTM D5949-96) temperatures of the fuel samples were measured using a Phase Technology Series 70V petroleum analyzer and are listed in Table 1. In addition, gas chromatography in combination with a mass spectrometer was used to determine the *n*-alkane (weight) distribution of the fuels. As already noted, *n*-alkane species are believed to be largely responsible for the freezing of jet fuel.

Solution of the governing equations requires low-temperature thermal properties of both liquid and solid jet fuel. Unfortunately, published properties of jet fuel at low temperatures, including density, viscosity, thermal conductivity, and specific heat are limited.^{4,8} Moreover, they are generally unavailable for temperatures below 233 K. Jet fuel properties vary widely depending on their source, whereas model accuracy depends on accurate measurements of these properties. Thus, property measurement for use in low-temperature simulations is warranted.

The density of jet fuel samples varies with refinery source. However, Fig. 2 shows that, although the measured density of three samples (445, 168, F3804) of JP-8 fuel varies, the difference is small (<3%) (Ref. 4). Moreover, Fig. 2 shows that the densities of samples of JP-8 and Jet A fuel are similar and have been represented by an aggregate linear function of temperature for the liquid phase [Coordinating Research Council (CRC), Ref. 8]. In the present work,

Table 1 Freeze point, cloud point, and pour point temperatures of jet fuel samples and phase change onset

Fuel	Freeze point, K (±0.5 K)	Cloud point, K (±1.0 K)	Pour point, K (±2.0 K)	Cell onset, K (±0.3 K)	DSC onset, K ±0.5 K
JP-8 (F3804)	224.9	221.2	215.2	221.2	220.8
Jet A (F3219)	227.2	222.2	217.2	220.5	222.2
Jet A (F3219) + additive (F3607)	227.2	221.6	213.4	218.5	221.2

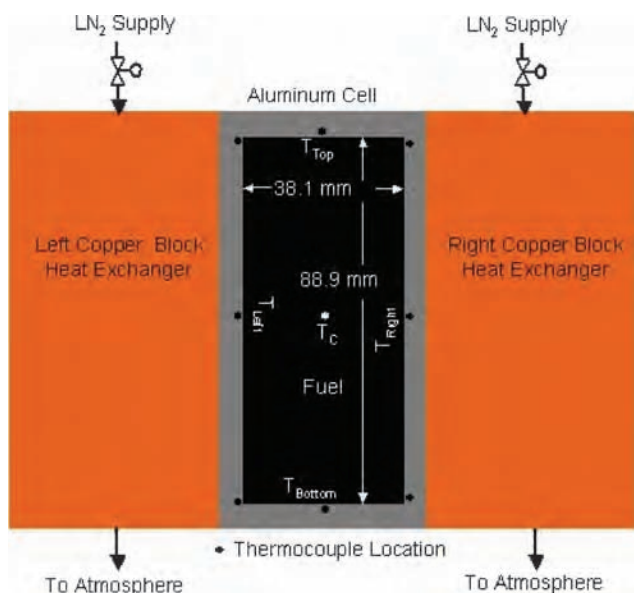
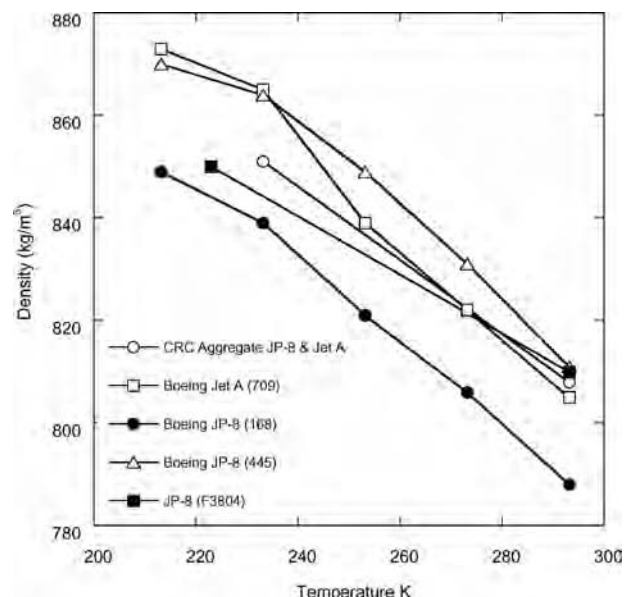


Fig. 1 Schematic of low-temperature optical cell.



334 Fig. 2 Jet fuel density for different fuel samples and temperatures.^{4,8}

the density of F3804 at 291.0 K was gravimetrically determined to be $810 \pm 1 \text{ kg/m}^3$, and the density at the onset of phase change (221.2 K) was measured with a pycnometer as $849.2 \pm 0.5 \text{ kg/m}^3$ (Ref. 9). Thus, the density of F3804 varies by less than 5% between 291.0 and 221.2 K. In addition, the densities of fuel samples F3219 and F3804 differed by 1% at 15°C. For simplicity, it is reasonable to assume that the densities of fuels F3804 and F3219 remain constant at 830 kg/m^3 except in the buoyancy source term (Boussinesq approximation) of the momentum equation. This density value is midway between the measured maximum and minimum density values for fuel F3804 in the temperature range of interest (208–291 K). During solidification, individual *n*-alkanes (C_8 – C_{17}) that are commonly found in jet fuel increase in density by roughly 6% (Ref. 10). These *n*-alkanes represent a fraction (about 25%) of the total fuel mass. Consequently, it is reasonable to assume that changes in density due to freezing *n*-alkanes are essentially negligible for simulation purposes.

A rotational viscometer (Tannas Company, Model Plus Two) was used to measure the dynamic viscosity of the F3804 fuel sample for temperatures between 291.0 and 221.2 K. A polynomial fit of the measured viscosity as a function of temperature reasonably represents the measured viscosity and is, $\mu = 2.444 \times 10^{-9}T^4 - 2.675 \times 10^{-6}T^3 + 1.097 \times 10^{-3}T^2 - 1.999 \times 10^{-1} + 13.66 \text{ kg/m} \cdot \text{s}$ (Fig. 3). For simplicity, liquid–solid mixture viscosity values below 221.2 K are assumed to follow extrapolation of the fit of Fig. 3 in simulations involving fuel F3804. Figure 3 shows a comparison of the polynomial fit with reported viscosities of Jet A and JP-8 fuels.^{4,8} Our measurements agree well with the previously measured values from 291 to 240 K. However, below 240 K, Fig. 3 shows that there are substantial differences between the measured viscosity of F3804 and the viscosities of fuel samples measured in the earlier studies. These differences are not surprising because we have observed that differences in viscosity measurements among fuel samples from different refinery sources become larger as the cloud-point (onset of crystallization) temperatures of the individual samples are approached. There was little difference between the measured viscosities of fuels F3804 and F3219 over the temperature range of Fig. 3. Thus, the viscosity measured here for fuel F3804 was used in all simulations. Moreover, the authors believe, after comparing viscosity measurements to three lower freeze-point JP-8 fuels, that the freeze-point specification minimum JP-8 sample (F3804) may potentially be used to predict the maximum hold-up.

To the best of our knowledge, published values of jet fuel thermal conductivity at low temperatures (below 253 K) do not exist.

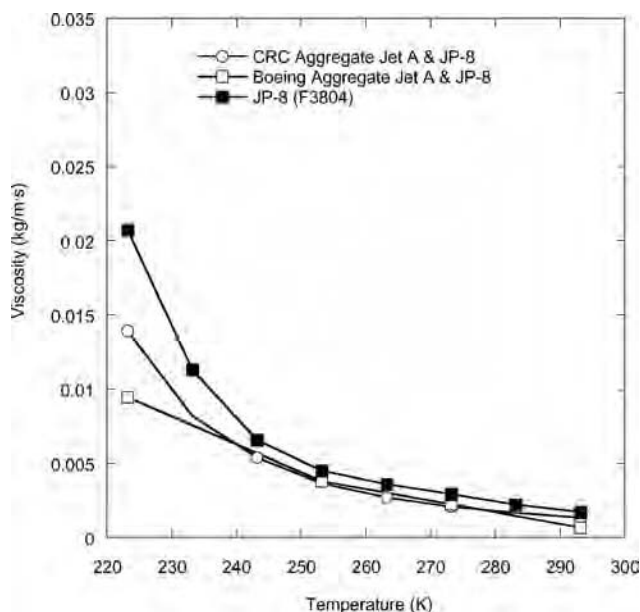


Fig. 3 Absolute viscosity of JP-8 and Jet A fuels for different temperatures.^{4,8}

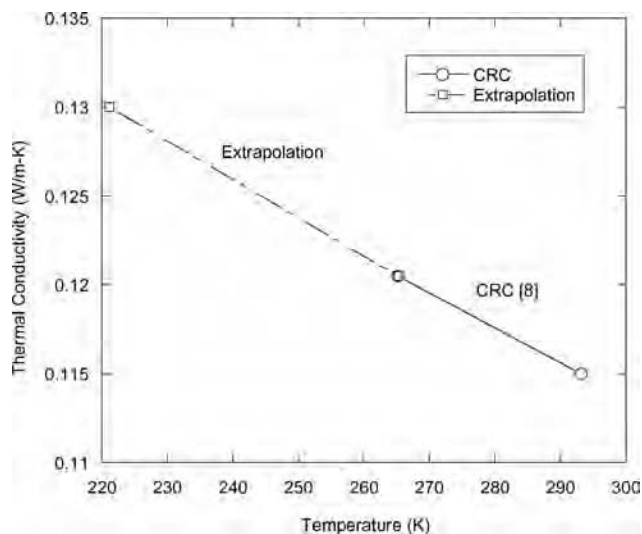


Fig. 4 Thermal conductivity of Jet A and JP-8.

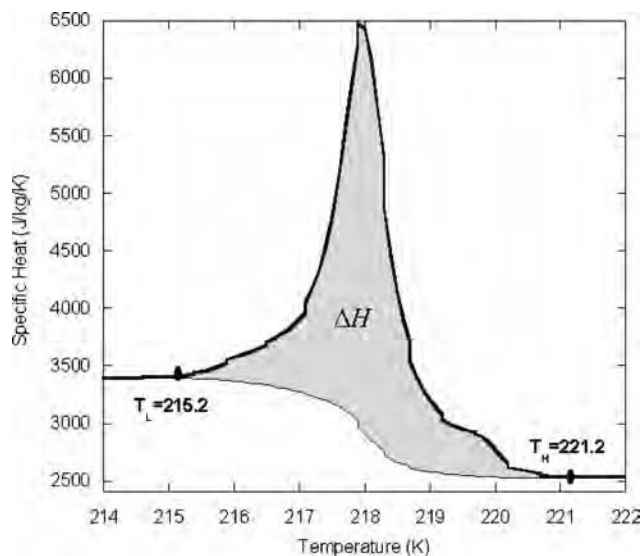


Fig. 5 Measured specific heat for fuel F3804 (JP-8).

Figure 4 shows that the thermal conductivity of liquid jet fuel varies linearly with temperature between 300 and 265 K (Ref. 8). Linear extrapolation to 221.2 K yields a value of approximately $0.13 \text{ W/m}^2 \cdot \text{K}$ for liquid jet fuel. This extrapolated value agrees well with thermal conductivity values of jet fuel *n*-alkane constituents, for example, tetradecane has a thermal conductivity of $0.1399 \text{ W/m}^2 \cdot \text{K}$ at the solidification temperature.¹¹ Thus, for simplicity, the thermal conductivity of the liquid jet fuel is assumed to be $0.12 \text{ W/m}^2 \cdot \text{K}$ at 291.0 K and increases linearly to $0.13 \text{ W/m}^2 \cdot \text{K}$ at 221.2 K in all simulations. The thermal conductivity of *n*-alkanes can increase by 25–50% upon crystallization.¹² Thus, for simplicity and the absence of thermal conductivity measurements, the thermal conductivity of the liquid–solid mixture below the solidification temperature (221.2 K for F3804 and 222.2 K for F3219) is assumed here to be $0.18 \text{ W/m}^2 \cdot \text{K}$.

The differential scanning calorimeter (DSC) can be used to determine specific heat and enthalpy as functions of temperature as well as indicate phase transition temperatures. A DSC (TA Instruments Model 2920, cooling rate 1 K/min) was used to determine the effective specific heat and heat of fusion for solidifying constituents within the fuel samples (F3219 and F3804). Figure 5 shows that the measured specific heat (F3804) varies less than 3% until the onset of solidification (221.2 K) and is approximately $2500 \text{ J/kg} \cdot \text{K}$. At 221.2 K (T_H , Fig. 5), the specific heat begins to increase due to

the onset of freezing within the hydrocarbon mixture. Additionally, Table 1 shows that temperatures measured at the onset of solidification, which was determined both visually in the optical cell and with the DSC, agree fairly well with the measured cloud-point temperatures. With continued cooling, the specific heat peaks, begins to decrease, and ultimately levels after the larger n -alkane constituents have solidified (T_L , Fig. 5). A similar procedure was followed for fuel F3219. The specific heat behavior during phase change varied significantly among the fuel samples. Thus, measured values of the specific heat obtained from the DSC for each fuel sample were used in the simulations. The JP-8 sample utilized represents a freeze-point specification minimum fuel, and the authors believe the measured thermal properties may potentially be used to predict the maximum hold-up.

Simulation Methodology

In the current work, the freezing of jet fuel in the rectangular cavity of Fig. 1 is simulated using primitive variables. The cavity is long in the viewing direction, and thus, the flow is essentially two dimensional. In addition, the buoyancy-induced flow is laminar in our experiments. We assume that the liquid fuel itself behaves as a Newtonian fluid and that the density is constant in all terms except the buoyancy source term (Boussinesq approximation).

In our simulations, we employ an enthalpy method that has been used previously to simulate the solidification of simple mixtures in buoyancy-driven flows.¹³ With the enthalpy method, the governing energy equation incorporates the heat of fusion due to phase change, and the heat of fusion must be accounted for on the advancing liquid–solid interface. The energy equation is written in terms of the liquid–solid enthalpy H ,

$$H = h + \Delta H \quad (1)$$

In Eq. (1), ΔH is the heat of fusion from solidifying constituents. The heat of fusion is incorporated over the entire liquid–solid region. Thus, the liquid and solid phases are not treated separately. Incorporating the heat of fusion enables a simple fixed grid to be used, avoiding the complexity of deforming grids that account for the moving liquid–solid interface. Such simplifications are advantageous for large computational domains as might be expected for simulations of an aircraft fuel tank. Admittedly, this enthalpy method has limitations.³ For example, details of the microstructure of the fuel crystals cannot be predicted, and local thermodynamic equilibrium is invoked. However, such limitations are not considered fatal for the prediction of fuel tank hold-up and flow.

For complex mixtures, such as jet fuel, that solidify over a temperature range, porous structures form that resist flow. It is believed that freezing jet fuel forms a matrix of crystals, but the nature of the matrix is not understood.⁷ A fixed grid formulation requires that a momentum exchange source term be added to the momentum equation to account for changes in velocity due to the added flow resistance. The flow rate through a porous material can be represented by the empirical D'Arcy¹⁴ relation (also see Ref. 15),

$$\mathbf{u} = -(K \nabla P / \mu) \quad (2)$$

In Eq. (2), \mathbf{u} is the superficial velocity (ensemble-average velocity), and is defined in terms of the porosity λ and the actual fluid velocity \mathbf{u}_l

$$\mathbf{u} = \lambda \mathbf{u}_l \quad (3)$$

The permeability is a property of the porous material that characterizes the ease with which a fluid flows under a pressure gradient. K is determined by pore geometry, which may, in reality, vary anisotropically and have a statistical distribution of sizes. Several empirical and semi-empirical representations for K exist, and the Kozeny¹⁶ relation is often invoked (also see Refs. 15 and 17),

$$K = C_0 \lambda^3 / \Sigma^2 \quad (4)$$

In Eq. (4), C_0 is a dimensionless constant that depends on the pore geometry. The actual flowpath may likely be indirect. Thus, the tortuosity τ , (ratio of tortuous flowpath length to material length) is sometimes included in Eq. (4)¹⁵:

$$K = C_0 \lambda^3 / \tau \Sigma^2 \quad (5)$$

In practice, C_0 is empirically determined, and measurements (if at all possible) of λ , Σ , and τ may have large uncertainties. Some researchers prefer a simpler expression,¹³

$$K = \lambda^3 / C(1 - \lambda)^2 \quad (6)$$

C of Eq. (6) is an empirical constant that includes the effects of Σ and τ together with the influence of pore shape, size, and orientation. For crystallization, C is assumed to characterize the morphology of the porous medium and is hereafter referred to as the morphology constant. Equation (6) can be used with the D'Arcy relation to give an expression for the pressure gradient in the two-phase coexistence region:

$$\nabla P = -C \mu [(1 - \lambda)^2 / (\lambda^3)] \mathbf{u} \quad (7)$$

Equation (7) shows that as the porosity approaches unity (liquid alone), pressure loss due to flow through the porous media decreases to zero. As the porosity approaches zero, the pressure drop increases to eliminate flow within a region of liquid–solid coexistence. Moreover as C is increased for a fixed μ , λ , and velocity, Eq. (7) shows that the flow resistance increases. Thus for jet fuel, crystallization behaviors that inhibit flow would tend to have larger values of C .

Results from analytical phase-separation techniques¹⁸ show that approximately 8% (mass) of the F3804 fuel sample actually solidifies at the minimum temperature of interest (215.2 K). As observed elsewhere, only a relatively small mass fraction of jet fuel solidifies, and this fraction consists essentially of n -alkanes.⁵ Here, the mass fraction of fuel that becomes solid is referred to as f_s , and the mass fraction that remains liquid is f_l . Thus, for fuel sample F3804, the maximum value of f_s is 0.08, which coincides with a minimum f_l of 0.92. As n -alkanes precipitate from solution, f_s increases while f_l , λ , and K decrease. Unfortunately, λ is difficult, if not impossible currently, to measure under the low-temperature conditions occurring with solidifying jet fuel. However, it is reasonable to assume that f_l is proportional to λ , and as an approximation, λ of Eq. (7) may be replaced with f_l ,

$$K = f_l^3 / C(1 - f_l)^2 \quad (8)$$

For convenience, f_l is normalized to vary between 0 and 1. Because there is a large uncertainty in C of Eq. (8), the use of a normalized f_l is acceptable. Here f_l is a function of temperature and is estimated using DSC measurements for a particular jet fuel sample. (In the remainder of this paper, f_l^* refers only to the normalized mass fraction of fuel that remains liquid. For simplicity, we also rename the product $C \mu$ [Eq. (7)] as C^* using appropriate units.) The momentum equations for buoyancy-dominated flow through a region that may have n -alkane crystal structures include the momentum source terms and are written in terms of the superficial velocity,^{13,19}

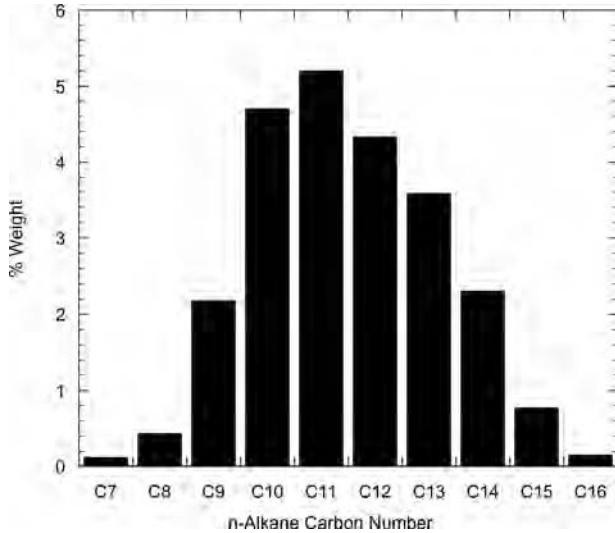
$$\frac{\partial(\rho v)}{\partial t} + \nabla \cdot (\rho \mathbf{u} v) = \nabla \cdot (\mu \nabla v) - \frac{\partial P}{\partial y} + \frac{C^*(1 - f_l^*)^2}{(f_l^*)^3} v \quad (9)$$

$$\frac{\partial(\rho w)}{\partial t} + \nabla \cdot (\rho \mathbf{u} w) = \nabla \cdot (\mu \nabla w) - \frac{\partial P}{\partial z} + \frac{C^*(1 - f_l^*)^2}{(f_l^*)^3} w + \frac{\rho g \beta (h - h_{\text{ref}})}{c} \quad (10)$$

Here, v and w are the scalar components of \mathbf{u} in the y and z directions. In the buoyancy source term of Eq. (10), the coefficient of thermal expansion for liquid jet fuel, β , is determined from temperature-dependent density values. Here h_{ref} is the enthalpy corresponding

Table 2 DSC and GC measurements for different jet fuel samples

Fuel	T_L , K (± 0.5 K)	T_H (± 0.5 K)	ΔH , J/kg (± 200 J/kg)	f_s	ΔH_e , J/kg	$f_{n\text{-alkane}}$ total
JP-8 (F3804)	215.2	221.2	4968	0.08	62100	0.238
Jet A (F3219)	217.2	222.2	3487	0.06	58117	0.187
Jet A (F3219) + additive (F3607)	213.4	221.6	3581	0.06	59683	0.187


Fig. 6 Measured distribution of n -alkanes for F3804 (JP-8).

to the lowest temperature achieved. In addition, the energy equation includes phase change and is written using H of Eq. (1),

$$\frac{\partial(\rho H)}{\partial t} + \nabla \cdot (H\rho\mathbf{u}) - \nabla \cdot (k\nabla T) = 0 \quad (11)$$

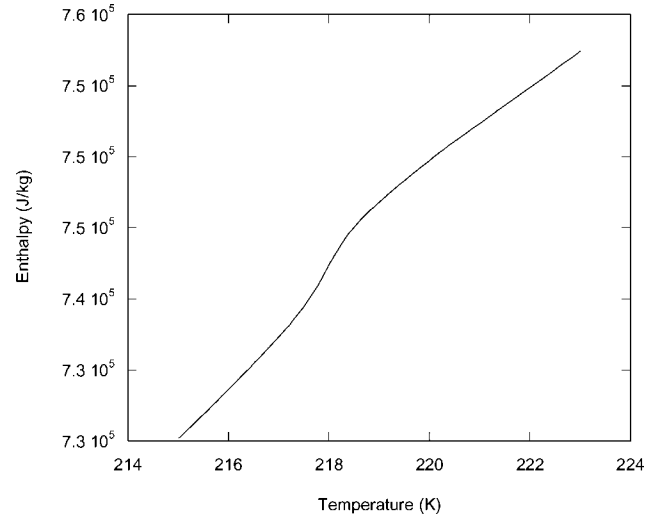
Equations (9–11), along with the continuity equation (12), represent the system of coupled governing partial differential equations used.

$$\nabla \cdot \mathbf{u} = 0 \quad (12)$$

Figure 5 shows how DSC measurements can be used to determine enthalpy as a function of temperature, which also incorporates the heat of fusion. Measurements for F3804 show that the specific heat may be reasonably assumed to be a constant until the onset of freezing (221.2 K) and a different constant after freezing is essentially complete (215.2 K). A sigmoidal baseline is used to compensate for the change in baseline that occurs during phase change.²⁰ The specific heat can be numerically integrated to yield the temperature-dependent enthalpy for the mixture. Thus, the shaded area of Fig. 5 represents the heat of fusion (ΔH) of precipitating n -alkanes under the solvent influence of the remaining hydrocarbon constituents. Because of the heat of fusion generated on cooling, the crystallization of large n -alkanes yields an exotherm measured by the DSC. Moreover, other fuel species, that is, isoparaffins, naphthenes, and aromatics, do not contribute significantly to this exotherm.²¹ Figure 6 shows the measured n -alkane distribution for F3804 and that the fuel has an n -alkane mass fraction $f_{n\text{-alkane}}$ of 0.238. As already stated, less than one-third of these n -alkanes actually solidify at the temperatures of interest, resulting in a maximum solidifying mass fraction f_s of 8%. The DSC measured heat of fusion is divided by f_s to estimate an effective latent heat, ΔH_e ,

$$\Delta H_e = \Delta H / f_s \quad (13)$$

For the present JP-8 sample (F3804), the measured $\Delta H = 4968$ J/kg (shaded area, Fig. 5), and $\Delta H_e = 62,100$ J/kg [Eq. (13)]. Similar DSC and gas chromatography (GC) measurements were performed for the Jet A (F3219) sample and the Jet A sample containing


Fig. 7 Derived enthalpy function for fuel sample F3804 (JP-8).

2000 mg/l of cold-flow additive F3607. These measurements are summarized in Table 2.

Although crystallization dynamics of jet fuels is not well understood, precipitating n -alkanes have been hypothesized to form a matrix that entraps other fuel species that remain in the liquid phase or possibly exist as a gel. Fuel cooled to the pour-point temperature does not flow and is, therefore, unavailable for use (referred to as fuel tank hold-up). Because the ability to predict the unavailable mass is important, the assumption that the fuel behaves as if it were essentially a nonflowing phase at 215.2 K is useful. T_H and T_L of Fig. 5 correlate well with the measured cloud- (onset of crystallization) and pour-point (gelation) temperatures, and this correlation suggests an approach to modeling. The enthalpy function of Fig. 7 was generated by numerical integration of the measured specific heat of Fig. 5. From T_H to T_L , Fig. 7 shows that the enthalpy varies nearly linearly with temperature and that f_i^* between T_H and T_L is estimated as

$$f_i^* = (T - T_L) / (T_H - T_L) \quad (14)$$

Thus, at temperatures above T_H , f_i^* is one and, at temperatures below T_L , f_i^* is zero.

Numerical

A commercially available and modifiable CFD code, CFD-ACE was selected for use.¹⁹ The program was modified to model solidification of mixtures as described here. An enthalpy formulation, fixed grid method was incorporated.¹³ The temperatures at which solidification begins, T_H , and solidification ends, T_L , are required as input. Density, viscosity, thermal conductivity, and specific heat as functions of temperature are also required. The entire domain is considered porous with varying porosity to account for momentum resistance of porous solid-liquid regions, and f_i^* is calculated. The program was also modified to accommodate the product of the morphology constant and viscosity, C^* .

CFD-ACE incorporates a finite volume approach using the SIMPLEC algorithm and offers a choice of spatial and temporal differencing options.¹⁹ For the present simulations, the governing equations are represented by a blend of (0.9) third-order and (0.1) upwind

Table 3 Grid refinement study for JP-8 at 1.0 K/min, $t = 3150$ s (values at optical cell center)

Grid size	Nodes	Cells	Temperature, K	f_i	Temperature % change	f_i % change	CPU time, s
8×15	120	98	221.02	0.971	—	—	813.76
15×30	450	406	221.18	0.997	0.07	2.7	3411.37
21×42	900	820	221.23	1.000	0.02	0.3	7250.67
30×60	1800	1711	221.29	1.000	0.02	0.0	17998.95

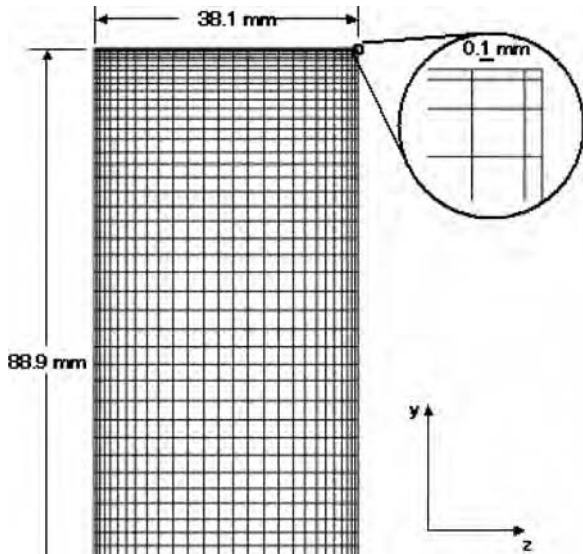


Fig. 8 Structured grid.

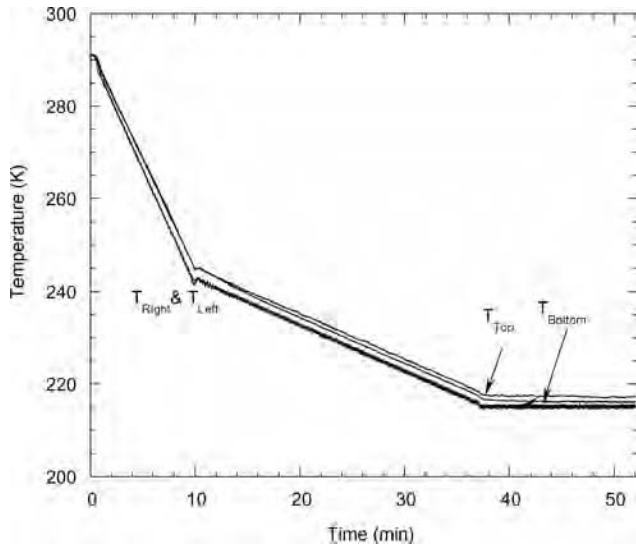


Fig. 9 Measured surface temperatures applied as thermal boundary conditions for optical cell calculations for JP-8 fuel.

spatial differencing. A Crank–Nicolson scheme is used for temporal differencing (see Ref. 19).

The rectangular computational domain used to represent the flow within the optical cell (Fig. 8) consists of a structured grid, clustered along each horizontal and vertical surface. The grid size and cluster spacing were determined after a grid refinement study for the neat JP-8 (F3804) fuel using the thermal boundary conditions of Fig. 9. The f_i^* and temperature at the center of the computational domain were calculated for grid densities of 8×15 , 15×30 , 21×42 , and

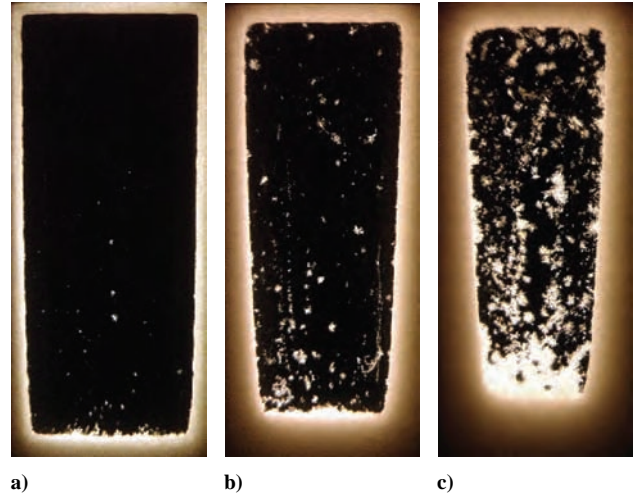


Fig. 10 Solidifying JP-8 (F3804) in the optical cell after a) 37.5 min, b) 42.5 min, and c) 47.5 min of the applied thermal boundary conditions shown in Figure 9.

30×60 . A time step δt of 1.0 s provided a stable solution and was small enough to resolve the unsteady convective motion for each grid density. The solution was considered complete for each time step if all variable residuals decreased by four orders of magnitude. A grid size of 30×60 was utilized based on the results of the grid refinement study (Table 3). The CPU (Pentium® III, 800 MHz) time for each solution is listed in Table 3 and shows a reasonable serial run time (approximately 5 h) for the selected grid. More complex geometries, such as actual aircraft wing tanks that include ribs and spars, may require a parallel computational solution to keep computational time manageable. The code selected is easily configured for parallel processing.

Results and Discussion

Simulations of the Solidification of JP-8

The JP-8 fuel sample (F3804) was subjected to the surface temperatures of Fig. 9. The vertical surfaces were cooled from room temperature at a rate of 5.0 K/min to 243.2 K to expedite the experiment by rapidly approaching the freeze-point temperature (224.9 K). The vertical surfaces were then more slowly cooled from 243.2 K to the pour-point temperature (215.2 K) at the desired rate of 1.0 K/min. The temperature of the optical cell vertical surfaces, T_{left} and T_{right} , were maintained at 215.2 K for a period of 15 min to ensure adequate solidification. Images were obtained at 5-min intervals (37.5, 42.5, and 47.5 min). The top and bottom surface temperatures of the cell, T_{top} and T_{bottom} , were not actively controlled, but were measured. The surface temperatures show in Fig. 9 were used as thermal boundary conditions in the simulations.

Figure 10 shows images of the JP-8 fuel sample obtained after 37.5, 42.5, and 47.5 min of cooling (Fig. 9). The use of cross polarized light eliminates light transmittance through liquid fuel, rendering images of the liquid as black regions. The formation of crystals depolarizes the light, and the crystals appear as the lightly colored regions. Figure 10 shows images of fuel solidifying on the cell surfaces and the liquid–solid region boundary advances symmetrically about the center axis of the cell. The symmetrical growth in time of the solidifying region is expected because of the symmetrical

thermal conditions (zero temperature difference between vertical surfaces).

Figure 10a shows the initial formation of free-floating crystals that drift within the liquid fuel. Figures 10b and 10c show that the number and size of these crystals increase with time. Similar behavior observed in metal alloy solidification research suggests that the origin of these crystals is nucleation within the liquid near a cool surface and dislodged or fractured adhered crystals.³ On initial inspection, the number and size of these free-floating crystals appear to be significant in Fig. 10c. However, the optical cell is 44.5 mm in depth, and the actual number of crystals present in any single two-dimensional plane is significantly less than the cumulative image of Fig. 10c. Thus, momentum exchange between the liquid and free-floating crystals is neglected because the adhered structures are a more dominant effect. Finally, Fig. 10 shows that the crystallization behavior of the JP-8 sample is similar to that of the Jet A sample (F3219) presented in previous work.⁷

Because C for the freezing of JP-8 and Jet A cannot be determined directly by crystal shape and size, C^* is obtained by adjustment until agreement between the measured and simulated cell center temper-

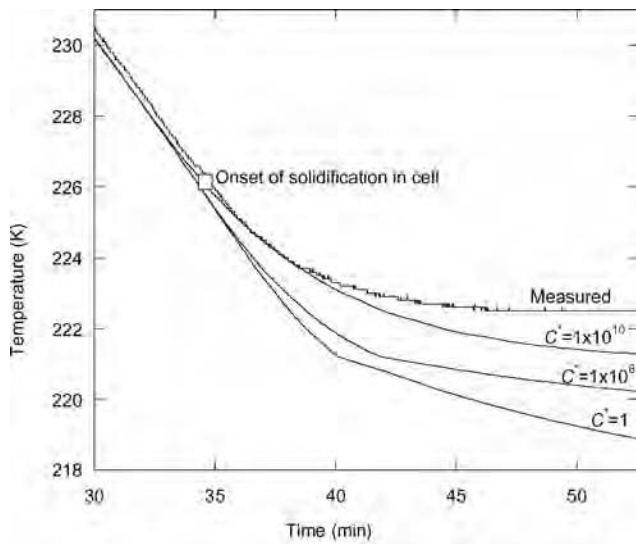


Fig. 11 Predicted and measured T_{center} for different values of C^* for JP-8 sample (F3804).

ature T_{center} for a given fuel sample. (The simulated temperature at the center of the optical cell should be the same for any value of C^* until the onset of solidification, 221.2 K for this JP-8 sample.) Figure 11 shows the measured temperature at the center of the optical cell, as well as the calculated temperature for three values of C^* . The measurement and simulation of the temperature at the cell center agree reasonably well (within 0.5 K) until solidification begins at 221.2 K. Once solidification begins, the solutions, which employ different C^* values, begin to deviate due to the effect of flow through liquid–solid regions. With $C^* = 1 \text{ kg/m}^3 \cdot \text{s}$, the lowest T_{center} is predicted. After 52.5 min, the predicted temperature is 218.1 K, which is 4.4 K below the measured temperature of 222.5 K. Figure 11 shows that a C^* of $1 \times 10^6 \text{ kg/m}^3 \cdot \text{s}$ increases the calculated T_{center} , and it more closely agrees with the measured temperature during solidification. Figure 11 shows that a C^* of $1 \times 10^{10} \text{ kg/m}^3 \cdot \text{s}$ brings the simulated T_{center} within 1.2 K (221.3 K predicted vs 222.5 K measured). Further increases in C^* do not yield better predictions. Thus, a $C^* = 1 \times 10^{10} \text{ kg/m}^3 \cdot \text{s}$ was used in all JP-8 simulations. Figure 11 shows that relatively large values of C^* are required for agreement between measured and simulated values of T_{center} .

It is known that precipitating n -alkanes form a crystalline matrix or network about cooled liquid jet fuel, but the physical aspects of this liquid-entrapping mechanism are not well understood. Thus, it is important to conduct visualization studies involving simultaneous flow and crystallization. For reference, Fig. 12a shows a two-dimensional view of an entire face of the optical cell. Figure 12b shows a magnified image of crystal structures that have grown outward from the vertical cell surfaces. Indicated by an arrow, newly formed crystals extend into the bulk liquid fuel. Crystals near the cooled vertical surface are believed to be more closely packed than the newly formed crystals protruding from the edge of the solidifying area. Individual jet fuel crystals (Fig. 12c) have platelike branches that extend in three dimensions, and these platelike crystals have been described as having an orthorhombic structure.⁵ As the jet fuel crystals nucleate and grow into the flowing thermal boundary layer due to temperature and concentration gradients, they accumulate in layers and appear to have a random orientation with respect to each other. Liquid surrounded by contacting crystals is then effectively trapped in localized regions because the crystal orientations inhibit flow in all directions. In the present experiments, gentle stirring of the liquid fuel does not disrupt the matrix. Elsewhere, the mass of the matrix structure in which the liquid and solid phases of fuel coexist was found to consist primarily of the liquid phase, and phase separation was achieved by physically disrupting the crystalline structure.¹⁸

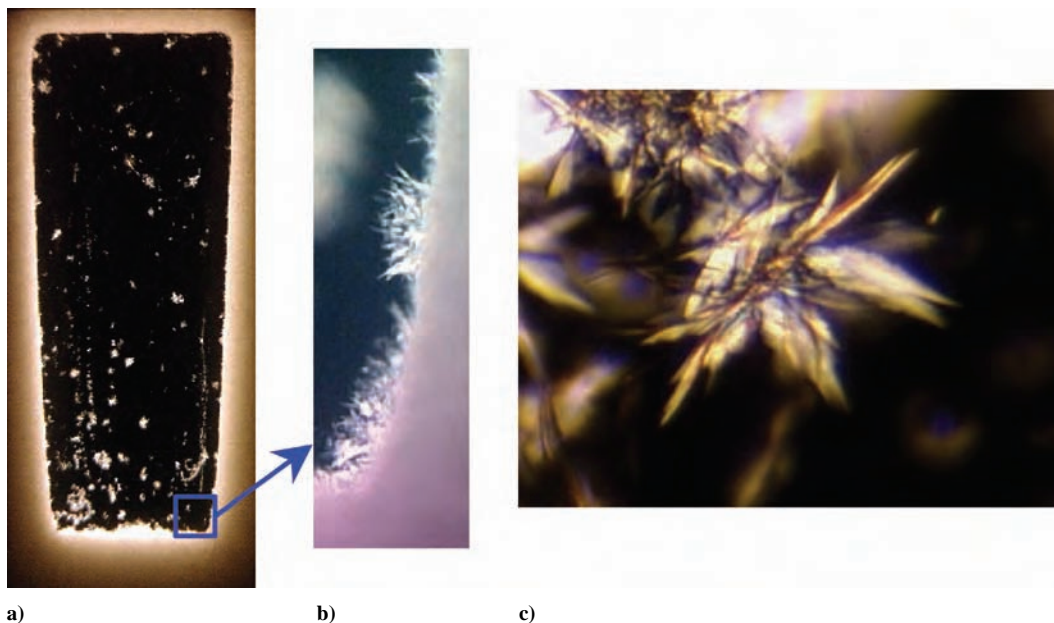


Fig. 12 Solidifying JP-8 (F3804) in the optical cell after 47.5 min of applied thermal boundary conditions (Fig. 9); a) two-dimensional view of the cell, b) crystals on the advancing solidification front, and c) three-dimensional geometry of crystals with platelike branches.

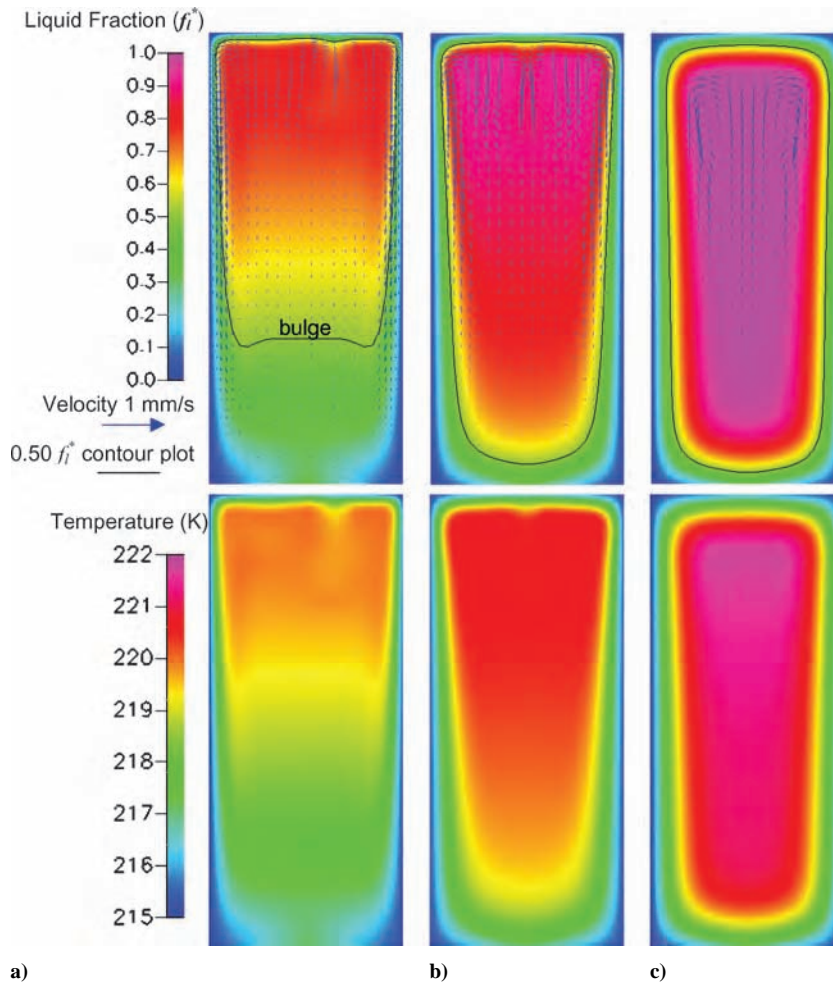


Fig. 13 Simulated liquid fraction, velocity, and temperature for JP-8 after 52.5 min of the applied thermal boundary conditions of Fig. 9 for a) $C^* = 1 \text{ kg/m}^3 \cdot \text{s}$, b) $C^* = 1 \times 10^6 \text{ kg/m}^3 \cdot \text{s}$, and c) $C^* = 1 \times 10^{10} \text{ kg/m}^3 \cdot \text{s}$.

Although the value of C^* in Eqs. (9) and (10) was selected by adjustment to match the temperature of the fuel at the center of the optical cell, it is important to understand the influence of C^* on the flow velocity and solidification. Figure 13 shows simulations of JP-8 in the optical cell after 52.5 min for three values of C^* . Flood diagrams for simulated f_l^* , temperatures, and velocity vectors are presented. (For reference, an f_l^* contour line of 0.5 is shown on the f_l^* flood diagrams.) Figure 13a ($C^* = 1 \text{ kg/m}^3 \cdot \text{s}$) shows the lowest predicted f_l^* (0.47) and T_{center} (218.1 K) relative to Figs. 13b and 13c. In addition, Fig. 13a shows the greatest area of solidification. In Fig. 13a, the f_l^* contour line of 0.5 has advanced from the lower portion of each vertical surface to the cell center. The protrusion or bulging of the solidifying structure is caused by significant flow in the porous liquid–solid region and is evident from the velocity vectors present there. Convection-induced bulges in liquid–solid regions have been observed in other studies of solidification within a cavity.¹³ Relative to Figs. 13b and 13c, the low value of C^* in Fig. 13a causes higher velocities in porous regions and the advancement of the solid region toward the cell center. Flow away from the colder lower regions on the vertical surfaces causes lower temperatures throughout the cell and overall greater solidification. Figure 13a shows the smallest area of solidification and highest temperatures to occur on the upper surfaces of the optical cell. Relatively warmer circulating fuel flow inhibits the growth of the solids on the upper surfaces.

Figure 13b shows simulations for $C^* = 1 \times 10^6 \text{ kg/m}^3 \cdot \text{s}$, and the velocity vectors show that less flow occurs in the liquid–solid regions relative to Fig. 13a. Consequently, reduced flow results in less heat transfer and higher temperatures throughout the cell. The temperature and f_l^* at the cell center are 220.1 K and 0.81, respectively.

The $0.50 f_l^*$ contour of Fig. 13b encompasses a much larger area than that of Fig. 13a, extending to the bottom of the optical cell with no discernable convection bulge. Figure 13b shows much less solidification in the optical cell relative to Fig. 13a. However, more solidification occurs in the upper region of the optical cell because the larger value of C^* reduces the heated return flow.

Figure 13c shows simulations for $C^* = 1 \times 10^{10} \text{ kg/m}^3 \cdot \text{s}$. For this condition, the calculated temperature at the center of optical cell is 221.3 K, and f_l^* is 1.0. The liquid fraction flood diagram shows that solidification has decreased overall. On the other hand, solidification has increased locally in the upper region of the optical cell. The velocity vectors show that flow has been substantially reduced in liquid–solid regions ($f_l^* < 1$). In addition, with this larger C^* value, there is a symmetric pair of vortices that extend in the vertical direction over much of the optical cell and assist the circulation of fuel between the upper and lower regions of the cell.

Figure 13 demonstrates the effect of C on the forming solidifying structures. The ability of freezing n -alkanes to trap liquid fuel and reduce buoyancy-driven flow (Fig. 12) is a behavior that will increase the magnitude of C for jet fuel. From Eq. (9), larger C^* values will reduce buoyancy-driven flow. As anticipated, Fig. 11 shows that the largest C^* value better predicts temperature. Results from visualization should correspond, therefore, to simulations where $C^* = 1 \times 10^{10} \text{ kg/m}^3 \cdot \text{s}$ (Fig. 13c).

Simulations of jet fuel freezing are useful if they can predict fuel tank hold-up or the volume of jet fuel unavailable for use because of solidification. Thus, it is important to define what portion of the fuel in the optical cell essentially does not flow and is a part of the crystalline matrix. For the largest value of C^* ($1 \times 10^{10} \text{ kg/m}^3 \cdot \text{s}$), 340 Fig. 14 shows a comparison of simulated f_l^* to the jet fuel after 37.5,

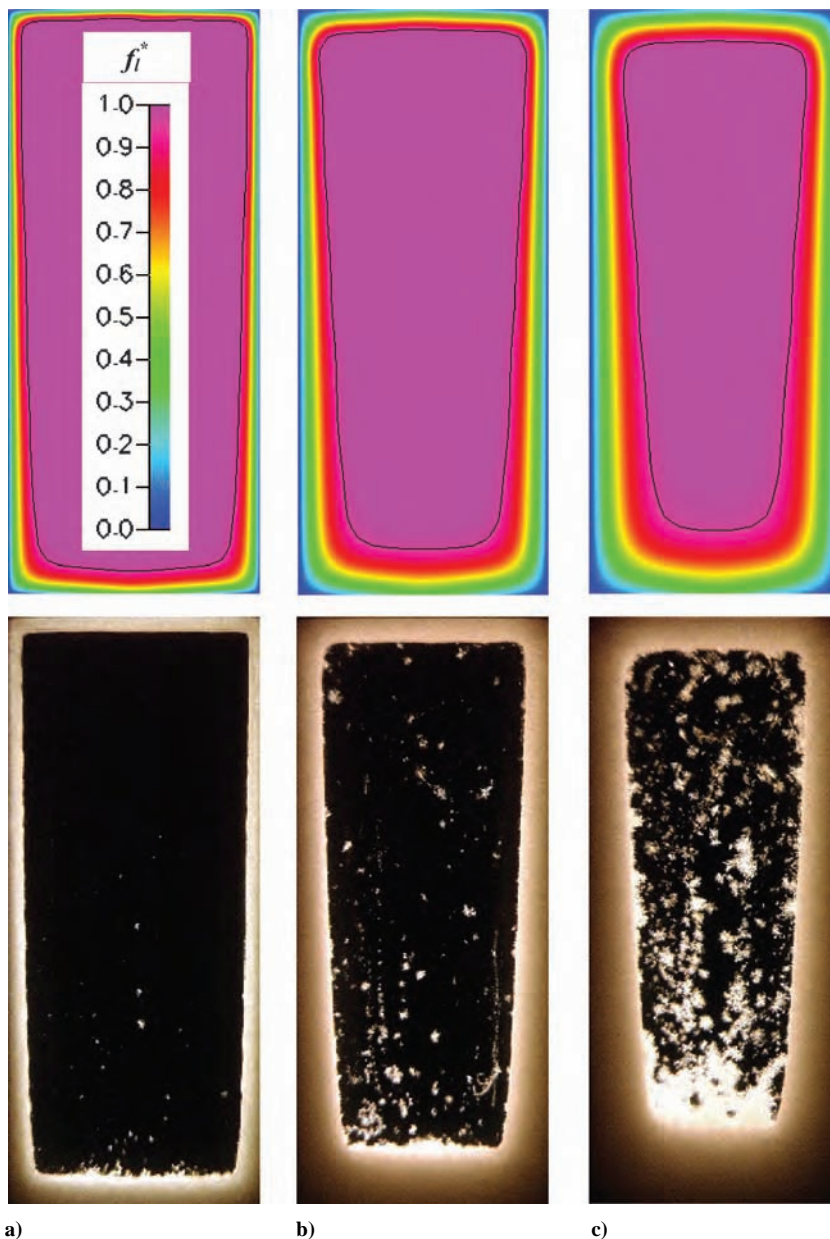


Fig. 14 Predicted liquid fraction with $C^* = 1 \times 10^{10} \text{ kg/m}^3 \cdot \text{s}$ for images of JP-8 (F3804) after a) 37.5 min, b) 42.5 min, and c) 47.5 min of applied thermal boundary conditions of Figure 9. A black contour line representing an f_l^* of 0.95 is shown for each condition.

42.5, and 47.5 min of cooling. The simulations show an increase in the adhered liquid–solid structures with time as demonstrated by the decreasing liquid fraction and predicts the shape and area of the adhered structures. Figure 14 demonstrates that the model simulates the liquid–solid advancement reasonably well spatially and temporally. A black contour line representing an $f_l^* = 0.95$ is shown in Fig. 14 and demonstrates the ability of the model to predict the shape of the solidifying structure. The area of adhered solidified structure predicted by this contour line is 1704 mm^2 . When the free-floating crystals and crystals that may settle by gravity on the bottom of the cell are neglected, the measured area of the two-phase region is 1680 mm^2 . Thus, the use of a liquid fraction contour line with a value near unity provides a method to estimate the two-dimensional area of solid and entrapped liquid fuel.

Simulations of the Solidification of Jet A

The applicability of the current approach for use with various jet fuels is desirable because different jet fuels may have dissimilar low-temperature properties. Moreover, low-temperature properties of individual jet fuel samples of the same type (Jet A fuel or JP-8), 341

may vary depending on the refinery source. Additional simulations were performed using properties of the Jet A fuel sample (F3219) and different thermal boundary conditions (Fig. 15). The use of other thermal boundary conditions can demonstrate the generality of the model. As with the JP-8 fuel sample, C^* was adjusted until the measured T_{center} agreed with the calculated value. As with the JP-8 fuel, Fig. 16 shows that a C^* value of $1 \times 10^{10} \text{ kg/m}^3 \cdot \text{s}$ provides the optimum prediction of T_{center} for the Jet A fuel. The model predicts the temperature to within 1.1 K of the measured temperature, which is similar to the accuracy of the JP-8 simulation shown in Fig. 11 (1.2 K). Figure 17 shows solidifying Jet A fuel (F3219) and that the crystal morphology and, thus, liquid fuel trapping mechanisms are similar to those of JP-8 (Figs. 10 and 12). Therefore, it is reasonable that the C^* found for the JP-8 fuel sample would be of the same magnitude as the C^* of the Jet A sample ($C^* = 1 \times 10^{10} \text{ kg/m}^3 \cdot \text{s}$).

Figure 18a shows a flood diagram of simulated f_l^* for the Jet A fuel sample using the measurements of Table 2. Figure 18b shows the image obtained from the optical cell for the same asymmetric thermal conditions used in the calculations. Figure 18a shows that a contour line corresponding to an $f_l^* = 0.95$ provides a good representation of the boundary between flowing liquid and the solid–liquid

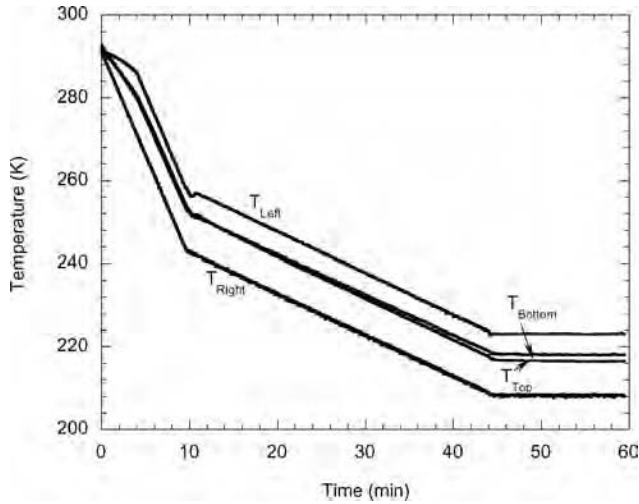


Fig. 15 Thermal boundary conditions applied to the optical cell for Jet A (F3219).

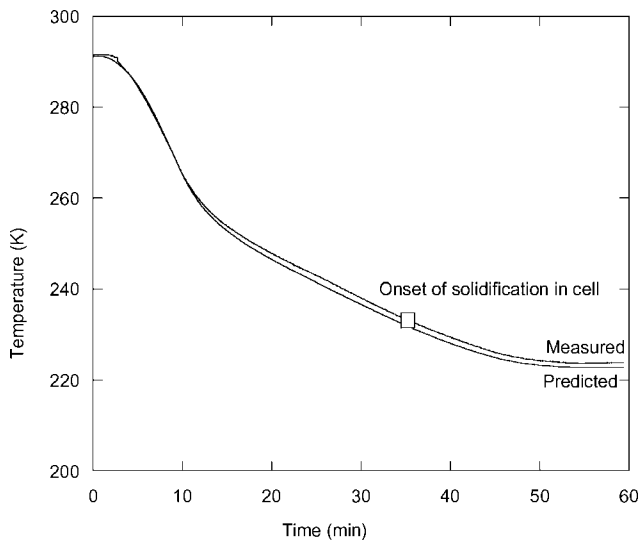


Fig. 16 Calculated and measured T_{center} for Jet A sample for a C^* value of $1 \times 10^{10} \text{ kg/m}^3 \cdot \text{s}$.

regions, as with the JP-8 sample. Differences between the simulated and measured solidification on the left vertical surface of the optical cell (Figs. 18a and 18b) are likely due to the uncertainty in the measured surface boundary temperature and its proximity to the cloud-point temperature (222.2 K, Table 1). The area of adhered solidified structure enclosed by the f_i^* contour line of 0.95 is 1039 mm^2 , and this value agrees well with the measured area (947 mm^2) of the solidifying region. Figures 16 and 18 together show that the model can simulate reasonably well the freezing behavior of another fuel type.

Simulations of the Freezing of Jet A Fuel Containing an Additive

There are potential commercial and military applications for developing additives to improve the low-temperature performance (reduced cloud point, increased flow ability) of Jet A and JP-8, fuels. Thus, it is desirable to simulate the freezing behavior of a jet fuel that contains a low-temperature additive. Here, the Jet A fuel sample is blended with 2000 mg/l of a proprietary additive (F3607), which has been observed to reduce the hold-up in large-scale tests. In experiments using a low-temperature microscope, the addition of the additive was found to change the platelike crystals of solidifying neat jet fuel into needlelike crystals.²² In addition, the additive shifts the DSC peak associated with phase change of the Jet A sample to lower temperatures and lowers the cloud-point temperature by 0.6 K (Table 1).

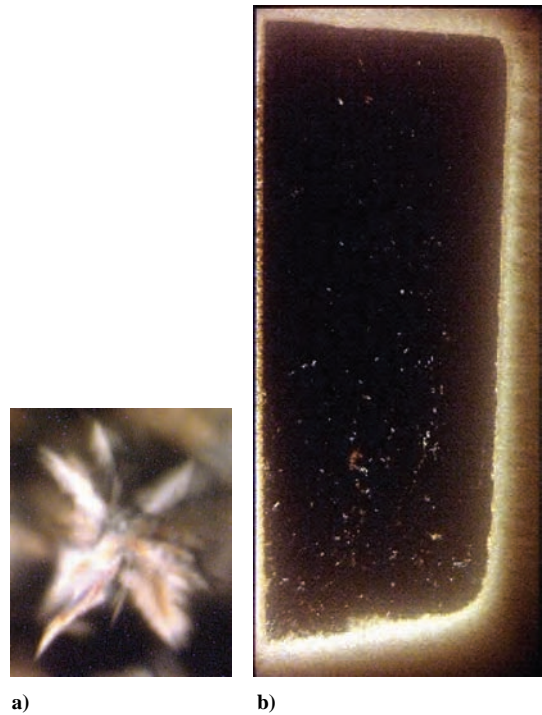


Fig. 17 Solidifying Jet A (F3219) after 50 min of applied thermal boundary conditions of Fig. 15: a) three-dimensional crystal geometry and b) two-dimensional view of the cell.

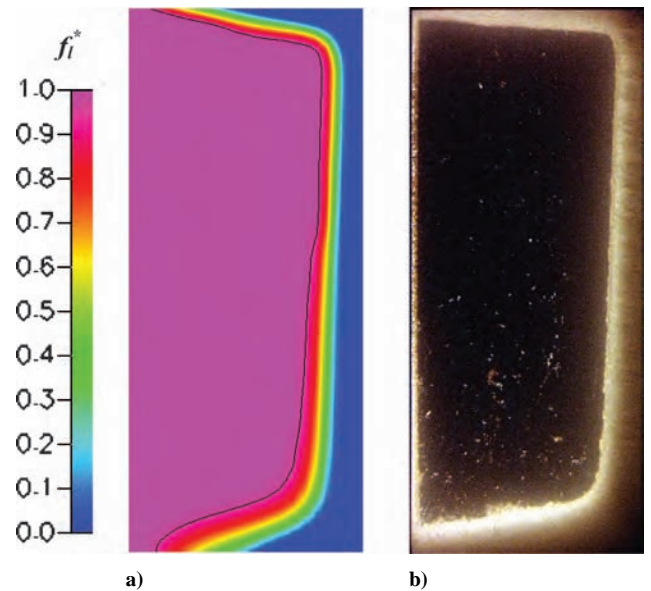


Fig. 18 Jet A (F3219) after 50 min of applied thermal boundary conditions of Fig. 15: a) flood diagram of simulated f_i^* ($C^* = 1 \times 10^{10} \text{ kg/m}^3 \cdot \text{s}$) with f_i^* contour of 0.95 and b) image of Jet A.

In previous work, it was observed that the solidification behavior of the fuel containing the additive is different from that of the neat Jet A fuel.⁷ The fuel containing the additive tends to have smaller crystals, which do not pack in the same way as those observed in the case of the neat fuel. In contrast to the behavior of the neat fuel, stirring the liquid fuel easily disrupts the accumulation of crystals and allows them to flow into the bulk fuel. Figures 19a and 19b show simulations of f_i^* for C^* values of 1×10^{10} and $1 \times 10^8 \text{ kg/m}^3 \cdot \text{s}$, respectively. Better agreement between the calculated and actual shape occurs with a C^* value of $1 \times 10^8 \text{ kg/m}^3 \cdot \text{s}$. With this C^* value, the calculated temperature at the center of the optical cell is within 3 K of the final measured value. The difference between the simulated and measured optical cell center temperatures for the fuel containing the additive is not as small as that for the neat fuels and

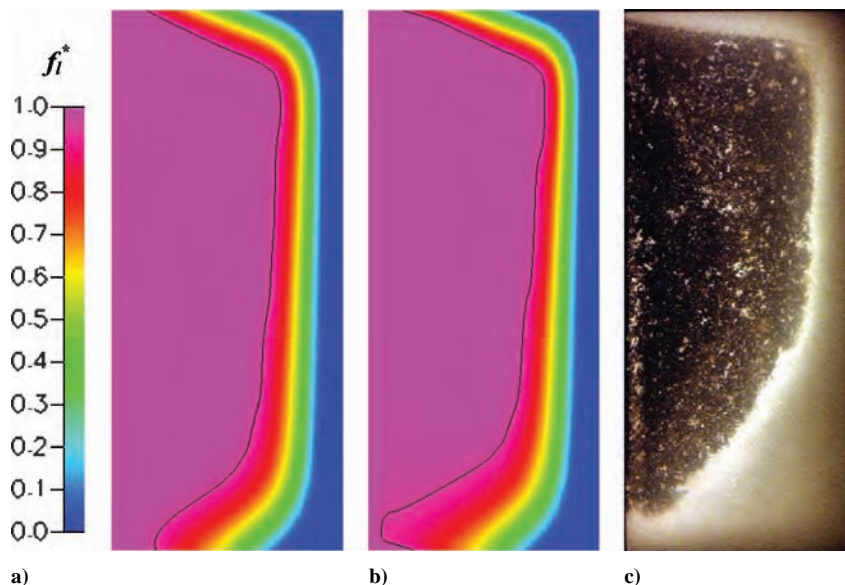


Fig. 19 Solidification of Jet A (F3219) with 2000 mg/l of additive F3607 after 60 min of applied thermal conditions of Fig. 15; calculated f_l^* for a) $C^* = 1 \times 10^{10} \text{ kg/m}^3 \cdot \text{s}$ and b) $C^* = 1 \times 10^8 \text{ kg/m}^3 \cdot \text{s}$ and c) fuel. The black contour line represents an f_l^* of 0.95.

suggests that other mechanisms are involved. Further understanding of the behavior of classes of low-temperature additives is required to enable the application of the model to fuels containing additives.

Discussion of the Morphology Constant, C

A fundamental concern to be addressed is the interpretation of the constant C , used in the flow resistance term. C represents the cumulative effects of Σ together with the influence of pore geometry and orientation. The use of C is a first step in simulating the freezing of jet fuel and permits reasonable simulations of T_{center} and solidified areas. Note that the Jet A and JP-8 fuel samples had similar crystal morphologies, and the same value of C^* ($C\mu$, $1 \times 10^{10} \text{ kg/m}^3 \cdot \text{s}$) yielded acceptable simulations of the growth of the two-phase coexistence region. In addition, the fuel containing the additive formed crystals that were irregularly shaped and needlelike and did not readily trap liquid fuel. With regard to Eqs. (9) and (10), it is observed as C^* is increased for a fixed λ and velocity that the flow resistance increases. Thus, for the jet fuel containing the additive, a lower C^* value ($1 \times 10^8 \text{ kg/m}^3 \cdot \text{s}$) might be anticipated. Indeed, a lower C^* value was observed for the fuel containing the additive. Relatively large values of C^* are shown here to be required for proper simulations. In simulations of metal alloy solidification, large C values were also necessary.¹³

Conclusions

A two-dimensional CFD model that reasonably predicts the solidification of jet fuels in a buoyancy-driven flow has been developed. The approach here uses DSC and GC measurements and enables the amount of hold-up due to fuel freezing to be estimated. Flow resistance caused by porous, adhered crystal structures was simulated using a momentum resistance source term. In addition, jet fuel properties were measured at low temperatures for use in the simulations. Optical cell flow-visualization experiments using polarized light enabled the measurement of areas of liquid–solid regions and the imaging of interactions between the flow and crystallization. The simulations agreed reasonably well with the solidified area and temperature measurements for the jet fuel samples and the thermal boundary conditions used. Thus, the current numerical model may be used as a tool by aircraft designers who need to predict fuel tank hold-up. The properties presented in the present work are specific to the fuels analyzed. Representative properties must be selected by the designer based on the level of model accuracy desired. The authors believe that the JP-8 sample utilized represents a freeze-point specification minimum fuel and the measured

properties may potentially be used to predict the maximum hold-up.

The ability of solidifying jet fuel to entrap liquids was shown to minimize the buoyancy-driven flow through adhered solidifying crystalline structures. Trapped liquid is unlikely to flow due to buoyancy forces for both the Jet A and JP-8 samples. Comparisons between simulations and the visualization experiments demonstrated that buoyancy-driven flow was minimal in regions of adhered solidifying fuel. Simulations with additives show promise; however, predicted temperatures agree less with measured temperatures. Thus, further understanding of low-temperature additive behavior and refinement of the model are necessary for the additive application.

Acknowledgments

This work was supported by the Dayton Area Graduate Studies Institute and the U.S. Air Force, Air Force Research Laboratory, Propulsion Directorate, Turbine Engines Division, Fuels Branch, Wright–Patterson Air Force Base, Ohio, under cooperative agreement F33615-03-2-2347. We would like to thank Marlin Vangsness and Linda Shafer for obtaining viscosity, density, and microscope images; Richard Striebich and Linda Shafer for obtaining gas chromatograph data; Nikki Widmor for obtaining differential scanning calorimeter data; and Kirsten Wohlwend (U.S. Air Force) and David Gollier for obtaining the freeze, pour, and cloud point temperature measurements.

References

- McConnell, P. M., Owens, S. F., and Kamin, R. A., "Prediction of Fuel Freezing in Airplane Fuel Tanks of Arbitrary Geometry—Part 1," *Aircraft Engineering*, Vol. 58, No. 9, 1986, pp. 20–23.
- McConnell, P. M., Owens, S. F., and Kamin, R. A., "Prediction of Fuel Freezing in Airplane Fuel Tanks of Arbitrary Geometry—Part 2," *Aircraft Engineering*, Vol. 58, No. 10, 1986, pp. 2–7.
- Beckermann, C., and Viskanta, R., "Mathematical Modeling of Transport Phenomena During Alloy Solidification," *Applied Mechanical Review*, Vol. 46, No. 1, 1993, pp. 1–27.
- Desmarais, L. A., and Tolle, F. F., "Fuel Freeze Point Investigations," Air Force Research Lab., Technical Rept. AFWAL-TR-84-2049, Wright–Patterson Air Force Base, OH, July 1984.
- Coutinho, J. A. P., "A Thermodynamic Model for Predicting Wax Formation in Jet and Diesel Fuels," *Energy and Fuels*, Vol. 14, No. 3, 2000, pp. 625–631.
- Leo, A., and von Meerwall, E., "Fuel Holdup and Component Diffusivity in a Cooled Cylindrical Tank," *Journal of Aircraft*, Vol. 26, No. 5, 1989, pp. 465–469.

- ⁷Atkins, D. L., and Ervin, J. S., "Freezing of Jet Fuel within a Buoyancy-Driven Flow in a Rectangular Optical Cell," *Energy and Fuels*, Vol. 15, No. 5, 2001, pp. 1233–1240.
- ⁸"Handbook of Aviation Fuel Properties," Coordinating Research Council, Technical Rept. 530, Atlanta, GA, May 1988.
- ⁹Savant Independent Lubricant Testing and Research Lab., Midland, MI, June 2003.
- ¹⁰He, B., and Setterwall, F., "Technical Grade Paraffin Waxes as Phase Change Materials for Cool Thermal Storage and Cool Storage Systems Capital Cost Estimation," *Energy Conservation and Management*, Vol. 43, No. 13, 2002, pp. 1709–1723.
- ¹¹"Thermal Conductivity of Liquid; Organic Compounds," *Chemical Properties Handbook* [online], URL: <http://www.knovel.com> [cited 2 March 2001].
- ¹²Yarbrough, D. W., and Kuan, C. E., "The Thermal Conductivity of Solid N-Eicosane, N-Octadecane, N-Heptadecane, N-Pentadecane, and N-Tetradecane," *Thermal Conductivity 17*, Plenum Press, New York, 1983, pp. 265–274.
- ¹³Voller, V. R., and Prakash, C., "A Fixed Grid Numerical Modeling Methodology for Convection-Diffusion Mushy Region Phase-Change Problems," *International Journal of Heat and Mass Transfer*, Vol. 30, No. 8, 1987, pp. 1709–1719.
- ¹⁴D'Arcy, H., *Les Fontaines Publiques de la Ville de Dijon*, Dalmont, Paris, 1856.
- ¹⁵Collins, R. E., *Flow of Fluids through Porous Materials*, Reinhold, New York, 1961, Chaps. 1–3.
- ¹⁶Kozeny, J. S., "Ueber kapillare Leitung des Wassers im Boden," *Sitzungsberichte, Akademie der Wissenschaften in Wien, Mathematisch-Naturwissenschaftliche Klasse*, Vol. 136, 1927, pp. 271–306.
- ¹⁷Carman, P., "Fluid Flow Through Granular Beds," *Transactions of the Institution of Chemical Engineers*, Vol. 15, May 1937, pp. 150–166.
- ¹⁸Moynihan, C. T., Mossadegh, R., and Bruce, A. J., "Determination of the Mass Fraction of Crystals in Partly Frozen Hydrocarbon Fuels," *Fuel*, Vol. 63, No. 3, March 1984, pp. 378–384.
- ¹⁹"CFD-ACE(U) Users Manual Version 2002," CFD Research Corporation, Huntsville, AL, March 2002.
- ²⁰Wendlandt, W. W., *Thermal Analysis*; Wiley, New York, 1986.
- ²¹Zabarnick, S., and Widmor, N., "Studies of Jet Fuel Freezing by Differential Scanning Calorimetry," *Energy and Fuels*, Vol. 15, 2001, pp. 1447–1453.
- ²²Widmor, N., Ervin, J. S., Zabarnick, S., and Vangsness, M., "Studies of Jet Fuel Freezing by Differential Scanning Calorimetry and Cold-Stage Microscopy," *Journal of Engineering for Gas Turbines and Power*, Vol. 125, No. 1, 2003, pp. 34–39.

APPENDIX Y

Simulations of Flowing Mildly-Cracked Normal Alkanes Incorporating Proportional Product Distributions

INTENTIONALLY LEFT BLANK

Simulations of Flowing Mildly-Cracked Normal Alkanes Incorporating Proportional Product Distributions

Thomas A. Ward,* Jamie S. Ervin,† Richard C. Striebich,‡ and Steven Zabarnick§
University of Dayton, Dayton, Ohio 45469-0116

Hydrocarbon fuels have been used as a cooling media in aircraft jet engines for many years. However, advanced aircraft engines are reaching a practical heat transfer limit beyond which the sensible heat transfer provided by fuels is no longer adequate. One solution is to use an endothermic fuel that absorbs heat through chemical reactions. A two-dimensional computational model is developed to calculate the heat and mass transport associated with a flowing fuel using a unique global chemical kinetics model. Most past models do not account for changes in the chemical composition of a flowing fuel and also do not adequately predict flow properties in the supercritical regime. The two-dimensional computational model presented calculates the changing flow properties of a supercritical reacting fuel by use of experimentally derived proportional product distributions. The calculations are validated by measured experimental data obtained from a flow reactor in which n-decane and n-dodecane are mildly cracked. It is believed that these simulations will assist the fundamental understanding of high-temperature fuel flow experiments.

Nomenclature

A	= preexponential factor (A -factor) in Arrhenius rate expression, s^{-1}
C_p	= specific heat, $J/kg \cdot K$
C_μ	= constant, 0.09
C_1	= constant, 1.47
C_2	= constant, 1.92
D	= reactor diameter, m
D_i	= diffusion coefficient of i th species, m^2/s
E_a	= activation energy in Arrhenius rate expression, cal/mol
G	= $\mu_t \left\{ 2 \left[\left(\frac{\partial u}{\partial z} \right)^2 + \left(\frac{\partial v}{\partial r} \right)^2 + \left(\frac{v}{r} \right)^2 \right] + \left(\frac{\partial v}{\partial z} + \frac{\partial u}{\partial r} \right)^2 \right\}$
g	= gravitational acceleration, m/s^2
h	= enthalpy, kJ/kg
i	= individual product species
k	= turbulent kinetic energy, kJ/kg
k_A	= Arrhenius rate constant
n	= number of parent fuel conversions of interest (from different experimental runs)
P_c	= critical pressure, n-decane, 2.10 MPa; n-dodecane, 1.81 MPa (Ref. 23)
p	= pressure, MPa
R	= molar gas constant, $1.987 cal/K \cdot moles$
RH	= parent fuel
r	= radial coordinate, m
S^Φ	= source term

T	= fuel temperature, $^\circ C$
T_c	= critical temperature, n-decane, $345^\circ C$; n-dodecane, $385^\circ C$
t	= time, s
u	= axial velocity component, m/s
v	= radial velocity component, m/s
Y_i	= mass fraction of i th cracked product species
Y_{RH}	= mass fraction of parent fuel
$Y_{\sum prod}$	= mass fraction of total products
y_i	= product mass fraction of an individual product species
y_{iav}	= averaged y_i over a range of parent fuel conversions (experimental conditions)
z	= axial coordinate, m
Γ^Φ	= transport coefficient
ε	= turbulence dissipation rate, W
κ	= thermal conductivity, $W/m \cdot K$
μ	= absolute viscosity, $kg/m \cdot s$
μ_t	= turbulent viscosity, $C_\mu \cdot \rho \cdot k^2/\varepsilon$, $kg/m \cdot s$
ρ	= density, kg/m^3
σ_k	= constant, 1.0
σ_{Y_i}	= constant, 1.0
σ_ε	= constant, 1.3
τ_w	= wall shear stress, N/m^2
Φ	= assigned variable in Equation 9
$\dot{\omega}_i$	= rate of production of i th specie, $kg/m^3 \cdot s$

Introduction

AVIATION fuels are circulated in military aircraft for cooling. Unfortunately, current aircraft engines are reaching a practical heat transfer limit beyond which the sensible heat transfer provided by fuels is no longer adequate.¹ Additionally hypersonic air vehicles, capable of flying at Mach numbers (Mach > 5) greater than conventional aircraft, are being considered for future military and commercial needs.² At hypersonic speeds, the high stagnation temperature of air precludes cooling with an air/fuel heat exchanger. Recirculation cooling via an external heat exchanger would add unacceptable weight. Cryogenic fuels can provide sufficient cooling but require large storage volume (due to their low densities) and significant insulation. An alternative solution is to use an endothermic fuel that absorbs heat through a series of chemical reactions.

With an endothermic fuel, additional cooling is obtained by endothermic reactions occurring simultaneously with traditional sensible convective heat transfer. The endothermic heat absorption rate

Received 31 January 2003; revision received 26 June 2003; accepted for publication 27 June 2003. This material is declared a work of the U.S. Government and is not subject to copyright protection in the United States. Copies of this paper may be made for personal or internal use, on condition that the copier pay the \$10.00 per-copy fee to the Copyright Clearance Center, Inc., 222 Rosewood Drive, Danvers, MA 01923; include the code 0748-4658/04 \$10.00 in correspondence with the CCC.

*Aerospace Engineer, Department of Aerospace and Mechanical Engineering; Thomas.Ward@wpafb.af.mil. Member AIAA.

†Professor, Department of Aerospace and Mechanical Engineering, Associate Fellow AIAA.

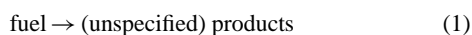
‡Professor, Department of Aerospace and Mechanical Engineering.

§Research Engineer, Research Institute.

can be over twice as much as the rate available by sensible convective cooling.¹ The most promising endothermic reaction mechanism is thermal cracking or pyrolysis.³ Significant thermal cracking of jet fuel occurs at fuel temperatures above approximately 500°C, where the bonds of hydrocarbon molecules are broken to produce several smaller molecules. In real fuel systems, cracking would result in thousands of chemical reactions. However, for low conversion (mild cracking) of normal alkanes, the primary degradation products have been observed to be smaller carbon number alkanes and alkenes.^{4–6} Mild cracking is defined here as a low conversion of the parent fuel caused by initial chemical reactions that form only 1–alkene, and n–alkane products in significant quantities. Other products may form in minute quantities but do not have a significant effect on the chemical kinetics and transport properties. This definition of mild cracking generally excludes secondary reactions that are common at higher conversions. Mild-cracking reactions of n–alkanes are of interest in endothermic fuel systems because aromatics, for example, benzene and toluene, do not form in substantial quantities. Combustion of aromatics are known to increase soot and pollutant emissions.⁷ Moreover, the formation of saturates and aromatics also drastically reduce the heat-absorbing potential of the reaction. Finally and most important, aromatics are thought to be deposition precursors, which can cause catastrophic system failure by obstructing fuel pathways.⁷ It is necessary to suppress surface deposition to utilize thermal cracking in an endothermic cooling system. Research of surface coatings and additives to reduce deposition is ongoing.⁸ Single-pass heat exchangers could potentially make use of the cooling benefits of mild cracking while avoiding the detrimental effects caused by the formation of deposits at higher conversions.

Although thermal cracking is an avenue to increase heat sink potential, there are numerous concerns that need to be studied. Numerical simulations can assist the understanding of experiments that involve endothermic fuels. For example, there is a strong coupling between the chemical kinetics and transport phenomena under the supercritical conditions expected for endothermic fuels. Under supercritical conditions, the transport properties may change drastically, which, in turn, influence the endothermic reaction rates.

Past modeling efforts have involved several different types of chemical kinetics models including detailed, lumped, and global mechanisms. Detailed modeling⁹ and lumped^{5,10} chemical mechanisms have generally been confined to nonflowing, one-dimensional, analytical models. Detailed modeling requires intricate knowledge of reaction pathways and rate constants that are generally unavailable for high carbon number n–alkanes.¹⁰ Because detailed modeling encompasses thousands of elementary reactions, incorporation into multidimensional fluid dynamics problems is not practical. In lumped mechanisms, components of a fuel/product mixture are grouped together into kinetic lumps, which are then treated as pseudocomponents. Unfortunately, information about individual components comprising the product distribution is lost, and therefore, the transport properties associated with the mixture may not always be adequately modeled. Most past numerical simulations of the thermal cracking of flowing jet fuel have included global chemical mechanisms.^{11–13} Global models are generally the most practical mechanisms for multidimensional fluid dynamics applications. However, global models used previously have not accounted for property changes due to the formation of cracked products in the fuel mixture. Most past global models employ the following reaction and do not specify individual cracked products.



One such global model was developed by LinhBao and Chen,¹¹ who developed a one-dimensional model for prediction of heat transfer using Norpar-12. A simple one-step reaction is used, and reaction rate constants are chosen to fit the data of Sobel and Spadaccini.¹ The heat transfer predictions were consistently lower than the experimental data. LinhBao and Chen concluded that this difference was due to the relative simplicity of the flow model and the global chemical kinetic representation.¹¹ Stewart¹² also developed a one-step global model of several cycloalkanes, for example, MCH, decalin, and tetralin. Cycloalkanes generally constitute a fraction (typically

5–20%) of jet fuels. In this work, laminar plug flow conditions (no gradients in the radial direction of the reactor) were assumed and fuel properties were calculated using ideal gas approximations. This assumption is usually invalid for supercritical conditions. However, some limited initial steps were taken to extrapolate the ideal gas model to supercritical conditions. Goel and Boehman¹³ conducted an experiment to measure the thermal degradation of n–dodecane in a flow reactor. In addition, they solved the governing equations of energy and mass using the method of lines.¹⁴ The model uses a one-step global reaction to simulate the degradation of n–dodecane. However, they did not simulate the products formed from thermal cracking and assumed that the transport properties remained constant. Sheu et al.¹⁵ developed a three-step lumped model to describe the thermal cracking of Norpar-13 under supercritical and near-critical conditions using a commercially available code. The composition of the species within the lumps was assumed to be constant and set to experimentally measured values at the specific conditions of interest. Unfortunately, because the model relies on empirical data, it is not applicable to different experimental conditions.

The focus of the current work is the development of a two-dimensional computational model of the heat transfer and chemistry in a flowing system to simulate mild cracking of n–alkanes. The salient feature of our approach over previous models is that it is a two-dimensional computational fluid dynamics (CFD) model representing fuel flow without idealized approximations such as plug flow or constant properties. The present model accounts for property changes as the fuel cracks. Because endothermic fuel systems will be expected to operate at supercritical temperatures and pressures, it is important to assess fuel behavior under supercritical conditions. Transition from liquid phase to supercritical state may drastically affect transport properties that ultimately determine the temperature field, reaction rates, and cooling capacity. The chemistry included is more detailed than past global models because it predicts cracked products based on experimentally measured proportional distributions (explained in the “Proportional Product Distribution Chemical Model” section). However, only one rate expression is required to define parent fuel degradation, and so it is practical for use in multi-dimensional flow simulations.

Experimental

The development of the chemical kinetics model was based on a set of experiments that studied cracked products of n–alkanes. Two n–alkanes, which have critical pressures and temperatures similar to actual jet fuels, were selected: n–decane (Aldrich 99+%) and n–dodecane (Aldrich 99+%). Also previous studies² have shown that n–alkanes have product distributions that are similar to real jet fuels. The experimental apparatus used was the system for thermal diagnostic studies (STDS), shown in Fig. 1. The STDS consists of a thermal reaction chamber, a gas chromatograph (GC) with mass spectrometer (MS), and a hydrogen flame ionization detector (FID). Product distribution samples from the exposure of liquid-phase and condensed-phase materials were collected through high-pressure liquid sampling valves and then injected into the GC–MS and FID. This technique is capable of measuring dissolved gases, such as oxygen and nitrogen, cracked gases, and condensed-phase reaction products of the parent fuel.

The fuels were sparged with gaseous helium before being pumped into the STDS to remove dissolved oxygen to prevent thermal-oxidative deposition. A constant delivery syringe pump was used to provide a constant flow rate through the reactor. Five flow rates (0.3, 0.4, 0.5, 0.6, and 0.7 ml/min) were used. A constant outlet pressure of 3.45 MPa (500 psig) was maintained throughout all of the experiments using a backpressure valve. The flow was pumped into (0.5 mm i.d.) 316 stainless-steel tubing and passed through a switch valve that either directed the fuel to the reactor assembly or allowed gaseous nitrogen to flow through the system (to prevent surface deposition in the reactor when not collecting data).

The thermal reaction chamber was housed in a GC oven (Hewlett–Packard Company 5890A) kept at 200°C. The oven is used for temperature control of the fuel transfer lines into the reactor. Contained inside this oven is a smaller high-temperature furnace that houses

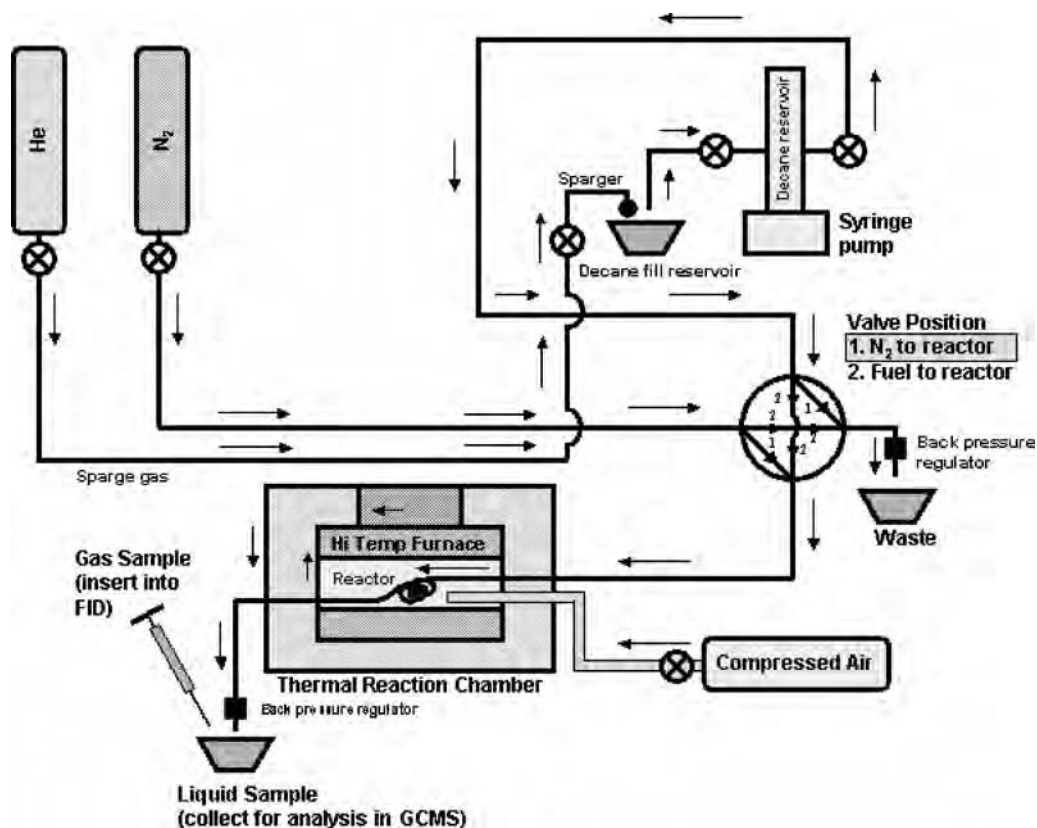


Fig. 1 STDS experimental apparatus.

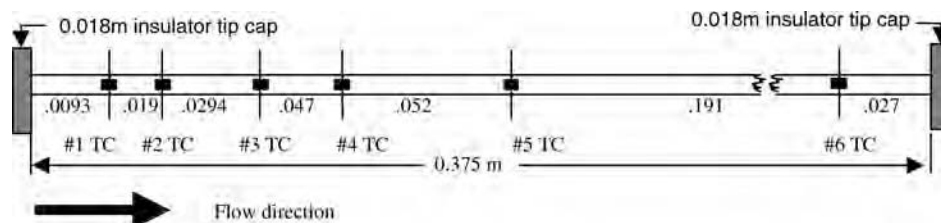


Fig. 2 Flow reactor schematic (not to scale, all units in meters) with thermocouple (TC) locations shown.

the flow reactor. The high-temperature furnace heats by electrical conduction coils that completely surround the reactor. The heating coils are surrounded by insulation to minimize convective heat loss into the low-temperature furnace. The reactor consists of a continuous coiled, stainless-steel fuel line (0.5 mm i.d., 37.5 cm in length) lying inside an insulated quartz tube and heated by the hinged reactor furnace. The quartz tube was also capped at both ends with a foam insulator to reduce convective heat loss. Six (type K) thermocouples were welded onto the outer wall of the reactor (Fig. 2). The measured wall temperature profiles (uncertainty of $\pm 2^\circ\text{C}$) were used as boundary conditions for the numerical model. Figures 3a–3c show the wall temperature profiles measured from the *n*-decane experiments. The *n*-dodecane experiments were similar and, thus, not shown. Three wall temperatures were studied (500, 550, and 600°C) for each of the five flow rates.

Chromatographic separation was performed in a second GC (Hewlett–Packard Company 5890A) with two detectors. Ultrahigh purity helium (99.999%) was used as the carrier gas. Gas product samples were collected directly from the thermal reaction chamber in a syringe and then injected into the FID. The mass of the total gas products was determined by measuring the volumetric flow rate with a bubble meter and calculated assuming ideal gas behavior. Quantification of the total gas product was necessary to normalize the gas product fractions (determined from the FID) to the liquid product fractions. Liquid products were collected for 2 min, weighed, and then analyzed offline using a GC–MS. Both the FID

and GC–MS were calibrated with known external standards spanning the entire range of products formed in the experiment. All of the product species were quantified based on these calibrations. Three replicates of the experimental runs were performed to obtain an indication of the experimental error. The maximum standard deviation of the measured parent fuel mass fraction from all of the experimental conditions was $\pm 3.5\%$.

Proportional Product Distribution Chemical Model

Previous mild thermal cracking experiments of *n*-alkane hydrocarbons have shown that the major products formed are predominately lower carbon number *n*-alkanes and 1-alkenes.^{4–6} Kossiakoff and Rice¹⁶ described this decomposition as occurring through a series of free radical reactions. Decomposition initiates by a carbon–carbon bond fission along the parent *n*-alkane chain to form the primary radicals. These radicals abstract hydrogen atoms from surrounding molecules to form secondary radicals plus *n*-alkanes. The secondary radicals can isomerize or decompose by a β -scission reaction to form an alkene and a smaller primary radical. The resulting small primary radical can then undergo further reactions until the final product is too small to decompose further. This mechanism describes thermal cracking of hydrocarbons in detail, but it encompasses thousands of chemical reactions (for *n*-decane or *n*-dodecane pyrolysis) and is too complex and, thus, impractical for use in most CFD applications. The focus of this work is to

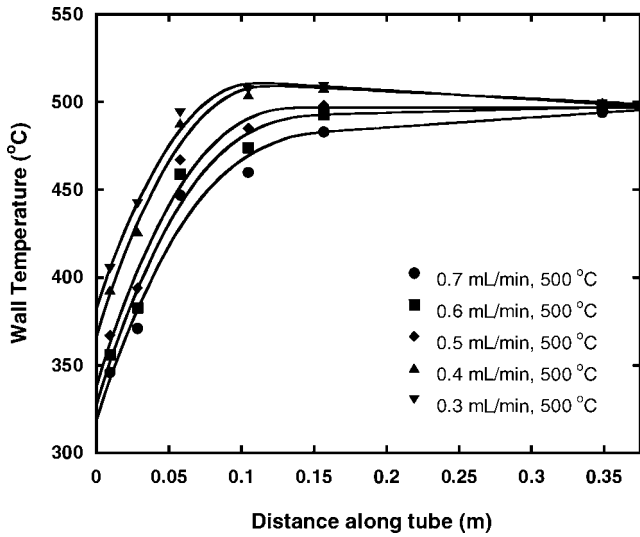


Fig. 3a Wall temperatures for n-decane experiment; steady-state wall temperature = 500°C.

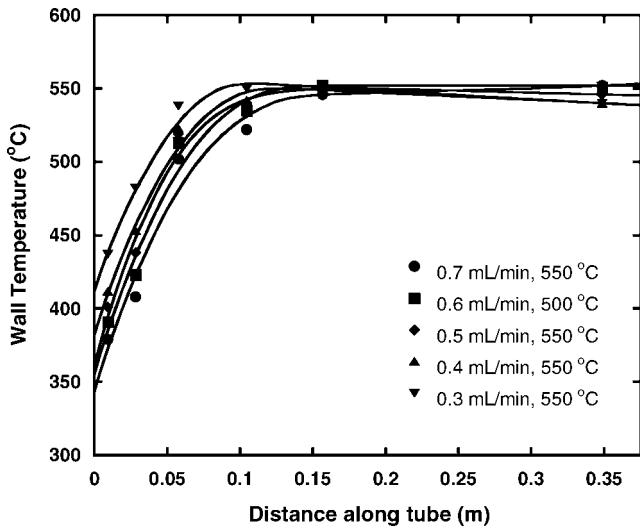


Fig. 3b Wall temperatures for n-decane experiment; steady-state wall temperature = 550°C.

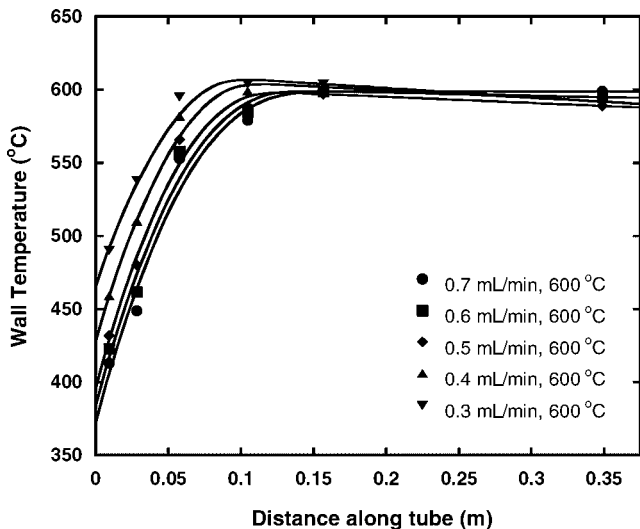


Fig. 3c Wall temperatures for n-decane experiment; steady-state wall temperature = 600°C.

develop a practical kinetic mechanism to predict the formation of cracked products and use it in two-dimensional CFD simulations of n-alkane fuels flowing through a reactor.

In the current model, one rate expression is used to predict the degradation of the parent fuel into products,

$$-\frac{d(RH)}{dt} = k_A[RH] \quad (2)$$

The rate constant k_A for the reaction of Eq. (2) is expressed in Arrhenius form as

$$k_A = A \cdot \exp(-E_a/RT) \quad (3)$$

In Eq. (3), E_a is the activation energy, and A is a preexponential factor (or A factor) of the reaction.

The total product mass fraction $Y_{\sum \text{products}}$ is defined in Eq. 4, where Y_{RH} is the parent fuel mass fraction.

$$Y_{\sum \text{products}} = 1.0 - Y_{RH} \quad (4)$$

Past mild-cracking experiments^{4,12} show that the products form at constant proportions with respect to the other products. Therefore, it may be possible to predict the mass fractions of the cracked products formed by taking advantage of these proportional product distributions. This hypothesis forms the basis of the proportional product distribution (PPD) model. The product mass fraction of species, i , y_i is measured from the experimental data,

$$y_i = \frac{Y_i}{Y_{\sum \text{products}}} \quad (5)$$

By the PPD assumption, y_i remains approximately constant with parent fuel conversion ($1.0 - Y_{RH}$). However, this will only be true within the limits of mild-cracking conditions, which assumes that there are no secondary cracking reactions. The measured values of y_i for a number n of different parent fuel conversions are averaged as

$$y_{iav} = \sum_n \frac{y_i}{n} \quad (6)$$

The mass fraction of each product Y_i is determined by multiplying the total product mass fraction by the average product fractions of each individual species y_{iav} .

$$Y_i = (1.0 - Y_{RH}) \cdot y_{iav} \quad (7)$$

CFD Simulations

The Navier–Stokes turbulent energy, enthalpy, and species equations were used to simulate the flow and heat and mass transport within the reactor.¹⁷ The fluid motion inside the reactor was assumed to be axisymmetric and steady. The governing equations written in the cylindrical, z and r , coordinate system for axisymmetric flow are

$$\frac{\partial \rho u}{\partial z} + \frac{\partial \rho v}{\partial r} + \frac{\rho v}{r} = 0 \quad (8)$$

$$\frac{\partial \rho u \Phi}{\partial z} + \frac{\partial \rho v \Phi}{\partial r} = \frac{\partial}{\partial z} \left(\Gamma^\Phi \frac{\partial \Phi}{\partial z} \right) + \frac{\partial}{\partial r} \left(\Gamma^\Phi \frac{\partial \Phi}{\partial r} \right) - \frac{\rho v \Phi}{r} + \frac{\Gamma^\Phi}{r} \frac{\partial \Phi}{\partial r} + S^\Phi \quad (9)$$

Equation (8) is the continuity equation, and Eq. (9) represents the momentum, energy, or species equation depending on the variable represented by Φ . Here ρ is the mixture density. Table 1 lists the transport coefficients Γ^Φ and the source terms S^Φ of the governing equations. The governing equations are discretized utilizing a second-order, central differencing scheme (except where the local Peclet number becomes greater than two, in which case a first-order upwind scheme is used). Wall functions were used to determine the flow variables near the wall.¹⁸ Because the purpose of the model is to simulate mild thermal cracking, resulting in very low surface deposition, deposition was not modeled.

The inlet velocity and temperature profile of the fuel are assumed to be uniform for simplicity. The inlet fuel temperature was 200°C, and the measured pressure of 3.45 MPa was used. When the velocity, pressure, turbulent kinetic energy, turbulent dissipation, enthalpy, and species global error residuals were all reduced below four orders of magnitude from their maximum values, the solution was considered converged.

The thermodynamic and transport properties were calculated at every grid point by incorporating SUPERTRAPP¹⁹ subroutines. SUPERTRAPP performs phase equilibrium calculations with the Peng–Robinson equation of state,²⁰ and transport properties are calculated with an extended corresponding states model. SUPERTRAPP provides well-behaved thermodynamic properties near the critical point and in the supercritical regime. However, it does not predict the molecular diffusivity. Determination of the diffusion coefficients for supercritical conditions is difficult, and there is little published data available. Stewart¹² showed that for most supercritical fluid flow applications the diffusion coefficient is of the order of 10^{-7} m²/s. For reference, liquids have a diffusion coefficient generally of the order 10^{-8} m²/s. In our experiment, the fluid transitions from an initial compressed liquid state into a supercritical fluid. Stewart¹² also showed that molecular diffusivity has a negligible effect on the reaction rate for large activation energy reactions of supercritical fluids under these experimental conditions. Furthermore, our experiment involved turbulent flows (outlet Reynolds numbers were greater than 2,000), further decreasing the influence of molecular diffusivity relative to the turbulent diffusivity of the flow. To evaluate the assumption that molecular diffusion is negligible for our experimental conditions, two simulations were performed. In the first simulation, the diffusion coefficient was set to a constant value of 10^{-7} m²/s. In the second simulation, the diffusion coefficient was set to a constant value of 10^{-8} m²/s. There was less than a 1% difference between the two runs in all flow properties. For all subsequent simulations, the diffusion coefficient was set to a constant value of 10^{-8} m²/s, where the fluid was subcritical and 10^{-7} m²/s at grid points where the fluid was supercritical.

Table 2 shows the rate constants used to predict the conversion of the parent fuel into products [Eq. (3)]. The rate constants used to predict n–decane conversion are within the error bounds of those determined by Stewart et al.²¹ from flow reactor experiments at slightly lower temperatures and pressures than in our experiment. The rate

constants used to predict n–dodecane conversion are within the error bounds of those determined by Zhou and Crynes²² using a batch reactor at lower temperatures but higher pressures than our experiment. (Most available studies provide rate constants obtained from batch reactor experiments, which only approximately apply to flow reactor experiments.) Because the rate constants were used to predict conversions at slightly different conditions than the literature values, a slight deviation from the mean literature values was required.

Simulations of flow through the reactor (0.5 mm i.d., 37.5 cm in length) were performed using different grid densities ($z \times r$): 80×15 and 200×25 . A comparison of the results obtained from the two grids indicated a negligible (less than 0.5%) difference in the bulk fuel temperature and reaction rate calculations. Run times using the 80×15 grid (on a 2.2-GHz Pentium 4 computer) were approximately three days, whereas the 200×25 grid required 17 days to complete. Because this high computational cost results in negligible accuracy gain, all subsequent solutions were calculated using the 80×15 grid. The primary reason for the lengthy run times are the number of iterative calculations that must be executed using SUPERTRAPP when cracked products are accounted for in the fuel mixture. The calculated flow properties using only the parent species were used to converge rapidly to an approximate initial estimation, before transitioning to the more time-consuming chemical model that accounts for cracked products. Using the initial estimate reduced the run time by 12%.

Results and Discussion

The experimental results were used to evaluate the assumptions made in deriving the PPD mechanism. Figure 4 shows measured mass fractions of some selected products, formed by cracking n–decane over the ranges of wall temperatures and flow rates used in the experiment. The products selected for Fig. 4 are representative of different classes of products formed in the experiments. At low n–decane conversions the formation rate of each product is essentially linear (demonstrated by the linear fits). However, at the higher conversions of Fig. 4 (20% and greater), the amount of ethylene exiting the reactor begins to exceed the linear rate observed at lower conversions. The formation rates of all of the (C₁–C₄) light

Table 1 Source terms and transport coefficients appearing in Eqs. (8) and (9)

Φ	Γ^Φ	S^Φ
u	$\mu + \mu_t$	$-\frac{\partial p}{\partial z} + \frac{\partial}{\partial z} \left(\Gamma^u \frac{\partial u}{\partial z} \right) + \frac{\partial}{\partial r} \left(\Gamma^u \frac{\partial v}{\partial z} \right) + \frac{\Gamma^u}{r} \frac{\partial v}{\partial z} + \rho g$
v	$\mu + \mu_t$	$-\frac{\partial p}{\partial r} + \frac{\partial}{\partial z} \left(\Gamma^v \frac{\partial u}{\partial r} \right) + \frac{\partial}{\partial r} \left(\Gamma^v \frac{\partial v}{\partial r} \right) + \frac{\Gamma^v}{r} \frac{\partial v}{\partial r} - 2\Gamma^v \frac{v}{r^2}$
k	$\mu + \frac{\mu_t}{\sigma_k}$	$G - \rho \epsilon$
ϵ	$\mu + \frac{\mu_t}{\sigma_\epsilon}$	$C_1 G \frac{\epsilon}{k} - C_2 \rho \frac{\epsilon^2}{k}$
h	$\frac{\kappa}{c_p} + \frac{\mu_t}{\sigma_h}$	0
Y_i	$\rho D_i + \frac{\mu_t}{\sigma_{Y_i}}$	$\dot{\omega}_i$

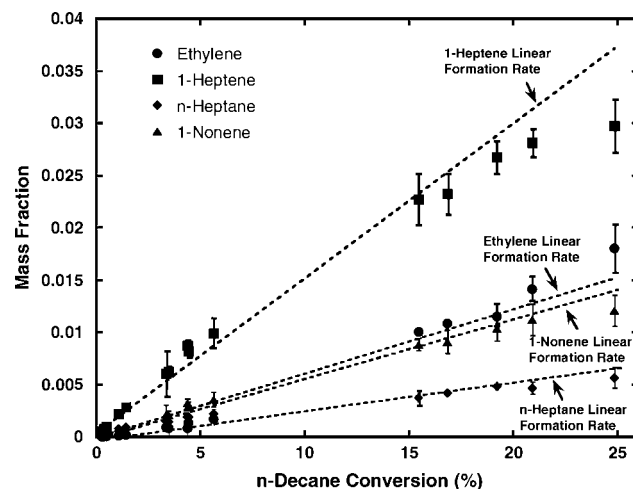


Fig. 4 Measured formation of select cracked n–decane products.

Table 2 Arrhenius rate parameters used in the CFD calculations

Parent fuel	Present models, $P = 3.45$ MPa and $T = 500$ – 600°C		Stewart et al., ²¹ $P = 2.96$ MPa and $T = 440$ – 535°C		Zhou and Crynes, ²² $P = 9.2$ MPa and $T = 250$ – 440°C	
	Activation energy E_a , kcal/mol	A factor A , s ⁻¹	Activation energy E_a , kcal/mol	A factor A , s ⁻¹	Activation energy E_a , kcal/mol	A factor A , s ⁻¹
n–Decane (C ₁₂ H ₂₆)	63	2.1×10^{15}	64 ± 2.4	$1.0 \times 10^{15.9 \pm 1.5}$	—	—
n–Dodecane (C ₁₄ H ₃₀)	65	1.0×10^{16}	—	—	65	3.7×10^{16}

products (measured but not shown in Fig. 4, methane, ethane, 1-propene, n-propane, 1-butene, and n-butane) behave similarly to ethylene. Figure 4 also shows that the outlet mass fractions of the heavier 1-alkene products (1-heptene and 1-nonene) initially form at a linear rate but begin to drop below this rate as more n-decane is converted. The formation rates of all of the higher carbon number 1-alkene products (measured but not shown in Fig. 4, 1-pentene, 1-hexene, 1-octene, and 1-decene) behave similarly to 1-heptene and 1-nonene. At high n-decane conversions, the 1-alkene formation rates drop below the initial linear rate because they undergo secondary cracking reactions. The light products (such as ethylene) increase beyond their initial linear rate as more light products form from these secondary-cracking reactions. As more of these secondary products form, they begin to have a significant influence on the fuel composition. At such conversions, the fuel can no longer be considered mildly cracked. The PPD mechanism is limited to mild-cracking reactions and does not account for secondary reactions. At high conversions, the error induced by secondary reactions becomes unacceptable, and thus, the PPD mechanism is no longer sufficiently accurate. Figure 4 also shows that n-heptane continues to form approximately at a linear rate for every conversion level. The formation rates of all of the other (C_5 – C_9) n-alkane products (measured but not shown in Fig. 4, n-pentane, n-hexane, n-octane, and n-nonane) behave similarly to n-heptane.

A set of experiments in which n-dodecane was cracked (not shown) were performed at the same conditions as the n-decane experiments. Evidence of secondary reactions appears between conversions of 25–30%. This is a slightly higher conversion than where secondary reactions were first observed in the n-decane experiments (20% n-decane conversion).

Figure 5 shows the product mass fraction [Eq. (5)] of two of the cracked n-decane product species (1-hexene and n-hexane) with increasing n-decane conversion (obtained by varying the wall temperature and flow rate). Figure 5 shows that the product mass fractions of both 1-hexene and n-hexane are nearly constant. Figure 5 provides more evidence that the products tend to form in constant proportions with respect to one another. At the highest conversion of Fig. 5, the product mass fraction of 1-hexene begins to diverge from the average value. As observed in Fig. 4, this divergence suggests that secondary reactions are beginning to occur more frequently. Figure 5 only shows two of the products for conciseness. Although not shown, the product mass fractions of all of the major products (n-alkanes and 1-alkenes) were also nearly constant, until the conversion point where secondary reactions begin. This was true for both the n-decane and n-dodecane cracking experiments.

Figures 6 shows the average product mass fractions [Eq. (6)] of each of the major product species formed in the n-decane cracking experiments. The error bars in Fig. 6 represent the standard deviation of each product mass fraction over the entire range of experimental conditions considered. These average product fractions form the basis of the PPD chemical mechanism. The PPD mechanism uses these averaged experimentally derived mass fractions to determine the product composition slate, given a parent fuel conversion [Eq. (7)]. Figure 7 shows the average product mass fractions

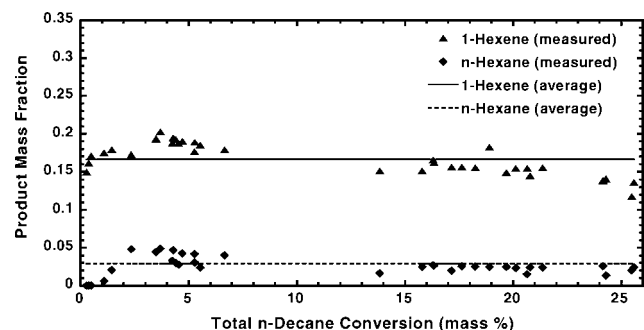


Fig. 5 Example of formation of products in constant ratios (cracked n-decane).

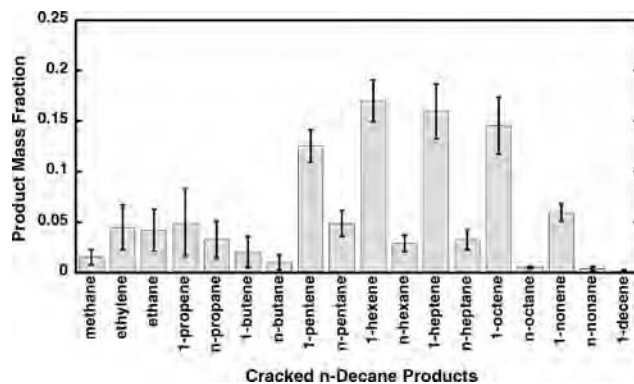


Fig. 6 Product mass fraction distribution of mildly cracked n-decane.

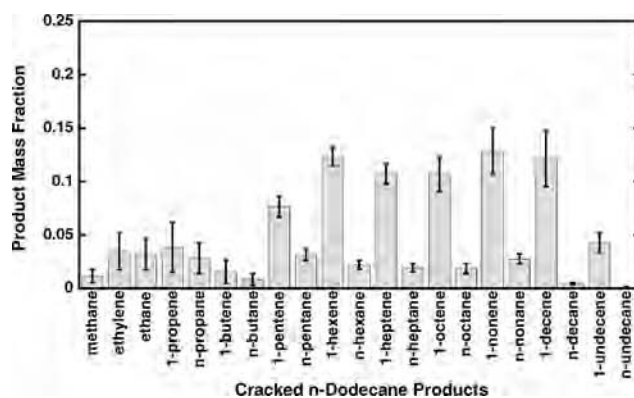


Fig. 7 Product mass fraction distribution of mildly-cracked n-dodecane.

formed in the n-dodecane cracking experiments [Eq. (6)].

The measured outlet bulk mass fraction of n-decane is compared with values predicted by the CFD simulations of Fig. 8. Two sets of calculations are shown in Fig. 8. One employs the PPD mechanism, and the other uses the simple mechanism [Eq. (1)], which assumes that the parent fuel alone contributes to the overall property calculations. Therefore, with respect to the simple mechanism's property calculations, the chemical composition of the parent fuel does not change as the fuel cracks. The three data sets (Figs. 8a–8c) correspond to the three wall temperatures used in the experiments. The error bars on the measurements are standard deviations of replicate runs of each set of conditions. Both the PPD and simple mechanisms use the same first-order reaction rate equation to predict parent fuel degradation [Eq. (3)]. Furthermore, the same Arrhenius rate constants are used in both models (Table 2). Differences between the PPD and simple mechanism results are due to transport property calculations. The PPD mechanism includes cracked products in these calculations and the simple mechanism does not.

Figure 8 shows that the PPD mechanism agrees reasonably well with the experimental data, until an upper conversion limit is reached. In Fig. 8a, the PPD predicted mass fractions diverge above a 20% n-decane conversion. At all other conditions (Figs. 8b–8c), the PPD mechanism predicts an outlet n-decane mass fraction within 3% of the measurement (usually within the measurement error bars at each condition). The PPD predictions diverge at the same conversion levels where secondary reactions were observed in Fig. 4. Secondary cracking is one reason the PPD mechanism results diverge from the measured values at these conditions. A second possible reason is self-inhibition. Fabuss et al.²³ described a decrease in the calculated first-order rate constant for high conversions. They attributed this phenomenon to increasing formations of alkenes that inhibit free-radical reactions. Decreasing the rate constants to account for self-inhibition may result in a better match with the measured data at high conversions. However, determining rate constants as a function of conversion greatly complicates the functionality of the PPD mechanism. Because the PPD mechanism is

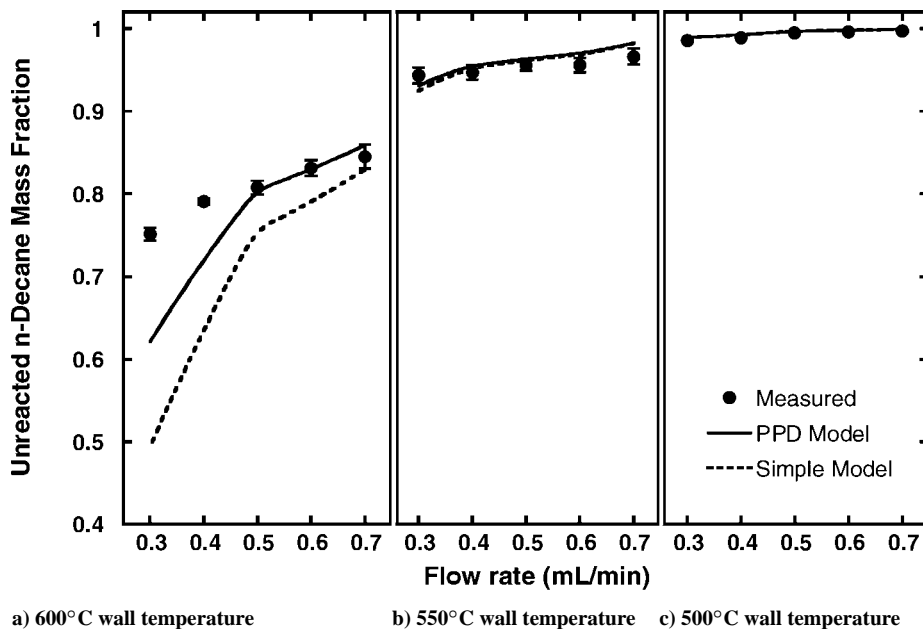


Fig. 8 Comparison of experimental vs calculated *n*-decane degradation for varying steady-state wall temperatures and flow rates.

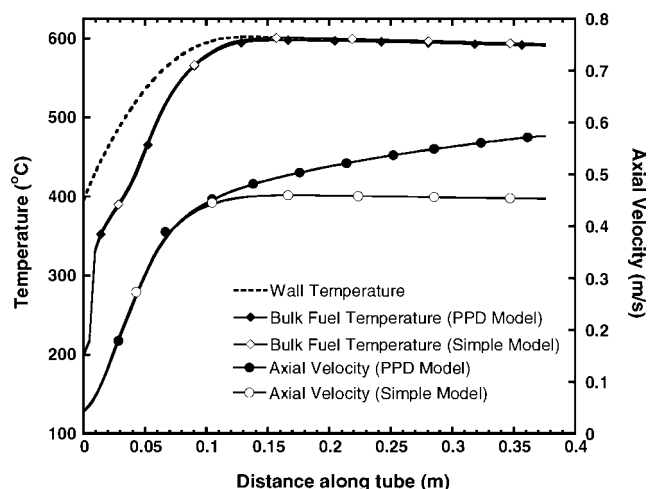


Fig. 9 Wall temperature, bulk fuel temperature, and axial velocity of cracked *n*-decane (0.5 ml/min, 600°C).

already limited by secondary reactions at high conversions (Fig. 4), it would not be advantageous to correct the rate constants to model the self-inhibition phenomenon.

Figure 8a also shows the differences between the PPD and simple mechanism results increase with higher *n*-decane conversion. The PPD mechanism predicts a slower conversion rate than the simple mechanism. As the concentrations of cracked products increase within the fuel mixture, they have a greater influence on the flow properties, whereas the influence of the *n*-decane on the transport properties becomes less dominant. The PPD mechanism predicts a slower conversion rate because it accounts for lighter cracked products as a portion of the fuel mixture. Formation of lighter cracked products produces a less dense fuel mixture, which results in turn in an increased flow velocity (by conservation of mass).

Figure 9 shows the wall temperature and a comparison of the bulk fuel temperature and axial velocity calculated by the PPD and simple mechanisms for one experimental condition. Although there is little difference between the bulk fuel temperature predictions, there is a significant axial velocity difference. After approximately 12 cm along the reactor, the predicted axial velocity of the simple mechanism becomes constant. However, the PPD mechanism predicts a linear rise in velocity. An increased fuel velocity results in a

decreased residence time for the fuel, thus, lowering the conversion rate. Figure 8 shows that by properly accounting for the cracked products, the PPD mechanism is more accurate (over a greater conversion range) than the simple mechanism. Figures 8 and 9 show that the density, flow velocity, and chemistry are coupled and have a profound effect on the conversion rate. Modeling these relationships correctly will be critical in endothermic fuel systems that experience significant flow changes, such as occurs with throttling, flowpath bends, valves, and nozzles. A way to understand the influence of these factors is to model adequately endothermic fuel systems using CFD methods that account for the formation of cracked products in the fuel composition.

The similarity between the fuel temperature predicted by the PPD and simple mechanisms (Fig. 9) implies that the simple mechanism may be sufficient if only the bulk fuel temperature is the desired result. However, the two-dimensional temperature profiles of Figure 10 show that the two mechanisms predict different radial temperature profiles. (The temperature contour scale of Fig. 10 is finer near the outlet to illustrate clearly the differences between the simple and PPD mechanism results.)

Figure 10 shows contour plots comparing the fuel temperature and mass fraction predictions of both the PPD and simple mechanisms for one set of experimental conditions (0.5 ml/min, 600°C). This set of conditions (Fig. 10) corresponds to the highest conversion of *n*-decane before the PPD mechanism diverges (Fig. 9). In Fig. 10, a dashed line axially divides each reactor. Figure 10a shows the PPD mechanism results, whereas Fig. 10b shows the simple mechanism predictions. Figure 10 shows that there is little difference between the two temperature calculations as the fuel is initially heated. Both models predict that the fuel reaches a maximum temperature and then cools as the fuel nears the end of the reactor. A wall temperature drop (near the end of the reactor) was consistently observed for many of the experimental conditions (Figs. 3a–3c). At the conditions of Fig. 10, a wall temperature decrease of 8°C (from a 600°C steady-state wall temperature) was measured near the end of the reactor. Two reasons could account for this: heat loss from the reactor wall to the outside surroundings (despite an insulating cap at the end) and an endothermic fuel reaction that cooled the wall from inside the reactor. The absence of a wall temperature reduction at the higher flow rates (lower residence times, thus, less cracking) in Figs. 3a–3c supports the view that endothermic reactions are the primary source of this cooling phenomenon. Figures 3a–3c would show a wall temperature reduction at every flow rate if insufficient insulation was the primary cause of this cooling. Figure 10 shows

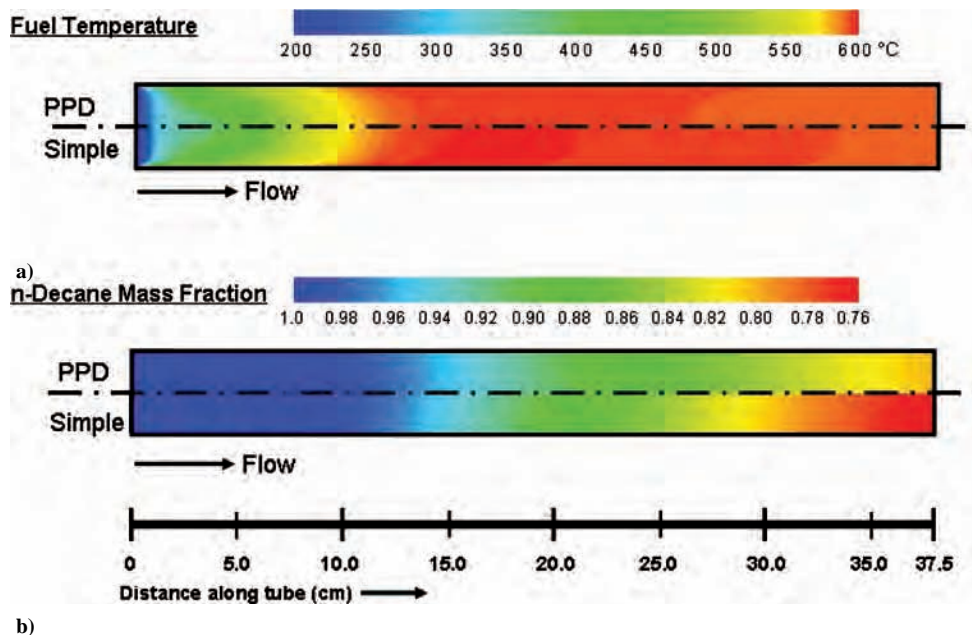


Fig. 10 Fuel temperature and *n*-decane degradation comparison between PPD and simple mechanism calculations; (*n*-decane, 0.5 ml/min, 600°C).

that, after the initial temperature rise, the PPD mechanism predicts a lower fuel temperature than the simple mechanism. Unlike the simple mechanism, the PPD mechanism accounts for enthalpy changes as cracked products form. These enthalpy changes cause the fuel temperature to drop, which is the endothermic effect produced by the thermal cracking reactions. This can be seen in comparing the radial temperature profile near the end of the reactor. The PPD mechanism calculates that the fuel near the center of the reactor cools faster (due to the endotherm) than fuel closer to the wall. The simple mechanism does not simulate enthalpy changes induced by product formation, so that it does not simulate an endotherm. Thus, with the simple mechanism the temperature reduction is due only to the decreasing wall temperature boundary condition (Fig. 3c).

Figure 10 also shows that the simple mechanism calculates a faster *n*-decane conversion rate. For both mechanisms, more conversion occurs close to the wall, where temperature is a maximum and the velocity is a minimum. Temperature or velocity discontinuities in a fuel system, for example, valves and nozzles, will cause changes in the local reaction rate. If mild cracking is desired in the fuel system design, then care must be taken to determine if higher conversions could occur at these discontinuities. Higher conversion rates could lead to deposition, which could impair the flow and possibly lead to catastrophic results. This illustrates the utility of multidimensional CFD models in understanding and designing fuel flow pathways, especially in endothermic fuel systems.

Figure 11 shows a comparison of the measured exit bulk mass fractions of the cracked *n*-decane products to the PPD mechanism results for the same conditions as Fig. 10. Figure 11 shows that most of the product mass is composed of 1-alkenes (between C_5 and C_{10}). The largest differences (over all experimental conditions) between measured and predicted product mass fractions occur for the light molecular weight products (C_1 – C_4). The maximum percent difference is 20% with 1-propene. However, because 1-propene is a very small fraction of the total fuel composition, calculating the percent difference of 1-propene with respect to the total fuel results in a difference of only 0.25%. Such a small difference has little effect on the overall fuel mixture and transport property calculations.

Although all of the products were supercritical while flowing through the reactor, at ambient conditions (where the samples were collected) they undergo a phase change. The light products transitioned into gases, whereas the heavier products condensed into liquids. The gas products were difficult to collect and measure

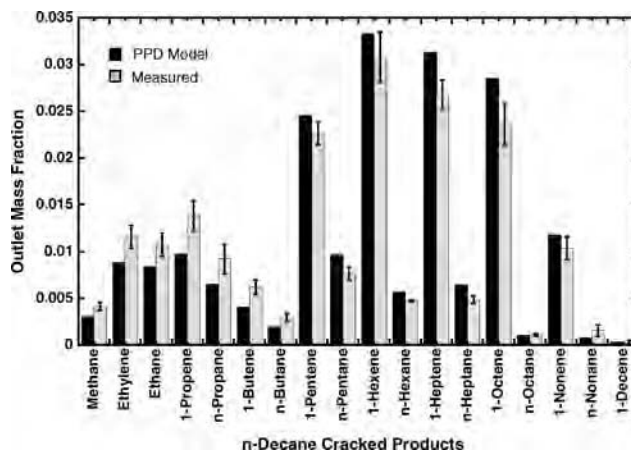


Fig. 11 Comparison of measured and calculated cracked products exiting the reactor; (*n*-decane, 0.5 ml/min, 600°C).

accurately. The largest single source of experimental error, observed through replicate experimental runs, is attributed to measurement of the gas products. Thus, it is not surprising that the largest differences between the measured and predicted products are the light products.

Figures 8–11 show results using *n*-decane; however, Fig. 12 shows the *n*-dodecane results. Figure 12 is a comparison of the experimental and calculated results of the thermal cracking of *n*-dodecane. The pressure, temperature, and flow rate conditions are identical to those in Fig. 8. The PPD and simple mechanism calculations generally match the measured values (within the error bars). In Fig. 12a, the PPD mechanism departs from the measured values near 30% *n*-dodecane conversion. This condition corresponds to the conversions (25–30%) where secondary reactions became evident in the measured data. Figure 12a shows a much larger difference between the PPD and simple mechanism results than in Fig. 8a because *n*-dodecane experiences more conversion into cracked products than *n*-decane. There is more conversion of *n*-dodecane relative to *n*-decane because *n*-dodecane is a longer chain *n*-alkane, which has more bonds that can potentially break to form a larger free-radical pool. Therefore, longer chained *n*-alkanes generally have an increased reaction rate over smaller *n*-alkane chains.²³

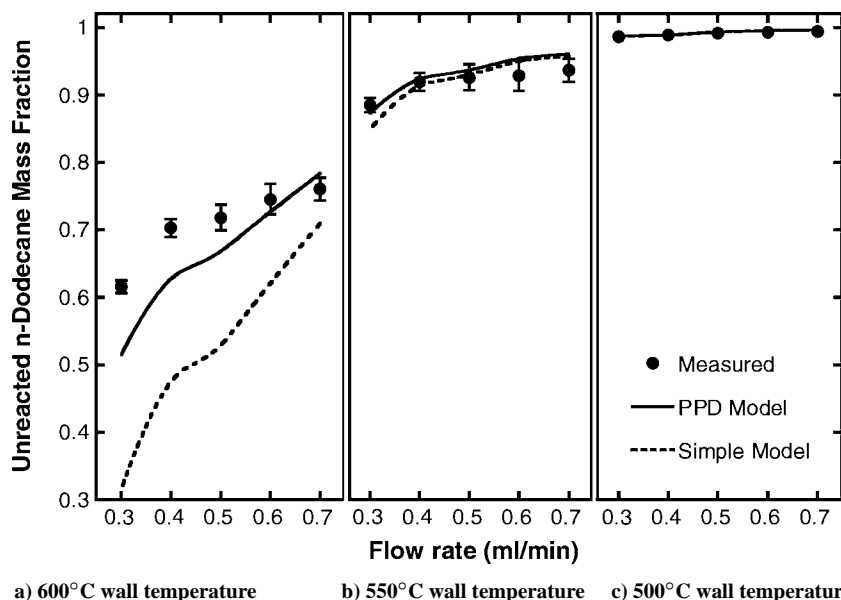


Fig. 12 Comparison of experimental vs calculated n-dodecane degradation for varying steady-state wall temperatures and flow rates.

Conclusions

The use of endothermic fuels is a promising method to expand the temperature limits of gas turbine engines. This computational model can assist in the fundamental understanding of high-temperature fuel flow experiments. The model accounts for property changes due to the formation of mildly cracked products in the fuel mixture. It was experimentally shown that mild cracking of n-alkanes generally form lower carbon number 1-alkenes and n-alkanes in constant proportions to one another. This forms the basis of a global chemical (PPD) mechanism to predict product formation. Thus, the necessity for a complex detailed chemical mechanism to predict product formation is avoided, making this model practical for use in a multi-dimensional CFD model. Comparisons of calculations (using the PPD mechanism) to measurements (involving the cracking of single-component n-alkanes) show that this method has merit. Comparisons of the PPD mechanism with simple mechanisms (often used in past thermal cracking studies) show a marked accuracy improvement in calculating reaction rates and transport properties such as the velocity and density of cracking fuel flows. Furthermore, calculated enthalpy changes due to the formation of cracked products simulate the endotherm produced in these reactions. It is anticipated that this model could serve as a building block to future models involving more complex fuel mixtures and fuel system structures.

Acknowledgments

This work was supported by the Dayton Area Graduate Studies Institute and the U.S. Air Force, Air Force Research Laboratory, Propulsion Directorate, Turbine Engines Division, Fuels Branch, Wright-Patterson Air Force Base, Ohio, under Contract F33615-03-2-2347.

References

- Sobel, D. L., and Spadaccini, L. J., "Hydrocarbon Fuel Cooling Technologies for Advanced Propulsion," *Journal of Engineering for Gas Turbines and Power*, Vol. 119, No. 2, 1997, pp. 344-351.
- Huang, H., Sobel, D. R., and Spadaccini, L. J., "Endothermic Heat-Sink of Hydrocarbon Fuels for Scramjet Cooling," AIAA Paper 2002-3871, July 2002.
- Heinrich, B., Luc-Bouhali, A., Ser, F., and Vigot, C., "Endothermic Liquid Fuels: Some Chemical Considerations on the Cooling Process," AIAA Paper 2001-1785, April 2001.
- De Witt, M. J., and Broadbelt, L. J., "Binary Interactions Between Tetradecane and 4-(1-Naphthylmethyl) Bibenzyl During Low- and High Pressure Pyrolysis," *Energy and Fuels*, Vol. 13, No. 5, 1999, pp. 969-983.
- Nigam, A., and Klein, M. T., "A Mechanism-Oriented Lumping Strategy for Heavy Hydrocarbon Pyrolysis: Imposition of Quantitative Structure-Reactivity Relationships for Pure Components," *Industrial and Engineering Chemistry Research*, Vol. 32, No. 7, 1993, pp. 1297-1303.
- Ranzi, E., Dente, M., Pierucci, S., and Biardi, G., "Initial Product Distributions from Pyrolysis of Normal and Branched Paraffins," *Industrial and*

Engineering Chemistry Fundamentals, Vol. 22, 1983, pp. 132-139.

⁷Glassman, I., *Combustion*, 2nd ed., Academic Press, San Diego, CA, 1987, pp. 360-375.

⁸Ervin, J. S., Ward, T. A., Williams, T. F., and Bento, J., "Surface Deposition within Treated and Untreated Stainless-Steel Reactors Resulting from Thermal-Oxidative and Pyrolytic Degradation of Jet Fuel," *Energy and Fuels*, Vol. 17, No. 3, 2003, pp. 577-586.

⁹Lindstedt, R. P., and Maurice, L. Q., "Detailed Chemical-Kinetic Model for Aviation Fuels," *Journal of Propulsion and Power*, Vol. 16, No. 2, 2000, pp. 187-195.

¹⁰Ligurias, D. K., and Allen, D. T., "Comparison of Lumped and Molecular Modeling of Hydrolysis," *Industrial and Engineering Chemistry Research*, Vol. 31, No. 1, 1992, pp. 45-53.

¹¹LinhBao, T., and Chen, L. D., "Heat Transfer Calculation of an Endothermic Fuel at Supercritical Conditions," AIAA Paper 98-3762, July 1998.

¹²Stewart, J. F., "Supercritical Pyrolysis of the Endothermic Fuels Methylcyclohexane, Decalin, and Tetralin," Ph.D. Dissertation, Dept. of Mechanical and Aerospace Engineering, Princeton Univ., Princeton, NJ, June 1999.

¹³Goel, P., and Boehman, A. L., "Numerical Simulation of Jet Fuel Degradation in Flow Reactors," *Energy and Fuels*, Vol. 14, No. 5, 2000, pp. 953-962.

¹⁴Schiesser, W. E., *The Numerical Method of Lines: Integration of Partial Differential Equations*, Academic Press, New York, 1991.

¹⁵Sheu, J. C., Zhou, N., and Krishnan, A., "Thermal Cracking of Norpar-13 Fuel under near-critical and Supercritical Conditions," AIAA Paper 98-3758, July 1998.

¹⁶Kossiakoff, A., and Rice, F. O., "Thermal Decomposition of Hydrocarbons, Resonance Stabilization and Isomerization of Free Radicals," *Journal of the American Chemical Society*, Vol. 65, No. 4, 1943, pp. 590-595.

¹⁷Katta, V. R., and Roquemore, W. M., "Numerical Method for Simulating the Fluid-Dynamic and Heat Transfer Changes in a Jet Engine Injector Feed-Arm due to Fouling," *Journal of Thermophysics and Heat Transfer*, Vol. 7, No. 4, 1993, pp. 651-660.

¹⁸Lauder, B. E., and Spalding, D. B., "The Numerical Computation of Turbulent Flows," *Computer Methods in Applied Mechanics and Engineering*, Vol. 3, No. 2, 1974, pp. 269-289.

¹⁹Ely, J. F., and Huber, M. L., NIST Standard Reference Database 4—NIST Thermophysical Properties of Hydrocarbon Mixtures, Ver. 3.0, National Inst. of Standards, Gaithersburg, MD, Oct. 1999.

²⁰Peng, D., and Robinson, D. B., "A New Two-Constant Equation of State," *Industrial and Engineering Chemistry Fundamentals*, Vol. 15, No. 1, 1976, pp. 59-64.

²¹Stewart, J., Brezinsky, K., and Glassman, I., "Supercritical Pyrolysis of Decalin, Tetralin, and n-decane at 700-800 K. Product Distribution and Reaction Mechanism," *Combustion Science and Technology*, Vol. 136, April 1998, pp. 373-390.

²²Zhou, P., and Crynes, B., "Thermolytic Reactions of Dodecane," *Industrial and Engineering Chemistry Process Design and Development*, Vol. 25, 1986, pp. 508-514.

²³Fabuss, B. M., Smith, J. O., and Satterfield, C. N., "Thermal Cracking of Pure Saturated Hydrocarbons," *Advances in Petroleum Chemistry and Refining*, Vol. 9, 1964, pp. 157-201.

INTENTIONALLY LEFT BLANK

APPENDIX Z

Simulation of the Effect of Metal-Surface Catalysis on the Thermal Oxidation of Jet Fuel

INTENTIONALLY LEFT BLANK

Simulation of the Effect of Metal-Surface Catalysis on the Thermal Oxidation of Jet Fuel

T. Dounghip,[‡] J. S. Ervin,^{*,†,‡} S. Zabarnick,^{†,‡} and T. F. Williams[†]

University of Dayton Research Institute, 300 College Park, Dayton, Ohio 45469-0116, and
Department of Mechanical and Aeronautical Engineering, University of Dayton,
300 College Park, Dayton, Ohio 45469-0210

Received April 24, 2003. Revised Manuscript Received July 28, 2003

Jet fuel is used for cooling in high-performance aircraft. Unfortunately, jet fuel reacts with dissolved O₂ in the presence of heat to form unwanted surface deposits. Computational fluid dynamics that incorporates pseudo-detailed chemical kinetics with a wall reaction is used to simulate the effects of treated and untreated stainless-steel surfaces on the liquid-phase thermal oxidation of jet fuel in both isothermal and nonisothermal heated-tube experiments. A hydroperoxide decomposition reaction is used to represent the surface chemistry. The effects of a treated surface on thermal oxidation were modeled by adjusting the activation energy of the surface reaction. Nonisothermal heated-tube experiments that measure dissolved O₂ are performed here, whereas isothermal flow experiments are performed elsewhere. Simulations of dissolved O₂ consumption in the presence of treated and untreated surfaces, which include the wall reaction, agree reasonably well with the dissolved O₂ measurements.

Introduction

Jet fuel is used in military aircraft for cooling purposes before it is burned in the combustor. As fuel flows through the fuel system, an autoxidation chain that involves heteroatomic fuel species proceeds, which results in the reaction of dissolved O₂ and the formation of oxidized products.¹ Oxidized products may subsequently react to form surface deposits that reduce fuel flow and degrade heat-transfer effectiveness. Moreover, catastrophic engine failure could occur if these deposits impair the operation of close-tolerance valves. Thus, it is important to study liquid-phase fuel oxidation and the involved surface reactions. Computational fluid dynamics, together with chemical kinetics, can show aircraft engine designers how fluid dynamics and heat transfer influence fuel oxidation and the accompanying surface reactions.

Three different types of chemical kinetic mechanisms have been used to simulate the thermal oxidation of jet fuel: global mechanisms, detailed mechanisms, and pseudo-detailed mechanisms.^{1,2} Generally, global kinetic mechanisms use one reaction to represent the thermal oxidation of jet fuel:



Although the thermal oxidation of jet fuel actually involves several reactions, the basic assumption of eq 1 is that the overall reaction of a mixture of compounds can be represented by one rate equation. This rate

equation consists of a rate constant multiplied by concentrations that have the same form as those in eq 2:

$$-\frac{d[\text{O}_2]}{dt} = k[\text{RH}][\text{O}_2]^n \quad (2)$$

In eq 2, the fuel is represented by a single compound RH. The rate constant k is represented by the product of an Arrhenius factor A and an activation-energy term. In addition, the order of the reaction is given by n . Because individual fuel samples are different, the factor A and the activation energy may have to be determined for different fuel samples.

Although a global mechanism consists of relatively few reactions, a detailed kinetics mechanism may consist of hundreds of reactions to represent the thermal oxidation of jet fuel. Moreover, a detailed kinetics mechanism would include a multitude of species that exist within the fuel. These species and their concentrations will change for each fuel sample. Thus, a detailed mechanism is not practical for a study of the thermal oxidation of jet fuel that also uses computational fluid dynamics. An alternative approach that has been used to simulate the thermal oxidation of jet fuel is the use of a pseudo-detailed chemical kinetics mechanism. Pseudo-detailed chemistry represents the dominant chemistry and the behavior of classes of species within the fuel.^{1–4} Pseudo-detailed chemistry is midway in complexity between global and detailed kinetics mechanisms and was previously used with reasonable success in simulating the thermal oxidation of jet fuel.

Because of their complexity, surface reactions have received little attention in previous computational studies of the liquid-phase thermal oxidation of jet fuel.^{1–4}

* Author to whom correspondence should be addressed. E-mail: jamie.ervin@notes.udayton.edu.

[†] University of Dayton Research Institute.

[‡] Department of Mechanical and Aeronautical Engineering, University of Dayton.

(1) Zabarnick, S. *Energy Fuels* 1998, 12, 547–553.

(2) Ervin, J. S.; Zabarnick, S.; Williams, T. F. *J. Energy Res. Technol.* 2000, 122, 229–238.

(3) Zabarnick, S. *Ind. Eng. Chem. Res.* 1993, 32, 1012–1017.

(4) Ervin, J. S.; Zabarnick, S. *Energy Fuels* 1998, 12, 344–352.

Table 1. Present Pseudo-Detailed Chemical Kinetic Mechanism

number	reaction	Arrhenius factor <i>A</i> (mol, L, s)	activation energy (kcal/mol)
Bulk Reaction			
1	I → R•	1 × 10 ⁻⁷	0
2	R• + O ₂ → RO ₂ •	3 × 10 ⁹	0
3	RO ₂ • + RH → ROOH + R•	3 × 10 ⁹	10
4	RO ₂ • + RO ₂ • → termination	3 × 10 ⁹	0
5	RO ₂ • + AH → ROOH + A•	3 × 10 ⁹	5
6	AO ₂ • + RH → AO ₂ H + R•	3 × 10 ⁵	10
7	A• + O ₂ → AO ₂ •	3 × 10 ⁹	0
8	AO ₂ • + AH → AO ₂ H + A•	3 × 10 ⁹	6
9	AO ₂ • + AO ₂ • → products	3 × 10 ⁹	0
10	R• + R• → R ₂	3 × 10 ⁹	0
11	ROOH → RO• + •OH	1 × 10 ¹⁵	42
12	RO• + RH → ROH + R•	3 × 10 ⁹	10
13	RO• → R _{prime} • + carbonyl	1 × 10 ¹⁶	15
14	•OH + RH → H ₂ O + R•	3 × 10 ⁹	10
15	RO• + RO• → termination	3 × 10 ⁹	0
16	R _{prime} • + RH → alkane + R•	3 × 10 ⁹	10
17	ROOH + SH → products	3 × 10 ⁹	16
Wall Reaction			
18	ROOH → RO• + •OH	1 × 10 ⁹	37–42

Here, we attempt to include the effects of surface catalysis on autoxidation. Isothermal experimental studies of the surface effects on the thermal oxidation of jet fuel have shown that the use of tubing with a surface treatment can delay dissolved O₂ consumption, relative to that of stainless steel.⁵ This surface treatment involved the chemical vapor deposition of a proprietary silica-based layer (Silcosteel tubing).⁶ The slower oxidation rate suggests that a surface that has been passivated by a surface treatment with an inert coating could delay or significantly reduce surface deposition. It is desirable to simulate the thermal oxidation of jet fuel using pseudo-detailed chemical kinetics and surface reactivity by including a wall reaction in the computational model. A goal of this work is to investigate if the surface-catalyzed decomposition of fuel hydroperoxides can be used to simulate the influence of surface type on the thermal oxidation of jet fuel. Studying the effects of a metal surface or a relatively inert surface on the oxidation of jet fuel is important because such research will ultimately assist the understanding of the surface deposition of jet fuel.

Simulation Methodology

Pseudo-detailed Chemical Kinetics. A pseudo-detailed chemical kinetics mechanism used to simulate the liquid-phase oxidation of jet fuel was first proposed by Zabarnick.³ Table 1 shows the present chemical kinetics mechanism, which consists of 17 bulk reactions and 1 wall reaction. The rate constant (*k*) for each reaction can be represented in Arrhenius form:

$$k = A \exp\left(-\frac{E_a}{RT}\right) \quad (3)$$

In eq 3, *A* is the pre-exponential factor, *E_a* the activation energy, *R* the universal gas constant, and *T* the absolute temperature.

Reactions 1–4 and reaction 10 of Table 1 comprise a simple chain mechanism that involves the formation of

free radicals that are due to hydrocarbon fuel oxidation. In reaction 1, species I is used to initiate the complex process that forms the free radical R• at a low reaction rate. Reaction 1 becomes negligible relative to other reactions after the chain begins. The single compound RH represents the bulk fuel and is assumed to have the chemical properties of a straight-chain alkane (such as *n*-dodecane). Reactions 5–9 in the table represent the antioxidant chemistry associated with the interception of an alkylperoxy radical by species AH. Species AH represents an antioxidant, such as butylated hydroxytoluene (BHT), that intercepts peroxy free radicals.

Reactions 11–16 in Table 1 represent alkylhydroperoxide decomposition chemistry, which occurs at a sufficiently high temperature and has an important role in accelerated O₂ consumption in the bulk fuel. Reaction 17 represents the reaction of fuel hydroperoxides with the hydroperoxide decomposing species SH. SH is believed to include sulfur species (sulfides and disulfides, for example) that decompose fuel hydroperoxides into nonradical products. Previous simulations including only bulk reactions have shown that reaction 17 (from Table 1) can slow the oxidation rate when fuel hydroperoxides in the bulk fuel react with the SH species.⁴ In addition, previous simulations have demonstrated that AH and SH can act synergistically to slow the oxidation rate.^{1,4} For simplicity, the pseudo-detailed chemical kinetics mechanism uses the concentration of antioxidants AH and SH to differentiate fuel samples.

Wall Reaction. Using a modified version of the pseudo-detailed chemical kinetics mechanism, Ervin and Zabarnick simulated the thermal oxidation of jet fuel that was flowing within stainless-steel tubes with reasonable success.⁴ In preliminary efforts during the current study, hydrocarbon oxidation on a passivated surface was simulated using the activation energy for the unimolecular hydroperoxide decomposition reaction assumed to occur in the bulk fuel. Unfortunately, agreement between experiment and simulation could not be obtained. In numerical simulations of the effects of different surfaces on the thermal oxidation of jet fuel, the use of surface reactions, rather than the arbitrary

(5) Jones, E. G.; Balster, L. M.; Balster, W. J. *Energy Fuels* **1996**, *10*, 813–836.

(6) Silcosteel tubing, Restek Corp., Bellefonte, PA.

modification of bulk reactions, is believed to be more representative of the actual chemistry.

Simulations of reactions between a gas-phase species and a metal surface have commonly been performed through the use of Langmuir–Hinshelwood mechanisms, which have been reported to provide reasonable descriptions of the surface chemistry.^{7–12} These mechanisms consist of three types of reactions: the adsorption of molecules, the reaction involving adsorbed molecules (catalytic reaction), and the desorption of adsorbed molecules. A variable number of site species on the active surface is required with their use. Thus, the physical and chemical properties of the site species on the active surface, including their interactions with species in the fluid, are usually known.^{7–12} However, this is not the case for reactions between fuel hydroperoxides, which are known to have an important role in thermal oxidation, and the surface species of stainless-steel tubing. With the stainless-steel tubes used in the present heated-tube experiments, the active site species and their population are unknown. Although it is agreed that active metal ions (such as Fe, V, Mn, Ni, and Cu) that comprise the surface have an important role in the catalysis of fuel hydroperoxide decomposition, little is known about the actual reactions between fuel hydroperoxides and site species on metal surfaces.¹² Moreover, adsorption and desorption processes on a real surface are extremely difficult, if not impossible, to model in detail in a computational fluid dynamics simulation.^{10,11}

The present work does not consider the actual elementary surface reactions, which are unknown for the stainless steel and treated (inert) surfaces used in this study. Instead, for simplicity, the complex surface reactions are represented by the single reaction



This hydroperoxide decomposition reaction is assumed to be catalyzed by an active surface and have a lower activation energy than the corresponding reaction in the bulk fuel. As a result, the rate of reaction of fuel hydroperoxide decomposition on the surface may be higher than the corresponding reactions in the bulk.^{5,13,14} In addition, the reactions between fuel hydroperoxides and the species that comprise the metal surfaces produce the free-radical species, RO^\bullet and $\bullet\text{OH}$, which diffuse into the bulk liquid and react further, increasing the local free-radical pool.^{5,13,14}

In the present study, a wall reaction (reaction 18, Table 1) that represents unimolecular alkylhydroper-

oxide decomposition is appended to the pseudo-detailed chemical kinetics mechanism of Ervin and Zabarnick.⁴ The rate equation of the hydroperoxide decomposition reaction at the wall is given here as

$$-\frac{d[\text{ROOH}]}{dt} = A \exp\left(-\frac{E_a}{RT}\right) [\text{ROOH}]^\alpha \quad (5)$$

In eq 5, α is the order of reaction for the hydroperoxide decomposition. In detailed studies of simple catalytic decomposition reactions, the order of the reaction is determined from the overall mechanism of the adsorption–surface reaction–desorption process.^{10,11} In this study, we do not have knowledge of these surface processes; therefore, the value of α was adjusted to study its influence on fuel oxidation.

The choice of the activation energy in eq 5 is used to represent the effects of a stainless-steel or passive surface on the thermal oxidation of jet fuel that is flowing within a heated tube. Generally, the activation energy of a surface reaction is less than that of the corresponding bulk reaction.^{7,8} However, for simplicity, the activation energy in eq 5 for the passive surface is selected to be 42 kcal/mol and is equal to that of the corresponding bulk hydroperoxide decomposition reaction.¹ Thus, flowing experiments that use a treated stainless-steel surface and a surrogate fuel can be performed to determine α and A for use in eq 5. In our approach, we assume that these values of α and A are equally valid for a stainless-steel surface. Although the E_a value of the fuel hydroperoxide decomposition reaction for a stainless-steel surface is unknown, it must be less than the E_a value of the more-passive Silcosteel surface. Experiments were performed to determine reasonable values of E_a for a stainless-steel surface, and the selection of E_a for stainless-steel surfaces is described later in this paper.

Calibration of the Mechanism. In previous work, a “calibration” of the kinetics mechanism was performed by adjusting (within acceptable kinetics limits) the pre-exponential factors and activation energy of reactions 3 and 11 (from Table 1) until the chemistry model reasonably represented the thermal oxidation of a hydrotreated fuel on a stainless-steel surface.⁴ However, the hydrotreated fuel may likely have contained small concentrations of naturally occurring antioxidants that were not taken into consideration. It is important to make the mechanism independent of the initial antioxidant concentration and reduce the influence of the surface material via the use of an inert surface. In the present work, a “calibration” is performed using computational fluid dynamics, together with the pseudo-detailed chemical kinetics mechanism, by simulating previous measurements of dissolved O_2 consumption using treated tubes (Silcosteel, 2.16-mm inner diameter (ID) \times 3.18-mm outer diameter (OD) and a heated length of 0.813 m) under isothermal flow conditions (wall temperature of 185 °C).^{15,16} In these experiments, the average residence time of the fuel (Exxsol D110, from Exxon–Mobil) in the heated tube was varied by adjusting the flow rate. Exxsol D110 is a hydrocarbon

(7) Masel, R. I. *Principle of Adsorption and Reaction on Solid Surfaces*; Wiley: New York, 1996.

(8) Anderson, A. W. *Physical Chemistry of Surfaces*; Wiley: New York, 1997.

(9) Myers D. *Surfaces Interface and Colloids, Principle and Application*; Wiley: New York, 1999.

(10) Coltrin, M. E.; Kee, R. J.; Rupley, F. M.; Meeks, E. *Surface Chemkin–III: A Fortran Package for Analyzing Heterogeneous Chemical Kinetics at a Solid–Surface–Gas–Phase Interface*, Technical Report No. SAND96–8217, Sandia National Laboratory, Albuquerque, NM, 1996.

(11) Stoltze, P. *Prog. Surf. Sci.* **2000**, *65*, 65–150.

(12) Hiatt, R. *J. Org. Chem.* **1968**, *33*, 1416–1441.

(13) Jones, E. G.; Balster, W. J.; Pickard, J. M. *J. Eng. Gas Turbines Power* **1996**, *118*, 286–291.

(14) Jones, E. G.; Balster, W. J.; Rubey, W. A. *Prepr. Am. Chem. Soc., Div. Pet. Chem.* **1995**, *40*, 655–659.

(15) Jones, E. G.; Balster, L. M. *Energy Fuels* **2000**, *14*, 640–645.

(16) *Handbook of Aviation Fuels Properties*; Coordinating Research Council: Atlanta, GA, 1983; pp 22–34.

Table 2. Source Term and Transport Coefficients Appearing in eq 7

Φ	Γ^Φ	S^Φ
u	$\mu + \mu_t$	$-(\partial P/\partial z) + (\partial/\partial z)[\Gamma^u(\partial u/\partial z)] + (\partial/\partial r)[\Gamma^u(\partial v/\partial z)] + (\Gamma^u/r)(\partial v/\partial z) + \rho g$
v	$\mu + \mu_t$	$-(\partial P/\partial r) + (\partial/\partial z)[\Gamma^v(\partial u/\partial r)] + (\partial/\partial r)[\Gamma^v(\partial v/\partial r)] + (\Gamma^v/r)(\partial v/\partial r) + 2\Gamma^v(v/r^2)$
k	$\mu + (\mu_t/\sigma_k)$	low-Reynolds $k-\epsilon$, $G - \rho(\epsilon + D)$ standard $k-\epsilon$, $G - \rho\epsilon$
ϵ	$\mu + (\mu_t/\sigma_\epsilon)$	low-Reynolds $k-\epsilon$, $C_{\epsilon_1}f_1(G\epsilon/k) - C_{\epsilon_2}f_2\rho(\epsilon^2/k) + E$ standard $k-\epsilon$, $C_1G(\epsilon/k) - C_2\rho(\epsilon^2/k)$
h	$(k/c_p) + (\mu_t/\sigma_h)$	0
Y_i	$\rho D_i + (\mu_t/\sigma_{Y_i})$	$\dot{\omega}_i$

^a $G = \mu_t[2((\partial u/\partial z)^2 + (\partial v/\partial r)^2 + (v/r)^2) + ((\partial v/\partial z) + (\partial u/\partial r))^2]$; $f_1 = 1.0$; $f_2 = 1 - 0.22 \exp[-(\text{Re}/6)^2]$; $E = -2v(\epsilon/\gamma^2) \exp(-0.5\gamma^+)$; $D = 2vk/\gamma^2$; $C_1 = 1.44$; $C_2 = 1.92$; $C_{\epsilon_1} = 1.35$; and $C_{\epsilon_2} = 1.8$.

solvent that is a combination of ~50 wt % paraffins, ~50 wt % cycloparaffin, and <1 wt % aromatics.¹⁵ It contains little, if any, antioxidants and, thus, oxidizes very rapidly.¹⁵ Moreover, Exxsol D110 has properties (density and viscosity, for example) that are similar to those of Jet A-1 and Jet A fuels.^{15,16}

For reaction 1 (from Table 1), a pre-exponential factor of $1 \times 10^{-7} \text{ s}^{-1}$ is selected for the representation of free-radical initiations that occur within Exxsol D110 in the current simulations. The use of this pre-exponential factor is reasonable, because it is small enough to initiate the autoxidation chain but produces a negligible production of R^{*} radicals after the chain begins. Except for reactions 3 and 11 (from Table 1), the pre-exponential factors and activation energies of the bulk reactions are the same as those used in our previous computational fluid dynamics simulations.⁴ With regard to reaction 11 from Table 1, the pre-exponential factor and activation energy originally used by Zabarnick to represent homogeneous ROOH decomposition are retained.³ Thus, to calibrate the mechanism, one rate parameter is adjusted within well-defined bounds. The activation energy of reaction 3 (from Table 1) can be in the range of 8–14 kcal/mol, and a value of 10 kcal/mol is selected, rather than that used previously (12 kcal/mol).^{1,4} In preliminary simulations, 10 kcal/mol was determined to represent the oxidation measurements better.

The order of the surface reaction influences the oxidation rate of Exxsol D110. Therefore, it is important to consider the effects of varying the order of the surface reaction on the thermal oxidation of Exxsol D110. When the order of the surface reaction is unity ($\alpha = 1$), the predicted oxidation rate of Exxsol D110 is slower than the measured oxidation rate. When α is decreased to 0.8, the dissolved O₂ is consumed more rapidly, and the predicted oxidation rates agree well with the measured rates. Decreasing α below unity increases the free-radical species concentration on the wall at a greater rate than when α is unity, because the ROOH concentration is a fractional value here. When α is decreased to a value below 0.8, the simulated oxidation rate is too rapid, and the simulated dissolved O₂ is completely consumed before the measured value. A pre-exponential factor of $1 \times 10^9 \text{ s}^{-1}$ was observed to provide the best agreement between simulation and measurement of the dissolved O₂ consumption in Exxsol D110. This value for A lies within the range of reported values for pre-exponential factors of metal surfaces (10^3 – 10^{12} s^{-1}).^{7,12} The aforementioned values of A and α are used in all the simulations that follow. In addition, it is assumed, for simplicity, that the activation energy of the surface

reaction is the same for all stainless steels considered (SS316 and SS304).

Computational Fluid Dynamics Code. To understand the effects of temperature, flow, and surface material on thermal oxidation, a commercially available computational fluid dynamics code (CFDACE) was used to simulate the flow and oxidative chemistry within a heated tube.¹⁷ The fuel motion inside the tube was assumed to be axisymmetric and steady. To simulate the fuel chemistry within the heated tubes, the species, temperature, and velocity distributions were obtained by finite volume solution of the species, enthalpy, Navier–Stokes, and turbulent energy equations. The properties of the fuel (density, viscosity, thermal conductivity, specific heat, and enthalpy) are dependent on the fuel temperature. The governing equations written for a cylindrical (z, r) coordinate system are

$$\frac{\partial(\rho u)}{\partial z} + \frac{\partial(\rho v)}{\partial r} + \frac{\rho v}{r} = 0 \quad (6)$$

$$\frac{\partial(\rho u \Phi)}{\partial z} + \frac{\partial(\rho v \Phi)}{\partial r} = \frac{\partial}{\partial z} \left(\Gamma^\Phi \frac{\partial \Phi}{\partial z} \right) + \frac{\partial}{\partial r} \left(\Gamma^\Phi \frac{\partial \Phi}{\partial r} \right) - \frac{\rho v \Phi}{r} + \frac{\Gamma^\Phi}{r} \frac{\partial \Phi}{\partial r} + S^\Phi \quad (7)$$

Equation 6 is the continuity equation, and eq 7 represents the momentum, species, turbulent energy ($k-\epsilon$), or energy equation, depending on the variable that is represented by Φ . Convective terms are represented by a third-order accurate upwind scheme, and a version of the SIMPLC (Semi-Implicit Method for Pressure-Linked Equations Consistent) algorithm is used in the solution procedure.¹⁷ Table 2 lists the transport coefficients, Γ^Φ , and the source terms, S^Φ , of the governing equations. For upward nonisothermal flow in a vertical tube, buoyancy forces are included in the simulations, and the gravity vector is in the opposite direction of the flow.

For the development of a thermal oxidative model, it is important to simulate the fluid dynamics and chemistry for different fuels and a range of flow and thermal conditions. Table 3 describes three experiments that measure dissolved O₂ consumption over a range of flow rates (residence times) and are used for comparison with numerical simulations. In research that has been performed elsewhere, Experiment I used isothermal (185 °C) laminar conditions (Reynolds numbers varied, from 40 at the inlet to 380 at the tube exit) within a heated tube (2.16-mm ID \times 3.18-mm OD, heated length of 0.813

(17) CFD-ACE Theory Manual Version 5.0; CFD Research Corporation: Huntsville, AL, 1998.

Table 3. Experiments Used for Simulations

experiment	Experiment I. isothermal flowing test rig ^a	Experiment II. nonisothermal horizontal flow rig ^b	Experiment III. nonisothermal vertical flow rig ^c
fuel	Jet A-1 (F2747), Jet A (F3219), Exxsol D110	Jet A-1 (F2747)	Jet A (F3219)
flow direction	horizontal	horizontal	vertical upward
surface	treated or untreated (SS304)	untreated (SS316)	treated or untreated (SS316)
wall temperature	185 °C	varies along tube length	varies along tube length
bulk exit temperature	185 °C	150–300 °C (varies with wall temperature profile)	150–225 °C (varies with wall temperature profile)
inlet flow rate	1–40 mL/min	16 mL/min	20 mL/min
pressure	2.3 MPa	2.48 MPa	4.5 MPa
inlet Reynolds number	20–80	90–150	120–180
exit Reynolds number	380–450	1100–2500	1200–2800
residence time	0.5–3 min	7 s	11 s

^a From refs 5, 15, and 18. ^b From ref 4. ^c From current experiments.

Table 4. Characteristics of Jet A-1 (F2747) and Jet A (F3219) Fuels

characteristic	Fuel Sample	
	Jet A-1 (F2747)	Jet A (F3219)
JFTOT breakpoint	332 °C (629.6 °F)	285 °C (545 °F)
sulfur content, total	0.004 wt %	0.0321 wt %
aromatics content	19 vol %	16.6 vol %
copper content	<5 ppb	<5 ± 5 ppb
iron content	N/A	<10 ± 5 ppb
zinc content	18 ppb	<10 ± 5 ppb
specific gravity at 60 °F	0.809	0.8109

m).^{5,15,18} The interior surface of the tube either was stainless steel (SS304) or was treated with a passive layer (Silcosteel). Because of its relatively simple flow conditions, Experiment I was also used to “calibrate” the current mechanism. Experiment II from our previous work used a horizontal tube with an imposed wall temperature profile.⁴ In Experiment II, the surface that was in contact with the fuel was stainless steel (SS316), and the horizontal flow transitioned from laminar to turbulent flow (Reynolds numbers varied from 90 at the inlet to 2500 at the tube exit). In the third experiment performed in the present study, the wall temperature profile was imposed on treated (Silcosteel) or untreated (SS316) tubes. The fuel flowed vertically upward and, thus, was assisted by buoyancy forces. As in Experiment II, there was a transition from laminar to turbulent flow (Reynolds number varied, from 120 at the inlet to 2800 at the tube exit).

For a numerical simulation to be useful, it is important to show that different fuel samples can be used. Table 4 lists characteristics of the Jet A-1 (F2747) and Jet A (F3219) fuels, which are the fuel samples that have been used in addition to Exxsol D110. The Jet A-1 (F2747) sample was hydrotreated and, thus, had a lower concentration of antioxidants than the Jet A (F3219) sample. In the current work, the thermal properties (density, viscosity, thermal conductivity, specific heat, and enthalpy) of JP-8 and Jet A are assumed to be identical and reasonably represent the properties of Exxsol D110 in the simulations.¹⁶

For the vertically upward flow of Experiment III, when the Reynolds number is >2000, a low-Reynolds-number $k-\epsilon$ turbulence model is applied in the computation.¹⁹ The low-Reynolds-number $k-\epsilon$ model used in the turbulent simulations allows the integration of the momentum and the $k-\epsilon$ equation from the tube center

to the wall. Moreover, this turbulence model includes the effects of molecular viscosity in the near-surface regions, which is important for the study of surface reactions at the wall of the heated tube. For the horizontal flow of Experiment II, the standard $k-\epsilon$ turbulence model was used when the Reynolds number was >2000. In previous work, the use of the standard $k-\epsilon$ turbulence model resulted in simulations of the fuel temperature and dissolved O₂ consumption that captured the early transition from laminar to turbulent flow and agreed well with measurements.⁴ Values of the constants used in the model of turbulent species transport are listed in the nomenclature. Wall temperatures for the nonisothermal conditions were imposed using polynomial fits of the experimental thermocouple measurements. The inlet velocity and temperature profiles were assumed to be uniform for simplicity, and the inlet temperature was assumed to be 20 °C.

Figure 1 shows the axisymmetric computational grid used in the present work. The grid density used in the simulations was 180 (axial cells) × 15 (radial cells) for the isothermal experiments (Experiment I), 90 (axial cells) × 15 (radial cells) for horizontal flow conditions (Experiment II), and 200 (axial cells) × 15 (radial cells) for vertically upward flow (Experiment III). Further grid refinement resulted in negligible changes in the solutions. The computational grid is clustered near the wall, and the first cell is located at a y^+ distance of <5. In this work, the deposition process itself is not simulated. The surface deposits are thin here; therefore, they are assumed to have a negligible influence on heat transfer and flow.

Figure 2 shows the grid used in the calculation at the surface boundaries. The rate equation that represents the wall reaction (hydroperoxide decomposition, reaction 18 from Table 1) is written for finite areas on the wall boundary. The results obtained through the use of the rate equation on the wall boundary are then set as the wall boundary condition for the next iterative calculation that involves the bulk reactions. When the global error residuals were reduced below 4 orders of magnitude from their maximum values, the solution was considered to be converged.

Table 5 shows initial concentrations of species used in the simulations. In this table, the small initial concentration of species I used in the present model is 4.0×10^{-8} mol/L, as used by Ervin and Zabarnick.⁴ An initial dissolved O₂ concentration of 70 ppm ($\sim 1.8 \times 10^{-3}$ mol/L) is assumed for the samples of Exxsol D110,

(18) Balster, L., private communication, March 2003.

(19) Chien, K. Y. *AIAA J.* **1982**, *20*, 33–38.

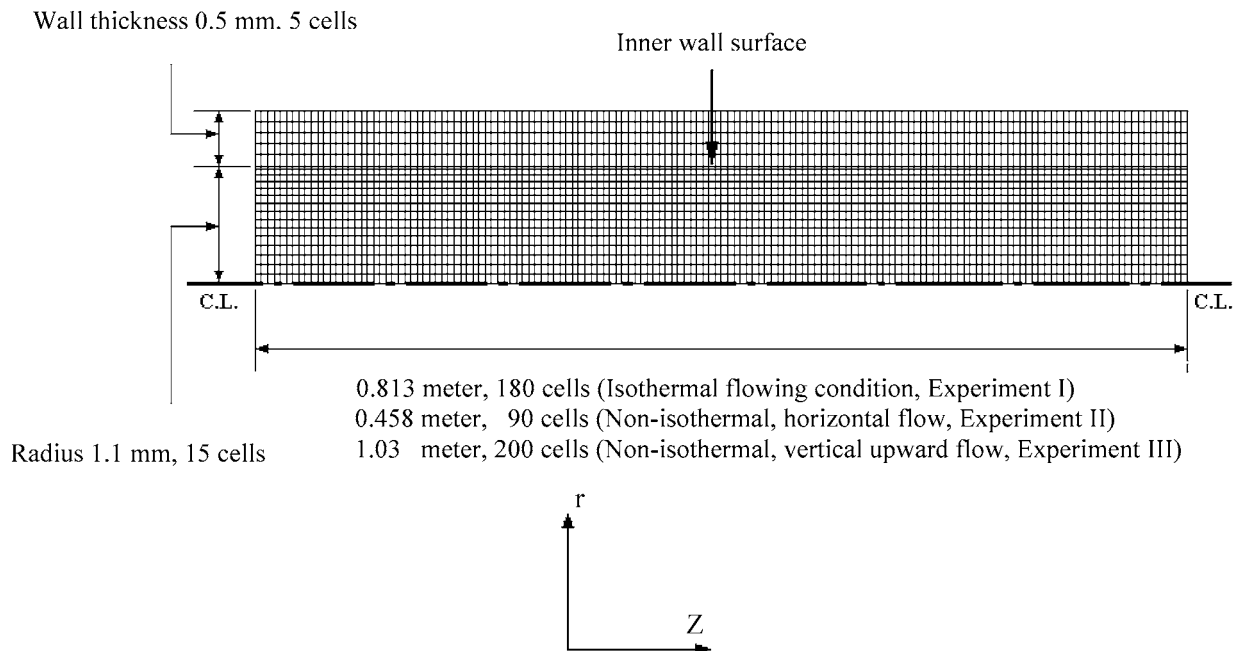


Figure 1. Computational grid.

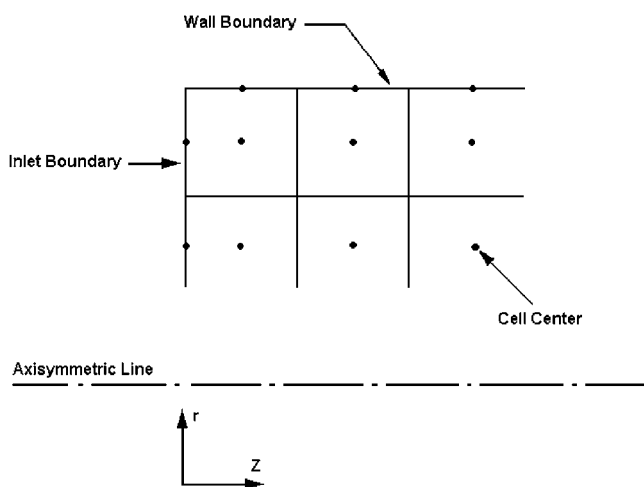


Figure 2. Computational cells and node points on boundaries.

Table 5. Initial Concentrations of Species^a

species	initial concentration (mol/L)
I	4.0×10^{-8}
RH	4.7
O ₂	1.8×10^{-3} (70 ppm)
AH	varies ($0-1.14 \times 10^{-4}$) (~25 mg/L)

^a Remaining species are set to zero.

Jet A-1 (F2747), and Jet A (F3219) fuels.⁴ Depending on the fuel type, the concentration of antioxidant AH of sample fuels varied, from 0 mol/L to 1.14×10^{-4} mol/L.

Experimental Section

To provide further validation of the mechanism used in the present work, experiments (Experiment III, Table 3) were conducted using Jet A fuel (F3219) flowing vertically upward within a tube (2.16-mm ID \times 3.18-mm OD) that was heated by a furnace. The surface that was in contact with the fuel was either stainless steel (SS316, ASTM grade A269/A213, surface roughness of 8–15 micro inches) or stainless steel

treated with a passive layer, which involves the chemical vapor deposition of a proprietary silica-based layer (Silcosteel). The silica coating has a nominal thickness of 10 000 Å and, thus, does not significantly influence the heat transfer from the wall to the fuel. The flow rate was maintained constant at 20 mL/min. Thermocouples welded to the outer surface of the tubing provided wall temperatures along the tube length, and the bulk fuel temperature at the tube outlet was measured (uncertainty of ± 10 °C). The exit bulk temperature of the fuel was varied from 150 °C (maximum wall temperature of 198 °C) to 225 °C (maximum wall temperature of 310 °C) by adjusting the furnace power. Dissolved O₂ levels were measured at the furnace outlet using a modified gas chromatograph. Additional details of the experimental apparatus may be found in the work of Ervin et al.²⁰

Results and Discussion

For model validation and improved fundamental understanding, it is beneficial to show how computational fluid dynamics, combined with the current kinetic mechanism, can simulate measured dissolved O₂ consumption for different flow conditions, fuels, and surface materials.

Simulations of Velocity Profiles. Fluid dynamics and heat transfer influence jet-fuel oxidation and antioxidant chemistry; however, the nature of this influence is not well understood. To better understand the oxidative processes for fuel that is flowing within a heated tube, it is important to simulate the flow behavior for both isothermal and nonisothermal conditions. Isothermal flow is not influenced by buoyancy. In contrast for a nonconstant wall temperature, the flow can be strongly influenced by buoyancy, depending on the magnitude of the local Reynolds number. Figure 3 shows simulated velocity profiles for the fuel under isothermal conditions (see Figure 3a, wall temperature 185 °C, Experiment I) and nonisothermal flow conditions (see Figure 3b, and the wall temperature profile

(20) Ervin, J. S.; Ward, T.; Williams, T. F.; Bento, J. *Energy Fuels* 2003, 17, 577–586.

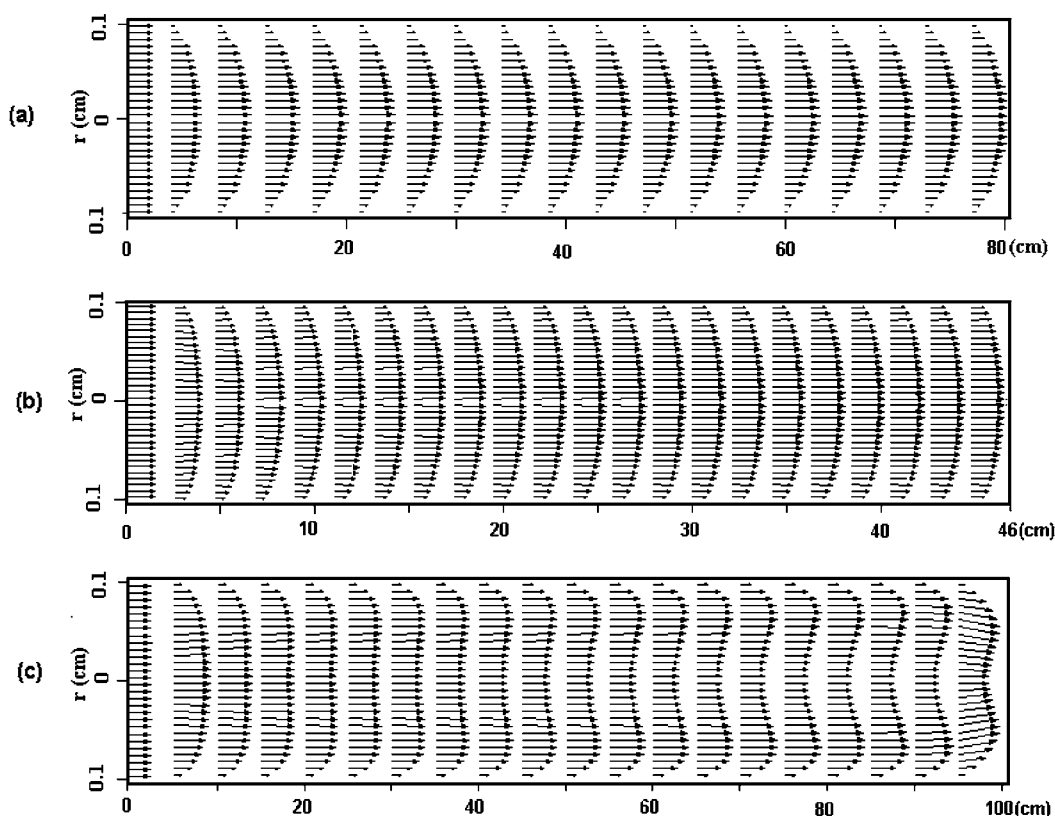


Figure 3. Velocity profiles of fuel flowing within either stainless-steel or treated tubes for (a) isothermal flow with a wall temperature of 185 °C (residence time of 1.25 min), (b) nonisothermal flow with the wall temperature profile of Figure 4, and (c) nonisothermal flow with the wall temperature profile of Figure 5.

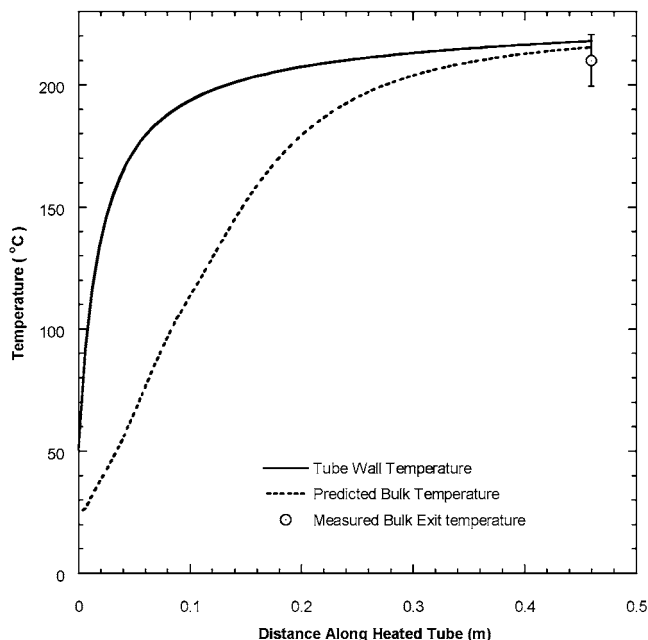


Figure 4. Bulk and tube wall temperature profiles along a heated tube (Experiment II, flow rate of 16 mL/min, heated length of 0.458 m).⁴

of Figure 4, Experiment II; and Figure 3c, wall temperature profile of Figure 5, Experiment III). Figure 3a shows that, for the constant wall temperature, the fuel reaches a fully developed laminar, parabolic profile early in the tube (near 5 cm) and, thus, the velocity profile downstream from this location does not change. For horizontal nonisothermal flow (Figure 3b), the fuel

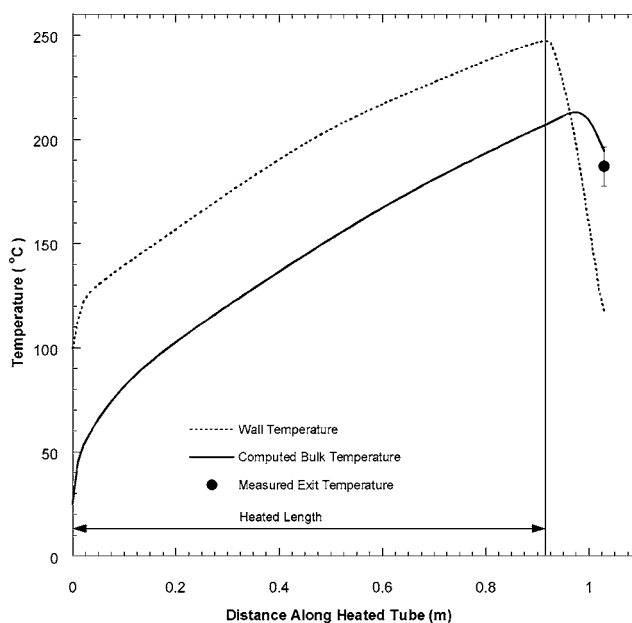


Figure 5. Computed and measured temperature of Jet A (F3219) fuel under nonisothermal flowing conditions with a wall temperature profile that provides an exit bulk temperature of 192 °C (Experiment III, flow rate of 20 mL/min).

reaches a velocity profile that is essentially fully developed near 2.8 cm. At the tube entrance, the flow is actually laminar but rapidly transitions to turbulent flow because of buoyancy-induced instabilities.¹⁹ Thus, the velocity profiles of Figure 3b are more flat than the parabolic profiles of Figure 3a. For the upward nonisothermal flow (Figure 3c), the velocity profile is flat near

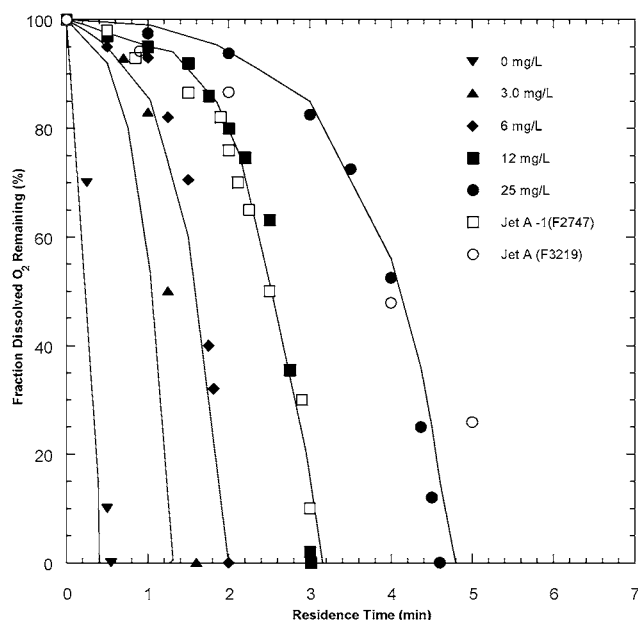


Figure 6. Measured and simulated fraction of dissolved O_2 remaining at the exit of the heated tube for Exxsol D110 containing different concentrations of BHT.¹⁵ In addition, dissolved O_2 consumption measurements for fuel samples F2747 and F3219 are shown.^{5,18} Flow is isothermal within the treated tube (Experiment I, wall temperature of 185 °C).

the center of the tube. As the wall temperature increases, the maximum velocity in radial direction begins (near 0.15 m) to shift from the tube center to a region midway between the wall and tube center, because of the growing influence of buoyancy. The velocity profile of Figure 3c never becomes fully developed because the wall temperature, transport properties, and buoyancy forces continuously change. With regard to oxidation, the lower-velocity regions in Figure 3 translate to regions of longer residence time. Thus, the shape of the velocity profile, as affected by buoyancy forces or turbulence, for example, influences fuel oxidation through the resulting fuel temperature distribution and residence time.

Studies of Exxsol D110 under Isothermal Conditions. Because Exxsol D110 is a less-complex mixture of hydrocarbons than a real jet fuel, the thermal-oxidative behavior of Exxsol D110 is easier to understand than that of a real jet fuel. Exxsol D110 is believed to contain minimal concentrations of antioxidants. In past isothermal flowing experiments, the concentration of butylated hydroxytoluene (BHT) was varied to study how the concentration of this antioxidant affects the rate of dissolved O_2 consumption.¹⁵ In numerical simulations, AH can be used to represent BHT. Thus, the measured oxidation rate of Exxsol D110 that contains different concentrations of antioxidant (AH) can be used to assess the present simulations (Table 3, Experiment I, variable flow rate).

Figure 6 shows measurements and predictions of dissolved O_2 concentration at the exit of the heated tube for Exxsol D110 that contained different concentrations of BHT.¹⁵ All measurements in Figure 6 were performed using a treated tube (wall temperature of 185 °C). Figure 6 shows that the present mechanism, which includes a wall reaction, reasonably predicts the oxidation rate of Exxsol D110 for BHT concentrations of 0–25

mg/L. As the concentration of BHT increases, Figure 6 shows that both the measured and simulated oxidation rates of Exxsol D110 decrease. Figure 6 shows that the measured oxidation rates of Exxsol D110 that contain 12 and 25 mg/L of BHT are similar to those of the Jet A-1 (F2747) and Jet A (F3219) fuel samples, respectively.^{5,18} These BHT concentrations are used to represent the initial concentration of AH for Jet A-1 (F2747, 5.45×10^{-5} mol/L) and Jet A (F3219, 1.14×10^{-4} mol/L) fuels in all simulations of jet fuel that follow. Moreover, because the Jet A-1 sample is hydrotreated, it is reasonable that the simulated value of AH is lower than that of the Jet A fuel. Fuel F2747 is similar to Exxsol D110, in that the naturally occurring antioxidants have been removed during hydrotreatment at the refinery, with an antioxidant (or antioxidants) being added later. The addition of a single or small number of synthetic antioxidants would result in the observed slow oxidation, followed by a rapid increase in oxidation rate after the antioxidant has been consumed. Fuels with naturally occurring inhibitors contain a large number of these species, which each have somewhat different reactivities. The result is that when the most easily oxidized species is consumed, a second slightly less easily oxidized species is consumed next. This can continue for many species. In addition, several species can be oxidizing, and, therefore acting as antioxidants simultaneously. The result is that the dissolved O_2 consumption curve for fuel F3219 has a more-linear shape than the curves for Exxsol D110 and fuel F2747. This more-linear O_2 consumption behavior of fuel F3219 could be better duplicated by adjusting AH and SH correctly to fit the O_2 measurements for fuel F3219. However, fitting the complex O_2 consumption behavior of the straight-run fuel F3219 is not a goal of the current work. In addition, fuel sample F2747 (similar to Exxsol D110) essentially does not contain a reactive sulfur species (SH, for example), which is in contrast to fuel F3219. Research is ongoing in regard to the development of measurement techniques for different AH and SH species, which we desire to add to the current model.

Studies of Jet A-1 (F2747) Fuel under Isothermal Conditions. Figure 7 (Experiment I, variable flow rate) compares the measured and simulated oxidations of fuel F2747 for stainless-steel and treated tubes for laminar flow. Figure 7 shows that, for the stainless-steel tube, the simulated dissolved O_2 concentration is completely consumed after a residence time of 1.8 min. For the passivated tube (surface activation energy of 42 kcal/mol), the predicted dissolved O_2 concentration is depleted after an average residence time of 3.25 min. Thus, the calculated oxidation rate is reduced for the treated surface. Moreover, Figure 7 shows that the prediction of dissolved O_2 consumption for fuel sample F2747 within isothermal laminar flow conditions agrees reasonably well with the measurements for both passive and active surfaces.

The concentration of AH that provides reasonable O_2 consumption rates for fuel F2747 in simulations was established in the Exxsol D110 studies. In addition, the oxidation rate of the Jet A-1 (F2747, hydrotreated) fuel sample was previously measured within either treated (Silcosteel) or untreated tubes (SS304) under isothermal flowing conditions (185 °C).⁵ Thus, the set of measure-

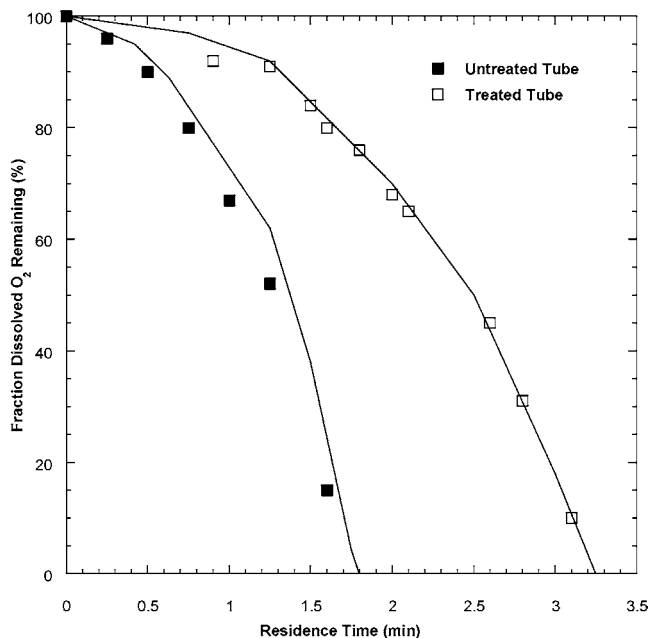


Figure 7. Measured and simulated dissolved O_2 fraction remaining for Jet A-1 (F2747) fuel for isothermal flow (Experiment I, wall temperature of $185\text{ }^\circ\text{C}$) within treated (42 kcal/mol) and untreated tubes (37 kcal/mol).⁵

ments for dissolved O_2 consumption for fuel flowing within the untreated tubes can be used to determine the activation energy for the surface reaction that occurs on a stainless-steel surface. By adjusting the activation energy for reaction 18 (from Table 1), a surface activation energy of 37 kcal/mol was determined to provide reasonable agreement between the measured and simulated oxidation rates. This value of the surface reaction activation energy is used in all subsequent simulations that involve stainless steel (304 or 316).

Figure 7 shows bulk averaged concentrations of dissolved O_2 at the exit of the tube. From a different perspective, Figure 8 shows simulated dissolved O_2 and ROOH mass fraction color contours of one condition selected from Figure 7 (Experiment I with a flow rate of 2.5 mL/min and a residence time of 1.25 min) within the heated tube for fuel F2747 as it flows through untreated and treated tubes. The flow in Figure 8a–d is laminar, with an inlet Reynolds number of 35 and an exit Reynolds number of 155. Dissolved O_2 and ROOH are two measurable species that are important for the understanding of fuel oxidation. Figure 8a shows the predicted dissolved O_2 mass fraction along the stainless-steel tube. In Figure 8a, the dissolved O_2 begins to be measurably consumed at a distance of 0.25 m from the tube inlet. As the fuel flows through the tube, the velocity close to the wall is lower than that near the tube center. Thus, the fuel resides relatively longer in the high-temperature region close to the wall, resulting in lower dissolved O_2 there. The computed bulk dissolved O_2 concentration that remains at the exit of the untreated tube (0.813 m) is 60%. Figure 8b shows the simulated dissolved O_2 mass fraction for the passivated tube. Significant consumption of the dissolved O_2 is delayed until a distance of 0.5 m from the tube inlet, and the computed bulk dissolved O_2 at the tube exit (0.813 m) is 90%. As might be expected for the more passive surface, the dissolved O_2 consumption has been

delayed significantly longer than that which occurs with the stainless-steel surface. Figures 8c and 8d show the predicted ROOH concentrations using passivated and stainless-steel tubes, respectively. Figure 8c shows that the predicted ROOH concentration from the use of a stainless-steel tube increases from 0 mol/L at the inlet to $8.7 \times 10^{-5}\text{ mol/L}$ at the exit. For the treated tube (Figure 8d), the ROOH concentrations increase from 0 mol/L at the inlet to $4.5 \times 10^{-6}\text{ mol/L}$ at the exit. The higher concentration of ROOH at the exit of the stainless-steel tube is due to the greater production of free radicals from the surface reactions on the untreated tube. Interestingly, the wall reaction consumes ROOH, which, in turn, increases radical production. The observed higher ROOH concentration for the stainless-steel tube shows that, under these conditions, the wall reaction results in a net increase in hydroperoxide production, despite being a result of wall-catalyzed peroxide decomposition. Figure 8 indicates that the concentration of dissolved O_2 decreases while the concentration of ROOH increases. Similar trends in the O_2 and ROOH concentrations along the tube have been previously observed.^{3,4}

Thermal Oxidation of Jet A-1 (F2747) Fuel under Nonisothermal Flowing Conditions. Because fuel oxidation is influenced by the temperature profile within the fuel and the level of turbulence and concomitant mixing, it is important to simulate oxidation within a turbulent flow and under different temperature conditions. In Table 3, a second set of experimental conditions (Experiment II), which involves the nonisothermal flow of fuel F2747, is shown. In these experiments, which have been detailed elsewhere, the tube (SS 316, 0.46 m long) is horizontal and clamped within a copper block that contains embedded cartridge heaters.⁴ Thus, a wall temperature profile is imposed by the heated copper block. For Experiment II, the inlet volumetric flow rate is 16 mL/min . Under these thermal and flow conditions for a horizontal orientation, buoyancy has been shown to produce a premature transition from laminar to turbulent flow.⁴ To obtain a range of bulk temperatures at the tube exit, different wall temperature profiles are imposed by adjusting the power input to the heaters. For the flow conditions of Experiment II, the predicted bulk temperature increases along the heated tube but never reaches the wall temperature. As an example, Figure 4 shows the wall and bulk temperatures along the tube for one power-input level. In addition, Figure 4 shows reasonable agreement between the predicted ($215\text{ }^\circ\text{C}$) and measured ($210\text{ }^\circ\text{C}$) exit bulk temperatures.

Figure 9 shows measured and simulated fractions of dissolved O_2 that remain at the exit of the tube for fuel F2747 flowing at a rate of 16 mL/min for different bulk exit temperatures. This figure shows that the predicted dissolved O_2 begins to be consumed at a bulk exit temperature of $180\text{ }^\circ\text{C}$, which is more than $10\text{ }^\circ\text{C}$ higher than the temperature corresponding to the initial consumption of the measured dissolved O_2 . Despite the initial delay associated with the simulated dissolved O_2 consumption, Figure 9 shows that the overall predicted dissolved O_2 behavior agrees reasonably well with the measurements. Moreover, Figure 9 shows that the measured and calculated temperatures associated with O_2 depletion agree well.

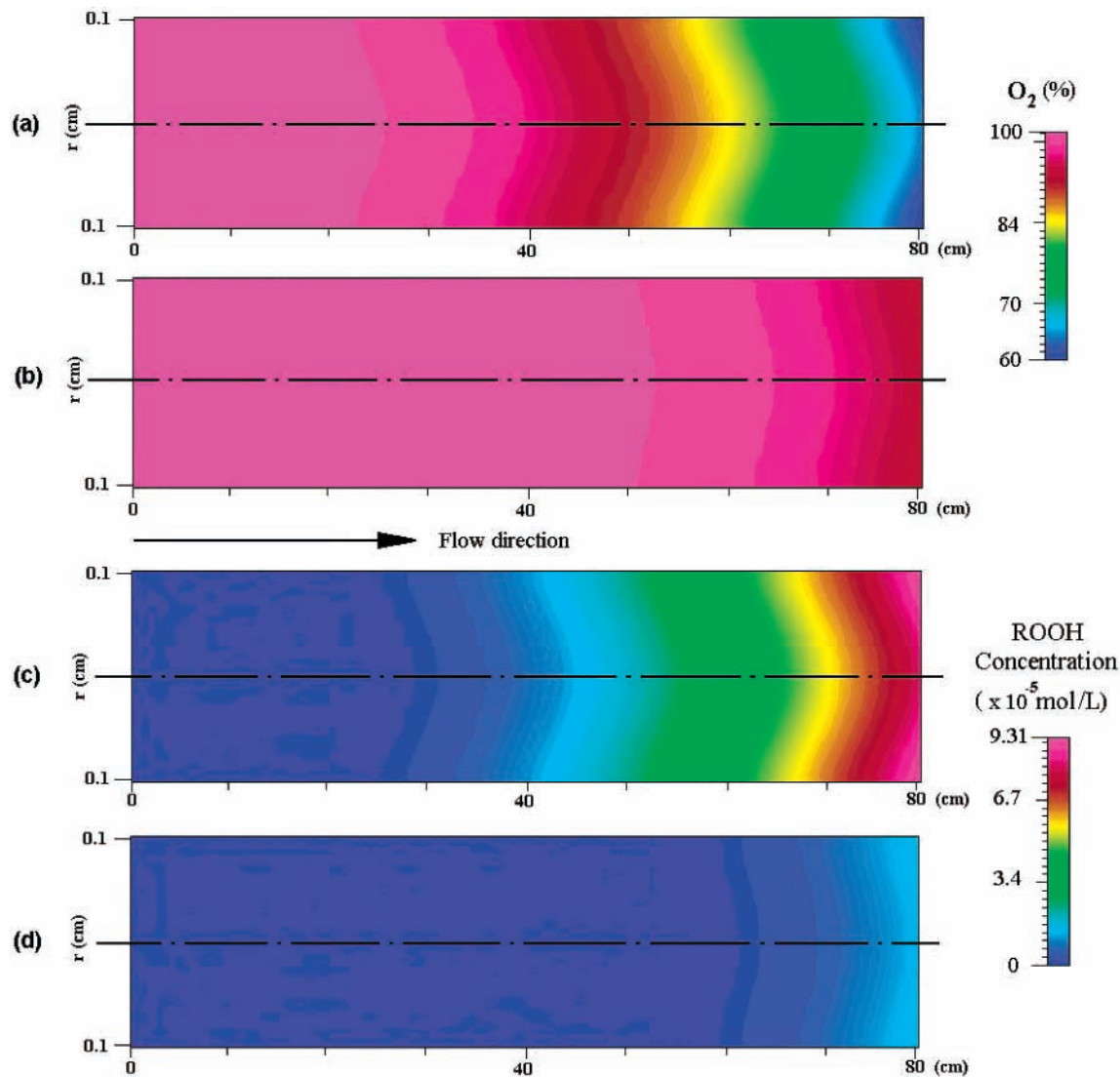


Figure 8. Dissolved O_2 and ROOH mass fractions at the exit of untreated (SS 316) and treated (Silcosteel) tubes for Jet A-1 (F2747) fuel at 2.5 mL/min and 185 °C (Experiment I): (a) predicted dissolved O_2 concentration along the untreated stainless-steel tube (surface activation energy of 37 kcal/mol), (b) predicted dissolved O_2 concentration along the treated tube (surface activation energy of 42 kcal/mol), (c) predicted ROOH concentration along the untreated stainless-steel tube, and (d) predicted ROOH concentration along the treated tube.

Because ROOH is another species that is important for the understanding of the thermal oxidation of fuel, it is useful to examine how well the current mechanism can simulate ROOH production and consumption. For Experiment II, Figure 10 shows measured and calculated ROOH concentrations for different exit bulk temperatures. This figure shows that the predicted ROOH concentration begins to increase at the exit bulk temperature of 185 °C. This delay in ROOH production (relative to the measured ROOH) agrees with the delay in the initial dissolved O_2 consumption of Figure 10. As the exit bulk temperature approaches 250 °C, Figure 10 shows that the simulated ROOH concentration increases rapidly until a maximum concentration of 0.0014 mol/L is reached. When the temperature further increases, the simulated ROOH concentration gradually decreases and is depleted near 360 °C. This figure shows that the temperatures associated with the peaks in measured and simulated ROOH concentrations agree reasonably well. Initially, relative to the measurements, the simulated amount of ROOH does not appear to decrease at sufficiently rapid rates beyond the peak

concentration. However, because of the large uncertainties in the ROOH measurements and additional reaction after the heated zone, it is believed that our simulations of ROOH provide acceptable results.

Thermal Oxidation of Jet A (F3219) Fuel under Nonisothermal Flowing Conditions. Different fuel samples can have very different thermal-oxidative properties; therefore, it is important to perform simulations of different fuel samples flowing over different surface types. Thus, for simulations of the third set of experiments (see Table 3), a straight-run Jet A (F3219) fuel is selected. This fuel is believed to contain a higher concentration of antioxidants and is a slower oxidizing fuel sample, relative to fuel F2747. As described earlier, the wall temperature varies continuously along the tube length for experiments that involve fuel F3219. For example, Figure 5 shows a selected (measured) wall temperature profile, together with the computed bulk temperature profile. The calculated bulk temperature at the tube exit (192 °C) is greater than the measured bulk temperature (187 °C); however, this temperature difference lies within the uncertainty of the measure-

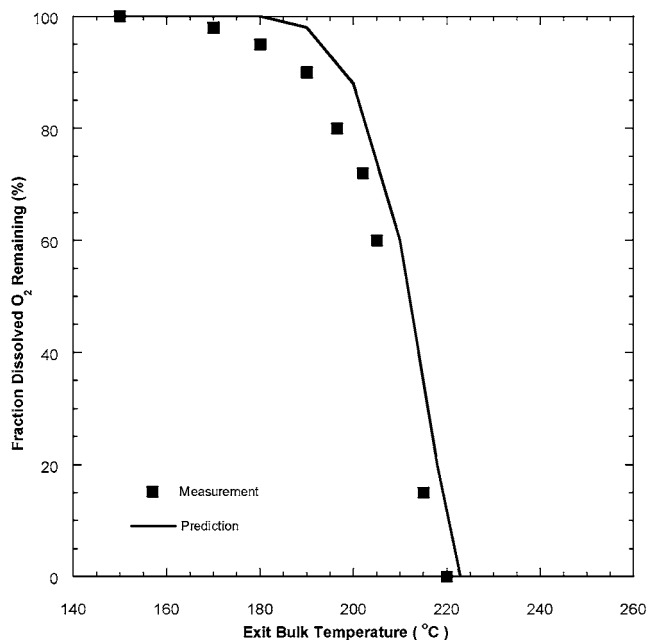


Figure 9. Fraction of dissolved O_2 remaining at the exit of the heated tube (Experiment II, flow rate of 16 mL/min, fuel sample F2747).

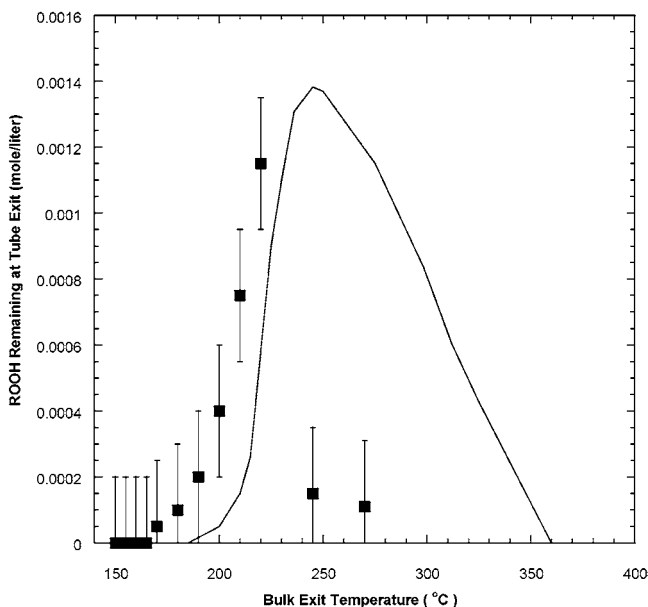


Figure 10. Measured and simulated ROOH concentration at the exit of the heated tube (Experiment II, flow rate of 16 mL/min, fuel sample F2747).⁴ Solid curve represents simulations.

ment. For a selected wall temperature profile (see Figure 5), Figure 3c shows a representative calculated velocity profile that results in an exit bulk temperature of 192 °C.

Figure 11 shows measured and predicted dissolved O_2 concentrations for Jet A (F3219) fuel for several outlet bulk temperatures for an entrance flow rate of 20 mL/min. With the more-active surface (SS 316), the dissolved O_2 is consumed more rapidly than with the treated tube, as observed for Exxsol D110 and fuel F2747. Figure 11 shows that the predicted dissolved O_2 concentration is completely consumed at the tube exit when the bulk temperature there is 216 °C for the untreated tube and 230 °C for the treated tube. This figure shows that simulations of dissolved O_2 consump-

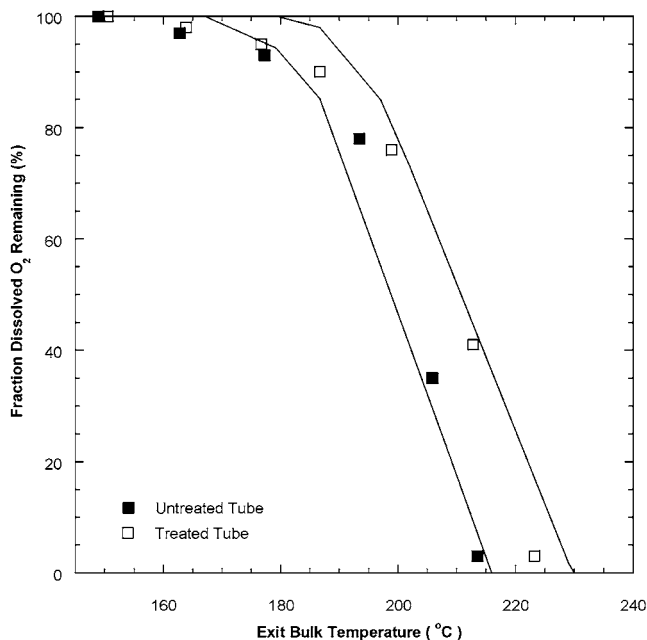


Figure 11. Measurement and simulation of the fraction of dissolved O_2 remaining at the tube exit for Jet-A (F3219) fuel under nonisothermal flowing conditions (Experiment III). Treated (42 kcal/mol) and untreated tubes (37 kcal/mol) tubes with varied exit bulk temperatures for a constant flow rate of 20 mL/min.

tion for both surface types agree reasonably well with the measurements, despite the relatively slower consumption predicted at relatively high dissolved O_2 concentrations (80%–100%) for both tube surfaces. Nevertheless, Figure 11 shows that the trends of the simulated oxidation rates obtained from using the present kinetics mechanism are correct.

Figure 12 shows contour plots of the predicted temperature, as well as the dissolved O_2 , ROOH, and AH concentrations along the heated tube for fuel F3219 that is flowing within the untreated (Figures 12b, 12d, and 12f) and treated (Figures 12c, 12e, and 12g) tubes for the wall temperature given in Figure 5. The flow is laminar, with an exit Reynolds number of 1400. Figure 12a shows that the simulated fuel temperature increases along the tube and that the temperature near the tube surface is higher than that at the tube center. However, at the exit of the tube, the wall temperature decreases, resulting in lower fuel temperatures near the surface than at the tube center. Figures 12b and 12c show that the dissolved O_2 begins to be measurably consumed at a distance of 0.7 and 0.9 m from the tube inlet for the untreated and treated tube, respectively. Figure 12b shows that, at a distance of 0.82 m from the inlet, the dissolved O_2 within the untreated tube is depleted at the wall, whereas, in contrast, the dissolved O_2 fraction near the tube center remains unreacted. Figures 12d and 12e show that the exit bulk concentration of ROOH for the treated tube (6×10^{-5} mol/L) is less than that of the untreated tube (1.67×10^{-4} mol/L). A lower ROOH concentration is reasonable here, because there is a lower rate of dissolved O_2 consumption. Figures 12b–e together show that as the concentration of dissolved O_2 decreases rapidly near the exit of the heated tube, the concentration of ROOH increases but is not fully consumed as in Figure 8 for fuel F2747. Figures 12b–e show lower O_2 and higher ROOH con-

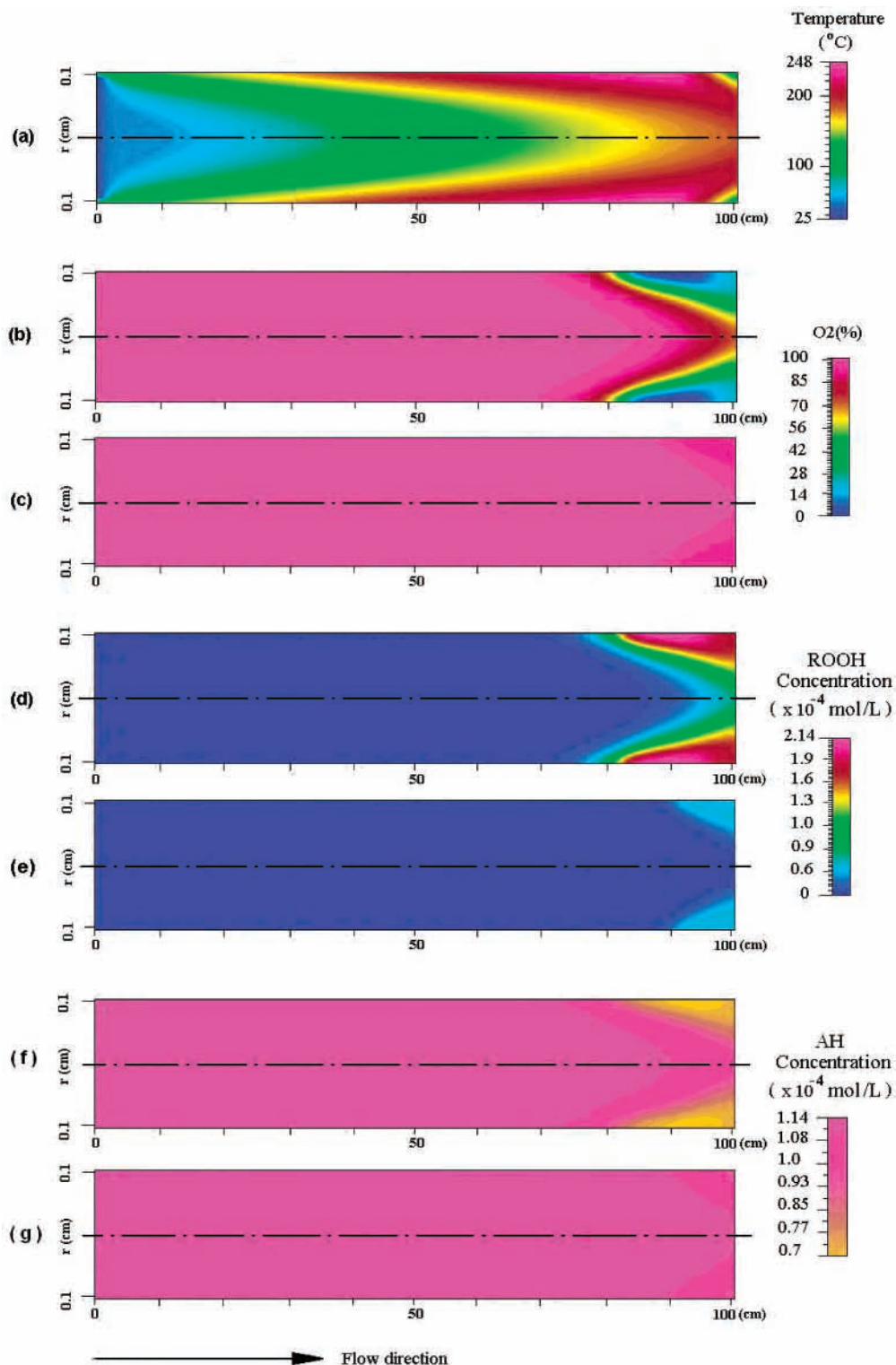


Figure 12. Simulations for fuel F3219 of (a) temperature, (b) dissolved O_2 fraction along the untreated tube (surface activation energy of $E_a = 37$ kcal/mol), (c) dissolved O_2 fraction along the treated tube (surface activation energy of $E_a = 42$ kcal/mol), (d) ROOH concentration along the untreated tube, (e) ROOH concentration along the treated tube, (f) AH concentration along an untreated tube, and (g) AH concentration along a treated tube. The tube is scaled to visualize temperature and species gradients. Total tube length is 1.03 m (heated length of 0.913 m).

centrations near the surface, rather than at the tube center, because the surface temperature is greater. Figures 12f and 12g show that the exit bulk concentration of AH for the untreated tube (2.42×10^{-5} mol/L) is lower than that for the treated tube (8.65×10^{-5} mol/L). A lower AH concentration for the untreated tube is

expected, because of a higher rate of dissolved O_2 consumption within the untreated tube.

Conclusions

In the present study, the effects of treated and untreated surfaces on the liquid-phase thermal oxida-

tion of different fuel samples were simulated for both isothermal and nonisothermal heated-tube experiments, using computational fluid dynamics and pseudo-detailed chemical kinetics with a surface reaction. The effects of the surface material on thermal oxidation were simulated using different activation energies for the fuel ROOH surface decomposition reaction for different surface materials (42 kcal/mol for treated surfaces and 37 kcal/mol for untreated stainless-steel surfaces). The oxidation measurements and simulations together show that the chemical reactions that occur at the tube surface influence the oxidation rate of jet fuels. Surface passivation has a marked effect in slowing the rate of dissolved O_2 consumption. Comparisons between the measurements and simulations of dissolved O_2 consumption on treated and untreated surfaces show that computational fluid dynamics that incorporate pseudo-detailed chemical kinetics with the selected wall reaction provide reasonable predictions of the dissolved O_2 consumption for jet fuel. Although the chemistry that occurs at the heated surface is complex, the influence of the surface material on the thermal oxidation of jet fuel can be reasonably simulated by the inclusion of a surface fuel hydroperoxide decomposition reaction.

Acknowledgment. This work was supported by the U.S. Air Force, Fuels Branch, Propulsion Directorate, Air Force Research Laboratory, Wright-Patterson AFB, OH (under Contract No. F33615-03-2-2347) and by the Dayton Area Graduate Studies Institute (under Grant No. PR-00-UD-12). The authors would also like to acknowledge Lori M. Balster for measuring the dissolved oxygen consumption in an isothermal flow experiment.

Nomenclature

- $C_1 = 1.44$ (constant)
 $C_2 = 1.92$ (constant)
 $C_{\epsilon_1} = 1.35$ (constant)
 $C_{\epsilon_2} = 1.8$ (constant)
 $C_{\mu} = 0.09$ (constant)
 D_i = diffusion coefficient of the i th species (m^2/s)
 $f_{\mu} = 1 - \exp(-0.0115y^+)$ (low-Reynolds-number $k-\epsilon$), 1.0 (standard $k-\epsilon$)
 g = gravitational acceleration (m/s^2)
 h = enthalpy (kJ/kg)
 k = thermal conductivity ($W m^{-1} K^{-1}$); turbulent kinetic energy (kJ/kg)
 p = pressure (MPa)
 S^{Φ} = source term
 u = axial velocity component (m/s)
 u_{τ} = friction velocity, $(\tau_w/\rho)^{1/2}$ (m/s)
 v = radial velocity component (m/s)
 $\dot{\omega}_i$ = rate of production of the i th species ($kg m^{-3} s^{-1}$)
 y = normal distance from wall (m)
 y^+ = dimensionless distance from wall, $\rho y u_{\tau}/\mu$
 Y_i = mass fraction of the i th species
 z = axial coordinate (m)
 Φ = assigned variable in eqs 1 and 2
 Γ^{Φ} = transport coefficient
 ϵ = dissipation rate ($kJ kg^{-1} s^{-1}$)
 ρ = density (kg/m^3)
 $\sigma_k = 1.0$ (constant)
 $\sigma_{\epsilon} = 1.3$ (constant)
 $\sigma_h = 1.0$ (constant)
 $\sigma_{\gamma i} = 1.0$ (constant)
 μ = absolute viscosity ($N s/m^2$)
 μ_t = turbulent viscosity, $C_{\mu} f_{\mu} \rho k^2/\epsilon$ ($N s/m$)

EF030098D

INTENTIONALLY LEFT BLANK

Appendix AA
Evaluation of Soot Particulate Mitigation Additives in a T63 Engine

INTENTIONALLY LEFT BLANK

Evaluation of soot particulate mitigation additives in a T63 engine

Edwin Corporan^{a,*}, Matthew DeWitt^b, Matthew Wagner^c

^a*Air Force Research Laboratory, AFRL/PRTG 1790 Loop Rd N, WPAFB OH 45433-7103, USA*

^b*University of Dayton Research Institute, 1790 Loop Rd N, WPAFB OH 45433-7103, USA*

^c*Air Force Research Laboratory, AFRL/PRTM 1790 Loop Rd N, WPAFB OH 45433-7103, USA*

Abstract

The performance of fuel additive candidates to mitigate soot particulate emissions in turbine engines was assessed in a T63 helicopter engine. Seventeen additives, including commercial compounds to reduce emissions in internal combustion engines, diesel cetane improvers, and experimental/proprietary additives, were evaluated. The additives were individually injected into the JP-8 fuel feed to the engine, and evaluated at a minimum of three concentration levels. The engine was operated at two conditions, idle and cruise, to investigate additive effects at different power settings or equivalence ratios. Particulate samples were collected from the engine exhaust using an oil-cooled probe, and analyzed using a suite of particulates instrumentation, which included a condensation nuclei counter (CNC), scanning mobility particle sizer (SMPS), laser particle counter (LPC) and a tapered element oscillating microbalance (TEOM). Results indicate that the diesel cetane improvers and commercial smoke abatement additives tested had minimal impact on particulate emissions in the T63 turboshaft engine. One proprietary additive was shown to reduce particle number density (PND) by up to 67% at the relatively high concentration of 3000 mg/l. These benefits were observed only at cruise condition, which may provide some insight into the mechanisms by which the additive suppresses the formation or enhances the oxidation of soot particles. Test results with blends of JP-8 and Norpar-13 (normal paraffins) show significant reductions in particulate emissions for both idle and cruise conditions demonstrating the potential environmental benefits of using blends of clean (low aromatic and low sulfur) fuels with JP-8. Comparisons of mass determination with different instruments and preliminary results of chemical characterization of particulate emissions with and without additives are also presented.

© 2004 Elsevier B.V. All rights reserved.

Keywords: Additives; Particulate; Engine

* Corresponding author. Tel.: +1-937-255-2008; fax: +1-937-255-3893.

E-mail address: edwin.corporan@wpafb.af.mil (E. Corporan).

1. Introduction

The United States consumes approximately 26 billion gallons of jet fuel per year [1]. Based on the International Civil Aviation Organization (ICAO) Emissions Index for particulate matter (PM), it is estimated that 7.0 million pounds of solid particulate are emitted each year by US aircraft. PM may either be emitted directly or formed in the atmosphere by transformations of gaseous emissions of compounds including nitrogen oxides (NO_x), volatile organic compounds (VOCs), and sulfur oxides (SO_x). Studies have shown that these airborne particles pose both health and environmental risks. The National Ambient Air Quality Standards (NAAQS) have a health-based regulation for particulate matter with diameters less than 10 μm (PM10). Research indicates that exposure to coarse particles (larger than 2.5 μm diameter) is associated with aggravation of asthma and increased respiratory illness [2]. Additionally, chronic health effects have been linked with long-term exposure to these coarse particles. However, there is increasing evidence that the PM10 regulation (annual arithmetic mean of 50 μg/m³, 24-h average of 150 μg/m³) is insufficient to eliminate serious health and environmental problems for particulate matter with diameters smaller than 2.5 μm (PM2.5). As a result, the EPA has adopted a revision of the particulate matter regulation to regulate PM2.5 particles (arithmetic annual average of 15 μg/m³, 24-h average 65 μg/m³) [3]. Recently, the U.S. Supreme Court upheld the constitutionality of the Clean Air Act and the EPA's decision on setting the new health-protective PM2.5 regulation. The health effects associated with PM2.5 can range from aggravation of respiratory and cardiovascular disease to premature mortality [4]. Most particulate matter from aircraft engines is PM2.5. Since these fine particles contain high amounts of carbon, they are usually referred to as soot in the combustion community. However, there is evidence that harmful polycyclic aromatic hydrocarbons (PAH) are present in these carbon-laden particles.

2. Experimental

2.1. T63 engine and fuel system

A T63-A-700 turboshaft engine, used primarily in helicopter applications, was used in this additive evaluation. The engine is located in the Engine Environment Research Facility (EERF) in the Propulsion Directorate at Wright-Patterson Air Force Base, and is used to evaluate turbine engine lubricants, fuels, and sensors in an actual engine environment. A schematic of the engine as installed in the EERF is shown in Fig. 1. The compressor draws atmospheric air through the inlet, compresses it via six axial stages and one centrifugal stage, and discharges it to two tubes which carry it to the combustor inlet on the aft end of the engine. The combustion gases flow forward through the combustor to two uncoupled two-stage turbine sections. The gas producer turbine drives the compressor, and the power turbine drives the output shaft, which is connected to a hydraulic dynamometer. After the power turbine, the exhaust gases turn 90° to enter two exhaust collectors to route the gases out of the test cell. Particulate emissions were taken

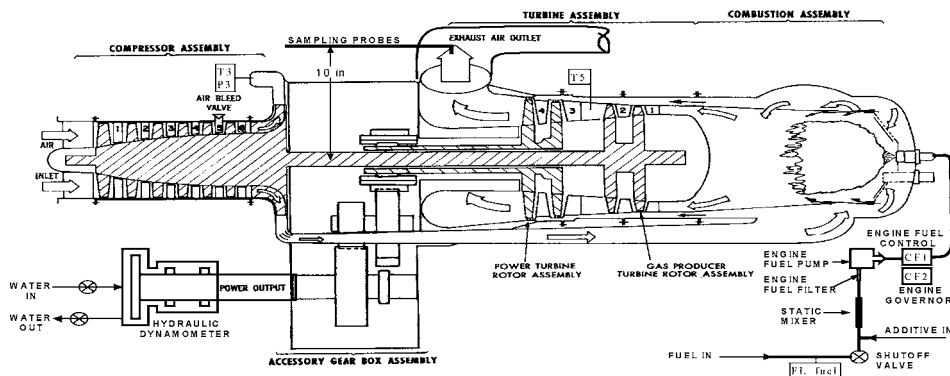


Fig. 1. Engine environment research facility setup.

via an oil-cooled sampling probe installed parallel to the flow into the exhaust duct 10 in. from the engine centerline.

JP-8 fuel was supplied to the T63 from an external tank, and the fuel flow rate was measured with a flow meter (FL_{fuel}). The additives were diluted to a predetermined concentration in JP-8 to improve their flowability, and injected via two ISCO Model 1000D syringe pumps immediately downstream of the fuel flow meter. The required additive flow was computed from the measured fuel flow rate and the desired additive concentration. The syringe pump displacement was adjusted via a computer-controlled feedback loop to provide the required additive flow rate. The fuel/additive passed through a static mixer (to ensure a homogeneous mixture) and entered the engine's fuel filter, fuel pump and the engine fuel control. The fuel control (CF1), in conjunction with the governor (CF2), metered the required amount of fuel/additive to the engine's pressure atomizing fuel nozzle and circulated the remaining fuel back through the fuel pump. For a given engine operating condition, the combined fuel/additive flow was held constant.

The engine was operated at two conditions, designated as Ground Idle (GI) and Normal Rated Power (NRP) (also referred to as cruise condition). Nominal values for operating parameters at these conditions are listed in Table 1. GI was attained by a fixed fuel control setting and no load on the dynamometer. NRP was attained by adjusting the governor control and dynamometer load to maintain the intra-turbine temperature (T_5) at 1280 °F and output shaft speed at 6000 rpm. For all tests, the total flow of fuel plus additive was computer-feedback controlled to maintain a constant T_5 . This approach assured the best run-to-run repeatability between tests conducted with and without the additives.

Table 1
Engine operating conditions—WP standard day (850 ft, 14.25 psia, 77 °F)

Power	P_3 (psia)	T_3 (°F)	T_5 (°F)	SHP (hp)	Fuel flow (lb/min)	Air flow (lb/min)	Overall F/A ratio	Burner F/A ratio
Idle	35	251	750	8	0.89	95	0.009	0.040
Cruise (NRP)	80	498	1280	238	2.92	169	0.017	0.075

2.2. Particulate measurement methodology and instrumentation

Currently, there is no standard methodology or instrumentation for measuring mass and particle number density (PND) for PM_{2.5} emissions from gas turbine engines. The EPA has a standard method for measuring particulate emissions from stationary sources called Method 5. The method consists primarily of collecting and weighing the carbon from the engine exhaust deposited on a quartz filter. The EPA Method 5 is very labor intensive, extremely slow (about 3 h per sample) and is susceptible to significant uncertainty from filter handling. An industry standard used for engine emissions certification is the smoke number. In this method, a known volume of engine exhaust is passed through a filter, and the change in filter optical reflectance is correlated to the quantity of particulate matter collected. However, it has been found that smoke number is largely the result of a few large diameter particles, and that the contribution of fine particles to the smoke number is minimal. As such, smoke number is considered an unsuitable method for measuring PM_{2.5} exhaust from turbine engines.

The methodology used in this effort was based on that used by the University of Missouri-Rolla (UMR). [5] Particulate emissions from the T63 engine were characterized using mainly commercially available particle counters and electrostatic classifiers. Precision errors of less than 5% (2σ) in the particle number measurements were observed for both engine conditions due to the steady operation of the engine. Particulate emissions were captured and transported to the analytical instruments (described in Table 2) via an oil-cooled probe. The probe design, shown in Fig. 2, was based on an AEDC/NASA/UMR design and consisted basically of three concentric tubes with three fluid passages. The outermost passage carried the recirculating cooling oil, the middle passage provided particle free dilution air, and the center passage transported the diluted sample to the instruments. The probe was installed facing the flow in the center and near the exit of the engine to help capture a “representative” sample of the engine exhaust and avoid diluting or contaminating with surrounding air. The exhaust sample was diluted with dry air at the tip of the probe to prevent water condensation and particulate loss to the wall due to high wall-sample temperature gradients, and to prevent saturation of the particulate instrumentation. Due to the high particle count from this engine, dilution rates of 94–98% were used (analyzed sample consisted only 2–6% of the exhaust). The corrected particle count was calculated for various dilution rates and found to be in excellent agreement (< 5% error). The diluted sample was drawn into the analytical instruments via a vacuum pump, and the air dilution and sample flows were controlled with high precision Brooks 5850 (0–10 SLPM) flow controllers. Dilution flows were initially set to 100% (only particle-free air through the system) and subsequently adjusted to the desired dilution ratio based on engine condition.

2.3. Description of additives

The additives evaluated are listed in Table 3. These include: diesel cetane improvers, detergent/dispersants for jet fuels, commercial additives for gasoline and diesel engines, and various research additives. The additives were nominally tested at $1\times$, $5\times$ and $10\times$ the recommended concentrations. They were diluted in JP-8 (to improve additive

Table 2
Particulate emissions instrumentation

Instrument and model number	Measurement	Description
<i>Condensation Nuclei Counter</i> (CNC) CPC TSI Model 3022A	Particle number density (PND) (#/cm ³)	Real-time count of particles per cm ³ . Uses principle of condensing supersaturated vapor on sub-micron size particles. Particles are counted with an optical detector via individual pulses (<10 ⁴ particles) or by photometric means. Capability up to 10 ⁷ particles per cm ³ .
<i>Scanning mobility particle sizer</i> (SMPS) TSI model 3936 Differential mobility analyzer (DMA) TSI model 3081 Condensation Nuclei Counter CPC TSI Model 3022A	Particle size distribution	Consists of an electrostatic classifier to determine particle size according to mobility through an electric field. A CNC is used to determine particle concentrations in a size bin. Particle diameter size range of 7–300 nm.
<i>Tapered element oscillating microbalance</i> (TEOM) Rupprecht & Patashnick Series 1105 diesel particle monitor	Direct particulate mass concentration (mg/m ³)	Collects particles on a filter attached to an oscillating tapered element. The mass on the filter is determined based on the change in natural frequency of the tapered element. Used only when significant changes in PN observed.
<i>Laser particle counter</i> (LPC) MetOne	Particulate count for particles larger than 300 nm	Number of particles determined via light scattering. Count of larger particles found to be negligible in T63.

flowability) before entering the syringe pumps and then injected into the fuel flow to the engine. Due to nondisclosure agreements between the Air Force and the additive companies, the chemical composition of proprietary and commercial additives cannot be disclosed. Nonetheless, this study evaluates the performance of these research compounds, diesel cetane improvers, and commercial additives in a turbine engine burning

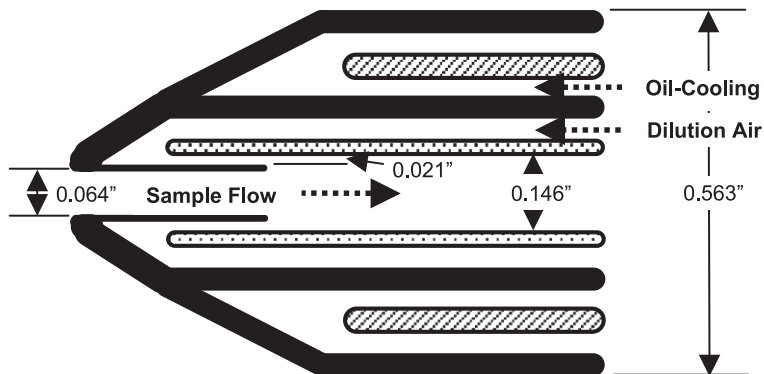


Fig. 2. Particulate matter probe design.

Table 3
Additives evaluated on the T63 combustor

Additive	Concentration tested (mg/l)	Additive type	Company
(1) Enviro max (EMP)	780–20000	fuel catalyst for gasoline and diesel	Maxma LC
(2) Enviro max (EMD) biodiesel	780–3900	fuel catalyst for gasoline and diesel with biodiesel	Maxma LC
(3) Wynn's emissions control + plus +	3000–60000	emissions reducer	Wynn's oil company
(4) Kleen fuel	3900–78000	combustion enhancer	Green fuel
(5) Fuel fix	205–822	high molecular weight polymer	Fuel Fix
(6) RXP biodiesel	780–15620	emissions reducer gasoline and diesel	RXP Products
(7) Viscon	780–3900	high molecular weight polymer	GTA Technologies
(8) Isobutyl nitrate	200–8000	cetane improver	Aldrich
(9) 2-Ethylhexyl nitrate	500–5000	cetane improver	Aldrich
(10) Norpar-13	10–30% by vol.	solvent (normal paraffins)	Exxon-Mobil
(11) Betz Dearborn 8Q462	256–10240	detergent/dispersant	Betz Dearborn
(12) PA-1	200–8000	similar to thermal cracking initiator	Synthesized
(13) PA-2	400–10000	detergent (PA-5 and PA-6 blend)	Lubrizol
(14) PA-3	200–4000	thermal stability (contains PA-4)	Lubrizol
(15) PA-4	200–2000	detergent type	Lubrizol
(16) PA-5	200–10000	detergent type	Lubrizol
(17) PA-6	200–2000	detergent type	Lubrizol

JP-8. Furthermore, it provides the additive companies an assessment of their additives in a jet engine and the opportunity to reformulate their products for jet fuel.

3. Results and discussion

3.1. Commercial additives

Commercial additives used in gasoline and diesel engines were evaluated. The companies supplied additives that have undergone testing in independent laboratories and have reportedly shown to be effective in reducing gaseous emissions and improving fuel economy. It has been proposed that the additives reduce emissions by improving the combustion process by chemical and/or physical means. A brief description of these commercial additives and their proposed function to reduce emissions is given below.

The *Fuel Fix* and *Viscon* additives employ a very similar approach; high molecular weight polymers are used to change the fuel's physical characteristics to modify the fuel's atomization and vaporization behavior. The proposed function of the additive is to prevent the rapid vaporization of the fuel's higher volatility components in the combustion

chamber and, therefore, promote the vaporization and combustion of all fuel components uniformly. Both additive manufacturers have observed significant reductions in gaseous emissions (CO, HC and NO_x) and fuel consumption with increased engine power with their additives in internal combustion engines. Test results in the T63 show that neither additive was effective in reducing particle number density (PND) or changing particle size distribution. However, both additives appeared to change the surface tension of JP-8 since the resultant treated fuel had an elastic-like consistency. The additives were blended at relatively high concentrations with JP-8 before entering the syringe pumps, and were noticeably more difficult to draw into the pumps. The negligible effects observed by these additives on the T63 emissions may indicate that this engine or its injection system (1960s technology) is fairly insensitive to changes in certain physical properties of the fuel. The additives will be tested in a high performance turbine engine combustor to investigate if physical changes in the fuel can impact emissions in newer engines. If benefits are observed with this class of additive, its pumping characteristics will be addressed.

Several commercial additives evaluated were expected to reduce emissions by chemically changing the combustion process. *Kleen Fuel* is a blend of aliphatic nitro compounds, which reportedly has active components that break down to release oxygen. The oxygen released from these nitroparaffin groups is used to burn the remaining unburned hydrocarbon components in the combustion chamber to improve engine performance and reduce emissions. *RxP* is a hydrocarbon blend that reportedly contains a molecule that absorbs a large portion of the infrared radiation emitted during the combustion process. The unburned fuel is preheated (producing higher combustion temperatures) and the heat loss to the combustor chamber wall is reduced to produce more efficient engine operation and lower emissions. *Enviro Max* is a combination of a heterogeneous catalyst and a combustion promoter. The homogenous catalyst consists of micron-sized particles of solid zinc oxide/peroxide suspended in selected solvents, which are blended with the proprietary combustion promoter and *tert*-butyl hydroperoxide (TBH). Two formulations of the *Enviro Max* additives were tested in this study, the EMP and EMD biodiesel. It should be noted that in the pre-mixed EMP/JP-8 blend a significant amount of the additive separated from the fuel and settled in the bottom of the fuel reservoir. This characteristic most likely prevented a homogenous fuel/additive mixture, and obviously makes the present formulation of EMP an undesirable additive for jet fuel. *Wynns Emissions Control+Plus* additive is also reported to be an emissions reduction additive; however, specific details about its functionality were not defined.

Tests results show that these commercial additives were all relatively ineffective in reducing PND or altering particle size distributions in the T63. Only the *Kleen* additive had a measurable effect by reducing PND by 19% at the cruise condition; however, it was added at a relatively high concentration of 7.8% by volume. Additionally, preliminary test results in an atmospheric combustor showed that *Kleen* (at ~ 1.5% by volume in JP-8) produced measurable reductions in PND with the combustor operating at fuel rich conditions ($\phi = 1.1$). Differences in combustor pressure, fuel nozzle characteristics, and equivalence ratios may explain the differences in additive effectiveness between the two combustors. During the preparation of this paper, additional experiments with the *Kleen* additive were being conducted to help explain its superior performance in the atmospheric combustor compared to the T63.

Further testing of these commercial additives on other engines is necessary to generalize their performance on all turbine engines. There are many reasons why an additive that is effective in reducing emissions on an IC engine may be ineffective in a jet-fueled turbine engine. In general, turbine engines operate at higher combustion efficiencies than their IC counterparts, and jet fuels have lower aromatics (proposed soot precursors) than both diesel and gasoline fuels. Furthermore, diesels (which produce considerably higher particulate exhaust than gasoline engines) operate at higher pressures and temperatures than jet engines, and the fuel distribution within its cylinders is nonuniform, which increases the fuel-rich zones and promotes the formation of soot particulate. The non-steady operation of the reciprocating engines is also likely to adversely impact emissions. Overall, jet-fueled turbine engines burn cleaner than IC engines, and therefore, the challenge of reducing harmful PM_{2.5} emissions from aircraft turbine engines is significantly greater.

3.2. Research additives

Additives used to increase fuel thermal stability (ability of fuel to resist carbon formation upon heating) were also investigated for their ability to reduce particulate emissions. The Betz Dearborn 8Q462 (+100 additive) is a commercially available additive package with a detergent/dispersant added at only 256 mg/l (about one quart per 1000 gal of fuel) to increase the thermal stability of JP-8 by 100 °F (JP-8 + 100) [6]. JP-8 + 100 is currently used in over 3000 Air Force aircraft (mostly fighters and trainers). Experience has demonstrated that JP-8 + 100 significantly reduces unscheduled maintenance, maintains engine components cleaner, and drastically reduces soot buildup on hot engine components [7–9]. The reduced soot buildup on engine turbine blades prompted an investigation into the potential of +100 to reduce soot particulate emissions. Unpublished, limited field data on a fighter aircraft engine showed significant reductions in PND emission index using JP-8 + 100 compared to operation with JP-8. Additionally, in recent tests at the United Technologies Research Center (UTRC), significant reductions in particle size, PND and smoke number were observed in an F119 single-nozzle combustor operated with JP-8 + 100 [10].

The PA-2 to PA-6 research additives were similar to the Betz + 100 as they contained detergent-type active ingredients. PA-2 is composed of detergents PA-5 and PA-6 diluted in a hydrocarbon carrier. PA-1 is an oxygen-containing additive with similar chemical structure as a proprietary compound used to accelerate fuel thermal cracking at high temperatures. The original compound could not be evaluated because it is no longer produced.

Results show that the +100, PA-1 and PA-6 additives had negligible effects on particulate emissions. The PA-3 and PA-4 additives actually increased PND by 10% to 25% at concentrations of 200–4000 mg/l with the largest increases occurring at cruise condition at the highest additive levels. Although the + 100 additive was tested at up to 40 times the recommended dose, minimal effects on particulate emissions were observed. Differences in injector design, combustor pressure and geometry, and JP-8 fuel batches between the T63 and the UTRC F119 single nozzle tests are believed to contribute to the significantly different results obtained in the two tests. Further studies on the effects of

+ 100 on the emissions of various aircraft and engines are underway under several Air Force programs [11]. It is believed that detergent-type additives may have long-term beneficial effects on emissions as fuel nozzles become cleaner and fuel atomization is improved. However, two detergent-type additives were shown to have an immediate positive effect on particulate emissions. The PA-2 additive reduced PND by up to 45%; however, undesirably high concentrations of 10,000 mg/l (~ 1.0% by volume) were required. In addition, the improvement was only observed at the cruise condition. Based on the reductions observed with PA-2, its two active ingredients (PA-5 and PA-6) were evaluated. As mentioned above, PA-6 had negligible effects on particulate emissions; however, significant reductions in PND were observed with PA-5. Fig. 3 displays the immediate reduction in PND as the PA-5 additive was added to the fuel, and the return to baseline PND upon removal of the additive. A maximum PND reduction of 67% at 3000 mg/l (~ 0.30% volume) was observed. As shown, the effectiveness of PA-5 decreased as the additive concentration was increased (e.g., 63% reduction at 2000 mg/l and 67% reduction at 3000 mg/l). Consistent with PA-2 these improvements were observed only at cruise conditions. Assuming a chemical interaction, we infer that the additive has a high activation energy, thus requiring higher flame temperatures to break down and produce radicals or other species that react to reduce the formation of soot and soot precursors. Further studies are needed to verify this hypothesis. In addition, studies on potential physical effects of additives on fuel atomization will be pursued.

The particle size distribution for the T63 using PA-5 is shown in Fig. 4. PA-5 was observed to increase the concentration of particles in the 7–10 nm diameter range. These smaller particles are believed to be products formed via breakdown of the additive or smaller soot particles from reduced soot surface growth and coagulation. Future detailed studies will be conducted on PA-5 and similar chemistry additives in the T63 and in a high

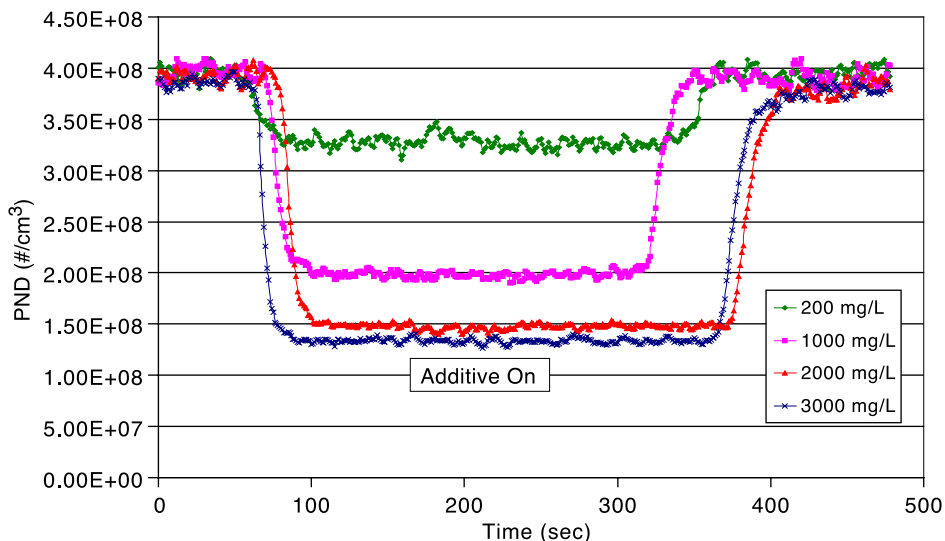


Fig. 3. Effects of PA-5 additive at various concentrations on particle number density (PND) in the T63 engine.

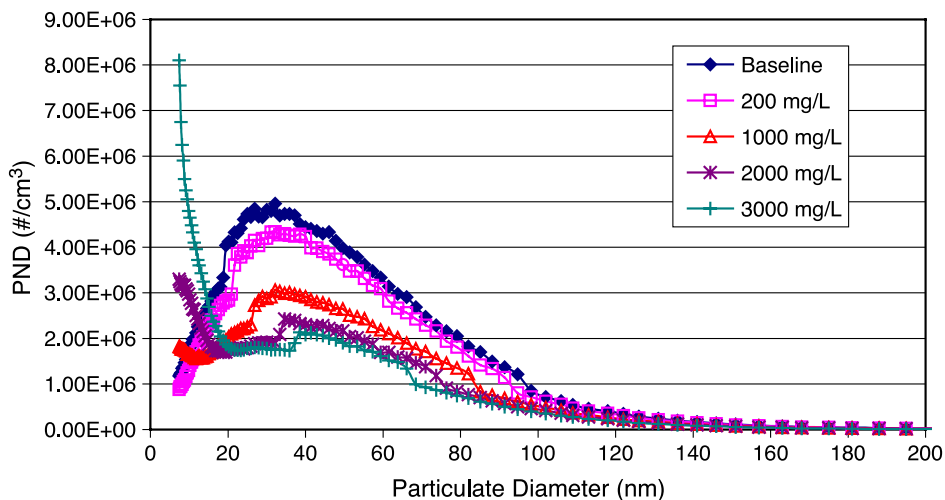


Fig. 4. Effects of PA-5 additive at various concentrations on particle size distribution of T63 engine exhaust at cruise condition.

performance single-nozzle combustor equipped with advanced laser diagnostics instrumentation. These studies will help elucidate mechanisms by which the additive reduces PND and alters particle size distribution. In addition, soot samples will be chemically characterized to ensure that the additive is not producing additional/other harmful pollutants.

Norpar-13, an Exxon solvent consisting mostly of normal paraffins averaging a carbon number of 13, was blended (10–30% by vol.) in JP-8 and evaluated in the T63. The objective was to reduce the aromatic concentrations (also increase the hydrogen-to-carbon ratio) in JP-8 to investigate their effect on particulate emissions. Also, the blend of Norpar-13 in jet fuel is expected to have similar emissions benefits as blends of synthetic (coal or natural gas) and petroleum derived jet fuels. As shown in Fig. 5 Norpar-13 dramatically reduced PND at both idle and cruise engine conditions. At idle, reductions of up to 52% were observed at Norpar-13 concentrations of 30% by volume. These results are consistent with previous studies that have found aromatics to be strong contributors to soot formation in hydrocarbon-fueled combustion systems. [12] Previous research has shown that at the range of temperatures found in the T63 combustor ($\sim 2000\text{--}2800$ °F), hydrocarbon aromatics produce soot via a fast route that involves condensation of the aromatic rings into soot nuclei [13]. The proposed mechanism begins with the transformation of the initial aromatic hydrocarbon into macromolecules via gas-phase reactions. The partial pressure of these macromolecules grows to supersaturation levels causing their condensation into liquid microdroplets, which eventually become soot nuclei. Subsequently formed gaseous macromolecules then contribute to nuclei growth. The addition of Norpar-13 reduced the relative aromatic-to-aliphatic ratio, thus reducing particle nucleation. As shown in Fig. 5, the benefits of Norpar-13 were more pronounced at idle than at cruise. The increased F/A ratio, and thus higher combustor temperatures and pressures, at the cruise condition, increased the reaction rates of soot production, which appear to slightly

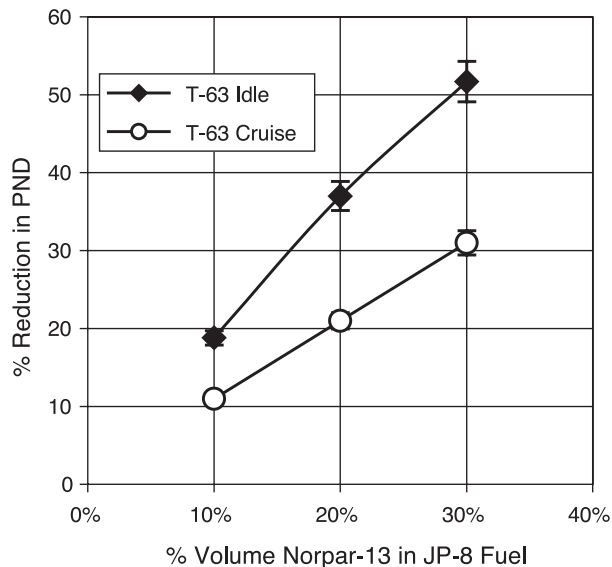


Fig. 5. Reduction in particle number density in the T63 engine as a function of percent of Norpar-13 in JP-8.

offset the benefits of reducing the overall aromatic concentration in the fuel. The size distribution curves in Fig. 6 show that Norpar-13 has only minor effects on the particle size distribution (peak particle diameter about 18 nm with or without Norpar-13). Apparently, reducing the aromatics in JP-8 mainly reduces soot particle nucleation, and has less of an

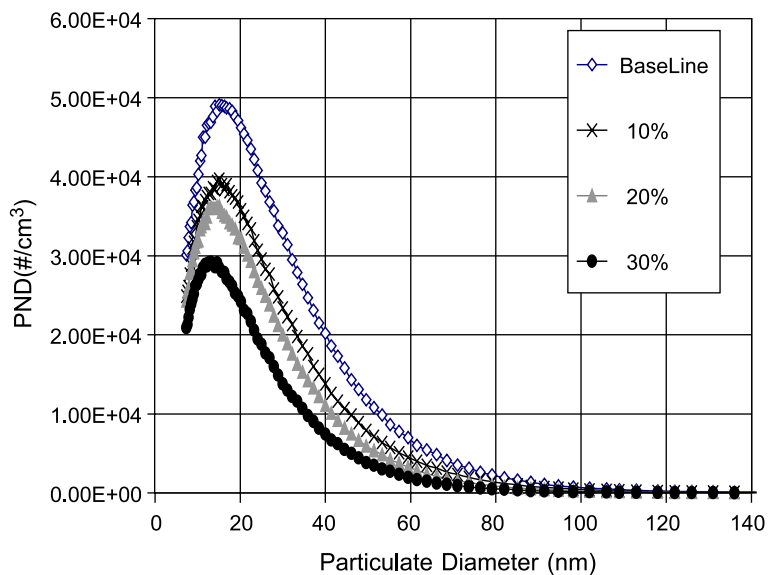


Fig. 6. Size distribution of particle emissions from T63 engine at idle for various JP-8/Norpar-13 blends.

impact on the surface growth and coagulation stages, which are the processes that affect particle size.

3.3. Cetane number improvers

Alkyl nitrates have been found to be effective cetane number improving additives. Increased cetane number diesel fuels have a lower ignition delay time, which result in improved engine performance and reduced emissions. Based on the dramatic improvements in diesel engine emissions with the ignition promoters, two cetane improvers were evaluated. The most widely used cetane-improving additive is 2-ethylhexyl nitrate (2-EHN). The additive is thermally unstable and decomposes at high temperatures to release radicals that accelerate oxidation, and thus, promote combustion. Isobutyl nitrate was also evaluated to assess effects of nitrates with different alkyl groups. Results show that the nitrate compounds were ineffective in reducing PND or affecting particle size in the T63. These results are consistent with previous research on a J79 combustor fueled with JP-5, which showed alkyl nitrates to be ineffective in reducing particulate emissions. [14] Furthermore, results in shock tube experiments have shown the ineffectiveness of 2-EHN in reducing ignition delay time of JP-8 even when added at 50% by volume [15]. Development of additives that reduce the ignition delay time of jet fuels are of interest since they may have similar beneficial effects on emissions as cetane improvers have on diesels.

3.4. Calculation of particulate matter (PM) mass emissions and identification of polycyclic aromatic hydrocarbon (PAH) chemical composition

In addition to measuring the PND and size distribution, it is important to consider the mass concentration and chemical composition of PM when characterizing the emissions from a combustion source. Since the total mass of PM emissions has both regulatory and health implications and the value is not easily inferred from the particle size data, direct measurement of the total mass is necessary. In addition, it is possible that alterations to the PND and size distribution may not directly correlate to changes in the total PM mass. Identification of the chemical composition of the PM is desirable since certain PAH species have been recognized as carcinogens. Therefore, it would be beneficial to determine how a chemical additive alters the total concentration of these species. Furthermore, quantitative information about the PAH composition may provide valuable insight into the mechanism of soot formation as these species have been identified as important precursors.

There are three methods for the measurement of PM mass emissions that can be employed in our laboratory: (1) collection of PM via flow-through filtration with subsequent off-line quantification, (2) on-line measurement using a tapered element oscillating microbalance (TEOM), and (3) calculation using particle size distribution data. During collection via a sample filtration, a quantified volume of undiluted combustor exhaust is sampled with a Roseco engine smoke emissions sampler, and PM is collected using Whatman QMA-type quartz filters. Quantification of the sample mass is conducted by off-line analysis with a LECO Multiphase Carbon Analyzer (assumes PM is primarily

comprised of carbon). The exhaust PM mass concentration is determined by normalizing this weight to the total volume of sample gas passed through the filter. Overall, this sampling approach has a high trapping efficiency for compounds of moderate to low volatility, and provides a PM sample that can be subsequently analyzed to determine its elemental and molecular composition. The major drawback of this method is that samples must be collected under a steady-state condition; therefore, data cannot be collected during the addition/removal of an additive to the engine fuel flow.

On-line measurement of PM mass emissions is possible using the TEOM. The major advantage to this approach is that PM mass emissions are measured real-time during steady or transient operation of the combustor. Therefore, dynamic changes in the mass emissions due to an additive can be observed (similar to that observed with the PND data shown in Fig. 3). A possible complication with this instrument is that the measurement can be significantly affected by adsorption/desorption of water and volatile organics on the filter element.

The third approach is to estimate PM mass using the particle size distribution data; however, assumptions for the particle geometry and density must be made. Typically, soot particles are assumed to have a spherical geometry and a density of approximately 1.8 g/cm^3 [10]. This density value is estimated as a compromise of the value for a representative PAH (e.g., 1.27 g/cm^3 for pyrene) and graphitic carbon ($\sim 2.2 \text{ g/cm}^3$), which are believed to encompass the range of organic species within the PM. Obviously, the mass estimation is significantly affected by the accuracy of the size distribution data and validity of the assumptions for particle geometry and density.

Due to the inherent complexity associated with the measurement of the PM mass emissions, these were not routinely made during initial additive evaluation on the T63. Rather, the measurements were made for additives that were identified to significantly alter PND or particle size distribution. Due to time constraints, only a small number of mass measurements were made during this study, and the results in this section will be limited in scope. As discussed previously, the addition of both PA-5 and Norpar-13 to the baseline JP-8 fuel rendered significant reductions in the measured PND. Therefore, mass emissions were measured during testing with these additives. For testing conducted at the cruise condition with PA-5, reductions in mass emissions measured with the TEOM and calculated using the particle size distribution data are compared to the reduction in the PND in Table 4.

As shown in Table 4, the reductions in the measured and calculated mass emissions were significantly lower than those observed for the PND. This indicates that the total

Table 4
Comparison of reduction in mass concentration and PND emissions for testing with various concentrations of PA-5 at cruise

Concentration of PA-5 (mg/l)	% Reduction in particle number density	% Reduction in mass concentration using TEOM	% Reduction in mass concentration using size distribution
1000	51	21	35
2000	63	25	47
3000	67	25	51

mass and particle size emissions are most likely not linearly related, which reiterates the necessity of these mass measurements. It can be observed that the mass emissions were further reduced with increases in PA-5 concentration for the calculated value, while it was independent of concentration for the TEOM measurement. In addition to the differences in the mass reduction values, a discrepancy in the absolute value of the mass concentrations for the various methods used was observed. At the baseline (no additive) cruise condition, the size distribution data rendered a calculated value of approximately 28.3 mg/m^3 while the TEOM measured approximately 7.6 mg/m^3 . When measured using the filtration method and LECO analysis, the mass concentration for this condition was approximately 16.8 mg/m^3 .

The filtration method was also used to measure mass concentrations of PM for testing with various blend percentages of Norpar-13. For testing with 25% Norpar-13 at the idle condition, the PND was reduced by approximately 45% relative to the neat conditions while the reduction in mass via the calculated and filtration methods were approximately 64% and 69%, respectively. Under these conditions, it appeared that blending with Norpar-13 was more effective at reducing the total mass of PM emissions than the PND emissions. This is an important observation because it demonstrates that alterations to the mass and PND emissions may not follow the same trends for different additives (i.e., mass always decreases at faster rate than PND). Discrepancies in the absolute mass concentration measurements—calculated value of 2.8 mg/m^3 and filtered value of 5.4 mg/m^3 for untreated JP-8 at the idle condition—were also observed. Efforts are underway to explain and minimize these differences in the future. Despite the discrepancies in the absolute value of the mass concentrations, it is reasonable to infer the effect of an additive on the PM mass emissions if the techniques are self-consistent when normalized.

There are several possible causes for the discrepancies in the absolute mass values between the various methods. With respect to the value calculated using the size distribution data, the major sources of error are most likely associated with the assumptions of the particle geometry and density. Varying either of these could lead to an increase or reduction in the total mass value and provide for better agreement with the other methods. The assumption that all particles have the same density is also a likely source of error. There may be significant differences in the physical characteristics of the PM depending upon the combustor operating conditions. Variations in the physical properties of the PM may explain the observation that the calculated mass at the cruise condition was higher than the other methods but the opposite was observed at the idle combustor condition. For the TEOM measurements, the major source of variability is most likely adsorption/desorption of moisture (which is high in concentration in the exhaust) and volatile organics on the filter element. This is also a concern for testing with the filtration measurements using the Roseco engine smoke emissions sampler. However, there is the added complication that the quantification for this method is performed off-line (must be transferred for analysis) with the assumption that the PM is primarily carbon; both can increase variability in the data. In addition, the filters were not preconditioned prior to use or analysis. Therefore, the quantity of volatile organics on the filter during analysis could vary depending on the history of the sample. Despite the difficulties with the filtration approach, it is believed to be the most accurate since assumptions regarding the physical characteristics of the particles are not made (e.g., calculation method) and it is

less affected by sampling artifacts (e.g., moisture adsorption on TEOM filter element) during measurement.

Information about the PM chemical composition can be obtained using an analytical method with the samples collected using the filtration method. The procedure involves the thermal desorption of the volatile PM fraction with subsequent identification and quantification using a Gas Chromatograph-Mass Spectrometer. This technique permits for the identification and quantification of a wide range (typically 16 separate species) of PAHs [16]. This method has been used to analyze the PM from a limited number of test conditions, and data analysis is in-progress. As a representative example of the data that can be obtained, the total PAH concentration was reduced from approximately $1.74 \times 10^{-1} \text{ mg/m}^3$ for the neat condition to $6.8 \times 10^{-2} \text{ mg/m}^3$ (61% reduction) for testing with 25% Norpar-13 at idle. Major reductions were observed for a number of individual PAHs, which included fluoranthene (62%) and pyrene (65%). Overall, this analytical approach provides the opportunity for a broader understanding of the effects of the chemical additives on PM emissions. It is anticipated that chemical characterization will be routinely employed during the subsequent evaluation of additives that are found to be effective at reducing PND emissions.

4. Conclusions

The first series of tests under a current Air Force program to develop and/or demonstrate fuel additives that reduce particulate emissions from turbine engines was completed. The performance of 17 additive candidates was assessed in a T63 helicopter engine. It was found that diesel cetane improvers and commercially available additives designed to reduce emissions in internal combustion engines were relatively ineffective in reducing particulate emissions from the T63. Tests with blends of JP-8 and Norpar-13 demonstrated the potential environmental benefits of blending JP-8 and a clean (low aromatic and low sulfur) fuel as it reduced PND by 52% when blended at 30% by volume in jet fuel. In addition, preliminary analysis of collected soot particles shows that Norpar-13 significantly reduced the concentration of PAHs in the samples. The thermal stability Betz + 100 additive was shown to be ineffective in the T63 even at concentrations up to 40 times the recommended value. One of the proprietary detergent-type additives, PA-5, was the most effective as it reduced PND by 67% at 3000 mg/l ($\sim 0.30\%$ volume). Although detergent-type additives are believed to have positive long-term effects on emissions, it was demonstrated that these could produce immediate reductions in particulate emissions depending on additive chemistry.

Additive companies have been informed on the performance of their additives, and several have provided additional formulations for evaluation. Future studies will evaluate these as well as model compounds. Studies will include testing in the T63 engine and in atmospheric and high-pressure combustors. The combustors will have optical access to employ laser-based techniques to investigate the effects of additives on soot formation, flame temperatures and OH radical production. These techniques will aid in understanding the mechanisms by which additives impact soot particulate formation and destruction in advanced and legacy turbine engine combustors.

Acknowledgements

The authors gratefully acknowledge Dr. Mel Roquemore for his technical advice, Mr. Gerald Ewing of AdTech Systems Research for his technical support in operating the T63 engine, and Mr. Joel Everhart for his assistance in reducing test data.

References

- [1] J. Bacha, F. Barnes, M. Franklin, L. Gibbs, G. Hemighaus, N. Hogue, D. Lesnini, J. Lind, J. Maybury, J. Morris, Aviation Fuels Technical Review, Chevron Products Co., San Ramon, CA, 2000.
- [2] Federal Register (July 18, 1997).
- [3] US Environmental Protection Agency (USEPA) Fact Sheet (July 17, 1997).
- [4] US Environmental Protection Agency (USEPA), Evaluation of Air Pollutant Emissions from Subsonic Commercial Jet Aircraft, Office of Mobile Sources, Ann Arbor, Michigan, report no. EPA420-R-99-013, Appendix A, 1999 (April).
- [5] D.E. Hagen, P.D. Whitefield, Particulate emissions in the exhaust plume from commercial jet aircraft under cruise conditions, *J. Geophys. Res., (Atmos.)* 101 (1996) 19551–19557.
- [6] S.P. Heneghan, S. Zabarnick, D.R. Ballal, W.E. Harrison III, JP-8 + 100: the development of high-thermal-stability jet fuel, *J. Energy Resour. Technol.* 118 (1996 Sept.) 170–179.
- [7] Universal Technology and C4e, JP-8 + 100 Performance Assessment at Portland and Kingsley ANG Units, 1998 (July). Distribution limited to US Department of Defence employees and contractors only.
- [8] Universal Technology, Engine Maintenance Trends at the 1st Fighter Wing, Langley AFB, VA after Conversion from JP-8 to JP-8 + 100, 1999 (February). Distribution limited to US Department of Defence employees and contractors only.
- [9] Universal Technology and C4e, Study of JP-8 + 100 Impact on C-130 Aircraft at 123 AW, KY ANG, 2000 (September). Distribution limited to US Department of Defence employees and contractors only.
- [10] D.S. Liscinsky, M.B. Colkett, D.J. Hautman, B. True, Effect of Fuel Additives on Particle Formation in Gas Turbine Combustors, AIAA 2001-3745, AIAA Joint Propulsion Conference, 2001.
- [11] E. Corporan, W.M. Roquemore, A. Jacobson, W.E. Harrison, D. Phelps, Air Force Programs to Reduce Particulate Emissions from Aircraft, AIAA 2002-3722, AIAA Joint Propulsion Conference, 2002.
- [12] A.W. Lefebvre, *Gas Turbine Combustion*, 1st ed., Hemisphere Publishing Corporation, New York, 1987.
- [13] C.A. Amann, D.C. Siegla, Diesel particulates—what they are and why, *Aerosol Sci. Technol.* 1 (1982) 73–1001.
- [14] M.W. Shayeson, Reduction of Jet Engine Exhaust Smoke with Fuel Additives, SAE Paper No. 670866, Society of Automotive Engineers, Inc., New York, 1967.
- [15] S.S. Sidhu, J.L. Graham, D.C. Kirk, L.Q. Maurice, Investigation of the ignition characteristics of jet fuels: JP-7, JP-8 and JP-10. 22nd International Shock tube and Shock Wave Symposium, London, UK, Paper No. 3810 1999 (July).
- [16] J.R. Klosterman, Direct thermal desorption of combustion residues by GC-MS, Proceedings of the Society of Advancement of Materials and Process Engineering (SAMPE), 46th International Symposium and Exposition, Long Beach, CA, 2001 (May).

Appendix BB
Modeling Soot Formation in a Stirred Reactor

INTENTIONALLY LEFT BLANK

GT2004-54001

MODELING SOOT FORMATION IN A STIRRED REACTOR

Meredith B. Colket, III
United Technologies Research Center
East Hartford, CT

Robert J. Hall
West Hartford, CT

Scott D. Stouffer
University of Dayton Research Institute
Dayton, OH

ABSTRACT

The formation of carbonaceous particulate matter and polycyclic aromatic hydrocarbons has recently been studied (Stouffer, et al, 2002 and Reich, et al, 2003) in a toroidal well-stirred reactor using ethylene as the fuel, with and without the additive ethanol. In the later work, modeling of the gas-phase species was performed and compared to the experimental trends. In the present study, a modified version of the CHEMKIN-based code for 'perfectly stirred reactors' has been used to model soot particle formation, including computations of particle mass and smoke number. Detailed soot formation routines have been extracted from Hall and coworkers (1997), who modeled soot formation in flames. Experimental trends are accurately modeled by the code with quantitative accuracies generally within 50%. The importance of accurate knowledge and control of reactor temperature is discussed. In fact, scatter in the original experimental study can be largely attributed to inadequate temperature control. Speculation for differences between the model and experiment are offered while additive effects and the well known 'soot bell' are discussed. For the initial experiments examined by Stouffer et al, the effect of the additive is largely due to temperature differences.

Keywords: Soot/smoke Formation, Modeling, Stirred Reactors, Ethylene, Fuel-Additives, Ethanol, Soot Bell

INTRODUCTION

Combustion-generated soot particles from both land-based and airborne sources pose a significant health risk and are the subject of stringent new EPA regulations (PM_{2.5}) in the United States. In addition, soot contributes to thermal radiation loads on combustor liners and turbine blades. A quantitative understanding of the soot growth and oxidation mechanism and the ability to model these processes are critical to the development of strategies to control emissions.

In recent studies on understanding the effects of additives on soot formation in a well-stirred reactor, Stouffer, et al (2002) and Reich, et al (2003) observed contrasting effects of the additive ethanol on soot formation during the combustion of ethylene. Generally, the same facility was utilized for the two sets of experiments. It was speculated by Reich, et al that the differences were due to a temperature effect due to reactor changes between the sets of experiments.

It is the objective of this study to analyze the experimental results and to perform some modeling of soot formation in a stirred reactor to help offer specific explanations for the contrary observations between the two experimental studies.

WELL-STIRRED REACTOR

A toroidal-shaped, well-stirred reactor (WSR) research combustor with a volume of 250 mL was used for the study. Experimental results analyzed in this study have previously been presented in detail by Stouffer, et al 2002. A cross section of the reactor and jet ring is shown in Figure 1. The design is a modification of an earlier WSR design by Nenniger et al (1984) and Zelina (1995) and features an Inconel jet ring with 48 fuel/air jets. The upper and lower halves of the toroidal reactor are cast from zirconia. (In subsequent studies, Reich, et al (2003) used silicon carbide because of its resistance to thermal cracking. The higher thermal conductivity of SiC presumably resulted in significant differences in the apparent experimental results.) The ceramic reactor is contained inside a steel housing, and has a 2-inch diameter stack connected to the exhaust port which forms the plug flow reactor (PFR) section. The jet ring is cooled by nitrogen impingement cooling to avoid autoignition of the fuel-air mixture within the jet ring manifold.

The three fuels used in the current study were neat ethylene and two ethylene-ethanol mixtures: one with 5% of the fuel mass from the oxygen in the ethanol (14.4% ethanol by mass) and the second with 10% oxygen. With these fuels the WSR

operates stably at high equivalence ratios ($1.8 < f < 2.6$), which allows measurement particulates and smoke in a range of conditions from soot inception through the formation of carbonaceous soot.

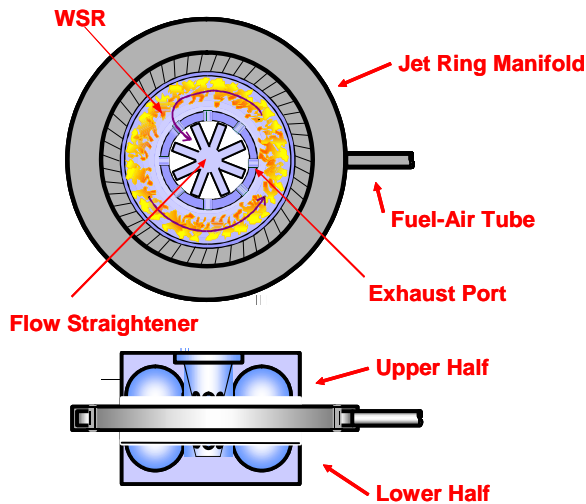


Figure 1. Schematic of WSR Design

A sampling probe penetrated the exhaust stack, entering the plug flow region above the reactor. Soot samples extracted with the probe were collected on filters from both the plug flow region 16 cm downstream of the WSR and from the inside of the toroidal WSR volume on paper. The gas sample was first pulled through a 25 cm-long oil-cooled probe with an inside diameter of 0.47 cm. The probe was cooled to 150°C by circulating oil through the outer jacket. The gas then passed through an electrically heated (constant surface temperature of 150°C) 2-meter long sample line before passing into a Roseco engine smoke emissions sampler.

The volume of the sample gas collected for each test was 7.08 liters. Each sample required 30-60 seconds to collect. The samples acquired on the paper filters (Whatman #4) were analyzed using the SAE ARP1179 procedure⁷ to determine the smoke number based on reflected light from the samples.

PSR MODELING APPROACH

The chemical kinetic modeling was performed utilizing a modified version of the CHEMKIN II-based code for stirred reactors (Glarborg, et al, 1988 and Kee, et al, 1991). A conceptual schematic of a stirred reactor is provided in Fig. 2.

For a perfectly stirred reactor (PSR), sufficiently intense mixing is assumed such the concentrations of all species and temperature are uniform throughout the reactor and that these values are identical to the exit conditions. Additional equations have been added to include computations of soot formation. The original equations treated by the PSR code include the species and energy conservation equations:

$$\dot{m}(Y_k - Y_k^*) - \dot{\omega}_k^g W_k V = 0, \quad k = 1, 2, \dots, K$$

$$\dot{m} \sum_{k=1}^K (Y_k h_k - Y_k^* h_k^*) + Q = 0$$

where Y_k is the mass fraction of the k th species (a total of K species); \dot{m} is the mass flow rate through the reactor volume, V ; W_k , the molecular weight of the k th species; $\dot{\omega}_k^g$, the molar rate of production by chemical reaction of the k th (gaseous) species per unit volume; h_k , the specific enthalpy per unit mass of the k th species; and Q , the reactor loss. The superscript (*) indicates the inlet conditions.

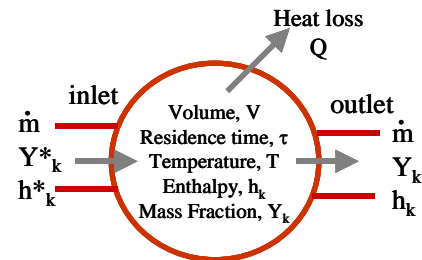


Figure 2. Schematic of Perfectly Stirred Reactor

The growth of soot spheroids in the reactor has been modeled as a classical aerosol dynamics problem, involving the division of the size range of interest into discrete intervals or size classes with a logarithmic transformation of the size range, and then deriving a source for the size class mass densities with terms representing inception, surface growth (or oxidation) and coalescence. The sectional analysis follows the analysis developed by Gelbard and Seinfeld (1980) and Gelbard, Tambour and Seinfeld (1980). The method used in this work incorporates selected algorithms of the well-known MAEROS program (Gelbard, 1982). Surface growth and coalescence are assumed to take the free molecular form and the spheroids consist of the single component carbon. Furthermore, it is assumed for this sectional analysis that the boundaries of the sections vary on a log scale. The total number of particle sections is M . Additional details of the application of the sectional analysis to modeling soot formation have been developed and described in detail by Hall, et al (1997). The extension to stirred reactors is made through the use of the modified governing equations:

$$\dot{m}(Y_k - Y_k^*) - (\dot{\omega}_k^g + \dot{\omega}_k^s) W_k V = 0, \quad k = 1, 2, \dots, K$$

$$\dot{m}(Y_k - Y_k^*) - \dot{Q}_k V = 0, \quad k = K + 1, K + 2, \dots, K + M$$

$$\dot{m} \sum_{k=1}^K (Y_k h_k - Y_k^* h_k^*) + Q = 0$$

where the extra equation (series) represents the conservation equations for the sectional (particulate) species. Y_k ($k = K+1$ to M) represent the mass fractions of the M sectional 'species' or

particulates; $\dot{\omega}_k^s$ is the molar rate of production of the k th gaseous species per unit volume due to reactions involving soot particulates (i.e., scrubbing/replenishment of gaseous species from surface reactions during soot growth/oxidation processes); and \dot{Q}_k is the net mass rate of change of particulates in section k per unit volume due to aerosol processes (including soot inception, surface growth and oxidation, as well as collisional dynamics). The enthalpy of all the sectional species were assumed equivalent to a large polycyclic aromatic hydrocarbon (PAH), that is, slightly larger, but nearly identical to that for condensed carbon (0.0 kcal/gm). A total of 20 soot sections were assumed for this study, ranging from an equivalent midpoint particle diameter of 0.78 nm to 10.8 μm (assuming a soot density of 1.8 gm/cc).

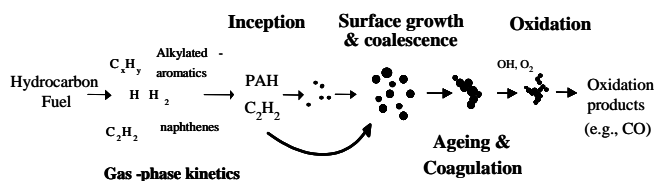


Figure 3. Sequence for Soot Formation and Oxidation

The soot dynamics model generally follows the schematic depicted in Figure 3. The model treats gas-phase kinetics, soot inception/nucleation, surface growth and oxidation, as well as collisional coalescence; ageing/carbonization and coagulation effects are not included. For simplicity, nucleation is computed based on the formation of naphthenyl radicals as described by Hall, et al (1997), although there is ample justification for using a higher molecular weight polycyclic aromatic hydrocarbon for description of inception rates. Surface growth is based upon the work by Harris and Weiner (1983) and hence acetylene is assumed to be the only surface growth species. Note, that since small PAH are treated as soot in this model, the mass growth due to PAH addition to soot is not excluded. Oxidation by OH (Neoh, et al, 1981) and O₂ (Nagle and Strickland-Constable, 1963) were included utilizing the formulism presented by Hall et al (1997). For this PSR modeling, the collisional efficiency of OH reaction with soot was reduced by a factor of three in an attempt to model the earlier data of Zelina (1995). Temperature data was not available for those simulations; hence, simulations were performed assuming adiabatic conditions.

For the atmospheric pressure conditions of this investigation, the coalescence rates were assumed to be in the free molecular regime; an average collisional enhancement factor of 1.5 has been utilized to simulate attractions from van der Waals forces (see, e.g., Harris and Kennedy, 1988).

The PSR model was run with the detailed reaction set for ethylene that has been utilized in previous soot modeling efforts (Colket and Hall, 1994 and Hall, et al, 1997) in laminar

premixed and diffusion flames. To this mechanism, species, reactions and related thermodynamics for ethanol chemistry originally developed by Marinov (1998), and as assembled by Song, et al, 2003 has been included. The total mechanism has 67 species and 388 reactions.

Normally, exit species concentrations and temperatures are determined by the PSR code; this modified code also computes the particle size distribution, from which total particle mass and number densities can be calculated. A correlation developed by Colket, et al (2003) for the relationship between smoke number and total particle mass, m , in mg/m^3 where the volume is based upon conversion of the flame gases to atmospheric pressure at 289K. Ambient conditions are utilized for the reactor studies as they are close to characteristic conditions for the smoke number (SN) measurement device. The correlations developed by Colket and coworkers are:

$$\begin{aligned} \text{if } m \text{ (mg/m}^3\text{)} < 2.5 \text{ then: } & \text{SN} = -1.8743 * m^2 + 12.117 * m \\ \text{if } m \text{ (mg/m}^3\text{)} > 2.5 \text{ then: } & \text{SN} = 12.513 * m^{0.4313} \\ \text{or} & \\ \text{if SN} < 18.7, \text{ then: } & m = 3.232 * (1 - (1 - \text{SN}/19.58)^{1/2}) \\ \text{if SN} > 18.7, \text{ then: } & m = 0.002751 * \text{SN}^{2.319} \end{aligned}$$

These empirical curves were shown to be in good agreement with other literature data (Champagne, 1971).

RESULTS AND DISCUSSION

The focus of the present work is the simulation of the experimental observations for the first reactor study (Stouffer et al, 2002). Note that temperature data presented in this study has not been previously reported.

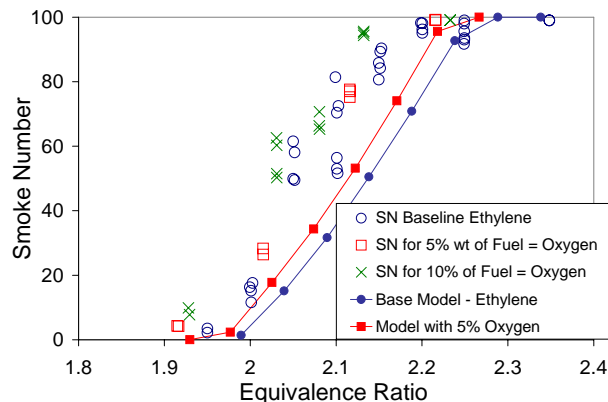


Figure 4. Experimental and Predicted Smoke Numbers for the Ethylene and Ethylene/Ethanol Fuel-Rich Mixtures

Simulations of the well-stirred reactor experimental studies were performed with this 'sooting' PSR code. Reactor volume and mass flow rates were matched to the experimental conditions for cases with pure ethylene as the fuel as well as for the ethylene/ethanol (5% oxygen) blend. Adiabatic conditions

were assumed; hence, the heat loss term, Q , was assigned to be zero. Based on mass flow rates, reactor volume and gas density, reactor residence times were computed to range from 8 to 8.5 milliseconds. Predicted smoke numbers (SN) are compared in Fig. 4 to the experimental data. Comparisons to experimental data sets indicate that the model under predicts the level of smoke produced in the experiment, although the trend is well matched. The model predicts a slight increase in smoke number when ethanol is added, consistent with an increase in smoke for both the cases in which 5% and 10% oxygen by mass was added (as ethanol) to the fuel (ethylene), as shown in Fig. 4. Note the relatively large scatter and the opposite trends with added ethanol in these initial experimental data relative to that reported more recently (Reich, et al, 2003).

To understand the trends and the large experimental scatter, recall that soot formation is known to be a strong function of temperature (Glassman, 1989). Equilibrium temperatures of the the two mixtures are just slightly different. As shown in Figure 5, however, the kinetically-limited (stirred reactor) temperatures are about 40K lower for the cases with the additized fuel. The difference in temperature contributes primarily to the different soot levels, as will be shown below. The dependence of soot formation on temperature depends on which side of the bell-shaped curve the experiments have been performed. The negative trend (decreasing soot with increasing temperature) suggests the tests have been performed on the high temperature side of the soot bell. For characterization of the 'soot bell', see Bauerle, et al, 1994 and included references.

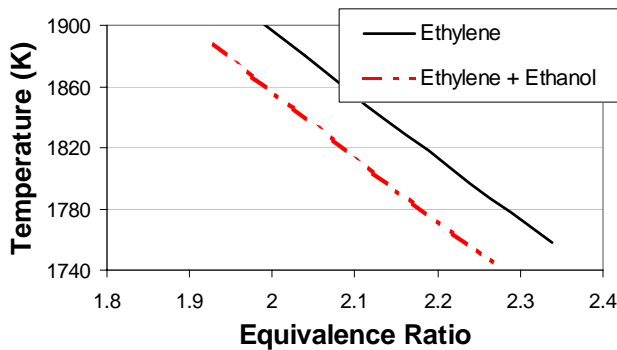


Figure 5. Kinetically Limited Temperatures Computed in the PSR

To determine which side of the soot bell the experiments were performed, reactor temperature data (not reported by Stouffer, et al, 2002) was utilized. Smoke number at the exit of the stirred reactor was plotted vs. the recorded temperature. The data (both ethanol-free and with ethanol) is shown in shown in Fig. 6. The trends are similar, for any given mixture with or without additive. (Some of the data sets have been averaged for purposes of clarity.) Recall that for these early experiments, the walls of the reactor were constructed out of zirconia. Zirconia has a low thermal conductivity and hence it took a long time for the reactor to stabilize. Data was collected during this period

and for a given equivalence ratio, several data points were collected, but at varying temperatures.

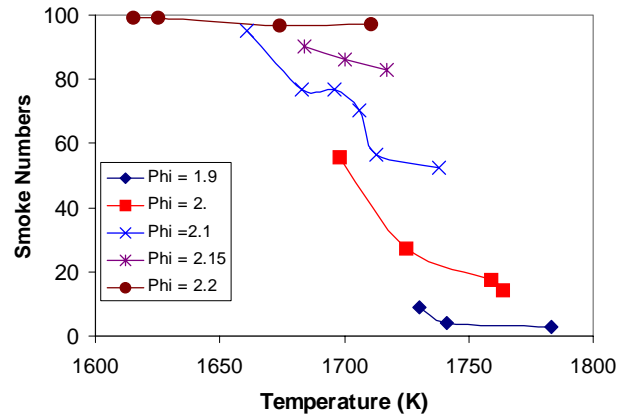


Figure 6. Measured Smoke Number as a Function of the Experimental Temperature

Whether the data from a fixed equivalence ratio or data for a range of equivalence ratios are considered, the data clearly show smoke/soot decreases with increasing temperature and hence the experiments of Stouffer, et al were performed on the high temperature side of the soot bell.

Modeling was performed to ensure consistency with this interpretation. For a fixed equivalence ratio (ϕ) of 2.0 and a fixed residence time of about 8.5 milliseconds, a series of computations were performed over the range of 1400-1900K with varying values of heat loss, Q . (Alternatively, fixed temperature computations could be performed.) The adiabatic reactor temperature for this mixture is about 1900K, a temperature at which little soot is formed. Also note for reference that the experimental temperatures for this set of conditions were about 1770K. The calculated smoke number results are shown in Fig 7. Recall that the oxidation rate (by OH) was suppressed by a factor of three.

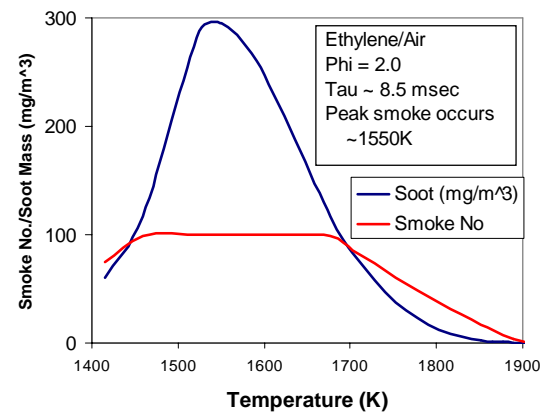


Figure 7. Predicted Temperature Dependence of Smoke/Soot in a Stirred Reactor at $\phi = 2.0$.

The artificial reduction of the OH oxidation rate by a factor of three enabled the simulations of both the Zelina data and the present data assuming adiabatic conditions. Note however, that in both cases, energy loss was not accounted for, which based on the present analysis would have increased the soot predictions. Had a better treatment on the energy loss been available, the higher rate of oxidation might have resulted in a reasonable soot prediction, without the altered oxidation rate. Treatment of such effects will be considered in future studies.

As temperature decreases from the adiabatic condition, soot particulates increase until the smoke number is saturated. As temperature decreases further, the soot production rate decays. The peak soot/smoke level can be estimated to be about 1550K for this mixture. Note that when computations are repeated with corrected oxidation rates, these predicted soot/smoke levels are expected to decrease significantly.

In the pyrolysis work by Bauerle, et al (1994), peak soot formation occurred around 1850K for ethylene and 1800K for benzene. The predicted soot formation in this present work occurs at much lower temperatures. The explanation for the difference is due to the presence of more oxidation species, first because this study involves a fuel-rich mixture ($\phi=2$) vs. pyrolysis and second because in a stirred reactor, the reactants (e.g., O_2) are intimately mixed with the products. Hence, we argue the shift of the soot curve is due to the following:

In shock tubes and at low temperatures when overall reaction rates and soot production follow parallel trends, the soot production is kinetically limited, as linked to overall hydrocarbon decomposition rates. Alternatively, on the high temperature side of the soot bell the thermal stability of aromatic species falls off with increasing temperature. Benzene and other aromatics are recognized to provide the foundation for soot formation (inception) and growth. Loss of these species directly inhibits the production of soot, causing a reduction in soot with increasing temperature. Specifically, the thermal decomposition of a key intermediate species (e.g., phenyl radical or C_6H_5) through $C_6H_5 \Rightarrow 1-C_6H_5 \Rightarrow C_4H_3 + C_2H_2$ increases rapidly with increasing temperature and becomes first competitive with and then dominates over growth reactions (e.g., as initiated by $C_6H_5 + C_2H_2 \Rightarrow C_8H_7$).

In the case of the stirred reactor, in which the reactants (e.g., molecular oxygen) are also present in the soot formation zone, low activation energy oxidation step(s) (such as $C_6H_5 + O_2 = C_6H_5O + O \Rightarrow$ oxidation products) shift the peak in the soot bell to much lower temperatures than are normally observed during pyrolytic studies in shock tubes. Stirred reactors are often utilized to simulate combustors, and the (changing) shape of the soot bell may be an important concern as this work is applied to soot formation in gas turbine engines.

In the subsequent study by Reich, et al (2003), the opposite trend with added ethanol was observed. In those experiments,

the ceramic walls were changed to silicon carbide. The primary objective of the hardware change was to minimize cracking of the walls, but in addition, the much higher thermal conductivity allowed for more rapid thermal stabilization of the reactor – at lower temperatures and with a stronger influence of the cooled external container. The computed curve in Fig. 7 indicates that even at temperatures 100K lower than the present study, there should still be some temperature sensitivity, i.e., lower temperatures should increase soot. However, the experimental data from Reich, et al indicate that soot decreases significantly with the additive; thus either the temperature sensitivity to soot production is lower than Fig 7 indicates, or the temperature difference between the experiments with the neat and additized fuels is negligible. While both effects may contribute, we tend to favor the latter explanation due to the mitigation effects of the silicon carbide walls. At lower temperatures, and at conditions such that the gas temperature between the ethylene and the ethylene/ethanol mixtures are much closer, then the chemical effects due to the presence of the additive should be apparent as described in detail in the latter study.

CONCLUSIONS

- Initial experiments investigating additive effects have been performed on the high temperature side of the soot bell.
- A temperature shift (decrease) due to the presence of the additive is the primary cause of the increase in soot observed in the initial experimental study by Stouffer, et al (2003)
- Better thermal control of the conditions in the work by Reich, et al (2003) enabled investigation of the kinetic mechanisms by which additives effect soot production.
- This work serves as a reminder of the importance of temperature control when comparing soot production rates
- While qualitative features were reproduced by a sooting PSR model, a revised soot model is expected to provide better quantitative predictions of particle mass and size distribution.

ACKNOWLEDGEMENTS

This material is based on research sponsored by Air Force Research Laboratory under agreement number F33615-03-2-2347. The U.S. Government is authorized to reproduce and distribute reprints for Governmental purposes notwithstanding any copyright notation thereon. The authors are very appreciative of Drs. D. Phelps and M. Roquemore of the Air Force Research Laboratories (Wright-Patterson AFB) who have been instrumental in supporting this work. The Strategic Environmental Research and Development Program is acknowledged for the financial support of these activities. The efforts of H. Hollick of United Technologies are very much appreciated for computational support. Finally, Prof. T. Litzinger of The Pennsylvania State University is gratefully

acknowledged for technical discussions and for sharing mechanisms and thermodynamics related to ethanol kinetics. The views and conclusions contained herein are those of the authors and should not be interpreted as necessarily representing the official policies or endorsements, either expressed or implied, of Air Force Research Laboratory or the U.S. Government.

REFERENCES

Bauerle, St., Karasevich, Y., Slavov, St., Tanke, D., Tappe, M., Thienel, Th., and Wagner, H. Gg., "Soot Formation at Elevated Pressures and Carbon Concentrations in Hydrocarbon Pyrolysis", Twenty-Fifth Symposium (International) on Combustion, The Combustion Institute, Pittsburgh, pp. 627-634, 1994.

Champagne, D.L., "Standard Measurement of Aircraft Gas Turbine Engine Exhaust Smoke," ASME 71-GT-88, 1971.

Colket, M. B., Liscinsky, D., Chiappetta, L. Leong, M., Madabhushi, R., Zeppieri, S., Hautman, D., "Mitigation of Particulate Emissions in Engines via Fuel Additives", Air Force Technology Investment Agreement F33615-00-2-2001. UTRC Report No. R03-6.100.0007-1, Donald Phelps, Program Manager, Air Force Research Laboratories, 2003.

Colket, M. B. and Hall, R. J., "Successes and Uncertainties in Modeling Soot Formation in Laminar, Premixed Flames", in Soot Formation in Combustion, H. Bockhorn, ed., Springer Verlag, Berlin, p 417- 470, 1994.

Frenklach, M. and Wang, H., "Detailed Modeling of Soot Particle Nucleation and Growth", Twenty-Third Symposium (International) on Combustion, The Combustion Institute, Pittsburgh, PA, pp. 1559 – 1566, 1991.

Gelbard, F., "MAEROS User Manual", NUREG/CR-1391, SAND80-0822, 1982.

Gelbard, F. and Seinfeld, J. H., *Journal of Colloidal and Interface Sciences*, Vol. 78, p. 485, 1980.

Gelbard, F., Tombour, Y., and Seinfeld, J. H., *Journal of Colloidal and Interface Sciences*, Vol. 76, p. 54, 1980.

Glarborg, P., Kee, R. J., Grcar, J.F., and Miller, J.A. (1986). "PSR: A Fortran Program for Modeling Well-Stirred Reactors", Sandia Report, SAND86-8209.

Glassman, I., "Soot Formation in Combustion Processes", Twenty-Second Symposium (International) on Combustion, The Combustion Institute, Pittsburgh, PA, p. 295- 311, 1989.

Hall, R. J., Smooke, M. D. and Colket, M. B., "Predictions of Soot Dynamics in Opposed Jet Flames", *Physical and*

Chemical Aspects of Combustion: A Tribute to Irvin Glassman, (R. F. Sawyer and F. L. Dryer, eds.) *Combustion Science and Technology Book Series*, Gordon and Breach, PA, pp. 189-230, 1997.

Harris, S. J. and Kennedy, I.M., *Combustion Science and Technology*, Vol. 59, pp. 443- 454, 1988.

Harris, S.J., and Weiner, A.M., *Combustion Science and Technology*, Vol. 31, p. 155, 1983.

Kee, R.J., Rupley, F.M., and Miller, J.A., "Chemkin-II: A Fortran Chemical Kinetics Package for the Analysis of Gas-Phase Chemical Kinetics", Sandia National Laboratories, Albuquerque, SAND89-8009, reprinted March 1991.

Marinov, N. N., *International Journal of Chemical Kinetics*, Vol. 31, pp 183-220, 1998.

Nagle, J. and Strickland-Constable, R. F., "Oxidation of Carbon Between 1000-2000°C", *Proceedings of the Fifth Carbon Conference*, Vol. 1, Pergamon Press, p. 154, 1963.

Nenniger, J. E., Kridiotis, A., Chomiak, J., Longwell, J. P., and Sarofim, A. F., "Characterization of a Toroidal Well Stirred Reactor," Twentieth Symposium (International) on Combustion, The Combustion Institute, pp. 473-479, 1984.

Neoh, K. G., Howard, J. B. and Sarofim, A. F. (1981), "Soot Oxidation in Flames," in *Particulate Carbon Formation during Combustion*, D. C. Siegla and G. W. Smith, eds., pp. 261-282-. Plenum., 1981.

Reich, R. F., Stouffer, S. D. Katta, V. R., Mayfield, H. T., Frayne, C. W., and Zelina, J., "Particulate Matter and Polycyclic Aromatic Hydrocarbon Determination using a Well-Stirred Reactor", AIAA 2003-0664, presented at the 41st AIAA Aerospace Sciences Meeting, Jan. 6-9, 2003.

Song, K. H., Nag, P., Litzinger, T., Haworth, D. C., "Effects of Oxygenated Additives on Aromatic Species in Fuel-Rich, Premixed Ethane Combustion: A Modeling Study" *Combustion and Flame*, Vol. 135, pp. 341-349, 2003.

Stouffer, S. D., Streibich, R. C., Frayne, C. W., and Zelina, J., "Combustion Particulates Mitigation Investigations in a Well-Stirred Reactor," Paper No. AIAA 2002-3723, 38th Joint Propulsion Conference, 2002.

Zelina, J., "Combustion Studies in a Well-Stirred Reactor," Ph.D. Thesis, University of Dayton, Dayton, OH, 1995.

Appendix CC

Modeling the Liquid-Phase Oxidation of Hydrocarbons over a Range of Temperatures and Dissolved Oxygen Concentrations with Pseudo-Detailed Chemical Kinetics

INTENTIONALLY LEFT BLANK



Modeling the liquid-phase oxidation of hydrocarbons over a range of temperatures and dissolved oxygen concentrations with pseudo-detailed chemical kinetics

Nicholas J. Kuprowicz^{a,b,*}, Jamie S. Ervin^{b,c}, Steven Zabarnick^{b,c}

^aPropulsion Directorate, Air Force Research Laboratory, Wright-Patterson Air Force Base, OH, 45433-7251, USA

^bDepartment of Mechanical and Aerospace Engineering, University of Dayton, Dayton, OH 45469-0210, USA

^cUniversity of Dayton Research Institute, Dayton, OH 45469-0116, USA

Received 28 August 2003; revised 23 March 2004; accepted 27 March 2004; available online 23 April 2004

Abstract

The ability of pseudo-detailed chemical kinetic modeling to simulate the oxidation behavior of Exxsol D-80, a paraffin blend whose oxidative characteristics are representative of severely hydrotreated jet fuels, is assessed. The effects of temperature and initial dissolved O₂ concentration on oxidation are considered. A 17-step pseudo-detailed mechanism is shown to provide reasonable simulations of Exxsol D-80 oxidation over a range of temperatures, but not over a range of initial dissolved O₂ concentrations. The addition of alkyl-peroxy radical isomerization to the pseudo-detailed mechanism did not reconcile the initial dissolved O₂ limitation. With the addition of a peroxy radical decomposition reaction to the original 17-step pseudo-detailed mechanism, reasonable simulations of Exxsol D-80 oxidation over a range of temperatures and initial dissolved O₂ concentrations were obtained. Analysis of the rate parameters associated with peroxy radical decomposition suggests that aromatic hydrocarbons play a significant role in the oxidation of fuels, even at low (<1% by weight) aromatic levels.

© 2004 Elsevier Ltd. All rights reserved.

Keywords: Autoxidation; Kinetics; Modeling

1. Introduction

Prior to combustion, the jet fuel in military aircraft is used as a cooling medium. Unfortunately, in the presence of dissolved oxygen and heat, jet fuel undergoes chemical reactions that result in solid deposit formation along heated surfaces. Numerical simulations assist the understanding of experimental measurements and provide a basis to explain complex thermal-oxidative degradation and deposition processes. There are three classes of chemical kinetic mechanisms that have been used by researchers in this area: (i) detailed, (ii) pseudo-detailed, and (iii) global. Simulating the oxidation behavior of a jet fuel by means of detailed kinetics is not practical due to the large number of different

compounds present and their variability among fuel samples. The need for a realistic model of jet fuel oxidation without the impracticality of a detailed kinetics approach has led to the use of pseudo-detailed modeling.

As a first step in modeling fuel additives for thermal-oxidative stability, a kinetic mechanism representing the dominant chemical kinetics of jet fuel thermal-oxidation chemistry has been developed [1,2]. The term pseudo-detailed is used to describe this mechanism, as it represents classes of compounds and is comprised entirely of reactions and rate parameters that are chemically realistic. Table 1(a) lists the 17-step pseudo-detailed mechanism of Zabarnick [2]. Fuel is modeled as a single species, RH, which is assumed to have chemical properties of a straight-chain alkane. Reactions 1 through 4, together with reaction 10, correspond to a simplified autoxidation chain. Chemistry associated with a peroxy radical inhibiting antioxidant molecule (AH) is represented by reactions 5 through 9. The unimolecular decomposition of hydroperoxides (RO₂H) is

* Corresponding author. Address: Air Force Research Laboratory, Propulsion Directorate, AFRL/PR 1950 Fifth Street, Wright-Patterson Air Force Base, OH 45433-7251, USA. Tel.: +1-937-255-5258; fax: +1-937-255-0082.

E-mail address: nicholas.kuprowicz@wpafb.af.mil (N.J. Kuprowicz).

Table 1
Pseudo-detailed chemical kinetic mechanisms

#	Reaction	(a)		(b)	
		A [mol, L, s]	E_a [kcal/mol]	A [mol, L, s]	E_a [kcal/mol]
1	$I \rightarrow R'$	1×10^{-3}	0.0	1×10^{-3}	0.0
2	$R' + O_2 \rightarrow RO_2'$	3×10^9	0.0	3×10^9	0.0
3	$RO_2' + RH \rightarrow RO_2H + R'$	3×10^9	12.0	3×10^9	12.0
4	$RO_2' + RO_2' \rightarrow$ termination	3×10^9	0.0	3×10^9	0.0
5	$RO_2' + AH \rightarrow RO_2H + A'$	3×10^9	5.0	3×10^9	5.0
6	$AO_2' + RH \rightarrow AO_2H + R'$	3×10^5	10.0	3×10^5	10.0
7	$A' + O_2 \rightarrow AO_2'$	3×10^9	0.0	3×10^9	0.0
8	$AO_2' + AH \rightarrow AO_2H + A'$	3×10^9	6.0	3×10^9	6.0
9	$AO_2' + AO_2' \rightarrow$ products	3×10^9	0.0	3×10^9	0.0
10	$R' + R' \rightarrow R_2$	3×10^9	0.0	3×10^9	0.0
11	$RO_2H \rightarrow RO' + \cdot OH$	1×10^{15}	42.0	1×10^{15}	39.0
12	$RO' + RH \rightarrow ROH + R'$	3×10^9	10.0	3×10^9	10.0
13	$RO' \rightarrow R_{\text{prime}} +$ carbonyl	1×10^{16}	15.0	1×10^{16}	15.0
14	$\cdot OH + RH \rightarrow H_2O + R'$	3×10^9	10.0	3×10^9	10.0
15	$RO' + RO' \rightarrow RO'_{\text{term}}$	3×10^9	0.0	3×10^9	0.0
16	$R_{\text{prime}} + RH \rightarrow$ alkane + R'	3×10^9	10.0	3×10^9	10.0
17	$RO_2H + SH \rightarrow$ products	3×10^9	0.0	3×10^9	0.0
18	$RO_2' \rightarrow R' + O_2$	N/A	N/A	1×10^{16}	19.0
19	$RO_2' + R' \rightarrow$ termination	N/A	N/A	3×10^9	0.0

(a) 17 Step Model of Zabarnick [2] (b) 19 step model of present work (Section 3.2).

represented by reaction 11, and the related free radical chemistry associated with this decomposition is represented by reactions 12 through 16. Finally, the chemistry associated with a peroxide decomposer species (SH) is represented by reaction 17. Rate constants for each reaction are also shown in the table.

The initial concentrations of peroxy radical inhibiting antioxidants (AH) and peroxide decomposers (SH) are used to model individual fuel samples. Antioxidant synergism of AH and SH, behavior that has been observed in experiments [3,4], is also correctly simulated with the pseudo-detailed mechanism [2]. The manner in which antioxidants are modeled is one distinguishing feature between pseudo-detailed models and the remaining type of jet fuel oxidation mechanisms-global mechanisms.

Global mechanisms capture thermal-oxidative degradation and deposition behavior through the use of empiricism. A review of global modeling [5] illustrates various techniques used to fit reaction rate parameters for individual fuel samples and experimental conditions. For design applications, where a knowledge of deposit growth is necessary, global chemistry mechanisms have previously been used in computational fluid dynamics (CFD) simulations for their simplicity [6]. In terms of CFD, the pseudo-detailed model has been successfully applied to 2D simulations of thermal-oxidation that did not include surface deposition [7]. The development of pseudo-detailed modeling has been driven by the practical need for CFD simulations that represent the underlying chemistry associated with thermal-oxidative degradation. The goal of this

paper is to extend the pseudo-detailed mechanism of fuel autoxidation to include a range of temperatures and initial dissolved oxygen levels.

As jet fuels are comprised primarily of paraffins and aromatics, knowledge of paraffin oxidation behavior is essential in high-temperature fuels research. Exxsol D-80, a commercially available (Exxon) solvent blend of normal, branched, and cyclic paraffins with less than 1% aromatics (by weight), is one particular paraffin blend that has been used in several oxidation studies [8–10]. As it is highly refined, it contains few naturally occurring antioxidants and, therefore, oxidizes rapidly. Its oxidative characteristics are representative of a highly hydrotreated jet fuel and, thus, should reasonably be represented by the pseudo-detailed mechanism with the assumption that no antioxidants are present.

Exxsol D-80 oxidation measurements of Pickard and Jones [9] involving a range of temperatures (408–438 K) and initial dissolved O_2 concentrations ($0.8\text{--}8 \times 10^{-3}$ M) are used here to investigate the accuracy and limitations of pseudo-detailed modeling. Two distinct aspects of oxidation behavior are examined: (i) the effect of temperature on oxidation for a fixed initial dissolved O_2 concentration ($[O_2]_0$), and (ii) the effect of $[O_2]_0$ on oxidation when temperature is held constant. Varying both the temperature and $[O_2]_0$ conditions provides a stringent test of the assumed mechanism. In addition, the current study addresses the importance of both alkyl-peroxy radical isomerization and alkyl-peroxy radical decomposition-behavior previously assumed negligible in the pseudo-detailed mechanism.

2. Methodology

Simulations of Exxsol D-80 oxidation were performed using the LSODA solver [11] to integrate the multiple differential equations defined by the pseudo-detailed mechanism in a manner consistent with Whitbeck's methodology [12] for chemical kinetic simulations. The computer program used is a modification of Whitbeck's REACT package that utilizes Visual Basic scripts to compute and post-process the simulations without the need for manual manipulation of files. In addition to the individual chemical reactions and their rate parameters (A and E_a), the initial species concentrations are required as input along with the reaction time, temperature, and tolerances for precision of the integration. The output for any simulation is concentration versus time for the species present in the reaction mechanism.

The initial dissolved O_2 concentrations used for the simulations in this work are 8.00×10^{-4} M (10% saturation), 1.68×10^{-3} M (21% saturation), 2.84×10^{-3} M (35% saturation), 4.05×10^{-3} M (50% saturation), 6.01×10^{-3} M (75% saturation), and 8.04×10^{-3} M (100% saturation). These values of $[O_2]_0$ correspond to the Exxsol D-80 measurements of Pickard and Jones [9], as do the temperatures of 408, 413, 423, and 438 K. The initial concentration of the initiator species $[I]_0$ is 1.00×10^{-8} M for all cases. This value of $[I]_0$ yields an initial R^\cdot radical production rate that is large enough to start the autoxidation chain, yet small enough to remain an insignificant source of free radicals once the chain has begun. For consistency with earlier pseudo-detailed modeling studies, an initial concentration of 4.4 M for the fuel species (RH) is used for all cases. Unless otherwise specified, all other initial species concentrations are set to zero.

3. Results and discussion

Comparing simulations with experimental oxidation data when variations in both temperature and $[O_2]_0$ conditions are considered provides a stringent test of the assumed mechanism. The 17 step mechanism, with the rate parameters given in Table 1(a), yielded simulations of oxidation that were appreciably slower than the measurements for all experimental conditions. To increase the overall rate of oxidation predicted by the 17 step mechanism, as will be discussed later in more detail, the activation energy associated with alkyl-hydroperoxide unimolecular decomposition (E_{a11}) was reduced within a kinetically reasonable range of values. Fig. 1 provides a comparison of the 17 step pseudo-detailed model simulations and Exxsol D-80 measurements [9] for the case of a fixed temperature of 413 K and two initial dissolved O_2 concentrations. Fig. 1 shows that with an alkyl-hydroperoxide decomposition activation energy (E_{a11}) of 39.5 kcal/mol, the mechanism provides a reasonable simulation of Exxsol D-80 oxidation for

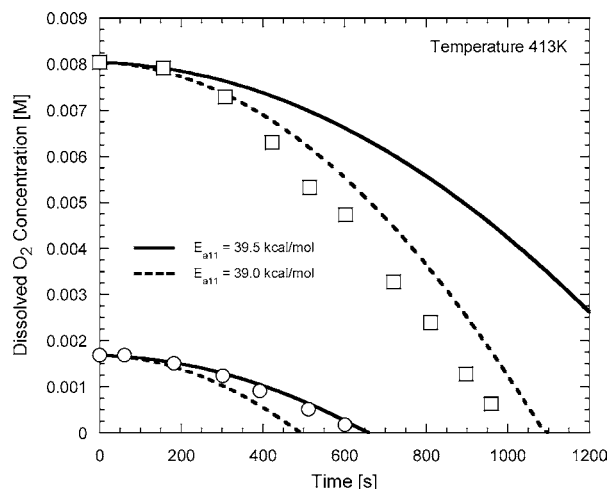


Fig. 1. Comparison of 17-step mechanism simulations and oxidation measurements at 413 K. The curves represent simulations, and the symbols represent measurements.

the lower $[O_2]_0$ level. However for the higher $[O_2]_0$ level, the figure shows that an E_{a11} value of 39.5 kcal/mol results in simulations that are significantly slower than the Exxsol D-80 measurements. By reducing E_{a11} to 39.0 kcal/mol, thereby increasing the overall rate of oxidation even further, the figure shows that the model provides reasonable simulations for the higher $[O_2]_0$ case. This reduced E_{a11} value, however, also results in pseudo-detailed model simulations for the lower $[O_2]_0$ case that are appreciably faster than the measurements. Thus, Fig. 1 shows that no single value of E_{a11} provides reasonable simulations of the Exxsol D-80 measurements over a range of $[O_2]_0$ at a constant temperature.

It is helpful to compare simulations with experimental data over a range of temperatures at a constant $[O_2]_0$. Fig. 2 shows Exxsol D-80 dissolved O_2 consumption

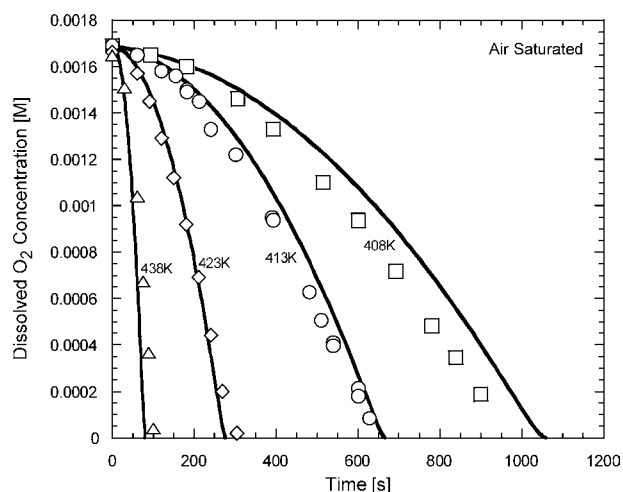


Fig. 2. Comparison of 17-step mechanism simulations and oxidation measurements under air-saturated conditions. The curves represent simulations (with an E_{a11} of 39.5 kcal/mol), and the symbols represent measurements.

measurements [9] as a function of residence time together with simulations of the mechanism (Table 1(a) with $E_{a11} = 39.5$ kcal/mol) for an $[O_2]_0$ of 1.68×10^{-3} M (air-saturated). The figure shows that the mechanism provides reasonable simulations of Exxsol D-80 oxidation over the temperature range 408–438 K. Together, Figs. 1 and 2 show that, for a fixed set of rate parameters and with the assumption that no antioxidants are present, the 17 step mechanism can correctly simulate Exxsol D-80 oxidation over a range of temperatures, but cannot correctly simulate oxidation over a range of $[O_2]_0$. The O_2 limitation is not caused by the selection of E_{a11} to control the overall rate of oxidation simulated by the model. Numerical studies involving parametric variations (within realistic limits) of initiation-related terms (A_1 , E_{a1} , and $[I]_0$) and additional rate parameters to which the model is highly sensitive (A_{11} , E_{a11} , and E_{a3}) yielded the same O_2 limitation.

Although Exxsol D-80 contains few (if any) naturally occurring antioxidants, this does not imply that antioxidants were not present in the Exxsol D-80 sample. Fuel samples may, over time, form species with antioxidant character during storage [13]. The possibility of antioxidants being responsible for the O_2 limitation shown in Fig. 1 was investigated. The increase in time for complete dissolved O_2 consumption due to combinations of AH and SH in the 17 step mechanism, however, was found to be weakly dependent on $[O_2]_0$. Thus, the mechanism of Table 1(a) is lacking important chemical reactions which either (i) increase the rate of oxidation at high dissolved O_2 concentrations or (ii) decrease the rate of oxidation at low dissolved O_2 concentrations. In previous pseudo-detailed chemical kinetic mechanisms for thermal oxidation [1,2], reactions involving alkyl-peroxy radical isomerization and alkyl-peroxy radical decomposition were assumed negligible for simplicity. The following sections describe these reactions and our investigation into their impact on pseudo-detailed modeling simulations.

3.1. Alkyl-Peroxy Radical Isomerization

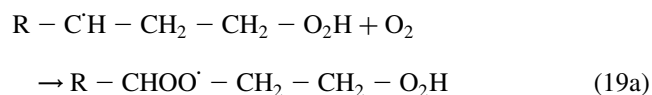
Intramolecular hydrogen abstraction chemistry occurs when a long chain alkyl-peroxy radical (RO_2) forms a five or six membered cyclic transition state to transfer a hydrogen atom from the alkyl chain to the oxygen radical site. The dominant chemistry may be represented by three reactions, where the first reaction is the production of the isomer itself. Isomerization of the alkyl-peroxy radical may be expressed as



where $R - \dot{C}H - CH_2 - CH_2 - O_2H$ is the isomerized molecule. A reasonable assumption for the activation energy associated with isomerization (E_{a18a}) is that it be within the range of 10–15 kcal/mol [14]. This range of activation energies is consistent with other reactions in

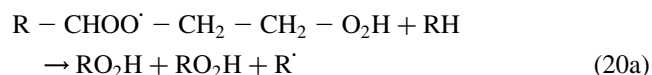
the mechanism (Table 1(a)) involving the extraction of a hydrogen atom from a fuel molecule. The Arrhenius pre-exponential multiplier (A) of unimolecular reactions involving intramolecular rearrangements, in general, has a range of $10^{12} - 10^{15} \text{ s}^{-1}$ [14]. In the present study, A_{18a} is treated as an independent variable, subject to this kinetic constraint, in order to numerically assess the overall influence of alkyl-peroxy radical isomerization on simulations.

The second reaction is the isomerized radical combining with an oxygen molecule, and may be expressed as



where $R - CHOO\dot{C} - CH_2 - CH_2 - O_2H$ is the product of bimolecular combination. The activation energy of this reaction (E_{a19a}) is taken as zero, as it is an addition reaction of a free radical. An Arrhenius pre-exponential multiplier value of $A_{19a} = 3 \times 10^9 \text{ s}^{-1}$ is used for consistency with other bimolecular reactions of the mechanism.

The third and final reaction is the extraction of a hydrogen atom from a fuel molecule by the $R - CHOO\dot{C} - CH_2 - CH_2 - O_2H$ radical. The products of this reaction are a di-alkyl-hydroperoxide species and an alkyl radical. For simplicity, the di-alkyl-hydroperoxide is modeled as two individual alkyl-hydroperoxides and the third reaction may be written as



Since reaction 20a is bimolecular, as in reaction 19a, an A-factor of $3 \times 10^9 \text{ s}^{-1}$ is used. Again, an activation energy E_{a20a} in the range of 10–15 kcal/mol is consistent with other reactions in the 17 step pseudo-detailed mechanism (Table 1(a)) involving the radical extraction of a hydrogen atom from a fuel molecule.

Reactions (18a), (19a), and (20a) were appended to the mechanism to investigate whether their inclusion could resolve the O_2 limitation. Since alkyl-peroxy radicals are formed by a reaction involving oxygen (reaction 2 in Table 1), and the isomerization of alkyl-peroxy radicals yields the production of hydroperoxide species (reaction (20a)) which can decompose to form radicals (reaction 11), it is conceivable that reactions (18a), (19a), and (20a) could result in increased dissolved O_2 consumption at high dissolved O_2 concentrations.

Fig. 3 provides a comparison of the appended mechanism (Table 1(a) with reactions (18a), (19a), and (20a)) simulations and Exxsol D-80 measurements [9] for the case of a fixed temperature of 413 K and two initial dissolved O_2 concentrations (1.68×10^{-3} M and 8.04×10^{-3} M). With an E_{a11} of 39.5 kcal/mol and an A_{18a} of 0.0 s^{-1} , the reactions initiated by isomerization are effectively ‘turned off’ and the model simulations (solid black curves in Fig. 3) are identical to those of the 17 step

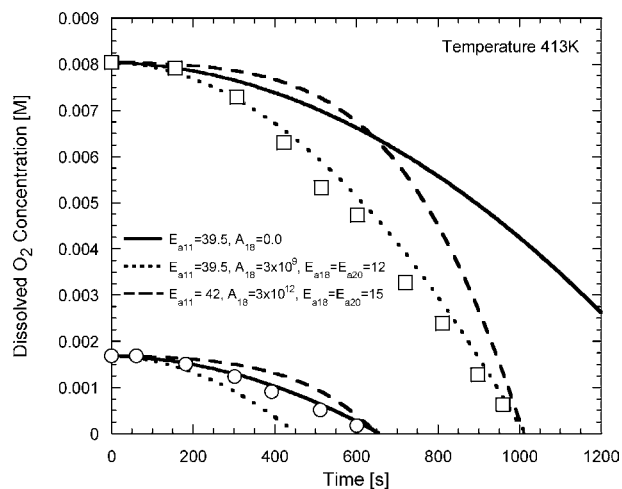


Fig. 3. Influence of alkyl-peroxy radical isomerization on pseudo-detailed modeling at 413 K. Solid black lines correspond to simulations with $E_{a11} = 39.5$ kcal/mol and $A_{18} = 0.0$ s $^{-1}$ (17-step mechanism). Dotted black lines correspond to simulations with $E_{a11} = 39.5$ kcal/mol, $A_{18} = 3 \times 10^9$ s $^{-1}$, and $E_{a18} = E_{a20} = 12.0$ kcal/mol. Dashed black lines correspond to simulations with $E_{a11} = 42.0$ kcal/mol, $A_{18} = 3 \times 10^{12}$ s $^{-1}$, and $E_{a18} = E_{a20} = 15.0$ kcal/mol. Symbols represent measurements.

mechanism. With A_{18a} increased to 3×10^9 s $^{-1}$, and $E_{a18a} = E_{a20a} = 12.0$ kcal/mol, Fig. 3 shows (dotted black curves) that the 20 step mechanism provides reasonable simulations of Exxsol D-80 oxidation for the high $[O_2]_0$ case but provides simulations that are appreciably faster than the measurements for the low $[O_2]_0$ case. It is important to note, however, that this value of A_{18a} (3×10^9 s $^{-1}$) is well below the acceptable kinetic range for A_{18a} described previously ($10^{12} - 10^{15}$ s $^{-1}$), and variations of E_{a18a} and E_{a20a} (each within the limits of 10–15 kcal/mol explained earlier) yield similar results. The dashed black curves in Fig. 3 correspond to $E_{a11} = 42.0$ kcal/mol (value from Table 1(a)), $A_{18a} = 3 \times 10^{12}$ s $^{-1}$, and $E_{a18a} = E_{a20a} = 15.0$ kcal/mol. Each of these rate parameters is reasonable, and the simulations for this case initially appeared promising in reconciling the O_2 limitation. Further analysis of the numerical results, however, revealed that a major fraction of RO_2 radicals were being consumed through the alternate pathway (reactions (18a), (19a), and (20a)) rather than by the autoxidation chain. It is known from hexadecane autoxidation studies at similar temperatures that isomerization is a minor pathway for such long chain peroxy radicals [15]. Thus, in the present system where long chain alkanes are one component of the Exxsol D-80 mixture, alkyl-peroxy radical isomerization is not a realistic explanation for increased dissolved O_2 consumption at high dissolved O_2 concentrations.

As an alternative to reactions which accelerate oxidation at high dissolved O_2 levels, reactions which slow oxidation at low dissolved O_2 levels could also reconcile the $[O_2]_0$ limitation of the mechanism. The decomposition of alkyl-peroxy radicals is now considered as a candidate reaction to reconcile the O_2 limitation.

3.2. Alkyl-peroxy radical decomposition

For simplicity, the decomposition of alkyl-peroxy radicals back into alkyl radicals and molecular O_2 (the reverse of reaction 2)



has been assumed negligible in earlier studies [1,2]. The addition of alkyl-peroxy radical decomposition (reaction (18b)) to the mechanism will result in a reduced rate of dissolved O_2 consumption. To determine whether this reduction is dependent on $[O_2]_0$, reaction (18b) was appended to the mechanism. The A-factor for simple unimolecular fission reactions, in general, has a range of $10^{15} - 10^{17}$ s $^{-1}$ [14]. In the present study, A_{18b} is varied subject to this constraint in order to assess the overall influence of alkyl-peroxy radical decomposition on the simulations. The activation energy E_{a18b} may be taken as the reaction enthalpy (ΔH_{298}^0) since the reverse reaction (reaction 2 in Table 1) has a zero activation energy and a negligible energy barrier [16,17]. Experimentally-derived values of ΔH_{298}^0 for reaction 18b exist for several alkyl species and range from 31.8 to 39.4 kcal/mol [17].

In addition to the self-termination reactions involving RO_2 and R already a part of the pseudo-detailed mechanism, the termination reaction



has been included to better simulate oxidation at near-zero dissolved O_2 concentrations. The activation energy of this reaction (E_{a19b}) is taken as zero, as it is an addition reaction of free radicals, and an Arrhenius pre-exponential multiplier value of $A_{19b} = 3 \times 10^9$ s $^{-1}$ is used for consistency with the other bimolecular reactions.

The rate parameters for the alkyl-peroxy radical decomposition reaction (A_{18b} and E_{a18b}) need to be specified, but for a fixed temperature it is the rate constant (k_{18b}) that influences model behavior. By varying k_{18b} , the impact of alkyl-peroxy radical decomposition on simulations of Exxsol D-80 oxidation at a constant temperature of 413 K was assessed. Values of k_{18b} near 1×10^6 s $^{-1}$ yielded simulations of dissolved O_2 consumption over a range of $[O_2]_0$ that appeared promising. Fig. 4 provides a comparison of simulations with $k_{18b} = 8.8 \times 10^5$ s $^{-1}$ and Exxsol D-80 measurements [9] for a temperature of 413 K and varying initial dissolved O_2 concentrations in the range of $0.8 - 8 \times 10^{-3}$ M (10–100% normal saturation). Fig. 4 suggests that the inclusion of alkyl-peroxy radical decomposition may reconcile the O_2 limitation of the original 17 step mechanism. Thus, consideration of A_{18b} and E_{a18b} values which yield a k_{18b} of 8.8×10^5 s $^{-1}$ at 413 K is warranted.

As explained earlier, the Arrhenius pre-exponential multiplier of reaction 18b (A_{18b}) has a range of $10^{15} - 10^{17}$ s $^{-1}$. For the case where $A_{18b} = 1 \times 10^{16}$ s $^{-1}$, the same pre-exponential used for alkoxy radical

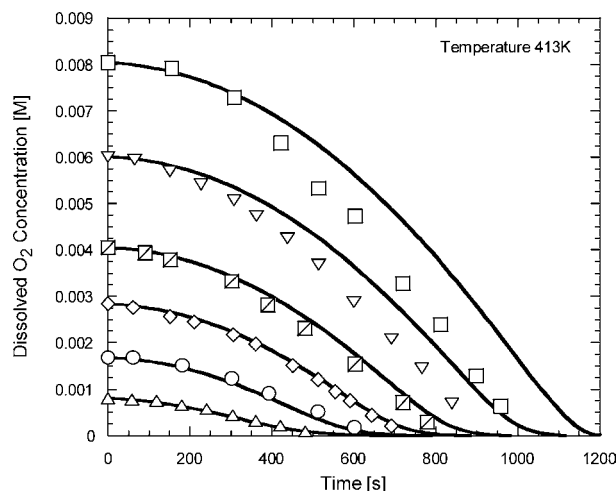


Fig. 4. Comparison of 19-step mechanism simulations and oxidation measurements at 413 K. The curves represent simulations (with $E_{a11} = 39.0$ kcal/mol and $k_{18b} = 8.8 \times 10^5 \text{ s}^{-1}$), and the symbols represent measurements.

decomposition (A_{13}), an activation energy E_{a18b} of 19.0 kcal/mol yields a k_{18b} of $8.8 \times 10^5 \text{ s}^{-1}$ at 413 K. This value of E_{a18b} is significantly less than values of ΔH_{298}^0 cited previously (31.8–39.4 kcal/mol [17]) but, interestingly, is quite close to group additivity estimates [14,18] of ΔH_{298}^0 for the case where R' is modeled as an alkyl-substituted aromatic benzylic radical. For example, when R' is represented by an ethyl benzene benzylic radical, group additivity estimates yield an ΔH_{298}^0 of 18.2 kcal/mol for reaction 18b. The difference in ΔH_{298}^0 values for paraffin and aromatic hydrocarbons involved in the reaction $\text{RO}_2 \rightarrow \text{R}' + \text{O}_2$ has previously been attributed to resonance stabilization of the benzylic radical [19]. For the case where aromatic hydrocarbons are involved, a reaction ΔH_{298}^0 of 20 kcal/mol has been reported [19]. The E_{a18b} value of 19.0 kcal/mol used in the 19 step pseudo-detailed mechanism, therefore, suggests that aromatic hydrocarbons may play a role in the oxidation of Exxsol D-80 although less than 1% aromatics (by weight) are present.

Analysis of the rate of reaction 3 ($\text{RO}_2 + \text{RH} \rightarrow \text{RO}_2\text{H} + \text{R}'$) provides some insight into the manner in which trace quantities of aromatic hydrocarbons may contribute to oxidation. By dividing the 'fuel' compound (RH) into constituent paraffin (RH_p) and aromatic (RH_a) compounds, reaction 3 may be interpreted as the following two reactions



each with its own Arrhenius pre-exponential multiplier and activation energy. For analysis purposes, it is reasonable to assume that the pre-exponentials are approximately equal ($A_{3-p} \approx A_{3-a}$). It follows that

the ratio of reaction rates of these reactions is

$$r_{3-a}/r_{3-p} = ([\text{RH}_a]/[\text{RH}_p]) \times \exp(\Delta E_{a3}/RT)$$

where

$$\Delta E_{a3} = E_{a3-p} - E_{a3-a}$$

For the case where $[\text{RH}_a]/[\text{RH}_p] = 0.01$ (approximately 1% aromatic content), and at a temperature of 413 K, a ΔE_{a3} value of 3.8 kcal/mol will result in the rates being equal. Denisov and Denisova [20] have calculated activation energies for the peroxy radical abstraction reaction (reaction 3) for various peroxy radicals and hydrocarbons. Their results indicate that the activation energy for abstraction from benzylic hydrogen containing species, such as ethyl benzene, is approximately 4 kcal/mol lower than for non-benzylic hydrocarbons, such as *n*-pentane. This indicates that even at low aromatic levels (<1%) reactions of aromatic species can play an important role in the autoxidation of fuels and hydrocarbon mixtures. As nearly all aromatic species in hydrocarbon fuels are alkyl-substituted, it is likely that a large fraction of these contain benzylic hydrogens.

Modeling the aromatic and paraffin compound classes individually in the pseudo-detailed mechanism is of sufficient complexity to warrant a separate study. With the assumption that reaction 18b involves aromatic peroxy radicals and that an E_{a18b} value of 19.0 kcal/mol is reasonable, we return our attention to simulations using the pseudo-detailed mechanism. The appended mechanism (including reactions 18b and 19b) is given in Table 1(b), and simulations of Exxsol D-80 oxidation at constant temperature using this mechanism were previously shown in Fig. 4. Simulations of air-saturated Exxsol D-80 oxidation over a range of temperatures (408–438 K) using this mechanism are provided in Fig. 5. Fig. 5 shows that the 19 step mechanism provides reasonable simulations of oxidation

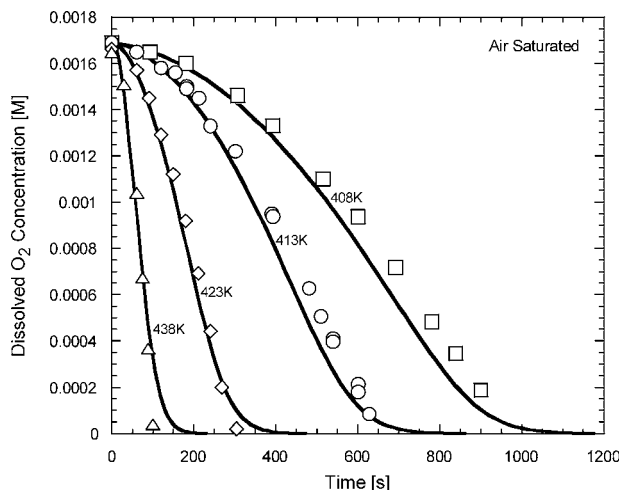


Fig. 5. Comparison of 19-step mechanism (Table 1(b)) simulations and oxidation measurements under air-saturated conditions. The curves represent simulations, and the symbols represent measurements.

over the entire range of temperatures. Together, Figs. 4 and 5 show that the addition of peroxy radical decomposition to the pseudo-detailed model resolves the O₂ limitation of the previous mechanism (Table 1(a)) without adversely affecting the capability of the model to simulate oxidation when the temperature is varied.

4. Summary

The present study investigated the use of pseudo-detailed chemical kinetic mechanisms to simulate the liquid-phase oxidation representative of severely-hydrated jet fuels over a wide range of temperatures and initial dissolved O₂ concentrations. Earlier kinetic mechanisms provide reasonable simulations of oxidation over a range of temperatures, but not over a wide range of initial dissolved O₂ concentrations. Alkyl-peroxy radical isomerization was shown to be unimportant in kinetic modeling of oxygen profiles in Exxsol D-80 oxidation. The addition of peroxy radical decomposition to the pseudo-detailed mechanism enables reasonable simulations of oxidation over a range of temperatures and dissolved O₂ concentrations. Analysis of reaction rate parameters used in the pseudo-detailed mechanism to simulate oxidation suggests that benzylic aromatic hydrocarbons, even at low concentrations, play a significant role in the oxidation of jet fuels. Further analysis, both modeling and experiment, of the relationship between paraffin content, aromatic content, and antioxidant additive concentrations in thermal-oxidative degradation and deposition processes is warranted.

Acknowledgements

This material is based on research sponsored by Air Force Research Laboratory under agreement number F33615-03-2-2347. The US Government is authorized to reproduce and distribute reprints for Governmental purposes notwithstanding any copyright notation thereon. The views and conclusions contained herein are those of the authors and should not be interpreted as necessarily representing the official policies or endorsements, either expressed or implied, of Air Force Research Laboratory or the US Government.

References

- [1] Zabarnick S. Chemical Kinetic Modeling of Jet Fuel Autoxidation and Antioxidant Chemistry. *Ind. Eng. Chem. Res.* 1993;32:1012–7.
- [2] Zabarnick S. Pseudo-detailed chemical kinetic modeling of antioxidant chemistry for jet fuel applications. *Energy Fuels* 1998;12:547–53.
- [3] Scott G. Antioxidants. *Chem Indus* 1963;271–81.
- [4] Zabarnick S, Mick MS. Inhibition of jet fuel oxidation by addition of hydroperoxide-decomposing species. *Ind Eng Chem Res* 1999;38:3557–63.
- [5] Katta VR, Jones EG, Roquemore WM. Modeling of deposition process in liquid fuels. *Combust Sci and Tech* 1998;139:75–111.
- [6] Katta VR, Roquemore WM. Numerical method for simulating fluid-dynamic and heat-transfer changes in jet-engine injector feed-arm due to fouling. *J Thermophys Heat Transfer* 1993;7:651.
- [7] Ervin JS, Zabarnick S. Computational fluid dynamics simulations of jet fuel oxidation incorporating pseudo-detailed chemical kinetics. *Energy Fuels* 1998;12:344–52.
- [8] Balster LM, Balster WJ, Jones EG. Thermal stability of jet-fuel/paraffin blends. *Energy Fuels* 1996;10:1176–80.
- [9] Pickard JM, Jones EG. Liquid-phase oxidation kinetics: paraffin blends. *Energy Fuels* 1998;12:1241–4.
- [10] Jones EG, Balster LM, Balster WJ. Autoxidation of neat and blended aviation fuels. *Energy Fuels* 1998;12:990–5.
- [11] Radhakrishnan, K, Hindmarsh, AC. Description and Use of LSODE, the livermore solver for ordinary differential equations. Report Number UCRL-ID-113855. Lawrence Livermore National Laboratory; 1993.
- [12] Whitbeck M. Numerical modeling of chemical reaction mechanisms. *Tetrahedron Comput Methodol* 1990;3:497–505.
- [13] Kauffman RE, Tirey DA. New techniques to predict and evaluate the effectiveness of antioxidants in jet fuels. *Am Chem Soc Preprints-Div Petrol Chem* 1992;37:412–9.
- [14] Benson SW. *Thermochemical Kinetics*. New York: Wiley; 1976.
- [15] Jensen RK, Korcek S, Zinbo M. Formation Isomerization, and cyclization reactions of hydroperoxyalkyl radicals in hexadecane autoxidation at 160–190 C. *J Am Chem Soc* 1992;114:7742–8.
- [16] Wagner AF, Slagle IR, Sarzynski D, Gutman D. Experimental and theoretical studies of the C₂H₅ + O₂ Reaction Kinetics. *J Phys Chem* 1990;94:1853–68.
- [17] Knyazev VD, Slagle IR. Thermochemistry of the R-O₂ bond in alkyl and chloroalkyl peroxy radicals. *J Phys Chem A* 1998;102:1770–8.
- [18] Ritter ER, Bozzelli JW. THERM: thermodynamic property estimation for gas phase radicals and molecules. *Int J Chem Kinet* 1991;23:767–78.
- [19] Foote CS, Valentine JS, Greenberg A, Liebman JF, editors. *Walling, C. Active Oxygen in Chemistry*. London: Chapman and Hall; 1995. 9. 24–65
- [20] Denisov ET, Denisova TG. *Handbook of Antioxidants*, 2nd ed. Boca Raton: CRC Press; 2000. pp. 26–28.

INTENTIONALLY LEFT BLANK

APPENDIX DD

**Lists of UDRI Publications, Patents, Presentations, Honors and Awards Obtained during
the Contract Period**

AWARDS, PUBLICATIONS, AND PRESENTATIONS
Air Force Cooperative Agreement No. F33615-03-2-2347
(April 2003 to September 2010)

Honors and Awards

1. J.S. Ervin, Faculty Research and Scholarship Award presented by University of Dayton Alumni, 2003.
2. J.S. Ervin, Invited Panelist, Fuel Storage Working Group, Consumer Energy Council of America, 2003.
3. S. Zabarnick, Outstanding Engineer and Scientist Award from the Affiliate Societies Council of the Engineering and Science Foundation of Dayton, 2003.
4. S. Zabarnick, Invitation for Membership on the Steering Committee, International Association of Stability and Handling of Liquid Fuels, 2003.
5. S. Zabarnick, Invited Lecture, Duquesne University Chemistry Department Distinguished Seminar Series, 2003.
6. S. Zabarnick, Session Chair, 8th International Conference on Stability and Handling of Liquid Fuels, Steamboat Springs, CO, 2003.
7. J.S. Ervin, Session Chair, 8th International Conference on Stability and Handling of Liquid Fuels, Steamboat Springs, CO, 2003.
8. S. Zabarnick, Promoted to Full Professor (Joint Appointee), Mechanical & Aerospace Engineering Department, 2003.
9. S.S. Sidhu, George Noland Research of the Year award from Sigma Xi Research Society, 2003.
10. S. Zabarnick, Invited Lecture, Ohio Valley Section of the American Institute of Chemical Engineers, 2004.
11. M. J. DeWitt, Session Chair, 29th Annual DCASS, March 2004.
12. S. Zabarnick, Session Chair, Jet Fuels, Division of Petroleum Chemistry, American Chemical Society National Meeting, Philadelphia, PA, August, 2004.
13. M. J. DeWitt, Granted joint appointment as Associate Professor, Chemical and Materials Engineering Department, 2004.

14. J.S. Ervin, DAGSI Panelist for Selection of Ph.D. Awards, January 2005.
15. R. Assudani, J.S. Ervin, and S. Zabarnick, Best Paper Award, 30th Dayton-Cincinnati Aerospace Sciences Symposium, March 2005.
16. S. Zabarnick, Board of Directors, International Association of Stability and Handling of Liquid Fuels, 2005.
17. M. J. DeWitt, Session Chair, 30th Annual DCASS, March 2005.
18. S. S. Sidhu, University of Dayton Humanities Fellowship for developing undergraduate research in Environmental Sustainability 2005-2006.
19. S. Zabarnick, Vice-Chair, Coordinating Research Council, Aviation Fuel Stability Group, January 2006.
20. M. J. DeWitt, Session Chair, 31st Annual DCASS, March 2006.
21. M. J. DeWitt, Session Chair, 32nd Annual DCASS, March 2007.
22. D.R. Ballal, U.S. National Academic Studies Committees on “Aerospace Propulsion” and “Re-engining of Aircraft” (2005-2008)
23. S. Zabarnick, Session Chair, 1st Ohio Summit on Supply Chain Opportunities in Alternative Energy, June 2007.
24. D. R. Ballal, Honorary Member of International Advisory Board, Gas Turbine Society of Japan, Tokyo, Japan (2006-2011).
25. S. Zabarnick, Chair, Student Awards Committee, International Association of Stability and Handling of Liquid Fuels, 2006-2009.
26. D. R. Ballal, Invited Faculty Seminar, Naval Postgraduate School, Monterey, CA (May 2007).
27. S. Zabarnick, Invited Lecture, Rolls-Royce plc, Derby, UK, June 2007.
28. D. R. Ballal, ASME Vice President for Gas Turbines (2006-2009).
29. D. R. Ballal, Editor-in-Chief, ASME Transactions, Journal of Engineering for Gas Turbines and Power.
30. S. Stouffer, V. Katta, W. Roquemore, G. Justinger, V. Belovich, A. Lynch, J. Miller, R. Pawlik, J. Zelina, S. Roy, K. Grinstead, and J. Gord, Second Prize Art-in-Science Competition AIAA DCASS, March 2007.
31. S. Stouffer, V. Katta, W. Roquemore, Garth Justinger, V. Belovich, A. Lynch, J. Miller, R. Pawlik, J. Zelina, S. Roy, K. Grinstead, and J. Gord, -- First Prize Combustion Art Competition and the 5th US National Meeting of the Combustion Institute, March 2007

32. D. R. Ballal, AIAA International Air Breathing Propulsion Award (2007).
33. S. Stouffer, Session Chair, 3rd Annual Dayton Engineering Sciences Symposium ASME, October 2007.
34. G. Justinger, S.D. Stouffer, R. Streibich, Best Presentation, 3rd Annual Dayton Engineering Sciences Symposium, ASME, October 2007.
35. M. J. DeWitt, Session Chair, 33rd Annual DCASS, March 2008.
36. S. Stouffer, G. Justinger, M. Roquemore, A. Lynch, V. Belovich, J. Gord, K. Grinstead, V. Katta, K. Frische, Second Place in Art-In Science Competition, 33rd Annual AIAA DCASS, March 2008.
37. S. Stouffer, G. Justinger, M. Roquemore, A. Lynch, V. Belovich, J. Gord, K. Grinstead, V. Katta, K. Frische, Third Place Combustion Art Competition, Central States Combustion Meeting, April 2008.
38. S. Stouffer, Session Chair, 4th Annual Dayton Engineering Sciences Symposium ASME, October 2008.
39. SERDP Project of the Year—Weapon Systems and Platforms, “A Comprehensive Program for Measurement of Emissions from military Aircraft,” Team Members: E. Corporan (AFRL), M. DeWitt and C. Klingshirn (UDRI), S. Mahurin and M-D. Cheng (ORNL), R. Kagann and R. Hashmonay (Arcadis), and R. Shores and B. Harris (EPA), November 2008.
40. S. Zabarnick, Session Chair, 34st Annual DCASS, March 2009.
41. S. Stouffer, Session Chair, 34st Annual DCASS, March 2009.
42. S. Stouffer, G. Justinger, M. Roquemore, A. Lynch, V. Belovich, J. Gord, K. Grinstead, V. Katta, K. Frische, Third Place in Art-In Science Competition, 34th Annual AIAA DCASS, March 2009.
43. S. Stouffer, Session Chair, 5th Annual Dayton Engineering Sciences Symposium ASME, October 2009.
44. J.S. Ervin, Affiliate Society Council of Dayton Outstanding Engineer Award, March 2009.
45. S. Stouffer, Session Chair, 35th Annual DCASS, March 2010.
46. M.J. DeWitt, Session Chair, 35th Annual DCASS, March 2010.
47. S. Stouffer, Second Place in Art-In Science Competition, 35th Annual AIAA DCASS, March 2010.
48. S. Zabarnick, Selected as At-Large Steering Committee Member of the Coordinating Research Council Aviation Meetings, May 2010.

49. M. Vangsness, Plenary Speaker, International Symposium on Aircraft Materials-ACMA 2010, Marrakech, Morocco, May 12-14, 2010.
50. S. Zabarnick, Organizer and Session Chair of Chemistry and Materials for Alternative Energy, Central Regional Meeting of the American Chemical Society (CeRMACS), Dayton, OH, June 16-19, 2010.
51. M.J. DeWitt, External Advisory Board Member, Mechanical, Industrial and Manufacturing Engineering Department of the University of Toledo, June, 2010.
52. K.E. Binns, Keynote Address, Joint Symposium of SAE-AE-5 and A-6 Committees, September, 2010
53. K.E. Binns, Special performance recognition award, SAE-6 Committee, September 2010.

Journal Articles & Conference Proceedings Publications

1. M.J. DeWitt, S. Zabarnick, J. Ervin and T. Williams, "Inhibition of Jet Fuel Deposition Within a Complete Oxygen Consumption Regime," Proceedings of the 8th International Conference on Stability and Handling of Liquid Fuels, Steamboat Springs, CO, 2003.
2. C.A. Obringer, J.S. Ervin, S. Zabarnick, T.F. Williams, M.D. Vangsness, L.M. Shafer, G.L. Dieterle, and K.E. Binns, "Development of Low Temperature Additives for Use in Jet Fuel," Proceedings of the 8th International Conference on Stability and Handling of Liquid Fuels, Steamboat Springs, CO, 2003.
3. L.M.T. Balster, S. Zabarnick, R.C. Striebich, and M. DeWitt, "Predicting the Thermal Stability of Jet Fuel: Analytical Techniques toward Model Validation," Proceedings of the 8th International Conference on Stability and Handling of Liquid Fuels, Steamboat Springs, CO, 2003.
4. J. S. Ervin, N. Widmor, S. Zabarnick, and M. Vangsness, "Studies of Jet Fuel Freezing by Differential Scanning Calorimetry and Cold-Stage Microscopy," *Transactions of ASME, Journal of Engineering for Gas Turbines and Power*, Vol. 125, pp. 34-39, 2003.
5. E. Corporan, M.J. DeWitt, O. Monroig, J. Everhart, and M. Wagner, "Effect of Fuel Character on the Particulate Emissions of a T63 Engine," Proceedings of the 8th International Conference on Stability and Handling of Liquid Fuels, Steamboat Springs, CO, 2003.
6. J.S. Ervin, T.A. Ward, T.F. Williams, J. Bento, "Surface Deposition within Treated and Untreated Stainless Steel Tubes Resulting from Thermal-Oxidative and Pyrolytic Degradation of Jet Fuel," *Energy & Fuels*, Vol. 17, pp. 577-586, 2003.
7. J.S. Ervin, D.L. Atkins, and A. Saxena, "Computational Model of the Freezing of Jet Fuel," Proceedings of the 8th International Conference on Stability and Handling of Liquid Fuels, Steamboat Springs, CO, 2003.
8. S. Zabarnick, M. Laber, J. Ervin, and R. Assudani, "Operation of Aircraft Fuel Systems at Low Temperatures," Proceedings of the 8th International Conference on Stability and Handling of Liquid Fuels, Steamboat Springs, CO, 2003.
9. E. Corporan, M. J. Dewitt, and M. Wagner, "Evaluation of Soot Particulate Mitigation Additives in a T63 Engine," *Fuel Processing Technology*, Vol. 85, pp. 727-742, 2004.
10. R.C. Striebich and J. Lawrence, "Thermal decomposition of high-energy density materials at high pressure and temperature," *J. Anal. Appl. Pyrolysis*, Vol. 70, pp. 339-352, 2003.
11. T.A. Ward, J.S. Ervin, R.C. Striebich, and S. Zabarnick, "Simulations of Flowing Mildly-Cracked Normal Alkanes Incorporating Proportional Product Distributions," *AIAA Journal of Propulsion and Power*, Vol. 20, No 3, pp. 394-402, May-June 2004.

12. T. Dounghthip, J.S. Ervin, and S. Zabarnick "Simulation of the Effects of Treated and Untreated Stainless-Steel Surfaces on Thermal Oxidation of Jet Fuel," *Energy & Fuels*, Vol. 18, pp. 425-437, 2004.
13. N.J. Kuprowicz, J.S. Ervin, and S. Zabarnick, "Modeling the Liquid-Phase Oxidation of Hydrocarbons over a Range of Temperatures and Dissolved Oxygen Concentrations with Pseudo-Detailed Chemical Kinetics," *Fuel*, Vol. 83, pp. 1795-1801, 2004.
14. M.B. Colket, R.J. Hall, S.D. Stouffer, "Modeling Soot Formation in a Well-Stirred Reactor," Paper GT2004-54001, Proceedings of the ASME Turbo Expo 2004 Power for Land, Sea and Air, June 14-17, 2004 Vienna, Austria.
15. L.M. Balster, S. Zabarnick and R.C. Striebich, "Division of Polar Species in Jet Fuel by their Relative Polarity and Molecule Type, and Possible Implications of these Sub-classes on Jet Fuel Thermal Stability," *Prepr.-Am. Chem. Soc., Div Pet. Chem.*, Vol. 49, pp. 477-480, 2004.
16. Z.J. West, S. Zabarnick and R.C. Striebich, "Determination of Hydroperoxides in Jet Fuel via Reaction with Triphenylphosphine," *Prepr.-Am. Chem. Soc., Div Pet. Chem.*, Vol. 49, pp. 481-483, 2004.
17. N. Widmor, J.S. Ervin and S. Zabarnick, "Calculations of Binary Interaction Energies for Solid-Liquid Phase Equilibria Calculations Involving Jet Fuel," *Prepr.-Am. Chem. Soc., Div Pet. Chem.*, Vol. 49, pp. 489-492, 2004.
18. M.D. Vangsness, L. Shafer, J.S. Ervin and S. Zabarnick, "Low-temperature Properties of Jet Fuel," *Prepr.-Am. Chem. Soc., Div Pet. Chem.*, Vol. 49, pp. 498-501, 2004.
19. R. Assudani, J.S. Ervin and S. Zabarnick, "Computational Fluid Dynamic Simulations of Jet Fuel Flow Near the Freeze Point Temperature," *Prepr.-Am. Chem. Soc., Div Pet. Chem.*, Vol. 49, pp. 502-505, 2004.
20. L.M. Shafer, J.S. Ervin and S. Zabarnick, "Effects of Low-temperature Additives on Phase Compositions of Jet Fuel," *Prepr.-Am. Chem. Soc., Div Pet. Chem.*, Vol. 49, pp. 506-509, 2004.
21. Z. West, S. Zabarnick and R. Striebich, "Determination of Hydroperoxides in Jet Fuel via Reaction with Triphenylphosphine," *Ind. Eng. Chem. Res.*, Vol. 44, pp. 3377-3383, 2005.
22. T. Edwards, W. Harrison, S. Zabarnick, M. DeWitt, C. E. Bentz, "Update on the Development of JP-8+100," AIAA 2004-3886.
23. T. Edwards, D. Minus, W. Harrison, E. Corporan, M. DeWitt, S. Zabarnick, L. Balster, "Fischer-Tropsch Jet Fuels – Characterization for Advanced Aerospace Applications," AIAA-2004-3885.

24. W. Williams, S. Popovic, L. Vuskovic, C. Carter, L. Jacobson, S. Kuo, D. Bivolaru, S. Corera, M. Kahandawala and S. Sidhu, "Model and Igniter Development for Plasma Assisted Combustion," AIAA 2004-1012.
25. E.A. Guliants, K. Novak, and C.E. Bunker, "The Effect of Thin Film Environment on Luminescent Properties of CdS Nanoparticles," submitted to *Applied Physics Letters*, 2004.
26. M. J. DeWitt, E. Corporan, S. Stouffer, D. Ostdiek, B. Mortimer, M. Wagner and R. Reich, "Impacts of Oxygenates on Pollutant Emissions of a JP-8 Fueled Turbine Engine," *Prepr.-Am. Chem. Soc., Div Pet. Chem.*, Vol. 49, pp. 521-524, 2004.
27. E. Corporan, O. Monroig, M. Wagner, and M. J. DeWitt, "Influence of Fuel Chemical Composition on Particulate Matter Emissions of a Turbine Engine," *Proceedings of ASME Turbo Expo*, GT2004-54335, Vienna, Austria, 14-17 June 2004.
28. E. Corporan, R. Reich, O. Monroig, M. J. DeWitt, V. Larson, T. Aulich, M. Mann, and W. Seames, "Impacts of Biodiesel on Pollutant Emissions of a JP-8 Fueled Turbine Engine," *A&WMA Annual Conference Proceedings*, Paper 751, 2004.
29. S. K. Chelgren, V. M. Belovich, E. Corporan, J. R. Gord, M. J. DeWitt, S. Roy and T. R. Meyer, "Influence of Fuel Type and Operating Conditions on Particulates in Gas-Turbine Combustors," *Proceedings of Joint International Combustion Symposium*, Maui, Hawaii, 10-13 October, 2004.
30. S.D. Stouffer, B.M. Mortimer, D.M. Ostdiek, M.J. DeWitt, R. Pawlik, R. Reich, and R. Mayfield, "Soot Reduction Research Using a Well-Stirred Reactor," AIAA 2005-1317.
31. E. Corporan, R. Reich, O. Monroig, M. J. DeWitt, V. Larson, T. Aulich, M. Mann, and W. Seames, "Impacts of Biodiesel on Pollutant Emissions of a JP-8 Fueled Turbine Engine," *Journal of the Air & Waste Management Association*, Vol. 55, pp. 940-949, 2005.
32. E. Corporan, M. J. DeWitt, O. Monroig, D. Ostdiek, B. Mortimer, and M. Wagner, "Reduction of Turbine Engine Particulate Emissions Using Synthetic Jet Fuel," *Prepr.-Am. Chem. Soc., Div Fuel Chem.*, Vol. 50, pp. 338-341, 2005.
33. O. Monroig, E. Corporan, M. J. DeWitt, B. Mortimer, D. Ostdiek, and M. Wagner, "Effects of Jet Fuel Aromatic Concentration on the Emissions of a T63 Engine," *Prepr.-Am. Chem. Soc., Div Fuel Chem.*, Vol. 50, pp. 335-337, 2005.
34. D. Atkins, J.S. Ervin, and L. Shafer, "Experimental Studies of Jet Fuel Viscosity at Low Temperatures, Using a Rotational Viscometer and an Optical Cell," *Energy & Fuels*, Vol. 19, pp. 1935-1947, 2005.
35. D.L. Atkins, J.S. Ervin, and A. Saxena, "Computational Model of the Freezing of Jet Fuel," *AIAA J. Propulsion and Power*, Vol. 21, pp. 356-367, March-April 2005.

36. T. A. Ward, J. S. Ervin, S. Zabarnick, and L. Shafer, "Pressure Effects on Flowing Mildly-Cracked n-Decane," *AIAA Journal of Propulsion and Power*, Vol. 21, pp. 344-355, March-April 2005.
37. S. Zabarnick, "Ab Initio and Density Functional Theory Calculations of the Energetics of Autoxidation Reactions," Preprints of Symposia – American Chemical Society, Division of Fuel Chemistry, Vol. 50, pp. 88-89, 2005.
38. R. Assudani, J.S. Ervin, and S. Zabarnick, "Experimental and Modeling Studies of Jet Fuel Flow Near the Fuel Freeze Point Temperature," *AIAA Journal of Propulsion and Power*, Vol. 22, pp.534-541, 2006.
39. L.M. Balster, E. Corporan, M.J. DeWitt, J.T. Edwards, J.S. Ervin, J.L. Graham, S.-Y. Lee, S. Pal, D.K. Phelps, L.R. Rudnick, R.J. Santoro, H.H. Schobert, L.M. Shafer, R.C. Striebich, Z.J. West, G.R. Wilson, R. Woodward, and S. Zabarnick, "Development of an Advanced, Thermally Stable, Coal-Based Jet Fuel," *Fuel Proc. Tech.*, Vol. 89, pp. 364-378, 2008.
40. J.L. Graham, R.C. Striebich, K.J. Myers, D.K. Minus, and W.E. Harrison, III, "The Swelling of Nitrile Rubber by Selected Aromatics Blended in a Synthetic Jet Fuel," *Energy & Fuels*, Vol. 20, pp. 759-765, 2006.
41. S.S. Sidhu, J.L. Graham, D.R. Ballal, and H.C. Mongia, "Investigation of Heptane Combustion at 50 ATM Using a Shock Tube," AIAA 2005-1447, 2005.
42. S.K. Chelgren, L.M. Balster, M.D. Vangsness, T.R. Denaro, E.M. Strobel, and J.N. Lang, "Characterization of the Bio-burden in Aviation Fuel using Direct Polymerase Chain Reaction (PCR) and other Analytical Techniques," Proceedings of the 9th International Conference on Stability, Handling, and Use of Liquid Fuels, Sitges, Spain, 2005.
43. S.K. Chelgren, L.M. Balster, M.D. Vangsness, T.R. Denaro, E.M. Strobel, and J.N. Lang, "Characterization of the Bio-burden in Aviation Fuel using Direct Polymerase Chain Reaction (PCR) and other Analytical Techniques," Proceedings of the National Petroleum Management Association (NPMA) Petro Conference and Exhibition, San Antonio, Texas, 2005.
44. S. Zabarnick, Z. West, N. Kuprowicz, L. Balster, J. Ervin, D. Minus, and R. Striebich, "Measurement of Key Species and Development of a Chemical Kinetic Model Toward the Prediction of Jet Fuel Thermal Stability," Proceedings of the 9th International Conference on Stability, Handling, and Use of Liquid Fuels, Sitges, Spain, 2005.
45. S. Zabarnick and D.K. Phelps, "Density Functional Theory Calculations of the Energetics and Kinetics of Jet Fuel Autoxidation Reactions," *Energy & Fuels*, Vol. 20, pp. 488-497, 2006.
46. R.C. Striebich, M.A. Motsinger, M.E. Rauch, S. Zabarnick, and M. DeWitt, "Estimation of Select Specification Tests for Aviation Turbine Fuels Using Fast Gas Chromatography," *Energy and Fuels*, Vol. 19, pp. 2445-2454, 2005.

47. E. Corporan, M. J. DeWitt, V. Belovich, T. Meyer, and A. Lynch, "Impacts of Synthetic Fuel on Emissions of Turbine Engine Combustors," Proceedings of the 9th International Conference on Stability, Handling, and Use of Liquid Fuels, Sitges, Spain, 2005.
48. O. Monroig, E. Corporan, and M. J. DeWitt, "Effects of Aromatic and Sulfur Concentration in Jet Fuel on the Emissions of a T63 Engine," Proceedings of the 9th International Conference on Stability, Handling, and Use of Liquid Fuels, Sitges, Spain, 2005.
49. M. J. DeWitt, T. Williams, L. Shafer, R. Striebich, L. Riehl and C. Delaney, "Investigation of the Effectiveness of DiEGME to Suppress the Solidification of Water in Aircraft Fuel Systems," Proceedings of the 9th International Conference on Stability, Handling, and Use of Liquid Fuels, Sitges, Spain, 2005.
50. M.S. Kahandawala, S.A. Corera and S.S. Sidhu, "Impact of additives on Soot Yields at 20 bar – A Shock Tube Study," *Shock Wave*, Proc. 25th International Shock tube and Shock Wave Symposium, Paper No. 1085-2a, pp. 636-644, 2005.
51. M.S. Kahandawala, S.A. Corera, S. Williams, C.D. Campbell, and S.S. Sidhu, "Investigation of Kinetics of iso-Octane Ignition under Scramjet Conditions," *Int. J. Chem. Kinet.*, Vol. 38, pp. 194-201, 2006.
52. W.E. Harrison and S. Zabarnick, "The OSD Assured Fuels Initiative – Military Fuels Produced from Coal," Proceedings of the 31st International Technical Conference on Coal Utilization & Fuel Systems, Clearwater, FL, 2006.
53. R. Assudani, J.S. Ervin, and L. Riehl, "Experiments and Simulations of the Freezing of Jet Fuel in Forced Flow," *AIAA J. Propulsion and Power*, Vol. 23, pp. 1123-1133, 2007.
54. L.M. Balster, S. Zabarnick, R.C. Striebich, L.M. Shafer, and Z.J. West, "Analysis of Polar Species in Jet Fuel and Determination of Their Role in Autoxidative Deposit Formation," *Energy & Fuels*, Vol. 20, pp. 2564-2571, 2006.
55. J.L. Graham, R.C. Striebich, K.J. Myers, D.K. Minus, W.E. Harrison, "The Swelling of Nitrile Rubber by Selected Aromatics Blended in a Synthetic Jet Fuel," *Energy and Fuels*, Vol. 20, pp. 759-765, 2006.
56. N.J. Kuprowicz, S. Zabarnick, Z. J. West, and J. S. Ervin, "The Use of Measured Species Class Concentrations with Chemical Kinetic Modeling for the Prediction of Autoxidation and Deposition of Jet Fuels," *Energy & Fuels*, Vol. 21, pp. 530-544, 2007.
57. L. M. Balster, S. K. Chelgren, E. M. Strobel, M. D. Vangness, and L. L. Bowen, "Characterization of the Bio-burden in United States Aviation Fuel: A Comparison of FTA Paper and Other Methods for Obtaining Genetic Material from Aviation Fuel Microbes," Preprints, 232nd American Chemical Society National Meeting, Division of Petroleum Chemistry, Vol. 51, No. 2, 2006.

58. T. Edwards, M.J. DeWitt, L. Shafer, D. Brooks, H. Huang, S.P. Bagley, J.O. Ona, M.J. Wornat, "Composition Influence on Deposition in Endothermic Fuels," Paper 2006-7973, Proceedings of the 14th AIAA/AHI Hypersonics Technology Conference, Canberra, Australia, 2006.
59. T. Edwards, L. Shafer, R. Striebich, J. Gomach, "Chemical Class Composition of Commercial Jet Fuels and Other Specialty Kerosene Fuels," Paper 2006-7972, Proceedings of the 14th AIAA/AHI Hypersonics Technology Conference, Canberra, Australia, 2006.
60. M.J. DeWitt, R. Striebich, L. Shafer, S. Zabarnick, W.E. Harrison, III, D.E. Minus, and T. Edwards, "Evaluation of Fuel Produced via the Fischer-Tropsch Process for Use in Aviation Applications," Paper 58b, Proceedings of AIChE Spring National Meeting, 2007.
61. E. Corporan, M.J. DeWitt, V. Belovich, R. Pawlik, A.C. Lynch, J.R. Gord, and T.R. Meyer, "Emissions Characteristics of a Turbine Engine and Research Combustor Burning a Fischer-Tropsch Jet Fuel," *Energy & Fuels*, Vol. 21, pp. 2615-2626, 2007.
62. E. Corporan, A. Quick, and M.J. DeWitt, "Characterization of Particulate Matter and Gaseous Emissions of a C-130H Aircraft," *Journal of Air & Waste Management Association*, Vol. 58, pp. 474-483, 2008.
63. M.D. Cheng, E. Corporan, M.J. DeWitt, C. Spicer, M. Holdren, K. Cowen, A. Laskin, B. Harris, R. Shores, R. Kaganan, R. Hashmonay, "Probing Emissions of Military Cargo Aircraft: Description of a Joint Field Measurement Environmental Research and Development Program," *Journal of Air & Waste Management Association*, Vol. 58, pp. 787-796, 2008.
64. E. Corporan, M.J. DeWitt, C.D. Klingshirn and R. Striebich, "DOD Assured Fuels Initiative: B-52 Aircraft Emissions Burning a Fischer-Tropsch/JP-8 Fuel Blend," Proceedings of the 10th International Conference on Stability, Handling and Use of Liquid Fuels, 2007.
65. J.L. Graham, R.C. Striebich, D.K. Minus, and W.E. Harrison III, "A Laboratory Assessment of the Compatibility of Fischer-Tropsch Derived (Iso-paraffinic Kerosene) and Blended FT-Petroleum-Derived Fuels with Non-Metallic Materials," Proceedings of the 10th International Conference on Stability, Handling and Use of Liquid Fuels, 2007.
66. M.J. DeWitt, S. Zabarnick, T. Williams, Z. West, L. Shafer, R. Striebich, S. Breitfield, C. Delaney, and D. Phelps, "Determination of Minimum Required FSII Dosage for Use on USAF Aircraft," Proceedings of the 10th International Conference on Stability, Handling and Use of Liquid Fuels, 2007.
67. S. Zabarnick, Z. West, M.J. DeWitt, L. Shafer, R. Striebich, C. Delaney, and D. Phelps, "Development of Alternative Fuel System Icing Inhibitor Additives that are Compatible with Aircraft Tank Topcoat Material," Proceedings of the 10th International Conference on Stability, Handling and Use of Liquid Fuels, 2007.

68. M. Vangsness, S. Chelgren, E. Strobel, L. Balster, L. Bowen, and S. Mueller, "Microbial Contamination Studies in JP-8 Fueled Aircraft," Proceedings of the 10th International Conference on Stability, Handling and Use of Liquid Fuels, 2007.
69. J.S. Ervin and T.M. Bartsch, "Simulations of Fuel Tank Temperatures within US Air Force Cargo Aircraft as part of a JP-8 Replacement Study," Proceedings of the 10th International Conference on Stability, Handling and Use of Liquid Fuels, 2007.
70. M.J. DeWitt, E. Corporan, J.L. Graham and D. Minus, "Effects of Aromatic Type and Concentration in Fischer-Tropsch Fuel on Emission Production and Material Compatibility," Proceedings of the 10th International Conference on Stability, Handling and Use of Liquid Fuels, 2007.
71. E.A. Nagley, P.I. King, F.R. Schauer, M.J. DeWitt and J.L. Hoke, "Fuel Composition Analysis of Endothermically Heated JP-8 Fuel for Use in a Pulse Detonation Engine," AIAA-2008-0109.
72. L.L. Bowen and S.S. Mueller, "Microbial Contamination of Biodiesel," Encyclopedia of Petroleum and Refining Science, Taylor & Francis, in press, 2010.
73. L.M. Balster, "Microbial Contamination in Jet Fuel," Encyclopedia of Petroleum Science and Engineering, Taylor & Francis, in press, 2010.
74. M.J. DeWitt, E. Corporan, J.L. Graham and D. Minus, "Effects of Aromatic Type and Concentration in Fischer-Tropsch Fuel on Emission Production and Material Compatibility," *Energy & Fuels*, Vol. 22, pp. 2411-2418, 2008.
75. R. Wills, A. Cole, H. Jiang, J. Sebastien, and J.S. Ervin, "Laboratory Development for the Study of Liquid Hydrocarbon -Cooled Rotating Equipment," AIAA-ASME Joint Propulsion Conference, East Hartford, July 2008.
76. M.S.P. Kahandawala, M.J. DeWitt, E. Corporan, and S.S. Sidhu, "Ignition and Emission Characteristics of Surrogate and Practical Jet Fuels," *Energy & Fuels*, Vol. 22, pp. 3673-3679, 2008.
77. G. Bessee and S. Zabarnick, "Evaluation of the Effects of TriEGME Fuel System Icing Inhibitor Candidate on Aviation Fuel Filtration," Proceedings of the 9th International Filtration Conference, 2008.
78. M. Roquemore, V. Katta, S. Stouffer, V. Belovich, R. Pawlik, M. Arstingstall, G. Justinger, J. Gord, A. Lynch, J. Zellina, and S. Roy, "Soot Studies of Laminar Diffusion Flames with Recirculation Zones," Proceedings of the Combustion Institute, in press, 2010.
79. R. Striebich, J. Contreras, L. Balster, Z. West, L. Shafer, and S. Zabarnick, "Identification of Polar Species in Aviation Fuels using Multidimensional Gas Chromatography-Time of Flight Mass Spectrometry," *Energy & Fuels*, Vol. 23, pp 5474-5482, 2009.

80. T. Litzinger, M. Colket, M. Kahandawala, V. Katta, S. -Y. Lee, D. Liscinsky, K. McNesby, R. Pawlik, M. Roquemore, R. Santoro, S. Sidhu, S. Stouffer, and J. Wu, "Fuel Additive Effects on Soot across a Suite of Laboratory Devices, Part 1: Ethanol," *Combustion Science and Technology*, Vol. 181, pp 310-328, 2009.
81. E. Corporan, M. J. DeWitt, C. D. Klingshirn, S. M. Mahurin, M.-D. Cheng, "Emissions Characteristics of a Legacy Military Aircraft," "Proceedings of ASME Turbo Expo, Power for Land, Sea and Air, Paper GT2009-59255, June 8-12, 2009.
82. L. M. Balster, E. M. Strobel, M. D. Vangsness, L. L. Bowen, S. S. Mueller, L. M. Brown, D. D. Pike, and D. L. Dalrymple, "Effect of FSII on Microbial Contamination: DiEGME and TriEGME," Proceedings of the 11th International Conference on Stability, Handling, and Use of Liquid Fuels (IASH), Prague, Czech Republic, 2009.
83. M. D. Vangsness, S. S. Mueller, L. L. Bowen, L. M. Brown, L. M. Balster, J. P. McComb, E. M. Strobel, "Biocontamination Diversity in JP-8 and Jet-A," Proceedings of the 11th International Conference on Stability, Handling, and Use of Liquid Fuels (IASH), Prague, Czech Republic, 2009.
84. S. Zabarnick, R. Adams, Z. West, M.J. DeWitt, L. Shafer, R. Striebich, C.L. Delaney, and D.K. Phelps, "Studies of the Compatibility of DiEGME and TriEGME Icing Inhibitor Additives with Aircraft Tank Topcoat Material," Proceedings of the 11th International Conference on Stability, Handling, and Use of Liquid Fuels (IASH), Prague, Czech Republic, 2009.
85. M.J. DeWitt, S. Zabarnick, S. Shaeffer, T. Williams, Z. West, L. Shafer, R. Striebich, S. Breitfield, R. Adams, R. Cook, C.L. Delaney, and D.K. Phelps, "Determination of Minimum Required FSII Use and Procurement Limits for USAF Aircraft," Proceedings of the 11th International Conference on Stability, Handling, and Use of Liquid Fuels (IASH), Prague, Czech Republic, 2009.
86. E. Corporan, L. Shafer, M.J. DeWitt, C. Klingshirn, S. Zabarnick, Z. West, R. Striebich, and J. Klein, "Initial Evaluation of Chemical, Thermal Stability and Emissions Characteristics of Jet Fuels from Alternative Sources," Proceedings of the 11th International Conference on Stability, Handling, and Use of Liquid Fuels (IASH), Prague, Czech Republic, 2009.
87. R.J. Allen, Z. West, and L. Shafer, "Hydrotreated Renewable Jet Fuels – A Comparison of Various Alternative Fuels with JP-8," Proceedings of the 11th International Conference on Stability, Handling, and Use of Liquid Fuels (IASH), Prague, Czech Republic, 2009.
88. S. Zabarnick, R. Adams, Z. West, M.J. DeWitt, L. Shafer, R. Striebich, C.L. Delaney, and D.K. Phelps, "Compatibility of DiEGME and TriEGME Fuel System Icing Inhibitor Additives with BMS 10-39 Aircraft Tank Topcoat Material," *Energy & Fuels*, Vol. 24, pp. 2614-2627, 2010.

89. M.D. Cheng, E. Corporan, M. J. DeWitt, and B. Landgraf, "Emissions of Volatile Particulate Components from Turbohaft Engines Operated with JP-8 and Fischer-Tropsch Fuels," *J. Aerosol Air Quality Res.*, Vol. 9, pp. 237-256, 2009.
90. M. Kahandawala, M. DeWitt, E. Corporan, S. Sidhu, "Ignition and Emission Characteristics of Synthetic Jet Fuels," *Combustion Generated Fine Carbonaceous Particles*, Bockhorn, H. (Ed.), Kit Scientific Publishing, Chap 12, pp. 173-185, 2009.
91. E. Shafer, R. Striebich, M.J. DeWitt, T. Edwards, and W.E. Harrison, "Variation of JP-8 Properties in CONUS and Potential Implications during Blending with Synthetic Paraffins," *Proceedings of the 11th International Conference on Stability, Handling, and Use of Liquid Fuels (IASH)*, Prague, Czech Republic, 2009.
92. E. Corporan, M.J. DeWitt, C. Klingshirn, "Emissions Evaluations of Diesel Engines Operated with JP-8 and a 50/50 Fischer-Tropsch/JP-8 Blend," *Proceedings of the 11th International Conference on Stability, Handling, and Use of Liquid Fuels (IASH)*, Prague, Czech Republic, 2009.
93. Corporan, E., DeWitt, M.J., Klingshirn, C.D., Striebich, R., and M.-D. Cheng, "Emissions Characteristics of Military Helicopter Engines with JP-8 and Fischer-Tropsch Fuels," *Journal of Propulsion and Power*, Vol. 26, pp. 317-324, 2010
94. L. M. Brown, J. P. McComb, M. D. Vangness, L. L. Bowen, S. S. Mueller, L. M. Balster, and C. A. Bleckmann, "Community Dynamics and Phylogenetics of Bacteria Fouling in Jet A and JP-8 Aviation Fuel," *International Journal of Biodeterioration & Biodegradation*, Vol. 64, pp. 253-261, 2010.
95. W.S. Anderson, M.D. Polanka, J. Zelina, D.S. Evans, S.D. Stouffer, and G. Justinger, "Effects of a Reacting Cross-Stream on Turbine Film Cooling," *ASME Journal of Engineering for Gas Turbines and Power*, Vol. 132, pp. 051501/1-051501/7, 2010.
96. W.K. Lewis, A.T. Rosenberger, J.R. Gord, C.A. Crouse, B.A. Harruff, K.A.S. Fernando, M.J. Smith, D.K. Phelps, J.E. Spowart, E.A. Guliants, and C.E. Bunker
"Multispectroscopic (FTIR, XPS, and TOFMS-TPD) Investigation of the Core-Shell Bonding in Sonochemically-Prepared Aluminum Nanoparticles Capped with Oleic Acid," *J. Phys. Chem. C*, Vol. 114, pp. 6377-6380, 2010.
97. S.W. Chung, E.A. Guliants, C.E. Bunker, P.A. Jelliss, S.W. Buckner, "Size-Dependent Al Nanoparticle Oxidation Enthalpy," *Prepr. Pap.-Am. Chem. Soc., Div. Fuel Chem.*, accepted for publication, 2010.
98. M.A. Burgers, C.D. Oberle, S.W. Chung, E.A. Guliants, V. Kalugotla, C.E. Bunker, D.W. Hammerstroem, P.A. Jelliss, S.W. Buckner, "Long-Term Air Stability of Organically-Capped Aluminum Nanoparticles," *Prepr. Pap.-Am. Chem. Soc., Div. Fuel Chem.*, accepted for publication, 2010.

99. H. Li, M.J. Meziani, A. Kitaygorodskiy, F. Lu, C.E. Bunker, K.A.S. Fernando, E.A. Guliants, Y.-P. Sun, "Preparation and Characterization of Alane Complexes for Energy Applications," *J. Phys. Chem. C*, Vol. 114, pp. 3318-3322, 2010.
100. C.E. Bunker, M.J. Smith, K.A.S. Fernando, B.A. Harruff, W.K. Lewis, J.R. Gord, E.A. Guliants, and D.K. Phelps "Spontaneous Hydrogen Generation from Organic-Capped Al Nanoparticles and Water," *ACS Appl. Mater. Interfaces*, Vol. 2, pp. 11-14, 2010.
101. H. Li, M.J. Meziani, F. Lu, C.E. Bunker, E.A. Guliants, Y.-P. Sun, "Templated Synthesis of Aluminum Nanoparticles – A New Route to Stable Energetic Materials," *J Phys. Chem. C*, Vol. 113, pp. 20539-20542, 2009.
102. S.W. Chung, E.A. Guliants, C.E. Bunker, D.W. Hammerstroem, Y. Deng, M.A. Burgers, P.A. Jelliss, S.W. Buckner, "Capping and Passivation of Aluminum Nanoparticles Using Alkyl-Substituted Epoxides," *Langmuir*, Vol. 25, pp. 8883-8887, 2009.
103. M.J. Meziani, C.E. Bunker, F. Lu, H. Li, W. Wang, E.A. Guliants, R.A. Quinn, Y.-P. Sun, "Formation and Properties of Stabilized Aluminum Nanoparticles," *ACS Appl. Mater. Interf.*, Vol. 1, pp. 703-709, 2009.
104. K.A.S. Fernando, M.J. Smith, B.A. Harruff, W.K. Lewis, E.A. Guliants, and C.E. Bunker, "Sonochemically-Assisted Thermal Decomposition of Alane *N,N*-Dimethylethylamine with Titanium (iv) Isopropoxide in the Presence of Oleic Acid to Yield Air Stable and Size Selective Aluminum Core-Shell Nanoparticles," *Journal of Physical Chemistry C*, Vol. 113, pp. 500-503, 2009.
105. A.B. Morgan, D.J. Wolf, E.A. Guliants, K.A. Shiral Fernando, W.K. Lewis, C.E. Bunker, "Heat Release Measurements on Micron and Nanoscale Aluminum Powders," *Thermochimica Acta*, Vol. 488, pp. 1-9, 2009.
106. A.M. Briones, J. Zelina, V. Katta, "Flame Stabilization in Small Cavities," *AIAA Journal*, Vol. 48, pp. 224-235, 2010.
107. A.M. Briones, J.S. Ervin, S. Putnam, L. Byrd, L. Gschwender, "Micrometer-sized Water Droplet Impingement Dynamics and Evaporation on a Flat Dry Surface," *Langmuir*, Vol. 26, pp. 13272–13286, 2010.
108. L. Shafer, J. Hinz, T. Edwards, B. Curtis, and W. Weisman, "Speciated Naphthalene Analysis in Liquid Transportation Fuels," manuscript in preparation, 2010.

Presentations and Pre-Prints

1. DeWitt, M. J., Zabarnick, S., Ervin, J. S., and Williams, T. F., "Inhibition of Jet Fuel Deposition Within a Complete Oxygen Consumption Regime," presented at the 8th International Conference on Stability and Handling of Liquid Fuels (IASH 2003), Steamboat Springs, Colorado, 14-19 September 2003.
2. Balster, L., Zabarnick, S., Ervin, J. S., Striebich, R., DeWitt, M. J., Dounghip, T., and Kuprowicz, N., "Predicting the Thermal Stability of Jet Fuel: Analytical Techniques Toward model Validation," presented at the 8th International Conference on Stability and Handling of Liquid Fuels (IASH 2003), Steamboat Springs, Colorado, 14-19 September 2003.
3. C.A. Obringer, J.S. Ervin, S. Zabarnick, T.F. Williams, M.D. Vangness, L.M. Shafer, G.L. Dieterle, and K.E. Binns, "Development of Low Temperature Additives for Use in Jet Fuel," presented at the 8th International Conference on Stability and Handling of Liquid Fuels (IASH 2003), Steamboat Springs, Colorado, 14-19 September 2003.
4. S. Zabarnick, M. Laber, J. Ervin, and R. Assudani "Operation of Aircraft Fuel Systems at Low Temperatures," presented at the 8th International Conference on Stability and Handling of Liquid Fuels (IASH 2003), Steamboat Springs, Colorado, 14-19 September 2003.
5. Corporan, E., DeWitt, M. J., Monroig, O., Everhart, J., and Wagner, M., "Effect of Fuel Character on the Particulate Emissions of a T63 Engine," presented at the 8th International Conference on Stability and Handling of Liquid Fuels (IASH 2003), Steamboat Springs, Colorado, 14-19 September 2003.
6. S. Zabarnick, "The Chemistry of Jet Fuel Oxidation and Deposition," Invited Lecture, Duquesne University Chemistry Department Distinguished Seminar Series, October 2003.
7. J.S. Ervin, D.L. Atkins, and A. Saxena, "Computational Model of the Freezing of Jet Fuel," presented at the 8th International Conference on Stability and Handling of Liquid Fuels (IASH 2003), Steamboat Springs, Colorado, 14-19 September 2003.
8. T. Ward, J.S. Ervin, and S. Zabarnick, "Simulations of Flowing Endothermic Fuels," presented at the Joint ASME-JSME Fluids Engineering Conference, Honolulu, Hawaii June 2003.
9. M. J. DeWitt, L. Shafer, and S. Zabarnick, "Development of Methodologies to Minimize the Oxidative Deposits of Jet Fuels," Presented at the CRC Aviation Fuels Meeting, Alexandria, VA, April 2003.
10. D. Goller, S. Zabarnick, and J. Ervin, "The Use of a Differential Scanning Calorimeter to Study Freezing of Jet Fuel," Presented at the 27th Annual Dayton-Cincinnati Aerospace Sciences Symposium, Dayton, OH, March 2002.

11. S. Zabarnick, "Improving Jet Fuels at High and Low Temperatures," Invited Lecture, Ohio Valley Section of the American Institute of Chemical Engineering, January 2004.
12. L. Balster, S. Zabarnick, and R. Striebich, "HPLC Methods for Fuel Analysis," Presented at the 28th Annual Dayton-Cincinnati, AIAA Aerospace Sciences Symposium, Dayton, OH, March 2003.
13. M. Kahandawala, J. Graham, and S. Sidhu, "Investigation of the Impact of Fuel Composition on Soot Emissions," The Proceedings of the Third Joint Meeting of the Sections of the Combustion Institute, March 16-19, 2003, Chicago, Illinois.
14. M.J. DeWitt, T. Williams, L. Shafer, R. Striebich, J. Ervin, and S. Zabarnick, "Investigation of Effectiveness of DiEGME to Suppress Solidification of Water in Aircraft Fuel Systems," Presented at Fuel Study Kickoff Meeting, Boeing, St. Louis MO, March 2004.
15. K. Froning, G. Garcia, J. Graham, R. Striebich, and D. Minus, "Interactions of Elastomers with Aviation Turbine Fuel," Poster Presentation, AIChE National Meeting, San Francisco CA., November 16-21, 2003.
16. J. Contreras and R.C. Striebich, "Determinations of Polar Components in Aviation Fuels Using MDGC-MS," Poster Presentation at the AIAA 100th Anniversary of Flight Symposium, Dayton, Ohio, July, 2003.
17. J.S. Ervin, "JP-8+100 LT Requirements," Presented to the Air Force Air Combat Command, Langley, VA, January 2004.
18. Z. West, S. Zabarnick and R.C. Striebich, "Development of a Rapid, Quantitative Method to Determine Hydroperoxide Concentration in Jet Fuel," presented at the 29th Annual Dayton-Cincinnati, AIAA Aerospace Sciences Symposium, Dayton, OH, March 2004.
19. R. Pawlik, S. D. Stouffer, R. F. Reich, B. M. Mortimer, C. W. Frayne, J. A. Kleinfeldt, "Effect of Additives on Soot Formation in a Well-Stirred Reactor," 29th AIAA Aerospace Science Symposium, Dayton, OH, 9 March 2004.
20. S. Williams, S. A. P. Corera, M. S. P. Kahandawala, C. D. Carter, J. L. Graham, S. S. Sidhu, "Investigation of Kinetics of iso-Octane Ignition under Scramjet Conditions," Presented at the 228th National Meeting of American Chemical Society, August 2004, Philadelphia, PA.
21. M. Kahandawala, S. Corera, J. Graham and S. Sidhu, "Impact of Nitro-compounds on Soot Yields at 20 Bar- A Shock Tube Study," presented at AIChE 2004 Annual Meeting, Austin, Texas, November 10, 2004.
22. R.F. Reich, S.D. Stouffer, R. Pawlik, C.W. Frayne, B.M. Mortimer, and H.T. Mayfield, "Effect on Soot Formation in a Well-Stirred Reactor with Nitromethane Addition," Partners in Environmental Technology Symposium & Workshop, Washington D.C., December 2003.

23. R.F. Reich, S.D. Stouffer, and H.T. Mayfield, "Real-Time Analysis of Trace Combustion Gases from a Well-Stirred Reactor Using Tandem Mass Spectrometry and Selected Ion Storage," Poster presentation at 51st American Society for Mass Spectrometry, Montreal, Canada, June 9, 2003.
24. N. Widmor, J.S. Ervin and S. Zabarnick, "Calculations of Binary Interaction Energies for Solid-Liquid Phase Equilibria Calculations Involving Jet Fuel," Presented at the Jet Fuels Session, Division of Petroleum Chemistry, American Chemical Society National Meeting, Philadelphia, PA, August, 2004.
25. M.D. Vangsness, L. Shafer, J.S. Ervin and S. Zabarnick, "Low-temperature Properties of Jet Fuel," Presented at the Jet Fuels Session, Division of Petroleum Chemistry, American Chemical Society National Meeting, Philadelphia, PA, August, 2004.
26. R. Assudani, J.S. Ervin and S. Zabarnick, "Computational Fluid Dynamic Simulations of Jet Fuel Flow Near the Freeze Point Temperature," Presented at the Jet Fuels Session, Division of Petroleum Chemistry, American Chemical Society National Meeting, Philadelphia, PA, August, 2004.
27. L.M. Shafer, J.S. Ervin and S. Zabarnick, "Effects of Low-temperature Additives on Phase Compositions of Jet Fuel," Presented at the Jet Fuels Session, Division of Petroleum Chemistry, American Chemical Society National Meeting, Philadelphia, PA, August, 2004.
28. T. Edwards, W. Harrison, S. Zabarnick, M. DeWitt, C. E. Bentz, "Update on the Development of JP-8+100," 40th AIAA/ASME/SAE/ASEE Joint Propulsion Conference and Exhibit, Fort Lauderdale, Florida, July 11-14, 2004
29. T. Edwards, D. Minus, W. Harrison, E. Corporan, M. DeWitt, S. Zabarnick, L. Balster, "Fischer-Tropsch Jet Fuels – Characterization for Advanced Aerospace Applications," 40th AIAA/ASME/SAE/ASEE Joint Propulsion Conference and Exhibit, Fort Lauderdale, Florida, July 11-14, 2004.
30. C.E. Bunker, J.J. Karnes, E.A. Guliants, J.D. Gord, and D.F. Phelps, "Sensors and Sensor Technologies for Jet Fuel Analysis," 228th ACS National Meeting, Philadelphia, PA, Aug. 2004.
31. E.A. Guliants, B.A. Haruff, J.R. Gord, and C.E. Bunker, "Photophysical Properties of CdS Nanoparticles in Thin Films for Opto-Chemical Sensing," MRS Spring Meeting, San Francisco, CA, Apr. 2004.
32. E.A. Guliants, J. Karnes, and C.E. Bunker, "Toward Highly Efficient CdS Nanoparticle Based Thin-Film Fuel Sensor," 2nd Annual Nano-Materials for Defense Applications Symposium, Maui, HI, Feb. 2004.
33. J. Karnes, N.L. Sanders, E.A. Guliants, and C.E. Bunker, "Preparation, Characterization, and Reactivity of Iron Core-Shell Nanoparticles," 2nd Annual Nano-Materials for Defense Applications Symposium, Maui, HI, Feb. 2004.

34. C.E. Bunker, N.L. Sanders, J.J. Karnes, R.J. Schwarb, and E.A. Guliants, "Temperature Induced Reactivity of Organic-Coated Core-Shell Nanoparticles," 36th ACS Great Lakes Regional Meeting 2004, Peoria, IL, Oct. 2004.
35. M. J. DeWitt, E. Corporan, S. Stouffer, D. Ostdiek, B. Mortimer, M. Wagner and R. Reich, "Impacts of Oxygenates on Pollutant Emissions of a JP-8 Fueled Turbine Engine," American Chemical Society National Meeting, Philadelphia, PA, August, 2004.
36. E. Corporan, O. Monroig, M. Wagner, and M. J. DeWitt, "Influence of Fuel Chemical Composition on Particulate Matter Emissions of a Turbine Engine," ASME Turbo Expo, Vienna Austria, June 14-17, 2004.
37. E. Corporan, R. Reich, O. Monroig, M. J. DeWitt, V. Larson, T. Aulich, M. Mann, and W. Seames, "Impacts of Biodiesel on Pollutant Emissions of a JP-8 Fueled Turbine Engine," A&WMA Annual Conference, Indianapolis, IN, June 22-25, 2004.
38. Z. J. West, S. Zabarnick, and R. C. Striebich, "Determination of Hydroperoxides in Jet Fuel via Reaction with Triphenylphosphine," 228th ACS National Meeting, Philadelphia, PA, August, 2004.
39. L. M. Balster, S. Zabarnick, and R. C. Striebich, "Division of Polar Species in Jet Fuel by Their Relative Polarity and Molecule Types, and Possible Implications of These Subclasses on Jet Fuel Thermal Stability," 228th ACS National Meeting, Philadelphia, PA, August, 2004.
40. J. L. Graham, R.C. Striebich, D.K. Minus, W.E. Harrison, "The Swelling Of Selected O-Ring Materials In Jet Propulsion And Fischer-Tropsch Fuels," Presented at the 228th National Meeting of American Chemical Society, August, 2004, Philadelphia, Pennsylvania.
41. S. Zabarnick, "High Heat Sink Fuels," Scientific Advisory Board Presentation, Air Force Research Laboratory Propulsion Directorate, Wright-Patterson AFB, OH, October 20, 2004.
42. S. Zabarnick, "Ab Initio and Density Functional Theory Calculations of the Energetics of Autoxidation Reactions," 229th American Chemical Society National Meeting, Division of Fuel Chemistry, San Diego, CA, March 13-17, 2005.
43. R. Assudani, J.S. Ervin, and S. Zabarnick, "Numerical and Experimental Studies of Jet Fuel Flow Near the Freeze Point Temperature," 30th Dayton-Cincinnati Aerospace Sciences Symposium, March 8, 2005.
44. L. Riehl and J.S. Ervin, "Visualization of Jet Fuel Solidification Occurring in Forced Flow," 30th Dayton-Cincinnati Aerospace Sciences Symposium, March 8, 2005.
45. P. Ramineni and J.S. Ervin, "Simulations of Jet Fuel Flow with Imposed High Heat Flux," 30th Dayton-Cincinnati Aerospace Sciences Symposium, March 8, 2005.

46. J.S. Ervin, L. Riehl, and D. Phelps, "Recent Progress in the JP-8+100LT Program," Northrop Grumman, San Bernardo Technical Facility, San Diego, CA, April 21, 2005.
47. S.D. Stouffer, B.M. Mortimer, D.M. Ostdiek, M.J. DeWitt, R. Pawlik, R. Reich, and H.T. Mayfield, "Soot Reduction Research Using a Well-Stirred Reactor," Presented at 43rd AIAA Aerospace Sciences Meeting and Exhibit 10-14 January, 2005, Reno, Nevada
48. S.D. Stouffer, D.R. Ballal, J. Zelina, D.T. Shouse, R.D. Hancock, H.C. Mongia, "Development and Combustion Performance of a High-Pressure WSR and TAPS Combustor," Presented at 43rd AIAA Aerospace Sciences Meeting and Exhibit 10-14 January, 2005, Reno, Nevada
49. S.D. Stouffer, E. Strader, M. Arstingstall, A. Lynch, and C. Frayne, "Design and Test of an Improved Smoke Mass Sampling System," 30th Dayton-Cincinnati Aerospace Science Symposium, Dayton, OH, 8 March 2005.
50. B.M. Mortimer, D.M. Ostdiek, S.D. Stouffer, and M.J. DeWitt, "The Effect of Volatile Compounds on Apparent Emission Characteristics," 30th Dayton-Cincinnati Aerospace Science Symposium, Dayton, OH, 8 March 2005.
51. D.M. Ostdiek, B.M. Mortimer, M.J. DeWitt, and S.D. Stouffer, "A Technique for Measuring Soot Density Using Typical Aerosol Instrumentation," 30th Dayton-Cincinnati Aerospace Science Symposium, Dayton, OH, 8 March 2005.
52. R. Pawlik, S. Stouffer, C. Frayne, and R. Reich, "Effect of Pyridine and Quinoline on Soot Formation," SERDP and ESTCP Partners in Environmental Technology Symposium and Workshop, Washington D.C., Nov 30-Dec 2 2004,
53. M. J. DeWitt, T. Williams, L. Shafer, R. Striebich, L. Riehl, J. Ervin, and S. Zabarnick, "Investigation of Effectiveness of DiEGME to Suppress Solidification of Water in Aircraft Fuel Systems," Presented at B-52 Fuel Tank Topcoat Peeling Briefing, Tinker AFB, August 2004.
54. M. J. DeWitt, T. Williams, L. Shafer, R. Striebich, L. Riehl, and J. Ervin, "Investigation of Effectiveness of DiEGME to Suppress Solidification of Water in Aircraft Fuel Systems," Presented at Additive Deletion Study Review Meeting, WPAFB, September 2004.
55. E. Corporan, M. J. DeWitt, O. Monroig, D. Ostdiek, B. Mortimer, and M. Wagner, "Reduction of Turbine Engine Particulate Emissions Using Synthetic Jet Fuel," American Chemical Society National Meeting, San Diego, CA, March, 2005.
56. O. Monroig, E. Corporan, M. J. DeWitt, B. Mortimer, D. Ostdiek, and M. Wagner, "Effects of Jet Fuel Aromatic Concentration on the Emissions of a T63 Engine," American Chemical Society National Meeting, San Diego, CA, March, 2005.

57. M. J. DeWitt, T. Williams, L. Shafer, R. Striebich, and L. Riehl, "Investigation of Effectiveness of DiEGME to Suppress Solidification of Water in Aircraft Fuel Systems," Presented at Additive Deletion Study Review Meeting, Radian, Alexandria, VA, April, 2005.
58. T.W. Selby, M. Vangsness L. Shafer, "Studies of the Flow and Gelation Response of Jet Fuels at Critical Low Temperatures," Presented at International Condition Monitoring Conference 2004 – Joint Oil Analysis Program, Pensacola, FL, April 2004.
59. M.D. Vangsness, L.M. Balster, J.N. Lang, S.K. Chelgren, and T.R. Denaro, "Jet Fuel Microbial Contamination," Presented at the CRC Aviation Fuels Meeting, Williamsburg, VA, May 2005.
60. J.L. Graham, R. Striebich, D. Minus, W.E. Harrison III, "Flexible JP-8 Program: Elastomer Compatibility," Presented at the Flexible JP-8 Program technical review, Pittsburg, PA, July 26, 2005.
61. S. K. Chelgren, L. M. Balster, M. D. Vangsness, T. R. Denaro, E. M. Strobel, and J. N. Lang, "Characterization of the Bio-burden in Aviation Fuel Using Direct Polymerase Chain Reaction (PCR) and other Analytical Techniques," poster presented at the Society of Industrial Microbiologists (SIM) Annual Meeting, Chicago, August 21-25, 2005.
62. S. K. Chelgren, L. M. Balster, M. D. Vangsness, T. R. Denaro, E. M. Strobel, and J. N. Lang, "Characterization of the Bio-burden in Aviation Fuel using Direct Polymerase Chain Reaction (PCR) and other Analytical Techniques," presented at the 9th International Conference on Stability, Handling, and Use of Liquid Fuels (IASH 2005) Sitges, Spain, September 18-22, 2005.
63. S. K. Chelgren, L. M. Balster, M. D. Vangsness, T. R. Denaro, E. M. Strobel, and J. N. Lang, "Characterization of the Bio-burden in Aviation Fuel using Direct Polymerase Chain Reaction (PCR) and other Analytical Techniques," presented at the National Petroleum Management Association Conference and Exhibition, San Antonio, Texas, October 16-19, 2005.
64. S. Zabarnick, Z. West, N. Kuprowicz, L. Balster, J. Ervin, D. Minus, and R. Striebich, "Measurement of Key Species and Development of a Chemical Kinetic Model Toward the Prediction of Jet Fuel Thermal Stability," Proceedings of the 9th International Conference on Stability, Handling, and Use of Liquid Fuels, Sitges, Spain, 2005.
65. E. Corporan, M. J. DeWitt, V. Belovich, T. Meyer, and A. Lynch, "Impacts of Synthetic Fuel on Emissions of Turbine Engine Combustors," Proceedings of the 9th International Conference on Stability, Handling, and Use of Liquid Fuels, Sitges, Spain, 2005.
66. O. Monroig, E. Corporan, and M. J. DeWitt, "Effects of Aromatic and Sulfur Concentration in Jet Fuel on the Emissions of a T63 Engine," Proceedings of the 9th International Conference on Stability, Handling, and Use of Liquid Fuels, Sitges, Spain, 2005.

67. M. J. DeWitt, T. Williams, L. Shafer, R. Striebich, L. Riehl and C. Delaney, "Investigation of the Effectiveness of DiEGME to Suppress the Solidification of Water in Aircraft Fuel Systems," Proceedings of the 9th International Conference on Stability, Handling, and Use of Liquid Fuels, Sitges, Spain, 2005.
68. L. M. Balster, S. K. Chelgren, E. M. Strobel, M.D. Vangsness, and L. L. Bowen, "DNA Analysis of Microbial Contaminants in Jet Fuel," 37th Annual AIAA Dayton-Cincinnati Aerospace Science Mini Symposium, Dayton, March 2006.
69. L. M. Balster, S. Zabarnick, R. C. Striebich, L. M. Shafer, and Z. J. West, "Qualitative and Quantitative Analysis of Polar Species in Jet Fuel by HPLC," 37th Annual AIAA Dayton-Cincinnati Aerospace Science Mini Symposium, Dayton, March 2006.
70. S. Zabarnick, "Prediction of Jet Fuel Oxidation and Deposition," CRC Aviation Fuels Meeting, Alexandria, VA, May 2006.
71. W.E. Harrison and S. Zabarnick, "The OSD Assured Fuels Initiative – Military Fuels Produced from Coal," The 31st International Technical Conference on Coal Utilization & Fuel Systems, Clearwater, FL, 2006.
72. J.L. Graham, R. Striebich, D. Minus, W.E. Harrison III, "Elastomer Compatibility," Presented at the Developing Sealing Guidance for Fuel Wetted Components in the Next Generation Warfighter Workshop, Dayton, OH, April 27-28, 2006.
73. J.L. Graham, R. Striebich, D. Minus, W.E. Harrison III, "Material Compatibility Testing With Fischer-Tropsch Fuel Blends," Presented at the Assessment of FT Fuel Blends for Air Force Aviation Use Workshop, Dayton, OH, October 27, 2006.
74. J.L. Graham, R. Striebich, D. Minus, W.E. Harrison III, "A Rapid Survey of the Compatibility of Selected Seal Materials with Conventional and Semi-Synthetic JP-8," Presented at the 2006 NASA Seal/Secondary Air System Workshop, Cleveland, OH, November 14-15, 2006.
75. S. K. Chelgren, E. M. Strobel, L. M. T. Balster, M. D. Vangsness, and L. L. Bowen, "Further Characterization of the Bio-burden in Aviation Fuel: A Comparison of FTA Paper, Direct PCR, and Traditional Culture Methods for Obtaining Genetic Material from Aviation Fuel Microbes," Society of Industrial Microbiologists 28th Symposium on Biotechnology for Fuels and Chemicals, Nashville, April 30-May 3, 2006.
76. L. M. Balster, S. K. Chelgren, E. M. Strobel, M. D. Vangsness, and L. L. Bowen, "DNA Analysis of Microbial Contaminants in Aviation Fuels," 232nd American Chemical Society National Meeting, San Francisco, September 10-14, 2006.
77. S. Zabarnick, "Fischer-Tropsch Transportation Fuels," Planning meeting on Third Frontier Proposal with Global Energy, Dayton, OH, October 2006.

78. T. Edwards, M.J. DeWitt, L. Shafer, D. Brooks, H. Huang, S.P. Bagley, J.O. Ona, M.J. Wornat, "Composition Influence on Deposition in Endothermic Fuels," Presented at the 14th AIAA/AHI Hypersonics Technology Conference, Canberra, Australia, 2006.
79. DeWitt, M. J., Williams, T., Shafer, L., Striebich, R., West, Z., Zabarnick, S., "Determination of Minimum Required FSII Dosage for Use on USAF Aircraft," Presented at B-52 Fuel Tank Topcoat Peeling Technical Review, Tinker AFB, August 2006.
80. L. M. Balster, S. K. Chelgren, E. M. Strobel, M. D. Vangsness, L. L. Bowen, and S. S. Mueller, "Jet Fuel Microbial Contaminants: Toxicity, Habitat, and Survival," 38th AIAA-DCASS, March 6, 2007.
81. L. L. Bowen, S. K. Chelgren, E. M. Strobel, M. D. Vangsness, L. M. Balster, and S. S. Mueller, "Microbial Contamination of Biodiesel," AIAA-DCASS, March 6, 2007.
82. S. Zabarnick, "Prediction of Jet Fuel Oxidation and Deposition," invited lecture, Rolls-Royce plc, Derby, UK, June 2007.
83. M.D. Vangsness, L. Balster, L. Bowen, S. Mueller, S. Brooks, E. Strobel, "Jet Fuel Bio-Contamination, 2005-2006" presented at IATA Aviation Fuel Systems Management seminar, Panama City, Panama, March 12-14, 2007.
84. M.J. DeWitt, R. Striebich, L. Shafer, S. Zabarnick, W.E. Harrison III, D.E. Minus, and T. Edwards, "Evaluation of Fuel Produced via the Fischer-Tropsch Process for Use in Aviation Applications," AIChE Spring National Meeting, 2007.
85. M. Roquemor, V. Katta, V. Belovich, R. Pawlik, A. Lynch, J. Miller, S. Stouffer, G. Justinger, J. Zelina, S. Roy, J. Gord, "Experimental and Numerical Investigations of Centerbody Flames" Presented at the 5th Joint Meeting of the US Sections of the Combustion Institute, March 25-27, San Diego, CA, 2007
86. S. Sidhu, V. Belovich, M. Colket, M. Kahandawala, V. Katta, D. Liscinsky, T. Litzinger, K. McNesby, M. Roquemore, R. Santoro, S. Stouffer, "The Effects of Phosphorus Compounds on PAH and Soot Across a Suite of Laboratory Devices," Presented at the 5th Joint Meeting of the US Sections of the Combustion Institute, March 25-27, San Diego, CA., 2007
87. T. Litzinger, M. Colket, M. Kahandawala, V. Katta, S.Y. Lee, D. Liscinsky, K. McNesby, R. Pawlik, M. Roquemore, R. Santoro, S. Sidhu, S. Stouffer, and J. Wu, "The Effects of Oxygenated Compounds on PAH and Soot Across a Suite of Laboratory Devices," Presented at the 5th Joint Meeting of the US Sections of the Combustion Institute, March 25-27, San Diego, CA., 2007
88. M. Colket, T. Litzinger, M. Kahandawala, V. Katta, S.Y. Lee, D.T. Liscinsky, K. McNesby, A. Menon, M. Roquemore, R. Santoro, S. Sidhu, and S. Stouffer, "The Effects of Nitrogen-Containing Compounds on PAH and Soot Across a Suite of Laboratory Devices," Presented at the 5th Joint Meeting of the US Sections of the Combustion Institute, March 25-27, San Diego, CA., 2007

89. B.M. Mortimer, S.D. Stouffer, and M.J. Dewitt, "Quantification of the Volatile Composition of the Volatile Composition of Soot Particles Below 200 nm," Presentation at the 32nd Dayton Cincinnati Aerospace Sciences Symposium, March 6, 2007.
90. M. Roquemore, V. Katta, V. Belovich, R. Pawlik, A. Lynch, J. Miller, S. Stouffer, G. Justinger, J. Zelina, S. Roy, J. Gord, "Experimental and Numerical Investigations of Centerbody Flames," Presented at the 5th Joint Meeting of the US Sections of the Combustion Institute, March 25-27, San Diego, CA., 2007.
91. S.D. Stouffer, R. Pawlik, G. Justinger, J. Heyne, J. Zelina, D. Ballal, "Combustion Performance and Emissions Characteristics for a Well-Stirred Reactor for Low Volatility Hydrocarbon Fuels," AIAA 2007-5673.
92. S.K. Shaeffer, "Loss of Fuel System Icing Inhibitor Additive During Fuel Transport and Storage," presented at the 10th International Conference on Stability, Handling and Use of Liquid Fuels, Tucson, AZ, Oct 2007 (presented by S. Zabarnick).
93. E. Corporan, M.J. DeWitt, C.D. Klingshirn and R.C. Striebich, "DOD Assured Fuels Initiative: B-52 Aircraft Emissions Burning a Fischer-Tropsch/JP-8 Fuel Blend," presented at the 10th International Conference on Stability, Handling and Use of Liquid Fuels, Tucson, AZ, Oct 2007.
94. J.L. Graham, R.C. Striebich, D.K. Minus, and W.E. Harrison III, "A Laboratory Assessment of the Compatibility of Fischer-Tropsch Derived (Iso-paraffinic Kerosene) and Blended FT-Petroleum-Derived Fuels with Non-Metallic Materials," presented at the 10th International Conference on Stability, Handling and Use of Liquid Fuels, Tucson, AZ, Oct 2007.
95. M.J. DeWitt, S. Zabarnick, T. Williams, Z. West, L. Shafer, R. Striebich, S. Breitfield, C. Delaney, and D. Phelps, "Determination of Minimum Required FSII Dosage for Use on USAF Aircraft," presented at the 10th International Conference on Stability, Handling and Use of Liquid Fuels, Tucson, AZ, Oct 2007.
96. S. Zabarnick, Z. West, M.J. DeWitt, L. Shafer, R. Striebich, C. Delaney, and D. Phelps, "Development of Alternative Fuel System Icing Inhibitor Additives that are Compatible with Aircraft Tank Topcoat Material," presented at the 10th International Conference on Stability, Handling and Use of Liquid Fuels, Tucson, AZ, Oct 2007.
97. M. Vangsness, S. Chelgren, E. Strobel, L. Balster, L. Bowen, and S. Mueller, "Microbial Contamination Studies in JP-8 Fueled Aircraft," presented at the 10th International Conference on Stability, Handling and Use of Liquid Fuels, Tucson, AZ, Oct 2007.
98. J.S. Ervin and T.M. Bartsch, "Simulations of Fuel Tank Temperatures within US Air Force Cargo Aircraft as part of a JP-8 Replacement Study," presented at the 10th International Conference on Stability, Handling and Use of Liquid Fuels, Tucson, AZ, Oct 2007.

99. M.J. DeWitt, E. Corporan, J. Graham, and D. Minus, "Effects of Aromatic Type and Concentration in Fischer-Tropsch Fuel on Emissions Production and Material Compatibility," poster presentation at the 10th International Conference on Stability, Handling and Use of Liquid Fuels, Tucson, AZ, Oct 2007.
100. S.K.C. Brooks, E.M. Strobel, L.L. Bowen, M.D. Vangsness, L.M. Balster, and S.S. Mueller, "A Microbiological Examination of a Biodiesel Sample Over Time," poster presentation at the 10th International Conference on Stability, Handling and Use of Liquid Fuels, Tucson, AZ, Oct 2007.
101. G. Justinger, S.D. Stouffer, R. Streibich, C. Tseng, R. Pawlik, and J. Zelina, "A Comparison of Gaseous and Particulate Emissions for JP-8 and Fischer-Tropsch Fuels in a Well-Stirred Reactor," 3rd Annual Dayton Engineering Sciences Symposium-ASME Oct 29, 2007.
102. S. Zabarnick and M.J. DeWitt, "AFRL Fuel System Icing Inhibitor Programs – FSII Reduction and DiEGME Replacement," SAE Aerospace Fuel, Oil, and Oxidizer Systems AE-5 Committee, Orlando, FL, April 2007.
103. S.K.C. Brooks, E.M. Strobel, M.D. Vangsness, L.L. Bowen, S.S. Mueller, "An Update on USAF Fuel Sampling: Testing for Microbial Contamination," Coordinating Research Council Aviation Meeting, May 2007.
104. L.M. Balster, S.K.C. Brooks, E.M. Strobel, M.D. Vangsness, L.M. Balster, L.L. Bowen, S.S. Mueller, "FSII Reduction and Biocidal Activity," Coordinating Research Council, May 2007.
105. L.L. Bowen, S.K.C. Brooks, E.M. Strobel, M.D. Vangsness, S.S. Mueller, "Microbial Contamination of Biodiesel," Coordinating Research Council, May 2007.
106. M.D. Vangsness, S.K. Brooks, E.M. Strobel, L.M. Balster, L.L. Bowen, S.S. Mueller, "Microbial Contamination Studies in JP-8 Fueled Aircraft," National Petroleum Management Association, October 2007.
107. E.M. Strobel, S.K.C. Brooks, L.L. Bowen, M.D. Vangsness, L.M. Balster, S.S. Mueller, L. Shafer, "A Microbiological Examination of a Biodiesel Sample Over Time," National Petroleum Management Association, October 2007.
108. M.D. Vangsness, L.M. Balster, L.L. Bowen, S.S. Mueller, S.K.C. Brooks, E.M. Strobel, "Microbial Contamination Studies in JP-8 Fueled Aircraft," PETRO 2007, San Antonio, TX, Nov. 2007.
109. E.M. Strobel, M. Rauch, S.K.C. Brooks, L.L. Bowen, M.D. Vangsness, L.M. Balster, S.S. Mueller, L. Shafer, "Microbial Contamination of Biodiesel," PETRO, January 2008.
110. E.M. Strobel, S.K.C. Brooks, L.L. Bowen, M.D. Vangsness, L.M. Balster, S.S. Mueller, L. Shafer, "Microbial Contamination in Fuel," 2nd Annual Alternative Energy NOW Conference, Feb. 2008.

111. L. M. Balster, E. M. Strobel, M. D. Vangsness, L. L. Bowen, S. S. Mueller, and L. M. Brown, "Effect of FSII on Microbial Growth in Jet Fuel: The Sequel," Coordinating Research Council (CRC) Meeting, Alexandria, VA, April 28th -May 1st, 2008.
112. S. S. Mueller, M. D. Vangsness, L. M. Balster, L. L. Bowen, L. M. Brown, D. Pike, and E. M. Strobel, "Bugs, Bugs, Who Has the Bugs? A Peek into the Microbial Life of Alternative Fuels," Coordinating Research Council (CRC) Meeting, Alexandria, VA, April 28 – May 1, 2008.
113. L. L. Bowen, S. S. Mueller, M. D. Vangsness, L.M. Balster, L.M. Brown, E.M. Strobel, D.D. Pike, "Through the Microscope: How Environmental Contaminants Affect Fuel," Society of Industrial Microbiology (SIM) Annual Meeting, San Diego, August 10-14, 2008.
114. S. S. Mueller, L.L. Bowen, M.D. Vangsness, L.M. Balster, L.M. Brown, E.M. Strobel, D. D. Pike, "Techniques in Recovering Microbial Contaminations in Aviation Fuel," Society of Industrial Microbiology (SIM) Annual Meeting, San Diego, August 10-14, 2008.
115. E. M. Strobel, D. D. Pike, D. L. Dalrymple, L. M. Balster, L. L. Bowen, L. M. Brown, S. S. Mueller, M. D. Vangsness, "Identification of Microbial Species in Alternative and Conventional Fuel," 3rd Annual Alternative Energy NOW Conference, Orlando, FL January 22-23, 2009.
116. D. Evans, P. King, M. Polanka, R. Anthony, J. Zelina, J. Gord, S. Stouffer, "The Impact of heat release on Turbine Film Cooling," Dayton-Cincinnati Aerospace Sciences Symposium, Miamisburg, OH, 4 March 2008.
117. J. Sebastian, D. Gasper, G. Hartman, S. Stouffer, and D. Shouse, "Nonstandard Threaded Hole Strength- Analysis and Experimental Data," Dayton-Cincinnati Aerospace Sciences Symposium, Miamisburg, OH, 4 March 2008.
118. A.M. Briones, S. Stouffer, A. Altman, H. Kang, A. Bichal, E. Corporan, and V. Belovich, "Performance of a Particulate Sampling Probe with Diluter under Gas-Turbine Conditions," Dayton-Cincinnati Aerospace Sciences Symposium, Miamisburg, OH, 4 March 2008.
119. R. Wills, A. Cole, H. Jiang, J. Sebastien, and J.S. Ervin, "Laboratory Development for the Study of Liquid Hydrocarbon -Cooled Rotating Equipment," AIAA-ASME Joint Propulsion Conference, East Hartford, CT, July 2008.
120. A.M. Briones, S. Stouffer, A. Bichal, H. Kang, A. Aaron, E. Corporan, and V. Belovich, "Aspiration Efficiencies of a Soot-particulate Sampling Probe with Dilution under Gas Turbine Conditions," AIAA-2008-4877, 44th Joint Propulsion Conference & Exhibit, Hartford, CT, 21 July 2008.
121. A.M. Briones. B. Sekar, J. Zelina, R. Pawlik, S. Stouffer, "Numerical Modeling of Combustion Performance for a Well-stirred Reactor for Aviation Fuels," AIAA-2008-4565, 44th Joint Propulsion Conference & Exhibit, Hartford, CT, 21 July 2008.

122. G. Bessee and S. Zabarnick, "Evaluation of the Effects of TriEGME Fuel System Icing Inhibitor Candidate on Aviation Fuel Filtration," 9th International Filtration Conference, San Antonio, TX, Oct 2008.
123. K. Taylor, R.C. Striebich, L. Shafer, Z. West, and S. Zabarnick, "Gas Chromatography of Alternate Sources of Aviation Fuels," Poster presented at University of Dayton Stander Symposium, Dayton OH, April 2008.
124. M.J. DeWitt, E. Corporan, T. Edwards, L. Shafer, R.C. Striebich, R.W. Morris, Jr., J.T. Datko, G. Parker, R.J. Allen, and S. Zabarnick, "Evaluation of Alternative Fuels for Aviation Applications," Poster presented at the University Clean Energy Alliance of Ohio Meeting, Columbus, OH, April 2008.
125. A. Briones, M. Dewitt, S. Stouffer, C. Klingshirn, M.-D. Cheng, and E. Corporan, "A Numerical Investigation on the Performance of a Low-flow Thermodenuder," 4th Annual Dayton Engineering Science Symposium, DESS08-0015, October 2008.
126. A. Briones, B. Sekar, K. Kundu, S. Stouffer, and J. Zelina, "Reduced Propane-air and Vitiated-Air Chemical Schemes for Gas Turbine Combustion Applications" AIAA-2009-256, 47th AIAA Aerospace Sciences Meeting including The New Horizons Forum and Aerospace Exposition, Orlando, Florida, Jan. 5-8, 2009.
127. D. Evans, P. King, M. Polanka, J. Zelina, W. Anderson, and S. Stouffer, "The Impact of Heat Release in Turbine Film Cooling," AIAA-2009-298, 47th AIAA Aerospace Sciences Meeting including The New Horizons Forum and Aerospace Exposition, Orlando, Florida, Jan. 5-8, 2009.
128. A. Bichal, A. Altman, A.M. Briones, and S.D. Stouffer, "Comparative Study Of Three Flow Diagnostic Techniques Applied To A Nearbody Flowfield," AIAA 2009-0884, 47th AIAA Aerospace Sciences Meeting including The New Horizons Forum and Aerospace Exposition, Orlando, Florida, Jan. 5-8, 2009
129. C.X. Lin, R.J. Holder, H. Thornburg, B. Sekar, J. Zelina, W. Anderson, M.D. Polanka, S.D. Stouffer, and A.M. Briones" Numerical Simulation of Film Cooling in Reactive Flow over a Surface with Shaped Coolant Hole," AIAA-2009-678, 47th AIAA Aerospace Sciences Meeting including The New Horizons Forum and Aerospace Exposition, Orlando, Florida, Jan. 5-8, 2009.
130. H. Thornburg, B. Sekar, J. Zelina, M. Polanka, C.X. Lin, R.J. Holder, A.M. Briones, and S.D. Stouffer, "Design Studies of Turbine Blade Film Cooling with Unburned Fuel in Cross Stream Flow," AIAA-2009-510, 47th AIAA Aerospace Sciences Meeting including The New Horizons Forum and Aerospace Exposition, Orlando, Florida, Jan. 5-8, 2009.
131. W. Anderson, M. Polanka, J. Zelina, S. Stouffer, and D. Evans, "Effect of Reacting Film Cooling," Paper presented at 34th Dayton-Cincinnati Aerospace Sciences Symposium, AIAA, March 3, 2009.

132. V.R. Katta, W.M. Roquemore, and S.D. Stouffer, "Dynamics of the Lifted Flame Supported by a Recirculation Zone," Paper 12H5, 6th US Combustion Institute Meeting, May 17-20, 2009.
133. V. R. Katta, R. A. Forlines, W. M. Roquemore, W. S. Anderson, J. Zelina, J. R. Gord, S. D. Stouffer, S. Roy, "Sooting Characteristics of Partially Premixed Flames in Centerbody Burner," Paper 31E4, 6th US combustion Institute Meeting, May 17-20, 2009.
134. L. M. Balster, L. L. Bowen, L. M. Brown, S. S. Mueller, M. D. Vangsness, E. M. Strobel, D. D. Pike, and D. L. Dalrymple, "Effect of FSII on Microbial Contamination in Jet Fuel: TriEGME," Coordinating Research Council (CRC) Aviation Meetings, New Orleans, May 4-7, 2009.
135. L. M. Brown, L. M. Balster, L. L. Bowen, S. S. Mueller, M. D. Vangsness, E. M. Strobel, D. D. Pike, and D. L. Dalrymple, "Estimating Bacterial Community Dynamics Among Fuels," Coordinating Research Council (CRC) Aviation Meetings, New Orleans, May 4-7, 2009.
136. M. D. Vangsness, S. S. Mueller, L. L. Bowen, L. M. Brown, L. M. Balster, "Microbial Contamination in Air Force Fuels, Past-Present-Future," PETRO conference April 26-29, 2009.
137. M. J. DeWitt and E. Corporan, "AFRL Research on Engine Emissions Characterization of Alternative Fuels," presented at FAA Aviation Emissions Characterization Roadmap 7th Annual Meeting, Washington, DC, June 9, 2009.
138. B. Sekar, H. J. Thornburg, A. M. Briones, and J. Zelina, "Effect of Trapped Vortex Combustion with Radial Vane Cavity Arrangements on Predicted Inter-Turbine Burner Performance," Joint IECEC/JPC Opening Panel: 40th Anniversary Apollo Panel, AIAA-2009-4603.
139. S. Zabarnick, M.J. DeWitt, R. Striebich, and J. Gomach, "Thermal Stability Evaluation via In-Situ Oxidation of Deposits," Coordinating Research Council (CRC) Aviation Meetings, New Orleans, May 4-7, 2009.
140. L.L. Bowen, M.D. Vangsness, E.M. Strobel, L.M. Balster, S.S. Mueller, L.M. Brown, D.L. Dalrymple, "Microbial Contaminants of Biodiesel and Diesel Fuel," Poster Presentation, Society for Industrial Microbiology (SIM) meeting in Toronto, ON Canada, July 26-29, 2009.
141. L. M. Balster, E. M. Strobel, M. D. Vangsness, L. L. Bowen, S. S. Mueller, L. M. Brown, D. D. Pike, and D. L. Dalrymple, "Effect of FSII on Microbial Contamination: DiEGME and TriEGME," 11th International Conference on Stability, Handling, and Use of Liquid Fuels (IASH), Prague, Czech Republic, October 18-22, 2009.

142. M. D. Vangsness, S. S. Mueller, L. L. Bowen, L. M. Brown, L. M. Balster, J. P. McComb, E. M. Strobel, "Biocontamination Diversity in JP-8 and Jet-A," 11th International Conference on Stability, Handling, and Use of Liquid Fuels (IASH), Prague, Czech Republic, October 18-22, 2009.
143. M. D. Vangsness, "Microbial Growth on Selected Aircraft Materials," Poster Presentation, 11th International Conference on Stability, Handling, and Use of Liquid Fuels (IASH), Prague, Czech Republic, October 18-22, 2009.
144. S. Zabarnick, R. Adams, Z. West, M.J. DeWitt, L. Shafer, R. Striebich, C.L. Delaney, and D.K. Phelps, "Studies of the Compatibility of DiEGME and TriEGME Icing Inhibitor Additives with Aircraft Tank Topcoat Material," 11th International Conference on Stability, Handling, and Use of Liquid Fuels (IASH), Prague, Czech Republic, October 18-22, 2009.
145. M.J. DeWitt, S. Zabarnick, S. Shaeffer, T. Williams, Z. West, L. Shafer, R. Striebich, S. Breitfield, R. Adams, R. Cook, C.L. Delaney, and D.K. Phelps, "Determination of Minimum Required FSII Use and Procurement Limits for USAF Aircraft," 11th International Conference on Stability, Handling, and Use of Liquid Fuels (IASH), Prague, Czech Republic, October 18-22, 2009.
146. E. Corporan, L. Shafer, M.J. DeWitt, C. Klingshirn, S. Zabarnick, Z. West, R. Striebich, and J. Klein, "Initial Evaluation of Chemical, Thermal Stability and Emissions Characteristics of Jet Fuels from Alternative Sources," 11th International Conference on Stability, Handling, and Use of Liquid Fuels (IASH), Prague, Czech Republic, October 18-22, 2009.
147. E. Shafer, R. Striebich, M.J. DeWitt, T. Edwards, and W.E. Harrison, "Variation of JP-8 Properties in CONUS and Potential Implications during Blending with Synthetic Paraffins," 11th International Conference on Stability, Handling, and Use of Liquid Fuels (IASH), Prague, Czech Republic, October 18-22, 2009.
148. R.J. Allen, Z. West, and L. Shafer, "Hydrotreated Renewable Jet Fuels – A Comparison of Various Alternative Fuels with JP-8," 11th International Conference on Stability, Handling, and Use of Liquid Fuels (IASH), Prague, Czech Republic, October 18-22, 2009.
149. M. Luo, J. Jones, A.E. Stewart, M.J. DeWitt, R.W. Morris and T. Williams, "Alternative Fuels Research Laboratory at the University of Dayton Research Institute," UCEAO Workshop, Columbus, OH, April 2009.
150. C.K. Klingshirn, M.J. DeWitt, and E. Corporan, "Preliminary Evaluation of Aerosol & Gaseous Emissions of Shale Oil Feedstocks & Improved Conventional Fuel Compared to a Specification JP-8," Presentation at the 34th Dayton Cincinnati Aerospace Sciences Symposium, March, 2009.
151. M.J. DeWitt, "Overview of R&D Efforts Related to Aviation Fuel Chemistry and Engineering," presented at University of Dayton Undergraduate Mechanical Engineering Seminar, March, 2009.

152. E. Corporan, M.J. DeWitt, and C.D. Klingshirn, "Emissions Evaluations of Diesel Engines Operated with JP-8 and a 50/50 FT Blend," 11th International Conference on Stability, Handling, and Use of Liquid Fuels (IASH), Prague, Czech Republic, October 18-22, 2009.
153. M.J. DeWitt, "Overview of R&D Efforts Related to Aviation Fuel Chemistry and Engineering," presented at University of Dayton Senior Chemical Engineering Seminar, March, 2010.
154. C.D. Klingshirn, M.J. DeWitt, E. Corporan, L. Shafer, S. Zabarnick, Z. West, R. Striebich, J.T. Edwards, and J. Klein, "Initial Evaluation of Chemical, Thermal Stability and Emissions Characteristics of Jet Fuels from Alternative Sources," Presentation at 5th Annual Dayton Engineering Sciences Symposium, Dayton, OH, 2009.
155. C.D. Klingshirn, M.J. DeWitt, and E. Corporan, "Preliminary Emissions Evaluations of Diesel Engines Operated with JP-8 and a 50/50 FT Blend," Presentation at Coordinating Research Council (CRC) Aviation Technical Meetings, New Orleans, LA , 2009.
156. S. S. Mueller, M. D. Vangsness, L. M. Balster, L. L. Bowen, L. M. Brown, E. M. Strobel, "Comparing Microbial Contamination in Different Types of Fuel," 4th Annual Alternative Energy NOW Conference, Orlando, FL, February 9-10, 2010.
157. E.A. Guliants and W.K. Lewis, "Ultra-Fine Highly Energetic Core-Shell Nanoparticles with Triggerable Protective Coatings," DTRA Basic Research Review, DC, October 27, 2009 (invited).
158. B.A. Harruff, D.L. Gillaugh, D.W. Bair, J. Gord, T.M. Sexton, M.C. Jochum, E.N. Stachler, E.A. Guliants, and C.E. Bunker, "Iron Core-Shell Nanoparticles in Thin Films and Small Scale Fuel Studies," SERMACS 2009 (South East Regional Meeting of the ACS), Puerto Rico, October 2009.
159. M.J. Smith, K.A.S. Fernando, N. McNamara, B.A. Harruff, E.A. Guliants, and C.E. Bunker, "Sonochemical Synthesis of Aluminum Core-Shell Nanoparticles with Different Shell Materials," SERMACS 2009 (South East Regional Meeting of the ACS), Puerto Rico, October 2009.
160. S.W. Buckner, S.W. Chung, D.W. Hammerstroem, M.A. Burgers, C.E. Bunker, E.A. Guliants, and P.A. Jelliss, "Alkyl-Substituted Epoxides as Capping Agents for Aluminum Nanoparticles," SERMACS 2009 (South East Regional Meeting of the ACS), Puerto Rico, October 2009.
161. D.W. Hammerstroem, S.W. Buckner, C.E. Bunker, E.A. Guliants, "Air Stability of Organically-Capped Aluminum Nanoparticles," SERMACS 2009 (South East Regional Meeting of the ACS), Puerto Rico, October 2009.
162. M.A. Burgers, S.W. Buckner, P.A. Jelliss, C.E. Bunker, E.A. Guliants, S. Chung, and D.W. Hammerstroem, "Stability of Organically-Capped Aluminum Nanoparticles," 44th Midwest Regional Meeting of the American Chemical Society, Oct. 21 - 24, 2009, Iowa City, Iowa.

163. C.D. Oberle, S.W. Buckner, P.A. Jelliss, C.E. Bunker, E.A. Guliants, S.W. Chung, and D.W. Hammerstroem, "Core-Shell Aluminum-Organic Nanomaterial Synthesis," 44th Midwest Regional Meeting of the American Chemical Society, Oct. 21 - 24, 2009, Iowa City, Iowa.
164. A.M. Briones, B. Sekar, H. Thornburg, and J. Zelina, "Effect of Vane Notch and Ramp Design on the Performance of a Rectangular Inter-Turbine Burner," 48th AIAA Aerospace Sciences Meeting including the New Horizons and Aerospace Exhibition," Orlando, FL, January, 2010.
165. H. Thornburg, B. Sekar, and A.M. Briones, "Analysis of Wake Characteristics of Several Two-dimensional Flame Holders for Combustion Systems," 34th Dayton-Cincinnati Aerospace Sciences Symposium, Dayton, OH, March, 2010.
166. B. Sekar, A.M. Briones, and H. Thornburg, "Analysis of Wake Characteristics of Several Two-dimensional Flame Holders for Combustion Systems," Augmentor Design Systems Conference, Jacksonville, FL, March, 2010.
167. L. M. Balster, L. L. Bowen, L. M. Brown, S. S. Mueller, L. M. Shafer, E. M. Strobel, M. Tsao, M. D. Vangsness, "Microbial Growth and Biofilm Formation: GC-MS Analysis and Traditional Culture of Jet A-1 and Alternative Fuels," Central Regional Meeting of the American Chemical Society (CeRMACS), Dayton, OH, June 16-19, 2010.
168. M.D. Vangsness and K. Lafdi, "Nano Technology Approach to Prevent Bacterial Contamination in Aircraft Fuel Systems," International Symposium on Aircraft Materials-ACMA 2010, Marrakech, Morocco, May 12-14, 2010.
169. M. D. Vangsness and E. M. Strobel, "Bio-Contamination Suppression by Antimicrobial Cotton Coalescer Element," Coordinating Research Council (CRC) Aviation Meeting, Alexandria, Virginia, May 3-6, 2010.
170. L. M. Balster, L. L. Bowen, L. M. Brown, S. S. Mueller, L. M. Shafer, E. M. Strobel, M. Tsao, M. D. Vangsness, "Microbial Growth and Biofilm Formation: Jet A-1 vs. Six Alternative Fuels," Coordinating Research Council (CRC) Aviation Meeting, Alexandria, Virginia, May 3-6, 2010.
171. H. Jiang, Z. West, S. Zabarnick, and J. Ervin, "Effects of a Step Change in Flow Geometry on the Surface Deposition from Jet Fuel within a Tube," Coordinating Research Council (CRC) Aviation Meeting, Alexandria, Virginia, May 3-6, 2010.
172. Z. West, R. Adams, and S. Zabarnick, "Homogeneous Catalysis of Hydroperoxide Decomposition in Liquid Hydrocarbons," Central Regional Meeting of the American Chemical Society (CeRMACS), Dayton, OH, June 16-19, 2010.
173. H.J. Robota, J. Jones, M. Luo, and A. Stewart, "Hexadecane Hydrotreating as a Surrogate for Fischer-Tropsch Upgrading to Aviation Fuel Using a Co/MoO₃/Silica-Alumina Catalyst," Central Regional Meeting of the American Chemical Society (CeRMACS), Dayton, OH, June 16-19, 2010.

174. E. Corporan, M. J. DeWitt, C. Klingshirn, J. Mantz and D. Anneken, "AFRL Efforts on Turbine Engine PM Emissions," SAE E31 Committee Meeting, Interlaken, Switzerland June 29, 2010.
175. B. Sekar, H. Thornburg, and A.M. Briones, "Design and Analysis of Flame Holders for Instability-Free Operation of Combustion Systems," Proceedings of the HPCMP User's Group Conference, Schaumburg, IL, June 14-17, 2010.
176. A.M. Briones and B. Sekar, "Characteristics of Multi-Cavity Trapped Vortex Combustors," ASME Turbo Expo 2010: Power for Land, Sea, and Air, Glasgow, Scotland, UK, June 14-18, 2010.
177. K.E. Binns, "Fueledraulic and Hydraulic Technology for Future Military Aircraft," Joint SAE AE-5 and A-6 Committee Meeting, Anchorage , Alaska, September 2010

Technical Reports

1. S. Zabarnick, J.S. Ervin, M.J. DeWitt, D.R. Ballal, K.E. Binns, T.F. Williams, and S. Stouffer, "Advanced Integrated Fuel/Combustion Systems," AFRL-TR-2005-2023.
2. S. Zabarnick, J.S. Ervin, M.J. DeWitt, D.R. Ballal, K.E. Binns, T.F. Williams, and S. Stouffer, "Advanced Integrated Fuel/Combustion Systems," UDR-TR-2004-00007.
3. T. Williams, M. D. Vangsness, J.R. Shardo, and J.S. Ervin, "Refueling Tanker Truck Temperature Measurements" AFRL-PR-WP-TR-2005-2103.
4. M. J. DeWitt, T. Williams, L. Shafer, R. Striebich, and L. Riehl, "Investigation of the Effectiveness of DiEGME to Suppress Solidification of Water in Aircraft Fuel Systems. Appendix A: Requirement for Static Dissipater Additive in Military Jet Fuels: An Evaluation of Safety Considerations for the Removal of Static Dissipater Additive," AFRL-PR-WP-TR-2005-2167.
5. S. Zabarnick, D.K. Phelps, Z.J. West, L.S. Shafer, J.S. Ervin, M.J. DeWitt, K.E. Binns, T.F. Williams, G.L. Dieterle, L.M. Balster, and W.E. Harrison, III, "Evaluation and Testing of the Suitability of a Coal-Based Jet Fuel," AFRL-RZ-WP-TR-2009-2063.
6. T. R. Denaro, S. K. Chelgren, J. N. Lang, E. M. Strobel, L. M. Balster, and M. D. Vangsness, "DNA Isolation of Microbial Contaminants in Aviation Turbine Fuel via Traditional Polymerase Chain Reaction (PCR) and Direct PCR--Preliminary Results," AFRL-WP-TR-2006-2049.
7. R.C. Striebich, C. Delaney, J.T. Edwards, 1LT J. O'Neill, A. Fletcher, J. Leone, and R. Osysko, "The Examination of Higher Levels of Total Acid Number and Mercaptan Sulfur on Jet Fuel Quality," AFRL-RZ-WP-TR-2008-2239.
8. R.C. Striebich, L.M. Shafer, M.J. DeWitt, Z.J. West, J.T. Edwards, and W.E. Harrison III, "Dependence of Fuel Properties During Blending of Iso-Paraffinic Kerosene and Petroleum-Derived Jet Fuel," AFRL-RZ-WP-TR-2009-2034.
9. S. Zabarnick and J.S. Ervin, "The Effects of Operating Jet Fuels Below the Specification Freeze Point Temperature Limit," DOT/FAA/AR-09/50, 2010.
10. M.J. DeWitt, S. Zabarnick, T.F. Williams, Z. West, L. Shafer, R. Striebich, S. Breitfield, R. Adams, R. Cook, D.K. Phelps, and C.L. Delaney, "Determination of the Minimum Use Level of Fuel System Icing Inhibitor (FSII) in JP-8 that will Provide Adequate Icing Inhibition and Biostatic Protection for Air Force Aircraft," AFRL-RZ-WP-TR-2009-2217.
11. E. Shafer, R. Striebich, M.J. DeWitt, T. Edwards, and W. Harrison, "Variation of JP-8 Properties in CONUS and Potential Implications During Blending with Synthetic Paraffinic Kerosene," AFRL-RZ-WP-TR-2010-2079.

12. L. M. Balster, M. D. Vangsness, L. L. Bowen, S. S. Mueller, L. M. Brown, E. M. Strobel, D. D. Pike, "Effects of Diethylene Glycol Monomethyl Ether (DiEGME) and Triethylene Glycol Monomethyl Ether (TriEGME) on Microbial Contaminants in Aviation Fuel," AFRL-RZ-WP-TR-2010-2094.
13. L. M. Balster, M. D. Vangsness, L. L. Bowen, S. S. Mueller, L. M. Brown, E. M. Strobel, "The Effect of DiEGME on Microbial Contamination of Jet Fuel: A Minimum Concentration Study," AFRL-RZ-WP-TR-2010-2002.
14. S. Zabarnick, M.J. DeWitt, R. Adams, Z.J. West, L.S. Shafer, T.F. Williams, R. Cook, R. Striebich, L.M. Balster, D.K. Phelps, and C.L. Delaney, "Evaluation of Triethyleneglycol Monomethyl Ether (TriEGME) as an Alternative Fuel System Icing Inhibitor for JP-8 Fuel, submitted for publication, AFRL-RZ-WP-TR-2010-xxxx, 2010, in press.

Student Theses/Dissertations

1. Alex Heltzel, "Molecular Modeling of Jet Fuel Solidification," M.S. Mechanical & Aerospace Engineering, 2003.
2. T.A. Ward, "Physical and Chemical Behavior of Flowing Endothermic Jet Fuel," Ph.D. Mechanical & Aerospace Engineering, 2003.
3. Thammarat Dounghthip, "Simulations of Jet Fuel Thermal-Oxidative Degradation and Flow Characteristics of Injected Jet Fuel under Supercritical Conditions," Ph.D. Mechanical & Aerospace Engineering, 2004.
4. Zachary West, "Determination of Hydroperoxides in Jet Fuel Via Reaction with Triphenylphosphine," M.S. Chemical Engineering, 2004.
5. Daniel Atkins, "Investigations into the Low Temperature Behavior of Jet Fuels: Visualization, Modeling, and Viscosity Studies," Ph.D. Mechanical & Aerospace Engineering, 2004.
6. Pradeep Ramineni, "Simulations of Jet Fuel Flow with Imposed High Heat Flux," M.S. Mechanical & Aerospace Engineering, 2005.
7. Nicholas Kuprowicz, "A Predictive Modeling Approach to Simulate Liquid-Phase Oxidation and Deposition of Jet Fuels," Ph.D. Mechanical & Aerospace Engineering, 2006.
8. Lee Riehl, "Experimental Study of the Solidification Of Jet Fuel Flowing in a Quartz Duct," M.S. Mechanical & Aerospace Engineering, 2006.
9. Benjamin Mortimer, "Development of an Experimental Technique to Quantify the Volatile Composition of Soot Particles Below 200 nm," M.S. Aerospace Engineering, 2006.
10. Jeff Gomach, "Development of an In-Situ Carbon Deposition Test for the Analysis of Thermal Stress on Jet Fuel," M.S. Chemical Engineering, 2006.
11. Rajee Assudani, "Computational Fluid Dynamics Simulations of Jet Fuel Flow Near and Below the Freeze Point Temperature," Ph.D. Mechanical & Aerospace Engineering, 2006.
12. Michael Frede, "Simulations Of The Flow Of A Hydrocarbon Fuel Under Different Body Force Conditions," M.S. Mechanical Engineering, July 2007.
13. J.L. Graham, "The Swelling of Nitrile Rubber by Selected Species in a Synthetic Jet Turbine Fuel," Ph.D. Thesis, University of Dayton, August, 2006.
14. J. P. McComb, "A Metagenomic Analysis of Microbial Contamination in Aviation Fuels," Masters Thesis, Air Force Institute of Technology (AFIT), March 2009.

15. Ryan K. Adams, "Determination of Fuel Tank Topcoat Material Compatibility with Diethylene Glycol Monomethyl Ether and Triethylene Glycol Monomethyl Ether," M.S. Chemical Engineering, University of Dayton, May 2009.
16. K.B. Taylor, "Comparative Study of Alternative Fuel Icing Inhibitor Additive Properties & Chemical Analysis of Metal Speciation in Aviation Fuels," M.S. Thesis Mechanical Engineering, University of Dayton, July 2010.

LIST OF ACRONYMS, ABBREVIATIONS, AND SYMBOLS

ACRONYM	DESCRIPTION
AAFRF	Assured Aerospace Fuels Research Facility
AFRL	Air Force Research Laboratory
AFRL/RZ	Air Force Research Laboratory Propulsion Directorate
AFRL/RZPF	Air Force Research Laboratory Fuels & Energy Branch
API	American Petroleum Institute
BMS 10-39	Topcoat material produced to Boeing Material Specification 10-39
BSA	Bovine serum albumen
CAST	Cold additive screening test
CFD	Computational fluid dynamics
CSTR	Continuous stirred tank reactor
CTL	Coal-to-liquids
DiEGME	Diethylene glycol monomethyl ether
DFT	Density functional theory
EDTST	Extended duration thermal stability test
EGME	Ethylene glycol monomethyl ether
EISA	Energy Independence and Security Act of 2007
FSII	Fuel system icing inhibitor
FAME	Fatty acid methyl ester
FT	Fischer-Tropsch
FTIR	Fourier-Transform Infrared Spectroscopy
FTTP	Fuel tank topcoat peeling
DMF	Dimethyl formamide
DNA	Deoxyribonucleic acid
FID	Flame ionization detector
GC	Gas chromatography
GC-MS	Gas chromatograph-mass spectrometer
GCxGC	Two dimensional gas chromatography
GO	Graphene oxide
GTL	Gas-to-liquids
HPLC	High performance liquid chromatography
HPLC-TOFMS	High performance liquid chromatography-time of flight mass spectrometry
HRJ	Hydroprocessed renewable jet fuel
ICP-MS	Inductively-Coupled Plasma Mass Spectrometry
JP-8+100	High temperature thermal stability jet fuel
JP-8+100LT	JP-8+100 fuel with low temperature flow improving additive
JRF	Jet reference fluid
LBO	Lean blowout
LCA	Life cycle analysis
LSWT	Low speed wind tunnel
LT	Low temperature
MCRT	Microcarbon residue tester
MDGC-TOFMS	Multidimensional gas chromatography-time of flight mass spectrometry
mL	milliliter
mM	millimolar
NIST	National Institute of Standards and Technology

ACRONYM	DESCRIPTION
NP	Nanoparticle
PCR	Polymerase chain reaction
PIDT	Particle image diagnostic technique
PIV	Particle image velocimetry
PL	Photoluminescence
PM	Particulate matter
PMMA	Polymethylmethacrylate
PPD	Proportional product distribution
ppm	part per million
ORNL	Oak Ridge National Laboratory
QCM	Quartz crystal microbalance
RTOC	Reduction in Total Ownership Cost
SERDP	Strategic Environmental Research and Development Program
SMR	Steam methane reformer
SPK	Synthetic paraffinic kerosene
SWNT	Single-walled carbon nanotube
TEOS	Tetraethyl orthosilicate
TERTEL	Turbine Engine Research Transportable Emissions Laboratory
TOFMS	Time of flight mass spectrometry
TPD	Temperature programmed desorption
TPP	Triphenylphosphine
TPPO	Triphenylphosphine oxide
TPPS	Triphenylphosphine sulfide
TriEGME	Triethylene glycol monomethyl ether
TVC	Trapped vortex combustor
UCC	Ultra-compact combustor
UD	University of Dayton
UDRI	University of Dayton Research Institute
UV	Ultra-violet
vol%	Volume percent
WSR	Well-stirred reactor
µg/mL	Microgram per milliliter